Challa S. S. R. Kumar *Editor*

UV-VIS and Photoluminescence Spectroscopy for Nanomaterials Characterization

Springer

UV-VIS and Photoluminescence Spectroscopy for Nanomaterials Characterization

Challa S.S.R. Kumar
Editor

UV-VIS and Photoluminescence Spectroscopy for Nanomaterials Characterization

With 278 Figures and 5 Tables

Springer

Editor
Challa S.S.R. Kumar
Center for Advanced Microstructures and Devices
Baton Rouge, LA, USA

ISBN 978-3-642-27593-7 ISBN 978-3-642-27594-4 (eBook)
DOI 10.1007/978-3-642-27594-4
Springer Heidelberg New York Dordrecht London

Library of Congress Control Number: 2013930307

Printed on acid-free paper

Springer is part of Springer Science + Business Media (www.springer.com)

Editor-in-Chief

Challa S.S.R. Kumar
Center for Advanced Microstructures and Devices
Baton Rouge, LA
USA

Contents

List of Contributors

Michael M. Adachi Department of Electrical and Computer Engineering, University of Waterloo, Waterloo, ON, Canada

X. Y. Chen Department of Physics, The University of Hong Kong, Pokfulam Road, Hong Kong

Rui Chen Division of Physics and Applied Physics, School of Physical and Mathematical Sciences, Nanyang Technological University, Singapore, Singapore

Mircea Cotlet Brookhaven National Laboratory, Upton, NY, USA

Masih Darbandi Faculty of Physics and Center for Nanointegration Duisburg-Essen (CeNIDE), University of Duisburg-Essen, Duisburg, Germany

Hilmi Volkan Demir Department of Electrical and Electronics Engineering, Department of Physics and UNAM—Institute of Materials Science and Nanotechnology, Bilkent University, Ankara, Turkey

Luminous! Centre of Excellence for Semiconductor Lighting and Displays, School of Electrical and Electronic Engineering, School of Physical and Mathematical Sciences, Nanyang Technological University, Singapore, Singapore

A. B. Djurišić Department of Physics, The University of Hong Kong, Pokfulam Road, Hong Kong

Ricardo M. Abraham Ekeroth Grupo de Óptica de Sólidos-Elfo, Centro de Investigaciones en Física e Ingeniería del Centro de la Provincia de Buenos Aires – Instituto de Física Arroyo Seco, Facultad de Ciencias Exactas, Universidad Nacional del Centro de la Provincia de Buenos Aires, Buenos Aires, Argentina

Consejo Nacional de Investigaciones Científicas y Técnicas CONICET, Buenos Aires, Argentina

Hao Jing Department of Chemistry and Biochemistry, University of South Carolina, Columbia, SC, USA

Karim S. Karim Department of Electrical and Computer Engineering, University of Waterloo, Waterloo, ON, Canada

Mohammedreza Khorasaninejad Department of Electrical and Computer Engineering, University of Waterloo, Waterloo, ON, Canada

Jae-Seung Lee Department of Materials Science and Engineering, Korea University, Seoul, Republic of Korea

Marcelo Lester Grupo de Óptica de Sólidos-Elfo, Centro de Investigaciones en Física e Ingeniería del Centro de la Provincia de Buenos Aires – Instituto de Física Arroyo Seco, Facultad de Ciencias Exactas, Universidad Nacional del Centro de la Provincia de Buenos Aires, Buenos Aires, Argentina

Consejo Nacional de Investigaciones Científicas y Técnicas CONICET, Buenos Aires, Argentina

Y. H. Leung Department of Physics, The University of Hong Kong, Pokfulam Road, Hong Kong

Dehui Li Division of Physics and Applied Physics, School of Physical and Mathematical Sciences, Nanyang Technological University, Singapore, Singapore

A. M. C. Ng Department of Physics, The University of Hong Kong, Pokfulam Road, Hong Kong

Nanostructure Institute for Energy and Environmental Research, Division of Physical Sciences, South University of Science and Technology of China, Shenzhen, China

Timothy O'Connor Department of Physics, Bowling Green State University, Bowling Green, USA

Kenji Okitsu Graduate School of Engineering, Osaka Prefecture University, Naka-ku, Sakai, Osaka, Japan

Umapada Pal Instituto de Física, Benemérita Universidad Autónoma de Puebla, Puebla, Puebla, Mexico

Ovidio Peña-Rodríguez Centro de Microanálisis de Materiales (CMAM), Universidad Autónoma de Madrid (UAM), Madrid, Spain

Instituto de Óptica, Consejo Superior de Investigaciones Científicas (IO-CSIC), Madrid, Spain

Simarjeet S. Saini Department of Electrical and Computer Engineering, University of Waterloo, Waterloo, ON, Canada

Jesica M. J. Santillán Centro de Investigaciones Ópticas (CIOp), CONICET La Plata-CIC, La Plata, Argentina

Departamento de Ciencias Básicas, Facultad de Ingeniería, Universidad Nacional de La Plata, La Plata, Argentina

Lucía B. Scaffardi Centro de Investigaciones Ópticas (CIOp), CONICET La Plata-CIC, La Plata, Argentina

Departamento de Ciencias Básicas, Facultad de Ingeniería, Universidad Nacional de La Plata, La Plata, Argentina

Daniel C. Schinca Centro de Investigaciones Ópticas (CIOp), CONICET La Plata-CIC, La Plata, Argentina

Departamento de Ciencias Básicas, Facultad de Ingeniería, Universidad Nacional de La Plata, La Plata, Argentina

Urartu Özgür Şafak Şeker Department of Electrical and Electronics Engineering, Department of Physics and UNAM—Institute of Materials Science and Nanotechnology, Bilkent University, Ankara, Turkey

Luminous! Centre of Excellence for Semiconductor Lighting and Displays, School of Electrical and Electronic Engineering, School of Physical and Mathematical Sciences, Nanyang Technological University, Singapore, Singapore

Handong Sun Division of Physics and Applied Physics, School of Physical and Mathematical Sciences, Nanyang Technological University, Singapore, Singapore

J. Toudert Instituto de Optica, CSIC, Madrid, Spain

Pol Van Dorpe imec vzw, Leuven, Belgium

Physics Department, KU Leuven, Leuven, Belgium

Fabián A. Videla Centro de Investigaciones Ópticas (CIOp), CONICET La Plata-CIC, La Plata, Argentina

Departamento de Ciencias Básicas, Facultad de Ingeniería, Universidad Nacional de La Plata, La Plata, Argentina

Moriaki Wakaki Department of Optical and Imaging Science & Technology, School of Engineering, Tokai University, Hiratsuka, Kanagawa, Japan

Hui Wang Department of Chemistry and Biochemistry, University of South Carolina, Columbia, SC, USA

Qihua Xiong Division of Physics and Applied Physics, School of Physical and Mathematical Sciences, Nanyang Technological University, Singapore, Singapore

Division of Microelectronics, School of Electrical and Electronics Engineering, Nanyang Technological University, Singapore, Singapore

Zhihua Xu Department of Chemical Engineering, University of Minnesota Duluth, Duluth, MN, USA

Jian Ye imec vzw, Leuven, Belgium

Chemistry Department, KU Leuven, Leuven, Belgium

Eisuke Yokoyama Department of Optical and Imaging Science & Technology, School of Engineering, Tokai University, Hiratsuka, Kanagawa, Japan

Mikhail Zamkov Department of Physics, Bowling Green State University, Bowling Green, USA

J. A. Zapien Department of Physics and Materials Science, City University of Hong Kong, Kowloon, Hong Kong

Li Zhang Department of Chemistry and Biochemistry, University of South Carolina, Columbia, SC, USA

Geometrically Tunable Optical Properties of Metal Nanoparticles

1

Hao Jing, Li Zhang, and Hui Wang

Contents

H. Jing • L. Zhang • H. Wang (✉)
Department of Chemistry and Biochemistry, University of South Carolina, Columbia, SC, USA

Challa S.S.R. Kumar (ed.), *UV-VIS and Photoluminescence Spectroscopy for Nanomaterials Characterization*, DOI 10.1007/978-3-642-27594-4_1,

1 Definition of the Topic

Noble metal nanoparticles exhibit fascinating geometrically tunable optical properties that are dominated by their localized surface plasmon resonances (LSPRs). By judiciously tailoring the geometric parameters of a metal nanoparticle, one can fine-tune the nanoparticle's optical responses in a precisely controllable manner and thereby selectively implement desired optical properties into nanomaterial systems or nanodevices for specific applications. In this chapter, we present a review on the recent experimental and theoretical advances in the understanding of the geometry–optical property relationship of metallic nanoparticles in various geometries.

2 Overview

Metal nanoparticles are an important class of subwavelength optical components whose optical properties can be fine-tuned over a broad spectral range by tailoring their geometric parameters. The fascinating optical characteristics of metallic nanoparticles are essentially determined by the collective oscillations of free electrons in the metals, known as plasmons. Metallic nanostructures possess geometry-dependent localized surface plasmon resonances, which has stimulated growing interests in a rapidly expanding array of metallic nanoparticle geometries, such as nanorods, nanoshells, nanoprisms, nanostars, and nanocages. The resonant excitation of plasmons also leads to large enhancements of the local electromagnetic field in close proximity to the nanoparticle surface, resulting in dramatically enhanced cross sections for nonlinear optical spectroscopies such as surface-enhanced Raman scattering. These highly tunable plasmonic properties of metal nanoparticles allow for the development of fundamentally new metal-based subwavelength optical elements with broad technological potential, an emerging field known as plasmonics.

The past decades have witnessed significant advances in scientific understanding of the origin of the optical tunability of metallic nanoparticle systems, primarily driven by the rapid advances in the geometry-controlled nanoparticle fabrication and assembly and electrodynamics modeling of nanoparticle systems. In this chapter, we present a state-of-the-art review on the geometrically tunable plasmonic properties of metallic nanostructures in various geometries. We describe, both experimentally and theoretically, the relationship between the particle geometry and optical properties in a series of nanoparticle geometries, including

strongly coupling multi-nanoparticle systems, to demonstrate how the optical responses of a nanoparticle can be fine-tuned by judiciously tailoring the geometric parameters of the particle and how the tunable optical properties can be used to tackle grand challenges in diverse fields, such as photonics, energy conversion, spectroscopies, molecular sensing, and biomedicine.

3 Introduction

Nanoparticles exhibit a whole set of fascinating size- and shape-dependent physical and chemical properties that are dramatically different from those of either the corresponding bulk materials or the atomic and molecular systems [1]. Nanoparticles of noble metals, such as Au, Ag, and Cu, have attracted tremendous attention due to their interesting geometry-dependent optical properties. Actually, the vivid, beautiful color of colloidal metal nanoparticles has been an object of fascination since ancient times. One of the oldest examples is the famous Lycurgus Cup (Byzantine Empire, fourth century AD) (Fig. 1.1). This glass cup shows a striking red color when light is shone into the cup and transmitted through the glass, while viewed in reflected light, it appears green. This peculiar behavior is essentially due to the small Au–Ag bimetallic nanoparticles embedded in the glass, which show a strong optical absorption of light in the green part of the visible spectrum.

While these optical characteristics of metal colloids have been known and used for centuries, our scientific understanding on the origin of these properties has emerged far more recently, beginning with the development of classical electromagnetic theory. About a century ago, Gustav Mie applied Maxwell's equations to explain the strong absorption of green light by a Au nanosphere under plane wave illumination [2], which established, for the first time, the rigorous scientific foundation for our understanding of this interesting phenomenon. Essentially, the fascinating optically resonant behaviors of metal nanoparticles are determined by the collective oscillations of free electrons in the metals, known as plasmons. A plasmon resonance can be optically excited when a photon is absorbed at the metal–dielectric interface and transfers the energy into the collective electron oscillations, which are coupled in-phase with the incident light at a certain resonant frequency. For metal nanoparticles, the plasmon resonance frequencies are dependent upon the size and shape of the nanoparticles as the oscillations of free electrons are confined by the particle boundaries over finite nanoscale dimensions. It is well-known that solid spherical Au nanoparticles of ~30 nm in diameter strongly absorb green light at ~520 nm when their characteristic dipole plasmon resonance is optically excited, giving rise to a deep red color when dispersed in colloidal solutions. Michael Faraday was the first person to observe this spectacular phenomenon [3]. In 1857, he prepared the first stable suspension of Au colloids by reducing gold chloride with phosphorus in water. Some of his original samples are still well preserved and on display at the Faraday Museum in London.

The past two decades have witnessed rapid advances in the geometry-controlled fabrication of metallic nanostructures and electrodynamics simulation of the

Fig. 1.1 Pictures of the Lycurgus Cup (on display in the British Museum)

nanoparticles' optical properties, which allow for the development of quantitative understanding of the structure–property relationship of a series of metallic nanoparticle geometries with increasing structural complexity. It has become increasingly apparent that by adjusting the geometric parameters of metal nanostructures, one can fine-tune the wavelengths at which the nanoparticles interact with the incident light in a highly precise manner [1, 4–8]. The plasmon resonance frequencies of a metal nanoparticle are not only a function of the electronic properties of the constituent metal and the dielectric properties of the surrounding medium but also, especially on the nanometer-length scale, more sensitively dependent upon the size and shape of the particle. It is of paramount importance to create highly tunable plasmon resonances of nanoparticles over a broad spectral range because it can open a whole set of new opportunities for photonic, optoelectronic, spectroscopic, and biomedical applications. For example, expanding the plasmonic tunability of metallic nanoparticles from the visible into the near-infrared (NIR) "water window" where tissues and blood are relatively transparent provides unique opportunities for the integrated high-contrast cancer imaging and high-efficiency photothermal therapy [9, 10]. This has, in turn, stimulated tremendous interests in a rapidly expanding array of metal nanoparticle geometries, such as nanorods [11–16] nanoprisms [17–21], nanoshells [22–24] nanostars [25, 26], and nanocages [27, 28]. A key feature of these nanostructures is that their plasmon resonances are geometrically tunable, which enables one to set the plasmon resonances at a specific laser wavelength or spectral region that match a particular application.

In this chapter, we present a comprehensive review on the geometrically tunable optical properties of metal nanostructures. In Sect. 4, we give a brief introduction to the fundamentals of plasmon resonances supported by metal nanoparticles, covering both the experimental measurements and the theoretical methods for plasmon modeling. In Sect. 5, we start from the optical properties of the simplest geometry, solid metal nanospheres, to discuss how the free carrier density of the materials, the electronic properties of metals, and the size of spherical particles determine the

particles' overall optical properties. We also talk about the optical tunability of bimetallic heterostructured and alloy nanospheres. In Sects. 6 and 7, we focus on two representative nanoparticle geometries, nanorods and nanoshells, respectively, to demonstrate how various geometric parameters determine the plasmon-dominated optical properties of the nanoparticles with a particular focus on fundamental understanding of the origin of the optical tunability in these nanoparticle geometries. Essentially, the frequencies of plasmon resonances of metallic nanorods are determined by the aspect ratio of the nanorods, whereas the highly tunable nanoshell LSPRs arise from the interactions between the plasmon modes supported by the inner- and outer-shell surfaces. In Sect. 8, we give a brief survey of the structure–property relationships of several representative nanoparticle geometries with anisotropic structures, such as nanoprisms, nanopolyhedra, nanostars, and nanocages. In Sect. 9, we set out to talk about the geometrically tunable optical properties of more complicated multi-nanoparticle systems in which strong plasmon coupling occurs. We particularly emphasize on how the plasmonic interactions between nanoparticle building blocks give rise to the hybridized plasmon modes of the multiparticle systems and further enhanced local fields in the interparticle junctions that are exploitable for surface-enhanced spectroscopies. Finally, in Sect. 10, we summarize the latest progress in nanoparticle plasmonics over the past two decades and briefly comment on how the geometrically tunable LSPRs of metal nanoparticle systems will broadly impact the fundamental research on nanophotonics and technological applications of metal nanostructures.

4 Localized Surface Plasmon Resonances (LSPRs)

4.1 Plasmons: Collective Oscillations of Free Electrons

Early understanding of the theory of nanoparticle plasmons dates back to the work done by Mie [2] and Faraday [3] more than a century ago. In this chapter, it is not intended to thoroughly cover the plasmon theories in detail, since a good number of excellent reviews, such as the books by Kreibig and Vollmer [29] and by Bohren and Huffman [30] as well as review articles by Mulvaney [31] and by El-Sayed [5], have already been published on this topic, and the readers are encouraged to read them for further details. Here we only want to give a brief introduction to the fundamentals of plasmon resonances of metal nanoparticles.

Essentially, plasmons arise from the collective oscillations of free electrons in metallic materials. Under the irradiation of an electromagnetic wave, the free electrons are driven by the electric field to coherently oscillate at a plasmon frequency of ω_B relative to the lattice of positive ions [29]. For a bulk metal with infinite sizes in three dimensions in vacuum, ω_B can be expressed as

$$\omega_B = \sqrt{\frac{4\pi e^2 n}{me}} \tag{1.1}$$

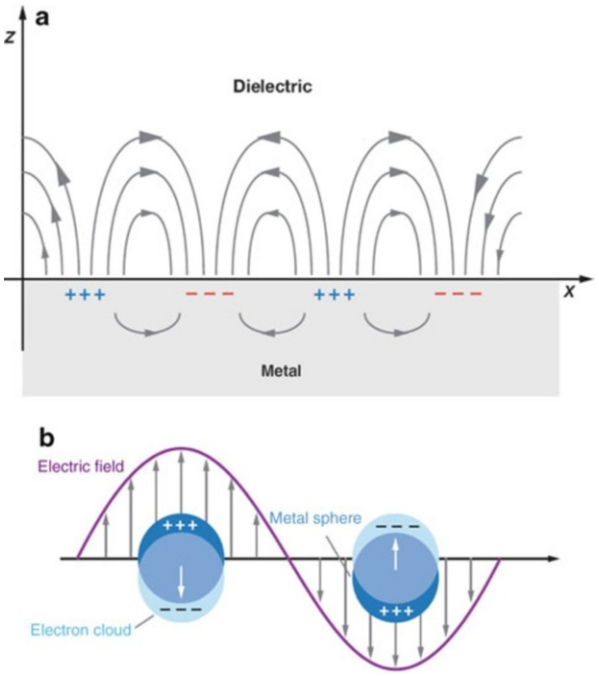

Fig. 1.2 Schematic illustrations of (**a**) a propagating plasmon at metal–dielectric interface and (**b**) a LSPR of a metal nanosphere (Adapted with permission from Ref. [33]. Copyright 2007 Annual Reviews)

where n is the number density of electrons and e and m_e are the charge and effective mass of electrons, respectively.

However, in reality, we have to deal with metallic structures of finite dimensions that are surrounded by materials with different dielectric properties. Since an electromagnetic wave impinging on a metal surface only has a certain penetration depth (~50 nm for Ag and Au), only the electrons on the surface are the most significant. Therefore, their collective oscillations are properly termed as surface plasmons [32]. At a metal–vacuum interface, application of the boundary conditions results in a surface plasmon mode with a frequency $\omega_{surf} = \frac{\omega_p}{\sqrt{2}}$. As is shown in Fig. 1.2a, such a surface plasmon mode represents a longitudinal charge density wave that travels across the surface [33], also widely known as a propagating plasmon. A surface plasmon mode can be excited through a resonance mechanism by passing an electron through a thin metallic film or by reflecting an electron or a photon from the surface of a metallic film when the frequency and wave vectors of both the incident light and the surface plasmon match each other.

In metallic nanoparticle systems, the collective oscillations of free electrons are confined to a finite volume defined by the particle dimensions. Since the plasmons of nanoparticles are localized rather than propagating, they are known as localized surface plasmon resonances (LSPRs). When the free electrons in a metallic nanostructure are driven by the incident electric field to collectively oscillate at a certain resonant frequency, the incident light is absorbed by the nanoparticles. Some of these photons will be released with the same frequency and energy in all directions,

which is known as the process of scattering. Meanwhile, some of these photons will be converted into phonons or vibrations of the lattice, which is referred to as absorption [30]. Therefore, LSPRs manifest themselves as a combined effect of scattering and absorption in the optical extinction spectra. As depicted in Fig. 1.2b, the free electrons of Au nanospheres oscillate coherently in response to the electric field of incident light [33]. The multipolar resonant frequencies can be represented as $\omega_{S.l} = \omega_B \sqrt{\frac{l}{2l+1}}$ (l = 1, 2, 3, 4. . .) when this process occurs in a vacuum. It has been known that the number, location, and intensity of LSPR peaks of Au or Ag nanoparticles are strongly correlated with both the shape and size of the nanoparticles.

4.2 Experimental Methodology of LSPR Measurements

There are generally two important effects associated with the excitation of LSPRs, the existence of optical extinction maxima at the plasmon resonance frequencies (far-field properties) and significantly enhanced electric fields in close proximity to the particle's surface (near-field properties). The far-field plasmonic properties of metal nanoparticles can be most conveniently measured by performing extinction spectroscopy measurements on colloidal nanoparticle suspensions or on thin films of nanoparticles immobilized on or embedded in a substrate at ensemble level using UV–visible–NIR spectrometers. In these measurements, both absorption and scattering contribute to the overall extinction. The polydispersity of the samples may introduce inhomogeneous broadening to the overall bandwidth and modify the line shape of the extinction spectra. To bypass the ensemble-averaging effects, one can use a dark-field microscope coupled with a spectrometer to probe the wavelength-dependent light-scattering properties of individual nanoparticles at single-particle level. Figure 1.3 shows a dark-field microscopy image of Au nanoparticles of different geometries and the corresponding scattering spectra of each individual nanoparticle [34]. The different nanoparticles exhibit dramatically different colors and intensities in the microscopy images and are resonant with the incident light at different wavelengths. By adding linear polarizers and other optical accessories to the dark-field microscope, the spatial distribution of the scattering light at a certain wavelength can be measured. By correlating the optical characteristics probed by dark-field microscopy with the detailed structural information obtained from electron microscopies at single-particle level, one can develop quantitative understanding of the structure–property relationship of individual nanoparticles without the ensemble-averaging effects. Since the electrodynamics simulations are mostly carried out on individual nanoparticles, the single-particle measurements provide unique opportunities to directly compare the experimental spectra to the simulated results.

In addition to the abovementioned far-field measurements, near-field scanning optical microscopy (NSOM) has been applied to the near-field measurements of LSPRs. NSOM is a powerful imaging tool which permits super-resolution imaging of samples through the interaction of the light with the samples close to the metal

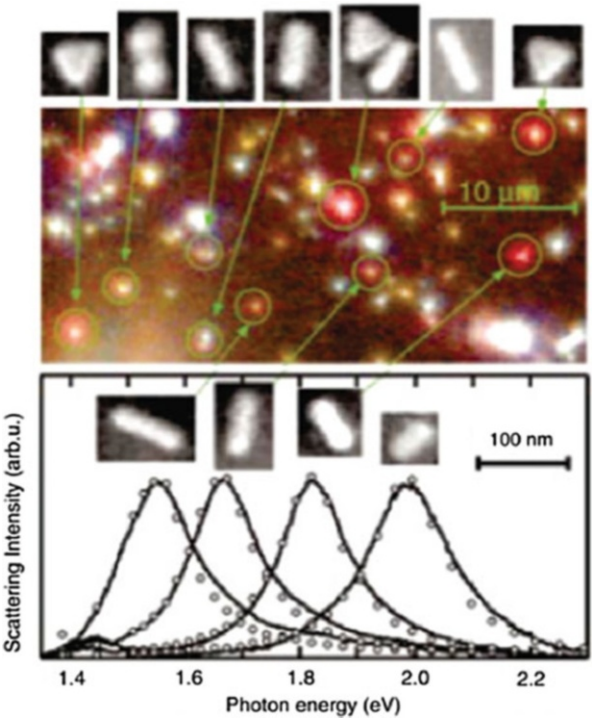

Fig. 1.3 Dark-field microscopy image, corresponding scanning electron microscopy images, and light-scattering spectra of Au nanocrystals of different shapes (Reprinted with permission from Ref. [34]. Copyright 2003 American Institute of Physics)

aperture, breaking the diffraction barrier of light [35–38]. However, for conventional aperture-type NSOM, the resolution is limited by the aperture size of the tip. Since the effective transmission area decreases as the fourth power of the aperture diameter [39, 40], the resolution improvement comes at the price of a sharp decrease in signal-to-noise ratio and contrast of NSOM images. Recently, differential near-field scanning optical microscopy (DNSOM) is introduced to improve the light transmission, which involves scanning a rectangular (e.g., a square) aperture (or a detector) in the near-field of the object of interest and recording the power of the light collected from the rectangular structure as a function of the scanning position [41].

Electron energy loss spectroscopy (EELS) is another powerful method for near-field mapping of LSPRs. When a material is exposed to a beam of electrons with a narrow range of kinetic energies, the constituent atoms can interact with these electrons via electrostatic (Coulomb) forces, resulting in elastic and inelastic scattering of electrons. Among them, inelastic scattering is associated with the energy loss of electrons, which can be measured via an electron spectrometer and interpreted in terms of what caused the energy loss [42]. EELS is a very powerful probe for the excitation on the surface and ultrathin films, in particular, for the collective excitations of electron oscillations (plasmons). Plasmon excitations are directly related to the band structure and electron density in a small volume of the particle probed by the focused electron beam [43]. With the recent proliferation of

aberration-corrected and monochromated transmission electron microscopes (TEMs), mapping the energy and spatial distribution of metallic nanoparticle plasmon modes on nanometer-length scales using EELS has become possible [44–47]. For example, Liz-Marzan and coworkers utilized a novel method relied on the detection of plasmons as resonance peaks in EELS to record maps of plasmons with sufficiently high resolution to reveal the dramatic spatial field variation over silver nanotriangles [48]. The near-field plasmon modes of isolated and coupled Au nanorods have also been imaged using EELS and energy-filtered transmission electron microscope (EFTEM) [49]. More recently, plasmon mapping of a series of high-aspect-ratio Ag nanorods using EELS was also reported [50]. These data indicate that correlated studies will ultimately provide a unified picture of optical and electron beam-excited plasmons and reinforce the notion that plasmon maps derived from EELS have direct relevance for the plethora of processes relying on optical excitation of plasmons.

The local field enhancements on the surface of nanoparticles arising from plasmonic excitations can also be indirectly probed by surface-enhanced spectroscopies. For example, the local field enhancements provide well-defined "hot spots" for surface-enhanced Raman scattering (SERS) [51–54]. Once the molecules get into these hot regions in vicinity to a metallic nanostructure, their spectroscopic signals can be dramatically amplified. It has been demonstrated that SERS enhancements are dependent on the fourth power of the local field enhancements. Therefore, the Raman enhancements of the probing molecules in close proximity to a metal nanostructure provide a way to evaluate the local field enhancements. Since Raman enhancements are sensitively dependent on the distance between molecules and metal surfaces, one can smartly construct molecular rulers to map out the local field enhancement profiles surrounding a nanoparticle based on SERS [55].

4.3 Simulations of LSPRs

The most commonly used theoretical methods for the modeling of the LSPRs of metallic nanoparticles include both analytical and numerical methods [56–59]. The analytical methods are either derived from Mie scattering theory for spheres or from the quasi-static (Gans) model as applied to spheroids. Most popular numerical methods for electrodynamics simulations include the discrete dipole approximation (DDA), the finite-difference time-domain (FDTD) method, the finite element method (FEM), and boundary element method (BEM).

It was realized almost a century ago that classical electromagnetic theory (i.e., solving Maxwell's equations for light interacting with a particle) based on Mie scattering theory provides a quantitative description of the scattering and absorption spectra of spherical nanoparticles. However, Mie's work is incapable of addressing shape effects. Although the quasi-static approximation developed later is an alternative to elucidate the optical properties of spheroids, the solution is even harder to use because of frequency-dependent dielectric functions included in Maxwell's

equations. Meanwhile, the numerical methods for solving Maxwell's equations come in many different flavors. For example, the discrete dipole approximation (DDA) is a frequency domain approach that approximates the induced polarization in a complex particle by the response of a cubic grid of polarizable dipoles. The finite different time domain (FDTD) method can be applied in both two and three dimensions, in which a clever finite differencing algorithm is applied to Maxwell's equation by Yee [60], using grids for the electric field **E** and magnetic field **H**, which are shifted by half a grid spacing relative to each other. Using the finite element method (FEM), the solutions to Maxwell's equations are expanded in locally defined basis functions chosen such that boundary conditions are satisfied on the surfaces of the elements. Boundary element method (BEM) is another numerical computational method of solving linear partial differential equations which have been formulated as integral equations. These numerical methods have been shown to be capable of simulating both the far-field and near-field plasmonic properties of metallic nanostructures of almost arbitrary structural complexity.

In addition to the analytical and numerical methods mentioned above, the time-dependent density functional theory (TDDFT) is one of the most convenient approaches for the fully quantum mechanical calculations of the optical properties of metallic nanoparticles [61–63]. TDDFT, an extension of density functional theory (DFT) with conceptual and computational foundations analogous to DFT, is to use the time-dependent electronic density instead of time-dependent wave function to derive the effective potential of a fictitious noninteracting system which returns the same density as any given interacting system.

Combined experimental and theoretical efforts over the past two decades have shed light on the interesting geometry dependence of plasmonic properties of metallic nanoparticles with increasing geometric complexity. In the following section, before moving onto those more complicated nanoparticle geometries, we will start from the simplest geometry, a nanosphere, to demonstrate how the LSPRs can be systematically tuned by changing the compositional and geometric parameters of the nanosphere.

5 LSPRs of Metallic Nanospheres

5.1 LSPRs of Single-Component Nanospheres

Strong optical scattering and absorption of light by noble metal nanospheres in visible spectral region due to LSPRs are a classical electromagnetic effect, which was described theoretically by Mie in 1908 by solving Maxwell's equations. Mie's theory is most useful in describing the plasmonic properties of metallic particles that are spherically symmetric. Mie scattering theory is the exact solution to Maxwell's electromagnetic-field equations for a plane wave interacting with a homogeneous sphere of radius R with the same dielectric constant as bulk metal. The extinction cross section of the spheres can be obtained as a series of multipolar oscillations if the boundary conditions are specified. Therefore, the

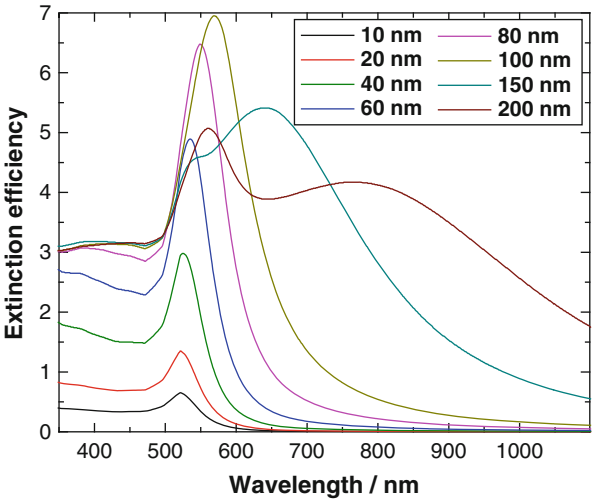

Fig. 1.4 Extinction spectra calculated using Mie scattering theory for Au nanospheres with diameters ranging from 10 nm to 200 nm dispersed in water. The calculated extinction is expressed as an efficiency, which is the ratio of the energy scattered or absorbed by the particle to the energy incident on its physical cross section

electrodynamics calculations can be simplified by only focusing upon low-order plasmon oscillations when the diameter of the spherical particle is much smaller than the wavelength of the radiation (within the quasi-static limit) and only dipole oscillation ($l = 1$) contributes to the extinction cross section which is a sum of both scattering and absorption. Based on this, the most popular form of Mie's theory for spherical nanoparticles within quasi-static limit is given as

$$C_{ext} = \frac{24\pi^2 R^3 {\varepsilon_m}^{3/2}}{\lambda} \bullet \frac{\varepsilon_2}{(\varepsilon_1 + 2\varepsilon_m)^2 + {\varepsilon_2}^2} \tag{1.2}$$

where C_{ext} is the extinction cross section of the spheres, ε_m is the dielectric constant of the surrounding medium, λ is the wavelength of the radiation, R is the radius of a homogeneous sphere, and ε_1 and ε_2 denote the real and imaginary part of the complex dielectric function of the particle material, respectively. A resonance occurs whenever the condition of $\varepsilon_1 = -2\varepsilon_m$ is satisfied, which explains the dependence of the LSPR extinction peak on the surrounding dielectric environment. It is this LSPR peak that accounts for the brilliant colors of a wide variety of metallic nanoparticles. The imaginary part of the dielectric function also plays a role in the plasmon resonance, relating to the damping, that is, resonance peak broadening in the spectrum.

For a small Au nanosphere within the quasi-static limit, its LSPR has an almost fixed resonance frequency and shows limited tunability. As shown in Fig. 1.4, the extinction spectra calculated using Mie theory for Au nanospheres smaller than 100 nm show that LSPR peaks are located in the green part of the visible region. According to the full Mie-theory solution, a limited red shift of LSPR wavelength and broadening of the resonant line shape appear as Au nanospheres progressively become larger within the sub-100-nm-size regime. As the particle size further

increases to the size regime beyond the quasi-static limit, the overall spectral line shape becomes more complicated as the higher-order multipolar resonances, such as quadrupole ($l = 2$) and octupole ($l = 3$), become increasingly significant in the extinction spectra in addition to the dipolar plasmon resonances due to the phase-retardation effects, resulting in further redshifted and broadened dipolar plasmon bands. Such size dependence of LSPRs has been experimentally observed to be in very good agreement with Mie scattering theory calculations for Au and Ag spherical or quasi-spherical particles over a broad size range both within and beyond the quasi-static limit [64, 65].

5.2 Effects of Materials' Electronic Properties on LSPRs of Nanospheres

In addition to the particle size, the frequencies of LSPRs of a nanosphere also rely on the electronic properties of the constituent materials. The LSPR frequency, although tunable by varying the nanoparticle size and local medium, is primarily controlled through the free electron density (N) of the material. Although LSPRs typically arise in nanostructures of noble metals, they are not fundamentally limited to noble metals and can also occur in other non-noble metals, conducting metal oxides and semiconductors with appreciable free carrier densities. Recently, Alivisatos and coworkers demonstrated that in analogy to noble metal nanoparticles, doped semiconductor quantum dots may also exhibit LSPRs whose resonance frequencies can be tuned by controlling the free carrier densities of the materials [66]. Figure 1.5 depicts the modulation of the LSPR frequency (ω_{sp}) of a spherical nanoparticle within the quasi-static limit through control over its free carrier concentration (N). In this figure, the LSPR frequency can be estimated using the following equation:

$$\omega_{SP} = \frac{1}{2\pi}\sqrt{\frac{Ne^2}{\varepsilon_0 m_e(\varepsilon_\infty + 2\varepsilon_m)}} \tag{1.3}$$

Here the high frequency dielectric constant (ε_∞) is assumed to be 10, the medium dielectric constant ε_m is set as 2.25 for toluene, and the effective mass of the free carrier m_e is assumed to be that of a free electron. e is the electronic charge, and ε_0 is the permittivity of free space. The top panel shows a calculation of the number of dopant atoms required for nanoparticle sizes ranging from 2 to 12 nm to achieve a free carrier density between 10^{17} and 10^{23} cm^{-3}. To achieve LSPRs in the visible region, a metallic material in which every atom contributes a free carrier to the nanoparticle is required. For LSPRs in the infrared, carrier densities of 10^{19}–10^{22} cm^{-3} are required. Below 10^{19} cm^{-3}, the number of carriers (for a 10-nm nanocrystal) may be too low (<10) to support an LSPR mode.

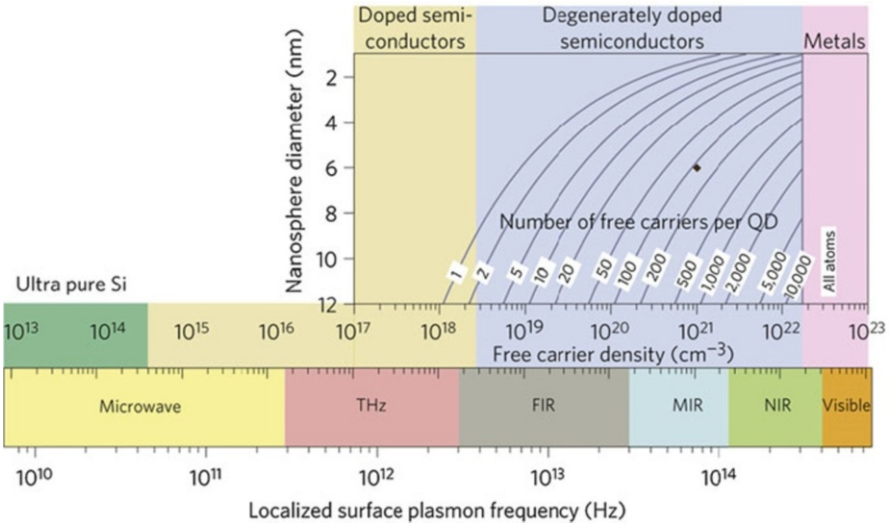

Fig. 1.5 LSPR frequency dependence on free carrier density and doping constraints (Reprinted with permission from Ref. [66]. Copyright 2011 Nature Publishing Groups)

The most commonly studied plasmonic materials so far are noble metals, such as Au, Ag, and Cu, which have free electron densities in the range of 10^{22}–10^{23} cm^{-3} with corresponding LSPRs in the visible. For non-noble metals, such as Pb, In, Hg, Sn, Cd, and Al, their LSPR frequencies lie in the UV region of the spectrum, and nanoparticles do not display well-defined LSPR bands that are as tunable as those of the noble metals. In addition, small particles of these non-noble metals are also chemically unstable and readily oxidized, making it difficult to measure their LSPRs. The LSPRs of doped semiconductor nanoparticles typically occur in the infrared and are not as strong and well-defined as those of noble metal nanoparticles. The geometry dependence of LSPRs of doped semiconductor nanoparticles is still poorly understood at the present stage. Therefore, we will only focus on the plasmonic properties of noble metal nanoparticles, Au and Ag nanoparticles in particular, because of not only their relatively high chemical and photostability but also more importantly their intense and geometrically tunable LSPRs across the visible and NIR regions.

In addition to the free electron densities of the materials, the optical properties of noble metal nanospheres are also strongly influenced by the electronic band structures of the constituent metal, which determine the metal's dielectric functions. The complex dielectric function of a material, denoted as $\varepsilon = \varepsilon_1 + i\varepsilon_2$, describes a material's response to an applied electric field. ε_1 determines the degree to which the material polarizes in response to an applied field, while ε_2 controls the relative phase of this response with respect to the applied field. Intrinsic loss mechanisms (e.g., electron scattering) of a material are all

condensed into ε_2. For the noble metals at optical frequencies, the dielectric function can be expressed as the sum

$$\varepsilon(m) = 1 + \chi_\infty + \chi_D(\omega) \tag{1.4}$$

where the background susceptibility χ_∞ arises from the core electron polarizability and interband (d → sp) transitions and χ_D is the Drude response of the conduction electrons. The background polarizability and free space response are often combined into $\varepsilon_\infty = 1 + \chi_\infty$ In the Drude model [30],

$$\chi_D(\omega) = -\frac{\omega_P^2}{\omega^2 + i\Gamma\omega} = -\frac{\omega_p^2}{\omega^2 + \Gamma^2} + i\frac{\omega_p^2\Gamma}{\omega(\omega^2 + \Gamma^2)} \tag{1.5}$$

where ω_P is the bulk plasmon frequency and Γ is the reciprocal electron relaxation time. In the visible and NIR, $\Gamma << \omega$; therefore,

$$\chi_D(\omega) \cong -\frac{\omega_P^2}{\omega^2} + i\frac{\omega_p^2}{\omega^3}\Gamma \tag{1.6}$$

To completely understand the role that the metal plays in determining the optical properties of metallic nanoparticles, it is necessary to examine and account for the effects of both the free-electron and electronic interband transition contributions to the metal's dielectric response. Figure 1.6 shows a comparison of dielectric functions of Ag, Au, and Cu, together with the calculated extinction spectra of Au, Ag, and Cu nanospheres that are 30 nm in diameter obtained using Mie scattering theory. The dielectric medium surrounding the nanoparticles is water. The spectral regions where interband transitions occur are shaded in green. The onset of electronic interband transitions from the valence band to the Fermi level causes a sharp increase in the imaginary part (ε_2) and a marked change in the slope of the real part (ε_1) of the dielectric functions. For 30-nm-diameter solid nanospheres, the relative spectral locations of the particle plasmon resonance and the constituent metal's interband transitions determine the nanoparticles' optical response, resulting in significant variations between Au, Ag, and Cu nanospheres. The Ag nanosphere has by far the strongest plasmon resonance because of the higher energy of the interband transitions (~3.8 eV), relative to the energy of the plasmon resonance, resulting in minimal damping of the plasmon. The Au nanosphere displays a well-defined plasmon resonance at ~520 nm, which is closer to the edge of the interband transitions region (~2.5 eV) than the case of Ag. With plasmon resonant energies well below the interband transitions, Au and Ag nanoparticles can be treated as free-electron systems whose optical properties are determined by the conduction electrons, with only a constant real background polarizability associated with the core electrons. The Cu nanosphere, however, has much weaker optical response in comparison to Ag and Au due to the nanosphere plasmon being resonant with the interband transition region (~2.1 eV)

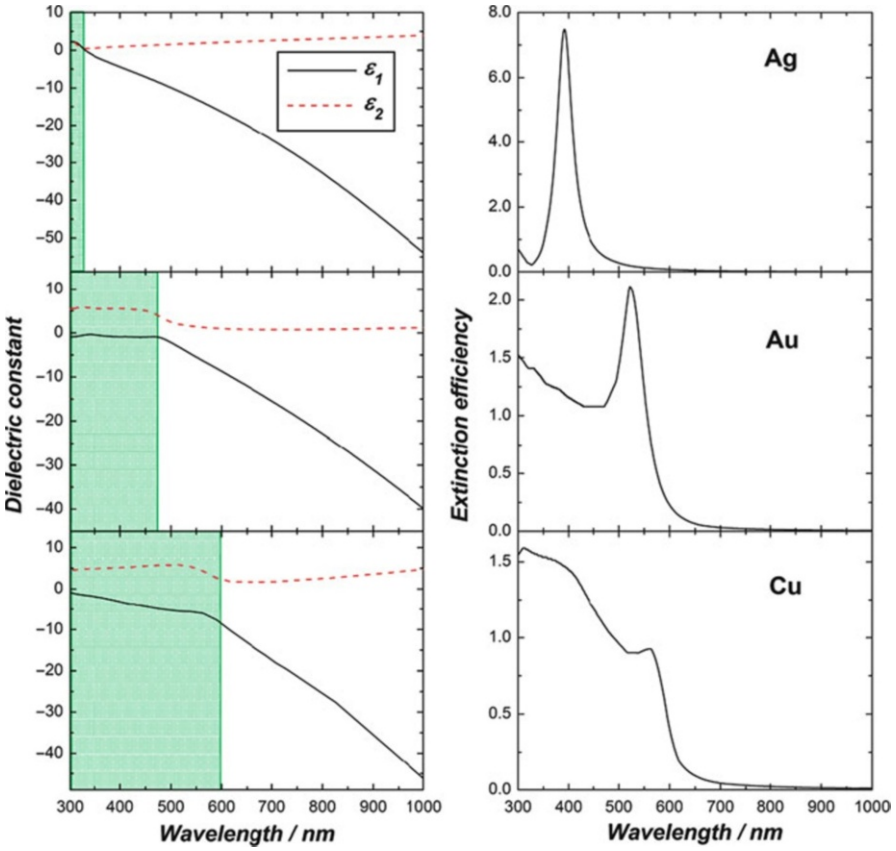

Fig. 1.6 Dielectric functions (*left column*) and calculated extinction spectra of a 30-nm-diameter nanosphere (*right column*) of Ag (*top*), Au (*middle*), and Cu (*bottom*)

of the spectrum. The interband transitions are responsible for a strong damping of the Cu nanosphere plasmon and the strong "background" absorption on top of which a weak plasmon resonance peak is visible.

5.3 Bimetallic Nanospheres

When multiple metallic components are integrated into one nanosphere, the resulting optical properties become dependent upon both the compositions and the compositional distribution inside the nanoparticle. Although various bimetallic nanoparticle systems have been studied, combinations of Au and Ag are of particularly interest largely for two reasons. First, both metals display intense and well-defined LSPR bands in the visible at around 400 and 520 nm for spherical nanoparticles of Ag and Au, respectively. Second, both Au and Ag form

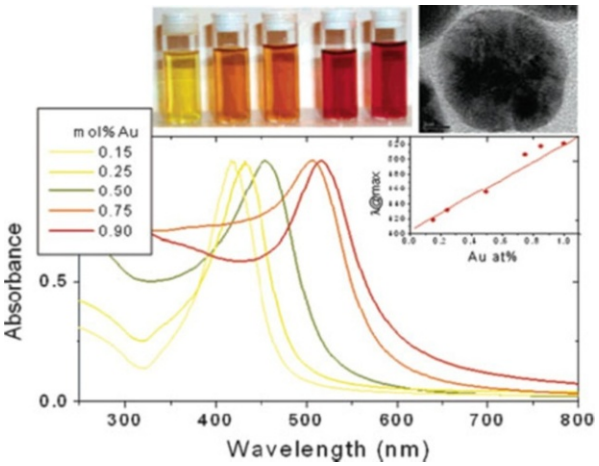

Fig. 1.7 UV–visible spectra of Au–Ag alloy nanoparticle colloids with varying compositions. A linear fit of the peak position of the experimental absorption band as a function of composition obtained using Mie theory is plotted (*inset*). HRTEM image shows the homogeneous distribution of Au and Ag atoms within the particles (Reprinted with permission from Ref. [80]. Copyright 2006 American Chemical Society)

face-centered cubic crystalline structures with very small lattice mismatch (lattice constants of 4.078 Å and 4.086 Å for Au and Ag, respectively), and therefore, they can form heteronanostructures through epitaxy growth or form alloy nanostructures with various compositional stoichiometries. Spherical nanoparticles of Au–Ag alloy [67–73], Au–Ag core–shell [74–78], and Ag–Au core–shell [74, 79] have been fabricated through various bottom-up chemistry approaches. Precise control over both the compositional stoichiometry and distribution enables one to systematically study the interesting optical tunability of bimetallic nanospheres.

For alloy nanospheres normally prepared by simultaneous reduction of the metal salts, it has been observed that the plasmon band of the alloy nanoparticles lies somewhere between those for pure Ag and pure Au nanoparticles [70, 71], and there is a linear relationship between the compositional stoichiometry and the wavelength of the plasmon band of the alloy particles. As shown in Fig. 1.7, a continuous color evolution from yellow to red can be clearly observed as the Au to Ag ratio progressively increases [80]. As shown in the inset plots of Fig. 1.7, the experimentally observed linear relationship between compositional stoichiometry and LSPR wavelength can be well reproduced by Mie scattering theory calculations. The LSPR shifts were initially modeled by assuming a linear combination of the dielectric functions of pure Au and Ag as input for the Mie scattering theory calculations, but El-Sayed and coworkers have demonstrated that the theoretical predictions agreed with the experimental results more accurately when experimentally measured dielectric functions for Au–Ag alloy films were used. The linear relationship between compositional stoichiometry and wavelength of LSPR band applies to alloy nanoparticles only and cannot be simply extended to core–shell heterostructured nanoparticles.

Core–shell heterostructured bimetallic nanoparticles can be fabricated either via segregation during simultaneous reduction or by successive reduction of the

different metals [68, 81, 82]. Recently, the creation of onion-like multilayer bimetallic nanoparticles obtained by successive reduction of $AgNO_3$ and $HAuCl_4$ with ascorbic acid in the presence of cetyltrimethylammonium bromide (CTAB) has been reported. The optical properties of these core–shell bimetallic nanoparticles are quite sensitive to the multilayer deposition, and the extinction spectral line shape are mostly dominated by the geometry of the outermost layer [83]. It is interesting that the core–shell heterostructured bimetallic nanoparticles may undergo alloying processes under appropriate conditions. For Au–Ag bimetallic nanoparticles, the core–shell heterostructures may be kinetically favorable during the particle formation, while the alloy particles are thermodynamically more stable. Therefore, the transitions from the core–shell heterostructures to alloy homostructures are in principle spontaneous at room temperature. By modifying the experimental conditions, such transitions may be accelerated and kinetically better controlled. For example, Hartland and coworkers [75] used nanosecond and picosecond lasers to melt the Au–Ag core–shell particles into homogeneously alloyed nanoparticles. Sun and coworkers [79] reported the formation of monodisperse Au–Ag alloy nanoparticles through interface diffusion of Ag–Au core–shell nanoparticles under solvothermal conditions in organic solvents. Recently, Tracy and coworkers [84] reported a facile method for the synthesis of Au–Ag core–shell nanoparticles and their subsequent transition to Au–Ag alloy nanoparticles through digestive ripening. By controlling the relative sizes of the Au core and Ag shell, the stoichiometry of the resulting Au–Ag alloy nanoparticles can be precisely controlled. The structural change of the particles during the alloying processes can be monitored through the shift of the LSPR bands. Precise control over the particle's geometry and compositions is important to the fine-tuning of the optical properties of the bimetallic nanoparticles as their LSPRs are sensitively dependent on both the stoichiometry and geometrical distribution of the metal compositions.

6 LSPRs of Metallic Nanorods

6.1 Geometrically Tunable LSPRs of Nanorods

Metal nanorods are elongated, anisotropic nanoparticles with polarization-dependent response to the incident light. The excitation of the electron oscillation along the short axis induces a plasmon band at wavelength similar to that of Au nanospheres, commonly referred to as the transverse band. The excitation of the electron oscillation along the long axis induces a much stronger plasmon band in the longer wavelength region, referred to as the longitudinal band. When Au nanorods are dispersed in a solvent, a steady-state extinction spectrum containing both bands of longitudinal and transverse plasmons can be observed due to the random orientation caused by the continuous Brownian motion of the particles. While the transverse band is insensitive to the size of the nanorods, the longitudinal band is redshifted significantly from the visible to NIR region with increasing aspect ratio (length/width) [85–87].

Because of the nonspherical shape, the plasmonic properties of nanorods cannot be fully described by Mie scattering theory. However, qualitative features of nanorod LSPRs are well reproduced by Gans theory [88] which is an extension of Mie theory for ellipsoidal nanoparticles. Gans theory puts depolarization factors for each direction in the Mie-theory expression to capture the optical anisotropy. In 1912, Gans predicted that for very small ellipsoids, where the dipole approximation holds, the plasmon mode would split into two distinct modes [88]. In Gans theory, the LSPRs are only dependent on the aspect ratio of the particles but not on the absolute dimensions. Gans theory gives the exact solution to Maxwell equations for ellipsoidal particles. The experimentally fabricated nanorods, however, are more like cylinders or sphere-capped cylinders than ellipsoids. Using numerical methods, such as DDA, one can more accurately model the exact shape of the particles. Nevertheless, Gans theory calculations match the experimental data adequately well in most cases and can further shed light on the origin of the geometry–property relationship of nanorods. To interpret the optical properties of small metal nanorods using Gans formula, it has been common to treat them as ellipsoids [11, 89].

The cross sections of absorption (C_{abs}), scattering (C_{csa}), and total extinction (C_{ext}) derived from Gans theory can be quantitative described by the following equations:

$$C_{abs} = \frac{2\pi}{3\lambda}\varepsilon_m^{3/2} V \sum_i \frac{\varepsilon_2/\left(n^{(i)}\right)^2}{\left(\varepsilon_1 + [(1-n^{(i)})/n^{(i)}]\varepsilon_m\right)^2 + \varepsilon_2^2} \tag{1.7}$$

$$C_{sca} = \frac{8\pi^3}{9\lambda^4}\varepsilon_m^2 V^2 \sum_i \frac{\left(\varepsilon_1 - \varepsilon_m\right)^2 + \varepsilon_2^2/\left(n^{(i)}\right)^2}{\left(\varepsilon_1 + [(1-n^{(i)}/n^{(i)}]\varepsilon_m\right)^2 + \varepsilon_2^2} \tag{1.8}$$

$$C_{ext} = C_{abs} + C_{sca} \tag{1.9}$$

where λ is the wavelength of light, V is the unit volume of the nanoparticle, and $n^{(i)}$ is the depolarization factor defined by:

$$n^{(a)} = \frac{2}{R^2-1}\left(\frac{R}{2\sqrt{R^2-1}} \ln\frac{R+\sqrt{R^2-1}}{R-\sqrt{R^2-1}} - 1\right) \tag{1.10}$$

$$n^{(b)} = n^{(c)} = (1-n^{(a)})/2 \tag{1.11}$$

where a, b, and c are the three axes of the nanoparticle, $a > b = c$, and aspect ratio, R is equivalent to a/b or a/c. The LSPRs of an ellipsoidal particle occur when the following equation applies:

$$\varepsilon_1 = -(1-n^{(i)}) \times \varepsilon_m/n^{(i)} \tag{1.12}$$

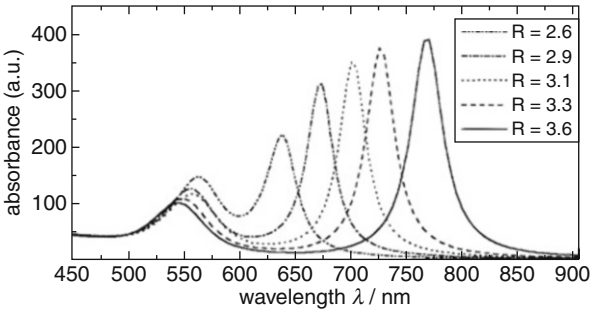

Fig. 1.8 Calculated extinction spectra of elongated Au ellipsoids with varying aspect ratio R using Gans theory (Reprinted with permission from Ref. [11]. Copyright 1999 American Chemical Society)

where $i = a$ for the longitudinal resonance and $i = b$ or c for the transverse resonance. At such resonance wavelengths, the absorption, scattering, and total extinction are all strongly enhanced, giving rise to the extinction peaks in the extinction spectra.

Gans equation predicts that for small ellipsoids embedded in the same medium, an almost linear correlation exists between longitudinal LSPR wavelength and aspect ratio of the ellipsoids. Figure 1.8 shows the calculated extinction spectra of nanorods with different aspect ratios. The longitudinal plasmon band is continuously shifted from the visible to NIR as the aspect ratio of the nanorods increases [11], while the transverse plasmon band exhibits a slight blue shift as aspect ratio increases.

In addition to aspect ratio, the longitudinal plasmon resonance frequency of metal nanorods is also sensitively dependent on the dielectric properties of the local environment. Figure 1.9 shows the calculated spectra of ellipsoidal Au nanoparticles with a fixed aspect ratio of 3.5 in dielectric media with varying refractive indices. As the refractive index of the surrounding medium increases, the longitudinal plasmon band progressively shifts to longer wavelength, exhibiting greatly enhanced sensitivity toward dielectric perturbations in comparison to Au nanospheres [87]. It has also been observed that the larger aspect ratio of the nanorod is, the greater the sensitivity to refractive index effects the nanorod has. Therefore, a single nanorod may serve as a nanoscale sensor that can be used to probe the local environment changes surrounding the particle based on the shift of its LSPR.

In comparison to metal nanospheres, nanorods exhibit greatly enhanced LSPR tunability over a much broader spectral range. In addition, metallic nanorods have further enhanced electric fields at the tips compared to nanospheres, which is crucial to the achievement of larger signal enhancements in surface-enhanced spectroscopies, such as SERS. As calculated by using classical electromagnetic theory and TDDFT, the maximum field enhancement is more pronounced for more elongated nanorods compared to ones with smaller aspect ratios (Fig. 1.10) [90]. Although the values of maximum field enhancement of nanorods with different aspect ratios are somewhat different, the spatial distributions of the field enhancements are similar for both TDDFT and classical calculations.

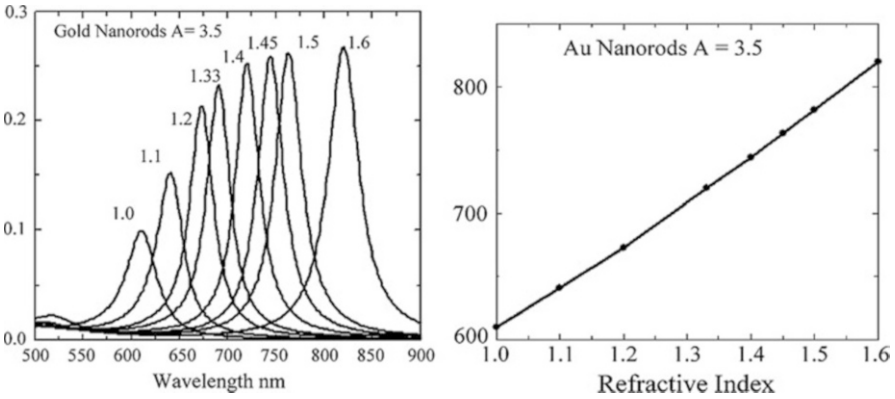

Fig. 1.9 Calculated spectra for Au ellipsoids with an aspect ratio of 3.5 in different media (*left*) and the LSPR band position as a function of the medium refractive index (*right*) (Reprinted with permission from Ref. [87]. Copyright 2005 Elsevier B. V.)

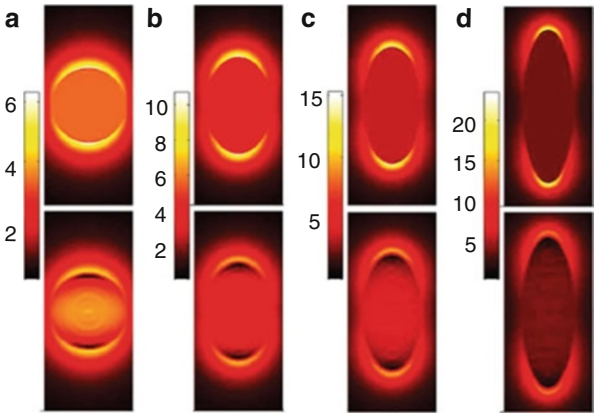

Fig. 1.10 Comparisons of the field distributions calculated using classical electromagnetic theory (*top panels*) and TDDFT (*bottom panels*) for aspect ratios of 1 (**a**), 1.5 (**b**), 2 (**c**), and 3 (**d**), respectively (Reprinted with permission from Ref. [90]. Copyright 2010 American Chemical Society)

6.2 Controllable Fabrication of Nanorods

Although the synthesis of spherical Au nanoparticles has a history of more than a century since the pioneering work by Faraday in 1857 [3], methods for the fabrication of colloidal Au nanorods with well-controlled aspect ratios emerged only during the past two decades. The controllability over the size and morphology enables us to experimentally study the geometrically tunable optical properties of metallic nanorods. Although there are successful examples of controllable fabrication of Ag and Cu nanorods [91–93], the fabrication of Au nanorods has received much more success with much better controllability over the yield, aspect ratio, and

uniformity of the samples. Here we give a brief outline of various synthetic approaches, including both bottom-up and top-down techniques, for the geometry-controlled fabrication of Au nanorods.

The template method for the synthesis of Au nanorods, first developed by Martin and coworkers [94], involves the electrochemical deposition of Au within the pores of nanoporous template membranes. Using this method, the diameter of the Au nanorods roughly equals to the pore diameter of the template membrane, which can be controlled during the membrane fabrication process. The length of the nanorods can be controlled by controlling the amount of Au deposited within the pores during the electrodeposition. More complicated one-dimensional metallic nanostructures, such as Au nanotubes, multicomponent coaxial nanocables, and bar-code heterojunction structures, can also be fabricated using this method [95].

In 1990s, Wang and coworkers developed an electrochemical method for the fabrication of Au nanorods with high yield [89, 96]. In this method, a metallic Au plate anode and a Pt plate cathode are immersed in an electrolytic solution containing a structural directing agent, CTAB, and a cosurfactant tetradodecylammonium bromide (TOAB). During the electrolysis, the bulk Au anode is consumed, forming $AuBr_4^-$ which are then complexed to the cationic surfactants, and migrates to the cathode where Au ions are reduced to metallic Au. A Ag plate is gradually inserted into the solution to control the aspect ratio of the nanorods. Sonication is needed to dissipate the nanorods away from the cathode to form free-standing colloidal Au nanorods. The redox reaction between Au ions generated from the anode and Ag metal leads to the formation of Ag ions and the concentration of Ag ions, and their release rate have been found to be the key factors that determine the aspect ratio of the nanorods, though the exact role of the Ag ions is still unclear at the present stage.

The seed-mediated growth method is so far the most popular method for the synthesis of colloidal Au nanorods [15, 85–87, 97]. The seed-mediated growth method has several advantages over other approaches, such as the simplicity of the procedure, high yield of nanorods, ease of tight control over aspect ratios, and flexibility for structural modifications. The anisotropic growth of Au nanoparticles was first reported in 1989 by Wiesner and Wokaun [98] who fabricated anisotropic Au colloids by introducing Au nuclei into $HAuCl_4$ growth solutions. This idea was further developed into a robust seed-mediated chemical approach for the controllable fabrication of Au nanorods originated in 2001 by Murphy and coworkers [99, 100]. For more explicit details about the seed-mediated growth of Au nanorods, the readers are referred to several excellent reviews by Murphy group [86, 97], El-Sayed group [85], and Mulvany group [87, 101].

The earliest version of nanorod fabrication protocol developed by Murphy group [99, 100] involves the addition of citrate-capped small Au nanospheres to a bulk $HAuCl_2$ growth solution obtained by the reduction of $HAuCl_4$ with ascorbic acid in the presence of CTAB surfactant and $AgNO_3$, which results in the formation of Au nanorods with aspect ratio of 1–7. In 2003, Nikoobakht and El-Sayed [13] made

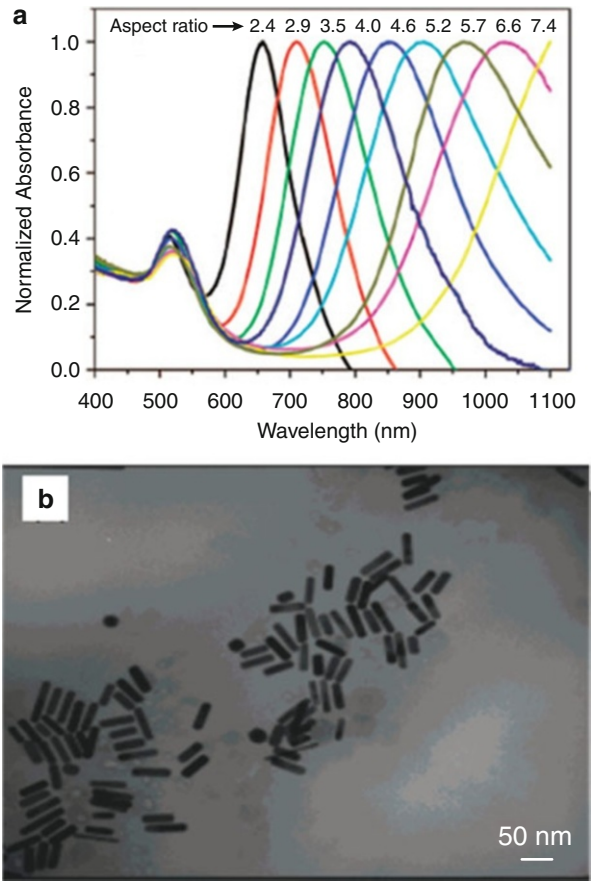

Fig. 1.11 (**a**) Extinction spectra of experimentally fabricated Au nanorods with different aspect ratios. (**b**) TEM image of nanorods of aspect ratio of 4.0 (Adapted with permission from Ref. [13]. Copyright 2003 American Chemical Society)

two modifications to this protocol: replacing sodium citrate with sodium borohydride, a stronger reducing agent in the seed formation process, and utilizing silver ions to control the aspect ratio of the resulting Au nanorods. This method produces high-yield Au nanorods (99 %) with aspect ratios from 1.5 to 4.5. To grow Au nanorods with further increased aspect ratios up to ~20, a three-step seeding method has been developed by Murphy and coworkers [12]. Another way to increase the aspect ratio of the resulting Au nanorods in high yield is to use a cosurfactant, such as benzyldimethylhexadecylammonium chloride (BDAC), in addition to CTAB. The BDAC–CTAB binary surfactant system produces nanorods with aspect ratios of up to 10 by changing the silver concentrations (Fig. 1.11) [13]. Using the Pluronic F-127 cosurfactant system, the aspect ratio can further increase up to 20 [43]. Introduction of other reagents into the growth solution can further adjust the kinetics of the nanorod growth and even longer nanorods can be obtained. For example, adding controllable amount of nitric acid into the growth solution

significantly enhances the production of nanorods with high aspect ratio over 20 [102]. Long Au nanorods with aspect ratios of up to 70 can be fabricated in high yield by controlling the volume of the growth solution [103].

Using the seed-mediated growth method, the yield, monodispersity, and aspect ratio of the resulting Au nanorods are all sensitively dependent on a whole set of experimental parameters, such as seed concentration, seed size, reducing agent, temperature, pH values, Au precursor concentration, surfactant concentration, the use of other cosurfactants, other additives, and even the nanorod aging time. Variation of experimental parameters of the nanorod fabrication protocol may also result in significant modifications to the typical cylindrical shape of the Au nanorods and even the formation of Au nanoparticles in other shapes, such as nanocubes, nano-dogbones, nanopolyhedral, and branched nanocrystals [104]. It is particularly worth mentioning that silver ions in the growth solution are the key factor that controls the dimensions of the resulting Au nanorods. In addition, the properties of the surfactants, such as chain length, head group structure, counterions, and even the purity of CTAB surfactant, play important roles in the nanorod growth. Korgel and coworkers [105] reported that even with exactly the same recipe, CTAB from different suppliers with different catalog numbers affects not only the aspect ratio but also the yield and monodispersity of the nanorods, due to the existence of impurities. They later found out that iodide, the low concentration impurity in CTAB, is the key shape-directing element that inhibits the nanorod growth [106].

Au nanorods can also be conveniently prepared by seedless photochemical growth in the presence of selected surfactants. Yang and coworkers first synthesized uniform Au nanorods with tunable aspect ratios in the range of 1–5 by irradiating gold ions in a micellar solution with a 254-nm ultraviolet light (420 $\mu W/cm^2$) for $\sim$30 h [107]. In analogy to the seed-mediated synthesis, the aspect ratio of the resulting Au nanorods can be controlled through the addition of silver ions using this photochemical approach [107–110]. In addition to the silver ions, the photochemical anisotropic growth of Au nanorods can also be controlled by other experimental parameters, such as irradiation light source and additives in the reaction solutions [111–113].

Lithographic techniques are top-down methods used in the production of Au nanostructures with highly controllable dimensions and orientation. Well-aligned Au nanorod structures supported on substrates have been fabricated using electron beam lithography (EBL) [114] and focused ion beam (FIB) lithography techniques [115]. However, these lithography techniques are not as widely used for nanorod fabrication as the bottom-up chemical approaches mentioned above due to three major reasons. First, lithographic techniques are much more expensive and time-consuming than bottom-up chemical approaches. Second, nanorods generated through lithography approaches are much larger than those from bottom-up chemical approaches due to the resolution limit of these top-down techniques. Third, nanostructures can be fabricated over a limit area of a substrate each time, and large-scale fabrication of free-standing nanorods is beyond the capability of lithographic techniques.

6.3 Geometry-Dependent LSPR Lifetimes of Au Nanorods

In addition to the LSPR frequencies, the LSPR linewidths of Au nanorods have also been observed to be dependent on the geometric parameters of the nanorods. Upon plasmonic excitation, the collective electron oscillations may undergo a number of damping or dephasing processes, either radiatively or nonradiatively, which ultimately result in the decay of the plasmon. Radiative damping occurs when the oscillating dipole moment of the plasmon gives rise to photon emission, while nonradiative damping occurs when the plasmon excites intraband or interband electronic transitions or through electron scattering processes at the surface of the nanostructures. The resonance linewidth provides a measure of these processes as it is inversely proportional to the plasmon lifetime [116]. Using ensemble spectroscopies to accurately characterize the intrinsic LSPR linewidth of nanoparticles has been challenging because the measured LSPR linewidth only provides ensemble-averaged information that includes both inhomogeneous broadening due to the size and shape distributions of the samples and the intrinsic band broadening of individual nanoparticles. Therefore, single-particle spectroscopic measurements have to be carried out to accurately probe the intrinsic LSPR linewidth of individual nanoparticles.

Sönnichsen et al. [117] used a dark-field microscope to measure the Rayleigh scattering from individual nanospheres of various sizes and individual nanorods with varying aspect ratios (see Fig. 1.12). They found that the longitudinal LSPRs of nanorods were significantly narrower than those of nanospheres and the LSPR linewidths of nanorods decreased as the aspect ratio of nanorods increased, indicating that the higher aspect ratios corresponded to longer LSPR lifetimes. There are numerous decay routes available to the longitudinal LSPR of nanorods. By tailoring the geometric parameters of nanorods, one can modify the plasmon decay pathways and achieve the optimized geometry that gives rise to the longest plasmon lifetimes [118]. The LSPR linewidths of nanorods have also been found to be determined by the width of the nanorods. Hartland and coworkers [116] measured the light scattering from individual Au nanorods of various widths but approximately the same aspect ratios. Keeping the aspect ratio constant ensures that the resonance frequencies and, therefore, the bulk dephasing contributions are similar for all samples. Due to the increased radiative damping associated with larger volumes, linewidth broadening was observed as the width of the nanorod increased. However, increased broadening for small nanorod widths was also observed due to the surface scattering of electrons occurring when the nanorod dimension became significantly smaller than the electronic mean free path of Au (~20 nm). These two competing processes lead to an optimum nanorod width in the range of 10–20 nm where the resonance is sharpest and the LSPR lifetime is the longest.

6.4 Geometrically Tunable Photoluminescence of Au Nanorods

Bulk materials of noble metals, such as Au, Ag, and Cu, exhibit extremely weak fluorescence with quantum yield on the order of 10^{-10} due to the rapid nonradiative

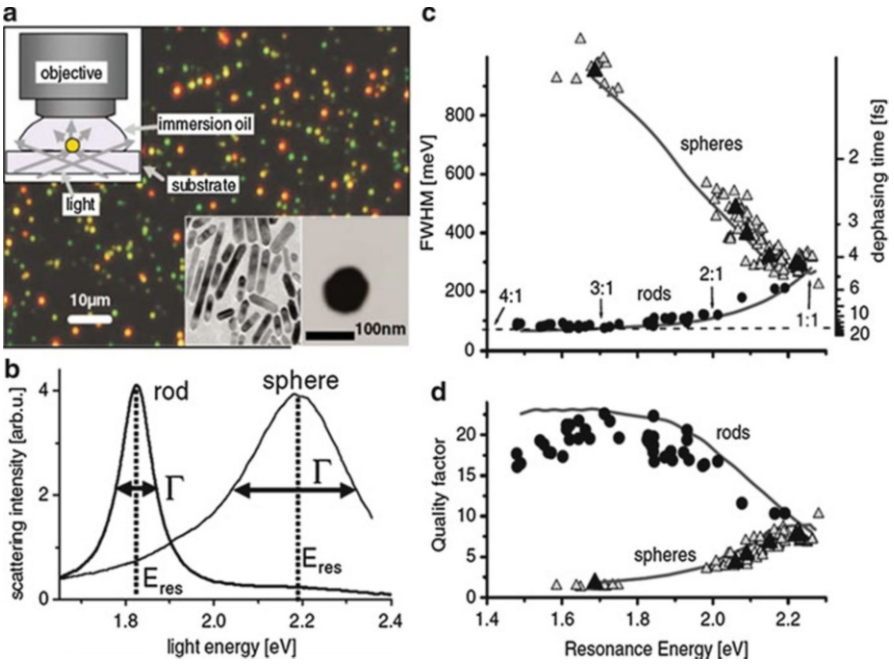

Fig. 1.12 (**a**) True color photograph of a sample of Au nanorods (*red*) and 60-nm nanospheres (*green*) in dark-field illumination (*inset upper left*). *Bottom right*: TEM images of a dense ensemble of nanorods and a single nanosphere. (**b**) Light-scattering spectra from a Au nanorod and a 60-nm Au nanosphere measured under identical conditions (light polarized along the long rod axis). (**c**) Measured linewidth Γ of plasmon resonances in single nanorods (*dots*) and nanospheres (*open triangles*) versus resonance energy E_{res}. (**d**) Same data plotted as quality factor $Q = E_{res}/\Gamma$ (Reprinted with permission from Ref. [117]. Copyright 2002 American Physical Society)

electron–hole recombinations [119]. Experimental and theoretical results published by Shen and coworkers [120] indicate that photoluminescence of noble metals can be attributed to an interband recombination of the electrons and holes. In contrast to the weak emission from bulk metals, large enhancement in emission on roughened metal surfaces has been observed largely due to local field enhancements around the surface of the metal [120].

Au nanorods exhibit interesting geometrically tunable photoluminescence properties. Although it essentially arises from interband recombinations of electrons and holes, the photoluminescence of Au nanorods is sensitively dependent on the tunable LSPRs. Mohamed and El-Sayed et al. [121] observed that Au nanorods with aspect ratios less than 3 have fluorescence quantum efficiency on the order of 10^{-4} to 10^{-3}, which is 6–7 orders of magnitude higher than that observed in the bulk materials, whereas almost no photoluminescence enhancements are observable for Au nanospheres. Such emission enhancements are directly related to the longitudinal LSPR of Au nanorods as the polarization of the emission is along the

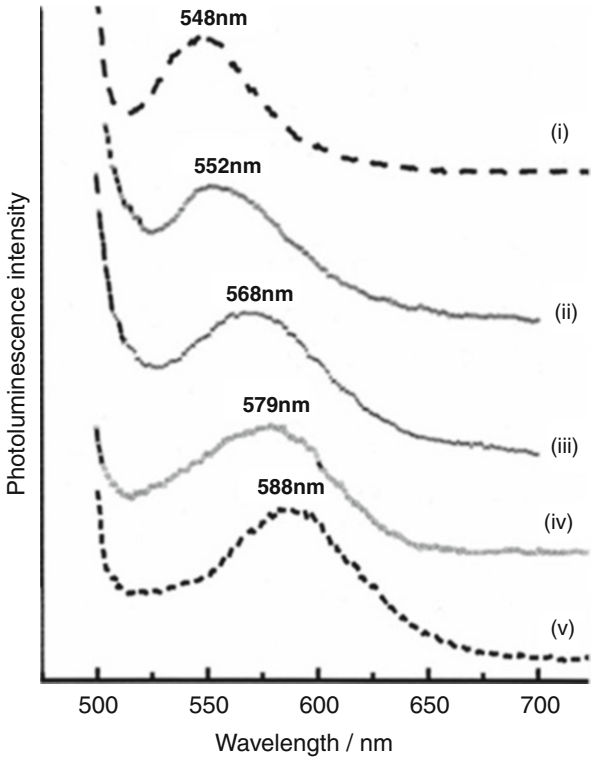

Fig. 1.13 Photoluminescence spectra i, ii, iii, iv, and v for Au nanorods of average aspect ratios of 2.0, 2.6, 3.3, 4.3, and 5.4, respectively. The excitation wavelength is 488 nm (Reprinted with permission from Ref. [121]. Copyright 2005 American Chemical Society)

long rod axis. The excitation of interband absorption simultaneously excites the longitudinal LSPR of Au nanorods, which results in enhanced local electric fields amplifying both excitation and emission fields. Interestingly, the photoluminescence maximum wavelength is found to increase linearly with increasing aspect ratio (Fig. 1.13) [122]. The quantum efficiency increases quadratically for aspect ratios below three and then begins to diminish thereafter. A detailed examination of the enhanced emission intensity was carried out for nanorods including high aspect ratios by Eustis and El-Sayed. Both the experimental data and simulation results show that the emission depends on three important factors: (1) the intensity of enhanced electric field associated with the longitudinal LSPRs, (2) the extent of spectral overlap between the interband absorption band and the LSPR band which determines the enhancement of the interband absorption of light, and (3) the overlap of the fluorescence spectrum of Au with the LSPR absorption band which determines the enhancement of the outgoing emitted fluorescence light. Because the LSPR absorption shifts to longer wavelengths as the nanorod aspect ratio increases,

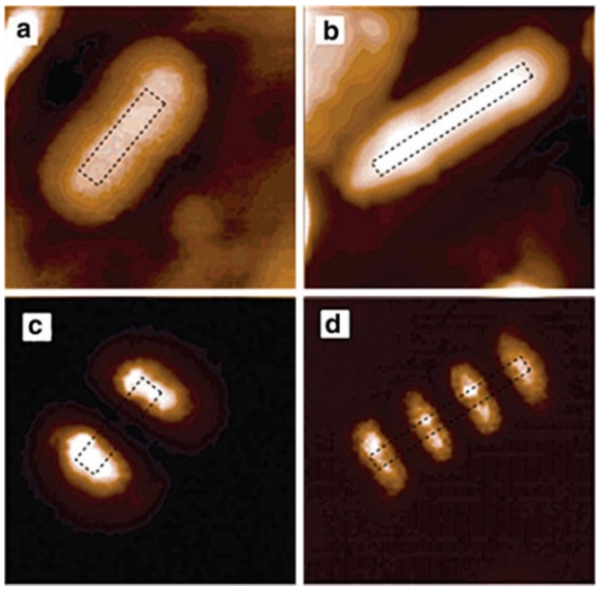

Fig. 1.14 (**a**, **b**) Topographic images of Au nanorods. (**c**, **d**) TPI-PL images for **a** and **b**, respectively (Reprinted with permission from Ref. [124]. Copyright 2004 American Chemical Society)

the extent of the overlap between the interband processes and the longitudinal LSPR absorption band will change accordingly. In the small aspect ratio regime, increase in the aspect ratio results in greater spectral overlap responsible for an emission enhancement. In the large aspect ratio regime, however, further increase in aspect ratio diminishes the degree of spectral overlap, resulting in decreased emission intensities.

Similar to one-photon photoluminescence, the two-photon-induced photoluminescence (TPI-PL) peaks of Au nanorods also redshift with increasing aspect ratio [123] and are more intense than that of spheres. The TPI-PL response originates from the sequential excitation of an intraband transition from just below the Fermi level, followed by a second d-band excitation to where the hole was created by the first excitation. Photoluminescence subsequently occurs when the remaining radiative charge–hole recombination takes place. Since two-photon optical processes involve an additional field enhancement, further enhanced photoluminescence is expected in comparison to the one-photon case. It has been reported by Okamoto and coworkers [124–126] that TPI-PL is also useful for revealing the near-field enhancements of individual Au nanorods associated with LSPR excitations (Fig. 1.14). Observation of TPI-PL from single nanoparticles enabled by NSOM measurements provides essential information for revealing the spatial distribution of the electric fields near the nanoparticle when a characteristic LSPR mode is excited. By locally exciting regions along the length of the nanorod while simultaneously monitoring the TPI-PL from the entire nanorod, the portions of the nanorod that yielded the strongest response can be mapped out [124–126]. Where the plasmon shows the strongest internal electric field, it also shows the strongest TPI-PL. Because of their interesting NIR TPI-PL properties, molecularly targeted

Au nanorods have been used as contrast agents for TPI-PL-based bioimaging both in vitro and in vivo [127, 128]. The TPI-PL signals from a single nanorod are found to be 57 times higher than those from a single rhodamine molecule [127].

7 Metallic Nanoshells

7.1 Tunable LSPRs of Nanoshells

Metal nanoshells are a class of fascinating subwavelength photonic particles with highly tunable plasmonic properties [24]. A nanoshell is composed of a spherical dielectric or semiconducting core homogenously coated with a concentric nanoscale metallic shell. By tailoring the geometric parameters of nanoshells, one can fine-tune the particles' light absorption and scattering properties all the way across the visible and NIR spectral regions, enabling widespread applications, such as optically triggered drug delivery [129], chemical and biomolecular sensing [130], surface-enhanced spectroscopies [131–134], and cancer diagnostic and photothermal therapy [9, 135, 136].

Because nanoshells are spherically symmetric, their LSPRs can be analytically described by Mie scattering theory. In 1951, Aden and Kerker [137] first proposed the model for simulating the absorption and scattering of electromagnetic waves from a spherical particle consisting of a dielectric core and a metallic shell based on Mie scattering theory. Neeves and Birnboim [138] proposed in 1989 that such a core–shell geometry could give rise to LSPR modes with their wavelengths tunable over a broad spectral range. The LSPRs of a nanoshell are extraordinarily sensitive to the inner and outer dimensions of the metallic shell layer. Figure 1.15 shows the optical extinction spectra of Au nanoshells calculated using Mie scattering theory [23]. In this set of calculations, the radius of the silica core was fixed at 60 nm, and the shell thickness was varied from 5 nm to 20 nm. Since the overall sizes of the Au nanoshells are beyond the quasi-static limit, both the dipole and quadrupole LSPR bands show up in the extinction spectra and progressively redshift as the shell thickness decreases. In this example, as the core radius–shell thickness ratio is varied between 3 and 12, the predicted resonances of the nanoshells span a range of 300 nm in wavelength. In contrast, if the order of these layers were inverted, that is, a Au core and a dielectric silica shell, less than a 20-nm optical resonance shift would be expected.

There is a long development gap between the original theoretical predictions about nanoshell plasmons and the experimental realization of the nanoshell geometry. The earliest example of experimentally fabricated nanoshells is Au_2S–Au core–shell nanoparticles produced by the reduction of $HAuCl_4$ in an aged Na_2S solution [22, 139]. By adjusting the amount ratios between $HAuCl_4$ and Na_2S, Au_2S–Au nanoshells can be grown with different core sizes and shell thicknesses. However, the tuning range of the overall size (<40 nm) and LSPR wavelength (600–900 nm) of the Au_2S–Au nanoshells is rather limited. Additionally, a large number of Au colloids are formed as a secondary product, generating an additional absorption peak at ~520 nm.

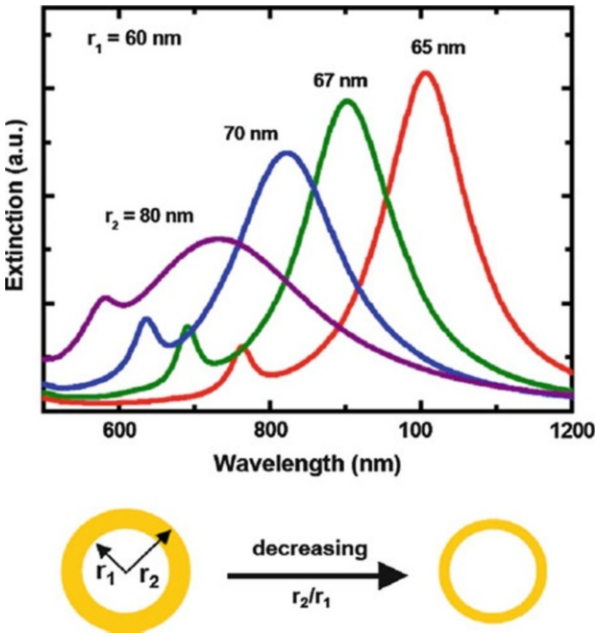

Fig. 1.15 Plasmonic tunability demonstrated for nanoshells with an inner silica core radius $r_1 = 60$ nm and an overall particle radius $r_2 = 65$, 67, 70, and 80 nm. The plasmon resonance (extinction) of the particles redshifts as r_1/r_2 increases (Adapted with permission from Ref. [23]. Copyright 1998 Elsevier B. V.)

Halas and coworkers have done pioneering work on the fabrication of metal nanoshells through a multistep, seed-mediated electroless plating approach [23]. In 1998, they controllably fabricated silica–Au core–shell nanoparticles, which overcame many of the limitations of the Au_2S–Au nanoshells. The whole procedure for the fabrication of the silica–Au nanoshells can be schematically illustrated in Fig. 1.16a. Highly monodisperse silica cores with precisely controlled diameters ranging from 50 to 800 nm are fabricated using the Stober method [140]. The surfaces of the silica core particles are then functionalized with amine groups, and small Au colloids (1–2 nm) are subsequently adsorbed onto the silica surfaces through Au–amine interactions. The immobilized Au colloids act as nucleation sites that catalyze the electroless plating of Au to form Au islands on the surface of silica. As increasing amount of Au is plated, the Au islands gradually grow larger and eventually coalesce to form a complete Au nanoshell. Figure 1.16b shows a set of TEM images that reveal the whole process of Au nanoshell growth on the surface of the silica cores. The final thickness of the Au nanoshells, which is typically in the range from 5 to 100 nm, can be precisely controlled by adjusting the amount ratio between silica and $HAuCl_4$ added. By using this seed-mediated electroless plating method, continuous Au [141–143], Ag [144, 145], Cu [146], and bimetallic nanoshells [147] with controllable core and shell dimensions have been successfully fabricated using silica, polymer, or cuprous oxide beads as core materials. The experimental extinction spectra of nanoshells show very good agreement with the calculated results using Mie theory, both at the ensemble [23, 148, 149] and single-nanoparticle levels [150].

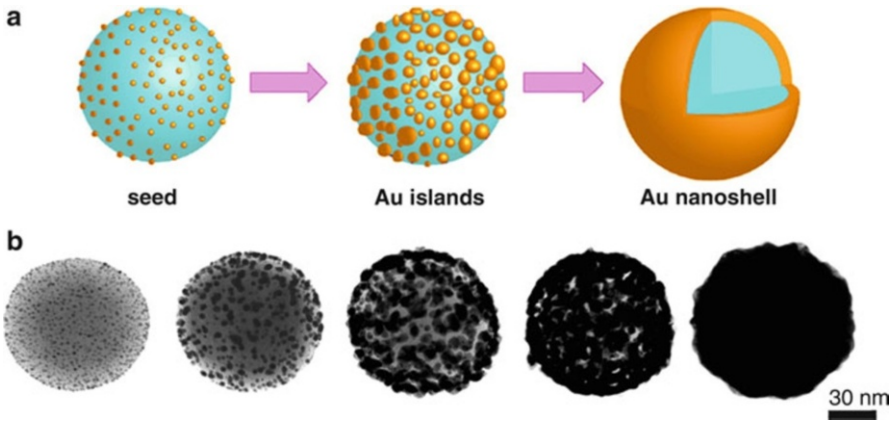

Fig. 1.16 (**a**) Scheme of seed-mediated electroless plating of Au nanoshells surrounding silica cores. (**b**) TEM images that reveal the whole process of Au nanoshell growth on the surface of silica cores (Reprinted with permission from Ref. [23]. Copyright 1998 Elsevier B. V.)

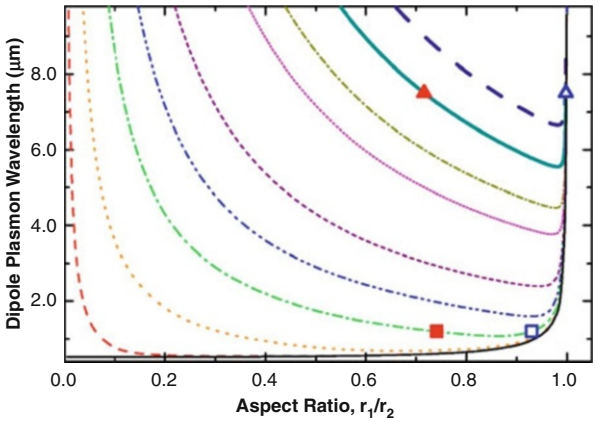

Fig. 1.17 Calculated dipole plasmon resonance of silica core–Au shell nanoshells with core radii of 0.1 (*solid*), 10 (*dashed*), 50 (*dotted*), 120 (*dash dotted*), 200 (*dash dot dotted*), 300 (*short dashed*), 500 (*short dotted*), 600 (*short dash dotted*), 750 (*thick solid*), and 900 nm (*thick dashed navy*). The *solid* and *hollow triangles* and *squares* are experimental data (Reprinted with permission from Ref. [151]. Copyright 2007 American Institute of Physics)

By tailoring the relative core–shell ratio and overall sizes of nanoshells, the frequencies of nanoshell LSPRs can be fine-tuned all the way across the visible, NIR, and mid-IR regions [23, 148, 151]. In Fig. 1.17, the optical resonance as a function of core–shell ratio is calculated for the silica–Au nanoshell system with varying overall dimensions both within and beyond the quasi-static limit [152]. These theoretical studies indicate that for small silica–Au nanoshells within the

quasi-static limit, inner–outer radius ratios close to 1 could in principle give rise to optical resonances shifted into the infrared as far as 10 μm in wavelength, though nanoshells with these extremely thin shells are impossible to fabricate experimentally. Known as phase retardation or finite size effects, the immediate impact of increasing particle size beyond the quasi-static limit results in a systematic shifting of the dipole plasmon to lower energies and a significant broadening of the plasmon resonance linewidth. Higher-order multipolar resonances appear as particle size is increased, as distinct spectral features at energies higher than that of the dipolar plasmon energy. Although the dipolar plasmon response of metallic nanoshells has been shown to be remarkably robust in the presence of defects or imperfections in the nanoparticle's metallic layer, the higher-order modes can be significantly damped by nanoscale surface texturing of the nanoshells [153, 154]. Practically, one can shift the nanoshell LSPRs deep into the IR region using nanoshells with relatively large core sizes and thin shell thicknesses. For small nanoshells within the quasi-static limit, the extinction properties are dominated by absorption rather than scattering, while for large nanoshells beyond the quasi-static limit, the extinction is dominated by scattering. Therefore, one can selectively tune the light absorption and scattering properties of nanoshells by controlling the overall size of the nanoshells.

Nanoshell LSPRs are also much more sensitive to local environment than solid nanospheres [149], significantly redshifting as the refractive index of surrounding medium increases. The sequence of LSPR sensitivity is typically dipole > quadrupole > octupole > higher-order modes. The LSPR sensitivity of nanoshells depends primarily on overall nanoparticle size and less sensitively on the core–shell ratio. Understanding how the geometrical parameters control LSPR sensitivities offers insight toward the design and engineering of nanoshell sensors for LSPR sensing applications.

Although the geometry dependence of nanoshell LSPRs can be analytically described by the Mie scattering theory, this classical electromagnetic theory provides little insights into the origin of nanoshells' optical tunability. Numerical computation methods, such as FDTD, have been used to simulate the plasmonic properties of nanoshells [155]; however, they do not provide a clear picture of the underlying physics behind the geometrically tunable nanoshell plasmons. In this context, plasmon hybridization theory, a plasmonic analog to the molecular orbital theory, has emerged as an effective and powerful method that can be used to fundamentally interpret the origin of the plasmonic tunability of metal nanoshells [156–158]. Next we will briefly introduce the basic ideas of plasmon hybridization model and demonstrate how it can be used to interpret the structure–property relationship of nanoshells. The plasmon hybridization picture extends to an entire family of nanoshell-based geometries with increasing structural complexity, such as multilayer shell-in-shell structures known as nanomatryushkas, nanoshells with offset cores known as nanoeggs, semi-nanoshell structures (half-shells, nanocups, and nanocaps), and spheroidal nanoshells known as nanorice. We will demonstrate how plasmon hybridization model can be used as a powerful tool to both predict and analyze the tunable optical properties of these complex nanoshell-based structures.

7.2 Plasmon Hybridization Model

Plasmon hybridization theory provides a conceptually enlightening method for calculating the plasmon resonance of complex nanostructures. The basic idea of plasmon hybridization theory is to deconstruct a nanoparticle or composite structure into more elementary shapes and then calculate how the primitive plasmons supported by the elementary geometries interact or hybridize with each other to form the hybridized plasmons of the composite structure. This theory enables scientists to draw on decades of intuition from molecular orbital theory to predict the plasmonic response of nanostructures with increasing structural complexity [159].

Plasmon hybridization model considers the conduction electrons of a metal to be a charged, incompressible, and irrotational fluid sitting on a rigid, uniform, and positive background charge representing the fixed ion cores. The deformation of the fluid can be expressed in terms of a scalar function η. Infinitesimal deformations in this fluid give rise to a surface charge density that interacts electrostatically, and plasmons are considered to be the self-sustained oscillations of this electron fluid. The Lagrangian for such a system is

$$L = \frac{n_0 m_e}{2} \int \eta \vec{\nabla} \eta \cdot dS - \frac{1}{2} \int \frac{\sigma(\vec{r}) \sigma(\vec{r}')}{|\vec{r} - \vec{r}'|} dS dS' \tag{1.13}$$

where n_0 is the free-electron density, m_e is the mass of electrons, and σ is the surface charge density,

$$\frac{d}{dt}\sigma = n_0 e \frac{d\eta}{d\hat{n}} \tag{1.14}$$

and the integrations are performed over all surfaces of the metal. The plasmon modes of the systems are obtained from the Euler–Lagrange equations.

In the context of plasmon hybridization model, the geometry-dependent nanoshell plasmon resonances result from the interaction between the essentially fixed-frequency plasmon response of a sphere and that of a cavity (Fig. 1.18a) [156, 157, 159]. Sphere and cavity plasmons are electromagnetic excitations at the outer and inner interfaces of the metal shell, respectively. Because of the finite thickness of the shell layer, the sphere and cavity plasmons interact with each other and hybridize in a way analogous to the hybridization between atomic orbitals. This interaction results in the splitting of the plasmon resonances into two new resonances, the lower-energy symmetric or "bonding" plasmon (ω_-) and the higher energy antisymmetric or "antibonding" plasmon (ω_+).

The hybridization of the cavity and the sphere plasmons depends on the difference in their energies $\omega_{C,l}$ and $\omega_{S,l}$ and on their interaction, which is determined by the thickness of the shell. To describe the geometry of a nanoshell, the notation (a, b) is adopted to indicate the inner radius a and the outer radius b of the shell. The hybridization between the cavity and sphere

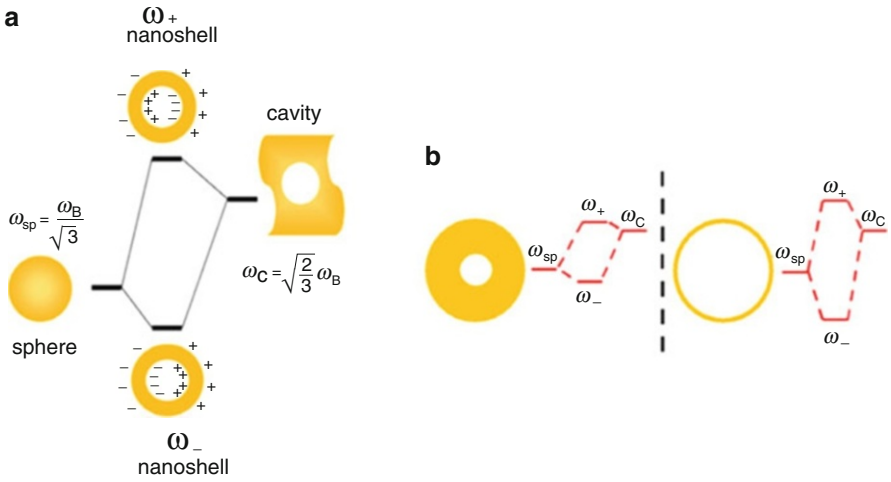

Fig. 1.18 Energy-level diagram (**a**) depicting plasmon hybridization in metal nanoshells and (**b**) illustrating the dependence of nanoshell plasmon energies on the strength of the interaction between the sphere and cavity plasmons, determined by the thickness of the metallic shell (Reprinted with permission from Ref. [159]. Copyright 2007 American Chemical Society)

plasmons gives rise to two hybridized plasmon modes $|\omega_+\rangle$ and $|\omega_-\rangle$ for each $l > 0$. The frequencies of these modes are

$$\omega_{l\pm}^2 = \frac{\omega_B^2}{2}\left\{1 \pm \frac{1}{2l+1}\left[1 + 4l(l+1)\left(\frac{a}{b}\right)^{2l+1}\right]^{1/2}\right\} \tag{1.15}$$

The $|\omega_+\rangle$ mode corresponds to antisymmetric coupling between the sphere and cavity modes, and the $|\omega_-\rangle$ mode corresponds to symmetric coupling between the two modes (see Fig. 1.18b). The ω_- plasmon interacts strongly with the incident optical field, while the ω_+ mode interacts weakly and, in the case of Au, is further damped by interband transitions at energies above the d-band to Fermi energy optical transitions at approximately 2.3 eV.

The validity of this expression for the nanoshell plasmon energies has been explicitly verified using fully quantum mechanical calculations [160]. Although the resulting plasmon energies are the same as what would be obtained from a Drude dielectric function and classical Mie scattering theory in the quasi-static limit, the present treatment very clearly elucidates the nature of the nanoshell plasmon resonances and, in particular, the microscopic origin of their sensitive dependence on geometry. For example, this picture provides a simple and intuitive explanation for why the energy of the optically active plasmon resonance shifts to lower energies with decreasing shell thickness: the decreased shell thickness leads to a stronger coupling between the sphere and cavity plasmons, increasing the splitting between the bonding and antibonding hybridized plasmons. The plasmon

hybridization model can also be used to interpret the LSPR sensitivity of nanoshells to surrounding medium. As illustrated in Fig. 1.18b, the optically bright plasmon mode (ω_-) is more sphere-like, while the optically dark plasmon mode (ω_+) is more cavity-like. Therefore, ω_- sensitively shifts upon a change in refractive index of the embedding medium, while ω_+ is more sensitive to the change of the core materials.

7.3 Nanomatryushkas

The plasmon hybridization picture extends naturally to more complicated multilayer nanoshell structures known as nanomatryushkas [156, 161]. The nanomatryushka geometry can be experimentally realized by first growing a uniform nanoscale layer of Au surrounding a silica nanoparticle, then coating this nanoparticle with a silica layer of controlled thickness, followed by the growth of a second thin Au layer. A schematic depicting the composition of this particle is shown in Fig. 1.19a. The plasmon responses of this structure can be understood as a hybridization of the plasmon resonances of the inner and outer nanoshells. As illustrated in Fig. 1.19b, for each multipolar symmetry, there are four linearly independent plasmon modes. Obviously, the thickness of the dielectric spacer layer $|a_2 - b_1|$ controls the strength of the coupling between the inner and outer nanoshells, whose plasmon resonances can each be tuned independently.

The energy-level diagram in Fig. 1.19b depicts the hybridization of the concentric nanoshell plasmons in terms of the mixing of the inner- and outer-shell plasmons. The experimentally observable eigenmodes correspond to the hybridization of the bonding plasmon modes of the two metal shell layers. Figure 1.19c shows the strong coupling case. Spectrum (1) shows the experimental and theoretical extinction spectra for the isolated inner-shell plasmon $\left|\omega_{-,NS1}\right\rangle$. Spectrum (2) is the theoretical extinction spectrum of the isolated outer-shell plasmon $\left|\omega_{-,NS2}\right\rangle$, calculated as though the inner-shell structure was replaced wholly by a dielectric (silica) core. Spectrum (3) is the experimental and theoretical extinction for the concentric nanoshell in which $\left|\omega^{+}_{-,CS}\right\rangle$ and $\left|\omega^{-}_{-,CS}\right\rangle$ plasmons are clearly apparent. The plasmon hybridization and splittings are quite strong because of the small interlayer spacing between inner- and outer-metal shell layers and the fact that the inner-shell plasmon $\left|\omega_{-,NS1}\right\rangle$ and outer-shell plasmon $\left|\omega_{-,NS2}\right\rangle$ are nearly resonant with each other. The hybridization of the plasmons appears to be strongly asymmetric primarily due to phase-retardation effects. A second contributing factor to the asymmetry is the small but finite interaction with the higher energy $\left|\omega_{+,NS1}\right\rangle$ and $\left|\omega_{+,NS2}\right\rangle$ plasmon modes. Figure 1.19d depicts a concentric nanoshell with a weak plasmon coupling between the inner and outer shell. In this case, the inner- and outer-plasmon resonances are detuned from each other in energy, as the spacing between inner and outer-metal layers is increased. Because the hybridization is weak, the concentric shell plasmon modes show only small shifts relative to the isolated shell plasmons. In Fig. 1.19e, a concentric nanoshell with a fully decoupled

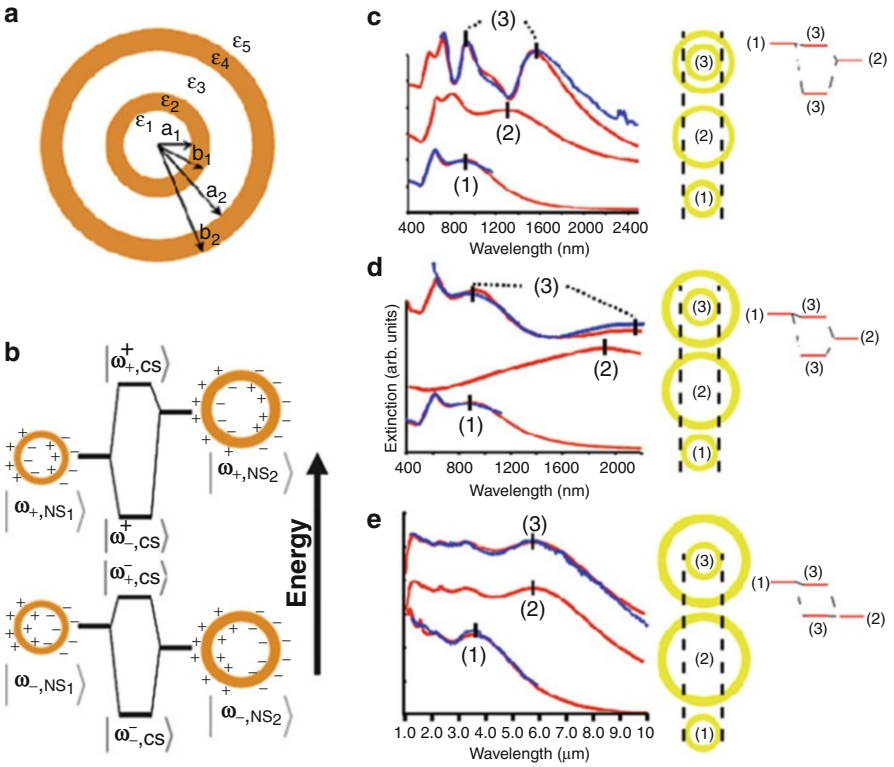

Fig. 1.19 (**a**) Concentric nanoshell geometry with concentric radii of core (a_1), inner shell (b_1), spacer layer (a_2), and outer shell (b_2) where ε_1 and ε_3 are assumed to be SiO_2, ε_2 and ε_4 are Au, and ε_5 is embedding medium. (**b**) Energy-level diagram of hybridization between the inner and outer nanoshell plasmons. (**c**) Experimental (*blue*) and theoretical (*red*) extinction spectra for concentric nanoshells (3), inner shell (1), and outer shell (2); the inner- and outer-nanoshell plasmons interact strongly, resulting in strongly hybridized plasmons. (**d**) The inner- and outer-nanoshell plasmons interact weakly with a relatively small change in the concentric nanoshell plasmon compared with single-nanoshell plasmons. (**e**) Noninteracting inner- and outer-shell plasmons (Adapted with permission from Ref. [156]. Copyright 2003 American Association for the Advancement of Science)

plasmon response is shown. In this case, the intershell spacing is so large that the concentric nanoshell response (3) appears to be almost indistinguishable from the calculated nanoshell response for the outer shell. Because of the large intershell spacing and the finite penetration depth of the light, the inner-nanoshell plasmon is not excited.

Recently, Halas and coworkers reported that the geometrically tunable optical properties of another type of nanomatryushkas are composed of a silica-coated gold nanosphere surrounded by a Au nanoshell layer in a sub-100-nm-size range [162]. The nanoshell was fabricated by seed-mediated electroless plating of Au onto silica-coated Au nanoparticles using CO as the reducing agent. This approach allows independent control over the size of the Au core, the silica layer thickness,

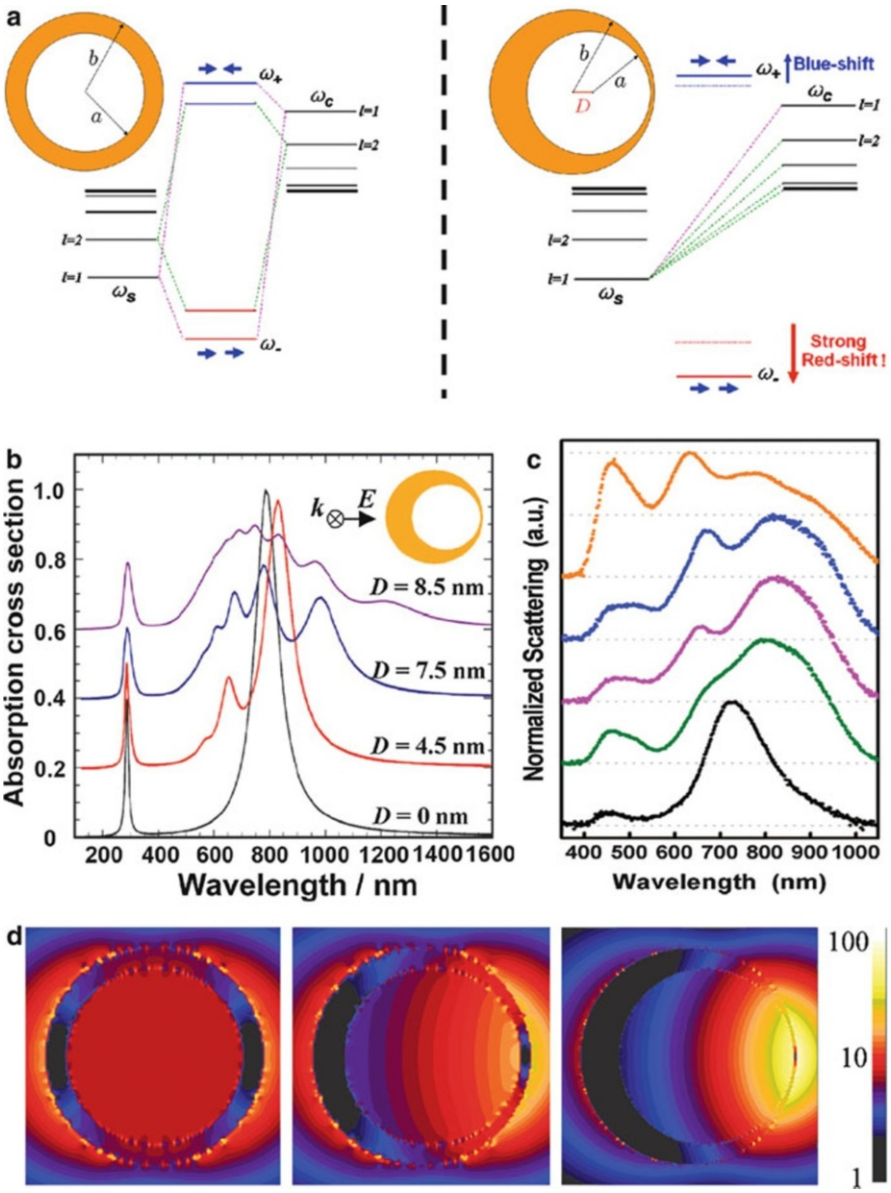

Fig. 1.20 (**a**) Schematic of plasmon hybridization in a nanoshell (*left*) and a nanoegg (*right*). (**b**) Theoretical absorption spectra as a function of offset D obtained by the plasmon hybridization method, for a $[a, b] = [39, 48]$-nm Au nanoshell with vacuum core. (**c**) Experimentally measured single-particle dark-field scattering spectra of a nanoshell (*black curve*, $[a, b] = [94, 103]$ nm.) and four nanoegg particles with varying core offset (*colored spectra*, D increases from bottom to top). (**d**) Near-field plots of $[a, b] = [39, 48]$-nm Au nanoshells with different offset cores and an empirically based dielectric function for Au. *Left*: $D = 0$ nm at $\lambda = 604$ nm. *Center*: $D = 4.5$ nm at

and the thickness of the Au nanoshell layer. Therefore, detailed investigation on plasmon hybridization between the Au nanosphere core and Au outer nanoshell becomes possible with minimized phase-retardation effects. As the core–shell interactions become stronger, a larger split between $\left|\omega^{+}_{-,CS}\right\rangle$ and $\left|\omega^{-}_{-,CS}\right\rangle$ can be observed with $\left|\omega^{-}_{-,CS}\right\rangle$ further redshifted and $\left|\omega^{+}_{-,CS}\right\rangle$ progressively blueshifts. The resulting plasmon resonances are in exact agreement with Mie scattering theory.

7.4 Nanoeggs

Symmetry breaking can introduce dramatic changes in the optical properties of the plasmonic nanoshells. The plasmon hybridization picture can be applied to a nanoshell with an offset core known as a nanoegg [163, 164]. For a spherically symmetric nanoshell, where the center of the inner-shell radius is coincident with the center of the outer-shell radius, plasmon hybridization only occurs between cavity and sphere plasmon states of the same angular momentum, denoted by multipolar index $l(\Delta l = 0)$. In the quasi-static limit, only the $l = 1$ dipolar bonding plasmon is excited by an incident optical plane wave. However, when the center of the inner shell is displaced with respect to the center of the outer shell, this selection rule is relaxed, and cavity and sphere plasmons of all multipolar indices hybridize. As a consequence, all plasmon modes can be optically excited, even in the dipole limit, resulting in a multipeaked and redshifted plasmonic response with increasing line-shape complexity as the core–shell displacement increases. The relaxation of the selection rules of plasmon hybridization due to symmetry breaking is schematically illustrated in Fig. 1.20a.

A nanoegg with a dielectric core of radius a displaced a distance D from the center of an outer shell of radius b can be denoted (a, b, D) and is schematically illustrated as an extension of the spherically symmetric nanoshell geometry in Fig. 1.20a. The deformation field can be expressed as a gradient of a scalar potential η [157], which takes the form

$$\eta(r_C, \Omega_C, r_S, \Omega_S) = \sum_{lm} \left[\sqrt{\frac{a^{2l+1}}{l+1}}\, \dot{C}_{lm}(t) {r_C}^{-l-1} Y_{lm}(\Omega_C) \right] + \sqrt{\frac{1}{l b^{2l+1}}}\, \dot{S}_{lm}(t) r_S^l Y_{lm}(\Omega_S) \tag{1.16}$$

Fig. 1.20 (continued) λ = 619 nm. *Right*: D = 7.5 nm at λ = 674 nm. Maximum field enhancements $|E|/|E_0|$ are 13.8, 24.5, and 67.7 from left to right. The incident field is horizontally polarized (Reprinted with permission from Ref. [163]. Copyright 2006 National Academy of Sciences of the United States of America)

where (r_C, Ω_C) are spherical coordinates centered in the cavity and (r_S, Ω_S) are spherical coordinates with an origin at the center of the spherical outer shell. The quantities of C_{lm} and S_{lm} are the amplitudes for the primitive cavity and sphere plasmons, respectively. For finite offset D, the spherical harmonics centered on the two different origins are no longer orthogonal for different l, resulting in interactions between the cavity and sphere modes in a manner analogous to the coupling between the individual nanoparticle plasmons of a nanoparticle dimer or in periodic structures of metallic nanoparticles in close proximity [158, 165, 166].

The Lagrangian for this system can be constructed directly from η. The structure of the resulting eigenvalue problem is illustrated in Fig. 1.20a [163]. The left panel shows the resulting plasmon modes for a spherically symmetric nanoshell. In this case, the plasmon energies depend on multipolar index l but not on the azimuthal index m which labels the $2l + 1$ possible orientations of the plasmon modes. For finite offset D (right panel), an interaction exists between all cavity and sphere modes of the same m. This leads to stronger hybridization and an admixture of all primitive cavity and sphere plasmons. For simplicity, we will refer to these reduced-symmetry nanoparticle plasmon modes by multipolar index l, corresponding to the spherical or zero-offset case, although for finite offset the plasmon modes contain an admixture of plasmons of all l for a given m. For the nonconcentric nanoshell, the coupling of the cavity and sphere plasmons depends on azimuthal m, but the resulting plasmon energy spectrum is only weakly dependent upon orientation. Figure 1.20b shows the theoretical optical absorption spectra of nanoeggs with $[a, b] = [39, 48]$ nm as a function of core-offset D obtained by the plasmon hybridization model. As D increases, the $l = 1$ mode is redshifted and the higher l modes, now also dipole active, contribute additional peaks to the spectrum, resulting in increased spectral line-shape complexity with increasing D. The calculated spectra using the plasmon hybridization model are in very good agreement with the results of FDTD simulations.

Nanoeggs are experimentally fabricated by anisotropically depositing additional metallic Au onto preformed silica − Au concentric nanoshells [163]. The Au nanoshells are first immobilized onto polyvinylpyridine-functionalized glass substrates as a sub-monolayer of isolated nanoshells. The nanoshell films are subsequently immersed in an aqueous solution containing an appropriate amount of chloroauric acid and potassium carbonate, where the addition of formaldehyde then initiates the electroless plating of Au onto the nanoparticle surfaces. The films are subsequently removed from the plating solution, rinsed, and dried. As a result, all the nanoeggs fabricated in this manner have the same orientation on the glass slides, with the point of contact with the glass substrate corresponding to the minimum in shell thickness for each nanoparticle. Increasing the time duration of the plating process results in an increase in the effective core offset of each nanoegg particle. The immobilized nanoeggs can be released into a solvent through sonication to form free-standing colloidal nanoegg particles. Figure 1.20c shows the single-particle scattering spectra of individual nanoeggs of increasing asymmetry. As the offset between the center of the inner- and outer-shell radius increases, the optical spectrum broadens and includes additional peaks adjacent to the original

dipolar plasmon resonance which is significantly redshifted. The experimentally obtained single-particle spectra clearly show the characteristic offset-dependent multipeaked features that are predicted by the plasmon hybridization model.

Another striking feature arising from the symmetry breaking is the near-field enhancement on the surface of nanoeggs. Figure 1.20d shows the local field enhancements calculated using the FDTD method for nanoeggs with a silica core and Au shell modeled using the empirically obtained dielectric function for Au. The largest field enhancements achievable on the outer surface dramatically increase as the core-offset D increases. Such large field enhancements on the open, exterior surface of an individual nanoparticle make nanoegg extremely promising for ultrasensitive molecular sensing based on surface-enhanced spectroscopies.

7.5 Semi-Shell Nanostructures

The case of nanoeggs has clearly demonstrated that the symmetry breaking of individual plasmonic nanostructures has profound impact to their optical properties. If a further reduction in symmetry of nanoeggs occurs when the shell is completely removed from one side of the spherical nanoparticle core, it would then result in partially broken semi-shell nanostructures known as half-shells, nanocups, or nanocaps, depending on how much of the shell is preserved in the final structures. The plasmonic responses of these semi-shell nanostructures become a sensitive function of the orientation of the nanostructure with respect to the incident light due to the asymmetry of the particle geometry.

Whitesides and coworkers fabricated semi-shell nanostructures at an approximately 50 % metal coverage (half-shell) by vertical evaporation of metal onto dielectric nanoparticles predeposited on a substrate [167]. These half-shell structures show highly tunable plasmonic properties that are significantly redshifted in comparison to the solid nanosphere plasmons. As demonstrated using Au half-shells [168], both decrease in shell thickness, and increase in core size will shift the LSPRs dramatically to longer wavelengths. Halas and coworkers [169] reported a chemical approach to two types of reduced-symmetry nanoparticles: nanocups, with approximately $70 - 80$ % metal coverage, and nanocaps, the inverse structure with approximately $20 - 30$ % metal coverage. The plasmon response of both nanocups and nanocaps was dependent upon the nanoparticle orientation with respect to incident light and polarization angle.

By carefully adjusting the angle of metal deposition with respect to the substrate orientation, Lee and coworkers [170] fabricated Au nanocup structures with sharp shell edges, which they called as nanocrescent moons (see Fig. 1.21). Unique multiple scattering peaks are observed in a single Au nanocrescent moon with dark-field white-light illumination. The sub-10-nm sharp edge of Au nanophotonic crescent moons incorporates the advantages of both metallic sharp nanotips and ultrathin nanorings and generates intense local electromagnetic-field enhancements. Lee's group later demonstrated [171] that by further incorporating magnetic components into the nanocrescent moons, each nanocrescent particle cannot only

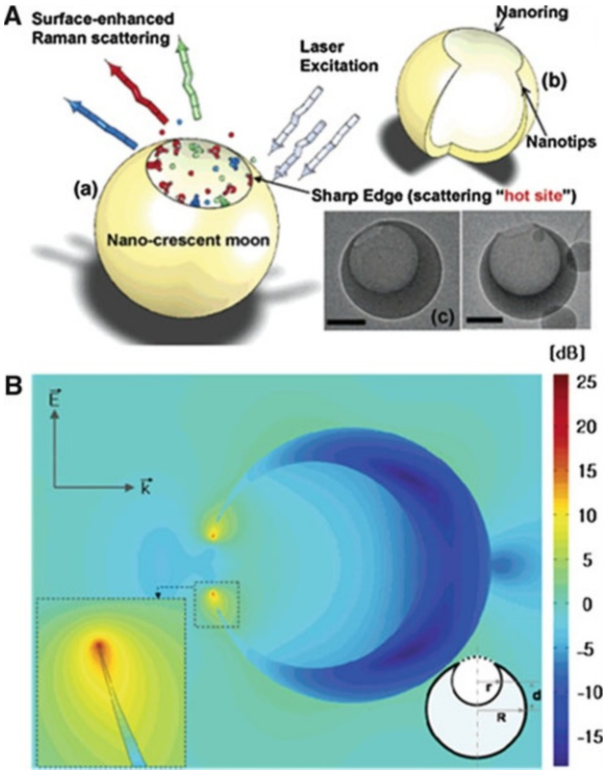

Fig. 1.21 (**A**) Au nanocrescent moons with sharp edges. (*a*) Conceptual schematics of a nanocrescent moon SERS substrate. The Au surface can be functionalized with biomolecular linker to recognize specific biomolecules. The sharp edge of the nanocrescent moon can enhance the Raman scattering intensity so that the biomolecules on it can be detected. (*b*) Geometrical schematics of a nanocrescent moon. A Au nanocrescent moon with sharp edges integrates the geometric features of nanoring and nanotips. (c) TEM images of two nanocrescent moons. Scale bars: 100 nm. (**B**) Local electric field amplitude distribution of a nanocrescent moon excited at 785 nm (Reprinted with permission from Ref. [170]. Copyright 2005 American Chemical Society)

serve as stand-alone SERS substrates with high local electromagnetic-field enhancement factors but also be manipulated by external magnetic fields to produce translational and rotational motion of the nanoprobes.

The nanocup structures can also be obtained through a unique electron-beam-induced ablation process as demonstrated by Halas and coworkers [172]. Using this approach, one can monitor the spectral evolution of individual particles as the particle morphology is reshaped from a symmetric nanoshell to an asymmetric nanoegg and eventually a nanocup. The optical response of the nanocups exhibits strong dependence on the particle orientations with respect to the polarization of the incident light due to the anisotropy of their geometry. Nanocups support both the "electric" and "magnetic" (electroinductive) plasmon modes, with potential applications as constituents in optical frequency magnetic materials or in metamaterials [173–175].

Halas and coworkers [173] systematically measured the plasmonic properties of Au nanocups and developed theoretical understanding of the origin of the plasmonic characteristics of nanocups. They showed that Au nanocups possess magneto-inductive modes that redirect scattered light in a direction dependent on particle orientation, an effect that also controls the interparticle coupling of plasmons in adjacent nanocups. As a true three-dimensional plasmonic nanoantenna, the Au nanocups exhibit unique light-bending properties.

Recently, a more complicated semi-shell nanostructure, perforated semi-shells, has been fabricated using a combination of clean-room techniques [176]. For a semi-shell with a single spherical perforation positioned on its symmetry axis, its plasmon modes strongly depend on the hole size and shape. Placing the perforation off the symmetry axis allows a family of higher-order modes to be excited in the nanostructure, along with complex near-field charge distributions for the various resonant modes. Two important variations of this structure: a semi-shell with multiple perforations in the shell layer and a semi-shell with a wedge-like "slice" in the shell layer were also investigated. A semi-shell with a wedge-like perforation can be thought of as a three-dimensional analog of a split-ring resonator, an important nanoscale component in metamaterial design.

7.6 Nanorice

Nanorice is a hybrid nanoparticle that combines the intense local fields of nanorods with the highly tunable plasmon resonances of nanoshells. This dielectric core–metallic shell prolate spheroid nanoparticle bears a remarkable resemblance to a grain of rice, inspiring the name "nanorice" (see Fig. 1.22a) [159]. This geometry possesses far greater structural tunability, along with much larger local field enhancements and far greater sensitivity as a LSPR sensor than either a nanorod or a nanoshell.

Halas and coworkers developed a seed-mediated electroless plating method for the fabrication of nanorice using spindle-shaped hematite nanoparticle cores [177]. In a typical procedure, the spindle-shape hematite (α-Fe_2O_3) nanoparticles are functionalized with (3-aminopropyl)trimethoxysilane (APTMS) to generate amine moiety-terminated surfaces. Then ultrasmall Au nanoparticles ($\sim$2 nm in diameter) were immobilized onto the surface of functionalized cores at a nominal coverage of $\sim$30 %. The immobilized Au colloids act as nucleation sites to catalyze the electroless Au plating onto the surface of core particles, leading to the gradual formation of a continuous and complete Au shell surrounding the hematite cores. By controlling the amount of Au deposited on the surface of each hematite core, the shell thickness of the nanorice can be precisely controlled. Figure 1.22b shows a SEM image of the as-fabricated hematite core–Au shell nanorice particles. Figure 1.22c shows the experimentally measured optical extinction spectra of nanorice with varying shell thicknesses. For each sample, two well-defined plasmon modes are observed. The strong plasmon resonance feature observed at longer wavelengths arises due to the excitation of longitudinal plasmon supported

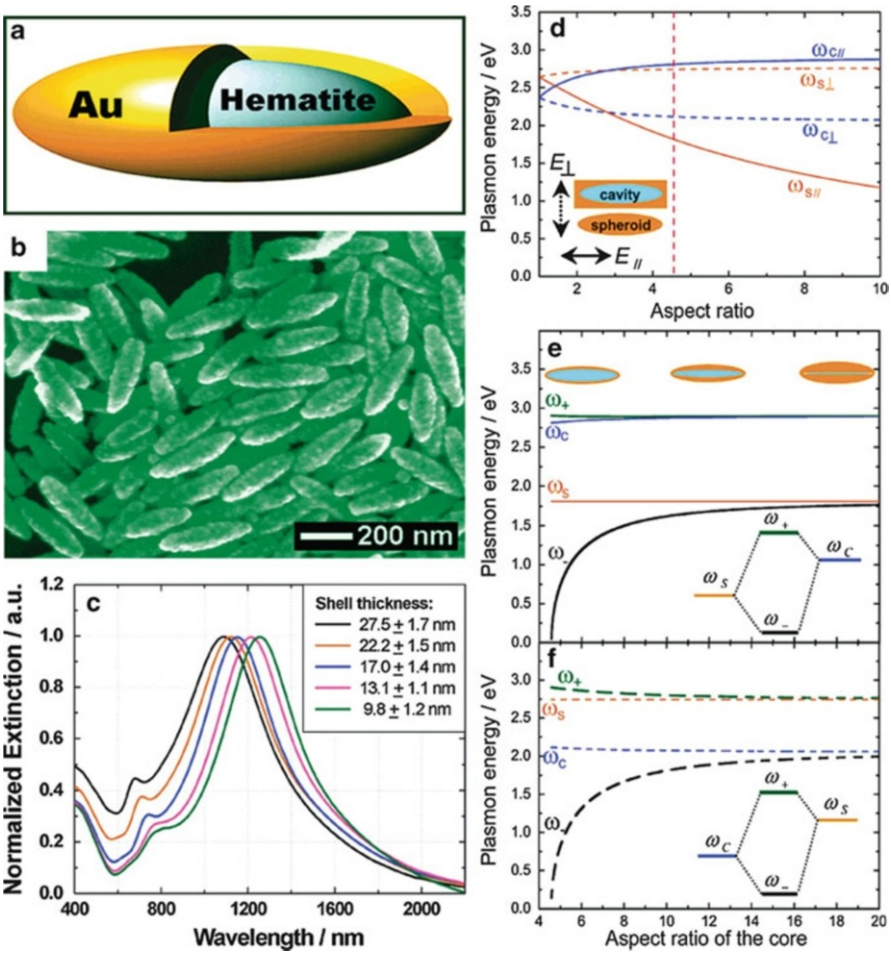

Fig. 1.22 (**a**) Illustration of nanorice, (**b**) SEM image, and (**c**) extinction spectra of nanorice with different shell thicknesses fabricated on a hematite core with longitudinal diameter of 340 ± 20 nm and transverse diameter of 54 ± 4 nm, (**d**) plasmon energy versus aspect ratio (major radius/minor radius) of the solid prolate spheroid and prolate cavity (*solid lines*, longitudinal plasmon; *dashed lines*, transverse plasmon), and (**e**) longitudinal and (**f**) transverse plasmon energies versus core aspect ratio for an aspect ratio of 4.575 (Reprinted with permission from Ref. [159]. Copyright 2007 American Chemical Society)

by the nanorice structure. The little shoulder at shorter wavelengths is mostly corresponding to the transverse plasmon mode of nanorice. Both the longitudinal and transverse plasmon resonances progressively redshift as the shell thickness decreases. The longitudinal plasmon mode exhibits a more sensitive structural dependence of its optical resonance on the shell thickness than the transverse plasmon.

It was found that both the longitudinal and transverse plasmons of nanorice redshift as the refractive index of solvents increases with a linear dependence of plasmon wavelength on refractive index [177]. Although the transverse plasmon is relatively insensitive to the local environment, the longitudinal nanorice plasmon resonance wavelength is highly sensitive to the surrounding dielectric medium, with LSPR sensitivity as high as over 800 nm per refractive index unit. The LSPR sensitivity of the longitudinal plasmon is maintained as shell thickness is varied, while that of the transverse plasmon decreases as shell thickness increases. Such environmental sensitivity of the nanorice plasmons holds great potential for monitoring local environmental changes during chemical and biological processes.

The sphere–cavity model for spherical nanoshells [156, 157] can be generalized to describe the plasmon resonances of nanorice as the result of the hybridization between plasmon modes of a solid prolate spheroid and an ellipsoidal cavity inside a continuous metal [152, 177]. For a solid prolate spheroidal particle of aspect ratio (semimajor/semiminor axis) = $\coth\alpha$, which consists of a metal with an electron density corresponding to a bulk plasmon frequency ω_B and a polarizability of ε_S (immersed in a dielectric with permittivity ε_E), the energies of the plasmon modes take the form

$$\omega^2_{S,lm}(\alpha) = \omega^2_B \frac{P'_{lm}(\cosh\,\alpha)Q_{lm}(\cosh\,\alpha)}{\varepsilon_S P'_{lm}(\cosh\,\alpha)Q_{lm}(\cosh\alpha) - \varepsilon_E P_{lm}(\cosh\,\alpha)Q'_{lm}(\cosh\,\alpha)} \tag{1.17}$$

For a prolate dielectric cavity of aspect ratio $\coth\alpha$ filled with a dielectric medium of permittivity ε_C in the same metallic material, the plasmon energies are

$$\omega^2_{C,lm}(\alpha) = \omega^2_B \frac{P_{lm}(\cosh\,\alpha)Q'_{lm}(\cosh\,\alpha)}{\varepsilon_S P_{lm}(\cosh\,\alpha)Q'_{lm}(\cosh\alpha) - \varepsilon_C P'_{lm}(\cosh\,\alpha)Q_{lm}(\cosh\,\alpha)} \tag{1.18}$$

Figure 1.22d shows the dependence on aspect ratio of the transverse and longitudinal plasmon resonances of a Au nanorod, modeled as a prolate spheroid (Eq. 1.17), and that of an elliptical dielectric cavity embedded in an infinite Au volume (Eq. 1.18). Each of these nanostructures supports longitudinal and transverse plasmon resonances strongly dependent upon aspect ratio, where an aspect ratio of 1 corresponds to the spherical particle and cavity case. The cavity plasmon described here corresponds to a void filled with a dielectric medium of dielectric constant $\varepsilon_C = 9.5$, that of hematite. For this large dielectric function, the cavity is strongly redshifted to energies lower than the solid spheroid plasmon resonance. As the aspect ratio increases, the energies of the longitudinal plasmon of the spheroid and the transverse plasmon of the cavity decrease, while the longitudinal plasmon of the cavity and the transverse plasmon of the spheroid increase. Varying the aspect ratio of the cavity and spheroid shifts the relative energy of the cavity and spheroid parent plasmon modes, which ultimately affects the way in which the cavity and spheroid plasmon states hybridize in the nanorice geometry.

In Fig. 1.22e and f, we show how the nanorice resonances vary as the aspect ratio of the core is varied, while the outer-shell aspect ratio is held constant at 4.575 for the longitudinal and transverse excitations, respectively. As the aspect ratio of the

core is decreased, the hybridization between the cavity and spheroid modes becomes progressively stronger, resulting in larger energy gaps between the bonding and antibonding plasmon modes. The lower-energy bonding plasmon modes of nanorice are much more sensitive to the core and shell dimensions than the antibonding plasmon modes for both the longitudinal and the transverse cases. The nanorice plasmon modes have a significantly increased geometric sensitivity and can be tuned across a broader spectral range than the parent solid spheroid and cavity plasmon modes. In particular, the bonding plasmon extends toward zero frequency in the thin shell limit, for both the transverse and longitudinal cases. For longitudinal polarization, the nature of the bonding plasmon is solid particle-like and the antibonding mode is cavity-like. For transverse polarization, the situation is reversed. Since the solid spheroidal plasmons have a much larger induced dipole moment and couple more strongly to incident light than cavity-like plasmons, the extinction cross section for longitudinal polarization is dominated by the bonding nanorice plasmon and, for transverse polarization, the spectrum is dominated by the antibonding plasmon mode. The difference in LSPR sensitivity of the longitudinal and transverse nanorice plasmons can also be explained in the context of the plasmon hybridization model, where the spheroid-like plasmon resonance has increased sensitivity to changes in its dielectric environment, while a cavity-like resonance has greater sensitivity to changes in the dielectric properties within the nanoparticle core [157].

The asperities of a nanorice particle support very strong local field intensity enhancements at wavelengths corresponding to the longitudinal plasmon resonance of nanorice [177]. The field enhancements are several times larger than those reported for nanofabricated bowtie junctions [178] and those measured in scanning probe junctions [179] and are similar in magnitude to the localized plasmon resonant "hot spots" occurring in junctions between metallic nanoparticles [158]. The nanorice local fields should give rise to intense SERS enhancements with the added advantage that the hot spots are completely open to the surrounding medium in this geometry. From this point of view, each nanorice particle can potentially serve as a stand-alone, optically addressable nanoscale substrate for surface-enhanced spectroscopies. Moreover, since the enhanced near-field intensities can extend several tens of nanometers from the surface of the nanorice, these particles may exhibit unique advantages in the spectroscopic sensing and characterization of large biomolecules, such as proteins and DNA, biological samples, or materials placed directly adjacent to the nanoparticles.

8 Other Metallic Nanostructures with Geometrically Tunable Optical Properties

Besides nanorods and nanoshells, a series of other nanoparticle geometries have also been found to possess geometrically tunable optical properties. Here we provide several representative examples, including nanoprisms, nanopolyhedrons, nanostars, and nanocages, to highlight how the geometric parameters profoundly impact the optical responses of these anisotropic nanostructures.

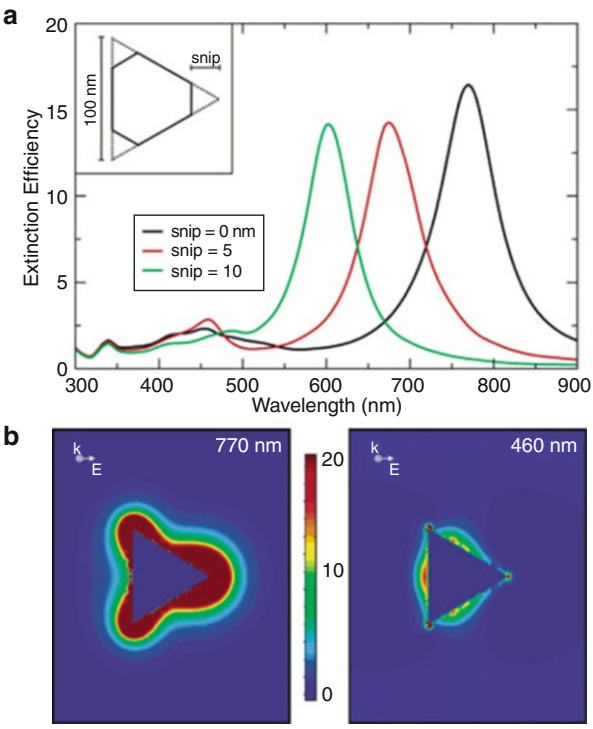

Fig. 1.23 (**a**) Orientation-averaged extinction efficiency for trigonal prisms based on a 100-nm edge dimension with snips of 0, 10, and 20 nm. The *inset* shows the shape of a snipped prism. The prism thickness is 16 nm. (**b**) E-field enhancement contours external to the Ag trigonal prism, for a plane that is perpendicular to the trigonal axis and that passes midway through the prism (Reprinted with permission from Ref. [56]. Copyright 2003 American Chemical Society)

8.1 Nanoprisms

Nanoprisms or triangular nanoplates display a wide range of geometrically tunable optical features [180]. Triangular nanoprisms contain three sharp vertices that contribute significantly to their optical properties. However, experimentally fabricated metallic triangular nanoprisms typically exhibit varying degrees of tip truncation. The LSPR band position of nanoprisms is essentially determined by the tip sharpness, the edge length, and the aspect ratio (lateral dimension/thickness). Sharper tips, larger edge lengths, and higher aspect ratios generally give rise to more redshifted resonances, while round and truncated tips and low aspect ratios result in oppositely blueshifted bands.

The LSPRs of triangular Ag nanoprisms have been simulated by Schatz and coworkers using DDA method [56, 181]. For the perfect triangular prism as shown in Fig. 1.23a, the extinction spectrum consists of three LSPR bands, a long wavelength peak at 770 nm (in-plane dipole), a weaker peak at 460 nm (in-plane quadrupole), and a small but sharp peak at 335 nm (out-of-plane quadrupole). A dipole plasmon resonance can be described as the electron cloud surrounding the nanoparticle moving either parallel or antiparallel to the applied field. For a quadrupole mode, half of the cloud moves parallel and half moves antiparallel. Since a nanoprism is anisotropic with respect to the propagation and polarization of

the incident light, both in-plane and out-of-plane excitation lead to dipole and quadrupole resonances; however, the out-of-plane dipole resonance at 430 nm is not resolved because it is a very broad resonance. Interestingly, the red-most peak is very sensitive to snipping, with the 20-nm snipped prism giving rise to a peak that is blueshifted by 100 nm as compared to the perfect triangular nanoprism, while the other peaks at shorter wavelengths are much less sensitive to snipping. As shown in Fig. 1.23b, the maximum enhancement for the dipole resonance is located around the tips, while for the quadrupole resonance, the regions of significant field enhancements are largely confined at the sides.

The experimentally fabricated nanoprisms typically have sufficiently large edge lengths of sub-100 nm and high aspect ratio over 10 and therefore exhibit both dipole and quadrupole plasmon resonances that shift in frequency as a function of nanoprism size, shape, and dielectric environment. With spherical particles smaller than 100 nm, quadrupole and dipole plasmon resonances are not distinguishable from each other as shown in Fig. 1.4; however, in an anisotropic nanoprism with similar size, these modes oscillate at markedly different frequencies (generally separated by 100–400 nm) and can be resolved experimentally for nanoprisms of both Au and Ag [17, 18, 182].

Ag nanoprisms have been synthesized with tight control over their aspect ratio in relatively high yield through photochemically induced growth [17, 182–185] or thermal reduction in organic solvents [19, 20, 186], while Au nanoprisms have been mostly fabricated through solution-phase seed-mediated growth approaches [18, 187–190]. In the photochemical synthesis, a variety of radiation wavelengths can be used to selectively tailor the architectural parameters of the resulting nanoprisms, such as thickness and edge lengths, and thereby to fine-tune the optical properties of nanoprisms (Fig. 1.24) [184]. In the solution-phase chemical synthesis of Au and Ag nanoprisms, the particle geometry can be tuned by adjusting a whole set of experimental conditions, such as reducing agents, reaction media, temperature, and surfactants. For more details about the fabrication of Ag and Au nanoprisms and mechanisms of nanoprism formation under various conditions, the readers are recommended to read a recently published review article by Mirkin and coworkers [180].

Ag nanoprisms may also undergo post-fabrication morphological changes under various conditions, introducing interesting modifications to the LSPRs. Therefore, post-fabrication treatments provide an alternative way to fine-tune the optical properties of Ag nanoprisms. The optical properties of Ag nanoprisms can be precisely tuned over a wide spectral range through a process of shape reconstruction induced by UV irradiation, in which the morphology of the nanoparticles is changed from thin triangular nanoprisms to thick round nanoplates [191]. It has been recently reported that Ag nanoprisms may also undergo an interesting sculpturing process due to chemical etching by halide ions [192–194]. Thermal treatments of Ag nanoprisms can also give rise to interesting reshaping of Ag nanoprisms, which results in systematic evolution of LSRPs [195]. The blueshift of LSPRs is a direct consequence of both tip truncation and size reduction during the thermal treatments.

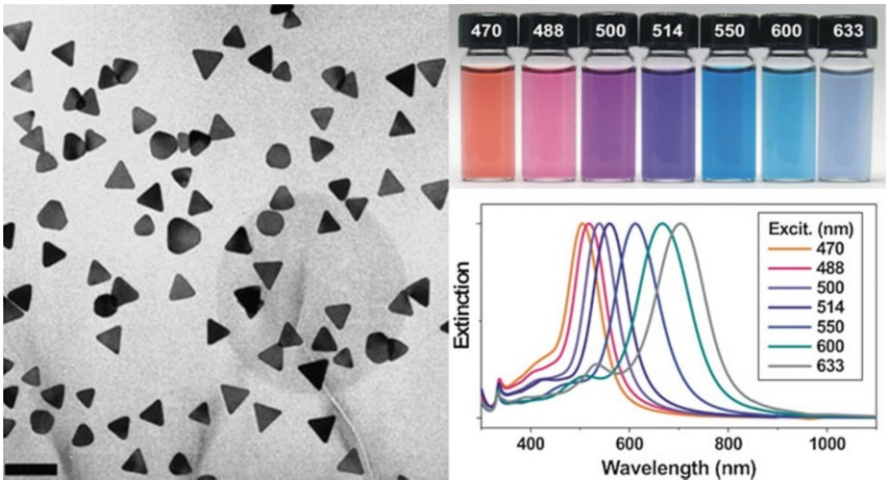

Fig. 1.24 TEM image of Au nanoprisms (*left*), extinction spectra, and corresponding solutions of Ag nanoprisms with varying edge length (*right*). Labeled vial and spectra numbers correspond to the wavelength of irradiation used to prepare the nanostructures (Reprinted with permission from [184]. Copyright 2007 John Wiley & Sons, Inc)

8.2 Nanopolyhedra

Controlling nanocrystal shapes in the mesoscopic size regime provides an elegant strategy for optical tuning. Whereas highly symmetric spherical particles within the quasi-static limit exhibit a single LSPR peak, anisotropic multifaceted nanoparticles such as cubes, bipyramids, and other polyhedra exhibit multiple scattering peaks in the visible and NIR regions due to their mesoscopic sizes beyond the quasi-static limit and highly localized charge polarizations at corners and edges.

Yang and coworkers systematically investigated LSPRs of metallic nanopolyhedrons both at the ensemble and single-particle levels [196] Monodisperse colloidal solutions of Ag nanocrystals with regular polyhedral shapes were synthesized in a highly controllable manner using the polyol method, where the metal salt is reduced by hot pentanediol at near-reflux temperature in the presence of PVP as the capping polymer. Silver nitrate and PVP were dissolved separately and injected into the system periodically, and specific polyhedral shapes can be obtained in high yield depending on how long the sequential additions are continued. Figure 1.25 shows the differences in LSPR modes for cubic, cuboctahedra, and octahedral nanoparticles, all of which exhibit highly complex plasmon signatures as a result of their geometric anisotropy.

8.3 Nanostars

Metallic nanostars are multipointed, branched metal nanoparticles, each of which may exhibit highly complex multipeaked extinction spectral line shapes [197].

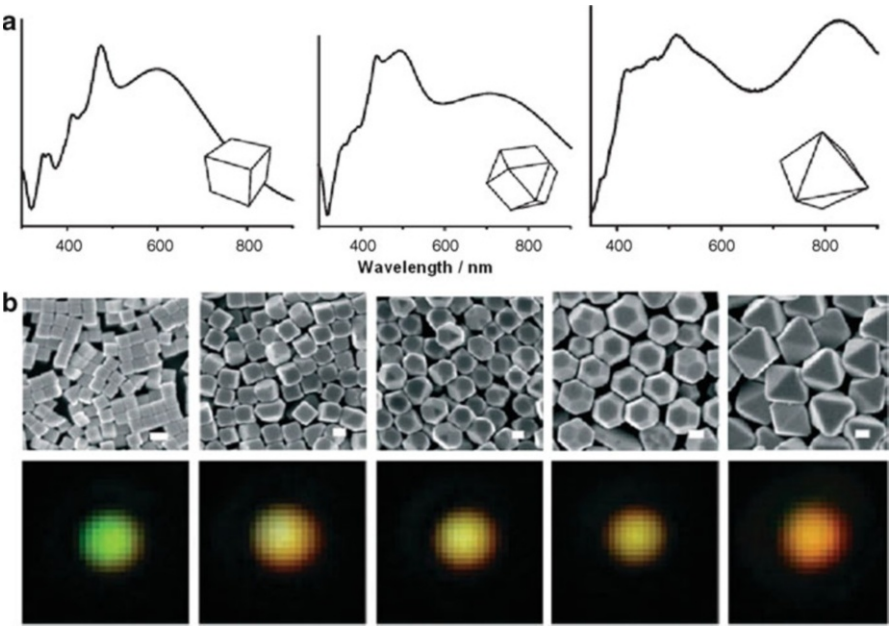

Fig. 1.25 (**a**) UV–visible spectra of colloidal dispersions of Ag nanocubes, cuboctahedra, and octahedra. (**b**) SEM and real color images taken with a digital camera displaying the different colors arising from plasmon-mediated scattering. Each spot corresponds to the light scattered from a single crystal. From *left to right*: *cube*, *truncated cube*, *cuboctahedron*, *truncated octahedron*, and *octahedron*. Scale bars: 100 nm (Reprinted with permission from Ref. [196]. Copyright 2006 John Wiley & Sons Inc)

For branched Au nanocrystals or nanostars, the precise control over particle morphology is often challenging because the number of branches or pods can vary within each preparation [25, 104, 198–201], which results in formation of mixtures of monopods, bipods, tripods, tetrapods, and other multipods in each sample. To synthesize Au nanostars with a specific number of branches, the utilization of structurally well-defined and multi-twinned Au nanoparticles, such as nanorods, bipyramids, and decahedra, is necessary as templates or seeds for the nanostar growth. Xia and coworkers [202] recently reported the facile synthesis of Au nano-hexapods by seeded growth with controllable arm lengths. During the seed-mediated growth, $HAuCl_4$ was reduced by *N*,*N*-dimethylformamide (DMF) in water in the presence of single-crystalline Au octahedra. The newly formed Au atoms preferentially nucleated and grew from the six vertices of an octahedral seed, leading to the formation of nano-hexapods. The LSPR peaks of the resultant Au nano-hexapods redshifted from the visible to the NIR depending upon the lengths of the arms, which could be controlled by varying the amount of $HAuCl_4$, the temperature, or both. The preparation and optical properties of penta-branched Au nanostars obtained using seed-mediated method have also been reported recently [26, 203–206]. The extinction spectra of the colloidal nanostars taken at

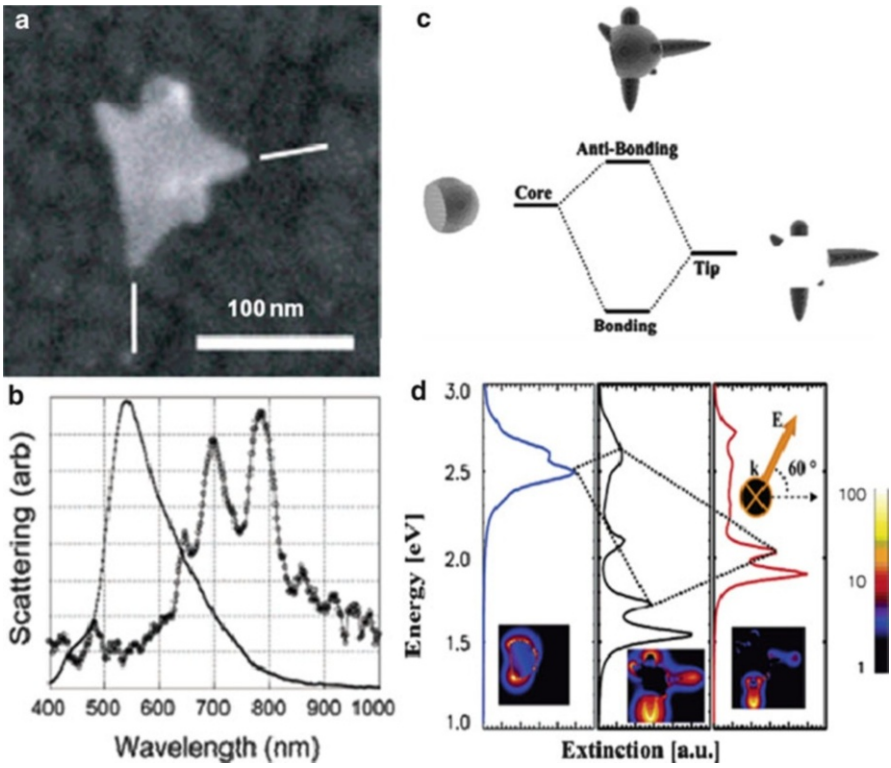

Fig. 1.26 (**a**) SEM image and (**b**) single-particle dark-field light-scattering spectrum (*open circles*) of a Au nanostar. The scattering spectrum of a 100-nm Au colloid is also plotted (*points*). (**c**) The plasmon hybridization picture of Au nanostar LSPRs. (**d**) The *left panels* show the extinction spectra of the individual core. The *right panels* show the spectra of the tips. The *middle panels* show the extinction spectra of the interacting nanostar system (Reprinted with permission from Refs. [26] and [207]. Copyright 2006 and 2007 American Chemical Society)

different time points demonstrate that there are two distinct peaks which correspond to short-wavelength transverse absorption band arising from the formation of fully developed side branches and redshifted longitudinal band due to the elongation of the developed branched nanocrystals.

To further shed light on the structure–property relationship of nanostars, Hafner and coworkers [26] studied the optical properties of individual Au nanostars at single-nanoparticle level. They used commercially available 10-nm-diameter Au colloids as the seed to produce star-shaped nanoparticles under the exact growth conditions suitable for nanorods in the presence of CTAB. Their single-particle light-scattering data show that nanostars have multiple plasmon resonances resulting in polarization-dependent scattering, which correspond to different tips of the star-shaped structure (Fig. 1.26a and b). The plasmon resonances are extremely sensitive to the local dielectric environment changes and that shows great promise for the nanostars to be used as LSPR sensors. Nordlander and

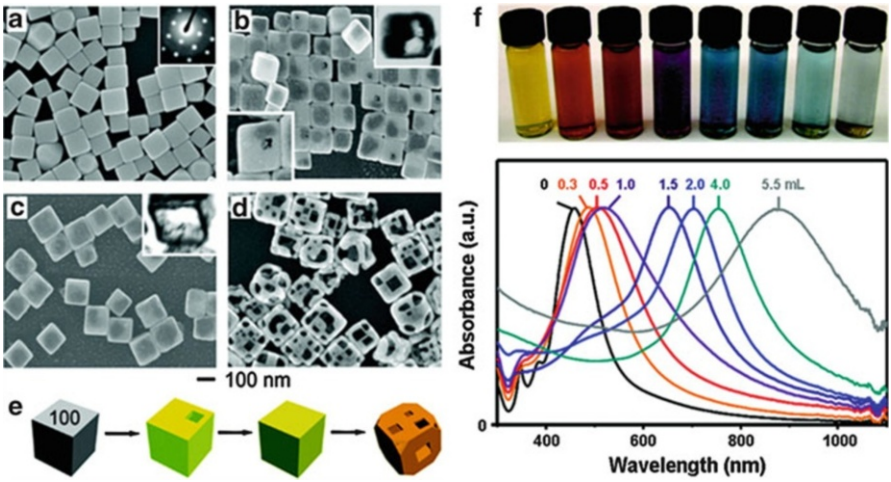

Fig. 1.27 SEM images of (**a**) Ag nanocubes and (**b–d**) Au–Ag porous nanocages. (**e**) Illustration summarizing morphological changes. (**f**) *Top panel*, vials containing Au nanocages prepared by adding different volumes of $HAuCl_4$ solution. Lower panel, the corresponding extinction spectra of Ag nanocubes and Au nanocages (Adapted with permission from Ref. [208]. Copyright 2008 American Chemical Society)

coworkers [207] interpreted the nanostar plasmons as a result of plasmon hybridization between the core and tips of the nanoparticle (Fig. 1.26c and d). The nanostar core serves as a nanoscale antenna, dramatically increasing the excitation cross section and the electromagnetic-field enhancements of the tip plasmons.

8.4 Nanocages

Metallic nanocages are a class of interesting photonic nanostructures possessing hollow interiors and porous walls [208]. They can be prepared in high yield through a remarkably simple galvanic replacement reaction between solutions containing metal precursor salts and metallic nanoparticle templates. Regarding the preparation of Au-based nanocages, Ag nanocubes prepared by polyol reduction [209, 210], can serve as a template for the galvanic reactions during which the produced Au is confined to the Ag nanocube surface, growing on it and adopting its morphology. Concurrent with this deposition, the interior Ag is oxidized and removed, together with alloying and dealloying, to produce hollow and, eventually, porous nanocage structures (see Fig. 1.27a–e). This approach is versatile and can be extended to the fabrication of multiple-walled Au nanorattles or nanotubes [211]. In addition to Au-based structures, switching the metal salt precursors to Na_2PtCl_4 and Na_2PdCl_4 allows for the preparation of Pt- and Pd-containing nanocages, respectively [212, 213].

Accompanying the compositional and morphological changes induced by the galvanic replacement reactions is the evolution of LSPRs of Au nanocages. The upper panel of Fig. 1.27f shows a picture of vials containing Au nanocages prepared by reaction between Ag nanocubes (edge length ≈ 40 nm) and different volumes of $HAuCl_4$ solution (0.1 mM) [211, 214]. As the photograph and corresponding extinction spectra (Fig. 1.27f, lower panel) indicate, the LSPR peak position of the Au nanocages is tunable throughout the visible and NIR. This observation makes Au nanocages attractive for colorimetric sensing and biomedical applications. The relative intensity of the scattering and absorption cross sections of Au nanocages can be tuned by varying their size. DDA simulations indicate that when Au nanocages are small (edge length<45 nm), light absorption predominates; however, light scattering prevails with larger Au nanocages [214]. Thus, one must consider their size and the magnitude of their scattering and absorption cross sections, in addition to LSPR position, when engineering nanocages for a specific application. The tunable LSPRs of nanocages hold great promise to biomedical applications. For example, Xia and coworkers have explored the use of Au nanocages as contrast enhancement agents for both optical coherence tomography and photoacoustic tomography [215–217], with significantly improved performance observed in each case.

9 Multi-nanoparticle Systems

In this section, we would like to expand our discussions to the geometrically tunable optical properties of more complicated multi-nanoparticle systems composed of multiple nanoparticles that are in close proximity to each other. The plasmonic interactions between neighboring nanoparticles give rise to further redshifted lowest-energy plasmon resonance, further increased complexity of extinction spectral line shapes, and significantly enhanced electric fields in the interparticle junctions [218]. The multi-nanoparticle systems possess more geometric parameters that one can adjust to further fine-tune the optical responses over a broader spectral range and, thus, may exhibit superior optical properties in comparison to individual nanoparticle building blocks. One striking example observed by colloidal chemists is the dramatic color change of noble metal colloids when a dilute suspension of nanoparticles forms nanoparticle aggregates upon the introduction of ions, such as Cl^-, or molecular linkers, such as DNA [52, 219–222]. When Au or Ag nanoparticles begin to aggregate, they form clusters of nanoparticles, and their extinction spectrum acquires a new band that is redshifted significantly from the extinction band of the isolated nanoparticles. In addition, the local electric fields can be enormously enhanced in the nanoscale gaps between the adjacent nanoparticles upon the excitation of the "aggregate" plasmons, providing "hot spots" for surface-enhanced spectroscopies. It is essentially these features that have been attributed to the enormous SERS enhancements reported for random colloidal aggregates, approaching single-molecule sensitivity for certain molecules [51, 52, 223–228].

The interesting optical properties of multi-nanoparticle systems can be essentially interpreted as results of plasmon coupling between individual nanoparticles that are in close proximity to each other [159, 218], in analogy to the hybridized molecular orbitals in a polyatomic molecule. In this context, individual nanoparticles can be regarded as artificial atoms, while a multi-nanoparticle system can be regarded as an artificial molecule. Plasmon hybridization model allows us to express the fundamental plasmon modes of these multiparticle systems as linear combinations of the primitive plasmons supported by individual nanoparticles. The geometry of individual constituent nanoparticles, the geometric arrangements of the nanoparticles, and the distance between adjacent nanoparticles are all key factors that profoundly impact the synergistic far-field and near-field optical properties of a multi-nanoparticle system. Halas and Nordlander [218] recently published a comprehensive review article on plasmons in strongly coupled metallic multi-nanoparticle systems, and the readers are strongly encouraged to read this review and the references cited therein to get a more complete and thorough understanding on this topic. In this section, we would like to focus on three representative systems, nanoparticle dimers, nanoparticle oligomers (clusters composed of a finite number of nanoparticles), and infinite nanoparticle arrays, to highlight how the plasmon coupling in multi-nanoparticle systems gives rise to a whole set of interesting optical properties that are exploitable for widespread applications, such as molecular sensing and surface-enhanced spectroscopies.

9.1 Nanoparticle Dimers

The simplest geometry of multi-nanoparticle systems is a pair of directly adjacent, interacting nanoparticles known as a nanoparticle dimer. The importance of the nanoparticle dimer geometry was first recognized from a theoretical point of view in the early 1980s [229], stimulating further theoretical investigations of this geometry ever since [158, 230–232]. In spite of the challenges associated with large-scale and high-yield synthesis of nanoparticle dimers, the optical properties of nanoparticle dimers have been studied in great detail at single-nanoparticle level using dark-field microscopy [233, 234]. The results of single-particle light-scattering measurements have been directly compared to electrodynamics simulations based on which detailed understanding of the plasmon coupling in nanoparticle dimers has been developed.

Figure 1.28a shows a diagram illustrating the plasmon coupling of a Au nanoparticle homodimer [158]. The plasmon hybridization between the two nanoparticles results in an increased redshift of the bonding $l = 1$ dimer mode with decreasing interparticle distance (Fig. 1.28b). This behavior is characteristic of a dimer excited by light polarized along its interparticle axis. For light polarized perpendicular to the dimer axis (Fig. 1.28c), interparticle coupling is minimal, and a small blueshift of the antibonding mode, which is optical "bright," is observed as the interparticle distance decreases, while the bonding plasmon mode is optically "dark."

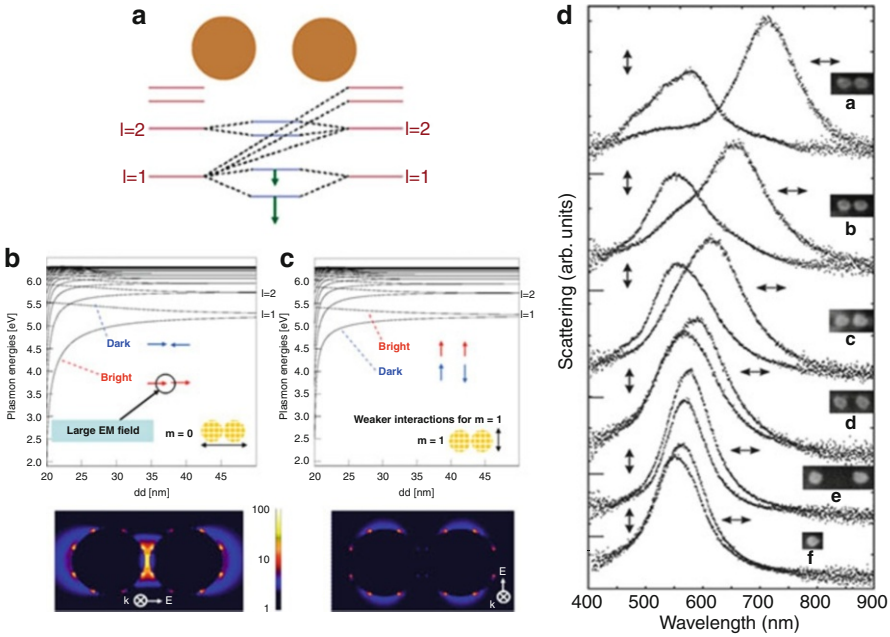

Fig. 1.28 (**a**) Schematic diagram of the dimer system and calculated plasmon energies versus dimer separation for a homodimer of Au nanospheres for (**b**) parallel and (**c**) perpendicular polarizations. (**d**) Dark-field spectra and SEM micrographs from isolated nanoparticle pairs with varying separations in parallel and perpendicular polarization, as indicated by *arrows*. (*Panels A–C*: adapted with permission from Ref. [158]. Copyright 2004 American Chemical Society. *Panel D*: reprinted with permission from Ref. [242]. Copyright 2005 American Chemical Society)

It is of particular interest that the local electric fields inside the interparticle gaps can be enormously enhanced when the bonding dipolar plasmon mode is optically excited for the polarization parallel to the dimer axis (Fig. 1.28b). Such local field enhancements in the nanoparticle junctions can fundamentally interpret the "hot-spots" effects in nanoparticle aggregates that are exploitable for surface-enhanced spectroscopies. Halas and coworkers have directly compared the SERS performance of individual nanoparticles vs. nanoparticle dimers [235]. They found that nanoparticle dimers exhibit much larger SERS enhancement than the individual nanoparticle primarily due to the hot spots in the interparticle junctions. Similar "hot-spots" effects have also been observed in dimers of Ag nanospheres [236], pairs of Ag nanocubes [237, 238], and metallic bowtie nanostructures (a nanoparticle dimer composed of two triangular nanoplates in close proximity with sharp tips directly pointing to each other) [239–241]. Figure 1.28d shows the experimentally measured scattering spectra from individual pairs of Ag nanoparticles with varying interparticle gaps [242]. The experimentally observed dependence of the dimer plasmon modes on the interparticle distance and dimer orientation with respect to the incident light polarization are in good agreement with the theory.

For a nanoparticle heterodimer, both the bonding and antibonding modes for both polarizations can be excited by the incident light because even for the hybridized plasmon modes in which the two dipole modes of individual nanoparticles are antiparallelly aligned, there is still a net dipole moment due to the asymmetry of the system. Halas and coworkers [233] have systematically studied the optical responses of plasmonic heterodimers and carefully correlated their experimental results with electrodynamics simulations. While a plasmonic homodimer can support both bright and dark modes, symmetry breaking relaxes selection rules and enhances coupling between all of the plasmon modes of a heterodimer nanostructure. In the case of two adjacent, mismatched nanoparticles, this allows modes with different characteristics, such as angular momentum or linewidth, to interact strongly with each other especially in the small gap regime, giving rise to more complicated spectral line shapes and asymmetric plasmon splitting. These interactions are a strong function of interparticle distance and relative energy level of primitive plasmons of the individual nanoparticles, resulting in energy shifts and avoided crossings of the plasmon modes as the constituent nanoparticles coalesce into the dimer structure. Interactions between broad and narrow resonant modes can occur, giving rise to a Fano resonance with its characteristically asymmetric line shape in nanoparticle heterodimer systems [233, 243].

Altering the symmetry of individual constituent nanoparticles inside a dimer will also introduce dramatic modifications to the optical properties of the dimer structure. For example, the shape anisotropy of metallic nanorods leads to different possible orientations within a dimer, resulting in different orientational modes of plasmon coupling [244–248]. Coupling of the nanorod longitudinal modes leads to bonding and antibonding interactions when the dimer is arranged end-to-end or side-to-side. Many other possible dimer geometries, including L-shaped and T-shaped dimers as well as dimers laterally and longitudinally displaced with respect to one another, may also form taking into consideration of the character of anisotropy.

Because of the strong dependence of the dimer plasmons on the interparticle distance, one can use nanoparticle dimers to construct “plasmon rulers” to measure distance changes over nanometer-length scale [249–253]. By using molecules as the linker between the two nanoparticles, the conformational changes of the molecular linker can be probed in real time simply based on the plasmon shift as the interparticle distance varies. Alivisatos and coworkers developed a single-molecule version of plasmon-based colorimetric sensing strategy using individual nanoparticle dimers as plasmon rulers to probe the DNA hybridization by monitoring the plasmon shift under a dark-field optical microscope [249]. Later, they further developed a DNA-linked nanoparticle dimer that can be used to probe the conformational dynamics of protein–DNA complexes and the kinetics of DNA digestion at single-molecular level [252]. In comparison to other nanoscale molecular rulers, such as fluorescence resonance energy transfer (FRET) [254], plasmon rulers have several unique advantages, such as high photostability of the probes (no blinking), long-lasting signals (no photobleach), and simplicity of instrumentation (colorimetric sensing based on dark-field scattering).

9.2 Nanoparticle Oligomers

The fundamental principles of plasmon hybridization described in the nanoparticle dimer systems can be further extended to more complicated nanoparticle oligomer structures. Just as molecular orbital theory can be applied to complex, polyatomic molecules, there has been interest in extending coupled plasmon systems beyond the plasmonic dimers to multi-nanoparticle systems. Because of the invariance of the interactions through symmetry transformations for a specific structure, group theory may be applied quite naturally to the analysis of plasmon modes of multi-nanoparticle systems with various symmetries. For example, symmetric linear combinations of plasmons corresponding to the underlying symmetry of the system can be used to interpret and classify the modes of a triangularly arranged nanosphere trimer (group D_{3h}) and squarely arranged quadrumer (group D_{4h}) [255]. The linear combinations of individual nanoparticle plasmons can be used to predict which modes have a dipole moment for a given polarization, resulting in a significant simplification of the problem.

Breaking the symmetry of a nanoparticle trimer will introduce interesting modifications to the plasmon coupling between the constituent nanoparticles. Chuntonov and Haran [256] followed the evolution of LSPR spectra of plasmonic trimers, assembled from equal-sized Ag nanoparticles, as gradual geometric alterations break their structural symmetry. The spectral modes of an equilateral triangle, the most symmetric structure of a trimer (D_{3h}), are degenerate. This degeneracy is lifted as the symmetry is lowered to C_{2v} and eventually to $D_{\infty h}$ as one of the vertex angles is gradually opened. This symmetry breaking leads to a subtle transition between bright and dark modes. The evolution of the plasmon modes across different symmetry groups was monitored through the scattering spectra of the symmetry-broken trimers, and the results can be well explained with the aid of group correlation tables and plasmon hybridization theory.

As the cluster size further increases, the spectral line shape of the plasmonic oligomers becomes increasingly more complicated due to the interaction and hybridization of more multipolar plasmon modes within these nanostructures. Highly asymmetric spectral line shapes due to pronounced Fano resonances have been observed in lithographically fabricated or chemically self-assembled planar symmetric plasmonic nanoparticle oligomers, such as quadrumers [257], pentamers [258] and heptamers [259–262]. These Fano resonances observed in planar plasmonic oligomers arise from interactions between a superradiant "bright" mode and a subradiant "dark" mode in a nanostructure, and they are characterized by a pronounced, asymmetric dip in the scattering spectra. As shown in Fig. 1.29, a self-assembled Au nanoshell heptamer cluster (one nanoparticle in the center of a six nanoparticle ring) on a planar substrate exhibits pronounced Fano resonance line shape in their extinction spectrum [259]. This Fano resonance line shape has also been observed in lithographically fabricated plasmonic heptamers by Hentschel et al. [261, 262] who symmetrically studied the effects of interparticle spacing and geometric arrangement on the frequency and line shape of the Fano resonance of the heptamers. The Fano resonances observed in plasmonic oligomers

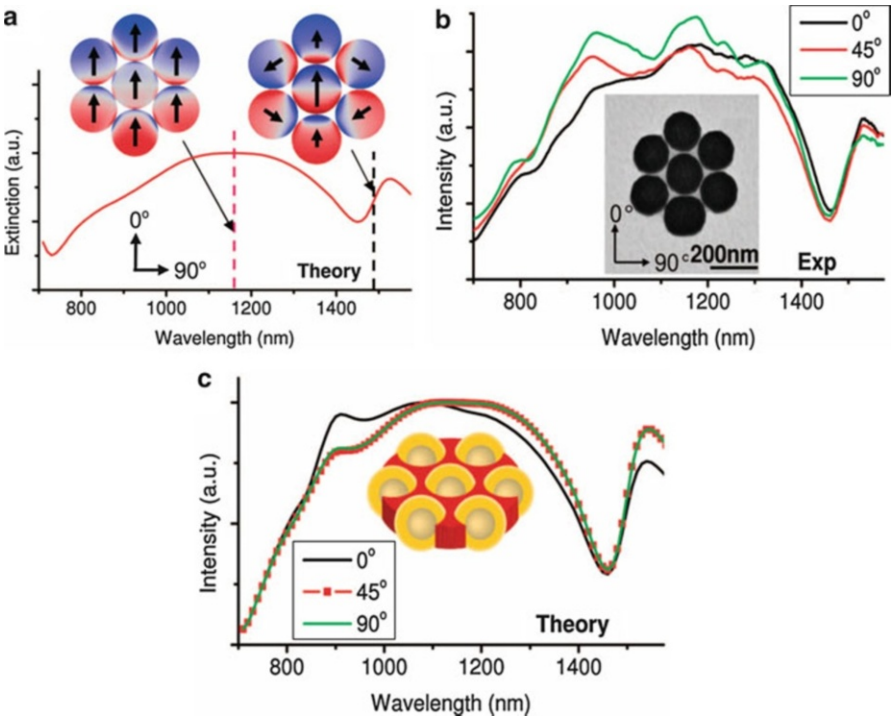

Fig. 1.29 Fano-resonant behavior of a plasmonic nanoshell heptamer. (**a**) Calculated extinction spectrum and charge density plots for a heptamer excited at normal incidence with a 0° orientation angle. (**b**) TEM image and spectra of a heptamer at three different incident electric-field orientation angles. (**c**) Calculated scattering spectra for a heptamer with a geometry matching that in (**a**), for the three orientation angles in (**b**) (Reprinted with permission from Ref. [259]. Copyright 2010 American Association for the Advancement of Science)

have relatively narrow linewidth and high sensitivity to the surrounding medium and thus are very attractive for LSPR sensing due to the great figure of merit (LSPR shift/linewidth).

9.3 Infinite 1D and 2D Nanoparticle Arrays

Periodic 1D and 2D nanoparticle arrays with homogeneous nanoparticle sizes and shapes as well as regular interparticle separations provided important geometries for far-field and near-field plasmon coupling to occur over a macroscopic area [263–268]. In nanoparticle arrays with the interparticle distance comparable to the LSPR wavelength of the isolated nanoparticles, far-field diffractive plasmon coupling leads to a spectral narrowing of the collective plasmon response [269, 270]. Hickes et al. investigated the line shape of an array of Ag nanoparticle chains and observed that the long wavelength shoulder in scattering spectra significantly

gained in intensity and narrowed spectrally for interparticle distances comparable to the resonance wavelength of an isolated nanoparticle [270]. Sharp, coherently coupled plasmon bands in 2D Ag nanoparticle arrays have also been observed by Chumanoc and coworkers [271, 272]. Simulations using the coupled dipole approximation have also shown that the bandwidth of the collective plasmon mode induced by far-field diffractive coupling can be smaller than 1 nm, which is important for applications such as LSPR sensing since the sensitivity improves for narrower linewidths [273].

Near-field plasmon coupling in linear nanoparticle chains has attracted significant attention because the plasmon modes are no longer localized on the individual nanoparticles but can propagate along the chain axis, which makes it possible to direct energy along a chain of nanoparticles [274–277] and allows for electromagnetic energy transport in waveguide structures smaller than the diffraction limit of the incident light [278–282]. It is very interesting to note that the characteristics of bending light around corners or splitting it into two or more branches can be achieved for nanoparticle arrays with complex geometries, such as T-shaped structures. Many research groups found that an increasing redshifted longitudinal plasmon resonance of the nanoparticle chains can be observed as increasing the number of nanoparticles from a dimer to a periodic linear chain while keeping the interparticle distance constant [283–285].

The synergistic optical properties of a 2D infinite nanoparticle array are sensitively dependent on the interparticle spacing. Yang and coworkers developed a Langmuir–Blodgett self-assembly approach for the fabrication of Ag nanoparticle arrays with fine-controlled interparticle spacing [286–288]. They found that when the interparticle spacing is relatively large with respect to individual particle size, the arrays exhibit plasmonic responses that are similar to individual nanoparticles due to lack of interparticle plasmon coupling. As the interparticle spacing gradually decreases, the plasmon coupling between nanoparticles becomes progressively stronger, giving rise to dramatic changes in the extinction spectral line shapes. As the interparticle spacing further decreases to a regime where the nanoparticles are almost touching, the optical properties become similar to those of a macroscopically continuous metallic film.

Tiny but nonzero interparticle gaps in 2D nanoparticle arrays are critical for the emergence of large local field enhancements in the interparticle junctions that are exploitable for surface-enhanced spectroscopies as demonstrated by several groups [289–293]. For example, Halas and coworkers developed a convenient and cost-effective chemical self-assembly approach to highly ordered Au nanosphere arrays with sub-10-nm interparticle spacing [291]. These sub-10-nm nanogaps between adjacent nanoparticles have been proved to be very crucial for reproducible, large, averaged SERS enhancements on the order of 10^8 for nonresonant molecules. 2D arrays of metallic nanoshells have recently been found to possess ideal properties as a substrate for combining SERS and surface-enhanced infrared absorption (SEIRA) spectroscopies [294]. For sub-10-nm interparticle distances, the multipolar plasmon resonances of individual nanoshells hybridize and form redshifted bands, a relatively narrow band in the NIR originating from quadrupolar nanoshell

resonances enhancing SERS and a very broad band in the mid-infrared (MIR) arising from dipolar resonances enhancing SEIRA. The resulting nanoshell arrays possess "hot spots" in the interparticle junctions that can enhance Raman scattering by a factor of 10^8–10^9 at near-infrared wavelengths and simultaneously provide broadband mid-infrared hot spots that can enhance infrared absorption by a factor of 10^4 on the same substrate [294]. Nordlander and coworkers [295] theoretically studied the origin of the interesting optical properties of metal nanoshell arrays. They systematically studied the evolution of optical properties from nanoshell oligomers to infinite nanoshell 2D arrays as the number of nanoshells gradually increases. They proposed that the large field enhancements in the MIR and at longer wavelengths are due to the lightning-rod effects and are well described with an electrostatic model.

10 Concluding Remarks

Over the past two decades, significant progress has been made on the controllable fabrication of metallic nanoparticle in various geometries through both top-down clean-room techniques and chemical bottom-up approaches. Tight control over particle geometries enables one to fine-tune the plasmon-dominated optical properties of metal nanoparticles or nanoparticle assemblies over broad spectral ranges. Classical electromagnetic theory and numerical electrodynamics simulations as well as plasmon hybridization model provide a powerful theoretical platform based on which the optical properties of nanostructures with almost arbitrary structural complexity can be predicted and quantitatively analyzed. All these are directly related to our capabilities to tackle grand challenges in energy conversion, photonics, spectroscopies, and biomedicine.

(a) Plasmon-Enhanced Absorption in Photovoltaic Devices
Plasmon-enhanced light absorption in photovoltaic devices has shown significant impact to advances in photovoltaics [296]. For solar cells, three distinct mechanisms for enhancing light absorption could be utilized, which are (1) the scattering from the metallic nanoparticles (far-field effect), (2) the near-field enhancement associated with the localized surface plasmon resonance of the nanoparticles, and (3) excitation of the propagating waveguide modes and direct generation of charge carriers within the thin absorbing or semiconductor layer [297–299]. Thin-film solar cells are currently widely used for low-cost photovoltaics. However, most photovoltaic materials face a trade-off between the necessary thickness for complete optical absorption and the requisite electronic quality for long minority carrier diffusion lengths [300]. The traditional method for enhancing absorption in a solar cell is to employ front or back surface texturing as a way of effective light trapping by increasing its path length [301–303], but this micrometer-sized method is inappropriate for thin-film solar cells because the total film thickness may be only a fraction of a wavelength. On the contrary, the incorporation of plasmonic nanostructures in photovoltaic devices has the potential to overcome this problem of light

trapping due to the ability of surface plasmons to guide and confine light in small volumes [304]. In addition, the feasibility of designing plasmonic nanoparticles with high effective scattering cross sections and geometrically tunable optical properties makes them the optimized candidates for photovoltaic devices. Hence, plasmonic nanoparticles have great potential to revolutionize the photovoltaic industry.

(b) Optical Antennas for Photonic Applications
Optical antennas are devices that convert freely propagating optical radiation into localized energy and vice versa. The control and manipulation of optical fields at the nanometer scale can be achieved using metallic nanoparticles as subwavelength antennas. From the first use of colloidal Au particles for localizing optical radiation on a simple surface proposed by Edward Synge in 1928 [305] to the subsequent experimental demonstrations followed by Dieter Pohl and Ulrich Fischer in 1995 [306] and applications to near-field microscopy [307], optical antennas have attracted tremendous attention. More importantly, LSPRs make optical antennas particularly efficient at selected frequencies [308–310]. Hence, metallic nanoparticles with geometrically tunable LSPRs are very promising candidates for this specific application. With the development of fabrication techniques, a wide range of applications including controlled single-photon sources for quantum information, light harvesting, data storage, nanoscale optical circuitry, and optical imaging beyond 10-nm resolution will emerge [311, 312].

(c) Plasmon-Enhanced Spectroscopies
The quantitative understanding of structure–property relationship of various metal nanoparticles provides critical insights into plasmon-enhanced spectroscopies. The SERS enhancement effect is essentially a result of the creation of plasmons that can transfer energy to the bound molecule through the associated electric field [313–317]. The first discovery of SERS showed that it was possible for a roughed noble metal surface to dramatically enhance the sensitivity and intensity of Raman spectroscopy [318, 319]. The most inspiring aspect is to consider the application of the marked enhancements afforded by SERS to the more challenging goal of single-molecule detection in the biological environment. The search for high-performance SERS substrates has been directly related to our capabilities to engineer the optical properties of metal nanostructures. As already demonstrated in nanoprism arrays fabricated by nanosphere lithography [320] and chemically fabricated metallic nanoshells [131, 132] strong correlation exists between the LSPR frequency of the substrate, the wavelength of excitation laser, and the SERS enhancements achievable on the nanoparticle surfaces. It is believed that as our capability of optimizing the nanoparticle geometries keeps developing, achieving large SERS enhancements at single-molecule sensitivity reproducibly will become possible. Plasmon-enhanced fluorescence (PEF) is another intriguing phenomena associated with plasmonic excitations. It has been known that fluorophore quenching occurs in close proximity to metallic surfaces (typically$<$50 Å) [321], while interesting coupling between the fluorophore and the enhanced

local electric field near the metal structure occurs at longer distances ranging from 5 to 200 nm, resulting in fluorescence enhancements due to increase in both absorption cross section and radiative decay rates. Correlating the plasmonic responses and fluorescence enhancements at single-nanoparticle level has provided crucial insights into how to use plasmonic nanoparticle to optimize the fluorescence behavior of fluorophores that are widely used in bioimaging [322, 323].

(d) Biomedical Imaging and Photothermal Therapy
Metal nanoparticles have widespread applications in biomedicine, such as cancer cell diagnostics [324, 325], and therapeutics [135, 326, 327]. The enhanced radiative properties of metallic nanoparticles derived from the large surface electric fields when interacting with resonant electromagnetic radiation make both the absorption and scattering cross section of orders of magnitude stronger than those of organic molecules. Therefore, metallic nanoparticles can act as exceptionally novel contrast agents for optical detections. The strongly absorbed radiation can be converted efficiently into heat on a picosecond time scale due to electron–photon and photon–photon processes, which is the so-called process of photothermal therapy. This is a promising new medical technology for cancer treatment and affords potential advantages of active targeting at specific cancer site, low toxicity, minimal side effects, and high efficacy.

In summary, this chapter provides a compelling and comprehensive story of geometrically tunable optical properties of various metallic nanoparticles including nanospheres, nanorods, nanoshells, nanoprisms, nanopolyhedrons, nanostars, nanocages, and multi-nanoparticle assemblies. Developing quantitative understanding of the structure–property relationship of these experimentally realizable metallic nanostructures with increasing structural complexity is directly related to our capabilities to further fine-tune their optical properties to optimize a whole set of important physical, chemical, and biomedical processes. Because of the highly diverse nature, we firmly believe that this field will maintain a fast rate of growth and innovation for many years to come. We predict the future of this field to be an innovative and exciting one with great efforts and inspirations devoted by the scientists and engineers from all over the world.

References

1. Burda C, Chen XB, Narayanan R, El-Sayed MA (2005) Chemistry and properties of nanocrystals of different shapes. Chem Rev 105(4):1025–1102
2. Mie G (1908) Articles on the optical characteristics of turbid tubes, especially colloidal metal solutions. Annalen Der Physik 25(3):377–445
3. Faraday M (1857) The bakerian lecture: experimental relations of gold (and other metals) to light. Philos Trans Roy Soc Lond 147:145–181
4. Link S, El-Sayed MA (2003) Optical properties and ultrafast dynamics of metallic nanocrystals. Annu Rev Phys Chem 54:331–366

5. Link S, El-Sayed MA (2000) Shape and size dependence of radiative, non-radiative and photothermal properties of gold nanocrystals. Int Rev Phys Chem 19(3):409–453
6. El-Sayed MA (2001) Some interesting properties of metals confined in time and nanometer space of different shapes. Acc Chem Res 34(4):257–264
7. Xia YN, Halas NJ (2005) Shape-controlled synthesis and surface plasmonic properties of metallic nanostructures. Mrs Bull 30(5):338–344
8. Jain PK, Huang XH, El-Sayed IH, El-Sayed MA (2008) Noble metals on the nanoscale: Optical and photothermal properties and some applications in imaging, sensing, biology, and medicine. Acc Chem Res 41(12):1578–1586
9. Loo C, Lowery A, Halas NJ, West J et al (2005) Immunotargeted nanoshells for integrated cancer imaging and therapy. Nano Lett 5(4):709–711
10. Huang XH, El-Sayed IH, Qian W, El-Sayed MA (2006) Cancer cell imaging and photothermal therapy in the near-infrared region by using gold nanorods. J Am Chem Soc 128(6):2115–2120
11. Link S, El-Sayed MA (1999) Spectral properties and relaxation dynamics of surface plasmon electronic oscillations in gold and silver nanodots and nanorods. J Phys Chem B 103(40):8410–8426
12. Busbee BD, Obare SO, Murphy CJ (2003) An improved synthesis of high-aspect-ratio gold nanorods. Adv Mater 15(5):414–416
13. Nikoobakht B, El-Sayed MA (2003) Preparation and growth mechanism of gold nanorods (nrs) using seed-mediated growth method. Chem Mater 15(10):1957–1962
14. Murphy CJ, Jana NR (2002) Controlling the aspect ratio of inorganic nanorods and nanowires. Adv Mater 14(1):80–82
15. Murphy CJ, Sau TK, Gole A, Orendorff CJ (2005) Surfactant-directed synthesis and optical properties of one-dimensional plasmonic metallic nanostructures. Mrs Bull 30(5):349–355
16. Jana NR, Gearheart L, Murphy CJ (2001) Wet chemical synthesis of silver nanorods and nanowires of controllable aspect ratio. Chem Commun 7:617–618
17. Jin RC, Cao YW, Mirkin CA, Kelly KL et al (2001) Photoinduced conversion of silver nanospheres to nanoprisms. Science 294(5548):1901–1903
18. Millstone JE, Park S, Shuford KL, Qin LD et al (2005) Observation of a quadrupole plasmon mode for a colloidal solution of gold nanoprisms. J Am Chem Soc 127(15):5312–5313
19. Pastoriza-Santos I, Liz-Marzan LM (2002) Synthesis of silver nanoprisms in dmf. Nano Lett 2(8):903–905
20. Sun YG, Xia YN (2003) Triangular nanoplates of silver: synthesis, characterization, and use as sacrificial templates for generating triangular nanorings of gold. Adv Mater 15(9): 695–699
21. Chen SH, Carroll DL (2002) Synthesis and characterization of truncated triangular silver nanoplates. Nano Lett 2(9):1003–1007
22. Averitt RD, Sarkar D, Halas NJ (1997) Plasmon resonance shifts of au-coated au_2s nanoshells: insight into multicomponent nanoparticle growth. Phys Rev Lett 78(22):4217–4220
23. Oldenburg SJ, Averitt RD, Westcott SL, Halas NJ (1998) Nanoengineering of optical resonances. Chem Phys Lett 288(2–4):243–247
24. Halas NJ (2005) Playing with plasmons. Tuning the optical resonant properties of metallic nanoshells. Mrs Bull 30(5):362–367
25. Hao E, Bailey RC, Schatz GC, Hupp JT et al (2004) Synthesis and optical properties of "branched" gold nanocrystals. Nano Lett 4(2):327–330
26. Nehl CL, Liao HW, Hafner JH (2006) Optical properties of star-shaped gold nanoparticles. Nano Lett 6(4):683–688
27. Chen JY, Wiley B, Li ZY, Campbell D et al (2005) Gold nanocages: engineering their structure for biomedical applications. Adv Mater 17(18):2255–2261
28. Chen JY, McLellan JM, Siekkinen A, Xiong YJ et al (2006) Facile synthesis of gold-silver nanocages with controllable pores on the surface. J Am Chem Soc 128(46):14776–14777

29. Kreibig U, Vollmer M (1995) Optical properties of metal clusters. Springer, Berlin
30. Bohren CF, Huffman DR (1998) Absorption and scattering of light by small particles. Wiley, New York
31. Mulvaney P (1996) Surface plasmon spectroscopy of nanosized metal particles. Langmuir 12(3):788–800
32. Raether H (1988) Surface plasmon on smooth and rough surfaces and on gratings. Springer, Berlin
33. Willets KA, Van Duyne RP (2007) Localized surface plasmon resonance spectroscopy and sensing. Annu Rev Phys Chem 58:267–297
34. Kuwata H, Tamaru H, Esumi K, Miyano K (2003) Resonant light scattering from metal nanoparticles: practical analysis beyond rayleigh approximation. Appl Phys Lett 83(22):4625–4627
35. Gan QQ, Song GF, Yang GH, Xu Y et al (2006) Near-field scanning optical microscopy with an active probe. Appl Phys Lett 88(12):121111
36. Mitsui T (2005) Development of a polarization-preserving optical-fiber probe for near-field scanning optical microscopy and the influences of bending and squeezing on the polarization properties. Rev Sci Instrum 76(4):043703
37. Betzig E, Chichester RJ (1993) Single molecules observed by near-field scanning optical microscopy. Science 262(5138):1422–1425
38. Betzig E, Trautman JK, Harris TD, Weiner JS et al (1991) Breaking the diffraction barrier–optical microscopy on a nanometric scale. Science 251(5000):1468–1470
39. Bethe HA (1944) Theory of diffraction by small holes. Phys Rev 66(7–8):163–182
40. de Abajo F (2002) Light transmission through a single cylindrical hole in a metallic film. Opt Express 10(25):1475–1484
41. Ozcan A, Cubukcu E, Bilenca A, Crozier KB et al (2006) Differential near-field scanning optical microscopy. Nano Lett 6(11):2609–2616
42. Egerton RF (1996) Electron energy-loss spectroscopy in the electron microscope second edition. Plenum, New York
43. Raether H (1980) Excitation of plasmons and interband transitions by electrons, vol 88. Springer, Berlin
44. Koh AL, Fernandez-Dominguez AI, McComb DW, Maier SA et al (2011) High-resolution mapping of electron-beam-excited plasmon modes in lithographically defined gold nanostructures. Nano Lett 11(3):1323–1330
45. Schaffer B, Grogger W, Kothleitner G, Hofer F (2010) Comparison of eftem and stem eels plasmon imaging of gold nanoparticles in a monochromated tem. Ultramicroscopy 110(8):1087–1093
46. Garcia de Abajo FJ (2010) Optical excitations in electron microscopy. Rev Mod Phys 82(1):209–275
47. Chu M-W, Myroshnychenko V, Chen CH, Deng J-P et al (2009) Probing bright and dark surface-plasmon modes in individual and coupled noble metal nanoparticles using an electron beam. Nano Lett 9(1):399–404
48. Nelayah J, Kociak M, Stephan O, Garcia de Abajo FJ et al (2007) Mapping surface plasmons on a single metallic nanoparticle. Nat Phys 3(5):348–353
49. N′Gom M, Li S, Schatz G, Erni R et al (2009) Electron-beam mapping of plasmon resonances in electromagnetically interacting gold nanorods. Phys Rev B 80(11):113411
50. Guiton BS, Iberi V, Li SZ, Leonard DN, Parish CM, Kotula PG, Varela M, Schatz GC, Pennycook SJ, Camden JP (2011) Correlated optical measurements and plasmon mapping of silver nanorods. Nano Lett 11(8):3482–3488
51. Campion A, Kambhampati P (1998) Surface-enhanced raman scattering. Chem Soc Rev 27(4):241–250
52. Kneipp K, Kneipp H, Itzkan I, Dasari RR et al (1999) Ultrasensitive chemical analysis by raman spectroscopy. Chem Rev 99(10):2957–2976

53. Schatz GC (1984) Theoretical-studies of surface enhanced raman-scattering. Acc Chem Res 17(10):370–376
54. Moskovits M (1985) Surface-enhanced spectroscopy. Rev Mod Phys 57(3):783–826
55. Lal S, Grady NK, Goodrich GP, Halas NJ (2006) Profiling the near field of a plasmonic nanoparticle with raman-based molecular rulers. Nano Lett 6(10):2338–2343
56. Kelly KL, Coronado E, Zhao LL, Schatz GC (2003) The optical properties of metal nanoparticles: the influence of size, shape, and dielectric environment. J Phys Chem B 107(3):668–677
57. Noguez C (2007) Surface plasmons on metal nanoparticles: the influence of shape and physical environment. J Phys Chem C 111(10):3806–3819
58. Riikonen S, Romero I, Garcia de Abajo FJ (2005) Plasmon tunability in metallodielectric metamaterials. Phys Rev B 71(23):235104
59. Gonzalez AL, Noguez C (2007) Influence of morphology on the optical properties of metal nanoparticles. J Comput Theoret Nanosci 4(2):231–238
60. Yee KS (1966) Numerical solution of initial boundary value problems involving maxwell's equations in isotropic media. IEEE Trans Antenn Propag AP14(3):302–307
61. Jensen LL, Jensen L (2009) Atomistic electrodynamics model for optical properties of silver nanoclusters. J Phys Chem C 113(34):15182–15190
62. Morton SM, Jensen L (2009) Understanding the molecule-surface chemical coupling in sers. J Am Chem Soc 131(11):4090–4098
63. Zangwill A, Soven P (1980) Density-functional approach to local-field effects in finite systems – photoabsorption in the rare-gases. Phys Rev A 21(5):1561–1572
64. Rodriguez-Fernandez J, Perez-Juste J, Garcia de Abajo FJ, Liz-Marzan LM (2006) Seeded growth of submicron au colloids with quadrupole plasmon resonance modes. Langmuir 22(16):7007–7010
65. Malynych S, Chumanov G (2007) Extinction spectra of quasi-spherical silver sub-micron particles. J Quan Spectros Radiat Trans 106(1–3):297–303
66. Luther JM, Jain PK, Ewers T, Alivisatos AP (2011) Localized surface plasmon resonances arising from free carriers in doped quantum dots. Nat Mater 10(5):361–366
67. Wang C, Yin H, Chan R, Peng S et al (2009) One-pot synthesis of oleylamine coated auag alloy nps and their catalysis for co oxidation. Chem Mater 21(3):433–435
68. Mulvaney P, Giersig M, Henglein A (1993) Electrochemistry of multilayer colloids - preparation and absorption-spectrum of gold-coated silver particles. J Phys Chem 97(27):7061–7064
69. Hostetler MJ, Zhong CJ, Yen BKH, Anderegg J et al (1998) Stable, monolayer-protected metal alloy clusters. J Am Chem Soc 120(36):9396–9397
70. Link S, Wang ZL, El-Sayed MA (1999) Alloy formation of gold-silver nanoparticles and the dependence of the plasmon absorption on their composition. J Phys Chem B 103(18):3529–3533
71. Mallin MP, Murphy CJ (2002) Solution-phase synthesis of sub-10 nm au-ag alloy nanoparticles. Nano Lett 2(11):1235–1237
72. Shibata T, Bunker BA, Zhang ZY, Meisel D et al (2002) Size-dependent spontaneous alloying of Au-Ag nanoparticles. J Am Chem Soc 124(40):11989–11996
73. Wilson OM, Scott RWJ, Garcia-Martinez JC, Crooks RM (2005) Synthesis, characterization, and structure-selective extraction of 1-3-nm diameter auag dendrimer-encapsulated bimetallic nanoparticles. J Am Chem Soc 127(3):1015–1024
74. Wilcoxon J (2009) Optical absorption properties of dispersed gold and silver alloy nanoparticles. J Phys Chem B 113(9):2647–2656
75. Hodak JH, Henglein A, Giersig M, Hartland GV (2000) Laser-induced inter-diffusion in auag core-shell nanoparticles. J Phys Chem B 104(49):11708–11718
76. Mallik K, Mandal M, Pradhan N, Pal T (2001) Seed mediated formation of bimetallic nanoparticles by uv irradiation: a photochemical approach for the preparation of "core-shell" type structures. Nano Lett 1(6):319–322

77. Wilcoxon JP, Provencio PP (2004) Heterogeneous growth of metal clusters from solutions of seed nanoparticles. J Am Chem Soc 126(20):6402–6408
78. Zhang J, Tang Y, Weng L, Ouyang M (2009) Versatile strategy for precisely tailored core@shell nanostructures with single shell layer accuracy: the case of metallic shell. Nano Lett 9(12):4061–4065
79. Wang C, Peng S, Chan R, Sun S (2009) Synthesis of auag alloy nanoparticles from core/shell-structured ag/au. Small 5(5):567–570
80. Liz-Marzan LM (2006) Tailoring surface plasmons through the morphology and assembly of metal nanoparticles. Langmuir 22(1):32–41
81. Rivas L, Sanchez-Cortes S, Garcia-Ramos JV, Morcillo G (2000) Mixed silver/gold colloids: a study of their formation, morphology, and surface-enhanced raman activity. Langmuir 16(25):9722–9728
82. Srnova-Sloufova I, Lednicky F, Gemperle A, Gemperlova J (2000) Core-shell (ag)au bimetallic nanoparticles: analysis of transmission electron microscopy images. Langmuir 16(25):9928–9935
83. Rodriguez-Gonzalez B, Burrows A, Watanabe M, Kiely CJ et al (2005) Multishell bimetallic auag nanoparticles: synthesis, structure and optical properties. J Mater Chem 15(17):1755–1759
84. Shore MS, Wang J, Johnston-Peck AC, Oldenburg AL et al (2011) Synthesis of au(core)/ag(shell) nanoparticles and their conversion to auag alloy nanoparticles. Small 7(2):230–234
85. Huang XH, Neretina S, El-Sayed MA (2009) Gold nanorods: from synthesis and properties to biological and biomedical applications. Adv Mater 21(48):4880–4910
86. Murphy CJ, San TK, Gole AM, Orendorff CJ et al (2005) Anisotropic metal nanoparticles: synthesis, assembly, and optical applications. J Phys Chem B 109(29):13857–13870
87. Perez-Juste J, Pastoriza-Santos I, Liz-Marzan LM, Mulvaney P (2005) Gold nanorods: synthesis, characterization and applications. Coord Chem Rev 249(17–18):1870–1901
88. Gans R (1912) The shape of ultra microscopic gold particles. Annalen Der Physik 37(5):881–900
89. Yu YY, Chang SS, Lee CL, Wang CRC (1997) Gold nanorods: electrochemical synthesis and optical properties. J Phys Chem B 101(34):6661–6664
90. Zuloaga J, Prodan E, Nordlander P (2010) Quantum plasmonics: optical properties and tunability of metallic nanorods. ACS Nano 4(9):5269–5276
91. Murphy CJ, Gole AM, Hunyadi SE, Orendorff CJ (2006) One-dimensional colloidal gold and silver nanostructures. Inorg Chem 45(19):7544–7554
92. Caswell KK, Bender CM, Murphy CJ (2003) Seedless, surfactantless wet chemical synthesis of silver nanowires. Nano Lett 3(5):667–669
93. Wiley BJ, Chen Y, McLellan JM, Xiong Y et al (2007) Synthesis and optical properties of silver nanobars and nanorice. Nano Lett 7(4):1032–1036
94. Martin CR (1996) Membrane-based synthesis of nanomaterials. Chem Mater 8(8):1739–1746
95. Mieszawska AJ, Jalilian R, Sumanasekera GU, Zamborini FP (2007) The synthesis and fabrication of one-dimensional nanoscale heterojunctions. Small 3(5):722–756
96. Chang SS, Shih CW, Chen CD, Lai WC et al (1999) The shape transition of gold nanorods. Langmuir 15(3):701–709
97. Murphy CJ, Thompson LB, Chernak DJ, Yang JA et al (2011) Gold nanorod crystal growth: from seed-mediated synthesis to nanoscale sculpting. Curr Opin Colloid Interf Sci 16(2):128–134
98. Wiesner J, Wokaun A (1989) Anisometric gold colloids - preparation, characterization, and optical-properties. Chem Phys Lett 157(6):569–575
99. Jana NR, Gearheart L, Murphy CJ (2001) Wet chemical synthesis of high aspect ratio cylindrical gold nanorods. J Phys Chem B 105(19):4065–4067
100. Jana NR, Gearheart L, Murphy CJ (2001) Seed-mediated growth approach for shape-controlled synthesis of spheroidal and rod-like gold nanoparticles using a surfactant template. Adv Mater 13(18):1389–1393

101. Grzelczak M, Perez-Juste J, Mulvaney P, Liz-Marzan LM (2008) Shape control in gold nanoparticle synthesis. Chem Soc Rev 37(9):1783–1791
102. Wu HY, Chu HC, Kuo TJ, Kuo CL et al (2005) Seed-mediated synthesis of high aspect ratio gold nanorods with nitric acid. Chem Mater 17(25):6447–6451
103. Chen HM, Peng HC, Liu RS, Asakura K et al (2005) Controlling the length and shape of gold nanorods. J Phys Chem B 109(42):19553–19555
104. Sau TK, Murphy CJ (2004) Room temperature, high-yield synthesis of multiple shapes of gold nanoparticles in aqueous solution. J Am Chem Soc 126(28):8648–8649
105. Smith DK, Korgel BA (2008) The importance of the ctab surfactant on the colloidal seed-mediated synthesis of gold nanorods. Langmuir 24(3):644–649
106. Smith DK, Miller NR, Korgel BA (2009) Iodide in ctab prevents gold nanorod formation. Langmuir 25(16):9518–9524
107. Kim F, Song JH, Yang PD (2002) Photochemical synthesis of gold nanorods. J Am Chem Soc 124(48):14316–14317
108. Giannici F, Placido T, Curri ML, Striccoli M et al (2009) The fate of silver ions in the photochemical synthesis of gold nanorods: an extended x-ray absorption fine structure analysis. Dalton Trans 46:10367–10374
109. Placido T, Comparelli R, Giannici F, Cozzoli PD et al (2009) Photochemical synthesis of water-soluble gold nanorods: the role of silver in assisting anisotropic growth. Chem Mater 21(18):4192–4202
110. Niidome Y, Nishioka K, Kawasaki H, Yamada S (2003) Rapid synthesis of gold nanorods by the combination of chemical reduction and photoirradiation processes; morphological changes depending on the growing processes. Chem Commun 18:2376–2377
111. Miranda OR, Ahmadi TS (2005) Effects of intensity and energy of cw uv light on the growth of gold nanorods. J Phys Chem B 109(33):15724–15734
112. Ahmed M, Narain R (2010) Rapid synthesis of gold nanorods using a one-step photochemical strategy. Langmuir 26(23):18392–18399
113. Nishioka K, Niidome Y, Yamada S (2007) Photochemical reactions of ketones to synthesize gold nanorods. Langmuir 23(20):10353–10356
114. Billot L, de la Chapelle ML, Grimault AS, Vial A et al (2006) Surface enhanced raman scattering on gold nanowire arrays: evidence of strong multipolar surface plasmon resonance enhancement. Chem Phys Lett 422(4–6):303–307
115. Dayal PB, Koyama F (2007) Polarization control of 0.85 mu m vertical-cavity surface-emitting lasers integrated with gold nanorod arrays. Appl Phys Lett 91(11):111–107
116. Hu M, Novo C, Funston A, Wang H et al (2008) Dark-field microscopy studies of single metal nanoparticles: understanding the factors that influence the linewidth of the localized surface plasmon resonance. J Mater Chem 18(17):1949–1960
117. Sonnichsen C, Franzl T, Wilk T, von Plessen G et al (2002) Drastic reduction of plasmon damping in gold nanorods. Phys Rev Lett 88(7):077402
118. Novo C, Gomez D, Perez-Juste J, Zhang Z et al (2006) Contributions from radiation damping and surface scattering to the linewidth of the longitudinal plasmon band of gold nanorods: a single particle study. Phys Chem Chem Phys 8(30):3540–3546
119. Mooradia A (1969) Photoluminescence of metals. Phys Rev Lett 22(5):185–187
120. Boyd GT, Yu ZH, Shen YR (1986) Photoinduced luminescence from the noble-metals and its enhancement on roughened surfaces. Phys Rev B 33(12):7923–7936
121. Mohamed MB, Volkov V, Link S, El-Sayed MA (2000) The 'lightning' gold nanorods: fluorescence enhancement of over a million compared to the gold metal. Chem Phys Lett 317(6):517–523
122. Eustis S, El-Sayed M (2005) Aspect ratio dependence of the enhanced fluorescence intensity of gold nanorods: experimental and simulation study. J Phys Chem B 109(34):16350–16356
123. Bouhelier A, Bachelot R, Lerondel G, Kostcheev S et al (2005) Surface plasmon characteristics of tunable photoluminescence in single gold nanorods. Phys Rev Lett 95(26):267405

124. Imura K, Nagahara T, Okamoto H (2004) Plasmon mode imaging of single gold nanorods. J Am Chem Soc 126(40):12730–12731
125. Imura K, Nagahara T, Okamoto H (2005) Near-field two-photon-induced photoluminescence from single gold nanorods and imaging of plasmon modes. J Phys Chem B 109(27):13214–13220
126. Imura K, Nagahara T, Okamoto H (2005) Near-field optical imaging of plasmon modes in gold nanorods. J Chem Phys 122(15):154701
127. Wang HF, Huff TB, Zweifel DA, He W et al (2005) In vitro and in vivo two-photon luminescence imaging of single gold nanorods. Proc Natl Acad Sci USA 102(44):15752–15756
128. Durr NJ, Larson T, Smith DK, Korgel BA et al (2007) Two-photon luminescence imaging of cancer cells using molecularly targeted gold nanorods. Nano Lett 7(4):941–945
129. Sershen SR, Westcott SL, Halas NJ, West JL (2000) Temperature-sensitive polymer-nanoshell composites for photothermally modulated drug delivery. J Biomed Mater Res 51(3):293–298
130. Hirsch LR, Jackson JB, Lee A, Halas NJ et al (2003) A whole blood immunoassay using gold nanoshells. Anal Chem 75(10):2377–2381
131. Jackson JB, Westcott SL, Hirsch LR, West JL et al (2003) Controlling the surface enhanced raman effect via the nanoshell geometry. Appl Phys Lett 82(2):257–259
132. Jackson JB, Halas NJ (2004) Surface-enhanced raman scattering on tunable plasmonic nanoparticle substrates. Proc Natl Acad Sci USA 101(52):17930–17935
133. Tam F, Goodrich GP, Johnson BR, Halas NJ (2007) Plasmonic enhancement of molecular fluorescence. Nano Lett 7(2):496–501
134. Kundu J, Le F, Nordlander P, Halas NJ (2008) Surface enhanced infrared absorption (seira) spectroscopy on nanoshell aggregate substrates. Chem Phys Lett 452(1–3):115–119
135. Hirsch LR, Stafford RJ, Bankson JA, Sershen SR et al (2003) Nanoshell-mediated near-infrared thermal therapy of tumors under magnetic resonance guidance. Proc Natl Acad Sci USA 100(23):13549–13554
136. Loo C, Lin A, Hirsch L, Lee MH et al (2004) Nanoshell-enabled photonics-based imaging and therapy of cancer. Technol Cancer Res Treat 3(1):33–40
137. Aden AL, Kerker M (1951) Scattering of electromagnetic waves from 2 concentric spheres. J Appl Phys 22(10):1242–1246
138. Neeves AE, Birnboim MH (1989) Composite structures for the enhancement of nonlinear-optical susceptibility. J Opt Soc Am B Opt Phys 6(4):787–796
139. Zhou HS, Honma I, Komiyama H, Haus JW (1994) Controlled synthesis and quantum-size effect in gold-coated nanoparticles. Phys Rev B 50(16):12052–12056
140. Stober W, Fink A, Bohn E (1968) Controlled growth of monodisperse silica spheres in micron size range. J Colloid Interf Sci 26(1):62–69
141. Shi WL, Sahoo Y, Swihart MT, Prasad PN (2005) Gold nanoshells on polystyrene cores for control of surface plasmon resonance. Langmuir 21(4):1610–1617
142. Bardhan R, Grady NK, Ali T, Halas NJ (2010) Metallic nanoshells with semiconductor cores: optical characteristics modified by core medium properties. ACS Nano 4(10):6169–6179
143. Brinson BE, Lassiter JB, Levin CS, Bardhan R et al (2008) Nanoshells made easy: improving au layer growth on nanoparticle surfaces. Langmuir 24(24):14166–14171
144. Jackson JB, Halas NJ (2001) Silver nanoshells: variations in morphologies and optical properties. J Phys Chem B 105(14):2743–2746
145. Jiang ZJ, Liu CY (2003) Seed-mediated growth technique for the preparation of a silver nanoshell on a silica sphere. J Phys Chem B 107(45):12411–12415
146. Wang H, Tam F, Grady NK, Halas NJ (2005) Cu nanoshells: effects of interband transitions on the nanoparticle plasmon resonance. J Phys Chem B 109(39):18218–18222
147. Liu JB, Dong W, Zhan P, Wang SZ et al (2005) Synthesis of bimetallic nanoshells by an improved electroless plating method. Langmuir 21(5):1683–1686

148. Oldenburg SJ, Jackson JB, Westcott SL, Halas NJ (1999) Infrared extinction properties of gold nanoshells. Appl Phys Lett 75(19):2897–2899
149. Tam F, Moran C, Halas NJ (2004) Geometrical parameters controlling sensitivity of nanoshell plasmon resonances to changes in dielectric environment. J Phys Chem B 108(45):17290–17294
150. Nehl CL, Grady NK, Goodrich GP, Tam F et al (2004) Scattering spectra of single gold nanoshells. Nano Lett 4(12):2355–2359
151. Tam F, Chen AL, Kundu J, Wang H et al (2007) Mesoscopic nanoshells: geometry-dependent plasmon resonances beyond the quasistatic limit. J Chem Phys 127(20):204703
152. Brandl DW, Nordlander P (2007) Plasmon modes of curvilinear metallic core/shell particles. J Chem Phys 126(14):144708
153. Wang H, Fu K, Drezek RA, Halas NJ (2006) Light scattering from spherical plasmonic nanoantennas: effects of nanoscale roughness. Appl Phys B Lasers Optics 84(1–2):191–195
154. Wang H, Goodrich GP, Tam F, Oubre C et al (2005) Controlled texturing modifies the surface topography and plasmonic properties of au nanoshells. J Phys Chem B 109(22):11083–11087
155. Oubre C, Nordlander P (2004) Optical properties of metallodielectric nanostructures calculated using the finite difference time domain method. J Phys Chem B 108(46):17740–17747
156. Prodan E, Radloff C, Halas NJ, Nordlander P (2003) A hybridization model for the plasmon response of complex nanostructures. Science 302(5644):419–422
157. Prodan E, Nordlander P (2004) Plasmon hybridization in spherical nanoparticles. J Chem Phys 120(11):5444–5454
158. Nordlander P, Oubre C, Prodan E, Li K et al (2004) Plasmon hybridization in nanoparticle dimers. Nano Lett 4(5):899–903
159. Wang H, Brandl DW, Nordlander P, Halas NJ (2007) Plasmonic nanostructures: artificial molecules. Acc Chem Res 40(1):53–62
160. Prodan E, Nordlander P (2003) Structural tunability of the plasmon resonances in metallic nanoshells. Nano Lett 3(4):543–547
161. Radloff C, Halas NJ (2004) Plasmonic properties of concentric nanoshells. Nano Lett 4(7):1323–1327
162. Bardhan R, Mukherjee S, Mirin NA, Levit SD et al (2010) Nanosphere-in-a-nanoshell: a simple nanomatryushka. J Phys Chem C 114(16):7378–7383
163. Wang H, Wu YP, Lassiter B, Nehl CL et al (2006) Symmetry breaking in individual plasmonic nanoparticles. Proc Natl Acad Sci USA 103(29):10856–10860
164. Wu Y, Nordlander P (2006) Plasmon hybridization in nanoshells with a nonconcentric core. J Chem Phys 125(12):124708
165. Shvets G, Urzhumov YA (2004) Engineering the electromagnetic properties of periodic nanostructures using electrostatic resonances. Phys Rev Lett 93(24):243902
166. Brandl DW, Oubre C, Nordlander P (2005) Plasmon hybridization in nanoshell dimers. J Chem Phys 123(2):024701
167. Love JC, Gates BD, Wolfe DB, Paul KE et al (2002) Fabrication and wetting properties of metallic half-shells with submicron diameters. Nano Lett 2(8):891–894
168. Liu J, McBean KE, Harris N, Cortie MB (2007) Optical properties of suspensions of gold half-shells. Mater Sci Engin B-Solid State Mater Advan Technol 140(3):195–198
169. Charnay C, Lee A, Man SQ, Moran CE et al (2003) Reduced symmetry metallodielectric nanoparticles: chemical synthesis and plasmonic properties. J Phys Chem B 107(30):7327–7333
170. Lu Y, Liu GL, Kim J, Mejia YX et al (2005) Nanophotonic crescent moon structures with sharp edge for ultrasensitive biomolecular detection by local electromagnetic field enhancement effect. Nano Lett 5(1):119–124
171. Liu GL, Lu Y, Kim J, Doll JC et al (2005) Magnetic nanocrescents as controllable surface-enhanced raman scattering nanoprobes for biomolecular imaging. Adv Mater 17(22):2683–2688

172. Lassiter JB, Knight MW, Mirin NA, Halas NJ (2009) Reshaping the plasmonic properties of an individual nanoparticle. Nano Lett 9(12):4326–4332
173. Mirin NA, Halas NJ (2009) Light-bending nanoparticles. Nano Lett 9(3):1255–1259
174. Cortie M, Ford M (2007) A plasmon-induced current loop in gold semi-shells. Nanotechnology 18(23):235704
175. Knight MW, Halas NJ (2008) Nanoshells to nanoeggs to nanocups: optical properties of reduced symmetry core-shell nanoparticles beyond the quasistatic limit. New J Phys 10:105006
176. Mirin NA, Ali TA, Nordlander P, Halas NJ (2010) Perforated semishells: far-field directional control and optical frequency magnetic response. ACS Nano 4(5):2701–2712
177. Wang H, Brandl DW, Le F, Nordlander P et al (2006) Nanorice: a hybrid plasmonic nanostructure. Nano Lett 6(4):827–832
178. Schuck PJ, Fromm DP, Sundaramurthy A, Kino GS et al (2005) Improving the mismatch between light and nanoscale objects with gold bowtie nanoantennas. Phys Rev Lett 94:017402
179. Sanchez EJ, Novotny L, Xie XS (1999) Near-field fluorescence microscopy based on two-photon excitation with metal tips. Phys Rev Lett 82(20):4014–4017
180. Millstone JE, Hurst SJ, Metraux GS, Cutler JI et al (2009) Colloidal gold and silver triangular nanoprisms. Small 5(6):646–664
181. Shuford KL, Ratner MA, Schatz GC (2005) Multipolar excitation in triangular nanoprisms. J Chem Phys 123(11):114713
182. Jin RC, Cao YC, Hao EC, Metraux GS et al (2003) Controlling anisotropic nanoparticle growth through plasmon excitation. Nature 425(6957):487–490
183. Callegari A, Tonti D, Chergui M (2003) Photochemically grown silver nanoparticles with wavelength-controlled size and shape. Nano Lett 3(11):1565–1568
184. Xue C, Mirkin CA (2007) pH-switchable silver nanoprism growth pathways. Angew Chem Int Ed 46(12):2036–2038
185. Xue C, Metraux GS, Millstone JE, Mirkin CA (2008) Mechanistic study of photomediated triangular silver nanoprism growth. J Am Chem Soc 130(26):8337–8344
186. Pastoriza-Santos I, Liz-Marzan LM (2002) Formation of pvp-protected metal nanoparticles in dmf. Langmuir 18(7):2888–2894
187. Malikova N, Pastoriza-Santos I, Schierhorn M, Kotov NA et al (2002) Layer-by-layer assembled mixed spherical and planar gold nanoparticles: control of interparticle interactions. Langmuir 18(9):3694–3697
188. Kim F, Connor S, Song H, Kuykendall T et al (2004) Platonic gold nanocrystals. Angew Chem Int Ed 43(28):3673–3677
189. Shankar SS, Rai A, Ankamwar B, Singh A et al (2004) Biological synthesis of triangular gold nanoprisms. Nat Mater 3(7):482–488
190. Millstone JE, Metraux GS, Mirkin CA (2006) Controlling the edge length of gold nanoprisms via a seed-mediated approach. Adv Funct Mater 16(9):1209–1214
191. Zhang Q, Ge JP, Pham T, Goebl J et al (2009) Reconstruction of silver nanoplates by uv irradiation: tailored optical properties and enhanced stability. Angew Chem Int Ed 48(19):3516–3519
192. Lee BH, Hsu MS, Hsu YC, Lo CW et al (2010) A facile method to obtain highly stable silver nanoplate colloids with desired surface plasmon resonance wavelengths. J Phys Chem C 114(14):6222–6227
193. An J, Tang B, Zheng XL, Zhou J et al (2008) Sculpturing effect of chloride ions in shape transformation from triangular to discal silver nanoplates. J Phys Chem C 112(39):15176–15182
194. Ciou SH, Cao YW, Huang HC, Su DY et al (2009) Sers enhancement factors studies of silver nanoprism and spherical nanoparticle colloids in the presence of bromide ions. J Phys Chem C 113(22):9520–9525

195. Tang B, An J, Zheng XL, Xu SP et al (2008) Silver nanodisks with tunable size by heat aging. J Phys Chem C 112(47):18361–18367
196. Tao A, Sinsermsuksakul P, Yang P (2006) Polyhedral silver nanocrystals with distinct scattering signatures. Angew Chem Int Ed 45(28):4597–4601
197. Khoury CG, Vo-Dinh T (2008) Gold nanostars for surface-enhanced raman scattering: synthesis, characterization and optimization. J Phys Chem C 112(48):18849–18859
198. Nehl CL, Hafner JH (2008) Shape-dependent plasmon resonances of gold nanoparticles. J Mater Chem 18(21):2415–2419
199. Xie JP, Lee JY, Wang DIC (2007) Seedless, surfactantless, high-yield synthesis of branched gold nanocrystals in hepes buffer solution. Chem Mater 19(11):2823–2830
200. Chen SH, Wang ZL, Ballato J, Foulger SH et al (2003) Monopod, bipod, tripod, and tetrapod gold nanocrystals. J Am Chem Soc 125(52):16186–16187
201. Bakr OM, Wunsch BH, Stellacci F (2006) High-yield synthesis of multi-branched urchin-like gold nanoparticles. Chem Mater 18(14):3297–3301
202. Kim DY, Yu T, Cho EC, Ma Y et al (2011) Synthesis of gold nano-hexapods with controllable arm lengths and their tunable optical properties. Angew Chem Int Ed 50(28):6328–6331
203. Wu HL, Chen CH, Huang MH (2009) Seed-mediated synthesis of branched gold nanocrystals derived from the side growth of pentagonal bipyramids and the formation of gold nanostars. Chem Mater 21(1):110–114
204. Liao HG, Jiang YX, Zhou ZY, Chen SP et al (2008) Shape-controlled synthesis of gold nanoparticles in deep eutectic solvents for studies of structure-functionality relationships in electrocatalysis. Angew Chem Int Ed 47(47):9100–9103
205. Burt JL, Elechiguerra JL, Reyes-Gasga J, Montejano-Carrizales JM et al (2005) Beyond archimedean solids: star polyhedral gold nanocrystals. J Cryst Growth 285(4):681–691
206. Yamamoto M, Kashiwagi Y, Sakata T, Mori H et al (2005) Synthesis and morphology of star-shaped gold nanoplates protected by poly(n-vinyl-2-pyrrolidone). Chem Mater 17(22):5391–5393
207. Hao F, Nehl CL, Hafner JH, Nordlander P (2007) Plasmon resonances of a gold nanostar. Nano Lett 7(3):729–732
208. Skrabalak SE, Chen J, Sun Y, Lu X et al (2008) Gold nanocages: synthesis, properties, and applications. Acc Chem Res 41(12):1587–1595
209. Sun YG, Xia YN (2002) Shape-controlled synthesis of gold and silver nanoparticles. Science 298(5601):2176–2179
210. Skrabalak SE, Au L, Li X, Xia Y (2007) Facile synthesis of ag nanocubes and au nanocages. Nat Protoc 2(9):2182–2190
211. Sun YG, Xia YN (2004) Mechanistic study on the replacement reaction between silver nanostructures and chloroauric acid in aqueous medium. J Am Chem Soc 126(12):3892–3901
212. Chen JY, Wiley B, McLellan J, Xiong YJ et al (2005) Optical properties of pd-ag and pt-ag nanoboxes synthesized via galvanic replacement reactions. Nano Lett 5(10):2058–2062
213. Cobley CM, Campbell DJ, Xia Y (2008) Tailoring the optical and catalytic properties of gold-silver nanoboxes and nanocages by introducing palladium. Adv Mater 20(4):748–752
214. Skrabalak SE, Chen J, Au L, Lu X et al (2007) Gold nanocages for biomedical applications. Adv Mater 19(20):3177–3184
215. Yang X, Skrabalak SE, Li Z-Y, Xia Y et al (2007) Photoacoustic tomography of a rat cerebral cortex in vivo with au nanocages as an optical contrast agent. Nano Lett 7(12):3798–3802
216. Chen J, Saeki F, Wiley BJ, Cang H et al (2005) Gold nanocages: bioconjugation and their potential use as optical imaging contrast agents. Nano Lett 5(3):473–477
217. Cang H, Sun T, Li ZY, Chen JY et al (2005) Gold nanocages as contrast agents for spectroscopic optical coherence tomography. Opt Lett 30(22):3048–3050

218. Halas NJ, Lal S, Chang W-S, Link S et al (2011) Plasmons in strongly coupled metallic nanostructures. Chem Rev 111(6):3913–3961
219. Jin RC, Wu GS, Li Z, Mirkin CA et al (2003) What controls the melting properties of DNA-linked gold nanoparticle assemblies? J Am Chem Soc 125(6):1643–1654
220. Storhoff JJ, Elghanian R, Mucic RC, Mirkin CA et al (1998) One-pot colorimetric differentiation of polynucleotides with single base imperfections using gold nanoparticle probes. J Am Chem Soc 120(9):1959–1964
221. Storhoff JJ, Lazarides AA, Mucic RC, Mirkin CA et al (2000) What controls the optical properties of DNA-linked gold nanoparticle assemblies? J Am Chem Soc 122(19):4640–4650
222. Tan SJ, Campolongo MJ, Luo D, Cheng WL (2011) Building plasmonic nanostructures with DNA. Nat Nanotechnol 6(5):268–276
223. Camden JP, Dieringer JA, Wang Y, Masiello DJ et al (2008) Probing the structure of single-molecule surface-enhanced raman scattering hot spots. J Am Chem Soc 130(38):12616–12617
224. Dieringer JA, Lettan RB II, Scheidt KA, Van Duyne RP (2007) A frequency domain existence proof of single-molecule surface-enhanced raman spectroscopy. J Am Chem Soc 129(51):16249–16256
225. Kneipp K, Kneipp H, Kneipp J (2006) Surface-enhanced raman scattering in local optical fields of silver and gold nanoaggregatess - from single-molecule raman spectroscopy to ultrasensitive probing in live cells. Acc Chem Res 39(7):443–450
226. Kneipp K, Wang Y, Kneipp H, Perelman LT et al (1997) Single molecule detection using surface-enhanced raman scattering (sers). Phys Rev Lett 78(9):1667–1670
227. Michaels AM, Nirmal M, Brus LE (1999) Surface enhanced raman spectroscopy of individual rhodamine 6g molecules on large ag nanocrystals. J Am Chem Soc 121(43):9932–9939
228. Nie SM, Emery SR (1997) Probing single molecules and single nanoparticles by surface-enhanced raman scattering. Science 275(5303):1102–1106
229. Aravind PK, Nitzan A, Metiu H (1981) The interaction between electromagnetic resonances and its role in spectroscopic studies of molecules adsorbed on colloidal particles or metal spheres. Surf Sci 110(1):189–204
230. Oubre C, Nordlander P (2005) Finite-difference time-domain studies of the optical properties of nanoshell dimers. J Phys Chem B 109(20):10042–10051
231. Su KH, Wei QH, Zhang X, Mock JJ et al (2003) Interparticle coupling effects on plasmon resonances of nanogold particles. Nano Lett 3(8):1087–1090
232. Hao E, Schatz GC (2004) Electromagnetic fields around silver nanoparticles and dimers. J Chem Phys 120(1):357–366
233. Brown LV, Sobhani H, Lassiter JB, Nordlander P et al (2010) Heterodimers: plasmonic properties of mismatched nanoparticle pairs. ACS Nano 4(2):819–832
234. Lassiter JB, Aizpurua J, Hernandez LI, Brandl DW et al (2008) Close encounters between two nanoshells. Nano Lett 8(4):1212–1218
235. Talley CE, Jackson JB, Oubre C, Grady NK et al (2005) Surface-enhanced raman scattering from individual au nanoparticles and nanoparticle dimer substrates. Nano Lett 5(8):1569–1574
236. Li W, Camargo PHC, Lu X, Xia Y (2009) Dimers of silver nanospheres: facile synthesis and their use as hot spots for surface-enhanced raman scattering. Nano Lett 9(1):485–490
237. Camargo PHC, Au L, Rycenga M, Li W et al (2010) Measuring the sers enhancement factors of dimers with different structures constructed from silver nanocubes. Chem Phys Lett 484(4–6):304–308
238. Camargo PHC, Rycenga M, Au L, Xia Y (2009) Isolating and probing the hot spot formed between two silver nanocubes. Angew Chem Int Ed 48(12):2180–2184
239. Fromm DP, Sundaramurthy A, Kinkhabwala A, Schuck PJ et al (2006) Exploring the chemical enhancement for surface-enhanced raman scattering with au bowtie nanoantennas. J Chem Phys 124(6):061101

240. Jackel F, Kinkhabwala AA, Moerner WE (2007) Gold bowtie nanoantennas for surface-enhanced raman scattering under controlled electrochemical potential. Chem Phys Lett 446(4–6):339–343
241. Schuck PJ, Fromm DP, Sundaramurthy A, Kino GS et al (2005) Improving the mismatch between light and nanoscale objects with gold bowtie nanoantennas. Phys Rev Lett 94(1):017402
242. Gunnarsson L, Rindzevicius T, Prikulis J, Kasemo B et al (2005) Confined plasmons in nanofabricated single silver particle pairs: experimental observations of strong interparticle interactions. J Phys Chem B 109(3):1079–1087
243. Pena-Rodriguez O, Pal U, Campoy-Quiles M, Rodriguez-Fernandez L et al (2011) Enhanced fano resonance in asymmetrical au:Ag heterodimers. J Phys Chem C 115(14):6410–6414
244. Shao L, Woo KC, Chen H, Jin Z et al (2010) Angle- and energy-resolved plasmon coupling in gold nanorod dimers. ACS Nano 4(6):3053–3062
245. Slaughter LS, Wu Y, Willingham BA, Nordlander P et al (2010) Effects of symmetry breaking and conductive contact on the plasmon coupling in gold nanorod dimers. ACS Nano 4(8):4657–4666
246. Yang Z-J, Zhang Z-S, Zhang W, Hao Z-H et al (2010) Twinned fano interferences induced by hybridized plasmons in au-ag nanorod heterodimers. Appl Phys Lett 96(13):131113
247. Funston AM, Novo C, Davis TJ, Mulvaney P (2009) Plasmon coupling of gold nanorods at short distances and in different geometries. Nano Lett 9(4):1651–1658
248. Jain PK, Eustis S, El-Sayed MA (2006) Plasmon coupling in nanorod assemblies: optical absorption, discrete dipole approximation simulation, and exciton-coupling model. J Phys Chem B 110(37):18243–18253
249. Sonnichsen C, Reinhard BM, Liphardt J, Alivisatos AP (2005) A molecular ruler based on plasmon coupling of single gold and silver nanoparticles. Nat Biotechnol 23(6):741–745
250. Jain PK, Huang W, El-Sayed MA (2007) On the universal scaling behavior of the distance decay of plasmon coupling in metal nanoparticle pairs: a plasmon ruler equation. Nano Lett 7(7):2080–2088
251. Liu GL, Yin Y, Kunchakarra S, Mukherjee B et al (2006) A nanoplasmonic molecular ruler for measuring nuclease activity and DNA footprinting. Nat Nanotechnol 1(1):47–52
252. Reinhard BM, Sheikholeslami S, Mastroianni A, Alivisatos AP et al (2007) Use of plasmon coupling to reveal the dynamics of DNA bending and cleavage by single ecorv restriction enzymes. Proc Natl Acad Sci USA 104(8):2667–2672
253. Reinhard BM, Siu M, Agarwal H, Alivisatos AP et al (2005) Calibration of dynamic molecular rule based on plasmon coupling between gold nanoparticles. Nano Lett 5(11):2246–2252
254. Roy R, Hohng S, Ha T (2008) A practical guide to single-molecule fret. Nat Methods 5(6):507–516
255. Brandl DW, Mirin NA, Nordlander P (2006) Plasmon modes of nanosphere trimers and quadrumers. J Phys Chem B 110(25):12302–12310
256. Chuntonov L, Haran G (2011) Trimeric plasmonic molecules: the role of symmetry. Nano Lett 11(6):2440–2445
257. Fan JA, Bao K, Wu C, Bao J et al (2010) Fano-like interference in self-assembled plasmonic quadrumer clusters. Nano Lett 10(11):4680–4685
258. Rahmani M, Lukiyanchuk B, Ng B, Liew A, Tavakkoli KG et al (2011) Generation of pronounced fano resonances and tuning of subwavelength spatial light distribution in plasmonic pentamers. Opt Expr 19(6):4949–4956
259. Fan JA, Wu C, Bao K, Bao J et al (2010) Self-assembled plasmonic nanoparticle clusters. Science 328(5982):1135–1138
260. Lassiter JB, Sobhani H, Fan JA, Kundu J et al (2010) Fano resonances in plasmonic nanoclusters: geometrical and chemical tunability. Nano Lett 10(8):3184–3189
261. Hentschel M, Dregely D, Vogelgesang R, Giessen H et al (2011) Plasmonic oligomers: the role of individual particles in collective behavior. ACS Nano 5(3):2042–2050

262. Hentschel M, Saliba M, Vogelgesang R, Giessen H et al (2010) Transition from isolated to collective modes in plasmonic oligomers. Nano Lett 10(7):2721–2726
263. de Waele R, Koenderink AF, Polman A (2007) Tunable nanoscale localization of energy on plasmon particle arrays. Nano Lett 7(7):2004–2008
264. Maier SA, Kik PG, Atwater HA (2003) Optical pulse propagation in metal nanoparticle chain waveguides. Phys Rev B 67(20):205402
265. Auguie B, Barnes WL (2008) Collective resonances in gold nanoparticle arrays. Phys Rev Lett 101(14):143902
266. Giannini V, Vecchi G, Rivas JG (2010) Lighting up multipolar surface plasmon polaritons by collective resonances in arrays of nanoantennas. Phys Rev Lett 105(26):266801
267. Vecchi G, Giannini V, Rivas JG (2009) Shaping the fluorescent emission by lattice resonances in plasmonic crystals of nanoantennas. Phys Rev Lett 102(14):146807
268. Chu YZ, Schonbrun E, Yang T, Crozier KB (2008) Experimental observation of narrow surface plasmon resonances in gold nanoparticle arrays. Appl Phys Lett 93(18):181108
269. Lamprecht B, Schider G, Lechner RT, Ditlbacher H et al (2000) Metal nanoparticle gratings: influence of dipolar particle interaction on the plasmon resonance. Phys Rev Lett 84(20):4721–4724
270. Hicks EM, Zou SL, Schatz GC, Spears KG et al (2005) Controlling plasmon line shapes through diffractive coupling in linear arrays of cylindrical nanoparticles fabricated by electron beam lithography. Nano Lett 5(6):1065–1070
271. Evanoff DD, Chumanov G (2005) Synthesis and optical properties of silver nanoparticles and arrays. Chemphyschem 6(7):1221–1231
272. Malynych S, Chumanov G (2003) Light-induced coherent interactions between silver nanoparticles in two-dimensional arrays. J Am Chem Soc 125(10):2896–2898
273. Zou SL, Schatz GC (2004) Narrow plasmonic/photonic extinction and scattering line shapes for one and two dimensional silver nanoparticle arrays. J Chem Phys 121(24):12606–12612
274. Mayshev AV, Malyshev VA, Knoester J (2008) Frequency-controlled localization of optical signals in graded plasmonic chains. Nano Lett 8(8):2369–2372
275. Sukharev M, Seideman T (2006) Phase and polarization control as a route to plasmonic nanodevices. Nano Lett 6(4):715–719
276. Nordlander P (2008) Plasmonics – subwavelength imaging in colour. Nat Photon 2(7):387–388
277. Kawata S, Ono A, Verma P (2008) Subwavelength colour imaging with a metallic nanolens. Nat Photon 2(7):438–442
278. Brongersma ML, Hartman JW, Atwater HA (2000) Electromagnetic energy transfer and switching in nanoparticle chain arrays below the diffraction limit. Phys Rev B 62(24):16356–16359
279. Zou SL, Schatz GC (2006) Metal nanoparticle array waveguides: proposed structures for subwavelength devices. Phys Rev B 74(12):125111
280. Nomura W, Ohtsu M, Yatsui T (2005) Nanodot coupler with a surface plasmon polariton condenser for optical far/near-field conversion. Appl Phys Lett 86(18):181108
281. Maier SA, Brongersma ML, Kik PG, Atwater HA (2002) Observation of near-field coupling in metal nanoparticle chains using far-field polarization spectroscopy. Phys Re B 65(19):193408
282. Maier SA, Brongersma ML, Kik PG, Meltzer S et al (2001) Plasmonics – a route to nanoscale optical devices. Adv Mater 13(19):1501–1505
283. Salerno M, Krenn JR, Hohenau A, Ditlbacher H et al (2005) The optical near-field of gold nanoparticle chains. Opt Commun 248(4–6):543–549
284. Bouhelier A, Bachelot R, Im JS, Wiederrecht GP et al (2005) Electromagnetic interactions in plasmonic nanoparticle arrays. J Phys Chem B 109(8):3195–3198
285. Maier SA, Kik PG, Atwater HA, Meltzer S et al (2003) Local detection of electromagnetic energy transport below the diffraction limit in metal nanoparticle plasmon waveguides. Nat Mater 2(4):229–232

286. Tao A, Sinsermsuksakul P, Yang P (2007) Tunable plasmonic lattices of silver nanocrystals. Nat Nanotechnol 2(7):435–440
287. Tao AR, Ceperley DP, Sinsermsuksakul P, Neureuther AR et al (2008) Self-organized silver nanoparticles for three-dimensional plasmonic crystals. Nano Lett 8(11):4033–4038
288. Tao AR, Huang J, Yang P (2008) Langmuir-blodgettry of nanocrystals and nanowires. Acc Chem Res 41(12):1662–1673
289. Wang HH, Liu CY, Wu SB, Liu NW et al (2006) Highly raman-enhancing substrates based on silver nanoparticle arrays with tunable sub-10 nm gaps. Adv Mater 18(4):491–495
290. Genov DA, Sarychev AK, Shalaev VM, Wei A (2004) Resonant field enhancements from metal nanoparticle arrays. Nano Lett 4(1):153–158
291. Wang H, Levin CS, Halas NJ (2005) Nanosphere arrays with controlled sub-10-nm gaps as surface-enhanced raman spectroscopy substrates. J Am Chem Soc 127(43):14992–14993
292. Wei A, Kim B, Sadtler B, Tripp SL (2001) Tunable surface-enhanced raman scattering from large gold nanoparticle arrays. Chemphyschem 2(12):743–745
293. Lee SJ, Morrill AR, Moskovits M (2006) Hot spots in silver nanowire bundles for surface-enhanced raman spectroscopy. J Am Chem Soc 128(7):2200–2201
294. Wang H, Kundu J, Halas NJ (2007) Plasmonic nanoshell arrays combine surface-enhanced vibrational spectroscopies on a single substrate. Angew Chem Int Ed 46(47):9040–9044
295. Le F, Brandl DW, Urzhumov YA, Wang H et al (2008) Metallic nanoparticle arrays: a common substrate for both surface-enhanced raman scattering and surface-enhanced infrared absorption. ACS Nano 2(4):707–718
296. Pillai S, Green MA (2010) Plasmonics for photovoltaic applications. Solar Energy Mater Solar Cells 94(9):1481–1486
297. Ferry VE, Sweatlock LA, Pacifici D, Atwater HA (2008) Plasmonic nanostructure design for efficient light coupling into solar cells. Nano Lett 8(12):4391–4397
298. Saeta PN, Ferry VE, Pacifici D, Munday JN et al (2009) How much can guided modes enhance absorption in thin solar cells? Opt Express 17(23):20975–20990
299. Pala RA, White J, Barnard E, Liu J et al (2009) Design of plasmonic thin-film solar cells with broadband absorption enhancements. Adv Mater 21(34):3504–3509
300. Ferry VE, Munday JN, Atwater HA (2010) Design considerations for plasmonic photovoltaics. Adv Mater 22(43):4794–4808
301. Yablonovitch E, Cody GD (1982) Intensity enhancement in textured optical sheets for solar-cells. IEEE Trans Elect Dev 29(2):300–305
302. Green MA (1984) Limits on the open-circuit voltage and efficiency of silicon solar-cells imposed by intrinsic auger processes. IEEE Trans Elect Dev 31(5):671–678
303. Campbell P, Green MA (1987) Light trapping properties of pyramidally textured surfaces. J Appl Phys 62(1):243–249
304. Catchpole KR, Polman A (2008) Plasmonic solar cells. Opt Expr 16(26):21793–21800
305. Novotny L (2007) Effective wavelength scaling for optical antennas. Phys Rev Lett 98(26):266802
306. Fischer UC, Pohl DW (1989) Observation of single-particle plasmons by near-field optical microscopy. Phys Rev Lett 62(4):458–461
307. Novotny L, Stranick SJ (2006) Near-field optical microscopy and spectroscopy with pointed probes. Ann Rev Phys Chem 57:303–331
308. Novotny L, van Hulst N (2011) Antennas for light. Nat Photon 5(2):83–90
309. Alu A, Engheta N (2008) Tuning the scattering response of optical nanoantennas with nanocircuit loads. Nat Photon 2(5):307–310
310. Muhlschlegel P, Eisler HJ, Martin OJF, Hecht B et al (2005) Resonant optical antennas. Science 308(5728):1607–1609
311. Stipe BC, Strand TC, Poon CC, Balamane H et al (2010) Magnetic recording at 1.5 pb m(-2) using an integrated plasmonic antenna. Nat Photon 4(7):484–488
312. Challener WA, Peng CB, Itagi AV, Karns D et al (2009) Heat-assisted magnetic recording by a near-field transducer with efficient optical energy transfer. Nat Photon 3(4):220–224

313. Otto A (2006) On the significance of shalaev's "hot spots' in ensemble and single-molecule SERS by adsorbates on metallic films at the percolation threshold. J Raman Spectros 37(9):937–947
314. Li KR, Stockman MI, Bergman DJ (2003) Self-similar chain of metal nanospheres as an efficient nanolens. Phys Rev Lett 91(22):227402
315. Stockman MI, Faleev SV, Bergman DJ (2001) Localization versus delocalization of surface plasmons in nanosystems: can one state have both characteristics? Phys Rev Lett 87(16):167401
316. Gresillon S, Aigouy L, Boccara AC, Rivoal JC et al (1999) Experimental observation of localized optical excitations in random metal-dielectric films. Phys Rev Lett 82(22):4520–4523
317. Tsai DP, Kovacs J, Wang ZH, Moskovits M et al (1994) Photon scanning-tunneling-microscopy images of optical-excitations of fractal metal colloid clusters. Phys Rev Lett 72(26):4149–4152
318. Albrecht MG, Creighton JA (1977) Anomalously intense raman-spectra of pyridine at a silver electrode. J Am Chem Soc 99(15):5215–5217
319. Jeanmaire DL, Vanduyne RP (1977) Surface raman spectroelectrochemistry. 1. Heterocyclic, aromatic, and aliphatic-amines adsorbed on anodized silver electrode. J Electroanal Chem 84(1):1–20
320. Haes AJ, Haynes CL, McFarland AD, Schatz GC et al (2005) Plasmonic materials for surface-enhanced sensing and spectroscopy. Mrs Bull 30(5):368–375
321. Lakowicz JR, Geddes CD, Gryczynski I, Malicka J et al (2004) Advances in surface-enhanced fluorescence. J Fluoresc 14(4):425–441
322. Chen Y, Munechika K, Ginger DS (2007) Dependence of fluorescence intensity on the spectral overlap between fluorophores and plasmon resonant single silver nanoparticles. Nano Lett 7(3):690–696
323. Munechika K, Chen Y, Tillack AF, Kulkarni AP et al (2010) Spectral control of plasmonic emission enhancement from quantum dots near single silver nanoprisms. Nano Lett 10(7):2598–2603
324. Wu XY, Liu HJ, Liu JQ, Haley KN et al (2003) Immunofluorescent labeling of cancer marker her2 and other cellular targets with semiconductor quantum dots. Nat Biotechnol 21(1):41–46
325. Alivisatos P (2004) The use of nanocrystals in biological detection. Nat Biotechnol 22(1):47–52
326. Melancon MP, Lu W, Yang Z, Zhang R et al (2008) In vitro and in vivo targeting of hollow gold nanoshells directed at epidermal growth factor receptor for photothermal ablation therapy. Mol Cancer Ther 7(6):1730–1739
327. Lu W, Xiong CY, Zhang GD, Huang Q et al (2009) Targeted photothermal ablation of murine melanomas with melanocyte-stimulating hormone analog-conjugated hollow gold nanospheres. Clin Cancer Res 15(3):876–886

Optical Properties of Metallic Semishells: Breaking the Symmetry of Plasmonic Nanoshells

2

Jian Ye and Pol Van Dorpe

Contents

1 Definition of the Topic

Symmetric metal colloids, for example, nanospheres and nanoshells, are very well-studied plasmonic nanostructures. Breaking the symmetry of originally symmetric nanostructures induces many interesting changes of optical properties and local near-field distribution. In this chapter, we present the fabrication and optical properties of symmetry-broken nanoshells, namely, semishells.

J. Ye (✉)
imec vzw, Leuven, Belgium

Chemistry Department, KU Leuven, Leuven, Belgium

P. Van Dorpe
imec vzw, Leuven, Belgium

Physics Department, KU Leuven, Leuven, Belgium

Challa S.S.R. Kumar (ed.), *UV-VIS and Photoluminescence Spectroscopy for Nanomaterials Characterization*, DOI 10.1007/978-3-642-27594-4_2,

2 Overview

Localized surface plasmon excitations in metal nanostructures have a strong impact on light scattering, absorption, and local electric field intensities at the nanoscale. Tweaking the nanoparticle shape, size, and material enables researchers to engineer the resonance wavelength position, the nanoparticles' local field enhancement, and their scattering properties. Initially, most of the work focused on symmetric nanoparticles such as nanoshells, consisting of a dielectric core and a thin metallic shell, which exhibit highly tunable optical properties. Interestingly, by breaking the symmetry of originally symmetric nanostructures, additional degrees of freedom can be explored. One particular example of a highly investigated nanostructure is so-called semishell (or nanocup or nanocap).

In recent years, a series of experimental and theoretical work on semishells have been performed, related to a wide set of optical properties. Different fabrication techniques have been introduced in order to address different sets of properties. However, no comprehensive review that addresses all these aspects has been published to the best of our knowledge. In this chapter, we will present an overview on the fabrication and plasmonic optical properties of metallic semishells and the related applications. First, we introduce the definition of the semishell and then present why the semishells are so important and interesting for the investigation in the plasmonic field. Second, a number of fabrication methods of semishells are reviewed and compared by showing different advantages. The fabrication strategy of semishells is important, since it determines the final structural geometry and orientation, which leads to different applications. In the third section, we discuss the optical properties of semishells with a symmetry-reduced geometry. Due to the anisotropic geometry, metallic semishells exhibit quite distinct optical features compared to nanoshells with respect to light scattering, absorption, and near-field information. Furthermore, the optical properties of semishells can be tuned by controlling the dimensions of semishells, for example, core size, shell thickness, height, shell metals, and light polarization, which are discussed in the third section as well. Additionally, we also discuss the potential applications of semishells in the surface-enhanced Raman scattering and plasmonically enhanced solar cells. In the end, various fabrication techniques of semishells are summarized and a future perspective on the applications based on the semishells is given in terms of SERS and solar cells.

3 Introduction

Metal-based plasmonic nanostructures manipulate and concentrate light in nanoscale regions that are much smaller than conventional optic components. When such nanostructures are illuminated with light, a collective oscillation of the quasi-free electrons called surface plasmon generates a strong optical resonance, consequently producing enhanced near fields in deep-subwavelength scales that enables applications, such as waveguides [1], biochemical sensors [2], and surface-enhanced Raman scattering (SERS) spectroscopy [3]. Plasmon resonances

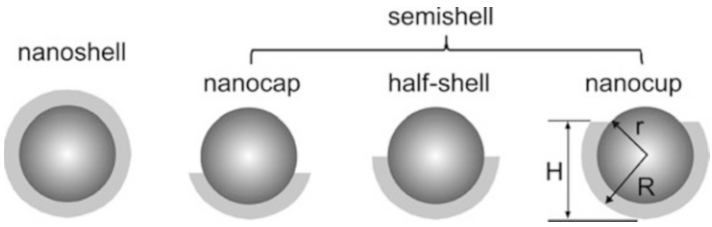

Fig. 2.1 Schematic of a nanoshell and semishells (including nanocap, half-shell, and nanocup)

of nanostructures strongly depend on their geometries and can be tailored throughout the visible and near-infrared (NIR) part of the spectrum with structures of different shapes, such as nanoshells [4] nanocubes [5], and nanorings [2].

Metallic nanoshells (see Fig. 2.1), concentric nanoparticles (NPs) consisting of a dielectric core (typically silica or polystyrene) and an ultrathin metallic shell, are one of interesting plasmonic nanostructures with unique and geometrically tunable optical resonances. Halas and coworkers are the first to prepare gold (Au) nanoshells with plasmon resonances in the NIR region by seeded metallization of colloidal silica particles [6]. The plasmon resonances of Au nanoshells can be tuned from the visible to the NIR region by controlling the relative ratio of the core size and shell thickness. The underlying reason lies beyond the classical electromagnetic theory, where plasmons hybridize in the same manner as the individual atomic wave functions in simple molecules [4]. Because nanoshells are able to absorb and scatter light in the NIR region, where absorption of light by biological tissue reaches a minimum, they are highly potential for in vivo biomedical imaging, drug delivery, and localized cancer thermotherapy application. In addition to Au nanoshells, the same preparation method has been applied to synthesize silver (Ag) [7] and copper (Cu) nanoshells [8].

Although Au and Ag have a highly symmetric, face-centered cubic crystal structure, some two-dimensional nanostructures with an asymmetric shape, for example, split-ring resonators (SRRs) [9] and nanocrescents [10], have been fabricated and have shown very novel optical properties and applications. They both have an incomplete ring shape geometry. Split-ring resonators are one of the most common elements used to fabricate metamaterials. Due to splits in the rings, the structure can support resonant wavelengths much larger than the diameter of the rings. This would not happen in closed rings. They mainly can excite magnetic dipoles directly. Split-ring resonators are widely used for research in negative index metamaterials, terahertz metamaterials, and plasmonic antennas. Due to the symmetry-broken geometry, nanocrescents show a larger refractive index sensitivity and a broader tunable range of localized surface plasmon resonance compared to the nanorings. Au nanocrescents are very useful for localized surface plasmon resonance sensing and surface-enhanced Raman scattering spectroscopy. Due to an analogous geometry, apparently, one may ask what the optical change is if we break the symmetry of the three-dimensional structure: nanoshells. We will answer this question in the following text.

The term semishell refers to an incomplete nanoshell and is a general denomination in contrast to the nanoshell (Fig. 2.1). Semishells ($r/R/H$) can be described by their inner radius (r), outer radius (R), and height (H). By varying H, semishell family members may include nanocaps ($H < R$), half-shells ($H = R$), and nanocups ($R < H < 2R$) (see Fig. 2.1). Semishells are a sort of three-dimensional symmetry-broken structure. Semishells exhibit quite distinct optical features in contrast to nanoshells, for example, a more pronounced red shift of LSPR bands by tuning the aspect ratio, a larger tuning range of optical properties, increased optical absorption at higher wavelengths, and more enhanced local electric fields. In addition, reduced symmetry results in two very different plasmon modes (electric and magnetic dipolar modes) of Au semishells when light is transversely or axially polarized. More interestingly, the magnetic mode exhibits a unique light-bending property. These new properties are potentially useful for a wide range of applications including biosensors, biological imaging, waveguide, and solar cells.

4 Experimental Methodology: Fabrication of Metallic Semishells

The fabrication of metallic semishells is typically analogous to that of nanoshells, in which a metal layer is chemically or physically deposited onto a template of a dielectric core in a controllable way. To date, there are a number of different techniques reported to prepare semishells. In general, they may be classified into two approaches: dry etching and template deposition.

4.1 Dry Etching

It is obvious that the semishells can be prepared by transforming the morphology from the nanoshells. Using some dry-etching methods, such as ion milling and electron beam etching, one can systematically remove a part of the full shell in a highly controlled way and consequently form a symmetry-broken semishell.

A versatile procedure using ion milling to fabricate Au semishells has been reported recently (see Fig. 2.2a) [11]. Au nanoshells were first synthesized by a wet-chemistry plating method from SiO_2 core templates (r) and immobilized in a submonolayer onto a 3-mercaptopropyltrimethoxysilane or poly(vinylpyridine)-coated substrate. The etching process was implemented over the whole substrate in an ion miller system for a number of seconds. Ion milling is a process in which an energetic ion beam of Xe ions is used to bombard the sample surface, thereby physically etching away the sample material. The etching rate is material dependent, and furthermore, its intrinsic working principle makes it a very directional-etching method. For a constant intensity beam of ions, the etching depth is controlled by the ion-milling time. Figure 2.2b shows TEM and SEM images of Au semishells with different sizes, clearly indicating the nanoapertures created

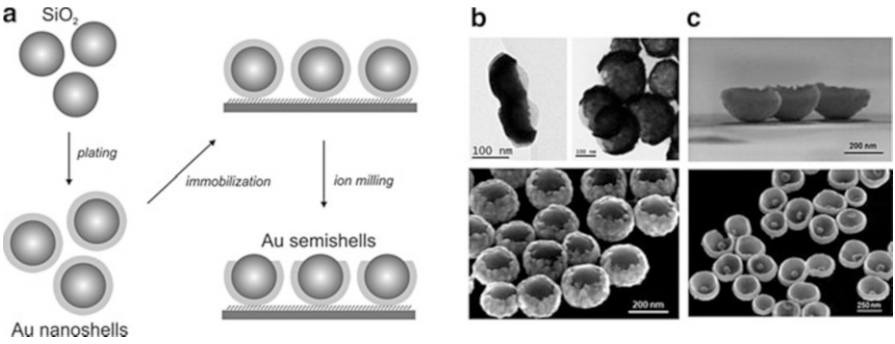

Fig. 2.2 (**a**) Schematic of the fabrication procedure for Au semishells via ion-milling technique [11] (**b**) TEM and SEM images of Au semishells with different sizes [11]. (**c**) SEM images of hollow Au nanobowls (*top*) and Au particle-in-nanobowl structures [12] (Reprinted with kind permission from Refs. [11, 12])

during the etching process. It is important to note that ion milling is a facile, fast, clean, and easily controllable technique. This technique is also applicable to etch away other metals, for example, Ag, Ni, Cu, and Ti. This method allows us to precisely control the reduced symmetric geometry, the upward orientation ("upward facing") of the created semishells. These features are rather favorable to the application of SERS. Furthermore, a vapor HF etching process is applicable to remove the SiO_2 core to produce hollow semishells, also call nanobowls (see Fig. 2.2c). Since vapor HF only reacts with SiO_2 and keeps Au material intact, this method provides a further possibility to prepare more complex structures such as Au particle-in-nanobowl (see Fig. 2.2c). Due to an extremely high near-field enhancement [13] this particle-in-nanobowl cavity structure may act as a suitable single-plasmonic-nanostructure platform for the study of plasmon hybridization, optical trapping, and SERS-based biosensing.

In addition, semishells can be prepared by using an electron beam-induced ablation process (see Fig. 2.3) [14]. Typically, this ablation process can be implemented using environmental scanning electron microscopy (ESEM). ESEM allows scanning electron microscopy to be performed on nonconductive samples through the introduction of H_2O vapor into the vacuum ESEM environment to stabilize surface charging. The electron beam continuously scans a small area ($\sim$500 nm^2) of the sample, allowing for simultaneous ablation and monitoring of the ablation process. A possible mechanism for this process is that the incident electron beam induces a net negative charge on the nanoparticle surface, which then attracts the positively charged H_2O ions to the nanoparticle, resulting in the sputtering of material from the nanoparticle.

Ion milling and electron beam-induced ablation are two similar directional-etching techniques. However, the former can create a great number of semishells spontaneously over a large area, and the latter is more suitable for local and controllable fabrication of single semishells.

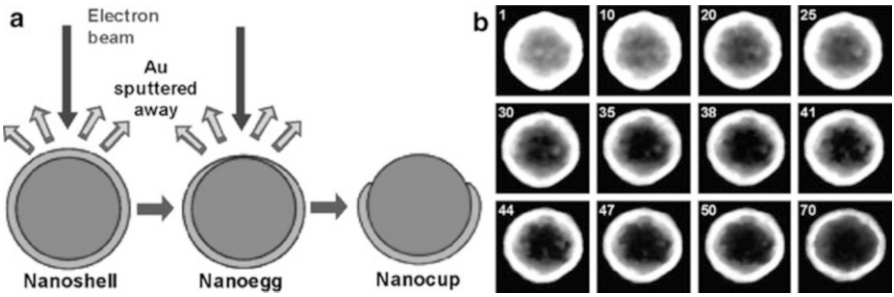

Fig. 2.3 (**a**) Schematic of the electron beam-induced ablation process for fabricating single Au semishells. (**b**) A selected representative sequence from 70 video frames imaging the transition between the initial nanoshell (*upper left frame*) and the final nanocup (*lower right frame*) (Reprinted with kind permission from Ref. [14])

4.2 Template Deposition

Semishells can be prepared directly by the metal deposition via evaporation or sputtering onto an ordered array of template cores such as silica or polystyrene (PS) on the substrate and then be separated off from the substrate by sonication (see Fig. 2.4a) [15]. Due to the shadow effect, an incomplete metallic shell can be formed on the template core to produce the asymmetric semishells. A wet-chemistry etching process, typically using HF for silica and toluene for polystyrene, may be further applied to remove the cores (see Fig. 2.4b–e). This method allows forming semishells consisting of different metals, like Au, platinum (Pt), and palladium (Pd) (see Fig. 2.4b–e). Although this method is rather simple, it can only obtain semishells with arbitrary orientations, which limits the investigation of optical properties and applications of the semishells. A simple way to achieve uniform orientation of semishells is to maintain the formed semishells on the substrate without sonication. Evaporation at normal incidence gives an ordered array of interconnected Au semishells (Fig. 2.4f) [18–20]. A less symmetric kind of semishells can be prepared by evaporation at an acute angle (Fig. 2.4g) [20]. The surface morphology of the metal deposited depends on the metal grain size and the conditions of the deposition (see Fig. 2.4f and h). Recently, a new method called orientation-preserving transfer has been reported to transfer the Au semishells from their growth substrate to an application substrate, chosen so that the orientation of semishells is preserved [21]. The new transfer method mainly includes the lifting of semishells via an elastomer film by Van der Waals force and the covalent binding between the semishells and the receiver substrate. This technique offers a possibility to study the optical properties of the semishells at the individual nanoparticle level (see Fig. 2.4i).

The semishells obtained via the deposition of continuous metal films on contiguous polystyrene (PS) arrays are to some extent difficult and complex systems to analyze the plasmonic properties of individual semishells since both delocalized Bragg plasmons and localized Mie plasmons are involved [19]. Moreover, direct

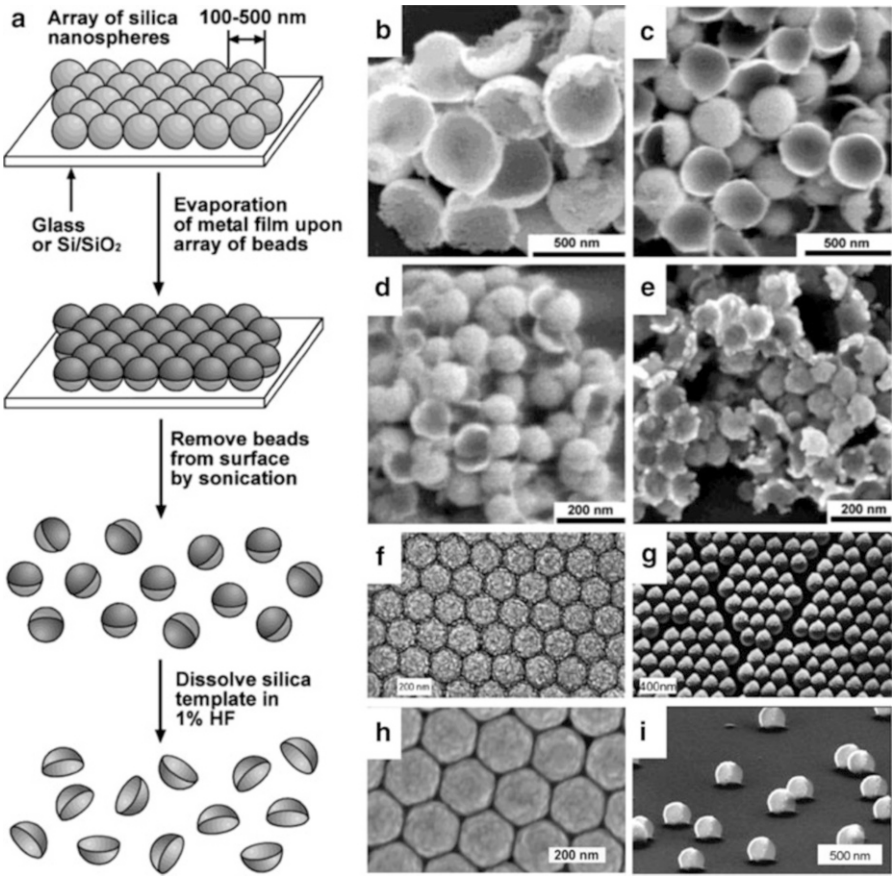

Fig. 2.4 (**a**) Schematic of the fabricating Au semishells via template deposition and (**b**–**e**) the corresponding SEM images of obtained different metallic semishells (**b**, **e**: Au, **c**: Pd, and **d**: Pt). SEM images of Au semishells deposited (**f**) at normal incident and (**g**) at an acute angle via thermal evaporation, showing a rough surface. (**h**) SEM image of Ag semishells via sputtering showing a smooth surface. (**i**) Separated Au semishells fabricated by orientation-preserving transfer method (Reprinted with kind permission from Refs. [15–21].

metal deposition on PS arrays also creates extra metallic truncated tetrahedral nanoparticles on the substrate [22–24], which give their own optical responses and complicate the accurate analysis of the plasmonic response from the individual semishells. Therefore, a new type of fabrication method has recently been reported for the semishells consisting of a polystyrene (PS) core and an arbitrary metal shell, embedded in a poly(dimethylsiloxane) (PDMS) polymer film (see Fig. 2.5) [25–27]. The structure of metallic semishells in PDMS is an interesting platform to investigate the plasmonic properties of individual semishells due to the absence of semishell aggregation, a tunable composition and thickness of the metal layer, and a well-controlled orientation of the semishells. The fabrication is based on

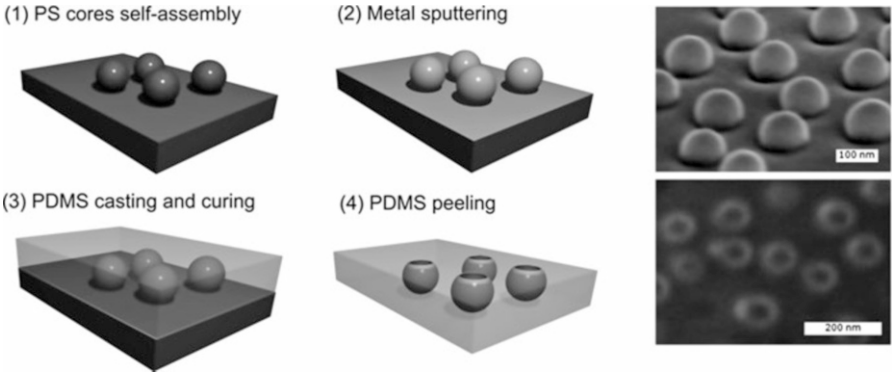

Fig. 2.5 (**a**) Schematic for fabricating metallic semishells in a polymer film and the corresponding SEM images in step 2 (*top*) and 4 (*bottom*) (Reprinted with kind permission from ref [25])

metal sputtering on a submonolayer of PS particles on the substrate, followed by a curing and peeling of a casted PDMS film on the metallic nanostructures. SEM images in Fig. 2.5 (top right) show that 100-nm-sized PS particles are uniformly distributed and isolated from each other. All PS particles are entirely covered by a continuous 30-nm-thick Au film except the parts that contact the substrate. This local discontinuity of the Au film makes it possible to separate the Au layer on the PS particles from the interparticle Au layer by the peeling process. The obtained Au semishells embedded in a PDMS matrix are shown in Fig. 2.5 (bottom right) from the side of the shell's apertures. A closer examination shows a 40−50-nm-sized nanoaperture on the top of each semishell, and all semishells are isolated from each other with a distance of 50−100 nm. Notably, the preparation method is suitable for noble metals such as Au and Ag but also for less commonly used plasmonic metals like Cu, Al, and Pt and may be applied to fabricate more complex symmetry-broken nanostructures consisting of multilayer shells with a varying composition. The PDMS matrix also reduces the oxidation of some metals, such as Ag, Cu, and Al, which provides more accurate optical measurement. By means of a slightly more elaborate procedure, bimetallic semishells can be prepared via selective hemisphere modification [28]. Secondary metal deposition on partially metal-free semishells embedded in a polystyrene film and dissolution in an organic solvent (to remove the polystyrene film) allows generating asymmetric core-shell bimetallic semishells.

Semishells can also be prepared by deposition of metals via chemical and electrochemical plating on the template cores [29, 30]. The former combines template nanoparticle deposition onto a substrate that provides a site for partial chemical passivation of the template surface, followed by subsequent nanoshell nucleation and deposition chemistry to selectively coat a specific section of the template surface with metal. One of advantages of this synthetic strategy is that it allows the preparation of semishells at arbitrary substrate. However, a conductive substrate is needed for the electrochemical plating method.

5 Key Research Findings

5.1 Optical Properties of Metallic Semishells

5.1.1 Symmetry-Reduced Effect

The optical properties of the Au semishells and the difference between the semishells and full nanoshells were assessed by full-vectorial, three-dimensional finite difference time domain (FDTD) calculations and spectrally resolved UV-Vis absorbance measurements. Figure 2.6a compares the calculated extinction spectra (top) and the experimental spectra (bottom) for two different sizes of Au nanoshells and semishells. The calculated and experimental spectra show a reasonable agreement and indicate an interesting trend: removing the top of the nanoshell results in a red shift of the plasmon resonance. This is corroborated by Fig. 2.6b, which shows the simulated dependence of the dipolar plasmon resonance peak on the aspect ratio R/(R-r) for both nanoshells and semishells. The red shift of the resonance position is consistent and becomes more pronounced as the aspect ratio increases.

FDTD calculations not only provide the optical spectra of semishells but also offer us their electric near-field distribution. Figure 2.6c shows the electric field profiles of the dipolar (*I* and *III*) and quadrupolar (*II* and *IV*) plasmon modes of a Au nanoshell and a Au semishell. For a large nanoshell (sample c), it exhibits a dipolar (*I*) and quadrupolar (*II*) mode. After breaking the symmetry, the resonance (*III*) still has a dipolar character but is dominated by the local charge buildup at the edges of the semishell (see Fig. 2.6c *III*). The charge buildup is accompanied by a strong enhancement of the local electric field as compared with the local enhancement of the nanoshell. This aspect provides interesting prospects for SERS application where signals depend strongly on the local electric field enhancement.

We also note that the biggest discrepancy between the experimental and simulated spectra exists in the relative ratio of the intensity between the dipolar plasmon mode and the quadrupolar mode of the Au nanoshell (sample c). This can be explained by the reports of Khlebtsov et al. [31] and Le et al. [32] where the dipolar resonance can be suppressed and the quadrupolar resonance is enhanced due to the strong interaction of dipolar plasmon resonances if some dimer, trimer, or high-ordered clusters of the nanoshells exist. Indeed, that is the case in our Au nanoshell monolayer structures in which $\sim$60 % coverage will induce many nanoshell clusters. However, we do not observe the suppressed dipolar phenomenon in Au semishell monolayer structures probably because the dipolar resonance is dominated by the local charge buildup at the nanoaperture. The locality of the excited mode, hence, makes the resonance of the semishells more robust toward changes in local packing density. The other discrepancies are most likely attributable to the polydisperse size and inherent rough shell surface of Au semishells [33].

Plasmonic hybridization theory is an effective tool to understand, design, and predict optical properties of metallic nanostructures [4, 34, 35]. Plasmonic properties of Au nanoshells have been explained by using the plasmon hybridization between the outer shell surface and the inner shell surface [36]. The symmetry breaking induced spectral changes of the Au semishells can also be explained in the

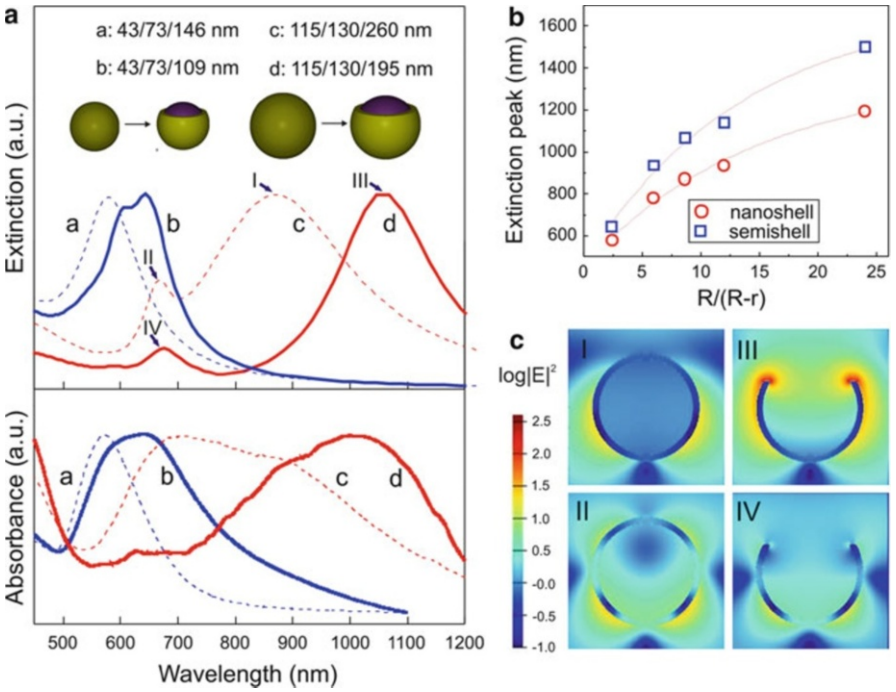

Fig. 2.6 (**a**) Finite difference time domain (FDTD)-simulated (*top*) and experimental optical spectra of Au nanoshells (a, c) and semishells (b, d). Horizontally polarized incident light illuminates the particle from the *top*. (**b**) Simulated dipolar plasmon resonance peaks of Au nanoshells and semishells as a function of aspect ratio: R/(R-r). (**c**) Electric field distribution of a Au nanoshell at resonance *I* and *II* and a Au semishell at resonance of *III* and *IV* (Reprinted with kind permission from Ref. [11])

framework of the plasmon hybridization model. Figure 2.7 shows the plasmon hybridization diagram for a hollow semishell (also called nanobowl). The symmetry-broken geometry allows the dipolar plasmons of nanoholes to interact with the dipolar and quadrupolar plasmons of nanoshells. Each interaction leads to a splitting with a low-energy "bonding" mode and a high-energy "antibonding" mode. Due to the limit of broken geometry, the hybridization between two dipolar modes is stronger than that between the quadrupolar mode and the dipolar mode, resulting in a greater energy splitting. The calculated surface charge distribution diagrams for the dipolar and quadrupolar resonance modes of nanoshells (see Fig. 2.7) before and after hybridization confirm that the plasmons on the outer and inner surfaces of the semishells have been redistributed by following the plasmon hybridization model. The red shift of the dipolar mode (*I* → *III* in Fig. 2.6a) can be attributed to the hybridization of the dipolar mode of the full nanoshell with the dipolar mode of the nanohole, and the red shift of the quadrupolar mode (*II* → *IV* in Fig. 2.6a) can be attributed to the hybridization of the quadrupolar mode of the full nanoshell with the dipolar mode of the nanohole.

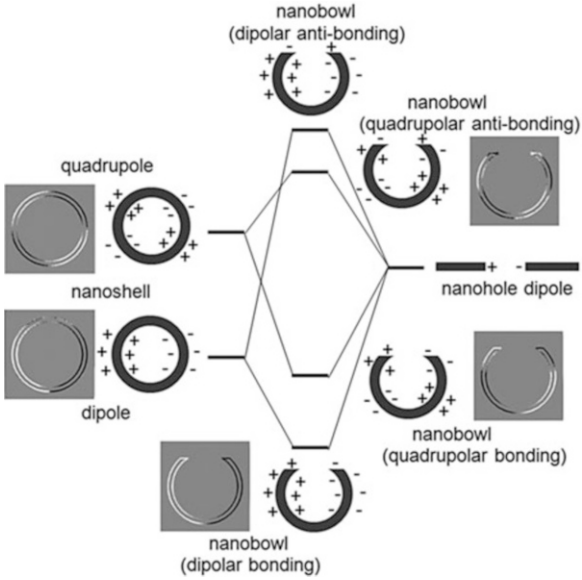

Fig. 2.7 Plasmon hybridization scheme and calculated surface charge distribution for a Au semishell resulting from interacting nanoshell and nanohole plasmons (Reprinted with kind permission from Ref. [49])

5.1.2 Height-Dependent Optical Properties

Ion-milling etching technique allows us to fabricate Au semishells with different fractional height ($H/2R$) by tuning the ion milling-time. This offers us the capability to precisely control the reduced symmetric geometry of Au semishells to obtain the aforementioned nanocups, half-shells, and nanocaps, respectively. Therefore, we can systematically investigate the fractional height ($H/2R$)-dependent optical properties of Au semishells. Figure 2.8a shows the theoretical calculations of the fractional height dependence on the optical properties of the Au semishells with an aspect ratio $(R/(R\text{-}r)) = 8.7$. A number of interesting results are found when the fractional height is changed. First, the dipolar plasmon mode (~870 nm) of nanoshells shifts to a higher wavelength in an earlier stage for $1 > H/2R > 0.625$ and shifts back to a lower wavelength, afterward, for $0.625 > H/2R > 0$, generating a "hyperbola-like" trend when $H/2R$ was decreased (from top to bottom in Fig. 2.8a). The maximum red shift from 870 to 1,080 nm occurs when $H/2R$ is 0.625. Second, the quadrupolar plasmon band (~670 nm) of nanoshells generally blue shifts and attenuates gradually ($1 > H/2R > 0.5$) and completely disappears when $H/2R$ is less than 0.5.

The red shift of the dipolar mode for $1 > H/2R > 0.625$ can be attributed to the hybridization of the dipolar resonance of the nanohole. The blue shift of the dipolar mode ($0.625 > H/2R > 0$) can be ascribed to a geometrical transition to nanocups, leading to a higher concentration of electromagnetic field lines inside of the metal [37]. The quadrupolar resonances also strongly couple to the dipolar mode of the nanohole, leading to a red shift for small apertures. As the aperture increases, the cavity length of the quadrupolar excitations shrinks, leading to a blue shift and attenuation [38]. Figure 2.8b displays the experimental fractional height-dependent

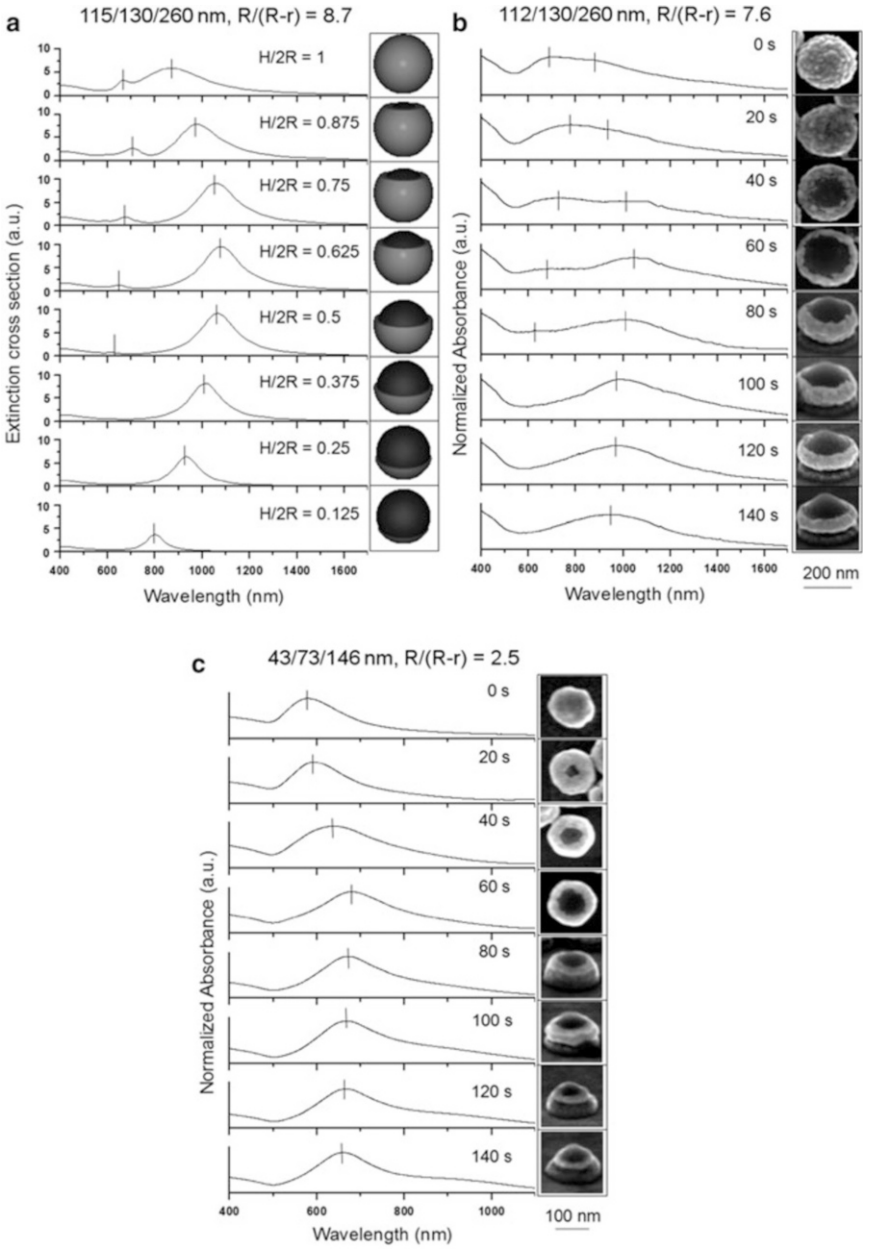

Fig. 2.8 (**a**) Simulated and (**b**, **c**) experimental fractional height (*H*/2*R*)-dependent optical properties of Au semishells with different aspect ratio (*R*/(*R*-*r*)). The experimental height (*H*) of the semishells is controlled by the ion-milling time from 0 to 120 s and measured by SEM images (Horizontally polarized incident light illuminates the particle from the *top*. Reprinted with kind permission from Ref. [11])

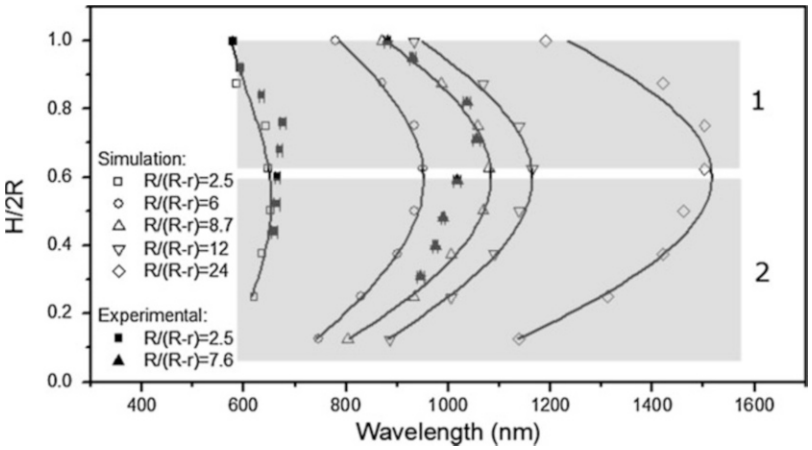

Fig. 2.9 (**a**) Simulated and experimental relationship between the fractional height (*H*/2*R*) and dipolar plasmon mode wavelength of Au semishells with different aspect ratios (*R*/(*R*-*r*)) (Reprinted with kind permission from Ref. [11])

optical properties of Au semishells with an aspect ratio of 7.6. The experimental height of the semishells is controlled by the ion-milling time from 0 to 140 s and visualized by SEM images. Although it is rather difficult to etch away the bottom part of Au shells due to the intrinsic directional character of the ion-milling technique, the experimental results reasonably fit the calculated results, showing a similar dipolar hyperbola shift trend and quadrupolar attenuation. For Au semishells with a smaller aspect ratio of 2.5, only a dipolar hyperbola shift was observed (Fig. 2.8c).

In the preceding text, we have demonstrated that both the aspect ratio (*R*/(*R*-*r*)) and fractional height ((*H*/2*R*) play important roles in tuning the optical properties of Au semishells. All calculated and experimental results about the plasmon resonance wavelength of Au semishells with different aspect ratios and fractional heights are summarized in Fig. 2.9. The calculation show that the dipolar plasmon modes of the Au semishells display a hyperbola shift with a decrease of the fractional height for all kinds of aspect ratio (2.5−24), and the "eccentricity" of the hyperbola becomes smaller when the aspect ratio increases. It also means that the dipolar modes shift in a broader wavelength range when the aspect ratio increases. No matter how the aspect ratio changes, the dipolar plasmon modes always shift a red shift for $1 > H/2R > 0.625$ (region 1) and a blue shift for $0.625 > H/2R > 0$ (region 2). Obviously, 0.625 is the inflection point in the full plasmon mode shifting curve. Two experimental results with aspect ratio of 2.5 and 7.6 reasonably fit the corresponding calculations. The discrepancies are mainly caused by the polydisperse size, surface roughness of the semishell, and the difficulties of the fractional height measurement. It is very important and useful to obtain the panorama of the optical properties possible with Au semishells with respect to the design and optimization of the particles' fabrication.

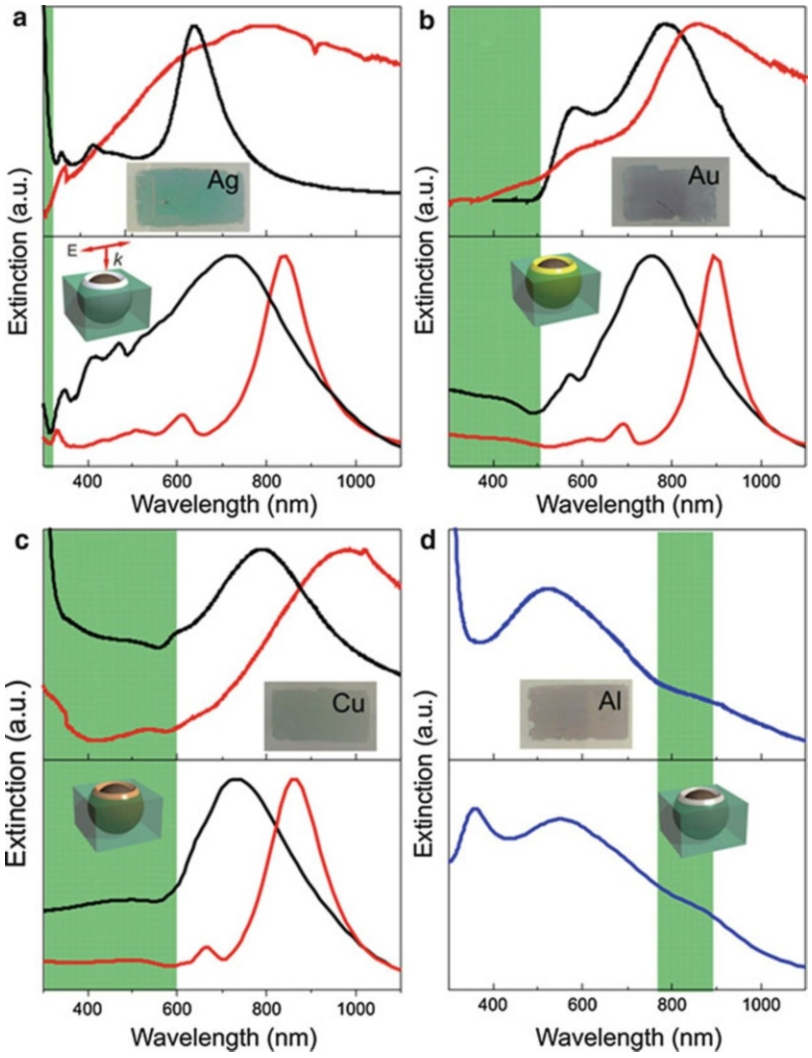

Fig. 2.10 Experimental (*top*) and calculated (*bottom*) extinction spectra of (**a**) Ag, (**b**) Au, (**c**) Cu, and (**d**) Al semishells with various shell thickness (*red*: 10 nm, *blue*: 20 nm, and *black*: 30 nm) in a PDMS film. The insets are the corresponding photographs (*top*) and schematics (*bottom*) of the metallic semishells. The *green-shaded areas* indicate the wavelength regions where interband transitions of the metals occur (Reprinted with kind permission from Ref. [25])

5.1.3 Shell Composition-Dependent Optical Properties

The metallic semishells in PDMS provide a favorable platform to investigate the plasmonic properties of nonaggregated semishells from different metals. Figure 2.10 compares the experimental and calculated extinction spectra of Ag, Au, Cu, and Al semishells with different shell thicknesses. Different plasmonic

behaviors are observed for the different semishells. For the Ag semishells (Fig. 2.10a), the experimental extinction spectra always show multiple LSPR bands, for instance, at 793, 650, and 349 nm for 10-nm-thick Ag semishells and at 639, 462, 412, and 341 nm for 30-nm-thick Ag semishells. The resonance bands at 793, 650, 639, 462, and 412 nm are assigned to the dipolar, quadrupolar, and even octupolar resonances of Ag semishells, which is consistent with previous reports [19, 20]. However, there are few reports and discussions about the resonance bands near the UV region, such as 349 nm for 10-nm Ag semishells and 341 nm for 30-nm Ag semishells, which are possibly attributed to higher-order modes or the dipole antibonding mode. We will return to this later on. For both the Au semishells of 10 and 30 nm in shell thickness, only two bands in the visible or NIR range are detected experimentally, and there is no plasmonic band near the UV range (Fig. 2.10b). The bands in the NIR and the visible range correspond to the dipolar and quadrupolar resonances of the Au semishells, respectively [11, 12]. For the Cu semishells with different thicknesses, the dipolar resonance is observed, while the quadrupolar resonance is dramatically damped and exhibits a rather weak spectral shoulder (Fig. 2.10c).

FDTD calculations are performed for individual 100-nm inner diameter semishells of different metals partially embedded in a PDMS matrix. Because the distance between the semishells in the samples is large enough to ignore the interparticle interaction, the calculation of individual semishells is a valid assumption. All calculated extinction spectra qualitatively reproduce the experimental spectra with respect to the number, position, and relative intensity of the resonance bands for the semishells of Ag, Au, and Cu with two different thicknesses (Fig. 2.10a–c). Some global features are apparent: (1) decreasing the shell thickness results in a pronounced red shift of the plasmon bands and (2) the number of plasmon bands is different for Ag, Au, and Cu semishells of the same size. The former phenomenon is possibly explained by the plasmon hybridization theory, where the thinner shell thickness leads to a stronger plasmon interaction between the inner and outer shell surface and consequently a lower-energy level of the resonance band. The latter reduction of the number of plasmon bands can be understood by the fact that the electronic interband transitions occur at different energy regions for Ag, Au, and Cu. The spectral regions in Fig. 2.4a–c, where interband transitions occur, are shaded in green [8, 39] The electronic transitions from the energetically deeper valence band into the conduction band form a steep absorption edge starting at the threshold frequency, above which all plasmon resonances are dramatically damped. This threshold energy for Ag is at ~3.8 eV (~326 nm), resulting in a minimal damping of plasmon resonances at short wavelengths. Au has a lower-energy onset of the interband transitions at ~2.5 eV (~500 nm), thus we may still observe the quadrupolar and dipolar modes of the Au semishells of 10- and 30-nm shell thickness. The interband transition in Cu at even lower energy of ~2.1 eV (~590 nm) results in an apparent damping of the quadrupolar mode of the Cu semishells. We have also found that the experimental plasmon bands are broadened compared to calculations for decreasing thickness of the shell. This can possibly be attributed to two effects: (1) an inhomogeneous or

a porous metal shell formed on the PS core during the sputtering of 10-nm-thick metal layers [40] and (2) a different extent of the oxidation of the metal. In an ensemble optical measurement, small structural differences may lead to a significantly broadened spectrum. Slight oxidation may also induce a dramatic change of the optical properties of Ag semishells, which explains the extremely broad spectrum of 10-nm Ag semishells compared to the other metals.

Unlike Ag, Au, and Cu, Al has a moderately strong interband transition in a narrow energy range of ~1.4(~890 nm) – 1.6 eV(~775 nm) [41], below and above which the interband activity is weak and Al behaves like a Drude metal. Figure 2.10d shows the experimental and calculated extinction spectra of Al semishells with 20-nm shell thickness. We can see a strong dipolar plasmon band at ~550 nm in both spectra, which are at the higher-energy side of and not damped by the interband transition of Al. An additional feature of a spectral shoulder at ~870 nm is clearly observed, which is located within the interband transition range of Al. This feature has also been reported previously by Langhammer et al. for Al nanodisks [42] It is not clear at present why we do not observe the quadrupolar mode (~360 nm) of the Al semishell in the experimental spectrum, (Fig. 2.10d) and further study is underway. An overview of all spectra of Ag, Au, Cu, and Al semishells tells us that the interband transitions of the metal can occur at the higher (e.g., Ag, Au, and Cu) or lower-energy side of the dipolar plasmon band (e.g., Al), leading to remarkably different plasmonic mode damping behaviors of metallic semishells.

A large discrepancy among the extinction spectra of Ag, Au, and Cu semishells is the presence of the resonance band at 340–350 nm for Ag semishells while absent for Au and Cu. To further understand the plasmonic modes of Ag semishells, a comparison of calculated extinction spectra of 10-nm-thick Ag nanoshells and Ag semishells and their corresponding electromagnetic field and charge distribution profiles are shown in Fig. 2.11. Figure 2.11a displays three pronounced plasmon resonance bands of Ag nanoshells at 770, 575, and 332 nm. The former two bands are attributed to the dipolar and quadrupolar modes, which are confirmed by the electric field and surface charge profiles at 770 nm (Fig. 2.11b) and 575 nm (Fig. 2.11c). The field enhancement inside the metal of the Ag shell and the absence of the enhancement on the inner and outer surface of the shell (see Fig. 2.11d) indicate an asymmetric distribution of the charges on the inner and outer surface, namely, an antibonding-like mode for the plasmon band at 332 nm [35]. Although the surface charge profile in Fig. 2.11d indicates the presence of multipolar modes as well, the antibonding mode dominates. It is easily understood that a multipolar mode is involved at a short wavelength since the diameter of the Ag semishell is close to half of the light wavelength at 332 nm. We therefore conclude that the resonance band at 332 nm is a mixture of a multipolar with the antibonding mode of the Ag semishell. Figure 2.11e shows an extinction spectrum of a 10-nm-thick Ag semishell with red-shifted dipolar and quadrupolar plasmon bands at 843 and 615 nm, respectively. These two modes are further elucidated by the electric field and surface charge profiles in Fig. 2.11f and g, respectively. The red shift of the dipolar and quadrupolar bands can be explained by the plasmon hybridization of the nanoshell and the nanoaperture, resulting in a lower-energy mode at a longer

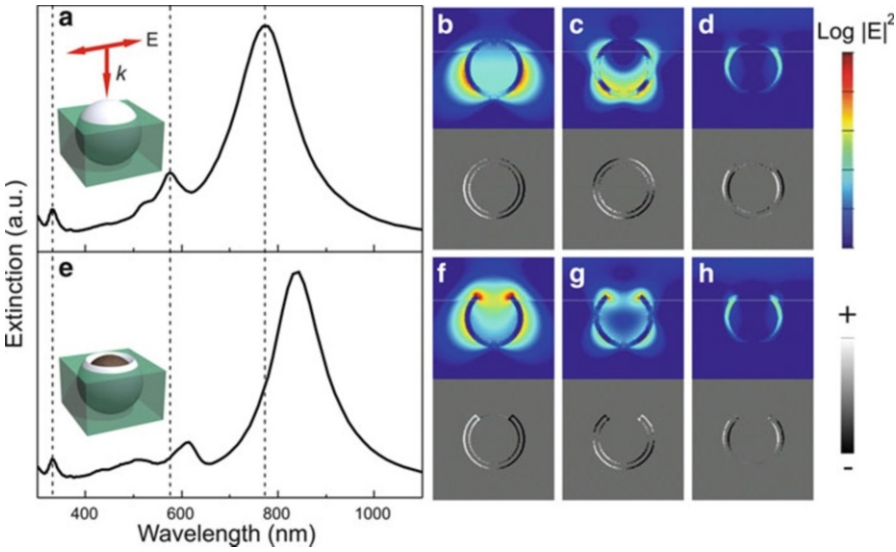

Fig. 2.11 Calculated extinction spectra of a 10-nm-thick (**a**) Ag nanoshell and (**e**) Ag semishell in a PDMS film. Their corresponding electric field ($\log|E|^2$) distribution profiles (*top*) and surface charge distribution (*bottom*) from horizontal cuts at the center of a Ag nanoshell at three on-resonance excitation wavelengths of (**b**) 770, (**c**) 575, and (**d**) 332 nm and a Ag semishell at three on-resonance excitation wavelengths of (**f**) 843, (**g**) 615, and (**h**) 332 nm are shown on the *right* (Reprinted with kind permission from Ref. [25])

wavelength. Additionally, a strong localized field enhancement at the top edges of the Ag semishell is observed compared to the Ag nanoshell at two on-resonance wavelengths. It is interesting to find that the plasmon band of the semishell at 332 nm remains at the same position as the Ag nanoshell (Fig. 2.11e). Removal of a small part on the top of the Ag nanoshell only affects the multipolar resonance and has almost no influence on the dominant antibonding mode, consequently resulting in no change of the position of the band. This is confirmed by the electric field and surface charge profile in Fig. 2.11h as well.

5.1.4 Polarization-Dependent Optical Properties and Light Bending

Symmetric nanoshells have one principal dipolar plasmon mode, of which the orientation of the electric dipole moment is solely controlled by the incident direction and polarization of light. In contrast, the symmetry-reduced geometry of the semishells generates two types of orthogonal dipole plasmon modes when the incident light is transversely or axially polarized [14, 19, 20, 43]. Figure 2.12a shows the calculated extinction spectra of a hollow Au semishell for two different polarizations. When light is transversely polarized, opposite charges accumulate on the edges of the semishell, forming a current loop or a magnetic plasmon mode (1) [21, 26, 43]. Under the same polarization, a higher-ordered mode, for example, quadrupolar mode (2) may be excited. By contrast, in the case of axial polarization, the electrons oscillate directly from the top to the bottom of the semishell, forming

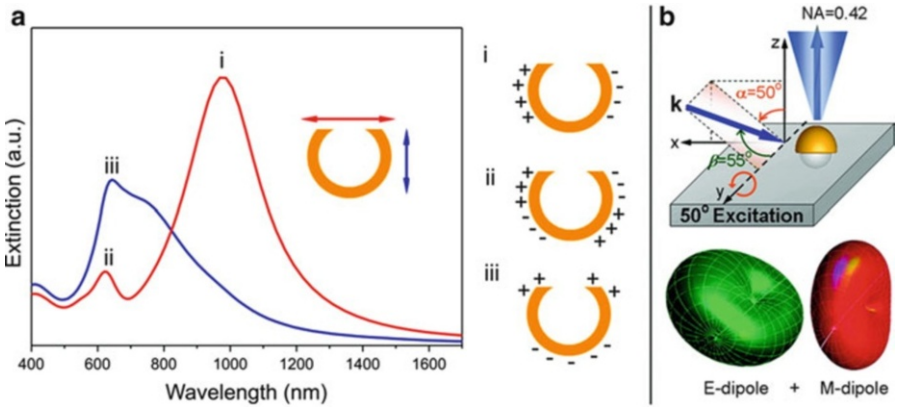

Fig. 2.12 (**a**) Calculated polarization-dependent optical properties of a hollow Au semishell (135/150/225) for transverse polarization (*red*) and axial polarization (*blue*). Surface charge distributions at the resonance modes i, ii, and iii are plotted on the right. (**b**) Schematic diagram of the dark-field scattering measurement of individual semishell with mixed excitation of the magnetic dipole mode and the electric dipole mode (Reprinted with kind permission from Ref. [21])

an electric dipole mode (3). The electrons oscillate in a shorter distance for the axial polarization and correspondingly at a higher frequency.

When light is polarized at an oblique angle, both the electric and magnetic modes can be simultaneously excited. However, these two modes have been shown to possess distinct light-scattering characteristics [21, 26]. The magnetic mode exhibits a unique light-bending property where incoming light from a broad cone of input angles is preferentially scattered in a direction normal to the semishell rim. In Fig. 2.12b, a semishell oriented at $\alpha = 0°$ is illuminated by light with incident **k** vector at $\alpha = 50°$ and $\beta = 55°$. The simulated "donut-shaped" scattering profile of the electric dipolar mode remains in the same plane as the illumination **k** vector, but the magnetic dipole plasmon mode is redirected by the semishell orientation (normal to the rim). Dark-field scattering measurements of single semishells confirm the differences in light scattering between the electric and magnetic dipolar modes. This new "light-bending" property is of particular interest for the solar cell application, where light may coupled from free space into planar structures. For instance, collection of diffuse light, for example, thin film photovoltaic devices or thin film devices that convert light into fuel solar cells may be enhanced significantly due to the integration of Au semishells.

5.2 Surface-Enhanced Raman Scattering on Semishells

5.2.1 SERS-Based Molecular Detection

Raman scattering from molecules adsorbed on metal nanostructures is strongly enhanced due to the excitation of the local electromagnetic field. This gives rise

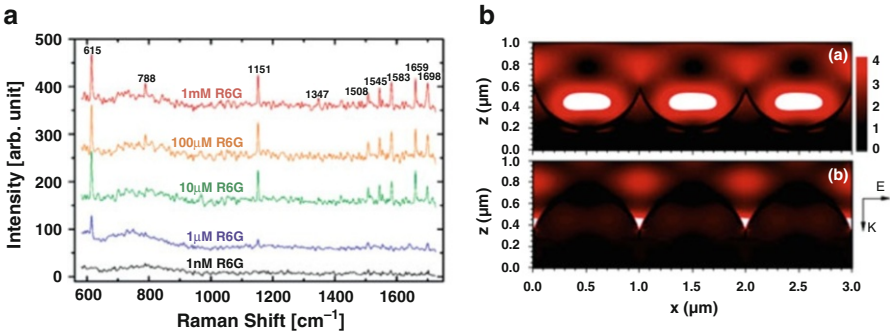

Fig. 2.13 (**a**) SERS spectra of different concentrations of R6G molecules adsorbed on a single Au semishell. (**b**) Simulated electric field distribution for the upward (*top*) and downward (*down*) Au semishell array (Reprinted with kind permission from Refs. [16] and [46])

to the well-known SERS, one of the best methods for label-free biomolecular detection and imaging. Due to the large electric field enhancement at the aperture edge, symmetry-reduced Au semishells have been proposed and demonstrated for SERS applications in ultrasensitive biomolecular detection [16, 44–46].

Lu et al. have presented Au semishells with a sub-10-nm sharp edge, which can enhance local electric field up to $\sim 10^{2.6}$, consequently a maximum Raman enhancement factor up to 10^{11} based on the numerical simulations [16]. The semishells used in that work were prepared by template evaporation method described in Sect. 4.2 and then be collected and redispersed on the substrate. The Raman scattering spectrum of Rhodamine 6G adsorbed on the single Au semishell has indicated a Raman enhancement factor larger than 10^{10}, which enables a detection of 1 μM R6G molecules (see Fig. 2.13a). However, this measurement is inconvenient in the SERS application from a practical point of view because of the uncontrollable or downward orientation of the semishells, which limits the molecular binding to the enhanced electromagnetic field regions. The Raman enhancement factors also differ from place to place on a substrate due to the random orientation of the semishells. In contrast to the above work, the fabrication methods based on the dry etching, such as ion milling and electron beam-induced ablation, are effective strategies to build stable, controllable, and predictable SERS substrates. Especially, ion milling can create semishells over a large area on the substrate, which will have a much better reproducibility of the SERS signals.

Au semishell arrays have also been utilized for the SERS-based molecular detection [45, 46]. It was observed that the Raman signal enhancement shows an obvious difference when reversing the orientations of the hollow Au semishell array in relation to the underlying dielectric substrate. The enhancement on an upward Au semishell array can be five-fold compared to that on a downward one, which can be explained by the fact that a strong localized cavity mode inside the hollow Au semishell is excited for the upward-orientated semishells (Fig. 2.13b) [46].

5.2.2 Location-Dependent SERS

The spatial localization of the electric field (|E|) enhancement gives rise to a stronger spatial localization of SERS intensity, which is roughly proportional to $|E|^4$. The investigation of the spatial inhomogeneity of SERS is of high importance for the theoretical interpretation and practical manipulation of single molecular detection. However, due to the diffraction limit of the excitation light, direct SERS measurement remains difficult as a scale of less than 100 nm. Although tip-enhanced Raman spectroscopy has achieved less than 30-nm spatial resolution on a flat surface, the fabrication of an extremely fine tip is challenging and, the measurement on 3D structures (e.g., nanocavities and nanogaps) is not straightforward.

Recently, a novel technique has been reported to examine, at the individual nanoparticle level, the spatial inhomogeneity of the SERS performance on a symmetry-reduced semishell. This is accomplished by using electron beam-induced deposition (EBID) method that allows us to precisely deposit a ~30-nm amorphous carbon nanoparticle (CNP) as a Raman reporter at different locations on individual Au semishell. The EBID of CNPs was performed in a custom-made device, where the liquid hexadecane was used as the precursor and a silicon-on-insulator wafer with nanochannels on freestanding membranes was used as the valve [47]. The EBID method renders us a rapid deposition of CNPs with tunable sizes in a highly controlled manner. Raman spectra were obtained when the position of the CNP was varied.

Figure 2.14a and b show a schematic geometry and TEM image of a Au semishell with a 87 ± 10-nm inner diameter (D) and a 30 ± 6-nm shell thickness (T), fabricated by ion-milling technique. Reshaping the geometry induces a charge accumulation at the edge of a semishell and a consequent spatial localization of the enhanced electric field. Two different positions (the edge, position I, and the center of the aperture, position II) on the top of a semishell are indicated in Fig. 2.14a–c. Because position I contains the enhanced electric field region while position II is on the surface of the dielectric SiO_2 core of the Au semishell, a 10^3–10^4 difference of SERS intensities between two positions is expected based on our numerical FDTD simulation (see Fig. 2.14c). To demonstrate this obvious spatial inhomogeneity of SERS on a single Au semishell, a ~30-nm CNP was placed by EBID on position I and II of a semishell (indicated by the blue circles in the top and middle of Fig. 2.14d), respectively. The corresponding SERS spectra of the CNP excited by a 633-nm laser reveals a broad Raman band at 1100–1,700 cm^{-1} for position I but no evident Raman band in the same range for position II (Fig. 2.14e). The broad Raman band on position I is a mixture of the D band (1,300–1,450 cm^{-1}) and the G band (1,550–1,580 cm^{-1}) of amorphous carbon, originated from the breathing mode of A_{1g} symmetry and the atomic displacement of E_{2g2} [48]. The strong band at 900–1,000 cm^{-1} in both spectra comes from the silicon substrate. The discrepancy of SERS intensity from CNPs deposited on position I and II directly indicates that the SERS hot spot is localized at the edge of the aperture of a semishell. For a comparison, a ~50-nm CNP is deposited on a 100-nm Au film, and no characteristic Raman bands of the CNP and silicon substrate are visible (bottom in Fig. 2.14d, e).

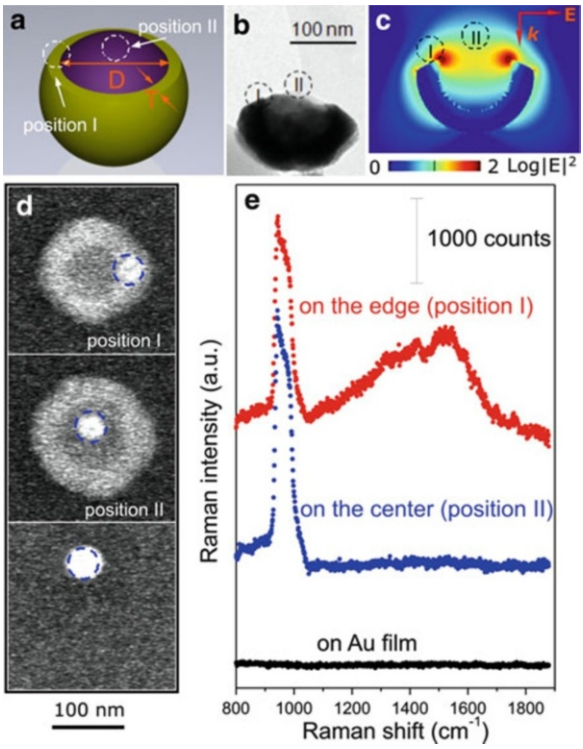

Fig. 2.14 (**a**) Schematic geometry, (**b**) TEM image, and (**c**) FDTD-simulated electric field profile of a Au semishell. (**d**) SEM images and (**e**) Raman spectra of carbon nanoparticles by EBID on different positions of a Au semishell: (*top*, position I) the edge of the aperture of a semishell, (*middle*, position II) the center of aperture of a semishell, and (*bottom*) 100-nm-thick Au film. Carbon nanoparticles are indicated by the *circles* in (**d**) (Reprinted with kind permission from Ref. [50])

6 Conclusions and Future Perspective

In summary, we have introduced a number of methods to fabricate metallic semishells consisting of different metals. Fabrication of the metallic semishells typically comprises an ensemble of techniques including bottom-up (e.g., wet-chemical synthesis or self-assembly of template cores) and top-down methods (e.g., metal evaporation, sputtering, ion milling). This hybrid approach allows to set the nanodimension of the structures by the bottom-up procedures and to set the geometry by the well-controlled top-down fabrication techniques. The combination of bottom-up and top-down technique offers a number of advantages: (1) simple and low cost, (2) semishells' geometry and dimension controllable, and (3) metal composition changeable.

For a number of emerging applications, such as plasmonically enhanced solar cells, rather than backscattering, forward scattering into the substrate is of relevance. It has been shown convincingly now, when excited properly, semishells do redirect light. It however strongly depends on details in the particle orientation and the quality and smoothness of the rim of the semishell. Moreover, the presence of a high-index substrate completely changes the picture. For future investigations, it would be beneficial to find out the exact portion of the light scattering into the

substrate or to free space, depending on particle orientation, permittivity of the substrate, or thickness of a spacer layer. Next to directional scattering, the versatility of the fabrication procedures allow also to embed any material or thin film layer stack, enabling, for example, magnetic control, embedded fluorescent, or SERS labels as well. Such versatile particles are prime candidates for targeted sensing and imaging in in vivo or in vitro applications.

References

1. Neutens P, Van Dorpe P, De Vlaminck I, Lagae L, Borghs G (2009) Electrical detection of confined gap plasmons in metal-insulator-metal waveguides. Nat Photonics 3(5):283–286
2. Sutherland DS, Larsson EM, Alegret J, Kall M (2007) Sensing characteristics of NIR localized surface plasmon resonances in gold nanorings for application as ultrasensitive biosensors. Nano Lett 7(5):1256–1263
3. Nie SM, Emery SR (1997) Probing single molecules and single nanoparticles by surface-enhanced Raman scattering. Science 275(5303):1102–1106
4. Prodan E, Radloff C, Halas NJ, Nordlander P (2003) A hybridization model for the plasmon response of complex nanostructures. Science 302(5644):419–422
5. Xia YN, Sun YG (2002) Shape-controlled synthesis of gold and silver nanoparticles. Science 298(5601):2176–2179
6. Oldenburg SJ, Averitt RD, Westcott SL, Halas NJ (1998) Nanoengineering of optical resonances. Chem Phys Lett 288(2–4):243–247
7. Halas NJ, Jackson JB (2001) Silver nanoshells: variations in morphologies and optical properties. J Phys Chem B 105(14):2743–2746
8. Halas NJ, Wang H, Tam F, Grady NK (2005) Cu nanoshells: effects of interband transitions on the nanoparticle plasmon resonance. J Phys Chem B 109(39):18218–18222
9. Aydin K, Cakmak AO, Sahin L, Li Z, Bilotti F, Vegni L, Ozbay E (2009) Split-ring-resonator-coupled enhanced transmission through a single subwavelength aperture. Phys Rev Lett 102(1):013904
10. Shumaker-Parry JS, Bukasov R (2007) Highly tunable infrared extinction properties of gold nanocrescents. Nano Lett 7(5):1113–1118
11. Ye J, Van Dorpe P, Van Roy W, Lodewijks K, De Vlaminck I, Maes G, Borghs G (2009) Fabrication and optical properties of gold semishells. J Phys Chem C 113(8):3110–3115
12. Ye J, Van Dorpe P, Van Roy W, Borghs G, Maes G (2009) Fabrication, characterization, and optical properties of gold nanobowl submonolayer structures. Langmuir 25(3):1822–1827
13. Ye JA, Chen C, Lagae L, Maes G, Borghs G, Van Dorpe P (2010) Strong location dependent surface enhanced Raman scattering on individual gold semishell and nanobowl particles. Phys Chem Chem Phys 12(37):11222–11224
14. Lassiter JB, Knight MW, Mirin NA, Halas NJ (2009) Reshaping the plasmonic properties of an individual nanoparticle. Nano Lett 9(12):4326–4332
15. Love JC, Gates BD, Wolfe DB, Paul KE, Whitesides GM (2002) Fabrication and wetting properties of metallic half-shells with submicron diameters. Nano Lett 2(8):891–894
16. Lu Y, Liu GL, Kim J, Mejia YX, Lee LP (2005) Nanophotonic crescent moon structures with sharp edge for ultrasensitive biomolecular detection by local electromagnetic field enhancement effect. Nano Lett 5(1):119–124
17. Liu JQ, McBean KE, Harris N, Cortie MB (2007) Optical properties of suspensions of gold half-shells. Mat Sci Eng B-Solid 140(3):195–198
18. Liu JQ, Maaroof AI, Wieczorek L, Cortie MB (2005) Fabrication of hollow metal "nanocaps" and their red-shifted optical absorption spectra. Adv Mater 17(10):1276

19. Maaroof AL, Cortie MB, Harris N, Wieczorek L (2008) Mie and Bragg plasmons in subwavelength silver semi-shells. Small 4(12):2292–2299
20. Liu JQ, Cankurtaran B, Wieczorek L, Ford MJ, Cortie M (2006) Anisotropic optical properties of semitransparent coatings of gold nanocaps. Adv Funct Mater 16(11):1457–1461
21. Zhang Y, Barhoum A, Lassiter JB, Halas NJ (2011) Orientation-preserving transfer and directional light scattering from individual light-bending nanoparticles. Nano Lett 11(4):1838–1844
22. Farcau C, Astilean S (2007) Probing the unusual optical transmission of silver films deposited on two-dimensional regular arrays of polystyrene microspheres. J Opt a-Pure Appl Op 9(9):S345–S349
23. Jensen TR, Malinsky MD, Haynes CL, Van Duyne RP (2000) Nanosphere lithography: tunable localized surface plasmon resonance spectra of silver nanoparticles. J Phys Chem B 104(45):10549–10556
24. Baia L, Baia M, Popp J, Astilean S (2006) Gold films deposited over regular arrays of polystyrene nanospheres as highly effective SERS substrates from visible to NIR. J Phys Chem B 110(47):23982–23986
25. Ye J, Verellen N, Van Roy W, Lagae L, Maes G, Borghs G, Van Dorpe P (2010) Plasmonic modes of metallic semishells in a polymer film. ACS Nano 4(3):1457–1464
26. Mirin NA, Halas NJ (2009) Light-bending nanoparticles. Nano Lett 9(3):1255–1259
27. Mirin NA, Ali TA, Nordlander P, Halas NJ (2010) Perforated semishells: far-field directional control and optical frequency magnetic response. ACS Nano 4(5):2701–2712
28. Correa-Duarte MA, Salgueirino-Maceira V, Rodriguez-Gonzalez B, Liz-Marzan LM, Kosiorek A, Kandulski W, Giersig M (2005) Asymmetric functional colloids through selective hemisphere modification. Adv Mater 17(16):2014
29. Chen Z, Dong H, Pan J, Zhan P, Tang CJ, Wang ZL (2010) Monolayer rigid arrays of cavity-controllable metallic mesoparticles: electrochemical preparation and light transmission resonances. Appl Phys Lett 96(5):051904
30. Charnay C, Lee A, Man SQ, Moran CE, Radloff C, Bradley RK, Halas NJ (2003) Reduced symmetry metallodielectric nanoparticles: chemical synthesis and plasmonic properties. J Phys Chem B 107(30):7327–7333
31. Khlebtsov BN, Khanadeyev VA, Ye J, Mackowski DW, Borghs G, Khlebtsov NG (2008) Coupled plasmon resonances in monolayers of metal nanoparticles and nanoshells. Phys Rev B 77(3):035440
32. Nordlander P, Le F, Brandl DW, Urzhumov YA, Wang H, Kundu J, Halas NJ, Aizpurua J (2008) Metallic nanoparticle arrays: a common substrate for both surface-enhanced Raman scattering and surface-enhanced infrared absorption. ACS Nano 2(4):707–718
33. Halas NJ, Wang H, Fu K, Drezek RA (2006) Light scattering from spherical plasmonic nanoantennas: effects of nanoscale roughness. Appl Phys B-Lasers O 84(1–2):191–195
34. Halas NJ, Wang H, Brandl DW, Nordlander P (2007) Plasmonic nanostructures: artificial molecules. Accounts Chem Res 40(1):53–62
35. Ye J, Van Dorpe P, Lagae L, Maes G, Borghs G (2009) Observation of plasmonic dipolar anti-bonding mode in silver nanoring structures. Nanotechnology 20(46):465203
36. Halas NJ (2005) Playing with plasmons. Tuning the optical resonant properties of metallic nanoshells. Mrs Bull 30(5):362–367
37. Wang F, Shen YR (2006) General properties of local plasmons in metal nanostructures. Phys Rev Lett 97(20):206806
38. Kelf TA, Sugawara Y, Cole RM, Baumberg JJ, Abdelsalam ME, Cintra S, Mahajan S, Russell, Bartlett PN (2006) Localized and delocalized plasmons in metallic nanovoids. Phys Rev B 74(24):245415
39. Johnson PB, Christy RW (1972) Optical-constants of noble-metals. Phys Rev B 6(12):4370–4379

40. Halas NJ, Wang H, Goodrich GP, Tam F, Oubre C, Nordlander P (2005) Controlled texturing modifies the surface topography and plasmonic properties of au nanoshells. J Phys Chem B 109(22):11083–11087
41. Ehrenreich H, Philipp HR, Segall B (1963) Optical properties of aluminum. Phys Rev 132(5):1918
42. Langhammer C, Schwind M, Kasemo B, Zoric I (2008) Localized surface plasmon resonances in aluminum nanodisks. Nano Lett 8(5):1461–1471
43. Cortie M, Ford M (2007) A plasmon-induced current loop in gold semi-shells. Nanotechnology 18(23):235704
44. Liu GL, Lu Y, Kim J, Doll JC, Lee LP (2005) Magnetic nanocrescents as controllable surface-enhanced Raman scattering nanoprobes for biomolecular imaging. Adv Mater 17(22):2683
45. Liu XF, Linn NC, Sun CH, Jiang P (2010) Templated fabrication of metal half-shells for surface-enhanced Raman scattering. Phys Chem Chem Phys 12(6):1379–1387
46. Chen L, Liu FX, Zhan P, Pan J, Wang ZL (2011) Ordered gold nanobowl arrays as substrates for surface-enhanced Raman spectroscopy. Chinese Phys Lett 28(5):057801
47. Chen C, Hutchison JA, Clemente F, Kox R, Uji-I H, Hofkens J, Lagae L, Maes G, Borghs G, Van Dorpe P (2009) Direct evidence of high spatial localization of hot spots in surface-enhanced raman scattering. Angew Chem Int Edit 48(52):9932–9935
48. Ferrari AC, Robertson J (2000) Interpretation of Raman spectra of disordered and amorphous carbon. Phys Rev B 61(20):14095–14107
49. Ye J, Lagae L, Maes G, Borghs G, Van Dorpe P (2009) Symmetry breaking induced optical properties of gold open shell nanostructures. Opt Express 17(26):23765–23771
50. Ye J, Chen C, Lagae L, Maes G, Borghs G, Van Dorpe P (2010) Strong location dependent surface enhanced raman scattering on individual gold semishell and nanobowl particles. Phys Chem Chem Phys 12:11222–11224

Exploiting the Tunable Optical Response of Metallic Nanoshells

3

Ovidio Peña-Rodríguez and Umapada Pal

Contents

1 Definition of the Topic

Metallic nanoshells, which are plasmonic nanostructures having alternating layers of dielectric and metal, exhibit a notable structural tunability of the plasmon frequencies. This interesting feature has been exploited for a myriad of applications. In this chapter, along with some synthesis approaches, we discuss the origin of the structural tunability and application potentials of these novel nanostructures in fields such as surface-enhanced Raman scattering, medicine, and photonics.

O. Peña-Rodríguez (✉)
Centro de Microanálisis de Materiales (CMAM), Universidad Autónoma de Madrid (UAM), Madrid, Spain

Instituto de Óptica, Consejo Superior de Investigaciones Científicas (IO-CSIC), Madrid, Spain

U. Pal
Instituto de Física, Benemérita Universidad Autónoma de Puebla, Puebla, Puebla, Mexico

Challa S.S.R. Kumar (ed.), *UV-VIS and Photoluminescence Spectroscopy for Nanomaterials Characterization*, DOI 10.1007/978-3-642-27594-4_3,

2 Overview

Plasmonic nanoparticles have become an emerging field of study in materials science due to their important applications, ranging from biology to optoelectronics. While the research carried out during the past decade have produced plasmonic nanostructures of different materials, different material combinations, and different geometries to manipulate the position and intensity of their surface plasmon resonance (SPR) emission in accordance with their application requirements, there is still a lot to be done to fully exploit the potentiality of these nanostructures. Nanoshells (NSs) are one of the most interesting plasmonic nanostructures. They present a hard-to-match mixture of interesting properties, combining a simple shape with a remarkable tunability of the optical response. So, it is not surprising that an enormous amount of works studying the synthesis, optical properties, and potential applications of these structures have been reported in recent years.

Naturally, different applications have different requirements in terms of size, composition, and morphology of the particles, as well as for the characteristics of the surface plasmon resonance. For example, most biological applications require the maximum of the surface plasmon resonance to be located in the near-infrared region of the spectrum, where biological tissues are transparent. Moreover, in vivo applications require that the nanoparticles are chemically inert and small enough to penetrate into the cells, while other applications such as surface-enhanced Raman scattering (SERS) require near electric fields as intense as possible. Therefore, there is no universal recipe for fabricating "good" nanoshells, but, instead, they must be optimized for each individual application. Two factors are of paramount importance for achieving this goal: (1) a detailed knowledge of the factors capable of modifying the optical response of these nanostructures and (2) utilization of synthesis methods suitable for enhancing one feature or the other.

In this chapter, we tried to highlight the progress made on the fabrication of metallic nanoshells, a special kind of plasmonic nanostructure; their application potentials, criteria, and possibilities for tuning their optical responses; advantages over other plasmonic nanostructures; and future application prospects in different fields.

3 Introduction

Metal nanoparticles (NPs) have attracted recently the attention of the scientific community due to their unique electronic and optical properties, which are dominated by the localized surface plasmon resonance (SPR), defined as collective oscillations of the free electrons. For solid nanoparticles, the SPR position barely depends on their geometrical parameters. This behavior is in stark contrast with that of metallic nanoshells [1–3] and their variants [4–6], which exhibit a notable structural tunability of the plasmon frequencies (Fig. 3.1), as has been demonstrated both theoretically [2, 3] and experimentally [7]. This feature makes nanoshells a very interesting kind of particle because, in spite of their simple shape, they can be

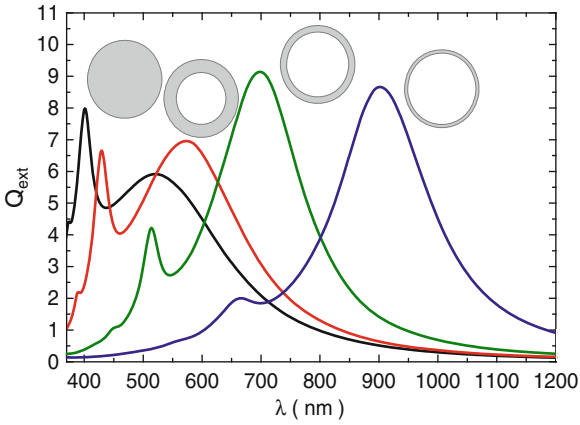

Fig. 3.1 Theoretically calculated optical extinction spectra of silver nanoshells ($r_2 = 60$ nm) for some selected core-to-shell ratios (from *left* to *right*: 0.0, 0.67, 0.83, and 0.92)

designed to absorb or scatter incident radiation of specific wavelengths, especially in the near-infrared [8]. Before continuing, it is necessary to define what a nanoshell is. It is commonly considered that a nanoshell is a spherical structure composed of a dielectric core and a metallic shell [9]. However, definitions as ample as that of any core-shell structure can also be found in the literature [10]. For the purposes of this chapter, we will define nanoshell as any plasmonic nanostructure having alternating layers of dielectric and metal.

Gold and silver have been traditionally the preferred materials for the synthesis of nanoshells [11–14], and both of them have some advantages and disadvantages. Silver NPs have a more intense SPR, which is of great advantage for surface-enhanced Raman scattering (SERS) and sensing applications. However, gold NPs have better biocompatibility and long-term stability, which make them superior materials for biological applications [1], especially in the form of nanoshells. Moreover, the chemical processes for synthesizing Au nanoshells are well known and easier to perform, allowing a better control over the nanoshell geometry [2].

For various applications like in medical diagnostics [15], immunoassay [16, 17], and studies of living cells and bacteria [18], it is necessary to shift the SPR to the near-infrared region (700–1,300 nm) where the biological tissues are transparent [16]. This can be achieved by increasing the core-to-shell ratio or, in other words, by decreasing the ratio between the thickness of the metallic shell and the total radius [3] of the NPs. Unfortunately, there is a practical limit of attainable red-shift in a conventional nanoshell, which is around 1,200 nm. To overcome this limitation, several attempts have been made to further manipulate the geometry of nanoshell structures. The nanorice [19, 20] (ellipsoidal nanoshells) and nonconcentric [21, 22] and multilayered [6, 23] nanoshells are just a few examples of this strategy, which have increased the limit of allowed red-shifts.

In this work, we intend to review the current state of the art on the fabrication and application of metallic nanoshells. It is somewhat surprising that, despite the intense current pace of research on this area, the summarizing efforts have been rather scarce to date. Probably the first overview of this topic was presented by

Kalele and colleagues in 2006 [10]. Later, in 2009, Erickson and Tunnell [24] published an excellent review chapter analyzing the use of gold nanoshells in biomedical applications. On the other hand, there have been some focused reviews that have compared the performance of nanoshells versus that of different kinds of particles for specific applications, such as the one published by Luk'yanchuk et al. [25] about Fano resonances in plasmonic nanostructures or the book about nanomedicine, edited by Sattler [26]. However, despite these precedents, there has been no effort known to us to present the up-to-date advancements on the fabrication and usage of metallic nanoshells in systematic and collective manner. We believe that this chapter would be of high interest to the scientific community working on design, fabrication, and application of plasmonic nanoshells.

This chapter is divided in four sections, starting with this brief introduction. The second section highlights the progress made on the synthesis of nanoshell structures as well as the theoretical methods used for calculating their optical properties. Precisely these unique optical properties, together with the underlying physics, and the various application prospects of nanoshells are the subjects of the third section. Finally, some concluding remarks have been presented in section four. We hope that this chapter would be useful both for experimental and theoretical researchers as a quick reference, as well as for beginners, to gain hands-on basic knowledge on different aspects of plasmonic nanostructures.

4 Experimental and Theoretical Methodologies

4.1 Synthesis

The first literature report on the synthesis of nanoshells is the one by Zhou et al. [27]. They obtained Au_2S@Au nanoshells via a two-step chemical process. Firstly, they dissolved chloroauric acid ($HAuCl_4$•$4H_20$) and sodium sulfide (Na_2S•$9H_2O$) into super pure water at room temperature to get $HAuCl_4$ and Na_2S solutions. Then, they mixed controlled amounts of the two solutions together to get unstable gold sulfide (Au_2S) particles. In a second step, they injected a little amount of Na_2S solution into the colloidal Au_2S solution. Finally, the surface of the Au_2S nanoparticles was reduced to obtain the Au_2S@Au nanoshells by injecting chloroauric acid solution. However, they failed to realize the origin of the observed red-shifts of the absorption bands in the composite nanoparticles and assigned them to quantum-size effects. It was not until a few years later when Averitt et al. [9, 28, 29] continued to study this type of nanoshells and determined the classical origin of the observed plasmon shifts.

Subsequently, Oldenburg et al. [2] and Westcott et al. [31, 32] pioneered a new scheme to synthesize nanoshells. In this method, previously manufactured metal nanoparticles were attached to the functionalized surface of a larger dielectric sphere (e.g., SiO_2), and then a complete metallic shell was grown either by further reduction of metal ions [31–34] or through layer-by-layer attachment of prefabricated metal nanoparticles [33, 35] (Fig. 3.2). Usually the preferred

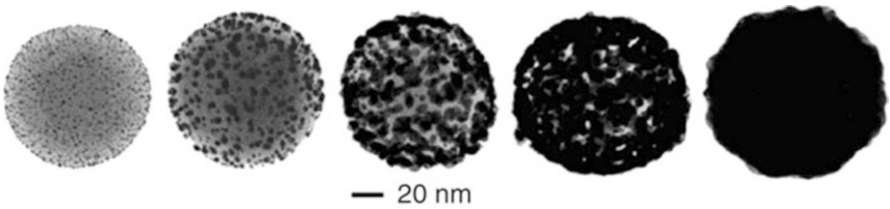

Fig. 3.2 Transmission electron microscopy images of gold nanoshell on a silica dielectric nanoparticle during shell growth [30]

materials for the dielectric core are SiO_2 [31, 32] and polystyrene (PS) [34]. The advantages of the former are its stability and the possibility of using the Stöber method [36] to grow particles of uniform sizes. Use of polystyrene, on the other hand, is advantageous as nanoparticles made of this material can be easily synthesized [37] as monodisperse suspensions, and they can be readily removed later, if desired, obtaining hollow nanoshells. Functionalization of dielectric core can be performed using an ω-terminated trialkoxyorganosilane in the case of SiO_2 [31, 32] or 2-aminoethanethiol hydrochloride in the case of polystyrene spheres [34].

In one of the latter incarnations of this method, Brinson et al. [38] reported a streamlined method for Au layer metallization on prefabricated nanoparticle surfaces using carbon monoxide as the reducing agent. This multistep process was initiated by functionalizing oxide nanoparticles with aminopropyltriethoxy or methoxysilane, followed by the binding of very small (1–2 nm diameter) Au nanoparticles onto the nanoparticle surface to a saturation coverage of nominally 25–30 % [19, 38]. This is subsequently followed by the chemical reduction of $Au^{3+}{}_{(aq)} \rightarrow Au^{0}{}_{(s)}$ onto the nanoparticle precursor surface. In the last reduction step, the tiny Au islands grow larger and ultimately merge, resulting in the formation of a continuous, multicrystalline metallic shell layer. They showed that the reduction of Au^{3+} by CO results in the formation of thin, uniform shell layers on these nanoparticles at lower Au^{3+} concentrations, while continuous shell layers were not achievable with existing liquid-phase reduction methods. Since this approach relies only on the introduction of $CO_{(g)}$ into the solution of prepared precursor nanoparticles and Au^{3+}, the shell layer morphology is not as susceptible to the reaction parameters, like the concentration of reductor or precursor solution, as in other chemical shell growth methods.

Finally, there has also been some interest in making nanoshells by coating SiO_2 and polystyrene spheres using seedless schemes [39–41]. For example, the solvent-assisted route has been used [39] to prepare a complete metal (Ag or Au) shell with controlled thickness on polystyrene colloids. Also, the electroless plating approach, based on electrostatic attraction, has been used to prepare a complete silver shell with controlled thickness on silica colloids. In the first step of the solvent-assisted route (Fig. 3.3a), the PS colloids synthesized by emulsion polymerization [37] are immersed in a mixed solvent of ethanol and acetone containing the metal salt.

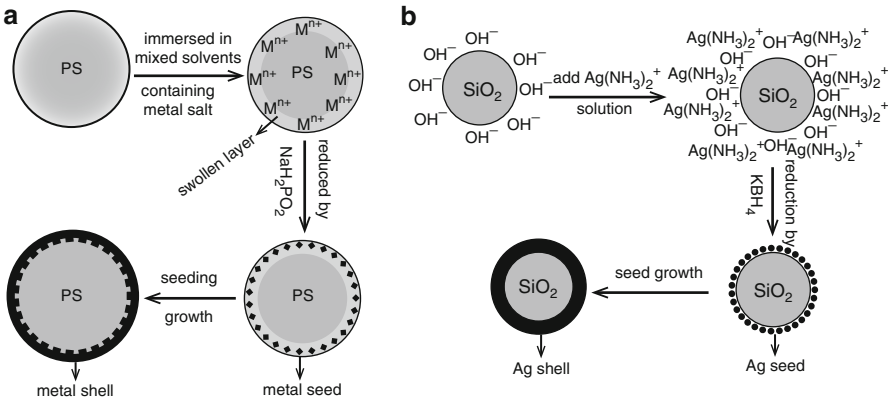

Fig. 3.3 Zhang's procedure for coating (**a**) polystyrene and (**b**) silica colloids with metal [39]

During the treatment process, the surface layer of the PS colloids gets swelled by the mixed solvent and permeated by the metal ions. Subsequently, sodium hypophosphite is used to reduce the metal ions in the swollen layer, and the swollen layer of the PS colloids is loaded uniformly with metal nanoparticles. After surface layer seeding, the PS colloids are dispersed in aqueous ethanol containing the metal salt (0.2 M), $C_6H_5O_7Na_3{\bullet}2H_2O$ (0.1 M), and ammonia solution (for Ag coating) or Na_2CO_3 (for Au coating). Then, HCHO (10 %) is added dropwise to grow the metal nanoparticles and increase the density and thickness of the metal shell. By varying the amount of (1) PS colloids after seeding, (2) HCHO, and (3) $C_6H_5O_7Na_3{\bullet}2H_2O$, the thickness and uniformity of the metal shell can be modified effectively.

On the other hand, Zhang's approach for coating silica with silver relies on the surface charge of the as-prepared colloids [36, 42], arising from the negatively charged Si-OH groups (Fig. 3.3b). The $[Ag(NH_3)_2]^+$ ions are absorbed onto the colloids' surface by the negatively charged Si-OH groups through electrostatic attraction. Subsequently, KBH_4 is used to reduce the $[Ag(NH_3)_2]^+$ ions, and the colloids' surface is covered uniformly with silver nanoparticles. The growth of the colloids after surface seeding is similar to that of the PS colloids after surface seeding. The main advantages of the above two coating routes are the following [39]:

1. Metal seeds are synthesized directly on the surface layer of the PS or silica core, avoiding the surface functionalization of the core and additional preparation of metal nanoparticles
2. The thickness and roughness of the metal shell can be effectively controlled through continuous dropwise addition of reductor solution, and the as-prepared core-shell colloids can crystallize into a long-range-ordered structure.
3. The routes are facile and versatile and suitable for the coating of other metals whose cations or complexes can be reduced in solution.

4.2 Theoretical Methods

The methods used for computing the scattering properties of small particles can be roughly divided in two groups: exact and approximated techniques. In general, the exact methods are more accurate than the approximated ones but are much more restricted with respect to the kind of particles they are suited for. All exact techniques for calculating electromagnetic scattering are based on solving the differential Maxwell equations or their integral counterparts in the time or frequency domain. To find an analytical solution, one has to solve the vector wave equations for the time-dependent electric fields outside and inside the particle, using the separation of variables technique. Then, the incident and internal fields are expanded in wave functions which are regular inside the scatterer, whereas the external scattered field is expanded in wave functions that behave as outgoing waves at infinity. Finally, using the requirement of continuity of the tangential component of the electric and magnetic fields at the particle boundary, the unknown coefficients in the internal and scattered field expansions can be determined from the known expansion coefficients of the incident field [43].

Unfortunately, the separation of variables technique generates only manageable solutions for a few simple cases. The first of such exact solutions was developed by Mie [44] for spherical particles. This model was later extended, first for the coated sphere [45] and then for the multilayered sphere [46–49]. Similar solutions have been found for homogeneous infinite circular cylinders [50], infinite elliptical cylinders [51], and homogeneous and core-mantle spheroids [52]. However, in the case of spherically symmetric particles, like most nanoshell variants, the exact methods can be used to generate accurate results for essentially any size parameter and relative refractive index values. Therefore, in this review we will focus mainly on the exact methods, and the approximate ones will be discussed only briefly, to show in which cases they can replace or supplement the exact solutions.

4.2.1 Quasi-static Approximation

When a particle's size is much smaller than the incident wavelength, the incident electric field may be regarded as spatially uniform over the extent of the particle; this is referred to as the quasi-static (QS) approximation. Despite its simplicity and lack of rigor, this approach is useful for qualitative understanding of the phenomena related to light scattering by nanoshells as it considerably simplifies the mathematical analysis. In this case, the electrostatic solution can be obtained by solving Laplace's equation of the potential.

The expressions needed to calculate the electric field of a core-shell particle in the quasi-static approach were first developed by Neeves and Birnboim [53]. Averitt et al. [28] subsequently extended the analysis, obtaining explicit formulas for the scattering and the absorption cross sections as well as for the geometric tunability of the surface plasmon resonance. In the core-shell geometry (Fig. 3.4), the first region is the core, characterized by a radius r_1 and dielectric function ε_1. The second region (the shell) has a thickness $t_2 = r_2 - r_1$ and a dielectric function ε_2, and, finally, the surrounding medium has a dielectric function ε_3. In general, there is

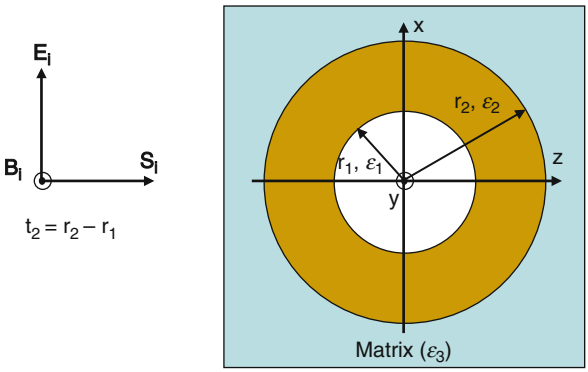

Fig. 3.4 Schematic representation of a typical metal nanoshell geometry

no especial requirement for the dielectric functions (i.e., each can be either real or imaginary), but this geometry becomes a metal nanoshell when the core is a dielectric material and ε_2 is the dielectric function of a metal. The general solution for the potential in each region is given by:

$$\Phi_i(r,\theta) = \left[A_i\, r + B_i/r^2\right]\, \cos\, \theta \tag{3.1}$$

where A_i and B_i are the constants multiplying the monopole and the dipole terms, respectively. $B_1 = 0$ in the core and the potential $\Phi_3 = -E_0\, r\, \cos\, \theta$ must be recovered in the surrounding medium, far from the shell, yielding $A_3 = -E_0$. Moreover, there must be continuity of the tangential and normal components of the electric field:

$$\left.\frac{\partial\, \Phi_i}{\partial\, \theta}\right|_{r=r_i} = \left.\frac{\partial\, \Phi_{i+1}}{\partial\, \theta}\right|_{r=r_i} \tag{3.2}$$

$$\varepsilon_i \left.\frac{\partial\, \Phi_i}{\partial\, r}\right|_{r=r_i} = \varepsilon_{i+1} \left.\frac{\partial\, \Phi_{i+1}}{\partial\, r}\right|_{r=r_i} \tag{3.3}$$

The application of the boundary conditions to Eq. 3.1, together with the known values of A_3 and B_1, results in a set of four equations and four unknowns that can be solved to obtain the constants A_1, A_2, B_2, and B_3, allowing the determination of the potential in the core, shell, and embedding medium. The electric field, in turn, can be obtained for each region using the expression $\mathbf{E_i} = -\nabla\Phi_i(r,\theta)$:

$$\mathbf{E}_1 = \frac{9\varepsilon_2\varepsilon_3}{\varepsilon_2\varepsilon_a - 2\varepsilon_3\varepsilon_b} E_0 \left(\cos\theta\, \hat{r} + \sin\theta\, \hat{\theta}\right) \tag{3.4}$$

$$\mathbf{E}_2 = \frac{3\varepsilon_3}{\varepsilon_2\varepsilon_a - 2\varepsilon_3\varepsilon_b} E_0 \left\{ \begin{array}{l} \left[(\varepsilon_1 + 2\varepsilon_2) + 2(\varepsilon_1 - \varepsilon_2)(r_1/r)^3\right]\, \cos\theta\, \hat{r} + \\ \quad + \left[(\varepsilon_1 + 2\varepsilon_2) - (\varepsilon_1 - \varepsilon_2)(r_1/r)^3\right]\, \sin\theta\, \hat{\theta} \end{array} \right\} \tag{3.5}$$

$$\mathbf{E}_3 = \left\{ 2\frac{\varepsilon_2\varepsilon_a - \varepsilon_3\varepsilon_b}{\varepsilon_2\varepsilon_a - 2\varepsilon_3\varepsilon_b}\left(\frac{r_2}{r}\right)^3 + 1 \right\} E_0 \cos\theta\, \hat{r} + \\ + \left\{ \frac{\varepsilon_2\varepsilon_a - \varepsilon_3\varepsilon_b}{\varepsilon_2\varepsilon_a - 2\varepsilon_3\varepsilon_b}\left(\frac{r_2}{r}\right)^3 - 1 \right\} E_0 \sin\theta\, \hat{\theta} \tag{3.6}$$

where

$$\varepsilon_a = \varepsilon_1(3 - 2P) + 2\varepsilon_2 P \tag{3.7}$$

$$\varepsilon_b = \varepsilon_1 P + \varepsilon_2(3 - P) \tag{3.8}$$

P is the ratio of the shell volume to the total particle volume. The induced field in the region outside the shell is the same as a dipole with an effective dipole moment of $\mathbf{p} = \varepsilon_3\ \alpha\ \mathbf{E}_{ind}$; then, the polarizability is given as:

$$\alpha = 4\pi\ \varepsilon_0\ r_2^3 \left[\frac{\varepsilon_2\varepsilon_a - \varepsilon_3\varepsilon_b}{\varepsilon_2\varepsilon_a - 2\varepsilon_3\varepsilon_b}\right] \tag{3.9}$$

where $\varepsilon_0 = 8.85 \times 10^{-12}$ F/m is the permittivity of free space. Finally, the scattering and absorption cross sections can be obtained from the polarizability, by using scattering theory [54]:

$$\sigma_{sca} = \frac{k^4}{6\pi\ \varepsilon_0^2}|\alpha|^2 = \frac{128\ \pi^5}{3\ \lambda^4}\varepsilon_3^2\ r_2^6 \left|\frac{\varepsilon_2\varepsilon_a - \varepsilon_3\varepsilon_b}{\varepsilon_2\varepsilon_a - 2\varepsilon_3\varepsilon_b}\right|^2 \tag{3.10}$$

$$\sigma_{abs} = \frac{k}{\varepsilon_0}\ \mathrm{Im}(\alpha) = \frac{8\ \pi^2}{\lambda}\sqrt{\varepsilon_3}\ r_2^3 \mathrm{Im}\left(\frac{\varepsilon_2\varepsilon_a - \varepsilon_3\varepsilon_b}{\varepsilon_2\varepsilon_a - 2\varepsilon_3\varepsilon_b}\right) \tag{3.11}$$

4.2.2 Mie Theory

The simplest exact solution is the original Mie formulation [44], which is based on solving Maxwell's equations in spherical polar coordinates for an incident electromagnetic (EM) plane wave impinging on a metallic sphere with a radius r embedded in a medium with a refractive index n_m. Now, let us consider an x-polarized incident electric field, $\mathbf{E_i} = E_0 \exp[i\,k\,r\,\cos(\theta)]\,\hat{e}_x$, with a time dependence of $\exp(-i\omega\,t)$. The interaction of this EM wave with small particles produces scattering and absorption of the incident plane wave [54]. The total energy loss of the incident radiation is the sum of the scattered and absorbed energies. These energy losses are expressed in a more convenient form by the cross sections, which are a measure of the probability that an event (scattering, absorption, or extinction) will take place. The total extinction cross section σ_{ext} is given by $\sigma_{ext} = \sigma_{sca} + \sigma_{abs}$, where σ_{sca} and σ_{abs} are the scattering and absorption cross sections, respectively.

In order to express these cross sections, it is convenient to define the size parameter x and the relative refractive index m, as:

$$x = k\, r = \frac{2\pi\, n_m\, r}{\lambda} \tag{3.12}$$

$$m = \frac{n_p}{n_m} \tag{3.13}$$

where r is the radius, λ is the light wavelength in vacuum, and n_p and n_m are the refractive indices of the sphere and the surrounding medium, respectively. Here, k and mk represent the wave number in the dielectric medium and in the metallic particle, respectively. The electromagnetic field is divided into two orthogonal subfields that can be deduced from a scalar potential. The solutions are expressed in terms of infinite series where the coefficient constants are obtained from the appropriate boundary conditions at the surface of the sphere. For this case, the cross sections can be calculated as:

$$\sigma_{ext} = \frac{2\pi}{k^2} \sum_{n=1}^{\infty} (2n+1)\mathrm{Re}\{a_n + b_n\} \tag{3.14}$$

$$\sigma_{sca} = \frac{2\pi}{k^2} \sum_{n=1}^{\infty} (2n+1)\left(|a_n|^2 + |b_n|^2\right) \tag{3.15}$$

$$\sigma_{abs} = \sigma_{ext} - \sigma_{dis} \tag{3.16}$$

The corresponding efficiency factors can be calculated for all the cross sections from the relation $Q_i = \sigma_i / A$, where $A = \pi\, r^2$ is the geometrical cross section of the particle. The scattering coefficients, a_n and b_n, can be calculated by the expressions:

$$a_n = \frac{m\psi_n(mx)\psi'_n(x) - \psi'_n(mx)\psi_n(x)}{m\psi_n(mx)\xi'_n(x) - \psi'_n(mx)\xi_n(x)} \tag{3.17}$$

$$b_n = \frac{\psi_n(mx)\psi'_n(x) - m\psi'_n(mx)\psi_n(x)}{\psi_n(mx)\xi'_n(x) - m\psi'_n(mx)\xi_n(x)} \tag{3.18}$$

where ψ_n and ξ_n are the Riccati-Bessel functions, defined as:

$$\psi_n(z) = z\, j_n(z), \qquad \xi_n(z) = z\, h_n(z) \tag{3.19}$$

being $j_n(z)$ and $h_n(z)$ the spherical Bessel and Hankel functions [55, 56], respectively. The expressions ψ'_n and ξ'_n indicate differentiation with respect to the argument in parentheses.

This Mie solution for the extinction by a single sphere also applies to any number of spheres provided that they have similar diameters and are randomly distributed with enough separations among them (distances larger than the incident wavelength). Under these circumstances, coherent light is not scattered by the spheres and the total scattered energy is equal to the energy scattered by one sphere multiplied by their total number.

Core-Shell Structures

Mie theory was subsequently extended by Aden and Kerker [45] in order to consider the scattering of light by a sphere with a concentric spherical shell embedded in a medium (core-shell structure with radii r_1 and r_2 for the core and the shell, respectively). They obtained new expressions to calculate the coefficients a_n and b_n (Eqs. 3.14–3.16) are still valid):

$$a_n = \frac{\psi_n(y)\left[\psi_n'(m_2y) - A_n\chi_n'(m_2y)\right] - \psi_n'(y)[\psi_n(m_2y) - A_n\chi_n(m_2y)]}{\xi_n(y)\left[\psi_n'(m_2y) - A_n\chi_n'(m_2y)\right] - \xi_n'(y)[\psi_n(m_2y) - A_n\chi_n(m_2y)]} \tag{3.20}$$

$$b_n = \frac{m_2\psi_n(y)\left[\psi_n'(m_2y) - B_n\chi_n'(m_2y)\right] - \psi_n'(y)[\psi_n(m_2y) - B_n\chi_n(m_2y)]}{m_2\xi_n(y)\left[\psi_n'(m_2y) - B_n\chi_n'(m_2y)\right] - \xi_n'(y)[\psi_n(m_2y) - B_n\chi_n(m_2y)]} \tag{3.21}$$

where

$$A_n = \frac{m_2\psi_n(m_2x)\psi_n'(m_1x) - m_1\psi_n'(m_2x)\psi_n(m_1x)}{m_2\chi_n(m_2x)\psi_n'(m_1x) - m_1\chi_n'(m_2x)\psi_n(m_1x)} \tag{3.22}$$

$$B_n = \frac{m_2\psi_n(m_1x)\psi_n'(m_2x) - m_1\psi_n(m_2x)\psi_n'(m_1x)}{m_2\chi_n'(m_2x)\psi_n(m_1x) - m_1\psi_n'(m_1x)\chi_n(m_2x)} \tag{3.23}$$

$$x = k\,r_1, \quad y = k\,r_2 \tag{3.24}$$

Multilayered Spheres

Mie theory can also be extended for the radially inhomogeneous (i.e., multilayered) sphere [46–49]. Similarly to the previous cases, the solution of the scattering by a multilayered sphere consists in expressing the EM fields in each layer l in terms of appropriate sets of spherical wave functions. Each layer is characterized by a size parameter $x_l = 2\pi\, n_m\, r_l/\lambda = k\, r_l$ and a relative refractive index $m_l = n_l/n_m$, $l = 1, 2, \ldots, L$, where λ is the wavelength of the incident wave in vacuum, r_l is the outer radius of the lth layer, n_m and n_l are the refractive index of the medium outside the particle and its lth component, respectively, and k is the propagation constant. In the region outside the particle, the relative refractive index is $m_{L+1} = 1$. The space is divided into two regions: the region inside the multilayered sphere and the

surrounding medium outside the particle. The electric and magnetic fields (inside and outside the sphere) are considered as the superposition of sets of spherical wave functions. For example, $\mathbf{E}_{in}$ and $\mathbf{E}_{out}$ can be expressed in terms of complex spherical eigenvectors [43]:

$$\mathbf{E}_{in} = \sum_{n=1}^{\infty} E_n \left[c_n^{(l)} \mathbf{M}_{o1n}^{(1)} - i\, d_n^{(l)} \mathbf{N}_{e1n}^{(1)} \right] \tag{3.25}$$

$$\mathbf{E}_{out} = \sum_{n=1}^{\infty} E_n \left[i\, a_n^{(l)} \mathbf{N}_{e1n}^{(3)} - b_n^{(l)} \mathbf{M}_{o1n}^{(3)} \right] \tag{3.26}$$

where $E_n = i^n E_0 (2n+1)/n(n+1)$, and $\mathbf{M}_{o1n}^{(j)}$ and $\mathbf{N}_{e1n}^{(j)}$ ($j = 1, 3$) are the vector harmonic functions with the radial dependence of the first kind of spherical Bessel function for $j = 1$ and the first kind of spherical Hankel function for $j = 3$. The explicit expressions for $\mathbf{M}_{o1n}^{(j)}$ and $\mathbf{N}_{e1n}^{(j)}$ can be found elsewhere, for instance, in ▶ Chap. 4, "UV-Vis Spectroscopy for Characterization of Metal Nanoparticles Formed from Reduction of Metal Ions During Ultrasonic Irradiation" of reference [54].

In the region outside the sphere, the total external field is the superposition of the incident and scattered fields, $\mathbf{E} = \mathbf{E}_i + \mathbf{E}_s$, which can be expanded as:

$$\mathbf{E}_i = \sum_{n=1}^{\infty} E_n \left[\mathbf{M}_{o1n}^{(1)} - i \mathbf{N}_{e1n}^{(1)} \right] \tag{3.27}$$

$$\mathbf{E}_s = \sum_{n=1}^{\infty} E_n \left[i\, a_n \mathbf{N}_{e1n}^{(3)} - b_n \mathbf{M}_{o1n}^{(3)} \right] \tag{3.28}$$

where a_n and b_n are the scattering coefficients. It can be deduced [43] that $a_n^{(1)} = b_n^{(1)} = 0$ and $c_n^{(L+1)} = d_n^{(L+1)} = 1$. The expansion coefficients ($a_n^{(l)}$, $b_n^{(l)}$, $c_n^{(l)}$, and $d_n^{(l)}$) and scattering coefficients (a_n and b_n) are obtained by matching the tangential components of EM fields at each interface and after some algebra (for details see reference [43]); the final coefficients in the series can be identified with the scattering coefficients [43]:

$$a_n = a_n^{L+1} = \frac{\left[H_n^a(m_L x_L)/m_L + n/x_L \right] \psi_n(x_L) - \psi_{n-1}(x_L)}{\left[H_n^a(m_L x_L)/m_L + n/x_L \right] \zeta_n(x_L) - \zeta_{n-1}(x_L)} \tag{3.29}$$

$$b_n = b_n^{L+1} = \frac{\left[m_L H_n^b(m_L x_L) + n/x_L \right] \psi_n(x_L) - \psi_{n-1}(x_L)}{\left[m_L H_n^b(m_L x_L) + n/x_L \right] \zeta_n(x_L) - \zeta_{n-1}(x_L)} \tag{3.30}$$

where ψ_n and ζ_n are the Riccati-Bessel functions (as defined in reference [57]), and the determinants H_n^a and H_n^b can be calculated by the expressions [43]:

$$H_n^a(m_1 x_1) = D_n^{(1)}(m_1 x_1) \tag{3.31a}$$

$$H_n^a(m_l x_l) = \frac{G_2 D_n^{(1)}(m_l x_l) - Q_n^{(l)} G_1 D_n^{(3)}(m_l x_l)}{G_2 - Q_n^{(l)} G_1}, \quad l = 2, \ldots, L \tag{3.31b}$$

$$H_n^a(m_l x_l) = \frac{G_2 D_n^{(1)}(m_l x_l) - Q_n^{(l)} G_1 D_n^{(3)}(m_l x_l)}{G_2 - Q_n^{(l)} G_1}, \quad l = 2, \ldots, L \tag{3.32a}$$

$$H_n^b(m_l x_l) = \frac{\tilde{G}_2 D_n^{(1)}(m_l x_l) - Q_n^{(l)} \tilde{G}_1 D_n^{(3)}(m_l x_l)}{\tilde{G}_2 - Q_n^{(l)} \tilde{G}_1}, \quad l = 2, \ldots, L \tag{3.32b}$$

and

$$D_n^{(1)}(z) = \psi_n'(z)/\psi_n(z) \tag{3.33}$$

$$D_n^{(3)}(z) = \zeta_n'(z)/\zeta_n(z) \tag{3.34}$$

$$Q_n^{(l)} = \frac{\psi_n(m_l x_{l-1})}{\zeta_n(m_l x_{l-1})} \Big/ \frac{\psi_n(m_l x_l)}{\zeta_n(m_l x_l)} \tag{3.35}$$

$$G_1 = m_l H_n^a(m_{l-1} x_{l-1}) - m_{l-1} D_n^{(1)}(m_l x_{l-1}) \tag{3.36}$$

$$G_2 = m_l H_n^a(m_{l-1} x_{l-1}) - m_{l-1} D_n^{(3)}(m_l x_{l-1}) \tag{3.37}$$

$$\tilde{G}_1 = m_{l-1} H_n^b(m_{l-1} x_{l-1}) - m_l D_n^{(1)}(m_l x_{l-1}) \tag{3.38}$$

$$\tilde{G}_2 = m_{l-1} H_n^b(m_{l-1} x_{l-1}) - m_l D_n^{(3)}(m_l x_{l-1}) \tag{3.39}$$

As before, Eqs. 3.14–3.16 remain valid for the calculation of the cross sections.

4.2.3 Plasmon Hybridization

As has been said earlier, for most nanoshell variants, Mie theory can be used to generate accurate results for essentially any size parameter and relative refractive index values. However, even if one can easily calculate the optical responses of such low-dimensional structures, it is often very difficult to understand the origin of the observed resonances. This problem can be overcome using the theory of plasmon hybridization [6], which is in good agreement with the Mie theory in the dipole limit (i.e., the quasi-static approximation). The theory of plasmon hybridization is an electromagnetic analog of molecular orbital theory, where the characteristics of the SPR can be explained in terms of the interactions between the plasmons of metallic nanostructures of simpler shapes. For example, the SPR of metallic nanoshells (Fig. 3.5) can be viewed as the interaction between the plasmons of a sphere and a cavity. The hybridization of the plasmon of the sphere

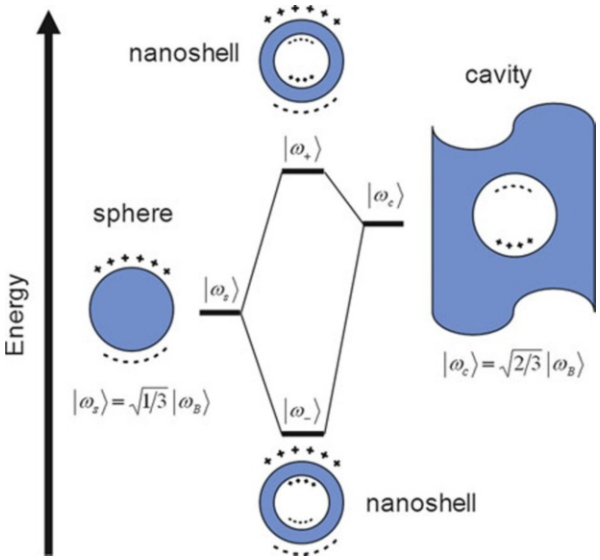

Fig. 3.5 Energy-level diagram describing the plasmon hybridization in metal nanoshells, resulting from the interaction between the sphere and cavity plasmons. The two nanoshell plasmons are an antisymmetrically coupled (antibonding) $|\omega_+\rangle$ plasmon mode and a symmetrically coupled (bonding) $|\omega_-\rangle$ plasmon mode

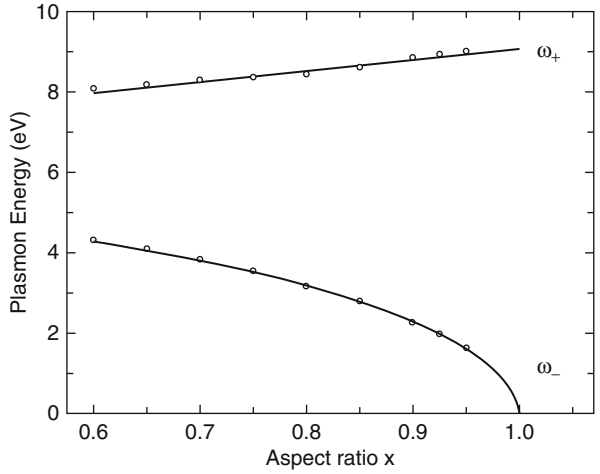

Fig. 3.6 Comparison of calculated symmetric ω_- and antisymmetric ω_+ plasmon resonances (*symbols*) for gold nanoshells, as a function of their aspect ratio $x = r_1/r_2$ with the result from the semiclassical approximation (Eq. 3.40) (*lines*) [58]

and the cavity creates two new plasmon oscillation modes (Fig. 3.6), i.e., the higher energy (antibonding) mode $|\omega_+\rangle$ and the lower energy (bonding) mode $|\omega_-\rangle$, corresponding to the antisymmetric and symmetric interactions between the $|\omega_s\rangle$ and $|\omega_c\rangle$ modes, respectively. The frequencies of these modes are [6]:

$$\omega_{l\pm}^2 = \frac{\omega_B^2}{2}\left[1 \pm \frac{1}{2\,l+1}\sqrt{1+4\,l(l+1)\left(\frac{r_1}{r_2}\right)^{2\,l+1}}\right] \tag{3.40}$$

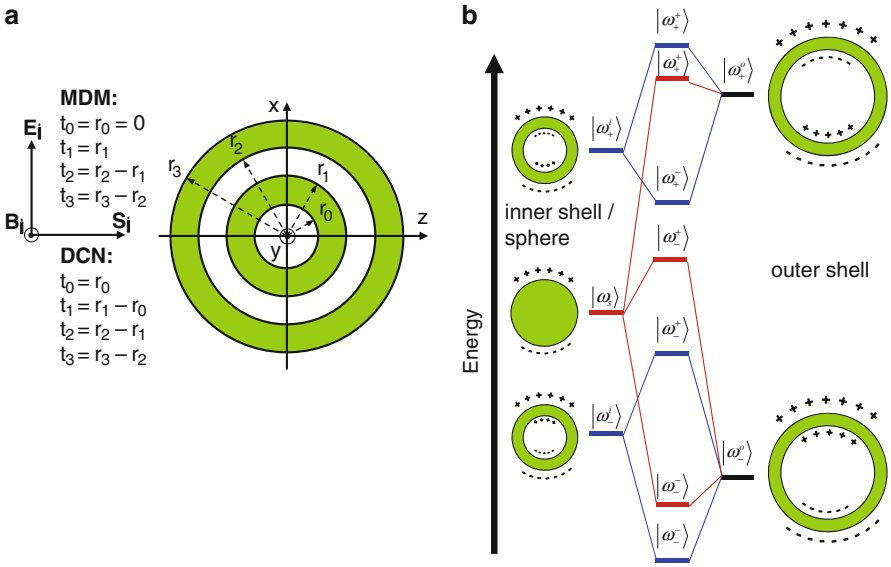

Fig. 3.7 (**a**) Schematic representation of the MDM and DCN structures (for the MDM $r_0 = t_0 = 0$) and (**b**) their corresponding energy diagrams, representing plasmon hybridization [59]. Plasmon hybridization for the MDM and DCN structures is represented in red and blue, respectively

being l the plasmon order ($l = 1$ is the dipolar plasmon, $l = 2$ the quadrupolar, and so on), ω_B the bulk plasmon frequency, and r_1 and r_2 the core and shell radii, respectively.

For composite metallic nanostructures of greater geometrical complexity, it is more difficult to obtain explicit expressions for the hybridized modes. However, this method remains as a useful tool to understand qualitatively their plasmon resonance behavior. Two particularly interesting multilayer geometries are metal-dielectric-metal (MDM) [5] and double concentric nanoshells (DCN) [60] structures (Fig. 3.7). The plasmon resonance in a MDM [DCN] structure can be viewed as the interaction between the plasmon responses of the inner sphere [nanoshell] ($|\omega_s\rangle$[$|\omega^i_-\rangle$ and $|\omega^i_+\rangle$]) and the outer ($|\omega^o_-\rangle$ and $|\omega^o_+\rangle$) nanoshell. Three hybridized modes are obtained for the MDM; the energy mode $|\omega^-_-\rangle$ corresponds to the antisymmetric coupling between the symmetric plasmon resonance modes of the outer ($|\omega^o_-\rangle$) nanoshell and the sphere plasmon. The coupling between the higher-energy antibonding mode of the outer nanoshell and the nanosphere plasmon modes is very weak, and only one hybridized mode is produced in this case ($|\omega^+_+\rangle$). In contrast, four hybridized modes are produced in the DCN structure because its inner nanoshell has two energy modes. The energy mode $|\omega^-_-\rangle$ ($|\omega^+_-\rangle$) corresponds to the antisymmetric (symmetric) coupling between the symmetric plasmon resonance modes of the inner ($|\omega^i_-\rangle$) and outer ($|\omega^o_-\rangle$) nanoshells. On the other hand, the energy mode $|\omega^-_+\rangle$ ($|\omega^+_+\rangle$) corresponds to the symmetric (antisymmetric) coupling between the antisymmetric plasmon resonance modes of the inner ($|\omega^i_+\rangle$) and outer

($|\omega_+^o\rangle$) nanoshells (Fig. 3.7). Although, in principle, there exists also a coupling between the antisymmetric and symmetric plasmons of the separate nanoshells, it has only a small influence on the hybridized modes, due to the large energy separation between those two modes [6].

4.2.4 Other Methods

Generally, the above mentioned methods are sufficient to study the optical properties of most of the classical nanoshells. However, there are some interesting cases such as nonconcentric [61], incomplete [41, 62–64], or ellipsoidal [19, 20] nanoshells that require the use of more elaborated techniques. These approximate techniques allow the study of virtually any shape. However, they have the disadvantage that their computational cost is much higher than that of the exact methods. Here, we will briefly discuss two of the methods that are frequently used for this task: the finite-difference in the time-domain (FDTD) method and the discrete dipole approximation (DDA).

The FDTD method, introduced in 1966 by Yee [65], is an electromagnetic modeling technique frequently used for the computation of light scattering by nonspherical or inhomogeneous particles. In this approach, the computational space and time are divided into a grid of discrete points, and the derivatives of the Maxwell equations are approximated by finite differences. The entire volume, containing the scatterer, is discretized into a cubical grid known as the Yee lattice; the basic element of this lattice is the Yee cell [65]. A finite differences method is then applied to evaluate the space and time derivatives of the field. This procedure is repeated iteratively for increasing values of time until a steady state solution is obtained. Absorbing boundary conditions are used to truncate the computational domain; this requires a layer of grid cells all around the computational domain. The absorbing boundary conditions ensure that the wave is not reflected at the open boundary of the discretized volume. Finally, a near- to far-field transformation is used to compute the scattered far-field from the near-field values of the computational domain.

The DDA method was originally developed by Purcell and Pennypacker [66] to model the interaction of light with dust particles in space. The main idea behind the DDA is to simulate the optical response to an electromagnetic field by approximating the particle with a finite number of polarizable entities on a cubic grid. Each dipole cell is assigned a complex polarizability, which can be computed from the complex refractive index of the bulk material and the number of dipoles in a unit volume. For a finite array of point dipoles, the scattering problem may be solved exactly, so the only approximation made in the DDA is the replacement of the continuum target by an array of N-point dipoles. The replacement requires specification of both the geometry (location of the dipoles) and the dipole polarizabilities. This method was further refined by Draine et al. [67, 68], who applied the Fast Fourier Transform and conjugate gradient method to calculate the convolution problem arising in the DDA methodology which allowed the calculation of scattering by larger targets.

5 Key Research Findings

5.1 Optical Properties

The main feature that differentiates nanoshells from solid particles is that, while the surface plasmon resonance of the former can be adjusted by varying the geometric parameters [2], that of the latter is essentially fixed. For example, coating of metallic shells on silica allows one to tune their absorption band from visible to infrared region. Moreover, by changing the shell thickness, one can tune the SPR band position in the desired wavelength range. Metal nanoshells having plasmon resonance in the infrared region are well suited for biological applications, as this range of the electromagnetic spectrum is transparent for biological tissues [69]. Thin metallic layers lead to larger SPR red-shifts, whereas thick layers have the opposite effect [58]. Small variations of shell thickness can displace the SPR in a wide spectral region, which can be optically monitored following the position of their SPR peaks. In this subsection, we will discuss the origin of this interesting feature and analyze the main factors affecting the optical properties of metallic nanoshells.

5.1.1 Surface Plasmon Resonance (SPR)

Physical properties of nanoparticles (NP) are intermediate between those of atoms and solids. The range of variation is large because these properties evolve in a nonlinear fashion with increasing number of atoms from a single atom to a dimer, a trimer, and so on, up to the physical properties of a bulk solid. Specifically, the optical properties strongly depend on the size and geometry of the NP [70]. In this respect, surface plasmon resonances (SPRs), coming from the resonant interaction between the collective oscillations of electrons in the conduction band and the incident radiation, play an important role in the optical properties of metals. They give rise to a strong absorption band in the visible range of the electromagnetic spectrum [54, 71]. When the electric field interacts with a metal, its electrons oscillate back and forth at the fluctuation frequency of the incident wave (see Fig. 3.8). The light is reflected because the electrons in the metal act as a shield against the incident electric field. However, there is a frequency fluctuation limit for which electrons can respond; i.e., if the fluctuations are too fast, the electrons can no longer respond. This limit, in which electron-plasma interactions give rise to the absorption of the photon energy, is called the plasmon frequency (ω_p). Light with frequency above the plasma frequency is transmitted. The plasmon frequency is responsible, among other things, for the color of bulk metals like gold and copper. In the free electron model, the plasmon energy can be estimated as:

$$\omega_p = \sqrt{\frac{n\, e^2}{\varepsilon_0\, m^*}} \tag{3.41}$$

where n is the density of free electrons, e is the electronic charge, ε_0 is the permittivity of free space, and m^* is the effective mass of the electrons.

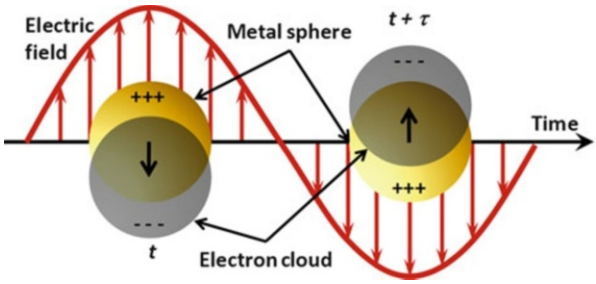

Fig. 3.8 Schematic representation of the surface plasmon resonance excited by light with a frequency 1/τ

Plasmon energy for bulk gold (9.2 eV [72]) and silver (9.0 eV [73]) lies in the UV range; however, for nanoparticles, the plasmon energy is smaller and lies in the UV-visible spectral range. As the electromagnetic wave striking the metal surface has small penetration depth, its interaction with the electrons of the metal surface becomes significant, and the collective oscillations of these surface electrons are known as surface plasmons. The extinction efficiency (Q_{ext}) for spherical metallic particles can be approximated by:

$$Q_{ext} = \frac{24\pi\, R\, \varepsilon_m^{3/2}}{\lambda} \frac{\varepsilon'}{(\varepsilon' + 2\,\varepsilon_m)^2 + (\varepsilon'')^2} \tag{3.42}$$

where R is the radius of the particle, λ the wavelength of the incident electromagnetic radiation, ε' and ε'' are the real and imaginary parts of the dielectric constant of the particles (i.e., $\varepsilon_p = \varepsilon' + i\,\varepsilon''$), respectively, and ε_m is the dielectric constant of the embedding medium. Then, the extinction would be maximum when $\varepsilon_1 + 2\varepsilon_m = 0$, which gives rise to a surface plasmon resonance (SPR) band. The position of the SPR band is dependent on the size and shape of the particle and dielectric constant of the medium in which the particles are dispersed [70].

5.1.2 Dielectric Functions

The optical properties of materials can be described by the complex refractive index ($\tilde{n} = n + i\,k$) or, alternatively, using the dielectric function ($\varepsilon = \varepsilon' + i\,\varepsilon''$). Both quantities are equivalent and are related by the expression: $\varepsilon = \tilde{n}^2$. They can be taken either from experimental results or from theoretical models. The most commonly used experimental data for the dielectric function of the noble metals comes from the measurements performed by Johnson and Christy in 1972 [74]. The experimental data published by Palik [75] has been frequently used as well. Unfortunately, the experimental data are not always suitable, as they might have gaps in certain regions of the spectrum or cannot be used with certain calculation algorithms (e.g., FDTD [76]). For this reason, in some cases, analytical expressions for $\varepsilon(\omega)$ are necessary. The more common approach to obtain such expressions consists in adding a certain number of Lorentzian terms to the free-electron (Drude) equation, in order to reproduce the interband transitions; this method is called the extended Drude model (EDM):

$$\varepsilon(\omega) = \varepsilon_\infty - \frac{\omega_p^2}{\omega^2 + j\omega\Gamma} + \sum_{i=0}^{n} L_i(\omega) \tag{3.43}$$

where the first two terms are the contributions of the standard Drude model, with a high-frequency limit dielectric constant ε_∞, a plasma frequency ω_p, and a (bulk) damping term Γ, while the $L_i(\omega)$ terms are the frequency-dependent Drude-Lorentz oscillators. Examples of the use of this approach are frequent in the literature. For instance, Vial et al. [77] provided an analytical fit to the gold data using only one Lorentzian term, while See et al. [78], Lee and Gray [79], and Moskovits et al. [80] have represented the dielectric function of silver using two, three, and four Lorentzian terms, respectively. Likewise, Hao and Nordlander [76] and Rakic et al. [81] fitted the dielectric functions of both Au and Ag using four and six Lorentzian terms, respectively.

More recently, Etchegoin et al. [82] have proposed a different approach: replacing the Lorentzian terms with a family of analytical models, called critical points (CPs), which have long been used for the analysis of interband transitions in semiconductors [83]. The advantage of using the CPs is that, unlike simple Lorentz oscillators, they allow for an easy adjustment of asymmetric line shapes [82, 84]. In this approach, the frequency-dependent dielectric function in the near-UV/visible region can be represented by the formula:

$$\varepsilon(\omega) = \varepsilon_\infty - \frac{\omega_p^2}{\omega^2 + j\omega\Gamma} + \sum_{i=0}^{n} G_i(\omega) \tag{3.44}$$

where $G_i(\omega)$ terms are the critical point oscillators, which can be described by the expression [85]:

$$G_i(\omega) = C_i\left[e^{j\varphi_i}(\omega_i - \omega - j\Gamma_i)^{\mu_i} + e^{-j\varphi_i}(\omega_i + \omega + j\Gamma_i)^{\mu_i}\right] \tag{3.45}$$

here, C_i is the amplitude, φ_i the phase, ω_i the energy of the gap, Γ_i the broadening, and μ_i the order of the pole. The form of the dielectric function described by Eqs. 3.45 and 3.46 conforms to the requirements of the Kramers-Kronig relations [80], as long as $\mu_i < 0$ [85].

Size Corrections

Although the optical properties of nanostructured materials differ from those of their bulk counterparts, it is possible to use the dielectric functions determined for bulk metals, $\varepsilon_{bulk}(\omega)$, if the appropriate size corrections are applied. These dielectric functions have contributions from interband and intraband transitions:

$$\varepsilon_{bulk}(\omega) = \varepsilon_{\text{inter}}(\omega) + \varepsilon_{\text{intra}}(\omega) \tag{3.46}$$

In metals, the electrons at the Fermi level can be excited by photons of very small energies, and therefore, they are considered "free" electrons. The contributions from free electrons to $\varepsilon_{\text{exp}}(\omega)$ can be described by the Drude model [54]:

$$\varepsilon_{\text{int } ra}(\omega) = 1 - \frac{\omega_p^2}{\omega^2 + i\omega\,\Gamma} \tag{3.47}$$

where ω_p is the plasma frequency and Γ the damping constant arising from the dispersion of the electrons. Γ is related with the mean free path of electrons (λ_e) by the expression $\Gamma = v_F/\lambda_e$, being v_F the Fermi velocity.

Now, we must consider that these free electrons can also be dispersed by the NP surface, as their mean free path is comparable or larger than the dimension of the particle. Therefore, it is necessary to modify the damping term to take into account the surface scattering of the "free" electrons:

$$\Gamma = \Gamma_{bulk} + \Gamma_R = \frac{v_F}{\lambda_e} + \frac{v_F}{R} \tag{3.48}$$

where Γ_R is the damping constant arising from the surface scattering associated with a particle of radius R.

From the Eq. 3.46, we obtain the input of the bound charges by subtracting the free electron contribution from the bulk dielectric function. The free electron contributions are calculated using the Drude model (Eq. 3.47) and ω_p is calculated using Eq. 3.41. Now, we include the surface damping contribution by adding the extra damping term v_F/R to the Drude model and obtain the size-dependent dielectric function, which includes the contributions of the free electrons, surface damping, and interband transitions, as:

$$\begin{aligned}\varepsilon(\omega,R) &= \varepsilon_{\text{inter}}(\omega) + \varepsilon_{\text{intra}}^{NP}(\omega,R) = \varepsilon_{bulk}(\omega) - \varepsilon_{\text{intra}}(\omega) + \varepsilon_{\text{intra}}^{NP}(\omega,R) \\ &= \varepsilon_{bulk}(\omega) + \frac{\omega_p^2}{\omega^2 + i\omega\,\Gamma_{bulk}} - \frac{\omega_p^2}{\omega^2 + i\omega\left(\Gamma_{bulk} + \frac{v_F}{R}\right)}\end{aligned} \tag{3.49}$$

Up to now we have considered a sphere of radius R, for which the surface damping is given by v_F/R. This correction can easily be extended for a nanoshell if instead of the radius we consider its thickness (t): v_F/t. In both cases, the smaller the particle size (its radius or thickness), the more important is the surface dispersion effect. It has been demonstrated that the surface dispersion effects do not change the location of the surface modes, but they affect the coupling of such modes with the applied field, making the resonance peaks wider and less intense [86].

Just to illustrate the importance of the above-described correction in the values of the dielectric functions, we can analyze how the damping constant changes due to the surface dispersion effect for the case of Cu, which has a Fermi velocity of 1.57×10^6 m/s and a mean free path of electrons of 3.9×10^{-8} m [87], and hence Γ_{bulk}^{Cu} has a value of $\sim 4.03 \times 10^{13}$ s^{-1}. For a Cu nanoshell with a thickness of 5 nm, $\Gamma_{t=5\,nm}^{Cu}$ is $\sim 3.54 \times 10^{14}$ s^{-1}, one order of magnitude higher than the damping constant for the bulk material.

5.1.3 Tuning the SPR

Plasmon Position

Perhaps the single most important characteristic of gold nanoshells is the tunability of their surface plasmon resonance. Among the three geometrical parameters of the nanoshells, the shell thickness (t_2), the radii of the inner core (r_1), and the outer shell (r_2), only two are independent, as: $r_2 = r_1 + t_2$. Consequently, the position of the SPR peak and the relative contributions of absorption and scattering to total extinction can be adjusted simply by varying two of these parameters (Fig. 3.10). Moreover, it has been shown that the position of the SPR depends only on the core-to-shell ratio (r_1/r_2) or, equivalently, on the shell thickness-to-total radius ratio (t_2/r_2) [28]. For greater core-to-shell ratios (thinner shells), the peak becomes shifted to longer wavelengths. This resonance condition can be obtained from Eq. 3.9, when the real part of the denominator becomes zero; i.e., Re ($\varepsilon_2\ \varepsilon_a + 2\varepsilon_3\ \varepsilon_b$) = 0. Now, if we assume that the core and the embedding medium are dielectrics (i.e., Im (ε_i) = 0; i = 1, 3), then the expression for the resonance condition as a function of wavelength can be described as [28]:

$$\frac{r_1}{r_2} = \left[1 + \frac{3}{2}\frac{\varepsilon_2'(\lambda)(\varepsilon_1 + 2\,\varepsilon_3)}{\left[\varepsilon_2'(\lambda)\right]^2 - \varepsilon_2'(\lambda)(\varepsilon_1 + 2\,\varepsilon_3) + \left\{\varepsilon_1\,\varepsilon_3 - \left[\varepsilon_2''(\lambda)\right]^2\right\}}\right]^{1/3} \tag{3.50}$$

where ε_2' and ε_2'' are the real and imaginary part of the shell's dielectric function, respectively.

Equation 3.50 gives the ratio of the core radius to the total radius needed to obtain a resonant condition at a particular wavelength. As can be seen in Fig. 3.9, there is always (within a certain range) a core-to-shell ratio capable of placing the maximum of the SPR in any desired wavelength. For example, the position of the resonant extinction peak of gold nanoshells can be selectively tuned from 590-600 nm to around 1,000 nm (Fig. 3.10a). This wavelength range is especially significant because it includes the "NIR tissue window" from 700 to 1,300 nm (Fig. 3.11) [88], where human tissues are mostly transparent to the incident radiation. In the NIR region, effective penetration depths vary from a few millimeters to several centimeters, depending on tissue type [89, 90]. Precisely this possibility of shifting the nanoshells' SPR to the NIR region is fundamental for their usage on in vivo applications.

Unfortunately, some problems arise when large red-shifts of the SPR are needed; as we have seen, this can only be achieved by increasing the r_1/r_2 ratio. This implies that we have to either reduce the thickness of the metal layer or to increase the particle size. Decreasing the thickness of the metal layer has the disadvantage that the intensity of the near-field is reduced, while increasing the particle size affects the Q_{abs}/Q_{sca} ratio. Both of these effects are unfavorable for some applications, such as surface-enhanced spectroscopy and thermal therapy of tumors [91]. Moreover, after a certain point, the SPR intensity is considerably reduced (Fig. 3.10b), eliminating most of the advantages obtained by the use of nanoshells. Finally,

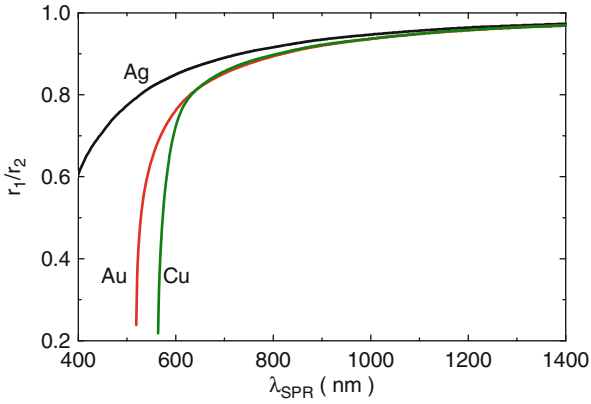

Fig. 3.9 Core-to-shell ratios necessary to shift the SPR peak to the desired wavelength position, calculated for the three noble metals using Eq. 3.50

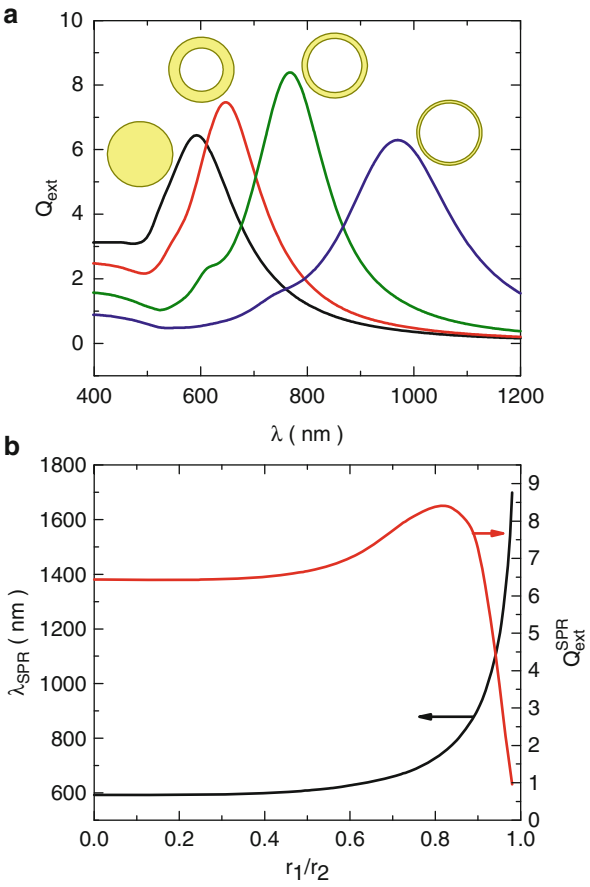

Fig. 3.10 (**a**) Theoretically calculated optical extinction spectra of gold nanoshells ($r_2 = 60$ nm) for some selected core-to-shell ratios (from *left to right*: 0.0, 0.67, 0.83, and 0.92). (**b**) Variation of calculated optical resonance wavelength (*black line*) and intensity (*red line*) with core-to-shell ratio for the same metal nanoshells

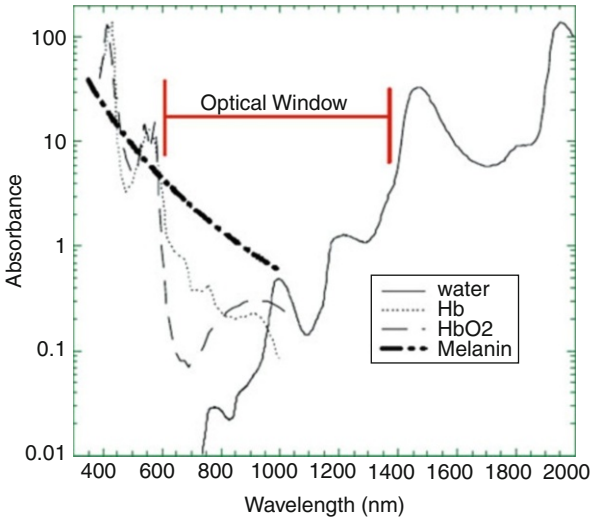

Fig. 3.11 Optical window in tissue due to reduced absorption of red and near-infrared wavelengths (700–1,300 nm) by tissue chromophores [88]

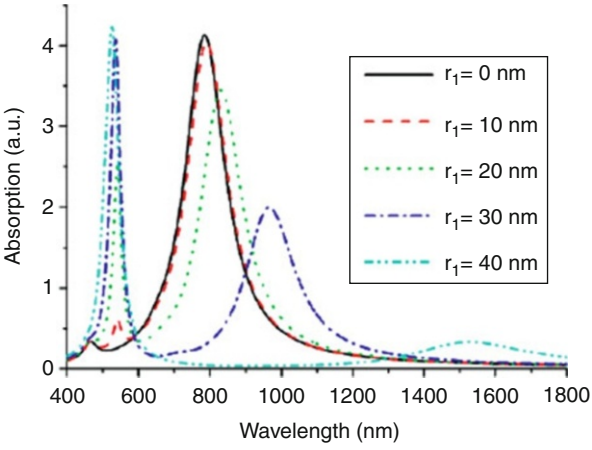

Fig. 3.12 Absorption spectra of MDM nanoshells suspended in free space with $r_1 = 0$ nm (*solid line*), 10 nm (*dashed line*), 20 nm (*dotted line*), 30 nm (*dash-dot line*), and 40 nm (*dash-dot-dot line*) [5]

smaller nanoparticles are preferred in certain cases. For instance, use of nanoshells as contrasting agents in biomedicine requires particles of a few tens of nanometer diameters to facilitate their penetration into the biological tissues.

A simple, yet effective, alternative to single nanoshells can be the structures with additional metallic layers, which can produce additional red-shifts through plasmon hybridization while maintaining the small size and strong surface plasmon resonance. For example, metal-dielectric-metal (MDM) hybrid nanostructures have been synthesized [23] and studied theoretically [5, 59, 92] in recent years, with excellent results (Fig. 3.12). Similarly, double concentric nanoshells (DCN), consisting of two concentric metallic nanoshells, have also been analyzed [59, 60] (Fig. 3.13) and fabricated [4, 6]. The advantage of these multilayered structures

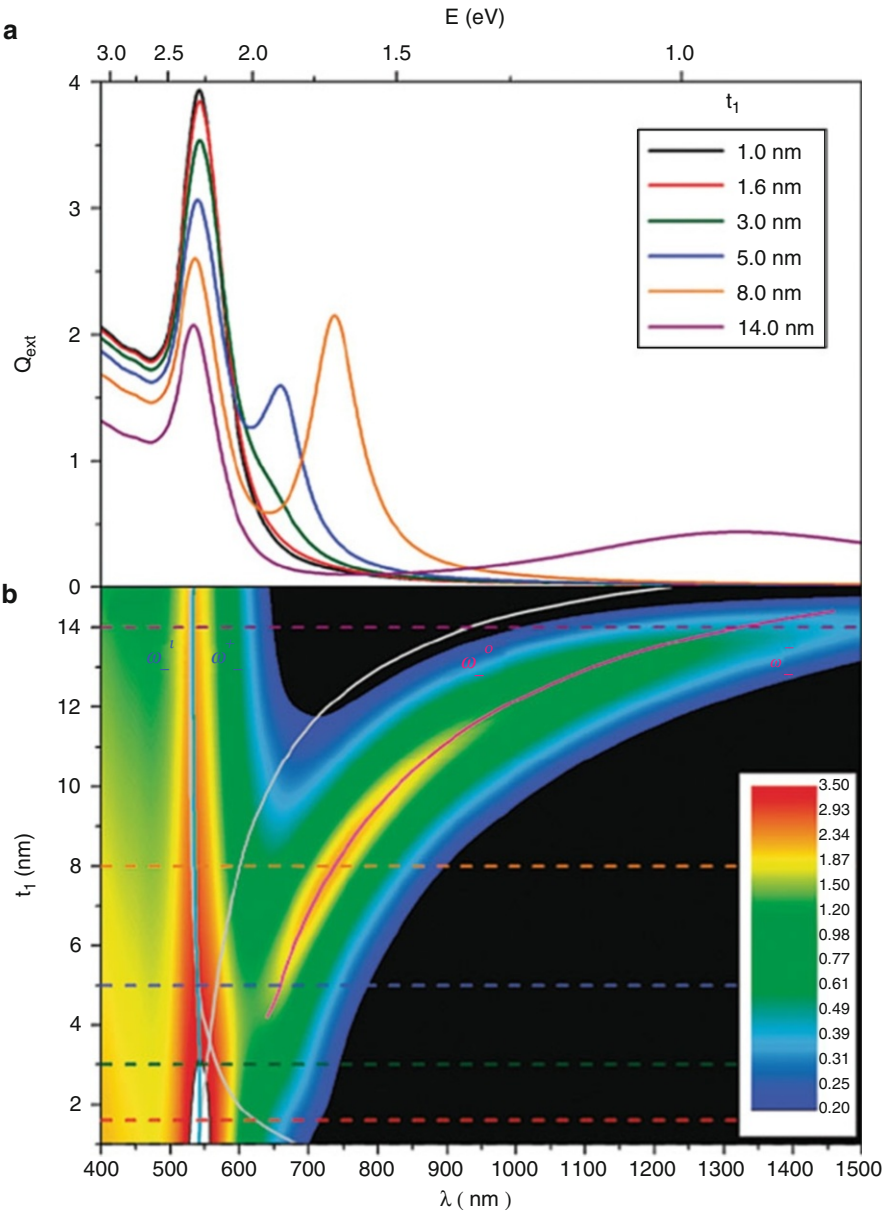

Fig. 3.13 Simulated extinction efficiency for a DCN, having $t_0 = t_2 = 5$ nm, while t_1 and t_3 are varied ($t_1 = 1,2,\ldots 15$ nm; $t_3 = 16$ nm $- t_1$) simultaneously. For clarity, Q_{ext} is presented for some selected values of t_1 (**a**) and for the whole interval (**b**) [60]

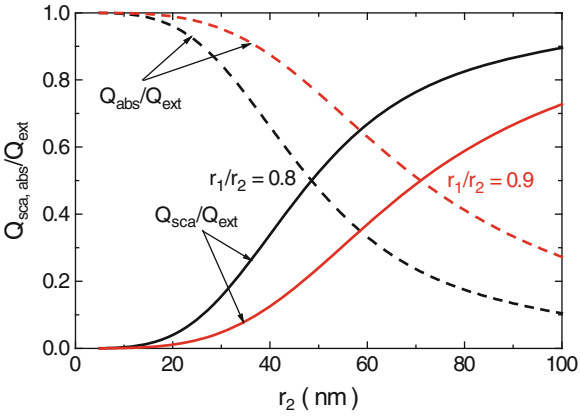

Fig. 3.14 Calculated absorption (*dashed lines*) and scattering (*solid lines*) ratios, for gold nanoshells with fixed core-to-shell ratios of 0.8 (*black*) and 0.9 (*red*). For core-to-shell ratios of 0.8 and 0.9, the absorption and scattering efficiencies are almost equal for outer radii of ca. 50 and 70 nm, respectively. The efficiency ratios were calculated at the SPR maximum

over nanoshells comes from the extra SPR tunability provided by the additional layers. Therefore, the size of the particles can be further reduced without affecting their optical properties.

Q_{abs}/Q_{sca} Ratio

In addition to spectral tunability, the absorption to scattering ratio of nanoshells can also be tuned by changing their outer radius (r_2). For smaller nanoshells, absorption dominates scattering, whereas for larger nanoshells the opposite is true. In between these two extremes, the contributions of absorption and scattering to total extinction can be controlled at will, depending on the total radius and on the core-to-shell ratio (Fig. 3.14). It is therefore possible to design nanoshells tailored for either diagnosis or therapy, where high scattering efficiencies facilitate scattering-based imaging and high absorption efficiencies facilitate photothermal therapy. In resume, by appropriately choosing the dimensions of r_1 and r_2, the position of the extinction peak and the relative amounts of absorption and scattering can be selected across a wide range of wavelengths. This geometrical tunability is an outstanding property. In contrast, a large number of conventional organic dyes would be necessary to cover the same wide spectral range [24].

Near-Field Enhancement

Metallic nanoparticles (including nanoshells) exhibit another unique property. They efficiently concentrate the incident electromagnetic radiation into the near-field region close to their surfaces [93–95]. For example, Jackson et al. [96] and Averitt et al. [28] have predicted near-field enhancements ($|\mathbf{E}|/|\mathbf{E}_0|$, being $\mathbf{E}$ and $\mathbf{E}_0$ the local and incident field, respectively) of around 30 and 3 for silver and gold nanoshells, respectively.

Hooshmand et al. [20], on the other hand, investigated systematically the effect of combining a nanoshell with a spheroid within the same nanostructure (i.e., a nanorice). They found that the plasmonic field enhancement is an order of magnitude larger for gold spheroidal nanoshells of aspect ratio 4 as compared to

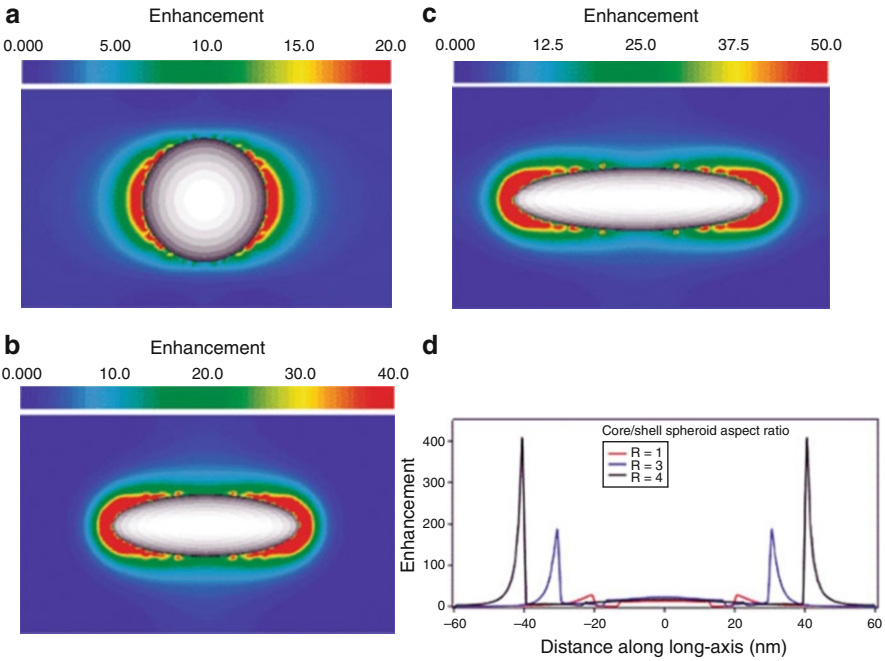

Fig. 3.15 Near-field enhancement in the vicinity of a spheroidal silica core-gold nanoshell as a function of the spheroidal aspect ratio for (**a**) a nanoshell with an aspect ratio of 1, an outer diameter of 40 nm, and a shell thickness of 7 nm; (**b**) a spheroidal nanoshell with an aspect ratio of 3, an outer dimension of 60 nm, and a shell thickness of 12 nm along the long axis; and (**c**) a spheroidal nanoshell with an aspect ratio of 4, an outer dimension of 80 nm, and a shell thickness of 16 nm along the long axis. (**d**) Line profile of the field enhancement along the long axis of the spheroid for all three aspect ratios [20]

spherical nanoshells of the same material (Fig. 3.15). Finally, Peña-Rodríguez and Pal [97] studied the plasmonic behavior of incomplete gold nanoshells, finding that during the initial stages of formation, well-separated, noninteracting metallic nanoparticles at the surface of a dielectric core behave like isolated particles, but intense and irregular local electric fields (with prominent hot spots that exhibit enhancements as high as 60) are created when the number of metallic spheres increases. Such enhancements are very important for applications like surface-enhanced Raman scattering (see Sect. 5.2.1) (Fig. 3.16) [98].

5.2 Applications

5.2.1 Surface-Enhanced Raman Scattering (SERS)

The first application of (gold) nanoshells in SERS was reported by Oldenburg et al. [98]. In this study, significant SERS signal was observed for p-mercaptoaniline (p-MA) in solution using gold nanoshells with plasmon resonance peak tuned to lie

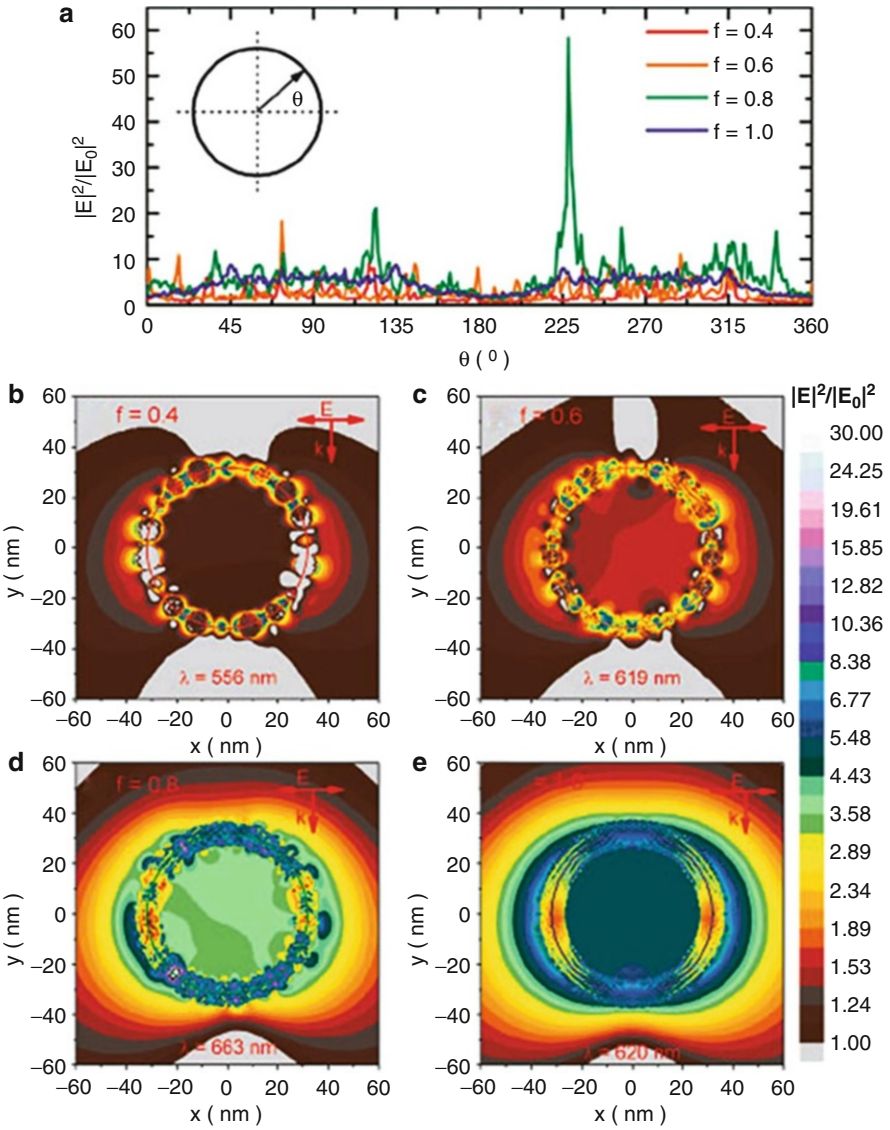

Fig. 3.16 Near-field contour plots in the section plane for some incomplete gold nanoshells. The structures shown have filling fractions of (**b**) 0.4, (**c**) 0.6, (**d**) 0.8, and (**e**) 1.0. (**a**) The field profiles through the middle of the metallic shell (marked with *solid lines* in the *contour plots*) are also shown, for clarity [97]

at the wavelength (1.06 μm) of the excitation source. The strongest Raman enhancements were obtained when enough gold was deposited on the silica cores to form a nearly complete metal shell. The SERS signal was found to be produced by two different factors: the local enhancement of the dielectric field via the

plasmon resonance of the nanostructure and the enhancement due to the localized regions of high field intensity provided by the nearly completed gold shell. A comparison between the SERS enhancements on complete nanoshell structures indicated the relative contribution of these two effects.

Silver nanoshells, owing to their intense SPR, are better SERS substrates than their gold counterparts, as has been observed by Jackson et al. [96]. They demonstrated that the variations of core diameter and shell layer thickness of a metallic nanoshell can tune the local surface electromagnetic field of the nanoparticle in a controlled manner, resulting in local field enhancements ($|\mathbf{E}|/|\mathbf{E}_0|$) of up to 30. Effective SERS enhancements of the order of 10^6 were obtained for these nanoshells in aqueous solution, which correspond to absolute enhancements $\sim 10^{12}$ when reabsorption of Raman emission by nearby nanoparticles is taken into account. Aggregates of composite Au/Ag nanoshells, fabricated on nanosized silica spheres by an aggregation-based method, also exhibited excellent optical properties, and their utility as substrates for surface-enhanced Raman scattering was demonstrated by Lu and coworkers [99]. Similarly, Jackson and Halas [100] found that SERS enhancements on Au and Ag nanoshell films are dramatically different from those observed on colloidal aggregates, measuring SERS enhancements as large as 2.5×10^{10} on Ag nanoshell films for the nonresonant molecule *p*-mercaptoaniline.

Goude and Leung [101] have applied the Gersten-Nitzan model to study the surface-enhanced Raman scattering from a molecule adsorbed on a spherical metallic nanoshell. They concluded that the nonlocal effects can be significant for very close molecule-shell distances and for shells with very small sizes and/or thickness, leading to smaller enhancement in general. On the other hand, Heck et al. [102] used SERS to provide the first direct evidence of the room-temperature catalytic hydrodechlorination of a chlorinated solvent through in situ the catalytic hydrodechlorination of 1,1-dichloroethene in H_2O. In this study, the authors employed Pd islands grown on Au nanoshell assembled films, exploiting the high enhancements and large active area of Au nanoshell SERS substrates, the transparency of Raman spectroscopy to aqueous solvents, and the catalytic activity enhancement of Pd by the underlying Au metal. The formation and subsequent transformation of several adsorbate species were observed.

Surface patterns of nanoshell arrays play an important role in diverse applications including SERS sensors, lithium-ion batteries, solar cells, and optical devices. Yang et al. [103] have described an innovative surface nanopatterning technique for realizing large-scale ordered arrays of spherical nanoshells with well-defined structures. Ag nanoshell arrays were fabricated using polystyrene sphere templates by an electrophoretic process in Ag colloidal solutions. With this fabrication process, it was possible to control various structural parameters of the nanoshell arrays, including the diameter, the surface roughness, and the inter-shell spacing. Tunable SERS and localized SPR of the nanoshell arrays were demonstrated by controlling the structural parameters. Moreover, Küstner et al. [104] have reported the silica encapsulation of a self-assembled monolayer (SAM) on metallic nanoparticles (Fig. 3.17). In this approach, the advantages of both the SAM and the silica shell

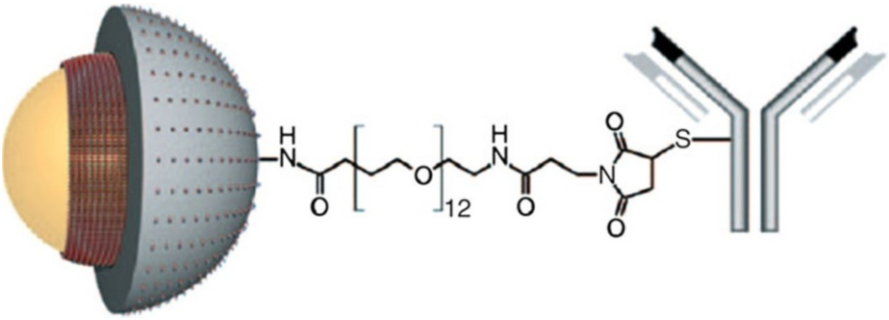

Fig. 3.17 Structure of silica-encapsulated and biofunctionalized SERS labels. *Left:* Gold/silver nanoparticle with a SAM of Raman label molecules (*red*) and a protective silica shell with amino groups (*gray*). *Middle*: heterobifunctional polyethylene glycol spacer. *Right*: monoclonal antibody for antigen recognition [104]

are integrated into a single functional unit. Using a SAM on gold/silver nanoshells optimized for red laser excitation, they found that these SERS labels give signals approximately 180 times more intense than those of other labels based on single gold particles.

Occurrence of SERS inside metal nanoshells was experimentally observed for the first time by Zhang and Guo [105]. They achieved giant enhancements of the order of 10^{11}–10^{14}, solely due to the electromagnetic enhancement in the near-field. Meanwhile, Gellner et al. [106] have reported the optical properties and SERS efficiency of Au/Ag alloy nanoshells with different shell thickness. The relative SERS efficiency of the Au/Ag nanoshells was determined with a self-assembled monolayer of 4-mercaptobenzoic acid (MBA) as a probe molecule. They presented quantitative predictions of SERS efficiencies as high as 0.9, based on calculated Mie scattering intensities. Additionally, a qualitative analysis of their relative SERS efficiency was performed using two dominant Raman bands of MBA.

The application of gold nanoshells as SERS platform for intracellular sensing in NIH-3T3 fibroblast cells was studied by Ochsenkühn et al. [107], using MBA-functionalized nanoshells as a pH sensor. For this, they used 151 ± 5-nm-sized solution-stable nanoparticles, finding the voluntary uptake of nanoshells by living cells. This controllable process was found to be independent of active cellular mechanisms, such as endocytosis. As a result, the cells showed no increase in necrosis or apoptosis. Nanoshell-based intracytosolic SERS spectra were measured using short acquisition times and low laser powers.

5.2.2 Surface-Enhanced Raman Optical Activity (SEROA)

Raman optical activity [108, 109] (ROA), which is defined as the difference between right- and left-circularly polarized Raman-scattering intensities, provides a spectroscopy that is sensitive to molecular chirality. The surface-enhanced version of ROA (SEROA) is even more sensitive and more selective than normal ROA spectroscopy. Acevedo et al. [110] have investigated SEROA theoretically for

molecules near a metal nanoshell. They calculated the SEROA excitation profiles and examined in detail the differential Raman scattering for a simple chiroptical model that provides analytical forms for the relevant dynamical molecular response tensors. This allowed a detailed investigation on the circumstances that simultaneously provide strong enhancement of differential intensities and selectivity to molecules with chirality. Moreover, Lombardini et al. [111] have examined SEROA in the same system for different experimental polarization schemes. Dual circular polarization strategies were found to have special advantages in these circumstances, and the corresponding excitation profiles for a simple chiroptical model were analyzed in detail to suggest preferred excitation wavelengths.

5.2.3 Medicine

Outstanding optical and chemical properties of metal (mainly gold) nanoshells make them interesting for medical applications [70], particularly in the areas of biomedical diagnostics, drug delivery, and thermal therapy of cancer [112, 113]. As the optical properties of these nanoshells are highly sensitive to the relative dimensions of the core and the shell, it is possible to design them to activate their plasmon frequencies in the near-infrared spectral range. In this energy range, the main components of body tissues, such as water, hemoglobin, and oxyhemoglobin, have weaker absorption (Fig. 3.11), making nanoshells useful for cancer treatment and/or detection [114]. Moreover, they can be tailored to either absorb or scatter EM radiation at this wavelength range, and, consequently, it can be controlled at will if the light is converted into heat or dispersed [115]. In the former case, the produced heat can be used to kill cancer cells or release drugs, while the scattering can be used to detect some types of malign cells.

In any case, nanoshells require adequate bio-conjugation for the attachment with biological cells. The bioconjugated nanoshells are then positioned specifically in the tumor to treat or detect the disease. Biomedical applications of nanoshells can be divided into two main categories: outside (i.e., in vitro) or inside (in vivo) the body. Among the former applications, we can find biosensors and biochips, which have been used to analyze various biological samples, particularly the blood, since 2002 [116]. For applications inside the body, researchers are working on the implementation of nanoshells tailored for enhanced thermal ablation of tumors, modulated drugs delivery, and cancer detection. In the following subsection, we will make a brief literature survey on the usage of nanoshells for medical applications.

Cancer Therapy

Complications associated with invasive malignant tumor excision have led to alternative treatment methods including chemotherapy, photodynamic therapy, and thermal coagulation. Metal nanoshells can provide a novel means for targeted photothermal therapy in tumor tissues, minimizing damage to the surrounding healthy tissues. Metal nanoshells have a strong tunable absorption, which can be placed in the near IR, where maximal penetration of light through biological tissues can be achieved. Moreover, when conjugated with a tumor-specific protein, these

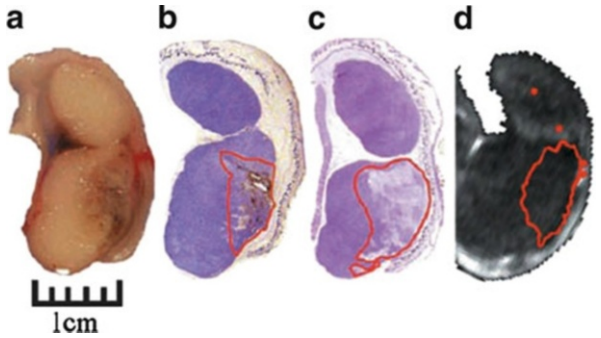

Fig. 3.18 (**a**) Gross pathology after in vivo treatment with nanoshells and NIR laser reveals hemorrhaging and loss of tissue birefringence beneath the apical tissue surface. (**b**) Silver staining of a tissue section reveals the region of localized nanoshells (outlined in *red*). (**c**) Hematoxylin/eosin staining within the same plane clearly shows tissue damage within the area occupied by nanoshells. (**d**) Likewise, MRTI calculations reveal an area of irreversible thermal damage of similar dimension to **a**, **b**, and **c** [91]

nanoshells could be systemically injected for the preferential attachment to the tumor sites. Up to date, cancer therapy using nanoshells has focused mainly in two directions: thermal ablation of tumors [91] and photothermally modulated drug delivery [117].

Thermal Ablation of Tumors

Phototherapy is a new therapeutic use of electromagnetic radiation for cancer treatment [118]. This type of therapy has the advantage of delivering a controlled amount of energy directly into the tumor mass. The laser energy delivered to the targeted tumors can induce localized photochemical, photomechanical, and photothermal reactions that kill the tumor cells [119]. However, the application of photothermal ablation is limited by the potential damage of the surrounding healthy tissues, as the heating from laser sources is nonspecific. Fortunately, nanoshells can be used to significantly enhance the efficiency of photothermal ablation because they exhibit a strong optical extinction at visible and near-infrared wavelengths, coming from the surface plasmon resonance. Moreover, these nanoparticles can be fabricated with well-defined core-shell ratio to absorb NIR light, resulting in a resonant and optimal transfer of thermal energies to the surrounding tissues. The absorption band in the NIR region is a desirable property because the normal tissues are relatively transparent to NIR light; thus, irradiation with NIR light causes minimal thermal injury to normal tissues [120]. Next, we will discuss the most significant advances that have been reported in the literature on the use of nanoshells for photothermal ablation of cancer cells.

Human breast carcinoma cells incubated with nanoshells in vitro were found to have undergone photothermally induced morbidity on exposure to NIR light (Fig. 3.18) [91]. In vivo studies under magnetic resonance guidance have also revealed that exposure of low doses of NIR light in solid tumors treated with

metal nanoshells attains average maximum temperatures capable of inducing irreversible tissue damage within 4-6 min. Tissues heated above the thermal damage threshold displayed coagulation, cell shrinkage, and loss of nuclear staining, which are indicators of irreversible thermal damage. Likewise, photothermally induced death of nanoshell-bound carcinoma cells in vitro, as well as in vivo [121] was demonstrated using an 821-nm diode laser combined with Au nanoshells fabricated to have their plasmon resonance at the same wavelength. Specific binding to tumor cells was achieved by conjugating antibodies against oncoproteins to nanoshells.

Laser-activated gold nanoshell-induced ablation has been found to be an effective and selective technique for both, an ectopic murine tumor model [122] and a subcutaneous murine colon tumor model [123]. In the former study, gold nanoshells of a total size of 110 nm with a 10-nm-thick metallic shell were designed to act as intense near-infrared absorbers, attaining temperatures up to 65.4 $^{\circ}$C in the treated group which resulted in 93 % of tumor necrosis and regression for the high-dose-treated group. The ablation zone was sharply limited to the laser spot size. There was no difference in the size or tumor histology in control groups, indicating a benign course for near-infrared laser treatment alone. The second work relied on the enhanced permeability and retention effect, by which nanoscale materials are preferentially deposited into the tumors (as opposed to normal tissue) due to the leaky nature of tumor vessels. They reported an effective nanoshell-induced photothermal ablation of the tumor using polyethylene glycol-coated Au nanoshells ($\sim$130 nm in diameter) which accumulated in the tumor passively after intravenous injection.

This structure also proved effective to mediate a thermally induced modulation of tumor vasculature in experimental prostate tumors [124]. It was demonstrated that after passive extravasation and retention of the circulating nanoshells from the tumor vasculature into the tumor interstitium, the enhanced nanoshells absorption of near-infrared irradiation over normal vasculature can be used to increase tumor perfusion or shut it down at powers which result in no observable effects on tissue without nanoshells. The results indicated that nanoshell-mediated heating can be used to improve perfusion and subsequently enhance drug delivery and radiation effects or be used to shut down perfusion to assist in thermal ablative therapy delivery.

Enhanced targeted delivery of the nanoshells has also been demonstrated using a new class of molecular specific photothermal coupling agents based on hollow gold nanoshells (average diameter $\sim$30 nm) covalently attached to monoclonal antibody directed at epidermal growth factor receptor (EGFR) [120]. The resulting anti-EGFR-NS exhibited excellent colloidal stability and efficient photothermal effect in the near-infrared region. EGFR-mediated selective uptake of anti-EGFR-NS in EGFR-positive A431 tumor cells but not IgG-NS control was shown in vitro by imaging scattered light from the nanoshells. Irradiation of anti-EGFR-NS treated A431 cells with near-infrared laser resulted in selective destruction of these cells. In contrast, cells treated with anti-EGFR-NS alone, laser alone, or IgG-NS plus laser did not show observable effect on cell viability. Using ^{111}In-labeled nanoshells, it was found that anti-EGFR-NS could be delivered to EGFR-positive tumors at 6.8 % ID/g,

and the microscopic image of excised tumor with scattering signal from nanoshells confirmed a preferential delivery of anti-EGFR-NS to A431 tumor compared with IgG-NS. The absence of silica core, the relatively small particle size and high tumor uptake, and the absence of cytotoxic surfactant required to stabilize other gold nanoparticles suggest that immuno-NS has the potential to extend to in vivo molecular therapy.

Mild-temperature hyperthermia generated by near-infrared illumination of gold nanoshell-laden tumors was reported to cause an early increase in tumor perfusion, reducing the hypoxic fraction of tumors [125, 126]. A subsequent radiation dose was used to induce vascular disruption with extensive tumor necrosis. The study determined that gold nanoshells sequestered in the perivascular space mediate these two tumor vasculature-focused effects to improve radiation response of tumors. This novel integrated antihypoxic and localized vascular disrupting therapy can potentially be combined with other conventional antitumor therapies. Similarly, local hyperthermia delivered by gold nanoshells plus radiation can eliminate radioresistant breast cancer stem cells [127]. In this work, it was confirmed that these cancer stem cells are responsible for accelerated repopulation in vivo and demonstrated that hyperthermia sensitizes this cell population to radiation treatment.

Active targeting of NSs to integrin $\alpha_v\beta_3$ increases its preferential accumulation in tumors and results in therapeutic nanoconstructs for effective cancer therapy [128]. Enzyme-linked immunosorbent assay (ELISA) and cell binding assay confirmed the binding affinity of NS-RGDfK to integrin $\alpha_v\beta_3$. Positron emission tomography/computed tomography imaging suggested that tumor targeting is improved by conjugation of NSs to cyclo(RGDfK) and peaks at ~20 h postinjection. In the subablative thermal therapy study, greater biological effectiveness of targeted NSs was implied by the greater degree of tumor necrosis.

Photothermally Modulated Drug Delivery

Another very important application of nanoshells that leverages the photothermal effect is the photothermally modulated drug delivery [129, 130]. Unfortunately conventional chemotherapeutic agents have poor specificity in reaching tumor tissues and are consequently restricted by dose-limiting toxicity. This limitation could be overcome using a combination of controlled release technology and targeted drug delivery. For this reason, a lot of recent efforts have been dedicated to the development of nanoscale delivery vehicles capable of controlling the release of chemotherapeutic agents directly inside the cancer cells [113]. This is achieved by combining a natural or synthetic polymer with a drug in such a way that the drug is encapsulated within the polymer system for subsequent release in a predetermined manner. One of the ways to obtain this goal is by means of photothermally modulated drug delivery. In this technique, optically active nanoshells are attached to thermally sensitive polymeric hydrogels, and the drug release is triggered with a laser emitting at the wavelength of the nanoshell SPR.

For example, composites of thermally sensitive hydrogels and optically active nanoparticles have been used to achieve significantly enhanced drug release in

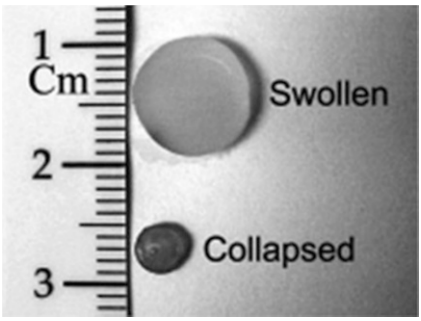

Fig. 3.19 NIPAAm-co-AAm-nanoshell-composite hydrogels in the swollen and collapsed states. The change in volume is induced by heating [131]

response to light irradiation [117, 131]. Copolymers of N-isopropylacrylamide (NIPAAm) and acrylamide (AAm) exhibit a lower critical solution temperature (LCST) that is slightly above the body temperature. When the temperature of the copolymer exceeds the LCST, the hydrogel collapses (Fig. 3.19), causing a burst release of any soluble material held within the hydrogel matrix. Gold-gold sulfide nanoshells had been incorporated into poly(NIPAAm-co-AAm) hydrogels for the purpose of initiating a temperature change with light. The 1,064-nm light was absorbed by the nanoparticles, and converted to heat, leading to the release of methylene blue and proteins of varying molecular weights. Additionally, these nanoshell-composite hydrogels could release multiple bursts of protein in response to repeated near-IR irradiation. The very same composites were also found suitable for delivering controlled pulsatile doses of insulin in response to near-IR irradiation [132]. The activity of the released insulin was determined by measuring glucose uptake by adipocytes that had been exposed to photothermally released insulin. The released insulin did not show a loss in activity as compared to the positive control (insulin in saline), thus demonstrating transdermal photothermally modulated drug deliver in vitro.

Near-complete liposome release within seconds was demonstrated by irradiating hollow gold nanoshells with a near-infrared pulsed laser, overcoming their usual slow release of the encapsulated drug [133]. Different coupling methods, such as having the gold NSs tethered to, encapsulated within, or suspended freely outside the liposomes, were tested, finding that all triggered liposome release but with different levels of efficiency. Microbubble formation and collapse due to the rapid temperature increase of the NS, resulting in liposome disruption, was suggested as the underlying content release mechanism.

Nanoshell-composite hydrogels have also been used to develop a photothermal modulated drug delivery system [134]. SiO_2-Au nanoshells of varying concentrations have been embedded within temperature-sensitive *N*-isopropylacrylamide-*co*-acrylamide (NIPAAm-*co*-AAm) hydrogels. The resulting composites had the extinction spectrum of the SiO_2-Au nanoshells in which the hydrogels collapsed reversibly in response to temperature (50°C) and laser irradiation. The degree of collapse of the hydrogels was controlled by the laser fluence as well as the concentration of SiO_2-Au nanoshells. Modulated drug delivery profiles for

methylene blue, insulin, and lysozyme were achieved by irradiation of the drug-loaded nanoshell-composite hydrogels, revealing that drug release depends on the molecular weight of the therapeutic molecules. Similarly, a drug-loaded structure comprising a PEGylated (PEG = polyethylene glycol) gold nanoshell on silica nanorattle spheres was demonstrated to obtain combined remote-controlled photothermal therapy with modulated drug delivery [135]. Tumor cells were killed with higher efficacy and less toxicity than the free drug.

Tissue Welding

Gold nanoshells with peak extinction matching the NIR wavelength of the exciting laser also proved to be good exogenous NIR absorbers to facilitate NIR laser-tissue welding [114]. Goblin et al. have performed the optimization work on ex vivo muscle samples and then translated into testing in an in vivo rat skin wound-healing model. Mechanical testing of nanoshell-solder welds in muscle revealed successful fusion of tissues with tensile strengths of the weld site equal to the uncut tissue. No welding was accomplished with this light source when using solder formulations without nanoshells. Mechanical testing of the skin wounds showed sufficient strength for closure and strength increased over time. Histological examination showed good wound-healing response in the soldered skin. Notably, the healing results were similar to the suture-treat control group until day 5, after which healing was shown to be better in the suture group.

Bio-sensing and Imaging

As important as the treatment of tumors is their detection. Thanks to its versatility and low toxicity, nanoshells have also found wide applications in this field. For instance, bioconjugated nanoshells have been used as contrast agents, to detect and image individual cancer cells in vitro and solid tumors in vivo. In this case, one attempts to maximize the scattering of light rather than the absorption, which allows the sensing and/or imaging of tumors, facilitating its detection.

Bio-sensing

Potential applications of NSs in bio-sensing [116, 136] arise from the dependence of their surface plasmon resonance frequency on the refractive index of surrounding environment [70]. For sensing applications, a high sensitivity of the SPR frequency to the change in the refractive index of the surroundings ($\Delta\lambda_{SPR}/\Delta n_m$) is required. Sun and Xia [116, 137] have shown that gold nanoshells are more sensitive than solid nanospheres to the changes in refractive index of the surrounding environment (306.6 and 65.5 nm/RIU, respectively) and that the observed peak shift varies linearly with n_m (Fig. 3.20). Similar results were obtained by Tam et al. [138], who could measure sensitivities of up to $\Delta\lambda_{SPR}/\Delta n_m = 555.4$ nm/RIU. In this subsection, we will do a brief literature survey on how this optical sensitivity to the surrounding environment exhibited by nanoshells has been exploited to detect biomarkers in simple absorbance assays [16, 139].

A rapid immunoassay capable of detecting analyte within complex biological media without any sample preparation has been demonstrated [16, 140, 141].

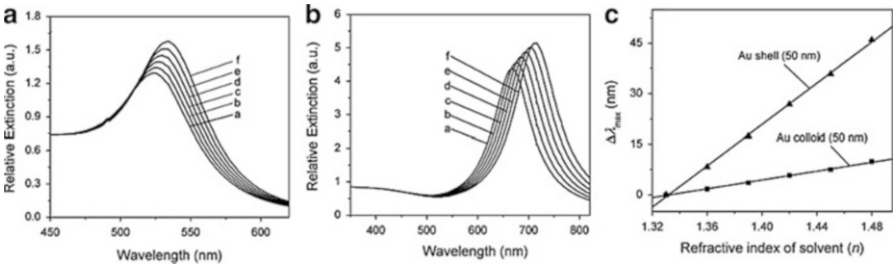

Fig. 3.20 Extinction coefficients computed for (**a**) a gold solid colloid with a diameter of 50 nm and (**b**) a gold nanoshell with a diameter of 50 nm and wall thickness of 4.5 nm. In simulation, the gold nanostructures are surrounded by solvents with increasing refractive indices: n = 1.33 (water), 1.36, 1.39, 1.42, 1.45, and 1.48. (**c**) Plots of the dependence of peak shift ($\Delta\lambda_{SPR}$, relative to the peak position calculated for water with n = 1.33) on the refractive index of surrounding medium. The sensitivity factors, $\Delta\lambda_{SPR}/\Delta n_m$, were 306.6 and 65.5 nm/RIU for gold nanoshell and 50-nm solid colloids, respectively. The interiors of these gold nanoshells were assumed to be filled by the external solvent [116]

This was accomplished using gold nanoshells as an immunoassay substrate. Near-infrared resonant gold nanoshells were labeled with antibodies specific to rabbit IgG analyte. Addition of analyte induced aggregation of antibody-nanoshell conjugates, causing a decrease in the SPR intensity. Successful detection of immunoglobulins was achieved in saline, serum, and whole blood. This simple immunoassay proved capable of quantitative detection of analyte within 10-30 min with sensitivities below 1 ng/mL. McFarland and Van Duyne [13] have used dark-field optical microscopy to demonstrate the localized surface plasmon resonance λ_{max} response of individual Ag nanoparticles and the formation of a monolayer of small-molecule adsorbates. They showed that the adsorption of fewer than 6×10^4 1-hexadecanethiol molecules on single Ag nanoparticles results in a localized surface plasmon resonance shift of 40.7 nm. Additionally, they found that the kinetics of the single nanoparticle response was comparable to that of other real-time sensor technologies.

Mie theory and the discrete dipole approximation method were used to calculate absorption, scattering efficiencies, and optical resonance wavelengths for three classes of nanoparticles commonly used for biological and cell imaging applications: gold nanospheres, silica-gold nanoshells, and gold nanorods [115]. In particular, gold nanoshells were found to have optical cross sections comparable to or even higher than nanospheres made of the same metal with the added advantage that their optical resonances lay favorably in the near-infrared region. The resonance wavelength could be rapidly increased by either increasing the total nanoshell size or increasing the ratio of the core-to-shell radius. The total extinction of nanoshells exhibits a linear dependence on their total size; however, it is independent of the core/shell radius ratio. It has also been found that the relative scattering contribution to the extinction can be rapidly raised by increasing the nanoshell size or decreasing the ratio of the core/shell radius.

Silica-gold nanoshells have also been used as solid-phase dot immunoassay [142, 143]. The principle of this assay is based on staining of a drop (1 μl) analyte on a nitrocellulose membrane strip by using silica-gold nanoshells conjugated with biospecific probing molecules. Experimental example was human IgG (hIgG, target molecules) and protein A (probing molecules). For 15-nm colloidal gold conjugates, the minimal detectable amount of hIgG was about 4 ng, but for nanoshell conjugates (silica core diameter of 70 nm and gold outer diameter of 100 nm), the detection sensitivity increased to about 0.5 ng. This finding has been explained by the difference in the monolayer particle extinction. Additionally, the optical mechanisms behind the efficiency of nanoparticle-labeled dot immunoassay have been addressed, both, theoretically and experimentally [144]. The experimental verification was performed with functionalized 15-nm colloidal gold nanospheres and silica-gold nanoshells. Three types of NSs, with silica core diameters of 100, 140, and 180 nm and a gold shell thickness of about 15 nm, were studied. A normal rabbit serum (the target IgG molecules) and sheep antirabbit antibodies (the probing molecules) were used as a biospecific model. It was found [139] that the minimal detection limit for IgG target molecules improves from 15 ng for 15-nm colloidal gold particles to around 0.25 ng in the case of 180/15-nm NSs and up to 0.5-1.0 ng for 100/15 and 140/15-nm NSs.

In yet another study, gold nanoshells were used as effective signal transducers in whole blood. First, NS self-assembled monolayers (SAMs) were formed on the surface of transparent glasses modified with 3-aminopropyltrimethoxysilane (APTES) [139]. Afterward, NS SAMs were modified with cystamine and biotin-NHS (N-hydroxysuccinimide) and used as a novel optical biosensor for real-time detection of streptavidin-biotin interactions in diluted human whole blood within short assay time, without any sample purification/separation. It has been shown that this biosensor featured a low detection limit ~3 μg/mL and a wide dynamic range ~3–50 μg/mL.

Gold precursor composites, preadsorbed onto the surface of ITO substrates, were also used successfully as nanoprobes in an antioxidant capacity assay [145]. Nanoshell precursor composites were enlarged to varying degrees with the treatment of modified electrodes immersed in the gold nanoparticle growth solution containing different phenolic acids. Obtained results revealed that the higher capacity of phenolic acid to reduce $AuCl^{4-}$ to Au^0 resulted in the intensified localized SPR features and reduced cathodic currents. The optical and electrochemical results could be used to evaluate the antioxidant capacity of phenolic acids with this simple method. Similarly, a series of phenolic acids were also tested for their ability to scavenge hydrogen peroxide (H_2O_2) by using a novel enzyme-free, spectrophotometry assay [146]. Gold nanoshell precursor composites were used as optical nanoprobes. This approach was based on the H_2O_2-induced growth of gold NSs. The addition of phenolic acids inhibits the formation of complete gold NSs, and the corresponding peak wavelength changed accordingly, acting as an optical signature. Caffeic acid was found to be the most efficient H_2O_2-scavenger with its H_2O_2-scavenging activity being 125×10^{-3} μM^{-1}, whereas trans-cinnamic acid exhibited the weakest activity (0.73×10^{-3} μM^{-1}).

Imaging

Optical imaging of tissues is a high resolution, noninvasive technique that has the potential to greatly contribute to cancer detection [30]. Unfortunately, these technologies are often limited by the inherently weak optical signals of endogenous chromophores and the subtle spectral differences of normal and affected tissues. This limitation can be overcome by using exogenous contrast agents, designed to probe the molecular specific signatures of cancer, which improve the detection limits and clinical effectiveness of optical imaging [147]. In recent years, nanoshells have been increasingly used for this task, due to their outstanding optical properties.

Imaging of tumors has been achieved by using diffuse optical spectroscopy (DOS) for the noninvasive measurement of gold nanoshell concentrations in tumors of live mice [148, 149]. In this study, the diffuse optical spectra (500-800 nm) were measured using an optical fiber probe placed in contact with the tissue surface. In vitro studies were performed on tissue phantoms illustrating an accurate measurement of silica-gold nanoshell concentration within 12.6 % of the known concentration. Subsequent in vivo studies were performed on a mouse xenograft tumor model. DOS spectra were measured at preinjection, immediately after injection, and at 1 and 24 h postinjection times. The nanoshell concentrations were verified using neutron activation analysis.

The effective use of gold nanoshells as a contrast agent for optical coherence tomography (OCT) may be hampered by the delivery of a wrong dose resulting in unwanted signal attenuation. A recent study has examined how the changes in the scattering coefficient (μ_s) due to concentration variations affect the OCT image and defined a dose range that would result in optimal values of μ_s to maintain an acceptable signal attenuation level [150]. The results obtained by Kah et al., using 81-nm-radius silica core and 23-nm shell thickness revealed that an increase in μ_s not only enhances the OCT signal near the surface but also attenuates the signal deeper into the sample. It was found that a concentration range of $5.6 \times 10^9 < c < 2.3 \times 10^{10}$ particles/mL provides adequate signal enhancement near the surface without severely compromising the imaging depth due to signal attenuation. Finally, the extraction of μ_s from the OCT signal to estimate the gold nanoshells' concentration in vivo has also been demonstrated. The estimated concentration of 6.2×10^9 particles/mL in a mouse tumor after intravenous delivery lies within this concentration range to effectively enhance the tumor imaging.

The in vivo control of optical contrast in a mouse tumor model with gold nanoshells as contrast agent has been examined [151]. Gold nanoshells were administered into mice, with varying injected dosage and particle surface parameters. The results reasserted that a high concentration of gold nanoshells in tumor only enhances the OCT signal near the tissue surface while significantly attenuating the signal deeper into the tissue. However, with an appropriate dosage, intravenous (IV) delivery of gold nanoshells allows a moderate concentration of 6.2×10^9 particles/mL in tumor to achieve a good OCT signal enhancement with minimal signal attenuation at higher depths. An increase in the IV dosage of gold nanoshells revealed a corresponding nonlinear increase in their tumor concentration.

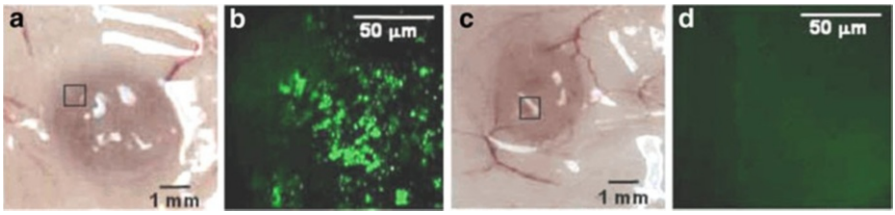

Fig. 3.21 Standard white light images and two-photon-induced photoluminescence (*TPIP*) images from subcutaneous tumors. (**a**), (**c**) *White light* images of tumor with and without nanoshells. (**b**), (**d**) TPIP images from tumors with and without nanoshells [152]

The fractional concentration could be improved with the use of antiepodermal growth factor receptor (EGFR) surface functionalization, which also reduced the time required for tumor delivery from 6 to 2 h.

Likewise, 3D microscopic imaging of gold nanoshells in tumors has been achieved using two-photon-induced photoluminescence [152–155]. This study took advantage of a new photo-physical property of nanoshells, whereby these particles glow brightly when excited by near-infrared light. Specifically, it was demonstrated that NSs excited at 780 nm produce strong two-photon-induced photoluminescence (TPIP, Fig. 3.21). The luminescence brightness of NSs was characterized and compared to that of fluorescein-labeled fluorescent beads (FB), finding that the former are 140 times brighter than the latter. 3D distribution of gold NSs targeted to murine tumors was imaged to demonstrate the potential application of this bright TPIP signal for biological imaging.

Gold NSs can be used as exogenous contrast agents for enhanced visualization of tumors using narrow band imaging (NBI) [156, 157]. NBI takes advantage of the strong NIR absorption of NSs to distinguish between blood and nanoshells in the tumor by imaging in narrow wavelength bands in the visible and NIR, respectively. First, the optimum wavelengths to enhance contrast between blood and NSs were determined using tissue-simulating phantoms. Then, these optimum wavelengths were used for ex vivo imaging of tumors extracted from human colon cancer xenograft-bearing mice injected with gold NSs. Systemically, delivered NSs accumulated passively in tumor xenografts due to the enhanced permeability and retention effects. Ex vivo NBI of tumor xenografts demonstrated tumor-specific heterogeneous distribution of NSs, with a clear distinction from the tumor vasculature.

The radiolabeling of gold nanoshells for positron emission tomography/computed tomography (PET/CT) imaging in rat tumor model has also been reported. For this purpose, the radionuclide ^{64}Cu was attached to the NSs via a conjugation method. In a first study [158], the resulting conjugates showed good labeling efficiency and stability in PBS and serum. The pharmacokinetics of ^{64}Cu-NS and the controls (^{64}Cu-DOTA and ^{64}Cu-DOTA-PEG2K) were determined in nude rats with a head and neck squamous cell carcinoma (HNSCC) xenograft by radioactive counting. In vivo distribution of ^{64}Cu-NSs and the controls in the tumor-bearing rats were monitored at various time points after their intravenous

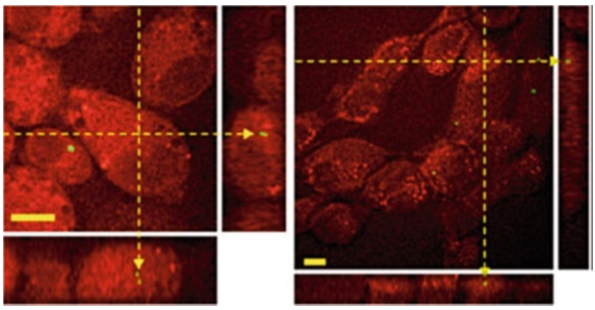

Fig. 3.22 Spatial distribution of gold NSs in live cultures of RAW 264.7 (*left*) and A431 (*right*). *Red contrast* corresponds with forward-detected CARS signal with pump and Stokes wavelengths tuned to excite the CH2 resonance (*red*). *Green signal* corresponds with gold NS signal. Both bars represent 10 μm [159]

injection using PET/CT imaging. Obtained results showed accumulation of ^{64}Cu-NSs in the tumors and other organs with significant difference from the controls. The organ biodistribution of rats at 46 h postinjection was analyzed by radioactive counting and compared between the ^{64}Cu-NS and the controls. Different clearance kinetics was indicated. Neutron activation analysis (NAA) of gold concentration was performed to quantify the amount of NSs in major tissues of the dosed rats, and the obtained results revealed similar distributions. Overall, PET images using ^{64}Cu had good resolution and therefore can be further applied to guide photothermal treatment of cancer. In vivo biodistribution and tumor specificity were analyzed in a similar study [128], using ^{64}Cu-radiolabeled untargeted and targeted NSs in live nude rats bearing HNSCC xenografts. ELISA and cell binding assay confirmed the binding affinity of NS-RGDfK to integrin $\alpha_v\beta_3$. PET/CT imaging suggested that tumor targeting is improved by conjugation of NSs to cyclo(RGDfK) and peaks at ~20 h postinjection.

Finally, plasmon-enhanced four-wave mixing microscopy combined with coherent anti-Stokes Raman scattering (CARS) microscopy has been used to visualize the distribution of 75-nm-radius gold NSs within live cells (Fig. 3.22) [159]. It was found that living cells containing plasmonic nanoshells could be exposed up to 2.5 mJ with no detectable photothermally induced necrosis. In contrast, above this irradiation energy threshold, cell death occurs, which is linearly proportional to the laser power. The majority of the detected NS signals were through plasmon-enhanced four-wave mixing process, along the epi-direction with the incident lasers tuned to the silent region of the Raman spectrum. Then, the distribution of NSs inside live cells was visualized by combining the epi-detected signal with the forward-detected CARS at the CH_2 resonance.

5.2.4 Photonics

Colloidal particles can be assembled to form a two- or three-dimensional crystal lattice with long-range periodicity, known as photonic bandgap materials. The behavior of photons in these materials is equivalent to that of electrons in

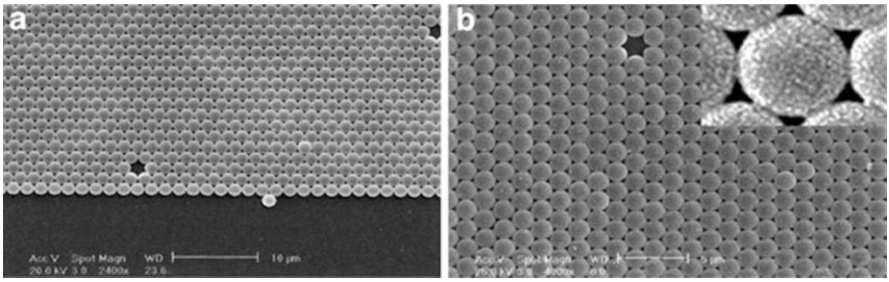

Fig. 3.23 (**a**) SEM image of a 2D colloidal crystal template composed of PS beads (diameter of 1,600 nm). (**b**) SEM image of the resultant 2D ordered array of metallodielectric composite microspheres. The inset in (**b**) shows the MD particles at a higher magnification. The silver shell thickness is about 45 ± 5 nm [160]

semiconductors. In this configuration, the gaps between the particles form a region of low refractive index, while the particles form a region of high refractive index. When photons are incident on these materials, they pass through regions with high and low refractive indices. For photons, this contrast in refractive index is similar to the periodic potential that an electron experiences while passing through a semiconductor. If the contrast in refractive index is large, then the photons are either totally reflected or confined inside the dielectric material. The colloidal crystal blocks wavelengths in the photonic bandgap while allowing other wavelengths to pass through. The photonic bandgap can be tuned by changing the size of the constituting particles.

Nanoshells are better suited than solid particles for this application because relative refractive index contrast in core and shell particles is higher [10]. Bandgap of such photonic crystals can be tuned from visible to IR range simply by changing index contrast [161]. For example, Zhan et al. [160] have studied the optical reflectance of a two-dimensional (2D) metallodielectric (MD) photonic crystal, composed of hexagonal array of close-packed silver shell polystyrene-core composite particles (Fig. 3.23). They observed a dramatic change in reflectivity behavior of the 2D MD film from a 2D colloidal crystal template and a homogeneous silver film. The phenomenon of strong reflectance bands of the 2D MD film was explained as a selective coupling of the incident light with surface plasmon of the 2D textured structure via the 2D grating.

Similarly, collective plasmonic modes in two- and three-dimensional periodic assemblies of metallic nanoshells were studied by means of full electrodynamic calculations [162, 163]. It was found that, in assemblies of metallic nanoshells, the plasmon resonances of the individual particles interact weakly between them and form narrow bands of collective plasmon modes that manifest themselves as resonance structures in corresponding transmission spectra and induce strong absorption. In contrast, for binary heterostructures, the collective plasmonic modes originating from the two building components coexist, leading to hybridization gaps, broadband absorption, and a rich structure of resonances over an extended range of frequencies.

5.2.5 Fano Resonances

Fano profiles are typical spectral features caused by the coupling of a discrete state with a continuum [164]. In particular, the all-plasmonic Fano resonance [25] was first described for a near-field coupled Au-Ag dimer, where the spectrally localized SPR of the silver nanoparticle (the discrete level) was coupled to the interband transitions of the gold nanoparticle (the continuum) [165]. In addition to fundamental scientific interests, Fano resonances in strongly coupled systems give rise to the so-called plasmon-induced transparency (PIT) [61], which is a phenomenon similar to the electromagnetically induced transparency, previously observed in atomic systems [166, 167]. In turn, PIT has a great potential for the fabrication of sub-wavelength waveguides, low-loss metamaterials, and chemical sensors [61, 168–171]. Therefore, it is not surprising that, apart from the original dimer, several plasmonic structures have been proposed as candidates for generating Fano resonances [61, 72, 168, 172, 173].

Fano resonances in modified MDM nanoshells (also referred as Fanoshells [174]) have been recently reported by Hu et al. [22] and Mukherjee et al. [61]. In these structures, the center of the metallic shell had been displaced with respect to the center of the metallic core. Then, the dipolar modes of the inner core interacted with quadrupolar and higher multipolar plasmon modes of the outer shell due to the symmetry breaking introduced by the displacement of the core, resulting in Fano interference. It was found that the resulting Fano resonance was almost isotropic (i.e., independent of the polarization of the incident light), opening the possibility of applying them as metamaterials.

6 Conclusions and Future Perspective

Research on metal nanoshells has had a short but intense life. The theoretical tools to calculate their optical properties existed since the 50s [45]. However, it was only in 1989 that Neeves and Birnboim [53] demonstrated, using theoretical calculations, that a composite spherical particle with a dielectric core and a metallic shell can produce SPR modes in a much larger range of wavelengths than solid ones. They predicted that those SPR wavelengths would be tunable by controlling the geometrical parameters of the core and shell. The first nanoshells, consisting of an Au_2S core surrounded by a gold shell, were synthesized a few years later by Zhou et al. [27] and allowed shifting the plasmon resonance peak from 520 nm (gold colloids) up to 900 nm. However, additional red-shifts were restricted by the chemistry of the synthesis reactions, which imposed a limit of around 40 nm on the maximum achievable size of nanoshells [9]. The process also produced large amounts of gold colloid as a secondary product, generating an additional absorption peak around 520 nm [9]. Most of the limitations of those first nanoshells were overcome by a new type of gold nanoshells, synthesized by Halas and coworkers [71]. The new method replaced the Au_2S core of the previous structure by monodisperse spherical silica particles, opening the possibility of much greater control over the spectral position of SPR in nanoshells [2].

After that, applications of nanoshells flourished. In 1999, Oldenburg et al. [98] demonstrated the use of nanoshells in surface-enhanced Raman scattering (SERS). A year later Sershen et al. [117] used them for photothermally modulated drug delivery. Sun and Xia [116] showed in 2002 that nanoshells are more sensitive than nanospheres to changes in the refractive index of the surrounding environment, opening the door to their use as sensors. Hirsh at al. [91] revealed its usefulness for thermal ablation of tumors in 2003. Goblin et al. [114] proved in 2005 that they can be good exogenous NIR absorbers to facilitate NIR laser-tissue welding. Last year (2010), Hu et al. [22] reported the appearance of Fano resonances in metal-dielectric-metal (MDM) nanoshells with the center of the metallic shell displaced with respect to the center of the metallic core.

Moreover, the methods of nanoshell synthesis have also been improved considerably, allowing an always-growing control over the morphology of the nanoshells that lead to several new variations such as the nanorice [19, 20] (ellipsoidal nanoshells) as well as nonconcentric [21, 22] and multilayered [6, 23] nanoshells. All of them have proved capable of increasing the upper limit of allowed red-shifts. However, despite all those advances made in the study of nanoshells, the possibilities of development are still very large. It is not hard to foresee that the current trend on nanoshell research will continue, achieving greater control over their morphology and size, while new applications appear and existing ones are improved. In the end, it will be possible to fabricate nanoshells with features tailored to the needs of each particular application.

References

1. Oldenburg SJ, Jackson JB, Westcott SL, Halas NJ (1999) Infrared extinction properties of gold nanoshells. Appl Phys Lett 75(19):2897–2899
2. Oldenburg SJ, Averitt RD, Westcott SL, Halas NJ (1998) Nanoengineering of optical resonances. Chem Phys Lett 288(2–4):243–247
3. Peña O, Pal U, Rodríguez-Fernández L, Crespo-Sosa A (2008) Linear optical response of metallic nanoshells in different dielectric media. J Opt Soc Am B 25(8):1371–1379
4. Radloff C, Halas NJ (2004) Plasmonic properties of concentric nanoshells. Nano Lett 4(7):1323–1327
5. Wu D, Liu X (2009) Tunable near-infrared optical properties of three-layered gold-silica-gold nanoparticles. Appl Phys B Lasers Optics 97(1):193–197
6. Prodan E, Radloff C, Halas NJ, Nordlander P (2003) A hybridization model for the plasmon response of complex nanostructures. Science 302(5644):419–422
7. Schwartzberg AM, Olson TY, Talley CE, Zhang JZ (2006) Synthesis, characterization, and tunable optical properties of hollow gold nanospheres. J Phys Chem B 110(40):19935–19944
8. Anker JN, Hall WP, Lyandres O, Shah NC, Zhao J, Van Duyne RP (2008) Biosensing with plasmonic nanosensors. Nat Mater 7(6):442–453
9. Averitt RD, Sarkar D, Halas NJ (1997) Plasmon resonance shifts of Au-coated Au_2S nanoshells: insight into multicomponent nanoparticle growth. Phys Rev Lett 78(22):4217
10. Kalele S, Gosavi SW, Urban J, Kulkarni SK (2006) Nanoshell particles: synthesis, properties and applications. Curr Sci 91(8):1038–1052
11. Sönnichsen C, Alivisatos AP (2005) Gold nanorods as novel nonbleaching plasmon-based orientation sensors for polarized single-particle microscopy. Nano Lett 5(2):301–304

12. Raschke G, Brogl S, Susha AS, Rogach AL, Klar TA, Feldmann J, Fieres B, Petkov N, Bein T, Nichtl A, Kurzinger K (2004) Gold nanoshells improve single nanoparticle molecular sensors. Nano Lett 4(10):1853–1857
13. McFarland AD, Van Duyne RP (2003) Single silver nanoparticles as real-time optical sensors with zeptomole sensitivity. Nano Lett 3(8):1057–1062
14. Xu H, Käll M (2002) Surface-plasmon-enhanced optical forces in silver nanoaggregates. Phys Rev Lett 89(24):246802
15. Allain LR, Vo-Dinh T (2002) Surface-enhanced Raman scattering detection of the breast cancer susceptibility gene BRCA1 using a silver-coated microarray platform. Anal Chim Acta 469(1):149–154
16. Hirsch LR, Jackson JB, Lee A, Halas NJ, West JL (2003) A whole blood immunoassay using Gold nanoshells. Anal Chem 75(10):2377–2381
17. Cui Y, Ren B, Yao J-L, Gu R-A, Tian Z-Q (2006) Synthesis of Ag_{core}-Au_{shell} bimetallic nanoparticles for immunoassay based on surface-enhanced Raman spectroscopy. J Phys Chem B 110(9):4002–4006
18. Premasiri WR, Moir DT, Klempner MS, Krieger N, Jones G, Ziegler LD (2005) Characterization of the surface enhanced Raman scattering (SERS) of bacteria. J Phys Chem B 109(1):312–320
19. Wang H, Brandl DW, Le F, Nordlander P, Halas NJ (2006) Nanorice: a hybrid plasmonic nanostructure. Nano Lett 6(4):827–832
20. Hooshmand N, Jain PK, El-Sayed MA (2011) Plasmonic spheroidal metal nanoshells showing larger tunability and stronger near fields than their spherical counterparts: an effect of enhanced plasmon coupling. J Phys Chem Lett 2(5):374–378
21. Wu Y, Nordlander P (2006) Plasmon hybridization in nanoshells with a nonconcentric core. J Chem Phys 125(12):124708
22. Hu Y, Noelck SJ, Drezek RA (2010) Symmetry breaking in gold-silica-gold multilayer nanoshells. ACS Nano 4(3):1521–1528
23. Xia X, Liu Y, Backman V, Ameer GA (2006) Engineering sub-100 nm multi-layer nanoshells. Nanotechnology 17(21):5435–5440
24. Erickson TA, Tunnell JW (2009) Gold nanoshells in biomedical applications. In: Kumar CSSR (eds) Nanomaterials for the life sciences: mixed metal nanomaterials, vol 3. Wiley-VCH, Weinheim, Germany, pp. 1-44.
25. Luk'yanchuk B, Zheludev NI, Maier SA, Halas NJ, Nordlander P, Giessen H, Chong CT (2010) The Fano resonance in plasmonic nanostructures and metamaterials. Nat Mater 9(9):707–715
26. Sattler KD (2010) Nanomedicine and nanorobotics. CRC Press, Baco Raton
27. Zhou HS, Honma I, Komiyama H, Haus JW (1994) Controlled synthesis and quantum-size effect in gold-coated nanoparticles. Phys Rev B 50(16):12052–12056
28. Averitt RD, Westcott SL, Halas NJ (1999) Linear optical properties of gold nanoshells. J Opt Soc Am B 16(10):1824–1832
29. Averitt RD, Westcott SL, Halas NJ (1998) Ultrafast electron dynamics in gold nanoshells. Phys Rev B 58(16):R10203
30. Loo C, Lin A, Hirsch L, Lee M-H, Barton J, Halas N, West J, Drezek R (2004) Nanoshell-enabled photonics-based imaging and therapy of cancer. Technol Cancer Res Treat 3(1):33–40
31. Westcott SL, Oldenburg SJ, Lee TR, Halas NJ (1998) Formation and adsorption of clusters of gold nanoparticles onto functionalized silica nanoparticle surfaces. Langmuir 14(19):5396–5401
32. Westcott SL, Oldenburg SJ, Lee TR, Halas NJ (1999) Construction of simple gold nanoparticle aggregates with controlled plasmon-plasmon interactions. Chem Phys Lett 300(5–6):651–655
33. Caruso F (2001) Nanoengineering of particle surfaces. Adv Mater 13(1):11–22
34. Shi W, Sahoo Y, Swihart MT, Prasad PN (2005) Gold nanoshells on polystyrene cores for control of surface plasmon resonance. Langmuir 21(4):1610–1617

35. Salgueiriño-Maceira V, Caruso F, Liz-Marzán LM (2003) Coated colloids with tailored optical properties. J Phys Chem B 107(40):10990–10994
36. Stöber W, Fink A, Bohn E (1968) Controlled growth of monodisperse silica spheres in the micron size range. J Colloid Interface Sci 26(1):62–69
37. Zhang J, Chen Z, Wang Z, Zhang W, Ming N (2003) Preparation of monodisperse polystyrene spheres in aqueous alcohol system. Mater Lett 57(28):4466–4470
38. Brinson BE, Lassiter JB, Levin CS, Bardhan R, Mirin N, Halas NJ (2008) Nanoshells made easy: improving Au layer growth on nanoparticle surfaces. Langmuir 24(24):14166–14171
39. Zhang J, Liu J, Wang S, Zhan P, Wang Z, Ming N (2004) Facile methods to coat polystyrene and silica colloids with metal. Adv Funct Mater 14(11):1089–1096
40. Lim YT, Park OO, Jung H-T (2003) Gold nanolayer-encapsulated silica particles synthesized by surface seeding and shell growing method: near infrared responsive materials. J Colloid Interface Sci 263(2):449–453
41. Peceros KE, Xu X, Bulcock SR, Cortie MB (2005) Dipole-dipole plasmon interactions in gold-on-polystyrene composites. J Phys Chem B 109(46):21516–21520
42. Zhang JH, Zhan P, Wang ZL, Zhang WY, Ming NB (2003) Preparation of monodisperse silica particles with controllable size and shape. J Mater Res 18(03):649–653
43. Yang W (2003) Improved recursive algorithm for light scattering by a multilayered sphere. Appl Opt 42(9):1710–1720
44. Mie G (1908) Beiträge zur optik trüber medien, speziell kolloidaler metallösungen. Ann Phys 330(3):377–445
45. Aden AL, Kerker M (1951) Scattering of electromagnetic waves from two concentric spheres. J Appl Phys 22(10):1242–1246
46. Wyatt PJ (1962) Scattering of electromagnetic plane waves from inhomogeneous spherically symmetric objects. Phys Rev 127(5):1837–1843
47. Wyatt PJ (1964) Scattering of electromagnetic plane waves from inhomogeneous spherically symmetric objects. Phys Rev 134(7AB):AB1–AB1
48. Bhandari R (1985) Scattering coefficients for a multilayered sphere: analytic expressions and algorithms. Appl Opt 24(13):1960–1967
49. Wait J (1963) Electromagnetic scattering from a radially inhomogeneous sphere. Appl Sci Res B 10(5):441–450
50. Wait JR (1955) Scattering of a plane wave from a circular dielectric cylinder at oblique incidence. Can J Phys 33(5):189–195
51. Kim CS, Yeh C (1991) Scattering of an obliquely incident wave by a multilayered elliptical lossy dielectric cylinder. Radio Sci 26(5):1165–1176
52. Asano S, Yamamoto G (1975) Light scattering by a spheroidal particle. Appl Opt 14(1):29–49
53. Neeves AE, Birnboim MH (1989) Composite structures for the enhancement of nonlinear-optical susceptibility. J Opt Soc Am B 6(4):787–796
54. Bohren CF, Huffman DR (1998) Absorption and scattering of light by small particles. Wiley-Interscience, New York
55. Abramowitz M (1965) Handbook of mathematical functions. Dover, New York
56. Arfken GB, Weber HJ, Harris F (2005) Mathematical methods for physicists, 6th edn. Academic, San Diego
57. Kai L, Massoli P (1994) Scattering of electromagnetic-plane waves by radially inhomogeneous spheres: a finely stratified sphere model. Appl Opt 33(3):501–511
58. Prodan E, Nordlander P (2003) Structural tunability of the plasmon resonances in metallic nanoshells. Nano Lett 3(4):543–547
59. Peña-Rodríguez O, Pal U (2011) Enhanced plasmonic behavior of bimetallic (Ag-Au) multilayered spheres. Nanoscale Res Lett 6(1):279
60. Peña-Rodríguez O, Pal U (2010) Geometrical tunability of linear optical response of silica-gold double concentric nanoshells. J Phys Chem C 114(10):4414–4417

61. Mukherjee S, Sobhani H, Lassiter JB, Bardhan R, Nordlander P, Halas NJ (2010) Fanoshells: nanoparticles with built-in Fano resonances. Nano Lett 10(7):2694–2701
62. Rohde CA, Hasegawa K, Deutsch M (2006) Coherent light scattering from semicontinuous silver nanoshells near the percolation threshold. Phys Rev Lett 96(4):045503
63. Preston TC, Signorell R (2009) Growth and optical properties of gold nanoshells prior to the formation of a continuous metallic layer. ACS Nano 3(11):3696–3706
64. Lin Q, Sun Z (2011) Optical extinction properties of aggregated ultrafine silver nanoparticles on silica nanospheres. J Phys Chem C 115(5):1474–1479
65. Yee K (1966) Numerical solution of initial boundary value problems involving maxwell's equations in isotropic media. IEEE Trans Antennas Propagation 14(3):302–307
66. Purcell EM, Pennypacker CR (1973) Scattering and absorption of light by nonspherical dielectric grains. Astrophys J 186:705–714
67. Draine BT (1988) The discrete-dipole approximation and its application to interstellar graphite grains. Astrophys J 333:848
68. Draine BT, Flatau PJ (1994) Discrete-dipole approximation for scattering calculations. J Opt Soc Am A 11(4):1491–1499
69. Halas N (2005) Playing with plasmons: tuning the optical resonant properties of metallic nanoshells. MRS Bull 30(05):362–367
70. Kelly KL, Coronado E, Zhao LL, Schatz GC (2003) The optical properties of metal nanoparticles: the influence of size, shape, and dielectric environment. J Phys Chem B 107(3):668–677
71. Hu M, Chen J, Li Z-Y, Au L, Hartland GV, Li X, Marquez M, Xia Y (2006) Gold nanostructures: engineering their plasmonic properties for biomedical applications. Chem Soc Rev 35(11):1084
72. Peña-Rodríguez O, Pal U (2011) Au@Ag core-shell nanoparticles: efficient all-plasmonic Fano-resonance generators. Nanoscale 3(9):3609–3612
73. Prodan E, Nordlander P, Halas NJ (2003) Electronic structure and optical properties of gold nanoshells. Nano Lett 3(10):1411–1415
74. Johnson PB, Christy RW (1972) Optical constants of the noble metals. Phys Rev B 6(12):4370–4379
75. Palik ED (1997) Handbook of optical constants of solids. Academic, New York
76. Hao F, Nordlander P (2007) Efficient dielectric function for FDTD simulation of the optical properties of silver and gold nanoparticles. Chem Phys Lett 446(1–3):115–118
77. Vial A, Grimault A-S, Macías D, Barchiesi D, de la Chapelle ML (2005) Improved analytical fit of gold dispersion: application to the modeling of extinction spectra with a finite-difference time-domain method. Phys Rev B 71(8):085416
78. See KC, Spicer JB, Brupbacher J, Zhang D, Vargo TG (2005) Modeling interband transitions in silver nanoparticle-fluoropolymer composites. J Phys Chem B 109(7):2693–2698
79. Lee T-W, Gray S (2005) Subwavelength light bending by metal slit structures. Opt Express 13(24):9652–9659
80. Moskovits M, Srnová-Sloufova I, Vlckova B (2002) Bimetallic Ag-Au nanoparticles: extracting meaningful optical constants from the surface-plasmon extinction spectrum. J Chem Phys 116(23):10435–10446
81. Rakic AD, Djurisic AB, Elazar JM, Majewski ML (1998) Optical properties of metallic films for vertical-cavity optoelectronic devices. Appl Opt 37(22):5271–5283
82. Etchegoin PG, Le Ru EC, Meyer M (2006) An analytic model for the optical properties of gold. J Chem Phys 125(16):164705
83. Etchegoin P, Kircher J, Cardona M (1993) Elasto-optical constants of Si. Phys Rev B 47(16):10292–10303
84. Campoy-Quiles M, Heliotis G, Xia R, Ariu M, Pintani M, Etchegoin P, Bradley DDC (2005) Ellipsometric characterization of the optical constants of polyfluorene gain media. Adv Funct Mater 15(6):925–933

85. Leng J, Opsal J, Chu H, Senko M, Aspnes DE (1998) Analytic representations of the dielectric functions of materials for device and structural modeling. Thin Solid Films 313–314:132–136
86. Noguez C (2005) Optical properties of isolated and supported metal nanoparticles. Opt Mater 27(7):1204–1211
87. Ashcroft NW, Mermin ND (1976) Solid state physics, 1st edn. Brooks Cole, Philadelphia
88. Hamblin MR (2006) Mechanisms of low level light therapy. Proc SPIE 6140:614001
89. Stolik S, Delgado JA, Pérez A, Anasagasti L (2000) Measurement of the penetration depths of red and near infrared light in human "ex vivo" tissues. J Photochem Photobiol B Biol 57(2–3):90–93
90. Ntziachristos V, Ripoll J, Wang LV, Weissleder R (2005) Looking and listening to light: the evolution of whole-body photonic imaging. Nat Biotechnol 23(3):313–320
91. Hirsch LR, Stafford RJ, Bankson JA, Sershen SR, Rivera B, Price RE, Hazle JD, Halas NJ, West JL (2003) Nanoshell-mediated near-infrared thermal therapy of tumors under magnetic resonance guidance. Proc Natl Acad Sci USA 100(23):13549–13554
92. Hasegawa K, Rohde C, Deutsch M (2006) Enhanced surface-plasmon resonance absorption in metal-dielectric-metal layered microspheres. Opt Lett 31(8):1136–1138
93. Oldenburg SJ, Hale GD, Jackson JB, Halas NJ (1999) Light scattering from dipole and quadrupole nanoshell antennas. Appl Phys Lett 75(8):1063
94. Wang H, Fu K, Drezek RA, Halas NJ (2006) Light scattering from spherical plasmonic nanoantennas: effects of nanoscale roughness. Appl Phys B Lasers Optics 84(1):191–195
95. Chien W-Y, Szkopek T (2008) Multiple-multipole simulation of optical nearfields in discrete metal nanosphere assemblies. Opt Express 16(3):1820–1835
96. Jackson JB, Westcott SL, Hirsch LR, West JL, Halas NJ (2003) Controlling the surface enhanced Raman effect via the nanoshell geometry. Appl Phys Lett 82(2):257
97. Peña Rodríguez O, Pal U (2011) Enhanced plasmonic behavior of incomplete nanoshells: effect of local field irregularities on the far-field optical response. J Phys Chem C. 115 (45):22271–22275
98. Oldenburg SJ, Westcott SL, Averitt RD, Halas NJ (1999) Surface enhanced Raman scattering in the near infrared using metal nanoshell substrates. J Chem Phys 111(10):4729
99. Lu L, Zhang H, Sun G, Xi S, Wang H, Li X, Wang X, Zhao B (2003) Aggregation-based fabrication and assembly of roughened composite metallic nanoshells: application in surface-enhanced raman scattering. Langmuir 19(22):9490–9493
100. Jackson JB, Halas NJ (2004) Surface-enhanced Raman scattering on tunable plasmonic nanoparticle substrates. Proc Natl Acad Sci USA 101(52):17930–17935
101. Goude ZE, Leung PT (2007) Surface enhanced Raman scattering from metallic nanoshells with nonlocal dielectric response. Solid State Commun 143(8–9):416–420
102. Heck KN, Janesko BG, Scuseria GE, Halas NJ, Wong MS (2008) Observing metal-catalyzed chemical reactions in situ using surface-enhanced Raman spectroscopy on Pd-Au nanoshells. J Am Chem Soc 130(49):16592–16600
103. Yang S, Cai W, Kong L, Lei Y (2010) Surface nanometer-scale patterning in realizing large-scale ordered arrays of metallic nanoshells with well-defined structures and controllable properties. Adv Funct Mater 20(15):2527–2533
104. Küstner B, Gellner M, Schütz M, Schöppler F, Marx A, Ströbel P, Adam P, Schmuck C, Schlücker S (2009) SERS labels for red laser excitation: silica-encapsulated SAMS on tunable gold/silver nanoshells. Angew Chem Int Ed 48(11):1950–1953
105. Zhang P, Guo Y (2009) Surface-enhanced Raman scattering inside metal nanoshells. J Am Chem Soc 131(11):3808–3809
106. Gellner M, Küstner B, Schlücker S (2009) Optical properties and SERS efficiency of tunable gold/silver nanoshells. Vibrat Spectros 50(1):43–47
107. Ochsenkuhn MA, Jess PRT, Stoquert H, Dholakia K, Campbell CJ (2009) Nanoshells for surface-enhanced Raman spectroscopy in Eukaryotic cells: cellular response and sensor development. ACS Nano 3(11):3613–3621

108. Barron LD, Buckingham AD (1971) Rayleigh and Raman scattering from optically active molecules. Mol Phys 20(6):1111–1119
109. Barron LD, Zhu F, Hecht L, Tranter GE, Isaacs NW (2007) Raman optical activity: an incisive probe of molecular chirality and biomolecular structure. J Mol Struct 834–836:7–16
110. Acevedo R, Lombardini R, Halas NJ, Johnson BR (2009) Plasmonic enhancement of Raman optical activity in molecules near metal nanoshells. J Phys Chem A 113(47):13173–13183
111. Lombardini R, Acevedo R, Halas NJ, Johnson BR (2010) Plasmonic enhancement of Raman optical activity in molecules near metal nanoshells: theoretical comparison of circular polarization methods. J Phys Chem C 114(16):7390–7400
112. West JL, Halas NJ (2003) Engineered nanomaterials for biophotonics applications: improving sensing, imaging, and therapeutics. Annu Rev Biomed Eng 5(1):285–292
113. Gu FX, Karnik R, Wang AZ, Alexis F, Levy-Nissenbaum E, Hong S, Langer RS, Farokhzad OC (2007) Targeted nanoparticles for cancer therapy. Nano Today 2(3):14–21
114. Gobin AM, O'Neal DP, Watkins DM, Halas NJ, Drezek RA, West JL (2005) Near infrared laser-tissue welding using nanoshells as an exogenous absorber. Lasers Surg Med 37(2):123–129
115. Jain PK, Lee KS, El-Sayed IH, El-Sayed MA (2006) Calculated absorption and scattering properties of gold nanoparticles of different size, shape, and composition: applications in biological imaging and biomedicine. J Phys Chem B 110(14):7238–7248
116. Sun Y, Xia Y (2002) Increased sensitivity of surface plasmon resonance of gold nanoshells compared to that of gold solid colloids in response to environmental changes. Anal Chem 74(20):5297–5305
117. Sershen SR, Westcott SL, Halas NJ, West JL (2000) Temperature-sensitive polymer-nanoshell composites for photothermally modulated drug delivery. J Biomed Mater Res 51(3):293–298
118. Fiedler VU, Schwarzmaier H, Eickmeyer F, Müller FP, Schoepp C, Verreet PR (2001) Laser-induced interstitial thermotherapy of liver metastases in an interventional 0.5 Tesla MRI system: technique and first clinical experiences. J Magn Reson Imaging 13(5):729–737
119. Vogel A, Venugopalan V (2003) Mechanisms of pulsed laser ablation of biological tissues. Chem Rev 103(2):577–644
120. Melancon MP, Lu W, Yang Z, Zhang R, Cheng Z, Elliot AM, Stafford J, Olson T, Zhang JZ, Li C (2008) In vitro and in vivo targeting of hollow gold nanoshells directed at epidermal growth factor receptor for photothermal ablation therapy. Mol Cancer Ther 7(6):1730–1739
121. Hirsch LR, Stafford RJ, Bankson JA, Sershen SR, Price RE, Hazle JD, Halas NJ, West JL (2002) Targeted photothermal tumor therapy using metal nanoshells. In: Proceedings of the 24th annual conference and the annual fall meeting of the biomedical engineering society EMBS/BMES conference, vol 1, Houston, TX, USA, pp 530–531
122. Stern JM, Stanfield J, Kabbani W, Hsieh J-T, Cadeddu JA (2008) Selective prostate cancer thermal ablation with laser activated gold nanoshells. J Urol 179(2):748–753
123. O'Neal DP, Hirsch LR, Halas NJ, Payne JD, West JL (2004) Photo-thermal tumor ablation in mice using near infrared-absorbing nanoparticles. Cancer Lett 209(2):171–176
124. Shetty A, Elliott AM, Schwartz JA, Wang J, Esparza-Coss E, Klumpp S, Taylor B, Hazle JD, Stafford RJ (2008) Use of gold nanoshells to mediate heating induced perfusion changes in prostate tumors. Proc of SPIE 6842:68420S
125. Diagaradjane P, Shetty A, Wang JC, Elliott AM, Schwartz J, Shentu S, Park HC, Deorukhkar A, Stafford RJ, Cho SH, Tunnell JW, Hazle JD, Krishnan S (2008) Modulation of in vivo tumor radiation response via gold nanoshell-mediated vascular-focused hyperthermia: characterizing an integrated antihypoxic and localized vascular disrupting targeting strategy. Nano Lett 8(5):1492–1500
126. Diagaradjane P, Shetty A, Wang J, Schwartz J, Park HC, Deorukhkar A, Stafford J, Cho S, Hazle J, Tunnell J, Krishnan S (2008) Modulation of in vivo tumor radiation response via vascular-focused hyperthermia-characterizing gold nanoshells as integrated anti-hypoxic and localized vascular disrupting agents. Int J Radiat Oncol Biol Phys 72(1 (Suppl 1)):S64

127. Atkinson RL, Zhang M, Diagaradjane P, Peddibhotla S, Contreras A, Hilsenbeck SG, Woodward WA, Krishnan S, Chang JC, Rosen JM (2010) Thermal enhancement with optically activated gold nanoshells sensitizes breast cancer stem cells to radiation therapy. Sci Trans Med 2(55):55ra79
128. Xie H, Diagaradjane P, Deorukhkar AA, Goins B, Bao A, Phillips WT, Wang Z, Schwartz J, Krishnan S (2011) Integrin $\alpha_v\beta_3$-targeted gold nanoshells augment tumor vasculature-specific imaging and therapy. Int J Nanomedicine 6(1):259–269
129. van Vlerken LE, Amiji MM (2006) Multi-functional polymeric nanoparticles for tumour-targeted drug delivery. Expert Opin Drug Deliv 3(2):205–216
130. Emerich DF, Thanos CG (2006) The pinpoint promise of nanoparticle-based drug delivery and molecular diagnosis. Biomol Eng 23(4):171–184
131. Sershen SR, Westcott SL, West JL, Halas NJ (2001) An opto-mechanical nanoshell-polymer composite. Appl Phys B Lasers Opt 73(4):379–381
132. Sershen SR, Halas NJ, West JL (2002) Pulsatile release of insulin via photothermally modulated drug delivery. In: Proceedings of the 24th annual conference and the annual fall meeting of the biomedical engineering society EMBS/BMES conference, vol 1, Houston, TX, USA, pp 490–491
133. Wu G, Mikhailovsky A, Khant HA, Fu C, Chiu W, Zasadzinski JA (2008) Remotely triggered liposome release by near-infrared light absorption via hollow gold nanoshells. J Am Chem Soc 130(26):8175–8177
134. Bikram M, Gobin AM, Whitmire RE, West JL (2007) Temperature-sensitive hydrogels with SiO_2-Au nanoshells for controlled drug delivery. J Control Release 123(3):219–227
135. Liu H, Chen D, Li L, Liu T, Tan L, Wu X, Tang F (2011) Multifunctional gold nanoshells on silica nanorattles: a platform for the combination of photothermal therapy and chemotherapy with low systemic toxicity. Angew Chem Int Ed 50(4):891–895
136. Alivisatos P (2004) The use of nanocrystals in biological detection. Nat Biotechnol 22(1):47–52
137. Sun Y, Xia Y (2003) Synthesis of gold nanoshells and their use in sensing applications. In: Unconventional approaches to nanostructures with applications in electronics, photonics, information storage and sensing symposium, vol 776, pp 31–36
138. Tam F, Moran C, Halas N (2004) Geometrical parameters controlling sensitivity of nanoshell plasmon resonances to changes in dielectric environment. J Phys Chem B 108(45):17290–17294
139. Wang Y, Qian W, Tan Y, Ding S (2008) A label-free biosensor based on gold nanoshell monolayers for monitoring biomolecular interactions in diluted whole blood. Biosens Bioelectron 23(7):1166–1170
140. Hirsch LR, Halas NJ, West JL (2002) A rapid, near infrared, whole blood immunoassay using metal nanoshells. In: Proceedings of the 24th annual conference and the annual fall meeting of the biomedical engineering society EMBS/BMES Conference, vol 2, Houston, TX, USA, pp 1646–1647
141. Hirsch LR, West JL, Jackson JB, Lee A, Halas NJ (2003) A rapid, whole blood immunoassay using metal nanoshells. Proceedings of the 25th annual international conference of the IEEE, vol 4, Cancun, Mexico, pp 3442–3443
142. Khlebtsov B, Dykman L, Bogatyrev V, Zharov V, Khlebtsov N (2006) A solid-phase dot assay using silica/gold nanoshells. Nanoscale Res Lett 2(1):6–11
143. Khlebtsov BN, Dykman LA, Bogatyrev VA, Khlebtsov NG (2007) Gold nanoshells as solid-phase dot assay labels. Proc SPIE 6534:65343L
144. Khlebtsov B, Khlebtsov N (2008) Enhanced solid-phase immunoassay using gold nanoshells: effect of nanoparticle optical properties. Nanotechnology 19(43):435703
145. Ma X, Qian W (2010) Phenolic acid induced growth of gold nanoshells precursor composites and their application in antioxidant capacity assay. Biosens Bioelectron 26(3):1049–1055
146. Ma X, Li H, Dong J, Qian W (2011) Determination of hydrogen peroxide scavenging activity of phenolic acids by employing gold nanoshells precursor composites as nanoprobes. Food Chem 126(2):698–704

147. Sokolov K, Follen M, Aaron J, Pavlova I, Malpica A, Lotan R, Richards-Kortum R (2003) Real-time vital optical imaging of precancer using anti-epidermal growth factor receptor antibodies conjugated to gold nanoparticles. Cancer Res 63(9):1999–2004
148. Zaman RT, Diagaradjane P, Wang JC, Schwartz J, Rajaram N, Gill-Sharp KL, Cho SH, Rylander HG, Payne JD, Krishnan S, Tunnell JW (2007) In vivo detection of gold nanoshells in tumors using diffuse optical spectroscopy. IEEE J Select Topics Quantum Electron 13(6):1715–1720
149. Zaman RT, Diagaradjane P, Wang JC, Schwartz J, Rajaram N, Gill-Sharp KL, Cho SH, Rylander HG III, Payne JD, Krishnan S, Tunnell JW (2008) Erratum to In vivo detection of gold nanoshells in tumors using diffuse optical spectroscopy. IEEE J Select Topics Quantum Electron 14(1):251–251
150. Kah JCY, Chow TH, Ng BK, Razul SG, Olivo M, Sheppard CJR (2009) Concentration dependence of gold nanoshells on the enhancement of optical coherence tomography images: a quantitative study. Appl Opt 48(10):D96–D108
151. Kah JCY, Olivo M, Chow TH, Song KS, Koh KZY, Mhaisalkar S, Sheppard CJR (2009) Control of optical contrast using gold nanoshells for optical coherence tomography imaging of mouse xenograft tumor model in vivo. J Biomed Opt 14(5):054015
152. Park J, Estrada A, Sharp K, Sang K, Schwartz JA, Smith DK, Coleman C, Payne JD, Korgel BA, Dunn AK, Tunnell JW (2008) Two-photon-induced photoluminescence imaging of tumors using near-infrared excited gold nanoshells. Opt Express 16(3):1590–1599
153. Park J, Estrada A, Schwartz JA, Payne JD, Dunn AK, Tunnell JW (2008) 3D microscopy of gold nanoshells in tumors using two-photon-induced photoluminescence. Proc SPIE 6869:68690L
154. Park J, Estrada A, Sharp K, Sang K, Schwartz JA, Smith DK, Coleman C, Donald PJ, Korgel BA, Dunn AK, Tunnell JW (2008) Two-photon-induced photoluminescence imaging of tumors using near-infrared excited gold nanoshells. In: Conference on lasers and electro-optics and conference on quantum electronics and laser science, vol 1, pp 1–2
155. Park J, Estrada AP, Diagaradjane K, Sharp K, Sang J, Schwartz A, Coleman C, Payne JD, Dunn AK, Krishnan S, Tunnell JW (2008) Microscopy of gold nanoshells in tumors using two-photon induced photoluminescence, Digest of the IEEE/LEOS Summer Topical Meetings, 1:71–72
156. Puvanakrishnan P, Park J, Diagaradjane P, Schwartz JA, Coleman CL, Gill-Sharp KL, Sang KL, Payne JD, Krishnan S, Tunnell JW (2009) Narrow band imaging of tumors using gold nanoshells. Proceedings of SPIE 7169:716912
157. Puvanakrishnan P, Park J, Diagaradjane P, Schwartz JA, Coleman CL, Gill-Sharp KL, Sang KL, Payne JD, Krishnan S, Tunnell JW (2009) Near-infrared narrow-band imaging of gold/silica nanoshells in tumors. J Biomed Opt 14(2):024044
158. Xie H, Wang ZJ, Bao A, Goins B, Phillips WT (2010) In vivo PET imaging and biodistribution of radiolabeled gold nanoshells in rats with tumor xenografts. Int J Pharm 395(1–2):324–330
159. Garrett N, Whiteman M, Moger J (2011) Imaging the uptake of gold nanoshells in live cells using plasmon resonance enhanced four wave mixing microscopy. Opt Express 19(18):17563–17574
160. Zhan P, Liu JB, Dong W, Dong H, Chen Z, Wang ZL, Zhang Y, Zhu SN, Ming NB (2005) Reflectivity behavior of two-dimensional ordered array of metallodielectric composite particles at large incidence angles. Appl Phys Lett 86(5):051108
161. Graf C, van Blaaderen A (2002) Metallodielectric colloidal core-shell particles for photonic applications. Langmuir 18(2):524–534
162. Tserkezis C, Gantzounis G, Stefanou N (2008) Collective plasmonic modes in ordered assemblies of metallic nanoshells. J Phys Condens Matter 20(7):075232
163. Stefanou N, Tserkezis C, Gantzounis G (2008) Plasmonic excitations in ordered assemblies of metallic nanoshells. Proceedings of SPIE 6989:698910

164. Fano U (1961) Effects of configuration interaction on intensities and phase shifts. Phys Rev 124(6):1866–1878
165. Bachelier G, Russier-Antoine I, Benichou E, Jonin C, Del Fatti N, Vallée F, Brevet P-F (2008) Fano profiles induced by near-field coupling in heterogeneous dimers of Gold and Silver nanoparticles. Phys Rev Lett 101(19):197401
166. Boller K-J, Imamolu A, Harris SE (1991) Observation of electromagnetically induced transparency. Phys Rev Lett 66(20):2593
167. Fleischhauer M, Imamoglu A, Marangos JP (2005) Electromagnetically induced transparency: optics in coherent media. Rev Mod Phys 77(2):633
168. Mirin NA, Bao K, Nordlander P (2009) Fano resonances in plasmonic nanoparticle aggregates. J Phys Chem A 113(16):4028–4034
169. Lassiter JB, Sobhani H, Fan JA, Kundu J, Capasso F, Nordlander P, Halas NJ (2010) Fano resonances in plasmonic nanoclusters: geometrical and chemical tunability. Nano Lett 10(8):3184–3189
170. Fan JA, Wu C, Bao K, Bao J, Bardhan R, Halas NJ, Manoharan VN, Nordlander P, Shvets G, Capasso F (2010) Self-assembled plasmonic nanoparticle clusters. Science 328(5982):1135–1138
171. Liu N, Weiss T, Mesch M, Langguth L, Eigenthaler U, Hirscher M, Sönnichsen C, Giessen H (2010) Planar metamaterial analogue of electromagnetically induced transparency for plasmonic sensing. Nano Lett 10(4):1103–1107
172. Verellen N, Sonnefraud Y, Sobhani H, Hao F, Moshchalkov VV, Dorpe PV, Nordlander P, Maier SA (2009) Fano resonances in individual coherent plasmonic nanocavities. Nano Lett 9(4):1663–1667
173. Peña-Rodríguez O, Pal U, Campoy-Quiles M, Rodríguez-Fernández L, Garriga M, Alonso MI (2011) Enhanced Fano resonance in asymmetrical Au:Ag heterodimers. J Phys Chem C 115(14):6410–6414
174. Halas NJ, Lal S, Chang W-S, Link S, Nordlander P (2011) Plasmons in strongly coupled metallic nanostructures. Chem Rev 111(6):3913–3961

UV-Vis Spectroscopy for Characterization of Metal Nanoparticles Formed from Reduction of Metal Ions During Ultrasonic Irradiation

4

Kenji Okitsu

Contents

1 Overview

The reduction processes of metal ions can be used to prepare metal nanoparticles in an aqueous solution, in which UV-Vis spectroscopy can be used as an excellent tool to characterize the properties of metal nanoparticles, in particular the size and shape of the metal nanoparticles and their surface property in the state of the colloidal dispersion system. In addition, UV-Vis spectroscopy enables the amount of precursor metal ions used during the formation of metal nanoparticles to be measured. In this chapter, the sonochemical reduction processes for Pd(II), Au(III), Pt(II), Pt(IV), Ag(I), and MnO_4^- are described on the basis of changes in the absorption

K. Okitsu
Graduate School of Engineering, Osaka Prefecture University, Naka-ku, Sakai, Osaka, Japan

Challa S.S.R. Kumar (ed.), *UV-VIS and Photoluminescence Spectroscopy for Nanomaterials Characterization*, DOI 10.1007/978-3-642-27594-4_4,

spectrum during ultrasonic irradiation to understand the sonochemical reduction mechanism of metal ions. In addition, the optical properties of the sonochemically formed metal nanoparticles such as the spherical nanoparticles of Pd, Au, Pt, Ag, MnO_2, and Au/Pd and the shape-controlled nanoparticles are reviewed to understand the formation processes during ultrasonic irradiation.

2 Introduction

Metal nanoparticles have attracted considerable attention in various fields of technology because of their useful physicochemical properties arising from the effects of the size of nanoparticles. The structure and shape of the nanoparticles are also important factors to control their properties. Therefore, various types of preparation methods such as controlled chemical methods with an appropriate reductant [1–4] as well as photochemical and radiation chemical methods [5, 6] have been actively developed. Although there are a number of methods available to prepare metal nanoparticles, a sonochemical method offers unique synthetic processes: the sonochemical method involves radical reactions and/or thermal reactions, which originate from extremely high temperatures and pressures generated in cavitation bubbles. In addition, strong shock waves and micro-jet flows are also induced by ultrasonic irradiation of a liquid as a consequence of a cavitation phenomenon.

The reduction processes can be conveniently used to prepare metal nanoparticles in an aqueous solution. As representative reactions, the following reactions proceed under ultrasonic irradiation in an aqueous solution containing an organic additive (RH) under a rare gas atmosphere [7]:

$$H_2O \rightarrow \bullet OH + \bullet H \tag{4.1}$$

$$RH + \bullet OH(\bullet H) \rightarrow \bullet R + H_2O(H_2) \tag{4.2}$$

$$RH \rightarrow \text{pyrolysis radicals and unstable products} \tag{4.3}$$

$$M^{n+} + \text{reductants} \rightarrow M^0 \tag{4.4}$$

$$nM^0 \rightarrow \left(M^0\right)_n \tag{4.5}$$

$$M^0 + \left(M^0\right)_n \rightarrow \left(M^0\right)_{n+1} \tag{4.6}$$

where M^{n+} and M^0 correspond to a metal ion and metal atom, respectively. Reactions (4.1)–(4.3) indicate the sonochemical formation of reductants: (4.1) •H is formed from the pyrolysis of water, (4.2) •R and H_2 are formed from the abstraction reaction of RH with •OH or •H, and (4.3) pyrolysis radicals and unstable products are formed via the pyrolysis of RH. Some of the pyrolysis radicals and unstable products act as reductants. In this mechanism, most of the organic

additives used, including general organic stabilizers such as surfactants or water-soluble polymers, correspond to RH. After the formation of M^0, some of the M^0 aggregate to form small particles, $(M^0)_n$, as Eqs. 4.4 and 4.5. In addition to such aggregation, the formed M^0 can be adsorbed on $(M^0)_n$ to give $(M^0)_{n+1}$, as Eq. 4.6. The general mechanisms for the formation of metal nanoparticles are studied elsewhere [1–4].

Sonochemical reduction processes can be used as eco-friendly techniques for the synthesis of nanoparticles, because these experiments can be conducted in a solution at around room temperature and the amounts of used reagents and/or reaction times can be reduced [7–10]. Since the sonochemical processes offer unique synthetic routes, they are expected to be promising ones to synthesize various types of novel functional nanoparticles.

Although there are some reviews about the sonochemical synthesis of metal nanoparticles, the UV-Vis spectrum analyses for the formation of the metal nanoparticles as well as the reduction of metal ions are not described comprehensively. Therefore, in this chapter, the comprehensive data for changes in the absorption spectrum of the sample solution during ultrasonic irradiation are shown and analyzed to understand the mechanism for the formation of metal nanoparticles and reduction of metal ions, where the synthesis of spherical metal nanoparticles of Pd, Au, Pt, Ag, MnO_2, and Au/Pd and the synthesis of shape-controlled nanoparticles of Au nanorods are described.

3 Experimental and Instrumental Methodology

Various types of sonicators and irradiation systems have been used for sonochemical reactions. An ultrasonic cleaning bath can be used conveniently; however, when the intensity of ultrasound is not high enough, the sonochemical reactions with OH or H radicals do not occur sufficiently. This is because hot cavitation bubbles do not generate sufficiently and thus the amounts of OH or H radicals formed are very small. On the other hand, a horn-type sonicator can be used as a high-intensity sonicator, which is often used as a strong homogenizer. Although a horn-type sonicator can produce hot cavitation bubbles, the frequency of ultrasound is generally limited to as low as 20–50 kHz. Stronger physical effects such as shock waves and micro-jet flows are also induced by the irradiation with a lower frequency sonicator. This is because changes in the size of the cavitation bubbles during ultrasonic irradiation are larger at the lower frequency.

In this chapter, a standing-wave-type irradiation system is mainly used for the sonochemical reduction of metal ions and formation of metal nanoparticles. The representative irradiation setup and the characteristics of the reaction vessel are shown in Fig. 4.1 [11]. In this system, standing waves are formed by overlapping the irradiated ultrasound with the ultrasound reflected at the top interface of the sample solution. The glass vessel is cylindrical and it has a Teflon valve and a port covered by a silicon septum for gas bubbling. The bottom of the vessel is planar, 1 mm thick and 55 mm in diameter. The vessel is mounted at a fixed position. Since

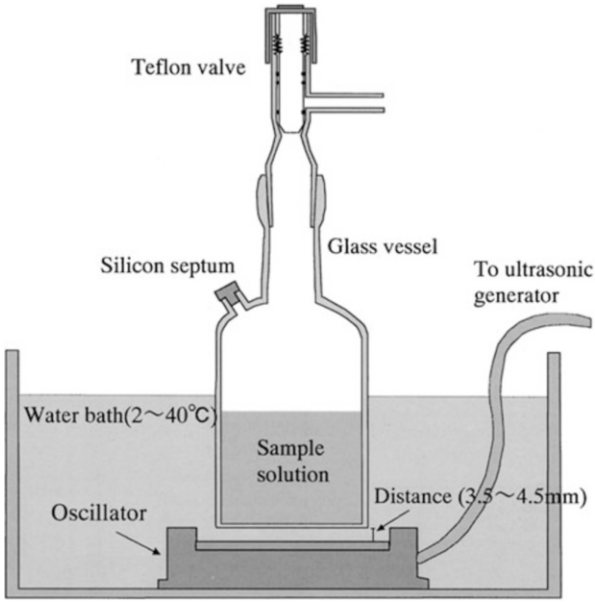

Fig. 4.1 One example of the irradiation setup and the characteristic of the reaction vessel in a standing-wave-type irradiation system (Reprinted with permission from Ref [11]. Copyright 2002 The Chemical Society of Japan)

the distance from the oscillator to the vessel bottom affects sonochemical efficiency [11], the distance from the oscillator must be controlled carefully. In general, the vessel bottom is fixed at the λ/2 distance from the oscillator to get high sonochemical efficiency, where λ is the wavelength of ultrasound in the sample solution.

As a sample solution, an aqueous solution of metal ions (e.g., 0.1–1.0 mM, 60 or 65 mL) is added to the vessel. Since a dissolved gas in the sample solution strongly affects sonochemical efficiency [11, 12], the solution should be purged with an appropriate gas. After purging, ultrasonic irradiation is carried out using an ultrasonic generator (4,021type; frequency, 200 kHz; Kaijo Co.) and a 65 mmϕ oscillator (Kaijo Co.), which is operated at ca. 20–200 W in a water bath maintained at a constant temperature. In this chapter, figures other than Fig. 4.11 are based on the results obtained by this irradiation system. After irradiation, small amounts of the sample solutions are drawn from the silicon septum by a syringe with a stainless-steel needle and then the sample solutions are analyzed by UV-Vis spectroscopy and/or various analytical methods.

As described in the reduction mechanism, organic compounds, which act as a precursor for the formation of reductants during ultrasonic irradiation, are added before or after gas purging. When a high-volatile organic compound is added to the sample solution, its vaporization property should be considered: the addition of a high-volatile compound should be performed after gas purging to avoid the decrease in the concentration by its vaporization.

As a matter of course, the physicochemical properties of the cavitation bubbles affect the reduction processes of the metal ions as well as various chemical reactions. Since the bubble temperature is one of the most important factors to

control the chemical effects of cavitation, it is important to understand the bubble temperature of the used irradiation system. To estimate the bubble temperature, analyses of sonoluminescence (light emission from a cavitation bubble) and reaction kinetics can be used. Here, we briefly present the analysis of reaction kinetics. Based on the literature [12–15], the bubble temperature can be estimated from the sonolysis of a *tert*-butyl alcohol (*t*-BuOH) aqueous solution in the presence of an appropriate rare gas. During the sonolysis of this solution, CH_3 radicals are formed by the pyrolysis of *t*-BuOH, which then react to form C_2H_2, C_2H_4, and C_2H_6. Since the product ratio $(C_2H_2 + C_2H_4)/C_2H_6$ is dependent on the temperature, the bubble temperature can be estimated by analyzing the yield of these products: the product ratio is equal to the ratio k_2/k_1, where k_1 (rate constant for $2CH_3 \rightarrow C_2H_6$) is $2.4 \times 10^{14}\ T^{-0.4}\ dm^3\ mol^{-1}\ s^{-1}$ and k_2 (rate constant for $2CH_3 \rightarrow C_2H_4 + H_2$) is $1.0 \times 10^{16}\ \exp(-134\ kJ/RT)\ dm^3\ mol^{-1}\ s^{-1}$. C_2H_2 is formed via the thermal reaction of C_2H_4.

Figure 4.2 shows the estimated bubble temperature as a function of the thermal conductivity of each rare gas [12]. It can be seen that the bubble temperature is about 3,900 K and is almost the same among all of the rare gases. In the analysis of sonoluminescence induced by using a horn-type 20-kHz sonicator, the bubble temperatures decrease with increasing thermal conductivity of the dissolved gases, where it is considered that the greater the conductivity of the gas, the more heat is dissipated to the surroundings, resulting in the decrease in the bubble temperature. Until now, the bubble temperatures estimated from analyses of the sonoluminescence, reaction kinetics, and a computer simulation are generally in the range between 3,900 and 30,000 K [12–21].

In addition to the measurement of the bubble temperature, chemical efficiency is often measured. The yield of H_2O_2 formed in the sonolysis of pure water can be regarded as the chemical efficiency [11, 22], because the yield of H_2O_2 can be connected to that of the OH primary radicals formed in the sonolysis of water.

$$2 \bullet OH \rightarrow H_2O_2 \tag{4.7}$$

Koda et al. [22] investigated the effect of frequency on the sonochemical efficiency in the frequency range of 19.5–1.2 MHz, where the yields of H_2O_2 were measured by KI oxidation and the Fricke reaction (Fe(II) oxidation) with a UV-Vis spectrophotometer. They showed that the highest chemical efficiency existed in the range of 96–500 kHz. In addition, the liquid height of the sample solution also affects the sonochemical efficiency [23]. Therefore, to get high chemical efficiency, the frequency and liquid height should be optimized as well as the configuration of the irradiation system.

As a reference, we introduce several examples for the effects of frequency on the chemical reactions. From the viewpoint of environmental remediation, the degradation of 1,4-dioxane and CCl_4 has been investigated. In the case of 1,4-dioxane, the rate of degradation was the highest at 358 kHz in the frequency range of 205–1,071 kHz [24]. In the case of CCl_4, the rate of degradation was the highest at around 500–618 kHz in the frequency range of 20–1,078 kHz [25]. On the other

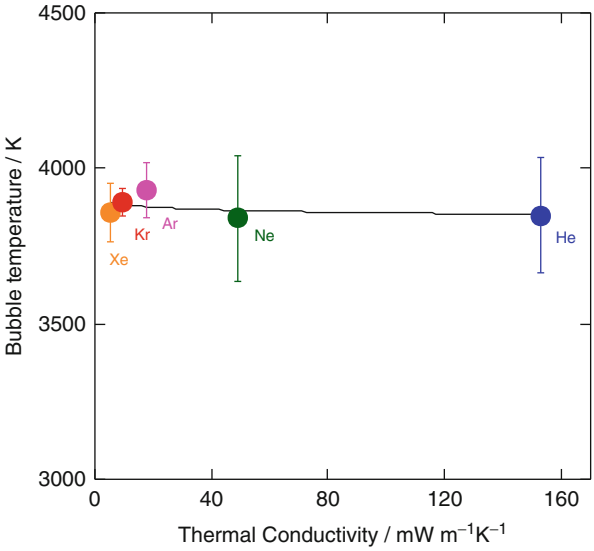

Fig. 4.2 Cavitation bubble temperature estimated in the presence of different rare gases from the analysis of reaction kinetics. Ultrasound (200 kHz) is irradiated to a *t*-BuOH aqueous solution at 20 °C (Reprinted with permission from Ref. [12]. Copyright 2006 American Chemical Society)

hand, from the viewpoint of the reduction of metal ions to form metal nanoparticles, the effect of frequency on the rate of reduction has been investigated. For example, the rate of Au^{3+} reduction in the presence of 1-propanol decreased with increasing frequency (213 kHz > 358 kHz > 647 kHz > 1062 kHz), and the rate was the lowest when a horn-type sonicator of frequency 20 kHz was used [26]. Here, UV-Vis spectroscopy acts as a strong tool for the measurement of the concentration of Au^{3+} in an aqueous solution during ultrasonic irradiation.

In the following section, the formation of metal nanoparticles is described in connection with the reduction behavior of metal ions based on the analysis of changes in the UV-Vis spectra during ultrasonic irradiation.

4 Key Research Findings

4.1 Pd Nanoparticles

Pd nanoparticles can be widely applied to catalysts for cross-coupling reactions, hydrogenations and oxidations [27–29]. As described in the Introduction section, various preparation methods have been studied to prepare Pd nanoparticles. The size and shape of the nanoparticles are important factors to control their catalytic properties, because the surface structure and electronic state change depending on the size and shape of the nanoparticles. For example, the amount ratio of Pd atoms on the facets, edges, and corners of the nanoparticles changes when the size and shape of the nanoparticles change, resulting in the different catalytic activity for the structure sensitive reactions. By using a sonochemical reduction method, we can prepare size-controlled Pd nanoparticles [30]. We can see the characteristics of

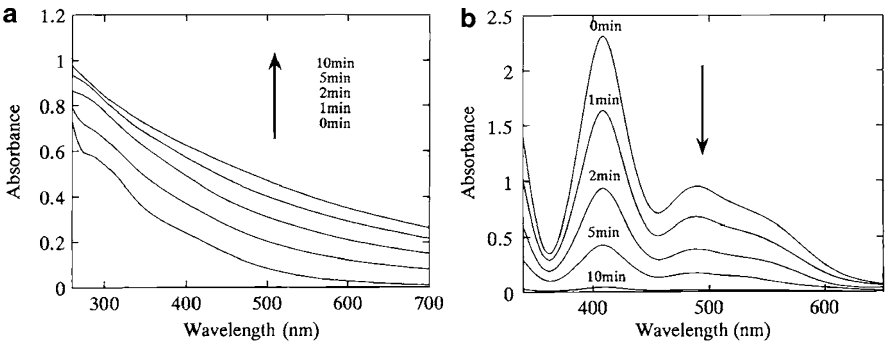

Fig. 4.3 (**a**) Changes in absorption spectra during ultrasonic irradiation of a Pd(II)-SDS aqueous solution under an argon atmosphere and (**b**) absorption spectra after addition of NaI to each sample solution of (**a**). Conditions: $PdCl_2 \cdot 2NaCl$ 0.5 mM, SDS 8 mM, cell length 0.5 cm (Reprinted with permission from Ref. [30]. Copyright 1996 American Chemical Society)

changes in the UV-Vis absorption spectra of a sample solution during ultrasonic irradiation.

Figure 4.3a shows changes in the absorption spectra during ultrasonic irradiation of an aqueous solution containing $PdCl_2 \cdot 2NaCl$ (hereafter, abbreviated to Pd(II)) and sodium dodecyl sulfate (SDS) under an argon atmosphere. Small absorption peaks at around 300 and 400 nm, characteristic of Pd(II), are observed before ultrasonic irradiation (corresponding to 0 min in Fig. 4.3a).

These peaks gradually disappear with irradiation and a broad absorption band between the UV and visible region appears. Based on the Mie theory [31], this broad band can be attributed to the spectrum of the solution containing colloidal Pd nanoparticles. The color of the solution changes from initial pale yellow to dark brown by ultrasonic irradiation. As a matter of fact, the formation of Pd nanoparticles must be confirmed by several analysis methods as described later.

To understand the mechanism of Pd(II) reduction and Pd nanoparticle formation, the concentration of Pd(II) should be measured as a function of irradiation time. However, it is impossible to determine the concentration of Pd(II) from the spectrum analysis of Fig. 4.3a. This is because the spectrum of Pd(II) in an aqueous solution consists of $[PdCl_x(H_2O)_{4-x}]^{(x-2)-}$ or $[PdCl_x(OH)_{4-x}]^{2-}$, which are dependent on the concentration of Pd(II) and the pH value of the solution. By using a NaI colorimetric method [30], the concentration of Pd(II) in the sample solution can be determined: the addition of an appropriate amount of a saturated NaI aqueous solution to the sample solution results in the formation of a Pd(II)-iodide complex with a large absorbance ($\varepsilon = 9{,}600\ M^{-1}\ cm^{-1}$ at wavelength of 408 nm) as seen in Eq. 4.8.

$$Pd(II) + 4I^- \rightarrow [PdI_4]^{2-} \tag{4.8}$$

In addition, since the aggregation of colloidal Pd nanoparticles occurs simultaneously, the aggregated Pd nanoparticles can be removed by filtration with

a membrane filter. Therefore, based on this method, the concentration of Pd(II) in the sample solution can be spectrophotometrically determined without interference from surfactants and colloidal Pd nanoparticles. Figure 4.3b shows the absorption spectra obtained from each of the irradiated Pd(II) solutions in the presence of SDS after NaI addition and filtration with a 0.2-μm pore size membrane filter. The absorption peak attributed to $[PdI_4]^{2-}$ is clearly observed at 408 nm before ultrasonic irradiation, and the peak gradually decreases with increasing irradiation time.

In the presence of polyethylene(40)glycol monostearate (PEG40MS) instead of SDS, changes in the absorption spectra during irradiation were similar to those in the presence of SDS. On the other hand, in the case of a Pd(II)-polyvinyl pyrrolidone (PVP; Mw, 40,000) aqueous solution and a Pd(II)-polyoxyethylene (20)sorbitan monolaurate (Tween20) aqueous solution, different absorption spectra were observed: when NaI was added to the sample solution of Pd(II)-PVP or Pd(II)-Tween20, the absorption intensity and peak considerably changed ($\varepsilon = 21{,}000\ M^{-1}\ cm^{-1}$ at wavelength of 342 nm). These changes in the absorption spectra would be due to the fact that the coordination of PVP and Tween20 to Pd(II) partly occurred. However, a good linear line dependence of absorbance versus concentration of Pd(II) was able to be obtained as in the SDS and PEG40MS solutions.

By using the colorimetric method, the rates of reduction of Pd(II) can be measured and analyzed. For example, when the types of added organic additives were changed, it was found from the analysis of the colorimetric method that the rates changed in the order of no organic additive (6.9 μM min^{-1}) < 1 g/L PVP (87 μM min^{-1}) < 8 mM SDS (130 μM min^{-1}) < 0.4 mM PEG40MS (230 μM min^{-1}) < 5 g/L Tween20 (400 μM min^{-1}), at an initial concentration of 1.0 mM of Pd(II) [30]. In addition, when the concentration of SDS was increased, the rates of reduction of Pd(II) also increased as 30 μM min^{-1} at 0.1 mM SDS < 100 μM min^{-1}, at 1 mM SDS < 130 μM min^{-1}, and at 8 mM SDS. Even in the case of the addition of alcohols or carboxylic acids, the rates can be changed. For example, the rates were 250 μM min^{-1} in a 10 mM *t*-BuOH aqueous solution and 300 μM min^{-1} in a 10 mM *n*-pentanoic acid aqueous solution. Based on these results, it was concluded that organic additives act as a precursor for the formation of reductants as described in the mechanism of the sonochemical reduction. Therefore, the concentration and types of organic additives are important factors to control the rates of reduction.

Figure 4.4 shows a TEM image of Pd nanoparticles formed from the sonolysis of a 1.0 mM Pd(II) and 0.4 mM PEG40MS aqueous solution. It can be seen that the size of the Pd nanoparticles is ca. 5 nm [10]. Since organic additives of PVP, SDS, PEG40MS, and Tween20 act as colloidal stabilizers to suppress the aggregation of Pd nanoparticles, the synthesis of the size-controlled Pd nanoparticles can be performed by using these stabilizers. The average size of the sonochemically formed Pd nanoparticles decreased with decreasing initial concentrations of Pd(II) [30]. In addition, the average size decreased with increasing rates of Pd(II) reduction [32].

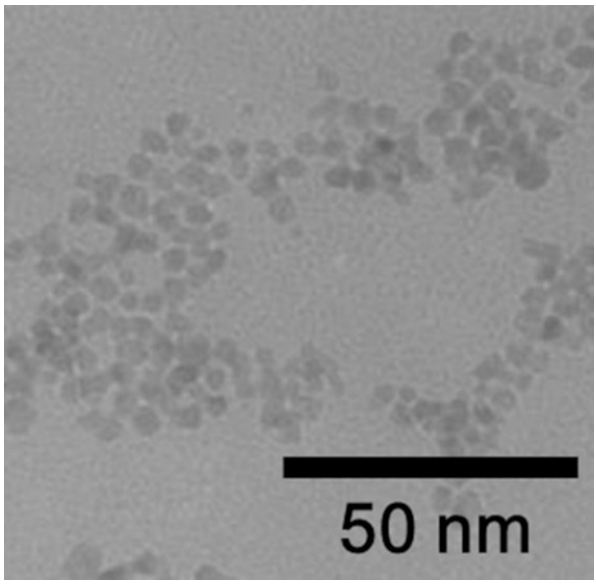

Fig. 4.4 TEM image of sonochemically prepared Pd nanoparticles from the reduction of 1.0 mM Pd(II) and 0.4 mM PEG40MS (Reprinted with permission from Ref. [10]. Copyright 1996 Elsevier)

The types of precursors also affect the reduction behavior of metal ions and formation behavior of metal nanoparticles. When a $[Pd(NH_3)_4]Cl_2$ aqueous solution is sonicated instead of $PdCl_2 \cdot 2NaCl$, the rate of reduction is different. Figure 4.5a shows changes in the absorption spectra of a $[Pd(NH_3)_4]Cl_2$ aqueous solution containing 2-propanol during ultrasonic irradiation [33]. A broad absorption band between the UV and visible region increases with increasing irradiation time, and an absorption peak can be observed at 225 nm at the irradiation times of 30, 60, and 120 min. Creighton and Eadon [31] reported that the calculated surface plasmon peak of spherical Pd nanoparticles of 10 nm diameter in water was located at 220–230 nm. In most cases, it is difficult to confirm the peak at 220–230 nm experimentally because it is often overlapped with other absorption spectra of coexisting solutes such as inorganic ions and organic stabilizers.

However, if the spectrum interference due to coexisting solutes was removed, the absorption spectra should become clearer. Figure 4.5b and c shows absorption spectra of sonochemically formed Pd nanoparticles before and after corrections in the region from 200 to 280 nm, where the corrected absorption spectra (Fig. 4.5c) are prepared by abstracting the spectra of $[Pd(NH_3)_4]Cl_2$ remaining in the irradiated solution from the spectra of Fig. 4.5b. In this case, the concentrations of $[Pd(NH_3)_4]Cl_2$ are measured first by the colorimetric method, and then, the overlapping spectra are removed from the uncorrected absorption spectra. Since the mole absorption coefficient of Cl^- and NH_4^+ ions is quite small compared with that of $[Pd(NH_3)_4]Cl_2$, the corrections for these ions are excluded. As seen in Fig. 4.5c, the clear peak corresponding to the surface plasmon of the Pd nanoparticles can be seen after the spectrum corrections.

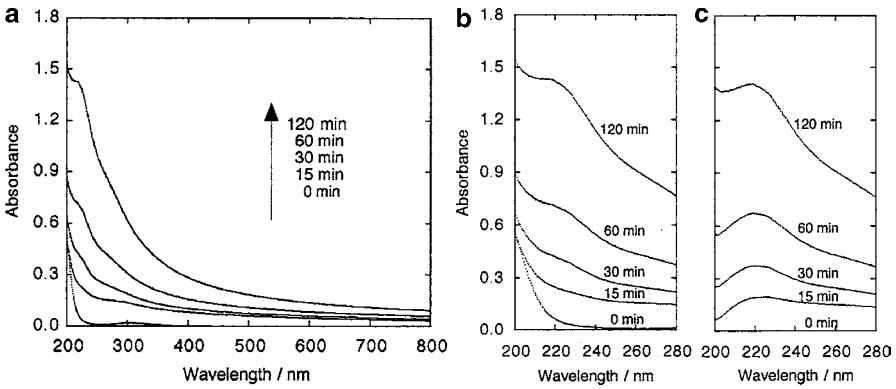

Fig. 4.5 (**a**) Changes in the absorption spectra of $[Pd(NH_3)_4]Cl_2$ solution in the presence of 2-propanol during ultrasonic irradiation. (**b**) Absorption spectra of sonochemically formed Pd nanoparticles before and (**c**) after corrections. Conditions: 0.2 mM $[Pd(NH_3)_4]Cl_2$, 100 mM 2-propanol, argon atmosphere, cell length, 0.5 cm (Reprinted with permission from Ref. [33]. Copyright 2002 The Chemical Society of Japan)

The TEM analysis indicated that the size of the formed Pd nanoparticles was about 20–30 nm. The Pd nanoparticles formed here were stable in the colloidal state for more than 6 months, although no stabilizer existed in the solution.

Based on the colorimetric method, we can measure the rates of $[Pd(NH_3)_4]^{2+}$ reduction during ultrasonic irradiation. Although the sonochemical reduction of $[Pd(NH_3)_4]^{2+}$ did not proceed in the absence of 2-propanol, it proceeded in the presence of 2-propanol, where the rate was estimated to be 2.1 μM min^{-1} at 0.2 mM $[Pd(NH_3)_4]^{2+}$. Consequently, it was found that the rate of $[Pd(NH_3)_4]^{2+}$ reduction was slower than that of the Pd(II) (= $PdCl_2{\cdot}2NaCl$) reduction, indicating that $[Pd(NH_3)_4]^{2+}$ is more stable than Pd(II) for the reducing species formed from the sonolysis of water and 2-propanol.

4.2 Au Nanoparticles

Au nanoparticles can be widely applied to various fields of nanotechnology such as catalysts [34–36], sensors [37, 38], and surface-enhanced Raman spectroscopy [39]. By using a sonochemical reduction method, we can prepare Au nanoparticles. Figure 4.6a shows a representative spectrum change in the solution containing $NaAuCl_4$ (hereafter, abbreviated to Au(III)) and SDS during ultrasonic irradiation [40]. The absorption peak at around 300 nm can be observed before ultrasonic irradiation. This peak corresponds to $[AuCl_{4-x}(OH)_x]^-$ [41]. After irradiation, a new absorption peak appears at around 530 nm, and its intensity gradually increases with increasing irradiation time, indicating the formation of Au nanoparticles. It is also clear that the

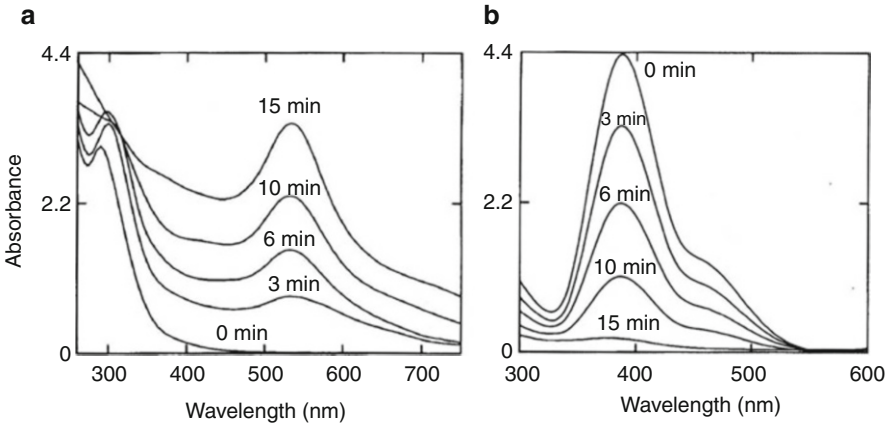

Fig. 4.6 (**a**) Changes in absorption spectra during ultrasonic irradiation of Au(III)-SDS aqueous solution under an argon atmosphere and (**b**) absorption spectra after addition of NaBr to the sample solution of (**a**). Conditions: $NaAuCl_4$ 1 mM, SDS 8 mM, cell length 1.0 cm (Reprinted with permission from Ref. [40]. Copyright 1996 Radiation Research Society)

absorption peak corresponding to $[AuCl_{4-x}(OH)_x]^-$ disappears at 15 min irradiation. In this case, the color of the sample solution gradually changes from initial yellow to reddish-violet by ultrasonic irradiation.

It is clear that the concentration of $[AuCl_{4-x}(OH)_x]^-$ cannot be measured correctly from the analysis of Fig. 4.6a because the spectrum of Au nanoparticles overlaps with that of $[AuCl_{4-x}(OH)_x]^-$ during ultrasonic irradiation, and thus, the peak corresponding to $[AuCl_{4-x}(OH)_x]^-$ shifts. However, when the addition of a NaBr solution to the sample solution of Fig. 4.6a is performed, the concentration of $[AuBr_4]^-$ formed from $[AuCl_{4-x}OH_x]^-$ can be measured as seen in Fig. 4.6b, where the following ligand exchange reaction occurs:

$$\left[AuCl_{4-x}(OH)_x\right]^- + 4Br^- \rightarrow [AuBr_4]^- + (4-x)Cl^- + xOH^- \qquad (4.9)$$

Simultaneously, the aggregation of colloidal Au nanoparticles occurs. Since the aggregated Au nanoparticles can be removed by filtration, the concentration of unreduced Au(III) can be determined, and the rate of reduction of Au(III) can be calculated to be 83 μM min^{-1}. The rates of reduction of Au(III) are strongly dependent on the types and concentrations of organic additives [40] and the types of dissolved gases [11].

The average size of the formed Au nanoparticles has been measured to be 10 and 9 nm from the analysis of dynamic light scattering and TEM, respectively [40]. Recently, Haiss et al. reported a simple method to estimate the size of Au nanoparticles from the analysis of an UV-Vis spectrum [42]. They plotted the ratio of the surface plasmon resonance peak (A_{spr}) to the absorbance at 450 nm (A_{450}) as a function of the logarithm of the particle diameter (D), where the plots

were prepared by use of the theoretical and experimental data, respectively. As a result, the linear relationship between A_{spr}/A_{450} and D was established in the size range from 5 to 80 nm as follows:

$$D = \exp(B_1 \frac{A_{spr}}{A_{450}} - B_2) \tag{4.10}$$

where B_1 is the inverse of the slope (m) of the linear fit, B_2 is B_0/m, and B_0 is the intercept. They found from the theoretical data that B_1 and B_2 were 3.55 and 3.11, respectively. On the other hand, from the experimental data, B_1 and B_2 were 3.00 and 2.20, respectively.

By using the theoretically and experimentally measured values of B_1 and B_2, the diameter of the sonochemically formed Au nanoparticles at 15 min irradiation in Fig. 4.6a can be calculated to be 8.8 and 9.7 nm, respectively. These values are in good agreement with those measured by dynamic light scattering and TEM. The size of the sonochemically formed Au nanoparticles can be controlled by various parameters such as types of organic additives and dissolved gas, intensity of ultrasound, frequency of ultrasound, and distance between the reaction vessel and the oscillator [11, 26].

4.3 Pt Nanoparticles

Pt nanoparticles can be applied to various catalysts for electrocatalytic oxidations [43, 44] and water-gas shift reactions [45]. A sonochemical reduction method can be used to prepare Pt nanoparticles [10, 46, 47]. Figure 4.7a shows changes in the absorption spectra during ultrasonic irradiation to an aqueous solution containing K_2PtCl_4 (hereafter, abbreviated to Pt(II)) and SDS [46]. Small absorption peaks at 380.5 and 317.5 nm attributed to Pt(II) gradually disappear, and a broad absorption band between the UV and visible region increases with increasing irradiation time. This spectrum change is due to the progress of the reduction of Pt(II) and formation of Pt nanoparticles.

The absorption spectrum of Pt(II) is unclear as seen in Fig. 4.7a, because Pt(II) in water consists of $[PtCl_x(H_2O)_{4-x}]^{(x-2)-}$ or $[PtCl_x(OH)_{4-x}]^{2-}$. However, the concentration of Pt(II) can be determined by the NaI colorimetric method as follows:

$$Pt(II) + 4I^- \rightarrow PtI_4^{2-} \tag{4.11}$$

Since the aggregated Pt nanoparticles that are induced by the addition of NaI can be removed by filtration, the absorption spectra of PtI_4^{2-} attributed to Pt(II) can be clearly measured as seen in Fig. 4.7b. The spectrum and TEM analyses indicated that the rate of Pt(II) reduction and the average size of the formed Pt nanoparticles were measured to be 26.7 μM min^{-1} and 2.6 nm, respectively [46].

In the following section, we look at the sonochemical reduction of the different valence of the Pt precursor. Figure 4.8a shows changes in the absorption spectra

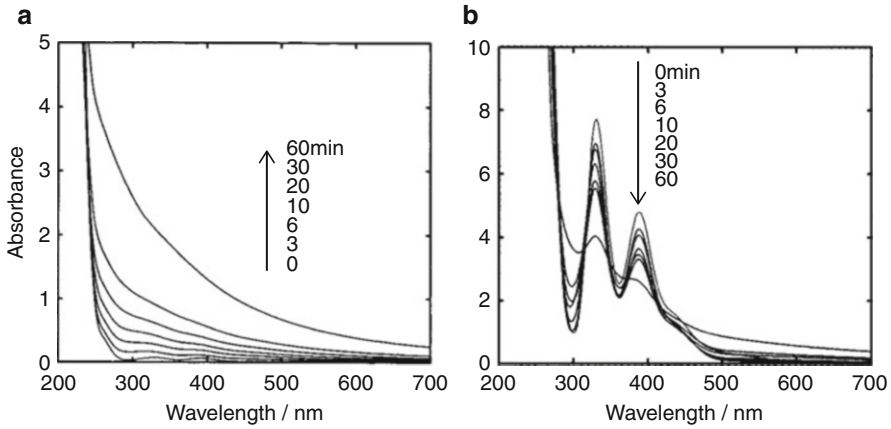

Fig. 4.7 (**a**) Changes in the absorption spectra of a solution of K_2PtCl_4 and SDS during ultrasonic irradiation under an argon atmosphere and (**b**) absorption spectra of NaI treated sample solution of (**a**). Conditions: K_2PtCl_4 1 mM, SDS 8 mM (Reprinted with permission from Ref. [46]. Copyright 1999 American Chemical Society)

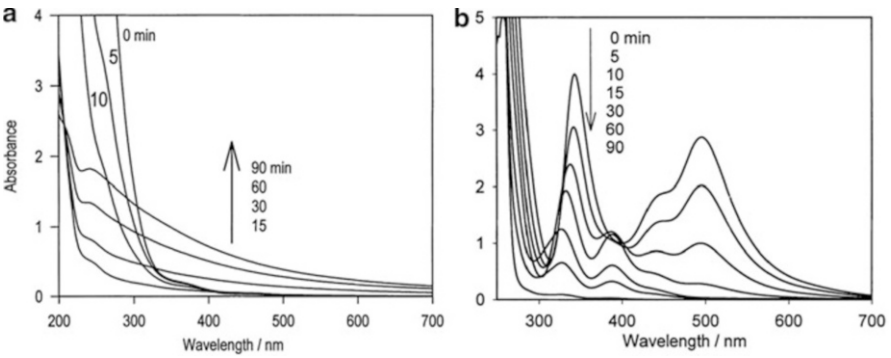

Fig. 4.8 (**a**) Changes in the absorption spectra of a solution of H_2PtCl_6 and SDS during ultrasonic irradiation under an argon atmosphere and (**b**) absorption spectra of NaI treated sample solution of (**a**). Conditions: H_2PtCl_6 1 mM, SDS 8 mM (Reprinted with permission from Ref. [47]. Copyright 2001 Elsevier)

during ultrasonic irradiation of an aqueous solution containing H_2PtCl_6 (hereafter, abbreviated to Pt(IV)) and SDS [47]. It can be seen that the absorbance in the UV region attributed to Pt(IV) decreases with increasing irradiation time from 0 min to 15 min. After 15 min irradiation, a broad absorption band between the UV and visible region increases with increasing irradiation time. This spectrum change is due to the consecutive progress of the reduction of Pt(IV) to Pt(II) and Pt(II) to Pt(0) (corresponding to the formation of Pt nanoparticles) as described later.

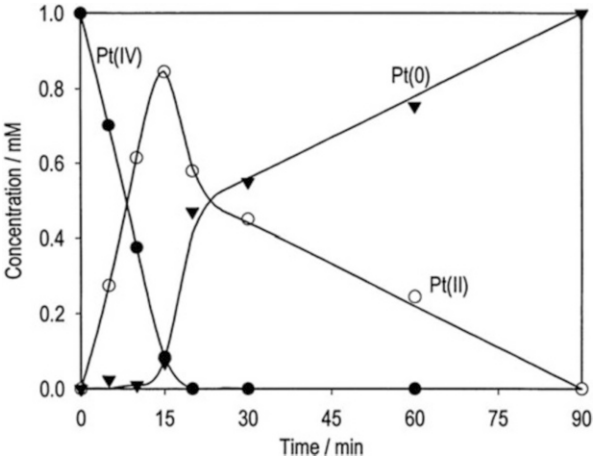

Fig. 4.9 Changes in the concentrations of Pt(IV), Pt(II), and Pt(0) during ultrasonic irradiation of an argon saturated aqueous solution containing 1 mM H_2PtCl_6 and 8 mM SDS (Reprinted with permission from Ref. [47]. Copyright 2001 Elsevier)

Similar to Pt(II), the following ligand exchange reaction of Pt(IV) (Pt(IV) in water consisting of $[PtCl_{6-x}(H_2O)_x]^{(2-x)-}$ or $[PtCl_{6-x}(OH)_x]^{2-}$) occurs after addition of a saturated NaI solution to the sample solution of Fig. 4.8a.

$$Pt(IV) + 6I^- \rightarrow PtI_6^{2-} \tag{4.12}$$

Therefore, the absorption spectra of PtI_6^{2-} attributed to Pt(IV) can be measured as seen in Fig. 4.8b, where the formation of PtI_4^{2-} (Pt(II)) is also confirmed as an intermediate during the sonochemical reduction of Pt(IV).

From the analysis of Fig. 4.8b, changes in the concentrations of Pt(IV), Pt(II), and Pt(0) during ultrasonic irradiation can be prepared as shown in Fig. 4.9. It is clear that the reduction of Pt(IV) proceeds to form Pt(II) and then the reduction of Pt(II) to Pt(0) proceeds consecutively [47].

It has also been reported that the reduction rates of Pt(IV) to Pt(II) were strongly affected by the concentration and types of organic stabilizers of SDS, PEG40MS, and sodium dodecylbenzenesulfonate, although those of Pt(II) to Pt(0) were hardly affected. The average sizes of the formed Pt nanoparticles at 8 mM SDS and 0.4 mM PEG40MS were measured to be ca. 3 nm and ca. 1 nm, respectively [47].

4.4 Ag Nanoparticles

Ag nanoparticles have been investigated actively from the fundamental point of view to understand the mechanism of Ag(I) reduction and Ag nanoparticle formation. This would be because Ag(I) is a simple monovalent metal cation, and the formed Ag clusters have a size-dependent absorption property. In addition, Ag nanoparticles can be widely applied to various technologies such as surface-enhanced Raman spectroscopy [48] and optical sensing [49, 50].

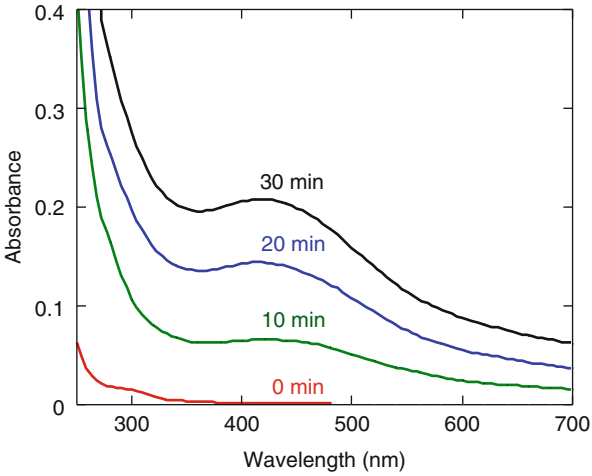

Fig. 4.10 Changes in absorption spectra of $AgNO_3$–PVP solution during ultrasonic irradiation under an argon atmosphere. Conditions: 0.5 mM of $AgNO_3$, 1 g/L of PVP [52]

Nagata et al. reported the formation of Ag nanoparticles from the sonochemical reduction of Ag(I), where $AgClO_4$ or $AgNO_3$ were used as precursors [51]. An example for changes in the absorption spectra of an aqueous solution containing $AgNO_3$ and PVP during irradiation is shown in Fig. 4.10 [52]. Although little absorption is observed before irradiation, a new absorption peak at around 420 nm gradually emerges with irradiation time. It is clear that the concentration of Ag(I) cannot be measured by analyzing the spectra of Fig. 4.10. To measure the amount of the formed Ag(0) colorimetrically, Nagata et al. used Eq. 4.13:

$$\mathrm{Ag(0)} + \mathrm{C(NO_2)_4} \rightarrow \mathrm{Ag(I)} + \mathrm{C(NO_2)^{3-}} + \mathrm{NO_2} \tag{4.13}$$

where the absorbance of $C(NO_2)^{3-}$ (ε =14,000 M^{-1} cm^{-1} at wavelength of 350 nm) was measured. By analyzing the amount of $C(NO_2)^{3-}$, the reduction rate of Ag(I) can be estimated. Ag nanoparticles can be also synthesized in the presence of other stabilizers such as SDS, PEG40MS and Tween20. The average size of the Ag nanoparticles formed from the sonochemical reduction of $AgClO_4$-PEG40MS was measured to be 13 nm, as determined by a dynamic light scattering photometer.

Gedanken et al. reported the formation of Ag nanoparticles from the sonochemical reduction of Ag(I) in the absence of organic additives under an argon-hydrogen atmosphere [53]. Zhu et al. reported the formation of Ag nanorods from the sonochemical reduction of Ag(I) in the presence of methenamine and PVP [54].

Xu and Suslick recently reported that very small Ag nanoparticles with a highly fluorescent property (hereafter, abbreviated to Ag nanoclusters) can be prepared by the sonochemical reduction of Ag(I) in the presence of polymethylacrylic acid (PMAA), which acts as a capping agent [55]. We can observe changes in the absorption spectra during the formation of Ag nanoclusters. They used a horn-type sonicator (1 cm^2 Ti horn at 20 kHz and 25 W cm^{-2}) to prepare Ag nanoclusters under an argon atmosphere at 20 °C. Figure 4.11a shows changes in the absorption

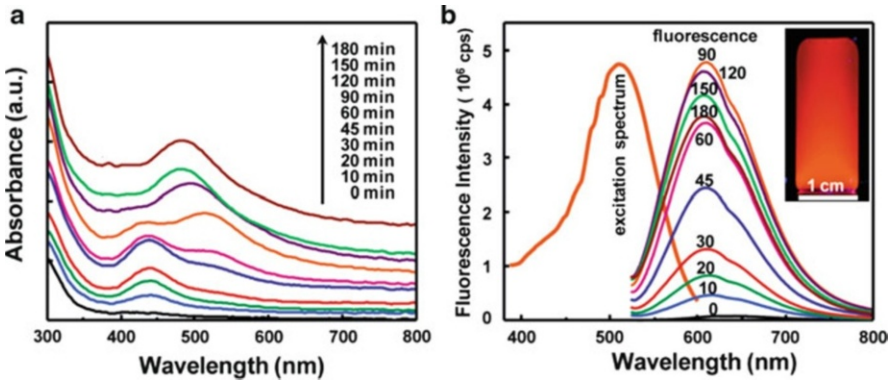

Fig. 4.11 (**a**) UV-Vis spectra and (**b**) fluorescence emission spectra of the solution containing PMAA and $AgNO_3$ after increasing length of sonication time; the excitation spectrum shown in (**b**) corresponds to the 90-min sample with an emission wavelength of 610 nm (*inset*: solution of the Ag nanoclusters illuminated by a UV lamp with 365-nm excitation) (Reprinted with permission from Ref. [55]. Copyright 2010 American Chemical Society)

spectra of an aqueous solution containing Ag(I) and PMAA during ultrasonic irradiation. The formation of Ag nanoclusters can be confirmed by an absorption peak at around 440–520 nm, which gradually emerges by ultrasonic irradiation. In this case, the color of the solution gradually changes from colorless (0 min) to pink (90 min) and then dark red (180 min). The formed Ag nanoclusters were measured to be less than 2 nm in diameter.

Since the carboxylic acid groups in PMAA have a strong affinity for Ag(I) ions and Ag metal surfaces, the aggregation of Ag nanoclusters would be suppressed. The formed Ag nanoclusters have a high fluorescent property, as seen in the inset of Fig. 4.11b. They also reported that the optical and fluorescence properties of the sonochemically synthesized Ag nanoclusters also change by modifying the stoichiometry of the carboxylate groups of PMAA to Ag(I) [55]. In general, Ag nanoclusters can be applied to fluorescent sensors for metal ions such as Cu(II) [49] and Hg(II) [50]. More recently, it has been reported that Au/Ag nanoclusters with a yellow emission can be synthesized by ultrasonic irradiation in the presence of bovine serum albumin [56].

4.5 Reduction Mechanism of Metal Ions

The reduction of Pd(II), Au(III), Pt(II), Pt(IV), and Ag(I) proceeds by ultrasonic irradiation as described before. Here, the reduction behavior among Pd(II), Au(III), Pt(II), and Ag(I) in the presence of SDS will be compared by analyzing the rates of reduction. Based on Eqs. 4.1–4.6, various types of reductants are formed in the sonolysis of SDS and water. Since each of the reductants should have different reducing potentials for metal ions, the rate of reduction of metal ions should depend on the reactivity of the metal ions with reductants.

In the case of 200 kHz ultrasonic irradiation under an argon atmosphere, the rates of the sonochemical reduction are reported to be in the order of 130 μM min^{-1} for Pd(II) > 83 μM min^{-1} for Au(III) > 19 μM min^{-1} for Pt(II) > 7 μM min^{-1} for Ag(I) [10]. Since metal ions have different valences, the rates of the sonochemical reduction should be corrected for comparison with each other. If the rates were corrected on the basis of the number of electron transfers (e.g., Pd(II) needs two electrons to form Pd(0) and Au(III) needs three electrons to form Au(0)), the order would become Pd(II) ≈ Au(III) > Pt(II) > Ag(I). This order does not agree with the order of the redox potential of each metal ion. It is found that the rates of the sonochemical reduction of Pt(II) and Ag(I) are considerably slower than those of Pd(II) and Au(III). From the analysis of the reduction behavior during gamma ray irradiation under a N_2O atmosphere [10], it is suggested that the sonochemical reduction of Pt(II) and Ag(I) proceeds mainly via the reduction by •R and H_2, which are formed by the abstraction reactions as Eq. 4.2. On the other hand, in the cases of Pd(II) and Au(III), the sonochemical reduction proceeds mainly via the reduction by pyrolysis radicals and unstable products, which are formed by the pyrolysis of RH as Eq. 4.3.

To evaluate the effects of •R and H_2 on the reduction of metal ions, the analysis of the amount of H_2O_2 formed in the sonolysis of pure water is useful, because the amount of H_2O_2 should be related to that of •R and H_2, taking into account Eqs. 4.2 and 4.7. As a result of this analysis, the effects of the pyrolysis radicals and unstable products on the reduction of the metal ions can also be evaluated as seen in the literature [10, 11, 26, 30, 32, 33, 40, 46, 47].

4.6 MnO_2 Nanoparticles

MnO_2 is a useful material for application to electrochemical capacitors, Li-batteries, sensors, and catalysts [57–60]. Okitsu et al. reported that the sonochemical reduction of MnO_4^- occurs to form MnO_2 nanoparticles [9]. Figure 4.12a and b shows changes in the absorption spectra of a MnO_4^- aqueous solution during ultrasonic irradiation, where no organic compound has been added. During irradiation, the color of the sample solution gradually changes from purple (0 min) to pale yellow (8 min) and finally turned to colorless (12, 14, 16 min). Figure 4.12a shows that several absorption peaks of MnO_4^- from 450 to 580 nm gradually disappear, and a new broad peak at around 360 nm emerges by ultrasonic irradiation. Based on the literature [61–64], this new peak can be attributed to colloidal MnO_2 particles. Therefore, a pale yellow color solution at 8 min irradiation corresponds to the formation of colloidal MnO_2 particles. In Fig. 4.12a, two isosbestic points are also observed at 504 and 580 nm, indicating that the reduction of MnO_4^- to MnO_2 proceeds consecutively by ultrasonic irradiation. Figure 4.12b shows changes in the absorption spectra following further irradiation. The peak at around 360 nm quickly decreases with increasing irradiation time. This is due to the progress of the reduction of MnO_2 to Mn^{2+} [62, 64].

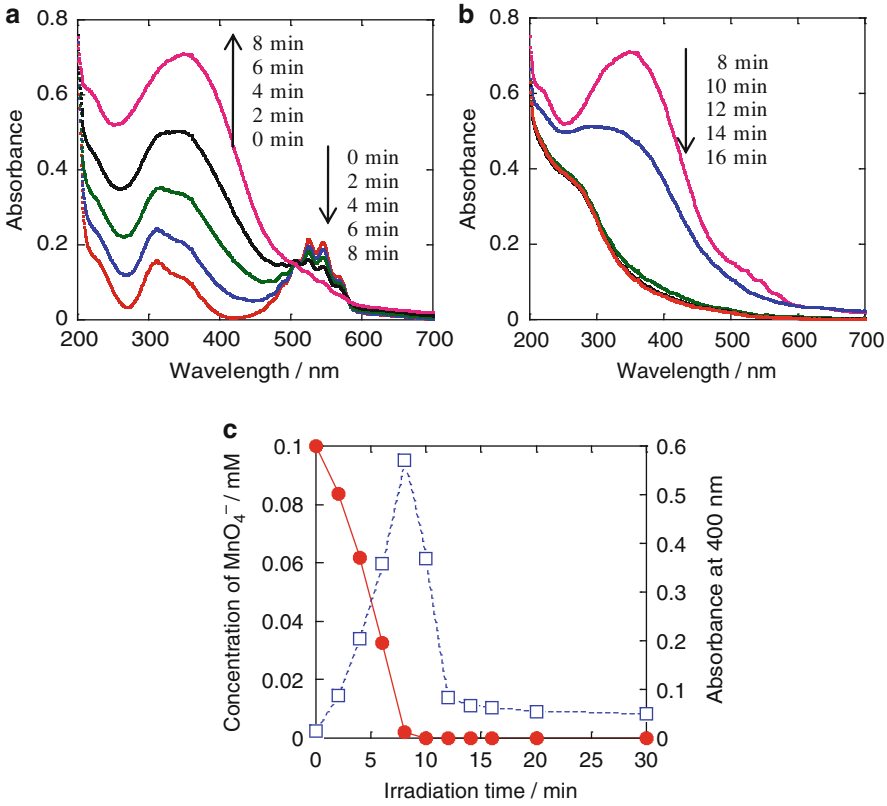

Fig. 4.12 (**a**) Changes in absorption spectra of MnO_4^- aqueous solution before and after 2, 4, 6, and 8 min ultrasonic irradiation and (**b**) after 8, 10, 12, 14, and 16 min ultrasonic irradiation. (**c**) Changes in the concentration of MnO_4^- (●) and absorbance at 400 nm (□) during ultrasonic irradiation. Initial concentration of MnO_4^-: 0.1 mM, argon atmosphere (Reprinted with permission from Ref. [9]. Copyright 2009 Elsevier)

Figure 4.12c shows changes in the concentration of MnO_4^- during ultrasonic irradiation. As an index of the amount of MnO_2 in the sample solution, changes in the absorbance at 400 nm are also plotted, where the absorbance at 400 nm is chosen to reduce the overlap of the MnO_4^- absorbance. It is clear that the formation of MnO_2 occurs along with the reduction of MnO_4^-, and the formed MnO_2 is reduced consecutively by further irradiation. From Fig. 4.12c, it is found that 8 min irradiation is the optimum irradiation time to prepare MnO_2 particles.

In this study, since no organic additive is added to the sample solution, the reduction of MnO_4^- proceeds as follows:

$$2MnO_4^- + 3H_2(\text{or } 6H) \rightarrow 2MnO_2 + 2OH^- + 2H_2O \tag{4.14}$$

$$2MnO_4^- + 3H_2O_2 \rightarrow 2MnO_2 + 3O_2 + 2OH^- + 2H_2O \tag{4.15}$$

where MnO_4^- can react with H_2O_2 because of the strong oxidizing agent of MnO_4^- [65]. As seen in Eqs. 4.14 and 4.15, the measurement of pH is also useful to understand the progress of the formation of MnO_2.

4.7 Au Core/Pd Shell Nanoparticles

Bimetallic nanoparticles of Au/Pd can be prepared by sonochemical reduction of the corresponding metal ions [66–69]. Au/Pd nanoparticles are recently researched as active catalysts that can be applied to various catalytic reactions such as alkene hydrogenation [67, 68], H_2O_2 production [70], and CO oxidation [71]. Figure 4.13a shows changes in the absorption spectra of the sample solution containing Au(III), Pd(II), and SDS during ultrasonic irradiation [66]. It can be seen that an absorption peak at around 520 nm gradually emerges with increasing irradiation time and becomes clear at 6 min irradiation. This peak is in good agreement with the surface plasmon peak of Au nanoparticles [31, 40]. After that, the peak becomes broader following further irradiation. The color of the solution gradually changes from pale yellow (0 min) to reddish-violet (6 min) and finally to dark brown (15 min) during ultrasonic irradiation.

Figure 4.13b shows changes in the concentrations of Au(III) and Pd(II) during ultrasonic irradiation, where the concentrations are measured using a colorimetric method [66]. It can be seen that the reduction of Au(III) starts at first and then the reduction of Pd(II) starts after completion of the reduction of Au(III). The TEM analysis indicated that the average size of the formed Au/Pd nanoparticles is ca. 8 nm and they have a Au core and a Pd shell nanostructure. Based on the formation of the core/shell nanostructure, it can be concluded that the reason why the surface plasmon peak of Au nanoparticles becomes broader at 9 min irradiation is because of the deposition of the sonochemically reduced Pd atoms on the formed Au nanoparticles. As seen in Fig. 4.13a and b, the analysis of the UV-Vis spectra is an important probe to understand the reduction behavior of Pd(II) and Au(III) as well as the formation behavior of Au core/Pd shell nanoparticles.

4.8 Au Nanorods

Rod-shaped Au nanoparticles (Au nanorods) have great potential in a wide variety of applications such as photothermal therapy of cancer cells [72] and optical data storage [73]. Okitsu et al. reported the synthesis of Au nanorods from the sonochemical reduction of Au(I) [74]. Figure 4.14 shows changes in the extinction spectra of the sample solution during ultrasonic irradiation at pH 3.5. Cetyltrimethylammonium bromide (CTAB), $AgNO_3$, and ascorbic acid are added to the solution of $HAuCl_4$, where CTAB and $AgNO_3$ act as shape-control agents and ascorbic acid acts as a weak reductant to reduce $HAuCl_4$ to Au(I). From this figure, the term of extinction is used instead of absorbance, because Au nanorods have a light scattering property depending on their size and shape. Therefore, the term of

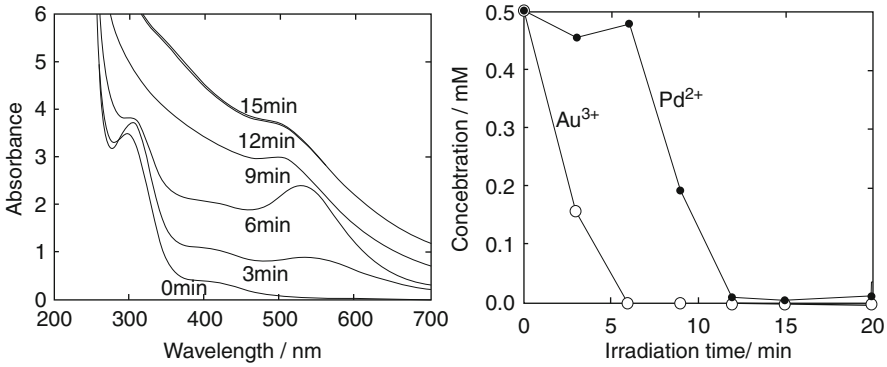

Fig. 4.13 (**a**) Changes in the absorption spectra of sample solution containing Au(III), Pd(II), and SDS during ultrasonic irradiation. (**b**) Changes in the concentrations of Au(III) and Pd(II) during ultrasonic irradiation of an aqueous solution. Conditions: 0.5 mM $NaAuCl_4$, 0.5 mM $PdCl_2 \cdot 2NaCl$ and 8 mM SDS, argon atmosphere (Reprinted with permission from Ref. [66]. Copyright 1997 American Chemical Society)

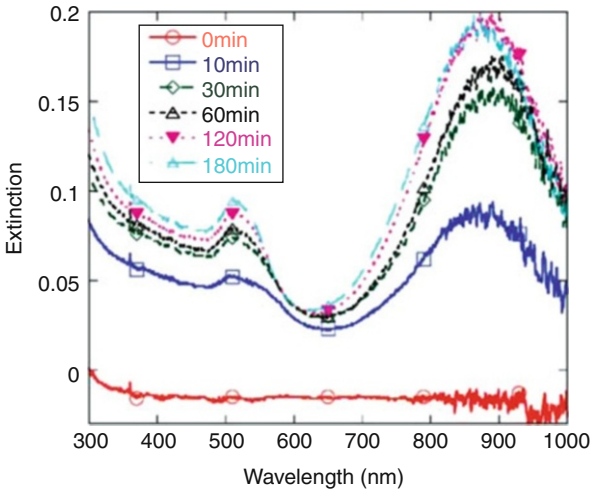

Fig. 4.14 Changes in extinction spectra of sample solution of Au(I) during ultrasonic irradiation under an argon atmosphere at pH 3.5. Cell length: 0.5 cm (Reprinted with permission from Ref. [74]. Copyright 2009 American Chemical Society)

extinction is appropriate for the results of UV-Vis spectroscopy. In Fig. 4.14, it can be seen that the extinction intensity gradually increases with irradiation time, and extinction peaks at around 510 and 880 nm are clearly observed at the irradiation time from 10 to 180 min. These peaks correspond with the surface plasmon bands of Au nanorods [3, 75, 76], indicating that the reduction of Au(I) to Au(0) proceeds and formation of Au nanorods occurs.

Figure 4.15a shows a TEM image of Au nanoparticles formed at 180 min irradiation in Fig. 4.14. It is clear that rod-shaped nanoparticles are formed in the size range of 10–50 nm. Figure 4.15b shows the distribution of the aspect ratio measured. It is found that the formation of nanorods with an aspect ratio

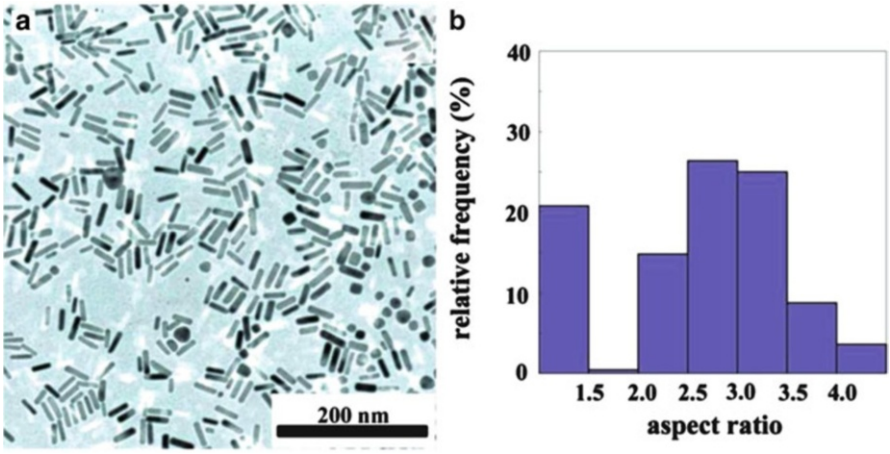

Fig. 4.15 (**a**) TEM image of Au nanorods and nanoparticles formed after irradiation of a sample solution of Au(I) under an argon atmosphere at pH 3.5 for 180 min. (**b**) Distribution of the aspect ratio of Au nanorods and nanoparticles (Reprinted with permission from Ref. [74]. Copyright 2009 American Chemical Society)

from 1.5 to 2.0 is almost zero. From Fig. 4.15a and b, spherical-, cubic-, and irregular-shaped particles with an aspect ratio of less than 1.5 are formed partly, and the total yield of these is measured to be ca. 20 %. The average aspect ratio of the formed nanorods was 3.0, when particles with an aspect ratio of less than 1.5 were excluded from the calculation of the average aspect ratio. Since Fig. 4.14 shows that the peak wavelength of the surface plasmon bands hardly changes during ultrasonic irradiation, it is possible that the formation of nanorods is determined at the initial growth stage of the formed Au seeds.

The pH of the solution is one of the important factors to control the sonochemical reduction of Au(I) and formation of Au nanoparticles. Figure 4.16 shows the extinction spectra of the sonochemically formed Au nanoparticles after 180 min irradiation of different pH solutions. It can be seen that the peak wavelength of the longitudinal plasmon band decreases as the pH of the solution increases.

The TEM analysis indicated that the average aspect ratio of Au nanorods synthesized at different pH solutions decreased as follows: 3.0 at pH 3.5 $<$ 2.2 at pH 5.0 and $<$ 2.1 at pH 6.5, where particles with an aspect ratio of less than 1.5 were excluded from the calculation of the average aspect ratio. This order can be connected to the order of the peak shift observed in the extinction spectra as seen in Fig. 4.16: the peak wavelength of the longitudinal plasmon band decreases with decreasing aspect ratio of the formed Au nanorods.

As seen in the results for Au nanorods, the extinction spectrum changes strongly depending on the aspect ratio of Au nanorods. In the case of the synthesis of shape-controlled nanoparticles with a surface plasmon peak, therefore, the analysis of the extinction spectrum is an important probe to know the average property of the

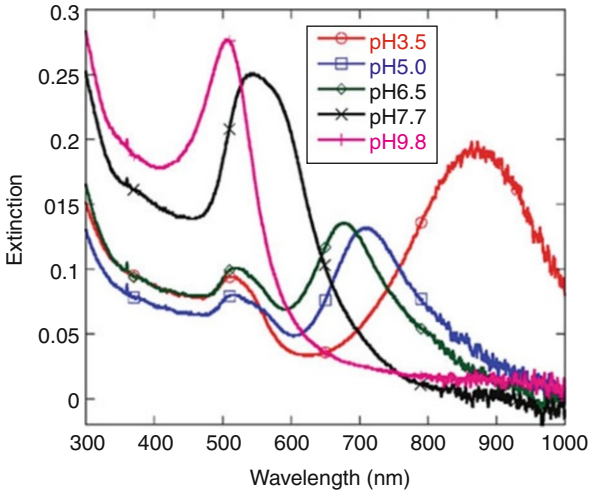

Fig. 4.16 Effects of pH on the extinction spectra of Au nanorods and nanoparticles formed after irradiation of sample solutions of Au(I) under an argon atmosphere for 180 min. Cell length: 0.5 cm (Reprinted with permission from Ref. [74]. Copyright 2009 American Chemical Society)

formed nanoparticles in the state of the colloidal dispersion system. In the analysis of a TEM image, a large number of particles must be analyzed to get the average information of the formed nanoparticles. In addition, it is possible that the preparation processes of the TEM specimens affect the formation of some aggregation with nanostructures. For example, the following phenomena may occur [74]: (1) during the processes of centrifugation to remove dissolved organic and inorganic species in solution, some aggregation of nanoparticles may occur, and (2) during the addition of a sample solution to a TEM grid or during the drying processes of a sample solution on a TEM grid, some aggregation of the nanoparticles may occur. In such a case, chemical reactions of the nanoparticles or unreduced metal ions with a TEM grid such as Cu may be induced to form some aggregation and/or unexpected nanostructures. Therefore, the results of TEM showing the formation of the unique shape should be compared with those of the extinction spectrum of the sample solution to confirm whether the formation of nanostructures occurs in the state of the colloidal dispersion system or not.

5 Conclusions and Future Perspective

UV-Vis spectroscopy provides important information about the sonochemical reduction processes of metal ions and the formation processes of metal nanoparticles in solution. In this chapter, the optical properties of spherical nanoparticles of Pd, Au, Pt, Ag, MnO_2, and core/shell bimetal nanoparticles and shape-controlled nanoparticles are described mainly on the basis of changes in the UV-Vis spectra during ultrasonic irradiation. It is noted that the UV-Vis spectrum has to be collected as a function of irradiation time to understand the effects of ultrasound on the synthesis of these nanoparticles. Since the reduction processes of metal ions can be linked to the formation processes of metal nanoparticles,

the analysis of both processes must be performed to understand the mechanism. In particular, since the analysis of the UV-Vis spectrum of the nanoparticle sample solution corresponds to real information for the formed metal nanoparticles in the state of a colloidal dispersion system, the analysis of the spectrum must be performed comprehensively. In the case of the synthesis of shape-controlled nanoparticles, it is probable that the analysis of TEM only leads to misunderstandings when the preparation and analysis of the TEM sample are not performed adequately. Therefore, to evaluate the formed nanoparticles correctly, the results of the TEM analysis should be compared with those of the UV-Vis spectrum.

In the sonochemical reduction methods, various parameters such as the types of organic additives and dissolved gas, intensity of ultrasound, frequency of ultrasound, and distance between the reaction vessel and the oscillator strongly affect the rates of the reduction of metal ions and properties of the formed metal nanoparticles [7]. If we changed the experimental parameters, the properties of the formed metal nanoparticles would change. However, there are still unclear points regarding the characteristics of the cavitation phenomenon such as the bubble temperatures and pressures, number and size distribution of the bubbles, and its dynamics. If we succeeded in clarifying the cavitation phenomenon in more detail, the sonochemical reduction methods would be promising ones to synthesize various types of novel functional nanoparticles. UV-Vis spectroscopy is expected to be an excellent tool to understand the reduction behavior of metal ions and the formation behavior of metal nanoparticles, as well as a means to understand the characteristics of the cavitation phenomenon.

References

1. Polte J, Ahner TT, Delissen F, Sokolov S, Emmerling F, Thünemann AF, Kraehnert R (2010) Mechanism of gold nanoparticle formation in the classical citrate synthesis method derived from coupled in situ XANES and SAXS evaluation. J Am Chem Soc 132(4):1296–1301
2. Pretzer LA, Nguyen QX, Wong MS (2010) Controlled growth of sub-10 nm gold nanoparticles using carbon monoxide reductant. J Phys Chem C 114(49):21226–21233
3. Pérez-Juste J, Pastoriza-Santos I, Liz-Marzán LM, Mulvaney P (2005) Gold nanorods: synthesis, characterization and applications. Coord Chem Rev 249(17–18):1870–1901
4. Fong Y-Y, Visser BR, Gascooke JR, Cowie BCC, Thomsen L, Metha GF, Buntine MA, Harris HH (2011) Photoreduction kinetics of sodium tetrachloroaurate under synchrotron soft X-ray exposure. Langmuir 27(13):8099–8104
5. Lee YW, Kim M, Han SW (2010) Shaping Pd nanocatalysts through the control of reaction sequence. Chem Commun 46:1535–1537
6. Belloni J (2006) Nucleation, growth and properties of nanoclusters studied by radiation chemistry: application to catalysis. Catalysis Today 113(3–4):141–156
7. Okitsu K (2001) Sonochemical synthesis of metal nanoparticles, chapter 5. In: Pankaj, Ashokkumar M (Eds) Theoretical and experimental sonochemistry involving inorganic systems. Springer, Dordrecht, pp 131–150
8. Anandan S, Ashokkumar M (2011) Sonochemical preparation of monometallic, bimetallic and metal-loaded semiconductor nanoparticles, chapter 6. In: Pankaj, Ashokkumar M (Eds) Theoretical and experimental sonochemistry involving inorganic systems. Springer, Dordrecht, pp 151–169

9. Okitsu K, Iwatani M, Nanzai B, Nishimura R, Maeda Y (2009) Sonochemical reduction of permanganate to manganese dioxide: the effects of H_2O_2 formed in the sonolysis of water on the rates of reduction. Ultrasonics Sonochem 16:387–391
10. Okitsu K, Mizukoshi Y, Bandow H, Maeda Y, Yamamoto T, Nagata Y (1996) Formation of noble metal particles by ultrasonic irradiation. Ultrason Sonochem 3:S249–S251
11. Okitsu K, Yue A, Tanabe S, Matsumoto H, Yobiko Y, Yoo Y (2002) Sonolytic control of rate of gold(III) reduction and size of formed gold nanoparticles: relation between reduction rates and sizes of formed nanoparticles. Bull Chem Soc Jpn 75(10): 2289–2296
12. Okitsu K, Suzuki T, Takenaka N, Bandow H, Nishimura R, Maeda Y (2006) Acoustic multibubble cavitation in water: a new aspect of the effect of rare gas atmosphere on bubble temperature and its relevance to sonochemistry. J Phys Chem B 110:20081–20084
13. Tauber A, Mark G, Schuchmann H-P, Von Sonntag C (1999) Sonolysis of tert-butyl alcohol in aqueous solution. J Chem Soc Perkin Trans 2(6):1129–1135
14. Hart EJ, Fischer C-H, Henglein A (1990) Sonolysis of hydrocarbons in aqueous solution. Radiat Phys Chem 36(4):511–516
15. Ashokkumar M, Grieser F (2005) A comparison between multibubble sonoluminescence intensity and the temperature within cavitation bubbles. J Am Chem Soc 127(15): 5326–5327
16. McNamara WB III, Didenko YT, Suslick KS (1999) Sonoluminescence temperatures during multi-bubble cavitation. Nature 401(6755):772–775
17. Didenko YT, McNamara WB III, Suslick KS (1999) Hot spot conditions during cavitation in water. J Am Chem Soc 121(24):5817–5818
18. Hilgenfeldt S, Grossmann S, Lohse D (1999) A simple explanation of light emission in sonoluminescence. Nature 398(6726):402–405
19. Flannigan DJ, Suslick KS (2005) Plasma formation and temperature measurement during single-bubble cavitation. Nature 434(7029):52–55
20. Young FR (1976) Sonoluminescence form water containing dissolved gases. J Acoust Soc Am 60(1):100–104
21. Yasui K (2001) Single-bubble sonoluminescence from noble gases. Phys Rev E Stat Nonlin Soft Matter Phys 63(3II):353011–353014
22. Koda S, Kimura T, Kondo T, Mitome H (2003) A standard method to calibrate sonochemical efficiency of an individual reaction system. Ultrason Sonochem 10(3):149–156
23. Asakura Y, Nishida T, Matsuoka T, Koda S (2008) Effects of ultrasonic frequency and liquid height on sonochemical efficiency of large-scale sonochemical reactors. Ultrason Sonochem 15(3):244–250
24. Beckett MA, Hua I (2001) Impact of ultrasonic frequency on aqueous sonoluminescence and sonochemistry. J Phys Chem A 105(15):3796–3802
25. Hung H-M, Hoffmann MR (1999) Kinetics and mechanism of the sonolytic degradation of chlorinated hydrocarbons: frequency effects. J Phys Chem A 103(15):2734–2739
26. Okitsu K, Ashokkumar M, Grieser F (2005) Sonochemical synthesis of gold nanoparticles: effects of ultrasound frequency. J Phys Chem B 109(44):20673–20675
27. Li Y, Boone E, El-Sayed MA (2002) Size effects of PVP-Pd nanoparticles on the catalytic Suzuki reactions in aqueous solution. Langmuir 18(12):4921–4925
28. Semagina N, Renken A, Laub D, Kiwi-Minsker L (2007) Synthesis of monodispersed palladium nanoparticles to study structure sensitivity of solvent-free selective hydrogenation of 2-methyl-3-butyn-2-ol. J Catal 246(2):308–314
29. Jia C-J, Schüth F (2011) Colloidal metal nanoparticles as a component of designed catalyst. Phys Chem Chem Phys 13(7):2457–2487
30. Okitsu K, Bandow H, Maeda Y, Nagata Y (1996) Sonochemical preparation of ultrafine palladium particles. Chem Mater 8:315–317
31. Creighton JA, Eadon DG (1991) Ultraviolet-visible absorption spectra of the colloidal metallic elements. J Chem Soc Faraday Trans 87(24):3881–3891

32. Okitsu K, Nagaoka S, Tanabe S, Matsumoto H, Mizukoshi Y, Nagata Y (1999) Sonochemical preparation of size-controlled palladium nano-particles on alumina surface. Chem Lett 28:271–272
33. Okitsu K, Yue A, Tanabe S, Matsumoto H (2002) Formation of palladium nanoclusters on Y-zeolite via a sonochemical process and conventional methods. Bull Chem Soc Jpn 75:449–455
34. Wittstock A, Zielasek V, Biener J, Friend CM, Bäumer M (2010) Nanoporous gold catalysts for selective gas-phase oxidative coupling of methanol at low temperature. Science 327(5963):319–322
35. Ma Z, Dai S (2011) Design of novel structured gold nanocatalysts. ACS Catalysis 1(7):805–818
36. Corma A, Garcia H (2008) Supported gold nanoparticles as catalysts for organic reactions. Chem Soc Rev 37:2096–2126
37. Liu C-Y, Tseng W-L (2011) Colorimetric assay for cyanide and cyanogenic glycoside using polysorbate 40-stabilized gold nanoparticles. Chem Commun 47(9):2550–2552
38. Xie J, Zheng Y, Ying JY (2010) Highly selective and ultrasensitive detection of Hg^{2+} based on fluorescence quenching of Au nanoclusters by Hg^{2+}-Au^{+} interactions. Chem Commun 46(6):961–963
39. Rodríguez-Lorenzo L, Álvarez-Puebla RA, De Abajo FJG, Liz-Marzán LM (2010) Surface enhanced Raman scattering using star-shaped gold colloidal nanoparticles. J Phys Chem C 114(16):7336–7340
40. Nagata Y, Mizukoshi Y, Okitsu K, Maeda Y (1996) Sonochemical formation of gold particles in aqueous solution. Radiat Res 146:333–338
41. Murphy PJ, LaGrange MS (1998) Raman spectroscopy of gold chloro-hydroxy speciation in fluids at ambient temperature and pressure: a re-evaluation of the effects of pH and chloride concentration. Geochim Cosmochim Acta 62(21–22):3515–3526
42. Haiss W, Thanh NTK, Aveyard J, Fernig DG (2007) Determination of size and concentration of gold nanoparticles from UV-Vis spectra. Anal Chem 79(11):4215–4221
43. Subhramannia M, Pillai VK (2008) Shape-dependent electrocatalytic activity of platinum nanostructures. J Mater Chem 18(48):5858–5870
44. Chen A, Holt-Hindle P (2010) Platinum-based nanostructured materials: synthesis, properties, and applications. Chem Rev 110(6):3767–3804
45. Ratnasamy C, Wagner J (2009) Water gas shift catalysis. Catalysis Rev Sci Engin 51(3):325–440
46. Mizukoshi Y, Oshima R, Maeda Y, Nagata Y (1999) Preparation of platinum nanoparticles by sonochemical reduction of the Pt(II) ion. Langmuir 15(8):2733–2737
47. Mizukoshi Y, Takagi E, Okuno H, Oshima R, Maeda Y, Nagata Y (2001) Preparation of platinum nanoparticles by sonochemical reduction of the Pt(IV) ions: role of surfactants. Ultrason Sonochem 8(1):1–6
48. Stamplecoskie KG, Scaiano JC, Tiwari VS, Anis H (2011) Optimal size of silver nanoparticles for surface-enhanced raman spectroscopy. J Phys Chem C 115(5):1403–1409
49. Shang L, Dong S (2008) Silver nanocluster-based fluorescent sensors for sensitive detection of Cu(II). J Mater Chem 18(39):4636–4640
50. Guo W, Yuan J, Wang E (2009) Oligonucleotide-stabilized Ag nanoclusters as novel fluorescence probes for the highly selective and sensitive detection of the Hg^{2+} ion. Chem Commun 23:3395–3397
51. Nagata Y, Watanabe Y, Fujita S, Dohmaru T, Taniguchi S (1992) Formation of colloidal silver in water by ultrasonic irradiation. J Chem Soc Chem Commun 1992:1620–1622
52. Okitsu K (1993) unpublished result
53. Salkar RA, Jeevanandam P, Aruna ST, Koltypin Y, Gedanken A (1999) The sonochemical preparation of amorphous silver nanoparticles. J Mater Chem 9(6):1333–1335
54. Zhu Y-P, Wang X-K, Guo W-L, Wang J-G, Wang C (2010) Sonochemical synthesis of silver nanorods by reduction of sliver nitrate in aqueous solution. Ultrason Sonochem 17(4):675–679

55. Xu H, Suslick KS (2010) Sonochemical synthesis of highly fluorescent Ag nanoclusters. ACS Nano 4:3209–3214
56. Liu H, Zhang X, Wu X, Jiang L, Burda C, Zhu J-J (2011) Rapid sonochemical synthesis of highly luminescent non-toxic AuNCs and Au@AgNCs and Cu (ii) sensing. Chem Commun 47(14):4237–4239
57. Thackeray MM (1997) Manganese oxides for lithium batteries. Progr Solid State Chem 25(1–2):1–71
58. Zhu S, Zhou H, Hibino M, Honma I, Ichihara M (2005) Synthesis of MnO_2 nanoparticles confined in ordered mesoporous carbon using a sonochemical method. Adv Funct Mater 15(3):381–386
59. Fischer AE, Pettigrew KA, Rolison DR, Stroud RM, Long JW (2007) Incorporation of homogeneous, nanoscale MnO_2 within ultraporous carbon structures via self-limiting electroless deposition: Implications for electrochemical capacitors. Nano Lett 7(2):281–286
60. Dong X, Shen W, Gu J, Xiong L, Zhu Y, Li H, Shi J (2006) MnO_2-embedded-in-mesoporous-carbon-wall structure for use as electrochemical capacitors. J Phys Chem B 110(12): 6015–6019
61. Fujimoto T, Mizukoshi Y, Nagata Y, Maeda Y, Oshima R (2001) Sonolytical preparation of various types of metal nanoparticles in aqueous solution. Scr Mater 44(8–9):2183–2186
62. Sostaric JZ, Mulvaney P, Grieser F (1995) Sonochemical dissolution of MnO_2 colloids. J Chem Soc Faraday Trans 91(17):2843–2846
63. Mulvaney P, Cooper R, Grieser F, Meisel D (1990) Kinetics of reductive dissolution of colloidal manganese dioxide. J Phys Chem 94(21):8339–8345
64. Baral S, Lume-Pereira C, Janata E, Henglein A (1985) Chemistry of colloidal manganese dioxide. 2. Reaction with O_2^- and H_2O_2 (pulse radiolysis and stop flow studies). J Phys Chem 89(26):5779–5783
65. Bowman MI (1949) The reaction between potassium permanganate and hydrogen peroxide. J Chem Educ 26(2):103–104
66. Mizukoshi Y, Okitsu K, Maeda Y, Yamamoto TA, Oshima R, Nagata Y (1997) Sonochemical preparation of bimetallic nanoparticles of gold/palladium in aqueous solution. J Phys Chem B 101(36):7033–7037
67. Okitsu K, Murakami M, Tanabe S, Matsumoto H (2000) Catalytic behavior of Au core / Pd shell bimetallic nanoparticles on silica prepared by sonochemical and sol-gel processes. Chem Lett 29(11):1336–1337
68. Mizukoshi Y, Fujimoto T, Nagata Y, Oshima R, Maeda Y (2000) Characterization and catalytic activity of core-shell structured gold/palladium bimetallic nanoparticles synthesized by the sonochemical method. J Phys Chem B 104(25):6028–6032
69. Nakagawa T, Nitani H, Tanabe S, Okitsu K, Seino S, Mizukoshi Y, Yamamoto TA (2005) Structural analysis of sonochemically prepared Au/Pd nanoparticles dispersed in porous silica matrix. Ultrason Sonochem 12(4):249–254
70. Pritchard JC, He O, Ntainjua EN, Piccinini M, Edwards JK, Herzing AA, Carley AF, Moulijn JA, Kiely CJ, Hutchings GJ (2010) The effect of catalyst preparation method on the performance of supported Au–Pd catalysts for the direct synthesis of hydrogen peroxide. Green Chem 12(5):915–921
71. Xu J, White T, Li P, He C, Yu J, Yuan W, Han Y-F (2010) Biphasic Pd-Au alloy catalyst for low-temperature CO oxidation. J Am Chem Soc 132(30):10398–10406
72. Huang X, El-Sayed IH, Qian W, El-Sayed MA (2006) Cancer cell imaging and photothermal therapy in the near-infrared region by using gold nanorods. J Am Chem Soc 128(6):2115–2120
73. Zijlstra P, Chon JWM, Gu M (2009) Five dimensional optical recording mediated by surface plasmons in gold nanorods. Nature 459:410–413

74. Okitsu K, Sharyo K, Nishimura R (2009) One-pot synthesis of gold nanorods by ultrasonic irradiation: the effect of pH on the shape of the gold nanorods and nanoparticles. Langmuir 25(14):7786–7790
75. Jana NR, Gearheart L, Murphy CJ (2001) Wet chemical synthesis of high aspect ratio cylindrical gold nanorods. J Phys Chem B 105(19):4065–4067
76. Nikoobakht B, El-Sayed MA (2003) Preparation and growth mechanism of gold nanorods (NRs) using seed-mediated growth method. Chem Mater 15(10):1957–1962

Size-Dependent Optical Properties of Metallic Nanostructures

5

Lucía B. Scaffardi, Daniel C. Schinca, Marcelo Lester, Fabián A. Videla, Jesica M. J. Santillán, and Ricardo M. Abraham Ekeroth

Contents

1 Definition of the Topic

Metallic nanostructures are a key component of current and future nanotechnology devices since their individual properties convey the appropriate characteristics for applications in several fields of science and technology. At the nanoscale size,

L.B. Scaffardi (✉) • D.C. Schinca • F.A. Videla • J.M.J. Santillán
Centro de Investigaciones Ópticas (CIOp), CONICET La Plata-CIC, La Plata, Argentina

Departamento de Ciencias Básicas, Facultad de Ingeniería, Universidad Nacional de La Plata, La Plata, Argentina

M. Lester • R.M.A. Ekeroth
Grupo de Óptica de Sólidos-Elfo, Centro de Investigaciones en Física e Ingeniería del Centro de la Provincia de Buenos Aires – Instituto de Física Arroyo Seco, Facultad de Ciencias Exactas, Universidad Nacional del Centro de la Provincia de Buenos Aires, Buenos Aires, Argentina

Consejo Nacional de Investigaciones Científicas y Técnicas CONICET, Buenos Aires, Argentina

Challa S.S.R. Kumar (ed.), *UV-VIS and Photoluminescence Spectroscopy for Nanomaterials Characterization*, DOI 10.1007/978-3-642-27594-4_5,

optical properties of metal structures depend not only on the type of material but also on the dimensions and geometry of the structure, suggesting the possibility of tuning optical resonances through appropriate engineering. In this chapter, we will describe methods for calculation of size-dependent optical properties of metal nanostructures and show the successful use of extinction spectroscopy technique to determine the size of nanoparticles (Np/Nps).

2 Overview

From a classical point of view, the optical properties of materials are condensed in the so-called constitutive parameters, namely, the electric permittivity and the magnetic permeability. Particularly, the dielectric function condenses the averaged response of the constitutive electrons of matter to an externally applied electric field. If this electric field varies in time, the dielectric function not only integrates the electron characteristics of the specific material but it will also depend on the frequency of the incoming field.

For metals at the nanoscale, the dielectric function behaves differently from its macroscopic (bulk) counterpart, since the electrons start to show confinement effects. This behavior includes an explicit dependence on particle size. In turn, the optical absorption, scattering, and extinction cross sections are functions of the metal dielectric function, thus translating the size dependence to the optical properties of the metallic nanostructure.

In this chapter, we overview the contribution of free and bound electrons to the metal dielectric function and apply different theoretical approaches to the calculation of optical extinction spectra of nanowires, nanotubes, and bare and core-shell nanoparticles. We then apply these results to fit experimental extinction spectra and determine the size of nanostructures which compare very well with high-resolution TEM.

3 Introduction

The developments in the nanotechnology area have been undoubtedly one of the greatest achievements of science in the late twentieth century. The particular interest in understanding the physical and chemical phenomena associated with nanoscale systems (clusters of several tends of atoms up to systems with characteristic distances of small fractions of a micron) is mainly due to its high technological potential. Nanotechnology has found wide applications in broad interdisciplinary science fields. We found significant developments in the biomedicine area, lasers, communications, and medical physics, to name a few.

This increasing trend toward nanoscience and nanotechnology makes it inevitable to study the optical properties and electromagnetic response (near and far field, resonances) on the nanometer scale. In particular, over the last two decades, the interest in metallic clusters, metallic nanoparticles (core-shell systems, nanowires), and systems with nanometric details has grown significantly ([1–15], and therein).

The term "nanoparticle" includes from small clusters, size range around 1 nm (tens of atoms), up to particles consisting of hundreds of thousands of atoms (or even greater) and having a diameter in the range of tens to hundreds of nanometers. In the literature, this kind of material has long been known as colloids, generally applied to suspensions of metal particles in an aqueous medium. In fact, colloidal gold has been used as a coloring pigment dating back to the Middle Ages [7].

The excitation at optical frequencies of "eigenmodes" (surface plasmon resonances in metallic nanoparticles, whispering gallery modes in the dielectric spheres, and other resonant phenomena) is probably one of the most spectacular electromagnetic effects in nanosystems. In particular, plasmon resonances lead to extremely strong fields in the vicinity of a nanoparticle. Such fields play, for example, a key role in surface-enhanced Raman scattering, wherein the Raman signal of a molecule deposited on the nanoparticle is enhanced by several orders of magnitude [16]. This enhancement can be large enough that the Raman spectrum of a single molecule can be detected [17, 18].

The large extinction cross section associated with plasmon resonances also produces a strong signal in the far field. This observation is the key to detect and investigate optical properties of nanoscopic particles. Plasmon resonance occurs for specific wavelengths and gives the particles ensemble its color. These resonance frequencies are sensitive not only to particle size but also its shape. The properties of the metal particles were used during the Middle Ages for the design of colored glass. This was mostly an empirical art, close to alchemy, where the relation between the metallic particle shape and its color (its spectrum of plasmon resonances as it is called today) was only known by the master glass-makers. In the nineteenth century, Faraday noted that there must be a relationship between the ruby red color of a colloidal gold suspension and the presence of aggregates of metal atoms, although he had no means of analyzing the size of these metallic nanoparticles by modern analytical techniques such as transmission electron microscopy (TEM).

The theoretical investigation of this problem remained however extremely limited. The exact treatment of the problem of scattering of electromagnetic waves by particles is limited only to a few very simple geometries such as spheres or ellipsoids in 3D, or a nanowire with a cylindrical or elliptical section in 2D [19–24]. In general, for simple situations, it can be solved using Mie theory or related semi-analytical techniques. Recently, through discrete dipole approximation or finite element approaches, it is possible to calculate the electromagnetic interaction between particles of different shapes and sizes. However, these calculations become very difficult when the particle size is smaller than 20 nm, extremely rapid variations of the field occur on very short distances. Using these techniques to study the resonance spectra of silver nanowires with a non-regular cross section, it was shown that nanowires had a complex spectrum, with many different resonances [25]. In particular, triangular wires seem to produce the most complex spectrum, as it was demonstrated in [26, 27], where nanowires with different convex polygonal sections were systematically investigated.

An interesting question that arises when studying the interaction of electromagnetic waves with nanoscale systems is about the validity of Maxwell's equations for these scales. The constitutive parameters characterize completely the system, but they are calculated for "macroscopic bodies." They represent an averaging of quantum phenomena that occur during the interaction over a large number of atoms to achieve an adequate bulk representation.

In general, for metals with characteristic dimensions on the order of the wavelength or larger, the bulk atoms contribute mainly to the dielectric function. For example, for systems with few cubic millimeters, the relationship between surface atoms and bulk atoms is less than 10^{-3}. When the volume is a few tens of nanometers, the relationship is about 0.1. However, for systems with few nanometers of characteristic dimensions, all atoms can be considered like surface atoms.

For these nanoscale systems, where optical properties are governed by surfaces effects (especially metals and semiconductors), an adjustment of the constitutive parameters with size is essential to maintain the validity of the classical equations. This chapter presents a review of a theoretical model to correct the constitutive parameters with system size, focusing on outlining the physical principles involved in the interaction of electromagnetic waves with nanometric systems. In the different sections, we will show results of several research groups, including ours, about the behavior of the dielectric function in the UV-visible to near-IR (infrared) range appropriately corrected for few nanoscopic dimensions, as well as its applications to sizing for different 2D and 3D nanostructures. We will focus on studying dilute clusters of particles (average distance between particles of some wavelengths) with revolution symmetry such as nanospheres, nanowires, metallic core-shell spheres, and metallic nanotubes, where the thicknesses of the metal layers are of a few nanometers. In this way, the dielectric function will not only depend on the frequency of the electromagnetic wave but also on the characteristic dimensions of the nanoscale systems [16]. One of the main challenges at theoretical level is the correct description of the optical parameters of systems with nanometric scale. This parameterization of the dielectric function with the size allows describing the optical response of the system under study with a macroscopic quasi-classic model, based on Maxwell's equations.

In this study, there are two kinds of approaches: One is the top-down approach, in which the study of the nanostructures is reached from the bulk, and the other is the bottom-up approach, where the analysis starts from the atoms toward large clusters.

We analyze at this point, the behavior of the dielectric function for different sizes, starting from experimental bulk values toward smaller sizes up to subnanometric nanoparticles.

4 Experimental and Instrumental Methodology

4.1 Experimental Extinction Spectroscopy

Traditional methods for nanoparticle sizing are based on optical or electron microscopy. These methods have, in many cases, drawbacks concerning the preparation of

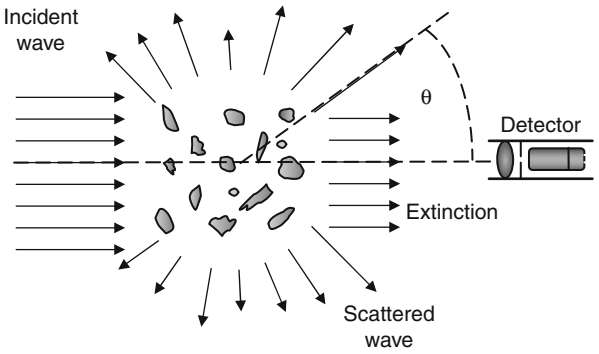

Fig. 5.1 Schematic for definition of extinction and scattering processes by an ensemble of particles

the sample or poor statistics. Optical spectroscopic techniques are often more suitable since measurements can be made without sample treatment, data acquisition can be very fast, they may be implemented for in situ analysis, and they are an excellent complement to electron microscopy.

Spectral extinction is one of these techniques which can be readily implemented using a commercial spectrophotometer. It is a very simple and suitable technique for sizing particles in the micron and submicron range, where it can be put in parallel with transmission electronic microscopy (TEM) and scanning electronic microscopy (SEM). Spectral extinction can be easily performed for dielectric [28, 29] and metallic nanoparticles [16, 25, 30–42] in diluted liquid suspensions. Figure 5.1 pictures a possible setup of the situation. When the detector is placed in the direction of the incident light, after the ensemble, it will measure an energy flux per unit area which is smaller than the power of the incoming wave.

Experimental results are fitted by Mie calculations (see Sect. 5.3.4) for spherical particles, where knowledge of the refractive index as a function of the wavelength for both the particle material and the solvent is necessary. For the metal dielectric function used in this Mie calculation, it is necessary to include the modifications for size for the free and bound electron contribution described in Sect. 5.1.

Spectrophotometers measure the extinction of light that is the fraction of light removed from the incident beam. Operatively, extinction can be derived from the relation given by the Lambert–Beer law:

$$I_t = I_i \exp\left(-\beta_{ext}\, l\right) \tag{5.1}$$

where I_i is the intensity incident over the sample, I_t is the transmitted irradiance, β_{ext} is the attenuation coefficient, and l is the length of the sample. When the dilution of the sample is such that the average interparticle distance in the medium is large enough so that incoherent scattering can be considered, it is possible to relate the attenuation coefficient of a sample of N particles per unit volume, with the single-particle cross section C_{ext}:

$$\beta_{ext} = N\, C_{ext} \tag{5.2}$$

When a set of measurements of I_t/I_i are performed over a range of wavelengths, the so-called extinction spectra is obtained. Results can be compared with the calculated spectral extinction efficiency, Q_{ext} (λ), for a given medium refractive index and for a given nanoparticle radius, which is used as fitting parameter. This spectral signature has information of the chemical composition of the sample as well as the size and distribution of sizes of the particles.

In general, samples consist of an ensemble of particles with a certain size distribution suspended in some liquid. To determine this distribution of radii, extinction measurements at a discrete set of wavelengths may be conducted, a method that is called multispectral extinction. Inversion of the experimental results should retrieve, in principle, the different radii values, although this is not a trivial task, since, in general, the scattering matrix is ill conditioned and a nonlinear inversion algorithm must be used to solve the problem.

For the case of large particles (compared with wavelength), when scattering is almost forward and the light can reach the detector, the measurement is not a pure extinction (scattering plus absorption) but an intermediate between absorption and extinction. Experimental results may be strongly altered unless special care is taken to avoid the unwanted forward-scattered light from reaching the detector. A small diameter pinhole placed at a suitable position between the sample and the detector will help enhance the reliability of the measurements. As the size of dielectric particles becomes smaller than the wavelength, the scattering spectrum smoothens its features and the spectral extinction technique loses gradually its power, thus making it an unsuitable method for measuring particles with mean radius below about 200 nm. However, it is interesting to notice that metal particles constitute one important exception to the rule mentioned above because their extinction spectra present clear size effects for radius well below the wavelength. For this reason, colloidal solutions of noble metals, like copper, gold, and silver, present intense color that is absent in bulk material. This behavior is due to surface modes, a class of electromagnetic modes that can couple light to particles in a very efficient way, as will be discussed in the next sections.

4.2 Experimental Fabrication and Fragmentation by Laser Ablation

The metal nanostructures which this chapter deals with were generated either by wet chemistry or by ultrashort pulse laser-based ablation methods. The former is extensively treated in the literature and will not be discussed here. The latter is centered in ablation of solid targets immersed in a cell with an appropriate liquid. Fabrication was performed focusing the laser beam over a sample of 1-cm diameter, which is placed over a PC controlled X-Y-Z translation stages with micrometer accuracy. The laser system was a Spectra Physics 100 fs pulse 800 nm wavelength Ti:Sa chirped amplified laser of 1 mJ pulse energy and 1 kHz repetition rate. After a few seconds of ablation, the liquid showed a typical coloring according to the ablated metal. Figure 5.2 shows the setup used to fabricate different metal Nps in solution with IR fs laser.

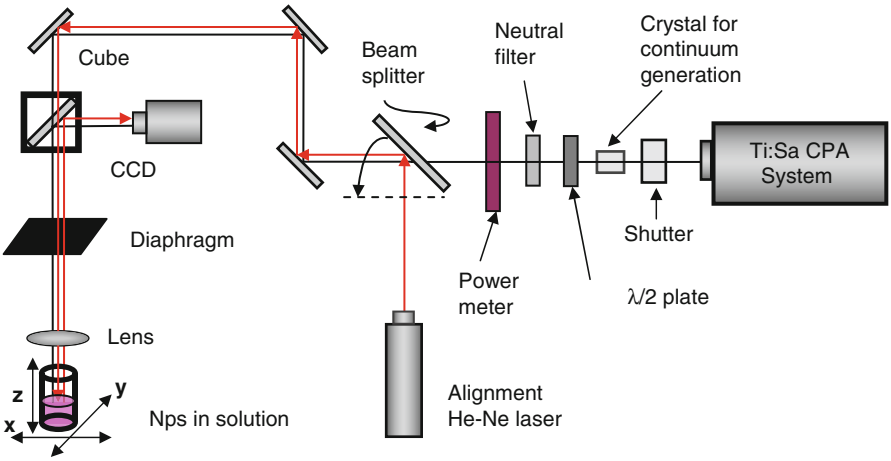

Fig. 5.2 Setup used to fabricate gold Nps in solution with IR fs laser and to perform fragmentation with SC generated using an external sapphire crystal

The second step consists in the fragmentation of the sample obtained before. This fragmentation process was carried out using two different sources of supercontinuum (SC) radiation: (1) SC produced by an external sapphire crystal and (2) SC produced by IR fs pulses in the same liquid solution. In both cases, radiation was applied to the solution during 30 min. This process enables to reach sizes of radius less than 2 nm. In the first case, the SC generated in the external sapphire crystal was focused on Nps solution to analyze the effect on size distribution after light interaction. A suitable IR cutoff filter could be inserted before the sample to filter out the 800-nm fundamental radiation [37, 38].

In the second case, fragmentation is carried out using the same setup, removing the sapphire crystal and the solid gold disk from the sample and leaving only the Nps solution. In this case, the IR radiation cannot be separated from the SC light generated in water. To characterize the size of gold Nps in water, optical extinction measurements in the 300–700 nm range by means of a commercial spectrophotometer were conducted.

5 Key Research Findings

5.1 About the Dielectric Functions of Metals

The optical parameters of metals determine many macroscopic characteristics such as shiny aspect and opacity to transmitted visible light. The reflection and transmission coefficients of light for different wavelength ranges may be described based on these optical parameters which, in turn, can be understood by assuming a simple model to characterize the microscopic structure of matter.

The electromagnetic response of matter is described by a frequency-dependent complex dielectric function, $\varepsilon(\omega) = \varepsilon'(\omega) + i\varepsilon''(\omega)$, which relates the value of the electric field $\vec{E}(\omega)$ with the displacement field $\vec{D}(\omega)$. The dielectric function for nanometric systems is not only a function of the wavelength (or frequency) of the incident radiation but also is sensitive to the size and shape of the particle [43–45]. As it was shown in the works of E. Coronado [43] and J. Kottmann [44], variations in the imaginary part of the dielectric function lead to dramatic changes in the optical response for nanoparticles and nanowires with asymmetric profiles.

The expression of the dielectric function for a nanoscopic particle is not trivial. Different approaches such as the jellium or quantum-chemistry models [16, 46, 47] may be used based on considerations related to electron collective behavior or in first principles calculations, respectively. However, if suitable and physically meaningful corrections are made, the classical concept of dielectric function can be extended down to nanometer sizes. This approach yields results that fit satisfactorily experimental data while giving physical insight about the electronic processes that give rise to macroscopic measurable parameters.

In general, this complex dielectric function for bulk metals can be decomposed into two terms, a complex free electron term and a complex interband (or bound electron) term. Since the dielectric function is additive [48], it can be written as:

$$\varepsilon(\omega) = \varepsilon_{free-electrons}(\omega) + \varepsilon_{bound-electrons}(\omega) = \varepsilon'(\omega) + i\varepsilon''(\omega)$$

So, real and imaginary parts of dielectric function have contributions from both complex free and bound electrons. In the following paragraphs, we will discuss briefly the separate contributions, introducing for each one an appropriate size dependence and will compare the results with available experimental data on real and imaginary parts of noble metal dielectric function. We will also analyze the influence of these size dependences on the optical extinction spectra of nanometric and subnanometric particles.

5.1.1 Free Electron Contribution

In order to model this response, a microscopic picture of matter is needed. One of the most basic models is the so-called Lorentz model, which assumes matter composed of electrons and ions as a collection of independent, identical, isotropic, and damped charged harmonic oscillators. So, optical properties are a consequence of the way in which these oscillators respond to electromagnetic fields.

For this model [49], the relative dielectric function ε defined as $\varepsilon = \in/\varepsilon_0$, corresponding to a collection of N damped harmonic oscillators per unit of volume, each with resonant frequency ω_0, can be written as:

$$\varepsilon = 1 + \frac{\omega_p^2}{\omega_0^2 - \omega^2 - i\gamma\omega}, \tag{5.3}$$

where $\omega_p^2 = N^* e^2/me_0$, e and m are the charge and mass of the electron, ε_0 is the permittivity of vacuum, and γ is the damping constant of the oscillators. For metals,

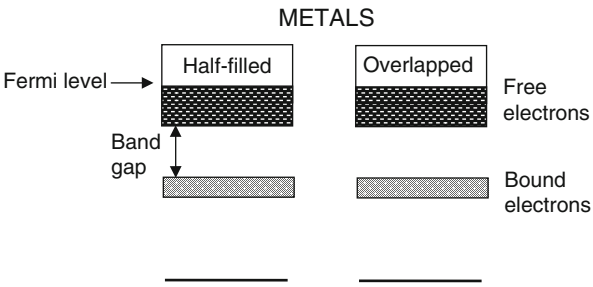

Fig. 5.3 Simplified electrons energy bands of solid metals

N^* is the density of free or conduction electrons that, in general, corresponds to one, two, or three electrons per atom.

Optical properties of materials are alternatively described by two sets of quantities: the real and imaginary parts of the complex refractive index, $N = n + ik$ or the real and imaginary parts of the dielectric function $\varepsilon = \varepsilon' + i\varepsilon''$. For nonmagnetic media, the relation $N = \sqrt{\varepsilon}$ holds. So, the real and imaginary parts of both parameters are related by:

$$\varepsilon' = n^2 - k^2, \tag{5.4}$$

$$\varepsilon'' = 2\,n\,k. \tag{5.5}$$

The energy states of electrons in solid materials may be represented by a nearly continuum energy levels grouped into different bands. For metals, the upper occupied band is partially filled with electrons or completely filled and overlapped with an upper empty band, as shown in a simplified form in Fig. 5.3.

Electrons in bulk metals are considered essentially "free" since they can be promoted to higher empty energy levels (from the top of the energy distribution, near the Fermi level) with very small photon energies. In this sense, it can be considered that they are not bound to the ion core, so their resonant frequency may be set equal to zero in the Lorentz model [50 (a, b)]. Therefore, the expression for the dielectric function of a "free electron metal" can be obtained according to the Drude Sommerfeld model, by putting $\omega_0 = 0$ in Eq. 5.3:

$$\varepsilon_{free}(\omega) = 1 - \frac{\omega_p^2}{\omega^2 + i\omega\,\gamma_{free}}, \tag{5.6}$$

with real and imaginary parts given by:

$$\varepsilon'_{free}(\omega) = 1 - \frac{\omega_p^2}{\omega^2 + \gamma_{free}^2}, \tag{5.7}$$

$$\varepsilon''_{free}(\omega) = \frac{\omega_p^2\,\gamma_{free}}{\omega\left(\omega^2 + \gamma_{free}^2\right)}. \tag{5.8}$$

The plasma frequency ω_p lies in the ultraviolet region of the spectrum and $\hbar\omega_p$ ranges from 4 to 20 eV. In the bulk metal, the damping constant γ_{free}, has a simple physical interpretation in terms of the average total time τ between collisions of free electrons with other electrons (electron–electron scattering), lattice vibrations (electron–phonon scattering), and imperfections. It can be expressed as:

$$\gamma_{free}^{bulk} = \frac{1}{\tau} = \frac{1}{\tau_{el-el}} + \frac{1}{\tau_{el-ph}} + \frac{1}{\tau_{im}} \tag{5.9}$$

For nanoparticles smaller than the electron mean free path (a few tens of nanometers for bulk metals), scattering of electrons with the particle's boundaries (surfaces) becomes important. This process reduces the electron mean free path, which in turn leads to an increase in the imaginary part of the dielectric function. This has been evidenced experimentally for spherical particles [16, 51–54]. In these works, it is shown that for particle sizes below 10 nm, the resonance width becomes broader.

To account for this fact, it is necessary to include an additive term in Eq. 5.9 which must be inversely proportional to the average time between collisions of the electrons with the boundary of the particle, $\frac{1}{\tau_r} = C\,\frac{v_F}{r}$, where v_F is the velocity of the electrons at the Fermi level and r is the radius of the nanoparticle. The proportionality constant C accounts for the details of the electron scattering processes at the boundary and may be calculated from electrodynamic theory or quantum box model [55 (a–d)]. For spheres, its value ranges from 0.75 to 1.15 [51].

With these considerations, a size-dependent damping constant may be introduced and expressed as:

$$\gamma_{free}^{size} = \gamma_{free}^{bulk} + C\frac{v_F}{r} \tag{5.10}$$

The second term of Eq. 5.10 becomes negligible for large radii r, and the size damping constant tends to the bulk value. When γ_{free} is replaced by the size-dependent expression of Eq. 5.10, Eqs. 5.7 and 5.8 take the form:

$$\varepsilon'_{free}(\omega,\ r) = 1 - \frac{\omega_p^2}{\omega^2 + \left(\gamma_{free}^{size}\right)^2} \tag{5.11}$$

$$\varepsilon''_{free}(\omega,\ r) = \frac{\omega_p^2\,\gamma_{free}^{size}}{\omega\left(\omega^2 + \left(\gamma_{free}^{size}\right)^2\right)} \tag{5.12}$$

Using Eqs. 5.11 and 5.12, a set of curves for different radii values can be obtained for the real and imaginary parts of the dielectric function. Figure 5.4 shows an example for the case of gold (Au), when it is plotted against wavelength.

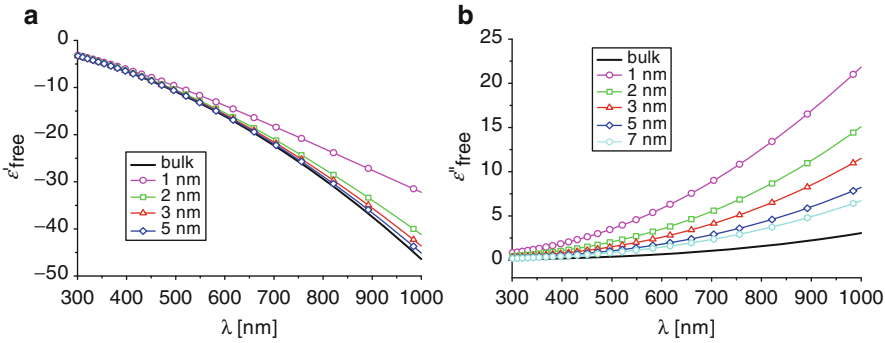

Fig. 5.4 Real (**a**) and imaginary (**b**) part of free electron contribution to the dielectric function for gold. Values used are: $C = 0.8$, $v_F = 14.1 \times 10^{14}$ nm/s Granqvist and Hunderi [56]

It can be seen that, as expected, each set of curves tends to a common wavelength-dependent curve (bulk) as the radius increases but presents clear differences for sizes between 1 and 10 nm, approximately, depending on the metal. It is clear then that it is possible to reproduce bulk values of the dielectric function by simply calculating Eqs. 5.11 and 5.12 for a radius close to 100 nm, since for these sizes, the second term in Eq. 5.10 is negligible. In this free electron approximation, all noble metals (Au, Ag, and Cu) behave alike and their dielectric functions are very similar, except for small differences arising from the different plasma frequency values.

5.1.2 Bound Electron Contribution (Bulk)

As it was mentioned at the beginning of Sect. 5.1, the complete expression for the complex dielectric function is made up by a free electron component and a bound electron component:

$$\varepsilon(\omega) = \varepsilon_{free}(\omega) + \varepsilon_{bound}(\omega) = \varepsilon'(\omega) + i\varepsilon''(\omega) \tag{5.13}$$

where $\varepsilon_{free}(\omega)$ can be made size-dependent through the Eqs. 5.11 and 5.12.

In a first approximation, the bound contribution may be considered non-size dependent. Its value may be determined from subtracting $\varepsilon_{free}(\omega)$ from the bulk experimental data $\varepsilon(\omega)$ taken from Palik or Johnson and Christy [57, 58] such as indicated in Eq. 5.13. For Nps with size smaller than 10 nm, the full complex dielectric function depends on size ($\varepsilon(\omega, r)$), and can be written as:

$$\varepsilon(\omega, r) = \varepsilon_{free}(\omega, r) + \varepsilon_{bound}(\omega) \tag{5.14}$$

where $\varepsilon_{free}(\omega, r)$ can be calculated by Eqs. 5.11 and 5.12.

Figures 5.5, 5.6, and 5.7 shows both the real and imaginary parts of dielectric function for Ag, Au, and Cu, respectively for bulk [58], and corrections for different radius of Nps calculated from Eq. 5.14.

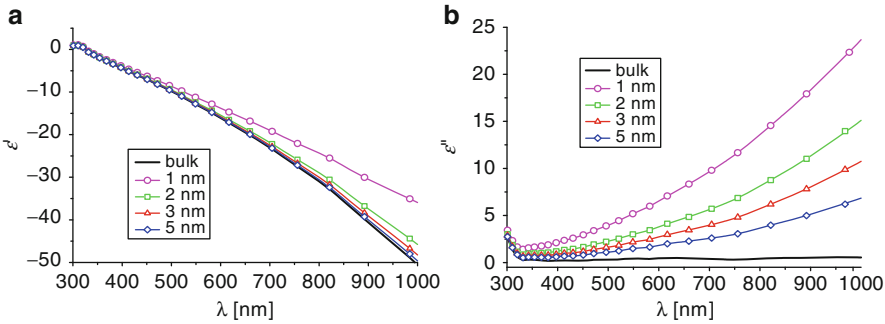

Fig. 5.5 Real (**a**) and imaginary part (**b**) for Ag dielectric function. In *black*, experimental bulk dielectric function [58]. In *color*, correction for a particle from 5 to 1 nm of radii [25]. See the panel for details

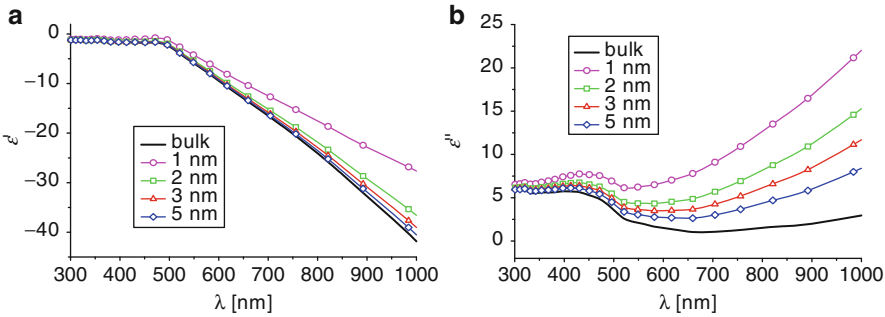

Fig. 5.6 Real (**a**) and imaginary part (**b**) for Au dielectric function. In *black*, experimental bulk values [58]. In *color*, correction for particles from 5 to 1 nm of radii [59]. See the panel for details

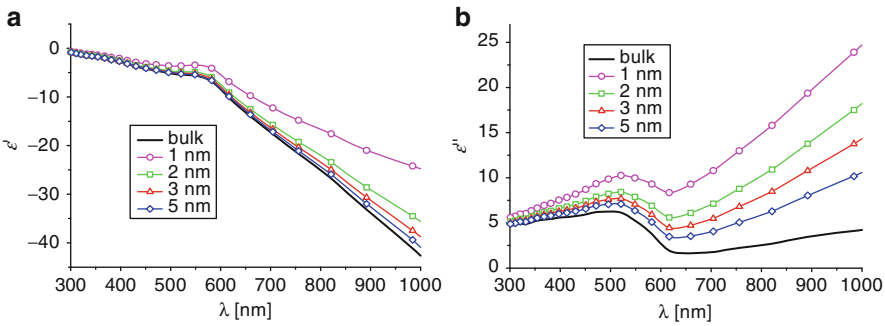

Fig. 5.7 Real (**a**) and imaginary part (**b**) for Cu dielectric function. In *black*, experimental bulk values [58]. In *color*, correction for particles from 5 to 1 nm of radii. See the panel for details

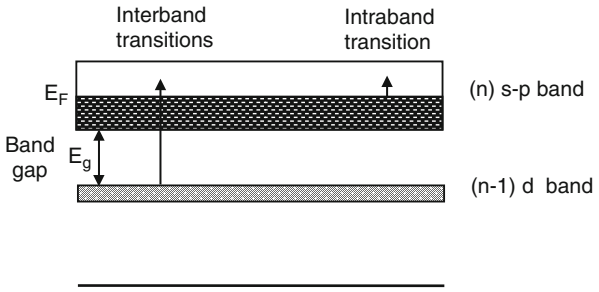

Fig. 5.8 Simplified electrons energy bands of noble metals

The real part shows an abrupt change of slope that is located at different wavelengths depending on the noble metal. The influence of bound electron is clearly associated for wavelengths smaller than the point of slope change. This is more dramatically evidenced in the behavior of the imaginary part, which shows a widened resonance at short wavelengths.

5.1.3 Bound Electron Contributions (Single Transition)

When the energy of the incoming photon is large enough to overcome the bandgap and promote valence (bound) electrons to the conduction band of the material, these electrons will add its contributions to the dielectric function. These kinds of transitions are called electronic interband transitions.

Figure 5.8 shows a simplified diagram for electrons energy bands of a noble metal at zero Kelvin. As *s-p* band is filled up to the Fermi energy, interband transitions can occur over a threshold energy value ($E_g + E_F$). Intraband transitions which correspond to free electrons can be excited with low energy photons.

The Drude model described above takes into account only electrons in the outer atomic orbitals (for example, 5s, 6s, and 4s states for silver, gold, and copper, respectively). However, interband transitions, such as the one from the 5d-band to the 6sp-band in gold, cannot be ignored when the incident light frequency falls in the visible region. This effect can be taken into account in ${\epsilon^L}_{bound}(\omega)$ by means of a standard Lorentz-like equation [4, 43, 61]:

$$ {\epsilon^L}_{bound}(\omega) = 1 + \frac{{\omega'_p}^2}{\left(\omega_0^2 - \omega^2\right) - i\gamma_{bound}\,\omega} \tag{5.15} $$

where ω'_p is introduced in analogy to the plasma frequency in the Drude model, γ_{bound} is the damping constant for the bound electron, and ω_0 is the resonance

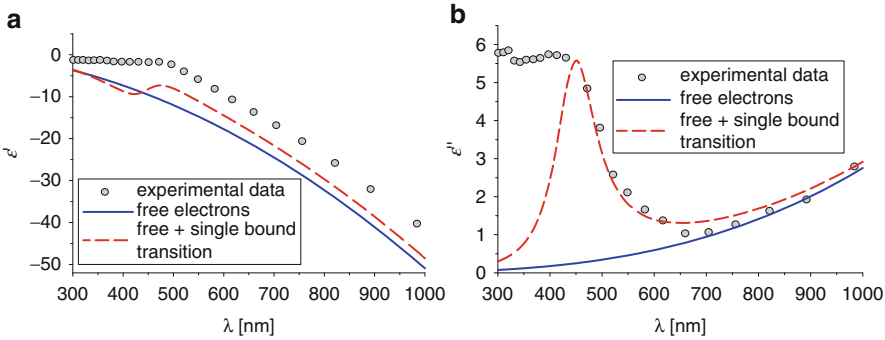

Fig. 5.9 Real (**a**) and imaginary (**b**) parts of the dielectric function for Au. *Open circles* correspond to the experimental bulk dielectric function from Johnson and Christy [58]. *Solid line*, free electron contribution for a bulk size; *dashed line*, free plus single bound electron contribution, also for a bulk size. Values used are: $\omega_0 = 4.19 \times 10^{15}$ Hz, $\omega'_p = 4.48 \times 10^{15}$ Hz and $\gamma_{\text{bound}} = 8.95 \times 10^{14}$ Hz [61]

frequency of the bound electron under the applied electric field. The real and imaginary parts are given by:

$$\varepsilon'^{L}{}_{bound}(\omega) = 1 + \frac{\omega'_p{}^2\left(\omega_0^2 - \omega^2\right)}{\left(\omega_0^2 - \omega^2\right)^2 + \gamma_{bound}^2\,\omega^2} \tag{5.16}$$

$$\varepsilon''^{L}{}_{bound}(\omega) = \frac{\omega'_p{}^2\gamma_{bound}\,\omega}{\left(\omega_0^2 - \omega^2\right)^2 + \gamma_{bound}^2\,\omega^2} \tag{5.17}$$

Since the dielectric function is additive, the complex expression can be written as:

$$\begin{aligned}\varepsilon(\omega,\ r) &= \varepsilon_{free}(\omega,\ r) + \varepsilon^{L}{}_{bound}(\omega) \\ &= 1 - \frac{\omega_p^2}{\omega^2 + i\omega\,\gamma_{free}^{size}(r)} + 1 + \frac{\omega'_p{}^2}{\left(\omega_0^2 - \omega^2\right) - i\,\gamma_{bound}\,\omega}\end{aligned} \tag{5.18}$$

The total contribution of free and bound electrons to the dielectric function can be evaluated from Eq. 5.18.

In Fig. 5.9, we plot the real (a) and imaginary (b) parts of the dielectric function of gold in the visible and near-infrared range of the spectrum, using Eq. 5.18 with $r = 100$ nm to consider a bulk size. The bulk dielectric function, plotted as open circles, is calculated by interpolation using experimental data measured by Johnson and Christy [58]. Solid line corresponds to free electron contribution while dashed line represents the sum of intraband and a single interband transition [61]. Concerning the real part, some authors add an arbitrary constant term called ε_∞, whose value ranges between 1 and 10 and represents other interband transitions [61, 62], to fit the experimental data. For wavelengths $\lambda > 650$ nm, $\varepsilon(\omega,\ r)$ is

governed by its large negative real part. This is a consequence of the fast response of conduction electrons to the external electromagnetic excitation. This quasi-free behavior is like a shield causing a very fast damping of the EM fields within the metal.

Concerning the imaginary part, at wavelengths $\lambda < 600$ nm, the free plus single-transition bound electron model does not reproduce the experimental data. For this model, ε'' departs from the experimental data between 300 and 450 nm. Thus, with the inclusion of a single interband correction (Eq. 5.15), an agreement with the experimental curve is only obtained for 450 nm $<\lambda<$1,000 nm.

Similar general behavior (including the disagreements) was observed for the case of silver and copper, both for real and imaginary parts. So it is clear that a more complete model that considers explicitly other interband transitions is necessary to describe the complex expression of $\varepsilon(\omega,\ r)$.

5.1.4 Bound Electron Contributions (Multiple Transitions)

Since the single-transition bound electron contribution model fails for particles sizes comparable to the mean free path of conduction electrons, there is a need for an adequate description of the optical properties for large clusters formed by hundreds of atoms (molecule-like properties), which may help to have a better agreement between theory and experiment for short wavelengths. This is a topic under discussion since more than 50 years ago [63, 64]. In this section, we show a theoretical formalism to evaluate the interband contribution to the dielectric function. This contribution was estimated in last section based on a semiempirical analysis.

Pinchuk et al. [59] have analyzed the influence of interband electronic transitions on the frequency, amplitude, and bandwidth of the surface plasmon resonance in small metal nanoclusters. Their theoretical results for silver and gold, including the interband transitions in the model, lead to a more reasonable value for the plasmon bandwidth. A first approximation was based on the concept that the contribution due to interband transitions remains unchanged when material goes from bulk to small particles. Afterward, in the previous section, this fact was modified, specially for noble metals, considering transitions of bound electrons to conduction levels with a characteristic frequency ω_0.

Now we take a step forward, considering that for the contribution of bound electron transitions to the dielectric function in actual solids, ω_0 should be extended to cover all the allowed transitions to conduction band levels, as indicated in Fig. 5.10.

If the density of states on this band is represented by $D(\omega_0)$, the relative dielectric function corresponding to the bound electrons contribution can be written as:

$$\varepsilon_{bound}(\omega) = \int D(\omega_0)\,(1-F)\,\varepsilon^{L}{}_{bound}(\omega,\ \omega_0)\ d\omega_0, \tag{5.19}$$

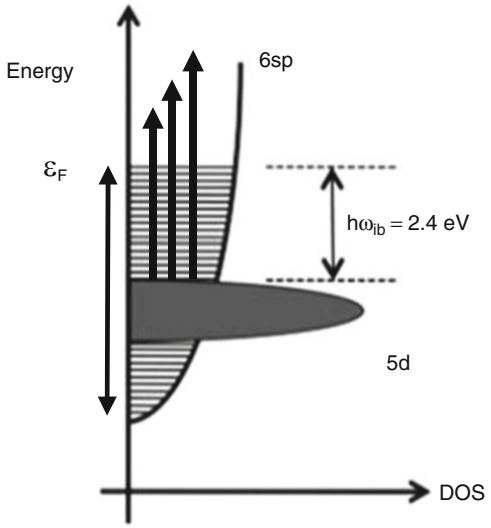

Fig. 5.10 Schematic diagram of energy levels for gold, showing interband transitions from d-state to sp-states (*vertical arrows*). *DOS* density of states

where F is the Fermi distribution, (1-F) is the probability that the upper state is not occupied, and $\varepsilon^{L}_{bound}(\omega,\ \omega_o)$ is the Lorentz dielectric function given by Eq. 5.15. Rosei et al. [60] and Rosei [65] have given an explicit form for $D\ (\omega_0)$ corresponding to noble metals like gold and silver, and they show also the way to calculate the limits of the integral in Eq. 5.19. Inouye et al. [66] have shown a simplified expression of this calculation for gold assuming that the curvature of the d-band can be ignored. In this case, the dielectric function can be written as:

$$\varepsilon_{bound}\ (\omega) = K_{bulk} \int_{\omega_g}^{\infty} \frac{\sqrt{x-\omega_g}}{x} [1 - F(x,T)] \times \frac{(x^2 - \omega^2 + {\gamma_b}^2 + i\ 2\ \omega\ \gamma_b)}{(x^2 - \omega^2 + {\gamma_b}^2)^2 + 4\ \omega^2\ {\gamma_b}^2}\ dx, \tag{5.20}$$

where $\hbar\omega_g$ is the gap energy (E_g); $F\ (x,\ E_F,\ T)$ is the Fermi energy distribution function of conduction electron of energy $\hbar\ x$ at the temperature T with Fermi energy E_F; γ_b represents the damping constant in the band to band transition; and K_{bulk} is a proportionality factor. The reference for the energy is assumed at the top of the d-band.

Figures 5.11 and 5.12 show calculated free electron (Eqs. 5.11, 5.12) and multiple transitions bound electron contribution (Eq. 5.20) to the dielectric function of gold and copper, respectively. The sum contribution (solid line) is compared with experimental data given in Ref. [58] for bulk. Some parameters were taken from the literature, while others were calculated previously by the authors [30]. These parameters such as K_{bulk}, E_g, E_F, and γ_b produce different and independent effects over the dielectric function.

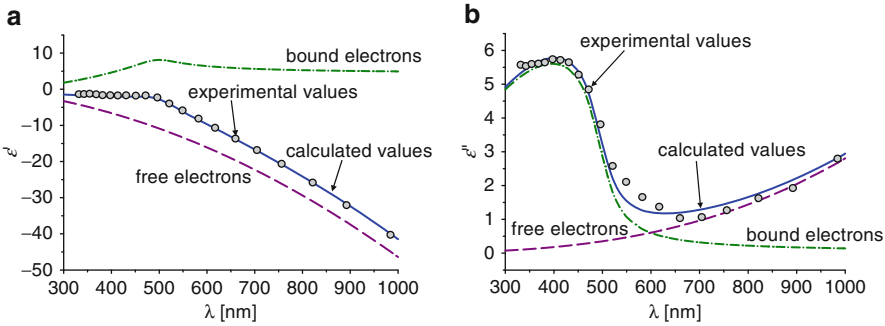

Fig. 5.11 Calculated free electron and multiple transitions bound electron contribution to the dielectric function of gold. The sum contribution (*solid line*) is compared with experimental data given in Ref. [58] for bulk

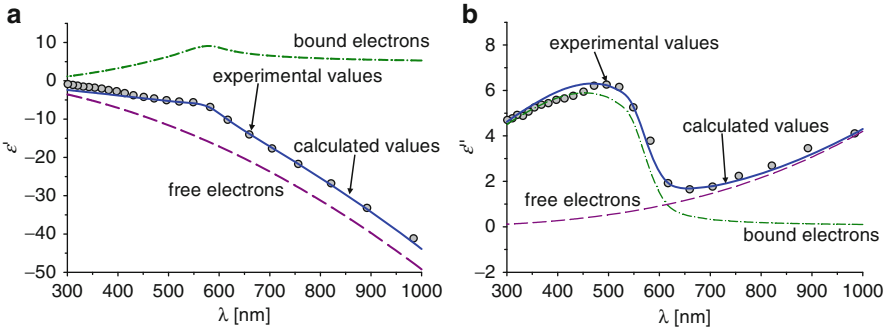

Fig. 5.12 Calculated free electron and multiple transitions bound electron contribution to the dielectric function of copper. The sum contribution (*solid line*) is compared with experimental data given in Ref. [58] for bulk

Fitting parameters and other relevant values for gold and copper are summarized in Table 5.1. It can be seen that with these parameters, the curves show excellent agreement with the experimental data without the need of adding an arbitrary constant.

For the contribution of bound electrons, no functional form is known to change the parameters in Eq. 5.20 as a function of the size of the particle. Some authors [16, 69, 70] introduced the idea that the electronic density of states is different for nanoparticles of different sizes. This fact affects Eq. 5.20 where part of the integrand is just the density of states in the upper band. Since small particles have larger spacing between electronic states, it is valid to conclude that the density of states will be smaller for very small Nps. It was proposed [16] to take account of this fact by changing the proportionality factor K_{bulk} in the contribution of bound electrons from its accepted bulk value to $K_{size} = K_{bulk}(1 - \exp(-R/R_0))$, where R is the radius of the particle and R_0 is a scale factor that represents the size for which the density of states can be considered to reach the value of the bulk.

Table 5.1 Optical parameters of bulk gold and copper

	Symbol	Value	Reference
Gold parameters			
Plasma frequency	ω_p	13×10^{15} Hz	Granqvist and Hunderi [56]
Damping constant for free electrons	γ_{bulk}	1.1×10^{14} Hz	Johnson and Christy [58]
Coefficient for bound electron contribution	K_{bulk}	2.3×10^{24}	Scaffardi and Tocho [30]
Gap energy	E_g	2.1 eV	Scaffardi and Tocho [30]
Fermi energy	E_F	2.5 eV	Scaffardi and Tocho [30]
Damping constant for bound electrons	γ_b	2.4×10^{14} Hz	Inouye et al. [66]
Copper parameters			
Plasma frequency	ω_p	13.4×10^{15} Hz	Cain and Shalaev [67]
Damping constant for free electrons	γ_{bulk}	1.45×10^{14} Hz	Johnson and Christy [58]
Coefficient for bound electron contribution	K_{bulk}	2×10^{24}	Santillán et al. [68]
Gap energy	E_g	1.95 eV	Santillán et al. [68]
Fermi energy	E_F	2.15 eV	Santillán et al. [68]
Damping constant for bound electrons	γ_b	1.15×10^{14} Hz	Santillán et al. [68]

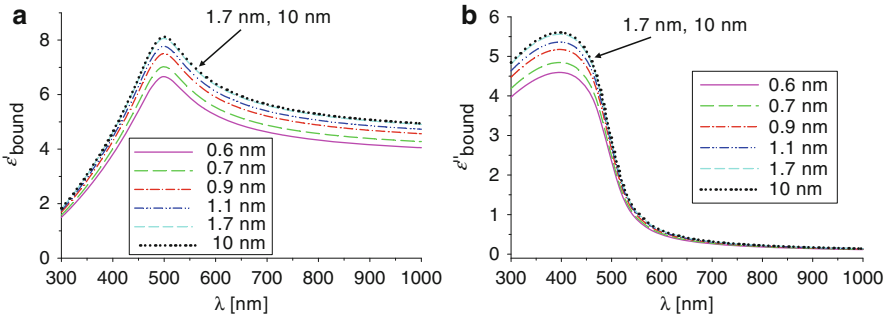

Fig. 5.13 Bound electron contribution to the dielectric function of gold, including correction for size. The correction is negligible for sizes close to 1.7 nm

Figures 5.13a, b show the spectral behavior of the real and imaginary parts of the bound electron contributions of gold for different nanometric and subnanometric sizes, using the Eq. 5.20 with the correction $K_{size} = K_{bulk}(1 - \exp(-R/R_0))$.

For the case of copper, Fig. 5.14a, b shows the spectral behavior of the real and imaginary parts of bound electron contribution for different subnanometric and nanometric sizes.

It can be observed from Figs. 5.13 and 5.14 that the curves corresponding to sizes larger than 2 nm are overlapped with each other. This is due to the fact that, for that size range, the correction included in the expression of K_{size} becomes negligible.

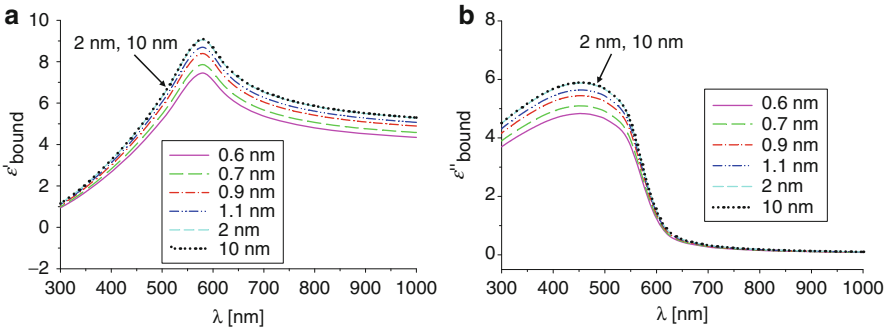

Fig. 5.14 Bound electron contribution to the dielectric function of copper, including correction for size. For sizes close to 2 nm, the correction is negligible

In the following section, we present results about the electromagnetic response of different nanometric systems. We show how changes in the dielectric function modify the optical properties of nanometric systems: metallic nanowires (2D scattering problem), nanotubes, spherical nanoparticles, and core-shell systems.

The different modification in the real and imaginary part of the dielectric function described above (arising from free and bound electron contribution) will be used in Sect. 5.3.4 to characterize experimentally the size of 3D spherical nanostructure from the features of their extinction spectrum.

5.2 Optical Extinction Spectroscopy

5.2.1 Nanoparticle Cross Section and Optical Theorem for Arbitrary Geometry

In this section, we outline the problem of the interaction of an electromagnetic wave with a nanometric sized particle [48, 71]. We use a rigorous 2D integral method based on Green's second identity and the extinction theorem for calculations of optical responses of arbitrary shaped particles. We then give a brief overview about the calculation of scattering and extinction cross section by small spherical particles following the method of Mie expansion, exploring the asymptotic behavior when the radius $a \to 0$.

Figure 5.15 shows the general problem of dispersion by a particle, considering that a polarized electromagnetic wave interacts with a particle of volume V with arbitrary geometry. The particle is characterized by a dielectric function $\varepsilon(\vec{r}) = \varepsilon'(\vec{r}) + i\,\varepsilon''(\vec{r})$.

Given the direction of incident electromagnetic field and the shape, size, and relative dielectric function $\varepsilon(\vec{r})$ of the scatterer, the goal is to determine the fields $\vec{E}(\vec{r})$ and $\vec{H}(\vec{r})$ at all points in space. The scatterer is assumed to be embedded in a homogeneous and isotropic lossless medium of dielectric constant ε_0. Electromagnetic fields must satisfy the macroscopic Maxwell's equations with the corresponding boundary condition on the particle [72]. In general, this is a complex problem that must be solved numerically, although analytical

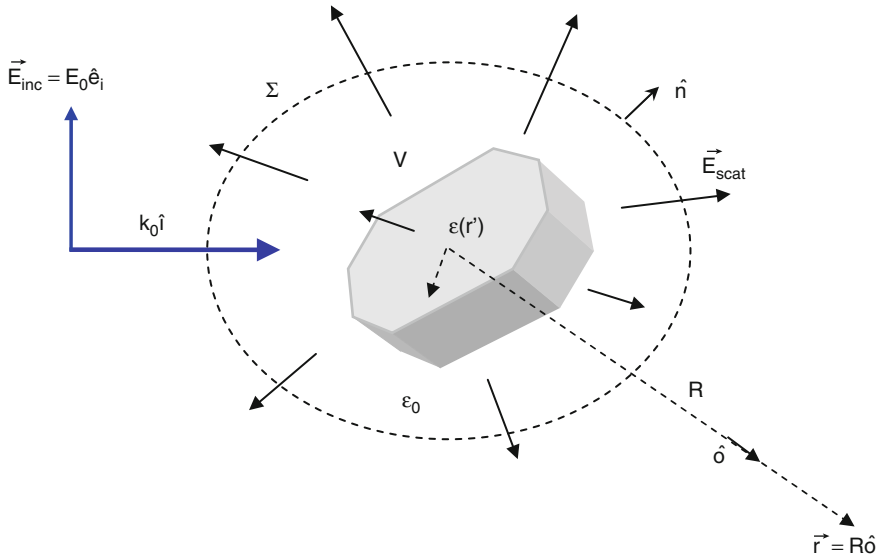

Fig. 5.15 Schematic for scattering calculation

expressions can be obtained for simple geometries or for certain approximations [58, 61, 73, 74].

In order to gain physical insight into the problem, we can write the total fields as a superposition of incident and scattered fields:

$$\vec{E} = \vec{E}_{inc} + \vec{E}_{scat}$$

$$\vec{H} = \vec{H}_{inc} + \vec{H}_{scat}$$

If we take a closed mathematical surface Σ containing the scatterer, the total energy flow per unit time and area that crosses this surface is given by the time-averaged Poynting vector $<\vec{\mathbf{S}}> = (1/2)\mathbf{Re}[\vec{\mathbf{E}} \times \vec{\mathbf{H}}^*]$, or

$$<\vec{S}> = <\vec{S}_i> + <\vec{S}_s> + <\vec{S}'> \tag{5.21}$$

It is interesting to note that the time-averaged Poynting vector for the total field can be written as a linear combination of energy flow per unit time for the incident field and scattered field plus a term that accounts for overlap of the fields:

$$<\vec{S}_i> = (1/2)\mathrm{Re}[\vec{\mathbf{E}}_{inc} \times \vec{H}^*_{inc}], <\vec{S}_s> = (1/2)\mathrm{Re}[\vec{\mathbf{E}}_{scat} \times \vec{H}^*_{scat}], \text{ and}$$
$$<\vec{S}'> = (1/2)\mathrm{Re}[\vec{\mathbf{E}}_{inc} \times \vec{H}^*_{scat} + \vec{\mathbf{E}}_{scat} \times \vec{H}^*_{inc}].$$

By integrating Eq. 5.21 through the closed surface Σ, we find a simple relation for energy present in the system. The energy term corresponding to the incident field results in zero, since we assumed a lossless host medium. Thus, the energy balance for a metallic scatterer is given by:

$$-W_a = W_s + W',$$

where

$$W_s = \oint_{\Sigma} <\vec{S}_s> \cdot \hat{n}\, da, \quad W' = \oint_{\Sigma} (\vec{\mathrm{E}}_{\mathrm{inc}} \times \vec{H}^*_{scat} + \vec{\mathrm{E}}_{scat} \times \vec{H}^*_{inc}) \cdot \hat{n}\, da \tag{5.22}$$

W_a is the energy absorbed by the particle and $\hat{n}$ is the normal to the Σ surface.

The integral W', the total energy removed from the incident field by both scattering and absorption, can be written in an analytic form when the electromagnetic fields are considered in the far field.

We consider an incident electromagnetic wave with a wave vector $\vec{k_0} = k_0\hat{i}$ and electric field of the form:

$$\vec{E_i} = E_0\hat{e}_i \ \exp[ik_0(\hat{i} \cdot \vec{r})]$$

The scattered waves, far from the scatterer, are considered spherical waves:

$$\vec{E}_{scat} = f(\hat{i}, \hat{o})\ \frac{\exp[ik_0 \cdot \vec{r}\,]}{R}; \quad \vec{H}_{scat} = \sqrt{\varepsilon_0}\ \left[\hat{o} \times f(\hat{i}, \hat{o})\right]\ \frac{\exp\ [i\vec{k_0} \cdot \vec{r}]}{R}$$

where $f(\hat{i}, \hat{o})$ is the so-called scattering amplitude, which depends on the observation angle.

By substituting the incident and scattered field into Eq. 5.22 and integrating when $R \to \infty$, we obtain:

$$-W' = W_a + W_s = \frac{2\pi}{k_0}\sqrt{\varepsilon_0}\ \mathrm{Im}\left[\hat{e}_i \cdot f(\hat{i}, \hat{i})\right].$$

Absorption and scattering remove energy from the incoming electromagnetic field when light interacts with particles. At this point, we can introduce the extinction cross section C_{ext}:

$$C_{ext} = \frac{W_a + W_s}{\left|<\vec{S}_i>\right|} = \frac{4\pi}{k_0}\mathrm{Im}[\hat{e}_i \cdot f(\hat{i}, \hat{i})] \tag{5.23}$$

and

$$C_{scat} = \frac{W_s}{\left|<\vec{S}_i>\right|} = \int_{4\pi} \left|f(\hat{o}, \hat{i})\right|^2 d\Omega, C_{abs} = \frac{W_a}{\left|<\vec{S}_i>\right|} = \int_V k_0\varepsilon''(\vec{r}\,')\left|\vec{E}(\vec{r}\,')\right| dV \tag{5.24}$$

Equation 5.21 is the so-called Optical Theorem or Forward Scattering Theorem [71, 75, 76], which is valid not only in electromagnetism but also in acoustics and quantum mechanics.

The electromagnetic problem reduces to find the scattering amplitude $f(\hat{o},\hat{i})$. A simple analysis shows the dependence of $f(\hat{o},\hat{i})$ with both the constitutive parameters and the shape of the nanoparticle. We first write Maxwell's equation in the following manner:

$$\vec{\nabla}\times\vec{E} = i\omega\mu_0\vec{H},$$

$$\vec{\nabla}\times\vec{H} = -i\omega\varepsilon_0\vec{E} + \vec{\xi}_e,$$

where $\vec{\xi}_e$ is consider like a source which generates the scattered waves and it is defined by [61]:

$$\vec{\xi}_e = \begin{cases} -i\omega\varepsilon_0[\varepsilon(\vec{r})-1]\,\vec{E} & in\ \ V \\ 0 & outside \end{cases}$$

If we write the scattered electromagnetic field as a function of the Hertz vector [62], we obtain:

$$\vec{E}_s(\vec{r}) = \vec{\nabla}\times\vec{\nabla}\times\vec{\Pi}_s(\vec{r}), \quad \vec{H}_s(\vec{r}) = -i\omega\varepsilon_0\vec{\nabla}\times\vec{\Pi}_s(\vec{r}), \tag{5.25}$$

where $\vec{\Pi}s(\vec{r}) = -\frac{1}{i\omega\varepsilon_0}\int_V G_0(\vec{r},\vec{r}\,')\xi_e(\vec{r}\,')\,dV'$.

$G_0(\vec{r},\vec{r}\,')$ is the free space Green's function. In the far field, we can write $G_0(\vec{r},\vec{r}\,')$ as (see Fig. 5.14):

$$G_0(\vec{r},\vec{r}\,') = \frac{\exp[ik_0R - ik_0\,\vec{r}\,'\cdot\hat{o}]}{4\pi R}.$$

Then, substituting $G_0(\vec{r},\vec{r}\,')$ for large R in to Eq. 5.25 we obtain:

$$\vec{E}_s(\vec{r}) = f(\hat{o},\hat{i})\,\frac{\exp[ik_0R]}{R},$$

and

$$f(\hat{o},\hat{i}) = \frac{k_0^2}{4\pi}\int_V \left\{-\hat{o}\times\left[\hat{o}\times\vec{E}(\vec{r}\,')\right]\right\}\{\varepsilon(\vec{r}\,')-1\}\exp[-ik0\vec{r}\,'\cdot\hat{o}]dV' \tag{5.26}$$

The scattering amplitude $f(\hat{o},\hat{i})$ depends on $\vec{E}(\vec{r}\,')$, the field inside the particle, and this magnitude is unknown in general. However, in many practical situations, it is possible to obtain a useful approximation to compute $f(\hat{o},\hat{i})$.

From a theoretical point of view, for particles with radii much smaller than the wavelength, a quasi-static limit can be used. Under this quasi-static approximation, if we consider the scatterer with a spherical symmetry, the electromagnetic field inside the sphere is constant and proportional to the incident field [77]:

$$E(\vec{r}') = \frac{3}{\varepsilon + 2} E_o \hat{e}_i,$$

Substituting this expression in Eq. 5.26 and considering a uniform dielectric function for the scatterer, we obtain:

$$f(\hat{o}, \hat{i}) = \frac{k_0^2}{4\pi} 3\alpha_0 \, V \sin(\theta_{obs}),$$

where $\alpha_0 = \frac{\varepsilon - 1}{\varepsilon + 2}$ and $\sin(\theta_{obs}) = -\hat{o} \times (\hat{o} \times \hat{e}_i)$.

Under this approximation, both the scattering and absorption cross sections are given by:

$$Q_{scat} = \frac{C_{scat}}{\pi \, a^2} = \frac{8}{3} (k_0 a)^4 |\alpha_0|^2, \quad Q_{abs} = \frac{C_{abs}}{\pi a^2} = 4 \, k_0 a \, \varepsilon'' \left| \frac{1}{\varepsilon + 2} \right|^2.$$

where a is the radius of the sphere.

A similar expression is obtained from an asymptotic Mie expansion (far field) for $ka \ll 1$, being a radii of the particle, as will be shown in Sect. 5.2.3.

For metallic particles, $\varepsilon' < 0$ at optical frequencies, so, the extinction cross section has a maximum when $\varepsilon' = -2$ for spheres and $\varepsilon' = -1$ for cylinders. This resonance is associated with collective oscillations of the free electrons at the metal induced by the incident electromagnetic fields. The physical region where the excitation into the metal occurs is given by the skin depth $\delta = \lambda \, / \, [4\pi \, \mathrm{Im}[\sqrt{\varepsilon}]]$. These collective electronic oscillations at the surface of the metal are known as surface plasmon [78]. In contrast to flat interfaces (films, diffraction gratings, rough interfaces), in the case of a nanoparticle, the surface plasmon is confined to the three dimensions of the nanostructure and it is then called localized surface plasmon [78, 79]. In this situation, the localized surface plasmon resonance depends on the metal dielectric function and on the geometry of the nanostructure.

For cross sections with different geometry to the spherical or circular one, the analytical calculation is not easy even under the small-particle approximation. One approach to estimate the condition of resonance is a generalization given by $\mathbf{Re}(\varepsilon) = 1 - 1/\Gamma$, where Γ is a geometrical factor or effective depolarization factor which depends on the shape of the particle [14, 79]. However, Γ can also include some first order corrections to the quasi-static model such as the dynamic depolarization or the radiation damping. Γ takes the value 1/2 for circular cylinders and thus the resonance condition will be $\mathrm{Re}(\varepsilon) = -1$. In first approximation, the Γ factor can be estimated from experimental curves for Q_{ext}. For ellipsoidal cross section, the value of Γ is related with the polarization of the incident wave: If the electric

field is along the major axis of the ellipsoid, Γ is smaller than 1/2, and if it is along the minor axis, Γ is greater than 1/2. Similar functional dependences are found for 3D nanowires [4, 14, 80].

The description of the scattering of electromagnetic waves by arbitrary nanosized obstacles has led to the development of several techniques to solve Maxwell's equations in inhomogeneous media. For example, the dipole discrete dipole approximation (DDA) [15, 81], finite difference methods in time domain (FDTD) [82, 83], multiple multipole expansion (MMP) techniques [84], transfer matrix methods [85, 86], or finite element methods in frequency domain [87] are among some of the most commonly used techniques to solve Maxwell's equations. All of them present advantages in certain aspects and disadvantages in others, but we will not go further into their description.

5.2.2 Scattering by Infinitely Long Wires

The method used to compute the scattered far field can deal with scattering problems of electromagnetic waves from systems formed by arbitrarily shaped bodies. Details of the general procedure can be found elsewhere [88–91]. In what follows we summarize the method applied to 2D systems with translations symmetry.

Let us consider a *s* or *p* incident polarized electromagnetic field with electric or magnetic vector $\vec{E}^{(inc)}(\vec{r},t)$ or $\vec{H}^{(inc)}(\vec{r},t)$, given by:

$$\vec{E}^{(inc)}(\vec{r},t) = (0, \phi_s{}^{(inc)}(\vec{r},\theta),\, 0)\exp[-i\omega t],$$

$$\vec{H}^{(inc)}(\vec{r},t) = (0, \phi_p{}^{(inc)}(\vec{r},\theta),\, 0)\exp[-i\omega t],$$

respectively. When these fields are incident upon a cylinder of cross section *S* limited by a curve *C*, and complex permittivity ε (Fig. 5.16), the expressions of the scattering field (per unit length) in each medium can be obtained using the extinction theorem for multiply connected scattering volumes [26]. The field is then represented in the form:

$$\phi_\alpha^{(0)}(\vec{r},\theta) = \phi_\alpha{}^{(inc)}(\vec{r},\theta) + \frac{i}{4}\int_{c^+} dl' \left[\frac{\partial G_0\left(\sqrt{\varepsilon_m}k_0|\vec{r}-\vec{r}\,'|\right)}{\partial \hat{n}'}\phi_\alpha^{(0)}(\vec{r}\,',\theta)\right.$$

$$\left. -G_0(\sqrt{\varepsilon_m}k_0|\vec{r}-\vec{r}\,'|)\frac{\partial \phi_\alpha^{(0)}(\vec{r}\,',\theta)}{\partial \hat{n}'}\right],\ if\ \vec{r}\in host\ medium$$

$$\phi_\alpha^{(0)}(\vec{r},\theta) = 0, \quad if\ \vec{r}\notin host\ medium \tag{5.27}$$

$$\phi_\alpha^{(1)}(\vec{r},\theta) = -\tfrac{i}{4}\int_{c^-} dl'\left[\tfrac{\partial G_1(\sqrt{\varepsilon}k_0|\vec{r}-\vec{r}\,'|)}{\partial \hat{n}'}\phi_\alpha^{(1)}(\vec{r}\,',\theta) - G_1(\sqrt{\varepsilon}k_0|\vec{r}-\vec{r}\,'|)\tfrac{\partial \phi_\alpha^{(1)}(\vec{r}\,',\theta)}{\partial \hat{n}'}\right],\quad if\ \vec{r}\in S$$

$$\phi_\alpha^{(1)}(\vec{r},\theta) = 0, if\ \vec{r}\notin S. \tag{5.28}$$

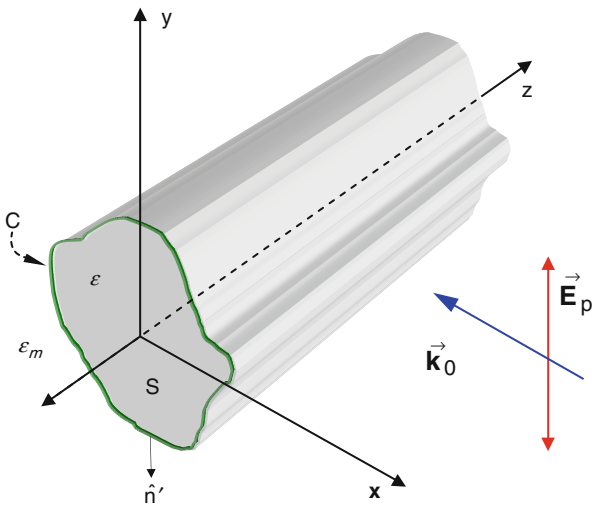

Fig. 5.16 Schematic for scattering calculation for infinitely long wires

α denotes s- or p-polarization, and $\phi_\alpha^{(j)}(\vec{r},\theta)$, with $j = 0,\ 1$, represents the complex amplitudes in the host medium (ε_m) and inside the cylinder, respectively. In a 2D configuration, the Green's functions are $G_j\left(\sqrt{\varepsilon_j}k_0|\vec{r}-\vec{r}'|\right) = i\pi H_0^{(1)}(\sqrt{\varepsilon_j}k_0|r-r'|)$, where $H_o^{(1)}$ are the zero-order, first class, Hankel functions and dl' is the differential element of line along the C contour. The symbol c^+ denotes that the integration variable $\vec{r}'$ tends to the contour C from outside of surface S(the normal $\hat{n}'$ points outward of surface S) and c^- denotes that the integration variable $\vec{r}'$ tends to the contour C from inside of surface S (the normal $\hat{n}'$ points inward of surface S). The electromagnetic field expressions for the far zone can be obtained from the previous equations making use of the asymptotic expressions for the Hankel functions for $|\vec{r}-\vec{r}'| \to \infty$, and the boundary conditions:

$$\phi_\alpha^{(0)}(\vec{r})\Big|_{\vec{r}\in c^+} = \phi_\alpha^{(1)}(\vec{r})\Big|_{\vec{r}\in c^-}, \quad \frac{\partial\phi_\alpha^{(0)}(\vec{r})}{\partial\hat{n}'}\Big|_{\vec{r}\in c^+} = \eta_\alpha \frac{\partial\phi_\alpha^{(1)}(\vec{r})}{\partial\hat{n}'}\Big|_{\vec{r}\in c^-},$$

where $\eta_p = \dfrac{\varepsilon_m}{\varepsilon}$ and $\eta_s = 1$.

In particular, the transmitted far field takes the form:

$$\phi_\alpha^{(t)}(r,\theta) = \sqrt{\frac{2}{\pi\sqrt{\varepsilon_m}k_0 r}}\exp\left[i\sqrt{\sqrt{\varepsilon_m}k_0 r - \pi 3/4}\right] T(\theta), \tag{5.29}$$

where

$$T(\theta) = \frac{i}{4}\oint_{c^+}\left[\left(\hat{n}'\cdot\vec{k}_t\right)\phi_\alpha^{(0)}(\vec{r}') - i\frac{\partial\phi_\alpha^{(0)}(\vec{r}')}{\partial\hat{n}'}\right]\exp(-i\vec{k}_t\cdot\vec{r}')\,ds', \tag{5.30}$$

is called the amplitude function of the scattering of the cylinder [56], and $\vec{k_t}$ is the propagation vector of the scattered wave, defined by,

$$\vec{k_t} = k_0\sqrt{\varepsilon_m}\,(\sin\theta_t, 0, \cos\theta_t). \tag{5.31}$$

A Gaussian incident beam of half-width W was considered. With this kind of beams, we can simulate a plane wave by setting W sufficiently large [25].

The optical properties of the cylinder material are introduced only through the frequency-dependent dielectric functions ε and ε_m that was used in Eqs. 5.27 and 5.28. Once the far field is calculated, the extinction cross section per unit length Q_{ext}, can be determined by using the optical theorem [48, 71, 76]:

$$Q_{ext} = C_{ext}/2a = \frac{2}{x}\mathrm{Re}[T(0)], \tag{5.32}$$

where $x = k_0\, a$ is the size parameter of the cylinder. Calculated Q_{ext} would be compared with experimental extinction spectra.

The method described here was extended to consider more complex systems such as nanotubes and coated wires [92].

5.2.3 Scattering by Spheres

This section is devoted to calculate 3D scattering for different structures such as bare-core or core-shell spherical nanoparticles. For calculations of cross sections, in this section, we resume the basic concepts involved in Mie Theory [48].

If a single spherical particle of radius a is considered, we can write the extinction cross sections (Eq. 5.23) in terms of the Mie [48] expansion coefficients a_n and b_n as:

$$C_{ext} = \frac{W_a + W_s}{\left|<\vec{S_i}>\right|} = \frac{2\,\pi}{k^2}\sum_{n=1}^{\infty}(2n+1)\ \ \mathrm{Re}\,(a_n + b_n) \tag{5.33}$$

where

$$a_n = \frac{\mu\, m^2 j_n(mx)\ [x\, j_n(x)]' - \mu_1\, j_n(x)\ [m\, x\, j_n(mx)]'}{\mu\, m^2 j_n(mx)\ \left[x\ h_n^{(1)}(x)\right]' - \mu_1\, h_n^{(1)}(x)\ [m\ x\, j_n(mx)]'} \tag{5.34}$$

$$b_n = \frac{\mu_1\, j_n(mx)\ [x\, j_n(x)]' - \mu_1\, j_n(x)\ [m\, x\, j_n(mx)]'}{\mu_1\, j_n(mx)\ \left[x' h_n^{(1)}(x)\right]' - \mu_1\, h_n^{(1)}(x)\ [m\, x\, j_n(mx)]'} \tag{5.35}$$

and the primes indicating derivatives with respect to the argument of the function; μ and μ_1 are the magnetic permeabilities of the surrounding medium and of

the spherical particle, respectively; $x = 2\,\pi\,N\,a/\lambda$ is the called *size parameter* with $N = \sqrt{\varepsilon_m}$ being the refractive index of the medium; $m = N_1/N$ is the relative refractive index. Finally, j_n and h_n are the spherical Bessel and Hankel functions, respectively.

If the size of the sphere is small compared with the incident wavelength, only the first two terms on the expansion are relevant (dipolar term). With the asymptotic form for a_1 and b_1 and considering the lowest order in x [48], the expressions for absorption and scattering efficiency factors Q are:

$$Q_{abs} = 4\,x\,\mathrm{Im}\left(\frac{\varepsilon_1 - \varepsilon_m}{\varepsilon_1 + 2\varepsilon_m}\right) \tag{5.36}$$

$$Q_{sca} = \frac{8}{3}\,x^4\,\left|\frac{\varepsilon_1 - \varepsilon_m}{\varepsilon_1 + 2\varepsilon_m}\right|^2 \tag{5.37}$$

These expressions are identical to that obtained from the electrostatic approximation using the Optical Theorem.

If scattering is small compared with absorption, the absorption cross section may be expressed as:

$$C_{abs} = k\,\mathrm{Im}(\alpha) \tag{5.38}$$

where $k = \frac{2\,\pi\,N}{\lambda}$ is the wavenumber in the medium surrounding the particle, λ is the wavelength of the incident light in vacuum, and α is the polarizability given by:

$$\alpha = 4\,\pi\,a^3\alpha_0 \tag{5.39}$$

For more complex structures, like core-shell spherical Nps, the expression of the polarizability is [48]:

$$\alpha = 4\,\pi R_2^3\,\frac{(\varepsilon_2 - \varepsilon_m)\,(\varepsilon_1 + 2\,\varepsilon_2) + f\,(\varepsilon_1 - \varepsilon_2)\,(\varepsilon_m + 2\,\varepsilon_2)}{(\varepsilon_2 + 2\,\varepsilon_m)\,(\varepsilon_1 + 2\,\varepsilon_2) + f\,(2\,\varepsilon_2 - 2\,\varepsilon_m)\,(\varepsilon_1 - \varepsilon_2)} \tag{5.40}$$

where $f = \left(\frac{R_1}{R_2}\right)^3$ is the ratio between inner and outer radius volumes; $R_1 = R_{core}$ is the metal central core; $R_2 = R_{core+coating}$ is the outer radius (metal core + shell); and $\varepsilon_1 = \varepsilon_1(\lambda,\ R_1)$, $\varepsilon_2 = \varepsilon_2(\lambda,\ R_2 - R_1)$, and ε_m are the dielectric functions of the core, coating (shell), and surrounding medium, respectively. When the metal dielectric function in the above expressions is modified by size according to Eqs. 5.11, 5.12, and 5.20, it is possible to calculate the extinction cross section for sizing small nanoparticles according to Eq. 5.38. This procedure will be used in Sect. 5.3.4 to fit experimental extinction spectra results in the visible-NIR range for bare-core and core-shell nanoparticles.

5.3 Theoretical and Experimental Results

In this section, we review some relevant results from the literature for the optical response of nanoscale systems. We show theoretical and experimental results of physical observables in the far field (optical cross sections) and how these observables depend on both the size and shape of the nanoparticle.

In recent years, great interest has developed in the study of nanoscale systems, from the synthesis and manufacture of nanoparticles, characterization and optical response up to their manipulation and physical properties control. Different areas of knowledge (chemistry, biology, physics, etc.) are making a significant amount of contributions to the subject. This is evidenced by the large number of interdisciplinary citations in recent reviews on the topics (see for instance Refs. [1, 2, 4, 7, 93–95]).

The optical properties of noble metals – in particular the structures of silver, gold, copper, aluminum, titanium – can be manipulated by appropriate engineering of nanoparticles (or nanostructures) and this subject is its main attraction. Understanding the optical response of nanoscale systems promote a variety of potential applications ranging from simple interaction molecules, optical crystals and photonic metamaterials. For instance, in surface-enhanced Raman spectroscopy [96–101], chemical and biological sensors have been proposed based on plasmon resonant particles [1, 102–104]. For scanning near-field optical microscopy, metallic particles provide large, yet well-localized near-field sources [105–113], and can therefore increase the resolution.

Small silver or gold particles and wires are also highly interesting for optical devices, as they provide efficient, frequency-selective scatters with sub-wavelength dimensions, allowing further device miniaturization. Moreover, silver and gold nanowires can guide electromagnetic modes over several microns [8, 114–118], coupled plasmon resonant nanoparticles can be used for evanescent optical transport [119–124], and nanoholes in metal films allow the filtering of optical signals [125–127]. Most recently, an active optical component, similar to a transistor, was proposed using the local field amplification associated with the excitation of plasmon resonances [12, 128] or the ablation of cancer cells in vivo [2, 7, 93, 94].

In general, numerical computations are necessary to understand the optical properties of arbitrarily shaped plasmon resonant particles in detail. In particular, the knowledge of the complex relationship between shape and size of the particles and its plasmon resonance spectrum allows designing nanoparticles for specific applications. This knowledge is required both for individual and interacting metal nanoparticles.

5.3.1 Electromagnetic Responses of Infinitely Long Nanowires: A 2D Scattering Problem

In this subsection, we deal with nanometric systems with translational symmetry. In particular, we show the electromagnetic response of metallic infinitely long nanowires and metallic nanotubes (2D metal dielectric core-shell systems). The solution of 2D problems allows qualitative and quantitative studies of the physical phenomena involved in electromagnetic interaction, without loss of generality.

As we mentioned in Sect. 5.2.1, the electron collective oscillation occurs within a narrow strip from the particle surface. The rapid response of free electrons in metals to external fields is the cause of the rapid damping of electromagnetic fields inside the metal giving rise to the skin effect. It is interesting to note that, for Ag particles, the skin effect depth is about 6–10 nm around the resonance frequency. Therefore, when the electromagnetic field falls on nanoparticles ($a < 10$ nm), the electromagnetic resonances related to the plasmon excitation practically occur in the volume of the particle. Due to these characteristics, we will call these resonances "eigenmodes of the system" which are a solution of the homogeneous problem.

The small metallic particle shows a complete polarization and the free electrons are confined to oscillate within its volume. Thus, the optical properties for these systems are substantially modified respect to larger ones. This behavior with size affects the constitutive parameters of the nanoparticle, as was shown in the Sect. 5.1.1

5.3.2 Nanowires

In Figs. 5.5, 5.6, and 5.7 (Sect. 5.1), we have shown results of applying the correction by size to Ag, Au, and Cu dielectric functions for particles with radii less than 7 nm. For infinitely long nanowires, a new condition is established: The permittivity depends on the polarization state of the illuminating wave. Two different dielectric functions may be defined: $\varepsilon(\omega)$ corresponding to silver bulk for *s*-waves (or TM), and $\varepsilon(\omega,r)$ for *p*-waves (or TE), where the size correction is included [25]. For this configuration, only p-waves show eigenmode resonances.

By inspection of the dielectric functions, we can see a clear increase of slope in the imaginary part as the particle radius decreases, while the real part displays much less variation, with a tendency to decrease its slope. This behavior of the dielectric constant (which is only corrected by size) is reflected in the cross section of extinction.

In Fig. 5.17, we show the evolution of the extinction cross section (p-waves) with the incident wavelength for different Ag and Au nanowires. The position of the resonant peak exhibits a clear dependence on the size. As the particle radius decreases, the resonant peak maximum is blueshifted.

This effect is particularly notorious for Ag nanowires (Fig. 5.17a). In Fig. 5.17b, we plot the peak position (resonant wavelength) depending on the radius, which clearly shows this blueshift. In the Fig. 5.17b too, we compare the same system but when it is immersed in index matching oil (refractive index approximately 1.52 at 500 nm). By comparing the peaks curve, we can see the redshifts of all resonance spectra due to change in the refractive index of the surrounding medium.

For the Au nanowires, the blueshift is less noticeable and for wires with radii less than 7 nm, the peak displacement is within the numerical error (see Fig. 5.17c). With respect to the displacement of the peaks with the particle size, there is not total agreement today. In the review of Link et al. [129], the authors devote a paragraph to comment about the disagreement in resonant peak shift. In the literature both redshifts and blueshifts of the peaks are reported. Recently, we can observe that this

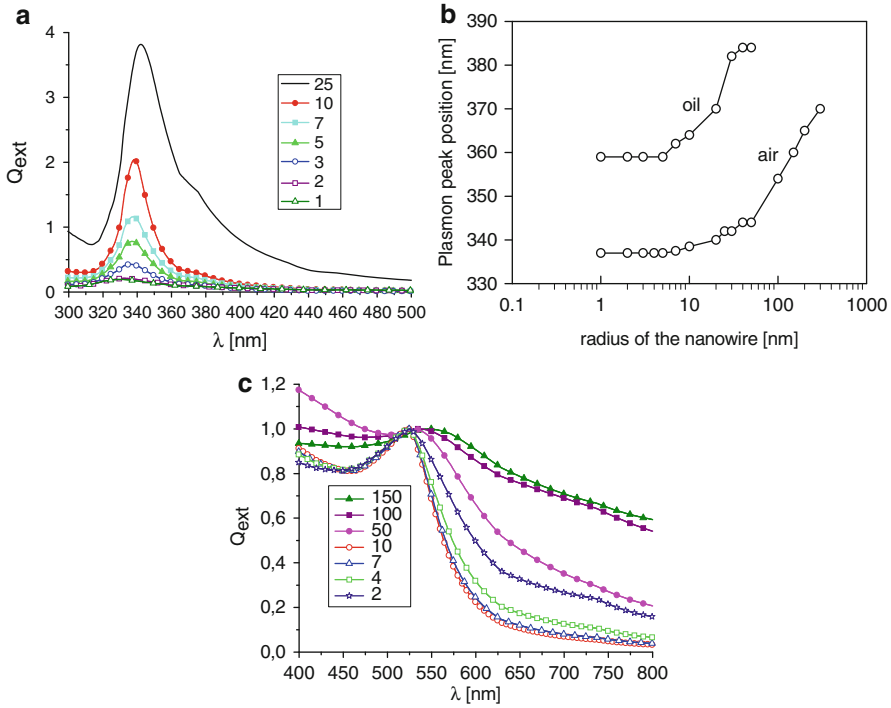

Fig. 5.17 (**a**) Behavior of Q_{ext} for p-polarized illumination with the wavelength for Ag nanowires with different radii. (**b**) Evolution of the resonant peak position with the radius. (**c**) Idem to (**a**) but Au nanowire normalized to the height of the resonance peak. In both cases, a blueshift is observed when the radius of the nanowire is reduced. Resonance peak position versus the radius of the silver nanowire for different host media: air and index matching oil

different behavior is produced by a nanoscopic shell due to the fabrication presses: oxide metal shell (i.e., in Ag nanoparticles) [130], surface modified in chemical process (i.e., in Au nanoparticles), etc.

In all cases studied, we observe a similar optical response: The position of the resonance peak does not change substantially with decreasing radius (less than 5 nm) and neither does the real part of the dielectric constant. As the radius decreases, the resonance peak broadens and decreases in height, while the imaginary part of the dielectric constant increases.

Another way, for s-waves, no eigenmode excitations are possible for 2D nanowires, but a clear difference in the spectra corresponding to different radii can be observed. In Fig. 5.18, we show the evolution for the extinction cross section with the wavelength for the incident s-wave. For radius larger than 10 nm, the contrast (relative difference between the maxima and the minima of the extinction cross section) between the ridge at 260–275 nm and the dip at 320–330 nm can be used to characterize the radii of the cylinders.

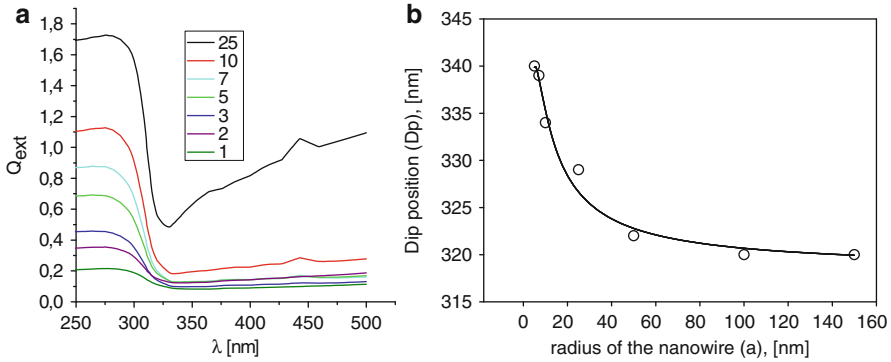

Fig. 5.18 (**a**) Evolution of Q_{ext} for s-polarized illumination as a function of wavelength for Au nanowires with different radii. (**b**) Evolution of the resonant peak position with the radius in air

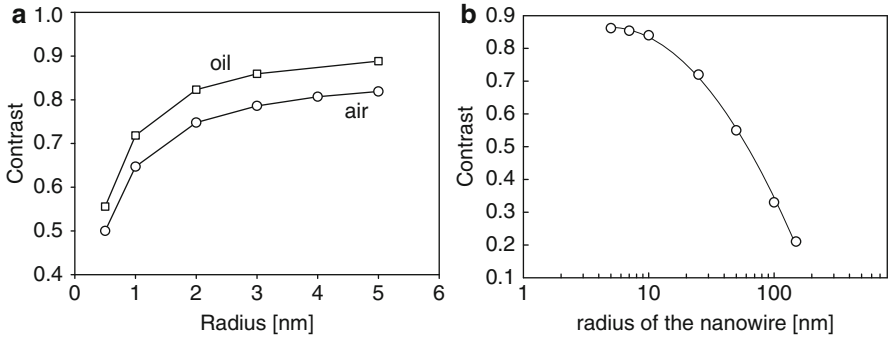

Fig. 5.19 Contrast curves as a function of Ag nanowire radius. (**a**) p-polarization for two host media, oil and air. (**b**) s-polarization in air

In Refs. [16, 25, 53], it has been proposed a useful tool based on contrast measurements. In Fig. 5.19, we show the contrast curves for characterizing the size of nanowires.

These qualitative optical properties are observed in 2D and 3D systems. The electromagnetic responses of metallic nanoparticles are not only sensitive to size of the particles, but also are sensitive to both the surrounding environment as well as its shape [74, 129].

In particular, the resonant frequencies of eigenmodes are sensitive to the geometry of the particles. The main attraction of the nanoparticles design is the possibility of tuning the resonant excitation of eigenmodes in a wide bandwidth, allowing a large number of applications, from the design of optical nanoantennas [123, 131], construction of plasmons waveguide of some nanometers wide [62, 121], development of more efficient solar cells, or the possibility of applying these resonant systems in detecting and/or destruction of cancer cells (photothermal therapy) [93].

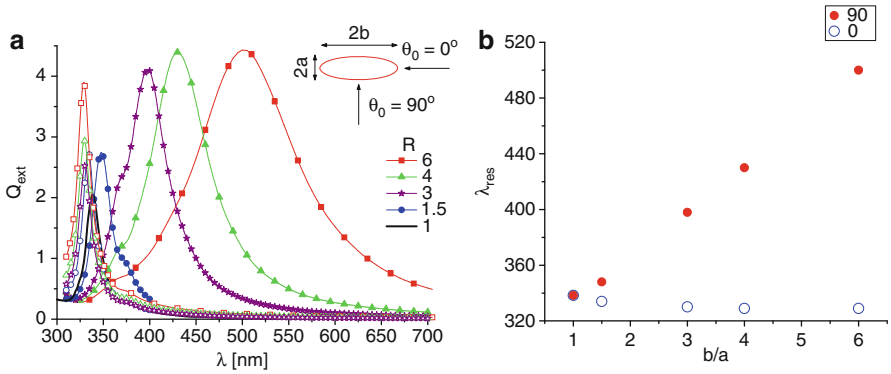

Fig. 5.20 Optical response for Ag nanowires with elliptic cross section and different aspect ratios. (**a**) Evolution of the extinction cross section $\boldsymbol{Q_{ext}}$ with wavelength for two different incident p-illumination modes: electric field parallel to major axis b ($\theta_0 = 90°$) – *solid symbols*; electric field parallel to the minor axis a ($\theta_0 = 0°$) – *hollow symbols*. (**b**) Evolution of the maximum of resonance peak as a function of the aspect ratio for both incidences. See the *insets* in panels (**a**) and (**b**)

A slight deviation from circular (spherical) geometry produces a splitting of the lower energy peak. This effect is noticeably for Ag particles, where eigenmode resonance shows a single well-defined peak for circular geometry (see Fig. 5.17a).

In Fig. 5.19, we show normalized extinction curves (respect to the geometrical shadow) as a function of wavelength for Ag nanoparticles with different aspect ratios (relationships between major and minor axes) $\mathbf{R} = \text{b/a}$: from $\mathbf{R} = 1$ (a = b = 10 nm) up to $\mathbf{R} = 6$ (a = 10 nm, b = 60 nm). As we can see in Fig. 5.19, two branches (channels) are opened which depend on the polarization of the incident wave. One of them, when the peak position shifts to shorter wavelengths, corresponds to the electric field parallel to the minor axis – open symbols – (incidence to 0°, see the inset in Fig. 5.20a) and the other one is redshifted when the electric field is along the major axis – solid symbol – (incidence to 90°).

In Fig. 5.20b, we show the evolution of the resonance peak versus the aspect ratio $\mathbf{R} = \text{a/b}$. The behavior of the resonant wavelengths is quasi-linear with **R**. With blue hollow circles, we show the evolution of resonance blueshifted peaks and with solid red circles, the redshifted peak ones. Because the minor axis is constant, the blueshift is not very pronounced, $\Delta\lambda = 9.4\,\text{nm}$ with respect to the perfect circle $\mathbf{R} = 1$.

A similar behavior is observed for Au nanowires with elliptical cross section. In Fig. 5.21, we show the evolution of the extinction cross section for identical geometrical parameters to Fig. 5.20.

A qualitative explanation of the optical response for particles with volume (surface) ellipsoidal can be given under the non-retarded field hypothesis. This theory is based on an electrostatic solution for the principal values of the polarizability tensor, α_j, with a relative complex dielectric function $\varepsilon(\lambda)$ [48].

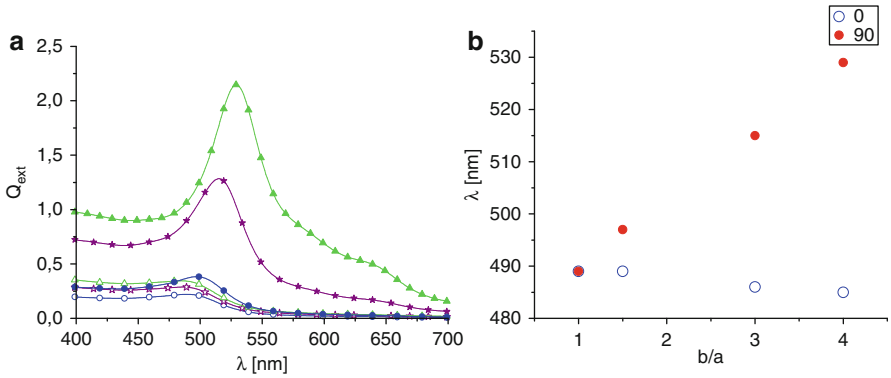

Fig. 5.21 Optical response for Au nanowires with elliptic cross section and different aspect ratios. (**a**) Evolution of the extinction cross section $\boldsymbol{Q_{ext}}$ with wavelength for two different incident p-illumination modes: electric field parallel to major axis b ($\theta_0 = 90°$) – *solid symbols*; electric field parallel to the minor axis a ($\theta_0 = 0°$) – *hollow symbols*. (**b**) Evolution of the maximum of resonance peak as a function of the aspect ratio for both incidences. See the *insets* in panels (**a**) and (**b**)

$$\alpha_j = 3V \frac{\varepsilon - 1}{3 + 3\Gamma_j(\varepsilon - 1)}, \tag{5.41}$$

V is the ellipsoidal volume and Γ_j are the geometrical depolarization factors. When the three axis of the ellipsoid are equal, the geometrical factor is degenerated and equals to 1/3 (or 1/2 for 2D problem). For small Rayleigh particles, the light-scattering contribution to the total extinction is usually neglected, so optical absorbance Q_{abs} is calculated through the absorption cross section averaged over random orientations of spheroids. Most papers on the optical properties of metal nanoparticles suspensions used the classic Gans theory. The qualitative behavior shown in Figs. 5.19 and 5.20 was observed experimentally in Au nanorods [13, 19].

Another way to control the frequency of excitation of eigenmodes in nanoparticles is through core-shell systems: dielectric particles coated with metal shell. In this case, controlling the thickness of the metal layer and the dielectric particle size is possible to tune the proper mode at determined frequency.

In the next section, we describe the optical response of metallic nanotubes. That is, hollow tubes with nanometric metallic walls and dielectric cylinders coated with a metallic layer.

5.3.3 Nanotubes

Geometrically, the nanotubes are formed by two coaxial cylinders forming an annular surface (wall of the nanotube) which is considered metallic. When the core of the nanotube is filled with a dielectric material, it is the 2D equivalent problem to the core-shell 3D system [42].

As it was shown for a single particle, the study of these 2D systems provides all the information necessary to understand the physical mechanisms involved in three-dimensional problems.

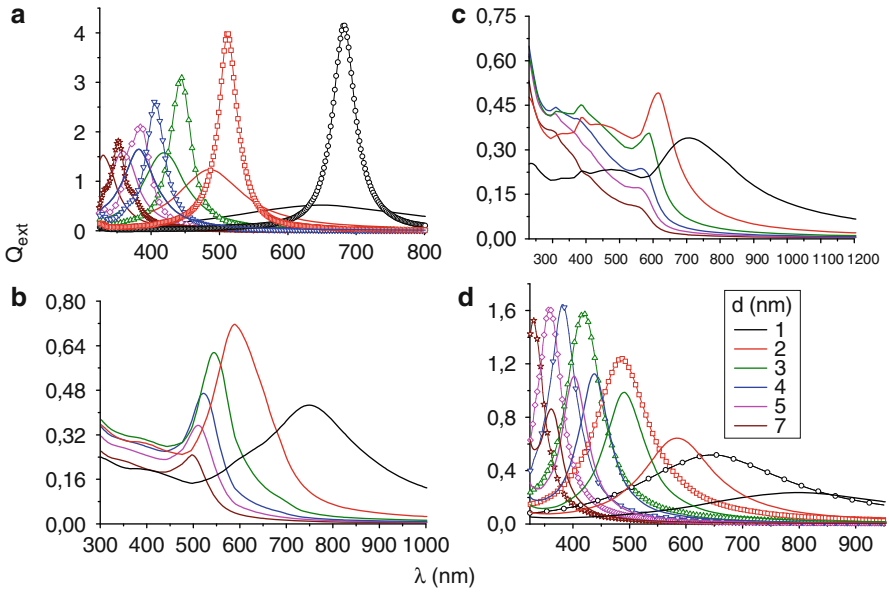

Fig. 5.22 Behavior of Q_{ext} as a function of the incident wavelength for different metallic nanotubes. (**a**) Ag nanotubes: in *solid line* Q_{ext} when the dielectric function is corrected by the thickness of the metallic shell and *hollow symbols* Q_{ext} for bulk dielectric function; (**b**) Q_{ext} for Au nanotubes; (**c**) idem to (**b**) for Cu nanotubes and (**d**) Q_{ext} curves for Ag nanotubes (*hollow symbols*) and Ag-shell silica-core (*solid line*) systems are compared. In all cases, the external radius is constant: $r_1 = 10$ nm and the internal radios r_2 is variable. *Line code* in (**a**–**c**) is the same as shown in (**d**)

Nanoshells and nanotubes are other example of tunable plasmonic nanostructures with important applications as nanoantennas [2, 42], light manipulators [132] and biomedical applications (http://halas.rice.edu/) [3]. Many recent studies have been focused on metallic nanoshells where the plasmon resonance can be tuned very simply by varying the shell thickness. In general, the models used to describe the response of systems with metallic shells are based on a quasi-static approximation and dipole interaction [133–137].

We focus on metallic shells with thickness from 1 to 10 nm, where the dielectric function of the metallic layer should be corrected by size [92], and the quasi-static approximation could be applicable. Results for larger systems (core radius larger than 50 nm) with thin shell layers, where the electromagnetic response is dominated by retarded effects, are also shown.

Numerical results for eigenmode excitation of metallic nanotubes corresponding to p-mode [138] are shown in Fig. 5.22 where the extinction cross section as a function of incident wavelength is depicted. For these examples and in this subsection, the external radius r_1 is constant and equal to 10 nm and the thickness ($d = r_1 - r_2$) of the nanotube is considered variable.

Figure 5.22a shows the extinction cross section for Ag nanotubes considering the dielectric function with (solid line) and without (hollow symbols) size correction.

Figure 5.22b shows the extinction cross section Au nanotubes with dielectric function thickness correction, (c) the extinction cross section for Cu nanotubes with corrected dielectric function, and (d) the extinction cross section for Ag nanotubes (hollow symbols) versus Ag/silica system (solid line) with dielectric function corrected. The inset in Fig. 5.22d shows the shell thickness code, valid also for panels (c) and (d). Hollow and solid symbols with the same color correspond to the same shell.

For these particle sizes, in general, $Q_{ext} \approx Q_{abs}$ and the extinction peaks observed in Fig. 5.7 are related with the excitation of eigenmodes. It is interesting to note that for the Ag shell, our model gives as a main result a significant widening of the resonance peak (due to the strong increase in the imaginary part of the dielectric function). The complex propagation constant solution to the homogeneous problem – eigenmode – moves away from the real axis into the complex plane as the thickness of the shell decreases. However, if the bulk dielectric function is used for all thicknesses, an opposite effect is observed: As the thickness of the shell decreases, the amplitude of the peaks increases and a more complicated evolution is observed for some cases (Au and Cu, for example). This behavior in the extinction cross-section spectra has been observed for all the examples shown in this section.

Extinction curves for Au nanotubes show a more complicated behavior. This effect can be associated to the multipole terms that play an important role for Au in the short wavelength range [137]. It can be observed in Fig. 5.22b that extinction curves for Au nanotubes present large and broad peaks for thin shells. The maximum of the extinction curves occurs for $d = 2$ nm in this configuration (see captions), while for $d = 1$ nm, the extinction peak is attenuated and strongly shifted to the IR zone. In all cases, the dipolar term dominates the extinction spectrum and the higher multipole orders have a perturbative character overlapped with the dipolar term. We can observe a similar behavior for Cu nanotubes (Fig. 5.22c) but with a more complex optical response in the short wavelength range.

In Fig. 5.22d, we compare electromagnetic response of Ag nanotubes with respect to a silica-core one ($\varepsilon_{\text{core}} = 2.25$), both with the same shell thickness. When a silica core is considered, all the spectra are shifted to the IR region, and the peaks are attenuated with respect to the same condition in the Ag nanotubes. The main cause of this shift is the relative value that the metal dielectric function takes with respect to the core dielectric constant. Therefore, the resonant coupling between surface plasmons (in both faces of the metallic shell), mainly dipolar, experiences a strong shifting to the IR zone and an intensity attenuation. This mechanism is consistent with that described by the method of hybridization [2].

Due to the size of this system (few nanometers), it is possible to compare our results with a non-retarded model. Moradi [133] proposes a non-retarded hybridization model to find the optical response of a core-shell 2D. Based on this model, it is possible to find an analytical expression to predict evolution of the peaks as a function of r_2/r_1 ratio.

In Fig. 5.23, we show the evolution of the isolated peaks of Fig. 5.22a ($\lambda_{\text{peak}} = \lambda^*$) is a function of the r_2/r_1 ratio, for both dielectric function, bulk and corrected,

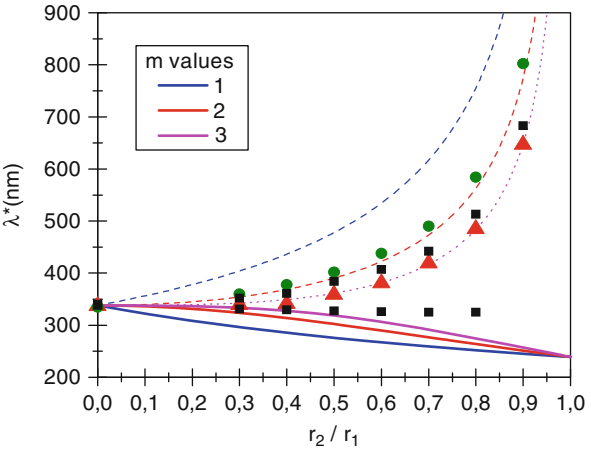

Fig. 5.23 Behavior of the extinction peaks λ^* versus r_2/r_1. *Dashed lines* represent the curves computed from [133]. The numbers labeled with m correspond to the angular momentum. *Black squares* for bulk dielectric function, *red triangles* for corrected dielectric function, and *green circles* for Ag-shell silica-core 2D nanoparticles

together with the silica-core metallic-shell systems (corresponding to Fig. 5.22d). In dashed lines, we show the dispersion relationship of plasmons from hybridization model corresponding to Ag nanotubes for three angular momenta m [133]. Squares and circles represent bulk dielectric function and triangles correspond to corrected dielectric function. Using the bulk dielectric function, it is possible to observe two branches, while only one branch can be detected when corrected dielectric function is used. Our calculations show that the fundamental excitation for an Ag nanotube (associated to the dipole order) dominates the extinction coefficient. In general, the principal extinction peaks follow a functional form like the predicted one by the plasmon hybridization model. The main discrepancy between the curves obtained by the non-retarded approximation and the maxima of extinction calculated by the integral method is due to the different dielectric functions used to model the systems. We observe that in the limit when $r_2 \to 0$ (solid wire), both the analytic curves and singles points (plasmonic excitations) converge to the same point.

In the quasi-static approach limit, it is possible to carry out an analysis of the interaction between eigenmodes: Eq. 6 in [133] can be rewritten in the incremental ratio form [92]:

$$\frac{\lambda_{res} - \lambda_{sp}}{\lambda_{sp}} = \frac{1}{\sqrt{1 - \left(1 - \frac{d}{r_1}\right)^m}} - 1, \tag{5.42}$$

where λ_{sp} corresponds to the wavelength for which the plasmon is excited in a solid wire with radius r_1. In this way, we can obtain a scaling law for the peaks shift that depends only on relative geometrical parameters. With this in mind, Fig. 5.24 plots $(\lambda_{\text{peak}} - \lambda_{sp})/\lambda_{sp}$ for the peak of low energy as a function of d/r_1 for different materials: Ag (circles), Au (squares), and Cu (triangles) nanotubes. Hollow symbols correspond to data extracted from Figs. 5.22a–c. In particular, for Ag nanotubes, we show in red solid circles results for a nanotube with $r_1 = 50$ nm

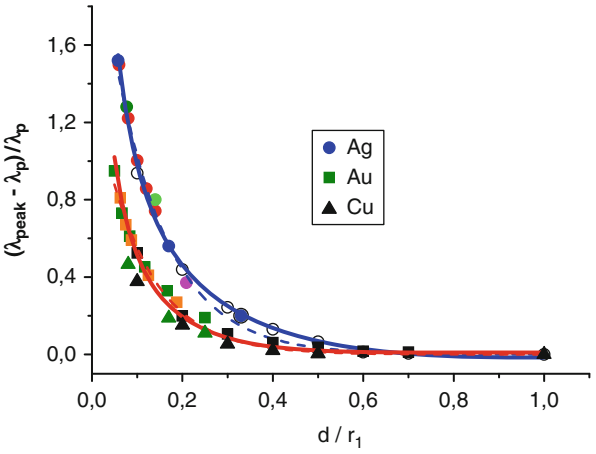

Fig. 5.24 Dependence of the relative shift $(\lambda_{peak} - \lambda_{sp})/\lambda_{sp}$ versus d/r_1 for the last peak eigenmode resonances for Ag (*circles*), Au (*squares*), and Cu (*triangles*) nanotubes. *Solid* and *dashed lines* correspond to the fitting curves: exponential and Eq. 5.43, for Ag nanotubes (*blue*) and Au, Cu nanotubes (*red*), respectively

and in green circles for $r_1 = 120$ nm. The rest of the circles shown were obtained for $r_1 = 60$ nm. For Au and Cu nanotubes, we can see that the curves are very close and differ slightly from that corresponding to Ag nanotubes. In these curves, solid black symbols (squares and triangles) correspond to $r_1 = 10$ nm, the green symbols to $r_1 = 60$ nm, and orange square symbols to $r_1 = 80$ nm.

It is remarkable to note that all the points, regardless of the size of the nanotubes, can be arranged on a single curve which can be adjusted by a single-exponential decay function. A similar law was found by Jain and El-Sayed for coated spheres and dimers [134].

As a first approximation, this extinction peak is due to a dipolar interaction between plasmons. We propose a functional form for the fitting equation like Eq. 5.42 with two degrees of freedom:

$$\frac{\lambda_{res} - \lambda_{sp}}{\lambda_{sp}} = \frac{a}{\sqrt{1 - \left(1 - \frac{d}{r_1}\right)^c}} - 1 \tag{5.43}$$

The best adjustment to the black hollow circles occurs for $a = 0.988 \pm 0.005$ and $c = 2.87 \pm 0.05$ (for the complete data $a = 0.98 \pm 0.02$ and $c = 2.7 \pm 0.1$). Due to the universality of the curve, therefore, all the points can be fitted by Eq. 5.43. In Fig. 5.23, we show the two fittings: in dashed line (blue and red), the exponential law, and in solid line, the fit corresponding to Eq. 5.43.

The black square and triangle data points (corresponding to the Au and Cu $r_1 = 10$ nm) can be adjusted by the same equation (the curves of Au and Cu show little difference between them). We found that the best adjustment for the Au nanotubes occurs for $a = 1.01 \pm 0.01$ and $c = 5.6 \pm 0.2$ (solid line in Fig. 5.23). This numerical exploration in order to fit the data with the hybridization model gives as a result high values for the parameter c (equivalent to the angular momentum for the Moradi's model). This high values found for c may indicate that the

non-retarded dipole approximation is not able to describe accurately the plasmon interaction through the nanotubes walls, at least for thin shells. Recently, Encina and Coronado [139] reached a similar conclusion for dimers with Ag nanospheres, where they also observe a separation between the "universal curves" between Ag and Au dimers.

We found that the shift of the excitation peaks toward the IR is directly associated with changes in the thickness of the wall of the nanotube. In addition, the thickness of the walls modifies the constitutive parameters and, as a consequence, the plasmon–plasmon interactions. This effect is clearly seen in the Ag nanotubes. It can be observed, in particular for these structures, that the effects of retardation should be included to describe correctly the interaction between plasmons when the thickness of the layer decreases, as occurs in Ag dimers. As a result, the fractional relative plasmon curve for Ag nanotubes is separated slightly from that corresponding to Au and Cu as the shell thickness decreases and the interband transitions start to be significant. For relationships $d/r_1 > 0.6$, these effects are attenuated and the "universal curve" appears to be recovered (at least for nanotubes). The presence of a dielectric core produces perturbations in the plasmon–plasmon interaction, and the extinction peaks are shifted toward the IR zone with respect to nanotubes in the same condition. Then, the fractional plasmon shift versus d/r_1 shows a difference when nanotubes and core-shell 2D nanoparticles – for the same external radii – are compared.

In Fig. 5.25, we compare the near-field intensities, for the three structures shown in this section in the resonance condition. Figure 5.25a corresponds to the near field at $\lambda = 338$ nm for Ag circular solid nanowire with 10 nm of radius (red line extinction curve with solid circles in Fig. 5.16a). Figure 5.25b shows an intensity map for a nanotube with 10 nm of external radius and Ag wall thickness of 3 nm at $\lambda = 448$ nm (solid green curve in Fig. 5.17a). Figure 5.25c, d show the near field for the same Ag ellipsoidal nanowire (a = 10 nm, b = 60 nm), for two fundamental electric field orientations: panel (c) electric field parallel to the minor axis, resonant wavelength 329 nm; panel (d) electric field parallel to the major axis at $\lambda = 500$ nm (see red curves in Fig. 5.20a). The arrows, in all cases, indicate the direction of the incidence.

The intensity maps shown in Fig. 5.25 for the eigenmode resonances are consistent with a dipolar response (the single peak shown in the spectra of extinction curve). Due to the size of the particles considered, the scattering cross section is negligible and the entire spectrum of extinction is due to absorption. Intensifications of fields due to local resonances are very short range and can reach up to two orders of magnitude of the incident field. The resonance occupies a small volume around the nanoparticle interface, similar to a point source. This high density of field is the tool for the thermal treatment of cancer cells. In the intensity maps, we can see the field penetration inside the metal structure. Almost, the entire volume (surface) of the nanoparticle is involved in the resonant phenomenon. Thus, part of the resonant energy of free electrons can be transmitted to the structure of the metal, causing an increase in kinetic energy resulting in an increase in metal temperature [93].

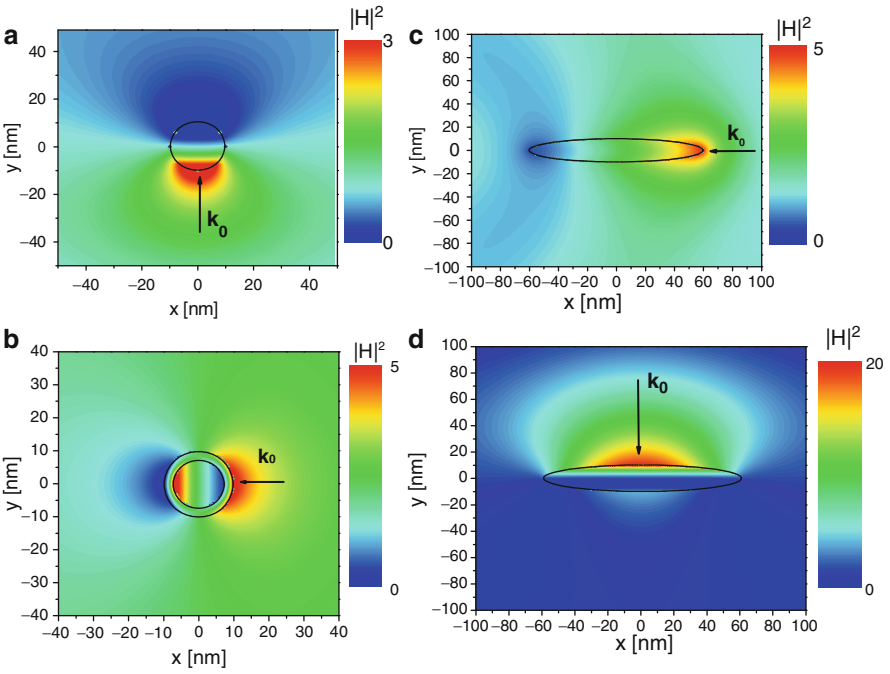

Fig. 5.25 Total near-field intensity maps $|H|^2$ (normalized to the incident intensity) for different Ag nanostructures in resonance. (**a**) *Solid circular* nanowire, $\lambda = 338$ nm, 10 nm of radius; (**b**) nanotube with 10 nm of external radius and 7 nm of the internal radius, $\lambda = 448$ nm. (**c**, **d**) Elliptical cross-section nanowire (aspect ratio $\mathscr{R} = 6$) for the two fundamental electric field orientations: parallel to the minor axis, $\lambda = 329$ nm and parallel to the major axis, $\lambda = 500$ nm, respectively. *Arrows* indicate the incident direction and the host medium is air

5.3.4 Experimental Results

The relation between the plasmon resonance maximum and the diameter of the spherical particle has been used by some authors as a tool to establish a range of sizes of studied metal Nps, TEM being the central technique for accurately measuring certain particles. Link et al. [140] studied laser-induced shape changes of colloidal gold nanorods after irradiating the sample with femtosecond and nanosecond laser pulses. The gold nanorods were prepared using an electrochemical method. The shape transformations of the gold nanorods are followed by two techniques: visible absorption spectroscopy by monitoring the changes in the plasmon absorption bands characteristic for gold nanoparticles and transmission electron microscopy (TEM) in order to analyze the final shape and size distribution. The extinction spectra are used to monitor the evolution of the plasmon resonances as the samples are irradiated with different pulselength lasers.

Mafuné et al. [141–147] studied the formation of noble metal (Au, Ag, and Pt) Nps under ns-regime laser ablation of solid targets in water and its relation with surfactant concentration. In all the series of papers, the authors use TEM to both

show the sphericity of the ablated Nps as well as determine their average diameter from sampling about 1,000 Nps. The extinction spectra are used to show the existence of the plasmon resonance and its dependence on different experimental parameters such as number of laser pulses, surface modifier concentration, etc.

Chen et.al [148] studied the induced alloying of Au–Pd and Ag–Pd colloidal mixtures by ns pulse laser irradiation. UV–vis absorption spectra of 1:1 and 2:1 molar ratios of Au/Pd colloidal suspensions are used to show the development of the mixture composition as a function of the laser exposure time, while the approximate sizing is performed by TEM analysis.

In a very interesting paper by Besner et al. [149], fragmentation of colloidal gold Nps by fs laser radiation is demonstrated by showing the expected blueshift of the plasmon resonance as the particle radius decreases.

In a similar way, Barcikowski and collaborators [150] study the influence of several parameters (such as pulse energy, dodecanthiol added to *n*-hexane) on gold Nps production using ultrashort pulse lasers. They show these influences by comparing extinction spectra from several treated samples, indicating the plasmon peak shift for different dodecanthiol concentrations in the liquid prior to fs laser ablation at two different laser fluences.

As a final example, Pyatenko et al. [151] produced silver nanoparticles by irradiating an Ag target with a 532 nm ns-regime laser in pure water. By working with high laser power and small spot sizes, the authors claimed to have synthesized very small spherical particles with a typical size of 2–5 nm. UV–vis extinction spectra for different beam spot sizes are used for estimating the amount of ablated Ag per pulse, according to a suggestion made by Mafuné et al. [141].

Our group has studied the relations between the different features of the extinction spectra and the size (or structure) of the Nps to use them for sizing purposes.

Scaffardi and Tocho [30] have explored the simultaneous modification of the free electron contribution to the dielectric function as well as the bound electron contribution, on the basis of Eqs. 5.11, 5.12, 5.13, 5.20, 5.38, and 5.40 to fit extinction spectra of very small nanoparticles (less than 2 nm radius). The contribution of electron transitions from the *d*-band to the conduction band was modeled using an integral expression for adding all the interband transitions across the bandgap. The dependence of the electronic density of states with size (the states begin to separate as the radius decreases) modulates the above integral expression and enables a much better fitting of the extinction spectra of very small gold nanoparticles, obtained by the inverse-micelle method. The fitting also permits the determination of microscopic parameters like the bound electron damping constant, the energy gap, and the Fermi energy of the particle.

Another application of extinction spectroscopy was developed by Roldán et al. [34], who described a method for preparation of Ag nanoparticles from chemical reduction of $AgNO_3$ in ethanol with ATS [*N*-[3-(trimethoxysilyl)propyl] diethylenetriamine] as surface modifier. While morphologic and structural characterizations of samples are conducted by Atomic Force Microscopy (AFM) and X-ray diffraction (XRD), UV–vis extinction spectroscopy interpreted through Mie theory is used to analyze the size evolution in the fabrication process of spherical silver

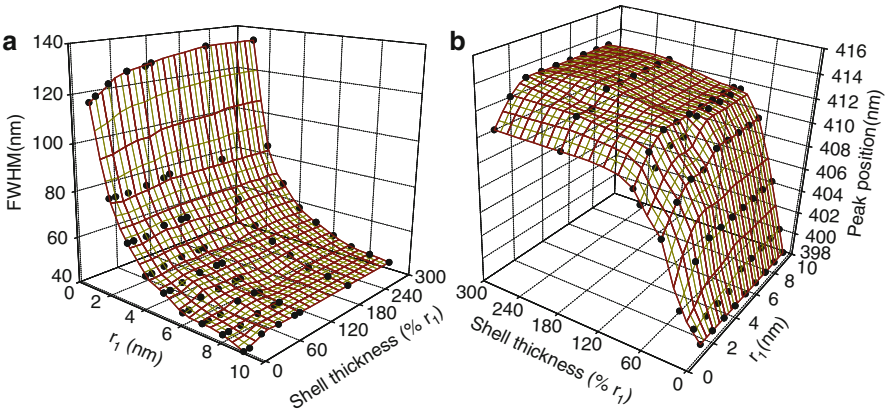

Fig. 5.26 (**a**) FWHM and (**b**) peak position of ATS-coated silver Nps immersed in ethanol as a function of core radius (r_1) and shell thickness

nanoparticles. This evolution is studied as a function of the time elapsed between the beginning of the reaction and the extraction of the sample and as a function of the temperature during the chemical reaction. The study was based on the inverse relation between the plasmon width (FWHM) and the mean radius, specially for values below 6 nm.

The optical extinction spectroscopy approach was also shown to be useful in sizing core-shell type Nps by Schinca and Scaffardi [35]. In Fig. 5.26, the authors made a detailed analysis of the dependence of plasmon resonance wavelength and FWHM with core radius and shell thickness of ATS-coated Ag Nps and were able to establish that, for sizes less than 10 nm, the plasmon peak wavelength depends almost exclusively on the shell thickness while the FWHM depends mainly on core radius. Based on these regularities, a simultaneous experimental measurement of plasmon width and plasmon peak position in extinction spectroscopy is proposed as a simple protocol for determining the mean size of noble metal core-shell nanospheres (in the size range smaller than 10 nm radius). The protocol was successfully applied to chemically and laser-ablation fabricated Ag Nps, the results of which agree with established TEM analysis.

A similar method was applied by Schinca et al. [36] to size small core-shell silver–silver oxide generated by ultrashort pulse laser ablation of solid target in water. Figure 5.27a, b show a TEM picture of the sample suspension and the corresponding size distribution histogram, respectively. In this case, the Ag Nps are capped with its own oxide during the ablation process, with a variety of thicknessess. A fit of the full experimental spectrum using Mie theory allows the determination of core size and shell thickness distributions as a function of fluence. The redshift of the plasmon peak wavelength with respect to the bare-core peak wavelength at 400 nm, produced by the oxide shell, may be easily measured even for very small thicknesses. It was found that the dominant silver oxide effective thickness is inversely proportional to the fluence, reaching a maximum of 0.2 nm

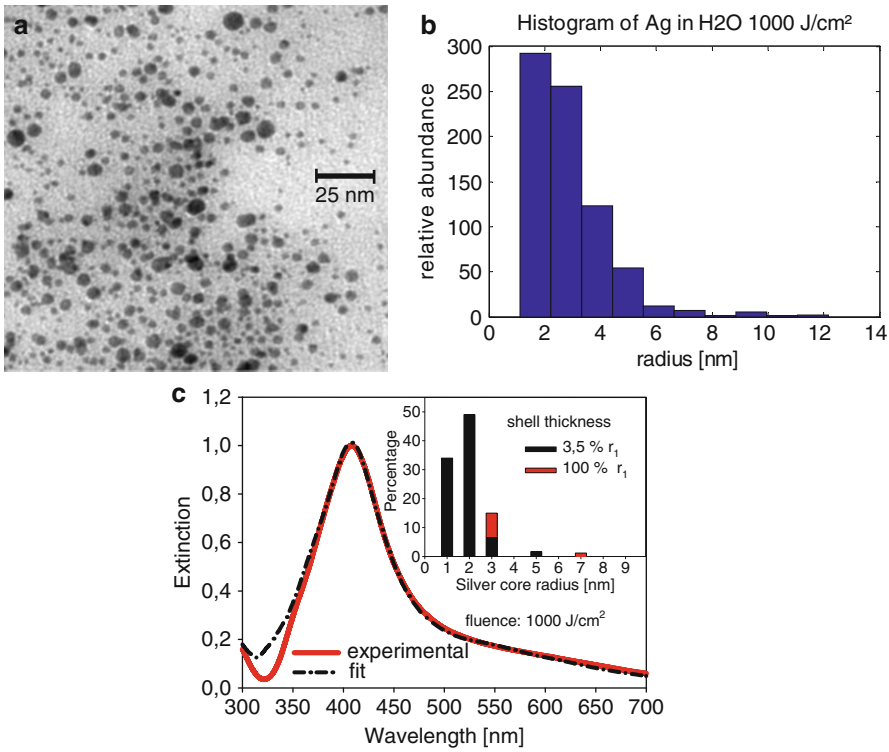

Fig. 5.27 (**a**) TEM image and (**b**) corresponding histogram of the sample of silver Nps immersed in water, fabricated at high fluence (1,000 J/cm^2); (**c**) Experimental extinction spectrum (*solid line*) and theoretical fit (*dot-dashed line*) for silver Nps in water at 1,000 J/cm^2 fluence. *Inset* shows size relative abundance distribution used for the fit

for a fluence of 60 J cm^{-2} and a minimum of 0.04 nm for a fluence of 1,000 J cm^{-2}, as it is shown in Fig. 5.27c.

For the case of Ag core-Ag_2O shell Nps, the relations depicted in Fig. 5.26 are a bit more complex than in the metal core dielectric shell case. Figure 5.28 shows the results of calculations of peak position (panel a), contrast (panel b) and FWHM (panel c) as a function of core radius and shell thickness. These 3D plots picture the interrelation between these three parameters. Although peak position is strongly dependent on shell thickness and almost independent of core radius, FWHM and contrast depend on both variables with similar strength. In spite of this complexity, Santillán et al. [41] have shown that a simple stepwise protocol to size oxide thickness growth over bare-core silver Np only from spectroscopic data could be devised and successfully applied to experimentally obtained single-particle extinction spectra.

Finally, the possibility of using optical extinction spectroscopy for the case of metal coated dielectric core Nps is also evident when the relation between the FWHM and peak resonance position as a function of core radius and shell thickness is analyzed. Figure 5.29 plots these relations for the case of a silica core and Ag shell.

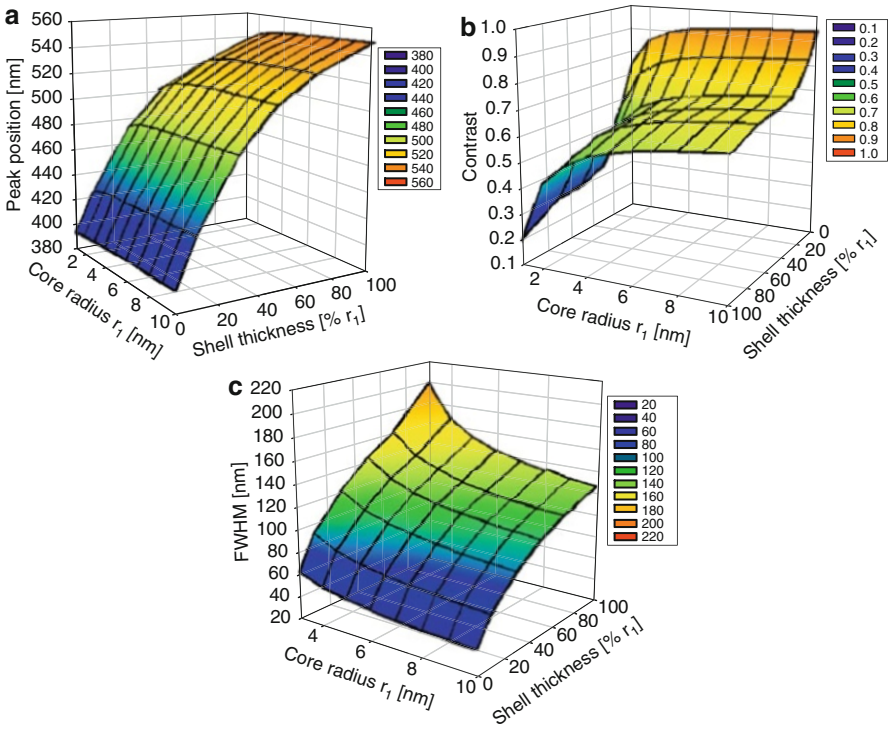

Fig. 5.28 (**a**) Plasmon peak wavelength, (**b**) Contrast and (**c**) FWHM as a function of core radius and shell thickness for Ag–Ag_2O core-shell Nps in water

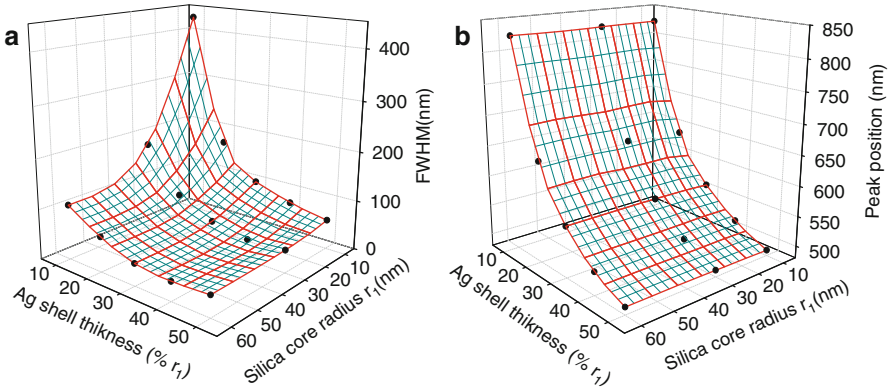

Fig. 5.29 (**a**) FWHM and (**b**) peak position of Ag-coated silica-core Nps immersed in ethanol as a function of core radius (r_1) and shell thickness

It can be seen that the peak position (panel b) is still strongly dependent on metal shell thickness and almost independent of silica-core radius, but FWHM depends on both Ag-shell thickness and silica-core radius. In this case, a measurement protocol may also be devised to size separately the core radius and metal shell thickness of single core-shell nanoparticles. These two last cases are important since researchers in the biological area are directing their interest in developing single-particle nanosensors for intracellular measurement of oxidative processes [152, 153].

6 Conclusions and Future Perspective

Throughout this chapter, we have shown results referring to the optical response of infinitely long metallic wires with cross section of the order of a few nanometers. The theoretical and numerical results suggest the concrete possibility of controlling this optical response with an appropriate engineering of nanoparticles. The relation of the constitutive parameters with particle size, coupled with interband transitions in the metal, gives a correct description of the experimentally measured optical observables. Our theoretical results show a slight blueshift of the resonance peak (for p-polarization) as the particle size decreases (most notorious for Ag nanowires).

The dependence of dielectric function on the particle size generates an anisotropy with the polarization of the incident wave: The size correction begins to be necessary for radii of the order of 7 nm and when the electric field vector is parallel to the cross section. This sensitivity of the eigenmodes with the orientation of the electric field can also be observed when the cross-sectional geometry deviates from the perfect circular symmetry. For the example studied in this work, oblong particles (two main axes), the orientation of the electric field determines two plasmonic resonances. The design of the geometry of the particle can "tune in" two-channel resonance. One channel is shifted to the blue and the other with a greater range of variability to the red (compared to the position of the plasmon for circular particle). Responsible for such behavior is an anisotropic tensor polarization induced by external fields.

The geometry of the nanoparticle and the surrounding medium significantly influence the optical response. A mixture of both conditions, along with size corrected dielectric function, can yield systems with multiple plasmonic excitations with redshifts of the resonant peak. While the physical principles involved in the electromagnetic interaction with the metal layer are the same (the excitation of free electrons), now couplings between resonant eigenmodes generated on both sides of the shell exist. This plasmon coupling reminds the orbital electronic coupling in diatomic molecules. The resonant couplings of the eigenmodes can be estimated in the small-particle limit, using a hybrid mix of "wave functions": eigenmodes corresponding to a solid particle with corresponding eigenmodes in a cavity. The interactions between surface plasmons generated on both sides of the metal shell determine the resonant channel, with possible shifts of the resonance peak toward blue or red.

The understanding of the physical mechanisms involved in the optical response of nanoscale systems (which results in the ability to "tune" these eigenmodes through the design of structures) opens a large number of practical applications. Today, these applications seem to be focusing strongly on biomedicine (optical tracers, heat treatment of tumors [93]), optical communications (plasmon waveguide-based nanocircuitry, optical antennas [4, 154]), and engineering of solar cells [155].

Acknowledgments This work was partially financed by Consejo Nacional de Investigaciones Científicas y Técnicas, CONICET (Grants PIP 0394 and PIP 0145), and by Facultad de Ingeniería de Universidad Nacional de La Plata (Grant 11/I151). LBS and ML belong to CONICET, DCS and FAV belong to the Comisión de Investigaciones Científicas de la Provincia de Buenos Aires (CICBA), Argentina, and JMJS and MRA are CONICET fellowship holders.

References

1. Yogeswaran U, Chen S-M (2008) A review on the electrochemical sensors and biosensors composed of nanowires as sensing material. Sensors 8:290–313
2. Halas NJ, Lal S, Chang W-S, Link S, Nordlander P (2011) Plasmons in strongly coupled metallic nanostructure. Chem Rev 111:3913–3961
3. Hirsch L et al (2006) Metal nanoshells. Ann Biomed Eng 34:15–22
4. Giannini V, Fernández-Domínguez AI, Heck SC, Maier SA (2011) Plasmonic nanoantennas: fundamentals and their Use in controllingthe radiative properties of nanoemitters. Chem Rev 111:3888–3912
5. Brambilla G (2010) Optical fibre nanowires and microwires: a review. J Opt 12:043001, 1–19
6. Macwan DP, Dave PN, Chaturvedi S (2011) A review on nano-TiO_2 sol–gel type syntheses and its applications. J Mater Sci 46:3669–3686
7. Huang X, El-Sayed MA (2010) Gold nanoparticles: optical properties and implementations in cancer diagnosis and photothermal therapy. J Adv Res 1:13–28
8. Wang W, Yang Q, Fan F, Hongxing X, Wang ZL (2011) Light propagation in curved silver nanowire plasmonic waveguides. Nano Lett 11:1603–1608
9. Ma L-C, Zhang Y, Zhang J-M, Ke-Wei X (2011) First-principles study on structural and electronic properties of copper nanowire encapsulated into GaN nanotube. Physica B 406:3502–3507
10. Long Y-Z, Li M-M, Changzhi G, Wan M, Duvail J-L, Liu Z, Fan Z (2011) Recent advances in synthesis, physical properties and applications of conducting polymer nanotubes and nanofibers. Prog Polym Sci 36:1415–1442
11. Barnard ES, Pala RA, Brongersma ML (2011) Photocurrent mapping of near-field optical antenna resonances. Nat Nanotechnol 6:588–593
12. Makino K, Tominaga J, Hase M (2011) Ultrafast optical manipulation of atomic arrangements in chalcogenide alloy memory materials. Opt Express 19:1260–1270
13. Alekseeva AV, Bogatyrev VA, Dykman LA, Khlebtsov BN, Trachuk LA, Melnikov AG, Khlebtsov NG (2005) Preparation and optical scattering characterization of gold nanorods and their application to a dot-immunogold assay. Appl Opt 49:6285–6295
14. Encina ER, Coronado EA (2007) Resonance conditions for multipole plasmon excitations in noble metal nanorods. J Phys Chem C 111(45):16796–16801
15. Perassi EM, Hernandez-Garrido JC, Moreno MS, Encina ER, Coronado EA, Midgley PA (2010) Using highly accurate 3D nanometrology to model the optical properties of highly irregular nanoparticles: a powerful tool for rational design of plasmonic devices. Nano Lett 10:2097–2104

16. Scaffardi LB, Pellegri N, de Sanctis O, Tocho LO (2005) Sizing gold nanoparticles by optical extinction spectroscopy. Nanotechnology 16:158–163
17. Mahmoud MA, Snyder B, El-Sayed MA (2010) Surface plasmon fields and coupling in the hollow gold nanoparticles and surface-enhanced Raman spectroscopy. Theory and experiment. J Phys Chem C 114:7436–7443
18. Ferrara MA, Rendina I, Basu SN, Dal Negro L, Sirleto L (2012) Raman amplifier based on amorphous silicon nanoparticles. Int J Photoenergy 2012:254946, 1–5
19. Eustis S, El-Sayed MA (2006) Determination of the aspect ratio statistical distribution of gold nanorods in solution from a theoretical fit of the observed inhomogeneously broadened longitudinal plasmon resonance absorption spectrum. J Appl Phys 100:044324, 1–7
20. Jian Z, Junwu Z, Yongchang W (2004) Influence of surface charge density on the plasmon resonance modes in gold nanoellipsoid. Physica B 353:331–335
21. Zhu J (2005) Shape dependent full width at half maximum of the absorption band in gold nanorods. Phys Lett A 339:466–471
22. Khlebtsov B, Khanadeev V, Pylaev T, Khlebtsov NA (2011) New T-matrix solvable model for nanorods: TEM-based ensemble simulations supported by experiments. J Phys Chem C 115:6317–6323
23. Encina ER, Perassi EM, Coronado EA (2009) Near-field enhancement of multipole plasmon resonances in Ag and Au nanowires. J Phys Chem A 113:4489–4497
24. Pavlovic G, Malpuech G, Gippius NA (2010) Dispersion and polarization conversion of whispering gallery modes in nanowires. Phys RevB 82:195328, 1–8
25. Scaffardi LB, Lester M, Skigin D, Tocho JO (2007) Optical extinction spectroscopy used to characterize metallic nanowires. Nanotechnology 18:315402, 1–8
26. Brambilla G (2010) Accurate 3D nanometrology to model the optical properties of highly irregular nanoparticles: a powerful tool for rational design of plasmonic devices. Nano Lett 10:2097–2104
27. Kottmann JP, Martin OJF, Smith DR, Schultz S (2000) Field polarization and polarization charge distributions in plasmon resonant particles. New J Phys 2:271–279
28. Scaffardi L, Tocho JO, Yebrin L, Cantera C (1996) Sizing particles used in the leather industry by light scattering. Opt Eng 35(1):52–56
29. Garcés Vernier I, Sotolongo O, Hernández MP, Scaffardi L, García-Ramos JV, Rivas L (2000) Determination of particle size distribution of particles on aerosols and suspensions by ultraviolet–visible-near infrared absorbance measurements. A new procedure for absorbing particles. Phys Status Solid B 220:583–586
30. Scaffardi LB, Tocho JO (2006) Size dependence of refractive index of gold nanoparticles. Nanotechnology 17:1309–1315
31. Scaffardi LB, Lester M, Skigin D, Tocho JO (2007) Optical extinction spectroscopy used to characterize metallic nanowires. Nanotechnology 18:315402–315410
32. Scaffardi LB, Tocho JO (2008) Absorption spectra of tiny gold and silver objects. J Luminisc 128(5–6):828–830
33. Torchia GA, Scaffardi LB, Méndez C, Moreno P, Tocho JO, Roso L (2008) Optical extinction for determining size distribution of gold nanoparticles fabricated by ultrashort pulsed laser ablation. Appl Phys A Mater Sci Process 93(4):967–971
34. Roldán MV, Scaffardi LB, de Sanctis O, Pellegri N (2008) Optical properties and extinction spectroscopy to characterize the synthesis of amine capped silver nanoparticles. Mater Chem Phys 112:984–990
35. Schinca DC, Scaffardi LB (2008) Core and shell sizing of small silver coated nanospheres by optical extinction spectroscopy. Nanotechnology 19:495712–495720
36. Schinca DC, Scaffardi LB, Videla FA, Torchia GA, Moreno P, Roso L (2009) Silver-silver oxide core-shell nanoparticles by femtosecond laser ablation. Characterization by extinction spectroscopy. J Phys D: Appl Phys 42:215102–215111
37. Videla FA, Torchia GA, Schinca DC, Scaffardi LB, Moreno P, Méndez C, Roso L, Giovanetti L, Lopez JR (2009) Role of supercontinuum in the fragmentation of colloidal gold nanoparticles in solution. Proc SPIE 7405:74050U-1–74050U-12

38. Videla FA, Torchia GA, Schinca DC, Scaffardi LB, Moreno P, Mendez C, Giovanetti L, Ramallo López J, Roso L (2010) Analysis of the main optical mechanisms responsible for fragmentation of gold nanoparticles by femtosecond laser radiation. J Appl Phys 107:114308-1–114308-8
39. Santillán JMJ, Scaffardi LB, Schinca DC, Videla FA (2010) Determination of nanometric Ag_2O film thickness by surface plasmon resonance and optical waveguide mode coupling techniques. J Opt 12:045002–045010
40. Videla FA, Torchia GA, Schinca DC, Scaffardi LB, Moreno P, Méndez C, Giovanetti LJ, RamalloLopez JM, Roso L (2010) Analysis of the main optical mechanisms responsible for fragmentation of gold nanoparticles by femtosecond laser radiation. Virtual J Sci Technol Ultrafast Sci Sect Photonics 9(7)
41. Santillán JMJ, Scaffardi LB, Schinca DC (2011) Quantitative optical extinction-based parametric method for sizing a single core–shell Ag–Ag_2O nanoparticle. J Phys D: Appl Phys 44:105104–105112
42. Abraham Ekeroth RM, Lester M, Scaffardi LB, Schinca DC (2011) Metallic nanotubes characterization via surface plasmon excitation. Plasmonics 6(3):435–444
43. Coronado E, Schatz G (2003) Surface plasmon broadening for arbitrary shape nanoparticles: a geometrical probability approach. J Chem Phys 7:3926–3934
44. Kottmann JP, Martin OJF (2001) Influence of the cross section and the permittivity on the plasmon-resonance spectrum of silver nanowires. Appl Phys B 73:299–304
45. Ranjan M, Oates TW, Facsko S, Mller W (2010) Optical properties of silver nanowire arrays with 35 nm periodicity. Opt Lett 35:2576–2578
46. Brack M (1993) The physics of simple metal clusters: self-consistent jellium model and semiclassical approaches. Rev Mod Phys 3:677–732
47. Bonacic-Koutecky V, Piercarlo Fantucci J, Koutecky J (1991) Quantum chemistry of small clusters of elements of groups Ia, Ib, and IIa: fundamental concepts, predictions, and interpretation of experiments. Chem Rev 91:1035–1108
48. Bohren CF, Huffman DR (1983) Absorption and scattering of light by small particles. Wiley, New York
49. Lorentz HA (1905) The motion of electrons in metallic bodies. Proc R Acad Sci Amst 7:438, 585, 684
50. (a) Drude P (1900) The theory of metals ions. Phys Zeitsch 1:161; (b) Drude P (1900) Zur elektronentheori der metalles 1 Teil. Ann Phys (Leipzig) 1:566
51. Kreibig U, Vollmer M (1995) Optical properties of metal clusters. Springer, Berlin
52. Kraus WA, Schatz GC (1983) Plasmon resonance broadening in small metal particles. J Chem Phys 79:6130–6139
53. Kraus WA, Schatz GC (1983) Plasmon resonance broadening in spheroidal metal particles. J Chem Phys 99:353–357
54. Doyle WT (1958) Absorption of light by colloids in alkali halide crystals. Phys Rev 111:1097–1077
55. (a) Genzel L, Martin TP, Kreibig U (1975) Dielectric function and plasma resonances of small metal particles, Z Physik B 21:339. http://www.springerlink.com/content/j2885x1521060275/; (b) Ruppin R, Yatom H (1976) Size and Shape Effects on the Broadening of the Plasma Resonance Absorption in Metals, Phys Status Solid B 74:647; (c) Wood DM, Ashcroft NW (1982) Quantum size effects in the optical propertiesof small metallic particles, Phys Rev B 25:6255; (d) Apell P, Penn DR (1983) Optical Properties of Small Metal Spheres:surface Effects, Phys Rev Lett 50:1316–1319
56. Granqvist CG, Hunderi O (1977) Optical properties of ultra fine gold particles. Phys Rev B 16:3513–3534
57. Palik ED (1985) Handbook of optical constants of solids. Academic, San Diego
58. Johnson PB, Christy RW (1972) Optical constants of noble metals. Phys Rev B 6:4370–4379
59. Pinchuk A, von Plessen G, Kreibig U (2004) Influence of interband electronic transitions on the optical absorption in metallic nanoparticles. J Phys D: Appl Phys 37:3133–3139

60. Rosei R, Antonangeli F, Grassano UM (1973) d bands position and width in gold from very low temperature thermomodulation measurements. Surf Sci 37:689–699
61. Novotny L, Hecht B (2006) Principles of nano-optics. Cambridge University Press, Cambridge
62. Maier S (2006) Plasmonic: metal nanoetructures for subwavelength photonic devices. IEEE J Sel Top Quantum Electron 12:1214–1220
63. Kreibig U (1970) Kramers kronig analysis of the optical properties of small silver particles. Z Phys 234:307–318
64. Kreibig U, Fragstein CV (1969) The limitation of electron mean free path in small silver particles. Z Phys 224:307–323
65. Rosei R (1974) Temperature modulation of the optical transitions involving the Fermi surface in Ag: theory. Phys Rev B 10:474–483
66. Inouye H, Tanaka K, Tanahashi I, Hirao K (1998) Ultrafast dynamics of nonequilibrium electrons in a gold nanoparticles system. Phys Rev B 57:11334–11340
67. Cain W, Shalaev V (2010) Optical metamaterials: fundamental and applications. Springer, Heidelberg
68. Santillán JMJ, Videla FA, Scaffardi LB, Schinca DC (2012) Plasmon spectroscopy for subnanometric copper particles: dielectric function and core-shell sizing. Plasmonics 1–8, doi:10.1007/s11468-012-9395-8
69. Logunov SL, Ahmadi TS, El-Sayed MA, Khoury JT, Whetten RL (1997) Electron dynamics of passivated gold nanocrystals probed by subpicosecond transient absorption spectroscopy. J Phys Chem B 101:3713–3719
70. Boyen H-G, Kästle G, Weigl F, Koslowski B et al (2002) Oxidation-resistant gold-55 clusters. Science 30:1533–1536
71. van de Hulst HC (1981) Light scattering by small particles. Dover, New York
72. Jackson JD (1999) Classical electrodynamics, 3rd edn. Wiley, New York
73. Zhao J, Pinchuk AO, McMahon JM, Li S, Ausman LK, Atkinson AL, Schatz GC (2008) Methods for describing the electromagnetic properties of silver and gold nanoparticles. Acc Chem Res 41(12):1710–1720
74. Kelly KL, Coronado E, Zhao LL, Schatz GC (2003) The optical properties of metal nanoparticles: the influence of size, shape, and dielectric environment. J Phys Chem B 107:668–677
75. Born M, Wolf E (1999) Principles of optics. Cambridge University Press, Cambridge
76. Ishimaru A (1997) Wave propagation and scattering in random media. IEEE Press/Oxford University, New York/Oxford
77. Straton JA (1941) Electromagnetic theory. Mc Graw-Hills, New York
78. Raether H (1988) Surface plasmons on smooth and rough surfaces and on grattings, vol 111, Springer tracts in modern physics. Springer, Berlin
79. Wokaun AW (1984) Surface enhanced electromagnetic processes. Solid State Phys 38:223–294
80. Pedersen TG, Jung J, Søndergaard T, Pedersen K Nanopar (2011) Nanoparticle plasmon resonances in the near-static limit. Optics Letters 36(5):713–715
81. Purcell EM, Pennypacker CR (1973) Scattering and absorption of light by non-spherical dielectric grains. Astrophys J 186:705
82. Miller EK (1994) Time domain modelling in electromagnetics. J Electromagn Waves Appl 8:1125–1172
83. Jerez S, Lara A (2011) A high resolution nonstandard FDTD method for the TM mode of Maxwell's equations. Math Comput Model 54:1852–1857
84. Hafner C, Ballist R (1983) The multiple multipole method (MMP). Int J Comput Electr Electron Eng 2:1–7
85. Pendry JB, MacKinnon A (1992) Calculation of photon dispersion relations. Phys Rev Lett 69:2772–2775
86. Khlebtsov B, Khanadeev V, Pylaev T, Khlebtsov N (2011) A new T-matrix solvable model for nanorods: TEM-based ensemble simulations supported by experiments. J Phys Chem C 115:6317–6323

87. (a) Jin J (2002) The finite element method in electromagnetics. Wiley, New York. (b) Nieto-Vesperinas M (1991) Scattering and diffraction in physical optics. Wiley, New York (Chaps 1 and 7)
88. Madrazo A, Nieto-Vesperinas M (1995) Scattering of electromagnetic waves from a cylinder in front of a conducting plane. J Opt Soc Am A 12:1298–1309
89. Lester M, Nieto-Vesperinas M (1999) Optical forces on microparticles in an evanescent laser field. Opt Lett 26:936–938
90. Lester M, Arias-González JR, Nieto-Vesperinas M (2001) Fundamentals and model of photonic-force microscopy. Opt Lett 26:707–709
91. Arias-González de la Aleja JR (2002) Electromagnetic resonances in the light scattering by objects and surfaces. Ph.D. thesis, Universidad Complutense de Madrid, Spain. ISBN: 84-669-1863-9. http://www.ucm.es/BUCM/tesis/fis/ucm-t26131.pdf
92. Abraham Ekeroth RM, Lester M, Scaffardi LB, Schinca DC (2011) Metallic nanotubes characterization via surface plasmon excitation. Plasmonics 6:435–444
93. Huang X, Jain PK, El-Sayed IH, El-Sayed MA (2008) Plasmonic photothermal therapy (PPTT) using gold nanoparticles. Lasers Med Sci 23:217–228
94. Huang X, Neretina S, El-Sayed MA, Nanorods G (2009) From synthesis and properties to biological and biomedical applications. Adv Mater 21:4880–4910
95. Pérez-Juste J, Pastoriza-Santos I, Liz-Marzán LM, Mulvaney P (2005) Gold nanorods: synthesis, characterization and applications. Coord Chem Rev 249:1870–1901
96. Moskovits M (1985) Surface-enhanced spectroscopy. Rev Mod Phys 57:783–826
97. Oates TWH, Sugime H, Noda S (2009) Combinatorial surface-enhanced Raman spectroscopy and spectroscopic ellipsometry of silver island films. J Phys Chem C 113:4820–4828
98. Aroca R (2006) Surface-enhanced vibrational spectroscopy. Wiley, Hoboken
99. Kneipp K, Wang Y, Kneipp H, Perelman LT, Itzkan I, Dasari RR, Feld MS (1997) Single molecule detection using surface-enhanced Raman scattering (SERS). Phys Rev Lett 78:1667–1670
100. Emory SR, Nie S (1997) Near-field surface-enhanced Raman spectroscopy on single silver nanoparticles. Anal Chem 69:2631–2635
101. Xu H, Bjerneld EJ, Kall M, Börjesson L (1999) Spectroscopy of single enhanced Raman scattering. Phys Rev Lett 83:4357–4360
102. Elghanian R, Storhoff JJ, Mucic RC, Letsinger RL, Mirkin CA (1997) Selective colorimetric detection of polynucleotides based on the distance-dependent optical properties of gold nanoparticles. Science 277:1078–1081
103. Lyon LA, Musick MD, Natan MJ (1998) Colloidal Au-enhanced surface plasmon resonance immunosensing. Anal Chem 70:5177–5183
104. Schultz S, Smith DR, Mock JJ, Schultz DA (2000) Single-target molecule detection with nonbleaching multicolor optical immunolabels. Proc Natl Acad Sci USA 97:996–1001
105. Sönnichsen C, Geier S, Hecker NE, von Plessen G, Feldmann J, Ditlbacher H, Lamprecht B, Krenn JR, Aussenegg FR, Chan VZ-H, Spatz JP, Möller M (2000) Spectroscopy of single metallic nanoparticles using total internal reflection microscopy. Appl Phys Lett 77:2949–2952
106. Specht M, Pedarnig JD, Heckl WM, Hänsch TW (1992) Scanning plasmon near-field microscope. Phys Rev Lett 68:476–479
107. Inouye Y, Kawata S (1994) Near-field scanning optical microscope with a metallic probe tip. Opt Lett 19:159–161
108. Hecht B, Sick B, Wild UP, Deckert V, Zenobi R, Martin OJF, Pohl DW (2000) Scanning near-field optical microscopy with aperture probes: fundamentals and applications. J Chem Phys 112:7761–7775
109. Stöckle RM, Suh YD, Deckert V, Zenobi R (2000) Nanoscale chemical analysis by tip-enhanced Raman spectroscopy. Chem Phys Lett 318:131–136
110. Sqalli O, Bernai MP, Hoffmann P, Marquis-Weible F (2000) Improved tip performance for scanning near-field optical microscopy by the attachment of a single gold nanoparticle. Appl Phys Lett 76:2134–2137

111. Milner RG, Richards D (2001) The role of tip plasmons in near-field Raman microscopy. J Microsc 202:66–71
112. Manjavacas A, García de Abajo FJ (2009) Robust plasmon waveguides in strongly interacting nanowire arrays. Nano Lett 9:1285–1289
113. Vogelgesang R, Dorfmüller J, Esteban R, Weitz RT, Dmitriev A, Kern K (2008) Plasmonic nanostructures in apertureless scanning near-field optical microscopy (aSNOM). Phys Status Solid B 245:2255–2260
114. Dickson RM, Lyon LA (2000) Unidirectional plasmon propagation in metallic nanowires. J Phys Chem B 104:6095–6098
115. Fang Z, Fan L, Lin C, Zhang D, Meixner AJ, Zhu X (2011) Plasmonic coupling of bow tie antennas with Ag nanowire. Nano Lett 11:1676–1680
116. Quinten M, Leitner A, Krenn JR, Aussenegg FR (1998) Electromagnetic energy transport via linear chains of silver nanoparticles. Opt Lett 23:1331–1333
117. Krenn JR, Dereux A, Weeber JC, Bourillot E, Lacroute Y, Goudonnet JP (1999) Squeezing the optical near-field zone by plasmon coupling of metallic nanoparticles. Phys Rev Lett 82:2590–2593
118. Bozhevolnyi SI, Erland J, Leosson K, Skovgaard PMW, Hvam JM (2001) Waveguiding in surface plasmon polariton band gap structures. Phys Rev Lett 86:3008–3011
119. Weeber J-C, Dereux A, Girard C, Krenn JR, Goudonnet J-P (1999) Plasmon polaritons of metallic nanowires for controlling submicron propagation of light. Phys Rev B 60:9061–9068
120. Lamprecht B, Schider G, Lechner RT, Ditlbacher H, Krenn JR, Leitner A, Aussenegg FR (2000) Metal nanoparticle gratings: influence of dipolar particle interaction on the plasmon resonance. Phys Rev Lett 84:4721–4724
121. Brongersma ML, Hartman JW, Atwater HA (2000) Electromagnetic energy transfer and switching in nanoparticle chain arrays below the diffraction limit. Phys Rev B 62:R16356–R16359
122. Krenn JR, Salerno M, Felidj N, Lamprecht B, Schider G, Leitner A, Aussenegg FR, Weeber JC, Dereux A, Goudonnet JP (2001) Light field propagation by metal micro- and nanostructures. J Microscopy 202:122–128
123. Lester M, Skigin D (2007) Coupling of evanescent s-polarized waves to the far field by waveguide modes in metallic arrays. J Opt A Pure Appl Opt 9:81–87
124. Skigin D, Letser M (2011) Optical nanoantennas: from comminications to super-resolution. J Nanophotonics 5:050303, 1–3
125. Martin-Moreno L, García-Vidal FJ, Lezec HJ, Pellerin KM, Thio T, Pendry JB, Ebbesen TW (2001) Theory of extraordinary optical transmission through subwavelength hole arrays. Phys Rev Lett 86:1114–1117
126. Lester M, Skigin D (2011) An optical nanoantenna made of plasmonic chain resonators. J Opt 13:035105–0345113
127. Barnard ES, Pala RA, Brongersma ML (2011) Photocurrent mapping of near-field optical antenna resonances. Nat Nanotechnol 6:588–593
128. Tominaga J, Mihalcea C, Büchel D, Fukuda H, Nakano T, Atoda N, Fuji H, Kikukawa T (2001) Local plasmon photonic transistor. Appl Phys Lett 78:2417–2420
129. Link S, El-Sayed MA (2000) Shape and size dependence of radiative, non-radiative and photothermal properties of gold nanocrystals. Int Rev Phys Chem 19:409–453
130. Santillán JMJ, Scaffardi LB, Schinca DC (2011) Quantitative optical extinction based parametric method for sizing a single core-shell Ag–Ag_2O nanoparticle. J Phys D: Appl Phys 44:105104, 1–8
131. Novotny L, van Hulst N (2011) Antennas for light. Nat Photonics 5:83–90
132. Silveirinha MG, Alu A, Engheta N (2008) Cloaking mechanism with antiphase plasmonic satellites. Phys Rev B 78:205109–205118
133. Moradi A (2008) Plasmon hybridization in metallic nanotubes. J Phys Chem Solid 69:2936–2838

134. Jain PK, El-Sayed MA (2007) Universal scaling of plasmon coupling in metal nanoestructures: extension from particles pair to nanoshells. Nano Lett 9:2854–2858
135. Park T, Nordlander P (2009) On the nature of the bonding and antibonding metallic film and nanoshell plasmons. Chem Phys Lett 472:228–231
136. Zhu J (2007) Theoretical study of the tunable second-harmonic generation (SHG) enhancement factor of gold nanotubes. Nanotechnology 18:225702
137. Wu D, Xu X, Liu X (2008) Influence of dielectric core, embedding medium and size on the optical properties of gold nanoshells. Solid State Commun 146:7–11
138. Calculations of cross sections in this section were performed with the integrated method outlined in Section 2, extended to cover the case of cylinders coated. For details of the method see [92]
139. Encina E, Coronado E (2010) Plasmon coupling in silver nanosphere pairs. J Phys Chem C 114:3918–3923
140. Link S, Burda C, Nikoobakht B, El-Sayed MA (2000) Laser-induced shape changes of colloidal gold nanorods using femtosecond and nanosecond laser pulses. J Phys Chem B 104(26):6152–6163
141. Mafuné F, Kohno J-y, Takeda Y, Kondow T, Sawabe H (2000) Structure and stability of silver nanoparticles in aqueous solution produced by laser ablation. J Phys Chem B 104(35):8333–8337
142. Mafuné F, Kohno J-y, Takeda Y, Kondow T (2002) Full physical preparation of size-selected gold nanoparticles in solution: laser ablation and laser-induced size control. J Phys Chem B 106(31):7575–7577
143. Mafuné F, Kohno J-y, Takeda Y, Kondow T, Sawabe H (2001) Formation of gold nanoparticles by laser ablation in aqueous solution of surfactant. J Phys Chem B 105:5114–5120
144. Mafuné F, Kohno J-y, Takeda Y, Kondow T, Sawabe H (2000) Formation and size control of silver nanoparticles by laser ablation in aqueous solution. J Phys Chem B 104:9111–9117
145. Mafuné F, Kohno J-y, Takeda Y, Kondow T (2002) Growth of gold clusters into nanoparticles in a solution following laser-induced fragmentation. J Phys Chem B 106:8555–8561
146. Mafuné F, Kohno J-y, Takeda Y, Kondow T (2001) Dissociation and aggregation of gold nanoparticles under laser irradiation. J Phys Chem B 105:9050–9056
147. Mafuné F, Kohno J-y, Takeda Y, Kondow T (2003) Formation of stable platinum nanoparticles by laser ablation in water. J Phys Chem B 107:4218–4223
148. Chen Y-H, Tseng Y-H, Yeh C-S (2002) Laser-induced alloying Au–Pd and Ag–Pd colloidal mixtures: the formation of dispersed Au/Pd and Ag/Pd nanoparticle. J Mater Chem 12:1419–1422
149. Besner S, Kabashin AV, Meunier M (2006) Fragmentation of colloidal nanoparticles by femtosecond laser-induced supercontinuum generation. Appl Phys Lett 89:233122–233125
150. Hahn A, Barcikowski S, Chichkov BN (2008) Influences on nanoparticle. Production during pulsed laser ablation. J Laser Micro/Nanoeng 3(2):73–77
151. Pyatenko A, Shimokawa K, Yamaguchi M, Nishimura O, Suzuki M (2004) Synthesis of silver nanoparticles by laser ablation in pure water. Appl Phys A 79:803–806
152. Novo C, Funston AM, Mulvaney P (2008) Direct observation of chemical reactions on single gold nanocrystals using surface plasmon spectroscopy. Nat Nanotechnol 3:598–602
153. Anker JN, Paige Hall W, Lyandres O, Shah N, Zhao J, Van Duyne R (2008) Biosensing with plasmonic nanosensors. Nat Mater 7:442–453
154. Alù A, Young M, Engheta N (2008) Design of nanofilter for optical nanocircuits. Phys Rev B 77:144107–144119
155. Cao L, Fan P, Vasudev AP, White JS, Yu Z, Cai W, Schuller JA, Fan S, Brongersma ML (2010) Semiconductor nanowire optical antenna solar absorbers. Nano Lett 10:439–445

Modeling and Optical Characterization of the Localized Surface Plasmon Resonances of Tailored Metal Nanoparticles

6

J. Toudert

Contents

1 Definition of the Topic

Metal nanoparticles present peculiar optical properties at their surface plasmon resonances, such as marked optical absorption, enhanced near-field and scattering to the far-field. From works involving the fabrication of tailor-made metal nanoparticles together with the accurate characterization of their optical response, it has been demonstrated that the plasmon-related optical features are sensitive to the size, shape, and environment of the nanoparticles. Such sensitivity is of

J. Toudert
Instituto de Optica, CSIC, Madrid, Spain

Challa S.S.R. Kumar (ed.), *UV-VIS and Photoluminescence Spectroscopy for Nanomaterials Characterization*, DOI 10.1007/978-3-642-27594-4_6,

particular interest for sensing applications and permits to tune the optical response of the nanoparticles, thus making them suitable for a wide range of applications in photonics. From a theoretical point of view, models and methods were developed in order to address the role of the previous structural parameters on the optical response of tailor-made nanoparticles.

2 Overview

This chapter reviews classical models and methods suitable for simulating the optical absorption, scattering, and near-field enhancement that arise at the surface plasmon resonances of tailor-made metal nanoparticles. After presenting modern methods for the controlled fabrication and optical characterization of metal nanoparticles, relevant predictions of each model are underlined in order to illustrate the role of the size, shape, and environment of Au and Ag nanoparticles on their optical response. Experimental data are also reported for comparison. Quasi-static calculations, which are valid for nanoparticle sizes insignificant compared to the wavelength of the incident light, highlight the sensitivity of the plasmonic response of an isolated nanoparticle to its shape (sphere or spheroid) and the nature of a surrounding dielectric medium. The macroscopic transmittance and specular reflectance of nanocomposite materials consisting of statistical ensembles of metal nanoparticles with a 2D or 3D organization in a dielectric film, or supported on a nonmetallic substrate, are derived from effective medium models, in the quasi-static approximation and assuming weak electrostatic interaction between nanoparticles. Predictions of the Mie theory are then reported to illustrate the consequences of dynamic effects on the optical response of an isolated spherical nanoparticle in the non quasi-static size regime. The effects of deviation from the spherical shape (spheroidal, disklike, or rodlike) and strong electromagnetic coupling in a pair of nearly touching nanoparticles are discussed from numerical simulations in the framework of classical electrodynamics. Limitations of classical models are evoked, at the light of recent works based on quantum calculations of the optical response of metal nanoparticles.

3 Introduction

3.1 Tuning, Characterization, and Modeling of Localized Plasmon Resonances

Many centuries ago, noble metals were already used as pigments for the coloration of glasses. A famous example of colored material obtained by melting small amounts of a noble metal with glass is the *Lycurgus cup*. It is now well known that the color of this piece of art results from the presence in the transparent glass matrix of small noble metal particles (from several nm to tens of nm in size) [1], which absorb light selectively around specific wavelengths in the visible range.

This peculiar optical behavior, not observed in the case of bulk metals, was underlined by Faraday, from his empirical works involving the synthesis of colloidal solutions of many elements (Ag, Pt, Cu, Fe, Zn, Hg,...) [2]. A crucial step toward the understanding of the interaction mechanisms of light with small metal particles was then permitted by Mie's theoretical works [3]. Mie solved Maxwell's equations in the case of a spherical particle excited by a sinusoidal plane wave, whose wavelength λ in the surrounding dielectric medium is longer or comparable to the particle's diameter D. After deriving the electromagnetic field inside and around the particle, it was shown that it may absorb and scatter the incident light, the importance and features of both phenomena depending on the D/λ ratio, nature of the particle and of the surrounding medium.

In the case of a spherical Ag particle with $D/\lambda << 1$ (known as the quasi-static limit), that is, several nm in size for near ultraviolet (N-UV), visible, or near infrared (N-IR) incident light, a strong optical absorption band is usually observed in the N-UV or visible, depending on the nature of the surrounding medium. At the peak wavelength, a strong enhancement of the electric field in the particle's nanometric surroundings (near-field) is expected, while scattering (to the far-field) is insignificant. The microscopic interpretation of this optical behavior involves the conduction electrons of the metal, which can be easily driven by the excitation electric field. Since $D/\lambda << 1$, this field is homogeneous over the whole particle volume and induces a coherent oscillation of the conduction electrons relative to the rigid ionic skeleton of the particle. A dipole-like distribution of surface charges thus appears, the interaction between them acting as a restoring force. The particle therefore behaves as an oscillating dipole, whose polarizability (and thus absorption and near-field) presents a resonant behavior with marked peak values. This phenomenon, which involves a coherent oscillation of electrons ("plasmon") and surface charges, is known as "surface plasmon resonance." Moreover, it is usually denoted as "localized," in order to distinguish it from plasmons propagating at the surface of metal films. Hereafter, we will be interested only in localized surface plasmon resonances, which will be denoted as "plasmon resonances," for the sake of simplicity.

Plasmon resonances can be excited optically at determined wavelengths in the N-UV, visible, and N-IR range in a metal in form of small entities, that is, from a few nm to hundreds of nm in size (in the following, such entities will be called nanoparticles). Nevertheless, the response of an arbitrary metal entity to the excitation field, which determines its absorption, near-field, and scattering properties, may strongly depart from that of the small spherical Ag nanoparticle evoked above. As it will be detailed later, deviation from the spherical shape drives the degeneracy breaking of the plasmon resonance and may induce stronger local values of the near-field. Moreover, upon gradually increasing the size, it follows from Mie's theory that a spherical nanoparticle behaves as an efficient resonant dipole scatterer and then supports several multipolar plasmon resonance modes peaking at distinct wavelengths [4]. In addition, the hypothesis of an isolated nanoparticle does not hold in many cases, for instance, as a result of electromagnetic interactions between nanoparticles or with a substrate [5]. Such interactions were early considered by effective medium models, which aimed at calculating the macroscopic optical

response of nanocomposite materials consisting of statistical ensembles of nanoparticles presenting simple shapes (such as spheres or spheroids), dispersed in a dielectric matrix or supported on a substrate.

Studying experimentally in a rigorous way the influence of nanoparticles size, shape, and interactions on their plasmon resonances has been allowed by the improvement of nanofabrication and optical characterization methods in the last 20 years. Metal nanoparticles with almost any desired size and shape can now be synthesized with a fine control of their organization, on substrates or in matrices. Optical probes have become sensitive enough to characterize single nanoparticles or agglomerates of a few nanoparticles. From a theoretical point of view, the increasing computer capabilities have permitted to realize extensive parametric studies involving analytical calculations and, above all, to implement numerical methods based on classical electrodynamics for calculating the optical response of finite but complex systems, for which analytical treatment is impossible. Such numerical simulations yield the absorption/scattering properties and near-field of single nanoparticles of complex shapes or finite systems of interacting nanoparticles, in the chosen illumination and detection conditions. Moreover, quantum calculations were performed in cases where classical hypotheses fail, that is, for instance, when nanoparticle diameter is only of a few nm, or for nearly touching nanoparticles. Coupling numerical calculations to adequate characterization of tailor-made nanoparticles has thus participated to important progresses in the understanding of the correlation between structural features and the plasmon resonance-driven optical properties. Theoretical predictions are also interesting from a technological point of view. Indeed, a good knowledge of the plasmonic response of nanoparticles is a guide to the development of devices taking profit of their specific properties. Among the possible applications, the tunability of the spectral position of the resonances may benefit to optical filtering, data storage, or encryption [6]. Nanoparticles with strong N-IR absorption may be used for local disease treatment by photothermal effect [7]. Enhanced near-fields are interesting for the realization of plasmonic circuitry [8], for luminescence enhancement [9], or for surface-enhanced Raman scattering (SERS) [10], while plasmonic scattering is thought to be useful for the development of improved solar cells [11]. In addition, modeling is important for the inverse problem, that is, the characterization of metal nanoparticles and their local surroundings from the features of their plasmon resonances. This approach is particularly interesting for nondestructive in-situ tracking of materials fabrication [12] or chemical sensing [13].

3.2 Aims and Outline

Due to the large number of recent publications dealing with the modeling of the optical response of metal nanoparticles and the nanocomposite materials built from them, several review papers were proposed in order to provide synthetic information about the existing models and their predictions. Nevertheless, from the author's point of view, a book chapter presenting a didactic and self-standing overview of

models and methods used in the last years in a wide range of cases (from an isolated nanoparticle of complex shape to nanocomposite materials built from nanoparticles) could be useful to a wide audience of material scientists and solid state physicists. Such a report should highlight the limitations of each model and provide comparisons between theoretical predictions and measurements on tailor-made systems. It should describe the correlation between the optical response of nanoparticles (resp. nanocomposite materials) and their nature, size, shape, and environment (resp. nanostructure) and discuss the physical meaning of these correlations. These are thus the purposes of this book chapter. Since the development of theoretical works is tightly linked to that of elaboration and characterization tools, we will first evoke the routes for fabricating metal nanoparticles in a controlled way (Sect. 4.1) and the techniques permitting to measure optical observables related to plasmon resonances (Sect. 4.2): the absorption and far-field scattering cross sections, the near-field distribution of a single nanoparticle or agglomerates of nanoparticles, and the macroscopic transmittance/specular reflectance of non-scattering nanocomposite materials. In Sect. 5.1, a first theoretical classical approach of the optical absorption and near-field enhancement of a spherical or spheroidal metal nanoparticle will be realized assuming $D/\lambda << 1$, so that simple quasi-static calculations can be made and scattering neglected. The influence of the nature of the metal and surrounding medium, as well as of nanoparticle's shape on the plasmonic response, will be shown. Finite-size effects, that become significant for nanoparticles a few nm in size, that is, the range in which the quasi-static approximation holds, will be discussed. Section 5.2 will be devoted to effective medium models relying on the quasi-static approximation and considering weak electrostatic interactions between nanoparticles. Recent applications of these models to non-scattering thin films based on random or anisotropically organized assemblies of metal nanoparticles will be reported. In Sect. 5.3, the main features of the classical Mie theory (for a spherical nanoparticle too big to satisfy quasi-static conditions) will be recalled, and the way the nanoparticle's diameter D affects its absorption/scattering cross sections and near-field will be discussed using recently reported theoretical and experimental data. Numerical calculation methods based on classical electrodynamics (multipole expansions, DDA, FEM, FDTD, surface integral methods) will be presented together with their predictions concerning the optical response of metal nanoparticles in specific but frequently encountered and didactic cases. An emphasis will be made on the evolution of the absorption, scattering, and near-field of prolate spheroids and cylindrical nanorods upon varying their aspect ratio and size, beyond the limits of the quasi-static approximation. Results concerning the optical response of metal nanoparticle dimers (pairs of spheres, prolate spheroids, or cylindrical nanorods) will also be reported, in order to describe the effect of interactions (from weak to strong) between nanoparticles on their plasmon resonances, as a function of their separation distance. Limitations of the classical approaches and recent results based on quantum calculations will be highlighted in Sect. 6. Finally, a few words will be said about the role of modern fabrication, characterization, and modeling techniques in the development of very recent trending topics in plasmonics.

4 Experimental and Instrumental Methodology: Fabrication and Optical Characterization of Tailor-Made Metal Nanoparticles

4.1 Fabrication Routes of Metal Nanoparticles

Today, physical or chemical fabrication routes permit to synthesize metal nanoparticles with a fine control of their size and shape. They can be functionalized and dispersed in gases, liquids, or organized on solid surfaces or in solid matrices. Nevertheless, each fabrication route presents different potentialities in terms of control of the nanostructure, which we discuss briefly in this section. We give examples of realizations permitted by each elaboration technique. Although nanoparticles of various compositions can be synthesized and plasmon resonances can be observed in many metals [5, 14–17], we will focus here on noble metals (mainly Ag and Au), since they are the most frequently used in the field of plasmonics.

Among the many existing lithography techniques (focused ion-beam lithography [18], UV lithography [19], electron-beam lithography [20], X-ray lithography [21], plasmon-mediated lithography [22], nanosphere lithography [23]), electron-beam lithography is a frequently used tool for designing metal nanoparticles supported on a substrate. It relies on a computer-driven process, in which the user draws the pattern to be imprinted by the electron beam on a layer of polymeric resist deposited on a usually flat substrate. Subsequent development, followed by metal deposition and washing out, converts the drawn pattern into metal nanostructures on the substrate. This method thus permits a fine control of the in-plane geometry of the nanoparticles, whereas their lateral sides are generally vertical, thus permitting to fabricate, for instance, nanocylinders [24], nanorings [25], nanorods [26], triangular nanoprisms [27], or nanocrosses [28]. Nanoparticles size can be tuned, as well as the interparticle separation in dimers, chains, or 2D periodic or random arrays of nanoparticles, however with an accuracy of only several nm. Thus, tuning the shape of nanoparticles for sizes below 10 nm is not possible, and the interparticle separation cannot be controlled with nanometric precision. The latter limitation is problematic for the reproducible fabrication of tailored systems of densely packed nanoparticles, whose optical response depends critically on the separation between nanoparticles. Therefore, electron-beam lithography is an excellent candidate for fabricating assembly of nanoparticles with typical dimensions of tens or hundreds of nm but has limited capabilities at the nanometer scale. In contrast, “bottom-up” elaboration routes provide a control, from reasonable to very good, over the nanoparticles size and shape even for sizes of a few nm. By such means, separation distance between the nanoparticles can be controlled at the nanoscale.

Physical deposition techniques involving ion-beam sputtering, evaporation or pulsed-laser ablation of a metal target in vacuum, and subsequent condensation of the ejected material onto a usually nonmetallic substrate permit the formation of assemblies of nanoparticles provided a Volmer-Weber-like growth occurs.

Deposition onto flat crystalline substrates in mild deposition conditions permits to grow nanoparticles with polyhedral shapes [29]. On amorphous flat substrates, a single layer of more or less truncated and flattened spheroidal or ellipsoidal nanoparticles can be formed, usually with quite broad size and shape distributions [30]. Assisting the growth with pulsed-laser light has been shown to allow reducing the distributions and controlling the flattening of nanoparticles of about 10 nm in size [31, 32]. In-plane auto-organization of nanoparticles has been achieved by deposition onto nanostructured templates, thus permitting the formation of parallel chains of almost touching Ag nanoparticles a few nm in size [33] or parallel nanostripes with lateral dimensions and separations of a few tens of nm [34, 35], presenting an in-plane anisotropic macroscopic optical extinction. Performing pulsed-laser treatment after deposition onto such templates has shown potential for tuning the morphology of Ag nanostripes without affecting their orientation [36]. Physical deposition techniques are not limited to the elaboration of a single layer of nanoparticles supported on a substrate and in contact with the air. Coating of such single layers by dielectric nanometric thin films is possible and permits to tune mildly the flattening of Ag nanoparticles around 10 nm in size, independently of their organization [30, 37]. Nanoparticles can also be embedded in a dense protective matrix, with a random distribution or a multilayer organization [38, 39] with a tunable period of a few nm. A clever use of multilayer deposition has permitted the growth of Ag nanorods oriented perpendicularly to the substrate [40, 41]. Nanocomposite materials containing almost monodisperse spherical nanoparticles with a tunable size below 10 nm can be formed by low energy cluster beam deposition (LECBD) [42]. This technique, as the previously cited ones, relies on the (laser) ablation of a target. Nevertheless, condensation of the ablated atoms and ions is provoked prior to deposition onto the substrate. Mass spectrometry sorting of the formed nanoparticles allows to select those of the desired size, which are then deposited onto the substrate.

Wet chemical synthesis, possibly seed-mediated, light-mediated, or template-mediated, provides control of nanoparticles size and allows efficient shape tailoring. A large variety of shapes [43–45] can be obtained such as spheres, rods, polyhedra, hollow structures such as nanoshells, and branched structures. Single nanoparticles can be capped with organic [46] or inorganic [47] shells. Complex assembling of previously synthesized metal nanoparticles can be achieved by using DNA as bridging agent or template, permitting to form the so-called plasmonic molecules (the simplest being the dimer), plasmonic polymers, or plasmonic crystals [48]. Since shell thicknesses and chain lengths can be tuned at the nanometer scale, chemical synthesis is a powerful tool for the investigation of electromagnetic coupling in systems of nearly touching nanoparticles. Infiltration of metals into inorganic templates is an efficient way to the fabrication of multifunctional nanocomposite materials. For instance, due to its photochromic properties, mesoporous TiO_2 impregnated with Ag is an interesting candidate for reversible recording of data by optical means [49, 50]. Infiltration methods were also used to grow materials organized at the nanoscale, for instance, consisting of periodic arrays of vertically oriented Au nanorods.

From a fundamental point of view, electron-beam lithography is thus ideal in view of parametric studies aiming at the understanding of the absorption, near-field, and scattering by nanoparticles as a function of their size and shape in the non quasi-static regime. Electromagnetic coupling between nanoparticles can also be probed, nevertheless with a limited precision when small separation distances and macroscopic measurements on statistical ensembles of nanoparticles are involved. Fine studies of the interaction between nearly touching nanoparticles are permitted in systems formed by chemical synthesis. Chemical routes or physical deposition techniques permit to fabricate nanoparticles small enough to fulfill quasi-static conditions. Statistical numbers of such nanoparticles can be incorporated into matrices or deposited onto a substrate in a controlled manner, in order to design model materials suitable for testing effective medium models. In addition, the monodisperse nanoparticles whose size is controlled below 5 nm provided, for instance, by LECBD have shown to be adequate for studies of the influence of small size effects involving quantum calculations.

4.2 Optical Characterization of Metal Nanoparticles

The most traditional way of probing the optical response of a nanoparticle consists in measuring the spectra of its absorption and scattering cross sections, σ_{abs} and σ_{sca}, respectively. They are defined as the fraction of electromagnetic power absorbed (P_{abs}) and scattered (P_{sca}) by the nanoparticle, with respect to the intensity I_0 of the incident plane sinusoidal wave: $\sigma_{abs} = P_{abs}/I_0$ and $\sigma_{sca} = P_{sca}/I_0$. They have the dimension of an area and depend on the wavelength of the incident light. The extinction cross section, $\sigma_{ext} = \sigma_{abs} + \sigma_{sca}$, is the physical quantity usually measured for nanoparticles in a liquid or gas. Indeed, assuming that a parallel light beam crosses a thickness z of a medium containing N identical nanoparticles per volume unit, the loss of intensity of this beam due to absorption and scattering losses is linked to σ_{ext} by Beer-Lambert's law :

$$\Delta I(z) = I_0(1 - \exp(-N\sigma_{ext}z)) \tag{6.1}$$

The transmitted intensity can be measured as a function of the wavelength in a spectrophotometer. In addition, if an integrating sphere is implemented on the setup, the scattered light can be collected. Let us underline that the intrinsic optical response of one nanoparticle can be determined from ensemble measurements following (Eq. 6.1) only if the N nanoparticles are in the free space, noninteracting, and identical. In contrast, macroscopic measurements on a statistical number of nanoparticles with size and shape distribution yield an average optical response that hinders the response of individual entities [5]. Optical techniques were thus developed during the last decade to measure selectively the response of a single nanoparticle, dimers, or aggregates. Spatial modulation spectroscopy [51] (see Fig. 6.1, top-left panel) gives access to the optical extinction spectrum of single metal nanoparticles down to a few nm in size deposited on a substrate. For supported

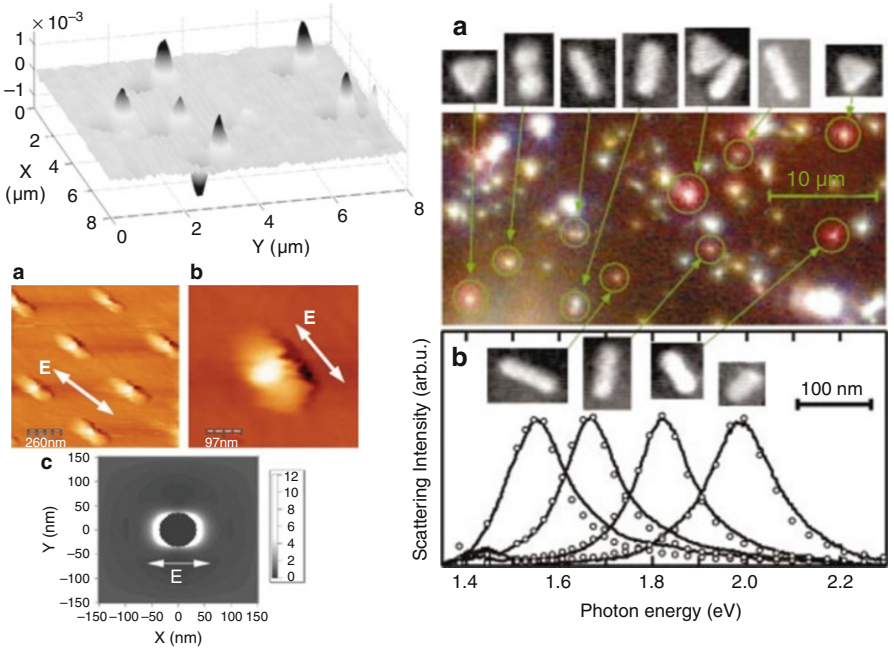

Fig. 6.1 (*Top-left panel*) Images of chemically synthesized Au nanoparticles deposited on a glass substrate recorded by spatial modulation spectroscopy. Reprinted with permission from [51], doi:10.1088/1464-4258/8/4/S28. Copyright 2006 Institute Of Physics. (*Bottom-left panel*) AFM images of cylindrical Ag nanoparticles fabricated by electron-beam lithography, capped by an organic shell grown by near-field-induced photopolymerization, and simulation of the near-field of one nanoparticle. Reprinted with permission from [59]. Copyright 2007 by the American Physical Society. (*Right panel*) Dark-field optical microscopy images of chemically synthesized Ag nanoparticles deposited on a substrate together with the corresponding SEM images and scattering spectra. Reprinted with permission from [159]. Copyright 2003, American Institute of Physics

nanoparticles of larger sizes, dark-field microscopy techniques [52–54] permit measurements of the scattering spectrum, as shown in Fig. 6.1 (right panel). Scanning near-field optical microscopy (SNOM) is used to image the near-field of metal nanostructures [55–57] however with limited spatial resolution. Alternative and recently developed physicochemical and physical approaches permit to take the fingerprint of the near-field of metal nanoparticles: near-field-induced photopolymerization (as shown in Fig. 6.1, bottom-left panel) [58, 59] and femtosecond laser near-field ablation [60]. Other recent methods for probing locally the plasmonic response of single or interacting metal nanoparticles, that is, electron energy loss spectroscopy [61–63] and cathodoluminescence [64], even if not optical, must be mentioned.

When a statistical ensemble of nanoparticles, small enough so that they do not scatter light, is supported on a flat substrate, embedded in a thin slab or in a bulk matrix, it forms a nanocomposite material that is frequently considered at the macroscopic scale as an effective medium. This medium absorbs and reflects the

incoming light, in a way that depends on its polarization and incidence angle, and interferences may occur if the material is under the form of a thin slab. Analysis of the optical response of the nanoparticles thus requires measuring the effective refractive index and extinction coefficient tensors, $[n_{eff}]$ and $[k_{eff}]$ (or in other words, the complex effective dielectric tensor $[\varepsilon_{eff}]$), of the nanocomposite material that reduce to scalar quantities n_{eff} and k_{eff} if its optical response is isotropic. Such a task is possible by fitting the transmittance and reflectance spectra of the material, which must be measured at several angles of incidence and for several polarizations of the (usually linearly polarized) light beam if the material presents optical anisotropy. In the case of a uniaxial anisotropic material whose optical axis is perpendicular to its (flat) surface, S-polarized light (electric field parallel to the surface) permits to characterize the in-plane response, whereas P-polarized light at oblique incidence (electric field in the plane of incidence) probes both components of the effective dielectric tensor (in-plane and along the optical axis). For characterizing biaxial materials presenting in-plane optical dichroism, measurements for different in-plane orientations of the electric field must be performed. The recent development of computer-controlled ellipsometers together with appropriate analysis software has permitted to extract from ellipsometry measurements the effective dielectric function or tensor of nanocomposite materials based on metal nanoparticles [65], presenting a uniaxial [66] or biaxial optical anisotropy [67]. In contrast with classical transmittance and reflectance measurements, ellipsometry yields information about the phase of the reflected or transmitted light.

5 Key Research Findings

5.1 Plasmon Resonances of a Metal Nanoparticle in the Quasi-Static Approximation

5.1.1 Polarizability of a Spherical Nanoparticle

Let us consider a spherical nanoparticle of diameter D in a transparent homogeneous dielectric medium, whose optical properties are described by local frequency-dependent dielectric functions, complex $\varepsilon_i(\omega)$ and real $\varepsilon_m(\omega)$, for the interior of the nanoparticle and surrounding medium, respectively. The magnetic permeability of both media is taken equal to 1. The nanoparticle is illuminated by a plane electromagnetic wave propagating along the x-axis and whose electric field $\mathbf{E_0} = E_0 e^{j(\omega t - kx)} \mathbf{e_z}$ is oriented along the z-axis (as shown on Fig. 6.2, left panel).

We assume that $D << \lambda$, λ being the wavelength of the incident light in the dielectric medium. The excitation field is thus homogeneous over the whole nanoparticle volume, so that it can be written as $\mathbf{E_0} = E_0 e^{j\omega t} \mathbf{e_z}$. In these conditions, known as "quasi-static," the laws of electrostatics are verified, the static permittivities being replaced by the frequency-dependent $\varepsilon_i(\omega)$ and $\varepsilon_m(\omega)$ dielectric functions (in the following, the ω dependence will be omitted). The electric potential ϕ inside (ϕ_i) and outside (ϕ_m) the sphere are determined by solving the Laplace equation with the appropriate boundary conditions and assuming that ϕ_m's limit at

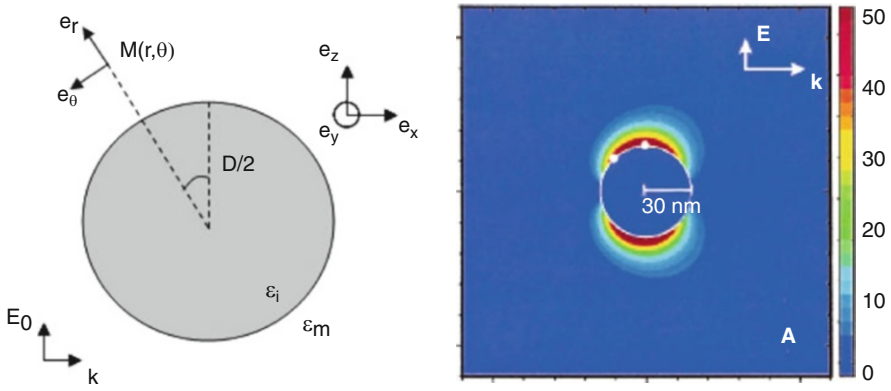

Fig. 6.2 (*Left panel*) Schematic representation of a spherical nanoparticle of dielectric function ε_i, in a homogeneous medium of dielectric function ε_m, illuminated by a plane electromagnetic wave. (*Right panel*) DDA-calculated map of the near-field enhancement factor around a spherical Ag nanoparticle (D = 60 nm) in water at the wavelength of its dipolar plasmon resonance. Reprinted with permission from [27]. Copyright 2003 American Chemical Society

a large distance from the sphere is the potential ϕ_0 of the applied field. One then obtains for the electric field $\mathbf{E_m}$ outside the sphere, at a point M defined by its polar coordinates (r,θ) [16]:

$$\mathbf{E}_m(r,\theta) = \left[E_0\cos\theta + E_0\cos\theta\frac{D^3}{4r^3}\frac{\varepsilon_i-\varepsilon_m}{\varepsilon_i+2\varepsilon_m}\right].\mathbf{e}_r + \left[-E_0\sin\theta + E_0\sin\theta\frac{D^3}{8r^3}\frac{\varepsilon_i-\varepsilon_m}{\varepsilon_i+2\varepsilon_m}\right].\mathbf{e}_\theta \tag{6.2}$$

This expression has the same form as the field at a distance r of a static point dipole in a medium of dielectric function ε_m, with its dipolar momentum $\mathbf{p} = p\mathbf{e_z}$, superimposed to a homogeneous field $\mathbf{E_0}$:

$$\mathbf{E}_m(r,\theta) = \left[\mathbf{E}_0\cos\theta + \frac{1}{4\pi\varepsilon_0\varepsilon_m}\frac{2p\cos\theta}{r^3}\right].\mathbf{e}_r + \left[-E_0\sin\theta + \frac{1}{4\pi\varepsilon_0\varepsilon_m}\frac{p\sin\theta}{r^3}\right].\mathbf{e}_\theta \tag{6.3}$$

After equating (6.2) and (6.3), and assuming that the dipole is induced by the field $\mathbf{E_0}$, that is, it satisfies the relation

$$\mathbf{p} = \varepsilon_0\varepsilon_m\alpha\mathbf{E_0} \tag{6.4}$$

one obtains the quasi-static polarizability α of the spherical nanoparticle of volume V:

$$\alpha = \frac{3(\varepsilon_i - \varepsilon_m)}{\varepsilon_i+2\varepsilon_m}V \tag{6.5}$$

5.1.2 Absorption and Scattering by a Spherical Nanoparticle

After inserting the polarizability given by (Eq. 6.5) in the expressions of the extinction and scattering cross sections σ_{ext} and σ_{sca} of an oscillating dipole [68], one obtains the well-known expressions

$$\begin{cases} \sigma_{ext} = \sigma_{abs} + \sigma_{sca} = k\mathrm{Im}(\alpha) = \dfrac{18\pi}{\lambda_0}\varepsilon_m^{3/2} V \dfrac{\varepsilon_2}{(\varepsilon_1 + 2\varepsilon_m)^2 + \varepsilon_2^2} \\ \sigma_{sca} = \dfrac{k^4}{6\pi}|\alpha|^2 = \dfrac{24\pi^3}{\lambda_0^4}\varepsilon_m^2 V^2 \dfrac{(\varepsilon_1 - \varepsilon_m)^2 + \varepsilon_2^2}{(\varepsilon_1 + 2\varepsilon_m)^2 + \varepsilon_2^2} \end{cases} \tag{6.6}$$

With $\varepsilon_i = \varepsilon_1 + j\varepsilon_2$, $k = 2\pi\varepsilon_m{}^{1/2}/\lambda_0$, λ_0 being the wavelength in vacuum. Since σ_{sca} and σ_{ext} scale as V^2 and V, respectively, one gets $\sigma_{abs} \approx \sigma_{ext} >> \sigma_{sca}$ for the small nanoparticle sizes for which the quasi-static approximation is valid. It then appears that σ_{abs} depends on the volume and nature of the sphere (through ε_1 and ε_2) and on that of the surrounding medium (through ε_m). In the case of most dielectrics, ε_m is usually constant in the visible and N-IR ranges. If ε_2 is taken independent of ω, it then comes from (Eq. 6.6) that σ_{abs} is maximized when

$$\varepsilon_1(\omega_R) = -2\varepsilon_m \tag{6.7}$$

Let us now take for ε_i the bulk dielectric function of Ag or Au. The dielectric functions of these metals are the sum of contributions from the Drude electrons and bounds electrons. The latter contribution is the result of "core polarization" and interband transitions [5]. In the case of Au, interband transitions can be excited in the visible range, as it can be seen from the nonzero values of ε_2 observed in Fig. 6.3a below a λ_0 value of approximately 650 nm. In contrast, interband transitions only occur in the N-UV for Ag, which behaves as a Drude metal (although with a contribution of dielectric screening due to the core electrons) in the visible. Both metals present comparable values of ε_1 and ε_2 in the N-IR.

Figure 6.3b presents the spectra of σ_{abs} calculated from (Eq. 6.6) using the dielectric functions of bulk Ag and Au shown in Fig. 6.3a [69], with $\varepsilon_m = 1$ (vacuum) and D = 10 nm. The Ag nanoparticle presents a sharp absorption peak at $\lambda_{0,R} \sim 350$ nm, with a maximum value $\sigma_{abs,R} = 140\ nm^2$ at the plasmon resonance, usually denoted as "dipolar" due to the topology of the electric field around the sphere. In the case of the Au nanoparticle, such a sharp peak is not observed, but a broad band with a maximum value $\sigma_{abs,R} = 20\ nm^2$ at $\lambda_{0,R} \sim 500$ nm. This absence of sharp resonance is due to the damping of the plasmon excitation by interband transitions in the visible for Au [5].

5.1.3 Near-field Enhancement Around a Spherical Nanoparticle

From (Eq. 6.2), one can calculate the near-field enhancement factor $\eta(r,\theta)$ defined as the intensity ratio between the total electric field at (r,θ) and the incident field $\mathbf{E_0}$:

$$\eta(r,\theta) = \frac{|E_m(r,\theta)|^2}{|E_0|^2} = \cos^2\theta \left| 1 + \frac{D^3}{4r^3}\frac{\varepsilon_i - \varepsilon_m}{\varepsilon_i + 2\varepsilon_m} \right|^2 + \sin^2\theta \left| -1 + \frac{D^3}{8r^3}\frac{\varepsilon_i - \varepsilon_m}{\varepsilon_i + 2\varepsilon_m} \right|^2 \tag{6.8}$$

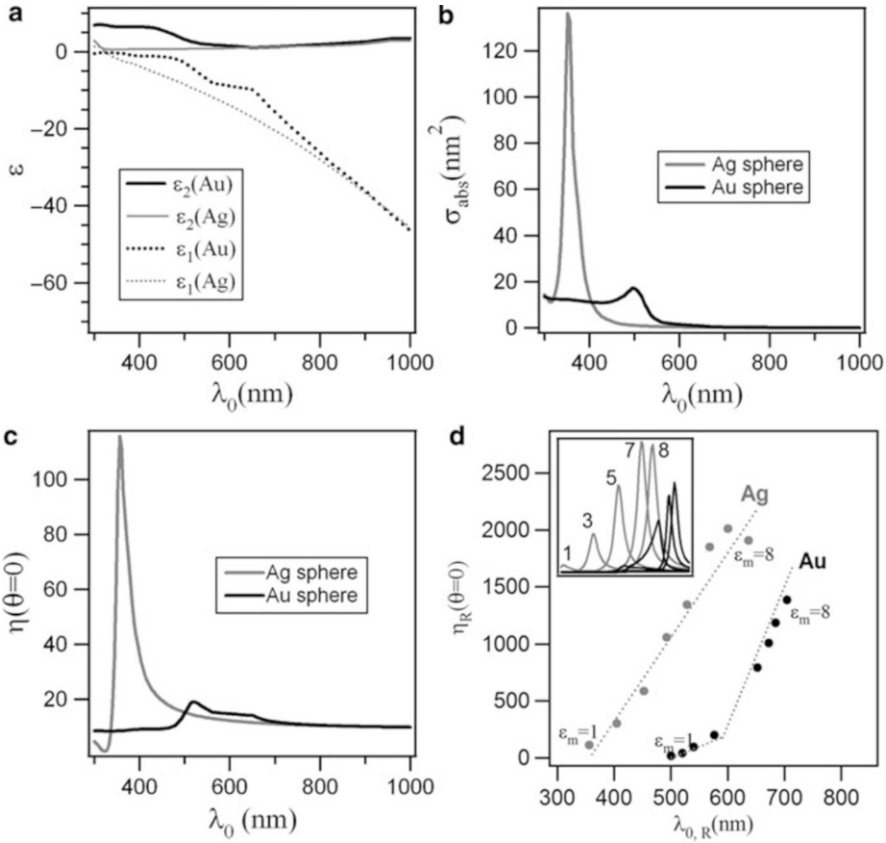

Fig. 6.3 (**a**) Bulk real and imaginary parts, ε_1 and ε_2, of the dielectric function ε_i of Ag and Au, taken from the Palik database [69]; (**b**) absorption cross sections calculated from (Eq. 6.6) with D = 10 nm, $\varepsilon_m = 1$, and with the metal dielectric functions shown in (**a**); near-field enhancement factor $\eta(\theta = 0)$ at the surface of the sphere calculated from (Eq. 6.8); and (**d**) evolution of the resonance wavelength $\lambda_{0,R}$ and of the peak value $\eta_R(\theta = 0)$ of $\eta(\theta = 0)$ as a function of ε_m. The *dotted lines* are a guide for the eye

Let us note that (Eq. 6.8) presents fastly decreasing D^3/r^3 terms, showing that the near-field enhancement only occurs at very short distances from the surface of the nanoparticle. This trend, as the dipolar geometry of the near-field, is observed in the near-field map presented in Fig. 6.2 (right panel). This map was simulated for an Ag nanoparticle with a 60-nm diameter, in the frameworks of electrodynamics [27, 70]. The slight asymmetry of the near-field with respect to the vertical axis, unexpected from (Eq. 6.8), is due to retardation effects that become important for such a nanoparticle size and are not taken into account in the quasi-static calculation. These effects will be described later. The highest value of the quasi-static near-field enhancement factor is obtained at the surface of the sphere (r = D/2) and for θ=0 (or π) where it is given by

$$\eta(\theta = 0) = \left| \frac{3\varepsilon_i}{\varepsilon_i + 2\varepsilon_m} \right|^2 \tag{6.9}$$

Figure 6.3c shows the spectra of $\eta(\theta = 0)$ calculated from (Eq. 6.9) using the bulk dielectric functions of Ag and Au shown in Fig. 6.3a and taking $\varepsilon_m = 1$. Their aspect is qualitatively comparable to that of the absorption spectra. In the case of a Ag nanoparticle, $\eta(\theta = 0)$ peaks sharply at the dipolar plasmon resonance, with a maximum value $\eta_R(\theta = 0)$ of about 120. Due to the absence of an intense resonance in the case of the Au sphere, no sharp peak can be seen in its spectrum of $\eta(\theta = 0)$, and a lower $\eta_R(\theta = 0)$ is obtained. Systematic quasi-static calculations of the $\eta(\theta = 0)$ spectra of spherical nanoparticles of various nature (Ag, Al, Au, Co, Cr, Cu, Ni, Pd, Pt, Sn, Ti) in vacuum can be found in the literature [16]. From these calculations, particularly high near-field enhancement values are expected at the plasmon resonance of Al nanoparticles, which peaks in the N-UV.

5.1.4 Influence of ε_m on the Absorption and Near-Field Enhancement of a Spherical Nanoparticle

Equations 6.6 and 6.9 show that the absorption cross section and near-field enhancement factor of the sphere depend not only on the nature of the metal but also on the dielectric function ε_m of the surrounding medium. In Fig. 6.3d, we plot the calculated values of $\lambda_{0,R}$ and $\eta_R(\theta = 0)$ in the case of Au and Ag spheres with D = 10 nm. For both Au and Ag spheres, the dipole plasmon resonance shifts toward longer wavelengths upon increasing ε_m, due to increased screening of the surface charges. $\eta_R(\theta = 0)$ evolves distinctly for the two metals: it increases quasimonotonously as a function of $\lambda_{0,R}$ in the case of Ag, whereas it remains constant at a low value until $\lambda_{0,R} \sim 600$ nm and then increases abruptly in the case of Au. This brutal jump occurs because interband transitions in Au do not occur above this wavelength, and the excitation of an intense dipolar plasmon resonance, comparable to that observed for Ag, is permitted. Plasmonic applications requiring high field enhancements in the N-IR can therefore be based on Au nanoparticles, which present the advantage of being chemically stable [45], in contrast with Ag nanoparticles that tend, for instance, to oxidize [71] or sulfidize [72].

5.1.5 Finite-Size Effects

As shown above, an isolated Ag or Au spherical nanoparticle in the quasi-static regime presents a strong peak value of the absorption and near-field enhancement provided a sharp and marked dipolar plasmon resonance develops. Optical spectra measured on Ag and Au nanoparticles for which the quasi-static approximation is valid do not generally present a plasmon resonance as sharp as observed in the previous simulations. Two important causes of the broadening of the plasmon resonances are the nanoparticles shape and size distribution and finite-size damping, the latter usually becoming important for nanoparticles a few nanometers in size. Classical interpretations of finite-size damping effects involve interactions of the conduction electrons of the metal with the nanoparticle/surrounding medium

interface (surface scattering [5] and/or chemical interface damping [73]). These interactions are currently taken into account in a phenomenological way, by adding a D-dependent term to the bulk collision frequency Γ_∞ of the conduction electrons in the metal, so that the electron collision frequency turns into [5]

$$\Gamma(D) = \Gamma_\infty + 2A\frac{v_F}{D} \tag{6.10a}$$

A size-dependent dielectric function $\varepsilon_i(D,\omega)$ is thus obtained for the nanoparticle:

$$\varepsilon_i(D,\omega) = \varepsilon_i(\omega) + \omega_p^2\left(\frac{1}{\omega^2+\Gamma_\infty^2} - \frac{1}{\omega^2+\Gamma^2(D)}\right) + i\frac{\omega_p^2}{\omega} \times \left(\frac{\Gamma(D)}{\omega^2+\Gamma^2(D)} - \frac{\Gamma_\infty}{\omega^2+\Gamma_\infty^2}\right) \tag{6.10b}$$

ω_p and v_F are the Drude plasma frequency and Fermi velocity of the bulk metal, and A is an adjustable coefficient that has been shown experimentally to be sensitive to the nature of the surrounding dielectric medium, yielding A values from 0 to 3 [74] and above. Using $\varepsilon_i(D,\omega)$ instead of $\varepsilon_i(\omega)$ for the calculation of σ_{abs} and $\eta(\theta = 0)$ damps the dipolar plasmon resonance, that is, lowers $\sigma_{abs,R}$ and $\eta_R(\theta = 0)$ and broadens the plasmon-related bands in the spectra of σ_{abs} (effect seen in Fig. 6.8, right panel) and $\eta(\theta = 0)$. Corrections accounting for finite-size damping are also reported in the case of nonspherical nanoparticles [75, 76]. Classical corrections of $\varepsilon_i(\omega)$ were also proposed to account for other finite-size effects, affecting the spectral position of the plasmon resonances, such as the spill-out of conduction electrons outside of the ionic skeleton of the nanoparticle [5] or lattice contraction of the metal [77].

5.1.6 Anisotropic Optical Response of Spheroidal and Ellipsoidal Nanoparticles

The Laplace equation can be solved in the case of nanoparticles of simple shapes, such as ellipsoids or spheroids (rotational ellipsoids). The far-field optical response of an ellipsoidal nanoparticle is that of a superposition of dipoles, located at the center of the nanoparticle and oriented along its three axes [68]. One defines the polarizability tensor of the nanoparticle, diagonal in the set of unity vectors ($\mathbf{e_a}$, $\mathbf{e_b}$, $\mathbf{e_c}$) attached to the axes of the ellipsoid [68]:

$$[\alpha] = \begin{pmatrix} \alpha_a & 0 & 0 \\ 0 & \alpha_b & 0 \\ 0 & 0 & \alpha_c \end{pmatrix} \tag{6.11}$$

with $\alpha_u = \frac{(\varepsilon_i - \varepsilon_m)V}{\varepsilon_m + L_u(\varepsilon_i - \varepsilon_m)}$ being the polarizability along $\mathbf{e_u}$ ($\mathbf{e_u} = \mathbf{e_a}$, $\mathbf{e_b}$, or $\mathbf{e_c}$) The L_u's are the depolarization factors, which depend on the axis half lengths a, b, and c, and are given by the analytical relations [68]:

$$L_u = \int_0^\infty \frac{abcdX}{(X + u^2)\sqrt{(X + a^2)(X + b^2)(X + c^2)}} \quad \text{with } u = a, b, \text{ or } c \tag{6.12}$$

In the case of a spheroid for which a = b = D/2 and c = H/2, one obtains $L_a = L_b = L_{transverse}$ and $L_c = L_{longitudinal}$ [68]:

$$\begin{cases} L_{transverse} = \frac{1}{2}\left[1 - \frac{1 - e^2}{2e^3}\left(\ln\left(\frac{1+e}{1-e}\right) - 2e\right)\right] \text{ if } H > D \\ L_{transverse} = L_a = L_b = \frac{1}{2}\left[1 - \frac{1 + e^2}{e^3}(e - \arctan(e))\right] \text{ if } H < D \end{cases} \tag{6.13}$$

and $L_{longitudinal} = 1 - 2L_{transverse}$

with $e = \left|1 - \left(\frac{D}{H}\right)^2\right|^{1/2}$

It is then straightforward that ellipsoidal and spheroidal nanoparticles present a shape-dependent optical response. Each of the polarizabilities in (Eq. 6.11) presents a resonant behavior at a wavelength depending on the corresponding depolarization factor. Thus, three (two) distinct plasmon resonance modes peaking at different wavelengths can be excited in an ellipsoidal (spheroidal) nanoparticle. Since the far-field response of spheroidal and ellipsoidal nanoparticles is that of a superposition of dipoles, the plasmon modes are usually denoted as "dipolar," and the contribution of each of them depends on the orientation of the electric field. Upon aligning it along one of the axes of the ellipsoid (spheroid), the corresponding plasmon mode can be selectively excited. Figure 6.4 presents the evolution of the spectral position $\lambda_{0,R}$ of the two plasmon resonances of a spheroidal Ag nanoparticle as a function of its axis ratio H/D. The values of $\lambda_{0,R}$ were obtained after calculation of the absorption cross section of the nanoparticle along (gray line) and perpendicularly to (black line) its revolution axis using (Eqs. 6.11, 6.13), and the relation $\sigma_u = k\mathrm{Im}(\alpha_u)$. ε_m was taken equal to 4, and the dielectric function of bulk Ag shown in Fig. 6.3 was used for ε_i.

The "longitudinal" ("transverse") plasmon mode excited by an electric field oriented along (perpendicularly to) the revolution axis of the nanoparticle shifts toward longer (shorter) wavelengths when H/D increases. The two modes are excited at the same wavelength in the case of a spherical nanoparticle (H/D = 1). For an oblate spheroid – H/D<1 (prolate spheroid – H/D>1) – the longitudinal mode peaks at a shorter (longer) wavelength than the transverse mode. The shift between the two modes can be qualitatively related with the shape-dependent distance between charges at opposite surfaces [78]. For a prolate spheroid, this distance is larger for a longitudinal excitation (charges at the tips of the spheroid) than for a transverse excitation. The restoring force between surface charges is thus

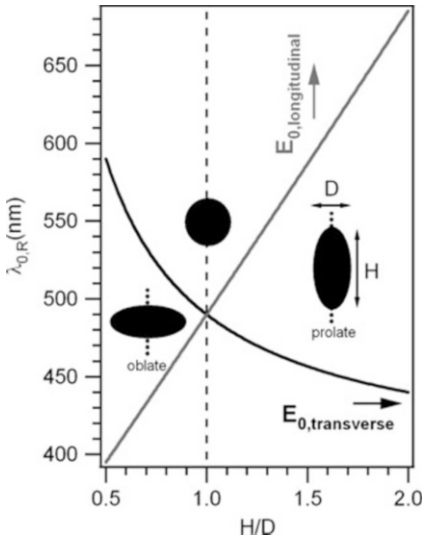

Fig. 6.4 Calculated spectral position $\lambda_{0,R}$ of the dipolar plasmon resonance modes of a spheroidal Ag nanoparticle as a function of its axis ratio H/D. The revolution axis of the spheroid is oriented vertically. The incident electric field $\mathbf{E_0}$ was oriented: along the revolution axis of the spheroid (*gray line*, longitudinal mode), perpendicularly to the revolution axis of the spheroid (*black line*, transverse mode). ε_m was taken equal to 4

weaker under longitudinal excitation than under transverse excitation, as expressed by the relation $L_{longitudinal}<L_{transverse}$ between the depolarization factors. As a consequence, the longitudinal plasmon mode is redshifted compared to the transverse mode.

Many studies were devoted to the synthesis and optical characterization of Au nanorods, presenting a cylindrical shape with rounded tips, and typical axis lengths in the 10–50 nm range. As a first approximation, it can be assumed that they behave optically as prolate spheroids in the quasi-static approximation [79]. As shown in Fig. 6.5 (left panel), the extinction spectra of solutions containing randomly oriented Au nanorods with a relatively sharp H/D distribution present two extinction bands in the visible-N-IR range [6] that are assigned to the two dipolar plasmon resonance modes of the rods: longitudinal and transverse [6, 79, 80]. The spectra are dominated by the intense longitudinal plasmon band, which peaks at a longer wavelength than the transverse plasmon band. In qualitative agreement with the trends observed in Fig. 6.4, the longitudinal plasmon mode red-shifts sensitively upon increasing the average aspect ratio, in contrast with the transverse mode that peaks at an almost constant wavelength [6, 79, 80]. From a technological point of view, tuning of the aspect ratio and spectral position of the dominant "longitudinal" dipolar plasmon mode of Au nanorods has been achieved by several means and, recently by pulsed-laser treatment [80], opening the way to optical data storage on such entities [6]. Due to the sensitivity of the longitudinal plasmon mode to H/D, measurements on a statistical number of nanorods with an H/D distribution yield a broader longitudinal plasmon band than measurements on a single nanoparticle [81]. This effect, known as "inhomogeneous broadening," is illustrated in Fig. 6.5 (left panel).

In other studies, the macroscopic optical response of columnar Ag nanoparticles with a relatively sharp H/D distribution, embedded in a dielectric thin film, was probed by transmittance measurements at normal or oblique incidence under

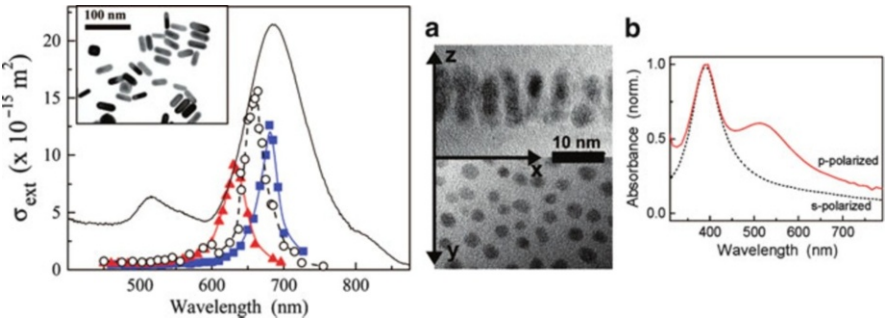

Fig. 6.5 (*Left panel*) Optical extinction spectra of single Au nanorods deposited on a substrate, as measured by spatial modulation spectroscopy with longitudinal polarization, and spectrum acquired on a solution of randomly oriented nanorods polydisperse in shape. Reprinted with permission from [81]. Copyright 2008 American Chemical Society. (*Right panel*) Cross section and plane-view TEM micrographs of a thin film containing Ag columnar nanoparticles oriented perpendicularly to the substrate and the corresponding optical absorbance spectra obtained by transmittance measurements at normal and oblique incidence with P-polarized light. Reprinted with permission from [41]. Copyright 2008 American Chemical Society

P-polarized light [82, 83]. The columnar nanoparticles – a few nm in size – are oriented with their revolution axis perpendicular to the surface of the film, as shown in Fig. 6.5 (right panel). At normal incidence, the electric field is oriented perpendicularly to the columnar nanoparticles and probes selectively the transverse plasmon mode. In this configuration, only one band of low transmittance is thus observed. This band only slightly blue-shifts upon increasing H/D [82, 83], in qualitative agreement with Fig. 6.4. At oblique incidence, the inclined orientation of the excitation field results in the presence of an additional band of low transmittance. It will be shown later (see Sect. 5.2) that this band cannot be attributed unambiguously to the longitudinal plasmon resonance of the nanocolumns. Indeed, this mode can be "dark" to transmittance measurements in the particular case of embedded prolate spheroids, nanorods, or nanocolumns with their revolution axis oriented perpendicularly to the film.

Let us remark that the discussion presented above is only qualitative. More advanced models than that of a single particle in a homogeneous environment are required for quantitative discussions. These models, which will be presented later, should take into account the real configuration of the system under study (ensembles of supported or embedded nanoparticles), possible electromagnetic interactions between nanoparticles and deviations from the quasi-static approximation when the nanoparticles size is of a few tens of nm.

5.1.7 Near-Field Enhancement by Spheroidal Nanoparticles

After resolution of the Laplace equation in the case of a prolate spheroid excited by an electric field $\mathbf{E_0}$ oriented along its revolution axis, one obtains the general form of the electric potential outside of the spheroid [68]. The near-field enhancement factor can then be derived. One obtains at the tip of the spheroid [84]:

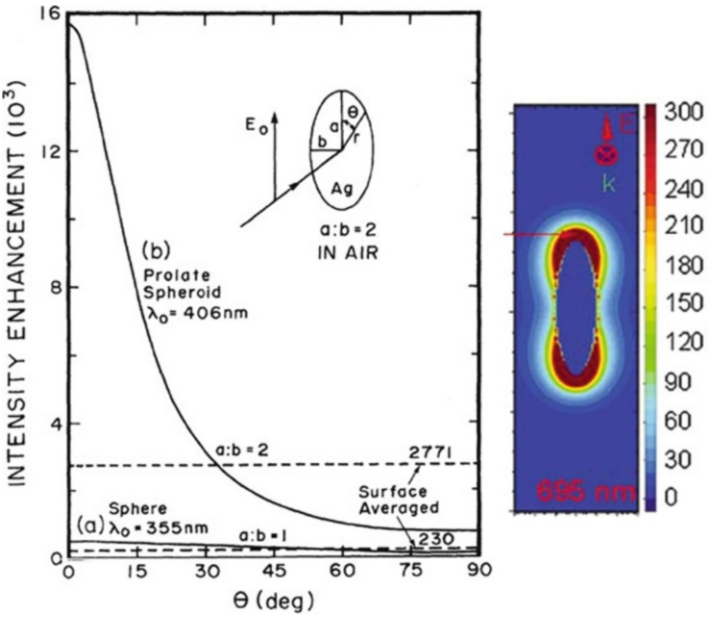

Fig. 6.6 (*Left panel*) Field enhancement factor $\eta_R(\theta)$ at the surface of a prolate Ag spheroid excited with a longitudinal electric field. The calculations were made in the quasi-static approximation, at the wavelength of the longitudinal dipolar plasmon resonance of the spheroid. The bulk dielectric function of Ag was used for the calculations. The same calculations were performed at the dipolar plasmon resonance of an Ag sphere for comparison. Reprinted with permission from [84]. Copyright 1983 by the American Physical Society. (*Right panel*) DDA-calculated map of the field enhancement factor around a Ag prolate spheroid (D = 20 nm, H = 68 nm) in water, at the wavelength of its longitudinal dipolar plasmon resonance. Reprinted with permission from [70] Copyright 2004, American Institute of Physics

$$\eta(\theta = 0) = \left| \frac{\varepsilon_i}{\varepsilon_m + (\varepsilon_i - \varepsilon_m) L_{\text{longitudinal}}} \right|^2 \tag{6.14}$$

The case of a prolate Ag spheroid in various dielectric environments, excited by a longitudinal incident electric field, was early studied in the quasi-static regime [84]. The spectra of the near-field enhancement factor $\eta(\theta = 0)$ at the tip of the spheroid and of the surface-averaged value $<\eta>$ were derived, both peaking at the wavelength $\lambda_{0,//R}$ of the longitudinal dipolar plasmon resonance. An increase in H/D was observed to induce an increase in the values $<\eta>_R$ and $\eta(\theta = 0)_R$ of the near-field enhancements at $\lambda_{0,//R}$. The angular evolution of η was also studied at the wavelength $\lambda_{0,//R}$. Figure 6.6 (left panel) presents the quasi-static $\eta_R(\theta)$ values for H/D = 2 and H/D = 1 in air [84] and (right panel) the near-field map of a prolate spheroidal Ag nanoparticle in water calculated in the framework of classical electrodynamics [70] (methods discussed later). The highest value of $\eta_R(\theta)$ is obtained at the tip of the spheroid, that is, for $\theta = 0$. The particularly high values

of the field enhancement at the tip of the spheroid in the quasi-static regime were attributed to the combination of two effects [85]: the excitation of the longitudinal plasmon resonance and the crowding of the field lines at the sharp tip of the spheroid, or "lightning-rod effect."

5.1.8 Some Other Cases Treated in the Quasi-Static Regime

In addition to the spherical, spheroidal, and ellipsoidal shapes, analytical expressions of the quasi-static polarizability tensor exist for the core-shell geometry [5, 16, 86, 87]. The optical responses of ensembles of nanoparticles in a homogeneous dielectric medium or of a nanoparticle supported on a nonmetallic substrate were also studied. When illuminated, the nanoparticles in an ensemble polarize and, if sufficiently closely packed, interact through the fields they generate. The polarization of each nanoparticle is thus driven by the fields created by the others, in addition to the external field $\mathbf{E_0}$. A simple way to treat such interacting systems consists in assuming that the nanoparticles behave as point dipoles experiencing non-retarded coupling. In the simplest cases of a dimer of identical spherical nanoparticles [88] or identical nanorods with several relative orientations [89], it was shown that an effective polarizability tensor can be derived to account for the response of the coupled dipoles. Using this approach, it comes that coupling between two identical spherical nanoparticles induces a splitting of the nanosphere plasmon resonance into two distinct dimer plasmon resonances [88], which can be excited selectively by orienting the external field along the revolution axis of the dimer (redshifted mode) or perpendicularly to it (blueshifted mode). Similarly, an anisotropic plasmonic response is observed when a spherical nanoparticle is supported on a dielectric substrate [90]. This optical anisotropy is due to the symmetry breaking induced by the presence of the substrate, and its importance depends on the contrast between the refractive index of the substrate and surrounding medium [90]. The field generated by the supported nanoparticle polarizes the substrate, which in turns affects the field exerted on the nanoparticle. Roughly, it can be assumed that the nanoparticle behaves as a point dipole and interacts with an image dipole virtually located inside the substrate. Under such an assumption, the effective polarizability of a single spherical nanoparticle [91] and of a dimer of spherical nanoparticles [92] deposited on a substrate was derived. In the case of a supported single nanoparticle, it comes that one dipolar resonance can be excited if the electric field is oriented in the plane of the substrate and another one for the field perpendicular to it.

These point dipole approaches are nevertheless not exact, neither for calculating the near-field of spheroids or ellipsoids nor for describing the interaction between a nanoparticle and a substrate or the interactions between two nearly touching nanoparticles. Several methods suitable to exact quasi-static calculations in these cases were thus developed. Approaches based on the resolution of the Laplace equation using multipolar expansions of the potential can be used to calculate the near- and far-field optical response of spheroidal or truncated spheroidal nanoparticles. Surface integral methods in the quasi-static approximation can be used to derive the effective properties of nanoparticles of more complex shapes,

such as nanocubes [93] and nanocylinders, possibly with surface roughness [94]. Moreover, plasmon hybridization methods permit exact quasi-static calculations of the optical response of nanoparticles of any shape or aggregates of nanoparticles [95]. All these methods and their predictions will be presented in the next sections.

5.2 Statistical Assemblies of Nanoparticles in the Quasi-Static Approximation: Effective Medium Modeling

The macroscopic optical response of ensembles of nanoparticles deposited on a flat substrate or embedded in a thin dielectric film (thus forming a nanocomposite material) cannot generally be simply derived from their individual extinction cross section by Beer-Lambert's law. Indeed, in real materials, the nanoparticles may experience electromagnetic interactions with the substrate or with neighboring particles. Their organization and orientation, which can be random or well defined, must therefore be taken into account, together with their size and shape distributions.

When the nanoparticles are small enough to fulfill the quasi-static approximation ($D<<\lambda$, and therefore, $\sigma_{sca}<<\sigma_{abs}$) and present a homogeneous 2D or 3D distribution, it is usually proposed that the nanocomposite material can be considered from a macroscopic point of view as a homogeneous effective medium. The optical properties of this effective medium are described by a dielectric tensor $[\varepsilon_{eff}]$ from which the transmittance, reflectance, and ellipsometry spectra can be calculated. The key of effective medium modeling thus relies in the determination of $[\varepsilon_{eff}]$, which must be linked to the features of the nanoparticles ensemble: size and shape distributions, organization, and orientation. Since the pioneering work of Maxwell-Garnett [96] that dealt with the simple case of dilute monodisperse spherical nanoparticles (considered as point dipoles) with a 3D distribution in a medium, many effective medium models of increasing complexity were developed [97, 98]. Only some of them, which can be considered as particularly intuitive, will be presented here in detail:

- The Maxwell-Garnett model and its extensions to polydisperse assemblies of nanoparticles, anisotropic shapes with a specific ensemble orientation.
- The Yamaguchi modeling for a single layer of weakly interacting spherical or spheroidal nanoparticles (considered as point dipoles) supported on a flat substrate or sandwiched between two dielectric layers (2D distribution). Its extensions to polydisperse systems, ellipsoidal nanoparticles, and nanoparticle chains will be described.
- The effective surface susceptibility method of Bedeaux and Vlieger and its applications (involving multipolar expansions of the potential) to the case of a single layer of truncated spheroidal nanoparticles supported on a flat substrate (2D distribution).

5.2.1 Maxwell-Garnett Model and Extensions

Maxwell-Garnett's approach [96] deals with the case of identical spherical nanoparticles dispersed homogeneously in an infinite matrix medium. Under

external electric excitation, the nanoparticles get polarized and thus alter the electric field in their surroundings. Each nanoparticle is supposed to be very small ($D<<\lambda$) and excited by a local field $\mathbf{E_{loc}}$ homogeneous over its whole volume. It is thus modeled as a point dipole of polarizability α and dipolar momentum $\mathbf{p} = \varepsilon_0\varepsilon_m\alpha\mathbf{E_{loc}}$, ε_m being the dielectric function of the matrix. $\mathbf{E_{loc}}$ results from contributions of the external excitation and the fields generated by the other nanoparticles. The exact way to take into account the latter contribution is to sum the fields created at a central nanoparticle by all the others. In order to simplify the problem, Maxwell-Garnett used the Lorentz sphere approach, that is, he considered the neighboring particles to act as a continuum. The local field was thus calculated using the Clausius-Mossotti-Lorenz-Lorentz formula $\mathbf{E_{loc}} = \mathbf{E} + \mathbf{P}/(3\varepsilon_0\varepsilon_m)$, $\mathbf{E}$ and $\mathbf{P}$ being the macroscopic electric field and polarization in the effective medium, respectively, and verify the relation $\mathbf{P} = N\mathbf{p} = \varepsilon_0(\varepsilon_{eff}\text{-}\varepsilon_m)\mathbf{E}$, N being the volume density of nanoparticles. After combining the previous relations and using Eq. 6.5 for the polarizability α, one gets the Maxwell-Garnett formula:

$$\varepsilon_{eff} = \varepsilon_m\left[1 + f\frac{(\varepsilon_i - \varepsilon_m)}{\varepsilon_m + \left(\frac{1-f}{3}\right)(\varepsilon_i - \varepsilon_m)}\right] \tag{6.15}$$

Except the dielectric functions of the metal and the host matrix, the only parameter is the metal volume fraction f verifying $f = NV$, V being the volume of one nanoparticle. This formula is frequently applied to the case of nanocomposite thin films consisting of nanoparticles randomly dispersed or with an isotropic 3D organization in a dielectric matrix. The film, of thickness t, is thus considered as a homogeneous material whose dielectric function ε_{eff} verifies (Eq. 6.15). Its reflectance, transmittance, or ellipsometry spectra can thus be calculated from the Abélès matrices taking into account in a coherent way the propagation of light and its transmission and reflexion at interfaces [99]. Comparison between absorbance spectra derived from (Eq. 6.15) and experimental spectra was reported, as, for instance, in the case of 100-nm-thick films built by stacking spherical core-shell Au/SiO_2 nanoparticles [100]. The core diameter was $D = 13$ nm, and the thickness of the shell was adjusted in order to tune the metal volume fraction f in the film. Simulations show a dipolar plasmon absorption band that red-shifts upon increasing f, as observed experimentally. A reasonable agreement between the simulated and experimental width and spectral position of the plasmon resonance band was observed for volume fractions f as high as 30 %.

The Maxwell-Garnett model was modified to treat the case of spherical particles consisting of an anisotropic nanocomposite material [101] or that of anisotropic nanoparticle shapes. The case of polydisperse ellipsoidal nanoparticles with a random orientation and distribution was studied [102]. Other extensions deal with monodisperse spheroidal nanoparticles with a specific orientation of their revolution axis, tilted of an angle θ [103] from the direction $\mathbf{e_z}$, defined as the normal to the nanocomposite material's flat surface. In such a case, the effective

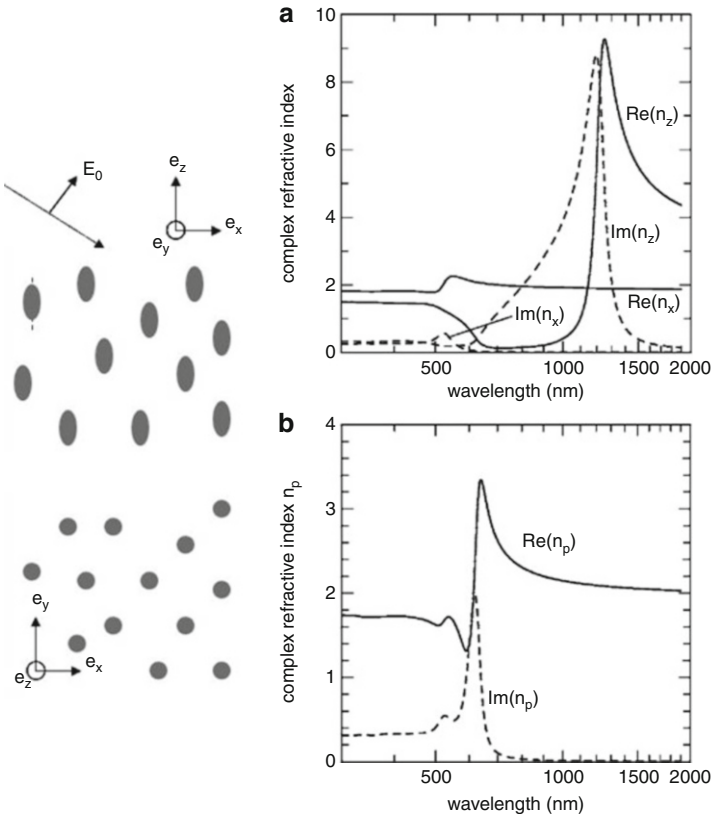

Fig. 6.7 (*Left panel*) Schematic representation of a composite medium whose effective dielectric function is calculated from (Eq. 6.16). It consists of spheroidal nanoparticles embedded in a matrix with their revolution axis along e_z. The incident electric field impinges obliquely onto the nanocomposite material's surface and is P-polarized. (*Right panel*) Spectra of the effective refractive indices n_x and n_z, respectively, in the (e_x, e_y) plane and along e_z, of a material containing Au nanocolumns oriented along e_z. Corresponding spectrum of the angle-dependent effective refractive index n_p, accounting for the response of the material illuminated at oblique incidence (60°) with P-polarized light. Reprinted with permission from [108]. Copyright 2006 by the American Physical Society

medium presents anisotropic optical properties, described by a tensor $[\varepsilon_{eff}]$ instead of a scalar quantity. If the revolution axis of the particles is perpendicular to the surface of the nanocomposite material ($\theta = 0$) [104, 105], as shown in Fig. 6.7 (left panel), $\mathbf{e_z}$ is the optical axis of the corresponding uniaxial effective medium and $[\varepsilon_{eff}]$ can be written under a simple form in the set of axes ($\mathbf{e_x}$, $\mathbf{e_y}$, $\mathbf{e_z}$):

$$[\varepsilon_{eff}] = \begin{pmatrix} \varepsilon_{eff,xy} & 0 & 0 \\ 0 & \varepsilon_{eff,xy} & 0 \\ 0 & 0 & \varepsilon_{eff,z} \end{pmatrix} \tag{6.16}$$

where $\varepsilon_{eff,u} = \varepsilon_m \left[1 + f \frac{(\varepsilon_i - \varepsilon_m)}{\varepsilon_m + (1-f)L_u(\varepsilon_i - \varepsilon_m)}\right]$ with u = xy or z

L_{xy} and L_z are the depolarization factors $L_{transverse}$ and $L_{longitudinal}$ defined in Sect. 5.1, respectively. Thus, (Eq. 6.16) takes into account the nanoparticles shape and specific orientation. The transmittance, reflectance, and ellipsometry spectra of a slab of such a nanocomposite material can then be derived using the anisotropic Abélès matrix method.

This uniaxial anisotropic form of Maxwell-Garnett's formula was applied to the case of Au nanocolumns embedded in a porous columnar Al_2O_3 matrix and elongated along the $\mathbf{e_z}$ axis [106]. In that case, it reproduced the blueshift of the transverse plasmon resonance, observed experimentally by transmittance measurements at normal incidence, upon increasing the nanoparticles aspect ratio H/D. It was also used to compute the transmittance spectra of columnar Ag nanoparticles considered as prolate spheroids, a few nm in size, embedded in TiO_2 [107] or BN [82] thin films with their revolution axis oriented along $\mathbf{e_z}$ and volume fractions below 10 %. In the latter case, the spectra were simulated for an excitation at oblique incidence with P-polarized light and showed two bands of low transmittance whose position agreed well with the experimental data. One of these bands corresponds to the transverse dipolar plasmon mode of the nanoparticles (i.e., in the ($\mathbf{e_x}$, $\mathbf{e_y}$) plane), which can be selectively excited by measurements at normal incidence. The origin of the other band, in contrast, is less trivial and cannot be interpreted using a model of isolated nanoparticle in the free space, as done in Sect. 5.1. Instead, let us consider a semi-infinite nanocomposite material, with its flat interface in the ($\mathbf{e_x}$, $\mathbf{e_y}$) plane and whose dielectric tensor is given by (Eq. 6.16). Under illumination from the outside, at oblique incidence with P-polarized light, its effective response is accounted for by an angle-dependent complex refractive index n_p [108]. Due to the intrinsic anisotropic properties of the effective medium, n_p is not a linear superposition of the refractive indices n_x and n_z defined as $n_x^2 = \varepsilon_{eff,xy}$ and $n_z^2 = \varepsilon_{eff,z}$ [108]. As seen in [108], a direct consequence of the nonlinear relation between n_x, n_z, and n_p is that a longitudinal resonance may not be observed directly by transmittance measurements. Figure 6.7 (right panel) shows the n_x and n_z spectra of a material presenting a transverse resonance (peaking at around 550 nm) and a longitudinal resonance (at around 1200 nm), respectively. The corresponding n_p spectrum at oblique incidence (60°, P-polarized light) presents a peak associated to the transverse resonance (at around 550 nm), another one at about 700 nm, but nothing at around 1200 nm [108]. Determining the spectral positions of the transverse and longitudinal plasmon modes of nanoparticles in a uniaxial anisotropic plasmonic material from transmittance measurements is thus not possible by simply indexing the peaks on the spectra. Instead, it is necessary to fit the experimental data with an anisotropic model in order to extract the n_x and n_y spectra.

5.2.2 Yamaguchi Model and Extensions

Since it is based on the concept of Lorentz sphere, the Maxwell-Garnett model is not suitable to the case of nanoparticles distributed in a plane, as it is however often

the case in real materials. Yamaguchi et al. [109] thus considered an assembly of monodisperse spheroidal nanoparticles with their revolution axis perpendicular to a nonmetallic flat substrate supporting them, that is, along $\mathbf{e_z}$, as shown in Fig. 6.8 (top-left panel). They assumed the nanoparticles to behave as point dipoles interacting between them. The interaction with the substrate was also taken into account, by the image-dipole method. The calculation of the effective dielectric tensor of the nanocomposite is then very similar to that of Maxwell-Garnett, except that the local field $\mathbf{E_{loc}}$ exerted at a given point dipole is calculated by a discrete sum over the contributions of other point dipoles and the image dipoles: $\mathbf{E_{loc}} = \mathbf{E_0} + \mathbf{E_{sub}} + \mathbf{E_{dip}}$, where $\mathbf{E_0}$, $\mathbf{E_{sub}}$, and $\mathbf{E_{dip}}$ are the incident field, that of the image dipole, and the sum of the contributions of the other dipoles (usually, the quasi-static component of their radiated field) and their images, respectively.

In the original calculations, the nanoparticles were assumed to be uncovered. Nevertheless, they can be straightforwardly extended to nanoparticles capped by a dielectric layer (with a dielectric function ε_{cap}), with the restriction that this layer is thick enough so that the nanoparticles do not interact significantly with the air/cap interface [110]. The macroscopic polarization of the thin slab of effective material reads $\mathbf{P} = \varepsilon_0([\varepsilon_{eff}]\text{-}\varepsilon_{cap})\mathbf{E} = N_s\varepsilon_0\varepsilon_{cap}[\alpha]\mathbf{E_{loc}}/t_{opt}$, where N_s is the surface density of particles, t_{opt} and $[\varepsilon_{eff}]$ the optical thickness and effective dielectric tensor of the slab, and $[\alpha]$ the polarizability tensor of a nanoparticle (relation (6.11) with $\varepsilon_m = \varepsilon_{cap}$). After calculating $\mathbf{E_{loc}}$, knowing the size and shape of the nanoparticles and their organization (on a square or hexagonal lattice in the $(\mathbf{e_x}, \mathbf{e_y})$ plane), and writing the continuity relations at the interface slab/cap and combining the equations, one obtains [109, 110]

$$\begin{cases} \varepsilon_{eff,xy} = \varepsilon_{cap}\left[1 + \dfrac{N_s V}{t_{opt}} \dfrac{\varepsilon_i - \varepsilon_{cap}}{\varepsilon_{cap} + F_{xy}(\varepsilon_i - \varepsilon_{cap})}\right] \\ \varepsilon_{eff,z} = \varepsilon_{cap}\left[1 - \dfrac{N_s V}{t_{opt}} \dfrac{\varepsilon_i - \varepsilon_{cap}}{\varepsilon_{cap} + F_z(\varepsilon_i - \varepsilon_{cap})}\right]^{-1} \end{cases} \tag{6.17}$$

Let us remark that the equations giving ε_{xy} and ε_z have distinct forms, due to the different continuity conditions for the fields in the $(\mathbf{e_x},\mathbf{e_y})$ plane and along $\mathbf{e_z}$. F_{xy} and F_z are effective depolarization factors that depend on the nanoparticle's shape (through their geometric depolarization factors L_{xy} and L_z) and on their organization [109, 110]:

$$\begin{cases} F_{xy} = L_{xy} - \dfrac{V}{4\pi H^3} \dfrac{\varepsilon_{sub} - \varepsilon_{cap}}{\varepsilon_{sub} + \varepsilon_{cap}} - \dfrac{1}{4\pi} \dfrac{2\varepsilon_{cap}}{\varepsilon_{sub} + \varepsilon_{cap}} \sum_j \left[\dfrac{3\cos^2(\varphi_j) - 1}{r_j{}^3}\right] V \\ F_z = L_z - \dfrac{2V}{4\pi H^3} \dfrac{\varepsilon_{sub} - \varepsilon_{cap}}{\varepsilon_{sub} + \varepsilon_{cap}} - \dfrac{1}{4\pi} \dfrac{2\varepsilon_{sub}}{\varepsilon_{sub} + \varepsilon_{cap}} \sum_j \left[-\dfrac{1}{r_j{}^3}\right] V \end{cases} \tag{6.18}$$

ε_{sub} is the dielectric function of the substrate, $\mathbf{r_j}$ are the positions of the dipoles. The second term in the expressions of F_{xy} and F_z accounts for the interactions between a central nanoparticle and its image dipole and the third term for the

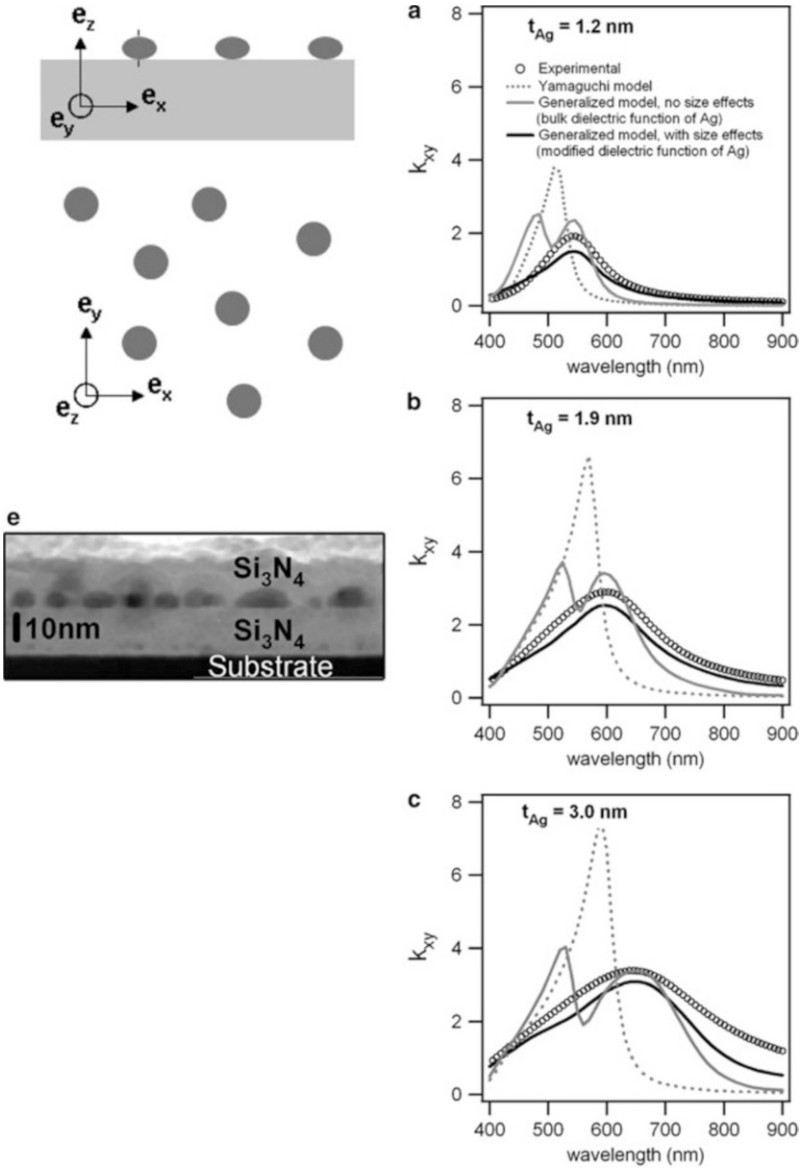

Fig. 6.8 (*Top-left panel*) Schematic representation of a composite medium whose effective dielectric function is calculated from (Eq. 6.17). (*Bottom-left panel*) Cross section TEM image of a thin film consisting of a single layer of Ag nanoparticles sandwiched between two Si_3N_4 layers. (*Right panel*) Spectra of the extinction coefficient of the single layer of Ag nanoparticles in the ($\mathbf{e_x}$, $\mathbf{e_y}$) plane for three of such thin films, containing different amounts of Ag. Simulations with different models (Yamaguchi, extension of the Yamaguchi model to ellipsoidal polydisperse nanoparticles, without and with finite-size damping effects) are compared to experimental spectra. Bottom-left and right panels reprinted with permission from [117] doi:10.1088/0957-4484/19/12/125709. Copyright 2008 Institute Of Physics

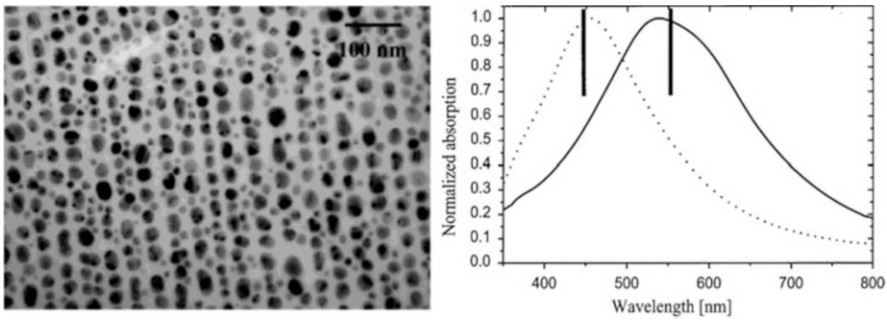

Fig. 6.9 (*Left panel*) Top view of parallel chains of Ag nanoparticles supported by an alumina rippled substrate – in the ($\mathbf{e_x}$,$\mathbf{e_y}$) plane. (*Right panel*) Corresponding absorbance spectra measured at normal incidence, for the incident electric field oriented along the chains (full line) or perpendicular to them (*dotted line*). Both panels reprinted with permission from [33]. Copyright 2003 American Chemical Society

interaction between this nanoparticle and the others, together with their image dipoles. Despite the fact that the image-dipole approach is not exact [111], calculations based on relations (6.17) were used in order to determine from in situ optical measurements the shape of Ag nanoparticles supported on substrates of various natures [112–114]. In addition, they permitted to reproduce satisfactorily the spectral position of the transverse dipole plasmon resonance of well-separated and weakly flattened Ag oblate spheroidal nanoparticles sandwiched between dielectric layers presenting a small refractive index contrast [37, 115]. Simulations in such cases, where interactions between nanoparticles are weak, show that the transverse plasmon mode of the nanoparticles red-shifts when the interparticle distance decreases.

The case of a single layer of polydisperse spheroidal nanoparticles embedded in a dielectric film was early treated [116]. An extension of these calculations was applied to the case of ellipsoidal nanoparticles randomly oriented in the ($\mathbf{e_x}$, $\mathbf{e_y}$) plane and presenting correlated size and shape distributions [117], as frequently observed in thin films grown by physical vapor deposition. Figure 6.8 (right panel) presents the measured spectra of the in-plane extinction coefficient of single layers of Ag nanoparticles sandwiched between Si_3N_4 layers (similar to that shown in the bottom-left panel of the same figure). They present an absorption band characteristic of the in-plane plasmonic response of the nanoparticles. The spectral position of this band is badly reproduced by simulations based on the Yamaguchi model, due to the non-spheroidal shape of the nanoparticles. In contrast, simulated spectra comparable to the measured ones are obtained if the nanoparticles are considered as ellipsoidal and if finite-size damping effects together with size and shape distributions are taken into account in the calculations.

Recently, physical vapor deposition on nanostructured substrates permitted to grow systems of parallel chains of nanoparticles, as shown in Fig. 6.9 (left panel). These materials display optical anisotropy in the ($\mathbf{e_x}$, $\mathbf{e_y}$) plane, as observed by transmittance measurements at normal incidence with linearly polarized light.

In such measurement conditions, a redshifted (blueshifted) plasmon resonance is probed for the electric field oriented along (perpendicular to) the chains [33, 118, 119]. The effective optical response of such systems was measured by generalized spectroscopic ellipsometry and shown to be described by a biaxial dielectric tensor [67]. Models based on Yamaguchi's approach were applied to derive in the point dipole approximation the effective dielectric tensor of parallel chains of supported spheroidal nanoparticles [118] or embedded ellipsoidal nanoparticles [36]. Simulations using these models suggest that the existence of two in-plane polarization-sensitive plasmon resonances may result from two contributions. First, a morphological effect may be involved [118]. Indeed, the nanoparticles sometimes present an in-plane elongation, with their long axis oriented along the chains. Second, since the interparticle distance is shorter along the chains than perpendicularly to them, a parallel incoming field may probe a more strongly coupled system than a perpendicular field and thus excite a redshifted plasmon resonance.

5.2.3 Limitations of the Yamaguchi and Maxwell-Garnett Approaches

Effective medium models like those of Maxwell-Garnett, Yamaguchi and their extensions are interesting from a qualitative point of view, since they rely on a few explicit parameters describing the structure of the nanocomposite materials. Therefore, they permit to get insights into the influence of the organization, orientation, and shape of the nanoparticles. They can also fit correctly experimental optical spectra in specific cases. Nevertheless, they very often suffer from the crude assumptions on which they rely. The point dipole approximation for modeling the interaction of a small nanoparticle with a substrate or other nanoparticles, although of practical interest, suffers from limitations. For instance, it rapidly fails to describe the interaction between two spherical nanoparticles when they almost touch, if the excitation electric field is oriented along the dimer [87]. This divergence from the point dipole behavior, that occurs even if the nanoparticles well behave as such when isolated, is linked to the strong inhomogeneity of the electric field between the two spheres. The hypothesis of a locally homogeneous excitation field made to obtain, for instance, Eq. 6.2 does not hold any more. Similarly, the validity of the image-dipole approach for modeling the interaction of a nanoparticle with a substrate has to be discussed. This approach is especially questionable in the case of spheroidal and ellipsoidal nanoparticles, because their near-field is not that of a point dipole [111]. Indeed, in the case of oblate spheroidal nanoparticles, the image-dipole method overestimates the nanoparticle-substrate interaction [111, 120]. Taking into account the near-field of the nanoparticle in a rigorous manner is thus necessary to describe its interaction with the substrate. Another weakness of the Yamaguchi and Maxwell-Garnett approaches is due to the hypothesis that the shape and size distributions are decoupled from the organization of the nanoparticles, which is not always the case experimentally. In addition, one has to define an optical thickness t_{opt} for the effective material. This is particularly problematic in the Yamaguchi case, in which this choice looks completely

arbitrary. Many models were developed to correct these weaknesses. An improvement of the Yamaguchi model taking into account the exact near-field of the spheroidal nanoparticles [111] was proposed. More general effective medium theories than those of Yamaguchi and Maxwell-Garnett were developed [121–126]. We evoke below that of Bedeaux and Vlieger [125, 126], which relies on an approach rubbing out the concept of optical thickness.

5.2.4 The Surface Susceptibility Method of Bedeaux and Vlieger

Bedeaux and Vlieger showed [125] that a thin perturbed layer located between two semi-infinite media can be described in terms of surface electromagnetic fields at the interface – ($\mathbf{e_x}$, $\mathbf{e_y}$) plane – between the two media. For nonmagnetic materials, the surface fields considered are the surface polarization $\mathbf{P^s}$, the surface electric displacement $\mathbf{D^s}$, and the surface electric field $\mathbf{E^s}$. If the thickness of the perturbed layer is insignificant compared to λ, a local relation is derived between these fields. The capability of the surface to polarize upon excitation is thus described by two surface susceptibilities γ and β, which account for the response in the ($\mathbf{e_x}$, $\mathbf{e_y}$) plane and along $\mathbf{e_z}$, respectively. Expressions of the Fresnel coefficients of the interface can then be calculated: they depend on the refractive indices of the substrate and ambient, the surface susceptibilities, the angle of incidence, and the polarization of the incoming light – while no optical thickness has to be used. Only the γ coefficient is involved for an S polarization of the incoming light, whereas both γ and β play a role at oblique incidence for a P polarization. In addition, the perturbed layer can be equally described as a slab of effective medium with an effective dielectric tensor [ε_{eff}] verifying the relation [125]:

$$\begin{cases} \gamma = t_{opt}(\varepsilon_{eff,xy} - \varepsilon_{cap}) \\ \beta = t_{opt}(\dfrac{1}{\varepsilon_{cap}} - \dfrac{1}{\varepsilon_{eff,z}}) \end{cases} \tag{6.19}$$

After these general preoccupations, the surface susceptibilities of a single layer of islands (with $D<<\lambda$) deposited on a nonmetallic flat substrate were calculated [126]. They were considered as point dipoles, without any assumption on their organization, with possible correlations between the size, shape, and position of the islands. The surface susceptibilities then read [126]:

$$\begin{cases} \gamma = \dfrac{\alpha^s_{0,xy}}{1 - \frac{1}{3}\kappa_{xy}\alpha^s_{0,xy}} \\ \beta = \dfrac{\alpha^s_{0,z}}{1 - \frac{1}{3}\kappa_z\alpha^s_{0,z}} \end{cases} \tag{6.20}$$

where $\alpha^s{}_{0,xy}$ and $\alpha^s{}_{0,z}$ are the average island polarizabilities per unit of surface, in the ($\mathbf{e_x}$, $\mathbf{e_y}$) plane and along $\mathbf{e_z}$, respectively. The $\kappa^s{}_{xy}$ and $\kappa^s{}_z$ coefficients are

calculated from the polarizabilities and exact positions of all the dipoles, retardation effects of their radiated fields being taken into account. These coefficients have simple expressions when assuming the nanoparticles size/shape to be decoupled from their position. Making this assumption, simulations of the optical transmittance of single layers of Ag nanoparticles supported on a substrate were comparable to experimental data [127]. Let us note that using (Eq. 6.20) with the adequate forms of κ^{s}_{xy} and κ^{s}_{z} leads to the Yamaguchi's effective dielectric functions extended to ellipsoidal nanoparticles [117].

Further refinements dealt with the accurate consideration of the nanoparticle/substrate and interparticle interactions. Interaction between a truncated spherical, truncated spheroidal, or cap-like-shaped nanoparticle (as frequently encountered experimentally) and a flat and optically isotropic dielectric substrate was studied in the quasi-static approximation [128, 129]. The electrostatic potential that verifies the Laplace equation was written in the nanoparticle, in the substrate, and in the ambient medium as sums of multipole terms weighted by unknown expansion coefficients. The boundary conditions at the different interfaces were taken into account, the image charge method [130] being used to account for the interfaces with the substrate. An infinite linear system involving the coefficients was thus obtained. Once the expansion coefficients determined numerically, the near-field around the nanoparticle can be calculated, as well as a renormalized polarizability tensor, describing the far-field optical response of the nanoparticle interacting with the substrate. Renormalized polarizabilities were also calculated in the case of a nanoparticle deposited on an optically anisotropic α-Al_2O_3 (1010) substrate [131]. The case of assemblies of supported nanospheres [132] interacting between them and with an optically isotropic substrate was also treated. The electric potential was calculated at a given point by summing the retarded multipole contributions of all the nanoparticles. Interactions in systems of supported nanoparticles can also be handled for truncated spheres [133] or truncated spheroids but at the expense of increased computational cost. Coupling multipolar calculations with the surface susceptibility approach – as implemented in the freely available Granfilm software [134] – permitted to analyze properly the spectroscopic ellipsometry spectra of single layers of colloidal Au nanoparticles on Si substrates [66] and to reproduce accurately the surface differential reflectivity of Ag nanoparticles deposited by evaporation onto MgO [135] or α-Al_2O_3 [136] substrates. In the latter case, the nanoparticles were modeled as identical hemispheres. Their renormalized polarizability tensor was calculated taking nanoparticle/substrate and dipole-dipole interparticle interactions into account. The surface polarizabilities $\alpha^{s}_{0,xy}$ and $\alpha^{s}_{0,z}$ and then the surface differential reflectance (SDR) spectrum of the single layer of nanoparticles were then derived from this tensor. Figure 6.10 (left panel) shows the excellent agreement between the simulated and experimental SDR spectra (oblique incidence 45°, S-polarized light). These spectra are dominated by a dipolar plasmon mode but also present quadrupolar contributions. The corresponding potential maps are shown also in Figure 6.10 (right panel), further discussion being given in [136].

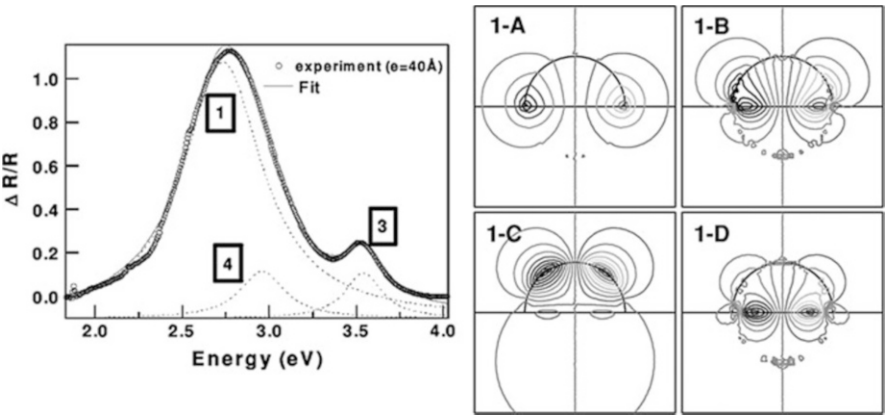

Fig. 6.10 (*Left panel*) Experimental SDR spectrum (45°, S-polarized light) of Ag nanoparticles deposited on a α-Al_2O_3 substrate and fitted theoretical spectrum obtained assuming a hemispherical shape for the nanoparticles. The individual contributions of the different plasmon modes are shown. (*Right panel*) Potential maps of the different in-plane plasmon modes. Both panels reprinted with permission from [136]. Copyright 2002 by the American Physical Society

5.3 Electrodynamic Calculations

5.3.1 Isolated Spherical Nanoparticle: Mie Theory

When D cannot be neglected versus λ, a spherical nanoparticle is not excited homogeneously by the incoming fields so that multipolar distributions of surface charges can set up. Moreover, due to the finite velocity of light, interactions between the polarization charges of the nanoparticle do not occur instantaneously but are affected by retardation effects. Therefore, the quasi-static approximation does not hold anymore. A more general approach, relying on electrodynamics, is thus required to study the optical response of the nanoparticle. The problem was treated by Mie [3], who found analytical solutions to Maxwell's equations, thus obtaining the extinction, scattering, and absorption cross sections of an isolated sphere in a nonabsorbing medium [5]:

$$\begin{cases} \sigma_{ext} = \dfrac{\lambda^2}{2\pi} \displaystyle\sum_{l=1}^{\infty} (2l+1)[\mathrm{Re}(a_l) + \mathrm{Re}(b_l)] \\ \sigma_{sca} = \dfrac{\lambda^2}{2\pi} \displaystyle\sum_{l=1}^{\infty} (2l+1)\left[|a_l|^2 + |b_l|^2\right] \end{cases} \quad \text{and} \quad \sigma_{abs=}\sigma_{ext} - \sigma_{sca} \tag{6.21}$$

The coefficients a_l and b_l are functions of the geometric (size-dependent) Bessel functions and of the dielectric functions of the sphere ε_i and surrounding medium ε_m. These coefficients represent the contributions of multipoles (linked to surface charges and surface currents) to the total response of the sphere. The dipolar

contribution is given by $l = 1$, the quadrupolar contribution by $l = 2$, etc. Let us note that Mie's approach also permits to derive the electric and magnetic fields. The extinction and scattering properties of the nanoparticles are usually described by their extinction and scattering efficiencies defined as the ratio between the extinction cross section given by (Eq. 6.21) and the real cross section of the nanoparticle: $Q_{ext} = \sigma_{ext}/\pi R^2$ and $Q_{sca} = \sigma_{sca}/\pi R^2$. Figure 6.11 (top panel) shows calculated extinction efficiency spectra for a spherical Ag and Au nanoparticle in water as a function of its size [137] (given by the radius R). For the Ag nanoparticle at $R \rightarrow 0$ (quasi-static limit), the extinction spectrum is dominated by the dipolar plasmon resonance peaking at around 400 nm. Upon increasing the nanoparticle size, the dipolar plasmon resonance red-shifts, while its peak value first increases slightly (until $R \approx 20$ nm) and then decreases due to a strong damping. Such a redshift and damping were also observed in the calculated spectra of the near-field of a Ag nanoparticle [138].

On one hand, the redshift of the dipolar plasmon resonance is linked to the finite velocity of light. Upon increasing R, the interaction between the opposite polarization charges of the nanoparticle cannot be considered as instantaneous as in the quasi-static regime. In contrast, they occur with a delay increasing with the particle size. Roughly, the dipolar resonance can be excited if the period of the external field remains much larger than this delay [139], that is, at a wavelength that increases with the size. This early known effect [140] is denoted as "dynamic depolarization." On the other hand, "radiation damping" is responsible for the broadening of the resonance in the frequency space [141].

Upon further increasing of the nanoparticle size, additional extinction bands appear in the violet region and then red-shift. They are attributed to multipolar distributions of surface charges [137]. The so-called multipolar plasmon resonances appear by order of increasing l values and suffer from dynamic depolarization and radiative damping as the dipolar mode. It comes from Mie's calculations that the contributions to extinction and scattering cross sections of the multipole l scale as $(kR)^{2l+1}/k^2$ and $(kR)^{2(l+1)}/k^2$, respectively. Thus, in the limiting case of $R \rightarrow 0$, (Eq. 6.21) reduces to (Eq. 6.6), and extinction is dominated by absorption. Upon increasing R, the relative contribution of dipolar scattering increases, followed by those of the quadrupole and poles of higher order. These trends are illustrated in Fig. 6.11 (bottom panel), which shows measured absorption, scattering, and extinction spectra of Ag nanoparticles in water with a controlled size (ranging from 29 to 136 nm) [142]. Similar trends are observed in the extinction efficiency spectra of Au but with plasmon modes shifted toward the red when compared to Ag. Dynamic depolarization, radiative damping, scattering [138], and higher order multipoles develop for larger values of R than in the case of Ag. The scattering pattern of the nanoparticle also depends on its size [5]: forward and backscattering are of comparable importance at small sizes (Rayleigh scattering). Then, upon increasing the size, forward scattering becomes predominant and contributions from multipoles can be observed.

Among all the plasmon modes, the dipolar mode is the one that leads to the highest near-field enhancement averaged over the nanoparticle surface [138].

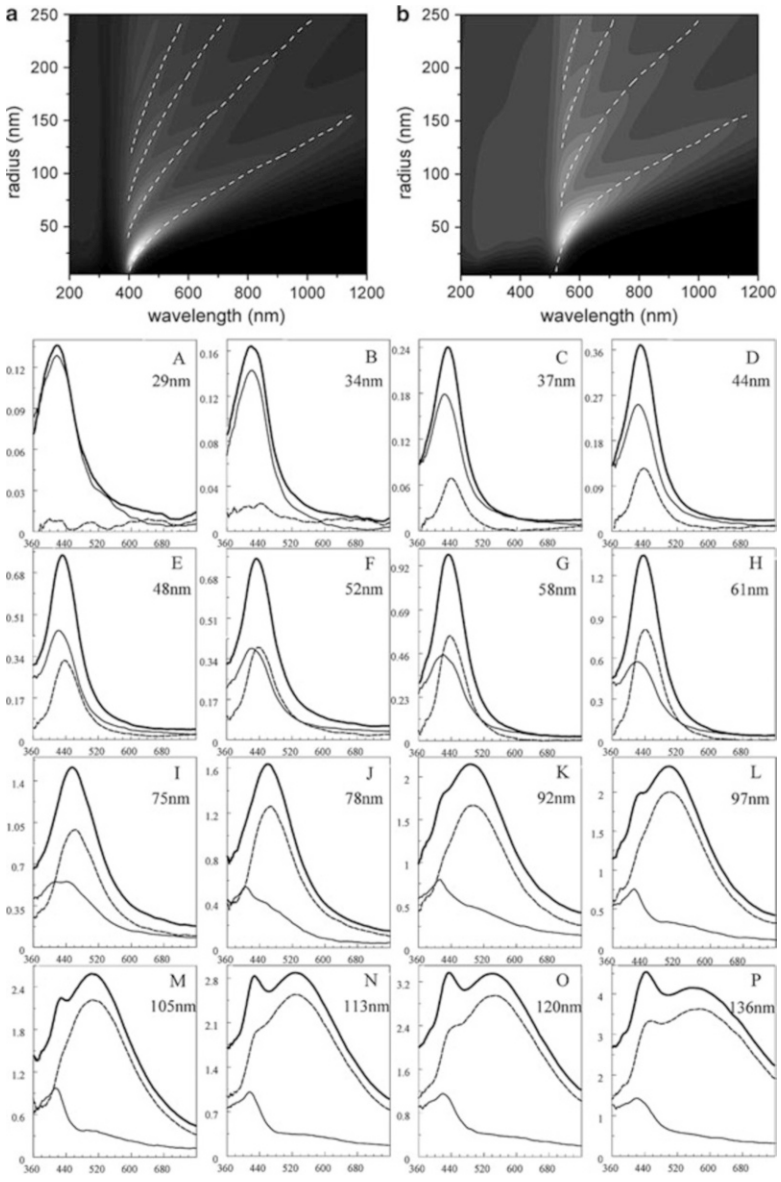

Fig. 6.11 (*Top panel*) Extinction efficiency of a Ag (**a**) and a Au (**b**) nanoparticle in water calculated as a function of the wavelength in vacuum and of the nanoparticle radius R. A *gray scale* is used for the extinction value: *black* for the lowest value and white for the highest one. The extinction efficiency ranges for Ag and Au where respectively 0–11 and 0–8. The bulk dielectric functions of Ag and Au were used for ε_i. Reprinted with permission from [137]. Copyright 2011 American Chemical Society. (*Bottom panel*) Measured extinction, scattering, and absorption spectra of spherical Ag nanoparticles in water, with an average diameter ranging from 29 nm (*A*) to 136 nm (*P*). Reprinted with permission from [142]. Copyright 2004 American Chemical Society

If R is small enough so that the multipolar contributions can be neglected, the optical response of the nanoparticle is usually described by a "dynamic polarizability" taking into account dynamic depolarization and radiation damping [143], the former scaling as R^2 and the latter as the volume $V = 4\pi R^3/3$. This polarizability substitutes to the static polarizability in (Eq. 6.6) to obtain the extinction and scattering cross sections of the nanoparticle.

5.3.2 Numerical Methods

After Mie's work, analytical solutions to Maxwell's equations were found for a sphere in an absorbing medium [144] or for nanoparticles presenting a simple shape, such as spheroids [145] or infinite cylinders, among others [146]. Nevertheless, when more complex shapes are involved, numerical approaches are required. A fast description of some frequently used approaches is given here. More complete information is given in the cited references or in textbooks, and related computer programs can be found [147]. Some of the methods available, such as the T-matrix [148, 149] or multiple multipole [88] methods, describe the fields inside and outside of the nanoparticle at a given wavelength as linear combinations of multipole terms. As in the works initiated by Bedeaux and Vlieger (although in the quasi-static approximation), the numerical task consists in determining the weighting coefficients in the sums. Volume discretization is the starting point of the discrete dipole approximation (DDA), the finite element method (FEM), and the finite difference time domain (FDTD). In DDA [150], a nanoparticle is described as a – generally cubic – array of coupled point dipoles whose polarizability is linked to the wavelength-dependent dielectric function of the metal. The momentum $\mathbf{p_j}$ of a given dipole is obtained from the local field, which is the sum of the incident field and retarded contributions of the other dipoles. The momentums of the N dipoles constituting the nanoparticle are thus linked by a system of N equations. After solving this system, one gets the $\mathbf{p_j}'$s, from which the electric field, extinction, and scattering cross sections are calculated at a given wavelength of the incident light. In FEM [151], the nanoparticle and its surroundings are divided into elements in which the fields are written as a linear combination of basis functions. Boundary conditions between neighbor elements lead to a system of equations that has to be solved for determining the weighting coefficients. FDTD [151, 152] solves Faraday's and Ampere's laws for an electromagnetic wave propagating in a grid-based domain containing the nanoparticle and its surroundings. In contrast with the previous approaches, which give wavelength-dependent results, FDTD yields a time-dependent electromagnetic field, from which spectral data can be derived by FFT treatment. Surface integral approaches, such as the boundary element method (BEM) [153], are also frequently employed. The electromagnetic field at a given wavelength is written as a function of boundary charges and currents at the surface of the nanoparticle. Boundary conditions are expressed by a system of surface integral equations that can be solved by discretization of the nanoparticle surface, thus yielding the boundary charges and currents and the electromagnetic field.

Since these methods rely on modal or spatial discretization, they do not yield the exact values of the electromagnetic field or absorption and scattering cross section. The error relative to exact calculations is tightly linked to the way the discretization is performed. Usually, the number of multipoles (MM and T-matrix) or number of dipoles (DDA) is increased, or the size of the volume or surface elements (FEM, FDTD, BEM) is decreased, until simulations of sufficient accuracy are obtained. Improving the quality of the calculations nevertheless increases their computational cost. Limitations in the computing capacity thus lead to select the calculation method as a function of the system under study. For instance, the T-matrix method could be more adequate for treating the case of large assemblies of spherical nanoparticles than DDA, which would involve a prohibitive number of dipoles. In contrast, DDA may take advantage in the case of single nanoparticles of complex shapes. Discussions of the advantages and drawbacks of the different methods can be found in the literature [139, 154], as well as benchmark studies comparing their performances in simple cases such as, for instance, Mie, FDTD, T-matrix, FEM, and DDA for a spherical Au nanoparticle [155]; MM, T-matrix, FEM, and DDA for a spheroidal Ag nanoparticle [156]; Mie versus FEM and FDTD for infinite Au cylinders [151]; MM versus BEM for a dimer of spherical Au nanoparticles [139]; DDA versus BEM for Au nanodecahedra [139]; and MM versus FEM for dimers of Ag and Ag nanoshells [157].

5.3.3 Spheroids

Retardation effects, scattering, and excitation of multipolar plasmon modes also occur upon increasing the size of nanoparticles presenting an anisotropic shape. Extensive studies were undertaken in order to quantify the influence of these effects on the optical response of nanoparticles with a revolution axis. Calculations of the near-field enhancement at the tip of prolate spheroidal Ag, Au, and Cu nanoparticles [84, 158] were early reported. As for spherical nanoparticles, increasing the nanoparticle effective diameter above some tens of nm was shown to cause a drastic decrease of the near-field enhancement at the longitudinal dipolar plasmon resonance. Peak enhancements of lower intensity were observed at the multipolar longitudinal plasmon resonances. Recently, a comprehensive DDA study of the extinction spectra of Au and Ag prolate and oblate spheroids as a function of the short axis length (varied from 5 nm to 30 nm) and axis ratio (H/D varied from 1/8 to 8) was realized [137]. The extinction spectra of the prolate and oblate spheroids are dominated by their longitudinal and transverse dipolar plasmon mode, respectively. As in the quasi-static case, these modes red-shift when the shape anisotropy increases – at a faster rate for the prolate spheroid. In addition, upon increasing the short axis length of the nanoparticles at fixed H/D, these dominant modes experience dynamic depolarization and radiation damping effects, while a blueshifted quadrupolar mode slightly grows. For a given H/D and short axis length, the volume of a prolate nanoparticle is smaller than that of its oblate counterpart, and the longitudinal prolate dipolar mode is less affected by the radiation damping-induced broadening than the transverse oblate dipolar mode. This property makes prolate spheroids interesting candidates for obtaining relatively sharp resonances peaking in the IR. In this wavelength range, Ag and Au nanoparticles with the

same shape and size present comparable extinction properties, due to similar Drude behavior of both metals, as already mentioned in Sect. 5.1.

Early works generalized the concept of dynamic polarizability, known for the dipolar plasmon mode of spheres, to spheroids [27]. The validity of the so-called modified long wavelength approximation (MLWA) was confirmed by DDA calculations in the case of the transverse dipolar plasmon mode of oblate Ag nanoparticles with an effective radius of 30 nm and axis ratios H/D as low as 0.1 [27, 143]. Similarly, a comparison between FDTD and analytical calculations showed that the concept of dynamic polarizability can be extended to Ag and Au prolate spheroids [159] with long axis length and axis ratio up to 120 nm and 5.5. The so-obtained analytical formulas, based on phenomenological parameters independent of the axis lengths, reproduced accurately scattering spectra of single Au nanorods measured by dark-field microscopy. Recent theoretical considerations about the dynamic polarizability in the case of spheroidal nanoparticles are reported [160], together with effective medium models using this concept [161].

5.3.4 Nanodisks and Nanorods

Computational works were realized for nanodisks [26] and, above all, for nanorods [162–168] which can, as prolate spheroids, support sharp longitudinal plasmon modes peaking in the IR. Their shape was taken into account rigorously, that is, as cylinders presenting possibly hemispherical tips, in contrast with previous studies in which they were approximated as spheroids [79]. DDA calculations of the extinction spectra of Au nanorods and spheroids with a short axis of 10 nm and H/D varying from 1 to 9 showed substantial differences in the positions of their longitudinal dipolar plasmon mode, peaking at a longer wavelength in the former case [163]. Assuming a cylindrical shape, a satisfactory agreement was obtained between the simulated and measured extinction spectra of Au nanorods, with D and H/D varying between 5 and 10 nm and 2 and 4, respectively [169]. The evolution of the spectral position of the longitudinal dipolar plasmon mode was studied for a Au nanorod as a function of the radius of the hemispherical tip and the total rod length, varied up to 600 nm [166]. In addition, spectrally well-separated multipolar plasmon modes were observed in the extinction spectra of such long Au nanorods [170]. Numerical calculations described their shift toward the red upon increasing the axis ratio [162, 167, 168]. Scaling laws linking the spectral position of each mode to the geometric parameters of the nanorods were derived from these works.

The contributions of absorption and scattering to the extinction spectra of Au nanorods was studied theoretically [162]. As seen in Fig. 6.12 (left panel), increasing the effective radius of the nanorod at a fixed axis ratio induces an increase of the scattering contribution. In addition, it is shown (Fig. 6.12, right panel) that the relative contribution of scattering increases with the axis ratio H/D at fixed volume and then remains almost constant. A similar behavior was observed experimentally [171] by dark-field microscopy on single Au nanorods of various aspect ratios and was attributed to the suppression of non-radiative desexcitation paths when the longitudinal dipolar plasmon resonance is shifted away from the interband region of Au.

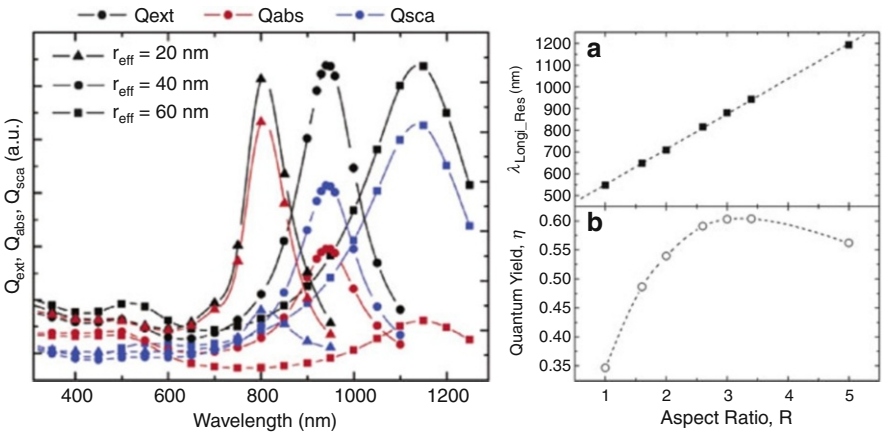

Fig. 6.12 (*Left panel*) Extinction, scattering, and absorption efficiency spectra of Au cylinders in water with an axis ratio H/D = R = 3.4 and for different values of the effective radius. (*Right panel*) Spectral position of the longitudinal dipolar mode of the Au cylinders and of the quantum yield (ratio between the peak values of the scattering and extinction efficiencies) as a function of R, for an effective radius of 40 nm. Both panels reprinted with permission from [162]. Copyright 2005 American Chemical Society

5.3.5 Other Nanoparticles Shapes

Metal nanoparticles with more complex shapes than spheres or rods can be designed. Varying the nanoparticles size and shape was shown experimentally to allow tuning their near-field, far-field optical response and index sensitivity [172]. Numerical calculations were performed in order to address the origin of the near-field and far-field plasmonic features for a wide range of nanoparticles shapes [70, 165] and to evaluate the related index sensibility. Studies are reported in the case anisotropic nanoparticles, such as triangular Ag nanoprisms [70] possibly with dipped edges, Ag truncated nanotetrahedra [27], Au nanodecahedra [173, 174], Ag nanocubes [175], Au nanostars [176], and nanodumbbells [177] (which are currently formed during the coalescence of spherical nanoparticles). Shell-like structures, such as Au nanorings [178] or spherical nanoshells [179], have been shown to present a dipolar plasmon resonance tunable from the visible to the IR upon varying the shell thickness, together with strong near-field enhancement and index sensitivity. Even higher tunability, near-field enhancement and index sensitivity are obtained in the case of spheroidal metal nanoshells – known as nanorice [180, 181].

5.3.6 Supported Nanoparticles: Scattering and Applications to Solar Cells

It is known that the scattering efficiency of a point dipole located at the interface between two transparent media is modified when compared to the free-space case, together with the angular distribution of the scattered light [182]. Under excitation at normal incidence, the main fraction of the scattered light is redirected into the medium presenting the highest refractive index [183]. Despite of the crudeness of

point dipole-based approaches, this property is considered of potential interest for the development of improved solar cells, since it may permit to increase the optical path length and thus the absorption efficiency in the photovoltaic material. Photocurrent enhancement in the range of low absorption of silicon solar cells was effectively observed after physical vapor deposition of Ag nanoislands [184] on their top face. Rigorous classical treatment of the problem of scattering by a spherical nanoparticle supported on a substrate was early done using multipole expansion methods [185]. Recent theoretical studies based on numerical calculations aimed at determining the conditions permitting to improve the fraction of light trapped in silicon: nanoparticles size and shape (cylinder, sphere, hemisphere) [186], nature of a buffer between the nanoparticles and the substrate [187], and distance between the nanoparticles and the substrate [188]. The recent advances in the field of plasmon-based photovoltaics are detailed in a recent review paper [11]. Particular interest was also devoted to the calculation of the scattered light of supported nanoparticles when observed using dark-field microscopes [90]. Besides, let us mention that numerical studies were also performed to study the effect of a metallic adhesion layer below cylindrical metal nanoparticles on their plasmon resonances [189].

5.3.7 Interacting Nanoparticles

Considering the nanoparticles as point dipoles coupled via the quasi-static component of their radiated field (as done, for instance, in Sect. 5.2.2) is generally a too crude approximation for describing the interactions between them. Indeed, on one hand, the electric field $\mathbf{E_{dipole}}$ radiated at $\mathbf{r} = (r,\theta)$ by an oscillating dipole excited by a field $\mathbf{E_0}$ involves a $1/r$ electrodynamic term in addition to the $1/r^3$ quasi-static term:

$$E_{\mathbf{dipole}} = \left[\frac{(1 - ik\mathbf{r})(3\cos^2\theta - 1)e^{ikr}}{\mathbf{r}^3} + \frac{k^2\sin^2\theta e^{ikr}}{\mathbf{r}}\right]\alpha\mathbf{E_0} \tag{6.22}$$

While the quasi-static term dominates at small r, the electrodynamic contribution plays an important role in the far-field coupling between nanoparticles. Indeed, it has been shown to affect the linewidth and spectral position of dipolar plasmon resonances in dimers [190], 2D arrays [191–194], 2D arrays [195] interacting with a substrate, and chains [196, 197] of nanoparticles, with pitches ranging from 100 nm to several hundreds of nm. On the other hand, when nanoparticles, even if small enough to behave as dipoles when isolated, come close enough one to another, the optical response of the coupled system involves multipolar orders [198]. We will focus here on the case of nearly touching nanoparticles, whose optical response is strongly sensitive to the interparticle distance, permitting the realization of "plasmonic molecular rulers" useful for biological sensing [199]. In addition, dense packing of the nanoparticles induces strongly enhanced fields – the so-called hot spots – in the gaps between nanoparticles [200]. Hot spots are identified as significant contributors to the SERS effect [10] and also likely play a role in the strong nonlinear susceptibility of almost percolated assemblies of

nanoparticles [201]. The simplest case for studying the optical response of strongly coupled nanoparticles is that of a dimer of identical nanospheres, sufficiently small to behave as dipoles when taken separately. The extinction of the dimer is generally studied as a function of the s/D or s/R ratio, s being the distance separating the nanoparticles surfaces. Decreasing s/D from a value at which the nanoparticles still present a dipole-like behavior first leads to a dipole-dipole interaction-induced redshift of the plasmon resonance observed under longitudinal excitation [88] (electric field along the revolution axis of the dimer). In contrast, a slight blueshift of the plasmon resonance is observed under transverse excitation. Upon further decrease in the separation distance, the longitudinal plasmon mode keeps redshifting, as shown in Fig. 6.13 (top-left panel) but at a faster rate than predicted assuming dipole-dipole interactions [88]. In addition, a blueshifted peak appears under longitudinal excitation [70, 88, 177]. The near-field corresponding to this peak involves distorded quadrupolar contributions, while that associated to the redshifted peak presents dipole-like contributions [70] (see Fig. 6.13, top-right panel). Simulations also show a very intense field enhancement in the gap [70, 177]. Upon reducing the separation distance down to very small values, calculations predict that the so-called dipolar mode loses strength as the quadrupolar-like mode and higher order (blueshifted) modes grow [177].

Theoretical findings are consistent with experimental data obtained on dimers of almost spherical or cylindrical metal nanoparticles [202–205] deposited on a substrate. Indeed, the redshift of the longitudinal dipolar plasmon is usually observed upon decreasing s/D. In the case of nearly touching nanoparticles, an additional blueshifted peak was revealed under longitudinal excitation (see Fig. 6.13, bottom-left panel) and was attributed to the quadrupolar-like mode [205]. Let us note at this point that due to accuracy limitations and, above all, due to fundamental inadequacy (as it will be explained in Sect. 6), numerical calculations based on local classical hypotheses are expected to fail in reproducing experimental trends in the s/D→0 limit.

A physical interpretation of plasmonic coupling between spherical nanoparticles [206, 207] and nanorods [208], and also in nanoshells [209, 210], or between a nanoparticle and a metallic surface [211], among many others [212], is provided by the plasmon hybridization method. This approach, which is valid in the quasi-static regime, has, for instance, proved to give values of the peak wavelengths of the plasmon resonances of a dimer of identical metal nanospheres in agreement with FDTD calculations [206]. At sufficiently large s/D, dipole-dipole coupling dominates and leads to the splitting of the "pure" single nanoparticle dipolar plasmon mode into lower energy (bonding) and higher energy (antibonding) hybridized dipolar dimer modes [79, 206]. One bonding and one antibonding mode are associated to each orientation of the excitation field and correspond to the two possible relative directions of the dipoles. The modes consisting of antiparallel dipoles present a zero total dipole moment and are optically "dark," that is, they cannot be probed by traditionnal optical far-field measurements. For a longitudinal (transverse) polarization, the dimer plasmon mode that can be probed – denoted as "bright" – is redshifted (blueshifted) from the "pure" single nanoparticle dipolar plasmon mode, the magnitude of the shift depending on the interaction strength, that is, on the polarization and

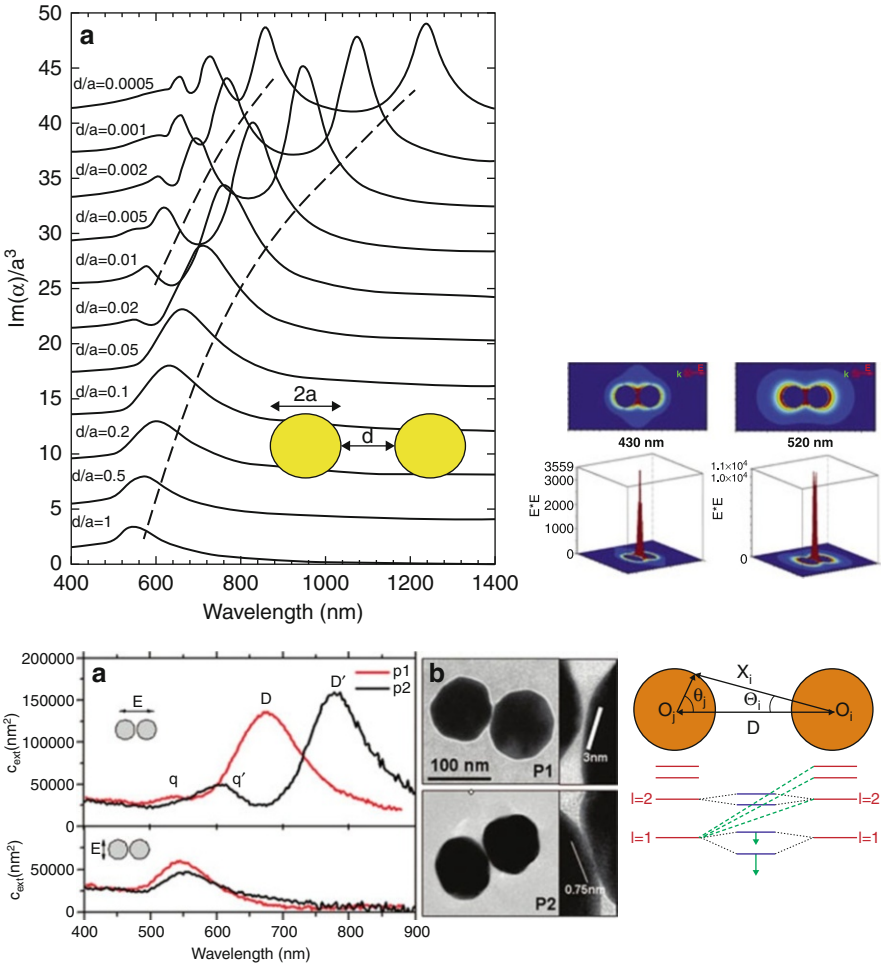

Fig. 6.13 (*Top-left panel*) Simulated extinction efficiency spectra of a dimer of Ag nanoparticles (diameter 60 nm), for the excitation field parallel to the dimer revolution axis. Reprinted after agreement from [177]. Copyright 2006 Optical Society of America. (*Top-right panel*) Simulated near-field distribution of a dimer of Ag nanoparticles (diameter 72 nm) for an excitation along its revolution axis, at the wavelength of the so-called quadrupolar and dipolar plasmon resonances. Reprinted with permission from [70]. Copyright 2004, American Institute of Physics. (*Bottom-left panel*) Experimental extinction spectra of two dimers of almost spherical Au nanoparticles, for a longitudinal and a transverse excitation. Reprinted with permission from [205]. Copyright 2009 American Chemical Society. (*Bottom-right panel*) Schematic representation of plasmon hybridization in a dimer of metal nanoparticles, in which the "pure" dipolar plasmon of one particle interacts with the "pure" multipolar plasmon of the other one. Reprinted with permission from [206]. Copyright 2004 American Chemical Society

separation distance. Due to the dipolar geometry of the near-field enhancement around a single spherical nanoparticle, stronger interparticle coupling and mode splitting are observed under longitudinal excitation of the dimer than under transverse excitation. Upon further decreasing of s/D and under longitudinal excitation, the "pure" dipolar plasmon mode of one nanoparticle interacts with the "pure" multipolar plasmon modes of the other one [206], as shown in Fig. 6.13 (bottom-right panel). This non-dipolar behavior leads to a faster redshift of the dipolar bonding mode than predicted by dipole-dipole interaction models and to the excitation of multipolar dimer plasmon modes peaking at a shorter wavelength than the dipolar bonding mode [206].

Works were also performed in the case of interacting metallic prolate spheroidal nanoparticles or nanorods sufficiently small so that their dipolar plasmon resonance dominates when isolated (maximum length around 100 nm). In contrast with spherical nanoparticles, the coupling depends on their relative orientation. Tip-to-tip (i.e., nanoparticles with their revolution axes being superposed) and side-to-side (i.e., with a plane of symmetry between the nanoparticles) configurations were investigated by DDA for a dimer of identical Au oblate spheroids [213]. Decreasing the separation distance in the tip-to-tip case leads to a weak blueshift and strong redshift of the transverse and longitudinal plasmon modes of the spheroidal nanoparticles, respectively. The situation is reversed in the side-to-side configuration, for which the shifts are weaker and the longitudinal mode blue-shifts while the transverse mode red-shifts. These trends are consistent with hybridization schemes, whose predictions are depicted in the weak dipole-dipole interaction regime in Fig. 6.14 [214]. Other orientations of the nanoparticles were also investigated by numerical and experimental means: dimer of identical Au nanorods with tip-to-tip and side-to-side configurations with a longitudinal offset (DDA) [214], dimer of identical Au nanorods with tilted orientations [215] (FDTD), or dimer of tip-to-tip nanorods of different length [216] (FDTD). The geometry of such dimers allows the observation of antibonding modes that are dark for identical rods with tip-to-tip and side-to-side geometries, as schematized in Fig. 6.14 [214].

Many other recent studies, which will not be detailed here, involving classical numerical calculations and devoted to the near-field interaction between metal nanoparticles can be found in the literature. A good agreement was obtained between the experimental and DDA-computed spectral positions of the transverse and longitudinal modes of an assembly of densely packed, vertically oriented Ag nanorods, thus in the side-to-side configuration, embedded in a-Al_2O_3 [217]. Scaling laws linking the spectral position of the longitudinal dipole plasmon of a dimer to a few structural parameters were derived in the case of dimers of spheres, spheroids, flat cylinders, and elongated cylinders with flat or rounded tips. Provided the separation distance s between the nanoparticles is not too small, an exponential function of the s/particle length ratio (or s/diameter ratio for spherical particles) has been obtained [218, 219]. Deviations from the exponential behavior were underlined in periodic arrays of dimers, in which far-field radiative coupling between the dimers plays a significant role [220]. Recently, Fano resonances [221] were observed in Au or Ag nanoparticle-based tailor-made plasmonic systems [212, 222], as a result of the

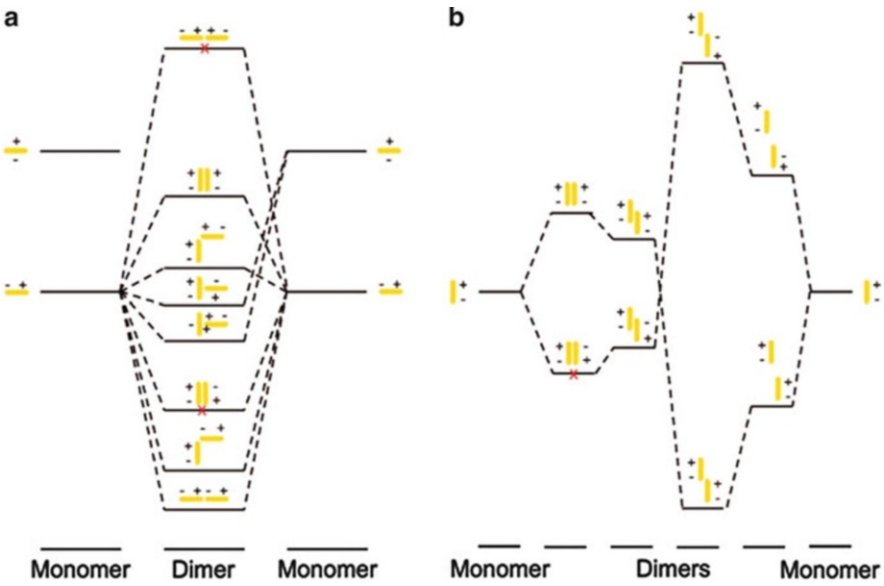

Fig. 6.14 Schematic representation of hybridization diagrams of dimers of Au nanorods, for different orientations, in the weak dipole-dipole interaction regime. Reprinted with permission from [214]. Copyright 2009 American Chemical Society

interaction between broad and sharp hybridized plasmon modes. Much effort has been made for modeling and tuning the features of the Fano optical transparency band, for instance in tailored clusters of nanoparticles [223–224], unveiling their strong potential for sensitive molecule [225] and nanoparticle [226] detection.

6 Conclusions and Future Perspective

In this chapter, the influence of the shape, size, and environment of Au and Ag nanoparticles on their plasmon resonances was reviewed through experimental data and simulations taken from the literature. The review was restricted to works dealing with the linear optical properties of nanoparticles in a passive environment, which represent only a fraction of the publications in the field of plasmonics. Indeed, it has to be mentioned that a huge number of studies, involving experimental and theoretical developments, were focused in the last years on the nonlinear optical response of metal nanoparticles [53, 227, 228], their temporal response [229–231], their vibrational properties [232], as well as on the interaction between metal nanoparticles and luminescent materials [9]. Moreover, the theoretical results reported in this chapter rely on the use of classical models, which assume the material constituting the nanoparticles to be described by a frequency-dependent (possibly size-dependent) dielectric function. In addition, the interface between a nanoparticle and its environment was considered as abrupt. These approximations are too rough in some

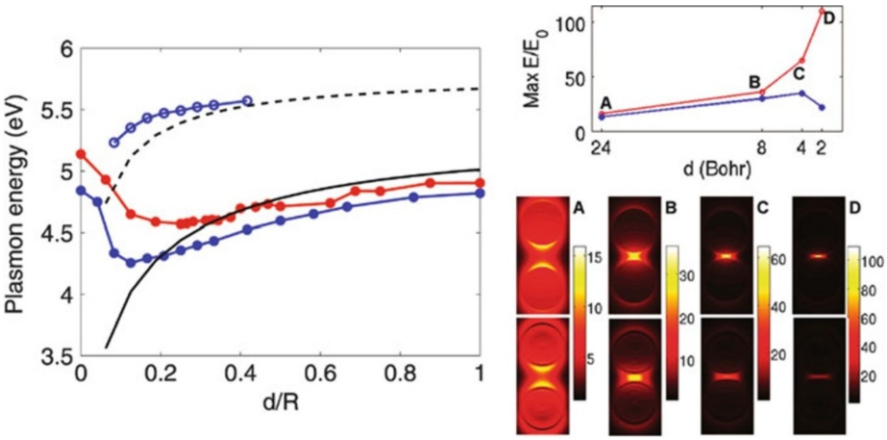

Fig. 6.15 (*Left panel*) Spectral position of the dipolar and quadrupolar plasmon resonances of a dimer of Ag nanoparticles, obtained from classical (*dark lines*) and quantum (*colored lines*) calculations. (*Right panel*) Near-field enhancement around the dimer for several separation distances, obtained from classical (*red*) and quantum calculations (*blue*). Both panels reprinted with permission from [234]. Copyright 2009 American Chemical Society

cases, for instance, for isolated nanoparticles, a few nm in size or nearly touching nanoparticles. Classical approaches based on nonlocal (i.e., frequency and wave vector dependent) dielectric functions for the metal were thus developed in order to provide a better description of such systems [233, 234]. The non-abruptness of the nanoparticle/environment interface due to spill-out of the electron cloud away from the rigid ionic skeleton of the metal was taken into account by quantum calculations [235], from which absorption spectra [236, 237] and near-field enhancements [239] of nanoparticles less than 5 nm in size were derived. From these calculations, it was pointed out that the near-field in the nanometric surrounding of a nanoparticle should be lower than predicted from classical calculations. Recently, discrepancies between classical and quantum calculations were evidenced in dimers of nearly touching Ag spherical nanoparticles [239] – as shown in Fig. 6.15 (left panel). Such discrepancies were attributed to the incapability of classical models to take into account electron tunneling between the nanoparticles, which occur at small separation distances and whose occurrence leads to lower field enhancements than those predicted by classical calculations [239] (see Fig. 6.15, right panel).

Although the results presented in this review are limited to relatively simple cases, it has to be pointed out that numerical calculations and modern nanofabrication and characterization techniques open the way to studies of more complex systems involving metal nanoparticles (consisting of any metal or alloy). In the last years, the potential of a broad range of elemental materials and alloys for plasmonics was discussed [240, 241], and works coupling experiments and modeling were undertaken in order to explore the optical response of tailored nanoparticles based on alternative plasmonic metals such as Al, Pt or Pd [15, 242, 243]. Coupling between

nanostructures of different natures, either in the core-shell geometry [244] or in compositionally asymmetric nanoparticle dimers [245–248] opens the way to a rich variety of plasmonic features and to the design of active hybrid systems with a possible interplay between plasmons and other physical or chemical properties. Specific illumination and collection conditions, as well as coupling between the nanoparticles and complex environments such as photonic structures, can be taken into account in classical calculations. Quantum calculations could also be useful for studies dealing with the interaction between metal nanoparticles and nearly touching active nanostructures. These developments, which have been at the focus of recent studies, may keep on being of significant interest in the near future.

References

1. Leonhardt U (2007) Optical metamaterials: invisibility cup. Nature Photonics 1:207
2. Faraday M (1857) Experimental relations of gold (and other metals) to light. Phil Trans Roy Soc Lon 147:145
3. Mie G (1908) Beiträge zur Optik trüber Medien, speziell kolloidaler Metallösungen. Ann Phys 3:377
4. Kreibig U, Zacharias P (1970) Surface plasma resonances in small spherical silver and gold particles. Z Phys 231:128
5. Kreibig U, Vollmer M (1995) Optical properties of metal clusters. Springer, Berlin
6. Ziljstra P, Chon JWM, Gu M (2009) Five-dimensional optical recording mediated by surface plasmons in gold nanorods. Nature 459:410
7. Huang X, El Sayed IH, Qian W, El Sayed MA (2006) Cancer cell imaging and photothermal therapy in the near-infrared region using gold nanorods. J Am Chem Soc 128:2115
8. Ozbay E (2006) Plasmonics: merging photonics and electronics at nanoscale dimensions. Science 311:189
9. Lakowicz JR, Ray K, Chowdhury M, Szmacinski H, Fu Y, Zhang J, Nowaczyk K (2008) Plasmon-controlled fluorescence: a new paradigm in fluorescence spectroscopy. Analyst 133:1308
10. Talley CE, Jackson JB, Oubre C, Grady NK, Hollars CW, Lane SM, Huser TR, Nordlander P, Halas NJ (2005) Surface-enhanced raman scattering from individual Au nanoparticles and nanoparticle dimer substrates. Nano Lett 5:1569
11. Atwater HA, Polman A (2010) Plasmonics for improved photovoltaic devices. Nat Mater 9:205
12. Simonot L, Babonneau D, Camelio S, Lantiat D, Guérin P, Lamongie B, Antad V (2010) In-situ optical spectroscopy during deposition of Ag:Si_3N_4 nanocomposite films by magnetron sputtering. Thin Sol Films 518:2637
13. Stewart ME, Anderton CR, Thompson LB, Maria J, Gray SK, Rogers JA, Nuzzo RG (2008) Nanostructured plasmonic sensors. Chem Rev 108:494
14. Wu PC, Kim T-H, Brown AS, Losurdo M, Bruno G, Everitt HO (2007) Real-time resonance tuning of liquid Ga nanoparticles by in-situ spectroscopic ellipsometry. Appl Phys Lett 90:103119
15. Langhammer C, Yuan Z, Zoric I, Kasemo B (2006) Plasmonic properties of supported Pt and Pd nanostructures. Nano Lett 6:833
16. Tanabe K (2008) Field enhancement around metal nanoparticles and nanoshells: a systematic investigation. J Phys Chem C 112:15721
17. Chan GH, Zhao J, Schatz GC, Van Duyne RP (2008) Localized plasmon resonant spectroscopy of triangular aluminium nanoparticles. J Phys Chem C 112:13958

18. Jiang XM, Ji Q, Ji LL, Chang A, Leung K (2003) Resolution improvement for maskless micro ion beam reduction lithography system. S Vac Sci Technol B 21:2724
19. Bender M, Otto M, Hadam B, Vratzov B, Spangenberg B, Kurz H (2000) Fabrication of nanostructures using a UV-based imprint technique. Microtech Eng 53:233
20. Vieu C, Carcenac F, Pepin A, Chen Y, Mejias M, Lebib A, Manin-Ferlazzo L, Couraud L, Launois H (2000) Electron beam lithography: resolution limits and applications. Appl Surf Sci 164:111
21. Cerrina F (2000) X-ray imaging: applications to patterning and lithography. J Phys D Appl Phys 33:R103
22. Xu Z, Yu W, Wang T, Zhang H, Fu Y, Lu H, Li F, Lu Z, Sun Q (2011) Plasmonic nanolithography: a review. Plasmonics 6:565
23. Haynes CL, Van Duyne RP (2001) Nanosphere lithography: a versatile nanofabrication tool for studies of size-dependent nanoparticle optics. J Phys Chem B 105:5599
24. Rechberger W, Hohenau A, Leitner A, Krenn JR, Lamprecht B, Aussenegg FR (2003) Optical properties of two interacting gold nanoparticles. Opt Comm 220:137
25. Banaee MG, Crozier KB (2010) Gold nanorings as substrates for surface-enhanced Raman scattering. Opt Lett 35:760
26. Grand J, Adam PM, Grimault AS, Vial A, Lamy de la Chapelle M, Bijeon JL, Kotscheev S, Royer P (2006) Optical extinction of oblate, prolate and ellipsoid shaped gold nanoparticles: experiments and theory. Plasmonics 1:13
27. Kelly KL, Coronado E, Zhao LL, Schatz GC (2003) The optical properties of metal nanoparticles: the influence of size, shape and dielectric environment. J Phys Chem B 107:668
28. Verellen N, Van Dorpe P, Vercruysse D, Vandenbosch GAE, Moschchalkov VV (2011) Dark and bright localized surface plasmons in nanocrosses. Opt Expr 19:11034
29. Henry CR (1998) Surface studies of supported model catalysts. Surf Sci Rep 31:231
30. Toudert J, Camelio S, Babonneau D, Denanot MF, Girardeau T, Espinos JP, Yubero F, Gonzalez Elipe AR (2006) Morphology and surface-plasmon resonance of silver nanoparticles sandwiched between $Si_3 N_4$ and BN layers. J Appl Phys 98:114316
31. Ouacha H, Hendrich C, Hubenthal F, Träger F (2005) Laser-assisted growth of gold nanoparticles: shaping and optical characterization. Appl Phys B 81:663
32. Wenzel T, Bosbach J, Goldmann A, Stietz F, Träger F (1999) Shaping nanoparticles and their optical spectra with photons. Appl Phys B 69:513
33. Fort E, Ricolleau C, Sau Pueyo J (2003) Dichroic thin films of silver nanoparticle chain arrays on facetted alumina templates. Nano Lett 3:65
34. Sánchez-Valencia JR, Toudert J, Boras A, López-Santos C, Barranco A, Feliu IO, Gonzalez-Elipe AR (2010) Tunable in-plane optical anisotropy of Ag nanoparticles deposited by DC sputtering onto SiO_2 nanocolumnar thin films. Plasmonics 5:241
35. Suzuki M, Maekita W, Wada Y, Nakayama K, Kimura K, Fukuoka T, Mori Y (2006) In-line aligned and bottom-up Ag nanorods for surface-enhanced Raman spectroscopy. Appl Phys Lett 88:203121
36. Sánchez-Valencia JR, Toudert J, Borras A, Barranco A, Lahoz R, de la Fuente GF, Frutos F, Gonzalez-Elipe AR (2011) Selective dichroic patterning by nanosecond laser treatment of Ag nanostripes. Adv Mater 24:848
37. Lantiat D, Babonneau D, Camelio S, Pailloux F, Denanot MF (2007) Evidence for capping-layer effects on the morphology and plasmon excitation of Ag nanoparticles. J Appl Phys 102:113518
38. Toudert J, Fernandez H, Babonneau D, Camelio S, Girardeau T, Solis J (2009) Linear and third-order nonlinear optical responses of multilayered Ag:Si_3N_4 nanocomposites. Nanotechnology 20:475705
39. Camelio S, Babonneau D, Girardeau T, Toudert J, Lignou F, Denanot M-F, Maître N, Barranco A, Guérin P (2003) Optical and structural properties of Ag-Si_3N_4 nanocermets prepared by means of ion-beam sputtering in alternate and codeposition modes. Appl Opt 42:674

40. Margueritat J, Gonzalo J, Afonso CN, Ortiz MI, Ballesteros C (2006) Production of self-aligned metal nanocolumns embedded in an oxide matrix film. Appl Phys Lett 88:093107
41. Burgin J, Langot P, Arbouet A, Margueritat J, Gonzalo J, Afonso CN, Vallée F, Mlayah A, Rossell MD, Van Tendeloo G (2008) Acoustic vibration modes and electron-lattice coupling in self-assembled silver nanocolumns. Nano Lett 8:1296
42. Perez A, Melinon P, Dupuis V, Jensen P, Prevel B, Tuaillon J, Bardotti L, Martet C, Treilleux M, Broyer M, Pellarin M, Vaille J-L, Palpant B, Lerme J (1997) Cluster assembled materials: a novel class of nanostructured solids with original structure and properties. J Phys D Appl Phys 30:709
43. Pérez-Juste J, Pastoriza-Santos I, Liz-Marzán LM, Mulvaney P (2005) Gold nanorods: synthesis, characterization and applications. Coord Chem Rev 249:1870
44. Sau TK, Rogach AL (2010) Non-spherical noble metal nanoparticles: colloidal-chemical synthesis and morphology control. Adv Mater 22:1781
45. Rycenga M, Cobley CM, Zheng J, Li W, Moran CH, Zhang Q, Qin D, Xia Y (2011) Controlling the synthesis and assembly of silver nanostructures for plasmonic applications. Chem Rev 111:3669
46. Shan J, Tenhu H (2007) Recent advances in polymer protected gold nanoparticles: synthesis, properties and applications. Chem Comm 44:4580
47. Liz-Marzán LM, Giersig M, Mulvaney P (1996) Synthesis of gold silica core-shell particles. Langmuir 12:4329
48. Tan SJ, Campolongo MJ, Luo D, Cheng W (2011) Building plasmonic nanostructures with DNA. Nat Nanotech 6:268
49. Ohko Y, Tatsuma T, Fujii T, Naoi K, Niwa C, Kubota Y, Fujishima A (2003) Multicolour photochromism of TiO2 films loaded with silver nanoparticles. Nat Mat 2:29
50. Crespo-Monteiro N, Destouches N, Bois L, Chassagneux F, Reynaud S, Fournel T (2010) Reversible, and irreversible laser microinscription on silver-containing mesoporous titania films. Adv Mater 22:3166
51. Muskens O, Christofilos D, Del Fatti N, Vallée F (2006) Optical response of a single noble metal nanoparticle. J Opt A Pure Appl Opt 8(4):S264–S272
52. Sönnichsen C, Geier S, Hecker NE, von Plessen G, Feldman J, Ditlbacher H, Lamprecht B, Krenn JR, Aussenegg FR, Chan VZ-H, Spatz JP, Möller M (2000) Spectroscopy of single metallic nanoparticles using total internal reflection microscopy. Appl Phys Lett 77:2949
53. Zijstra P, Orrit M (2011) Single metal nanoparticles: optical detection, spectroscopy and applications. Rep Prog Phys 74:106401
54. Gunnarsson L, Rindzevicius T, Prikulis J, Kasemo B, Käll M, Zou S, Schatz GC (2005) Confined plasmons in nanofabricated single silver particle pairs: experimental observation of strong interparticle interactions. J Phys Chem B 109:1079
55. Wiederrecht GP (2004) Near-field optical imaging of noble metal nanoparticles. Eur Phys J Appl Phys 28:3
56. Bouhelier A, Novotny L (2007) Near-field optical excitation and detection of surface plasmons; in surface plasmon nanophotonics. Springer, Berlin, p 139
57. Okamoto H, Imura K (2009) Near-field optical imaging of enhanced electric fields and plasmon waves in metal nanostructures. Prog Surf Sci 84:199
58. Hubert C, Rumyantseva A, Lerondel G, Grand J, Kotscheev S, Billot L, Vial A, Bachelot R, Royer P (2005) Near-field photochemical imaging of noble metal nanostructures. Nano Lett 5:615
59. Ibn El Ahrach H, Bachelot R, Vial A, Lérondel G, Plain J, Royer P, Soppera O (2007) Spectral degeneracy breaking of the plasmon resonances of single metal nanoparticles by nanoscale near-field photopolymerisation. Phys Rev Lett 98:107402
60. Plech A, Leiderer P, Bonneberg J (2009) Femtosecond laser near field ablation. Laser Photon Rev 3:435

61. Bosman M, Keast VJ, Watanabe M, Maaroof AI, Cortie MB (2007) Mapping surface plasmon at the nanometre scale with an electron beam. Nanotechnology 18:165505
62. Nelayah J, Kociak M, Stéphan O, Garcia de Abajo FJ, Tencé M, Henrard L, Taverna D, Pastoriza-Santos I, Liz-Marzan LM, Colliex C (2007) Mapping surface plasmons on a single metallic nanoparticle. Nature 3:349
63. Chu MW, Myroshnychenko V, Chen CH, Deng JP, Mou CY, Garcia de Abajo FJ (2009) Probing bright and dark surface-plasmon modes in individual and coupled noble metal nanoparticles using an electron beam. Nano Lett 9:399
64. Chaturvedi P, Hsu KH, Kumar A, Fung KH, Mabon JC, Fang NX (2009) Imaging of plasmonic modes of silver nanoparticles using high-resolution cathodoluminescence spectroscopy. ACS Nano 3:2965
65. Losurdo M, Bergmair M, Bruno G, Cattelan D, Cobet C, de Martino A, Fleischer K, DohcevicMitrovic Z, Esser N, Galliet M, Gajic R, Hemzal D, Hingerl K, Humlicek J, Ossikovski R, Popovic ZV, Saxl O (2009) Spectroscopic ellipsometry and polarimetry for materials and systems analysis at the nanometer scale: state-of-the-art, potential, and perspectives. J Nanopart Res 11:1521
66. Woormeester H, Kooij ES, Poelsema B (2003) Unambiguous optical characterization of nanocolloidal gold films. Phys Rev B 68:085406
67. Oates TWH, Ranjan M, Facsko S, Arwin H (2011) Highly anisotropic effective dielectric functions of silver nanoparticle arrays. Opt Expr 19:2014
68. Bohren CE, Huffman DR (2004) Absorption and scattering of light by small particles. Wiley-VCH, Weinheim
69. Palik ED (1997) Handbook of optical constants of solids. Academic, New York
70. Hao E, Schatz GC (2004) Electromagnetic fields around silver nanoparticles and dimers. J Chem Phys 120:357
71. Bi H, Cai W, Kan C, Zhang L, Martin D, Träger F (2002) Optical study of redox processes of Ag nanoparticles at high temperatures. J Appl Phys 92:7491
72. Kim B, Park C-S, Muruyama M, Hochella MF Jr (2010) Discovery and characterization of silver sulphide nanoparticles in sewage sludge products. Environ Sci Technol 44:7509
73. Hövel H, Fritz S, Hilger A, Kreibig U, Vollmer M (1993) Width of cluster plasmon resonances: bulk dielectric functions and chemical interface damping. Phys Rev B 48:18178
74. Kreibig U, Bour G, Hilger A, Gartz M (1999) Optical properties of cluster matter: influence of interfaces. Phys Stat Sol A 175:351
75. Kraus WA, Schatz GC (1983) Plasmon resonant broadening in small metal particles. J Chem Phys 79:6130
76. Coronado E, Schatz GC (2003) Surface plasmon broadening for arbitrary shape nanoparticles: a geometrical probability approach. J Chem Phys 119:3926
77. Cai W, Hofmeister H, Dubiel M (2001) Importance of lattice contraction in surface plasmon resonance shift for free and embedded silver particles. Eur Phys J D 13:245
78. Stockman M (2011) Nanoplasmonics: the physics behind the applications. Physics Today 64:38
79. Link S, Mohamed MB, El-Sayed MA (1999) Simulation of the optical absorption spectra of gold nanorods as a function of their aspect ratio and the effect of the medium dielectric constant. J Phys Chem B 103:3073
80. Link S, Burda C, Nikoobakht B, El-Sayed MA (2000) Laser-induced shape changes of colloidal gold nanorods using femtosecond and nanosecond laser pulses. J Phys Chem B 104:6152
81. Muskens OL, Bachelier G, Del Fatti N, Vallée F, Brioude A, Jiang X, Pileni M-P (2008) Quantitative absorption spectroscopy of a single gold nanorod. J Phys Chem C 112:8917
82. Toudert J, Babonneau D, Camelio S, Girardeau T, Yubero F, Espinós JP, Gonzalez-Elipe AR (2007) Using ion beams to tune the nanostructure and optical response of co-deposited Ag: BN thin films. J Phys D Appl Phys 40:4614

83. Margueritat J, Gonzalo J, Afonso CN, Mlayah A, Murray DB, Saviot L (2006) Surface plasmons and vibrations of self-assembled silver nanocolumns. Nano Lett 6:2037
84. Barber PW, Chang RK, Massoudi H (1983) Electrodynamic calculation of the surface-enhanced electric intensities on large Ag spheroids. Phys Rev B 27(12):7251
85. Jersch J, Demming F, Hildenhagen LJ, Dickmann K (1998) Field enhancement of optical radiation in the nearfield of scanning microscope tips. Appl Phys A 66:29
86. Averitt RD, Westcott SL, Halas NJ (1999) Linear optical properties of gold nanoshells. J Opt Soc Am B 16:1824
87. Wu D, Xu X, Liu X (2008) Electric field enhancement in bimetallic gold and silver nanoshells. Sol State Comm 148:163
88. Khlebtsov B, Melnikov A, Zharov V, Klebtsov N (2006) Absorption and scattering of light by a dimer of metal nanospheres: comparison of dipole and multipole approaches. Nanotechnology 17:1437
89. Gluodenis M, Foss CA Jr (2002) The effect of mutual orientation on the spectra of metal nanoparticle rod-rod and rod-sphere pairs. J Phys Chem B 106:9484
90. Knight MW, Wu Y, Lassiter JB, Nordlander P, Halas NJ (2009) Substrate matters: influence of an adjacent dielectric on an individual plasmonic nanoparticle. Nano Lett 9:2188
91. Pinchuk A, Hilger A, von Plessen G, Kreibig U (2004) Substrate effect on the optical response of nanoparticles. Nanotechnology 15:1890
92. Pinchuk A, Schatz G (2005) Anisotropic polarizability tensor of a dimer of nanospheres in the vicinity of a plane substrate. Nanotechnology 16:2209
93. Fuchs R (1975) Theory of the optical properties of small ionic crystal cubes. Phys Rev B 11:1732
94. Pecharromán C, Pérez-Juste J, Mata-Osoro G, Liz-Marzán LM, Mulvaney P (2008) Redshift of surface plasmon modes of small rods due to their atomic roughness and end-cap geometry. Phys Rev B 77:035418
95. Davis TJ, Gómez DE, Vernon KC (2010) Simple model for the hybridization of surface plasmon resonances in metallic nanoparticles. Nano Lett 10:2618
96. Maxwell-Garnett JC (1904) Colours in metal glasses and in metallic films. Phil Trans R Soc Lond 203:385
97. Theiss W (1993) The use of effective medium theories in optical spectroscopy. Adv Sol State Phys 33:149
98. Venger EF, Goncharenko AV, Dmitruk ML (1999) Optics of small particles and disperse media. Naukova Dumka, Kyiv
99. Azzam RMA, Bashara NM (1999) Ellipsometry and polarized light. Elsevier, North Holland
100. Ung T, Liz-Marzán LM, Mulvaney P (2001) Optical properties of thin films of Au@SiO_2 particles. J Phys Chem B 105:3441
101. Levy O, Stroud D (1997) Maxwell-Garnett theory for mixtures of anisotropic inclusions: Applications for conducting polymers. Phys Rev B 56:13
102. Goncharenko AV, Lozvski VZ, Venger EF (2001) Effective dielectric response of a shape distributed system. J Phys Condens Matter 13:8217
103. Gilliot M, En Naciri A, Johann L, Stoquert JP, Grob JJ, Muller D (2007) Optical anisotropy of shaped oriented cobalt nanoparticles by generalized spectroscopic ellipsometry. Phys Rev B 76:045424
104. Galeener FL (1971) Submicroscopic-void resonance: the effect of internal roughness on optical absorption. Phys Rev Lett 27:421
105. Barrera RG, Giraldo J, Mochán WL (1993) Effective dielectric response of a composite with aligned spheroidal inclusions. Phys Rev B 47:14
106. Hornyak GL, Patrissi CJ, Martin CR (1997) Fabrication, characterization, and optical properties of gold nanoparticles/porous alumina composites: the non-scattering Maxwell-Garnett limit. J Phys Chem B 101:1548
107. Dakka A, Lafait J, Sella C, Berthier S, Abd-Lefdil M, Martin JC, Maaza M (2000) Optical properties of Ag-TiO2 nanocermet films prepared by cosputtering and multilayer deposition techniques. Appl Opt 39:2745

108. Atkinson R, Hendren WR, Wurtz GA, Dickson W, Zayats AV, Evans P, Pollard RJ (2006) Anisotropic optical properties of arrays of gold nanorods embedded in alumina. Phys Rev B 73:235402
109. Yamaguchi T, Yoshida S, Kinbara A (1974) Optical effect of the substrate on the anomalous absorption of aggregated thin silver films. Thin Sol Films 21:173
110. Dalacu D, Martinu L (2001) Optical properties of discontinuous gold films: finite-size effects. J Opt Soc Am B 18:85
111. Fedotov VA, Emel'yanov VI, MacDonald KF, Zheludev NI (2004) Optical properties of closely packed nanoparticle films: spheroids and nanoshells. J Opt A Pure Appl Opt 6:155
112. Hilger A, Cüppers N, Tenfelde M, Kreibig U (2000) Surface and interface effects in the optical properties of silver nanoparticles. Eur Phys J D 10:115
113. Hilger A, Tenfelde M, Kreibig U (2001) Silver nanoparticles deposited on dielectric surfaces. Appl Phys B 73:361
114. Wenzel T, Bosbach J, Stietz F, Träger F (1999) In-situ determination of the shape of supported silver clusters during growth. Surf Sci 432:257
115. Babonneau D, Lantiat D, Camelio S, Toudert J, Simonot L, Pailloux F, Denanot M-F, Girardeau T (2008) Gold and silver nanoparticles embedded in dielectric-capping layers studied by HAADF-STEM. EPJ Appl Phys 44:3
116. Yoshida S, Yamaguchi T, Kinbara A (1971) Optical properties of aggregated silver films. J Opt Soc Am 61:62
117. Toudert J, Babonneau D, Simonot L, Babonneau D, Camelio S, Girardeau T (2008) Quantitative modelling of the surface plasmon resonances of metal nanoclusters sandwiched between dielectric layers: the influence of nanocluster size, shape and organization. Nanotechnology 19(12):125709
118. Camelio S, Babonneau D, Lantiat D, Simonot L, Pailloux F (2009) Anisotropic optical properties of silver nanoparticle arrays on rippled dielectric surfaces produced by low-energy erosion. Phys Rev B 80:155434
119. Maier SA, Brongersma ML, Kik PG, Atwater HA (2002) Observation of near-field coupling in metal nanoparticle chains using far-field polarization spectroscopy. Phys Rev B 65:193408
120. Valamanesh M, Borensztein Y, Langlois C, Lacaze E (2010) Substrate effect on the plasmon resonance of supported flat silver nanoparticles. J Phys Chem C 115:2914
121. Bergman DJ (1979) Dielectric constant for a two-component granular composite: a practical scheme for calculating the pole spectrum. Phys Rev B 19:2359
122. Tuncer E (2005) Extracting the spectral density function for a binary composite without a priori assumptions. Phys Rev B 71:012101
123. Fu L, Resca L (1994) Electrical response of heterogeneous systems with inclusions of arbitrary structure. Phys Rev B 49:6625
124. Fu L, Macedo PB, Resca L (1993) Analytical approach to the interfacial polarization of heterogeneous systems. Phys Rev B 47:13818
125. Bedeaux D, Vlieger J (1973) A phenomenological theory of the dielectric properties of thin films. Physica 67:55
126. Vlieger J, Bedeaux D (1980) A statistical theory for the dielectric properties of thin island films. Physica 69:107
127. Bedeaux D, Vlieger J (1983) A statistical theory for the dielectric properties of thin island films: application and comparison with experimental results. Thin Sol Films 102:265
128. Wind MM, Vlieger J, Bedeaux D (1987) The polarizability of a truncated sphere on a substrate I. Physica A 141:33
129. Lazzari R, Simonsen I, Bedeaux D, Vlieger J, Jupille J (2001) Polarizability of truncated spheroidal particles supported by a substrate: model and applications. Eur Phys J B 24:267
130. Jackson JD (1975) Classical electrodynamics. Wiley, New York

131. Flores-Camacho JM, Sun LD, Saucedo-Zeni N, Weidlinger G, Johage M, Zeppenfeld P (2008) Optical anisotropies of metal clusters supported on a birefringent substrate. Phys Rev B 78:075416
132. Harmaans MT, Bedeaux D (1993) The polarizability and the optical properties of lattices and random distributions of small metal spheres on a substrate. Thin Sol Films 224:117
133. Simonsen I, Lazzari R, Jupille J, Roux S (2000) Numerical modelling of the optical response of supported metal particles. Phys Rev B 61:7722
134. Lazzari R, Simonsen I (2002) Granfilm: a software for calculating thin-layer dielectric properties and Fresnel coefficients. Thin Solid Films 419:124
135. Lazzari R, Renaud G, Revenant C, Jupille J, Borensztein Y (2006) Adhesion of growing nanoparticles at a glance: surface differential spectroscopy and grazing incidence small angle x-ray scattering. Phys Rev B 79:125428
136. Lazzari R, Roux S, Simonsen I, Jupille J, Bedeaux D, Vlieger J (2002) Multipolar plasmon resonances in supported silver particles: the case of Ag/α-Al_2O_3 (0001). Phys Rev B 65:235424
137. Kooij ES, Ahmed W, Zandvliet HJW, Poelsema B (2011) Localized plasmons in noble metal nanospheroids. J Phys Chem C 115:10321
138. Messinger BJ, von Raben KU, Chang RK, Barber PW (1981) Local fields at the surface of noble-metal microspheres. Phys Rev B 24:649
139. Myroschnychenko V, Rodríguez-Fernández J, Pastoriza-Santos I, Funston AM, Novo C, Mulvaney P, LizMarzán LM, Garcia de Abajo FJ (2009) Modelling the optical response of gold nanoparticles. Chem Soc Rev 37:1792
140. Meier M, Wokaun A (1983) Enhanced fields on large metal particles: dynamic depolarization. Opt Lett 8:581
141. Wokaun A, Gordon JP, Liao PF (1982) Radiation damping in surface-enhanced Raman scattering. Phys Rev Lett 48:957
142. Evanoff DD Jr, Chumanov G (2004) Size-controlled synthesis of nanoparticles. 2. Measurement of extinction, scattering and absorption cross-sections. J Phys Chem B 108:13957
143. Jensen T, Kelly L, Lazarides A, Schatz GC (1999) Electrodynamics of noble metal nanoparticles and nanoparticle clusters. J Clust Sci 10:295
144. Hu L, Chen X, Chen G (2008) Surface-plasmon enhanced near-bandgap light absorption in silicon photovoltaics. J Comp Theo Nanosci 5:2096
145. Asano S, Yamamoto G (1975) Light scattering by a spheroidal particle. Appl Opt 14:29
146. Ghosh SK, Pal T (2007) Interparticle coupling effects on the surface plasmon resonance of gold nanoparticles: from theory to applications. Chem Rev 107:4797
147. www.scattport.org
148. Mischenko MI, Travis LD, Mackowski DW (1999) T-matrix computations of light scattering by non-spherical particles: a review. J Quant Spectrosc Radiat Transfer 55:535
149. Mischenko MI, Videen G, Babenko VA, Khlebtsov NG, Wriedt T (2004) T-matrix theory of electromagnetic scattering by particles and its applications: a comprehensive reference database. J Quant Spectrosc Radiat Transfer 88:357
150. Draine BT, Flatau PJ (1994) Discrete-dipole approximation for scattering calculations. J Opt Soc Am A 11:1491
151. Grosges T, Vial A, Barchiesi D (2005) Models of near-field spectroscopic studies: comparison between finite-element and finite-difference methods. Opt Expr 13:8483
152. Yee K (1966) Numerical solution of initial boundary value problems involving Maxwell's equations in isotropic media. IEEE Trans Ant Propag 14:302
153. Garcia de Abajo FJ, Howie A (2002) Retarded field calculation of electron energy loss in inhomogeneous dielectrics. Phys Rev B 65:115418
154. Zhao J, Pinchuk AO, McMahon JM, Li S, Ausman LK, Atkinson AL, Schatz GC (2008) Methods for describing the electromagnetic properties of silver and gold nanoparticles. Acc Chem Res 41:1710

155. Barnes WL (2009) Comparing experiments and theory in plasmonics. J Opt A Pure Appl Opt 11:114002
156. Karamehmedovic M, Schuh R, Schmidt V, Wriedt T, Matyssek C, Hergert W, Stalmashonak A, Seifert G, Stranik O (2011) Comparison of numerical methods in near-field computation for metallic nanoparticles. Opt Expr 19:8939
157. Khoury CG, Norton SJ, Vo-Dinh T (2009) Plasmonics of 3-D nanoshell dimers using multipole expansion and finite element method. ACS Nano 3:2776
158. Zeman EJ, Schatz GC (1987) An accurate electromagnetic theory study enhancement factors for Ag, Au, Cu, Li, Na, Al, Ga, In Zn and Cd. J Phys Chem 91:634
159. Kuwata H, Tamaru H, Esumi K, Miyano K (2003) Resonant light scattering from metal nanoparticles: practical analysis beyond Rayleigh approximation. Appl Phys Lett 83:4625
160. Moroz A (2009) Depolarization field of spheroidal particles. J Opt Soc Am B 26:517
161. Golovan LA, Zabotnov SV, Timoshenko VY, Kashkarov PK (2009) Consideration for the dynamic depolarization in the effective-medium model for description of optical properties for anisotropic nanostructured semiconductors. Semiconductors 43:218
162. Lee K-S, El-Sayed MA (2005) Dependence of the enhanced optical scattering efficiency relative to that of absorption for gold metal nanorods on aspect ratio, size, end-cap shape, and medium refractive index. J Phys Chem B 109:20331
163. Kooij ES, Poelsema B (2006) Shape and size effects in the optical properties of metallic nanorods. Phys Chem Chem Phys 8:3349
164. Khlebtsov BN, Khlebtsov NG (2007) Multipole plasmons in metal nanorods: scaling properties and dependence on particle size, shape, orientation, and dielectric environment. J Phys Chem C 111:11516
165. Jain PK, Lee K-S, El-Sayed IH, El-Sayed MA (2006) Calculated absorption and scattering properties of gold nanoparticles of different sizes, shape and composition: applications in biological imaging and biomedicine. J Phys Chem B 110:7238
166. Bryant GW, Garcia de Abajo FJ, Aizpurua J (2008) Mapping the plasmon resonances of metallic nanoantennas. Nano Lett 8:631
167. Encina ER, Coronado EA (2007) Resonance conditions for multipole plasmon excitations in noble metal nanorods. J Phys Chem C 111:16796
168. Encina ER, Coronado EA (2008) Plasmonic nanoantennas: angular scattering properties of multipole resonances in noble metal nanorods. J Phys Chem C 112:9586
169. Brioude A, Jiang XC, Pileni MP (2005) Optical properties of gold nanorods: DDA simulations supported by experiments. J Phys Chem B 109:13138
170. Payne EK, Shuford KL, Park S, Schatz GC, Mirkin CA (2006) Multipole plasmon resonances in gold nanorods. J Phys Chem B 110:2150
171. Sönnichsen C, Franzl T, Wilk T, von Plessen G, Feldmann J, Wilson O, Mulvaney P (2002) Drastic reduction of plasmon damping in gold nanorods. Phys Rev Lett 88:077402
172. Chen H, Kou X, Yang Z, Ni W, Wang J (2008) Shape- and size-dependent refractive index sensitivity of gold nanoparticles. Langmuir 24:5233
173. Noguez C (2007) Surface plasmons on metal nanoparticles: the influence of shape and physical environment. J Phys Chem C 111:3806
174. Rodríguez-Fernández J, Novo C, Myroshnychenko V, Funston AM, Sánchez-Iglesias A, Pastoriza-Santos J, Pérez-Juste J, Garcia de Abajo FJ, Liz-Marzán LM, Mulvaney P (2009) Spectroscopy, imaging and modelling of individual gold decahedra. J Phys Chem C 113:18623
175. Sherry LJ, Chang SH, Schatz GC, Van Duyne RP, Wiley BJ, Xia Y (2005) Localized plasmon resonance spectroscopy of single silver nanocubes. Nano Lett 5:2034
176. Hao E, Bailey RC, Schatz GC, Hupp JT, Li S (2004) Synthesis and optical properties of "branched" gold nanocrystals. Nano Lett 4:327
177. Romero I, Aizpurua J, Bryant GW, Garcia de Abajo FJ (2006) Plasmon in nearly touching metallic nanoparticles: singular response in the limit of touching dimers. Opt Expr 14:9988

178. Aizpurua J, Hanarp P, Sutherland DS, Käll M, Bryant GW, García de Abajo FJ (2003) Optical properties of gold nanorings. Phys Rev Lett 90:057401
179. Jain PK, El-Sayed MA (2007) Universal scaling of plasmon coupling in metal nanostructures: extension from particle pairs to nanoshells. Nano Lett 7:2854
180. Wang H, Brandl DW, Le F, Nordlander P, Halas NJ (2006) Nanorice: a hybrid plasmonic nanostructure. Nano Lett 6:827
181. Hooshmand N, Jain PK, El-Sayed MA (2011) Plasmonic spheroidal metal nanoshells showing larger tunability than their spherical counterparts: an effect of enhanced plasmon coupling. J Phys Chem Lett 2:374
182. Mertz J (2000) Radiative absorption, fluorescence, and scattering of a classical dipole near a lossless interface: a unified description. J Opt Soc Am A 17:1906
183. Schmid M, Klenk R, Lux-Steiner MC, Topic M, Krc J (2011) Modeling plasmonic scattering combined with thin-film optics. Nanotechnology 22:025204
184. Pillai S, Catchpole KR, Trupke T, Greene MA (2007) Surface plasmon enhanced silicon solar cells. J Appl Phys 101:093105
185. Videen G (1991) Light scattering from a sphere on or near a surface. J Opt Soc Am A 8:483
186. Catchpole KR, Polman A (2008) Design principles for particle plasmon enhanced solar cells. Appl Phys Lett 93:191113
187. Beck FJ, Polman A, Catchpole KR (2009) J Appl Phys 105:114310
188. Catchpole KR, Polman A (2008) Plasmonic solar cells. Opt Expr 16:21793
189. Vial A, Laroche T (2007) Description of dispersion properties of metal by means of the critical points model and application to the study of resonant structures using the FDTD method. J Phys D Appl Phys 40:7152
190. Dahmen C, Schmidt B, von Plessen G (2007) Radiation damping in metal nanoparticle pairs. Nano Lett 7:318
191. Zhao LL, Lance Kelly KL, Schatz GC (2003) The extinction spectra of silver nanoparticle arrays: influence of array structure on plasmon resonance wavelength and width. J Phys Chem B 107:7343
192. Haynes CL, McFarland AD, Zhao L, Van Duyne RP, Schatz GC, Gunnarsson L, Prikulis J, Kasemo B, Käll M (2003) Nanoparticle optics: the importance of radiative dipole coupling in two-dimensional nanoparticle arrays. J Phys Chem B 107:7337
193. Zou S, Janel N, Schatz GC (2004) Silver nanoparticle array structures that produce remarkably narrow plasmon lineshapes. J Chem Phys 120:10871
194. Auguié B, Barnes WL (2008) Collective resonances of gold nanoparticle arrays. Phys Rev Lett 101:1439021
195. Auguié B, Bendaña XM, Barnes WL, Garcia de Abajo FJ (2010) Diffractive arrays of gold nanoparticles near an interface: critical role of the substrate. Phys Rev B 82:155447
196. Hicks EM, Zou S, Schatz GC, Spears KG, Van Duyne RP (2005) Controlling plasmon line shapes trough diffractive coupling in linear arrays of cylindrical nanoparticles fabricated by electron beam lithography. Nano Lett 5:1065
197. Zou S, Schatz GC (2006) Theoretical studies of plasmon resonances in one-dimensional nanoparticle chains: narrow lineshapes with tunable widths. Nanotechnology 17:2813
198. Ruppin R (1982) Surface modes of two spheres. Phys Rev B 26:3441
199. Reinhard BM, Siu M, Agarwal H, Alivisatos AP, Liphardt J (2005) Calibration of dynamic molecular rulers based on plasmon coupling between gold nanoparticles. Nano Lett 5:2246
200. Grésillon S, Aigouy L, Boccara AC, Rivoal JC, Quelin X, Desmarest C, Gadenne P, Shubin VA, Sarychev AK, Shalaev VM (1999) Experimental observation of localized optical excitations in random metal-dielectric film. Phys Rev Lett 82:4520
201. Del Coso R, Requejo-Isidro J, Solis J, Gonzalo J, Afonso CN (2004) Third order nonlinear susceptibility of Cu:Al_2O_3 nanocomposites: from spherical nanoparticles to the percolation threshold. J Appl Phys 95:2755
202. Tamaru H, Kuwata H, Miyazaki HT, Miyano K (2002) Resonant light scattering from individual Ag nanoparticles and particle pairs. Appl Phys Lett 80:1826

203. Su K-H, Wei Q-H, Zhang X, Mock JJ, Smith DR, Schultz S (2003) Interparticle coupling effects on plasmon resonances on nanogold particles. Nano Lett 3:1087
204. Atay T, Song J-H, Nurmikko A (2004) Strongly interacting plasmon nanoparticle pairs: from dipole-dipole interaction to conductively coupled regime. Nano Lett 4:1627
205. Marhaba S, Bachelier G, Bonnet C, Broyer M, Cottancin E, Grillet N, Lermé J, Vialle J-L, Pellarin M (2009) Surface plasmon resonance of gold nanodimers near the conductive contact limit. J Phys Chem C 113:4349
206. Nordlander P, Oubre C, Prodan E, Li K, Stockman MI (2004) Plasmon hybridization in nanoparticle dimers. Nano Lett 4:899
207. Brown LV, Sobhani H, Lassiter JB, Nordlander P, Halas NJ (2010) Heterodimers: plasmonic properties of mismatched nanoparticle pairs. ACS Nano 4:819
208. Willingham B, Brandt DW, Nordlander P (2008) Plasmon hybridization in nanorods dimers. Appl Phys B 93:209
209. Prodan E, Radloff C, Halas NJ, Nordlander P (2003) A hybridization model for the plasmon response of complex nanostructures. Science 302:419
210. Prodan E, Nordlander P (2004) Plasmon hybridization in spherical nanoparticles. J Chem Phys 120:5444
211. Nordlander P, Prodan E (2004) Plasmon hybridization in nanoparticles near metallic surfaces. Nano Lett 4:2209
212. Halas NJ, Lal S, Chang W-S, Link S, Nordlander P (2011) Plasmons in strongly coupled metallic nanostructures. Chem Rev 111:3913
213. Jain PK, Eustis S, El-Sayed MA (2006) Plasmon coupling in nanorod assemblies: optical absorption, discrete dipole approximation simulation, and exciton-coupling model. J Phys Chem B 110:18243
214. Funston AM, Novo C, Davis TJ, Mulvaney P (2009) Plasmon coupling of gold nanorods at short distances and in different geometries. Nano Lett 9:1651
215. Shao L, Woo KC, Chen H, Wang J, Lin H-Q (2010) Angle- and energy-resolved plasmon coupling in gold nanorods dimers. ACS Nano 4:3053
216. Slaughter LS, Wu Y, Willingham BA, Nordlander P, Link S (2010) Effects of symmetry breaking and conductive contact on the plasmon coupling in gold nanorods dimers. ACS Nano 4:4657
217. Marty R, Arbouet A, Girard C, Margueritat J, Gonzalo J, Afonso CN (2007) Sculpting nanometer-sized landscape with plasmonic nanocolumns. J Chem Phys 131:224707
218. Jain PK, El-Sayed MA (2008) Surface plasmon coupling and its universal size scaling in metal nanostructures of complex geometry: elongated particle pairs and nanosphere trimers. J Phys Chem C 112:4954
219. Jain PK, Huang W, El-Sayed MA (2007) On the universal scaling behaviour of the distance decay of plasmon coupling in metal nanoparticle pairs: a plasmon ruler equation. Nano Lett 7:2080
220. Dridi M, Vial A (2011) Improved description of the plasmon resonance wavelength shift in metallic nanoparticle pairs. Plasmonics Published online
221. Miroshnichenko AE, Flach S, Kivshar YS (2010) Fano resonances in nanoscale structures. Rev Mod Phys 82:2257
222. Luk'Yanchuk B, Zheludev NI, Maier SA, Halas NJ, Nordlander P, Giessen H, Chong CT (2010) The Fano resonances in plasmonic nanostructures and metamaterials. Nature Mat 9:707
223. Lassiter JB, Sobhani H, Knight MW, Mielczarek WS, Nordlander P, Halas NJ (2012) Designing and deconstructing the Fano lineshape in plasmonic nanoclusters. Nano Lett 12:1058
224. Rahmani M, Lei DY, Giannini V, Lukiyanchuk B, Ranjbar M, Liew TYF, Hong M, Maier SA (2012) Subgroup decomposition of plasmonic resonances in hybrid oligomers: modeling the resonance lineshape. Nano Lett 12:2101

225. Wu C, Khanikaev AB, Adato R, Arju N, Yanik AA, Altug H, Shvets G (2012) Fano-resonant asymetric metamaterials for ultrasensitive spectroscopy and identification of molecular monolayers. Nat Mater 11:69
226. Wen F, Ye J, Liu N, Van Dorpe P, Nordlander P, Halas NJ (2012) Plasmon transmutation: inducing new modes in nanoclusters by adding dielectric nanoparticles. Nano Lett 12 (9):5020–5026
227. Palpant B (2006) Third order nonlinear optical response of metal nanoparticles, in nonlinear optical properties of matter. Springer, Dordrecht
228. Canfield BK, Husu H, Laukkanen J, Bai B, Kuittinen M, Turunen J, Kauranen M (2007) Local field asymmetry drives second-harmonic generation in non-centrosymmetric nanodimers. Nano Lett 7:1251
229. Del Fatti N, Vallée F, Flytzanis C, Hamanaka Y, Nakamura A (2000) Electron dynamics and surface plasmon resonance non-linearities in metal nanoparticles. Chem Phys 251:215
230. Link S, El Sayed MA (1999) Spectral properties and relaxation dynamics of surface plasmon electronic oscillations in gold and silver nanodots and nanorods. J Phys Chem B 103:8410
231. Lamprecht B, Leitner A, Aussenegg FR (1999) SHG studies of plasmon dephasing in nanoparticles. Appl Phys B 68:419
232. Palpant B, Portales H, Saviot L, Lermé J, Prevel B, Pellarin M, Duval E, Perez A, Broyer M (1999) Quadrupolar vibrational mode of silver clusters from plasmon-assisted Raman scattering. Phys Rev B 60:17107
233. García de Abajo FJ (2008) Nonlocal effects in the plasmons of strongly interacting nanoparticles, dimers, and waveguides. J Phys Chem C 112:17983
234. McMahon JM, Gray SK, Schatz GC (2010) Calculating nonlocal optical properties of structures with arbitrary shape. Phys Rev B 82:035423
235. Morton SM, Silverstein DW, Jensen L (2011) Theoretical studies of plasmonics using electronic structure methods. Chem Rev 111:3962
236. Palpant B, Prével B, Lermé J, Cottancin E, Pellarin M, Treilleux M, Perez A, Vialle JL, Broyer M (1998) Optical properties of gold clusters in the size range 2-4 nm. Phys Rev B 57:1963
237. Prodan E, Nordlander P, Halas NJ (2003) Electronic structure and optical properties of gold nanoshells. Nano Lett 3:1411
238. Zuloaga J, Prodan E, Nordlander P (2010) Quantum plasmonics: optical properties and tunability of metallic nanorods. ACS Nano 4:5269
239. Zuloaga J, Prodan E, Nordlander P (2009) Quantum description of the plasmon resonances of a nanoparticle dimer. Nano Lett 9:887
240. Blaber MG, Arnold MD, Ford MJ (2010) A review of the optical properties of alloys and intermetallics for plasmonics. J Phys Condens Matter 22:143201
241. Blaber MG, Arnold MD, Ford MJ (2010) Designing materials for plasmonic systems: the alkali-noble intermetallics. J Phys Condens Matter 22:095501
242. Zoric I, Zach M, Kasemo B, Langhammer C (2011) Gold, platinum and aluminium nanodisk plasmons: material independence, subradiance and damping mechanisms. ACS Nano 5:2535
243. Pakizeh T, Langhammer C, Zoric I, Apell P, Käll M (2009) Intrinsic Fano interference of localized plasmons in Pd nanoparticles. Nano Lett 9:882
244. Cortie MB, Mc Donagh AM (2011) Synthesis and optical properties of hybrid and alloy plasmonic nanoparticles. Chem Rev 111:3713
245. Bachelier G, Russier-Antoine I, Jonin C, Del Fatti N, Vallée F, Brevet PF (2008) Fano profiles induced by near-field coupling in heterogeneous dimers of gold and silver nanoparticles. Phys Rev Lett 101:197401
246. Chen F, Alemu N, Johnston RL (2011) Collective plasmon modes in a compositionally asymmetric nanoparticle dimer. AIP Adv 1:032134

247. Peña-Rodriguez O, Pal U, Campoy-Quiles M, Rodríguez-Fernández L, Garriga M, Alonso MI (2011) Enhanced Fano resonances in asymmetrical Au:Ag heterodimers. J Phys Chem C 115:6410
248. Antosiewicz T, Apell SP, Wadell C, Langhammer C (2012) Absorption enhancement in lossy transition metal elements of plasmonic nanosandwiches. J Phys Chem C 116:20522

Tailoring the Optical Properties of Silver Nanomaterials for Diagnostic Applications

7

Jae-Seung Lee

Contents

1 Definition of the Topic

Metallic silver (Ag) nanostructures play an essential role in determining sensitivity, specificity, and application in the context of the optical diagnostic techniques. In order to obtain the best sensitivity, some detection techniques require stringent Ag nanostructures, and it is for this reason that most such methods have not yet been commercialized. As many of the detection or enhancement phenomena are associated

J.-S. Lee
Department of Materials Science and Engineering, Korea University, Seoul, Republic of Korea

Challa S.S.R. Kumar (ed.), *UV-VIS and Photoluminescence Spectroscopy for Nanomaterials Characterization*, DOI 10.1007/978-3-642-27594-4_7,

with the optical properties of the metallic silver nanostructures such as surface plasmon resonance (SPR), fluorescence quenching/enhancement, and surface-enhanced Raman scattering (SERS), the quest for the "ideal" nanostructured silver materials to provide the best response has been central to the situation.

2 Overview

The dramatic development of genomics and proteomics in the last several decades has attracted researchers to investigate how the two fields merge together at the molecular level. For example, the desire to understand how proteins are expressed and what genes cause the expression has strongly motivated researchers to investigate proteins or genes in vivo or in vitro under various experimental conditions. To accomplish this task, they have taken advantage of current molecular biology techniques such as mass spectrometry, tap-tags, ELISAs, microarrays, and blottings associated with gel electrophoresis. To date, however, the need to develop alternative assays that are rapid, sensitive, and selective is growing significantly because the progress of the current research is hampered by the low throughput, high cost, slowness, and, in certain cases, limited reproducibility of the conventional methods.

Emerging nanotechnologies are considered to be promising to solve these problems. Owing to their unique and characteristic properties that have not been observed in macroscopic worlds previously and that excel the conventional materials in efficiency, nanomaterials have been intensively investigated and utilized in a variety of applications in diagnostics and therapeutics. Among the large number of nanomaterials that have been synthesized, silver nanomaterials have been used as probes in numerous detection schemes for biomolecule targets such as oligonucleotides and proteins. The unique chemical and physical properties of silver nanomaterials that stem from their nanostructures offer high sensitivity and selectivity in such applications. The following is a summary of the progress made toward understanding the optical properties of silver nanoparticles and their applications for biological sensing, with common methods and outlooks. To begin with, a brief introduction of oligonucleotides, proteins, silver nanoparticles, and oligonucleotide-silver nanoparticle conjugates (oligo-AgNPs) will be given in this section.

3 Introduction

3.1 Oligonucleotides

An oligonucleotide is a short nucleic acid, or polymer of nucleotides, with typically fewer than 100 bases. Although it can be obtained by cleaving longer DNA or RNA strands, oligonucleotides often refer to "synthetic" ones synthesized by polymerizing individual nucleotide precursors utilizing phosphoramidite chemistry. Because their chemical identity is the same as that of longer DNA or RNA except in terms of length, oligonucleotides have most of the same chemical and physical properties:

they (1) exhibit a UV absorbance at 260 nm, (2) form duplexes via base pairing, (3) have binding interactions with proteins, and (4) form monomolecular secondary structures, such as G-quadruplexes. In addition, a variety of modified bases and nucleotide linkages (e.g., 2′-O-methylated RNA bases, phosphorothioate-modified phosphate backbones, and locked nucleic acids (LNA)) have been developed to control their properties, in particular to enhance their stability.

One of the most important properties of oligonucleotides is the reversible duplex formation. Based upon the pairing of the four bases (adenine (A)-thymine (T) and guanine (G)-cytosine (C)) via hydrogen bonds, an oligonucleotide sequence can reversibly bind or hybridize to the complementary sequence. During the hybridization process, its absorbance at 260 nm decreases due to hypochromism. When heated, however, the duplexed oligonucleotides dehybridize into two complementary single strands with an increase in absorbance at 260 nm. If this dehybridization, or "melting" process, is monitored as a function of temperature using UV-vis spectroscopy (at 260 nm), a broad curve (full width at half maximum (FWHM) $\sim$10 °C) is observed, whose midpoint is considered to be the melting temperature (T_m) of the duplex system. The T_m, which is the representative value of the stability of the duplex pair, can be controlled by changing the salt concentration of the solution, the length of the sequence or the number of mismatched bases.

Synthetic oligonucleotides, terminally modified with functional chemical moieties such as thiols, amines, carboxyls, fluorophores, quenchers or biotin groups, are getting more and more widely utilized in nanotechnology applications, including microarrays, DNA origami, assembly of nanomaterials, and so on. As regards oligonucleotides, we will cover how oligonucleotides that are conjugated with nanomaterials, specifically silver nanoparticles, play a significant role as a "smart" material based upon the aforementioned properties.

3.2 Proteins

Proteins are biochemical polymeric molecules that are composed of polypeptides typically folded into various three-dimensional forms, facilitating crucial biological functions. A polypeptide is a single-chained linear polymer composed of up to 20 different amino acids joined together by peptide bonds between the carboxyl and amino groups of adjacent amino acid residues. Like other biological macromolecules such as polysaccharides and nucleic acids, proteins are essential parts of organisms and participate in virtually every process within cells. For example, enzymatic proteins catalyze biochemical reactions that are vital to metabolism. All proteinogenic amino acids except proline possess common structural features, including an α-carbon to which an amino group, a carboxyl group, and a variable side chain are bonded.

Some proteins are membrane proteins that act as receptors, whose main function is to bind a signaling molecule and induce a biochemical response in the cell. Many receptors have a binding site exposed on the cell surface and an effector domain within the cell, which may have enzymatic activity or may undergo a conformational change detected by other proteins within the cell. Antibodies

are protein components of an adaptive immune system whose main function is to bind antigens or foreign substances in the body, and target them for destruction. Antibodies can be secreted into the extracellular environment or anchored in the membranes of specialized B cells known as plasma cells. Whereas enzymes are limited in their binding affinity for their substrates by the necessity of conducting their reaction, antibodies have no such constraints. An antibody's binding affinity to its target is extraordinarily high, and thus it can be used as a target-recognition moiety as a part of silver nanomaterials-antibody conjugates.

3.3 Surface Plasmon Resonance (SPR)

Most metallic nanostructure-based diagnostic techniques, especially for silver or gold, are based on the physical phenomenon of SPR. Surface plasmons are coherent oscillations of electrons that occur at the interface between conductors and dielectrics (Fig. 7.1) [1]. When such a thin film or nanoparticle structures are excited by different wavelengths of light, there will be an absorbance maximum that occurs at a specific measurement configuration. When the nanoparticle is excited by a specific wavelength, the local electric field near the surface of the particle can be greatly enhanced, which provides a way of enhancing the vibration of the molecules attached to that surface. When two or more nanoparticles are in close proximity, the coupling of the electric field during external light excitation also changes the wavelength and strength of the local electric field. The optical properties of thin films and particles respond very sensitively to the dielectric constant change of their local environment, which is generally utilized by SPR-based sensors. In fact, the enhanced detection sensitivity really depends on how sensitively the nanostructures respond to such changes. Some of these SPR-based techniques are already commercially available.

3.4 Silver Nanoparticles: Chemical and Physical Properties

Colloidal silver nanoparticles (AgNPs) have been investigated by many researchers because of their unusual properties that include relatively high stability, low toxicity, catalytic activity, surface plasmon resonance (SPR), surface-enhanced Raman scattering (SERS), and chemical tailorability. Also, these structures can support multiple functionalities on their surface. Spherical AgNPs with various diameters (between 2 and 250 nm) can be prepared in aqueous media in relatively monodisperse forms using several synthetic methods. In addition, anisotropic AgNPs with various shapes and sizes exhibit a variety of colors fully ranging in the wavelengths of visible light. The unique and intense colors of these AgNPs are associated with their SPR. This SPR is observed in the visible region of the spectrum and stems from the collective oscillations of the free electrons in the conduction band interacting with the electromagnetic field of the incoming light. For example, monodisperse spherical AgNPs in solution ($\sim$20 nm in diameter) exhibit a yellow color, indicative of a surface plasmon band centered at $\sim$400 nm.

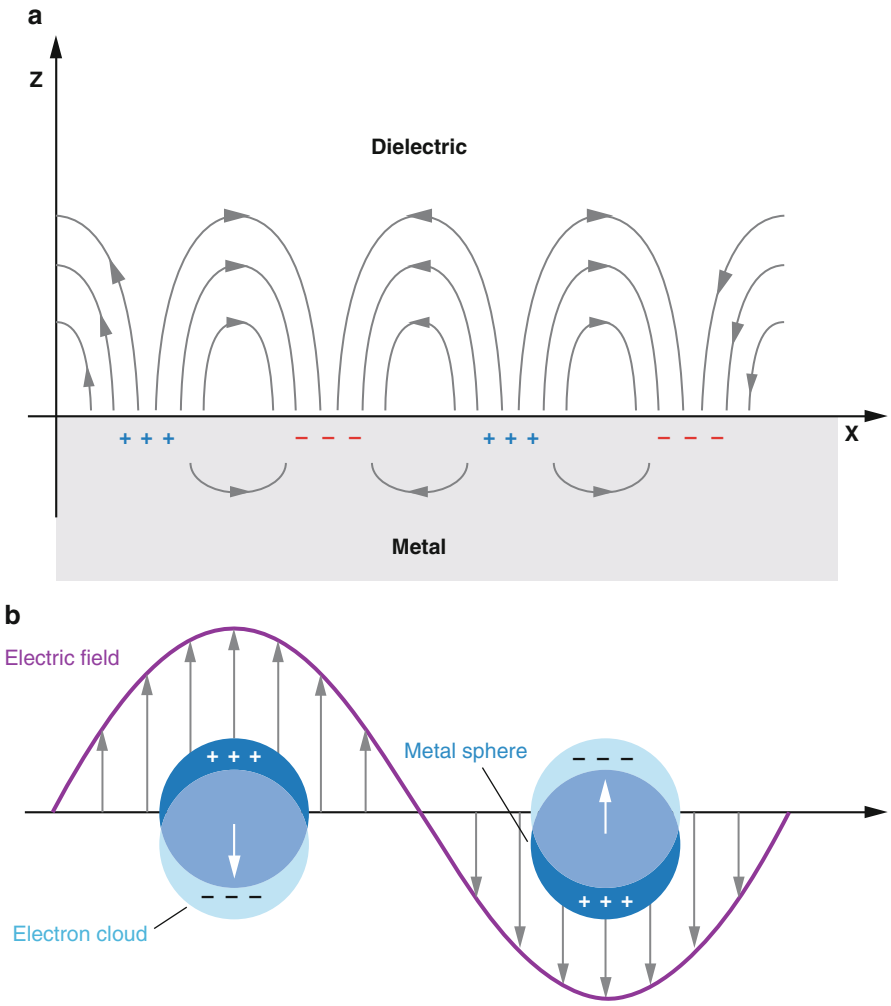

Fig. 7.1 Schematic diagrams illustrating (**a**) a surface plasmon polariton (or propagating plasmon) and (**b**) a localized surface plasmon (Reprinted with permission from Willets and Van Duyne [1]. Copyright 2007, Annual Reviews)

Because AgNPs, especially those stabilized with charged ligands, are exceedingly sensitive to changes in solution dielectric, the addition of sodium chloride (NaCl) shields the surface charge of these AgNPs and leads to a concomitant decrease in interparticle distance and eventual particle aggregation. A solution containing aggregated AgNPs appears purple or pink in color, corresponding to a characteristic red shift of the SPR of these particles, to around 600 nm. This distance-dependant optical property forms the basis of certain colorimetric detection schemes that employ nanoparticle-biomolecule conjugates as probes.

3.5 General Properties of Oligo-AgNPs

An Oligo-AgNP is a two-component system comprised of thiol-oligonucleotide strands and their nanoparticle scaffold. The properties of these inorganic nanoparticle core/organic-biomolecular ligand hybrids stem from not only each component of the hybrids but also synergistically from the combination of those two materials. The yellow color exhibited by Oligo-AgNPs in aqueous media is from the surface plasmon resonance (SPR) of the silver nanoparticles, which shows a narrow absorption in the visible range around 400 nm. However, the chemical recognition abilities of these structures are derived from the oligonucleotide shell. When two complementary Oligo-AgNPs are combined they form three-dimensional networks through DNA-DNA duplex interconnects and an effective shift of the SPR (100 nm or more) takes place with a concomitant yellow-to-pink color change. Owing to the reversible hybridization properties of oligonucleotides, however, the assembled Oligo-AgNPs disassemble at an elevated temperature (or at a reduced salt concentration) returning back to yellow. Importantly, melting analyses of the hybridized particle aggregates show sharper melting transitions (FWHM $\sim$2 °C) than free DNA duplexes. The sharpness of this melting transition is explained by a cooperative mechanism that originates from the presence of the multiple DNA interconnects between the Oligo-AgNPs and the melting cascade that takes place as counter ions are rapidly released from the aggregate. The sharp melting transition of the assembled Oligo-AgNPs is the representative synergetic result of cooperative interactions between the AgNP and surrounding oligonucleotides.

4 Experimental and Instrumental Methodology

4.1 Synthesis of DNA-Silver Nanomaterial Conjugates

In a typical experiment, silver nanomaterials with various shapes (nanospheres, nanoprisms, nanowires, nanorods, nanocubes, etc.) are synthesized using a silver precursor ($AgNO_3$), structure-directing reagents, a reductant, and other chemicals. Prior to the DNA-conjugation, excess chemicals are removed from the silver nanomaterial solutions by centrifugation of the silver material, removal of the supernatant, and redispersion of the materials in a solution containing appropriate protecting reagents and surfactants. The monothiol DNA sequences are deprotected by 0.10 M dithiothreitol in a phosphate buffer (0.17 M, pH 8.0) and purified by an NAP-5 column. The DNA is combined with 1 mL of silver nanomaterial solution (the final [DNA] = $\sim$10 μM). The nanomaterial solution is salted (0.15 M NaCl and 0.01 % SDS), buffered in 10 mM phosphate at pH 7.4, and incubated at 25 °C for 12 h. The optical properties of DNA-silver nanomaterials conjugates before and after salting are characterized by UV-vis spectroscopy.

4.2 Diagnostic Applications Using UV-Vis Spectroscopy

Two batches of DNA-silver nanomaterial probes, each with the two complementary thiol-modified DNA sequences, respectively, are combined with the target DNA strands in a series of concentrations and kept at 25 °C for 12 h to induce DNA-silver nanomaterial assembly formation. The melting experiments are conducted by monitoring the extinction at λ_{MAX} while heating the assembled DNA-silver nanomaterials from 25 °C to 85 °C. The melting experiment for the single base-mismatched target sequence was also performed in the same way.

5 Key Research Findings

5.1 Fluorescence

In the past, fluorescent dyes have been used extensively for biodetection, imaging, and diagnostics. Fluorescence in the life sciences is used generally as a nondestructive way of tracking or analysis of biological molecules by means of the fluorescent emission at a specific frequency where there is no background from the excitation light. In fact, a protein or other component can be "labeled" with an extrinsic fluorophore dye, which can be a small molecule, protein, or quantum dot, finding a large use in many biological applications. When an organic dye molecule is placed on a metal surface, its florescence signal would be quenched owing to the charge transfer between the dye molecule and the metal surface. In certain cases, however, dye molecules that are placed a small distance (a few tens of nanometers) away from the metal surface exhibit greatly enhanced florescence signal. Depending upon the distance and geometry, silver surfaces or nanoparticles can cause either a quenching or an enhancement of the fluorescence by factors of up to 1,000.

This so-called metal-enhanced florescence on fluorophores is usually observed by separating the fluorophore molecules from the metal surface by a distance of 10 nm, or more. Many of the reported studies of fluorescence associated with silver nanomaterials have used Ag islands, Ag nanoparticles, Ag surfaces or films, or mirrors, with the more dramatic effects having been found for islands and colloids rather than for continuous metallic surfaces. This type of technique has been widely used to study DNA hybridization and imaging-related diagnostics.

5.2 Surface-Enhanced Raman Scattering (SERS)

When photons are scattered from an atom or molecule, most photons are elastically scattered, such that the scattered photons have the same frequency and wavelength as the incident photons. A very small portion of that light, however, will shift its wavelength (usually lower than the frequency of the incident photons) because

of an interaction with different vibrational modes of the molecules. This type of light–molecule interaction phenomenon is known as Raman scattering. The locations of the Raman peaks reflect certain vibration bonds in the molecules, and these can be used as fingerprint to identify or differentiate different molecules. The Raman scattering technique is also one of the most useful methods in materials research. Usually, the Raman scattering cross section is extremely small compared to florescence spectroscopy, and is not suitable for low-concentration analyte detection. During the 1970s, however, it was discovered that the Raman scattering intensity could be significantly enhanced ($\sim$100 fold) when molecules were placed near rough Ag surfaces. Since then, this SERS has emerged as a powerful analytical tool that extends the possibilities of vibrational spectroscopy to solve a vast array of chemical and biochemical problems. SERS provides detailed information about the materials under investigation, often at a molecular level. In general, two primary mechanisms that differ substantially are believed to be responsible for the SERS enhancement: (1) a long-range classical electromagnetic (EM) effect [2] and (2) a short-range chemical (CHEM) effect [3]. These two mechanisms contribute simultaneously to the overall enhancement; the EM mechanism is proposed to contribute the most to the observed intensity enhancement, while the CHEM mechanism is thought to contribute a lesser amount.

5.3 SPR-Based Diagnostic Applications: Arrayed Silver Nanoparticles on a Flat Surface

Several research groups have begun to develop large-scale nanoparticle array systems that enable the real-time, parallel monitoring of multiple targets, and to explore alternative strategies for optical biosensors and chemosensors based on the extraordinary optical properties of silver nanoparticles. Nanoscale chemosensors and biosensors were demonstrated through shifts in the surface plasmon band of triangular silver nanoparticles (Fig. 7.2). These wavelength shifts are caused by adsorbent-induced local refractive index changes in competition with charge-transfer interactions at the nanoparticle surface. Arrayed silver nanoparticles can function as extremely sensitive and selective nanoscale affinity chemosensors and biosensors. These nanoscale biosensors based on SPR spectroscopy operate by transducing small changes in refractive index near the silver nanoparticle surface into a measurable wavelength shift response.

The wavelength of SPR on a silver thin film depends on the dielectric constant of the material, the film thickness, the morphological film structure, and the dielectric constant of the environment surrounding the thin film. Any changes in these parameters could induce a shift in the SPR resonant wavelength, thus give a sensing response. For most chemical and biological sensing, a change usually occurs in the surrounding environment of the thin film, such as the binding of antibody or proteins on the surface, and this causes an alteration in the dielectric constant of the environment.

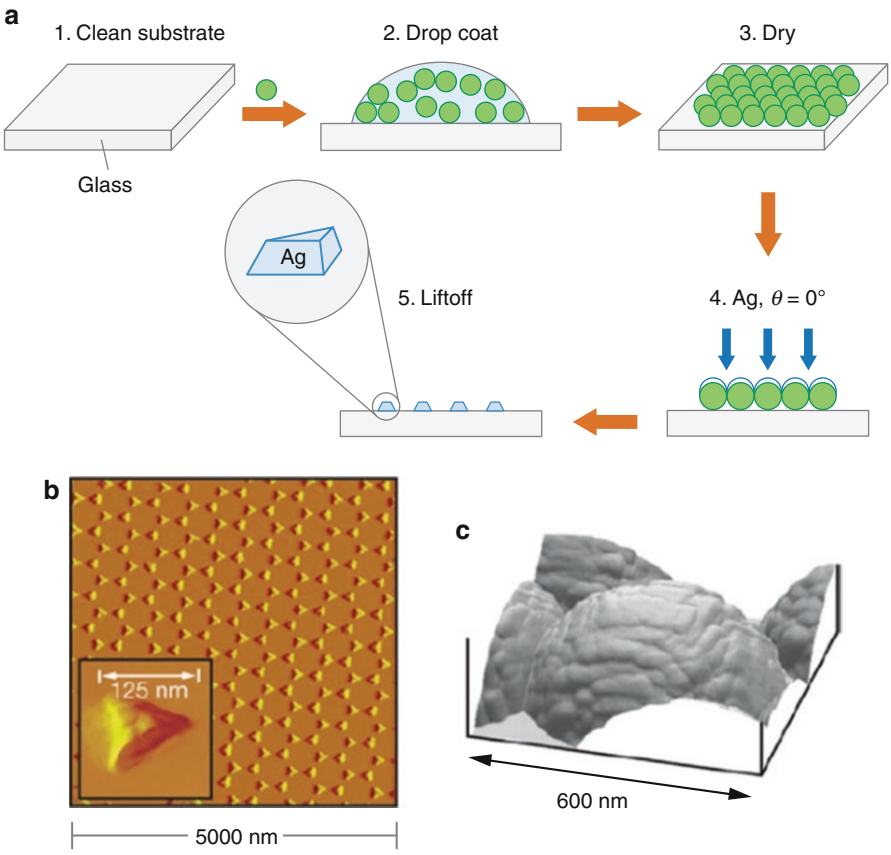

Fig. 7.2 (**a**) Illustration of the process of nanosphere lithography (NSL) in which nanospheres are drop-coated onto a surface and allowed to self-assemble into a hexagonally close-packed array (steps 1–3), followed by metal deposition (step 4), and (optional) removal of the nanosphere mask. (**b**) Atomic-force-microscope image of an NSL-fabricated nanoparticle array in which the nanosphere mask has been removed. (**c**) Atomic-force-microscope image of a film-over-nanosphere (FON) substrate in which the nanospheres remain on the surface (Reprinted with permission from Willets and Van Duyne [1]. Copyright 2007, Annual Reviews)

5.4 SPR-Based Diagnostic Applications: Assembly of Silver Nanomaterials

DNA-silver nanomaterial conjugates have been widely used in the assembly-based diagnostics owing to their intense optical properties, enhanced binding properties, sharp melting transitions, and high DNA loading. Depending on the type of assay, different properties are more or less beneficial and the ability to tail the DNA-AgNP synthesis for the specific assay can be critical. These materials have been used as probes in biodiagnostic assays for DNA and proteins. They could be potentially

used for the detection of small organic molecules and metal ions, considering the applications of their gold analogues. Because of the unique combination of properties exhibited by DNA-AgNPs, many of the assays using these materials have higher sensitivity and selectivity than conventional detection methods. The following sections will describe the different types of assays designed using the assembly of DNA-AgNPs for the detection of DNA target molecules.

5.4.1 Spherical Silver Nanoparticles

The development of DNA-spherical silver nanoparticle conjugates (DNA–AgNPs) in 2007 has opened up opportunities for fundamental studies of their novel properties as well as their application in the assembly of advanced superstructures, the detection of nucleic acids, proteins, metal ions, and small molecules, and as gene silencing agents [4, 5]. The utility of DNA–AgNPs is, in part, due to their intense optical, catalytic, and synthetically programmable recognition properties. In addition, when chemically modified in the appropriate manner, they can exhibit highly cooperative binding properties, which are typically characterized by extremely sharp melting transitions. The identification of this cooperativity demonstrated great possibility that can potentially lead to the development of molecular diagnostic probes that exhibit much higher selectivity and sensitivity for target analytes than conventional molecular fluorophore probes, and "antisense particle" agents that are significantly more effective at gene knockdown than free DNA-based antisense agents, as their gold analogues demonstrated.

In fact, silver nanoparticles (AgNPs) have generated significant scientific and technological interest. These particles exhibit higher extinction coefficients relative to gold nanoparticles of the same size, and are electrochemically and catalytically active. As has been extensively demonstrated with gold analogues, a common method used to functionalize the surface of noble metals is the adsorption of thiol-containing molecules. Until 2007, however, there have been only a few reports of thiol-functionalized AgNPs [6, 7], and of the structures prepared, they all (1) show limited stability in saline buffer (up to 0.3 M salt concentration), (2) typically require lengthy synthetic procedures (more than 2 days), and (3) do not exhibit highly cooperative binding as determined by melting analyses (the melting transitions for the hybridized particle aggregates span $\geq$10 °C). Moreover, the possible oligonucleotides that can be used to stabilize the particles are limited with respect to sequence (e.g., poly adenine (A) sequences). These limitations are primarily owing to the chemical degradation of the AgNPs under the functionalization conditions and the susceptibility of the silver surface to oxidation [8, 9].

As a result of these limitations, alternative approaches have been developed to enable the conjugation of DNA to AgNPs. Attempts to modify the AgNP surface with more tailorable and robust materials such as gold, silica, or polymers have been considered [8, 10–12]. Unfortunately, however, they require additional cumbersome chemical modification steps. Later, a method to functionalize AgNPs with oligonucleotides modified with terminal cyclic disulfide groups was developed (Fig. 7.3) [4]. These DNA-functionalized silver particles (DNA-Ag NPs) can be synthesized in less than 30 min and show stability at high salt concentrations (1.0 M NaCl).

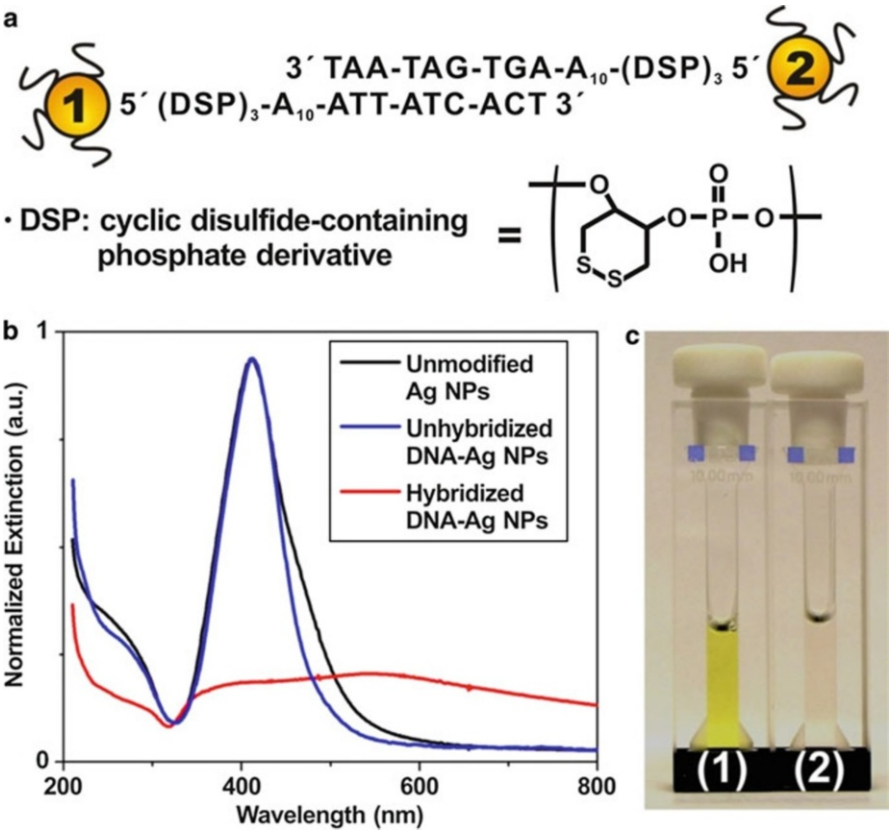

Fig. 7.3 (**a**) Schematic illustration of the hybridization of two complementary DNA-AgNPs. (**b**) UV-vis spectra of unmodified AgNPs (*black line*), unhybridized DNA-AgNPs (*blue line*), and hybridized DNA-AgNPs (*red line*). Note that the wavelength at which the maximum of the extinction of AgNPs is obtained remains the same after DNA-conjugation. After hybridization, however, the band of DNA-AgNPs broadens and red-shifts significantly from 410 to 560 nm. (**c**) Colorimetric change responsible for the assembly process of DNA-AgNPs. The intense yellow color of the unhybridized AgNPs (c1) turns to pale red (c2) as the particle aggregation proceeds. Heating of (c2), however, results in the return of the solution color to yellow (c1) (Reprinted with permission from Lee et al. [4]. Copyright 2007, American Chemical Society)

Significantly, the DNA-AgNPs also exhibit high cooperativity as characterized by their sharp DNA-melting transitions (full width at half-maximum: ~2 °C).

The cyclic disulfide anchoring group was designed based on two previous results: (1) Multiple thiol groups increase the binding affinity of oligonucleotides for the AuNP surface, which results in nanoparticle probes with higher stabilities. (2) Oligonucleotides containing a cyclic disulfide-anchoring group bind readily to Au NPs with higher affinity than monothiol or acyclic disulfide groups. The first strategy is based upon the fact that polydentate ligands often form more

substantially stable metal-ligand complexes than monodentate ligands. Therefore, utilization of multiple anchoring groups on the oligonucleotides should lead to higher stability AgNP-oligonucleotide conjugates.

5.4.2 Silver Nanoprisms

Anisotropic silver nanomaterials of different shapes and sizes are an important subject in chemistry, physics, and materials science. These materials demonstrate structurally and optically attractive properties in that they are typically nonspherical, range from several nanometers to submicrometers in size, and exhibit strong extinction owing to SPR that sensitively depends upon their shape and size. Specifically, plate-like triangular silver nanoprisms (AgNPRs), along with other silver anisotropic nanostructures such as rods, cubes, wires, disks, and polyhedrons, have been extensively investigated with respect to their controlled syntheses and various applications. Importantly, recent synthetic developments for AgNPRs based upon photochemical [13, 14] or thermal reactions [15, 16] have achieved a very high yield and the systematic and precise control over structural parameters, enabling their fundamental study and versatile application in diagnostics, optics, and electronics [17–19]. These advances in the synthesis and characterization of AgNPRs have offered substantial opportunities for the synthesis of high-quality DNA-silver nanoprism conjugates (DNA-AgNPRs) that would exhibit unique chemical and physical properties not only from AgNPRs and DNA but also from the conjugates themselves, which are analogous to DNA-conjugated isotropic plasmonic nanoparticles such as spherical gold and silver nanoparticles [20, 21]. Synthesis of the polyvalent DNA-AgNPRs, however, has not been demonstrated until 2009 [22], despite the highly developed silver surface chemistry with flat silver surfaces and spherical silver nanoparticles.

Controlled assembly of such anisotropically nanostructured DNA conjugates is another complicated and important issue [23–26]. In fact, anisotropic nanomaterials as well as isotropic ones are known to exhibit different chemical and physical properties depending upon how they are assembled. To date, several methods have been developed to control the assembly formation of anisotropic nanomaterials, such as gold nanorods, gold nanoprisms, silver nanoprisms, and silver nanocubes. Significantly, these novel assembly structures have provided scope for understanding the specific ways in which assemblies are constructed and have opened up an avenue for their fundamental study and application. These methods, however, usually require selective surface modifications of different facets or with different chemicals. In certain cases, the assembly formation of a given nanomaterial is limited to two dimensions on a surface and hardly exhibits anisotropy, despite the highly anisotropic nature of the individual nanoparticles. Only few studies, however, have yet demonstrated the reversibility of anisotropic assembly formation of anisotropic nanoparticles, which could lead to a variety of applications based upon the unique distance-dependent and assembly structure–dependent optical properties of the same material.

Recently, the synthesis of DNA-silver nanoprism conjugates and their thermodynamically controlled anisotropic assemblies in aqueous media are reported (Fig. 7.4) [22].

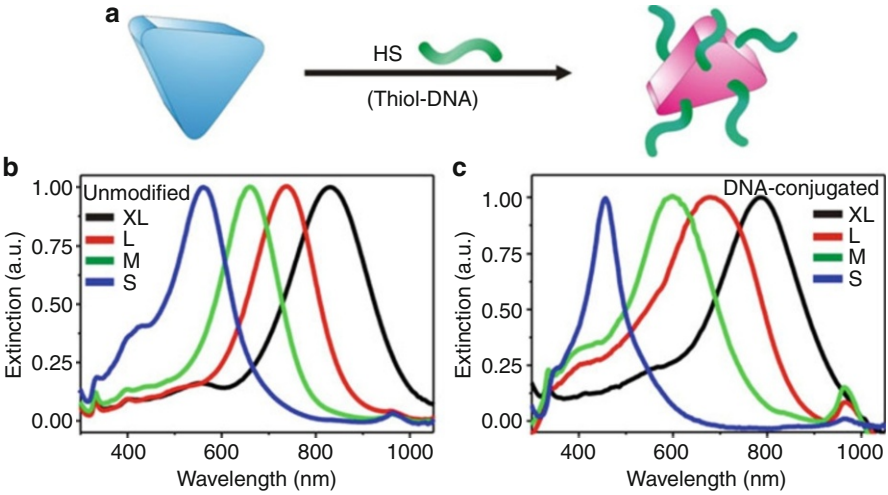

Fig. 7.4 (**a**) A scheme depicting the conjugation of thiol-DNA to a silver nanoprism (AgNPR). (**b**) UV-vis spectra of unmodified AgNPRs. (**c**) UV-vis spectra of DNA-conjugated AgNPRs (Reprinted with permission from Kim and Lee [22]. Copyright 2010, American Chemical Society)

The DNA-silver nanoprism conjugates (DNA-AgNPRs) exhibit the reversible assembly formation of the conjugates based upon the DNA-DNA duplex interconnects and assemble in an anisotropic manner that is controlled by thermodynamic conditions. Importantly, the noncovalently assembled anisotropic structures are observed not only ex situ, by electron microscopy, but also in situ, in a solution using UV-vis spectroscopy, which is strongly indicative of the programmable assembly formation not only by the DNA sequence, nanoparticle size, or simple drying effect, but also by the shape of the nanoparticle. These unique distance-dependent optical properties and programmable assembly properties are very important because they can be used in versatile diagnostic applications.

In fact, the distance-dependent optical properties of DNA-plasmonic nanoparticle conjugates have been widely utilized for the colorimetric detection of a variety of targets. Most of them, however, are based upon the SPR of individual gold or silver spherical nanoparticles, whose initial colors are limited to red (Au) or yellow (Ag). To expand the window of the initial colors, recently, gold nanoparticle clusters with various colors were synthesized whose optical properties were precisely regulated to exhibit colors such as red, purple, violet, and blue [27]. This diversity of color is significantly expanded with silver nanoprisms whose SPR ranges from the late UV region (~350 nm) to the early NIR region (~900 nm). To demonstrate the versatility of DNA-AgNPRs for the colorimetric detection of oligonucleotide targets, two sets of DNA-AgNPR probes, each of which was complementary to each half of the target (Fig. 7.5), were designed. When combined with targets of various concentrations (1, 5, 10, 25, and 50 nM), the probes

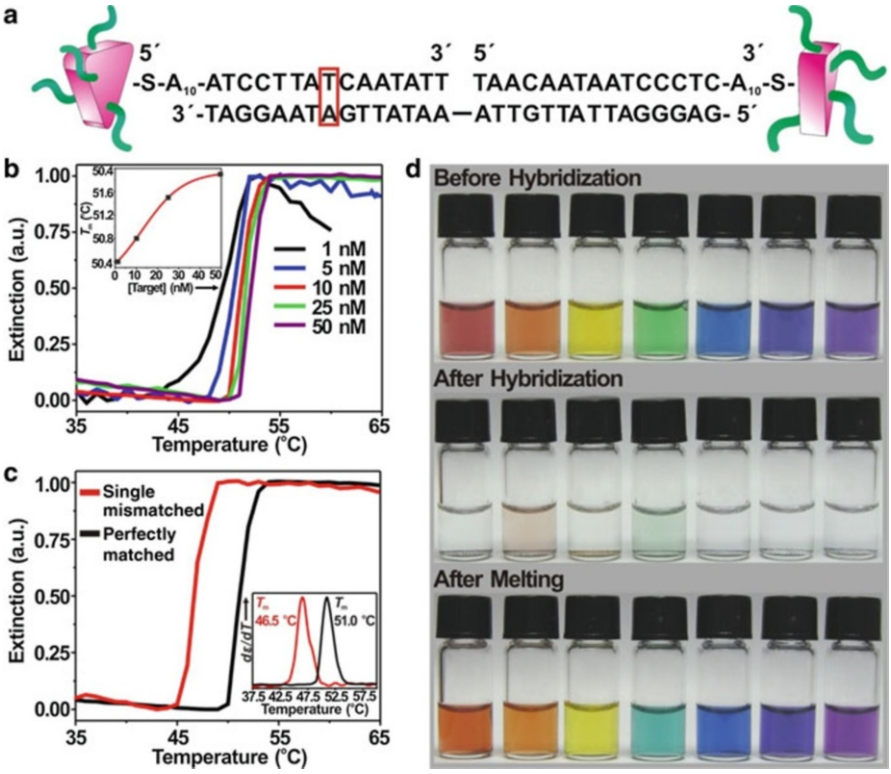

Fig. 7.5 (**a**) A scheme depicting the design of the colorimetric detection system. One of the target sequence bases is changed from adenine to thymine to examine a single-base mismatch target, and is designated in a *red box*. (**b**) Melting transitions of DNA-AgNPR aggregates with respect to various target concentrations. The melting temperature (T_m) is plotted as a function of the target concentration (*inset*). (**c**) Melting transitions of DNA-AgNPR aggregates formed with a perfectly matched target (*black line*) and a single-based mismatch target (*red line*). The first derivatives of melting transitions are shown in the inset. (**d**) Rainbow colors exhibited by two complementary DNA-AgNPRs of various sizes before hybridization (*top*), after hybridization (*center*), and after melting (*bottom*) (Reprinted with permission from Kim and Lee [22]. Copyright 2010, American Chemical Society)

aggregated and turned almost colorless. As the aggregates were heated, however, they disassembled immediately to turn light blue at certain temperatures depending upon the target concentration.

The quantitative aspect of the detection system was investigated by obtaining a series of melting transitions of the DNA-AgNPR aggregates with different target concentrations, and demonstrated by plotting the T_m as a function of the target concentration (Fig. 7.5). The plot of the T_m and the target concentration clearly demonstrates an almost linear correlation between them, indicating that this system is highly quantitative for measuring the target concentration. The limit of detection (LOD) under unoptimized conditions was determined to be 1 nM, comparable to or

better than those of other colorimetric DNA detection systems based upon the DNA-plasmonic nanoparticle conjugates. The detection system also demonstrates the excellent selectivity for distinguishing a single-base mismatch. The most important aspect of this system is its capability to provide full and continuous spectral coverage in the entire visible region by either modulating the size and shape of the nanoprisms or combining two types of nanoprisms with different colors.

5.4.3 Silver Nanowires

The syntheses and applications of one-dimensional silver nanostructures have been extensively investigated for the past decade, mainly because of their intriguing chemical and physical properties [28–33]. Specifically, silver nanowires (AgNWs) whose aspect ratio is generally much higher than their shorter rod forms exhibit excellent optical, thermal, and electrical properties, typically suitable for conductive films, plasmon resonators, electrodes, and building blocks for other nanostructures. One of the most successful methods based upon the chemical reduction of silver precursors is the polyol synthesis of silver nanowires, which takes advantage of polymeric materials such as polyvinylpyrrolidone (PVP) as a structure-directing reagent, often with external seeds [34]. While powerful and highly reproducible, this method requires the high reaction temperature (>150 °C) and cumbersome preparation of anhydrous polyols such as ethylene glycol, in certain cases with a mechanical syringe pump [35]. Alternatively, several investigations have reported the synthesis of AgNWs in aqueous media using citrate or ionic surfactants such as cetyltrimethylammonium bromide (CTAB) and sodium dodecylsulfonate [36–38].

Of particular interest is the seed-mediated growth approach owing to the rapid reaction rate and the capability to control the length distribution with different seed concentrations. Unfortunately, however, the length distribution of nanowires synthesized using this method was still broad, which could be an obstacle for analytical and quantitative applications. Subsequently, two seedless methods have been developed either with or without a surfactant [36, 37]. Unfortunately, however, these methods still exhibit relatively broad length distributions and require a high reaction temperature (100 °C). Therefore, considering the fundamental unique properties and various applications of AgNWs, the development of a significant facile synthetic method for AgNWs with well-defined structures for their biodiagnostic applications was required.

Recently, a method to synthesize AgNWs with a uniform diameter and controllable lengths using poly(sodium 4-styrenesulfonate) (PSSS) as a structure-directing reagent was reported (Fig. 7.6) [39]. PSSS molecules were chosen for two reasons: (1) they are highly soluble in aqueous media where the AgNW growth reaction takes place because of the linear, ionic structure and relatively low molecular weight (MW = 70,000), and (2) they are capable of forming micelles owing to the hydrophilic sulfonate and hydrophobic benzene ring, which can be used for templates of nanostructures [16]. The PSSS molecules on the surface of AgNWs are easily removed by simply exchanging the media with PSSS-free water, which

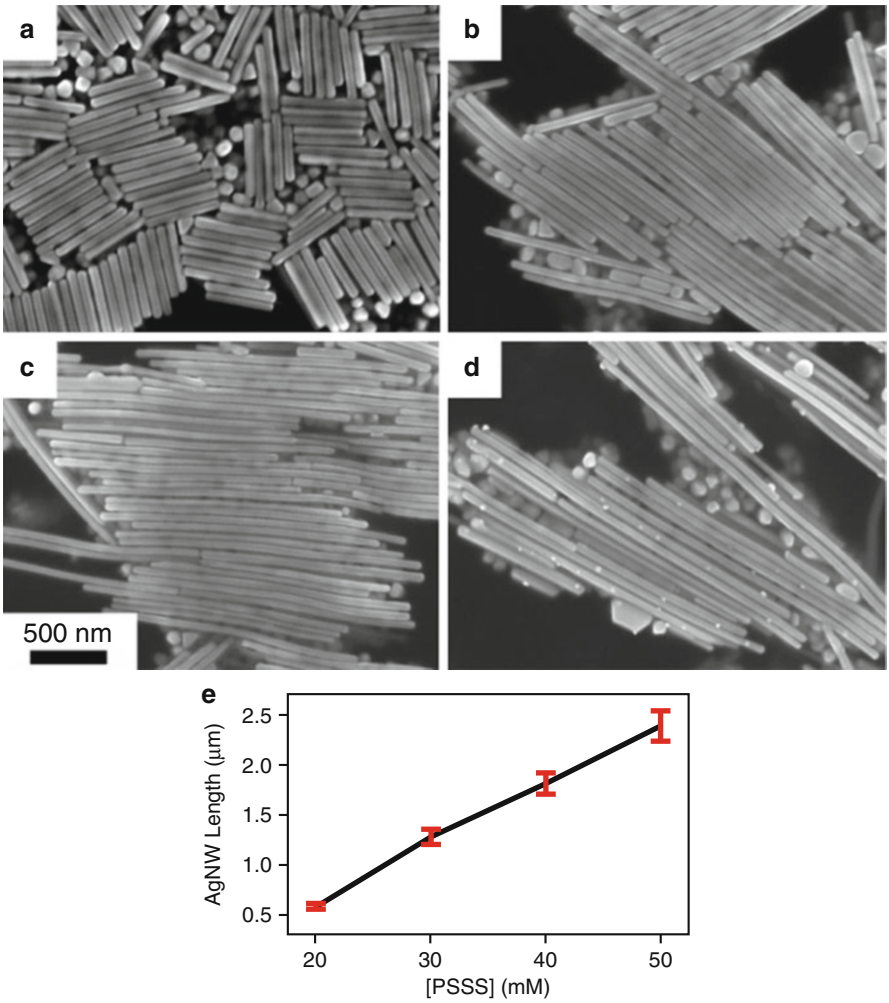

Fig. 7.6 AgNWs synthesized with (**a**) 20 mM, (**b**) 30 mM, (**c**) 40 mM, and (**d**) 50 mM of PSSS. (**e**) The linear correlation between the length of AgNWs and PSSS. Note that the length distribution of AgNWs of each length is almost negligible (Reprinted with permission from Han and Lee [39]. Copyright 2012, American Chemical Society)

enables the effective synthesis of DNA-AgNW conjugates (DNA-AgNWs) containing biochemically functional DNA sequences. Importantly, the length of the DNA-AgNWs can be precisely and accurately controlled from 0.5 to 2.5 μm with an extremely narrow length distribution, which would result in significantly improved and regulated properties of the DNA-AgNWs for quantitative analysis of given targets. Unlike the conventional AgNW synthesis, this method employs very mild conditions such as room temperature and aqueous media without using any organic solvent.

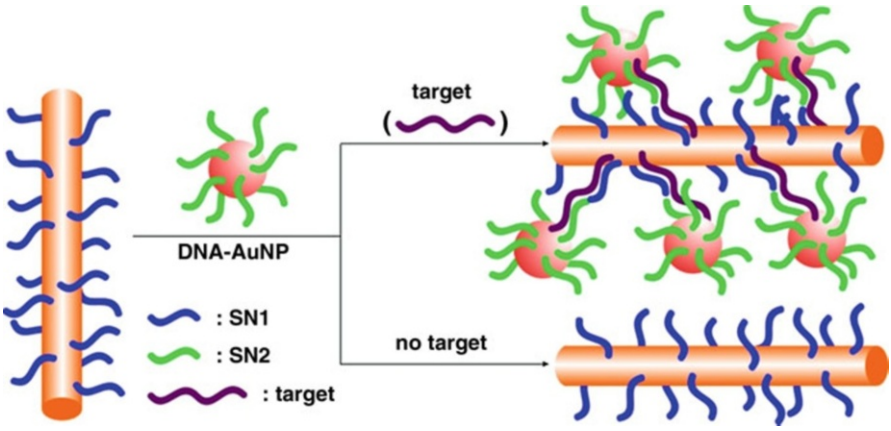

Fig. 7.7 A scheme depicting the detection of DNA targets using DNA-AgNW probes and DNA-AuNP probes, each conjugated with two complementary sequences (SN1 and SN2), respectively (Reprinted with permission from Han and Lee [39]. Copyright 2012, American Chemical Society)

The surface functionalization and assembly properties of AgNWs are particularly important for biodiagnostic applications based upon their controlled length and uniformity. A DNA detection system can be designed such that the DNA-AgNW conjugates (DNA-AgNWs) and DNA-AuNP conjugates (DNA-AuNPs) are complementary to each half of the target sequence (Fig. 7.7). In the presence of the target, the DNAAuNP probes are supposed to hybridize onto the DNA-AgNW probes, whose quantity would be proportional to the target concentration and could be analyzed by simply counting the particles on the nanowires in the SEM images. Alternatively, the extinction at 525 nm in the UV-vis spectrum of the DNA-AuNPs can be obtained after their [salt]-induced dehybridization [40]. In fact, PVP molecules on the conventional PVP-based AgNWs were reported to remain still on the nanowire surface even when exposed to excess thiol chemicals for displacement, often leading to incomplete and inhomogeneous conjugation with thiol functionalities [41]. In contrast, however, the PSSS-based AgNWs have demonstrated high coverage with thiol-DNA sequences, proven by the sharp melting profile of hybridized DNA-AgNW and DNA-AuNP assemblies. Subsequently, solutions containing a series of target concentrations were each combined with a mixture solution containing DNA-AgNW probes and DNA-AuNP probes (finally, [DNA-AuNP] = 10 nM, [NaCl] = 1 M). The mixtures were allowed to hybridize and were observed by SEM (Fig. 7.8). Significantly, in the absence of target, only a few AuNPs (<2) per AgNW were observed on average, indicating extremely low nonspecific binding between the two probes even at very high [NaCl]. As the target concentration increased, however, the number of AuNPs per AgNW distinctively increased, demonstrating a highly quantitative nature of this detection system because of the accurately controlled length and diameter of the monodisperse AgNWs. Alternatively, the DNA-AuNPs were released from the DNA-AgNWs by the addition of buffer without salt ([salt]-induced dehybridization), obtained

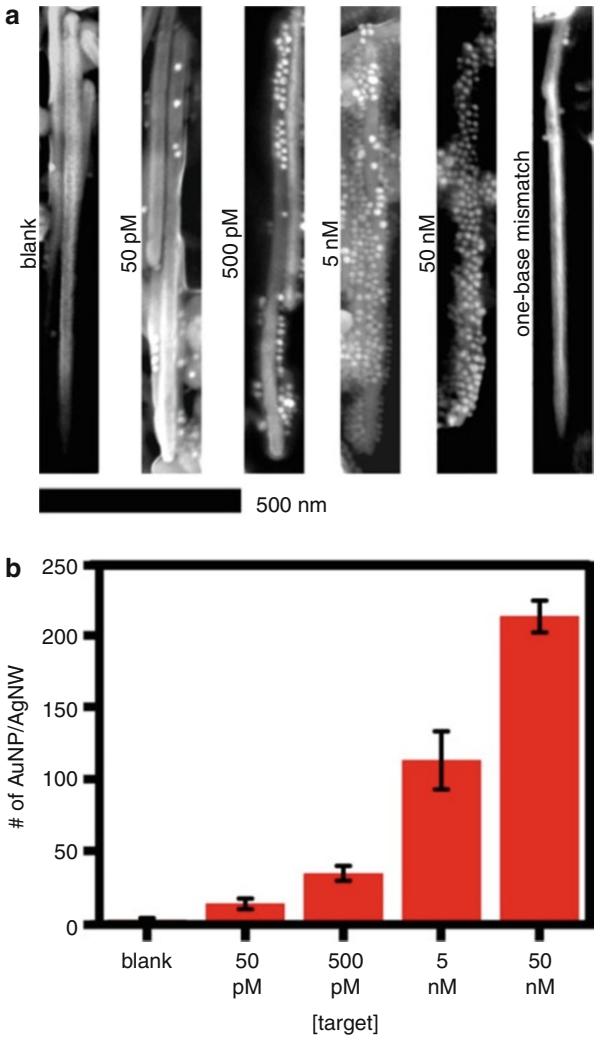

Fig. 7.8 (**a**) SEM images of DNA-AgNW probes hybridized with DNA-AuNP probes and target DNA of various concentrations. (**b**) A graph showing the number of DNA-AuNPs per DNA-AgNW as a function of the target DNA concentration (Reprinted with permission from Han and Lee [39]. Copyright 2012, American Chemical Society)

their UV-vis spectra, and plotted their extinction at 525 nm as a function of the target concentration (Fig. 7.8). The limits of detections in both cases were determined to be 50 pM under the conditions studied, which can be further improved by increasing the [NaCl] or [DNA-AuNP]. This system can also selectively and efficiently discriminate a one-base mismatch target.

5.4.4 Silver Nanocubes

Among nonspherical silver nanostructures, silver nanocubes (AgNCs) are particularly attractive from a structural point of view, because they have an isotropic structure analogous to spherical nanoparticles but contain only six flat surfaces without any curvature. The unique optical properties of AgNCs based upon surface plasmon

resonance (SPR) are more intense than AuNPs of the same size, which would provide a better opportunity to design their optical application schemes. Importantly, considering that the curvature of spherical nanoparticles plays significant roles in the cooperative disassembly properties of their DNA conjugates, the synthesis and reversible assembly of DNA-silver nanocube conjugates would be a very interesting topic to investigate in the context of DNA-mediated assembly of nanomaterials.

Polyvalent DNA-silver nanocube conjugates (DNA-AgNCs) and their reversible assembly properties are highly shape dependent and efficiently controlled by various chemical parameters. The distance-dependent optical properties of DNA-AgNCs based upon their SPR are taken advantage of for the colorimetric detection of DNA targets with a distinctive yellow-to-pink color change that is distinguished from conventional DNA-AuNP probes (Fig. 7.9). These DNA-AgNCs are also used for investigating their quantitative aspect and potential for diagnostic applications to detect target DNA strands (Fig. 7.10). A pair of DNA-AgNC probes were synthesized, each of which is conjugated with DNA sequences that are complementary to each half of the target DNA, respectively. The probes were combined with the DNA target whose concentration varied from 1 to 100 nM and allowed to hybridize to form large macroscopic assemblies. The gradual shift of the melting transitions obtained from the assemblies was observed, which become sharper as the target concentration increases. The corresponding T_ms are analyzed and plotted as a function of the target concentration, which clearly exhibits linearity up to 10 nM of the target and subsequently a plateau from 25 to 100 nM. The limit of detection is evaluated to be 1 nM, which is comparable to or better than those of other colorimetric DNA detection systems based upon only the DNA-nanoparticle conjugates without any enzymatic or chemical amplification. During the hybridization and melting process, the corresponding concurrent color changes from yellow to pale pink and back to yellow (Fig. 7.10) were also observed, which demonstrate the capability of the assay to visualize the result to the naked eye without any complicated instruments. Importantly, the detection system can also distinguish a single-base mismatched target from the target with a 40% larger difference in T_m ($T_m = \sim 44\ ^\circ C$, $\Delta T_m > 7\ ^\circ C$) than that of the conventional DNA-AuNP clusters or DNA-AgNPRs using the same sequences (typically the difference in Tm caused by a single-base mismatch target in the conventional systems is $\sim 5\ ^\circ C$).

6 Conclusions and Future Perspective

Nanotechnology is still in its infancy as far as bio-detection systems are concerned. The majority of work in this area has centered on proof-of-concept studies, which are vital when developing new methodologies. Proof-of-concept work allows scientists to control most of the variables in a system, so that problems can be easily solved in the laboratory. Once the simple systems have been characterized, however, the successful transition to patient or environmental samples must be shown in order for the technology to be broadly applied. This is where the majority of work on detection systems using silver nanomaterials lies. For protein detection,

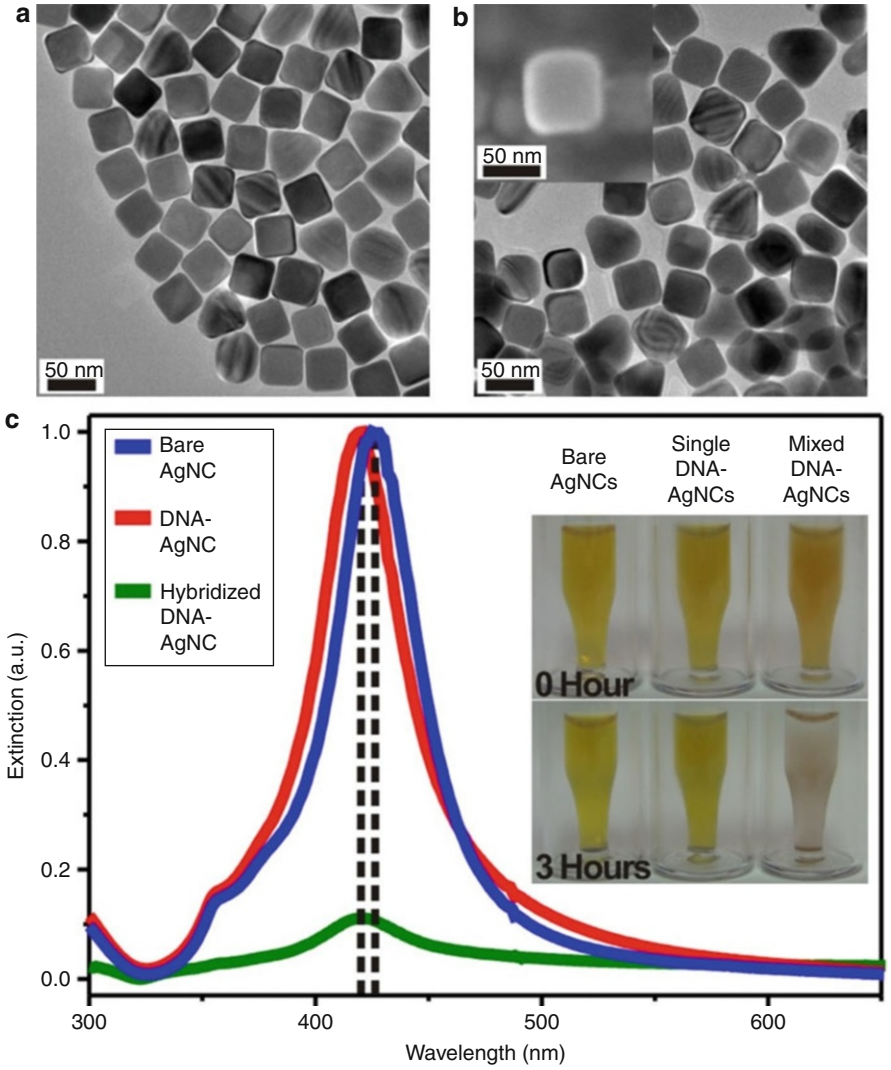

Fig. 7.9 (**a**) Unmodified bare silver nanocubes (AgNCs) and (**b**) DNA-AgNC conjugates. The *cubes* are slightly truncated after the DNA conjugation (**b**, *inset*). (**c**) UV-vis spectra of bare AgNCs, DNA-AgNCs and hybridized DNA-AgNCs. Note that the extinction of the DNA-AgNC conjugates at 420 nm significantly decreases with asymmetric transformation of the spectrum after the hybridization, leading to a color change of DNA-AgNCs from *yellow* to *pale pink* (*inset*) (Reprinted with permission from Park et al. [42]. Copyright 2012, American Chemical Society)

researchers are interested in looking at varying protein levels in the blood of cancer patients who are in remission and monitor relapses. As an example, it is projected that the bio-barcode assay and modifications on it will redefine several aspects of modern biodiagnostics for many types of cancer, heart disease, HIV, and

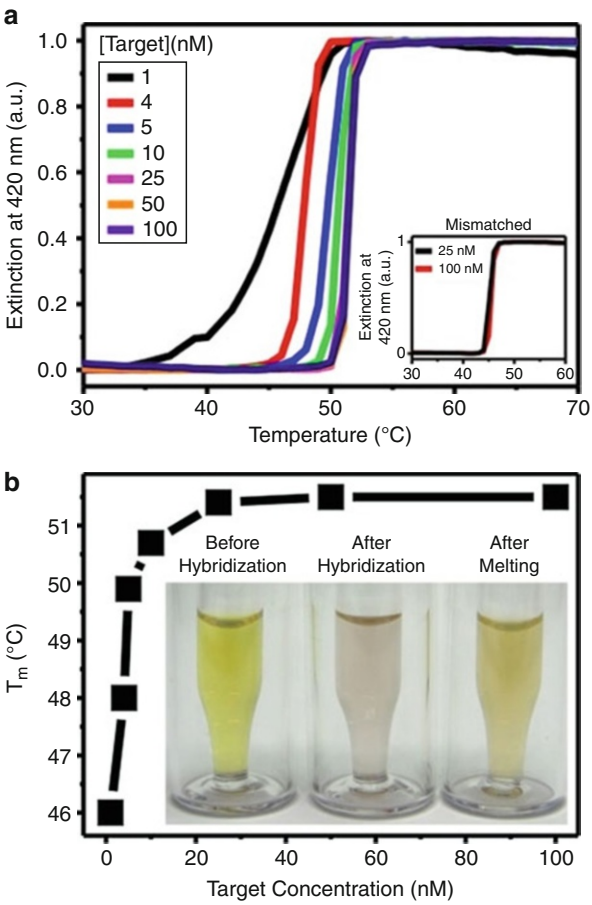

Fig. 7.10 (**a**) Melting transitions of DNA-AgNCs hybridized with various concentrations of *Target* (1, 4, 5, 10, 25, 50, and 100 nM) and *Mismatched* (25 and 100 nM, *inset*). (**b**) T_ms plotted as a function of the target concentration, and the color changes of the DNA-AgNCs before hybridization, after hybridization, and after melting (*inset*) (Reprinted with permission from Park et al. [42]. Copyright 2012, American Chemical Society)

neurodegenerative diseases such as Alzheimer's disease and Parkinson's disease. As for nucleic acid detection, the next big step is to prove that the detection systems can work with genomic DNA from bacteria and higher mammals, along with RNA. Though the majority of work with silver nanomaterials is interested in practical applications, fundamental investigations are still very important. In addition, there will no doubt be new and innovative uses for the silver nanomaterial systems.

Today, with the advance of new nanofabrication techniques, metal-based structures – either simple component or mixtures of multiple components – with better enhanced detection capabilities are emerging. Yet, even if these goals are achieved, the silver nanostructure–based diagnostic techniques may often still be impractical, generally because the environment in which the detection is carried out can also cause problems. For example, in the detection of viruses and/or bacteria, systems were tested using only purified viruses or bacteria, whereas in a practical diagnostic test, the detection of a specimen or analyte must overcome

often-complex biological matrices that affect the thresholds of both sensitivity and specificity. Only the tip of the iceberg has been scraped with regard to the synthetic mechanism of various silver nanomaterials. Much investigation remains to be done before cohesive understandings of the thermodynamics of nucleic acid binding in the context of the nanoparticle system are fully understood. Additionally, comprehensive studies into oligonucleotide loading and stability with silver nanomaterials will be needed if these probes are to be transitioned from a research lab into commercial applications.

References

1. Willets KA, Van Duyne RP (2007) Localized surface Plasmon resonance spectroscopy and sensing. Annu Rev Phys Chem 58:267–297; Annual Reviews: Palo Alto
2. Campion A, Kambhampati P (1998) Surface-enhanced Raman scattering. Chem Soc Rev 27:241–250
3. Lombardi JR, Birke RL (2008) A unified approach to surface-enhanced Raman spectroscopy. J Phys Chem C 112:5605–5617
4. Lee J-S, Lytton-Jean AKR, Hurst SJ, Mirkin CA (2007) Silver nanoparticle-oligonucleotide conjugates based on DNA with triple cyclic disulfide moieties. Nano Lett 7:2112–2115
5. Thompson DG, Enright A, Faulds K, Smith WE, Graham D (2008) Ultrasensitive DNA detection using oligonucleotide-silver nanoparticle conjugates. Anal Chem 80:2805–2810
6. Tokareva I, Hutter E (2004) Hybridization of oligonucleotide-modified silver and gold nanoparticles in aqueous dispersions and on gold films. J Am Chem Soc 126:15784–15789
7. Vidal BC, Deivaraj TC, Yang J, Too H-P, Chow G-M, Gan LM, Lee JY (2005) Stability and hybridization-driven aggregation of silver nanoparticle-oligonucleotide conjugates. New J Chem 29:812–816
8. Cao Y, Jin R, Mirkin CA (2001) DNA-modified core-shell Ag/Au nanoparticles. J Am Chem Soc 123:7961–7962
9. Yin Y, Li Z-Y, Zhong Z, Gates B, Xia Y, Venkateswaran S (2002) Synthesis and characterization of stable aqueous dispersions of silver nanoparticles through the Tollens process. J Mater Chem 12:522–527
10. Liu S, Zhang Z, Han M (2005) Gram-scale synthesis and biofunctionalization of silica-coated silver nanoparticles for fast colorimetric DNA detection. Anal Chem 77:2595–2600
11. Quaroni L, Chumanov G (1999) Preparation of polymer-coated functionalized silver nanoparticles. J Am Chem Soc 121:10642–10643
12. Chen Y, Aveyard J, Wilson R (2004) Gold and silver nanoparticles functionalized with kown numbers of oligonucleotides per particle for DNA detection. Chem Commun 2804–2805
13. Jin R, Cao YC, Hao E, Metraux GS, Schatz GC, Mirkin CA (2003) Controlling anisotropic nanoparticle growth through plasmon excitation. Nature 425:487–490
14. Jin R, Cao Y, Mirkin CA, Kelly KL, Schatz GC, Zheng JG (2001) Photoinduced conversion of silver nanospheres to nanoprisms. Science 294:1901–1903
15. Metraux GS, Mirkin CA (2005) Rapid thermal synthesis of silver nanoprisms with chemically tailorable thickness. Adv Mater 17:412–415
16. Aherne D, Ledwith DM, Gara M, Kelly JM (2008) Optical properties and growth aspects of silver nanoprisms produced by a highly reproducible and rapid synthesis at room temperature. Adv Funct Mat 18:2005–2016
17. Chen Y, Munechika K, Ginger DS (2007) Dependence of fluorescence intensity on the spectral overlap between fluorophores and plasmon resonant single silver nanoparticles. Nano Lett 7:690–696

18. Sherry LJ, Jin R, Mirkin CA, Schatz GC, Van Dyune RP (2006) Localized surface plasmon resonance spectroscopy of single silver triangular nanoprisms. Nano Lett 6:2060–2065
19. Metraux GS, Cao YC, Jin R, Mirkin CA (2003) Triangular nanoframes made of gold and silver. Nano Lett 3:519–522
20. Mirkin CA, Letsinger RL, Mucic RC, Storhoff JJ (1996) A DNA-based method for rationally assembling nanoparticles into macroscopic materials. Nature 382:607–609
21. Jin R, Wu G, Li Z, Mirkin CA, Schatz GC (2003) What controls the melting properties of DNA-linked gold nanoparticle assemblies? J Am Chem Soc 125:1643–1654
22. Kim JY, Lee JS (2010) Synthesis and thermodynamically controlled anisotropic assembly of DNA-silver nanoprism conjugates for diagnostic applications. Chem Mater 22:6684–6691
23. Glotzer SC, Solomon MJ (2007) Anisotropy of building blocks and their assembly into complex structures. Nat Mater 6:557–562
24. Grzelczak M, Vermant J, Furst EM, Liz-Marzan LM (2010) Directed self-assembly of nanoparticles. ACS Nano 4:3591–3605
25. Baker JL, Widmer-Copper A, Toney MF, Geissler PL, Alivisatos AP (2010) Device-scale perpendicular alignment of colloidal nanorods. Nano Lett 10:195–201
26. Jones MR, Macfarlane RJ, Lee B, Zhang J, Young KL, Senesi AJ, Senesi AJ, Mirkin CA (2010) DNA-nanoparticle superlattices formed from anisotropic building blocks. Nat Mater 9:913–917
27. Kim J-Y, Lee J-S (2009) Synthesis and thermally reversible assembly of DNA-gold nanoparticle cluster conjugates. Nano Lett 9:4564–4569
28. Wiley B, Sun Y, Xia Y (2007) Synthesis of silver nanostructures with controlled shapes and properties. Acc Chem Res 40:1067–1076
29. Sun YG (2010) Silver nanowires – unique templates for functional nanostructures. Nanoscale 2:1626–1642
30. Murphy CJ, Gole AM, Hunyadi SE, Orendorff CJ (2006) One-dimensional colloidal gold and silver nanostructures. Inorg Chem 45:7544–7554
31. Zhang J, Langille MR, Mirkin CA (2011) Synthesis of silver nanorods by low energy excitation of spherical plasmonic seeds. Nano Lett 11:2495–2498
32. Chang S, Chen K, Hua Q, Ma Y, Huang W (2011) Evidence for the growth mechanisms of silver nanocubes and nanowires. J Phys Chem C 115:7979–7986
33. Kim TY, Kim WJ, Hong SH, Kim JE, Suh KS (2009) Ionic-liquid-assisted formation of silver nanowires. Angew Chem Int Ed 48:3806–3809
34. Sun YG, Gates B, Mayers B, Xia YN (2002) Crystalline silver nanowires by soft solution processing. Nano Lett 2:165–168
35. Sun YG, Xia YN (2002) Large-scale synthesis of uniform silver nanowires through a soft, self-seeding, polyol process. Adv Mater 14:833–837
36. Caswell KK, Bender CM, Murphy CJ (2003) Seedless, surfactantless wet chemical synthesis of silver nanowires. Nano Lett 3:667–669
37. Hu JQ, Chen Q, Xie ZX, Han GB, Wang RH, Ren B, Zhang Y, Yang ZL, Tian ZQ (2004) A simple and effective route for the synthesis of crystalline silver nanorods and nanowires. Adv Funct Mater 14:183–189
38. Jana NR, Gearheart L, Murphy CJ (2001) Wet chemical synthesis of silver nanorods and nanowires of controllable aspect ratio. Chem Commun 617–618
39. Han SH, Lee J-S (2012) Synthesis of length-controlled polyvalent silver nanowire-DNA conjugates for sensitive and selective detection of DNA targets. Langmuir 28:828–832
40. Oh J-H, Lee J-S (2010) Salt concentration-induced dehybridisation of DNA-gold nanoparticle conjugate assemblies for diagnostic applications. Chem Commun 46:6382–6384
41. Andrew P, Ilie A (2007) Functionalised silver nanowire structures. J Phys: Conf Ser 61:36–40
42. Park H-G, Joo JH, Kim H-G, Lee J-S (2012) Shape-dependent reversible assembly properties of polyvalent DNA silver nanocube conjugates. J Phys Chem C 116:2278–2284

Optical Properties of Oxide Films Dispersed with Nanometal Particles

8

Moriaki Wakaki and Eisuke Yokoyama

Contents

1 Definition of the Topic

Solid materials reveal some special behaviors like quantum effects in semiconductors and surface-enhanced effects in metals by decreasing their diameters. In this review, the enhancement of the optical response due to the electric field of the light is reviewed as the recent active field of plasmonics. The production methods of various metal nanoparticles are summarized for the bared state and for the embedded state within the dielectric medium. The features of the optical properties of

M. Wakaki (✉) • E. Yokoyama
Department of Optical and Imaging Science & Technology, School of Engineering, Tokai University, Hiratsuka, Kanagawa, Japan

Challa S.S.R. Kumar (ed.), *UV-VIS and Photoluminescence Spectroscopy for Nanomaterials Characterization*, DOI 10.1007/978-3-642-27594-4_8,

these nanoparticles are reviewed, and typical formula to reproduce the absorption spectra due to the surface plasmon resonance is summarized. Several applications of these systems are shortly introduced.

2 Overview

The optical responses of metal nanoparticles are different to those of the conventional bulk metals and are actively studied as the field of plasmonics. The interesting optical behavior comes from the enhanced surface effect and called surface-enhanced plasmon resonance (SPR). The basic researches and application studies are introduced. The synthesis methods for the bared nanoparticles and the composite films dispersed with metal nanoparticles are briefly introduced. Basic optical theories describing the optical properties of metal nanoparticles at both bared and embedded states are reviewed. The detailed optical study of the composition dependence of the silver nanoparticles within a ZrO_2 matrix is introduced, and the applicability of the Maxwell–Garnett and Bruggeman theories is discussed. Finally, recent application researches of metal nanoparticles are briefly summarized.

3 Introduction

A metal nanoparticle is defined as the particle composed of a limited number of metal atoms with the size of nm order ($\sim 10^{-9}$ m). The dimensions of these groups of materials are much larger than those of metal complexes or clusters and smaller than so-called fine particles with the size of micrometer order ($\sim 10^{-6}$ μm) (Fig. 8.1). As an example of gold nanoparticle, the minimum one is consisted of 13 atoms and the diameter is 0.86 nm. The particle becomes larger as the number of the atoms increases. The particles with the diameter of 1.44 nm, 2.02 nm, and 2.6 nm contain the number of 55, 147, and 309 atoms, respectively.

The background of the researches for these nanoparticles in the early stage is summarized as follows:

1. These materials belong to the interdisciplinary region between bulk materials, and atoms/molecules and have been few chances to be the target of research.
2. Means to observe objects with these dimensions like TEM were not popular.
3. It was difficult to obtain a large quantity of nanoparticles with a same size because of the lack of needs for applications.

As a result, few reports have been submitted by several physicists and researchers of a colloid interface. Recently, researches on metal nanoparticles have expanded rapidly as the basic materials for the nanotechnology in accordance with the establishment of the synthesis method with simple and reproducible ways using a wet process and also with the progress of the observation techniques possible to characterize down to nanoscale order using high-resolution TEM, SEM, and surface probe microscopes like AFM.

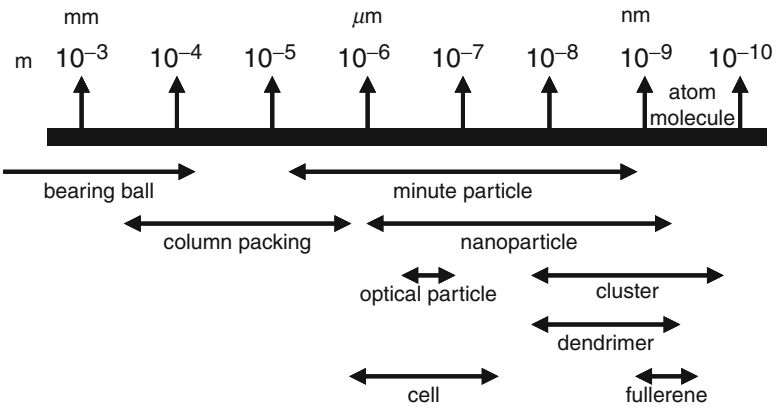

Fig. 8.1 Classification of materials according to particle size

The nanotechnology is considered as the innovative technology to bring about an industrial revolution in this era and is actively studied through the world. Especially, metal nanoparticles attract interests as the basic materials in the nanotechnology. The metal nanoparticles have many features, and the most of them are related with a surface or an interface. The surface area (total surface area) of the particles per unit weight becomes larger as the size of the particle becomes smaller. For instance, the specific surface area of the particle with the diameter of 5 nm is two million times larger compared with that with the diameter of 1 cm. A single atom has 100 % of surface area. Surface positions are occupied by 12 atoms (92 % of total atoms) in the nanoparticle consisted of 13 atoms and occupied by 42 atoms (76 %) in the nanoparticle consisted of 55 atoms.

Light cannot penetrate into a bulk metal which has been mainly used as a mirror. The resonance phenomenon (surface plasmon resonance: SPR) between the electric field of light and the surface plasmon mode of the metal has been found out by reducing metals to the nanoscale size. This effect has been known well as the origin of the color in stained glasses. As the interest to the nanophotonics becomes stronger, this effect is strongly correlated between electrons and light-attracted eyes of researchers. The optical technology utilizing this effect is called plasmonics like electronics and photonics and has the following features which cannot be compared with conventional optical technologies:

(a) Confinement of light within the nanoscale region beyond the diffraction limit
(b) Enhancement of the local electric field on the vicinity of the object inducing a SPR
(c) High sensibility of the resonance condition to the state of the surface of the metal nanoparticle

Applications in the fields of nonlinear optics and near-field optics have been developed according to these effects, and the researches on the second harmonic generation (SHG), optical switching, optical logic circuits, etc., are actively carried out. Especially, the noble metals like gold and silver have the resonance wavelength

in the visible region, and various applications for optical devices can be expected. A gold nanoparticle with the diameter of around 20 nm exhibits a red color, and it becomes a dark brownish color by reducing the diameter further [1, 2]. The origin of the red color ascribed to the absorption caused by the SPR and the effect has been utilized for the red color in the stained glass. Faraday first succeeded to obtain the red-colored gold nanoparticles in the dispersed colloidal system 150 years ago by controlled adding of yellow phosphor to the tetrachloroaurate [3, 4]. He also found out that such gold sol becomes stabilized by adding a protective colloid like a gelatin. Turkevich et al. observed directly these gold nanoparticles in 1951 using a SEM after 50 years of Faraday's works [5]. They also tried to make clear the generation mechanism of nanoparticles by preparing various sizes of gold nanoparticles [6]. Further, they succeeded to synthesize alloy nanoparticles like Pt–Au, Pt–Pa, etc., without protective colloids [7]. On the other hand, Nord et al. reported the preparation of nanoparticles with protective polymers like polyvinyl alcohol [8–10].

The nanoparticles which exhibit a plasmon absorption in the visible region are typically gold, silver, copper, and other metal nanoparticles that generally show stronger absorptions in the longer wavelength region giving a brownish color. The features brought by reducing metals to a nanoscale size are not only colors but also catalytic behaviors coming from the extremely large specific surface area [11–13]. Haruta et al. recently discovered the function of gold nanoparticles as an effective catalyst which have been known inactive as a catalyst [14]. Furthermore, it was found that nanoparticles of Pt group work as the catalyst for an effective hydrogenation and also as the catalyst to extract hydrogen from water [15–17].

The review articles on the topics of metal nanoparticles have been issued recently reflecting the active researching field of plasmonics [18–26]. Most of the reviews are discussed about the synthesis and optical behaviors of metal nanoparticles. There are few reviews commented on the composite materials between dielectric materials and metal nanoparticles [27]. In these reviews, the optical behaviors of the composite materials consisting of oxide materials and noble metal nanoparticles are especially reviewed minutely using various mixing models for the effective permittivity of the composite materials.

4 Experimental and Analytical Methodology

4.1 Fabrication Methods of Metal Nanoparticles

Production methods of metal nanoparticles can be divided into two types in a larger sense. One is the top-down method where nanoparticles are obtained by breaking down the bulk metals physically, and the other is the bottom-up method where nanoparticles are synthesized by extracting metal atoms from the precursors of metal salt or metal complex followed by cohesion and growth (Fig. 8.2). It is said generally to get homogeneous nanoparticles is difficult by the former method, and the latter method is often used. Chemical methods to synthesize nanoparticles are summarized on Table 8.1.

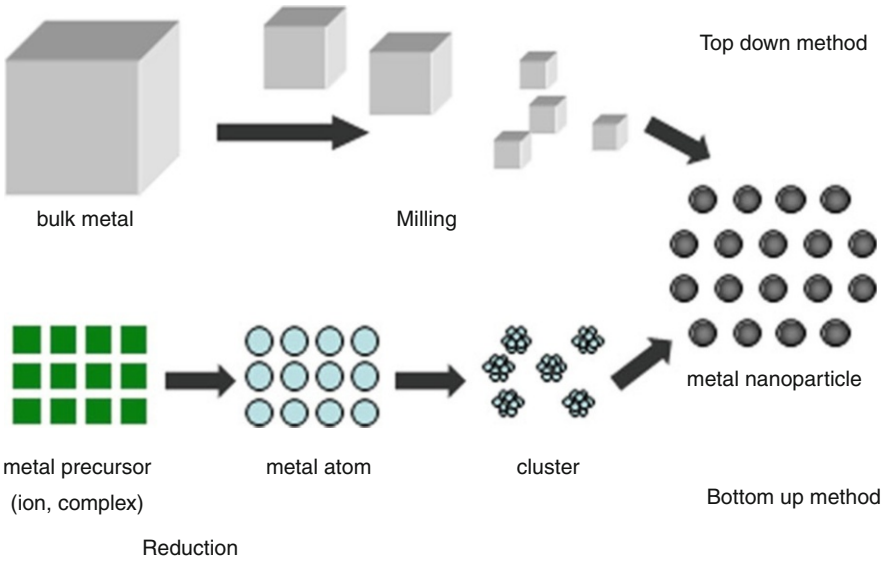

Fig. 8.2 Basic principles to prepare nanoparticles with physical and chemical methods

Table 8.1 Classification of synthesis methods of nanoparticles by chemical process

Reduction	Applicable metals	Capping
Alcohol	Noble metals	Water-soluble polymer
Polyol	Transition metals, alloy	Polymer
Amino alcohol	Gold, silver	Polymer
Diborane	Gold, palladium, alloy	Phosphine ligand
Hydrogen	Noble metals, transition metals	Amphiphilic molecule, long-chain amine
Citric acidAscorbic acid	Gold, silver, palladium, platinum	Polymer, metal ligand
Hydrazine	Noble metals, copper	Amphiphilic molecule, polymer
Borohydride	Noble metals, transition metals	Metal ligand, amphiphilic molecule
Light	Noble metals	Amphiphilic molecule, polymer
Gamma ray	Noble metals, transition metals	Amphiphilic molecule, polymer
Supersonic wave	Noble metals	Polymer
Laser	Noble metals	Amphiphilic molecule
Thermal decomposition	Gold, silver	Amphiphilic molecule, metal ligand
Electrochemical	Metals	Amphiphilic molecule
Supercritical fluid	Metals	Polymer

In the wet method, metal atoms (0 valence) are obtained by introducing the precursors like metal ions or metal complexes into the solution followed by the thermal decomposition of metal complex (0 valence) or the reduction of metal ions. Metals with 0 valence are generally derived from the complexes by a thermal

decomposition [28]. On the other hand, the reagents like alcohol [29–31], polyol [32–35], aldehyde, citric acid and its salt, ascorbic acid and its salt, hydrazine [36], hydrogen [37, 38], diborane [39], boron hydride, alkylammonium salt [40–43], alcohol amines, phosphor, etc., are used as the agents to reduce metal ions. The physical energy like γ-ray [44–47], X-ray, ultraviolet and visible light [48–50], heat, ultrasonic wave, etc., are also used (Table 8.1).

4.2 Fabrication Methods of Dielectric Films Dispersed with Metal Nanoparticles

The typical methods to synthesize composite materials of metal nanoparticles and dielectric materials as a matrix are a melt and quench method [51–53], a sputtering method [54–56], an ion implantation method [57–59], etc.

The melt and quench method has been known well since olden time and applied to stained glasses according to their brilliant purple-red colors. The method is still used widely for color filters. In the method, the mixtures of SiO_2, Al_2O_3, and Na_2O together with the trace of metal (Au, Ag, or Cu) are put into a Pt crucible and melted at over 1,000 °C. High-quality glasses with less content of impurities and small departure from the stoichiometry are synthesized. After melting, the melt is poured among the twin rollers and quenched to the glassy state. After the process, metal ions melted within the glass are condensed to form aggregates of metal nanoparticles by thermal annealing at the temperature around the softening temperature of the glass to produce composite materials. The size and the density of the metal nanoparticles strongly depend on the composition of the glass, the temperature, and the time of thermal annealing. Large homogeneous glasses dispersed with metal nanoparticles are possible to fabricate at a low cost. However, there are several problems that the maximum content of the metal nanoparticles is limited below the solubility limit of about 0.1 vol.%, and it is also difficult to prepare the glass dispersed with high density of metal elements because metal elements are evaporated out during the high temperature process.

The sol–gel method is well known as the technique to synthesize glasses and ceramics by a hydrolysis reaction of a metal alchoxide solution [60, 61]. By using this technique, glass fibers, antireflection films, and contact lenses hybridized with a polymer are fabricated industrially. It is possible to synthesize bulk, fiber, and thin-film materials by this method. Composite materials dispersed with metal or semiconductor nanoparticles are possible to fabricate by the sol–gel method.

The fabrication process of SiO_2 films dispersed with gold nanoparticles is shortly explained as a typical example. TEOS and metal salt as source materials, ethanol and water as solvents, and acid as a catalyst are mixed to form a sol solution. By using the sol solution, a gel-like thin film is coated on a substrate by the dip or the spin-coating method. Metal atoms dissolved within the glass are precipitated to form metal nanoparticles by heating the gel film. The thickness of the film is controlled by the withdrawal speed of the substrate during the dip coating, and

the size of the metal nanoparticle is controlled by the annealing temperature. Both bulk-like and film-like glasses dispersed with metal nanoparticles are possible to fabricate with the relatively simple system.

An ion implantation technique is mainly used for the doping of impurities or the surface modification of solids in the semiconductor industry. Colloidal metal nanoparticles are possible to be precipitated within a glass by a higher doping than a conventional doping density. By using this method, it is possible to disperse nanoparticles into various matrix materials and control the size of nanoparticles by the thermal annealing after the implantation. However, strains induced by the damage are remained in the substrate due to the high doping ($\sim 10^{17}$dose), and very expensive systems are required.

The sputtering method is widely used for many fields as a thin-film coating technique on various types of substrates. Especially, insulators and materials with high melting temperatures are easily deposited by using a high-frequency sputtering. By the method, the dielectric matrix films dispersed with metal nanoparticles at high density are possible to deposit.

As other methods, film depositions by vacuum evaporation using resistive heating, by laser ablation, etc., have been reported.

4.3 Basic Theory on the Optical Properties of Nanoparticles

The optical responses of materials are described by using dielectric functions. The dielectric functions depend on the frequency of light and take specific values depending on the materials. The major particles to respond in the visible wavelength region are electrons. In view of this response, the related materials are classified into insulators or conductors which are featured by the motions of bound or free electrons, respectively. The optical responses of these materials are described using Maxwell's equations.

The size and shape of the material strongly affect the optical response. Such effects are reflected in the boundary conditions on solving Maxwell's equations. However, the quantum effects appear by reducing the size of the material to a nanoscale, and the dielectric function varies largely due to the discrete electronic states. Furthermore, the surface effects are enhanced by reducing the volume and peculiar optical responses which are not observed when bulk materials appear.

4.3.1 Drude Model for Free Electrons in Metal

The Drude model assumes that the electrons with an effective mass m* move under the electric field of light E receiving a friction force with the average scattering time of $\tau(=1/\gamma)$ as shown in Fig. 8.3. The equation of motion for a free electron is given as

$$m^*\ddot{r} + m^*\gamma\dot{r} = -e\boldsymbol{E} \tag{8.1}$$

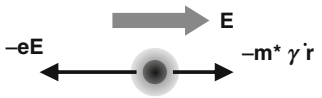

Fig. 8.3 Drude model illustrating the optical response of the free electron in metal

where $\boldsymbol{r}$ and $-e$ are the displacement and charge of the electron. This equation is solved as follows assuming an incident light with the electric field $\boldsymbol{E} = \boldsymbol{E_0}e^{-i\omega t}$ of the angular frequency ω:

$$\boldsymbol{r} = \frac{e\boldsymbol{E}}{m^*\omega(\omega + i\gamma)} \tag{8.2}$$

The dipole moment of an electron is defined as $-e\boldsymbol{r}$, and the dipole moment per unit volume (polarization P) is given as follows using the number of electrons N per unit volume:

$$\boldsymbol{P} = -eN\boldsymbol{r} \tag{8.3}$$

As a result, the dielectric function $\varepsilon(\omega)$ is given as

$$\varepsilon(\omega) = 1 - \frac{{\omega_p}^2}{\omega(\omega + i\gamma)} \tag{8.4}$$

where ω_p is the plasma frequency defined as

$$\omega_p = \sqrt{\frac{4\pi Ne^2}{m^*}} \tag{8.5}$$

In the visible region, the average scattering time τ is longer enough than the period of the light frequency 2π/ω. As a result, the dielectric function is approximated as

$$\varepsilon(\omega) = 1 - \frac{{\omega_p}^2}{\omega^2} \tag{8.6}$$

and the behavior is shown in Fig. 8.4. As shown in the figure, ε takes negative values below the plasma frequency. The relation among the permittivity, refractive index, and reflectivity are given as

$$\tilde{n}(\omega) = n(\omega) + i\kappa(\omega) = \sqrt{\varepsilon(\omega)} \tag{8.7}$$

$$R(\omega) = \left|\frac{\tilde{n}(\omega) - 1}{\tilde{n}(\omega) + 1}\right|^2 = \left|\frac{n + i\kappa(\omega) - 1}{n + i\kappa(\omega) + 1}\right|^2 \tag{8.8}$$

where $\tilde{n}(\omega), n(\omega)$, and $\kappa(\omega)$ are the complex refractive index, real refractive index, and extinction coefficient, respectively. The complex refractive index $\tilde{n}(\omega)$ becomes

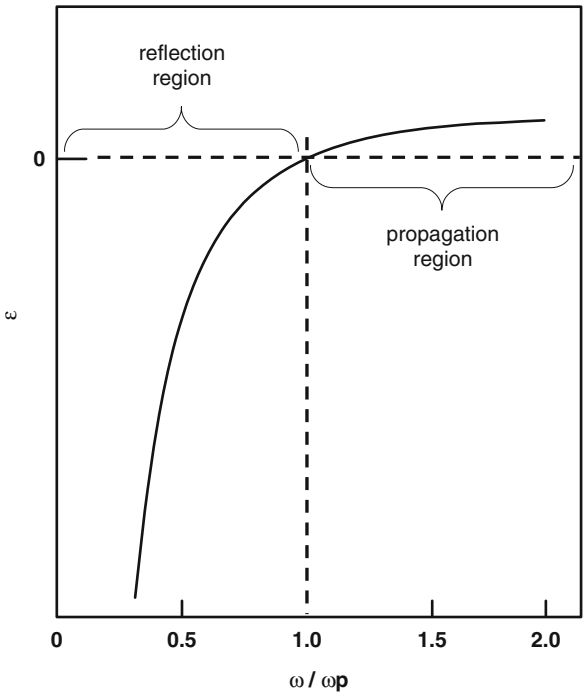

Fig. 8.4 Frequency response of the dielectric function $\varepsilon(\omega)$of free electrons. ω_p is the plasma frequency of the electrons

pure imaginary $i\kappa(\omega)$ in the frequency region where ε takes the negative value. As a result, the electromagnetic wave damps exponentially in the metal, and the reflectivity becomes 1. On the other hand, the refractive index becomes real at the higher frequency than the plasma frequency, and light transmits through the metal. The high reflectivity below the plasma frequency is the origin of the metallic luster, and the color of the metal is closely related with the value of the plasma frequency.

The plasma frequency corresponds to the frequency of the free oscillation mode of the longitudinal wave in a homogeneous metal. The wave transmits as the coupled mode between the polarization of the free electron and the depolarization field induced by the polarization. The restoration force of the oscillation becomes stronger as the density of the free electrons becomes larger. Free electrons within the metal are possible to respond for light at lower frequency than the plasma frequency which gives the high reflectivity of light. However, free electrons cannot respond to light at higher frequency than the plasma frequency, and light can penetrate into the metal.

The real and imaginary parts of the dielectric function are given as follows considering the scattering process of the free electrons:

$$\varepsilon_1(\omega) = 1 - \frac{{\omega_p}^2}{\omega^2 + \gamma^2} \tag{8.9}$$

$$\varepsilon_2(\omega) = \frac{{\omega_p}^2}{\omega^2 + \gamma^2}\frac{\gamma}{\omega} \tag{8.10}$$

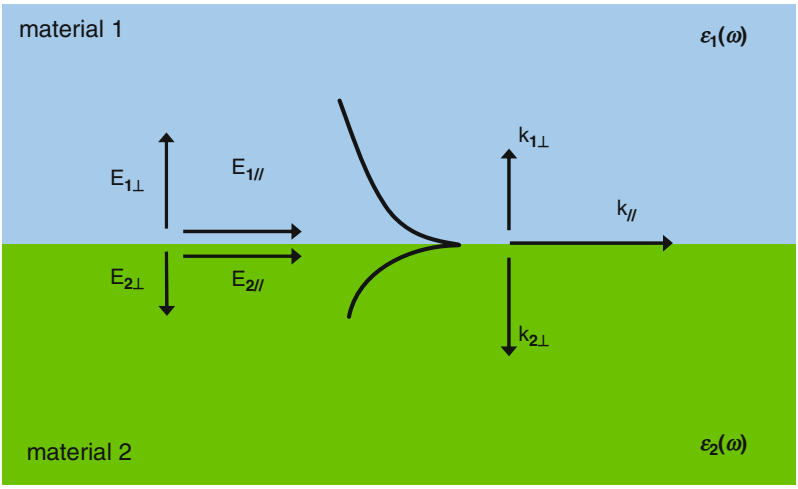

Fig. 8.5 Surface mode traveling along the interface between mediums 1 and 2

4.3.2 Surface Wave Mode

The eigenmodes for the electromagnetic wave existing at the planar interface between two materials with different dielectric functions $\varepsilon_1(\omega)$ and $\varepsilon_2(\omega)$ satisfy following conditions for the electric vector parallel and vertical to the interface as shown in Fig. 8.5:

$$E_{1//} = E_{2//} \tag{8.11}$$

$$\varepsilon_1(\omega)E_{1\perp} = -\varepsilon_2 E_{2\perp} \tag{8.12}$$

By combining these relations with the Maxwell equations, following relation is derived:

$$\frac{k_{1\perp}}{\varepsilon_1(\omega)} + \frac{k_{2\perp}}{\varepsilon_2(\omega)} = 0 \tag{8.13}$$

To satisfy this relation, either dielectric function ε_1 or ε_2 must take a negative value, which implies that there is an exponentially damping mode perpendicular to the interface. In other words, this condition is required to activate the eigenmodes existing at the interface. As mentioned previously, the permittivity of metal takes a negative value below the plasma frequency. By using the conservation of wavenumber at respective material, following relations are derived:

$$k_{//}{}^2 + k_{1\perp}{}^2 = \varepsilon_1 k_0{}^2, \qquad k_{//}{}^2 + k_{2\perp}{}^2 = \varepsilon_2 k_0{}^2 \tag{8.14}$$

$$k_{//}{}^2 = \frac{\varepsilon_1 \varepsilon_2}{\varepsilon_1 + \varepsilon_2} k_0{}^2 \tag{8.15}$$

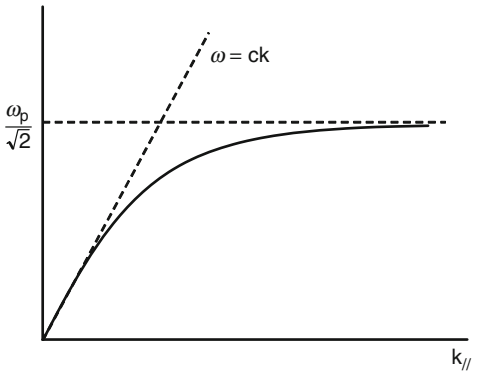

Fig. 8.6 Dispersion relation of surface plasmon

Either ε_1 or ε_2 is negative, and $\varepsilon_1 + \varepsilon_2$ is also requested to be negative to satisfy the equation.

The dispersion relation for the surface plasmon is shown in Fig. 8.6, assuming medium 1 as air and medium 2 as metal and applying the simplified dielectric function $\varepsilon(\omega) = 1 - \omega_p^2/\omega^2$. The surface plasmon mode exists in the region $\omega < \omega_p/\sqrt{2}$, which corresponds to the condition of negative value of $\varepsilon_1 + \varepsilon_2$. The wavenumber of the surface plasmon becomes larger as ω closes to ω_p. The dispersion curve of light in vacuum does not cross the dispersion curve of the surface wave, which means the surface waves cannot be excited by irradiating light upon the metal surface from vacuum. As the excitation method of the surface plasmon, the irradiation of light from the dielectric layer in the three-layer system consisting of the dielectric, metal, and air layers is often used. The wavenumber of light within the dielectric medium becomes larger according to the refractive index of the medium, and the steepness in the dispersion curve becomes smaller to cross the dispersion curve of surface plasmon as illustrated in Fig. 8.7.

4.3.3 Point Dipole

The electric field induced at the distance $\boldsymbol{r}$ by an oscillating point dipole moment $\boldsymbol{p}$ located at the original point is given as

$$\boldsymbol{E}(\boldsymbol{r}) = \left[(\boldsymbol{n} \times \boldsymbol{p}) \times \boldsymbol{p} \frac{k^2}{\boldsymbol{r}} - \{3(\boldsymbol{n} \cdot \boldsymbol{p})\boldsymbol{n} - \boldsymbol{p}\} \frac{ik}{\boldsymbol{r}^2} + \{3(\boldsymbol{n} \cdot \boldsymbol{p})\boldsymbol{n} - \boldsymbol{p}\} \frac{1}{\boldsymbol{r}^3} \right] e^{ikr} \quad (8.16)$$

where $\boldsymbol{n}$ and $\boldsymbol{k}$ are the unit vector toward $\boldsymbol{r}$ direction and wave vector, respectively. The first term corresponds to the field induced by the accelerating movement of the charge and damps slowly as 1/r form the dipole. This component of the radiation field extends to long distance and can be observed by our eyes. The energy distribution (Poynting vector) by this component emitted from the electric dipole moment is shown in Fig. 8.8. The second term called an inductive electric field is induced from the movement of the charge and damps rapidly as $1/r^2$. The third term corresponds to the quasistatic electric field generated from the static charge and damps very rapidly as $1/r^3$ and can be neglected at far field from the point dipole.

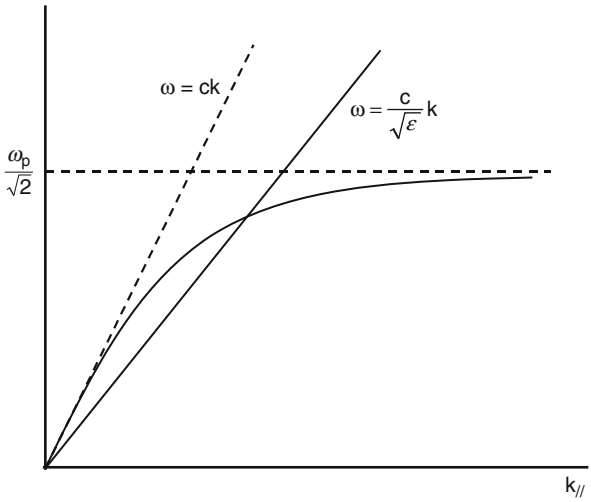

Fig. 8.7 Principle illustrating the excitation method of surface plasmon using dielectric, metal, and air layers by irradiating light from the dielectric medium

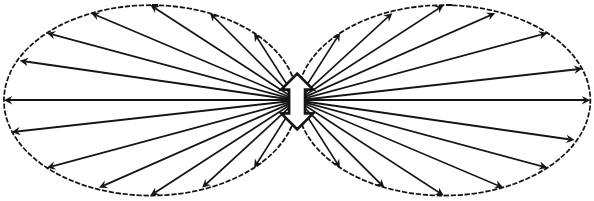

Fig. 8.8 Radiation (Poynting vector) distribution emitted from the oscillating electric dipole moment

The electric field distribution induced by the dipole is illustrated in Fig. 8.9. As seen in the figure, the induced electric field along the dipole moment has the same direction with the dipole moment vector, and the electric field perpendicular to the moment has the reverse direction to the moment, which is the most important factor to treat the interaction between particles and light in the nanoscale region.

4.3.4 Dipole Moment of Nanoparticle

The optical response of the metal particle changes largely depending on the size, shape, and surrounding medium in the frequency region where the dielectric function takes negative values in the lower frequency region than the plasma frequency. Apart from the point dipole model, it is required to consider the model which takes the shape and environment of the particle into consideration to understand such phenomena.

It is possible to apply the response theory to the static field if the quasistatic field approximation may hold. The dielectric polarization occurs for the particle placed in the light field E_0 as shown in Fig. 8.10. The surface charges are induced on the surface of the dielectrics with the charge density of σ given as

$$\sigma = \boldsymbol{n} \bullet \boldsymbol{P} \tag{8.17}$$

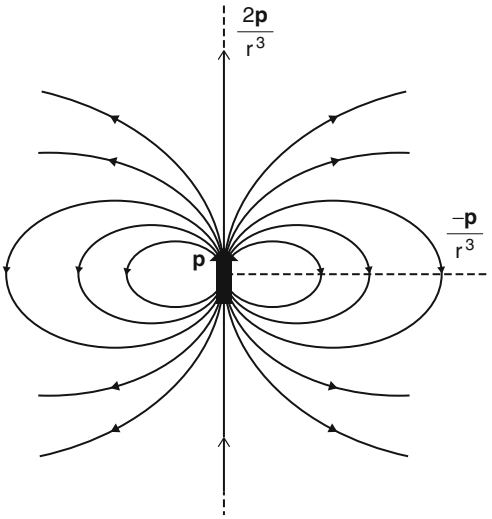

Fig. 8.9 Electric field distribution induced by the static electric dipole

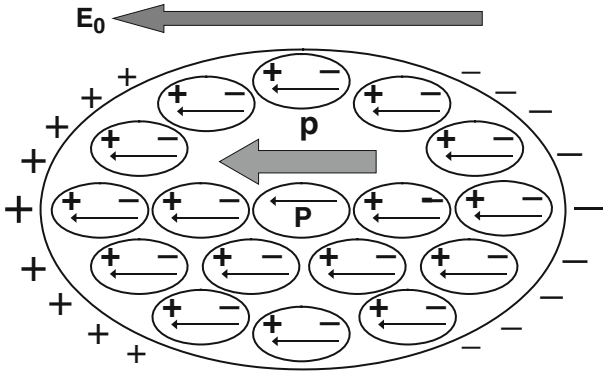

Fig. 8.10 Dipole moment $\boldsymbol{P}$ induced by applying the electric field $\boldsymbol{E_0}$ of light with longer wavelength than the particles

where $\boldsymbol{P}$ and $\boldsymbol{n}$ are the density of the polarized dipole moment and the unit vector perpendicular to the surface, respectively. The surface charges depend on the shape of the particle and surrounding medium and play an essential role in the optical response of the nanoparticle. The internal field $\boldsymbol{E}$ is different from the external field $\boldsymbol{E_0}$ and composed of the summation of the contribution from all dipoles as shown in Fig. 8.11. The summation is proved equal to the electric field $\boldsymbol{E_1}$ induced by the surface charge σ in vacuum, and the electric field $\boldsymbol{E}_1$ is called a depolarization electric field as the direction is reverse to the external field E_0. As a result, the internal field $\boldsymbol{E}$ within a dielectric material polarized homogeneously is given as

$$\boldsymbol{E} = \boldsymbol{E_0} + \boldsymbol{E_1} \tag{8.18}$$

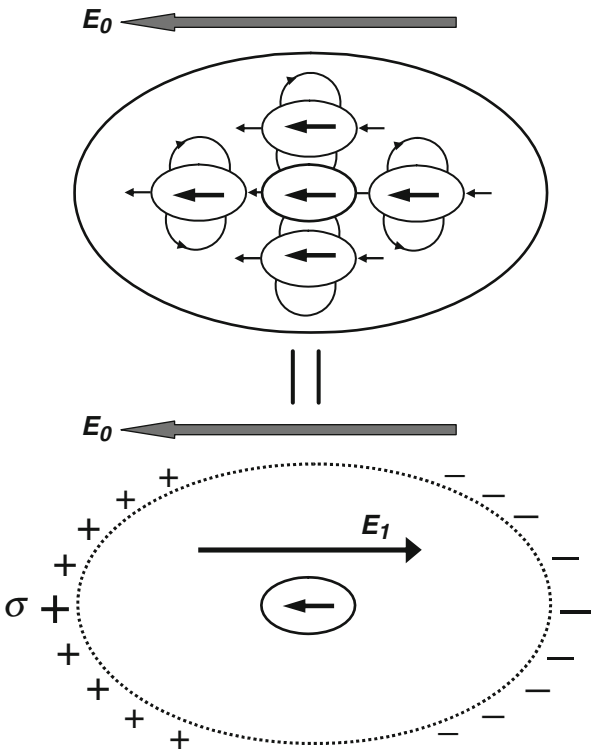

Fig. 8.11 Diagram illustrating the effective field $\boldsymbol{E_1}$ induced by the surface charge

The shapes of most particles are approximated as rotating ellipsoids. The component of the depolarization field along the principal axis of the ellipsoid $\boldsymbol{E}_{1\mathrm{i}}$ is given as

$$\boldsymbol{E}_{1i} = N_i \boldsymbol{P}_i, \tag{8.19}$$

where P_i ($\mathrm{i} = x, y, z$) is the component of the polarization along the principal axes of the ellipsoid. $\mathrm{N_i}$ is called a depolarization factor and has the rule taking a constant value of the summation ($\mathrm{N_x + N_y + N_z = 4\pi}$). The depolarization factors for the particle with the typical shapes like a sphere, rod, and disk are shown in Fig. 8.12.

The homogeneous polarization $\boldsymbol{P}$ is related with the internal field $\boldsymbol{E}$ using a dielectric susceptibility χ as

$$\boldsymbol{P} = \chi \boldsymbol{E} \tag{8.20}$$

The internal field $\boldsymbol{E}$ is written as follows if the external field $\boldsymbol{E}_0$ is parallel to the principal axis of the ellipsoid and the depolarization factor is N:

$$\boldsymbol{E} = \boldsymbol{E_0} + \boldsymbol{E_1} = \boldsymbol{E_0} - N\boldsymbol{P} \tag{8.21}$$

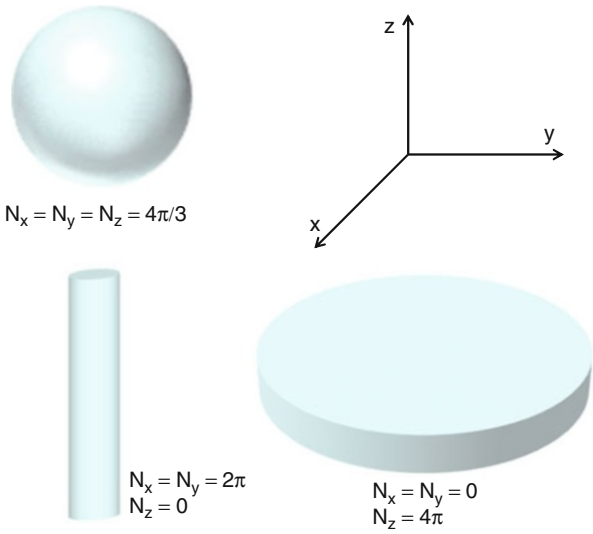

Fig. 8.12 Depolarization of electric fields along the principal axes of the particles with typical shapes (*sphere*, *rod*, and *disk*)

As a result, the polarization $\boldsymbol{P}$ is expressed by the external field $\boldsymbol{E}_0$ as

$$\boldsymbol{P} = \frac{\chi}{1 + N\chi}\boldsymbol{E}_0 \tag{8.22}$$

As is seen from this equation, the induced polarization is different depending on the shape even if the particle has same susceptibility. The dipole moment $\boldsymbol{p}$ of the particle with the volume V is expressed as follows using the dielectric function:

$$\boldsymbol{p} = V\boldsymbol{P} = \frac{\varepsilon(\omega) - 1}{4\pi + N(\varepsilon - 1)}V\boldsymbol{E}_0 \tag{8.23}$$

In the case of a sphere, the dipole moment $\boldsymbol{p}$ is given as

$$\boldsymbol{p} = \frac{\varepsilon(\omega) - 1}{\varepsilon(\omega) + 2}a^3\boldsymbol{E}_0 \tag{8.24}$$

4.3.5 Surface Plasmon Resonance (SPR)

The dipole moment induced for the sphere particle depends on the wavelength of the incident light according to the dielectric dispersion of the material as shown in Eq. 8.24. The large polarization is induced resonantly especially at the frequency where the permittivity takes a value $\varepsilon(\omega) = -2$. As a result, the electric field around the particle is enhanced. In the case of a metal, such resonant oscillation of the electric polarization is called a localized surface plasmon. The dielectric function of

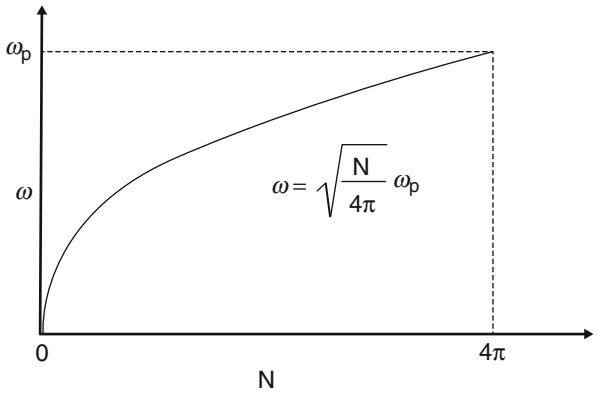

Fig. 8.13 Relation between resonance frequency ω and depolarization factor N

the metal takes negative values at the lower frequency than the plasma frequency as shown in Fig. 8.4. The resonance phenomenon occurs in the visible wavelength region in the case of Au and Ag, because the plasma frequencies of these metals locate near the visible region. The condition where the denominator of the Eq. 8.23 becomes 0 in the Drude model gives the following relation between the resonance frequency and depolarization factor:

$$\omega = \sqrt{\frac{N}{4\pi}}\omega_p \tag{8.25}$$

The resonance frequency ω becomes lower as the depolarization factor becomes smaller as illustrated in Fig. 8.13.

The practical nanoparticles do not exist at isolated state and are generally embedded in some medium or attached on the substrate. The influences of the medium on the optical response of the nanoparticle are discussed shortly compared with the isolated state. In the case of the particle embedded within a homogeneous medium ε' shown in Fig. 8.14, the surface charges induced by the light irradiation are partly canceled by the polarization of the surrounding medium. As a result, the resonance occurs at the frequency where the particle has a larger value of permittivity and the condition can be expressed by replacing ε in Eq. 8.23 by ε/ε'. The relation between the resonance frequency and ε' is derived for the sphere metal particle using Drude model as

$$\omega = \frac{\omega_p}{\sqrt{1+2\varepsilon'}} \tag{8.26}$$

The result implies this resonance phenomenon is sensitive to the shape of the particle and also the surrounding medium.

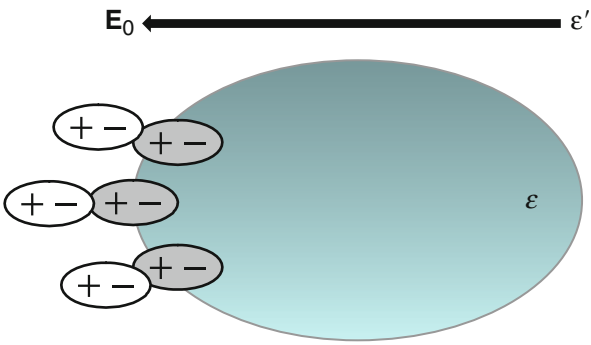

Fig. 8.14 Diagram illustrating the optical response of the nanoparticle with the permittivity ε embedded within a medium with the permittivity ε'

5 Key Research Findings

5.1 Shape Control Techniques of Nanoparticles

The nanostructure materials of noble metals are expected for wide range of applications in the fields of catalytic reactions, electronics, surface plasmon resonance (SPR), surface-enhanced Raman scattering (SERS), and biological and medical researches [62–64]. A specific shape of the nanostructure is required to optimize the performance for the application in the field. For example, of the application for catalysts, it is required to disperse the noble metal nanostructure on the ceramics with the large surface area. Nanowires are required for the observation of electric transport properties and the connection among electronic devices. On the other hand, the shape of the structure becomes the parameters to enhance and control the sensibility of the performance of noble metal nanostructures. The shapes of the nanostructure of Au or Ag determine the SPR properties and also become the important factors in the SERS measurement [65]. It is quite important to control the shape of the nanostructure of noble metals to improve the performance in various application fields.

The final morphology of the noble metal nanostructure in the liquid-phase synthesis is mainly determined by the twinned structure of the seed crystal and the growth rate of each crystal plane. The precursor compounds are decomposed or reduced to change to atoms with zero valence, and clusters called nuclei with flexible structures are formed. When the clusters grow beyond the critical size, they tend to take some specific structures to form seed crystals. The seed crystals play a role to connect between atoms and nanostructures and form single crystals or multiply twinned crystals as illustrated in Fig. 8.15 [66]. The twinned structure of the seed crystal is actually possible to control by the manipulation of the reduction rate. In case of the faster reduction rate, thermodynamically stable structures like single crystals or multiply twinned crystals are dominant. Depending on the reaction conditions, the single crystals grow to octahedron or cubic structures, and the multiply twinned structure to decahedron or pentagonal nanowire. In case of slow

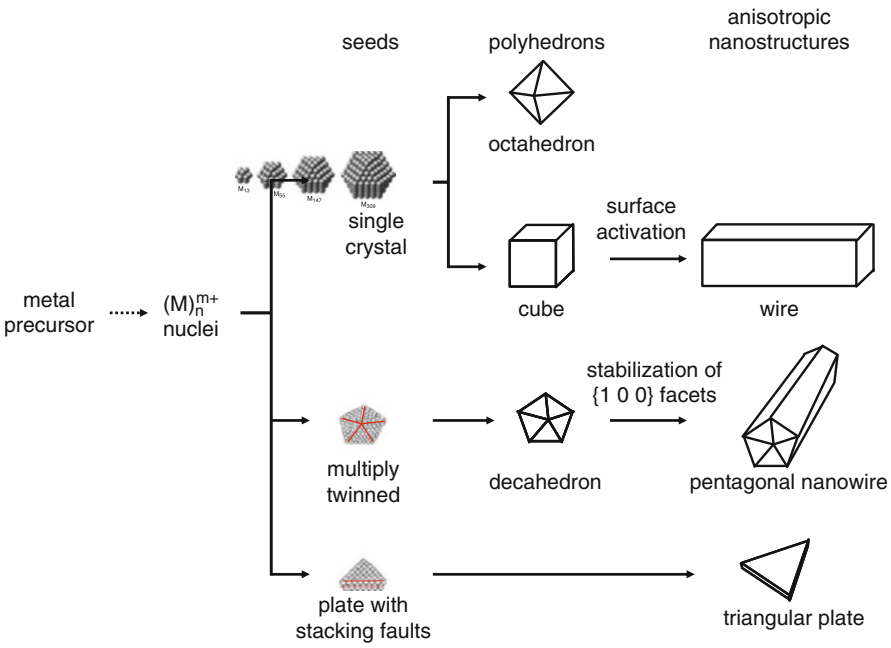

Fig. 8.15 Systematic diagram illustrating the flow from metal precursor to nanostructures

reduction rate, the reaction is controlled by the kinetic process. In this case, planer seed crystals having flat defect like stacking fault are formed at the first nuclei-forming process, and hexagonal and triangular nanoplates which depart largely from the thermodynamically preferable morphology are formed.

In most case, the relative free energy of respective crystal plane changes by introducing a capping agent with high selectivity according to the intense reaction with a specific crystal plane. Such process is the important means to control the relative growth rate of respective crystal plane. This type of chemical adsorption or surface capping strongly affects the final morphology of the metal nanostructure. For instance, polyvinylpyrrolidone (PVP) is a polymer capping agent in which oxygen atoms strongly couple with the (100) plane of Ag and the formation of Ag nanowire or nanocube is enhanced [67, 68].

5.1.1 Polyol Process in Nanostructures

The polyol process is the general method used to grow noble metal nanostructures with a specific morphology. At the first stage of this process, glycol aldehyde is synthesized using the following oxidation reaction by heating a metal salt (precursor of the noble metal) together with ethylene glycol (EG) up to 140–160 °C under the existence of a capping agent like PVP in order to create metal atoms [69]:

$$2HOCH_2CH_2OH + O_2 \rightarrow 2HOCH_2CHO + 2H_2O$$

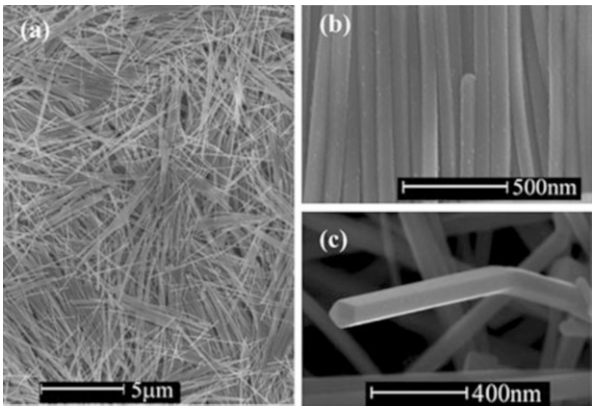

Fig. 8.16 SEM images showing (**a**) a large concentration of Ag nanorods, (**b**) assembly of the Ag nanorods during preparation of the specimen, and (**c**) pentagonal profile of the cross section of Ag nanorods [71]

Polyol can decompose many metal salts, and its reduction ability depends on the temperature. As a result, the process is appropriate to synthesize noble metal nanostructures like Ag, Au, Pd, Pt, Rh, Ru, and Ir.

5.1.2 Silver Nanoparticles

The nanostructure silver is a well-known material which engineering properties like SPR (surface plasmon resonance) depend on the morphology [69]. The structure is used to produce the substrate for SERS (surface-enhanced Raman spectroscopy) and also works as an excellent catalyst to epoxide ethylene. Homogeneous Ag nanowires are possible to synthesize by adding $CuCl_2$ to the typical polyol reduction of $AgNO_3$ using EG [70, 71]. Cu(II) ions are reduced to Cu(I) ions by EG, and both ions play an important role in this synthesis. The mechanism is shortly introduced below. Oxygen adsorbed on the metal surface is consumed in the oxidation from Cu(I) to Cu(II), and the oxygen concentration around the surface decreases, which prevent multiply twinned crystals to dissolve by oxidation etching to increase the sites for Ag to deposit and promote the growth of wire. Ethylene glycol makes recycle of Cu(II) to Cu(I), and adding of small quantity of Cu(II) ions is required for the adjustment of the oxygen concentration. Further, chloride ions control the isolated Ag^+ concentration in the solution by forming AgCl, which makes slow the reduction rate and promotes the preferential growth of Ag at the high-energy twinned boundary on the top of the wire. In the typical synthesis, PVP plays a role to protect preferentially (100) side plane of nanowire. Other trace ion species are important to control the morphology of Ag nanostructures. In the polyol reduction of $AgNO_3$, silver nanocubes are possible to synthesize homogeneously in large quantities by adding a small quantity of sulfates in the form of either Na_2S or NaHS [10–12]. The SEM images of Ag nanorods and nanocubes synthesized by polyol process are shown in Figs. 8.16 and 8.17, respectively. UV–Vis–NIR absorption spectra of the reaction mixture at various reaction times during the synthesis of Ag nanocubes are shown in Fig. 8.18 [71]. The resonance peaks show the red shift depending on the reaction time.

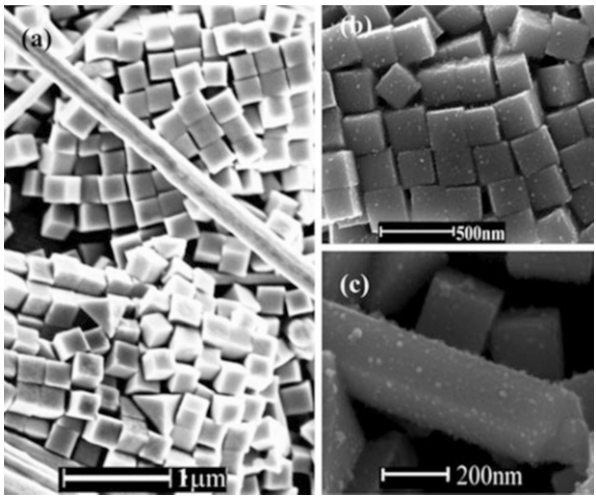

Fig. 8.17 FE-SEM images of the final products. (**a**) Uniform nanocubes with a few Ag nanorods, (**b**) a magnified image showing Ag nanocubes with many small Ag nanoparticles attached on the facets, and (**c**) the features of Ag nanorods formed in the sample of Ag nanocubes [71]

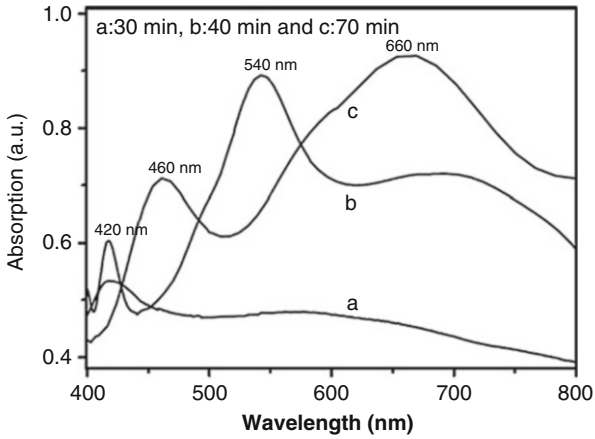

Fig. 8.18 UV–Vis–NIR absorption spectra of the reaction mixtures at various reaction times during the synthesis of Ag nanocubes: (*a*) 30 min, (*b*) 40 min, and (*c*) 70 min [71]

Calculated UV–Vis extinction (black), absorption (red), and scattering (blue) spectra of silver nanostructures were shown in Fig. 8.19 [70]. It is shown the shape of the nanostructure strongly affects its spectral characteristics. The absorption spectrum of an isotropic sphere (A) exhibits a single resonance peak. On the other hand, the spectra of anisotropic cubes (B), tetrahedra (C), and octahedra (D) exhibit multiple, red-shifted resonance peaks. The resonance frequency of a sphere with a hollow shows red shift (E), and a sphere with thinner shell walls shows further red shift (F) [70].

UV–Vis–NIR extinction (black), absorption (red), and scattering (blue) spectra of silver nanostructures calculated using the discrete dipole approximation (DDA) method are shown in Fig. 8.20 [70]. It is shown that 2D anisotropies affect strongly

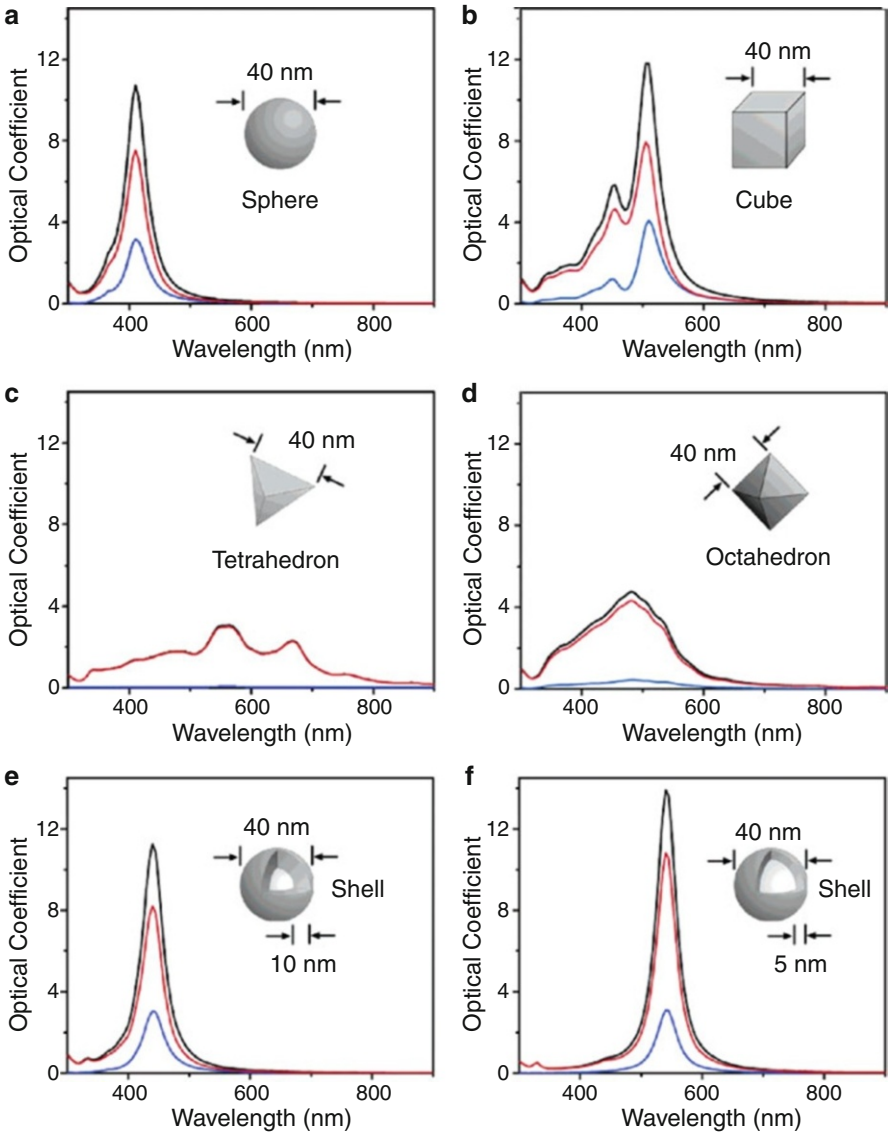

Fig. 8.19 Calculated UV–Vis extinction (*black*), absorption (*red*), and scattering (*blue*) spectra of silver nanostructures for an isotropic sphere (**a**), an anisotropic cube (**b**), a tetrahedron (**c**), and an octahedron (**d**). The absorption spectra of spheres with a hollow (**e**) and a thinner shell wall (**f**) are also shown [70]

their spectroscopic features. Resonance peaks show red shift depending on the anisotropy of a triangular plate (A) and circular disk (B). The resonance peaks of silver nanorings of two different thicknesses (C) and (D) show larger red shift for thinner rings.

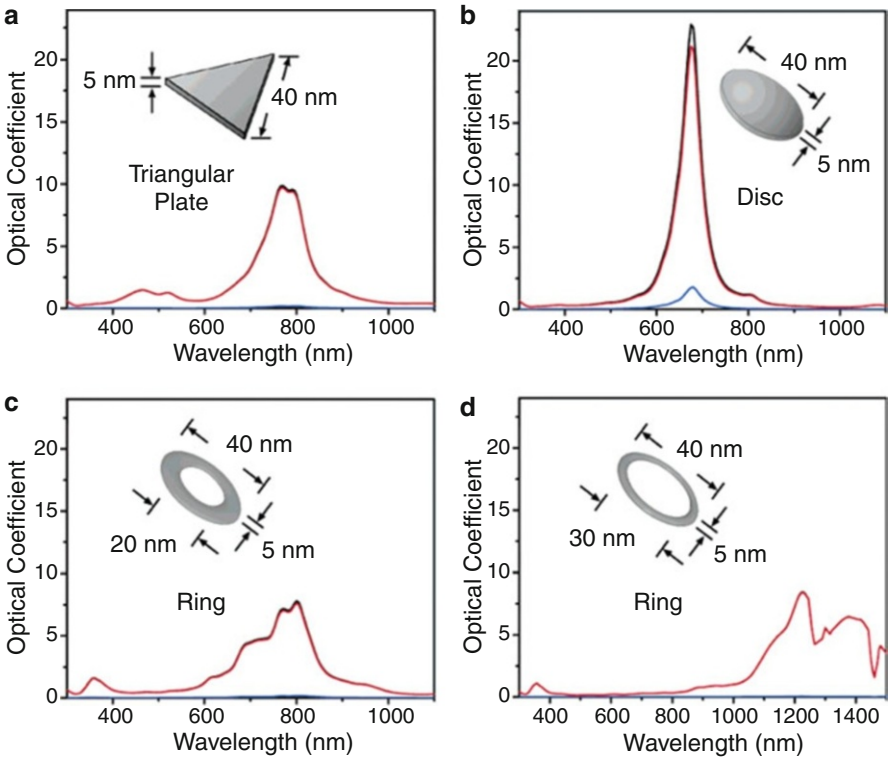

Fig. 8.20 UV–Vis–NIR extinction (*black*), absorption (*red*), and scattering (*blue*) spectra of silver nanostructures calculated by the DDA method for a triangular plate (**a**) and a circular disk (**b**). Absorption spectra of silver nanorings with two different widths are also shown in (**c**) and (**d**) [70]

5.1.3 Gold Nanoparticles

Gold nanostructures attract the intentions according to their excellent chemical stability, biological inactivity, SPR/SERS properties, and unique catalytic performance. Many methods have been tried to control the morphology of the Au nanostructures [72–75]. As mentioned for the Ag system previously, the selection of reducing or stabilizing agents and reaction temperatures are important to form a specific morphology. In the Au system, the polyol reduction also promotes to form thermodynamically preferable polygon of Au nanostructure using strong reducing agents. But there are several different points compared with Ag. It is considered that the bonding of PVP to Au is not strong enough to promote the formation of (100) plane in contrast to the Ag system. As a result, the single crystal and multiply twinned polygon surrounded by (111) planes like octahedron, decahedron, and icosahedron are the preferable nanocrystals of Au in the polyol process. For example, Au octahedrons are synthesized at high yields by the improved polyol process using polyethylene glycol 600 as the reducing agent [76]. Polyethylene

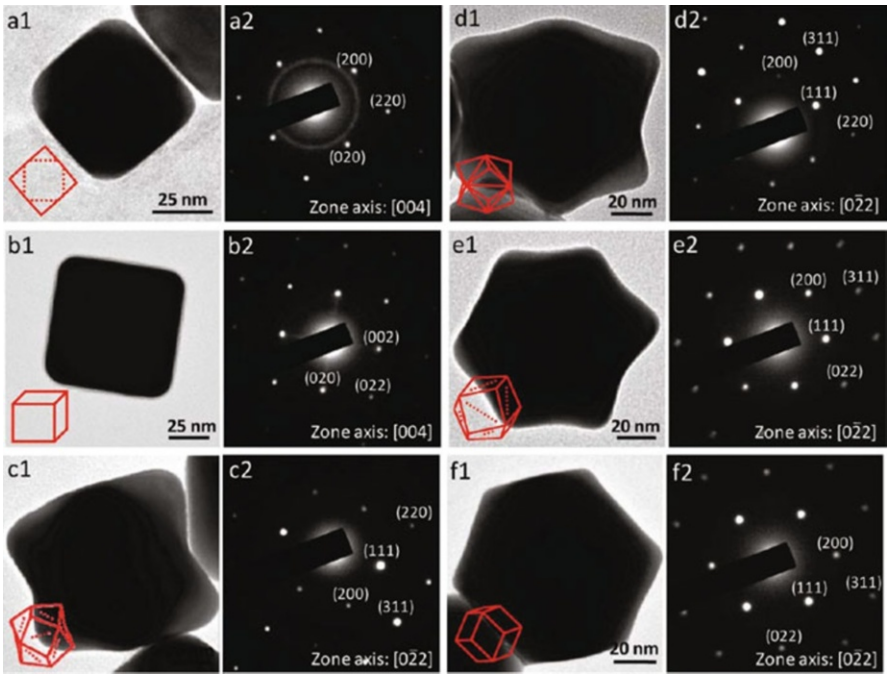

Fig. 8.21 TEM images of (**a1**) a *truncated cube*, (**b1**) a *cube*, (**c1**) a type I transitional particle, (**d1**) a *trisoctahedron*, (**e1**) a type II transitional particle, and (**f1**) a *rhombic dodecahedron*. Morphologies of the nanocrystals are also illustrated in the figures. The corresponding SAED patterns and their zone axes are also provided [75]

glycol 600 is used also as a solvent in this synthesis. The small addition of $NaBH_4$ before adding an $AuCl_3$ water solution is the key to obtain homogeneous Au octahedrons. The added $NaBH_4$ works as a strong reducing agent and rapid reduction of Au precursor proceeds. On the other hand, multiply twinned nanostructures of Au can be synthesized by increasing the PVP concentration in the polyol reducing process of $HAuCl_4$ using diethylene glycol [77].

TEM images of (a1) a truncated cube, (b1) a cube, (c1) a type I transitional particle, (d1) a trisoctahedron, (e1) a type II transitional particle, and (f1) a rhombic dodecahedron are shown in Fig. 8.21 [75]. Drawings of the corresponding nanocrystals are shown for reference. The corresponding SAED patterns and their zone axes are also provided. UV–Vis absorption spectra observed for gold nanocubes and rhombic dodecahedra with different sizes are shown in Fig. 8.22 [75]. The absorption band maxima show slight red shifts as the size becomes larger.

5.1.4 Palladium Nanoparticles

Palladium is an important catalyst used in the various reactions like hydrogenation and dehydrogenation and also used in the reactions to produce C–C bond like Suzuki coupling, Heck coupling, and Stille coupling. The major morphology of

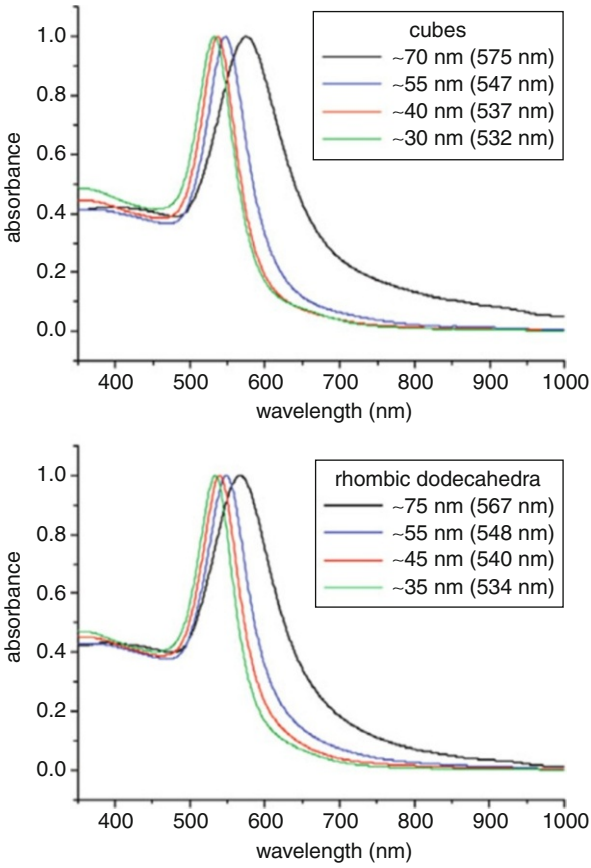

Fig. 8.22 UV–Vis absorption spectra of gold nanocubes and rhombic dodecahedras with different sizes. The maximum wavelengths of the absorption bands are also given in parentheses [75]

Pd nanostructure in the polyol reduction of Na_2PdCl_4 using EG takes an octahedron [78]. The morphologies of Pd nanostructures are controlled by the introduction of a specific capping agent like Br ions or by the oxidation etching. Pd nanobars are possible to synthesize by adding Br ions to the polyol reduction of Na_2PdCl_4 [79, 80]. Bromide ions bond strongly to the (100) plane of Pd, and seed crystals of cubic Pd are formed at the nucleation stage. In this process, the oxidation etching occurs locally on one of the six planes of the cubic seed crystal, and a part of Br ions is removed, which promotes the selective growth of the cubic seed crystal along one direction to form Pd nanobars surrounded with (100) planes.

As an another example, Pd triangle nanoplates are formed by introducing Fe(III) species during the polyol process, which is due to the large decrease of reducing rate by using Fe(III) species and O_2/Cl pairs as the wet etching liquid for Pd(0) [81]. These Pd nanoplates exhibit a SPR peak in the visible region as the size becomes larger and are possible to use as the SERS active substrate owing to their sharp corners and edges.

Electron microscope images of Pd triangular nanoplates prepared at 85 °C in the presence of 0.36 mM $FeCl_3$ and 5 mM HCl are shown in Fig. 8.23 [81]. The molar ratio

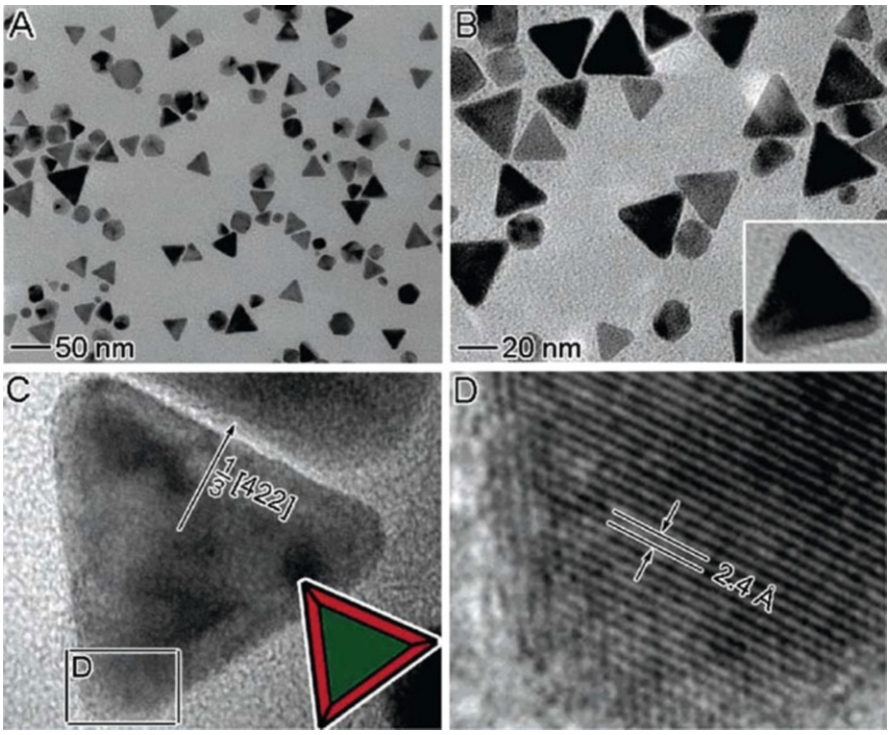

Fig. 8.23 TEM images (**a**) and (**b**) and high-resolution TEM images (**c**) and (**d**) of Pd triangular nanoplates. The *inset* in (**b**) gives the TEM image of a titled triangular nanoplate, and the *inset* of (**c**) shows a schematic drawing of the triangular nanoplate, where the red and green colors represent the (100) and (111) facets, respectively [81]

of PVP to Pd precursor is 5 where the concentration given in the figure caption is the final value in the reaction solution. UV–Vis extinction spectra of as-prepared triangular and hexagonal nanoplates are shown in Fig. 8.24a [81]. The extinction, absorption, and scattering coefficients of a triangular nanoplate calculated using the DDA method are shown in Fig. 8.24b [81], where all random configurations of the plate with respect to the incident light were averaged. The optical coefficients were defined as $C/\pi\alpha_{eff}{}^2$ where C was the cross sections obtained directly from DDA calculation and α_{eff} was defined through the concept of an effective volume equal to $4\pi\alpha_{eff}{}^3/3$ for the plate.

5.2 Spectral Analysis on the Absorption Spectra of Dielectric Films Dispersed with Metal Nanoparticles

5.2.1 Spectral Analysis on the Absorption Spectra by Surface Plasmon Using Mie Theory

The charges within a sphere are forced to oscillate when light incidents on the sphere. Such movement of charge emits light inside and outside of the sphere.

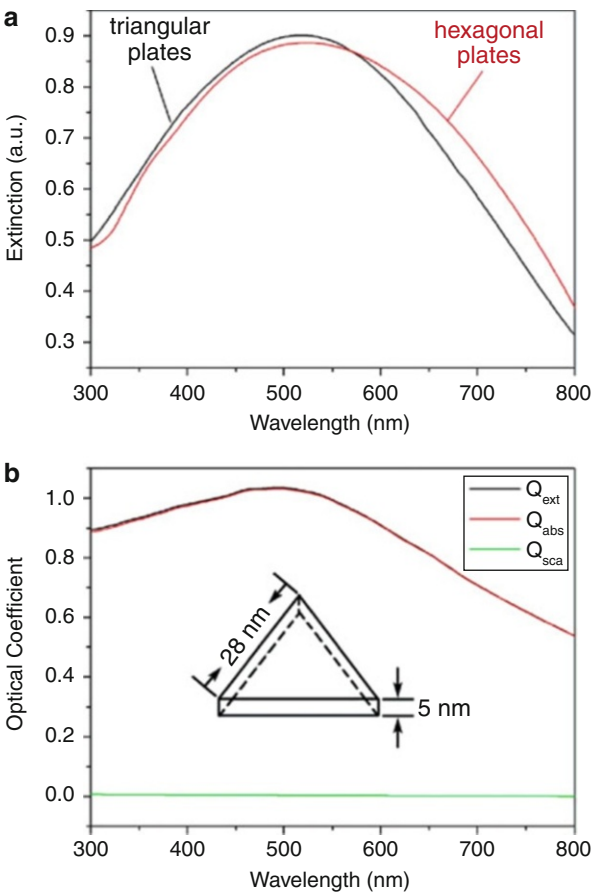

Fig. 8.24 UV–Vis extinction spectra of as-prepared triangular and hexagonal nanoplates (**a**) and the extinction (*blue*), absorption (*red*), and scattering (*green*) coefficients of a triangular nanoplate calculated using the DDA method (**b**) [81]

As a result, the electromagnetic field at any point is the superposition of electromagnetic fields of incident and emitted light, and so-called diffraction occurs. In olden time, this phenomenon gave the basic theory for the Rayleigh scattering of solar ray by air molecules, which was the proof of the blue sky. In recent time, it gives the basic theory for the optical properties of the photonic crystal composed of ordered spheres.

The electric field of incident light E_i can be expanded by vector spherical wave functions assuming a liner polarized plane wave traveling to z direction described as follows:

$$E_i = g_x E_0 e^{i(k_z z - \omega t)} = E_0 e^{-i\omega t} \sum_{n=1}^{\infty} i^n \frac{2n+1}{n(n+1)} \left(m_{o1n}^{(1)} - i n_{e1n}^{(1)} \right) \tag{8.27}$$

where g_x is the x component of the amplitude vector g. The amplitude vector component of the magnetic field H_i is given as g_y because the direction of the

magnetic field is perpendicular to that of the electric field. Utilizing Eq. 8.27, H_i is given as

$$H_i = g_y \frac{k_2}{\mu_2 \omega} E_0 e^{i(k_z z - \omega t)} = -\frac{k_2}{\mu_2 \omega} E_0 e^{-i\omega t} \sum_{n=1}^{\infty} i^n \frac{2n+1}{n(n+1)} \left(m_{o1n}^{(1)} - i n_{e1n}^{(1)} \right) \quad (8.28)$$

When light incidents into the sphere, two types of components of light occur. One is departing from the sphere, and the other is trapped within the sphere after the reflection and transmission. The former component should vanish apart enough from the sphere and expressed by spherical Bessel function of the third kind, that is, Hankel function. On the other hand, the component within the sphere should be finite at the center of the sphere and described as the same expression with the incident electromagnetic field.

The electromagnetic field out of the sphere (R > a) is written as

$$\begin{aligned} E^e &= E_0 e^{-i\omega t} \sum_{n=1}^{\infty} i^n \frac{2n+1}{n(n+1)} \left(a_n^e m_{o1n}^{(3)} - i b_n^e n_{e1n}^{(3)} \right) \\ H^e &- \frac{k_2}{\mu_2 \omega} E_0 e^{-i\omega t} \sum_{n=1}^{\infty} i^n \frac{2n+1}{n(n+1)} \left(b_n^e m_{o1n}^{(3)} + i a_n^e n_{e1n}^{(3)} \right) \end{aligned} \quad (8.29)$$

where $z_n(k_2R)$ in the expression of $m^{(3)}{}_{e1n,\ o1n}$ and $n^{(3)}{}_{e1n,\ o1n}$ is replaced by the Hankel function $h^{(1)}n(k_2R)$. On the other hand, the electromagnetic field within the sphere (R < a) is written as

$$\begin{aligned} E^i &= E_0 e^{-iwt} \sum_{n=1}^{¥} i^n \frac{2n+1}{n(n+1)} \left(a_n^i m_{o1n}^{(1)} - i b_n^i n_{e1n}^{(1)} \right) \\ H^i &- \frac{k_1}{m_1 w} E_0 e^{-iwt} \sum_{n=1}^{¥} i^n \frac{2n+1}{n(n+1)} \left(b_n^i m_{o1n}^{(1)} + i a_n^i n_{e1n}^{(1)} \right) \end{aligned} \quad (8.30)$$

The electromagnetic fields in and out of the sphere can be calculated by getting a_{ien} and b_{ien}. The values of a_{ien} and b_{ien} are determined by using the boundary conditions which claims that the tangential components of the electromagnetic fields at the surface of the sphere should be continuous:

$$\begin{aligned} \boldsymbol{i}_1 \times (\boldsymbol{E_i} + \boldsymbol{E^e}) &= \boldsymbol{i}_1 \times \boldsymbol{E^i} \\ \boldsymbol{i}_1 \times (\boldsymbol{H_i} + \boldsymbol{H^e}) &= \boldsymbol{i}_1 \times \boldsymbol{H^i} \end{aligned} \quad (8.31)$$

Next relations are derived at R = a by substituting Eq. 8.30 for Eq. 8.31 and by setting the condition that the coefficients for P 1n(cosθ) and ∂P 1n(cosθ)/∂θ are equal each other:

$$\begin{aligned} & j_n(k_1 a) a_n^i - h_n^{(1)}(k_2 a) a_n^e = j_n(k_2 a) \\ & [k_1 a j_n(k_1 a)]' b_n^i - \frac{k_1}{k_2} \left[k_2 a h_n^{(1)}(k_2 a) \right]' b_n^e = \frac{k_1}{k_2} [k_2 a j_n(k_2 a)]' \end{aligned} \quad (8.32)$$

$k_1 a = N\rho$ is obtained by putting $k_1 \equiv Nk_2$ and $\rho \equiv k_2 a$, and following relations are derived from Eq. 8.32:

$$\begin{aligned} j_n(N\rho)a_n^i - h_n^{(1)}(\rho)a_n^e &= j_n(\rho) \\ [N\rho j_n(N\rho)]' b_n^i - N\left[\rho h_n^{(1)}(\rho)\right]' b_n^e &= N[\rho j_n(\rho)]' \end{aligned} \tag{8.33}$$

Next relations are derived with similar way:

$$\begin{aligned} \mu_2 N j_n(N\rho)b_n^i - \mu_1 h_n^{(1)}(\rho)b_n^e &= \mu_1 j_n(\rho) \\ \mu_2 [N\rho j_n(N\rho)]' a_n^i - \mu_1\left[\rho h_n^{(1)}(\rho)\right]' a_n^e &= \mu_1 [\rho j_n(\rho)]' \end{aligned} \tag{8.34}$$

Following relations are derived from Eqs. 8.33 and 8.34:

$$\begin{aligned} a_n^i &= \frac{\mu_1 j_n(\rho)\left[\rho h_n^{(1)}(\rho)\right]' - \mu_1 h_n^{(1)}(\rho)[\rho j_n(\rho)]'}{\mu_1 j_n(N\rho)\left[\rho h_n^{(1)}(\rho)\right]' - \mu_2 h_n^{(1)}(\rho)[N\rho j_n(N\rho)]'} \\ b_n^i &= \frac{\mu_1 N h_n^{(1)}(\rho)[\rho j_n(\rho)]' - \mu_1 N j_n(\rho)\left[\rho h_n^{(1)}(\rho)\right]'}{\mu_1 h_n^{(1)}(\rho)[N\rho j_n(N\rho)]' - \mu_2 N^2 j_n(N\rho)\left[\rho h_n^{(1)}(\rho)\right]'} \\ a_n^e &= -\frac{\mu_1 j_n(N\rho)[\rho j_n(\rho)]' - \mu_2 j_n(\rho)[N\rho j_n(N\rho)]'}{\mu_1 j_n(N\rho)\left[\rho h_n^{(1)}(\rho)\right]' - \mu_2 h_n^{(1)}(\rho)[N\rho j_n(N\rho)]'} \\ b_n^e &= -\frac{\mu_1 j_n(\rho)[N\rho j_n(N\rho)]' - \mu_2 N^2 j_n(N\rho)[\rho j_n(\rho)]'}{\mu_1 h_n^{(1)}(\rho)[N\rho j_n(N\rho)]' - \mu_2 N^2 j_n(N\rho)\left[\rho h_n^{(1)}(\rho)\right]'} \end{aligned} \tag{8.35}$$

The values a_{ien} and b_{ien} increase largely due to the resonance effect as the ω of incident light becomes close to the angular frequency of the WG mode. The light scattering intensity from the sphere becomes enhanced by exciting the WG mode.

Gustav Mie was the first to rigorously explain the colors exhibited by metal colloids using Maxwell's equations. However, exact solutions to Maxwell's equations are known only for spheres, shells, spheroids, and infinite cylinders, and an approximation is required to solve the equations for other geometries. The approximation of choice is called the discrete dipole approximation (DDA) [70–72, 82, 83]. In a DDA calculation, the nanoparticle is discretized into a cubic array of N polarizable points, with each point representing the polarizability of a discrete volume of material. The presence of an electromagnetic field (light) gives these points a dipole moment. In the steady state limit, each dipole is polarized by an electric field that includes contributions from incident light and every other dipole in the array. The polarization at each point (P_j) must thus be calculated through an iterative procedure, which can be accelerated with FFT methods (thus the periodicity of the array). The polarization P_j can be plugged into an equation to determine the scattering and absorption cross sections of the particle, which in turn are divided by the cross-sectional area to give the dimensionless optical coefficients. As the

coefficients can be solved exactly for this N-point array, the only approximation is in the number of points. A greater N increases the accuracy of the calculation at the expense of computation time.

5.2.2 Spectral Analysis on the Absorption Spectra by Surface Plasmon for the Dielectric Materials Dispersed with Metal Nanoparticles Using Effective Medium Approximation (EMA) Theory

The interaction between light and a metal sphere is treated by the Mie theory. However, real metal nanoparticles take various shapes, and the theories for other shapes like ellipsoids are required. The interaction between nanoparticles is also related for the high concentration of nanoparticles. The process parameters with which one can control the macroscopic properties of the composite (dielectric materials dispersed with metal nanoparticles) are related to the individual material phases, their relative fractional volumes, and the shapes of the inclusions. The effective medium theories to treat the composite media dispersed with nanoparticles with extended shape parameters are reviewed.

The EMA theory is the approximation which assumes the composite material as a homogeneous medium with an effective permittivity. The theoretical model to mix the components of the composite is featured by the effective permittivity. Classical mixing formulae, like the Maxwell–Garnett and Bruggeman [84, 85], have been widely used to calculate the effective permittivity of such mixtures. These formulae work very well in some fields of applications. For example, in the area of the remote sensing, the contrasts of the permittivity among various phases of the heterogeneous structures are not very large. In the case, both Maxwell–Garnett and Bruggeman mixing formulae predict reasonably accurate results.

However, in the case of applications to the material science, the contrast of the permittivity between the matrix and the inclusion is often very large. In some cases, the composites are required to be constructed using a polymer matrix because of desired mechanical properties. The contrast of the electrical conductivity between the matrix and the metal nanoparticles may be extremely large, even several thousands. In addition, the volume filling ratio of inclusions changes over wide range. The combination of highly packed inclusions with the high electrical contrast leads to the situation where two mixing equations should be used simultaneously. The choice of the mixing theory to give the desired effective permittivity of the composite is very difficult when one must find out general principles to choose the best material combination for the given application. Another shortcoming of the semiempirical models is that the parameters do not correspond to separate physical properties of the mixture. For example, if one parameter is responsible for the percolation threshold of the mixture, a change in this parameter also changes the volume filling ratio properties of the mixture. The effective permittivity of the composite with very low filling ratios of spheres is dominated by the shape of the inclusions. As a result, the percolation parameter is also dependent on the shape of the inclusions.

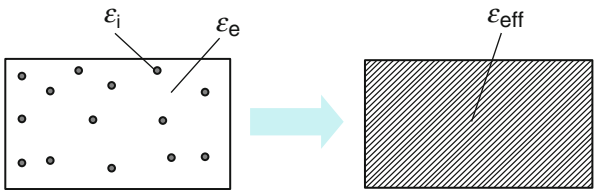

Fig. 8.25 Schematic diagram illustrating EMA model

Classical Mixing Formulae for the Composite Materials

The schematic illustration of a composite material is shown in Fig. 8.25 where a material with the permittivity ε_i and the volume filling fraction f is dispersed in the matrix material with the permittivity ε_e and volume fraction *1-f*. The basic idea behind all classical mixing formulae for the composite materials is to try to estimate and define the effective permittivity ε_{eff} for the mixture with the assumption that the dimension of inhomogeneity within the composite is much smaller than the wavelength of the incident light into the material.

If the shape of the inclusions can be modeled as spheres or ellipsoids, several mixing rules have been proposed in the literatures. General mixing rules to define the effective permittivity are listed on Table 8.2. In the table, f is the volume filling fraction of the dispersed spheres or ellipsoids in the mixture, ε_i is the permittivity of the inclusions, and ε_e is the permittivity of the matrix. The depolarization factor of the dispersed ellipsoids is denoted by $N_{x,y,z}$. The factor of the spheres is $N_x = N_y = N_z = 1/3$. The depolarization factors for general ellipsoids contain elliptic integrals, but closed-form expression can be written for spheroids.

For the prolate spheroids ($a_z > a_x = a_y$), the depolarization factors are written as

$$N_z = \frac{1-e^2}{2e^3}\left(\ln\frac{1+e}{1-e} - 2e\right), \qquad N_x = N_y = \frac{1}{2}(1-N_z) \tag{8.36}$$

where the eccentricity is $e = (1 - a_x{}^2/a_z{}^2)^{1/2}$.

For the oblate spheroids ($a_z < a_x = a_y$), the factors are written as

$$N_z = \frac{1+e^2}{e^3}\left(e - \tan^{-1}e\right), \qquad N_x = N_y = \frac{1}{2}(1-N_z) \tag{8.37}$$

where $e = (a_x{}^2/a_z{}^2 - 1)^{1/2}$, and a_x , a_y, and a_z are the three semiaxes of the ellipsoid. Depolarization factors for any ellipsoid satisfy $N_x + N_y + N_z = 1$.

The first attempt to describe optical constants of inhomogeneous materials with effective refractive index dates back to 1904 (the so-called Maxwell–Garnett rule [84]). Bruggeman derived an independent mixing rule for the effective dielectric constant of inhomogeneous materials [85]. Both the Maxwell–Garnett and Bruggeman rules are based on the assumption of the Rayleigh size of the inhomogeneity but consider different internal structures of the mixtures. Maxwell and Garnett (M–G) initiated the study of nanocomposites as they investigated the optical properties of metal colloids with minute metal spheres embedded in an

Table 8.2 General mixing rules based on EMA theories

1. Conventional effective medium theories
(a) Separated-grain topology
(a-1) Maxwell–Garnett model [84] $\frac{\varepsilon-\varepsilon_m}{\varepsilon+2\varepsilon_m}=f_i\frac{\varepsilon_i-\varepsilon_m}{\varepsilon_i+2\varepsilon_m}.$
(a-2) Inverse Maxwell–Garnett model [84] $\frac{\varepsilon-\varepsilon_i}{\varepsilon+2\varepsilon_i}=f_m\frac{\varepsilon_m-\varepsilon_i}{\varepsilon_m+2\varepsilon_i}.$
(a-3) Coherent potential model [86] $\frac{\varepsilon-\varepsilon_m}{4\varepsilon+2\varepsilon_m}=f_i\frac{\varepsilon_i-\varepsilon_m}{\varepsilon_i+3\varepsilon-\varepsilon_m}$
(a-4) Inverse coherent potential model [86] $\frac{\varepsilon-\varepsilon_i}{4\varepsilon+2\varepsilon_i}=f_m\frac{\varepsilon_m-\varepsilon_i}{\varepsilon_m+3\varepsilon-\varepsilon_i}$
(b) Aggregated-grain topology
(b-1) Bruggeman model [85] $f_i\frac{\varepsilon_i-\varepsilon}{\varepsilon i+2\varepsilon_i}+f_m\frac{\varepsilon_m-\varepsilon}{\varepsilon_m+2\varepsilon}=0$
(b-2) Looyenga model [87] $\varepsilon^{1/3}=f_i\varepsilon_i^{1/3}+f_m\varepsilon_m^{1/3}$
(b-3) Lichtenecker model [88, 89] $\log\varepsilon_{eff}=f\log\varepsilon_i+(1-f)\log\varepsilon_e$
2. Extended effective medium theories
(a) Stroud and Pan model [90] $\sum_{j=i,m}f_i\left(\frac{\varepsilon_j-\varepsilon}{\varepsilon_j+2\varepsilon}+\frac{x_j^2}{30}(\varepsilon_j-\varepsilon)\right)=0$
(b) Wachniewski and McClung model [91] $\sum_{j=i,m}f_i\left(\varepsilon\frac{\varepsilon_j-\varepsilon}{\varepsilon_j+2\varepsilon}+\frac{x_j^2}{10}[6\varepsilon(\varepsilon+\varepsilon_j)\frac{5\varepsilon_j-10\varepsilon+(\varepsilon_j/\varepsilon)\varepsilon_j+4(\varepsilon_j/\varepsilon)}{(\varepsilon_j+2\varepsilon)^2}$ $-(\varepsilon+\varepsilon_j)(\varepsilon_j/\varepsilon+1)\frac{3\varepsilon}{\varepsilon_j+2\varepsilon}-(\varepsilon+\epsilon_j)-(\varepsilon+\varepsilon_j)\frac{5\varepsilon}{3\varepsilon+2\varepsilon_j}$ $+2\varepsilon\left(\sqrt{\varepsilon_j/\varepsilon}+1\right)+4\varepsilon\sqrt{\varepsilon_j/\varepsilon}]\Big)=0.$

optically linear host material. The size of the inclusions is assumed to be much smaller than the wavelength of the incident light, and the composite can be treated as one homogeneous medium with the effective permittivity as shown in Fig. 8.25. In the classical Maxwell-Garnett mixing rule, it is assumed that the local electric field on each ellipsoid is the superposition of the average external field and the average field caused by other spheres. The result for the effective permittivity is also known as the Clausius–Mossotti equation. Unfortunately, the Maxwell-Garnett model is restricted to relatively small volume fraction of the inclusions because of the assumptions imposed on the model. The Maxwell–Garnett rule assumes that the composite material is composed of a matrix material with embedded inclusions. As a result, the effective refractive index depends on which material is considered as

the matrix and which as the inclusions. The Bruggeman rule avoids this problem by considering the medium composed of a set of randomly distributed cells of different materials. For large volume fraction of the inclusions and for randomly intermixed constituents, Bruggeman (Polder–van Santen) derived the EMA model by considering the host material as an effective medium. It assumes asymmetry between nanoparticles and the matrix phase. The formula similar to the Maxwell-Garnett equation was derived for the small volume fractions of nanoparticles. These two mixing rules have been generalized to adapt to the multiphase mixtures including magnetic, anisotropic, and chiral components; polydispersions of inhomogeneity; nonspherical (ellipsoidal, cylindrical, cubic, Jakes, and rods) and stratified inclusions. Even though the Maxwell–Garnett and Bruggeman rules still remain as the most general mixing rules, a variety of other effective medium theories have been developed. One of the most essential developments of the effective medium theories was suggested by Stroud and Pan [90]. It allows the inhomogeneity to be modeled not as infinitely small like Rayleigh particles but as larger particles which size is limited only by the condition that the attenuation length (mean free path of photon) is large compared to the characteristic particle dimension.

Three mathematical approaches were used to derive the mixing rules: direct calculation of the average polarizability of the composite material (see, e.g., [92]), the T-matrix method [93], and the method based on the requirement that the complex forward scattering amplitude of the light passing through the mixture should be zero [94] when it is immersed in a medium of the effective refractive index. Classification of EMA theories based on the physical description of the composite materials looks more illustrative, and it is described below. The physical description depends on the properties of the inclusions and on their arrangement inside the composite material. The main property of the inclusions is their size. The majority of EMA theories were developed within the flamework of "quasistatic approximation." They were derived at zero frequency, that is, inclusions are considered as very small like Rayleigh particles that can be treated as dipoles. As was mentioned above, the paper by Stroud and Pan suggested a new approach in the framework by which a number of EMA theories for inclusions of larger size have been developed. This method is known as the "dynamic approximation" or extended EMA theory [95] because it extends the effective medium approach to finite frequencies, using a full multipole expansion to treat scatterings from small particles. Within this method, the scattering by inclusions is represented by multipole coefficients obtained from the exact solution of the Maxwell equations for particles that have the same shape as the inclusions (spheres, spheroids, cylinders, etc.). The further classification of EMA theories as well as extended EMA theories can be done according to the number of components in the mixture, the shape and the size distributions of the inclusions, and other properties of the individual inclusions, including their structures (for instance, core–mantle inclusions can be considered), magnetic properties, anisotropy, chirality, etc.

Another important characteristic is the internal structure (topology) of the composite material. The main structures usually treated in EMA theories are aggregated- or separated-grain topologies. "Separated-grain" means that the

composite material can be represented as the matrix of a main material with the inclusions inside that are separated from each other by the matrix material. One of the most popular separated-grain EMA theories is the Maxwell–Garnett mixing rule. The separated-grain EMA theories give different results depending on which component of the mixture is chosen to be the matrix. The aggregated-grain topology represents the mixture as a set of "cells" made of one or the other component of the mixture. In this case, mixing rules are symmetric relative to which component is called matrix and which is called inclusions. The most popular aggregated-grain EMA theory is the Bruggeman mixing rule. Recent development of EMA theories for the astronomical application resulted in some new versions of EMA theories based on the aggregated-grain topology. They allow more complicated fractal, percolated, radially varying internal structures of composite materials [96].

5.2.3 Spectral Analysis on the Absorption Spectra by Surface Plasmon of ZrO_2 Films Dispersed with Ag Nanoparticles Synthesized by Sol–Gel Method

The aim of this study is the examination of the applicability of the effective medium theory to the synthesized ZrO_2–Ag composite materials [97–99]. The silver nanoparticle/ZrO_2 thin-film composites were prepared by a sol–gel method with various silver fill fractions. The synthesized films were analyzed by a UV–Vis–NIR spectrophotometer, a transmission electron microscope (TEM) and an X-ray diffractometer (XRD). The absorption spectra due to the silver surface plasmon resonance were simulated using the dielectric functions reflecting the M–G and the Bruggeman mixture rules. In this study, the composite materials are consisted of metal nanoparticles and dielectric materials, and two typical mixing models of Maxwell–Garnett and Bruggeman are applied to check the applicability for the simulation of the optical spectra. ZrO_2 thin films dispersed with silver nanoparticles were synthesized by the sol–gel method. The starting solution was prepared from zirconium n-propoxide, acetylacetone, 1-propanol, 2-propanol, and distilled water. The silver solution was prepared from silver nitrate and diethylenetriamine. The resulting solutions were mixed with the following molar ratios: Zr:Ag = 90:10, 80:20, 70:30, 60:40, 50:50, 40:60, and 30:70. These densities of silver correspond to the volume fractions of 5.3 %, 11.1 %, 17.7 %, 25.0 %, 33.3 %, 42.9 %, and 53.9 %, respectively. X-ray diffraction measurements were performed in a 2θ scan configuration in the range of 10–80° using an X-ray diffractometer with Cu Kα radiation (MacScience, MXP18HF). The X-ray diffraction peaks were observed at 2θ of 38.1°, 44.3°, 64.5°, and 77.5° which were identified by JCPDS card as (1 1 1), (2 0 0), (2 2 0), and (3 1 1) planes of silver, respectively. A clear peak of ZrO_2 was not observed. It is supposed that the matrix material of ZrO_2 takes an amorphous structure. TEM images of silver nanocrystallites in the zirconia films are shown in Fig. 8.26 [97] for the nominal Ag to Zr molar ratio [Ag]/[Zr] of 0.25, 1.00, and 2.33, respectively. The silver nanoparticles can be clearly seen, embedded in the ZrO_2 matrix. For the nominal Ag to Zr molar ratio [Ag]/[Zr] = 0.25 (Fig. 8.26a [97]), the particles are well separated from each other and their shapes are basically spherical. For the nominal Ag to Zr molar ratio [Ag]/[Zr] = 2.33 (Fig. 8.26c [97]), the particles

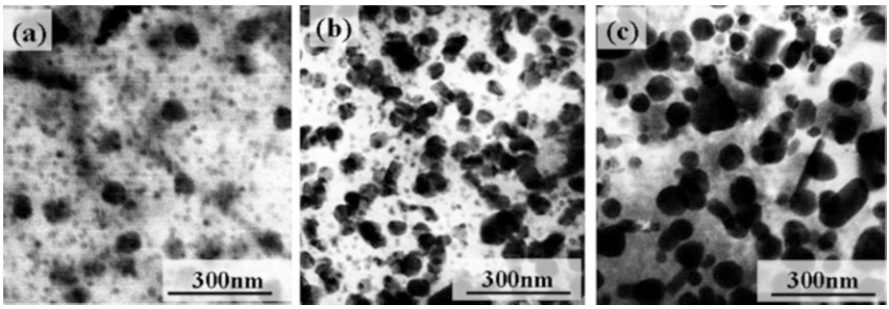

Fig. 8.26 TEM images of ZrO_2–Ag composite films with different molar ratios of silver: (**a**) $80ZrO_2$:20Ag mol%, (**b**) $50ZrO_2$:50Ag mol%, and (**c**) $30ZrO_2$:70Ag mol% [97]

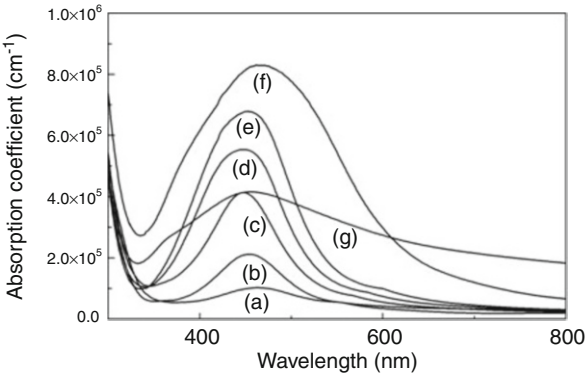

Fig. 8.27 Absorption spectra of ZrO_2–Ag films with different densities of silver nanoparticles: (*a*) 10 mol%, (*b*) 20 mol%, (*c*) 30 mol%, (*d*) 40 mol%, (*e*) 50 mol%, (*f*) 60 mol%, and (*g*) 70 mol% of silver [98]

become coagulated and their shapes changed to an oval shape. For [Ag]/[Zr] = 1.00 (Fig. 8.26b [97]), the particles show both spherical and oval shapes, and the appearance of coagulation lies in the middle in Fig. 8.26 [97]. With the case of any silver density, silver took a particle phase but not matrix.

The optical absorption spectra of ZrO_2 thin films doped with silver nanoparticles at various molar ratios are shown in Fig. 8.27 [98]. The films exhibit an absorption band centered at about 450 nm due to the surface plasmon resonance of silver nanoparticles. The absorption intensities become stronger as the densities of silver increase from 10 mol% to 50 mol%, while the peak wavelength remains constant. The FWHM of the peaks remains almost constant till the Ag density of 30 mol% and becomes relatively larger above the density. On the other hand, red shift of the absorption maximum to around 480 nm and the broadening of the peak were observed for the densities of silver above 60 %.

The observed absorption spectra were analyzed using the EMA model. In the EMA model, the effective permittivity ε_{eff} was described using the permittivity of the inclusion ε_i, the permittivity of matrix ε_e, the volume fraction of inclusion f, and the depolarization factor N. The following dielectric equation is given from the M–G model:

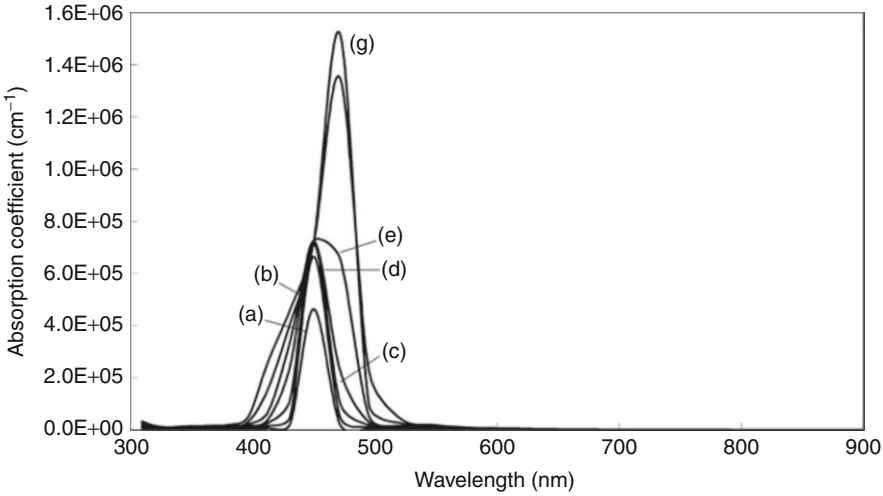

Fig. 8.28 Absorption spectra calculated by Maxwell–Garnett model of a ZrO_2 matrix with Ag nanoparticles for different values of the volume fraction f: (*a*) 5.3 %, (*b*) 11.1 %, (*c*) 17.7 %, (*d*) 25.0 %, (*e*) 33.3 %, (*f*) 42.9 %, and (*g*) 53.9 % [97]

$$\frac{\varepsilon_e - \varepsilon_{eff}}{\varepsilon_e + \kappa\varepsilon_{eff}} = f\frac{\varepsilon_i - \varepsilon_{eff}}{\varepsilon_i + \kappa\varepsilon_{eff}} \tag{8.38}$$

$$\varepsilon_{eff} = \varepsilon_e + \frac{N\alpha}{1 - N\alpha\gamma}, \quad \gamma \equiv \frac{1}{3\varepsilon_e} + \frac{K}{4\pi\varepsilon_e}, \quad \alpha = \frac{4\pi R^3(\varepsilon_i - \varepsilon_e)}{3[\varepsilon_e + \beta(\varepsilon_i - \varepsilon_e)]} \tag{8.39}$$

where R is the mean diameter of the nanoparticle for an ellipsoidal shape $R = (xyz)^{1/3}$, in which x, y, z represent the ellipsoid semiaxis, and β is the parameter depending on the particle geometry related with the depolarization factor N which takes a value of 1/3 for spherical shapes. The parameter K represents the ratio between the electric fields created at the particle position by the adjacent particles and created by the rest of the material.

The behaviors of the absorption spectra are simulated for the ZrO_2 matrix containing spherical silver nanoparticles by the Maxwell-Garnett model for different volume fractions f using the dielectric parameters of $\varepsilon_m = 3.57$ (dielectric constant of ZrO_2 matrix), $\beta = 1/3$ (spherical silver nanoparticles), and $R = 25$ nm (mean diameter of Ag nanoparticles) as shown in Fig. 8.28 [97]. In the case of silver densities from 10 mol% to 40 mol%, the peak intensities become stronger keeping same spectral profile as the density of silver increases. This result shows that the dielectric property of the ZrO_2–Ag composite does not depend on the silver density in the low volume fraction region. On the other hand, in the case of larger silver volume fraction region such as over 60 mol%, the absorption peak wavelength shows red shift from 450 to 480 nm and the spectral profile becomes broader, which cannot be simulated by the Maxwell-Garnett model.

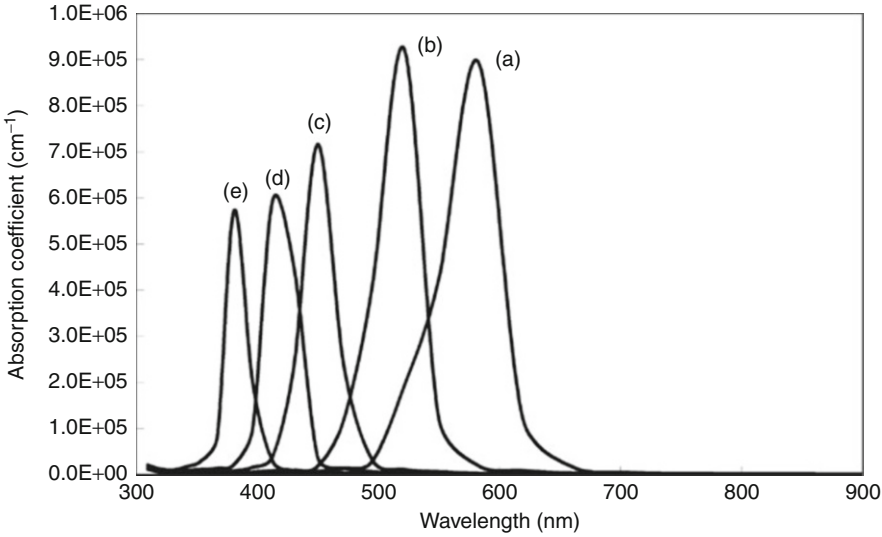

Fig. 8.29 Absorption spectra calculated by Maxwell–Garnett model for ZrO_2 matrix dispersed with Ag nanoparticles for different values of the shape parameter β: (*a*) 1/5, (*b*) 1/4, (*c*) 1/3, (*d*) 1/2.5, and (*e*) 1/2 [97]

Geometrical deviations of the nanoparticles from the perfect spherical shape correspond to the deviations of β parameter from 1/3. The absorption spectra calculated for the ZrO_2–Ag composite with various shapes of silver nanoparticles ranging β parameter from 1/5 to 1/2 are shown in Fig. 8.29 [97]. These values of β parameter define the particle aspect ratio from two times to half against the incident light direction, respectively. The absorption peak wavelength strongly depends on the β value. The peak position shifts toward shorter wavelength from 580 to 380 nm as the parameter β increases.

In order to check the applicability of the Maxwell-Garnett model for metal-dielectric composite quantitatively, the experimental results of ZrO_2 thin films containing 20 mol% of Ag nanoparticles were fitted. The particle diameter was fixed as 25 nm in the calculation from the TEM observation. The absorption spectrum calculated according to the M–G model is shown in Fig. 8.30a. The calculated absorption peak wavelength is well fitted to the experimental result except the difference in band width. The FWHM of the observed absorption band takes considerably larger value. This broadening of the band is considered caused by the distribution of the particle shape and size. Much better agreement with the experimental results was obtained when the particle shape distribution was considered as shown in Fig. 8.30a [97]. Excellent fit between the Maxwell-Garnett theory and experimental spectrum was found by assuming the particle geometry distribution corresponding to β parameters from 1/5 to 1/2 as shown in Fig. 8.30b [97]. The real distribution of the shape was observed for the synthesized composite system using a TEM, and the aspect ratio distribution of the particles from 1.0 to 2.75 was observed. This result supports the validity of the particle shape distribution used in the calculation.

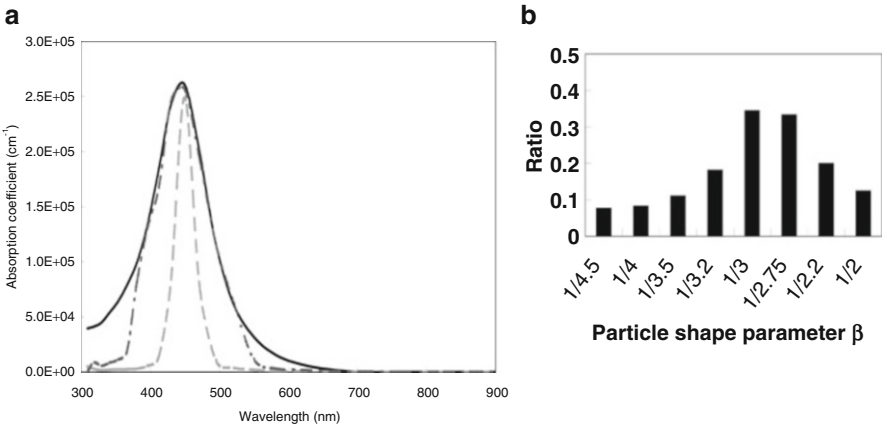

Fig. 8.30 (**a**) Experimental absorption spectrum (*solid curve*) of ZrO_2 matrix dispersed with Ag nanoparticles at the volume fraction of 20 mol% fitted by the M–G model (*dashed curve*) and the proposed model according to parameter value of β (*dash-dotted curve*). (**b**) Shape distribution of silver nanoparticles used for the profile simulation of the observed spectrum [97]

On the other hand, the calculated spectrum using the Maxwell-Garnett model did not agree well with the experimental one in the case of larger volume fraction region over 50 mol% of silver. In general, the Bruggeman model can be applied well to the larger volume fraction region. In the Bruggeman model, the effective dielectric constant of ZrO_2–Ag composite is calculated by using the following equation:

$$f\frac{\varepsilon_i - \varepsilon_{eff}}{\varepsilon_i + k\varepsilon_{eff}} + (1-f)\frac{\varepsilon_e - \varepsilon_{eff}}{\varepsilon_e + k\varepsilon_{eff}} = 0 \tag{8.40}$$

$$\varepsilon_{eff} = \frac{-c \pm \sqrt{c^2 + 4(1-\beta)\beta\varepsilon_e\varepsilon_i}}{4(1-\beta)}, \quad c = (\beta - f)\varepsilon_e + [\beta - (1-f)]\varepsilon_i \tag{8.41}$$

The absorption spectrum calculated according to the Bruggeman model was fitted well with the experimental spectra at the volume fraction of 70 mol% of silver as shown in Fig. 8.31 [97]. Comparing with the Maxwell-Garnett model, the Bruggeman model reproduced the absorption peak that shifted to longer wavelength with a broadened spectral shape. However, in the case of 60 mol% of silver, both the absorption peak wavelength and the spectral shape calculated by the Maxwell-Garnett and Bruggeman model did not fit well with the experimental spectrum. As a result, the applicability of the Maxwell-Garnett model is limited to smaller densities than 50 mol% and that of the Bruggeman model is over 70 mol % of silver density. It was suggested that a new model connecting the Maxwell-Garnett model and the Bruggeman model is necessary in the middle volume fraction region of silver.

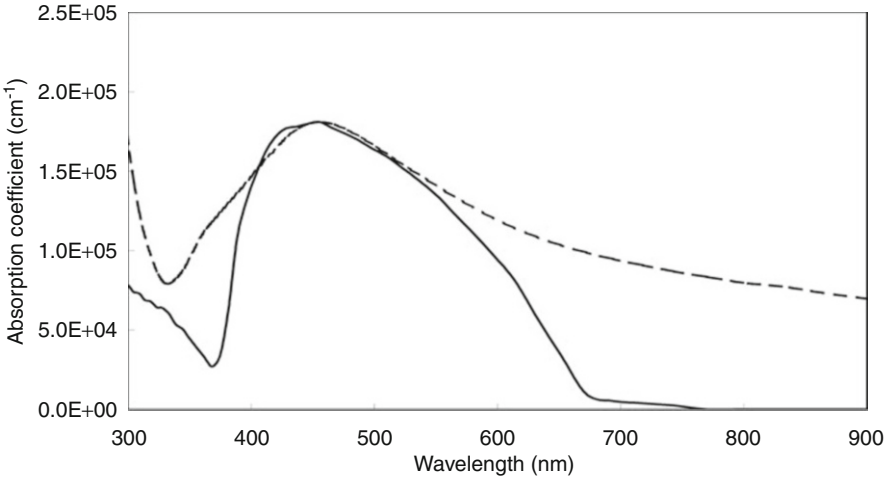

Fig. 8.31 Experimental absorption spectrum (*solid curve*) of ZrO_2 matrix dispersed with Ag nanoparticles at the volume fraction of 70 mol% fitted using the Bruggeman model (*dashed curve*) [97]

5.3 Applications of Metal Nanoparticles to Various Optoelectric Fields

5.3.1 Application to Immobilization by Light and Gilding

Giant particles of around several hundred nm grow by irradiating the near-infrared laser light of 1,064 nm upon the gold nanoparticles tailored with dodecanethiol (DT). During the process, immobilization phenomena proceed. By utilizing the phenomena, a new type of gilding is developed. Nanoparticles are immobilized on a glass substrate depending on the photomask by irradiating the pulsed laser light of 532 nm through the mask after dipping the glass substrate into the colloidal solution mentioned above. In case of immobilization of the catalyst within the flow channel to fabricate the electric line, it is required to fabricate before formation of flowing channel. However, the process becomes possible after forming the flow channel by using this technique [100, 101].

5.3.2 Photoelectric Conversion Technique Utilizing the Enhanced Electric Field

The aggregates of gold nanoparticles function as porous electrodes with the 3-dimensional structures under the condition electric conductivity are maintained. As a result, the surface area of the electrode increases, and the enhancement of the efficiency of molecular excitations by the localized enhanced electric field is expected. In case of the electrodes, the enhancement of photocurrent was observed in the wavelength region where the surface plasmon is excited by copying a single layer of gold nanoparticles onto the transparent electrode. The enhancement of florescence is also observed due to the increase of the excitation efficiency of dye molecules by the enhanced local electric field [102, 103].

5.3.3 Application for Optical Memories

The rod-like gold nanoparticles are known to exhibit two plasmon bands according to the difference in the resonance condition of the surface plasmon for longer and shorter axes [104]. One of the features of this gold nanorod is the deformation by the heat induced by the light. The development of application to optical memory is possible by utilizing this light-induced deformation within polymer. Polyvinyl alcohol dispersed with gold nanorods is used as a recording medium, and the plasmon band for a longer axis is excited selectively by irradiating the linear polarized laser light of 1,064 nm to induce the deformation of nanorods with the longer axis aligned to the direction of polarization. After the process, the spectra originating from the rods without the deformation are observed. On the other hand, the plasmon band for shorter axis is excited by irradiating the laser light of 532 nm, and the rods aligned vertically regarding to the excitation of 1,064 nm deform selectively. It is possible to write and read using the polarized light with two colors by this principle.

5.3.4 Applications for Sensing

The localized enhanced electric field is extremely effective to the surface-enhanced Raman scattering (SERS). The mechanism of SERS has not yet been made clear, but it is utilized as an ultrahigh sensitive measuring method because the normal Raman scattering intensity is enhanced by 10^{10}. But the degree of enhancement is quite sensitive to the nanostructure, and the reproducible fabrication method of a SERS chip has not been established. The researches of SERS utilizing the aggregates of gold nanoparticles and other spectroscopic methods are advancing steadily, and the transmission type of sensing of the localized plasmon resonance is proposed.

6 Conclusions and Future Perspective

It is requested to derive an easy to use mixing formula for material engineering applications, which combines the feature of low volume filling ratio properties in the Maxwell–Garnett mixing equation to that of percolation properties in the Bruggeman mixing equation. The equation should not involve any adjustable-free parameters, and the derivation is based only on the electromagnetic field analysis. The required parameters are the shape and volume fraction of inclusions and the permittivity of the matrix and inclusions. The new mixing equation can predict accurately the effective permittivity as a function of volume fraction of inclusions in the case where the shape of inclusions can be modeled as ellipsoids and their shape parameter is evenly distributed. With small volume filling fractions of inclusions, the Maxwell–Garnett mixing equation should be applied, because it takes the effect of the shape of inclusions correctly into account. When approaching the percolation threshold, the Bruggeman equation should be effective.

In this section, the main result of the new mixing equation [105] that combines the desired properties of both Maxwell–Garnett and Bruggeman models is

introduced. The derivation of the Maxwell–Garnett equation is based on combining the polarizability of an isolated particle with the averaged polarization effect of the effective medium. The drawback of the Maxwell–Garnett model is that when the volume filling ratio of spheres increases and the inclusion becomes connected to each other, the Maxwell–Garnett model underestimates the effective permittivity. In the derivation of the Bruggeman model, the internal field of spheres is calculated by assuming that the sphere is surrounded by the effective permittivity ε_{eff}, not by the permittivity of the environment phase ε_e. As a result, the Bruggeman equation is in good agreement with the simulated and measured values of the effective permittivity when the volume fraction of the inclusions is above the percolation threshold. However, when the volume fraction is below the percolation threshold, the Bruggeman tends to overestimate the effective permittivity.

The effective permittivity of a mixture ε_{eff} can be calculated using the Taylor expansion when the original background permittivity is ε_e and a differential amount of spheres is added:

$$\frac{\Delta\varepsilon_{eff}}{\varepsilon_e} = \frac{n\Delta\alpha}{\varepsilon_e} + \frac{\alpha\Delta n}{\varepsilon_e}, \quad \alpha = \frac{3\varepsilon_{eff}(\varepsilon_i - \varepsilon_{eff})V}{\varepsilon_i + 2\varepsilon_{eff}}, \quad \Delta\alpha = \frac{3V\varepsilon_i}{\varepsilon_i + 2\varepsilon_{eff}}\Delta\varepsilon_{eff} \tag{8.42}$$

where V is the volume of inclusion sphere, n is the number of spheres in the mixture, and Δn is the change in the number of spheres. α and $\Delta\alpha$ are the polarizability and the change in the polarizability, respectively. Equation 8.42 can be written as

$$\frac{\Delta\varepsilon_{eff}}{\varepsilon_e} = \frac{3\varepsilon_{eff}(\varepsilon_i - \varepsilon_{eff})}{\varepsilon_e(\varepsilon_i + 2\varepsilon_{eff})}\Delta f + \frac{3f\varepsilon_i}{\varepsilon_e(\varepsilon_i + 2\varepsilon_{eff})}\Delta\varepsilon_{eff} \tag{8.43}$$

where $f = nV$ is the volume fraction of spheres. The corresponding differential equation finally gives the resulting differential mixing rule as

$$\frac{d\varepsilon_{eff}}{df} = \frac{3\varepsilon_e(\varepsilon_i - \varepsilon_{eff})}{\varepsilon_i + 2\varepsilon_{eff} - 3f\varepsilon_i} \tag{8.44}$$

with the initial value $\varepsilon_{eff} = \varepsilon_e$ for the zero filling value $f = 0$. This differential equation is easy to solve numerically by starting from $\varepsilon_{eff} = \varepsilon_e$ with f = 0. For practical reasons, it is actually easier to solve the inverse function $df/d\varepsilon_{eff}$, especially if the electrical contrast between ε_i and ε_e is large. Even if no limiting value for $f = 1$ is assumed, the limit for ε_{eff} seems to be within ε_i for all filling ratios. If the inverse $df/d\varepsilon_{eff}$ is solved for $\varepsilon_e \leq \varepsilon_{eff} \leq \varepsilon_i$, then volume filling ratios are always exactly in the range $0 \leq f \leq 1$.

The solution for the inverse function of the differential equation with real values of ε_i and ε_e leads to the following equation:

$$f = 1 - \frac{1}{3}\frac{\varepsilon_i - \varepsilon_{eff}}{\varepsilon_i - \varepsilon_e}\left(2 + \left(\frac{\varepsilon_i - \varepsilon_{eff}}{\varepsilon_i - \varepsilon_e}\right)^{\varepsilon_i/\varepsilon_e - 1}\right) \tag{8.45}$$

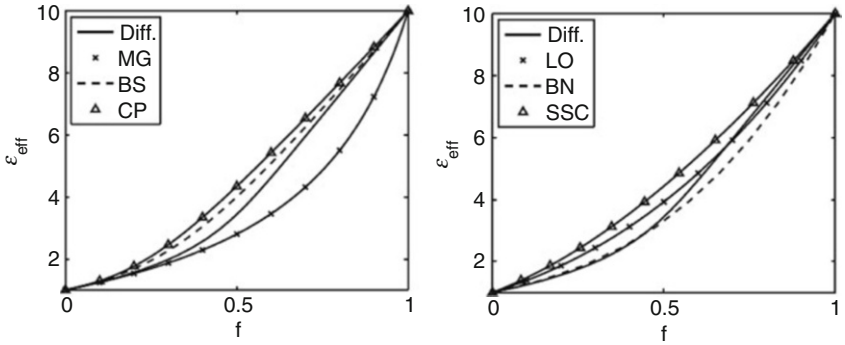

Fig. 8.32 Effective permittivity as a function of the volume filling ratio of spheres. The relative permittivity of the inclusions is $\varepsilon_i = 10$ and that of the environment is $\varepsilon_e = 1$ [105]

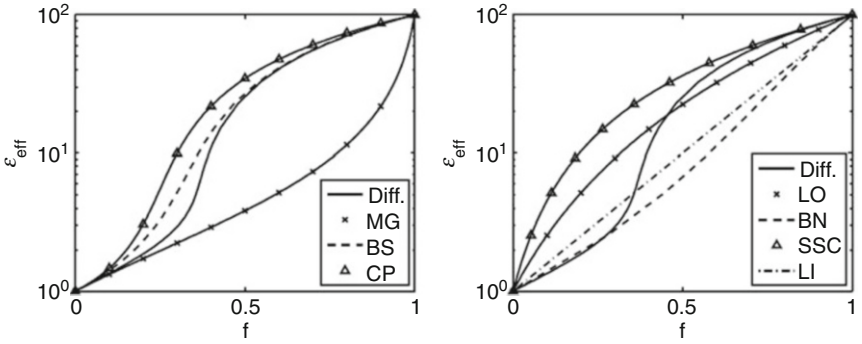

Fig. 8.33 Effective permittivity as a function of the volume filling ratio of spheres, where the relative permittivity of the inclusions is $\varepsilon_i = 100$ and that of the environment is $\varepsilon_e = 1$. The vertical scale is logarithmic [105]

The effective permittivity of the new mixing equation is shown in Fig. 8.32 as a function of volume fraction of spherical inclusions with the permittivity $\varepsilon_i = 10$ and $\varepsilon_e = 1$. On the left-hand side, the result of the differential equation (Diff.) is presented together with those of the Maxwell–Garnett (M–G), Bruggeman (BS), and coherent potential (CP) formulae and, on the right-hand side, with the Looyenga (LO), Bruggeman nonsymmetric (BN), and Sen–Scala–Cohen (SSC) formulae. The results of the same formulae are plotted for the higher contrast of the permittivity, $\varepsilon_i = 100$ and $\varepsilon_e = 1$ in Fig. 8.33. Note that the vertical axis is logarithmic in these figures.

Figures 8.32 and 8.33 show that the effective permittivity according to the differential mixing equation shifts smoothly from the Maxwell–Garnett model to the symmetric Bruggeman model as the volume fraction of spheres increases. Figure 8.33 shows clearly that the derivative of the effective permittivity in the limit $f \to 0$ is the same for all models on the left-hand side, but on the right-hand

side, it is very different for the Looyenga and Sen–Scala–Cohen models. It is required to check the validity of the new model using real materials and to make clear the limit of applications through further research.

References

1. Hosoya Y, Suga T, Yanagawa T, Kurokawa Y (1997) Linear and nonlinear optical properties of sol-gel-derived Au nanometer-particle-doped alumina. J Appl Phys 81:1475
2. Gang Y, Song-You W, Ming X, Liang-Yao C (2006) Theoretical calculation of the optical properties of gold nanoparticles. J Korean Phys Soc 49:2108
3. Faraday M (1857) Experimental relations of gold (and other metals) to light. Philos Trans R Soc 147:145
4. Kerker M (1986) Classics and classicists of colloid and interface science: 1. Michael Faraday. J Colloid Interf Sci 112:302
5. Turkevich J, Stevenson PC, Hiller J (1951) A study of the nucleation and growth processes in the synthesis of colloidal gold. Disc Faraday Soc 11:55
6. Turkevich J (1985) Colloidal gold. Part II Colour, coagulation, adhesion, alloying and catalytic properties. Gold Bull 18:86
7. Aika K, Ban LL, Oukra I, Namba S, Turkevich J (1976) Chemisorption and catalytic activity of a set of platinum catalysts. J Res Inst Catal Hokkaido Univ 24:54
8. Rampio LD, Nord FF (1941) Preparation of palladium and platinum synthetic high polymer catalysts and the relationship between particle size and rate of hydrogenation. J Am Chem Soc 63:2745
9. Rampio LD, Nord FF (1941) Applicability of palladium synthetic high polymer catalysts. J Am Chem Soc 63:3268
10. Dunsworth WP, Nord FF (1950) Investigations on the mechanism of catalytic hydrogenations XV. Studies with colloidal iridium. J Am Chem Soc 72:4197
11. Hirai H, Chawanya H, Toshima N (1985) Selective hydrogenation of cyclooctadienes using colloidal palladium in poly(N-vinyl-2-pyrrolidone). Bull Chem Soc Jpn 58:682
12. Yonezawa T, Waseda Y, Muramatsu A (2004) Morphology-controlled materials: advanced materials processing and characterization. Springer, Berlin, pp 85–112
13. Toshima N, Yonezawa T (1998) Bimetallic nanoparticles-novel materials for chemical and physical applications. New J Chem 22:1179
14. Haruta M (2002) Catalysis of gold nanoparticles deposited on metal oxides. CATTECH 6:102
15. Komiyama M, Hirai H (1983) Colloidal rhodium dispersions protected by cyclodextrins. Bull Chem Soc Jpn 56:2833
16. Lewis LN, Lewis N, Uriate RJ (1992) In homogeneous transi- tion metal catalyzed reactions. Adv Chem Ser 230:541
17. Larpent C, Brisse-Le Menn F, Ptin H (1991) New highly water-soluble surfactants stabilize colloidal rhodium(0) suspensions useful in biphasic catalysis. J Mol Catal 65:25
18. Henry A, Bingham J, Ringe E, Marks L, Schatz G, Van Duyne R (2011) Correlated structure and optical property studies of plasmonic nanoparticles. J Phys Chem C 115:9291
19. Sau T, Rogach A, Jaeckel F, Kuar T, Feldman J, Klar T (2010) Properties and applications of colloidal nonspherical noble metal nanoparticles. Adv Mater 22:1805
20. Sau T, Rogach A (2010) Nonspherical noble metal nanoparticles: colloid-chemical synthesis and morphology control. Adv Mater 22:1781
21. Cuenya B (2010) Synthesis and catalytic properties of metal nanoparticles: size, shape, support, composition, and oxidation state effects. Thin Solid Films 518:3127

22. Khlebtsov N, Dykman L (2010) Optical properties and biomedical applications of plasmonic nanoparticles. J Quant Spectrosc Radiat Transfer 111:1
23. Noguez C, Garzon I (2009) Optically active metal nanoparticles. Chem Soc Rev 38:757
24. Sakamoto M, Fujistuka M, Majima T (2009) Light as a construction tool of metal nanoparticles: synthesis and mechanism. J Photochem Photobiol C 10:33
25. Love S, Marquis B, Haynes C (2008) Recent advances in nanomaterial plasmonics: fundamental studies and applications. Appl Spectrosc 62:346A
26. Schwartzberg A, Zhang J (2008) Novel optical properties and emerging applications of metal nanostructures. J Phys Chem C 112:10323
27. Karmakar B, Som T, Singh S, Nath M (2010) Nanometal-glass hybrid nanocomposites: synthesis, properties and applications. Trans Indian Ceram Soc 69:171
28. Abe K, Hanada T, Yoshida Y, Tanigaki N, Takiguchi H, Nagasawa H, Nakamoto M, Yamaguchi T, Yase K (1998) Two-dimensional array of silver nanoparticles. Thin Solid Films 327:524
29. Hirai H, Nakao Y, Toshima N (1978) Preparation of colloidal rhodium in poly(vinyl alcohol) by reduction with methanol. J Macromol Sci A12:1117
30. Hirai H, Nakao Y, Toshima N (1979) Preparation of colloidal transition metals in polymers by reduction with alcohols or ethers. J Macromol Sci A13:727
31. Hirai H (1979) Formation and catalytic functionality of synthetic polymer-noble metal colloid. J Macromol Sci A14:633
32. Toshima N, Wang Y (1993) Novel preparation, characterization, and catalytic properties of Cu/Pd bimetallic clusters. Chem Lett 22:1611
33. Wang Y, Liu H, Toshima N (1996) Nanoscopic naked Cu/Pd powder as air-resistant active catalyst for selective hydration of acrylonitrile to acrylamide. J Phys Chem 100:19533
34. Lu P, Toshima N (2000) Catalysis of polymer-protected Ni/Pd bimetallic nano-clusters for hydrogenation of nitrobenzene derivatives. Bull Chem Soc Jpn 73:751
35. Lu P, Teranishi T, Asakura K, Miyake M, Toshima N (1999) Polymer-protected Ni/Pd bimetallic nano-clusters: preparation, characterization and catarysis for hydrogenation of nitrobenzene. J Phys Chem B 103:9673
36. Sapieszko RS, Matijevic E (1981) Hydrothermal formations of (hydrous) oxides on metal surfaces. Corrosion 37:152
37. Yonezawa T, Tominaga T, Richard D (1996) Stabilizing structure of tertiary amine-protected rhodium colloid dispersions in chloroform. J Chem Soc Dalton Trans 1996:783
38. Drognat Landre P, Richard D, Draye M, Gallezot P, Lemaire M (1994) Colloidal Rhodium: a new catalytic system for the reduction of dibenzo-18-crown-6 ether. J Catal 147:214
39. Schmid G, Pfell R, Bose R, Bandermann F, Meyer S, Calls GHM, van der Velden JWA (1981) Au55[P(C6H5)3]12Cl6 – a gold cluster of unusual size. Chem Ber 114:3634
40. Brust M, Fink J, Bethell D, Schiffrin DJ, Kiely CJ (1994) Synthesis of thiol-derivatised gold nanoparticles in a two-phase Liquid–Liquid system. J Chem Soc Chem Commun 1994:801
41. Yamanoi Y, Yonezawa T, Shirahata N, Nishihara H (2004) Immobilization of gold nanoparticles onto silicon surfaces by Si − C covalent bonds. Langmuir 20:1054
42. Yonezawa T, Matsune H, Kimizuka N (2001) Self-organized superstructures of fluorocarbon-stabilized silver nanoparticles. Adv Mater 13:140
43. Yonezawa T, Genda H, Koumoto K (2003) Cationic silver nanoparticles dispersed in water prepared from insoluble salts. Chem Lett 32:194
44. Henglein A, Tausch-Treml R (1981) Optical absorption and catalytic activity of subcolloidal and colloidal silver in aqueous solution: a pulse radiolysis study. J Collid Interface Sci 80:84
45. Belloni J, Delcourt MO, Leclere C (1982) Radiation-induced preparation of metal catalysts: iridium aggregates. Nouv J Chim 6:507
46. Torigoe K, Remita H, Beaunier P, Belloni J (2002) Radiation-induced reduction of mixed silver and rhodium ionic aqueous solution. Rad Phys Chem 64:215
47. Belloni J, Mostafavi M, Remita H, Marignir JL, Delcourt MO (1998) Radiation-induced synthesis of mono- and multi-metallic clusters and nanocelloids. New J Chem 22:1239

48. Toshima N, Takahashi T, Hirai H (1988) Polymerized micelle-protected platinum clusters preparation and application to catalyst for visible light-induced hydrogen generation. J Macromol Sci Chem A25:669
49. Hada H, Yonezawa Y, Yoshida A, Kuratake A (1976) Photoreduction of silver ion in aqueous and alcoholic solutions. J Phys Chem 80:2728
50. Toshima N, Takahashi T (1992) Colloidal dispersion of platinum and palladium cluster embedded in micelles. Preparation and application to catalysis for hydrogenation of olefins. Bull Chem Soc Jpn 65:400
51. Kreibig U (1977) Anomalous frequency and temperature dependence of the optical absorption of small gold particles. J Physique 38:97
52. Bloemer MJ, Haus JW, Ashley PR (1990) Degenerate four-wave mixing in colloidal gold as a function of particle size. J Opt Soc Am B7:790
53. Doremus RH, Rao P (1996) Optical properties of nanosized gold particles. J Matter Res 11:2834
54. Kineri T, Mori M, Kadono K, Sakaguchi T, Miya M, Wakabayashi H, Tsuchiya T (1993) Preparation and optical properties of gold-dispersed BaTiO3 thin films. J Ceram Soc Jpn 101:1340
55. Tanahashi I, Yoshida M, Manabe Y, Tohda T (1996) Characterization and optical properties of Au/SiO_2 composite thin films. Suf Rev Lett 3:1071
56. Tanahashi I, Manabe Y, Tohda T, Sasaki S, Nakamura A (1996) Optical nonlinearities of Au/SiO_2 composite thin films prepared by a sputtering method. J Appl Phys 79:1244
57. Yang L, Osborne DH, Haglund RF Jr, Magruder RH, White CW, Zuhr RA, Hosono H (1996) Probing interface properties of nanocomposites by third-order nonlinear optics. Appl Phys A62:403
58. Magruder RH, Yang LI, Haglund RF Jr, White CW, Yang L, Dorsinville R, Alfano RR (1993) Optical properties of gold nanocluster composites formed by deep ion implantation in silica. Appl Phys Lett 62:1730
59. Arnold GW (1975) Near-surface nucleation and crystallization of an ion-implanted Lithia-alumina-silica glass. J Appl Phys 46:4466
60. Matsuoka J, Mizutani R, Kaneko S, Nasu H, Kamiya K (1992) Preparation of Au-doped silica glass by sol-gel method. J Ceram Soc Jpn 100:599
61. Matsuoka J, Mizutani R, Kaneko S, Nasu H, Kamiya K, Kadono K, Sakaguchi T, Miya M (1993) Sol-gel processing and optical nonlinearity of gold colloid-doped silica glass. J Ceram Soc Jpn 101:53
62. Trimm DL, Onsan ZI (2001) Onboard fuel conversion for hydrogen-fuel-cell-driven vehicles. Catal Rev 43:31
63. Wiley B, Sun Y, Xia Y (2007) Synthesis of silver nanostructures with controlled shapes and properties. Acc Chem Res 40:1067
64. Skrabalak SE, Chen J, Au L, Lu X, Li X, Xia Y (2007) Gold nanocages for biomedical applications. Adv Mater 19:3177
65. McLellan JM, Li ZY, Siekkinen AR, Xia Y (2007) The SERS activity of a supported Ag nanocube strongly depends on its orientation relative to laser polarization. Nano Lett 7:1013
66. Xia Y, Xiong Y, Lim B, Skrabalak SE (2009) Shape-controlled synthesis of metal nanocrystals: simple chemistry meets complex physics? Angew Chem Int Ed 48:60
67. Wiley BJ, Sun Y, Xia Y (2005) Polyol synthesis of silver nanostructures: control of product morphology with Fe(II) or Fe(III) species. Langmuir 21:8077
68. Sun Y, Xia Y (2002) Shape-controlled synthesis of gold and silver nanoparticles. Science 298:2176
69. Skrabalak SE, Wiley BJ, Kim M, Formo EV, Xia Y (2008) On the polyol synthesis of silver nanostructures: glycolaldehyde as a reducing agent. Nano Lett 8:2077
70. Wiley BJ, Im SH, Li ZY, McLellan J, Siekkinen A, Xia Y (2006) Maneuvering the surface plasmon resonance of silver nanostructures through shape-controlled synthesis. J Phys Chem B 110:15666
71. Kan C-X, Zhu J-J, Zhu X-G (2008) Silver nanostructures with well-controlled shapes: synthesis, characterization and growth mechanisms. J Phys D 41:155304

72. Siekkinen AR, McLellan JM, Chen J, Xia Y (2006) Rapid synthesis of small silver nanocubes by mediating polyol reduction with a trace amount of sodium sulfide or sodium hydrosulfide. Chem Phys Lett 432:491
73. Lim B, Camargo PH, Xia Y (2008) Mechanistic study of the synthesis of Au nanotadpoles, nanokites, and microplates by reducing aqueous HAuCl4 with poly(vinyl pyrrolidone). Langmuir 24:10437
74. Lu X, Yavuz MS, Tuan HY, Korgel BA, Xia Y (2008) Ultrathin gold nanowires can be obtained by reducing polymeric strands of oleylamine – AuCl complexes formed via aurophilic interaction. J Am Chem Soc 130:8900
75. Wu H-L, Kuo C-H, Huang MH (2010) Seed-mediated synthesis of gold nanocrystals with systematic shape evolution from cubic to trisoctahedral and rhombic dodecahedral structures. Langmuir 26:12307
76. Lu X, Tuan TY, Korgel BA, Xia Y (2008) Facile synthesis of gold nanoparticles with narrow size distribution by using AuCl or AuBr as the precursor. Chem Eur J 14:1584
77. Li C, Shuford KL, Park QH, Cai W, Li Y, Lee EJ, Cho So O (2007) High-yield synthesis of single-crystalline gold nanooctahedra. Angew Chem Int Ed 46:3264
78. Seo D, Yoo CI, Chung IS, Park SM, Ryu S, Song H (2008) Shape adjustment between multiply twinned and single-crystalline polyhedral gold nanocrystals: decahedra, icosahedra, and truncated tetrahedra. J Phys Chem C 112:2469
79. Xiong Y, Chen J, Wiley B, Xia Y (2005) Understanding the role of oxidative etching in the polyol synthesis of Pd nanoparticles with uniform shape and size. J Am Chem Soc 127:7332
80. Xiong Y, Cai H, Wiley BJ, Wang J, Kim MJ, Xia Y (2007) Synthesis and mechanistic study of palladium nanobars and nanorods. J Am Chem Soc 129:3665–75
81. Xiong Y, McLellan JM, Chen J, Yin Y, Li ZY, Xia Y (2005) Kinetically controlled synthesis of triangular and hexagonal nanoplates of Pd and their SPR/SERS properties. J Am Chem Soc 127:17118
82. Korte KE, Skrabalak SE, Xia Y (2008) Rapid synthesis of silver nanowires through a CuCl- or CuCl2-mediated polyol process. J Mater Chem 18:437
83. Draine BT, Flatau PJ (1994) Discrete dipole approximation for scattering calculations. J Opt Soc Am A 11:1491
84. Maxwell Garnett JC (1904) Colours in metal glasses and in metallic films. Philos Trans Roy Soc A 203:385–420
85. Bruggeman DAG (1935) Berechnung verschiedener physikalischer Konstanten von heterogenen Substanzen. I. Dielektrizitatskonstanten and Leitfahigkeiten der Mischkorper aus isotropen Substanzen. Annalen der Physik 24:636–64
86. Elliot RJ, Krumhansl JA, Leath PL (1974) The theory and properties of randomly oriented disordered crystals and related physical systems. Rev Modern Phys 46:465–543
87. Looyenga H (1965) Dielectric constants of heterogeneous mixtures. Physica 31:401–6
88. Lichtenecker K (1926) Dielectric constant of natural and synthetic mixtures. Phys Z 27:115
89. Moulson A, Herbert J (2003) Electroceramics. Wiley, New York
90. Stroud D, Pan FP (1978) Self-consistent approach to electromagnetic wave propagation in composite media: application to model granular metals. Phys Rev B 17:1602–10
91. Wachniewski A, McClung HB (1986) New approach to effective medium for composite materials: application to electromagnetic properties. Phys Rev B 33:8053–9
92. Bohren C, Huffman D (1983) Absorption and scattering of light by small particles. Wiley, NewYork
93. Bussemer P (1989) Optical properties of inhomogeneous media: T-matrix approach (Review). Astron Nachr 310:311–4
94. Chylek P, Srivastava V (1983) Dielectric constant of a composite inhomogeneous medium. Phys Rev B 27:5098–105
95. Chylek P, Videen G, Geldart D, Dobbie J, Tso HW (2000) Effective medium approximation for heterogeneous particles, in light scattering by nonspherical particles: theory, measurements, and geophysical applications. Academic, New York, pp 273–308

96. Stognienko R, Henning T, Ossenkopf V (1995) Optical properties of coagulated particles. Astron Astrophys 296:797–809
97. Wakaki M, Yokoyama E (2010) Dielectric analysis on optical properties of zro_2 thin films dispersed with silver nanoparticles. J Nonlinear Opt Phys Mater 19:835
98. Yokoyama E, Sakata H, Wakaki M (2009) Sol-gel synthesis and characterization of Ag nanoparticles in ZrO_2 thin films. J Mater Res 24:2541
99. Wakaki M, Yokoyama E (2011) Optical properties of dielectric films dispersed with metal nanoparticles and applications to optically functional materials. Proc SPIE 8173:81731 G.1
100. Niidome Y, Hori A, Sato T, Yamada S (2000) Enormous size growth of thiol-passivated gold nanoparticles induced by near-IR laser light. Chem Lett 129:310
101. Niidome Y, Hori A, Takahashi H, Goto Y, Yamada S (2001) Laser-induced deposition of gold nanoparticles onto glass substrates in cyclohexane. Nano Lett 1:365
102. Akiyama T, Nakada M, Terasaki N, Yamada S (2006) Photocurrent enhancement in a porphyrin-gold nanoparticle nanostructure assisted by localized plasmon excitation. Chem Commun 28:395–397
103. Akiyama T, Aiba K, Hoashi K, Wang M, Sugawa K, Yamada S (2010) Enormous enhancement in photocurrent generation using electrochemically fabricated gold nanostructures. Chem Commun 46:306
104. Yamada S, Niidome Y (2006) Gold nanorods: preparation, characterization, and applications to sensing and photonics. In: Kawata S, Masuhara H (eds) Nanoplasmonics from fundamentals to applications, vol 2. Elsevier, Amsterdam, p 255
105. Jylha L, Sihvola A (2007) Equation for the effective permittivity of particle-filled composites for material design applications. J Phys D 40:4966

Optical Properties of Silicon Nanowires

9

Optical Properties of Silicon Nanowires and Other Nanostructures

Michael M. Adachi, Mohammedreza Khorasaninejad, Simarjeet S. Saini, and Karim S. Karim

Contents

1 Definition of the Topic

Silicon nanowires exhibit strong antireflective properties and are capable of enhancing optical absorption over that of bare bulk crystalline silicon. Low-dimensional silicon nanowires also exhibit luminescence visible to the naked eye under laser excitation. This chapter summarizes recent theoretical and experimental studies on the optical properties of silicon nanowires. The optical properties of silicon nanocones and core-shell nanowires are also discussed. Silicon nanowires are characterized by UV–VIS-NIR and photoluminescence spectroscopy.

M.M. Adachi (✉) • M. Khorasaninejad • S.S. Saini • K.S. Karim
Department of Electrical and Computer Engineering, University of Waterloo, Waterloo, ON, Canada

Challa S.S.R. Kumar (ed.), *UV-VIS and Photoluminescence Spectroscopy for Nanomaterials Characterization*, DOI 10.1007/978-3-642-27594-4_9,

2 Overview

One-dimensional silicon growth dates back to the early 1960s when Wagner and Ellis discovered the growth of catalyst-assisted single-crystalline silicon "whiskers" from vapor phase. However, study of the optical properties of silicon nanowires has been relatively recent. In this chapter, recent reports on the theoretical and experimental optical properties of silicon nanowires are summarized. Modeling of silicon nanowires is discussed to explain why nanowires improve absorption. Silicon nanowires and nanocones have been experimentally shown to exhibit strong antireflective properties and be capable of having high broadband optical absorption. The reflection spectrum of an array of silicon nanowires can also be tuned by controlling the diameter or periodicity of the nanowires. In addition, low-dimensional nanowires have been reported to emit light upon excitation by a laser. Applications that make use of these unique optical properties are also discussed.

3 Introduction

Silicon is an ideal material for a vast range of electronic and photonic applications because it readily forms thermally grown silicon dioxide and is stable after oxidation, is nontoxic, is abundant in the Earth's crust, and is cost-effective. Additionally, silicon-based device fabrication technology is mature and well established in the microelectronic industry. However, the optical properties of silicon are less than ideal mainly because of its indirect bandgap. In other words, recombination and generation of electrons require a phonon interaction. As a result, thick layers are necessary to efficiently absorb light, and light emission is inefficient. A number of methods have been developed to overcome these limitations, one of which is to use an array of nanostructures with sizes comparable to the wavelength of incident light. One such nanostructure is the nanowire, which has a very high length-to-diameter aspect ratio and a diameter on the order of nanometers to hundreds of nanometers. Silicon nanowires with diameters on the order of tens to hundreds of nanowires have been shown to exhibit strong antireflective properties and can enhance optical absorption as compared to bulk crystalline silicon. In addition, nanowires with diameters on the order of nanometers to tens of nanometers can exhibit strong luminescence visible to the naked eye when excited by a laser.

Over the last decade, considerable research has gone into investigating the unique optical properties of silicon nanowires not observed in bulk silicon. Although a number of review chapters have been published on the synthesis and structural characterization of inorganic nanowires, this chapter differs in that the topic of discussion focuses on the optical properties of silicon nanowires. The term "quasi-nanowire" will be used to refer to nanowires with a small aspect ratio (also known as nanorods) and the term "nanocone" to nanowires that are tapered.

The antireflective property of an array of subwavelength-sized structures was first discovered by Bernhard, et al. In 1967, Bernhard showed that a periodic array of conical perturbations on the corneal lens of a moth eye-suppressed optical

reflection [1]. He proposed that the perturbations gave rise to a gradient in the refractive index between that of air and the lens material and showed by upscaled reflection measurements that such perturbations significantly lowered reflection as compared to a smooth cornea sample. Clapham, in 1973, fabricated artificial moth eye structures by patterning photoresist on glass and showed that they reduced the integrated specular reflection of white light to 0.2 % [2]. In 1979, Gittleman et al. showed that an array of silicon pillars with diameters and spacing small compared to the incident wavelength of light lowered specular reflection to values of 10^{-3} or less at wavelengths below 1 μm [3]. Similarly, Craighead et al. 1980 showed that submicron texturing lowered thin film amorphous silicon reflection to nearly zero over the visible spectrum [4]. Since then, various groups have reported strong antireflective properties in silicon nanowires [5, 6], quasi-nanowires (i.e., nanorods) [7–9], tapered nanostructures [10, 11], and other nanoscale structures [12–14].

The optical absorption of silicon nanowires was first studied in bottom-up grown nanowires. Holmes et al. [15] observed that the "absorbance" of small-diameter (4–5 nm) silicon nanowires suspended in hexane exhibited discrete peaks. The peaks were strongly blue-shifted with respect to the bandgap of bulk silicon of 1.1 eV. In larger-diameter nanowires on the order of tens to hundreds of nanometers, strong optical absorption enhancement can be attained [16–19]. A number of theoretical studies have since shown that silicon nanowires, of appropriate diameter and periodicity, can significantly enhance optical absorption for solar cells applications [16–18]. Experimental measurements of silicon nanowires on glass substrates have also shown that silicon nanowires can enhance absorption over the entire solar spectrum [19].

Arrays of silicon nanowires have been incorporated into solar cells by a number of groups [5, 6, 20–26]. The overall performance of these devices remains lower than that of the highest recorded crystalline silicon conversion efficiency of 24.7 % [27]. One of the main challenges in nanowire solar cells is the increase of surface recombination velocity due to the high surface area of silicon nanowires [5]. Nonetheless, silicon nanowire solar cells have demonstrated ultralow reflection losses [6] and increased photo-generated current density compared to a planar silicon solar cell used as a control [24, 26]. Furthermore, the high aspect ratio of nanowires can improve collection efficiency in radial p-n junction solar cells for materials with low minority-carrier diffusion lengths [28].

Silicon nanowires with diameters on the order of nanometers to tens of nanometers have also exhibited strong luminescence at room temperature. Yu et al. [29] in 1998 showed that silicon nanowires with uniform diameters around 15 nm emitted blue light visible to the naked eye when excited by a 325-nm laser. Due to the large diameter of nanowires, the luminescence was attributed to the 2-nm-thick silicon oxide sheath that coated the nanowires rather than to quantum size effects. Low-dimensional nanowires have also exhibited photoluminescence (PL), attributed to quantum confinement effects [15, 30] and possibly surface states. Further details of photoluminescence from silicon nanowires are discussed in Sect. 3.3.

Top-down and bottom-up fabrication techniques of silicon nanowires are described in Sect. 2. The instrumentation methodology of UV–VIS and photoluminescence spectroscopy is also presented in this section. Both theoretical and experiment key research findings are presented in Sect. 3. Modeling of the optical properties of silicon nanowires is discussed in subsection 3.1 to better understand how nanowires can enhance absorption over that of bulk silicon. Experimental measurements of the reflection and absorption of silicon nanowires are summarized in subsection 3.2. Absorption in crystalline-amorphous silicon core-shell nanowires and nanocones are also discussed in this subsection. Finally, photoluminescence measurements exhibiting blue-shifted light emission from small-diameter silicon nanowires is discussed in subsection 3.3.

4 Experimental and Instrumental Methodology

4.1 Fabrication of Silicon Nanowires

Fabrication of silicon nanowires can be categorized into two approaches: top-down and bottom-up as illustrated in Fig. 9.1. In the top-down approach, a crystalline silicon wafer or silicon thin film is etched either by metal-induced (usually Ag) chemical etch using a HF-based solution [5], electrochemical etching [31], or dry etching [32, 33] to form vertical nanowires. During the metal-induced chemical etch process, a metal induces excessive local oxidation at the silicon surface, and submersion in HF solution leads to silicon dissolution [5]. This fabrication technique is weakly dependent on silicon crystal orientation and can therefore also be used in multicrystalline [22] or polycrystalline silicon [5]. Nanowires can also be formed by a two-step process of nanosphere [32] or electron beam [33] lithography for defining an etch mask followed by a reactive ion etch (RIE) or electrochemical etch [31]. In nanosphere lithography, a monolayer of nanospheres can be formed by a number of methods such as spin coating [34], floating-transferring technique [35], or the Langmuir-Blodgett technique [24, 32]. Alternatively, self-powered parallel electron lithography can be used to pattern photoresist into a periodic array with sub-35-nm high resolution [33]. Nanowires fabricated by the top-down approach are typically aligned vertically but can also be fabricated to be slanted [21].

There are two bottom-up nanowire growth approaches: the well-known metal-catalyzed vapor-liquid–solid (VLS) technique [36] and the oxide-assisted technique [37]. In both techniques, nanowires can be directly grown on various substrates such as glass, silicon wafer, and metal foils. The VLS growth mechanism involves the chemical reaction between a silicon source gas such as SiH_4, Si_2H_6, SiI_2, or $SiCl_4$ and a droplet of metal catalyst. At elevated temperatures, the silicon source gas and metal droplet form a liquid alloy, and supersaturation of the liquid alloy causes nanowire nucleation and growth to occur. Silicon atoms diffuse through the catalyst droplet and crystallize at the liquid–solid interface resulting in one-dimensional growth. The diameter of the nanowire is therefore controlled by the catalyst size.

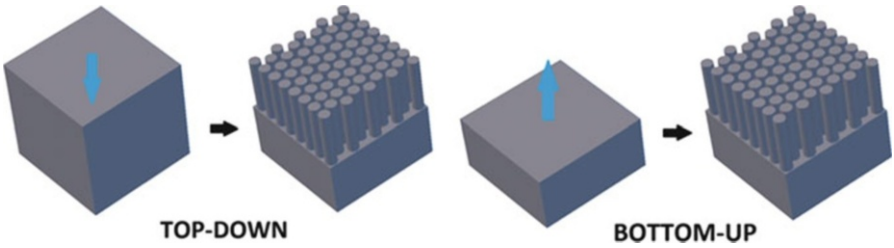

Fig. 9.1 Illustration of the top-down and bottom-up fabrication approaches. The top-down approach involves etching a silicon wafer or film by chemical or dry etching. The bottom-up approach involves growing nanowires from gas or liquid phase onto various substrates such as glass, silicon, or metal foil

The most common method for forming the catalyst droplet is by annealing a thin film of metal causing it to agglomerate into separate nano-sized droplets. Other methods of fabrication include spin coating of presynthesized nanoparticles or patterning of a thin film metal into islands by lithography. The most common catalyst used is Au, but various elements have been used such as Pt, Ag, Pd, Cu, Ni [36], Al [38], Fe [29], Ga[39], In[40], Zn [41], Ti [42], and Sn [43]. During nanowire growth, Au from the catalyst droplet wets the nanowire sidewall, eventually depleting the droplet at which point nanowire growth stops [44]. In addition, according to the Gibbs-Thomson effect, the nanowire growth ceases below a critical minimum diameter $d_c \leq 0.1$ μm [45]. Nonetheless, nanowires with single crystal silicon core diameters as small as 2 nm have been prepared using SiH_4 as the source gas and well-defined presynthesized Au nanoclusters as the catalyst [46]. Silicon nanowires can be grown by the VLS method over a wide range of temperatures ranging from about 950°C down to 320°C [47]. However, nanowires grown at low temperatures are more susceptible to growth defects such as kinks and bends [47]. Alternatively, very small-diameter nanowires (e.g., 4–5 nm) can be grown from a solution-phase source (e.g., Diphenylsilane) heated and pressurized beyond its critical point (e.g., 500°C and 270 bar respectively) [15].

The crystal orientation of silicon nanowires grown by VLS method can be controlled by using a monocrystalline silicon substrate [36, 48]. Using photolithography to define the location of catalyst islands and a silicon (111) substrate acting as a crystalline seed, a periodic array of vertically aligned nanowires can be fabricated [49].

The second bottom-up growth method is the oxide-assisted growth technique in which nanowires are synthesized by thermal evaporation or laser ablation of silicon powder mixed with silicon dioxide or pure silicon monoxide powder. In this method, oxides play a key role in the nucleation and growth of silicon nanowires [37, 50]. Fabrication is carried out in the temperature range of 850 °C and 1,200 °C, and nanowires consist of a crystalline silicon core surrounded by an oxide shell. Diameters approaching 1 nm [51, 52] are achievable with this method and the growth direction is mainly <112> and <110> [50]. A comparison between the bottom-up and top-down fabrication methods is given in Table 9.1.

Table 9.1 Advantages and disadvantages of the top-down and bottom-up fabrication approaches

	Top-down	Bottom-up
Advantages	Nanowires have identical crystal structure and doping properties as the initial substrate [5]	Nanowires are highly crystalline or single crystal [36]
	Simple fabrication is feasible at near room temperature [5]	Nanowires can be grown on nonsilicon substrates for large area applications
	Vertical alignment is common	Low-dimensional diameters down to 1 nm are possible [51, 52]
		Extremely high aspect ratios are possible (up to 100,000) [54]
		Nanowires can be doped in situ axially [55] and radially [56]
Disadvantages	Fabrication requires a starting silicon wafer or film	Catalysts used during VLS growth introduce impurities
	Carrier lifetimes are known to increase after dry etching [53] and chemical etching [5]	Nanowires are not directionally aligned when grown on a nonsilicon substrate
	Aspect ratios can be limited	Growth requires temperatures to be $\geq$ 320°C [47]
		Nanowires grown at low temperatures and high pressures are susceptible to bending and kinking [47]

4.2 Instrumental Methodology

The measured optical properties of silicon nanowires discussed in this chapter are characterized by two methods: ultraviolet–visible-near-infrared (UV–VIS-NIR) and photoluminescence spectroscopy. Spectrophotometry is the measurement of the reflection, transmission, and absorption of electromagnetic radiation. Ultraviolet–visible (UV–VIS) spectroscopy covers the spectral range of ultraviolet (200–400 nm) and visible (400–800 nm) wavelengths in which electron transitions occur between energy bands. Transmittance, T, is defined as the ratio of the intensity of light that passed through a sample, I_T, to the intensity of light before passing through the sample, I_o (i.e., $T(\lambda) = I_T(\lambda)/I_o(\lambda)$). Similarly reflectance, R, can be defined as the ratio of the intensity of light that is reflected by a sample, I_R, to the intensity of incoming light, I_o (i.e., $R(\lambda) = I_R(\lambda)/I_o(\lambda)$). This chapter defines absorption as $A = 1-T-R$, where T is the total transmission (including both specular and diffuse components) and R is the total reflection (including both specular and diffuse components). Specular reflection corresponds to reflected light which has the same angle with respect to the surface normal as the incident light, and diffuse reflection is the reflected light which is randomly distributed. Similarly, specular transmission corresponds to unscattered transmitted light and diffuse transmission refers to transmitted light that is randomly distributed.

An integrating sphere, a hollow sphere with an interior surface that has high diffuse reflectivity (i.e., near-Lambertian reflectivity), is used to measure total R and T. Note that there is another measurement in spectroscopy called "absorbance" which is only a function of transmission, defined as $-log(T)$.

UV–VIS spectrophotometers typically make measurements over the wavelength range of 200–1,000 nm, depending on the detector, light source, and integrating sphere used. UV–VIS-NIR spectrophotometers use a near-IR detector, such as a PbS detector, to extend the range of near-infrared detection to wavelengths of about 3,300 nm. The extended wavelength range is important in the case of silicon nanowires because nanowires have strong near-infrared absorption, and impurity defects can result in subbandgap absorption.

Photoluminescence spectroscopy involves the excitation of a sample with a monochromatic light source and the detection of the emitted light. The excitation source is usually a laser with a wavelength typically ranging from 270 to 514.5 nm. A spectrum of photoluminescence is obtained by scanning and measuring the emitted light over a range of wavelengths. A monochromator is used to select narrow bands of wavelengths of the emitted light from the sample which is measured using a detector such as a photomultiplier, photodiode, or charge-coupled device.

5 Key Research Findings

This section summarizes both theoretical and experimental findings on the optical properties of silicon nanowires. First, the optical modeling of vertically aligned silicon nanowires is discussed in subsection 3.1. Here, the effect of nanowire diameter, length, and periodicity on the optical reflection, transmission, and absorption is summarized. Experimentally measured reflection and absorption spectra of arrays of silicon nanowires, characterized by UV–VIS-NIR spectroscopy, are presented in subsection 3.2. Finally, photoluminescence of silicon nanowires is discussed in subsection 3.3.

5.1 Optical Modeling

The modeling of ordered and disordered silicon nanowire arrays requires different modeling methodologies to predict and optimize reflection and absorption. Ordered nanowire arrays are easier to model as periodic boundary conditions can be used to reduce the simulation domain. Low-dimensional nanowires exhibit quantum confinement [57] which changes the optical properties significantly. Some of these experimentally observed phenomena will be discussed later in subsection 3.3. For the discussions below, only larger-diameter nanowires which do not exhibit quantum confinement are considered. In this case, the absorption coefficients are considered to be the same as that of bulk silicon.

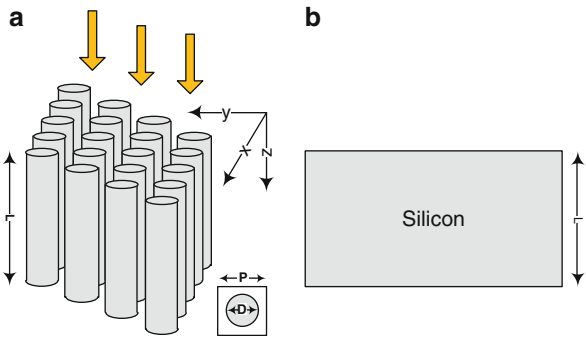

Fig. 9.2 Schematic diagram of (**a**) an infinite array of silicon nanowires and (**b**) thin film silicon. D represents the diameter of silicon nanowires and P is the periodicity of the unit cell

5.1.1 Ordered Silicon Nanowires

Figure 9.2a shows a schematic diagram of an ordered array of silicon nanowires. The design parameters include the diameter of the nanowires (D), the length of the nanowires (L), and the periodicity (P) of the array. In this schematic, a square lattice is used. Similarly, other periodic arrangements such as hexagonal lattice can also be used. In order to model an array, the structure is considered infinite in the transverse directions, x and y. For solar cell applications, the incident light can be considered as a plane wave. This allows defining a unit cell consisting of a nanowire with a periodicity of P and using periodic boundary conditions in the transverse directions. Thus, the simulation boundary can be reduced to a very small size, equal to that of the periodicity. Maxwell's equations under an input excitation can be solved for the unit cell using well-established numerical techniques such as the transfer matrix method (TMM), full wave finite element (FE) and finite difference time domain (FDTD). All these methods solve the same problem with periodic boundary conditions and lead to similar results. The main difference between these methods is the computational resources required. TMM is one of the most commonly used numerical techniques because it is an efficient frequency-domain method based on simple matrix operations. In this method, the structure is initially divided into a number of sections. At the beginning of each section, electromagnetic field components are calculated by means of numerical methods such as the finite element or finite difference methods. TMM is then used to calculate how the electromagnetic field components change through each section based on a transfer matrix.

The effect of diameter, pitch, and length on absorption of silicon nanowire arrays has been studied over the last few years. Hu et al. [16] simulated arrays of silicon nanowires for solar cell applications. The absorptance, reflectance, and transmittance of nanowires with a diameter of 50 nm and periodicity of 100 nm are shown in Fig. 9.3. The incident wave is normal to the x-y plane as illustrated in Fig. 9.2a. A few interesting results are apparent from the figure. The reflection from the silicon nanowire arrays was very low over the complete spectral range. The absorption is also very high compared to bulk silicon at high energies ($>\sim$2.8 eV) resulting in most of the incident photons being absorbed. This increased absorption mainly resulted from low reflection allowing more light to

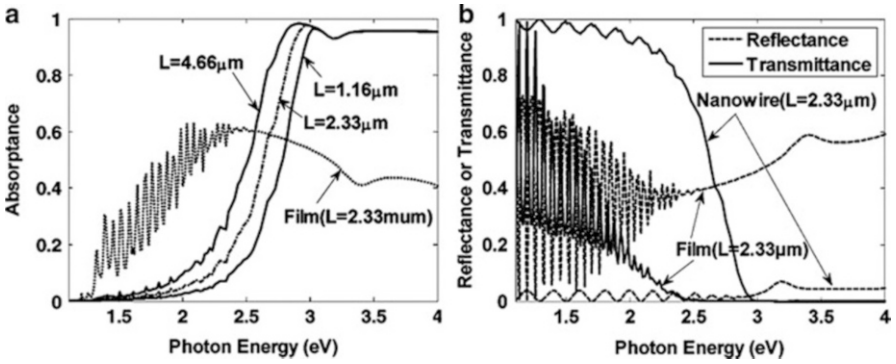

Fig. 9.3 (**a**) Absorptance spectra for silicon nanowires with diameter and periodicity of 50 nm and 100 nm respectively, for different length of 1.16, 2.33, and 4.66 μm, the silicon thin film is shown for comparison. (**b**) Reflectance and transmittance spectra for nanowires and thin film (Reprinted with permission from [16]. Copyright 2007, American Chemical Society)

penetrate into the silicon nanowires. Further, as the length was increased, the absorption edge shifted to the lower-energy spectrum. However, at lower energies, the absorption of the silicon nanowire array was still less than that of a reference silicon thin film. Consequently, the overall absorption efficiency of silicon nanowires integrated over the solar spectrum was lower than the silicon thin film for these designs.

In the above simulations, the array of nanowires was considered to be floating, surrounded by air above and below. This creates a Fabry-Perot cavity within the nanowires and light bounces back and forth in the vertical direction. As a consequence, ripples in the reflection and transmission spectra can be observed. This Fabry-Perot effect makes it difficult to differentiate the light trapping by nanowire arrays in the transverse direction (due to scattering and recapturing of light by nanowires) and the light trapped in the longitudinal direction due to the Fabry-Perot resonances. In order to understand whether absorption can be increased by light trapping in the transverse direction of nanowires compared to bulk silicon, it is therefore useful to model a semi-infinite array of silicon nanowires where the nanowires are considered to be infinitely long in the bottom direction. Figure 9.4 shows the reflection (a) and absorption (b) characteristics of periodic nanowire structures after transmitting through the first 1 μm of the nanowires at normal incidence. A perfectly matched layer (PML) (i.e., artificially absorbing layer with no reflections) was used at the bottom interface to simulate the semi-infinite nanowire length condition [58]. The absorption and reflection is also shown for different diameters while keeping the diameter-to-periodicity ratio constant at D/P = 0.5. The absorption and reflection for semi-infinite bulk silicon is shown for reference. Again, a similar shift of the absorption band edge as reported by Hu et al. was observed. However, interestingly light trapping by a resonance effect in the silicon nanowires was also observed, increasing the absorption compared to bulk silicon within a certain energy band. For example, when D = 100 nm, the

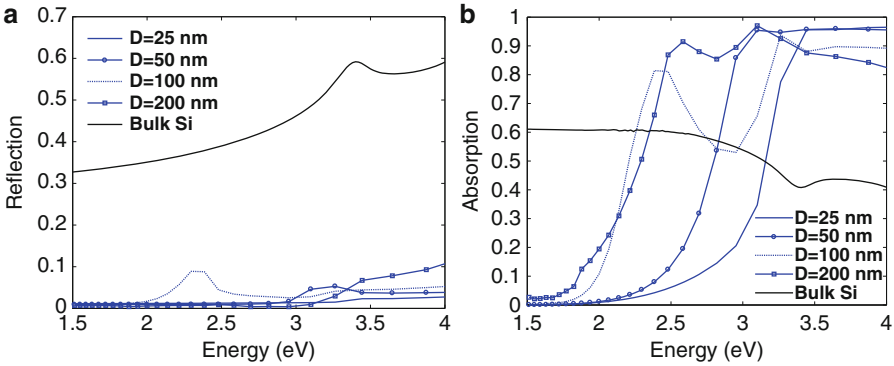

Fig. 9.4 (**a**) Reflection and (**b**) absorption of a periodic array of silicon nanowires after passing through the first 1 μm of the nanowires with different diameters and periodicity. For all simulation, D/P = 0.5. The nanowires are semi-infinitely long with no reflections at the bottom surface. Reflection and absorption through bulk silicon is also shown for comparison

absorption is increased at energies between 2.0 and 2.5 eV and at energies above 3.0 eV. Note that nanowires can be considered as cylindrical optical waveguides. At high energies, the confinement of the optical mode within the nanowires is large resulting in high absorption. When these nanowires are brought together in an array, a "supermode" can result over a certain wavelength region from constructive phase coupling of the modes of neighboring nanowires [59]. Nanowires with different diameters have resonances at different energies which are observable in Fig. 9.4. This suggests that depending on the application, one can optimize the nanowire array dimensions for enhanced absorption of light over a specific energy range. From an optical waveguide perspective, larger-diameter nanowires result in improved optical confinement within the silicon nanowires resulting in increased absorption.

Rigorous optimization of the diameter and the periodicity for 2.33-μm-long nanowires has been investigated by Lin et al. [17]. For solar cell applications, larger-diameter nanowires showed higher total conversion efficiency as compared to smaller diameters. The optimized design consisted of a diameter of 540 nm and a periodicity of 600 nm (i.e., D/P = 0.9), resulting in an efficiency improvement of 72.4 % in nanowire solar cells as compared to that of silicon thin film devices with equal thickness and no antireflective coatings. Even with an optimized single layer antireflective coating on the thin film silicon, the ultimate efficiency of silicon nanowires was 17.2 % higher than that of silicon thin film. The design of silicon nanowire arrays for solar cell application was also studied by Li et al. in which the nanowire length was 5 μm [18]. The absorption, reflection, transmission, and ultimate efficiency results are shown in Fig. 9.5. Again, the incident light is parallel to the nanowire axis. For a low periodicity of P = 100 nm, absorption was significant at higher energies (>2.5 eV) as had been previously shown by Hu et al. [16]. By increasing P to 300 nm, the absorption edge was shifted toward lower energies as shown in Fig. 9.5a. However, further increase in P to 600 and

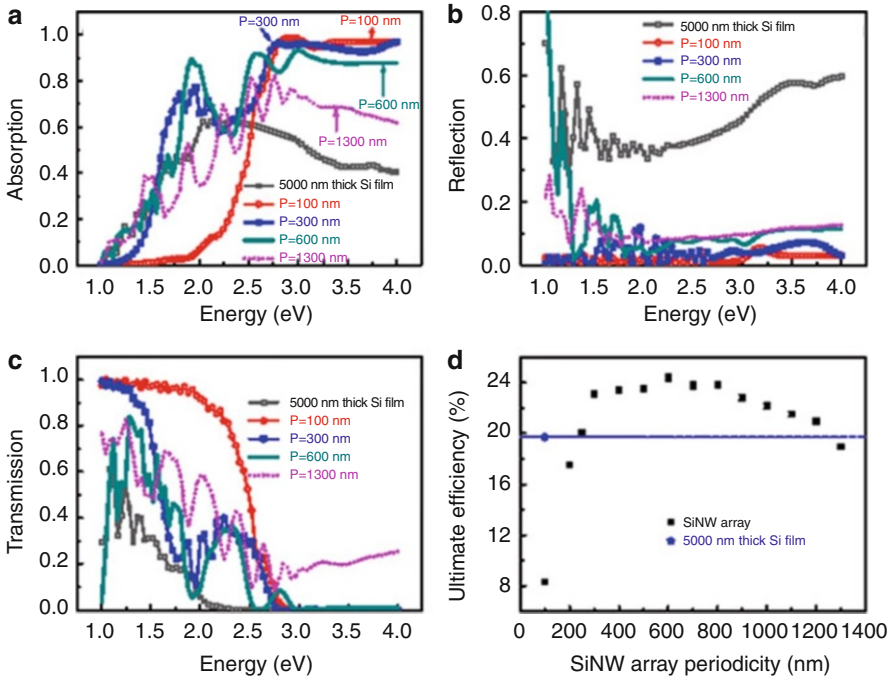

Fig. 9.5 (**a**) Absorption, (**b**) reflection, and (**c**) transmission spectra of silicon nanowire (SiNW) arrays for different periodicities, P. D/P = 0.5 for all cases. (**d**) The ultimate efficiency of a silicon nanowire array as a function of periodicity. The ultimate efficiency of a 5,000-nm-thick silicon film is shown for reference (Reprinted with permission from [18]. Copyright 2009, American Institute of Physics)

1,300 nm resulted in a decrease in absorption at high energies due to an increase in reflection, shown in Fig. 9.5b. In order to compare the absorption efficiency of silicon nanowires with a silicon thin film, the ultimate efficiency (η) for various periodicities was calculated, shown in Fig. 9.5d. As P was increased, η increased significantly, exceeding that of the 5-μm-thick silicon film at around P = 250 nm and reached a maximum efficiency of ~24 % at P ~ 600 nm. For P greater than 600 nm, η decreased due to an increase in reflection. The maximum η was found when the periodicity was between 300 and 900 nm as shown in Fig. 9.6. A maximum efficiency of 30.5 % was calculated for a D/P value of about 0.8 and P = 600 nm.

A configuration consisting of periodic vertically aligned silicon nanowires on top of an 800-nm-thick film of silicon was also simulated [60]. In this analysis, the silicon nanowire diameter is considered to be half of the periodicity between the nanowires in the array, and the length was 1 μm. Figure 9.7 shows the ultimate efficiency as a function of the silicon nanowire periodicity. A maximum efficiency of 27 % was predicted for the periodicity of 500 nm and diameter of 250 nm. The ultimate efficiency for the composite structure was considerably higher than the silicon thin film with equal total thickness and was comparable to ultimate efficiency of the 5,000-nm-long silicon nanowire array in Fig. 9.6.

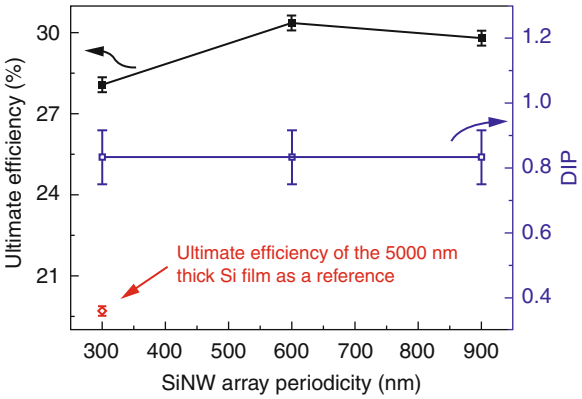

Fig. 9.6 The maximum ultimate efficiency of silicon nanowire arrays as a function of periodicity, P. The ultimate efficiency of a 5,000-nm-thick silicon film is shown for reference. The corresponding D/P ratios are also shown, indicating an optimal ratio of ~0.8 (Reprinted with permission from [18]. Copyright 2009, American Institute of Physics)

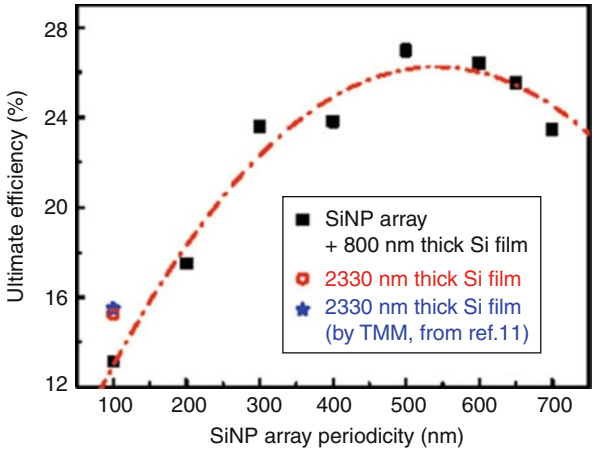

Fig. 9.7 The ultimate efficiency of a configuration consisting of 1-μm-long silicon nanowires on top of an 800-nm-thick film of silicon as a function of periodicity, P. The star indicates the ultimate efficiency of 2,330-nm-thick silicon film adopted from ref. [16] (Reprinted with permission from [60]. Copyright 2009, American Institute of Physics)

5.1.2 Disordered Nanowire Arrays

Thus far, we have considered an ideal case where the nanowire diameter and position were well defined and aligned vertically. While such nanowires can be fabricated by e-beam lithography followed by dry etching [61], most other fabrication methods result in nanowires with disordered characteristics. From a modeling perspective, disorder can be considered in which the diameter, pitch, and length of the nanowires vary randomly about average values. Bao et al. [62] used a pseudorandom process to study the effect of randomness in these physical parameters of silicon nanowire arrays on optical properties. Subcells measuring 200 nm × 200 nm containing an individual nanowire were considered. The position and the diameter within this subcell were determined randomly around an average value. The length of the nanowires was 2 μm. Sixteen of these units cells in a matrix of

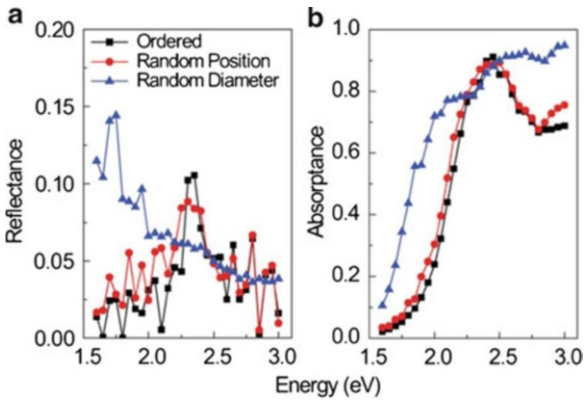

Fig. 9.8 Calculated (**a**) reflection and (**b**) absorption spectra for ordered and random silicon nanowire arrays (Reprinted with permission from [62])

4 × 4 were grouped together to form a single unit cell. Periodic boundary conditions were applied on the composite unit cell to simulate a nanowire array. Thus, while the nanowires were random in the groups of 16, the pattern repeated itself in the traverse directions. For each parameter they studied, simulations were performed for eight different random configurations and the results were averaged. Figure 9.8 shows the absorption and reflection from these pseudorandom nanowire arrays for two different configurations. In the first configuration, the diameter of the nanowire in a subcell is randomly chosen between 60 and 140 nm but the nanowires are positioned in the center of the subcell. In the second configuration, the position of the nanowire is randomly chosen within the subcell but the diameter was kept constant at 100 nm. Results for ordered nanowires with a single diameter of 100 nm are shown for reference. For an array consisting of random diameter nanowires, the reflection at low energies increased compared to ordered nanowires. However, the net absorption increased significantly and broadened to lower energies because the variation in diameter gave rise to different resonant frequencies and absorption peaks. In contrast, randomly located nanowires showed a similar absorption and reflectance spectra as the ordered nanowires. Furthermore, nanowires with random lengths, while keeping the diameter and position constant, also showed absorption enhancement compared to ordered arrays due to optical scattering by the nanowires (not shown) [62].

Nanowires grown by the bottom-up approach are characteristic of consisting of a range of diameter, position, length, and growth orientation. The simulation methodology used so far is not appropriate for such simulations as it will be computationally prohibitive. Purely disordered nanowires have however been analyzed semianalytically by assuming the nanowires to be a scattering mat in front of a partial reflecting surface (i.e., the substrate) [63].

5.2 UV–VIS-NIR Spectroscopy Measurements

UV–VIS-NIR spectroscopy is used to measure reflection, transmission, and absorption as a function of wavelength or angle of incidence. The reflection and absorption

for both top-down- and bottom-up-fabricated silicon nanowires are discussed in this subsection. The effect of diameter on absorption of crystalline-amorphous core-shell silicon nanowires is also considered, followed by a discussion of the enhanced optical absorption observed in silicon nanocones.

5.2.1 Reflection of Silicon Nanowires

Silicon is the most prevalent material used in solar cells but reflection of bare-polished crystalline silicon is very high in air (>30 % over the solar spectrum). Therefore, solar cells usually employ an antireflection coating to lower reflection losses. However, antireflection coatings (ARCs) have their own disadvantages such as limited wavelength range of operation in single layer antireflection coatings, an increase in fabrication complexity since precise thickness control is required or degradation over time when concentrators are used.

Microstructured or nanostructured surfaces are also commonly used to lower reflection. Surface texturing of (100)-oriented silicon into anisotropically etched pyramids has been shown to improve device performance in nonreflecting (black silicon) solar cells [64]. A well-textured silicon substrate can lower the average reflection to about 0.1 over the solar spectrum at normal incidence which can be further lowered to about 0.03 using an antireflective coating [65]. A nanostructured surface can also achieve ultralow reflection over a wide range of wavelengths. For example, an array of silicon nanowires fabricated by etching in HF-H_2O_2 solution can lower reflection to values of 2.1 % or less in the wavelength range of 300–1,100 nm [66].

Broadband antireflective properties of nanowires have also been observed in both vertically aligned nanowires as well as disordered nanowires. This subsection summarizes recent findings on the optical properties of silicon nanowires fabricated by both the top-down and bottom-up approaches. Since nanowires grown by these two approaches differ in terms of structure (e.g., aspect ratio, directional alignment, variation in diameter), doping method, and fabrication conditions (e.g., substrate type, temperature), their discussion will be treated separately.

Nanowires fabricated by the top-down approach can be etched either by chemical or dry etching. An array of vertically aligned silicon nanowires fabricated by etching the surface of a monocrystalline (111)-oriented silicon wafer using an aqueous HF/$AgNO_3$ solution for 20 min. at 50°C is shown in Fig. 9.9a [5]. The nanowires after etching were confirmed by TEM to have an identical crystalline orientation as the initial substrate. Figure 9.9b compares the hemispherical reflection of these nanowires with a bare-polished silicon substrate, porous silicon substrate, and a nanowire array synthesized from a polycrystalline silicon wafer. The reflection was observed to drop to about 5 % or less over the wavelength range of 300–1,000 nm, significantly lower than the starting silicon substrate and also lower than the porous silicon sample. A very similar low reflection spectrum was measured for nanowires etched from a polycrystalline silicon substrate also shown in Fig. 9.9b [5].

Periodic quasi-nanowires, fabricated using a combination of nanosphere lithography and etching, also have excellent antireflective properties [7, 31]. For example, periodic quasi-nanowires fabricated by Au-assisted electrochemical

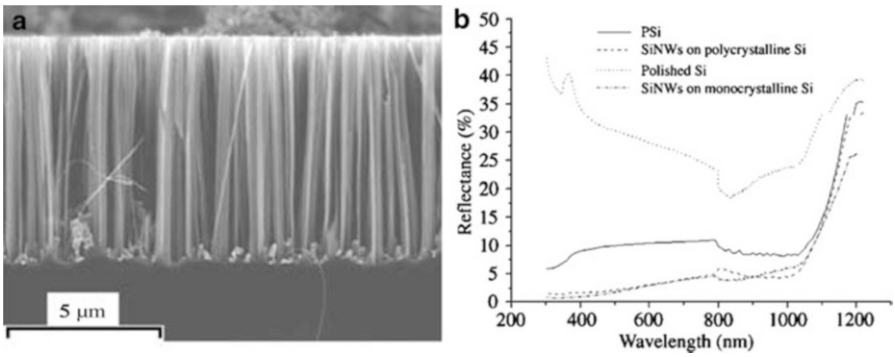

Fig. 9.9 (**a**) SEM cross-section image of a silicon nanowire array synthesized by etching a p-type (100)-oriented silicon substrate in an aqueous HF/$AgNO_3$ solution. (**b**) Hemispherical reflection measurements of polished crystalline silicon, porous silicon (PSi), and silicon nanowire (SiNW) arrays prepared on polycrystalline silicon and monocrystalline silicon substrates (Reprinted with permission from [5])

etching have been reported to have a total reflectance of <15 % for a short nanowire length of 332 nm and <3 % for longer lengths of 2.12, 3.80, and 5.33 μm over the wavelength range of 250–1,200 nm [31]. The reflection spectra can also be tuned by adjusting the nanowire diameter [67] or periodicity [68]. For example, periodic nanowires with varying radii of 45–70 nm have been shown to have distinctly different colors covering the entire visible spectrum [67]. The reflection spectra of nanowires dipped at wavelengths depending on the radius of nanowire. Nanowire arrays with radii of 45, 55, and 70 nm appeared red, blue, and green, respectively. The shift in reflection dip was attributed to the guided mode properties of individual nanowires. Shift in reflection peak to higher wavelengths has also been observed in tapered silicon quasi-nanowires with increasing periodicity [68] and crystalline-amorphous core-shell nanowires with increasing shell thickness [69]. Such color filtering effect could find application in image sensor devices.

Disordered silicon nanowires fabricated by the bottom-up approach have also exhibited antireflective properties. A cross-section SEM of an array of silicon nanowires grown by the VLS method using an Au catalyst on crystalline silicon substrate is shown in Fig. 9.10a. The average diameter of the nanowires was about 50 nm. The diffuse reflection (thin line) and specular reflection (thick line), shown in Fig. 9.10b, were significantly lower than that the reflectance of a bare silicon substrate (dashed line), particularly at low energies. The specular reflection decreased for increasing photon energy to near-zero values above 1.5 eV, but the diffuse reflection increased up to 33 % at 2.2 eV due to scattering. Suppression of the diffuse reflectance is possible by filling the space between nanowires with an intermediate refractive index medium such as indium tin oxide (ITO) or changing the nanowire diameter [70].

VLS grown nanowires incorporated into a thin film solar cell have demonstrated ultralow specular reflection. Tsakalakos et al. showed that nanowire solar cells

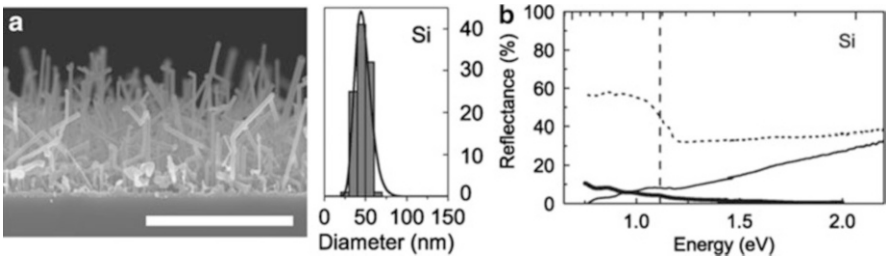

Fig. 9.10 (**a**) Cross-section SEM image of silicon nanowires fabricated by MOVPE growth and histogram of nanowire diameter. *Scale* bar of the SEM image is 2 μm. (**b**) Diffuse reflection (*thin line*) and coherent beam specular reflectance (*thick line*) of the silicon nanowires on crystalline silicon substrates. The reflectance of a bare silicon substrate is shown by the dashed line for comparison (Reprinted with permission from [70]. Copyright 2008 American Chemical Society)

consisting of p-type nanowires (diameter = 109 ± 30 nm) coated by a conformal 40-nm-thick n^+ a-Si film and 200-nm-thick ITO had a specular reflection of <1 % over the wavelength range of 300–1,100 nm [6]. Compared to a thin film p-i-n a-Si solar cell, the specular reflection of the nanowire solar cell was one to two orders of magnitude lower over the same spectral range. Although the conversion efficiency of the nanowire device was low (~0.1 %), it demonstrated photovoltaic response over a broad wavelength range showing potential for collection efficiency enhancement.

5.2.2 Absorption of Silicon Nanowires

The absorption spectrum can also be obtained by UV–VIS-NIR spectroscopy. Absorption is defined as $A = 1 - T - R$, where T is the total transmission and R is the total reflection. The transmission measurement of nanowires requires a transparent substrate such as glass [19, 20], growth in solution phase [15], or embedding in a transparent polymer and removed from a substrate such as crystalline silicon [71]. Therefore, absorption measurements are more common in bottom-up grown nanowires since they can be grown directly onto a transparent. Nonetheless, absorption measurements in nanowire arrays fabricated by etching a thin film of silicon on glass [22, 32] or etching a silicon-on-insulator substrate followed by removing the supporting silicon substrate [33] are also possible.

Figure 9.11(iii) shows the absorption spectra of silicon nanowires (curves a–c) grown by the VLS method on glass as well as that of a 11-μm silicon film (curve d) for comparison [19]. The absorption of silicon nanowires grown using three different catalyst thicknesses of 5 nm (curve c), 2.5 nm (curve b), and 1 nm (curve c) were noticeably high at low wavelengths between 300 and 450 nm as compared to the silicon thin film. The highest absorption was observed in the densest nanowire array, grown using an Au thickness of 5 nm, which was higher than the silicon film over a broad wavelength range of 300–2,000 nm. Interestingly, absorption at infrared wavelengths that correspond to energies below the bandgap of silicon was also very high. This subbandgap absorption was attributed to defect states and is also known to occur in silicon microspikes [72].

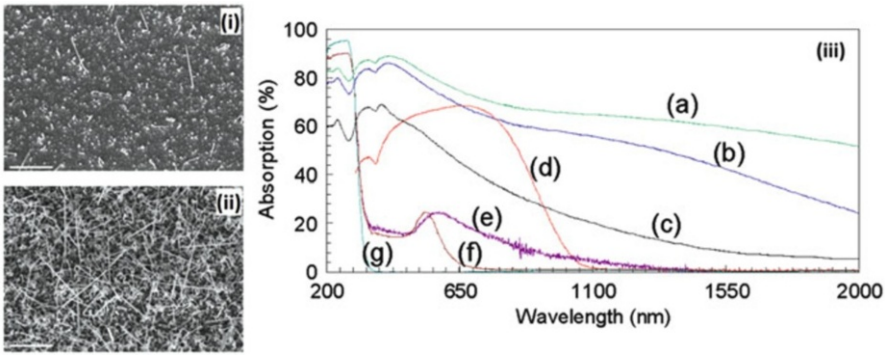

Fig. 9.11 SEM image of silicon nanowires grown by the VLS method using an Au catalyst thickness of (i) 1.0 nm and (ii) 5.0 nm. The scale bar is 4 μm. (iii) Optical absorption for nanowires using a catalyst thickness of (**a**) 5 nm, (**b**) 2.5 nm, and (**c**) 1 nm. The absorption of **a** (**d**) 11-μm-thick silicon film and a 5-nm Au film on glass substrate (**e**) before annealing and (**f**) after annealing and **a** (**g**) bare glass substrate are shown for comparison (Reprinted with permission from [19])

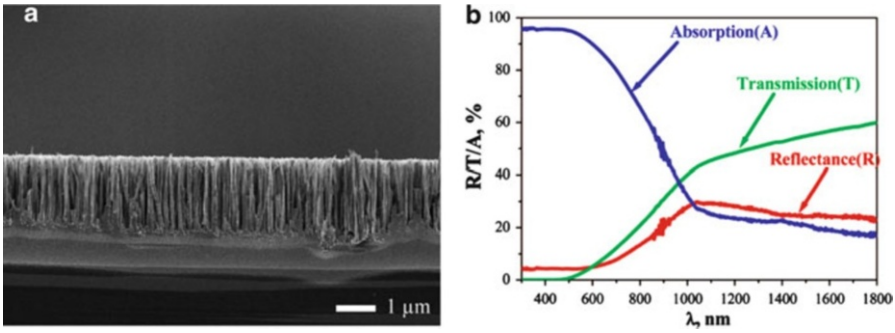

Fig. 9.12 (**a**) Cross-section SEM of $AgNO_3$/HF etched 2.7-μm-thick multicrystalline silicon film on glass. (**b**) Absorption, transmission, and reflection spectra of the nanowire sample (Reprinted with permission from [22]. Copyright 2009 American Chemical Society)

The absorption of top-down fabricated nanowires has also been shown to be high, particularly at low wavelengths. A cross sectional SEM of silicon nanowires on glass is shown in Fig. 9.12a. Nanowires were fabricated by $AgNO_3$/HF etching a 2.7-μm-thick multicrystalline silicon thin film. The highly dense array consists of nanowires with diameters ranging from 20 to 100 nm and an etch depth of about 2.3–2.5 μm with respect to the surface. The absorption, transmission, and reflection spectra of the nanowires are shown in Fig. 9.12b. At wavelengths between 300 and 500 nm, transmission through the silicon nanowires was zero, reflection was <10 %, and absorption was >90 %. Furthermore, the absorption of the nanowire array was higher than the silicon film of same thickness at wavelengths >550 nm [22].

Silicon nanowires with micron-sized diameters synthesized by the VLS method have also showed high absorption characteristics [71]. A periodic array of vertically

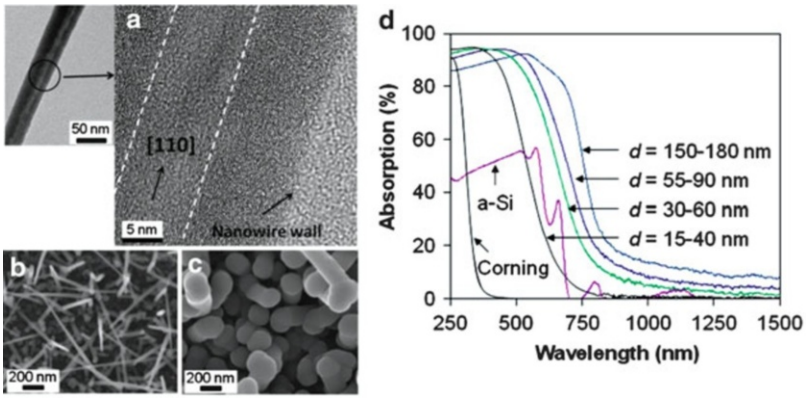

Fig. 9.13 (**a**) TEM image of a core-shell silicon nanowire consisting of a highly crystalline silicon core with a diameter of about 9 nm surrounded by an amorphous silicon shell. Plan-view SEM images of an array of crystalline-amorphous core-shell silicon nanowires with total diameters ranging from (**b**) 15–40 nm and (**c**) 150–180 nm. (**d**) Absorption $(1-T-R)$ as a function of wavelength for silicon nanowires grown on Corning glass with various total diameters, d. The absorption of a thin film of a-Si with a thickness of $t = 400$ nm is also shown for comparison. For the lowest diameter silicon nanowire array of $d = 15$–40 nm, the short wavelength absorption was very high (95 %) but dropped abruptly to <2 % for longer wavelengths, $\lambda > 780$ nm. The absorption edge of silicon nanowires shifted to longer wavelengths for the larger total diameter nanowire arrays beyond the absorption edge of the thin film amorphous silicon (Reprinted with permission from [69]. Copyright American Chemical Society)

aligned nanowires was fabricated by the VLS method on a <111> silicon wafer and later removed by embedding them in a transparent polymer called polydimnethlysiloxane (PDMS) and peeling them off. Due to the vertical orientation of the wires, the absorption of the nanowire array was low (<50 %) at normal incidence but increased with increasing incident angle. Incorporating a metal back contact and a $SiN_{\times}$ antireflective coating and adding Al_2O_3 particles to the PDMS improved normal incidence absorption to 96 %. This absorption enhancement was demonstrated while using about 1 % of the material used in a bulk silicon solar cell device [71].

5.2.3 Crystalline-Amorphous Core-Shell Silicon Nanowires

One method of adding functionality to silicon nanowires is by surrounding the crystalline core with a shell material with differing electronic bandgap or doping type [56]. For example, crystalline-amorphous core-shell silicon nanowires have found applications in battery electrodes [73] and electrical switches [74]. Furthermore, intrinsic amorphous silicon can also provide excellent surface passivation for crystalline silicon or upon doping can create a p-n heterojunction with crystalline silicon [75]. The radial thickness of the amorphous silicon shell can be increased by conformal deposition, providing a convenient method to study the effect of diameter on the optical properties of nanowires. Figure 9.13a shows a high-resolution TEM image of a core-shell silicon nanowire consisting of a highly crystalline

silicon with a diameter of about 9 nm surrounded by an amorphous silicon shell [69]. The nanowire core was grown by the VLS growth method using plasma-enhanced chemical vapor deposition (PECVD), and the conformal amorphous silicon shell was deposited in situ, also by PECVD.

Plan-view SEM images of core-shell silicon nanowires with a total diameter ranging from 15–40 nm to 150–180 nm are shown in Fig. 9.13b and c, respectively. The absorption of nanowire arrays with different total diameters are shown in Fig. 9.13d. The absorption of an amorphous silicon film (400 nm in thickness) on glass is also shown for comparison. The absorption of an amorphous silicon thin film was limited to <55 % over all wavelengths due to high reflection. The core-shell nanowires on the other hand showed absorption of up to 95 % at short wavelengths. The absorption edge of silicon nanowires shifted to longer wavelengths from about 550 to 760 nm as the diameter was increased. Moreover, absorption of the largest diameter nanowires, d = 150–180 nm, remained high (>50 %) at a wavelength of 750 nm, at which the absorption of the a-Si thin film was approximately zero.

Another interesting feature of the absorption curves in Fig. 9.13d was the sudden drop in absorption at long wavelengths near the bandgap of a-Si (1.78 eV). In fact the absorption of the smallest diameter nanowires (d = 15–40 nm) dropped to <2 % at wavelengths, $\lambda > 780$ nm. The nanowires grown in this case used a tin (Sn) catalyst which has been reported to have a high threshold concentration before degrading device performance in crystalline silicon solar cells [76]. In contrast, VLS method grown nanowires using an Au catalyst (Fig. 9.11 (iii)) showed high subbandgap absorption (at infrared wavelengths) suggesting that the catalyst type has a strong influence on the subbandgap optical absorption. In fact, strong subbandgap absorption has also been reported in silicon microspikes in which case the chemical species introduced during the fabrication process were found to be a key contributor to infrared absorption [77].

5.2.4 Silicon Nanocones

Nanocones also have promising optical properties. They are structurally similar to quasi-nanowires but are tapered with a larger base diameter than tip diameter. Vertically aligned nanocones can effectively grade the refractive index between air and bulk material rather than an abrupt transition from air (n = 1) to the incident material [32, 78]. When the index of refraction is graded, the net reflection becomes a combination of a collection of incremental changes of the refractive index [79]. The antireflective property of graded refractive index was mathematically studied for thin layers as far back as 1880 by Rayleigh [80] and has been shown to have broadband and omnidirectional antireflective characteristics [81, 82]. Furthermore, an array of aperiodic silicon nanotips (tapered nanostructures with sharp tips) has also been shown to suppress reflection ranging from ultraviolet wavelengths to terahertz frequencies [11].

Low broadband reflection has been measured in various tapered silicon subwavelength structures fabricated by dry etching [10, 11, 72, 83–86] or chemical etching [78] a silicon wafer. In 1999, Kanamori et al. showed that an array of periodic silicon nanocones fabricated by a combination of electron beam

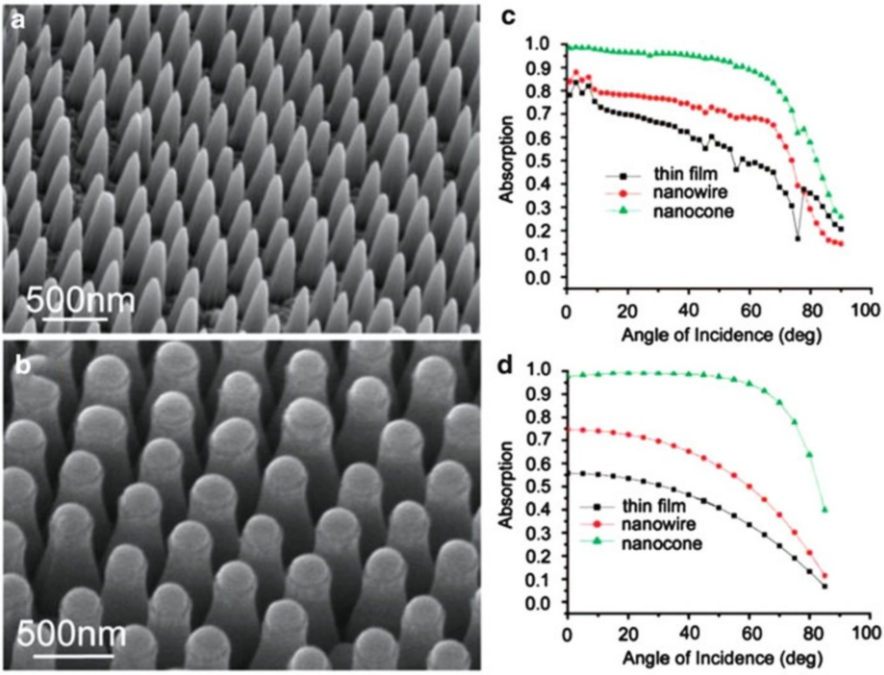

Fig. 9.14 (**a**) SEM images of amorphous silicon (**a**) nanocone and (**b**) quasi-nanowire arrays. Silica nanoparticles can be seen at the top of each quasi-nanowire. (**c**) Measured and (**d**) simulated absorption of the quasi-nanowire, nanocone, and amorphous silicon thin film samples as a function angle of incidence (Reprinted with permission from [32]. Copyright American Chemical Society)

lithography and fast atom beam etching with SF_6 gas could lower reflectivity to less than 3 % in the wavelength range of 200–1,000 nm [10]. The periodicity of the array was 150 nm and height of the nanocones was ~350 nm.

Nanocones fabricated by the top-down approach from thin films of amorphous silicon [32] and crystalline silicon [33] have also demonstrated high broadband absorption. Figure 9.14a and b show an SEM image of amorphous silicon nanocones and quasi-nanowire, respectively, fabricated by dry etching a 1-μm-thick layer of amorphous silicon on ITO-coated glass [32]. Quasi-nanowires had a diameter of about 300 nm and height of about ~600 nm, whereas the nanocones had a tip diameter of ~20 nm, base diameter of ~300 nm, and a height of ~600 nm. The absorption of the quasi-nanowire and nanocone arrays as well as that of a 1-μm-thick film of a-Si is shown in Fig. 9.14c as a function of incident angle. The measured absorption of the nanocone sample was an impressive 98.4 % at normal incidence (0°) which was higher than that of both the quasi-nanowire array (85 %) and the thin film (75 %). In addition, the nanocones exhibited absorption of >90 % for an incident angle of up to 60°. The simulated absorption using the

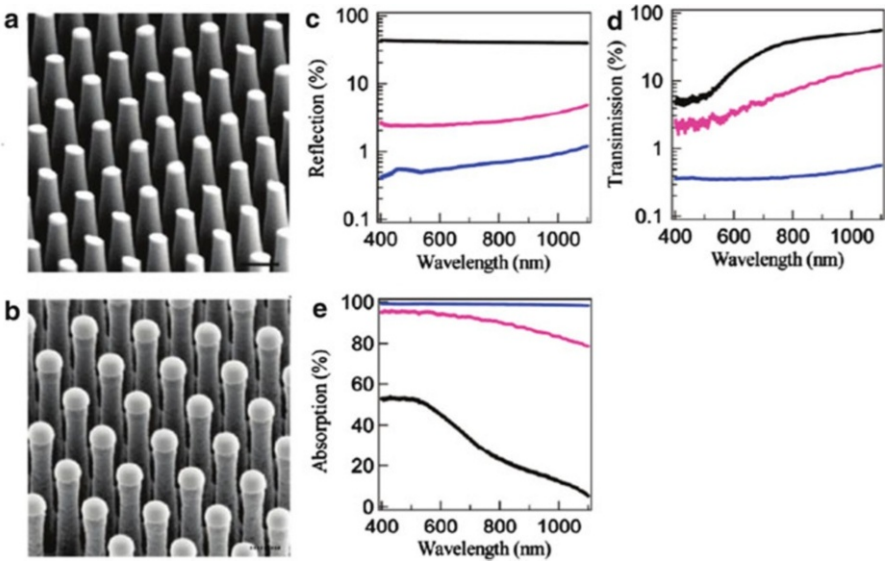

Fig. 9.15 45°-angled SEM images of ordered (**a**) silicon nanocone arrays and (**b**) quasi-nanowire arrays. Nanocones had a top radius of 170 nm and base radius of 400 nm. The height of both the silicon quasi-nanowires and nanocones was 3.5 μm. Each sample was on top of 1.5 μm of planar silicon and 2 μm of buried oxide. The scale bars are 400 nm. The (**c**) reflection, (**d**) transmission, and (**e**) absorption are shown at normal incidence on ordered silicon nanocone (*blue*), silicon quasi nanowires (*pink*), and control bare silicon (*black*) (Reprinted with permission from [33]. Copyright 2010 American Chemical Society)

rigorous coupled wave analysis method is shown in Fig. 9.14d which agreed with the experimental measurements [32].

A periodic vertical array of silicon nanocones fabricated from a crystalline silicon-on-insulator (SOI) wafer has also exhibited very high broadband absorption [33]. Nanocones and quasi-nanowires were fabricated by patterning a 5-μm layer of silicon on an insulator wafer by electron lithography, followed by RIE etching. SEM images of the silicon nanocones and quasi-nanowire arrays are shown in Fig. 9.15a and b, respectively. The slant angles, 3.8° for nanocones and 0° for quasi-nanowire, were achieved by changing the RIE conditions. Each sample consisted of 3.5 μm of ordered silicon nanocones/quasi-nanowires on top of 1.5 μm of planar silicon and 2 μm of buried oxide. The reflection, transmission, and absorption (1−T−R) spectra are shown in Fig. 9.15c–e, respectively, for nanocones (blue), quasi nanowires (pink), and a control bare silicon sample consisting of a 5-μm-thick layer of silicon on top of 2 μm of buried oxide (black). An array of nanocones with a lattice constant of 800 nm exhibited an extremely high absorption of 99 % and ultralow reflection of <1 % between the wavelength region of 400–1,100 nm. The nanocones were also incorporated into a radial p-n junction solar cell that demonstrated a conversion efficiency of 10.8 % and short-circuit current density of 26.4 mA/cm^2 [33].

5.3 Photoluminescence Measurements

Bulk crystalline silicon does not emit light due to its indirect bandgap. However, since the discovery of strong room temperature light emission in electrochemically etched porous silicon [87], a great deal of research has gone into studying silicon nanostructures for optoelectronic applications. Silicon nanowires also exhibit visible luminescence for nanowire diameters ranging from 1 nm to tens of nanometers [15, 29, 30, 88]. The origin of luminescence has been attributed to quantum confinement effects [15, 30, 52, 88–91], surface states [15], defects in the silicon oxide sheath [29, 52, 90], or interface states between the crystalline silicon core and silicon oxide sheath [90, 92, 93]. Potential applications include light emitting devices [94], nanoscale interconnects, and biosensors [95].

Holmes et al. [15] showed that the PL peak in 4–5 nm diameter silicon nanowires with lengths of several microns was blue shifted with respect to the bandgap of crystalline silicon of 1.1 eV. In addition, the crystal orientation had a strong effect on the PL spectra: <100> -oriented wires showed a sharp PL peak at 3.75 eV, whereas <110> -oriented wires showed three peaks at 3.35, 2.9, and 2.55 eV. Luminescence was attributed to quantum confinement effects and possibly surface states [15]. Further evidence of quantum confinement effects was observed by Zhang et al. [30] who showed that photoluminescence blue-shifted with reduction in nanowire diameter. In this case, silicon nanowires were fabricated by the oxide-assisted growth technique and, the nanowire diameter was controlled by changing the ambient gas. Nanowires with a diameter distribution peak at 6 nm, grown in N_2 ambient, showed a PL peak of 1.99 eV. Slightly larger-diameter nanowires with a diameter distribution peak at 9.5 nm grown in Ar (5 % H_2) ambient had a red-shifted PL peak at 1.58 eV. Furthermore, the nanowires having the largest diameter distribution peak at 13.2 nm, grown in the ambient, showed no photoluminescence.

Alternatively, the PL peak energy can be tuned using a combination of etching and thermal oxidation [91]. A hydrofluoric acid (HF) etchant was first used to remove the native oxide layer, and thermal oxidization was used to decrease the nanowire diameter. The average diameter of $TiSi_2$-catalyzed nanowires grown by VLS method as a function of oxidation time is shown in Fig. 9.16a. The starting average diameter was 20 nm and decreased to values between 16 and 3.5 nm depending on the oxidation time. The luminescence band, shown in Fig. 9.16b, shifted to higher energies for decreasing nanowire diameter. After 10 min. of oxidation, the PL peak energy shifted to 1.55 eV, and after 120 min., the PL peak energy saturated at about 1.66 eV. These results reasonably agreed with other theoretical studies based on nanowire diameter [91].

While PL results were reported for low-dimensional silicon nanowires, light emission has also been observed in larger-diameter silicon nanowires. Figure 9.17a shows a TEM image of silicon nanowires with an average diameter of about 15 nm which consist of a crystalline silicon core surrounded by a thin layer of silicon oxide. After the silicon oxide was removed by an HF etch, nanowires consisted of a crystalline silicon core with an average diameter of around 10 nm, shown in Fig. 9.17b [29]. The PL spectrum of the nanowires is shown in Fig. 9.17c, which

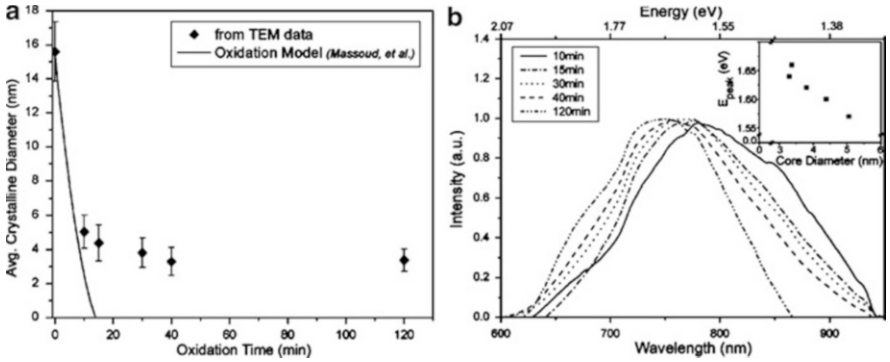

Fig. 9.16 (**a**) Average nanowire diameter versus oxidation time. The *diamonds* represent measured values from transmission electron microscopy analysis, and the *solid line* was predicted using an oxidation model for a planar surface. (**b**) Photoluminescence spectra taken after 10, 15, 30, 40, and 120 min. of oxidation of silicon nanowires. Inset shows the photoluminescence peak energy as a function of core diameter (Reprinted with permission from [91]. Copyright 2006 American Chemical Society)

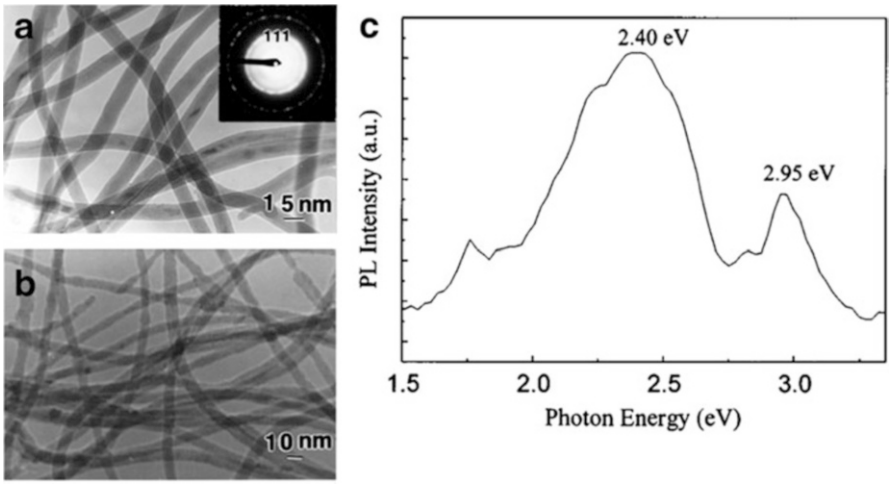

Fig. 9.17 (**a**) A TEM image of silicon nanowires with an average diameter of around 15 nm. (**b**) TEM image of the silicon core with an average diameter of around 10 nm after HF etch. (**c**) PL spectrum of the silicon nanowires showing two peaks at around 2.4 and 2.95 eV (Reprinted with permission from [29]. Copyright 1998, American Institute of Physics)

consisted of two PL peaks at 2.40 and 2.95 eV. Due to the large diameter, photoluminescence was not likely due to quantum confinement but instead, was attributed to the amorphous silicon oxide layer that coated the nanowires. Luminescence in nanowires with diameters larger than 10 nm has also been attributed to the interface between silicon and silicon oxide and quantum confinement effects of the silicon crystallites embedded in the oxide [90, 92]. Strong

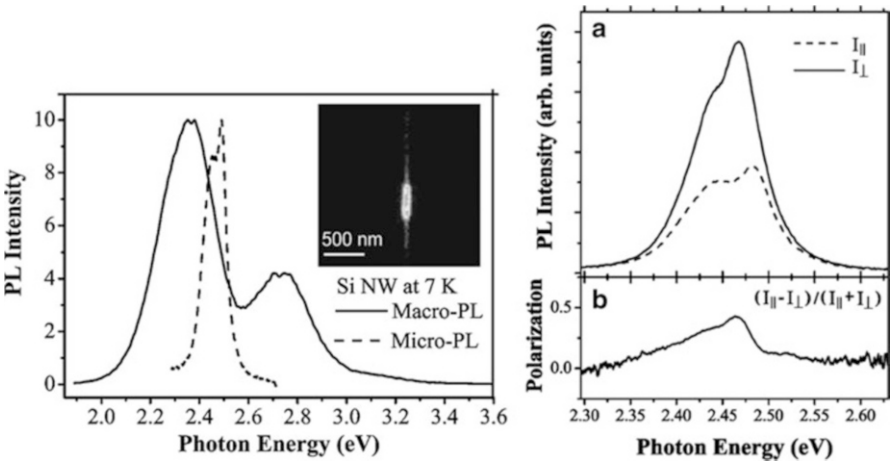

Fig. 9.18 (*Left*) Normalized silicon nanowire PL spectra measured by macro-PL for a large number of nanowires (*solid line*) and by micro-PL for a single nanowire (*dashed line*). (*Right*) PL spectra of a single nanowire at different polarization directions (Reprinted with permission from [88]. Copyright 2003, American Institute of Physics)

photoluminescence emission has also been observed in silicon nanowires surrounded by a SiC sheath [96].

Photoluminescence of an individual silicon nanowire has also been studied and compared to that of a large number of nanowires as shown in Fig. 9.18 (left). A narrow PL band (85 meV) was measured from an individual silicon nanowire, whereas a large number of nanowires exhibited a broadband PL ranging from blue to green wavelengths [88]. Interestingly, optical anisotropy has also observed by photoluminescence measurements in both single nanowires [88] and a high-density array of silicon nanowires [97]. The maximum-polarized PL was observed in the direction parallel to the nanowire axis in which case there was strong light-nanowire interaction. The PL spectrum of a single silicon nanowire with different polarization directions and the calculated degree of polarization is shown in Fig. 9.18 (right). Polarization was attributed to the abrupt change in dielectric constant between the crystalline core and the surrounding silicon oxide sheath [88]. Such polarization dependence could find application in photonic integrated circuits.

6 Conclusion and Future Perspective

Modeling of the optical properties of silicon nanowires revealed that nanowires can both enhance and reduce absorption at particular wavelengths depending on diameter, length, and periodicity. Superior light absorption compared to a thin film silicon of equal thickness can be achieved when the nanowire periodicity is between 250 and 1,200 nm. Optimal absorption was attained when the periodicity was 600 nm and diameter-to-periodicity ratio was about 0.8.

Both top-down-fabricated and bottom-up-grown silicon nanowires exhibited very low measured reflection compared to that of thin film silicon or bare silicon wafer. The reflection spectrum can also be tuned over all visible wavelengths by controlling the nanowire diameter or periodicity. Alternatively, growing a conformal amorphous silicon shell around the crystalline core can also shift the absorption edge to infrared wavelengths. Furthermore, top-down-fabricated nanocones exhibited extremely high absorption of up to 99 % and reflection of <1 % over the wavelength range of 400–1,100 nm.

The above-mentioned optical properties of silicon nanowires and nanocones are attractive for a number of applications. For example, ultralow reflection and high broadband optical absorption in well-designed nanowires and nanocones are promising for photovoltaic and photodetector applications. Individual or interconnected nanowires could also be used to power nanoelectronic devices [98, 99]. Wave guiding with high optical confinement for diameters greater than 100 nm can be achieved in nanowires which could be used in photonic wire devices [100]. In addition, strong luminescence upon laser light excitation has been observed in both low-dimensional silicon nanowires and silicon nanowires covered with a silicon oxide or SiC sheath. Such light emission offers exciting possibilities in applications such as light emitting and silicon-based optoelectronic devices.

Acknowledgments The authors are grateful to M. P. Anantram for support and helpful discussions.

References

1. Bernhard CG (1967) Structural and functional adaptation in a visual system. Endeavour 26:79–84
2. Clapham PB, Hutley MC (1973) Reduction of lens reflexion by the “Moth Eye” principle. Nature 244:281–282
3. Gittleman JI, Sichel EK, Lehmann HW, Widmer R (1979) Textured silicon: a selective absorber for solar thermal conversion. Appl Phys Lett 35:742–744
4. Craighead HG, Howard RE, Tennant DM (1980) Textured thin-film Si solar selective absorbers using reactive ion etching. Appl Phys Lett 37:653–655
5. Peng K, Xu Y, Wu Y, Yan Y, Lee ST, Zhu J (2005) Aligned single-crystalline Si nanowire arrays for photovoltaic applications. Small 1:1062–1067
6. Tsakalakos L, Balch J, Fronheiser J, Korevaar BA, Sulima O, Rand J (2007) Silicon nanowire solar cells. Appl Phys Lett 91:233117-1–233117-3
7. Sun C, Jiang P, Jiang B (2008) Broadband moth-eye antireflection coatings on silicon. Appl Phys Lett 92:061112
8. Min WL, Jiang P, Jiang B (2008) Large-scale assembly of colloidal nanoparticles and fabrication of periodic subwavelength structures. Nanotechnology 19:475604
9. Huang Z, Fang H, Zhu J (2007) Fabrication of silicon nanowire arrays with controlled diameter, length, and density. Adv Mater 19:744–748
10. Kanamori Y, Sasaki M, Hane K (1999) Broadband antireflection gratings fabricated upon silicon substrates. Opt Lett 24:1422–1424
11. Huang YF, Chattopadhyay S, Jen YJ, Peng CY, Liu TA, Hsu YK, Pan CL, Lo HC, Hsu CH, Chang YH, Lee CS, Chen KH, Chen LC (2007) Improved broadband and

quasi-omnidirectional anti-reflection properties with biomimetic silicon nanostructures. Nat Nanotechnol 2:770–774
12. Lalanne P, Morris GM (1997) Antireflection behavior of silicon subwavelength periodic structures for visible light. Nanotechnology 8:53–56
13. Hadobás K, Kirsch S, Carl A, Acet M, Wassermann EF (2000) Reflection properties of nanostructure-arrayed silicon surfaces. Nanotechnology 11:161
14. Koynov S, Brandt MS, Stutzmann M (2006) Black nonreflecting silicon surfaces for solar cells. Appl Phys Lett 88:203107
15. Holmes JD, Johnston KP, Doty RC, Korgel BA (2000) Control of thickness and orientation of solution-grown silicon nanowires. Science 287:1471–1473
16. Hu L, Chen G (2007) Analysis of optical absorption in silicon nanowire arrays for photovoltaic applications. Nano Lett 7:3249–3252
17. Lin C, Povinelli ML (2009) Optical absorption enhancement in silicon nanowire arrays with a large lattice constant for photovoltaic applications. Opt Express 17:19371–19381
18. Li J, Yu HY, Wong SM, Li X, Zhang G, Lo PGQ, Kwong DL (2009) Design guidelines of periodic Si nanowire arrays for solar cell application. Appl Phys Lett 95:243113-1–243113-3
19. Tsakalakos L, Balch J, Fronheiser J, Shih M, LeBoeuf SF, Pietrzykowski M, Codella PJ, Korevaar BA, Sulima OV, Rand J, Davuluru A, Rapol U (2007) Strong broadband optical absorption in silicon nanowire films. J Nanophotonics 1:013552
20. Stelzner T, Pietsch M, Andra G, Falk F, Ose E, Christiansen S (2008) Silicon nanowire-based solar cells. Nanotechnology 19:295203
21. Fang H, Li X, Song S, Xu Y, Zhu J (2008) Fabrication of slantingly-aligned silicon nanowire arrays for solar cell applications. Nanotechnology 19:255703
22. Sivakov V, Andra G, Gawlik A, Berger A, Plentz J, Falk F, Christiansen SH (2009) Silicon nanowire-based solar cells on glass: synthesis, optical properties, and cell parameters. Nano Lett 9:1549–1554
23. Gunawan O, Guha S (2009) Characteristics of vapor-liquid–solid grown silicon nanowire solar cells. Sol Energy Mater Sol Cells 93:1388–1393
24. Garnett E, Yang P (2010) Light trapping in silicon nanowire solar cells. Nano Lett 10:1082–1087
25. Li X, Li J, Chen T, Tay BK, Wang J, Yu H (2010) Periodically aligned Si nanopillar arrays as efficient antireflection layers for solar cell applications. Nanoscale Res Lett 5:1721–1726
26. Kumar D, Srivastava SK, Singh PK, Husain M, Kumar V (2011) Fabrication of silicon nanowire arrays based solar cell with improved performance. Sol Energy Mater Sol Cells 95:215–218
27. Zhao J, Wang A, Green MA, Ferrazza F (1998) 19.8 % efficient 'honeycomb' textured multicrystalline and 24.4 % monocrystalline silicon solar cells. Appl Phys Lett 73:1991–1993
28. Kayes BM, Atwater HA, Lewis NS (2005) Comparison of the device physics principles of planar and radial p-n junction nanorod solar cells. J Appl Phys 97:114302-1–114302-3
29. Yu DP, Bai ZG, Ding Y, Hang QL, Zhang HZ, Wang JJ, Zou YH, Qian W, Xiong GC, Zhou HT, Feng SQ (1998) Nanoscale silicon wires synthesized using simple physical evaporation. Appl Phys Lett 72:3458–3458
30. Zhang YF, Tang YH, Peng HY, Wang N, Lee CS, Bello I, Lee ST (1999) Diameter modification of silicon nanowires by ambient gas. Appl Phys Lett 75:1842–1844
31. Wang X, Pey KL, Yip CH, Fitzgerald EA, Antoniadis DA (2010) Vertically arrayed Si nanowire/nanorod-based core-shell p-n junction solar cells. J Appl Phys 108:124303, 5 pp
32. Zhu J, Yu Z, Burkhard GF, Hsu CM, Connor ST, Xu Y, Wang Q, McGehee M, Fan S, Cui Y (2009) Optical absorption enhancement in amorphous silicon nanowire and nanocone arrays. Nano Lett 9:279–282
33. Lu Y, Lal A (2010) High-efficiency ordered silicon nano-conical-frustum array solar cells by self-powered parallel electron lithography. Nano Lett 10:4651–4656

34. Jiang P, McFarland MJ (2004) Large-scale fabrication of wafer-size colloidal crystals, macroporous polymers and nanocomposites by spin-coating. J Am Chem Soc 126:13778–13786
35. Burmeister F, Schäfle C, Matthes T, Böhmisch M, Boneberg J, Leiderer P (1997) Colloid monolayers as versatile lithographic masks. Langmuir 13:2983–2987
36. Wagner RS, Ellis WC (1964) Vapor-liquid–solid mechanism of single crystal growth. Appl Phys Lett 4:89–90
37. Wang N, Tang YH, Zhang YF, Lee CS, Lee ST (1998) Nucleation and growth of Si nanowires from silicon oxide. Phys Rev B (Condens Matter) 58:16024–16026
38. Wang Y, Schmidt V, Senz SD, Gosele U (2006) Epitaxial growth of silicon nanowires using an aluminium catalyst. Nat Nanotechnol 1:186–189
39. Sunkara MK, Sharma S, Miranda R, Lian G, Dickey EC (2001) Bulk synthesis of silicon nanowires using a low-temperature vapor-liquid–solid method. Appl Phys Lett 79:1546–1548
40. Iacopi F, Vereecken PM, Schaekers M, Caymax M, Moelans N, Blanpain B, Richard O, Detavernier C, Griffiths H (2007) Plasma-enhanced chemical vapour deposition growth of si nanowires with low melting point metal catalysts: an effective alternative to Au-mediated growth. Nanotechnology 18:505307-1
41. Yu J, Chung S, Heath JR (2000) Silicon nanowires: preparation, device fabrication, and transport properties. J Phys Chem B 104:11864–11870
42. Kamins TI, Williams RS, Basile DP, Hesjedal T, Harris JS (2001) Ti-catalyzed Si nanowires by chemical vapor deposition: microscopy and growth mechanisms. J Appl Phys 89:1008–1016
43. Parlevliet D, Cornish JCL (2007) Silicon nanowires: growth studies using pulsed PECVD. Mater Res Soc Symp Proc 989:537–544
44. Hannon JB, Kodambaka S, Ross FM, Tromp RM (2006) The influence of the surface migration of gold on the growth of silicon nanowires. Nature 440:69–71
45. Givargizov EI (1975) Fundamental aspects of VLS growth. J Cryst Growth 31:20–30
46. Cui Y, Lauhon LJ, Gudiksen MS, Wang J, Lieber CM (2001) Diameter-controlled synthesis of single-crystal silicon nanowires. Appl Phys Lett 78:2214–2216
47. Westwater J, Gosain DP, Tomiya S, Usui S, Ruda H (1997) Growth of silicon nanowires Via gold/silane vapor-liquid–solid reaction. J Vac Sci & Technol B (Microelectron Nanometer Struct) 15:554–557
48. Ge S, Jiang K, Lu X, Chen Y, Wang R, Fan S (2005) Orientation-controlled growth of single-crystal silicon-nanowire arrays. Adv Mater 17:56–61
49. Kayes BM, Filler MA, Putnam MC, Kelzenberg MD, Lewis NS, Atwater HA (2007) Growth of vertically aligned Si wire arrays over large areas (1 cm^2) with Au and Cu catalysts. Appl Phys Lett 91:103110
50. Zhang R, Lifshitz Y, Lee S (2003) Oxide-assisted growth of semiconducting nanowires. Adv Mater 15:635–640
51. Ma DDD, Lee CS, Au FCK, Tong SY, Lee ST (2003) Small-diameter silicon nanowire surfaces. Science 299:1874–1877
52. Li CP, Sun XH, Wong NB, Lee CS, Lee ST, Teo BK (2002) Ultrafine and uniform silicon nanowires grown with zeolites. Chem Phys Lett 365:22–26
53. Kumaravelu G, Alkaisi MM, Bittar A, Macdonald D, Zhao J (2004) Damage studies in dry etched textured silicon surfaces. Curr Appl Phys 4:108–110
54. Park WI, Zheng G, Jiang X, Tian B, Lieber CM (2008) Controlled synthesis of millimeter-long silicon nanowires with uniform electronic properties. Nano Lett 8:3004–3009
55. Gudiksen MS, Lauhon LJ, Wang J, Smith DC, Lieber CM (2002) Growth of nanowire superlattice structures for nanoscale photonics and electronics. Nature 415:617–620
56. Lauhon LJ, Gudlksen MS, Wang D, Lieber CM (2002) Epitaxial core-shell and core-multishell nanowire heterostructures. Nature 420:57–61

57. Zhao X, Wei CM, Yang L, Chou MY (2004) Quantum confinement and electronic properties of silicon nanowires. Phys Rev Lett 92:236805
58. Taflove A, Hagness SC (2000) Computational electrodynamics: the finite-difference time-domain method. Artech House, Boston
59. Yariv A, Yeh P (2006) Photonics: optical electronics in modern communications, 6th edn. Oxford University Press, New York
60. Li J, Yu HY, Wong SM, Zhang G, Sun X, Lo PGQ, Kwong DL (2009) Si nanopillar array optimization on Si thin films for solar energy harvesting. Appl Phys Lett 95:033102-1–033102-3
61. Henry MD, Walavalkar S, Homyk A, Scherer A (2009) Alumina etch masks for fabrication of high-aspect-ratio silicon micropillars and nanopillars. Nanotechnology 20:255305
62. Bao H, Ruan X (2010) Optical absorption enhancement in disordered vertical silicon nanowire arrays for photovoltaic applications. Opt Lett 35(20):3378–3380
63. Street RA, Wong WS, Paulson C (2009) Analytic model for diffuse reflectivity of silicon nanowire mats. Nano Lett 9(10):3494–3497
64. Haynos J, Allison J, Arndt R, Meulenberg A (1974) The COMSAT nonreflective silicon solar cell: a second generation improved cell. International Conference of Photovoltaic Power Generation, Hamburg, p 487
65. Sopori BL, Pryor RA (1983) Design of antireflection coatings for textured silicon solar cells. Solar Cells 8:249–261
66. Peng K, Wang X, Lee ST (2008) Silicon nanowire array photoelectrochemical solar cells. Appl Phys Lett 92:163103-1–163103-3
67. Seo K, Wober M, Steinvurzel P, Schonbrun E, Dan Y, Ellenbogen T, Crozier KB (2011) Multicolored vertical silicon nanowires. Nano Lett 11:1851–1856
68. Boden SA, Bagnall DM (2008) Tunable reflection minima of nanostructured antireflective surfaces. Appl Phys Lett 93:133108-1–133108-3
69. Adachi MM, Anantram MP, Karim KS (2010) Optical properties of crystalline-amorphous core-shell silicon nanowires. Nano Lett 10:4093–4098
70. Muskens OL, Rivas JG, Algra RE, Bakkers EP, Lagendijk A (2008) Design of light scattering in nanowire materials for photovoltaic applications. Nano Lett 8:2638–2642
71. Kelzenberg MD, Boettcher SW, Petykiewicz JA, Turner-Evans DB, Putnam MC, Warren EL, Spurgeon JM, Briggs RM, Lewis NS, Atwater HA (2010) Enhanced absorption and carrier collection in Si wire arrays for photovoltaic applications. Nat Mater 9:239–244
72. Wu C, Crouch CH, Zhao L, Carey JE, Younkin R, Levinson JA, Mazur E, Farrell RM, Gothoskar P, Karger A (2001) Near-unity below-band-gap absorption by microstructured silicon. Appl Phys Lett 78:1850–1852
73. Chan CK, Peng H, Liu G, McIlwrath K, Zhang XF, Huggins RA, Cui Y (2008) High-performance lithium battery anodes using silicon nanowires. Nat Nanotechnol 3:31–35
74. Dong Y, Yu G, McAlpine MC, Lu W, Lieber CM (2008) Si/a-Si core/shell nanowires as nonvolatile crossbar switches. Nano Lett 8:386–391
75. Taguchi M, Kawamoto K, Tsujge S, Baba T, Sakata H, Morizane M, Uchihashi K, Nakamura N, Kiyama S, Oota O (2000) HIT^{TM} cells-high-efficiency crystalline Si cells with novel structure. Prog Photovoltaics Res Appl 8:503–513
76. Rohatgi A, Davis JR, Hopkins RH, McMullin PG (1983) A study of grown-in impurities in silicon by deep-level transient spectroscopy. Solid State Electron 26:1039–1051
77. Younkin R, Carey JE, Mazur E, Levinson JA, Friend CM (2003) Infrared absorption by conical silicon microstructures made in a variety of background gases using femtosecond-laser pulses. J Appl Phys 93:2626–2629
78. Jung J, Guo Z, Jee S, Um H, Park K, Lee J (2010) A strong antireflective solar cell prepared by tapering silicon nanowires. Opt Express 18:A286–A292
79. Wilson SJ, Hutley MC (1982) The optical properties of moth eye antireflection surfaces. J Mod Opt 29:993–1009

80. Rayleigh FRS (1880) On reflection of vibrations at the confines of two media between which the transition is gradual. Proc Lond Math Soc 11:51–56
81. Southwell WH (1983) Gradient-index antireflection coatings. Opt Lett 8:584–586
82. Poitras D, Dobrowolski JA (2004) Toward perfect antireflection coatings. 2. theory. Appl Opt 43:1286–1295
83. Zaidi SH, Ruby DS, Gee JM (2001) Characterization of random reactive ion etched-textured silicon solar cells. IEEE Trans Electron Devices 48:1200–1206
84. Yu Z, Gao H, Wu W, Ge H, Chou SY (2003) Fabrication of large area subwavelength antireflection structures on si using trilayer resist nanoimprint lithography and liftoff. J Vac Sci Technol B 21:2874–2877
85. Lee C, Bae SY, Mobasser S, Manohara H (2005) A novel silicon nanotips antireflection surface for the micro sun sensor. Nano Lett 5:2438–2442
86. Chang C, Wang Y-F, Kanamori Y, Shih J-J, Kawai Y, Lee C-K, Wu K-C, Esashi M (2005) Etching submicrometer trenches by using the bosch process and its application to the fabrication of antireflection structures. J Micromech Microeng 15:580–585
87. Canham LT (1990) Silicon quantum wire array fabrication by electrochemical and chemical dissolution of wafers. Appl Phys Lett 57:1046–1050
88. Qi J, Belcher AM, White JM (2003) Spectroscopy of individual silicon nanowires. Appl Phys Lett 82:2616–2618
89. Bhattacharya S, Banerjee D, Adu KW, Samui S, Bhattacharyya S (2004) Confinement in silicon nanowires: optical properties. Appl Phys Lett 85:2008–2010
90. Sham TK, Naftel SJ, Kim P-SG, Sammynaiken R, Tang YH, Coulthard I, Moewes A, Freeland JW, Hu Y-F, Lee ST (2007) Electronic structure and optical properties of silicon nanowires: a study using x-ray excited optical luminescence and x-ray emission spectroscopy. Phys Rev B (Condens Matter Mater Phys) 70:45313-1
91. Guichard AR, Barsic DN, Sharma S, Kamins TI, Brongersma ML (2006) Tunable light emission from quantum-confined excitons in $TiSi_2$-catalyzed silicon nanowires. Nano Lett 6:2140–2144
92. Dovrat M, Arad N, Zhang X-H, Lee S-T, Sa'ar A (2007) Optical properties of silicon nanowires from cathodoluminescence imaging and time-resolved photoluminescence spectroscopy. Phys Rev B (Condens Matter Mater Phys) 75:205343-1
93. Zhang ZY, Wu XL, Shen JC, Yang LW, Shi Y, Chu PK, Siu GG (2005) Light emission from as-prepared and oxidized Si nanowires with diameters of 5–15 nm. J Cryst Growth 285:620–626
94. Nassiopoulos AG, Grigoropoulos S, Papadimitriou D (1996) Electroluminescent device based on silicon nanopillars. Appl Phys Lett 69:2267–2267
95. Patolsky F, Lieber CM (2005) Nanowire nanosensors. Mater Today 8:20–28
96. Zhou XT, Zhang RQ, Peng HY, Shang NG, Wang N, Bello I, Lee CS, Lee ST (2000) Highly efficient and stable photoluminescence from silicon nanowires coated with SiC. Chem Phys Lett 332:215–218
97. Ma DDD, Lee ST, Shinar J (2005) Strong polarization-dependent photoluminescence from silicon nanowire fibers. Appl Phys Lett 87:33107-1
98. Tian B, Zheng X, Kempa TJ, Fang Y, Yu N, Yu G, Huang J, Lieber CM (2007) Coaxial silicon nanowires as solar cells and nanoelectronic power sources. Nature 449:885–889
99. Kelzenberg MD, Turner-Evans DB, Kayes BM, Filler MA, Putnam MC, Lewis NS, Atwater HA (2008) Photovoltaic measurements in single-nanowire silicon solar cells. Nano Lett 8:710–714
100. Khorasaninejad M, Saini SS (2010) Silicon nanowire optical waveguide (SNOW). Opt Express 18:23442–23457

Optical Properties of Oxide Nanomaterials 10

A. B. Djurišić, X. Y. Chen, J. A. Zapien, Y. H. Leung, and A. M. C. Ng

Contents

A.B. Djurišić (✉) • X.Y. Chen • Y.H. Leung
Department of Physics, The University of Hong Kong, Pokfulam Road, Hong Kong

J.A. Zapien
Department of Physics and Materials Science, City University of Hong Kong, Kowloon, Hong Kong

A.M.C. Ng
Department of Physics, The University of Hong Kong, Pokfulam Road, Hong Kong

Nanostructure Institute for Energy and Environmental Research, Division of Physical Sciences, South University of Science and Technology of China, Shenzhen, China

Challa S.S.R. Kumar (ed.), *UV-VIS and Photoluminescence Spectroscopy for Nanomaterials Characterization*, DOI 10.1007/978-3-642-27594-4_10,

1 Definition of the Topic

This chapter discusses different methods of optical characterization of various metal oxide materials. Photoluminescence (room temperature, temperature-dependent, and time-resolved), cathodoluminescence, electroluminescence, UV-Vis spectroscopy, and Raman spectroscopy are discussed.

2 Overview

In this chapter, we will discuss different experimental techniques for characterization of optical properties of metal oxide nanostructures. We will first discuss the basic principles of each technique, together with common experimental problems, various experimental artifacts, and suggestions to avoid artifacts during measurement. Then, we will provide an overview of recent reported results on using those techniques to characterize various metal oxide nanostructures. We will consider all binary oxide materials of interest in various practical applications, although most of the discussion will be devoted to ZnO as a material which has to date been the most comprehensively studied by different optical techniques. In addition to nanostructures, where relevant and needed, we will discuss the results obtained on bulk samples which are applicable to nanostructures (e.g., origins of defect bands or bound exciton lines). We will discuss the issues of optical properties dependence on the nanostructure size and emphasize the need for careful and proper assignment of observed dependences to the appropriate physical phenomena (quantum confinement, surface effects, extended defects, etc.).

3 Introduction

In the last decade, there has been a rapid growth of nanoscience and nanotechnology. Different morphologies of various materials have been synthesized, their growth, optical, and electronic properties have been studied, and various applications have been investigated as well. Among different materials, metal oxide nanostructures are of particular interest due to their potential for a variety of applications, for example, in optoelectronics, sensing, and photocatalysis. In many of these applications, the optical properties of materials are of interest. In addition, optical characterization is useful for obtaining more information about the material, such as types and concentrations of different native defects. Native defects in metal oxides are very common, and there have been ongoing debates for several decades on the origin of common defect emission bands in metal oxide semiconductors, such as green emission band in ZnO.

Different optical characterization techniques can be employed to characterize the optical properties of metal oxide nanostructures. We will briefly explain the possible problems with some of the techniques, and we will discuss the possible experimental artifacts and how to avoid them. Experimental artifacts are

unfortunately common in the reports on the optical properties and characterization of nanostructures, and they sometimes lead to erroneous identification of defect emissions and erroneous conclusions about the material quality and properties. Furthermore, for more reliable study of the material properties, it is essential to employ multiple techniques and to comprehensively and critically analyze whether the obtained results are consistent. This is frequently not the case in the literature. For example, due to the simplicity and ease of measurement, room temperature photoluminescence is often used as an indicator of the crystal quality of the material, with the argument that "no or weak defect emission" implies excellent crystal quality. However, this disregards the possible presence of nonradiative defects, and the fact that the ratio of near-band edge emission to defect emission is strongly dependent on the measurement conditions.

After discussing individual experimental techniques, we will present recent progress in the characterization of different metal oxide nanostructures. In addition to discussing issues related to the size dependence of different spectral features, we will also discuss common problems in the explanations of size dependences. Other features in the optical spectra, which are not size-dependent, will also be discussed, with reference to bulk samples where necessary. For example, for understanding the differences in optical properties of nanostructures with different morphologies, examinations of single crystal samples with different surface orientations may be helpful. Furthermore, single crystals frequently exhibit sharper and more prominent bound exciton lines, which make them more convenient for studies aiming at reliable identification of the chemical identity of donors or acceptors responsible for bound exciton emissions.

4 Experimental and Instrumental Methodology

4.1 Emission Spectroscopy: Photoluminescence, Cathodoluminescence, and Electroluminescence

Photoluminescence (PL) is a very common emission spectroscopy characterization technique for studying the properties of nanomaterials, since it is simple and straightforward. A common experimental setup for photoluminescence measurements is illustrated in Fig. 10.1a, and it typically consists of a laser, sample holder, optics, and a monochromator with a detector. For characterization of nanostructures, obtaining the spectra from individual nanostructures is often of interest. This can be achieved using cathodoluminescence (CL) or using microPL, which is illustrated in Fig. 10.1b. For the measurement of quantum efficiency of the emission, an integrated sphere needs to be included in the setup, as illustrated in Fig. 10.1c. Instead of a laser, an excitation source can also be a Xe lamp, and in that case, another monochromator is needed for the excitation wavelength tuning. Setups using a Xe lamp as an excitation source are of interest for photoluminescence excitation (PLE) measurements. Spectra can be collected by a spectrometer either using focusing optics or optical fibers. Additional items, which can be

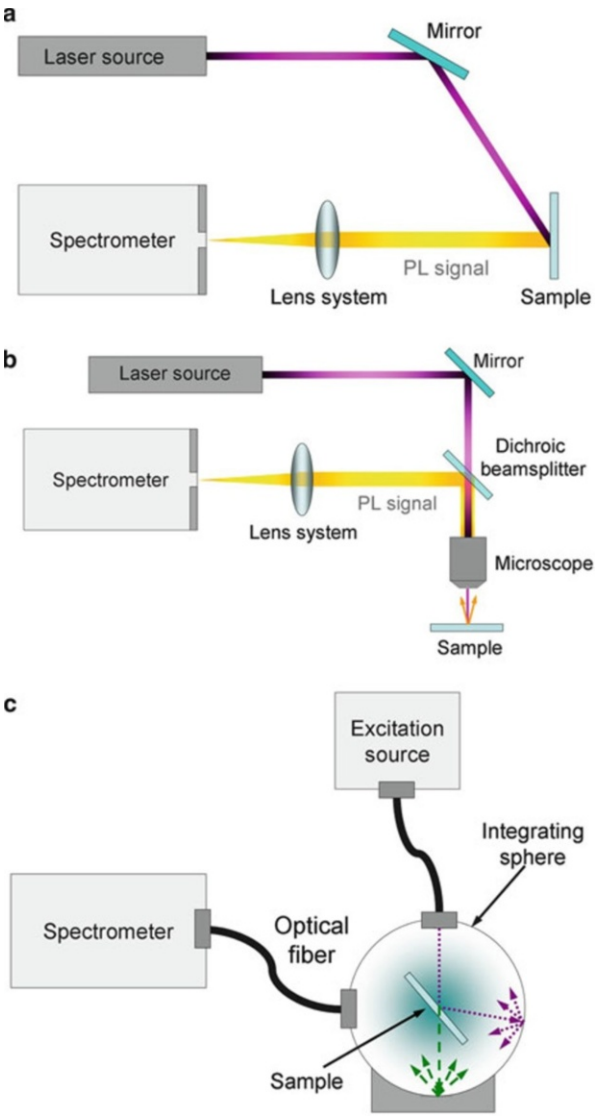

Fig. 10.1 Schematic diagrams of (**a**) PL setup, (**b**) microPL setup, (**c**) quantum efficiency measurement setup

included in the basic PL setup, are a chopper and a lock-in amplifier, which enable the enhancement of the signal-to-noise ratio and which are needed for the measurements of weakly emitting samples. It should be noted that the intensity of the signal can be increased by widening the slit on the monochromator, but this also increases the intensity of the noise. The use of a lock-in amplifier is a preferable way to improve the quality of the measured data for weakly emitting samples. In case of a variable temperature measurement, sample is placed in a cryostat with a suitable window for optical measurements. It should be noted that nanostructure measurements can in some cases be affected by the type of cryostat (e.g., cold finger vs.

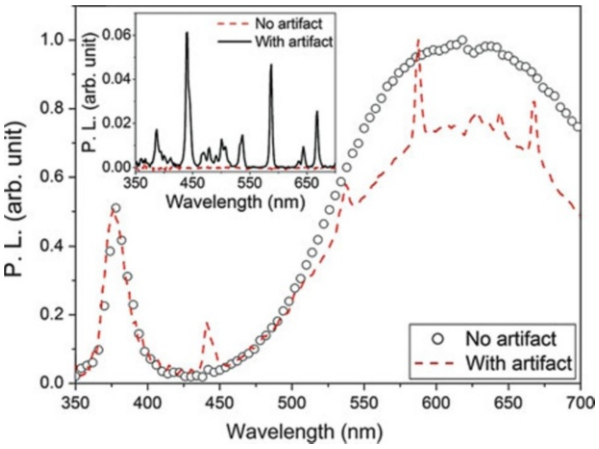

Fig. 10.2 PL spectra of ZnO nanorods with different alignment. The *inset* shows the PL spectra of a bare Si substrate with different alignment

immersion cryostat). This is because a loosely packed nanostructure powder sample may be in a poor thermal contact with a cold finger, resulting in a temperature difference between the actual temperature of the sample and that of the cold finger.

Another issue, which can potentially result in artifacts in PL measurements, is the alignment of the measurement setup. Poor alignment or the inappropriate choice of components in a PL system can result in various artifacts in the measured spectra. For example, lasing from ZnO covering the spectral range of 340–725 nm has been reported [1]. A number of sharp lines can be observed in the experimental spectra. Nevertheless, considering the bandgap and optical properties of ZnO, it is unlikely that such an emission spectrum originated from ZnO. Figure 10.2 illustrates the alignment issues using HeCd laser as an excitation source and a fiber-optic spectrometer for spectra collection. The artifacts occur when a reflective substrate such as Si is used, when the signal is weak, and when unsuitable position of the fiber and the angle between the excitation laser beam and the sample are selected. The fact that sharp lines represent experimental artifacts is obvious when bare Si substrate is measured.

Photoluminescence can also be measured using fluorometers or fluorescence spectrometers, as described in detail in Ref. [2]. Fluorescence spectrometers are much easier for operation, since they do not require careful alignment needed for a conventional PL system. However, spectra measured in such instruments are often very broad and have different shapes compared to typical luminescence of a material (for an example of ZnO PL spectra measured in such an instrument, see Refs. [3–6], while an example for SnO_2 can be found in Ref. [7]). A comparison of a PL spectrum from ZnO nanoparticles measured in a conventional setup and in a fluorescence spectrometer is shown in Fig. 10.3. It is obvious that the spectral features are fundamentally different. In this case, the measurement of a bare substrate does not provide any clues on whether the observed spectral shape is an artifact or not. From the actual examination of the emitted light by naked eyes (color of the emitted light), it is obvious that the emission spectrum obtained by the fluorescence spectrometer is not representative of the actual emission from the

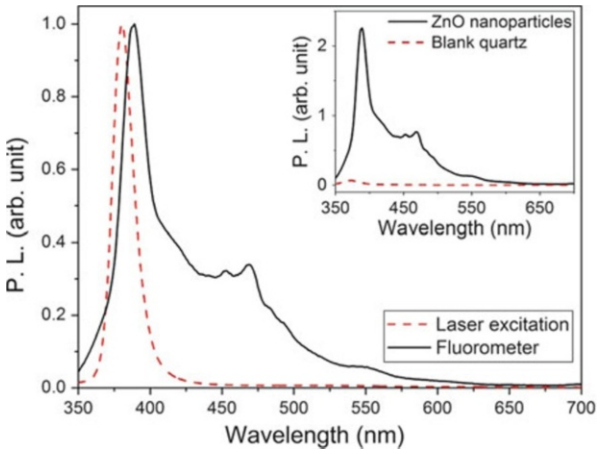

Fig. 10.3 PL spectra from ZnO nanoparticles measured in a conventional experimental setup using a HeCd laser (325 nm) as an excitation source and measured in a Photon Technology International (*PTI*) Fluorescence QuantaMaster Series QM1 spectrophotometer (325-nm excitation wavelength). The *inset* shows the comparison of the emission spectra measured in fluorescence spectrometer for ZnO nanoparticles on quartz substrate and the bare substrate

material. Such problems do not usually occur for very strongly emitting samples with broad emissions, such as various organic molecules.

In addition to excitation by photons with energy higher than bandgap, excitation with lower energy light can be also used for luminescence measurements. Two-photon spectroscopy has several potential advantages for studying the optical properties of a material [8]. Due to longer penetration depth, the influence of surface defects on the emission spectra will be smaller, and the influence of scattered light on emission detection is unlikely since the excitation wavelength is far away from the emission wavelength [8]. In some cases, stimulated emission due to inelastic exciton-exciton scattering in ZnO has been observed only under two-photon excitation, due to a significant effect of nonradiative surface recombination under one-photon pumping [9]. Two-photon spectroscopy is also of interest for potentially coupling the near-infrared radiation into ZnO nanostructures for local photodynamic therapy applications [10].

Another method for exciting the light emission from the sample is using electrical excitation, either by an electron beam in CL or by injection of the charge carriers in electroluminescence (EL). Schematic diagrams of these two techniques are illustrated in Fig. 10.4. The use of CL for nanostructure characterization has been recently reviewed [11]. It has been emphasized that while CL is useful as a qualitative technique, quantitative analysis of the CL is difficult since the obtained intensity depends on a number of factors, such as electron beam parameters, sample damage, internal light absorption, secondary excitation, etc. [11]. The sample damage by the electron beam can include creation or activation of defects, charging of surfaces, as well as adsorption/desorption from the surfaces [11] which makes it

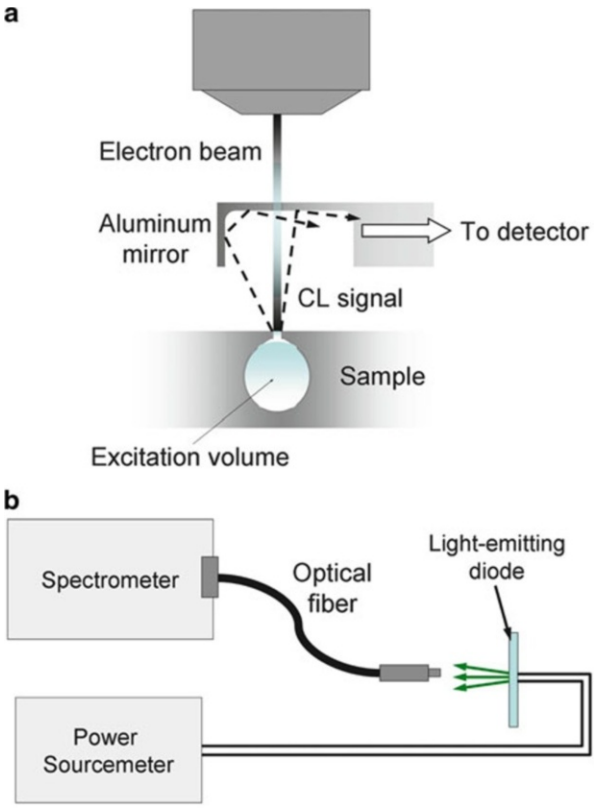

Fig. 10.4 Schematic diagrams of (**a**) CL and (**b**) EL experimental setups

difficult to analyze the origins of different defect emission bands. For EL measurements, it is essential that a good electrical contact to a nanomaterial measured can be achieved. For such purpose, nanoparticle or nanocrystalline films and nanorod or nanowire arrays are the most convenient since they can be processed using conventional techniques for thin film devices. In the case of nanorod/nanowire arrays, it is often necessary to fill the gaps between the nanowires/nanorods with an insulating material, but this can be achieved in a straightforward way by spin-coating polymers or spin-on-glass (with optimized spin-coating conditions and/or followed by etching to expose the tips of the nanostructures). Poor contact and device nonuniformity could result in artifacts in the EL spectra.

It should also be noted that the various emission spectra are frequently measured in arbitrary units. For the measurements of intensity, or luminance, or radiance in absolute units, very careful calibration of the optical setup using suitable calibration sources is needed. Radiance or luminance measurements can be performed using suitable instruments for such measurements, but in those cases as well, it is advisable to double check the instrument accuracy by characterizing the source with known brightness (calibration lamps).

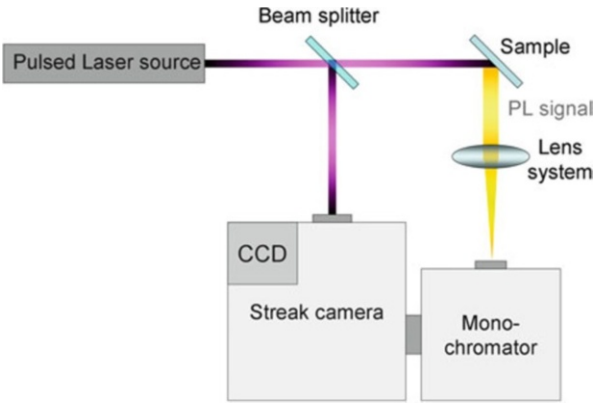

Fig. 10.5 Schematic diagrams of TRPL experimental setup

In addition to steady-state emission spectroscopies, transient measurements such as time-resolved photoluminescence (TRPL) are also of interest. TRPL allows us to study the spectral information from dynamic processes like energy relaxation, charge recombination, and transfer within semiconductors [12, 13]. Unlike steady-state photoluminescence spectroscopy, a pulse excitation source with duration in picosecond or femtosecond scale is used in TRPL. The emission signal from the sample is captured and recorded right after the excitation. An example of an experimental setup is shown in Fig. 10.5. There are various techniques for signal measurement: time-correlated single-photon counting (TCSPC), streak cameras, ultrafast optical (Kerr) gating, etc. [2, 12–14]. In all techniques used, it is necessary to take into account the instrument response time for accurate analysis [2]. Among different techniques, TCSPC modules and streak cameras are commercially available, while TCSPC is the most commonly used method. In TCSPC technique, the sample of interest is excited periodically, and the time delay between the emitted photon and the excitation pulse is recorded. Histograms with the measured time delay values can then be used to characterize the dynamics of the emission [12, 13]. Streak cameras convert emitted light signals into electrical signals (i.e., electrons) by photoelectric effects. The photogenerated electrons are accelerated toward the multichannel plate detector and swept by the electric field perpendicular to the propagation of the electrons. The sweeping rate of the electric field is synchronized with the excitation pulse; hence, the spatial location of the electrons hitting the detector is related to the temporal information of the emission [12, 13].

For detailed discussion of time-resolved and pump-probe techniques, see Ref. [2].

4.2 UV-Vis Spectroscopy

Absorption spectroscopy is typically performed using a spectrometer (for a detailed discussion, see Ref [2]). Spectrometer use is very simple, and the majority of commercial models can be used by any personnel even without training or

knowledge of optical instrumentation [2]. However, there are several artifacts which can occur in the measurements. Spectrometers for absorption measurements can have one or two channels, with a two-channel instrument being less sensitive to the fluctuations in the light source intensity [2]. It also has an advantage of being able to eliminate the influence of a cuvette and solvent for liquid samples in a straightforward manner, as opposed to more involved measurement procedure in a single-channel instrument [2]. The instruments can measure transmittance, or estimate absorbance from the transmittance. It should however be noted that this disregards any reflectance from the samples. Some spectrometer models enable measurement of both transmittance and reflectance, but they are typically more complex to operate. Also, the scattering from the nanoparticle samples can thus result in extended absorption tails. The scattered light intensity is proportional to $1/\lambda^4$ [2], so that any spectral features resembling this dependence, especially in a wide bandgap material, likely occur due to scattering. Other artifacts that can occur are the baseline shifts, either due to instability of the spectrometer or the environment in which it has been placed. This can be minimized by repeating the baseline measurement from time to time [2]. It is also advisable to wait for some time after turning on the instrument for the light source to stabilize before starting the measurement.

4.3 Raman Spectroscopy

Raman spectroscopy (RS) detects information from molecular vibrations that is then used to identify the molecular bonds in a sample as well as to provide specific details on their environment (structural, orientation, and chemical information) with a high degree of specificity. When monochromatic light interacts with matter, a portion of incident light undergoes Rayleigh scattering and it is deflected from its original path without transfer of energy within the sample. Rayleigh scattering is thus an elastic process where the scattered light presents the same energy, or frequency, as the incident light. In contrast, Raman scattering involves the exchange or transfer of energy between the molecules of a given material and the photons incident upon them. In this case, the scattered photons will have new frequencies, or characteristic energies, that correspond to that of the incident photon plus (or minus) the natural frequencies of the thermally excited vibrational molecular states of the material. The Raman effect is named after the Indian physicist Sir C. V. Raman who reported this phenomenon in 1928 [15, 16]. Historical perspectives can be found in the account of Rajinder Singh [17] and Cardona and Merlin [18], as well as references within.

The increasing ability to fabricate, and more importantly to find exceptional advantages and/or unique applications, to nanostructured materials has resulted in an ever increasing demand for characterization tools able to provide detailed information of materials and processes at the nanoscale. In this regard, RS holds a unique position with proven successful applications for the characterization of nanostructures; it has been argued that RS is one of the preferred nanomaterials

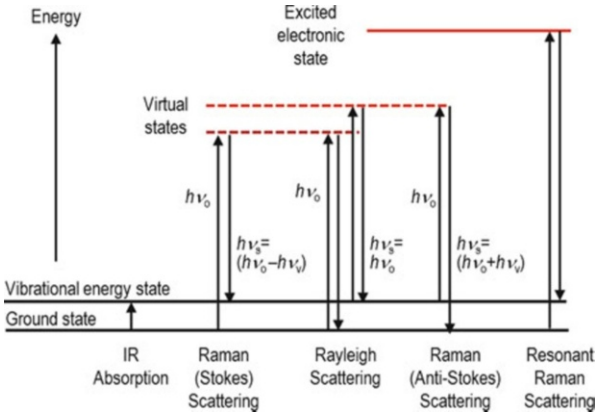

Fig. 10.6 Energy level transitions for IR-absorption, Rayleigh and Raman scattering. The excitation laser frequency is v_0, and v_1 is the frequency of the concerned vibrational mode (After Ref. [23])

characterization tools surpassed only by transmission and scanning electron microscopies (TEM, SEM), X-ray diffraction (XRD), and atomic force microscopy (AFM) [19]. The purpose of this section is to provide a critical review of the potential and advantages unique to this technique rather than attempting an exhaustive review. The basic theory of Raman spectroscopy has been discussed in a number of books and we only present, briefly, the basic concepts involved; the reader is directed to Ref. [20] for a detailed description of the semiclassical theory of Raman scattering or to Ref. [21, 22] for a more complete treatment. Raman spectroscopy considers an incident monochromatic wave of angular frequency v_0 interacting with a vibrational mode of frequency v_v. Scattered light, with frequency v_s, occurs through one of three channels (see energy-level diagrams): (1) elastic (Rayleigh) scattering such that the energy of the scattered photon, hv_s, is unchanged in which case $hv_s = hv_0$; inelastic collisions such that the scattered photon is of (2) lower energy, $hv_s = h(v_0 - v_v)$ called Stokes scattering; or (3) higher energy, $hv_s = h(v_0 + v_v)$, called anti-Stokes scattering, as illustrated in Fig. 10.6. These transitions occur through so-called virtual states that result from distortion of the electron distribution by the electric field of the incident light and have expected lifetimes of $\sim 10^{-12}$ to 10^{-13} s. Because the energy levels of the molecule are discrete and well defined, energy can be lost or gained by the molecule only in quantized or discrete amounts that result in the measured Raman lines (sometimes also denoted as bands, peaks, or modes). Raman spectra are usually represented in terms of intensity of the scattered light (usually in arbitrary units) on the ordinate axis vs. frequency, expressed in wave numbers $\tilde{\nu}$ with units of (cm^{-1}) according to

$$\tilde{\nu} = \frac{1}{\lambda_0} - \frac{1}{\lambda_v} \tag{10.1}$$

where λ_0 and λ_v denote the wavelengths (in unites of cm) of the incident and scattered light. Clearly, the incident and Rayleigh scattered light have a shift value of $\tilde{\nu} = 0$, whereas each vibrational mode in the sample results in a Raman line that is shifted by a value representative of its own energy (frequency).

Some factual remarks regarding the characteristics of Raman scattering follow:

- The intensity of the Raman effect is inherently weak since only about 1 in 10^6 to 10^8 of the photons scattered undergoes Raman scattering. This feature made the detection of Stokes radiation a complicated experimental problem before the development of lasers [24].
- Anti-Stokes scattering occurs only for molecules in an excited vibrational or rotational state before scattering. Therefore, the relative intensities of the Stokes (I_S) and anti-Stokes (I_{AS}) lines can be correlated to the local temperature of the molecule [25].
- The Raman effect results from changes in polarizability of the molecule as its internal motion state is perturbed by the incident electric field; this imposes selection rules in RS: if a vibrational mode is to be Raman active, the vibration must alter the polarizability tensor of the molecule [24].
- Resonant Raman scattering (RRS) occurs when the frequency of the excitation light is close to the frequency of an electronic transition; in this case, strong scattering enhancements (typically 10^3 but up to 10^6) can be observed [24].

For long time since its discovery in 1928, Raman spectroscopy was primarily a specialized research technique. Several milestones changed this, most notably, the successive developments of laser, single photon detection, multichannel detectors, and Fourier transform Raman [26]. Nowadays, RS is routinely used as a, primary or secondary, characterization tool with diverse applications. Like many other characterization techniques, there is no best instrument that will produce optimum results for every sample. Instead, there are trade-offs and multiple considerations in selecting a Raman instrument, or configuration, for a given application. Even after selecting a specific type of instrument, dispersive (monochromator based) or Fourier transform (interferometer-based), there are many choices to be made that will ultimately affect the quality and reliability of the results, including excitation laser line, experiment geometry, collecting optics, and detector. The subject is broad and will only be discussed here, largely following References [23, 24, 26] to illustrate experimental problems or artifacts that might be encountered when collecting the Raman signature of a given sample with a preselected, as it is usually the case, Raman spectrometer. Our presentation will focus on Raman microscopy and dispersive instruments. More specialized cases as time-resolved RS [27] and tip-enhanced Raman spectroscopy (TERS) [28] will not be included.

4.3.1 Excitation Wavelength Considerations

The intensity of the Raman scattering signal is proportional to the power density incident upon the sample (usually in W/cm^2) and to the fourth power of the frequency (ν^4) used to excite the sample [24]. While it might be tempting to simply use UV lasers and to increase the power density as much as possible, such choices are not always practical or desirable. The inexperienced user might be tempted to surrender to the perceived added benefit of decreasing the experiment time by using an exceedingly large laser power with disastrous consequences for the sample and or data reliability. Both the use of large power densities and UV lasers could result in larger energy absorption and potential degradation (burning) of the sample [24].

Even when no actual sample degradation occurs, the resulting local heating can lead to erroneous interpretation of Raman laser shifts; this effect is of particular concern for nanostructured materials which might have poor thermal contact with a suitable heat sink (see discussion of temperature effects in RS).

4.3.2 Sample Fluorescence and Foreign Raman Signals

Fluorescence is another important effect that should be taken into consideration. While the severity of fluorescence is sample and excitation frequency-dependent, it has been pointed out that generally it is a more serious problem with visible excitation as compared to NIR or UV and that under some conditions even fingerprints can cause significant fluorescence [24]. Attention should also be taken to avoid confusing Raman signal from unaccounted impurities/contamination with that of the sample. This can result in severe interpretation errors even for small amounts as the Raman cross section of materials can vary by at least six orders of magnitude [26]. Should the foreign Raman signal happen to be in resonance with the excitation frequency, its Raman signature could be further amplified by several orders of magnitude through resonant Raman scattering (RRS) [24]. Therefore, checks and precautions should be routinely followed to prevent unaccounted signals from substrates, solvents, solutions, and containers that might be used on a particular RS experiment. Special attention should be taken for unknown/new samples and procedures; it has been pointed out [24] that there are multiple published examples where such simple precautions have been ignored yielding wrong conclusions which subsequently were shown to originate in contamination.

4.3.3 Experiment Considerations

Raman spectroscopy is well known for needing little or no sample preparation; furthermore, Raman spectra of samples in gas, vapor, aerosol, liquid, or solid form can usually be collected by placing the sample directly on the spectrometer beam [24, 26]. For modern microscope-based Raman spectrometers, such aim-and-shoot exercise allows one to focus the sample under the microscope and simply collect the spectra. There are, however, several basic but critically important aspects that need careful consideration to avoid spurious data. Besides laser damage/heating and foreign Raman signals, as previously discussed, the user should consider artifact effects from leaking ambient light (neon lights are particularly notorious for their sharp spectra) which could have significant effect under special collection settings (large collection times, high sample reflectivity, objectives with large working distance, etc.). Raman microscopes simplify data collection, and it is certainly an advantage when studying distinctive parts of a complex sample; alternatively, overlooking the inhomogeneous nature of a sample can easily become a source of potential problems and even result in publication of misleading information. Most modern instruments are equipped with mapping capabilities, and they are a great source of detailed information as long as a consistency check is made to ensure that all the sampled area is under focus and issue of greater relevance for confocal microscopy. As a general rule, one can never be too careful; in particular, laboratories with multiple users should run thorough protocol tests before attempting to

collect weak Raman spectra. One can never be too surprised to learn that a microscope objective has been contaminated leaving behind debris that produce, under most collection modes, no significant spectra. The effects of such dirt on the resolution and spectral response can be easily overlooked for days, if not months, as microscopes used for RS are rarely used for diffraction-limited imaging, and quantitative RS is still used by few specialized laboratories.

4.3.4 Calibration Issues

The importance of Raman shift and spectral response calibration is usually highlighted along with their inherent difficulties [24, 26]. Shift calibration is usually based on measurement of atomic emission lines or on Raman shift from standard compounds. The strengths and weakness are discussed in the reference textbooks [23, 24, 26]; it is pointed out that an ASTM standard (ASTM E 1840) has been established for wave number calibration with reported standard deviations smaller than $\sim$1 cm^{-1} [24]. On the other hand, calibration of the spectral response (intensity) is rarely used; a fact that has been attributed to the relative complexity of the procedure and its dependence on sample positioning and instrument settings [29]. The underlying calibration intensity problem is that RS is a single-beam technique with no internal response calibration; in fact, the lack of reliable and simple intensity calibration procedures is regarded as one of the main obstacles for qualitative and broad RS acceptance [21, 22, 26, 29]. Whereas regulatory authorities, largely relating to pharmaceutical industry, have played a key role to push for the implementation and use of standard calibration solutions [24], the scientific community, on the other hand, largely continues to publish data with significant shift variations reportedly as large as ± 5 cm^{-1} [23]. Researchers working in nanomaterials should take a lead in reversing this state of affairs; small changes in Raman shift can provide a wealth of information particularly relevant for nanomaterials research that face added sample complexity and/or need to use advanced data analysis procedures. While modern Raman microscope providers routinely quote spectral reproducibility specifications $< \pm 2$ cm^{-1}, it is ultimately the users responsibility to confirm and maintain correct shift calibration. The reader is encouraged to consult the calibration and validation chapter in Ref. [23].

4.3.5 Data Manipulation and Analysis

The lack of intensity calibration, as is usually the case, results in limited capability to compare relative intensities between different groups and indeed between different operating conditions of the same instrument [29]. With this in mind, even the simplest data analysis, such as confirming the presence of a given material phase by comparing the collected Raman lines against a given standard or literature report, should be approached with care. Study of new samples, and indeed even routinely studied materials prepared by new procedures, grants a thorough revision of system checks to rule out spurious data as outlined earlier; see also page 63 in Ref. [24]. Even without intensity calibration, however, users should be aware of the intensity of the measured Raman lines as compared to the noise in the flat portions of the spectra and to the Raman signal of standard samples measured with the same experimental

conditions. Unusually weak signals could help to identify potential problems such as the need of larger sample quantities, poor sample preparation or alignment, strong signal from diluents or contamination, etc. Finally, extreme caution is recommended regarding data manipulation such as smoothing, baseline flattening, spectral subtraction, and other cosmetic procedures that are unfortunately too easily accessible in modern handling programs [24]. Even the apparently straightforward exercise of background subtraction can be subjective and dependent on user experience and knowledge and can result in irreproducible results unsuitable for advanced Raman spectra interpretation. These issues provide strong motivation for the development of automated background subtraction techniques [30, 31].

4.3.6 Perturbation Effects in RS

The representation of the Raman effect in terms of energy levels associated to vibrational and virtual states by means of the excitation energy of the incident photon highlights two important characteristics. First, the Raman line shift depends on the relative positions of the molecules vibrational energy states; therefore, any perturbation affecting them (strain, thermal excitation, chemical potential, etc.) should be expected to affect the Raman peak position. Second, the strength of the Stokes and anti-Stokes lines is related to the population of those vibrational modes and therefore to the local molecules temperature [25]. In what follows, we consider the effects of pressure and temperature briefly highlighting their relevance in the study of nanomaterials.

We will first discuss the effects of pressure and phase transitions. Understanding structural factors (such as domain size, boundary geometries, and defects) of materials and in particular the atomistic processes during phase formation/transformation provides important information of technological relevance in applications as diverse as mechanical stability, ferroelectric response, and even mass and electron transport properties [32]. While the study of such mechanisms in bulk solids is still an open question complicated by the presence of multidomains and high defect concentrations [32], nanosize materials can show novel bonding geometries with thermodynamics and kinetic processes of phase transitions significantly different from the bulk [33]. It has been argued that differences arise because bulk materials convert at pressures above their thermodynamic transition pressure via fragmentation into finite domains that are, nevertheless, larger than nanocrystals [34]. Accordingly, the study of structural transformations on nanomaterials under high pressure can serve multiple purposes: (1) to characterize the mechanical stability of these building blocks as prerequisite to enable future potential applications [35], (2) as prototypes for single-domain phase transformation studies [32], and (3) as model systems to study the size-dependent structural stability of nanometer size solids [33].

X-ray diffraction (XRD) has been a leading technique to study phase transformation in bulk and nanosized materials [32–34, 36, 37]. It has been pointed out, however, that XRD capabilities are limited for very small particles, less than a few nanometers in size, due to peak broadening, whereas RS maintains demonstrated potential to study their structural evolutions [38]. In addition, the amount of surface

atoms inside the observation volume of a Raman microscope can be large enough to enable the observation of surface vibrational modes enabling the study of surface reactions and adsorbed species characterization [38].

Next, we will discuss the effects of temperature. Assuming that the distribution of electrons on the energy levels of a molecule follows a Boltzmann distribution, then for a given temperature T, most atoms occupy the lowest energy state and higher energy states are populated with an exponentially decreasing number of electrons [25]. In this case the relative intensities of the Stokes (I_S) and anti-Stokes (I_{AS}) lines can be correlated to the local temperature of the molecule as [25]

$$\frac{I_S}{I_{AS}} = \left(\frac{v_0 - v_u}{v_0 + v_v}\right)^4 \exp[hv_v/k_BT] \tag{10.2}$$

where v_0 and v_v are the laser and phonon frequencies, respectively, and h and k_B are the Planck and Boltzmann constants, respectively. While Eq. 10.2 above is used regularly, it has also been shown that temperature determination of diamond over a large range (300–2,000 K) by means of Raman line position is a more straightforward and reliable measurement with ±10 K accuracy [39].

Unwanted temperature effects arising from the excitation laser have been intensively studied for Si nanowires (Si NWs) [40–45]. It has been shown that laser heating depends on (1) the thermal contact with the substrate, (2) the thermal conductivity of the ambient surrounding the SiNWs, and (3) the laser power density at the measuring position, which is significantly different for the micro or macro setup. However, studies of temperature effects on metal oxide nanostructures have been scarce.

The temperature dependence of RS shift in nanomaterials has been reviewed recently from the, more detailed, atomistic point of view [46]. It has been argued [46] that the observed temperature dependence of the red shift of Raman peaks in nanostructures can be explained by the following effects: (1) size-induced red shift: dominated by the bond-order deficiency of undercoordinated surface atoms, (2) temperature-induced red shift: resulting from thermal bond expansion and bond weakening, and (3) lower frequency and larger vibration magnitude of atoms surrounding a defect or at a surface. It was pointed out that more work is needed to clarify the mechanisms behind the size- and temperature-induced Raman shifts and that such studies are justified given the importance of surface phonons that influence directly the electrical, optical, and dielectric properties in semiconductor materials and devices [46].

Finally, we will discuss size effects. The size effects on RS has been a subject of several recent reviews [47–49] that include details on the three theoretical approaches used to investigate phonon confinement including (1) Gaussian confinement model originally proposed by Richter et al. [50] and generalized by Campbell and Fauchet [51], (2) rigorous continuum theory used to obtain the optical vibrational modes in a spherical quantum dot [52], and (3) microscopic

lattice dynamical calculations with few thousand atoms [53–55]. The basic principles, as well as limitations of such models, have been discussed in the cited references; here, we will only point out the main practical details relevant to data interpretation. Nanotechnology enables exciting perspectives based on unique and tunable properties of materials as function of their size. Not surprisingly, the initial goal of nanofabrication techniques is to control the nanoscale properties by correlating the synthesis parameters to the resulting nanosize [49]. Since the translational symmetry of a nanosized crystal is broken at its grain boundaries, it is expected that the resulting Raman spectrum of nanomaterials presents a signature of its size characteristics. However, such phonon confinement effects are noticeable only when the particle size is smaller than typically 20 lattice parameters; stated differently, changes are minor if the particle size is larger than 10 nm. Phonon confinement effects can be weaker if the nanoparticles are embedded in a host matrix such that the phonon dispersion curves of particles and host overlap partially or completely [48]. We emphasize that the exquisite sensitivity of RS to a number of sample characteristics and measurement conditions is also present in the measurement of nanostructures. In this regard, size effects become an added complexity in the analysis of Raman spectra that need careful and controlled experimental conditions to differentiate it from other, potentially larger, contributions such as residual stress, contamination, homogeneous or inhomogeneous laser heating, and disorder among others.

To illustrate the need to carefully analyze the data on nanoparticles to distinguish the effects of size from other contributions, we will discuss the Raman analysis on an example of CeO_2 nanoparticles. The need to rely on complex mechanisms beyond the phonon confinement model, namely, size-dependent phonon relaxation, to explain the Raman peak energy decrease and line width increase with decreasing particle size was called into question by Spanier [56]. The detailed Raman analysis of CeO_2 nanoparticles in Ref. [56] showed that changes in the Raman spectrum with particle size could be explained when taking into account the combined effects of (1) strain (increasing lattice constant relative to the bulk resulting from the presence of Ce_{31} ions and oxygen vacancies), (2) dispersion in the particle size distribution (inhomogeneous strain broadening), and (3) phonon confinement [56]. The effects are illustrated in Fig. 10.7.

Therefore, RS is a powerful research tool to investigate a large variety of phenomena in nanomaterials based on the interrogation of their vibrational spectra as determined from the Raman effect. Furthermore, advances in commercial instrumentation, ease of sample preparation, and ability to perform in a large variety of extreme conditions have made RS one of the preferred tools in nanoscience and nanotechnology. We have highlighted the strengths and applications of RS to characterize pressure, temperature, and size effects in nanomaterials and directed the reader toward potential practical applications of such studies as appropriate. The practical aspects of the technique including excitation source, fluorescence and foreign Raman signals, calibration issues, and data manipulation were reviewed with emphasis in the risks of collecting spurious data and highlighting consistency checks and procedures to avoid them.

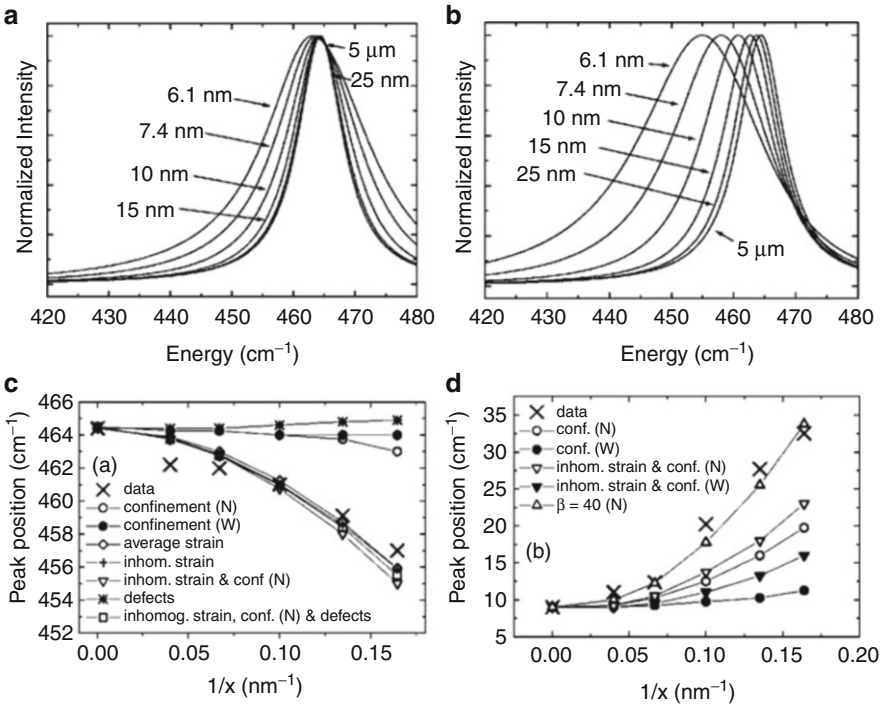

Fig. 10.7 Modeling of Raman spectra for selected CeO_2 nanoparticle sizes for the cases of (**a**) confinement only and (**b**) the combination of inhomogeneous strain and confinement. (**c**) and (**d**) show the peak position and line width, respectively, for the 464-cm^{-1} Raman line as a function of particle size for the experimental data (denoted by X) and several models including one or a combination of several factors considered. The model predictions with combined inhomogeneous strain and confinement (open inverted triangles, denoted $\beta = 40$) fit well the experimental data; further details can be found in Ref. [56]

5 Key Research Findings in Recent Years (2005–2011)

5.1 Emission Spectroscopy: Photoluminescence, Cathodoluminescence, and Electroluminescence

5.1.1 Photoluminescence

Photoluminescence measurements are commonly used for studying the properties of metal oxide nanomaterials. Among various metal oxides, ZnO has been extensively studied (both ZnO nanostructures and ZnO in general, bulk or thin film) due to its strong light emission, controversial issues in explanations of optical properties on which no consensus has been reached, as well as great potential for practical applications. The progress in studying ZnO has been described in several recent reviews [57–60]. Defects in ZnO and their effect on electronic and optical

properties have also been reviewed [59, 61]. Here, we will summarize the relevant findings related to optical properties of ZnO obtained by different techniques. Even though this chapter is primarily concerned with the optical properties of metal oxide nanostructures, it should be taken into account that research work on bulk (single crystal or thin film) samples can be relevant in establishing the origin of certain spectral features which are not expected to be size-dependent (especially in larger nanostructures). For example, the visible photoluminescence was investigated in ZnO thin films with different surface orientations, and it was found that the surface orientation significantly affected the intensity of the green defect emission, which was attributed to surface oxygen vacancies [62]. Impurity incorporation can also be different for different crystal faces of ZnO [63]. This could possibly affect the defect emission and result in significant differences in the emission spectra of nanostructures with different morphologies. Another investigation in bulk samples considered hydrogen passivation to investigate the origin of the yellow-green emission [64]. It was found that the yellow emission at ~2.1 eV disappeared after hydrogenation, while green emission at ~2.43 eV was unchanged [64]. Consequently, the yellow emission was attributed to oxygen vacancies, while green emission was attributed to complexes consisting of oxygen vacancies and other defects [64]. However, green emission in N-doped ZnO films was attributed to donor-acceptor transitions [65].

Regardless of the sample morphology, the origin of various defect emissions is still unresolved. Different hypotheses have been proposed in reported studies. Among the most commonly proposed defects to explain the green defect emission is the oxygen vacancy. The assignment of green emission to oxygen vacancy based on previous work by Vanheusden et al. [66] is still very common. Often, the assignment is performed by a simple discussion of the effects of morphology and a literature citation, without any more detailed investigation of optical properties, impurities, defect types, and concentrations. In some cases, misidentification of electron spin resonance (ESR) peak at g ~1.96 as corresponding to singly ionized oxygen vacancy also based on Ref. [66] still occurs, for example, in recent study of oxygen defects in ZnO nanoparticles [67], even though there have been several reviews of ZnO properties which clearly explain this misidentification [58, 61]. In some cases, it has even been clearly stated that it should not be assumed that green emission occurs due to oxygen vacancies [61].

In addition to oxygen vacancy hypothesis proposed both experimentally [66] and theoretically [68], other hypotheses have been proposed as well [57, 58]. Green emission frequently exhibits structured peaks at low temperatures [69]. Such structured transitions were attributed to two electronic transitions related to deep acceptors which had strong electron-phonon coupling [69]. Structured emissions in older works have also been attributed to external impurities, such as copper [57, 58]. Another common hypothesis to explain green emission is that it occurs due to surface defects [58]. For example, green luminescence in ZnO nanoparticles has been attributed to surface defects (oxygen vacancy for 490 nm, oxygen antisite for 520 nm) [70]. Also, the involvement of surface defects in the deep level emission from ZnO nanowires was confirmed by spatially resolved CL measurements [71].

However, green emission was also attributed to the defect complex consisting of zinc vacancy and interstitial zinc, while the surface defect complex consisting of zinc vacancy and water resulted in the reduction of the green emission [72].

Nevertheless, significant change in the emission spectra with surface modification is a strong indicator that surface defects are indeed involved in that particular emission. Thus, green emission has been attributed to surface defects (oxygen vacancies), and it has been demonstrated that it can be passivated with modifying the surface of ZnO nanoparticles with surfactants [73]. Passivation with alumina shell also reduced surface-state emissions but had no effect on the orange (2.1 eV) defect emission in ZnO [74]. It was also reported that ZnO nanostructures in ethanol did not exhibit visible emission, while such emission was observed for ZnO nanostructures in air [75]. This was attributed to the participation of adsorbed oxygen molecules in visible emission [75]. However, it should be noted that it is possible that the emission simply originates from surface defects, which are passivated in ethanol.

In addition, it was reported that "green" defect emission ($\sim$17,000 cm^{-1} or $\sim$590 nm) in ZnO nanoparticles is associated with the presence of OH groups and could be suppressed by capping the nanoparticles with dodecylamine [76]. In another work on hydrothermally grown ZnO nanorods, emission associated with surface adsorbates such as OH groups has been labeled yellow, but the peak position is similar ($\sim$580–600 nm) [77]. Green and orange-red emissions were attributed to defect complexes, some of which may include zinc vacancies [77]. The yellow (580 nm) emission was also attributed to oxygen vacancies [78].

Less frequently than the green and orange luminescence in ZnO, other emission bands such as violet emission [58] have also been observed in ZnO. Violet emission was attributed to zinc vacancies or zinc vacancy containing complexes [79]. The presence of blue emission (440 nm) was attributed to the involvement of amine groups on ZnO nanoparticles [80]. Blue emission was also attributed to zinc interstitials, while green and orange-red emissions were attributed to oxygen vacancies and oxygen interstitials, respectively [81].

PL studies of defect emissions also involved more complex investigations, such as variable temperature measurements, combinations with other measurement techniques, and the use of an additional excitation beam. Temperature dependence of different defect emission bands in ZnO has been studied on different nanostructured morphologies of ZnO [82, 83]. For ZnO nanoneedles, it was found that UV emission exhibited red shift, green emission exhibited blue shift, while violet emission exhibited S-shaped dependence of the peak position on temperature [82]. For other ZnO nanostructures (where no violet emission at $\sim$3 eV was observed, but blue emission at $\sim$2.8 eV was present at low temperatures), no shift or a small blue shift of defect emissions were observed [83]. It was also found that the PL spectra as well as conductivity in ZnO could be affected by a second excitation beam, which was most significant for the green excitation [84]. The observed phenomena were attributed to surface oxygen vacancies, with the hypothesis proposed that isolated V_o^+ act as green emission centers while V_o^+ complexes act as nonradiative recombination centers [84].

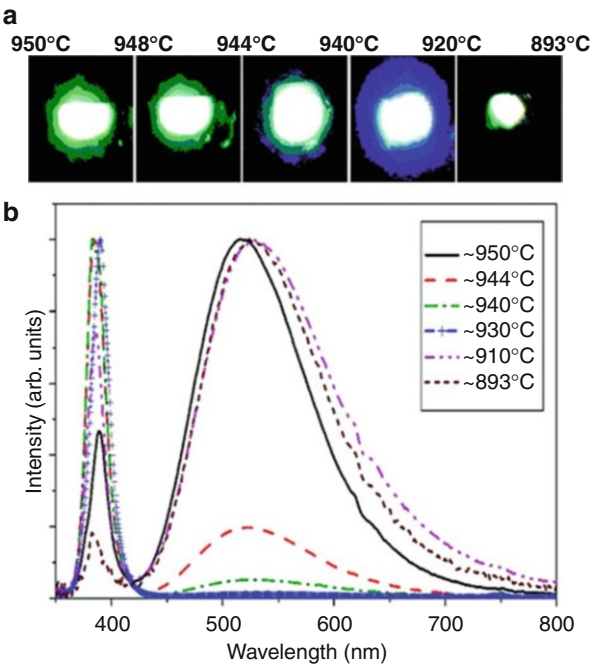

Fig. 10.8 (**a**) Photograph of luminescence from areas with different substrate temperatures. (**b**) PL spectra of tetrapods grown at different substrate temperatures. The intensities of the spectra have been normalized for easier comparison of UV and green emission ratios (Reprinted with permission from J Phys Chem B 112, 16286. Copyright 2008 American Chemical Society)

Obviously, ZnO exhibits very complex defect chemistry. Samples prepared by different methods frequently exhibit drastically different optical properties as a consequence of the fact that the defects in ZnO are strongly influenced by the growth conditions. Growth temperature is one of the significant parameters which affects the optical quality of ZnO nanostructures. It has been shown that there is a narrow temperature window in which high optical quality tetrapods can be grown [85], as illustrated in Fig. 10.8. Similarly, quantum efficiency of ZnO nanowires exhibited very prominent temperature dependence, where a narrow temperature window (900–920 °C) for the optimal ZnO properties was also found [86]. In addition, it has been found that excitons in ZnO tetrapods have long lifetime [87], and the photoluminescence decay in tetrapods can actually be longer than that of high-quality single crystals [85, 87]. Tetrapods also had low density of nonradiative defects [85]. Low nonradiative defect density was observed in other ZnO nanostructures as well, such as ZnO nanowires grown by metal organic vapor phase epitaxy [88].

Although primarily determined by the growth conditions, the optical properties of ZnO nanostructures can be improved by postdeposition treatments, such as annealing [77, 89], or hydrothermal treatment [90–92]. It should be noted, however, that the absence of defect emission in the room temperature PL spectra does not imply high crystal quality of the samples, since in some cases low positron diffusion length indicating high defect concentration is observed even in the absence of defect emission [89]. Also, the ratio of the UV-to-visible emission does not necessarily represent a good measure of the sample quality, since it is dependent

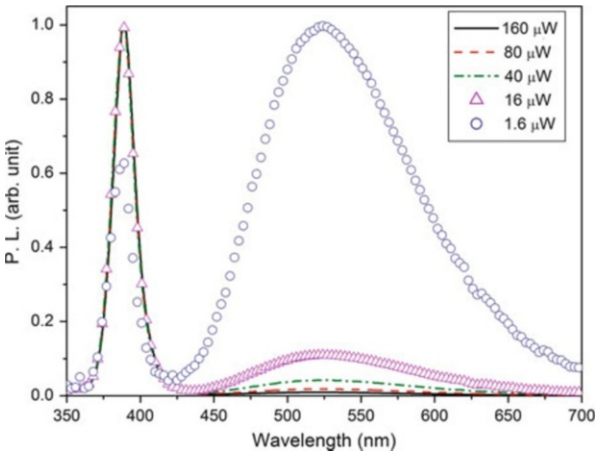

Fig. 10.9 PL spectra from ZnO tetrapods measured for different excitation powers

on the measurement conditions. PL spectra of ZnO tetrapods measured at different excitation powers are illustrated in Fig. 10.9. It can be clearly observed that the UV-to-visible ratio is significantly affected by the excitation power. Nevertheless, ratio of UV-to-visible emission is a useful indicator of relative difference among the samples measured under identical conditions and as such can be used to evaluate influence of the growth factors or the postgrowth treatments on the sample quality. The outcome of both annealing and hydrothermal treatment was found to be dependent on the starting properties of ZnO nanostructures [77, 92]. The improvement in the optical properties after the hydrothermal treatment has been attributed to the removal of Cl in the electrodeposited ZnO [90] and the elimination of native defects via reaction with water molecules [90, 91]. The treatment time had a significant effect on the optical properties [90, 92], and it was also found that in the case of ZnO growth on Si during hydrothermal treatment, there is out-diffusion of Si [92]. It should also be noted that treatment conditions have a huge influence on the treatment results. ZnO is extremely sensitive to the water vapor exposure. It has been shown that morphology and properties of ZnO nanocrystals can be altered in ambient with exposure to humid air [93]. This phenomenon is not limited to nanostructures only, since the formation of nanomounds and change in the zinc vacancy concentration in the surrounding region as a consequence of ambient exposure have been observed in ZnO single crystals [94].

Another method of changing the optical properties is the addition of impurities, intentional or unintentional. For example, hydrogen is a common impurity which is very difficult to avoid, and it is likely responsible for the *n*-type conductivity of unintentionally doped ZnO. It is well known that hydrogen can passivate defects in ZnO [95]. However, information on how exactly the passivation occurs has been scarce. Nevertheless, there have been some studies of hydrogen in defect complexes in ZnO. For example, defect complex between zinc vacancy and two hydrogen atoms has been studied by infrared absorption spectroscopy [95]. The passivation of defects can also result in the enhancement of conductivity and

stability of ZnO films [96]. The enhancement of near-band edge PL in ZnO nanowires due to unintentional incorporation of hydrogen during metal sputtering was also reported [97]. Furthermore, the appearance of a violet emission after hydrogen implantation was attributed to hydrogen-oxygen vacancy defect complex [98]. In addition to the effect on the optical properties of ZnO, hydrogen also has an effect on the electronic properties. It was proposed that hydrogen passivates acceptor defects and introduces new donor states interstitial hydrogen and hydrogen-oxygen vacancy complex [99]. These donor states (interstitial hydrogen at bond-centered position and hydrogen trapped at an oxygen vacancy) were proposed to be responsible for *n*-type doping in ZnO based on Hall, PL, and Raman measurements [100]. The hydrogen-oxygen vacancy complex is stable for annealing temperatures up to 400 °C and anneals out at ∼500 °C [99]. Thus, hydrogen can have undesirable effect on electronic properties in the attempt of *p*-type doping, since it results in creation of donor states and it can also passivate nitrogen acceptors [101].

Other elements can also have significant effect on the optical spectra. For example, it has been shown that doping with Ga can increase the ratio of UV-to-visible emission in ZnO nanorods grown by hydrothermal method [102]. Also, the quenching of surface exciton emission was achieved by Ti plasma immersion ion implantation [103].

Therefore, defect emissions from ZnO have been comprehensively studied on both nanostructured and bulk samples. Even though no consensus has been reached, it appears likely that optical properties are strongly affected by the growth temperature and that the green emission could be reduced by hydrogen passivation and/or surface passivation. The exact chemical origin of this emission and other defect emission bands, however, is still unresolved. In addition to the studies of the origin of the defect emission, high-quality bulk single crystal samples combined with thorough experimental characterization techniques are also of interest for correctly identifying bound exciton lines in the low temperature PL spectra [104]. Significant differences compared to earlier work summarized in different reviews [57, 58] are the observation of the Fano resonance for 1-LO replica line I_{6a}^{1LO}, difference in the exciton-phonon coupling strength of bound and free excitons, and the identification of one donor-bound exciton lines as possibly associated with Pb impurities [104]. The identification of a line corresponding to aluminum shallow donor (3.3607 eV) has also been reported recently [105]. I_{12} line at ∼3.3465 eV in ZnO thin films, which were grown on MgO buffer layer or highly doped ZnO, was attributed to an exciton bound to a neutral donor [106]. A peak at 3.3665 eV was attributed to surface excitons in ZnO nanorods, and it dominated the spectra at low temperature [107]. Surface excitons were also observed in ZnO nanowire/nanowall structures [108]. The surface exciton peak at ∼3.367 eV in ZnO nanostructures was attributed to surface adsorbates, likely OH group-containing species [109]. The intensity of the surface exciton peak was found to be dependent not only on surface-to-volume ratio but also additional morphology and crystal quality factors [109].

Other techniques can be combined with PL to conclusively identify bound exciton lines. Magnetophotoluminescence spectroscopy technique can be helpful

for identifying bound excitons in ZnO [110, 111], since it allows determination of charge states of defect centers [110]. Free and bound excitons can also be studied with a combination of polarized photoreflectance and PL spectroscopy [112]. The use of radioactive isotopes is also helpful in conclusive identification of bound exciton lines [113, 114]. Thus, I_8 line at 3.3600 eV and I_1 line at 3.3718 eV were attributed to gallium (neutral and ionized, respectively) [113], feature at 3.225 eV was attributed to Ge [113], while I_9 line at 3.3572 eV was attributed to In donors [114].

Furthermore, based on PL studies of implanted samples, it was proposed that arsenic preferentially occupies Zn site, which has potential implications on *p*-type doping [115]. Another issue, which has implications on *p*-type doping, is the origin of the optical transition at ~3.31 eV. This transition is of interest since it is frequently observed in *p*-type ZnO, and different explanations of its origin have been proposed in the literature. Emission at ~3.31 eV was proposed to be associated with an unknown acceptor level and not with the surface states [74], as suggested by other studies [116]. Although the emission at ~3.31 eV is often considered to be associated with *p*-type doping of ZnO nanostructures, it has been shown to be related to crystal defects in ZnO (studied on microcrystalline and nanoparticle samples) [117]. Evidence for association between structural defects and this emission has also been found by other groups and using different techniques, so that at present evidence that this emission originates from structural defects appears conclusive. For example, deeply bound exciton transition at ~3.333 eV was attributed to excitons bound to extended structural defects based on the comprehensive investigation of optical properties by a variety of techniques, and this emission was found to have inverse correlation with green defect emission [118]. Assignment of the line at ~3.311 eV to structural defects based on spatially and wavelength-resolved cathodoluminescence measurement on ZnO nanocrystals was also reported [119]. More specifically, the emission at ~3.314 eV was attributed to acceptor states located at basal plane stacking faults [120, 121]. Presence of this feature in samples with attempted *p*-type doping may indicate that the doping likely results in presence of stacking faults [120]. Thus, whenever studying doping in ZnO, it is necessary to consider whether the observed properties arise due to the dopant atoms or due to the changes in native defects concentrations (including both point defects and extended structural defects). Finally, it should be noted that similar to green defect emission, these structural defects can be passivated by hydrogen [122].

One aspect of optical properties of nanostructures, which is of significant interest, is the size dependence of various aspects of their optical properties, such as bandgap, PL decay time, temperature dependences of different emission bands, etc. Based on temperature-dependent PL studies, it was proposed that in ZnO quantum dots (4 nm), acceptor bound excitons are dominant transitions at all temperatures [123]. For ZnO nanocrystals (20 nm), acceptor-bound excitons were dominant below 150 K, while above this temperature, donor-bound excitons were dominant transitions [123]. It should be noted, however, that ZnO nanostructures with different sizes have different native defect and/or impurity concentrations,

which is not necessarily related to the difference in the surface-to-volume ratio (since different sizes may require different growth conditions or growth times). Thus, it is difficult to conclusively establish which phenomena are direct consequences of different nanostructure size.

In studying the influence of size on the luminescence and absorption of nanomaterials, emission shift due to quantum confinement is of significant interest. It was shown that the quantum confinement effects (blue shift of the emission with decreasing size) can be observed in very small ZnO quantum dots [124–127]. The intensities of the Raman modes were also found to increase with decreasing size, which was attributed to a change in the Raman cross section [125]. However, no shift of Raman modes was observed [127]. Quantum confinement effects on the defect emission in small (2.2–7.8 nm) ZnO quantum dots were also reported, and the defect emission was attributed to a transition between the deep donor level and the valence band [128]. However, it should be noted that this phenomenon will occur only for nanostructures with size smaller or comparable to Bohr radius. The majority of various nanostructured materials (nanowires, tetrapods, nanorods, etc.) are significantly larger than that and quantum confinement would not occur. For example, the influence of the particle size on the luminescence has been studied in ZnO nanoparticles [129]. The nanoparticles were in the size range from 25 to 73 nm, so that no quantum confinement is expected (Bohr radius in ZnO is ~2.34 nm) [129]. It was found that both UV and visible emission increased with particle size, which was attributed to higher concentrations of nonradiative defects in smaller particles [129]. In general, the surface properties of nanomaterials are known to have significant effect on their overall properties due to their large surface-to-volume ratio. However, surfaces typically contain various defects. It has been demonstrated that UV luminescence of ZnO can be considerably enhanced by a polymer (poly(methyl methacrylate)) coating [130]. In spite of the known facts that nanostructures need to be sufficiently small for quantum confinement to occur and that surface properties have a significant effect on nanostructure properties, the shift of the emission peaks with size of ZnO grains or nanostructures is sometimes mistakenly attributed to the effects of quantum confinement in larger nanostructures despite their size (significantly larger than Bohr radius) [131]. This means that there are other factors responsible for any spectral shifts observed in larger ZnO nanostructures. It is quite common that different nanostructures exhibit different positions of the UV emission peak in room temperature PL spectra, as illustrated in Fig. 10.10.

Several possible phenomena have been proposed to explain spectral shifts of the UV emission in ZnO. If the nanostructures are significantly larger than the Bohr radius, one or more of these phenomena will be responsible for spectral shifts rather than quantum confinement. It has been shown that a variation in coupling of excitons and phonons results in a shift of emission peak at room temperature (since the peak is a combination of exciton emission and phonon replicas) [132]. Blue shift of the emission with decreased diameter of ZnO nanorods was attributed to the reduced exciton-phonon interaction [133]. Surface defects were also found to affect the exciton-phonon interaction and could result in peak shift of the UV

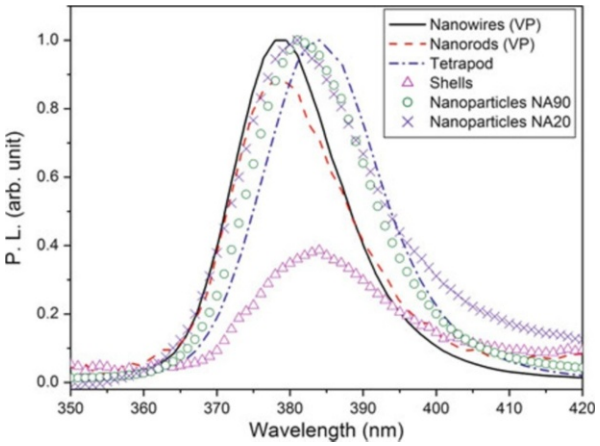

Fig. 10.10 PL spectra from different ZnO nanostructures. NA denotes commercial nanoparticles obtained from Nanostructured & Amorphous Materials Inc

emission in ZnO [134, 135]. While the parameters affecting exciton-phonon interactions in ZnO nanostructures are likely having complex interplay (size, surface roughness, defect concentrations), it is likely that spectral shifts observed for different sizes or morphologies of ZnO could be explained as a result of different contributions of free excitons and phonon replica emissions to the broad room temperature UV luminescence. Blue shift of UV luminescence in ZnO nanowires was also attributed to Burstein-Moss effect [136]. In addition, blue shift could occur due to the dominance of surface effects in PL spectra of thin nanostructures [137]. In some cases, no shift occurs due to opposite effects of the change in exciton-phonon coupling due to surface defects and the surface resonance effects [138]. Furthermore, the blue shift of the near-band edge emission in ZnO nanorods was attributed to surface recombination centers, and it was proposed that the rods having diameters larger than 620 nm will have the bulk properties [139]. The energy shift exhibited linear dependence on $1/d$ where d is the diameter of the nanorod [139]. Thus, it is essential to carefully consider all the possible reasons for spectral shifts before drawing any conclusions based on the position of the UV emission peak in the room temperature PL spectra.

In addition to the size dependence of the position of the absorption edge and near-band edge emission, other effects of size on the optical properties of ZnO have also been investigated. For example, size-dependent recombination in ZnO has been studied, and it was found that the lifetime of a bound exciton transition (at ~3.365 eV) decreases with decreasing dimensions due to increased surface recombination [140]. Also, the transitions at 3.341 eV and 3.314 eV were attributed to surface states [140]. Another phenomenon, which can occur in small ZnO nanostructures (such as ZnO nanorods with 5-nm thickness and 30-nm length), is the stabilization of exciton emission even at high excitations where electron-hole plasma emission would occur in the bulk [141]. This was attributed to an increase in the exciton binding energy with decreasing nanostructure size [141]. Finally, nanomaterial size also has an effect on the achievement of stimulated emission,

since increased number of surface defects and surface states can result in increased losses. Under sufficiently strong optical excitation, stimulated emission from various ZnO nanostructures is very common [142]. Time-resolved studies of stimulated emission from ZnO nanoneedles have been reported [142]. However, in ZnO nanoparticles the dependence of appearance of stimulated emission and the transition to electron-hole plasma emission with increasing excitation were found to be dependent on the particle size, which was attributed to increased nonradiative recombination with size reduction [143]. On the other hand, larger ZnO nano- and microstructures frequently exhibit stimulated emission and can exhibit waveguiding effects if they are sufficiently large. For example, exciton-polariton lasing has been observed in whispering gallery mode ZnO microcavities [144, 145].

Nanostructures of other metal oxides have been less commonly studied compared to ZnO. Nevertheless, there have been studies of gallium oxide, tin oxide, indium oxide, titanium dioxide, etc. Size dependence of photoluminescence has been studied in Ga_2O_3 nanoparticles [146]. Size dependence of luminescence was also studied for SnO_2 nanowires [147]. The nanowires exhibited yellow defect emission and the emission intensity decreased with decreasing diameter at room temperature [147]. For metal oxide nanostructures other than ZnO, defect emissions are also commonly observed. Different origins have been proposed for those defect emissions, although the defect emission in other oxides besides ZnO is also frequently attributed to oxygen vacancies. For example, green emission in germanium oxide nanowires was attributed to oxygen-related defect states (oxygen vacancies) [148]. While in this case X-ray absorption near-edge structure data were provided [148], frequently an assignment of defect emission to oxygen vacancies is done without additional supporting data, with just a reference to other works in the literature which also commonly fail to provide further evidence for the oxygen vacancy hypothesis. For example, broad orange-red emission in Cr-doped $In_2O_{3-\delta}$ was attributed to oxygen vacancies [149]. However, orange luminescence intensity in In_2O_3 octahedron structures was attributed to indium interstitials and complexes containing In interstitials rather than oxygen vacancies [150]. In SnO_2, red defect emission is also commonly attributed to oxygen vacancies or surface defects. For example, red defect emission in SnO_2 nanoribbons was attributed to combined oxygen vacancy (singly and doubly ionized) centers, based on photoluminescence, ESR, and Fourier transform infrared spectroscopy (FTIR) results [151]. It should be noted however that similar to ZnO, PL measurements before and after annealing in different environments cannot be considered as conclusive evidence to identify the defects (although they can disprove a hypothesis), while theoretical calculations often have significant uncertainties of actual energy level positions, which make conclusive identification of a certain optical transition difficult. Nevertheless, calculations predicted that surface bridging vacancies could result in formation of surface bands in agreement with the observed PL spectra [152]. Surface defects were proposed to explain visible luminescence in SnO_2 nanowires and nanobelts [153]. Ultrafast pump-probe spectroscopy was also used to study defect levels due to surface states in SnO_2 [154].

Both blue-green (~480 nm) and red (~600 nm) emissions in SnO_2 nanowires were attributed to oxygen vacancies [155]. It should be noted that for metal oxide nanowires grown at high temperatures on Si substrates which exhibit blue emission, it is necessary to conclusively rule out any presence of SiO_x to establish the origin of this emission.

The blue defect emission in Ga_2O_3 was assigned to a donor-acceptor pair recombination, and the binding energies of donors and acceptors were found to be size-dependent [146]. Finally, it was also found that surface trapping sites affect the recombination by competing with the acceptors for the photogenerated holes, so that the passivation of surface trapping sites results in the increase of defect emission [146], different from the reports on the green emission in ZnO [58, 59]. Photoluminescence studies of mesoporous titania have also been reported, and the emission in the violet-UV part of the spectrum (peak center 394–402 nm) was observed [156]. PL emission from different titania nanostructures has also been studied [80]. UV emission was attributed to self-trapped excitons at TiO_6 octahedra, while the emissions at longer wavelengths were attributed to oxygen vacancies [80]. Very intense blue-green emission was observed from MgO core/TiO_2 shell nanorods under 325-nm excitation, and the emission intensity was strongly dependent on the shell thickness [157].

Near-band edge emission in metal oxide nanostructures different from ZnO is rarely observed. Nevertheless, there have been reports of UV emission from tin oxide and indium oxide. Ultraviolet luminescence from SnO_2 is rarely reported, but there have been detailed studies of temperature-dependent UV PL spectra from high-quality SnO_2 nanowires [158, 159]. Ultraviolet emission has also been reported for ultrathin In_2O_3 nanowires, and different features corresponding to free and bound excitons, longitudinal optical phonon replicas, and donor-acceptor transitions have been identified in temperature-dependent PL spectra [160].

5.1.2 Time-Resolved Photoluminescence and Two-Photon Spectroscopy

Several studies have reported time-resolved PL of different ZnO nanostructures. Using PL and time-resolved PL, it has been demonstrated that homoepitaxial and heteroepitaxial ZnO nanowires have comparable properties [161]. A study of PL from colloidal ZnO nanocrystals reported that initial fast shift of the emission occurs due to fast hole cooling [162]. Biexponential decay was observed, with fast decay time independent on particle size and attributed to a nonradiative process, while slow decay time dependent on the particle size which was attributed to traps [162]. Size-dependent time-resolved studies have also been performed for ZnO nanoparticles with different sizes, and it was found that the fluorescence lifetime decreased with decreasing nanoparticle size [163]. This phenomenon was attributed to increased nonradioactive decay due to surface states with decreased nanoparticle size [163]. In ZnO nanorods, it was found that decay time increased with nanorod size increase in the range 150–600 nm [164]. However, it should be noted that in larger ZnO structures such as tetrapods, PL decay times as long or longer than in single crystals could be obtained [85].

Time-resolved measurements can also be used as additional technique in identification of the origin of the defect emissions. It was proposed that the green luminescence is a superposition of emission bands associated with oxygen and zinc vacancies, which exhibited different decay curve dependences on excitation wavelength and different dependencies of emission intensities on temperature [165]. Annealing in different environments was used to obtain samples with different densities of oxygen and zinc vacancies [165]. Other uses of time-resolved optical techniques include studies of conductivity and charge transport. Time-resolved terahertz spectroscopy, which can determine far-infrared photoconductivity, is useful for studying the conductivity of metal oxide materials [166]. The technique has been applied to thin films as well as nanowires and nanoparticles [166].

In addition to single-photon excitation, two-photon and multiphoton excitation have also been used to study ZnO nanostructures. Decay times in ZnO tetrapods were similar under one-photon and two-photon excitation, confirming low defect concentration in these materials [167]. UV luminescence in ZnO induced by multiphoton excitation has been demonstrated [10]. UV and visible emission peaks induced by two-photon excitation were also observed in ZnO microtubes [168]. In addition, stimulated emission achieved by two-photon [169] and multiphoton [170] excitation has been reported. Furthermore, nonlinear optical properties of ZnO quantum dots were studied, and three-photon induced four-photon absorption was observed [171]. It was also reported that ZnO nanopowders prepared by a sol-gel method have a low threshold (smaller than 18 W/cm^2) for the appearance of nonlinear emission peaks (free biexciton and inelastic exciton-exciton scattering) [172]. Furthermore, two-photon spectroscopy (both time-resolved and time-integrated) has been used to investigate spatial heterogeneity of electron-hole plasma formation in ZnO nanorods [173]. It was found that electron-hole plasma formed near the end of the nanorod, and the spatial pattern was affected by the whispering gallery modes [173].

5.1.3 Cathodoluminescence

Cathodoluminescence is a useful tool for studying correlation between luminescence and spatial features. It was found that dislocations and stacking faults result in quenching of the emission attributed to free-to-bound electron acceptor luminescence [174]. CL measurements were also used to identify association of 3.314 eV emission with basal plane stacking faults in ZnO [120]. In addition, CL is useful for studying bulk samples, since depth-resolved measurements can provide information on spatial distribution of defects [175], which is useful in identification of defect emissions and studying ZnO surfaces and interfaces with other materials. CL was also used to study the influence of nanoindentation on the ZnO emission [176]. It was found that indentation results in a reduction of the UV emission and the enhancement of the visible defect emission, where at least two different defect states contribute to the visible emission band [176].

In addition, CL spectroscopy is particularly useful in studying the spatial distribution of emission in nanostructures. This can be applied to study the location

of defect emissions, influence of the strain if any, distribution of impurities, etc. For example, CL has been used to study the luminescence from an aligned ZnO nanorod array [177]. It was found that there was a different distribution of defects on the nanorod top surface and sidewalls, with considerably stronger green emission observed from the sidewalls [177]. CL spectroscopy was also used to demonstrate that different emission bands (UV and green) can be obtained from the opposite ends of ZnO nanorods, which was attributed to different concentrations of oxygen along the length of the nanorod, so that reduced oxygen concentration resulted in the dominance of green emission attributed to oxygen vacancies [178]. Furthermore, CL has been used to study spatial variation of luminescence of ZnO/MgZnO coaxial nanowire arrays, and it was found that luminescence intensity was dependent on the MgZnO shell thickness [179]. This effect was attributed to the carrier confinement and surface passivation by MgZnO shell [179]. In addition, CL has been applied to study the emission from single ZnO nanopillars [180]. This study demonstrated that the luminescence from the wetting layer was very weak, while the nanopillars exhibited sharp exciton emission lines with no spectral shift along the pillar (detection of spectral shift can indicate the presence of strain) [180]. Furthermore, the use of CL to detect the incorporation of Al from the substrate near the bottom of the pillar, as well as unintentional doping by Ga, has been demonstrated in this study [180]. CL has also been used for characterizing the distribution of impurities in ZnO nanotubes grown on sapphire [181]. For ZnO grown on Si, a nonuniform distribution of Al donors was also observed [182].

In addition to bulk samples and nanorods/nanowires, CL [183, 184], together with temperature-dependent PL [183], was used to study the emission from ZnO tetrapods. It was found that defect emission increased for smaller size tetrapods (smaller than 500 nm) [184]. It was also found that suppression of the no phonon line was strongly dependent on morphology, and it was attributed to readsorption after multiple internal reflections in faceted structures [183]. In addition, the studies of the spatial distribution of the emission using CL spectroscopy are helpful in explaining unusual angular dependences observed in other measurements, such as PL, which can occur due to inhomogeneity of the emission along the nanorods [185]. Cathodoluminescence was also used to visualize localized photon modes in ZnO microrods with one metal (Al) mirror [186]. Furthermore, CL intensity can be dependent on the nanostructure morphology. Enhanced emission intensity was reported for ZnO nanocone arrays compared to ZnO nanowire arrays [187].

In general, the majority of the CL studies of metal oxide nanostructures have been performed at room temperature. Also, most of the reported results have been obtained for ZnO, which is likely due to the fact that ZnO typically exhibits very bright emission. Weaker emission can be more difficult to detect using CL, since higher sensitivity can be achieved easier with PL. CL spectroscopy studies at low temperature have been scarce [188–190]. CL spectroscopy at low temperature (77 K) was performed on ZnO nanobelts [190]. It was found that at low temperatures, free exciton emission was suppressed due to large surface-to-volume ratio of the nanobelts, and that discrepancies in estimated binding energy from CL and PL can occur due to momentum transfer from electrons to excitons in the CL [190].

Low temperature CL studies also revealed that ZnO nanowires emitted sharp and prominent bound exciton emission (I_8 line) at low temperature, while the emission from the wetting layer was much weaker and occurred at lower energies [189]. Due to lattice mismatch, defect density can be higher near the ZnO nanorod/substrate interface, which has been recently shown for ZnO growth on *p*-type 4H-SiC [188]. CL can also be used to study the effects of strain on the near-band edge emission, as demonstrated in ZnO nanowires [191].

5.1.4 Electroluminescence

ZnO is of great interest for applications in short wavelength light emitting devices, but the limiting factor is availability, reliability, and stability of *p*-type doping in ZnO. Consequently, ZnO-based light emitting diodes (LEDs) frequently contain another material, such as GaN, as a *p*-type semiconductor. These devices can exhibit a variety of performance behaviors in terms of turn-on voltages, I–V curve shapes, and emission colors, depending on the device structure and the properties of GaN and ZnO [192]. The identification of the emission peaks in the EL spectra is commonly performed by comparing the EL and PL spectra [193] or comparing EL spectra and literature reports on different defect levels in the material [194]. However, in some cases different emission (yellow) was observed in EL spectra compared to the PL spectra of ZnO nanorod-based LEDs [195]. The emission spectra obtained were also strongly dependent on the properties of ZnO/GaN interface (seed layer, if any) [196]. It has been proposed recently that some of the emissions observed in ZnO/GaN LEDs, which are commonly attributed to ZnO, actually originate from GaN, in spite of the absence of these features in the PL spectra of *p*-GaN [197]. Since such spectral features can occur in the absence of ZnO (i.e., Schottky contact on *p*-GaN), obviously they can originate from GaN films though they are absent in the PL spectra, and this possibility cannot be excluded even if similar spectral features are observed in PL spectra of ZnO [197]. Therefore, comprehensive study of the devices is necessary before emission peaks can be conclusively assigned to one type of material or one type of defect.

In addition to GaN, other materials can also be used as a *p*-type semiconductor in ZnO-based LEDs, and white emission has been reported for several material combinations [193, 197]. It should also be noted that the majority of EL reports on ZnO are concerned with room temperature measurements. Variable temperature EL studies have been scarce [198], although variable temperature measurements can provide additional information on the material properties and device operation. Furthermore, ZnO-nanostructure-based devices are frequently described as "high brightness" [199–201]. However, actual brightness or efficiency numbers are rarely given [197]. Thus, it would be desirable if electrical characterization of ZnO-nanostructure-based LEDs would include brightness measurements in addition to EL spectra.

While LEDs are of interest, possible development of electrically pumped UV lasers based on ZnO is even more interesting. In recent years, there have been several reports of electrically pumped lasing in ZnO [202–212]. The reported threshold currents in the literature vary significantly, so that various values such

as 0.8 mA [211], 1.1 mA [206], 6.5 mA [209], 12 mA [202], 20 mA [203], 25 mA [210], 27 mA [207], 28 mA [205], 48 mA [204], and 50 mA [208] have been reported. The majority of devices exhibited multiple emission modes, although stable single-mode operation has also been reported [206, 207]. A strategy to reduce the threshold by incorporating Zn_2TiO_4 nanoparticles into ZnO film for low threshold random lasers was also proposed [213]. Unfortunately, the majority of the reports provide only basic characterization, such as EL intensity dependence on the pumping current, and emission spectra below and above the threshold [202, 203]. In some cases, the emission spectra below the threshold are very noisy [203]. Also, I–V curves frequently show large leakage currents under reverse bias [204, 205, 207, 209–211]. In some devices, negative differential resistance regions were observed under both forward and reverse bias [208]. Spectra of optical and electrical pumping are rarely given in the same work, with the majority of the papers not reporting optically pumped stimulated emission from their devices. In some cases, EL spectra were measured in a fluorescence spectrometer [211], which could possibly result in some artifacts. Also, in some cases where both optical and electrical pumping are given, they have not been measured on exactly the same device structure [202]. Nevertheless, occasionally detailed characterization of the emission under both optical and electrical pumping has been performed [204, 206]. However, in spite of more convincing evidence for the achievement of electrically pumped lasing, leaky I–V curve could be observed [204]. This indicates that significant improvements in the material quality are needed to improve the performance of ZnO-based laser diodes. Also, there has been a recent report on recognizing electrically pumped lasing in organic semiconductors [214]. Many arguments are also applicable to electrically pumped lasing in ZnO, and more comprehensive characterization and analysis of the obtained data would be beneficial.

5.1.5 Other Techniques

In addition to optical and electrical (by applied bias or by electron beam) excitation, luminescence can be achieved using other sources of excitation. For example, depth-resolved luminescence of oriented ZnO nanowire arrays using X-ray excitation was reported [215]. Varying the incidence angle in the range 2–33° enabled changing the penetration depth in the range 3–132 nm for X-rays with the energy of 600 eV [215]. Using this technique, it was found that surface defect regions (for emission close to 2 eV) had a depth of ~14 nm [215]. X-ray-induced luminescence was also used to study the defect emission in ZnO [216]. Near-field spectroscopy can also be useful in studying the properties of nanostructures. For example, near-field studies of ZnO nanorods with ZnMgO quantum wells have been reported [217].

5.2 UV-Vis Spectroscopy

UV-Vis spectroscopy is of particular interest for characterizing nanomaterials for applications where their absorption properties are important, for example, in photocatalysis. Direct absorption or transmission measurements of nanomaterials

can be difficult due to scattering effects on aggregated nanostructures. However, relevant information can still be obtained from diffuse reflectance spectroscopy. This technique has been used, for example, to characterize mesoporous titania [156]. Absorption spectra can also be measured on ZnO colloids, which are useful for characterization of different capping agents for ZnO nanoparticles [218]. However, it was also demonstrated on ZnO nanoparticles in ethanol solution that illumination can result in charging of the nanoparticles and consequently shifts in the absorption and photoluminescence excitation (spectra).

In some cases, absorption spectra of the nanostructures are reported without providing measurement details [153]. However, this could result in significant measurement uncertainties. Thus, it was reported that the bandgap of SnO_2 nanowires was 3.74 eV and SnO_2 nanobelts was 3.81 eV, which were higher than the bulk bandgap of SnO_2 (claimed to be 3.62 eV) [153]. This was attributed to quantum size effect [153]. However, the size of the nanowires and nanobelts was too large to expect any quantum size effects. Measurement uncertainties, fitting uncertainties, or other causes of spectral shift (defects, Burstein-Moss shift, etc.) are thus more likely explanation for the observed differences in the bandgap.

5.3 Raman Spectroscopy

Raman spectroscopy, in combination with other characterization techniques, can be used to obtain useful information about nanostructures in terms of composition, defects, and phonon interactions. For example, Raman spectroscopy in combination with other techniques has been used to study hydrogen donors in ZnO [219–221]. These studies enabled the identification of the two types of hydrogen donors, H at the bond-centered lattice site and hydrogen bound in an oxygen vacancy [219]. The latter had an ionization energy of 47 meV and was responsible for the I_4-bound exciton emission at 3362.8 meV [219, 220]. However, the hydrogen donor at bond-centered lattice site resulted in the PL emission peak at 3.360 eV [220, 221]. Raman spectroscopy can also be used to detect phase segregation in doped ZnO [222]. This has been demonstrated on Co:ZnO, since detection of phase segregation is very important for understanding the magnetic properties of dilute magnetic semiconductors [222]. Defect densities can also be studied with Raman spectroscopy. For example, it has been used to estimate the density of oxygen vacancy defects in SnO_2 nanocrystals [223].

Raman spectroscopy has also been used for studying MgZnO nanoparticles, and spectral shift with increasing Mg content was observed [224]. Composition determination from the position of the first-order longitudinal optical phonon line position is possible in MgZnO nanocrystals [225]. However, disorder introduced by alloying would also result in broadening of the observed spectral features [225]. Other parameters are also dependent on the Mg content in MgZnO nanostructures, such as position of PL emission peak and exciton binding energy, which can be determined from PL measurements [226]. For a comprehensive optical characterization of MgZnO, it would be advisable to combine both PL and Raman measurements.

While Raman spectra of nanostructures frequently exhibit same features as those observable in the bulk materials, in some cases features that are specific to nanomaterials can be observed, such as peak shifts, unusual phenomena in exciton-phonon coupling, or the appearance of new peaks in the spectra. Raman peak shifts in nanostructures can possibly occur due to spatial confinement, phonon localization by defects, and local heating effects [227]. Local heating effects were found to be significant for resonant Raman excitation (325 nm), while no significant local heating was observed for nonresonant excitation (488 nm) [227]. Resonant Raman scattering under sub-bandgap excitation has been observed in ZnO, and the degree of enhancement was dependent on the defect density in ZnO nanostructures [228]. Also, electron-LO-phonon coupling strength was found to be dependent on disorder, so that decrease in correlation length rather than nanocrystal size resulted in the decrease of coupling strength [228]. On the other hand, for small ZnO quantum dots with average radius of ~2.3 nm, strong charge carrier-phonon coupling (coupling coefficient of 980 meV) was reported [229]. However, this estimate has been made by modeling temperature dependences of PL spectra [229]. In some cases, additional Raman lines are observed in nanostructures, which could not be observed in the bulk [230]. For example, the activation of a Raman-forbidden mode and additional modes attributed to defects was observed in SnO_2 nanowires [230].

6 Conclusions and Future Perspective

Optical properties of various metal oxide nanomaterials have been extensively studied. ZnO is one of the most commonly studied metal oxide materials, due to its bright emission under optical excitation and interest for a variety of practical applications. In spite of the progress made in understanding its optical properties, the exact chemical origins of different defect emission bands have still not been resolved. Furthermore, there are many examples in the literature for various artifacts in experimental characterization of nanostructures as well as erroneous explanations of physical phenomena responsible for the observed properties. A typical example of an artifact is PL spectra measured in fluorometers, while typical example of erroneous data interpretation is the claim of quantum confinement in large nanostructures based on the observed blue shift of the emission. Therefore, there is a need for a careful and comprehensive measurements as well as data interpretation when characterizing optical properties of metal oxide nanostructures. Future works should include combinations of different experimental techniques in order to obtain more conclusive information about remaining unresolved problems. As for other metal oxides, the situation is similar, with the additional factor and that is the need for the improvement of material properties. In several metal oxides different from ZnO, only defect emission can be observed in the room temperature photoluminescence data. Thus, necessary work to be done includes both material quality improvement and more comprehensive characterization.

Acknowledgment The authors would like to thank Prof. Raymond W. Y. Wong from Hong Kong Baptist University for access to a fluorescence spectrometer.

References

1. Govender K, Boyle DS, O'Brien P, Binks D, West D, Coleman D (2002) Room-temperature lasing observed from ZnO nanocolumns grown by aqueous solution deposition. Adv Mater 14(17):1221–1224
2. Tkachenko NV (2006) Optical spectroscopy methods and instrumentations, 1st edn. Elsevier, Amsterdam
3. Wang XF, Zhao FL, Xie PB, Deng SZ, Xu NS, Wang HZ (2006) Surface emission characteristics of ZnO nanoparticles. Chem Phys Lett 423(4–6):361–365
4. Wang HQ, Wang GZ, Jia LC, Tang CJ, Li GH (2007) Polychromatic visible photoluminescence in porous ZnO nanotubes. J Phys D Appl Phys 40(21):6549–6553
5. Irimpan L, Nampoori VPN, Radhakrishnan P, Deepthy A, Krishnan B (2007) Size dependent fluorescence spectroscopy of nanocolloids of ZnO. J Appl Phys 102(6):063524
6. Ghosh A, Choudhary RNP (2009) Microstructural aspects for defect emission and E_2^{high} phonon mode of ZnO thin films. J Appl Phys 105(12):124906
7. Senthilkumar V, Vickraman P (2010) Structural, optical and electrical studies on nanocrystalline tin oxide (SnO_2) thin films by electron beam evaporation technique. J Mater Sci Mater Electron 21(6):578–583
8. He TC, Chen R, Lin WW, Huang F, Sun HD (2011) Two-photon-pumped stimulated emission from ZnO single crystal. Appl Phys Lett 99(8):081902
9. He JH, Hsu JH, Wang CW, Lin HN, Chen LJ, Wang ZL (2006) Pattern and feature designed growth of ZnO nanowire arrays for vertical devices. J Phys Chem B 110(1):50–53
10. Kumar DS, Biswas M, Byrne D, Bock M, McGlynn E, Breusing M, Grunwald R (2010) Multiphoton-absorption induced ultraviolet luminescence of ZnO nanorods using low-energy femtosecond pulses. J Appl Phys 108(4):043107
11. Dierre B, Yuan XL, Sekiguchi T (2010) Low-energy cathodoluminescence microscopy for the characterization of nanostructures. Sci Technol Adv Mater 11(4):043001
12. Gilliland GD (1997) Photoluminescence spectroscopy of crystalline semiconductors. Mater Sci Engin R-Rep 18(3–6):99–399
13. Prasankumar RP, Taylor AJ (2011) Optical techniques for solid-state materials characterization. CRC Press, Boca Raton
14. Lakowicz JR (2006) Principles of fluorescence spectroscopy, 3rd edn. Springer, New York
15. The Nobel Prize in Physics (1930). Nobelprize.org. http://www.nobelprize.org/nobel_prizes/physics/laureates/1930/
16. Wood RW (1928) Wavelength shifts in scattered light. Nature 122(3071):349
17. Singh R (2002) C.V. Raman and the discovery of the Raman effect. Phys Perspect 4(4):399–420
18. Cardona M, Merlin R (2007) Light scattering in solids IX. volume 108 of topics in applied physics, Springer, Berlin, pp 1–15
19. Popović ZV, Dohčević-Mitrović Z, Šćepanović M, Grujić-Brojčin M, Aškrabić S (2011) Raman scattering on nanomaterials and nanostructures. Annalen Der Physik 523(1–2, SI): 62–74.
20. Hamaguchi C (2001) Basic semiconductor physics. Springer, Berlin
21. Cardona M (1983) Light scattering in solids I: introductory concepts, vol 8, Topics in applied physics. Springer, Berlin
22. Cardona M, Guntherodt G (1982) Light scattering in solids II: basic concepts and instrumentation, vol 50. Topics in applied physics, Springer, Berlin
23. McCreery RL (2000) Raman spectroscopy for chemical analysis. Wiley, New York
24. Smith E, Dent G (2005) Modern Raman spectroscopy - a practical approach. Wiley, England

25. Amer MS (2010) Raman spectroscopy, fullerenes and nanotechnology. The Royal Society of Chemistry, Cambridge
26. Laserna JJ (1996) Modern techniques in Raman spectroscopy. Wiley, England
27. Frontiera RR, Mathies RA (2011) Femtosecond stimulated Raman spectroscopy. Laser Photon Rev 5(1):102–113
28. Verma P, Ichimura T, Yano T, Saito Y, Kawata S (2010) Nano-imaging through tip-enhanced Raman spectroscopy: stepping beyond the classical limits. Laser Photon Rev 4(4):548–561
29. Ray KG, McCreery RL (1997) Simplified calibration of instrument response function for Raman spectrometers based on luminescent intensity standards. Appl Spectros 51(1):108–116
30. Schulze G, Jirasek A, Yu MML, Lim A, Turner RFB, Blades MW (2005) Investigation of selected baseline removal techniques as candidates for automated implementation. Appl Spectros 59(5):545–574
31. Rowlands C, Elliott S (2011) Automated algorithm for baseline subtraction in spectra. J Raman Spectros 42(3):363–369
32. Leoni S, Ramlau R, Meier K, Schmidt M, Schwarz U (2008) Nanodomain fragmentation and local rearrangements in CdSe under pressure. Proc Nat Acad of Sci USA 105(50):19612–19616
33. Tolbert SH, Alivisatos AP (1995) The wurtzite to rock-salt structural transformation in CdSe nanocrystals under high-pressure. J Chem Phys 102(11):4642–4656
34. Tolbert SH, Alivisatos AP (1994) Size dependence of a first-order solid-solid phase-transition - the wurtzite to rock-salt transformation in CdSe nanocrystals. Science 265(5170):373–376
35. Khachadorian S, Papagelis K, Scheel H, Colli A, Ferrari AC, Thomsen C (2011) High pressure Raman scattering of silicon nanowires. Nanotechnology 22(19):195707
36. Qadri SB, Skelton EF, Dinsmore AD, Hu JZ, Kim WJ, Nelson C, Ratna BR (2001) The effect of particle size on the structural transitions in zinc sulfide. J Appl Phys 89(1):115–119
37. Wang ZW, Saxena SK, Pischedda V, Liermann HP, Zha CS (2001) In situ x-ray diffraction study of the pressure-induced phase transformation in nanocrystalline CeO_2. Phys Rev B 64(1):012102
38. Pagnier T, Boulova M, Sergent N, Bouvier P, Lucazeau G (2007) Nanopowders and nanostructured oxides: phase transitions and surface reactivity. J Raman Spectros 38(6):756–761
39. Cui JB, Amtmann K, Ristein J, Ley L (1998) Noncontact temperature measurements of diamond by Raman scattering spectroscopy. J Appl Phys 83(12):7929–7933
40. Piscanec S, Cantoro M, Ferrari AC, Zapien JA, Lifshitz Y, Lee ST, Hofmann S, Robertson J (2003) Raman spectroscopy of silicon nanowires. Phys Rev B 68(24)
41. Khachadorian S, Scheel H, Cantoro M, Colli A, Ferrari AC, Thomsen C (2009) The morphology of silicon nanowire samples: a Raman study. Phys Status Solidi B Basic Solid State Phys 246(11–12SI):2809–2812
42. Scheel H, Reich S, Ferrari AC, Cantoro M, Colli A, Thomsen C (2006) Raman scattering on silicon nanowires: the thermal conductivity of the environment determines the optical phonon frequency. Appl Phys Lett 88(23):233114
43. Adu KW, Gutiérrez HR, Kim UJ, Eklund PC (2006) Inhomogeneous laser heating and phonon confinement in silicon nanowires: a micro-Raman scattering study. Phys Rev B 73(15):155333
44. Gupta R, Xiong Q, Adu CK, Kim UJ, Eklund PC (2003) Laser-induced Fano resonance scattering in silicon nanowires. Nano Letters 3(5):627–631
45. Adu KW, Xiong Q, Gutierrez HR, Chen G, Eklund PC (2006) Raman scattering as a probe of phonon confinement and surface optical modes in semiconducting nanowires. Appl Phys A Mater Sci Proc 85(3):287–297
46. Gu MX, Pan LK, Tay BK, Sun CQ (2007) Atomistic origin and temperature dependence of Raman optical redshift in nanostructures: a broken bond rule. J Raman Spectros 38(6):780–788

47. Gouadec G, Colomban P (2007) Raman spectroscopy of nanostructures and nanosized materials. J Raman Spectros 38(6):598–603
48. Arora AK, Rajalakshmi M, Ravindran TR, Sivasubramanian V (2007) Raman spectroscopy of optical phonon confinement in nanostructured materials. J Raman Spectros 38(6):604–617
49. Gouadec G, Colomban P (2007) Raman spectroscopy of nanomaterials: how spectra relate to disorder, particle size and mechanical properties. Progr Crystal Growth Characteriz Mater 53(1):1–56
50. Richter H, Wang ZP, Ley L (1981) The one phonon raman-spectrum in microcrystalline silicon. Solid State Commun 39(5):625–629
51. Campbell IH, Fauchet PM (1986) The effects of microcrystal size and shape on the one phonon raman-spectra of crystalline semiconductors. Solid State Commun 58(10):739–741
52. Roca E, Trallerogine C, Cardona M (1994) Polar optical vibrational-modes in quantum dots. Phys Rev B 49(19):13704–13711
53. Zi J, Zhang KM, Xie XD (1997) Comparison of models for Raman spectra of Si nanocrystals. Phys Rev B 55(15):9263–9266
54. Fu HX, Ozolins V, Zunger A (1999) Phonons in GaP quantum dots. Phys Rev B 59(4):2881–2887
55. Cheng W, Ren SF, Yu PY (2003) Theoretical investigation of the surface vibrational modes in germanium nanocrystal. Phys Rev B 68(19):193309
56. Spanier JE, Robinson RD, Zheng F, Chan SW, Herman IP (2001) Size-dependent properties of CeO_{2-y} nanoparticles as studied by Raman scattering. Phys Rev B 64(24):245407
57. Özgür Ü, Alivov YI, Liu C, Teke A, Reshchikov MA, Dogan S, Avrutin V, Cho SJ, Morkoç H (2005) A comprehensive review of ZnO materials and devices. J Appl Phys 98(4):041301
58. Djurišić AB, Leung YH (2006) Optical properties of ZnO nanostructures. Small 2(8–9):944–961
59. Djurišić AB, Ng AMC, Chen XY (2010) ZnO nanostructures for optoelectronics: material properties and device applications. Progr Quant Electron 34(4):191–259
60. Willander M, Nur O, Zhao QX, Yang LL, Lorenz M, Cao BQ, Zuniga Perez J, Czekalla C, Zimmermann G, Grundmann M, Bakin A, Behrends A, Al-Suleiman M, El-Shaer A, Che Mofor A, Postels B, Waag A, Boukos N, Travlos A, Kwack HS, Guinard J, Dang DLS (2009) Zinc oxide nanorod based photonic devices: recent progress in growth, light emitting diodes and lasers. Nanotechnology 20(33):332001
61. McCluskey MD, Jokela SJ (2009) Defects in ZnO. J Appl Phys 106(7):071101
62. Shen JH, Yeh SW, Mao SW, Huang HL, Huang YS, Gan D (2011) Visible photoluminescence of the $(11\bar{2}0)$, $(10\bar{1}1)$ and (0001) surfaces of ZnO nanofilms. Mater Lett 65(21–22):3333–3335
63. Lautenschlaeger S, Sann J, Volbers N, Meyer BK, Hoffmann A, Haboeck U, Wagner MR (2008) Asymmetry in the excitonic recombinations and impurity incorporation of the two polar faces of homoepitaxially grown ZnO films. Phys Rev B 77(14):144108
64. Kim MD, Oh JE, Kim SG, Yang WC (2011) Hydrogen passivation effect on the yellow-green emission band and bound exciton in n-ZnO. Solid State Commun 151(10):768–770
65. Chen H, Gu SL, Tang K, Zhu SM, Zhu ZB, Ye JD, Zhang R, Zheng YD (2011) Origins of green band emission in high-temperature annealed N-doped ZnO. J Luminescence 131(6):1189–1192
66. Vanheusden K, Seager CH, Warren WL, Tallant DR, Voigt JA (1996) Correlation between photoluminescence and oxygen vacancies in ZnO phosphors. Appl Phys Lett 68(3):403–405
67. Sharma PK, Pandey AC, Zolnierkiewicz G, Guskos N, Rudowicz C (2009) Relationship between oxygen defects and the photoluminescence property of ZnO nanoparticles: a spectroscopic view. J Appl Phys 106(9):094314
68. Kim Y, Kang S (2011) Investigation of photoluminescence mechanisms of ZnO through experimental and first-principles calculation methods. Acta Mater 59(1):126–132
69. Chen R, Tay Y, Ye J, Zhao Y, Xing GZ, Wu T, Sun HD (2010) Investigation of structured green-band emission and electron-phonon interactions in vertically aligned ZnO nanowires. J Phys Chem C 114(41):17889–17893

70. Wang ZG, Zu XT, Zhu S, Wang LM (2006) Green luminescence originates from surface defects in ZnO nanoparticles. Phys E-Low-Dimen Syst Nanostruct 35(1):199–202
71. Xue HZ, Pan N, Zeng RG, Li M, Sun X, Ding ZJ, Wang XP, Hou JG (2009) Probing the surface effect on deep-level emissions of an individual ZnO nanowire via spatially resolved cathodoluminescence. J Phys Chem C 113(29):12715–12718
72. Bera A, Basak D (2009) Correlation between the microstructure and the origin of the green luminescence in ZnO: a case study on the thin films and nanowires. Chem Phys Lett 476(4–6):262–266
73. Gong YY, Andelman T, Neumark GF, O'Brien S, Kuskovsky IL (2007) Origin of defect related green emission from ZnO nanoparticles: effect of surface modification. Nanoscale Res Lett 2(6):297–302
74. He HP, Yang Q, Liu C, Sun LW, Ye ZZ (2011) Size-dependent surface effects on the photoluminescence in ZnO nanorods. J Phys Chem C 115(1):58–64
75. Wang FF, Cao L, Pan AL, Liu RB, Wang X, Zhu X, Wang SQ, Zou BS (2007) Synthesis of tower-like ZnO structures and visible photoluminescence origins of varied-shaped ZnO nanostructures. J Phys Chem C 111(21):7655–7660
76. Norberg NS, Gamelin DR (2005) Influence of surface modification on the luminescence of colloidal ZnO nanocrystals. J Phys Chem B 109(44):20810–20816
77. Djurišić AB, Leung YH, Tam KH, Hsu YF, Ding L, Ge WK, Zhong YC, Wong KS, Chan WK, Tam HL, Cheah KW, Kwok WM, Phillips DL (2007) Defect emissions in ZnO nanostructures. Nanotechnology 18(9):095702
78. Kahn ML, Cardinal T, Bousquet B, Monge M, Jubera V, Chaudret B (2006) Optical properties of zinc oxide nanoparticles and nanorods synthesized using an organometallic method. Chemphyschem 7(11):2392–2397
79. Kurbanov SS, Panin GN, Kim TW, Kang TW (2009) Strong violet luminescence from ZnO nanocrystals grown by the low-temperature chemical solution deposition. J Luminescence 129(9):1099–1104
80. Alam Khan M, Jung HT, Yang OB (2006) Synthesis and characterization of ultrahigh crystalline TiO_2 nanotubes. J Phys Chem B 110(13):6626–6630
81. Ahn CH, Kim YY, Kim DC, Mohanta SK, Cho HK (2009) A comparative analysis of deep level emission in ZnO layers deposited by various methods. J Appl Phys 105(1): 013502
82. Cao BQ, Cai WP, Zeng HB (2006) Temperature-dependent shifts of three emission bands for ZnO nanoneedle arrays. Appl Phys Lett 88(16):161101
83. Djurišić AB, Leung YH, Tam KH, Ding L, Ge WK, Chen HY, Gwo S (2006) Green, yellow, and orange defect emission from ZnO nanostructures: influence of excitation wavelength. Appl Phys Lett 88(10):103107
84. Shih HY, Chen YT, Huang NH, Wei CM, Chen YF (2011) Tunable photoluminescence and photoconductivity in ZnO one-dimensional nanostructures with a second below-gap beam. J Appl Phys 109(10):103523
85. Zhong Y, Djurišić AB, Hsu YF, Wong KS, Brauer G, Ling CC, Chan WK (2008) Exceptionally long exciton photoluminescence lifetime in ZnO tetrapods. J Phys Chem C 112(42):16286–16295
86. Gargas DJ, Gao HW, Wang HT, Yang PD (2011) High quantum efficiency of band-edge emission from ZnO nanowires. Nano Lett 11(9):3792–3796
87. Lee SK, Chen SL, Hongxing D, Sun L, Chen Z, Chen WM, Buyanova IA (2010) Long lifetime of free excitons in ZnO tetrapod structures. Appl Phys Lett 96(8):083104
88. Robin IC, Gauron B, Ferret P, Tavares C, Feuillet G, Dang LS, Gayral B, Gérard JM (2007) Evidence for low density of nonradiative defects in ZnO nanowires grown by metal organic vapor-phase epitaxy. Appl Phys Lett 91(14):143120
89. Tam KH, Cheung CK, Leung YH, Djurišić AB, Ling CC, Beling CD, Fung S, Kwok WM, Chan WK, Phillips DL, Ding L, Ge WK (2006) Defects in ZnO nanorods prepared by a hydrothermal method. J Phys Chem B 110(42):20865–20871

90. Lupan O, Pauporté T, Tiginyanu IM, Ursaki VV, Sontea V, Ono LK, Roldan Cuenya B, Chow L (2011) Comparative study of hydrothermal treatment and thermal annealing effects on the properties of electrodeposited micro-columnar ZnO thin films. Thin Solid Films 519(22):7738–7749
91. Lupan O, Pauporté T (2010) Hydrothermal treatment for the marked structural and optical quality improvement of ZnO nanowire arrays deposited on lightweight flexible substrates. J Cryst Growth 312(16–17):2454–2458
92. Chen XY, Ng AMC, Djurišić AB, Ling CC, Chan WK (2012) Hydrothermal treatment of ZnO Nanostructures. Thin Solid Films 520:2656–2662
93. Ali M, Winterer M (2010) ZnO nanocrystals: surprisingly 'Alive'. Chem Mater 22(1):85–91
94. Merz TA, Doutt DR, Bolton T, Dong Y, Brillson LJ (2011) Nanostructure growth-induced defect formation and band bending at ZnO surfaces. Surface Sci 605(9–10):L20–L23
95. Bastin D, Lavrov EV, Weber J (2011) Metastable state of the $V_{Zn}H_2$ defect in ZnO. Phys Rev B 83(19):195210
96. Chang HP, Wang FH, Wu JY, Kung CY, Liu HW (2010) Enhanced conductivity of aluminum doped ZnO films by hydrogen plasma treatment. Thin Solid Films 518(24SI):7445–7449
97. Dev A, Richters JP, Sartor J, Kalt H, Gutowski J, Voss T (2011) Enhancement of the near-band-edge photoluminescence of ZnO nanowires: important role of hydrogen incorporation versus plasmon resonances. Appl Phys Lett 98(13):131111
98. Wang DF, Lu HB, Li JC, Wu Y, Tian Y, Lee YP (2009) Effects of low-energy hydrogen ion implantation on optical properties of ZnO nanowires. Mater Res Bull 44(1):41–44
99. Cai PF, You JB, Zhang XW, Dong JJ, Yang XL, Yin ZG, Chen NF (2009) Enhancement of conductivity and transmittance of ZnO films by post hydrogen plasma treatment. J Appl Phys 105(8):083713
100. Dong JJ, Zhang XW, You JB, Cai PF, Yin ZG, An Q, Ma XB, Jin P, Wang ZG, Chu PK (2010) Effects of hydrogen plasma treatment on the electrical and optical properties of ZnO films: identification of hydrogen donors in ZnO. ACS Appl Mater Interf 2(6):1780–1784
101. Li XN, Keyes B, Asher S, Zhang SB, Wei SH, Coutts TJ, Limpijumnong S, Van de Walle CG (2005) Hydrogen passivation effect in nitrogen-doped ZnO thin films. Appl Phys Lett 86(12):122107
102. Escobedo-Morales A, Pal U (2008) Defect annihilation and morphological improvement of hydrothermally grown ZnO nanorods by Ga doping. Appl Phys Lett 93(19):193120
103. Yang Y, Tay BK, Sun XW, Sze JY, Han ZJ, Wang JX, Zhang XH, Li YB, Zhang S (2007) Quenching of surface-exciton emission from ZnO nanocombs by plasma immersion ion implantation. Appl Phys Lett 91(7):071921
104. Mendelsberg RJ, Allen MW, Durbin SM, Reeves RJ (2011) Photoluminescence and the exciton-phonon coupling in hydrothermally grown ZnO. Phys Rev B 83(20):205202
105. Herklotz F, Lavrov EV, Weber J, Mamin GV, Kutin YS, Volodin MA, Orlinskii SB (2011) Identification of shallow Al donors in ZnO. Phys Status Solidi B Basic Solid State Phys 248(6):1532–1537
106. Brandt M, von Wenckstern H, Benndorf G, Lange M, Dietrich CP, Kranert C, Sturm C, Schmidt-Grund R, Hochmuth H, Lorenz M, Grundmann M, Wagner MR, Alic M, Nenstiel C, Hoffmann A (2010) Identification of a donor-related recombination channel in ZnO thin films. Phys Rev B 81(7):073306
107. Al-Suleiman M, Che Mofor A, El-Shaer A, Bakin A, Wehmann HH, Waag A (2006) Photoluminescence properties: catalyst-free ZnO nanorods and layers versus bulk ZnO. Appl Phys Lett 89(23):231911
108. Grabowska J, Meaney A, Nanda KK, Mosnier JP, Henry MO, Duclère JR, McGlynn E (2005) Surface excitonic emission and quenching effects in ZnO nanowire/nanowall systems: limiting effects on device potential. Phys Rev B 71(11):115439
109. Biswas M, Jung YS, Kim HK, Kumar K, Hughes GJ, Newcomb S, Henry MO, McGlynn E (2011) Microscopic origins of the surface exciton photoluminescence peak in ZnO nanostructures. Phys Rev B 83(23):235320

110. Ding L, Li BK, He HT, Ge WK, Wang JN, Ning JQ, Dai XM, Ling CC, Xu SJ (2009) Classification of bound exciton complexes in bulk ZnO by magnetophotoluminescence spectroscopy. J Appl Phys 105(5):053511
111. Meyer BK, Sann J, Eisermann S, Lautenschlaeger S, Wagner MR, Kaiser M, Callsen G, Reparaz JS, Hoffmann A (2010) Excited state properties of donor bound excitons in ZnO. Phys Rev B 82(11):115207
112. Nam YS, Lee SW, Baek KS, Chang SK, Song JH, Song JH, Han SK, Hong SK, Yao T (2008) Anisotropic optical properties of free and bound excitons in highly strained A-plane ZnO investigated with polarized photoreflectance and photoluminescence spectroscopy. Appl Phys Lett 92(20):201907
113. Johnston K, Henry MO, McCabe D, McGlynn E, Dietrich M, Alves E, Xia M (2006) Identification of donor-related impurities in ZnO using photoluminescence and radiotracer techniques. Phys Rev B 73(16):165212
114. Müller S, Stichtenoth D, Uhrmacher M, Hofsäss H, Ronning C, Röder J (2007) Unambiguous identification of the PL-I_9 line in zinc oxide. Appl Phys Lett 90(1):012107
115. Johnston K, Cullen J, Henry MO, McGlynn E, Stachura M (2011) Evidence for As lattice location and Ge bound exciton luminescence in ZnO implanted with ^{73}As and ^{73}Ge. Phys Rev 83(12):125205
116. Fallert J, Hauschild R, Stelzl F, Urban A, Wissinger M, Zhou HJ, Klingshirn C, Kalt H (2007) Surface-state related luminescence in ZnO nanocrystals. J Appl Phys 101(7): 073506
117. Tainoff D, Masenelli B, Mélinon P, Belsky A, Ledoux G, Amans D, Dujardin C, Fedorov N, Martin P (2010) Competition between exciton-phonon interaction and defects states in the 3.31 eV band in ZnO. Phys Rev 81(11):115304
118. Wagner MR, Callsen G, Reparaz JS, Schulze JH, Kirste R, Cobet M, Ostapenko IA, Rodt S, Nenstiel C, Kaiser M, Hoffmann A, Rodina AV, Phillips MR, Lautenschläger S, Eisermann S, Meyer BK (2011) Bound excitons in ZnO: structural defect complexes versus shallow impurity centers. Phys Rev B 84(3):035313
119. Kurbanov SS, Panin GN, Kang TW (2009) Spatially resolved investigations of the emission around 3.31 eV (A-line) from ZnO nanocrystals. Appl Phys Lett 95(21): 211902.
120. Thonke K, Schirra M, Schneider R, Reiser A, Prinz GM, Feneberg M, Sauer R, Biskupek J, Kaiser U (2010) The role of stacking faults and their associated 0.13 eV acceptor state in doped and undoped ZnO layers and nanostructures. Phys Status Solidi B-Basic Solid State Phys 247(6): 1464–1468.
121. Schirra M, Schneider R, Reiser A, Prinz GM, Feneberg M, Biskupek J, Kaiser U, Krill CE, Thonke K, Sauer R (2008) Stacking fault related 3.31-eV luminescence at 130-meV acceptors in zinc oxide. Phys Rev B 77(12): 125215
122. Hamby DW, Lucca DA, Lee JK, Nastasi M, Kang HS, Lee SY (2006) Effects of hydrogen implantation on the photoluminescence and carrier mobility of ZnO films. Nucl Inst Meth Phys Res Sect B Beam Interact Mater Atoms 249:196–199
123. Fonoberov VA, Alim KA, Balandin AA, Xiu FX, Liu JL (2006) Photoluminescence investigation of the carrier recombination processes in ZnO quantum dots and nanocrystals. Phys Rev B 73(16):165317
124. Lin KF, Cheng HM, Hsu HC, Lin LJ, Hsieh WF (2005) Band gap variation of size-controlled ZnO quantum dots synthesized by sol-gel method. Chem Phys Lett 409(4–6): 208–211
125. Cheng HM, Lin KF, Hsu HC, Hsieh WF (2006) Size dependence of photoluminescence and resonant Raman scattering from ZnO quantum dots. Appl Phys Lett 88(26):261909
126. Lu JG, Ye ZZ, Zhang YZ, Liang QL, Fujita SZ, Wang ZL (2006) Self-assembled ZnO quantum dots with tunable optical properties. Appl Phys Lett 89(2):023122
127. Fu ZD, Cui YS, Zhang SY, Chen J, Yu DP, Zhang SL, Niu L, Jiang JZ (2007) Study on the quantum confinement effect on ultraviolet photoluminescence of crystalline ZnO nanoparticles with nearly uniform size. Appl Phys Lett 90(26):263113

128. Zhang LY, Yin LW, Wang CX, Lun N, Qi YX, Xiang D (2010) Origin of visible photoluminescence of ZnO quantum dots: defect-dependent and size-dependent. J Phys Chem C 114(21):9651–9658
129. Xiong G, Pal U, Serrano JG (2007) Correlations among size, defects, and photoluminescence in ZnO nanoparticles. J Appl Phys 101(2):024317
130. Liu KW, Chen R, Xing GZ, Wu T, Sun HD (2010) Photoluminescence characteristics of high quality ZnO nanowires and its enhancement by polymer covering. Appl Phys Lett 96(2):023111
131. Yang BQ, Kumar A, Feng P, Katiyar RS (2008) Structural degradation and optical property of nanocrystalline ZnO films grown on Si (100). Appl Phys Lett 92(23):233112
132. Voss T, Bekeny C, Wischmeier L, Gafsi H, Boerner S, Schade W, Mofor AC, Bakin A, Waag A (2006) Influence of exciton-phonon coupling on the energy position of the near-band-edge photoluminescence of ZnO nanowires. Appl Phys Lett 89(18):182107
133. Zhang XX, Liu DF, Zhang LH, Li WL, Gao M, Ma WJ, Ren Y, Zeng QS, Niu ZO, Zhou WY, Xie SS (2009) Synthesis of large-scale periodic ZnO nanorod arrays and its blue-shift of UV luminescence. J Mater Chem 19(7):962–969
134. Hong WK, Jo G, Choe M, Lee T, Sohn JI, Welland ME (2009) Influence of surface structure on the phonon-assisted emission process in the ZnO nanowires grown on homoepitaxial films. Appl Phys Lett 94(4):043103
135. Ahn CH, Mohanta SK, Lee NE, Cho HK (2009) Enhanced exciton-phonon interactions in photoluminescence of ZnO nanopencils. Appl Phys Lett 94(26):261904
136. Yang YH, Chen XY, Feng Y, Yang GW (2007) Physical mechanism of blue-shift of UV luminescence of a single pencil-like ZnO nanowire. Nano Lett 7(12):3879–3883
137. Chang PC, Chien CJ, Stichtenoth D, Ronning C, Lu JG (2007) Finite size effect in ZnO nanowires. Appl Phys Lett 90(11):113101
138. Mohanta SK, Tripathy S, Soh CB, Kim DC, Kong BH, Cho HK (2010) Emission characteristics of ZnO nanorods on nanosilicon-on-insulator: competition between exciton-phonon coupling and surface resonance effect. J Phys D Appl Phys 43(14):145404
139. Chen CW, Chen KH, Shen CH, Ganguly A, Chen LC, Wu JJ, Wen HI, Pong WF (2006) Anomalous blueshift in emission spectra of ZnO nanorods with sizes beyond quantum confinement regime. Appl Phys Lett 88(24):241905
140. Reparaz JS, Gueell F, Wagner MR, Hoffmann A, Cornet A, Morante JR (2010) Size-dependent recombination dynamics in ZnO nanowires. Appl Phys Lett 96(5):053105
141. Kim SY, Yeon YS, Park SM, Kim JH, Song JK (2008) Exciton states of quantum confined ZnO nanorods. Chem Phys Lett 462(1–3):100–103
142. Kwok WM, Djurišić AB, Leung YH, Chan WK, Phillips DL (2005) Time-resolved photoluminescence study of the stimulated emission in ZnO nanoneedles. Appl Phys Lett 87(9):093108
143. Suzuki K, Inoguchi M, Fujita K, Murai S, Tanaka K, Tanaka N, Ando A, Takagi H (2010) High-density excitation effect on photoluminescence in ZnO nanoparticles. J Appl Phys 107(12):124311
144. Dai J, Xu CX, Sun XW, Zhang XH (2011) Exciton-polariton microphotoluminescence and lasing from ZnO whispering-gallery mode microcavities. Appl Phys Lett 98(16):161110
145. Czekalla C, Nobis T, Rahm A, Cao BQ, Zúñiga Pérez J, Sturm C, Schmidt-Grund R, Lorenz M, Grundmann M (2010) Whispering gallery modes in zinc oxide micro- and nanowires. Physica Status Solidi B-Basic Solid State Phy 247(6):1282–1293
146. Wang T, Radovanovic PV (2011) Size-dependent electron transfer and trapping in strongly luminescent colloidal gallium oxide nanocrystals. J Phys Chem C 115(38):18473–18478
147. Lee SY, Shin YH, Kim Y, Kim S, Ju S (2011) Emission characteristics of diameter controlled SnO_2 nanowires. J Luminescence 131(12):2565–2568
148. Peng MF, Li Y, Gao J, Zhang D, Jiang Z, Sun XH (2011) Electronic structure and photoluminescence origin of single-crystalline germanium oxide nanowires with green light emission. J Phys Chem C 115(23):11420–11426

149. Xing GZ, Yi JB, Wang DD, Liao L, Yu T, Shen ZX, Huan CHA, Sum TC, Ding J, Wu T (2009) Strong correlation between ferromagnetism and oxygen deficiency in Cr-doped $In_2O_{3-\delta}$ nanostructures. Phys Rev B 79(17):174406
150. Kumar M, Singh VN, Singh F, Lakshmi KV, Mehta BR, Singh JP (2008) On the origin of photoluminescence in indium oxide octahedron structures. Appl Phys Lett 92(17):171907
151. Chen HT, Wu XL, Xiong SJ, Zhang WC, Zhu J (2009) Red photoluminescence mechanism in SnO_2 nanostructures. Appl Phys A Mater Sci Process 97(2):365–368
152. Lettieri S, Causà M, Setaro A, Trani F, Barone V, Ninno D, Maddalena P (2008) Direct role of surface oxygen vacancies in visible light emission of tin dioxide nanowires. J Chem Phys 129(24):244710
153. Luo SH, Fan JY, Liu WL, Zhang M, Song ZT, Lin CL, Wu XL, Chu PK (2006) Synthesis and low-temperature photoluminescence properties of SnO_2 nanowires and nanobelts. Nanotechnology 17(6):1695–1699
154. Kar A, Stroscio MA, Meyyappan M, Gosztola DJ, Wiederrecht GP, Dutta M (2011) Tailoring the surface properties and carrier dynamics in SnO_2 nanowires. Nanotechnology 22(28):285709
155. Luo SH, Chu PK, Liu WL, Zhang M, Lin CL (2006) Origin of low-temperature photoluminescence from SnO_2 nanowires fabricated by thermal evaporation and annealed in different ambients. Appl Phys Lett 88(18):183112
156. Das SK, Bhunia MK, Bhaumik A (2010) Self-assembled TiO_2 nanoparticles: mesoporosity, optical and catalytic properties. Dalton Trans 39(18):4382–4390
157. Jin C, Kim H, Lee WI, Lee C (2011) Ultraintense luminescence in semiconducting-material-sheathed MgO nanorods. Adv Mater 23(17):1982–1987
158. Chen R, Xing GZ, Gao J, Zhang Z, Wu T, Sun HD (2009) Characteristics of ultraviolet photoluminescence from high quality tin oxide nanowires. Appl Phys Lett 95(6):061908
159. Liu B, Cheng CW, Chen R, Shen ZX, Fan HJ, Sun HD (2010) Fine structure of ultraviolet photoluminescence of tin oxide nanowires. J Phys Chem C 114(8):3407–3410
160. Wei ZP, Guo DL, Liu B, Chen R, Wong LM, Yang WF, Wang SJ, Sun HD, Wu T (2010) Ultraviolet light emission and excitonic fine structures in ultrathin single-crystalline indium oxide nanowires. Appl Phys Lett 96(3):031902
161. Pfüller C, Brandt O, Flissikowski T, Grahn HT, Ive T, Speck JS, Den-Baars SP (2011) Comparison of the spectral and temporal emission characteristics of homoepitaxial and heteroepitaxial ZnO nanowires. Appl Phys Lett 98(11):113113
162. Yamamoto S, Yano H, Mishina T, Nakahara J (2007) Decay dynamics of ultraviolet photoluminescence in ZnO nanocrystals. J Luminescence 126(1):257–262
163. Pozina G, Yang LL, Zhao QX, Hultman L, Lagoudakis PG (2010) Size dependent carrier recombination in ZnO nanocrystals. Appl Phys Lett 97(13):131909
164. Hong SS, Joo T, Park WI, Jun YH, Yi GC (2003) Time-resolved photoluminescence of the size-controlled ZnO nanorods. Appl Phys Lett 83(20):4157–4159
165. Klason P, Borseth TM, Zhao QX, Svensson BG, Yu A, Kuznetsov P, Bergman J, Willander M (2008) Temperature dependence and decay times of zinc and oxygen vacancy related photoluminescence bands in zinc oxide. Solid State Commun 145(5–6):321–326
166. Baxter JB, Schmuttenmaer CA (2006) Conductivity of ZnO nanowires, nanoparticles, and thin films using time-resolved terahertz spectroscopy. J Phys Chem B 110(50):25229–25239
167. Zhong YC, Wong KS, Djurišić AB, Hsu YF (2009) Study of optical transitions in an individual ZnO tetrapod using two-photon photoluminescence excitation spectrum. Appl Phys B Lasers Optics 97(1):125–128
168. Zhang CF, Dong ZW, You GJ, Qian SX, Deng H, Gao H, Yang LP, Li Y (2005) Observation of two-photon-induced photoluminescence in ZnO microtubes. Appl Phys Lett 87(5):051920
169. Zhang CF, Zhang F, Sun XW, Yang Y, Wang J, Xu J (2009) Frequency-upconverted whispering-gallery-mode lasing in ZnO hexagonal nanodisks. Opt Lett 34(21):3349–3351
170. Zhang CF, Dong ZW, Liu KJ, Yan YL, Qianb SX, Deng H (2007) Multiphoton absorption pumped ultraviolet stimulated emission from ZnO microtubes. Appl Phys Lett 91(14):142109

171. Chattopadhyay M, Kumbhakar P, Tiwary CS, Mitra AK, Chatterjee U, Kobayashi T (2009) Three-photon-induced four-photon absorption and nonlinear refraction in ZnO quantum dots. Opt Lett 34(23):3644–3646
172. Chia CH, Lai YJ, Han TC, Chiou JW, Hu YM, Chou WC (2010) High-excitation effect on photoluminescence of sol-gel ZnO nanopowder. Appl Phys Lett 96(8):081903
173. House RL, Kirschbrown JR, Mehl BP, Gabriel MM, Puccio JA, Parker JK, Papanikolas JM (2011) Characterizing electron-hole plasma dynamics at different points in individual ZnO rods. J Phys Chem C 115(43):21436–21442
174. Sieber B, Addad A, Szunerits S, Boukherroub R (2010) Stacking faults-induced quenching of the UV luminescence in ZnO. J Phys Chem Lett 1(20):3033–3038
175. Brillson LJ, Mosbacker HL, Doutt DL, Dong Y, Fang ZQ, Look DC, Cantwell G, Zhang J, Song JJ (2009) Nanoscale depth-resolved cathodoluminescence spectroscopy of ZnO surfaces and metal interfaces. Superlattices Microstruct 45(4–5):206–213
176. Coleman VA, Bradby JE, Jagadish C, Phillips MR (2006) Observation of enhanced defect emission and excitonic quenching from spherically indented ZnO. Appl Phys Lett 89(8): 082102
177. Foley M, Ton-That C, Phillips MR (2008) Cathodoluminescence inhomogeneity in ZnO nanorods. Appl Phys Lett 93(24):243104
178. Kuo CL, Wang RC, Huang JL, Liu CP, Lai YF, Wang CY, Chung HC (2008) ZnO nanorods with two spatially distinct light emissions. Nanotechnology 19(28):285703
179. Liu WZ, Liang Y, Xu HY, Wang LL, Zhang XT, Liu YC, Hark SK (2010) Heteroepitaxial growth and spatially resolved cathodoluminescence of ZnO/MgZnO coaxial nanorod arrays. J Phys Chem C114(39):16148–16152
180. Schirra M, Reiser A, Prinz GM, Ladenburger A, Thonke K, Sauer R (2007) Cathodoluminescence study of single zinc oxide nanopillars with high spatial and spectral resolution. J Appl Phys 101(11):113509
181. Yuan XL, Dierre B, Wang JB, Zhang BP, Sekiguchi T (2007) Spatial distribution of impurities in ZnO nanotubes characterized by cathodoluminescence. J Nanosci Nanotechnol 7(9):3323–3327
182. Biswas M, Kwack HS, Dang LS, Henry MO, McGlynn E (2009) Spatial inhomogeneity of donor bound exciton emission from ZnO nanostructures grown on Si. Nanotechnology 20(25):255703
183. Chen SL, Lee SK, Chen WM, Dong HX, Sun L, Chen ZH, Buyanova IA (2010) On the origin of suppression of free exciton no-phonon emission in ZnO tetrapods. Appl Phys Lett 96(3):033108
184. Zollfrank C, Rambo CR, Batentschuk M, Greil P (2007) Spatially resolved luminescence properties of ZnO tetrapods. J Mater Sci 42(15):6325–6330
185. Kurbanov SS, Cho HD, Kang TW (2011) Effect of excitation and detection angles on photoluminescence spectrum from ZnO nanorod array. Opt Commun 284(1):240–244
186. Gruzintsev AN, Emelchenko GA, Redkin AN, Volkov WT, Yakimov EE, Visimberga G, Romanov SG (2009) Visualization of localized photon modes of ZnO nanorods by scanning cathodoluminescence. Semiconductors 43(4):468–471
187. Bae J, Shim EL, Park Y, Kim H, Kim JM, Kang CJ, Choi YJ (2011) Direct observation of enhanced cathodoluminescence emissions from ZnO nanocones compared with ZnO nanowire arrays. Nanotechnology 22(28):285711
188. Bano N, Hussain I, Nur O, Willander M, Wahab Q, Henry A, Kwack HS, Dang DLS (2010) Depth-resolved cathodoluminescence study of zinc oxide nanorods catalytically grown on p-type 4H-SiC. J Luminescence 130(6):963–968
189. Fan HJ, Scholz R, Zacharias M, Gösele U, Bertram F, Forster D, Christen J (2005) Local luminescence of ZnO nanowire-covered surface: a cathodoluminescence microscopy study. Appl Phys Lett 86(2):023113
190. Yang J, Li S, Li ZW, McBean K, Phillips MR (2008) Origin of excitonic emission suppression in an individual ZnO nanobelt. J Phys Chem C 112(27):10095–10099

191. Xue HZ, Pan N, Li M, Wu YK, Wang XP, Hou JG (2010) Probing the strain effect on near band edge emission of a curved ZnO nanowire via spatially resolved cathodoluminescence. Nanotechnology 21(21):215701
192. Ng AMC, Xi YY, Hsu YF, Djurišić AB, Chan WK, Gwo S, Tam HL, Cheah KW, Fong PWK, Lui HF, Surya C (2009) GaN/ZnO nanorod light emitting diodes with different emission spectra. Nanotechnology 20(44):445201
193. Willander M, Nur O, Bano N, Sultana K (2009) Zinc oxide nanorod-based heterostructures on solid and soft substrates for white-light-emitting diode applications. New J Phys 11:125020
194. Alvi NH, Ul Hasan K, Nur O, Willander M (2011) The origin of the red emission in n-ZnO nanotubes/p-GaN white light emitting diodes. Nanoscale Res Lett 6:130
195. Chen XY, Ng AMC, Fang F, Djurišić AB, Chan WK, Tam HL, Cheah KW, Fong PWK, Lui HF, Surya C (2010) The influence of the ZnO seed layer on the ZnO nanorod/GaN LEDs. J Electrochem Soc 157(3):H308–H311
196. Ng AMC, Chen XY, Fang F, Hsu YF, Djurišić AB, Ling CC, Tam HL, Cheah KW, Fong PWK, Lui HF, Surya C, Chan WK (2010) Solution-based growth of ZnO nanorods for light-emitting devices: hydrothermal versus electrodeposition. Appl Phys B Lasers Optics 100(4):851–858
197. Chen XY, Ng AMC, Fang F, Ng YH, Djurišić AB, Tam HL, Cheah KW, Gwo S, Chan WK, Lui HF, Fong PWK, Surya C (2011) ZnO nanorod/GaN light-emitting diodes: the origin of yellow and violet emission bands under reverse and forward bias. J Appl Phys 110(9):094513
198. Zimmler MA, Voss T, Ronning C, Capasso F (2009) Exciton-related electroluminescence from ZnO nanowire light-emitting diodes. Appl Phys Lett 94(24):241120
199. Zhang XM, Lu MY, Zhang Y, Chen LJ, Wang ZL (2009) Fabrication of a high-brightness blue-light-emitting diode using a ZnO-nanowire array grown on p-GaN thin film. Adv Mater 21(27):2767–2770
200. Lupan O, Pauporté T, Viana B (2010) Low-Voltage UV-Electroluminescence from ZnO-nanowire array/p-GaN light-emitting diodes. Adv Mater 22(30):3298–3302
201. Alvi NH, Riaz M, Tzamalis G, Nur O, Willander M (2010) Fabrication and characterization of high-brightness light emitting diodes based on n-ZnO nanorods grown by a low-temperature chemical method on p-4H-SiC and p-GaN. Semicond Sci Technol 25(6):065004
202. Dai J, Xu CX, Sun XW (2011) ZnO-microrod/p-GaN heterostructured whispering-gallery-mode microlaser diodes. Adv Mater 23(35):4115–4119
203. Liu CY, Xu HY, Ma JG, Li XH, Zhang XT, Liu YC, Mu R (2011) Electrically pumped near-ultraviolet lasing from ZnO/MgO core/shell nanowires. Appl Phys Lett 99(6):063115
204. Chu S, Wang GP, Zhou WH, Lin YQ, Chernyak L, Zhao JZ, Kong JY, Li L, Ren JJ, Liu JL (2011) Electrically pumped waveguide lasing from ZnO nanowires. Nat Nanotechnol 6(8):506–510
205. Zhu H, Shan CX, Li BH, Zhang ZZ, Shen DZ, Choy KL (2011) Low-threshold electrically pumped ultraviolet laser diode. J Mater Chem 21(9):2848–2851
206. Liang HK, Yu SF, Yang HY (2010) ZnO random laser diode arrays for stable single-mode operation at high power. Appl Phys Lett 97(24):241107
207. Guo Z, Zhao DX, Liu YC, Shen DZ, Yao B, Zhang ZZ, Li BH, Guo Z, Liu YC (2010) Electrically pumped single-mode lasing emission of self-assembled n-ZnO microcrystalline film/p-GaN heterojunction diode. J Phys Chem C 114(36):15499–15503
208. Chen PL, Ma XY, Li DS, Zhang YY, Yang DR (2009) Electrically pumped ultraviolet random lasing from ZnO-based metal-insulator-semiconductor devices: dependence on carrier transport. Opt Expr 17(6):4712–4717
209. Zhu H, Shan CX, Zhang JY, Zhang ZZ, Li BH, Zhao DX, Yao B, Shen DZ, Fan XW, Tang ZK, Hou XH, Choy KL (2010) Low-threshold electrically pumped random lasers. Adv Mater 22(16):1877–1881
210. Chu S, Olmedo M, Yang Z, Kong JY, Liu JL (2008) Electrically pumped ultraviolet ZnO diode lasers on Si. Appl Phys Lett 93(18):181106

211. Zhu H, Shan CX, Yao B, Li BH, Zhang JY, Zhang ZZ, Zhao DX, Shen DZ, Fan XW, Lu YM, Tong ZK (2009) Ultralow-threshold laser realized in zinc oxide. Adv Mater 21(16):1613–1617
212. Ma XY, Pan JW, Chen PL, Li DS, Zhang H, Yang Y, Yang DR (2009) Room temperature electrically pumped ultraviolet random lasing from ZnO nanorod arrays on Si. Opt Expr 17(16):14426–14433
213. Li YP, Ma XY, Xu MS, Xiang LL, Yang DR (2011) Remarkable decrease in threshold for electrically pumped random ultraviolet lasing from ZnO film by incorporation of Zn_2TiO_4 nanoparticles. Opt Expr 19(9):8662–8669
214. Samuel IDW, Namdas EB, Turnbull GA (2009) How to recognize lasing. Nat Photonics 3(10):546–549
215. Rosenberg RA, Abu Haija M, Vijayalakshmi K, Zhou J, Xu S, Wang ZL (2009) Depth resolved luminescence from oriented ZnO nanowires. Appl Phys Lett 95(24):243101
216. Rosenberg RA, Shenoy GK, Tien LC, Norton D, Pearton S, Sun XH, Sham TK (2006) Anisotropic x-ray absorption effects in the optical luminescence yield of ZnO nanostructures. Appl Phys Lett 89(9):093118
217. Yatsui T, Ohtsu M, Yoo J, An SJ, Yi GC (2005) Near-field measurement of spectral anisotropy and optical absorption of isolated ZnO nanorod single-quantum-well structures. Appl Phys Lett 87(3):033101
218. Wu YL, Tok AIY, Boey FYC, Zeng XT, Zhang XH (2007) Surface modification of ZnO nanocrystals. Appl Surf Sci 253(12):5473–5479
219. Lavrov EV (2009) Hydrogen in ZnO. Physica B-Condensed Matter 404(23–24):5075–5079
220. Lavrov EV, Herklotz F, Weber J (2009) Identification of two hydrogen donors in ZnO. Phys Rev B 79(16):165210
221. Lavrov EV (2010) Hydrogen in ZnO. Proceedings of SPIE 7603:76030J
222. Wang XF, Xu JB, Yu XJ, Xue K, Yu JG, Zhao XJ (2007) Structural evidence of secondary phase segregation from the Raman vibrational modes in $Zn_{1-x}Co_xO$ ($0 < x < 0.6$). Appl Phys Lett 91(3): 031908
223. Li TH, Liu LZ, Li XX, Wu XL, Chen HT, Chu PK (2011) Oxygen vacancy density-dependent transformation from infrared to Raman active vibration mode in SnO_2 nanostructures. Opt Lett 36(21):4296–4298
224. Bergman L, Morrison JL, Chen XB, Huso J, Hoeck H (2006) Ultraviolet photoluminescence and Raman properties of MgZnO nanopowders. Appl Phys Lett 88(2):023103
225. Ye JD, Teoh KW, Sun XW, Lo GQ, Kwong L, Zhao H, Gu SL, Zhang R, Zheng YD, Oh SA, Zhang XH, Tripathy S (2007) Effects of alloying and localized electronic states on the resonant Raman spectra of $Zn_{1-x}Mg_xO$ nanocrystals. Appl Phys Lett 91(9):091901
226. Lu JG, Zhang YZ, Ye ZZ, Zeng YJ, Huang JY, Wang L (2007) Rational synthesis and tunable optical properties of quasialigned $Zn_{1-x}Mg_xO$ nanorods. Appl Phys Lett 91(19): 193108
227. Alim KA, Fonoberov VA, Shamsa M, Balandin AA (2005) Micro-Raman investigation of optical phonons in ZnO nanocrystals. J Appl Phys 97(12):124313
228. Šćepanović M, Grujić-Brojčin M, Vojisavljević K, Srećković T (2011) Defect induced variation in vibrational and optoelectronic properties of nanocrystalline ZnO powders. J Appl Phys 109(3):034313
229. Kukreja LM, Misra P, Das AK, Sartor J, Kalt H (2011) Anomalous optical processes in photoluminescence from ultrasmall quantum dots of ZnO. J Vac Sci Technol A 29(3): 03A120
230. Zhou JX, Zhang MS, Hong JM, Yin Z (2006) Raman spectroscopic and photoluminescence study of single-crystalline SnO_2 nanowires. Solid State Commun 138(5):242–246

UV-VIS Spectroscopy/Photoluminescence for Characterization of Silica Coated Core-shell Nanomaterials

11

Masih Darbandi

Contents

1 Definition of the Topic

Silica as a coating material promises an unparalleled opportunity for enhancement of physiochemical properties and functions by using core–shell rational designs and profiting from its synthetic versatility. This chapter provides a brief overview of recent progress in the synthesis of silica-coated nanomaterials and their characterization by UV-VIS spectroscopy/Photoluminescence.

2 Overview

Synthetic methods for high-quality near-monodispersed nanoparticles of metals, metal oxides, and quantum dots in organic solvents are well developed, but their

M. Darbandi
Faculty of Physics and Center for Nanointegration Duisburg-Essen (CeNIDE), University of Duisburg-Essen, Duisburg, Germany

Challa S.S.R. Kumar (ed.), *UV-VIS and Photoluminescence Spectroscopy for Nanomaterials Characterization*, DOI 10.1007/978-3-642-27594-4_11,

applications are restricted due to the lack of water dispersiblity and tailored surface chemistry.

In recent years, new strategies for silica coating of inorganic nanoparticles and organic nanomaterials, which differ from the classical methodologies, have emerged at the forefront of materials science. The use of silica as a coating material mainly lies in its anomalously high stability, especially in aqueous media, but other reasons include easy regulation of the coating process, chemical inertness, controlled porosity, processability, and optical transparency. These advantages render silica an ideal, low-cost material to tailor surface properties. Additionally, this coating could endow the cores with several beneficial properties, such as the possibility of subsequent functionalization and biocompatibility, which pave the way to apply this kind of nanoparticles in different fields.

UV-VIS spectroscopy/photoluminescence in combination with other physical techniques (like TEM, SEM, etc.) could be used to characterize final product regarding the quality and quantity point of view. Most importantly it could play an important role in verifying suggested mechanism for synthesis or encapsulation.

3 Introduction

Most syntheses for high-quality, near-monodispersed nanoparticles of semiconductors, metals, and metal oxides involved nonaqueous solvents and coating with monolayers of hydrophobic surfactants [1–5]. Such nanoparticles could not be used directly for biofunctionalization as they were water insoluble and did not have suitable functional groups for bioconjugation.

Silica coating is one of the facile approaches to render the nanoparticles with characteristic properties. Several methods of encapsulation were introduced and various techniques were applied to characterize silica-coated nanoparticles (Fig. 11.1).

Silica is a very interesting shelling material for various kinds of nanoparticles, because it is optical transparent, chemical inert, nontoxic, water dispersible, moderate buffer stable, and easy to functionalize. As mentioned, outstanding properties makes silica shell one of the most popular inert materials for surface protection [6–11].

To date, almost any kind of available nanoparticle has been coated with silica shell [12–20]. Nevertheless, very different methods for preparation were adopted, due to the different nature of the core particles. Most importantly, the optical properties of the resulting core/shell nanoparticles are of major interest, because almost any application relies on well luminescent nanoparticles. Unfortunately there is a lack of review on combining the synthesis of silica-coated nanocomposites and UV-VIS spectroscopy/photoluminescence characterization. Therefore the first part of this chapter introduces different synthesis methods for silica encapsulation of colloidal nanoparticles. The optical properties of silica-coated nanoparticles are discussed in the second part of this chapter.

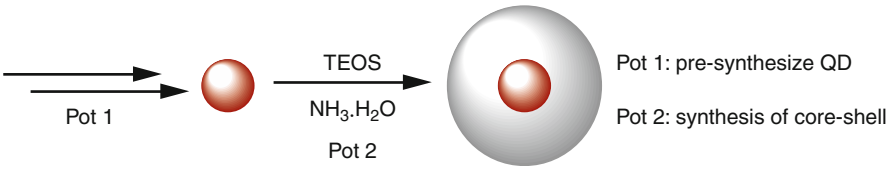

Fig. 11.1 General process for synthesis of silica-coated nanocomposites

4 Experimental Methodology

4.1 Stöber Method

The use of silica coatings itself is certainly not new. Stöber et al., in 1968, reported a pioneering method for the synthesis of spherical and monodisperse silica nanoparticles from aqueous alcohol solutions of silicon alkoxides in the presence of ammonia as a catalyst [21]. In this pioneering work, Stöber et al. developed a process capable of forming well-defined silica particles in the range of micrometer. The silica particles produced had a narrow size distribution and could be size-tuned by controlling the solution pH, composition of reactants and temperature. The process was typically carried out at room temperature and at a pH value of approximately 10. The Stöber method is very popular and currently many industrial manufacturing processes are based on this process [22–29].

Since the hydrolysis of TEOS is very slow, either an acid or a base (typically ammonia) is used as a catalyst. The former supports the growth of gel structures, while the latter is a morphological catalyst producing spherical particles. Stoichiometrically, the reaction proceeds as follows:

$$\mathrm{Si(OC_2H_5)_4 + 2H_2O \leftrightarrow SiO_2 + 4C_2H_5OH} \tag{11.1}$$

which is actually a hydrolysis

$$\mathrm{Si(OC_2H_5)_4 + 4H_2O \leftrightarrow Si(OH)_4 + 4C_2H_5OH} \tag{11.2}$$

followed by a condensation step

$$\mathrm{Si(OH)_4 \leftrightarrow SiO_2 + 2H_2O} \tag{11.3}$$

Polymerization of silicic acid may occur in two ways. In acidic solutions, initially chain-like or open-branched polymers are produced by the condensation of silane groups. Polymerization in alkaline solutions takes place by internal condensation and cross-linking to result in particles, where the four silicon-oxygen bonds and the hydroxyl groups are attached to the surface of the particles only [30–35].

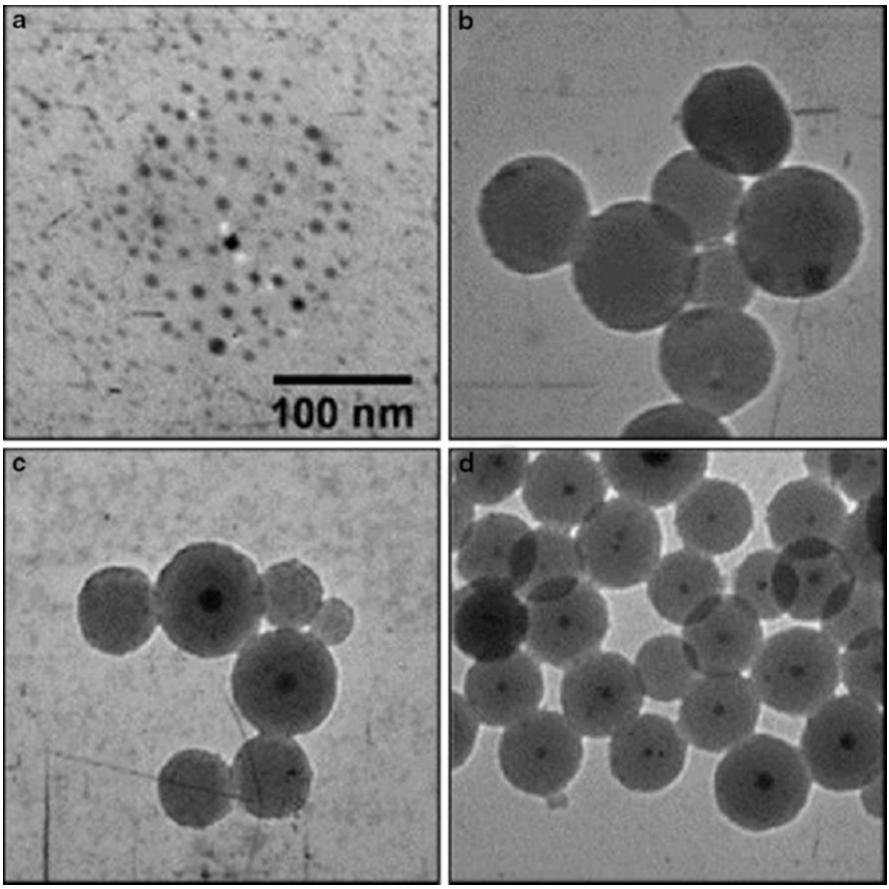

Fig. 11.2 TEM images of Ag nanoparticles (**a**) and Ag@SiO_2 prepared by TEOS hydrolysis using different bases (**b–d**) (From Ref. [8])

The silica coating of colloidal particles has been studied extensively during the past decade with a significant progress especially with noble-metal nanocrystals such as Au and Ag (Fig. 11.2).

As an alternative synthetic route, the silane coupling method, in which the use of a surface primer (a silane coupling agent) was necessary to provide the surface with silanol anchor groups has been used. Thereby, the nanoparticles surface was rendered vitreophilic via its complexation with the functional groups of the silane coupling agent. This enables the deposition of thin, dense silica layers in aqueous solution. An organosilane monolayer forms at the interface between core and shell (Fig. 11.3).

This coating process was also extended to silver and cadmium sulfide particles. A similar approach has been employed to produce silica-coated magnetite particles [36–39].

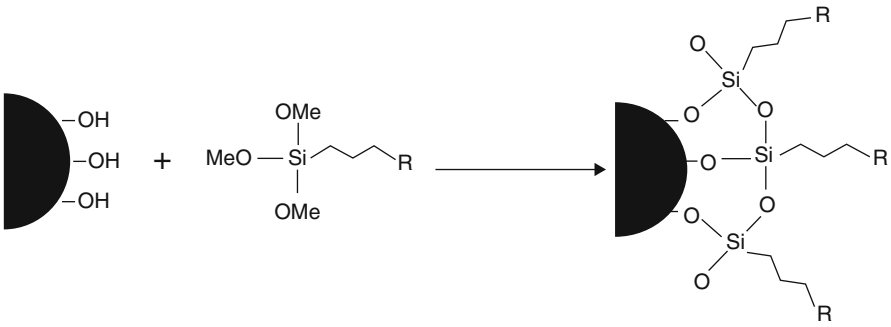

Fig. 11.3 Silica encapsulation by silane-coupling agent

Other studies have shown, that under certain conditions, silica shells can be formed on vitreophobic materials such as gold or silver nanoparticles without pretreatment of the particle surface using the Stöber method. Xia and coworkers [40, 41], for instance, prepared silica-coated gold and silver nanoparticles through hydrolysis and condensation of tetraethyl orthosilicate (TEOS) in ethanol. Similarly, Hardikar et al. [42] performed the coating of silver particles stabilized with Daxad. More recently, Graf et al. [10] used poly(vinylpyrrolidone) as a stabilizer to transfer gold and other nanoparticles into ethanol and perform a direct silica coating with TEOS. Ohmori et al. [43] optimized coating conditions and coated hematite (Fe_2O_3) particles with silica layers by hydrolysis of the tetraethoxysilane (TEOS) in 2-propanol.

Major disadvantages of the Stöber method for silica encapsulation are the high requirements on purity of the reactants, the difficulty and multiplicity of the preparation steps, and the fact that nanoparticles with nonpolar ligands cannot be coated easily or directly. Furthermore, it is very difficult and sometimes impossible to prevent co-nucleation of pure silica nanoparticles with this method.

Additionally, in the case of hydrophobic nanoparticles, Stöber's condition is difficult to apply as the nanoparticles are insoluble in the alcohol-water media. Various modifications have been reported for the effective silica coating of hydrophobic nanoparticles. These included the modification of Stöber's condition, the use of lipophilic silane monomers, the use of trialkoxysilanes that minimized the shell thickness, and the application of hydrophilic silanes that induced water dispersiblity for the final nanoparticles.

Since either of the above-mentioned methods require pretreatment or chemicals are quite expensive (for encapsulation of organically capped nanoparticles), the water-in-oil (W/O) microemulsion system in conjunction with other methods has also been used for the preparation of silica-coated nanoparticles.

4.2 Microemulsion Method

Microemulsions are isotropic and thermodynamically stable single phases, formed by at least three components; two of them are non-miscible, and a third, called

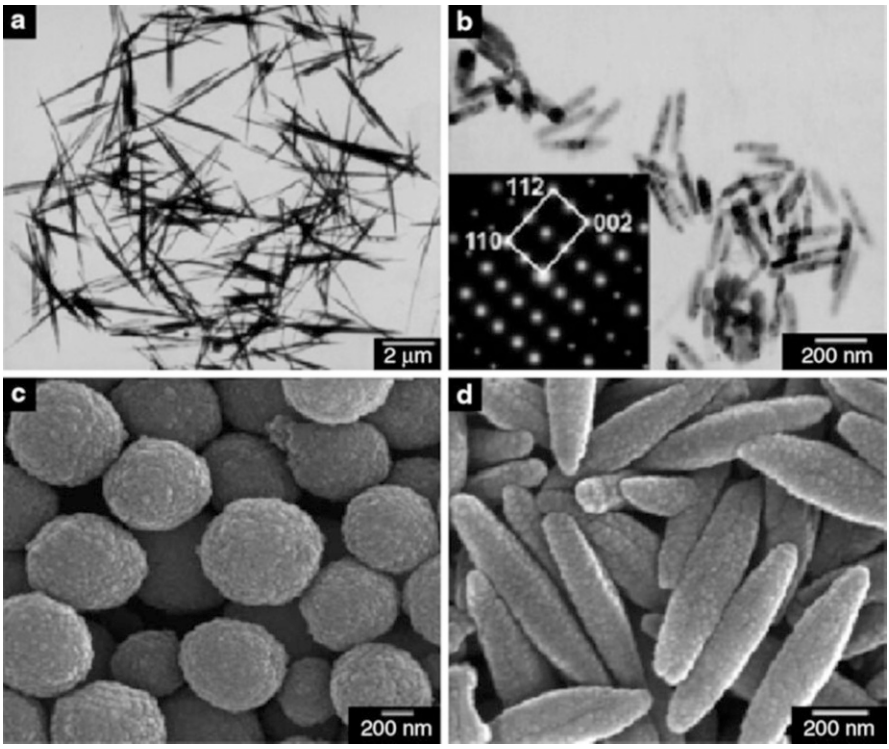

Fig. 11.4 TEM images of nanocrystals synthesized by microemulsion method (From Ref. [47])

surfactant, has an amphiphilic behavior. Surfactant monolayers separate aqueous and oil domains and hence reduce the unfavorable oil–water contact. In contrast to macroscopic emulsions, which are thermodynamically unstable, nanosized microemulsion droplets are formed spontaneously and are thermodynamically stable. The surfactant molecule lowers the interfacial tension between water and oil resulting in the formation of a transparent solution.

Reverse micellar synthesis (water-in-oil microemulsion) of materials belongs to the class of wet materials synthesis procedures, and exhibits, in general, all the advantages that usually accompany other wet approaches. Particles prepared by the reverse microemulsion method show good promise in size control and further miniaturization (Fig. 11.4).

In simple terms, nanoparticles prepared with reverse microemulsions, are usually "precipitated" within the water pool of the microemulsion. The size of these "nanoreactors" thus governs the size of the resulting particles. It is thus possible to control the sizes of reverse micelles by controlling the molar ratio of water to surfactant [44–51].

Adair et al. have used the microemulsion method primarily to prepare various core/silica shell nanoparticles in a one-pot, two-step microemulsion reaction [52, 53].

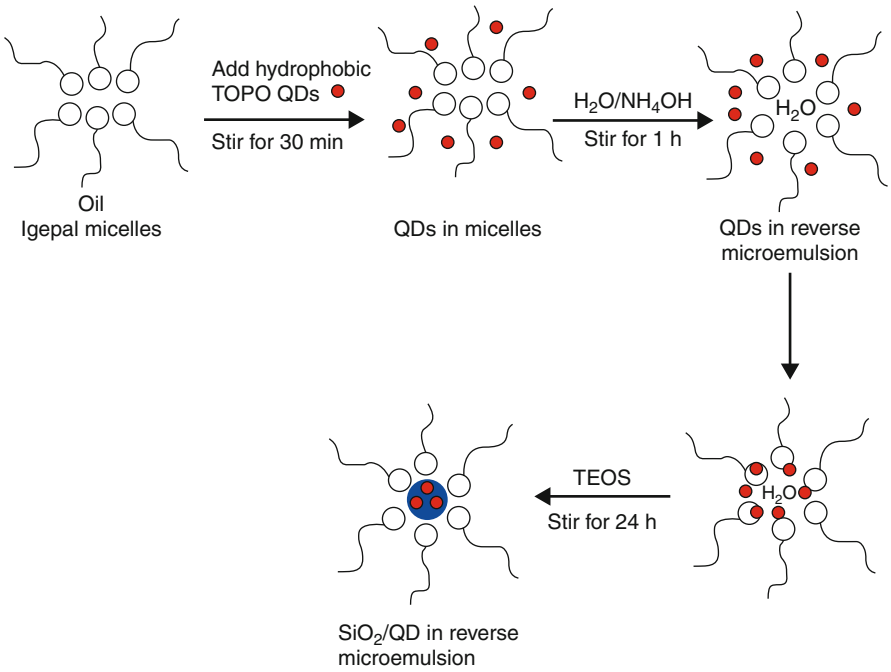

Fig. 11.5 Experimental process for silica encapsulation of nanoparticles in microemulsion (From Ref. [58])

Typically, they synthesize core nanoparticles or crystals first and add TEOS and an ammonia catalyst subsequently. This method is very elegant, because it is easy, and the resulting nanoparticles contain usually one core per silica shell.

W/O microemulsions (also termed "reverse microemulsions") have been found to be extremely useful as nanoreactors for the confined synthesis and silica coating of nanometer-sized particles [54–59], since they can efficiently dissolve both inorganic salts and organometallic precursors, as well as pre-synthesized nanocrystals, thus providing sufficient flexibility to synthesize nanostructures with diverse sizes, shapes, and functions. As compared to the Stöber silica coating on nanoparticles, the reverse microemulsion method shows as main advantage the higher control over silica nucleation, which is limited to the interior of the nanometer-sized droplets. The addition of tetraethyl orthosilicate (TEOS) directly to the microemulsion, results in a hydrolysis and polymerization reaction. This reaction rate is much slower in microemulsion systems compared with the bulk aqueous solution. Therefore, with time, as the polymerization reaction proceeds, a thin layer of uniform silica coating is formed onto each nanoparticle. Since the size of the nanoparticles is dependent on the size of the water pools, the size of the shell can be controlled and tuned by changing the water-to-surfactant molar ratio (Fig. 11.5).

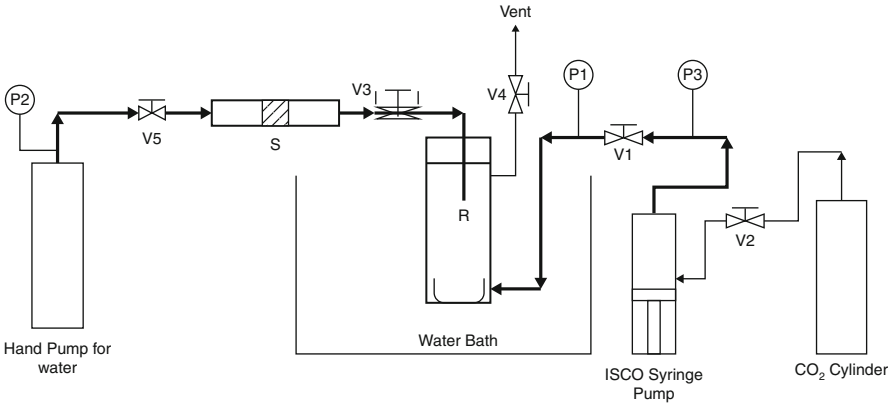

Fig. 11.6 Schematic of the apparatus for silica coating using supercritical CO_2 (From Ref. [64])

Alternatively, supercritical CO_2 has also been used as both reactant and antisolvent to encapsulate nanoparticles using AOT (sodium bis-(2-ethylhexyl) sulfosuccinate) W/O microemulsions. Some advantages of using this coating method are the less aging time (less than 1 min) and the absence of a base in the reaction medium [54, 60–63]. Thakur et al. [64] developed a supercritical antisolvent method for silica formation using a water-in-oil microemulsion. In this method, supercritical CO_2 acts both as an anti-solvent and as a reactant (Fig. 11.6).

The fact that QDs with hydrophobic ligands (such as TOPO) are homogeneously silica-coated within a microemulsion system is surprising. Darbandi et al. [65] suggested that the QDs have to undergo a spontaneous phase transfer as a result. They explained the findings with two hypothetical mechanisms: first, phase transfer without ligand exchange and second, phase transfer with ligand exchange. QDs with hydrophobic ligands can be easily transferred to water by means of tensides. With the first suggested mechanism, the surfactant could form an "inverse" bilayer around the TOPO-ligated QDs. On addition of the ammonia catalyst, the silica could grow between the tensid layers. With the second suggested mechanism, the ligands of the QDs are exchanged with, for example, TEOS, and subsequently transferred to the hydrophilic phase of the microemulsion. On addition of the ammonia catalyst, the TEOS is polymerized from the QD surface (Fig. 11.7).

The preparation of nanoparticles within microemulsions has been shown to be a convenient route toward monodisperse particles of controllable size. This method exploits two useful properties: the capacity to dissolve reactants in the water pool and the constant exchange of the aqueous phase among micelles. Thus, by mixing microemulsions containing different reactants, it is possible to perform chemical reactions within reverse micelle water pools by using them as a nanoreactor.

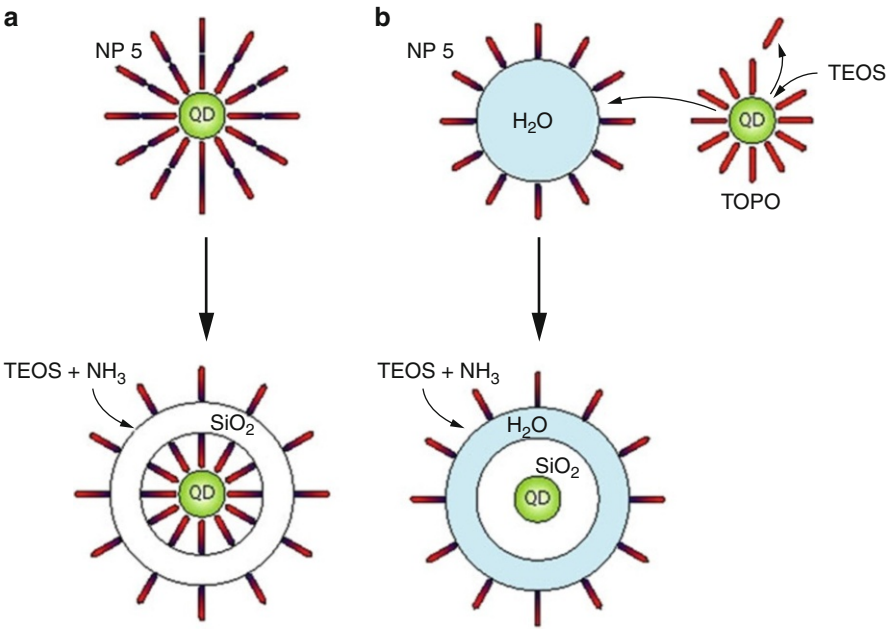

Fig. 11.7 Proposed mechanisms for silica growth on QDs: (**a**) Silica growth without ligand exchange and (**b**) with ligand exchange (Reprinted with permission from Ref. [65])

5 Key Research Findings

5.1 UV-VIS Spectroscopy/Luminescence as Promising Tool for Characterization of Silica-Coated Nanocomposites

UV-VIS spectroscopy/photoluminescence in combination with other techniques (like TEM, SEM, etc.) has been used to characterize silica-coated nanocomposites. Here we bring different examples from the literature regarding this issue.

5.1.1 Syntheses of Silica-Coated QDs with Tunable Size and Optical Properties

For many applications of silica-coated core–shell nanoparticles, such as biolabeling, etc., it is of paramount importance to precisely control the thickness of the shell in parallel with control over the optical property of the final product. Darbandi et al. [66] demonstrated a practical and straightforward method for the synthesis of silica-coated QDs of different sizes and with varying photoluminescence properties. In which silica encapsulation and increasing the thickness of silica shell has been done via in situ and one-pot method (silica encapsulation and control on the thickness of the final product and luminescence properties take place

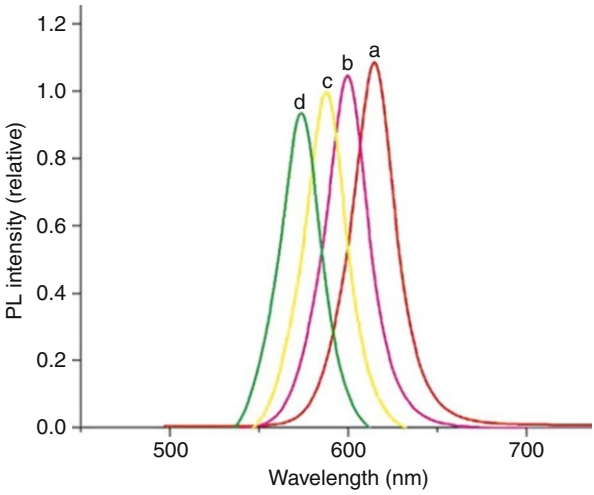

Fig. 11.8 Luminescence spectra of CdSe/ZnS/silica nanocomposites prepared with different initial amount of TEOS as time interval addition: (*a*) 50 μl, (*b*) 2 × 50 μl, (*c*) 3 × 50 μl, (*d*) 4 × 50 μl (From Ref. [66])

in the same reactor). A time interval addition of silica precursor method has been used to increase the size of the silica shell and in parallel to tune the photoluminescence property. The resulting nanocomposites were characterized by different techniques like transmission electron microscopy, photoluminescence spectroscopy, and zeta-potential measurements.

The influence of the silica layer on the optical properties of the final nanocomposites in water is shown in Fig. 11.8. Varying the TEOS concentration had noticeable effects on the luminescence properties of the core–shell nanoparticles. A gradual blue shift (of maximum peak position) and decrease in the photoluminescence intensity was reported with the addition of TEOS.

Additionally, they used different silica precursor for silica encapsulation (with the same concentration). Figure 11.9 shows that the luminescence property of the silica-coated CdSe/ZnS nanoparticles (exciting by single wavelength of 360 nm) changes dramatically with different silica precursor. The inset of Fig. 11.9 represents the photograph of three silica-coated QDs obtained with different silica agents, taken under illumination by a 60 W UV lamp operating at 360 nm.

5.1.2 Syntheses of Hollow Silica Nanospheres

Inorganic hollow nanospheres with well-defined architectures are of interest because of their low density, low toxicity, large surface area, high chemical and thermal stability, and surface permeability. Such hollow capsules have strong applications in catalysis, such as in the stationary phase for selective separation, controlled drug delivery, artificial cells, light fillers, low-dielectric-constant prosthetic materials, or photonic crystals [67–72].

Hollow inorganic particles were mostly made by removing a core material from core/shell nanoparticles, by either annealing at high temperature or dissolving the core with acids, alkalis, or an appropriate organic solvent [67, 73–77].

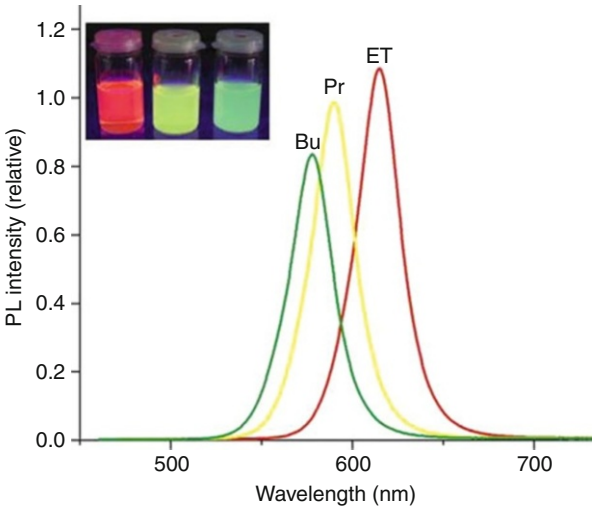

Fig. 11.9 Luminescence spectra of CdSe/ZnS/silica nanocomposites prepared with different silica precursor: TEOS (*red line*), TPOS (*yellow line*), and TBOS (*green line*). *Inset*: photograph of final product with different silica precursor TEOS (*left*), TPOS (*middle*), and TBOS (*right*) under UV lamp (From Ref. [66])

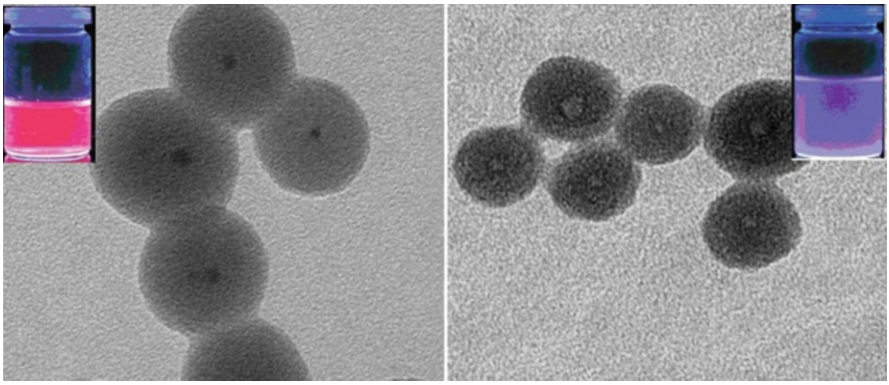

Fig. 11.10 TEM micrographs of core/shell-structured CdSe/ZnS/SiO_2 Particles and related photograph of final product under UV lamp (*left*) and TEM micrograph of hollow silica nanoparticles and related photograph of final product under UV lamp (*right*) (From Ref. [78])

Darbandi et al. [78] have described a novel, room temperature, and mild synthesis process for hollow silica nanoparticles using luminescent CdSe/ZnS nanoparticles as templates. Silica encapsulation and dissolution of the core particles has been done simultaneously (in situ) by modification of the reaction conditions. The size and shape of the hollow spheres has been controlled by the dimensions of the core nanoparticles. The progression of the reaction has been monitored by the luminescence (and vanishing of luminescence) of the functional nanoparticles (Fig. 11.10).

Scheme 11.1 displays the various options which have been used to prepare monodisperse hollow silica nanoparticles. When the concentration of ammonia was above the optimum conditions, the core particles started to dissolve

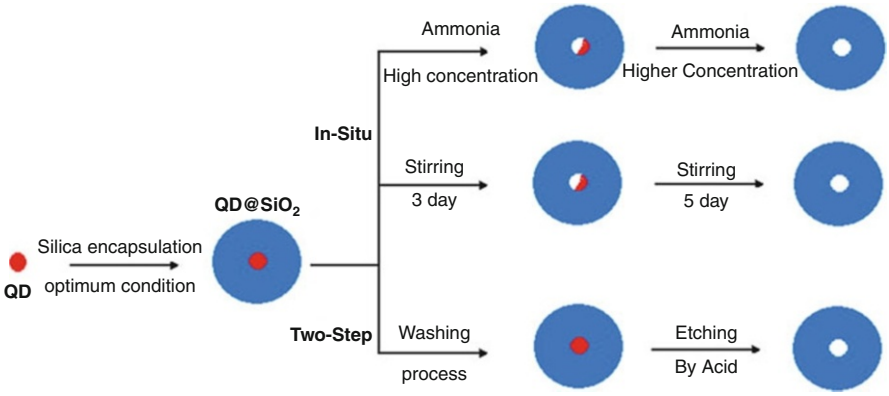

Scheme 11.1 Schematic diagram of the preparation of hollow silica spheres (From Ref. [78])

incompletely. Perfect hollow spheres were obtained with an increasing concentration of ammonia. A similar result has been reached with increasing reaction time. High concentrations of ammonia, added prior to the washing process, resulted in hollow silica spheres, as well as addition of an acidic solution after workup of the core/shell nanoparticles (two-step process).

5.1.3 Reverse Synthesis of Cores in Hollow Silica Nanospheres

The synthesis of noble metals (like Au, Ag) by wet chemical methods is based on the reduction of an inorganic or organometallic precursor in the presence of a stabilizing agent [79–81]. The surface of nanoscaled materials is very reactive and needs to be protected by surface ligands to avoid irreversible growth and agglomeration.

Cavaliere-Jaricot et al. [82] presented the synthesis of silica-coated gold nanoparticles ($Au@SiO_2$) by means of hollow silica nanospheres used as nanoreactors in which the metal particles were grown in situ, in the internal cavity of the previously prepared hollow silica particles (Fig. 11.11).

The strategy was exploited to transfer gold precursor and reducing compound into the silica's empty cavity, giving rise to the $Au@SiO_2$ nanocomposites. They let the metal precursor ($HAuCl_4$) diffuse into the holes, and then they added an excess amount of $NaBH_4$ as the reducing agent. The latter could be diffused into the cavity of the silica spheres, which were filled with Au^{3+} cations, and reduced. The metal nanoparticle formation took place by nucleation and growth of Au(0) atoms. The silica shell avoided further growth of the nanoparticles, acting as a template (as confinement factor), and finally stabilized them. Therefore the final product was a gold nanoparticle surrounded by a silica shell.

They characterized the yielded nanocomposites by different techniques like transmission electron microscopy (TEM), energy-dispersive X-ray analysis (EDAX), and UV-VIS spectroscopy.

The UV-VIS analysis of the silica-encapsulated gold nanoparticles presented quite a broad absorption peak with a λmax situated at 550 nm (Fig. 11.12) which

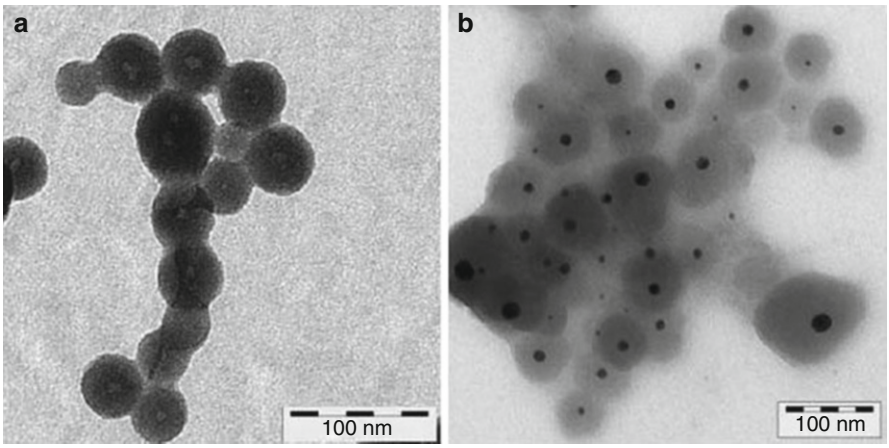

Fig. 11.11 TEM micrographs of (**a**) hollow silica nanoparticles and (**b**) the Au@SiO_2-derived nanocomposites (From Ref. [82])

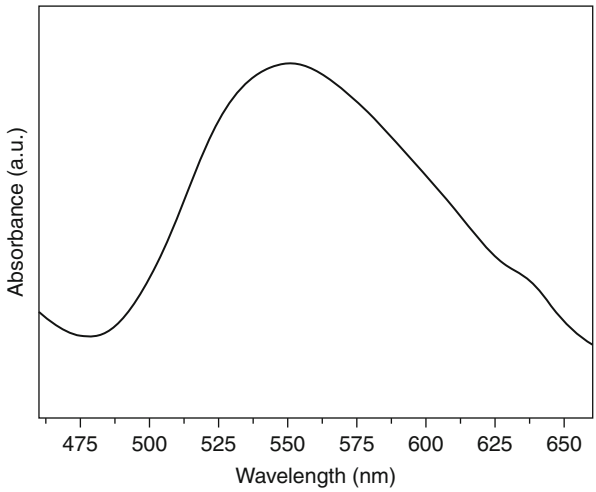

Fig. 11.12 UV-VIS spectrum of the Au@SiO_2 nanocomposites (From Ref. [82])

was clearly attributed to the Plasmon band of Au(0). The position and the width of the signal were in agreement with the TEM data, which showed the size dispersion of the core gold nanoparticles around the average value of 10 nm.

5.1.4 Silica-Coated Nanoparticles as Detectors

The quantum dots core offers the possibility of an optical sensing. In fact, they are known to have interesting photoluminescence (PL) properties, with size-dependent emission wavelength, continuous excitation spectrum, intense brightness, and good stability compared to organic dyes [83–85]. However, their luminescence is easily quenched, for example, by chemicals which adsorb on

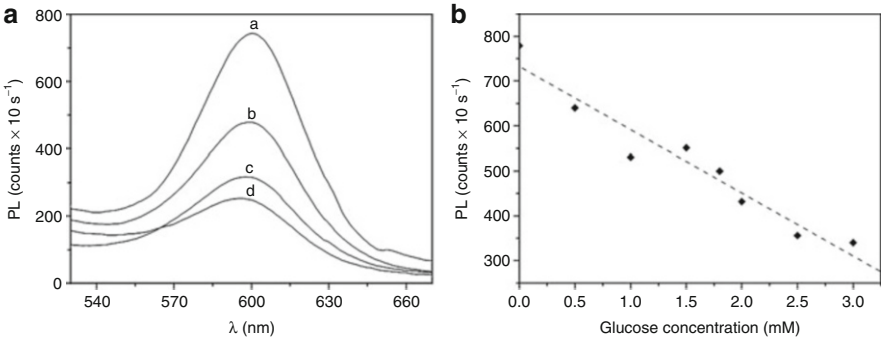

Fig. 11.13 (**A**) PL spectra of QDs@SiO_2 in the presence of 0 mM (*a*), 2 mM (*b*), 3 (*c*) and 5 mM (*d*) glucose. (**B**) Averaged PL intensities of QDs@SiO_2 as a function of glucose concentration (From Ref. [89])

the surface and first oxidize the surface or subsequently provide additional relaxation pathways for the excited electrons, which decreases the luminescence properties in general.

Nowadays, quantum dots and their fluorescence are used in few glucose sensors.

Zou et al. [86] presented a chemical sensor with CdSe nanocrystal films, which shows a linear dependency between the electrochemiluminescence signal of the nanocrystals and hydrogen peroxide up to 100 mM. Zayats et al. [87] have developed a sensor based on the hydrogen peroxide biocatalytical growth of gold NPs. The glucose concentration (related to the H_2O_2 production) was then optically monitored, with the plasmon absorbance changes with nanoparticle size growth. Cordes et al. [88] have reported a sensor based on the luminescence recovery by viologen-quenched QDs after the addition of glucose.

Cavaliere-Jaricot et al. [89] reported the application of silica-coated quantum dots (QDs@SiO_2) in glucose detection which is an indirect optical technique based on the photoluminescence quenching of QDs by hydrogen peroxide produced during glucose oxidation. Additionally, the amorphous nature of the silica shell and their mesopores can provide sufficiently opened channels to enable small molecules to diffuse toward the cores. H_2O_2 is then likely to reach the quantum dot surface, decreasing its photoluminescence intensity, the oxidation of glucose being proportional to the production of hydrogen peroxide.

Figure 11.13a shows the obtained spectra with different amount of added sugar. The addition of glucose led to the diminution of the PL signal due to quantum dots. The further increase in glucose concentration corresponded to the progressive decrease of the luminescence intensity. The dependence of the luminescence intensity from the glucose amount is presented in Fig. 11.13b.

5.1.5 Surface Functionalization on Silica-Coated Nanoparticles

Almost any potential application of silica-encapsulated nanoparticles requires further derivatization of the silica surface. This is applicable especially for bio/medical applications. Finding ways to effectively introduce effective functional

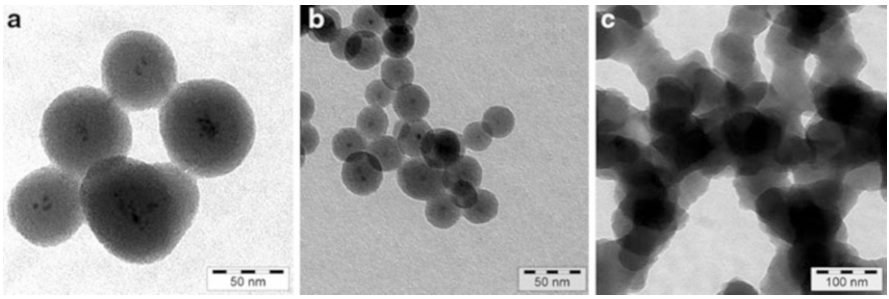

Fig. 11.14 TEM micrographs of CdSe/ZnS/SiO_2 nanoparticles with in situ, one-pot functionalization: (**a**) APS before hydrolysis reaction, (**b**) APS after hydrolysis reaction, and (**c**) MPS before hydrolysis reaction (From Ref. [90])

groups onto the surfaces of silica particles has been the object of intensive interest and investigation since the surface properties of silica materials are largely influenced by the nature of the surface functional groups. Most importantly a critical element in designing surface-functionalized particles for surface-imprinting or immobilization of ions, organic molecules, or biomolecules is achieving the maximum expression of desired functional groups on the particle surface.

Darbandi et al. [90] reported a systematic study of the design and development of surface modification schemes for silica-coated nanocomposite via an in situ, one-pot way. Silica-coated CdSe/ZnS nanoparticles were prepared in a water-in-oil microemulsion and subsequently surface-modified via addition of various organosilane reagents to the microemulsion system.

Depending on the reaction conditions, a single or multiple particles were coated with silica, respectively, to form a nanocomposite.

They demonstrated that depending on the sequence of addition of silica precursors and organosilanes the product can show bright luminescence or considerable colloidal stability. The organosilanes molecules which they used, act both as a stabilizer of the microemulsion system (regarding the charge compensation) and as a functional group on final product at top of silica shell.

When the APS (3-aminopropyltris (methyloxy) silane) was added before TEOS (Tetraethyl orthosilicate) hydrolyzing reaction, the final product were big silica spheres with multi-QD core (Fig. 11.14a). A high percentage of organosilanes were incorporated into the interior of the particles (most of the amine groups from APS were buried in the texture of the silica particles). Therefore the final product were multiple silica-coated nanocomposites with bright photoluminescence (Fig. 11.15c).

The addition of APS after hydrolyzing of TEOS (Fig. 11.14b) caused very uniform and monodisperse silica particles with a single QD in the center. A greater percentage of functional groups will be expressed at the particle surface rather than be incorporated in the interior of the particles. Negatively charged silica intermediates cause more negatively charged QDs to distribute evenly throughout the microemulsion during synthesis. Therefore, the core particle is located in center of the silica shell with moderate photoluminescence property (Fig. 11.15b).

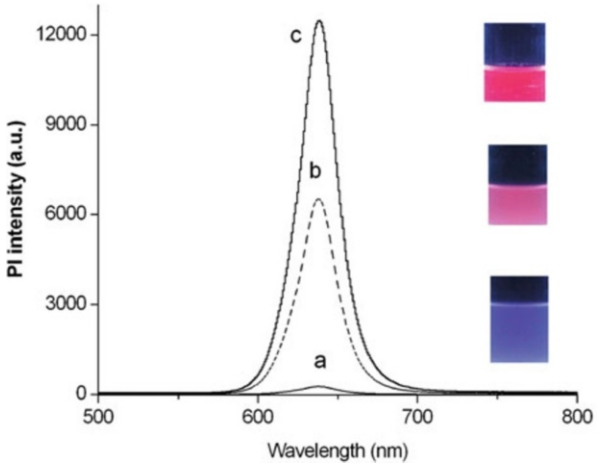

Fig. 11.15 Photoluminescence spectra of final CdSe/ZnS/SiO_2 nanoparticles functionalized with MPS (*a*), APS after (*b*), APS before (*c*) hydrolysis reaction, (*right*) photograph of final products under UV excitation, from up to down: APS functionalized before, APS functionalized after, MPS functionalized before hydrolysis of TEOS (From Ref. [90])

In the case of MPS as a silane coupling agent, the final product was a polymeric gel (Fig. 11.14c) without any core–shell structure, irrespective of whether MPS was added before or after the hydrolysis reaction. Charge repulsion could be enhanced and it can destabilize the microemulsion system (because of the negative charge from MPS molecules at high pH, in presence of ammonia) in which QDs will be pushed out of water pool. Therefore, the final product is an irregular structure that does not exhibit any photoluminescence (Fig. 11.15a).

5.1.6 Silica Encapsulation of Multifunctional Nanoparticles

The multifunctional probes offer great advantages for optical- and magnetic-based imaging applications. The magneto-fluorescent NPs, or in short magnetic QDs, are useful for fluorescence-based labeling applications, magnetic-based cell harvesting, tracking, and drug targeting, which can be detected by imaging techniques such as magnetic resonance imaging (MRI), fluorescence imaging, tomography, confocal microscopy, and flow cytometry. The synthesis of these bimodal magnetic-fluorescent probes has drawn great interest in recent years [91, 92].

Yi et al. [57] reported the synthesis of a water-dispersible hybrid material consisting of quantum dots (QDs) and magnetic nanoparticles (MPs) encapsulated in a silica shell (Fig. 11.16).

Bare CdSe showed an absorption peak at 530 nm and an emission peak at 554 nm. As the silica coating reaction proceeded from 8 to 48 h, the absorption peak shifted to lower wavelength and became less pronounced. This blue shift was also observed in the fluorescence spectra, and the excitonic band became broader (Fig. 11.17a). The quantum yield (QY) of the emission was estimated to be 11.4% for CdSe and 3.2% and 1.1% for SiO_2/MP-QD 8 and 48 h after the coating reaction,

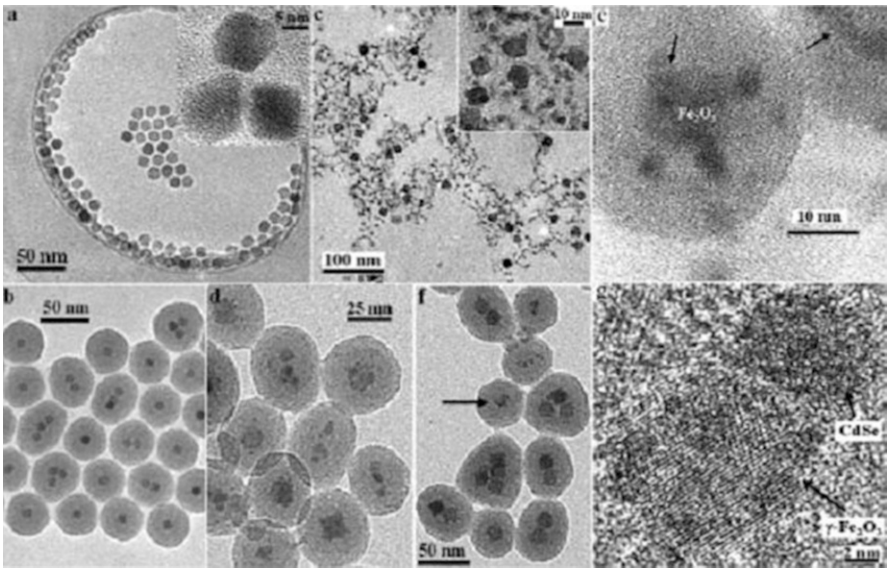

Fig. 11.16 TEM micrographs of (**a**) MPs, (**b**) SiO_2/MP, (**c**) interconnected MPs and CdSe QDs (after 8 h of SiO_2/MP-QD reaction), (**d**, **e**) SiO_2/MP-QD nanocomposites (after 48 h of SiO_2/MP-QD reaction), and (**f**) SiO_2/MP-QD nanocomposites formed at a lower CdSe concentration. (**g**) High-resolution TEM micrograph of the area marked by the *arrow* in (**f**), showing the presence of CdSe QDs and MPs (From Ref. [57])

respectively. The QY of SiO_2/MP-QD was increased to 4.8% when ZnS-capped CdSe QDs (QY) 14.5% were used. They also performed magnetic characterization using a superconducting quantum interference device (SQUID).

They proved that the SiO_2/MP-QD nanocomposite particles preserved the unique magnetic property of MP and optical property of CdSe QDs.

6 Conclusions and Future Perspective

In this report, we have described various methodologies for the silica coating of nanoparticles and related nanomaterials, while providing information regarding UV-VIS spectroscopy/photoluminescence as strong characterizing tool. These nanostructured core–shell architectures are fascinating hybrid materials that combine the chemical and physical stability of silica and the function provided by different types of cores. However, the potential payoff of undertaking the use of silica as a coating material is still considerable, because silica-coated core–shell nanoparticles are currently among the most important and widely studied architectures in colloid science and nanotechnology.

To date, it is possible to encapsulate almost any kind of nanoparticle with a silica shell. In other words: silica nanoparticles with dimensions in the lower nanometer size regime can be equipped with almost any optical or magnetic property with

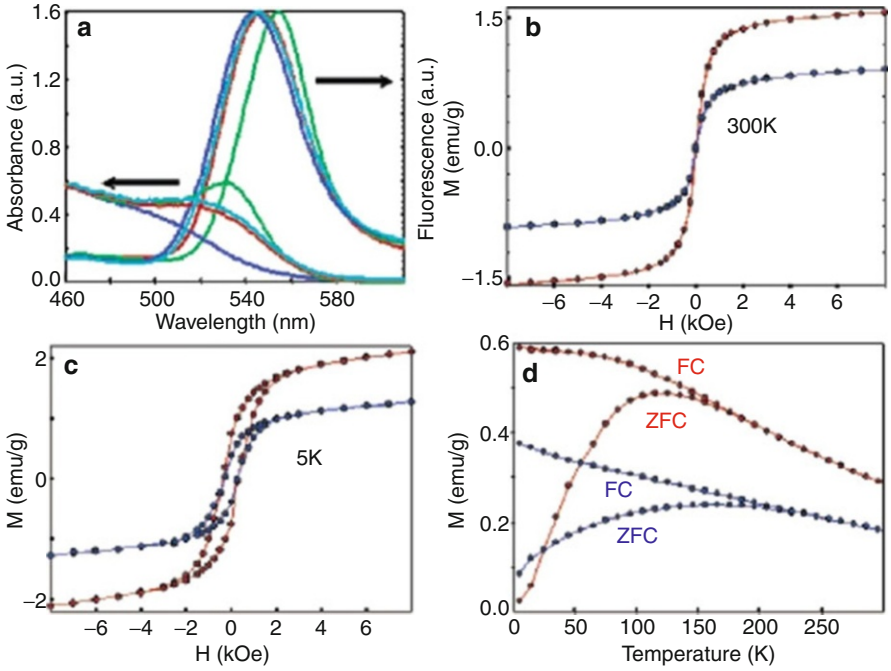

Fig. 11.17 (**a**) UV-VIS and normalized fluorescence spectra of CdSe QDs (*green*), SiO_2/MP-CdSe after 8 h (*red*) and 48 h (*blue*) of reaction, and SiO_2/MP-ZnS-capped CdSe after 48 h of reaction (*cyan*). Field-dependent magnetization at (**b**) 300 K and (**c**) 5 K, and (**d**) temperature-dependent magnetization at 100 Oe for SiO_2/MP (*red*) and SiO_2/MP-CdSe (*blue*) (From Ref. [57])

a choice of different core nanoparticles. Such a toolbox could be potentially used for the assembly of sophisticated nanosystems in the future. Therefore, it is important to bear the optical behavior of silica nanoparticles in mind, which is different compared to "macroscopic" particles. An increasing understanding of the optical behavior of nanoparticles in the nanometer size regime paves the way for application of this kind of material in controlled assembly, attachment of biomolecules, or other sophisticated bottom-up approaches.

References

1. Na M, Park H, Ahn M, Lee H, Chung I (2010) Syntheis of organic-inorganic hybrid sols with nano silica particles and organoalkoxysilanes for transparent and high-thermal-resistance coating films using sol-gel reaction. J Nanosci Nanotechnol 10(109):6992
2. Iwakai K, Tago T, Konno H, Nakasaka Y, Masuda T (2011) Preparation of nano-crystalline MFI zeolite via hydrothermal synthesis in water/surfactant/organic solvent using fumed silica as the Si source. Microporous Mesoporous Mater 141(1–3):167

3. Terskaya IN, Sal'nikov DS, Makarov SV, Yarovaya OV, Lilin SA (2008) Chemical synthesis of stable nano-sized water-organic copper dispersions. Prot Met 44(5):468
4. Lee YJ, Jun KW, Park JY, Potdar HS, Chikate RC (2008) A simple chemical route for the synthesis of gamma-Fe2O3 nano-particles dispersed in organic solvents via an iron-hydroxy oleate precursor. J Ind Eng Chem 14(1):38
5. Nakamura S, Sakamoto W, Yogo T (2006) In situ synthesis of nano-sized cobalt ferrite particle/organic hybrid. J Mater Res 21(5):1336
6. Darbandi M, Nann T (2006) One-pot synthesis of YF_3@silica core/shell nanoparticles. Chem Commun 776
7. Ow HD, Larson R, Srivastava M, Baird BA, Webb WW, Wiesner U (2005) Bright and stable core–shell fluorescent silica nanoparticles. Nano Lett 5:113
8. Kobayashi Y, Katakami H, Mine E, Nagao D, Konno M, Liz-Marzàn LM (2005) Silica coating of silver nanoparticles using a modified Stöber method. J Colloid Interface Sci 283:392
9. Eggenberger K, Merkoulov A, Darbandi M, Nann T, Nick P (2007) Direct immunofluorescence of plant microtubules based on semiconductor nanocrystals. Bioconjug Chem 18:1879
10. Graf C, Vossen DLJ, Imhof A, Van Blaaderen A (2003) A general method to coat colloidal particles with silica. Langmuir 19:6693
11. Mornet S, Elissalde C, Hornebecq V, Bidault O, Duguet E, Brisson A, Maglione M (2005) Controlled growth of silica shell on $Ba_{0.6}Sr_{0.4}TiO_3$ nanoparticles used as precursors of ferroelectric composites. Chem Mater 17:4530
12. Chawla S, Ravishanker, Khan AF, Yadav A, Chander H, Shanker V (2011) Enhanced luminescence and degradation resistance in Tb modified Yttrium Borate core-nano silica shell phosphor under UV and VUV excitation. Appl Surf Sci 257(16):7167
13. Wu CL, Hong JQ, Guo XQ, Huang CB, Lai JP, Zheng JS, Chen JB, Mu X, Zhao YB (2008) Fluorescent core-silica shell nanoparticles as tunable precursors: towards encoding and multifunctional nano-probes. Chem Commun 750
14. Badr Y, Mahmoud MA (2006) Photocatalytic degradation of methyl orange by gold silver nano-core/silica nano-shell. J Phys Chem Solid 68(3):413
15. Li YS, Church JS, Woodhead AL, Moussa F (2010) Preparation and characterization of silica coated iron oxide magnetic nanoparticles. Spectrochim Acta A Mol Biomol Spectrosc 76(5):484
16. Greenwood P, Gevert BS, Otterstedt JE, Niklasson G, Vargas W (2010) Novel nanocomposite particles: titania-coated silica cores. Pigment Resin Technol 39(3):135
17. Bazin L, Gressier M, Taberna PL, Menu MJ, Simon P (2008) Electrophoretic silica-coating process on a nano-structured copper electrode. Chem Commun 5004
18. Hsieh CT, Wu FL, Yang SY (2008) Superhydrophobicity from composite nano/microstructures: carbon fabrics coated with silica nanoparticles. Surf CoatTechnol 202(24): 6103
19. Yuan JJ, Zhou SX, You B, Wu LM (2005) Organic pigment particles coated with colloidal nano-silica particles via layer-by-layer assembly. Chem Mater 17(14):3587
20. Park JS, Han YH (2005) Nano size $BaTiO_3$ powder coated with silica. Ceram Int 31(6):777
21. Stöber W, Fink A, Bohn E (1968) Controlled growth of monodisperse silica spheres in the micron size range. J Colloid Interface Sci 26:62
22. Canton G, Ricco R, Marinello F, Carmignato S, Enrichi F (2011) Modified Stober synthesis of highly luminescent dye-doped silica nanoparticles. J Nanopart Res 13(9):4349
23. Rosa ILV, Oliveira LH, Longo E, Varela JA (2011) Synthesis and photoluminescence behavior of the $Eu^{(3+)}$ ions as a nanocoating over a silica Stober matrix. J Fluoresc 21(3):975
24. Brambilla R, Radtke C, dos Santos JHZ, Miranda MSL (2010) Silica-magnesia mixed oxides prepared by a modified Stober route: structural and textural aspects. Powder Technol 198(3):337
25. Park I, Ko SH, An YS, Choi KH, Chun H, Lee S (2009) Kim, G, monodisperse polystyrene-silica core-shell particles and silica hollow spheres prepared by the Stober method. J Nanosci Nanotechnol 9(12):7224

26. Kobayashi Y, Shimizu N, Misawa K, Takeda M, Ohuchi N, Kasuya A, Konno M (2008) Preparation of amine free silica-coated AgI nanoparticles with modified Stober method. Surf Eng 24(4):248
27. Barnakov YA, Yu MH, Rosenzweig Z (2005) Manipulation of the magnetic properties of magnetite-silica nanocomposite materials by controlled Stober synthesis. Langmuir 21(16):7524
28. Lee MH, Beyer FL, Furst EM (2005) Synthesis of monodisperse fluorescent core-shell silica particles using a modified Stober method for imaging individual particles in dense colloidal suspensions. J Colloid Interface Sci 288(1):114
29. Kobayashi Y, Katakami H, Mine E, Nagao D, Konno M, Liz-Marzan LM (2005) Silica coating of silver nanoparticles using a modified Stober method. J Colloid Interface Sci 283(2):392
30. Masalov VM, Sukhinina NS, Kudrenko EA, Emelchenko GA (2011) Mechanism of formation and nanostructure of Stober silica particles. Nanotechnology 22(27):275718
31. Terleczky P, Nyulaszi L (2009) The effect of the primary solvate shell on the mechanism of the Stober silica synthesis. A density functional investigation. J Phys Chem A 113(6):1096
32. Chou KS, Chen CC (2008) The critical conditions for secondary nucleation of silica colloids in a batch Stober growth process. Ceram Int 34(7):1623
33. Xu Y, Wu D, Sun YH, Gao HC, Yuan HZ, Deng F (2007) A new study on the kinetics of Stober synthesis by in-situ liquid Si-29 NMR. J Sol-Gel Sci Technol 42(1):13
34. Nozawa K, Gailhanou H, Raison L, Panizza P, Ushiki H, Sellier E, Delville JP, Delville MH (2005) Smart control of monodisperse Stober silica particles: effect of reactant addition rate on growth process. Langmuir 21(4):1516
35. Liu RL, Xu Y, Li ZH, Wu D, Sun YH, Gao HC, Yuan HZ, Deng F (2004) Liquid-state Si-29 NMR study on the chemical kinetics of Stober synthesis. Acta Chimica Sinica 62(1):22
36. Sun DX, Miao X, Zhang KJ, Kim H, Yuan YG (2011) Triazole-forming waterborne polyurethane composites fabricated with Silane coupling agent functionalized nano-silica. J Colloid Interface Sci 361(2):483
37. Mallakpour S, Barati A (2011) Efficient preparation of hybrid nanocomposite coatings based on poly (vinyl alcohol) and silane coupling agent modified TiO(2) nanoparticles. Prog Org Coat 71(4):391
38. Sabzi M, Mirabedini SM, Zohuriaan-Mehr J, Atai M (2009) Surface modification of TiO(2) nano-particles with silane coupling agent and investigation of its effect on the properties of polyurethane composite coating. Prog Org Coat 65(2):222
39. Zhao HJ, Zhang ZJ, Fan JW (2008) The effects of addition of silane-coupling agents on the performance of magnetic nano-sized composite microspheres (MCM). Rare Met Mater Eng 37:733
40. Lu Y, Yin Y, Li ZY, Xia Y (2002) Synthesis and self-assembly of Au@SiO_2 core–shell colloids. Nano Lett 2:785
41. Yin Y, Lu Y, Sun Y, Xia Y (2002) Silver nanowires can be directly coated with amorphous silica to generate well-controlled coaxial nanocables of silver/silica. Nano Lett 2:427
42. Hardikar VV, Matijevic E (2000) Coating of nanosize silver particles with silica. J Colloid Interface Sci 221:133
43. Ohmori M, Matijevic E (1993) Preparation and properties of uniform coated inorganic colloidal particles: 8. Silica on iron. J Colloid Interface Sci 160:288
44. Teng HH, Xu SK, Wang M (2010) Controllable synthesis of different dimensions nano-ZnO by microemulsion and photocatalytic activity. J Inorg Mater 25(10):1034
45. Chung CY, Lu CH (2010) Reverse-microemulsion preparation of visible-light-driven nano-sized BiVO(4). J Alloys Compd 502(1):L1
46. Solanki JN, Murthy ZVP (2010) Highly monodisperse and sub-nano silver particles synthesis via microemulsion technique. Colloids Surf A Physicochem Eng Asp 359:31
47. Cao M, Wu X, He X, Hu C (2005) Microemulsion-mediated solvothermal synthesis of $SrCO_3$ nanostructures. Langmuir 21:6093

48. Mi Y, Huang ZY, Zhou ZG, Hu FL, Meng QF (2009) Room-temperature preparation of BaMoO(4) nano-octahedra by microemulsion method. Chem Lett 38(5):404
49. Zhu ZF, Geng CL, Yang J, Li JP, Yu WJ (2008) Microemulsion synthesis of ZrO(2) nanopowders and their properties. Rare Met Mater Eng 37:800
50. Pithan C, Shiratori Y, Waser R, Dornseiffer J, Haegel FH (2006) Preparation, processing, and characterization of nano-crystalline $BaTiO_3$ powders and ceramics derived from microemulsion-mediated synthesis. J Am Ceram Soc 89(9):2908
51. Wu DC, Fu RW, Dresselhaus MS, Dresselhaus G (2006) Fabrication and nano-structure control of carbon aerogels via a microemulsion-templated sol-gel polymerization method. Carbon 44(4):675
52. Bae DS, Han KS, Adair JH (2002) Synthesis of platinum/silica nanocomposite particles by reverse micelle and sol–gel processing. J Am Ceram Soc 85:1321
53. Bae DS, Han KS, Adair JH (2002) Synthesis of Cu/SiO_2 nanosize particles by a reverse micelle and sol-gel processing. J Mater Sci Lett 21:53
54. Chung SH, Lee DW, Kim MS, Lee KY (2011) The synthesis of silica and silica–ceria, core–shell nanoparticles in a water-in-oil (W/O) microemulsion composed of heptane and water with the binary surfactants AOT and NP-5. J Colloid Interface Sci 355(1):70
55. Mokari T, Sertchook H, Aharoni A, Ebenstein Y, Avnir D, Banin U (2005) Nano@micro: general method for entrapment of nanocrystals in sol–gel-derived composite hydrophobic silica spheres. Chem Mater 17:258
56. Li T, Moon J, Morrone AA, Mecholsky JJ, Talham DR, Adair JH (1999) Preparation of Ag/SiO_2 nanosize composites by a reverse micelle and sol–gel technique. Langmuir 15:4328
57. Yi DK, Selvan ST, Lee SS, Papaefthymiou GC, Kundaliya D, Ying JY (2005) Silica-coated nanocomposites of magnetic nanoparticles and quantum dots. J Am Chem Soc 127:4990
58. Selvan ST, Tan TT, Ying JY (2005) Robust, non-cytotoxic, silica-coated CdSe quantum dots with efficient photoluminescence. Adv Mater 17:1620
59. Gao X, Yu KM, Tam KY, Tsang SC (2003) Colloidal stable silica encapsulated nano-magnetic composite as a novel bio-catalyst carrier. Chem Commun 2998
60. Wang GN, Wang C, Dou WC, Ma Q, Yuan PF, Su XG (2009) The synthesis of magnetic and fluorescent bi-functional silica composite nanoparticles via reverse microemulsion method. J Fluoresc 19(6):939
61. Charpentier PA, Li XS, Sui RH (2009) Study of the sol-gel reaction mechanism in supercritical CO(2) for the formation of SiO(2) nanocomposites. Langmuir 25(6):3748
62. Jiao JX, Xu Q, Li LM, Tsubasa T, Kobayashi T (2008) Effect of PEG with different M-W as template direction reagent on preparation of porous TiO_2/SiO_2 with assistance of supercritical CO_2. Colloid Polym Sci 286(13):1485
63. Jiao JX, Xu Q, Li LM (2007) Porous TiO_2/SiO_2 composite prepared using PEG as template direction reagent with assistance of supercritical CO_2. J Colloid Interface Sci 316(2):596
64. Thakur R, Gupta RB (2005) Supercritical CO_2 based silica coating of gold nanoparticles using water-in-Oil microemulsions. Ind Eng Chem Res 44:3086
65. Thomann R, Nann T (2005) Single quantum dots in silica spheres by microemulsion synthesis. Chem Mater 17(23):5720
66. Darbandi M, Urban G, Kruger M (2010) A facile synthesis method to silica coated CdSe/ZnS nanocomposites with tuneable size and optical properties. J Colloid Interface Sci 351(1):30
67. Xiao Y, Gao ZY, Wu DP, Jiang Y, Liu N, Yi R, Jiang K (2011) Synthesis of nano-sized EuF(3) hollow spheres via one step chemical conversion. Mater Chem Phys 129:161
68. Tang YW, Chen Y, Zhou P, Zhou YM, Lu LD, Bao JC, Lu TH (2010) Electro-catalytic performance of PdCo bimetallic hollow nano-spheres for the oxidation of formic acid. J Solid State Electrochem 14(11):2077
69. Chen HM, Liu RS, Lo MY, Chang SC, Tsai LD, Peng YM, Lee JF (2008) Hollow platinum spheres with nano-channels: synthesis and enhanced catalysis for oxygen reduction. J Phys Chem C 112(20):7522

70. Koo HJ, Kim YJ, Lee YH, Lee WI, Kim K, Park NG (2008) Nano-embossed hollow spherical TiO_2 as bifunctional material for high-efficiency dye-sensitized solar cells. Adv Mater 20(1):195
71. Watanabe M, Yamashita H, Chen X, Yamanaka J, Kotobuki M, Suzuki H, Uchida H (2007) Nano-sized Ni particles on hollow alumina ball: catalysts for hydrogen production. Appl Catal Environ 71:237
72. Liu ZX, Park JN, Abdi SHR, Park SK, Park YK, Lee CW (2006) Nano-sized carbon hollow spheres for abatement of ethylene. Top Catal 39:221
73. Bernard S, Salles V, Li JP, Brioude A, Bechelany M, Demirci UB, Miele P (2011) High-yield synthesis of hollow boron nitride nano-polyhedrons. J Mater Chem 21(24):8694
74. Wang FL, Liu JR, Kong J, Zhang ZJ, Wang XZ, Itoh M, Machida K (2011) Template free synthesis and electromagnetic wave absorption properties of monodispersed hollow magnetite nano-spheres. J Mater Chem 21(12):4314
75. Li Y, Guo YQ, Tan RQ, Cui P, Li Y, Song WJ (2010) Selective synthesis of SnO(2) hollow microspheres and nano-sheets via a hydrothermal route. Chin Sci Bull 55(7):581
76. Hosokawa S, Iwamoto S, Inoue M (2008) synthesis of nano-hollow-shaped rare earth oxides by glycothermal treatment of rare earth acetates and subsequent calcination. J Alloys Compd 457:510
77. Tsai MS, Li MJ, Yen FH (2008) Synthesis of nano grade hollow silica sphere via a soft template method. J Nanosci Nanotechnol 8(6):3097
78. Darbandi M, Thomann R, Nann T (2007) Hollow silica nanospheres: In situ, semi-in situ, and two-step synthesis. Chem Mater 19(7):1700
79. Chen B, Jiao XL, Chen DR (2010) Size-controlled and size-designed synthesis of nano/submicrometer Ag particles. Cryst Growth Des 10(8):3378
80. Shi XL, Wang S, Duan XL, Zhang QX (2008) Synthesis of nano Ag powder by template and spray pyrolysis technology. Mater Chem Phys 112(3):1110
81. Tomonari M, Ida K, Imanishi H, Yonezawa T, Mori K, Yamashita H (2008) Effects of preparation conditions on the synthesis off nano-sized Ag metal particles by the wet-process using 3-mercapto-propionic acid. Res Chem Intermed 34:641
82. Cavaliere-Jaricot S, Darbandi M, Nann T (2007) Au-silica nanoparticles by "reverse" synthesis of cores in hollow silica shells. Chem Commun 2031
83. Demchenko D, Robinson RD, Sadtler BC, Erdonmez K, Alivisatos AP, Wang LW (2008) Formation mechanism and properties of CdS-Ag_2S nanorod superlattices. ACS Nano 2:627
84. Peng P, Milliron DJ, Hughes SM, Johnson JC, Alivisatos AP, Saykally RJ (2005) Femtosecond spectroscopy of carrier relaxation dynamics in type II CdSe/CdTe tetrapod heteronanostructures. Nano Lett 5:1809
85. Liz-Marzan LM, Mulvaney P (2003) The assembly of coated nanocrystals. J Phys Chem B 107:7312
86. Zou G, Ju H (2004) Electrogenerated chemiluminescence from a CdSe nanocrystal film and its sensing application in aqueous solution. Anal Chem 76:6871
87. Zayats M, Baron R, Popov I, Willner I (2005) Biocatalytic growth of Au nanoparticles: from mechanistic aspects to biosensor design. Nano Lett 5:21
88. Cordes DB, Gamsey S, Singaram B (2006) Fluorescent quantum dots with boronic acid substituted viologens to sense glucose in aqueous solutions. Angew Chem 118:3913
89. Cavaliere-Jaricot S, Darbandi M, Kucur E, Nann T (2008) Silica coated quantum dots: a new tool for electrochemical and optical glucose detection. Microchim Acta 160:375
90. Darbandi M, Urban G, Kruger M (2012) Bright luminescent, colloidal stable silica coated CdSe/ZnS nanocomposite by an in-situ, one-pot surface functionalization. J Colloid Interface Sci 365:41–45
91. Salgueiriño-Maceira V, Correa-Duarte MA, Spasova M, Liz-Marzán LM, Farle M (2006) Composite silica spheres with magnetic and luminescent functionalities. Adv Funct Mater 16:509
92. Quarta A, Corato RD, Manna L, Ragusa A, Pellegrino T (2007) Fluorescent-magnetic hybrid nanostructures: preparation, properties, and applications in biology. IEEE Trans Nanobioscience 6:298

Optical and Excitonic Properties of Crystalline ZnS Nanowires

12

Rui Chen, Dehui Li, Qihua Xiong, and Handong Sun

Contents

1 Definition of the Topic

The interaction between light and matter can provide us a great deal of information about the properties of materials. Starting from the study of basic optical property, we will thus be able to investigate the superior property of the materials and make

R. Chen • D. Li • H. Sun (✉)
Division of Physics and Applied Physics, School of Physical and Mathematical Sciences, Nanyang Technological University, Singapore, Singapore

Q. Xiong
Division of Physics and Applied Physics, School of Physical and Mathematical Sciences, Nanyang Technological University, Singapore, Singapore

Division of Microelectronics, School of Electrical and Electronics Engineering, Nanyang Technological University, Singapore, Singapore

Challa S.S.R. Kumar (ed.), *UV-VIS and Photoluminescence Spectroscopy for Nanomaterials Characterization*, DOI 10.1007/978-3-642-27594-4_12,

best use of them. Zinc sulfide (ZnS), an important II–VI group semiconductor compound, has been of growing interest owing to the promising application in ultraviolet excitonic optoelectronic devices. In this chapter, we will describe the application of optical spectroscopy to investigate the optical and excitonic property of one-dimensional ZnS nanowires, a developing material star.

2 Overview

One-dimensional semiconductor nanowires (NWs) are of great scientific and technical interest because of their unique properties and potential to revolutionize broad areas of nanotechnology. Recently, wide-bandgap semiconductor NWs, e.g., gallium nitride (GaN) and zinc oxide (ZnO), have received considerable attention due to their promising application in highly efficient ultraviolet (UV) light source, waveguides, photodetectors, and nanolasers. Because of the direct wide bandgap, the presence of polar surfaces, excellent transport properties, good thermal stability, and high electronic mobility, zinc sulfide (ZnS) semiconductor has received more and more attention, and the relevant research in ZnS NWs has seen remarkable progress.

Here, we describe the optical and excitonic property of low-dimensional ZnS NWs based on optical spectroscopy. The content of this chapter are arranged as follows. Firstly, a general introduction of ZnS NWs will be presented. Secondly, the experimental techniques about different methods to synthesize ZnS NWs and basic knowledge about optical characterizations will be introduced. In the fifth section, recent key research findings about visible emission, near band-edge emission, exciton-phonon interaction, and exciton dynamics, as well as lasing from ZnS NWs, will be summarized and discussed. Finally, the potential future directions of ZnS NWs will be drawn. At the end of this chapter, a selection of references will be given for further reading which penetrate deeper into the topic, or give a more detail description.

3 Introduction

The research into one-dimensional (1-D) semiconductor nanowires (NWs) can be dated back to the 1960s when Wagner proposed the well-known vapor–liquid–solid (VLS) growth model to explain silicon and germanium microwhiskers' growth from metal islands with a feedstock of vapor source [1]. Over the past few decades, considerable research attention has been devoted toward this research field because of the unique properties and potential applications in nanoelectronics, photonics, luminescent materials, lasing materials, and biological and medical sensing based on 1-D semiconductor NWs [2–4]. Notable achievements have been witnessed by group IV elements (Si and Ge), [5] III–V compound semiconductors (GaN and GaAs), [2, 6] II–VI compound semiconductors (ZnS, CdS, and CdSe), [7–9] and

oxide semiconductor such as ZnO, SnO_2, and In_2O_3 [10–13]. Recent progress has also discovered a novel van der Waals epitaxy mechanism utilizing layered substrates, e.g., mica, to achieve large-scale high-quality NWs arrays, in which only van der Waals interaction is involved without the restriction of lattice matching [14]. The research suggests that semiconductor NWs are still a rising field with much room to explore in this decade. Nowadays, the motivation of the research about nanomaterials and nanostructures are mainly due to the competitive ability in the field of science and technology [15–17]. Moreover, the in-depth research of nanomaterials and nanostructures is imperative for generating new principles, new techniques, and new methods, and it is possible to lead to breakthrough in great science problems.

The recent surge of research activities in wide-bandgap semiconductors has risen from the demand of electronic devices capable of operation at high power level, high temperature, and caustic environments, and in parallel, a need for optoelectronic materials, especially emitters that are active in the blue and ultraviolet (UV) wavelength region [18]. Therefore, semiconductors with wide bandgap and stable excitonic emission are preferred. That is because the emission from excitonic recombination has larger efficiency than that of the interband transition, so excitonic lasing is expected to show superior properties.

ZnS, an important II–VI semiconductor, possesses a wide bandgap (3.68 eV for cubic phase and 3.70 eV for hexagonal wurtzite phase at room temperature) [19] and relatively large exciton binding energy (40 meV) [20, 21]. In fact, ZnS is one of the first semiconductors discovered showing remarkable fundamental property versatility [22–25]. In order to achieve high-efficiency room-temperature photonic devices, it is important to achieve high crystalline quality of the semiconductor. Despite their advantageous bandgap, bulk or thin-film ZnS materials have not been able to be used for light-emitting diode (LED) due to tendency of defect formation. In contrast, ZnS in NWs form may circumvent this difficulty because very high crystalline quality can be readily achieved in 1-D VLS growth mechanism. Therefore, there are lots of attentions devoted to the synthesis of 1-D ZnS NWs. With the efforts from the research community, 1-D ZnS nanostructures with various morphologies and shapes have been successfully synthesized via a variety of techniques.

Based on a good understanding of basic optical property of 1-D ZnS NWs, we will be able to make use of them. Furthermore, the basic research enables the optimization of device performance. Therefore, optical spectroscopy, a basic and important tool, is needed to understand the fundamental optical properties of 1-D ZnS NWs. However, up till now, the investigations about ZnS NWs were mainly focused on the synthesis method, surface morphology, and growth mechanism, and the studies on the optical and excitonic property were just initiated in the last several years. Since this is a rapidly expanding field in which some unique properties have been discovered, as well as some potential applications have been achieved, this chapter intends to provide the state-of-the-art research activities about the optical and excitonic properties of crystalline ZnS NWs.

4 Experimental and Instrumental Methodology

In this section, the main experimental means used for 1-D ZnS NWs synthesis and various optical characterizations will be briefly described. The principle of the experimental techniques will be introduced. The purpose of this section is to provide a fundamental description of the experimental and instrumental methodology which is necessary for understanding the experimental results to be presented later.

4.1 Material Growth

There are two basic approaches of synthesizing NWs: top-down and bottom-up approach. In a top-down approach, a large piece of material is diced into small pieces through standard microfabrication technique or electrophoresis, whereas in a bottom-up approach, the NW is synthesized by the combination of constituent adatoms. Most of the synthesis techniques are based on bottom-up approach. Up till now, the most popular bottom-up approach for NW growth is vapor transport method. Generally speaking, the mechanism of the vapor transport approach is the introduction of a catalytic liquid alloy phase which can rapidly adsorb a vapor to supersaturation levels, and from which crystal growth can subsequently occur from nucleated seeds at the liquid–solid interface [1]. In order to achieve ZnS nanostructure arrays, various kinds of approaches such as template-assisted growth, [26–28] heteroepitaxial growth, [29–31] homoepitaxial growth, [32, 33] hydrothermal/solvothermal reaction, [34] conversion from other nanostructures, [35–37] thermal evaporation process, [38] plasma-assisted metal organic chemical vapor deposition (MOCVD), [32, 39] molecular beam epitaxy (MBE), [40] VLS, [41] and subsequent heat-treatment process have been successfully developed [34].

Another method which combines laser ablation cluster formation and VLS growth, also called pulse laser vaporization (PLV), can be also used for the synthesis of ZnS NWs [42, 43]. In this process, laser ablation was used to prepare nanometer-diameter catalyst clusters that define the size of wires produced by VLS growth. Briefly, a pulsed Nd:YAG (yttrium-aluminum-garnet) laser with a pulse width of 15 ns and a repetition rate of 10 Hz was used to vaporize the Au/ZnS target, which was centered in a ~1-m-long quartz tube with an inner diameter of 25 mm. A tube furnace was used to control the temperature of the target, which was maintained at ~950 °C, and monitored by a thermocouple placed just above the target. After the system was pumped down to 20 mTorr and flushed several times with Ar gas, the temperature was increased to 850–890 °C and the carrier gas of 100 sccm Ar (5 % H_2) was introduced between the inner and outer quartz tubes, allowing the gas to be preheated before entering the reaction zone (pressure ~225 Torr). The laser beam was focused on the target to a spot size of ~2 mm and rastered slowly across the target surface. After the ablation or vaporization process, the laser was then shut down, and the power for the furnace was turned off, allowing the system to cool slowly to room temperature in ~3 h under flowing

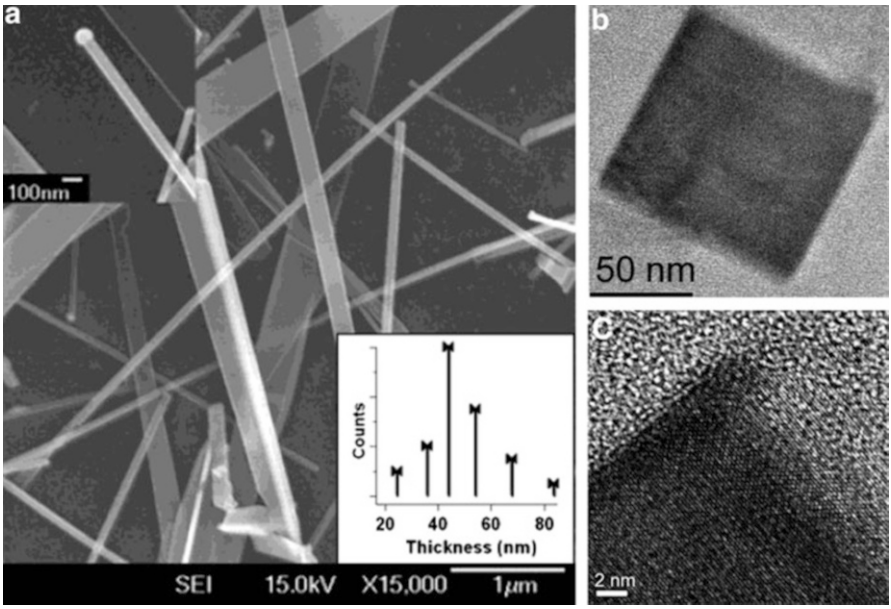

Fig. 12.1 (**a**) FESEM image of ZnS NWs dispersed on a piece of Si wafer. The inset at the *upper left* corner shows an NW growth tip with higher magnification. The inset to the *bottom right* corner shows a thickness distribution. (**b**) and (**c**) TEM and HRTEM images of the cross section of the ZnS NWs (Reproduced with permission from [42]. Copyright 2004 American Chemical Society)

Ar/H_2 gas. The as-grown ZnS NWs were collected from the inner quartz tube downstream by ~40 cm from the target, which appeared as a white powder.

Field emission scanning electron microscopy (FESEM) image of ZnS NWs deposited on a Si substrate was shown in Fig. 12.1a. A solidified metal particle was observed at one end of NWs indicating the VLS growth mechanism. The average thickness of the NWs was found to be ~49 nm, as shown in the bottom right inset of Fig. 12.1a. Figure 12.1b, c show the transmission electron microscopy (TEM) and high-resolution TEM (HRTEM) images of the cross sections of ZnS NWs. It is interesting to note that most of the NWs have a rectangular or nearly square cross section.

4.2 Optical Characterization

In the following section, the optical and excitonic properties of crystalline ZnS NWs will be discussed in detail by means of optical spectroscopy. Different kinds of measurement techniques will be involved for the discussion. In this section, brief introduction of different kinds of optical spectroscopy techniques, including optical absorption, photoluminescence (PL), and time-resolved photoluminescence (TRPL) will be presented.

4.2.1 Optical Absorption

The dielectric function $\varepsilon(\omega)$ connects the macroscopic electromagnetic phenomena of light propagation through media, such as absorption and reflection, with the microscopic electronic structure of a material, such as electron band structure and elemental excitation. $\varepsilon(\omega)$ is given as,

$$\varepsilon(\omega) = \varepsilon_r(\omega) + i\varepsilon_i(\omega) \tag{12.1}$$

Here, $\varepsilon_r(\omega)$ and $\varepsilon_i(\omega)$ are the real and imaginary part of the dielectric function, respectively. They are connected with Kramers-Krönig (KK) relations [44]. The dielectric function $\varepsilon(\omega)$ shows distinctive features at the so-called critical points, where the density of state possesses singularities; examples are the conjunction of valence band maximum and conduction minimum of a direct bandgap semiconductor, as well as various excitonic resonances. Therefore, by measuring absorption, one can obtain the intrinsic optical property of a semiconductor.

The dielectric function $\varepsilon(\omega)$ and the complex refraction index $\tilde{n}$ have a direct relationship. For an isotropic medium, it is,

$$\widetilde{n}(\omega) = n(\omega) + i\kappa(\omega) = \sqrt{\varepsilon(\omega)} \tag{12.2}$$

where $n(\omega)$ is the refractive index, whose physical meaning is that the wavelength of light in the medium becomes $1/n(\omega)$ of the wavelength in vacuum. $\kappa(\omega)$ is the extinction which describes the damping of the light in the direction of propagation. The attenuation of the light intensity I of plane wave of light propagation in z-direction is identified by,

$$I(\omega, z) = I(\omega, 0)\exp[-\alpha(\omega)z] \tag{12.3}$$

where the coefficient $\alpha(\omega)$ can be written as,

$$\alpha(\omega) = \frac{2\omega}{c}\kappa(\omega) \tag{12.4}$$

Here, $\alpha(\omega)$ is macroscopic value, which can be directly obtained from optical measurements. There are two contributions of $\alpha(\omega)$ here. The first one is absorption, which means the transformation of the energy of light into the media and brings the carriers into excited states. The other contribution is the coherent scattering of light. However, for the sample discussed herein, the scattering due to grain boundaries and phonon can be neglected because they are weak compared to the excitonic absorption. Therefore, in the following parts, $\alpha(\omega)$ is only the absorption coefficient and the contribution from light scattering is neglected.

The sample thickness (d) should be carefully chosen to perform the absorption measurement. The most convenient regime is $1 < \alpha(\omega)\, d < 3$. If d is too thin, then the absorption may be too weak to detect. In comparison, if d is too thick, some information will miss due to overabsorption, which influences the accuracy of the

data obtained. In an absorption process, energy is removed from an incident electromagnetic wave while electron–hole pairs inside the semiconductor are created. In absorption spectrum measurements, a lamp is used to provide the continuous light source. Different lamps will be used for different measurement. For example, a deuterium lamp was used for UV wavelength range, while tungsten-halogen lamp was used for visible and near-infrared measurement. The absorption coefficient can be determined from the transmission spectrum.

4.2.2 Photoluminescence

There are two important optical processes involved with emission of radiation from the semiconductors, namely, luminescence and inelastic scattering of light (also known as Raman) [44]. In a typical luminescent process, electrons on the ground state are excited to a higher energy state, and after some energy loss (relaxation), the excited electrons return to the ground state accompanying with the emission of a photon. To excite an electron, one possible way is to inject an external current, leading to electroluminescence (EL) [45]. Another common method is to use an irradiation of light with photon energy higher than the bandgap of semiconductor, which is known as PL. As is well known, PL is a powerful tool to study optical properties of semiconductors. This is because PL provides very rich information on both the intrinsic recombination processes and various radiative recombination processes associated with imperfections of a sample. With low-temperature PL spectra, more detailed information about the semiconductor properties could be obtained, such as exciton, phonon, donor binding energy, etc. These are very useful in giving a good picture of the optical quality of semiconductor material.

Usually, there are several important transitions which may occur during the PL process, depending on measurement conditions such as temperature and excitation energy [46]. Again, under optical excitation, a large number of carriers are excited from valence band to the conduction band of the semiconductors. The carriers relax rapidly to the energy states near the minimum of the conduction band in the case of electrons and near the maximum of the valence band in the case of holes. The carriers may be considered to be in quasi-thermal equilibrium state and their distribution can be represented by invoking quasi-Fermi levels. The excess carrier density decays by recombination via one of means illustrated in Fig. 12.2. There are (a) band-to-band recombination, (b) band-to-acceptor transition, (c) donor-to-valence recombination, and similarly (d) donor-to-acceptor-pair transition. These transitions where two bound particles recombine with each other are radiative. In contrast to these radiative transitions, recombination via a deep center can be (e) radiative or (f) nonradiative. Also, there is another nonradiative process (g) of band-to-band Auger recombination.

In the case of semiconductor with strong Coulomb interaction between electron and hole, instead of the free carrier recombination processes, corresponding excitonic recombination processes such as free exciton, exciton bound to a donor, and exciton bound to an acceptor will take place. The donor or acceptor can be either neutral at low temperature or ionized at high temperatures. The transition energy difference between these excitonic emission and the free carrier recombination processes is the exciton binding energy [47].

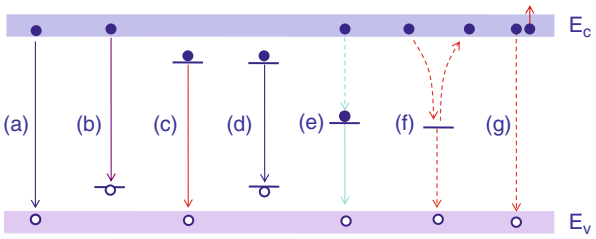

Fig. 12.2 Recombination process in a semiconductor. (**a**) Band-to-band recombination. (**b**) Band-to-acceptor transition. (**c**) Donor-to-valence transition. (**d**) Donor-to-acceptor-pair transition. (**e**) Recombination via a deep center. (**f**) Nonradiative recombination via an intermediate state. (**g**) Band-to-band Auger recombination

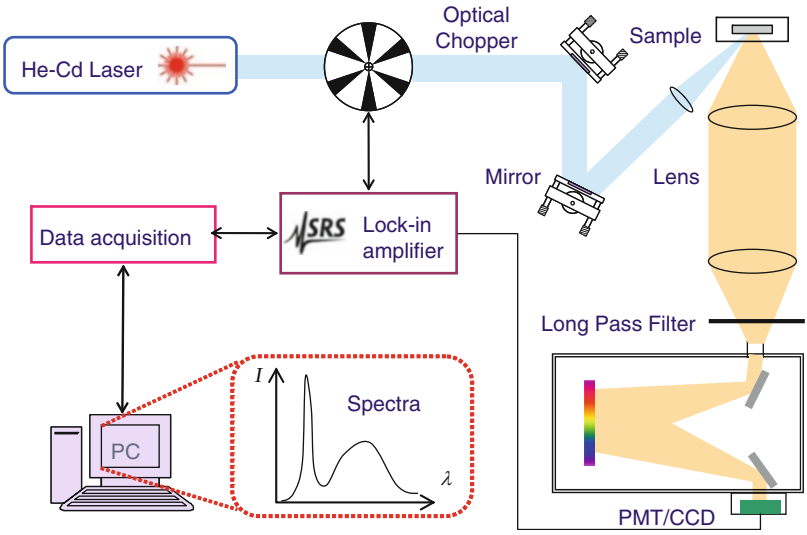

Fig. 12.3 The schematic experimental setup used for PL measurement

Typical experimental setup for the PL measurement is shown in Fig. 12.3. The PL measurements were performed in a closed-cycle helium cryostat which can provide variable temperature from 10 to 300 K. A pulsed Nd:YAG fourth harmonic (266 nm) laser was used as the PL excitation source. The pulse width and repetition rate of the laser are about 1 ns and 60 Hz, respectively. The laser was focused on the sample, and the emitted PL signal was collected into a 750-mm spectrometer and detected by either a photomultiplier or charge-coupled device (CCD). An aperture is usually inserted into the optical path to allow only a small solid angel of transmitted light to be collected to avoid the influence from stray light and luminescence. During the measurement, a standard lock-in amplifier technique was used to amplify the PL signal from the sample. It is needed to mention that suitable long pass filters are necessary to put at the entrance slit of the monochromator to block the laser beam.

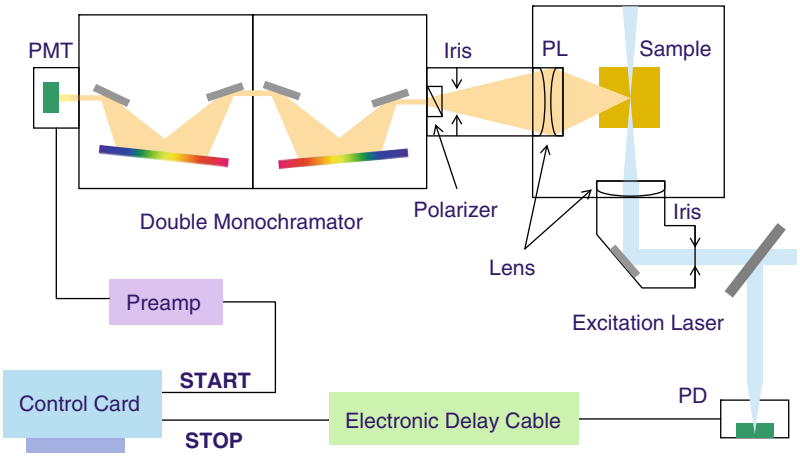

Fig. 12.4 The schematic experimental setup used for TRPL measurement

4.2.3 Time-Resolved Photoluminescence

The development of ultrafast laser has allowed the dynamics of the optical excitations in semiconductors to be measured directly in the time domain. TRPL spectroscopy is a powerful analysis tool which can provide us information about the complex dynamics in the semiconductor [46]. However, it is difficult to record the time decay profile of the signal from a single excitation-emission cycle because the decay is very fast, typically only some hundred picoseconds to some tens of nanoseconds. Moreover, the light available may be simply too weak to sample an analogue time decay. One of solutions to both problems is time-correlated single photon counting (TCSPC) [48]. With periodic excitation (e.g., from a laser), it is possible to extend the data collection over multiple cycles and one can reconstruct the single cycle decay profile from single photon events collected over many cycles. The method is based on the repetitive, precisely timed registration of single photons. A very important issue for this is the timing reference, which is supplied by excitation pulse. A photomultiplier tube (PMT) can be used as a single photon sensitive detector. If the probability of more than one photon generated per cycle is low, then the histogram of photon arrivals per time bin represents the time decay. So after a totting-up process during many circles, an exponential drop of counts toward later times will be obtained. This is the time decay of the wavelength monitored.

Figure 12.4 shows the schematic diagram of a typical TCSPC TRPL system. The excitation laser is the second or third harmonic from the Ti: sapphire laser with pulse width and repetition rate of 100 fs and 80 MHz. The laser source provides the transistor-transistor logic (TTL) signal for the timing we mentioned above. Iris is used to adjust the intensity of the source. There are two focus lenses before and after the laser shining on the sample, used for focusing the laser and collection. The PL signal is guided into a double-monochromator setup for dispersion. The relevant signals are collected by MCP-PMT and amplified according to TTL signal. There is

polarizer before the monochromator which can let light with certain polarization go through. The photodiode (PD) is used to collect the emission edge of pulse signal used for the totting-up process.

5 Key Research Findings

At ambient conditions, ZnS has two kinds of crystal structures, namely, cubic zinc blende (ZB) and hexagonal wurtzite (WZ) structure, and the bandgap at room temperature is 3.68 and 3.70 eV, respectively. Both the ZB and WZ structures of ZnS are covalently bounded solids. However, it was found that WZ-phase ZnS is much more desirable for its optical properties than the ZB phase [49, 50]. As mentioned above, the optical spectroscopy investigation of ZnS NWs is just initiated in the past several years. In fact, there is not many papers discussing about this issue, and some of the mechanism is still controversial. This section will summarize the optical and excitonic property in terms of visible emission, near band-edge absorption and emission, exciton-phonon interaction, and carrier dynamics, as well as lasing properties form 1-D ZnS NWs.

5.1 Visible Emission from ZnS Nanowires

From the journal papers, several visible emission bands (blue, green) can be usually observed from 1-D ZnS NWs synthesized using different methods [51–60]. For example, single-crystalline WZ ZnS NWs based on thermal evaporation of sulfide powders under controlled conditions with the presence of Au catalyst has been reported [51]. The room-temperature PL emission of these ZnS NWs shows two emission bands located at 450 and 520 nm, which are attributed to trapped luminescence arising from the surface states and emission due to unintentional doping from the Au catalyst, respectively. Moreover, ZnS NWs with a WZ phase synthesized in a horizontal ceramic tube furnace through the direct reaction of Zn and S powders placed in an alumina boat in an Ar atmosphere have been reported [52]. Two emission bands located at 421 and 530 nm were also observed. However, there is other report observed emission at ~535 nm under excitation in the range of 250–480 nm with a decay rate as short as 860 ps, which was related to elemental S species on the surface of the ZnS according to the investigation [53].

Recently, the synthesis of ZnS NWs with periodically alternating twins along the growth direction of wires via a thermal evaporation method has been demonstrated [54]. Structural characterizations reveal that both ZB and WZ phase coexist in the synthesized NWs, and the room-temperature emission displays two emission bands peaked at 329 and 410 nm. In 2005, single-crystalline and hexagonal cross-section ZnS nanotubes have been observed, with a uniform outer diameter of 100–200 nm and a tube-wall thickness of ~10 nm [55]. The formation of these nanotubes is a self-assisted growth process because no templates or metal catalysts have been used. Typical PL emission at room temperature consists of a weak blue emission centered at 439 nm and a strong green emission centered at ~538 nm. The authors

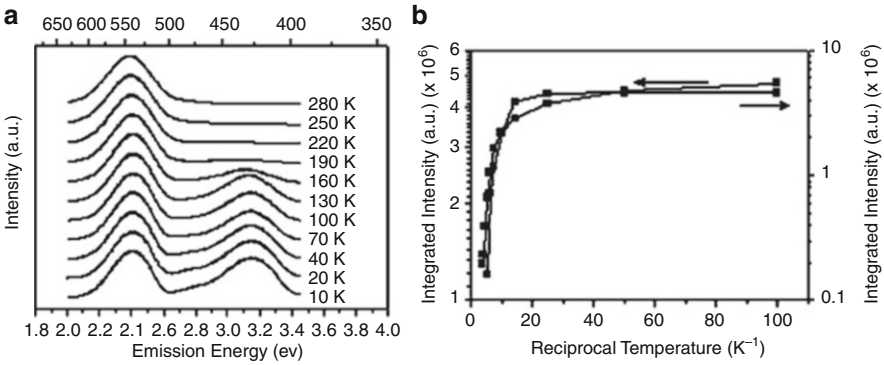

Fig. 12.5 (**a**) PL spectra of sulfur-rich ZnS nanobelts from 10 to 280 K. All spectra are normalized and shifted in the vertical direction for clarity. (**b**) Integrated PL intensity as a function of temperature for the green emission (*left*) and the blue emission (*right*), respectively, of the sulfur-rich ZnS nanobelts. *Squares* are experimental data, and curves are the fitting results (Reproduced with permission from [57]. Copyright 2006 American Institute of Physics)

have assigned the emission to arise from the surface of the nanotubes and the stoichiometric defects including self-activated centers, vacancy states, and interstitial states. As an alternative method, using hydrazine hydrate as a solvent, bundles of WZ ZnS NWs with diameters of 10–25 nm and lengths of ~5–8 μm have been synthesized via a solvothermal route [56]. The PL measurements show that one weak peak at 465 nm and two strong peaks at 413 and 438 nm, which may due to the S atoms and the surface states. The authors suggested that the S atoms and the surface states could be responsible for the strong emission bands at 413 and 438 nm and a weak peak at 465 nm, respectively.

More detail optical investigations have been carried out over the temperature range from 10 to 280 K for S-rich ZnS nanobelts [57]. As shown in Fig. 12.5a, two emission bands can be observed, which are located at blue (~430 nm) and green (~550 nm) regions. From the experimental data, the activation energies obtained for the two emissions are 157 and 65 meV as shown in Fig. 12.5b, respectively. It is noted that the activation energy of the blue emission is close to the delocalization energy of 167 meV of electrons from the strong localized state in the unsaturated orbital of surface S species [58]. Therefore, the blue emission may correspond mainly to the complete delocalization of electrons and captured by nonradiative channels. In contrast, the activation energy of the green band is much smaller than the localization energy, which may be ascribed to the potential barrier for the electrons escaping from the S vacancy donor sites to other energy levels and giving off the energy by nonradiative process.

Beside ZnS NWs and nanobelts, tetrapod-like ZnS nanopods and single-crystalline ZnS nanoawls were successfully synthesized [59, 60]. For example, single-crystalline ZnS nanoawls were achieved at a large scale by a simple two-step deposition at a low temperature of 800 °C using a mixture of commercial ZnS and SnO_2 and graphite powders [60]. Similar to the discussion above, strong green

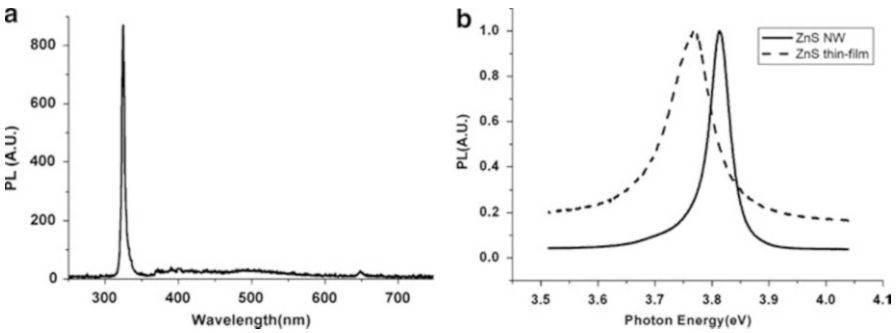

Fig. 12.6 (**a**) The PL spectrum of the ZnS NWs sample measured at 10 K. (**b**) The band-edge emission spectra of the ZnS NWs sample and the ZnS thin-film sample taken at 10 K (Reproduced with permission from [40]. Copyright 2008 Springer)

emission band centered at 513 nm and a weaker blue emission band centered at 447 nm can be observed. The authors suggested that the blue emission could be ascribed to the transitions involving vacancy states, whereas the green emission had been caused by some self-activated centers, vacancy states, or interstitial states associated with the peculiar nanostructures.

Due to the wide bandgap of ZnS semiconductor materials, the visible emission is related to radiative recombination from deep-level defect states. However, for 1-D ZnS NWs, the large surface-to-volume ratio makes this different from case to case because the surface of the NWs is very sensitive to synthetic techniques and conditions. Although there is no consistent conclusion on the mechanism of visible emission from ZnS NWs, more and more investigations will make the mystery clearer. To study possible origin of other visible peaks, the experiments are still ongoing.

5.2 Ultraviolet Absorption and Emission from ZnS Nanowires

Although some researches have been devoted to the optical properties, such as PL investigation of 1-D ZnS nanostructures as discussed above, very few studies have been reported on their possible UV bandgap emission at room temperature [7, 40, 42]. This is mainly due to high sensitivity of the optical properties of 1-D ZnS nanostructure to the synthetic conditions, crystal size and shape, and intrinsic defects such as vacancies, interstitials, etc.

In 2008, ultrathin ZnS NWs were grown on a sapphire substrate at 430 °C by the MBE technique using self-assembled Au droplets as the catalyst [40]. It was found that these NWs mainly consist of the cubic phase but a small portion was in the hexagonal phase. As shown in Fig. 12.6a, the PL spectrum of the ZnS NWs was measured at 10 K using the third harmonic of the amplifier output at 267 nm of a regenerative amplified Ti-sapphire laser with 200-fs-width pulses running at a repetition rate of 1 kHz. A near band-edge emission peaked at 325 nm and

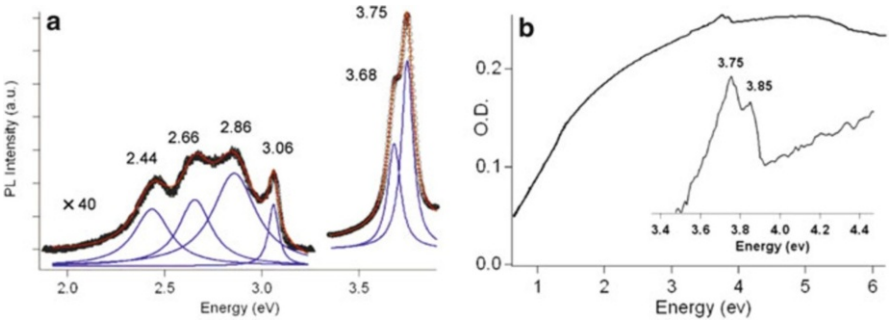

Fig. 12.7 (**a**) PL spectrum of ZnS nanowires taken at room temperature excited by a 266-nm UV laser. Two strong emission bands near band-edge and four weak defect luminescence bands were observed. *Blue curves* are Lorentzian line shape analyses after a least-squares multi-Lorentzian fit (*red curves*). (**b**) Optical density plot versus photon energy of ZnS nanowires. The inset shows a zoomed view at the vicinity of the fundamental absorption edge (Reproduced with permission from [42]. Copyright 2004 American Chemical Society)

a deep-level defect-related emission band covering 350–700 nm can be observed. At temperature lower than 150 K, the PL spectra are dominated by the near band-edge emission.

Figure 12.6b shows the comparison of the near band-edge emission of the ZnS NWs and the ZnS thin-film sample taken at 10 K. The emission from NWs clearly demonstrates a 46-meV blue shift. If we assume the ZnS NWs as a cylindrical box, then the quantum size effect on the excitons confined in the NWs can be calculated by solving the time-independent Schrödinger equation in the cylindrical coordinate system. Therefore, the confinement energy of the ground state was found to be,

$$E = \frac{\hbar^2}{2}\left(\frac{1}{m_e^*} + \frac{1}{m_h^*}\right)\left(\frac{2.4}{r}\right)^2 - \frac{1}{4\pi\varepsilon\varepsilon_0}\frac{e^2}{r} \tag{12.5}$$

where $m_e^* = 0.22\ m_0$ and $m_h^* = 1.76\ m_0$ are the effective mass of electron and hole, respectively. r is the radius of the ZnS NWs, and ε is the dielectric constant of ZnS which is ~8.0 [40]. The first term of the equation corresponds to the sum of the lift-up amounts of the single-particle ground-state energies due to the confinement in the radial dimension, and the second term corresponds to the Coulomb attraction of a confined exciton. Taking the blue shift of 46 meV as the confinement energy, the size of the NWs can be calculated to be 6.7 nm. This is in good agreement with the range of the size of the NWs obtained from the HRTEM image, which is ~5–8 nm.

In 2004, ZnS NWs was achieved by PLV method [42]. Figure 12.7a shows the PL emission from ZnS NWs, while Fig. 12.7b depicts the optical absorption for the sample. The inset of Fig. 12.7b gives a magnified view of the optical density near the position of the band edge in the bulk. First of all, it is found that the absorption edge is very broad, which is due to strong band tailing stemming from the

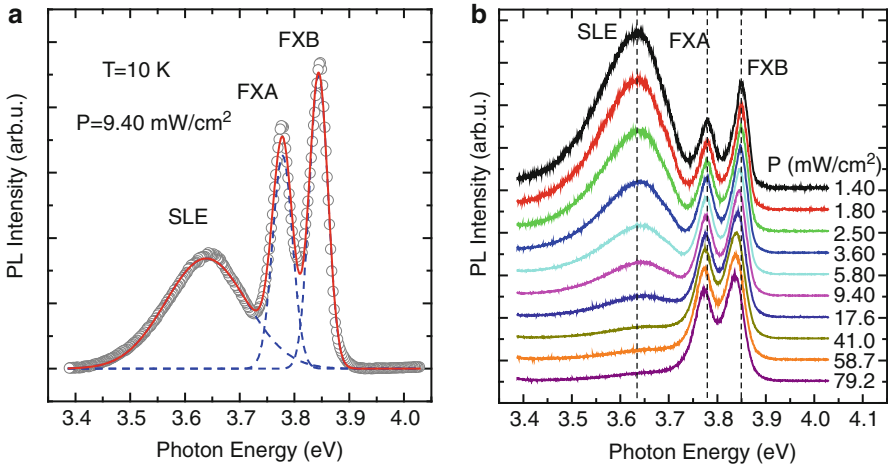

Fig. 12.8 (**a**) The band-edge emission spectra of ZnS NWs sample obtained at 10 K. *Open circles* are the experimental data, and *blue dashed lines* and a *red solid line* are the multi-Gaussian fitting of the spectra. (**b**) Evolution of the PL spectra measured at 10 K under different excitation densities. The *dashed vertical lines* are a guide for the eyes (Reproduced with permission from [7]. Copyright 2010 American Chemical Society)

stoichiometric defects [61]. Two peaks in the optical density are observed at 3.75 and 3.85 eV, which are close in energy to the structure obtained from the PL emission. Together with the information presented in Fig. 12.7a, the features of 3.68, 3.75, and 3.85 eV observed in PL and absorption spectrum are assigned to the free exciton A (FXA), B (FXB) and C (FXC), respectively. The energy splitting obtained are approximately 100 and 70 meV, which is close to the spin-orbit coupling and crystal field splitting energies which are 89 and 57 meV [19]. Moreover, the reason that no 3.68-eV absorption peak was observed is probably that these features are masked by the strong band tailing. And the absence of emission ~3.85 eV is due to the exciton states may decay rapidly to lower-energy exciton states, i.e., FXA and FXB. At photon energy bigger than 5.0 eV, a slight decrease in absorption, associated with diminished high-energy oscillator strength has been observed [42].

More recently, high-crystalline quality rectangular cross-sectional ZnS NWs have been successfully synthesized by PLV [7]. From the X-ray powder diffraction (XRD) spectrum of the ZnS NWs using Cu K_{α} radiation, all the peaks are identified with the WZ 2 H polytype of ZnS, and the lattice constant obtained are in good agreement with the powder XRD data for the bulk. Figure 12.8a shows the low-temperature (10 K) PL emission from ZnS NWs under a pulsed Nd:YAG fourth harmonic (266 nm) laser excitation with an average excitation density ~9.40 mW/cm^2. Very strong UV emission can be detected, which can be well fitted by multiple Gaussian line shape function. The blue dashed curves depict the deconvoluted Gaussian bands. In WZ ZnS, due to the spin-orbit interaction and crystal field splitting, the topmost valence band splits into three bands, and the respective exciton states are denoted as FXA, FXB and FXC [19].

The splitting energies are 89 meV (FXC-FXB) and 57 meV (FXB-FXA), respectively. Thus, the observed emissions at 3.778 and 3.844 eV (with an energy difference of 66 meV) can be assigned to FXA and FXB. The absence of FXC may be due to the faster decay. Moreover, on the low-energy side, an emission band peaked at 3.639 eV, which is attributed to the shallow-level emission (SLE). It is needed to mention that there is SLE observed at room temperature as shown in Fig. 12.7a. That is because the thermal energy is big enough to dissociate the shallow-level carriers, which will be discussed later.

Due to the different density of states, the relative intensity of the defect and free exciton transition shows a very different trend by varying excitation densities. Figure 12.8b depicts the PL spectra measured at 10 K under various excitation densities (displayed next to the curves). All the spectra are normalized by the peak intensity of FXB and shifted in y-coordinate for better comparison. It is interesting to note that for excitation density increasing by around two orders of magnitude, the emission band of SLE demonstrates a faster saturation compared with FXA and FXB and could not be resolved at excitation density higher than 41.0 mW/cm^2. The peak energies of FXA and FXB show a gradual red shift with increased excitation density, while the peak position of SLE is insensitive to photon flux. This may be the reason that this peak was absent in some previous studies, as the excitation power was probably high enough to saturate the SLE. The total shifts from 1.40 to 79.2 mW/cm^2 of FXA and FXB are 8 and 12 meV, respectively. This phenomenon can be ascribed to laser-heating effect commonly observed in other nanostructures [62].

At present, the room-temperature bandgap of ZnS material is still under controversial discussion [20, 40, 63]. The reported data in the previous literature range from 3.560 to as high as 3.764 eV [20]. It is worth mentioning that the laser excitation intensity will influence the determination of the real bandgap emission as indicated in Fig. 12.8b. Therefore, in order to determine the bandgap of ZnS NWs, a suitable laser power density should be chosen to minimize the laser-heating effect. It is also found that the WZ-phase ZnS is much more desirable for its optical properties than the ZB phase [49, 50]. Due to the crystal file and spin-orbit coupling, exciton state in WZ-phase ZnS will associate with electron–hole pair in each of the valance bands, and the topmost valence band will split into three bands, which make the situation more complex [7, 19]. Moreover, as can be seem from the papers reported, not every ZnS NWs can emit the UV light. That is because superior crystalline quality is imperative to obtain efficient near band-edge UV luminescence. At present, many approaches have been developed to synthesize ZnS NWs with very high crystalline quality, and the research in this field calls more detail optical investigation to understand the fundamental properties of ZnS NWs.

5.3 Exciton-Phonon Interaction in ZnS Nanowires

An exciton is a quasiparticle consisting of a bound state of an electron and a hole in semiconductor crystals by the electrostatic Coulomb force [46]. Excitons behave like a bosonic particle freely moving in the lattice of a semiconductor.

Compared with free carriers, excitons demonstrate the following superior characteristics. First of all, the oscillator strength of excitons is much larger than the transition possibility of the recombination of the band-edge free carriers. Second, exciton has a very narrow energy distribution of optical gain [64]. Therefore, excitonic lasing is expected to have lower threshold. Third, as a quasiparticle, excitons can interact with either excitons themselves or other quasiparticles in a semiconductor, such as electrons and phonons. This kind of interaction is very important because new emission mechanisms with even higher efficiency than exciton recombination may appear, such as biexciton recombination (M-band) [65] and inelastic exciton-exciton scattering (P-band) [66] which offer very large optical gain. Last but not the least, an exciton has a dynamical electric dipole, which can couple with electromagnetic wave, or light [67]. That means that inside a suitable optical cavity or photonic crystal structure, excitons will strongly couple with the cavity mode and form cavity polaritons [68]. In principle, this coupling between particle (exciton) and field (electromagnetic cavity mode) can be used to achieve zero threshold laser diodes [69–71].

Therefore, it is more preferable of excitonic emission for photonic device application. Generally speaking, the coupling between excitons and phonons is an important parameter in determining the electronic and optical properties of semiconductors [72]. That is because the applicability of the materials from the point of view of excitonic devices depends upon the strength of the room-temperature excitonic resonances. In order to achieve room-temperature photonic devices, it is necessary to have excitons which can exist up to room temperature, and there are two approaches which can achieve this. The first one is to use the materials with high exciton binding energy [12, 73]. Another alternative approach is to seek suitable materials that have stable exciton, which means the exciton emission is not much influenced by phonons [7]. As is well known, temperature-dependent PL spectroscopy is a very useful method to study the interaction between exciton and phonon because by changing the thermal energy, the coupling strength between exciton and phonon can be extracted.

Detailed temperature variations of the optical bandgap from the near band-edge of the cubic ZnS NWs and the thin-film sample have been carried out comparatively [40]. It is found that the bandgap energies of both samples vary linearly from room temperature down to about 150 K. The temperature coefficient, defined as dE_g/dT, is around -5.2×10^{-4} eV/K for the NWs and -4.8×10^{-4} eV/K for the thin-film sample. Both data are close to the previously reported value of -6.67×10^{-4} eV/K for a ZnS bulk sample [40]. Moreover, detail investigation about the electron–phonon interaction has been carried out by comparing the variation of bandgap at different temperature with a phenomenological expression. The model is introduced with the renormalization of electronic states due to the interaction with phonons with an average phonon frequency. The expression contains the Bose-Einstein statistical factor, and is expressed as, [74]

$$\Delta E_g(T) = a_B \frac{2}{\exp(\theta/T) - 1} \tag{12.6}$$

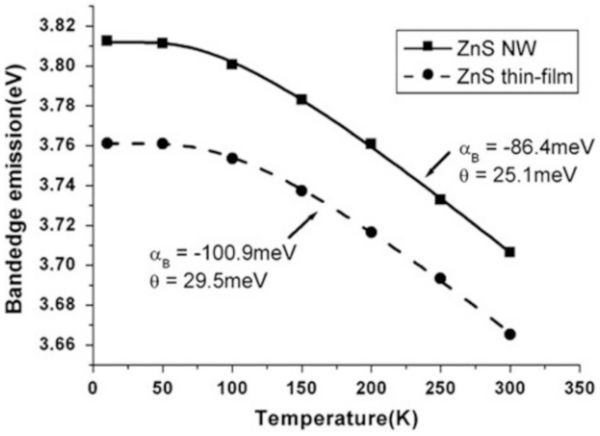

Fig. 12.9 The temperature variation of the band-edge emission peaks of the NWs sample and the thin-film sample. The *solid* and *dashed lines* are the least-squares fitting curves according to Eq. 12.6 (Reproduced with permission from [40]. Copyright 2008 Springer)

where θ is related to the average phonon frequency and a_B describes the strength of the interaction.

The solid and dashed curves in Fig. 12.9 are the least-squares fitting curves of the expression to the measured peak values of the PL spectra at different temperature. The fitted values are θ and a_B and are displayed next to the curves in Fig. 12.9, in which the average phonon frequency θ for the ZnS NWs sample and the thin film are 25.1 meV (291.2 K) and 29.5 meV (342.0 K), respectively [40], The author found that both the average phonon frequency and the strength of the electron–phonon interaction are lower for the NWs sample compared to the data for thin film. This implies that the phonon component of 1-D structure can be suppressed as compared that of two-dimensional structure, pointing out an approach to reduce the unwanted electron–phonon interactions in optoelectronic devices.

More detail investigations about the temperature-dependent PL emission from ZnS NWs have been carried out recently [7]. To minimum the laser-heating effect as discussed above, the laser excitation density was controlled as low as 9.40 mW/cm^2. Figure 12.10a shows the normalized PL spectra of the ZnS NWs measured at various temperatures. Different peak positions of the individual spectra are indicated by dashed lines. It can be seen that the peak position of SLE remains unchanged, while the PL intensity fades out gradually with increasing temperature and completely disappears at temperature higher than 140 K. This verifies our assignment that this peak is related to SLE rather than shallow donor-bound exciton, because otherwise the peak position will show a gradual red shift with increasing temperature [12]. It is also worth noting what shallow donor or acceptor impurities can introduce such SLE levels. Considering that the ionization is ~200 meV, one possible contamination NaCl gives rise to shallow Na acceptor or Cl donor level with ionization energies in the range of 170–250 meV [19].

As shown in Fig. 12.10a, the emission peaks of FXA and FXB show conventional bandgap shrinkage. Compared to Fig. 12.8b, the temperature of the sample is around 90 K under excitation density of ~79.2 mW/cm^2 due to the laser-heating effect. The thermal shift of the bandgap of the semiconductors is believed to arise

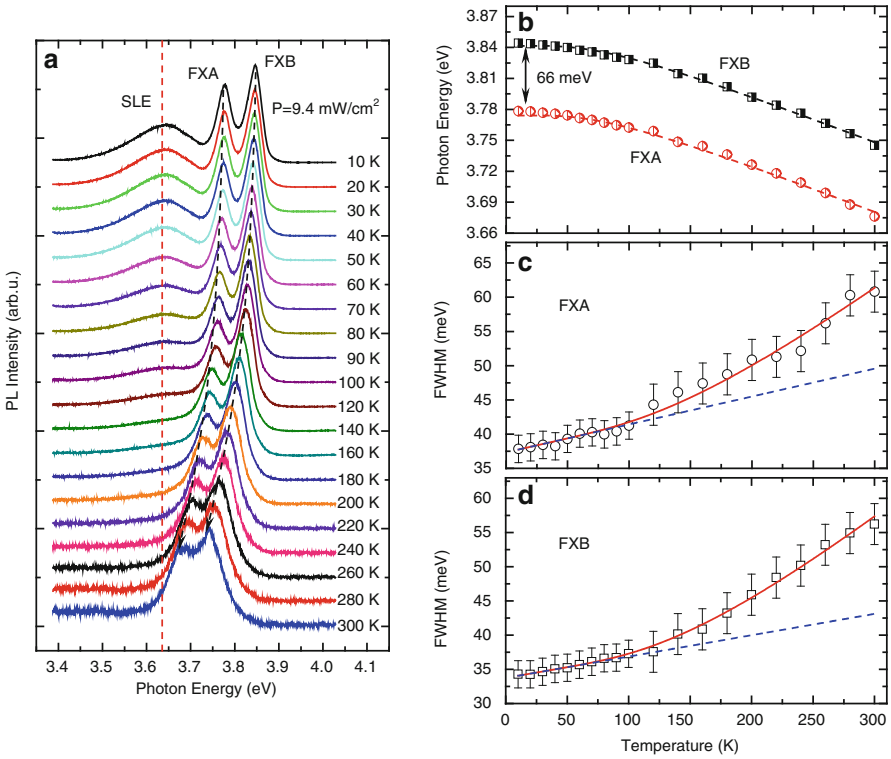

Fig. 12.10 (**a**) Temperature-dependent PL spectrum of ZnS NWs sample measured at low excitation density. All data were normalized by FXB intensity, and the dashed lines follow the peak positions. (**b**) Temperature-dependent peak energies and *dashed lines* are the fitting according to the Bose-Einstein expression. Temperature dependence of the peak widths of FXA (**c**) and FXB (**d**), respectively. The *solid lines* are the fitting of the experimental data based on Eq. 5.5, while dashed lines are the contributions from the inhomogeneous broadening and acoustic-phonon scattering (Reproduced with permission from [7]. Copyright 2010 American Chemical Society)

from the thermal dilation of the crystal lattice, as well as electron–phonon interactions. The temperature dependence of this characteristic can be described by the Varshni formula, [75] or the following Bose-Einstein expression:[76]

$$E(T) = E(0) - \frac{\lambda}{\exp(\hbar\omega/k_B T) - 1} \tag{12.7}$$

where *E(0)* is the bandgap at a temperature of 0 K, λ is the proportional coefficient, and $\hbar\omega$ is the effective phonon energy. Figure 12.10b shows the variation of the PL peak energies of FXA and FXB as a function of temperature. Dashed lines are the least-squares fitting curves of the expression to the measured peak values of the FXB spectra at different temperatures, then shift by 66 meV vertically. The fitting

Table 12.1 E_g is the bandgap at room temperature, E_b is the exciton binding energy, $\hbar\omega_{LO}$ is the LO-phonon energy, λ is the proportional coefficient, $\hbar\omega$ is the effective phonon energy, γ_{ph} is the coupling strength of exciton-acoustic phonon, and γ_{LO} the coupling strength of exciton-Lo phonon

Material		E_g (eV)	E_B (eV)	$\hbar\omega_{LO}$ (meV)	λ (meV)	$\hbar\omega$ (meV)	γ_{ph} $(\mu eV/K)$	Γ_{LO} (meV)
ZnS	FXA	3.716	40	42.95	108.40	19.89	40.78	50.40
	FXB	3.785					31.23	60.85
GaN[a]	FXA	3.42	26	91.5	121.00	27.30	21	525
	FXB						22	495
ZnO[b]	FXA	3.37	60	72	20.90	11.44	11.3	876.1
	FXB				11.48	21.80	26.5	783.3
ZnSe[c]		2.69	19	31.4	32.10	9.90	64.2	126

Note: [a]Viswanath et al. [72]
[b]Makino et al. [77]
[c]Bogani et al. [78]

parameters obtained are summarized in Table 12.1, and data for a GaN [72] and ZnO film [77], as well as a ZnSe bulk crystal [78], are also listed for comparison. The peak positions of FXA (FXB) at room temperature and 10 K are 3.676 eV (3.745 eV) and 3.778 eV (3.844 eV). Taking the exciton binding energy of 40 meV into account, the fundamental bandgap deduced from our measurement are 3.716 eV (3.785 eV) and 3.818 eV (3.884 eV) at room temperature and 10 K, respectively.

Moreover, thermal broadening of the excitonic peak is generally interpreted as an exciton-phonon interaction. The temperature dependence of (full width at half-maximum) FWHM can be approximately described by the following equation: [47, 64, 72, 79]

$$\Gamma(T) = \Gamma_{inh} + \gamma_{ph}T + \frac{\Gamma_{LO}}{[\exp(\hbar\omega_{LO}/k_BT) - 1]} \tag{12.8}$$

where Γ_{inh}, γ_{ph}, Γ_{LO} and $\hbar\omega_{LO}$ are the inhomogeneous peak width at zero temperature, the coupling strength of exciton-acoustic phonon, the coupling strength between exciton and LO phonon, and the LO-phonon energy, respectively. Figure 12.10c, d show the temperature dependence of the FWHM of the FXA and FXB, respectively. Solid lines represented the fitting results based on Eq. 12.8. It is found that a reasonably good fit is obtained, and the results are summarized in Table 12.1. Here, we have taken the LO-phonon energy $\hbar\omega_{LO} = 42.95$ meV for each fitting, which is obtained from previous Raman measurements (346.4 cm^{-1}) [42, 80]. In parts (c) and (d) of Fig. 12.10, the dashed lines are the contributions from the inhomogeneous broadening and acoustic-phonon scattering [$\Gamma(0) = \Gamma_{inh} + \gamma_{ph}T$]. It is noted that the acoustic-phonon contributes up to 120 K very significantly, but the contribution from LO phonon is negligible up to this temperature. From 120 K onward, the participation of the LO phonon causes the FWHM to increase further.

The exciton-LO phonon coupling strength (Γ_{LO}) for FXA and FXB deduced from the fitting is comparable. However, those parameters are quite small compared

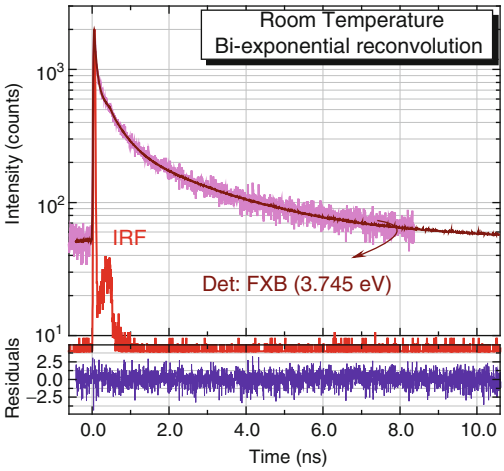

Fig. 12.11 Room-temperature TRPL data for ZnS NWs monitored at FXB. *Solid* curves are the fitting according to Eq. 12.9, and the separate plot shows the weighted residuals during the reconvolution (Reproduced with permission from [7]. Copyright 2010 American Chemical Society)

to the other wide-bandgap materials like GaN, ZnO, and ZnSe. As is well known, the exciton line width broadening is due to a *1S* exciton either dissociating into the free electron–hole continuum or scattering within the discrete exciton band by absorbing one LO phonon via the Fröhlich interaction. Here, Γ_{LO} is related to materials' polarity and the magnitude of the exciton binding energy relative to the LO-phonon energy [64]. It can be seen from Table 12.1 that the exciton binding energy and the LO-phonon energy of ZnS are comparable. Therefore, the dissociation of the 1S exciton into continuum states is suppressed, and Γ_{LO} is small. It is also emphasized that the small value of Γ_{LO} implies that excitons are less probable to be disassociated by LO phonons. So, excitons in ZnS are very stable even though the exciton binding energy in ZnS is not as high as that of ZnO; it is quite stable and not affected by optical phonons. Therefore, ZnS can be served as a suitable candidate for excitonic light-emitting devices.

5.4 Carrier Dynamics in ZnS Nanowires

For further application such as LED and photodetectors, the study of carrier dynamics remains an important task because the performance of the photonic device is highly sensitive to the respective carrier lifetimes in the semiconductor [7]. Therefore, in order to determine the free carrier or exciton lifetime of ZnS NWs, TRPL was carried out at room temperature.

Figure 12.11 shows the TRPL data for ZnS NWs monitored at the peak position of FXB. The decay curve can be well fitted by a biexponential fit with reconvolution,

$$I(t) = \int_{-\infty}^{t} IRF\left(t'\right) \sum_{i=1}^{2} A_i e^{-\frac{t-t'}{\tau_i}} dt' \tag{12.9}$$

Table 12.2 Decay constants and the amplitudes obtained from the fitting based on Eq. 12.9

					Fractional intensity (%)	
Detection energy (eV)	A_1	$\tau_1(ns)$	A_2	$\tau_2(ns)$	τ_1	τ_2
3.815	0.71	0.42	0.29	2.66	27.9	72.1
3.745 (FXB)	0.71	0.43	0.29	2.61	28.7	71.3
3.676 (FXA)	0.72	0.48	0.28	2.71	31.3	68.7
3.615	0.72	0.46	0.28	2.68	30.6	69.4

where A_i is the amplitude of the i^{th} component at time zero, τ_i is the corresponding lifetime and IRF is the instrument response function. A separate plot shows the weighted residuals, and the straight line indicates a good fitting.

Table 12.2 summarizes the decay constants and the amplitudes obtained from the fits for varying detection wavelengths. It can be seen that all the detected wavelengths exhibit similar carrier dynamics. The fast decay component τ_1 is ~0.45 ns, and the slow decay component τ_2 is ~2.7 ns. The biexponential behavior strongly suggests that two different decay or capture processes are involved in the emission.

The biexponential decay of the PL could be explained by exciton diffusion from the surface region to the bulk region. It is expected that excitons diffuse away from the surface while simultaneously undergoing nonradiative recombination and emitting exciton luminescence. These processes were presumed to occur on a fast timescale and would correspond to the fast component of the PL decay, whereas the slow component would correspond to relaxation once the excitons have diffused and equilibrated throughout the volume of the ZnS NW. However, due to the large absorption coefficient of ZnS at the excitation energy ($a_{exc} = 2.5 \times 10^5$ cm^{-1}), [81, 82] the effective penetration depth of optical excitation is estimated to be ~40 nm. It is noted that the penetration depth is comparable to the diameter of the ZnS NWs, and thus, the carriers are expected to generate uniformly throughout the whole NWs. Therefore, the surface-bulk diffusion can be excluded for the reason of biexponential decays.

Compared to the reported data, the fast decay component is comparable to what has been measured for bulk ZnO (~0.43 ns) and has been associated with nonradiative recombination [83]. The nonradiative process here is considered to be generated by certain defect species such as nonradiative surface traps. The fast decay component is much more prominent for ZnS NWs ($A_1 \sim 0.7$) compared to bulk single-crystal ZnO ($A \sim 0.3$) [83]. Generally speaking, in the case of NW, as the sample's surface-to-volume ratio increases, the relative density of nonradiative surface traps would increase, and the weight of fast decay component (associated with free exciton plus nonradiative surface recombination) would increase. For the slow decay component for ZnS NWs, the decay time ~2.7 ns can be attributed to the intrinsic radiative lifetime of the free exciton. This value is comparable to bulk single-crystal ZnO which is ~3.0 ns [83]. From the decay constants and the amplitudes listed in Table 12.2, the relative fractional intensity ($A_i\tau_i$) of each component can be determined. It can be seen that the slow decay component is the dominant contribution to the whole PL intensity, which confirms our assignment that it is related to effective free exciton lifetime.

5.5 Ultraviolet Lasing Properties of ZnS Nanowires

The realization of semiconductor lasers emitting short-wavelength UV light is of considerable interest for a wide range of applications including optical computing, high-density data storage and material processing, and chemical/biochemical microanalysis [3, 33, 84–86]. Room-temperature UV lasing has been demonstrated in for the ZnO and GaN NWs systems with epitaxial arrays, combs, and single NW [2, 3, 84]. ZnS is another wide-bandgap semiconductor which is suitable for UV-blue optoelectronic applications. Moreover, the binding energy for excitons in ZnS is 40 meV, [20] which is much higher than the thermal energy at room temperature (~26 meV), making ZnS become an ideal candidate for efficient excitonic laser action at room temperature. Up till now, UV lasing from ZnS NWs has been reported by several papers [26, 87, 88]. And the corresponding lasing mechanism can be classified into Fabry-Pérot lasing and coherent random lasing.

5.5.1 Fabry-Pérot Lasing

NWs with flat end facets can be exploited as optical resonance cavities to generate coherent light on the nanoscale, which has been observed in ZnO NWs [3, 89]. In 2004, single nanoribbon laser from optically pumped individual single-crystal ZnS NW was observed [87]. It is found that the high-quality facets with a refraction index larger than air serve as reflecting mirrors. The rectangular ZnS nanoribbons thus form potential optical waveguides/resonant cavities tens of microns long, few microns wide, and ~100 nm thick. The PL measurements were obtained using the fourth harmonic of a Nd:YAG laser (266 nm) as an excitation source, and the PL signal was detected with an UV optical fiber coupled to a 0.5 m spectrograph using a 1200 groove/mm grating and an intensified CCD detector. Figure 12.12a shows the PL emission from a single ZnS nanoribbon with an acceptance angle ~33°. The insets show the single ZnS nanoribbon dispersed on a TEM grid used for all the measurements and the PL intensity versus excitation power. The PL above a threshold power of ~60 kW/cm^2 exhibits a narrow (~2-nm FWHM) and intense peak at ~338 nm (~3.66 eV). The narrowing of the PL peak and the concurrent superlinear increase of peak intensity with excitation power indicates lasing action.

Moreover, the angular dependence of the emission intensity from a single ZnS nanoribbon was carried out, and Fig. 12.12b shows the PL obtained with a small acceptance angle. The insets show the sharp modes and the PL intensity change with the detection angle with respect to the nanoribbon long axis. It is straightforward to show that $2Ln = \lambda^2/\Delta\lambda$, where $\Delta\lambda$ is the spacing between adjacent resonant modes. For the ZnS nanoribbon, the modulation of $\Delta\lambda = 0.4$ nm corresponds to a cavity length of 60 mm. Therefore, the entire single nanoribbon serves as an active medium as well as an optical resonant cavity and a waveguide with very intense narrow modes.

Following the work about ZnS nanoribbon, investigation about UV lasing from ZnS NWs has been carried out. In 2004, high-density and uniform-sized gold particle arrays have been prepared electrochemically on anodic aluminum oxide (AAO) templates [26]. The gold particles were used as catalysts to synthesize ZnS NWs.

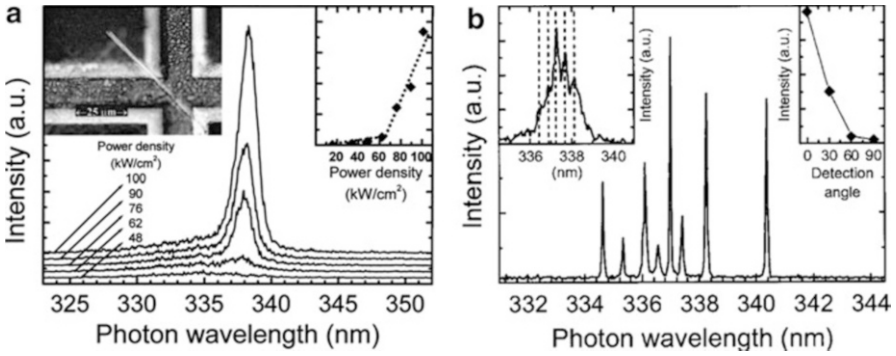

Fig. 12.12 (**a**) PL of a single ZnS nanoribbon excited by a 266-nm laser beam with different power densities. The insets show the single ZnS nanoribbon dispersed on a TEM grid used for all the measurements and the PL intensity versus excitation power. (**b**) PL obtained with an acceptance angle of ~2° and an angle of ~5° between the optical fiber and the plane of the TEM grid. The insets show the sharp modes and the PL intensity change with the detection angle with respect to the nanoribbon long axis (Reproduced with permission from [87]. Copyright 2004 American Institute of Physics)

The as-grown NWs had a WZ single-crystal structure and were aligned perpendicularly to the AAO template. Under high-power density optical excitation using the fourth harmonic (266 nm, 5 ns pulse width) Nd:YAG laser at room temperature, the author observed amplified stimulated emission at 338 nm (3.67 eV) with narrow resonant cavity modes (FWHM ~0.3 nm). It is found that the mode separation measured at high excitation power densities corresponds to a cavity length of ~30 μm, which is close to the NW length measured by scanning electron microscope (SEM). Therefore, these results indicate that the ZnS nanowires act as optical waveguide resonators.

More recently, cross arrays of ZnS NWs and aligned arrays of ZnS nanoribbons via homoepitaxial growth on micrometer-wide single-crystal ZnS nanoribbon substrates have been reported [90]. Figure 12.13 shows the PL spectra of bandgap emission versus excitation power. Low excitation powers result in a broad and weak PL (peaked at 338 nm). At a threshold power of ~100 $kWcm^{-2}$, a narrow PL peak at 338.4 nm appears, and an additional peak at 339.8 nm emerges as the excitation power increases to 240 $kWcm^{-2}$. Further increase of the power to 350 $kWcm^{-2}$ leads to two new narrow and intense peaks at ca. 337.2 and ca. 339.4 nm, and several weak but distinguishable resonant modes with the same peak separation can be observed, which indicates clearly the lasing action in different modes. The emission peak narrows with the increase of pump power because of the preferential amplification of frequencies close to the maximum of the gain spectrum, which is similar to the oriented ZnO NWs grown on sapphire substrates [22, 91–93]. From the discussion, the author found that the lasing occurs from ZnS NWs arrays of different lengths. Moreover, angle-dependent PL measurement shows that the arrays of epitaxial ZnS nanowires can function as Fabry-Pérot cavities, but the symmetric cross array arrangement of the NWs leads to lasing emission predominantly in two specific directions.

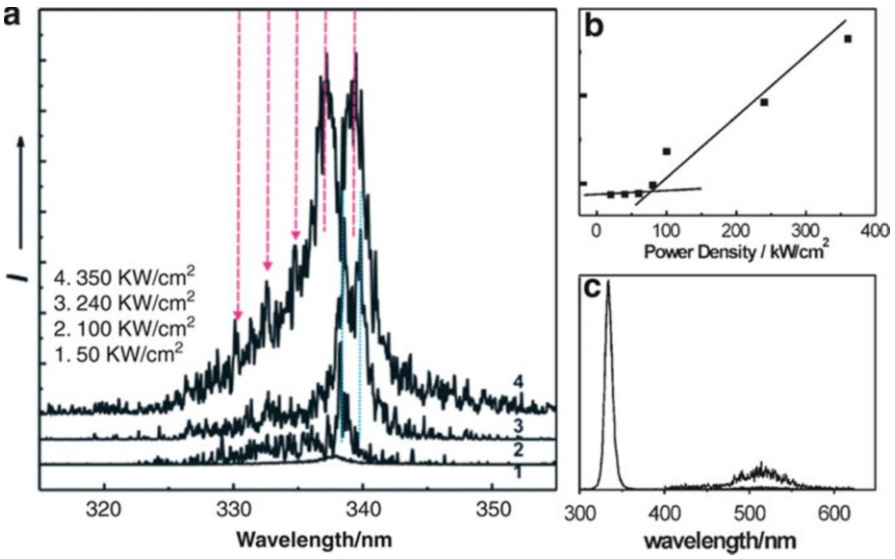

Fig. 12.13 (**a**) Room-temperature PL spectra of ZnS nanobelts versus excitation power. The *dotted* and *dashed lines* indicate the location of lasing modes. (**b**) The accumulated intensity of 100 pulses versus input power density. (**c**) The whole PL spectrum (Reproduced with permission from [90]. Copyright 2006 Wiley-VCH)

5.5.2 Coherent Random Lasing

In a regular laser, the light bounces back and forth between two mirrors that form a cavity. After several passes through the amplifying material in the cavity, the gain amplification can be large enough to produce laser light [94]. However, for random laser, the cavity is absent, but multiple scattering between particles in the disordered material keeps the light trapped long enough for the amplification to become efficient and for laser light to emerge in random directions [95–97].

In 2010, lasing phenomenon of randomly assembled ZnS nanosheets has been observed at room temperature [88, 98]. Under optical excitation, sharp lasing peaks emitted at around 332 nm with an FWHM less than 0.4 nm was observed in all directions, as shown in Fig. 12.14a. From the corresponding light-light curves, lasing action can be confirmed by the nonlinear increase of the emission intensity, and the corresponding pump threshold was determined to be 0.2 MW/cm^2. It is needed to emphasize that the large contrast in refractive index between ZnS and air may provide strong scattering. Hence, it is believed that the sharp peaks represent a closed-loop path of light, which randomly forms a cavity mode inside the randomly packed ZnS nanosheets, due to the coherent optical feedback of scattering light. Moreover, the author observed that the emission spectrum is different when observed from different directions [88].

As shown in Fig. 12.14b, the dependence of excitation area on the lasing spectrum was also studied. It is found that before a critical area, no sharp lasing peak is observed. However, when the excitation area exceeds the critical area, sharp

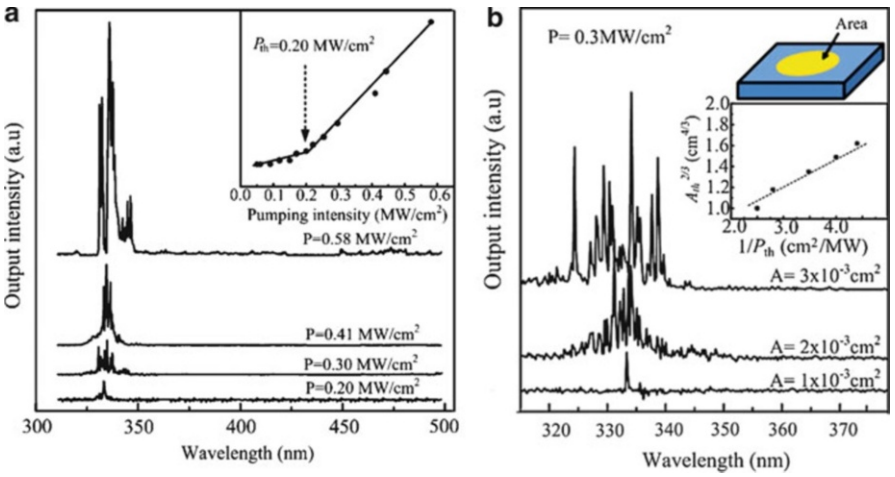

Fig. 12.14 (**a**) Emission spectra of the randomly assembled ZnS nanosheets under the excitation of 266-nm optical pumping. (**b**) Emission spectra versus different excitation areas. The insert shows the relation between excitation area and lasing threshold of the randomly assembled ZnS nanosheets (Reproduced with permission from [88]. Copyright 2010 Springer)

lasing peaks with FWHM of less than 0.4 nm appear. Moreover, the relation of critical area and the threshold obtained under different excitation area was discussed. And the results indicate that the randomly assembled ZnS nanosheet film should behave like a quasi three-dimensional (3-D) random medium (i.e., a 3-D random medium with transverse optical confinement of scattering light along the random medium), [89, 99] which provides very strong scattering which enable the observation of coherent random lasing action.

The realization of semiconductor lasers emitting short-wavelength UV light is of considerable interest for a wide range of applications including optical computing, high-density data storage and material processing, and chemical/biochemical microanalysis. These results have clearly demonstrated that the highly oriented ZnS NWs arrays indeed serve as an excellent nanoscopic laser cavity with room-temperature UV lasing.

6 Conclusions and Future Perspective

In summary, recent developments of the optical and excitonic properties of 1-D crystalline ZnS NWs have particularly been highlighted in this chapter. First of all, a general introduction of ZnS NWs is presented. Secondly, the experimental techniques about different methods to synthesize ZnS NWs and basic knowledge about optical characterizations are introduced. In the experimental section, description of the experimental and instrumental methodology is shown. Moreover, recent key research findings about visible emission, near band-edge emission,

exciton-phonon interaction, and exciton dynamics, as well as lasing from ZnS NWs, are discussed. The main conclusions drawn from the literatures are summarized as follows:

1. Blue and green emissions are usually observed from 1-D ZnS NWs synthesized using different methods, which is related to radiative recombination from deep-level defect states. Although there is no consistent conclusion on the mechanism of visible emission from ZnS NWs, it is more reasonable to ascribe the transitions to vacancy states, some self-activated centers, or interstitial states associated with the peculiar nanostructures. And there calls more investigation to reveal the possible origin of visible emission from ZnS NWs.
2. Near band-edge UV emissions have been observed from ZnS NWs with high crystalline quality. The emission from small NWs shows bigger photon energy compared to the thin-film sample indicates the existence of quantum confinement effect. For rectangular cross-sectional WZ ZnS NWs synthesized by PLV, several free exciton absorption and emission can be observed at room temperature and low temperature. Moreover, emission band peaked at 3.639 eV has been observed, which is attributed to the shallow-level emission.
3. Temperature-dependent PL measurements have been carried out, and the fundamental bandgap deduced are 3.716 eV (3.785 eV) and 3.818 eV (3.884 eV) at room temperature and 10 K, respectively. Moreover, the results indicate that the phonon component of 1-D structure can be suppressed as compared that of two-dimensional structure. Therefore, exciton in ZnS is very stable even though its exciton binding energy is not comparable with ZnO. This superior optical property made ZnS a suitable candidate for excitonic devices.
4. The intrinsic radiative lifetime of the free exciton for ZnS NWs is deduced to be ~2.7 ns, which is comparable to bulk single-crystal ZnO (~3.0 ns). Therefore, ZnS NWs can be envisaged as a potential material for technically important UV light emitter at nanoscale.
5. UV lasing have been observed from ZnS NWs, nanobelts, and nanosheets, and the corresponding lasing mechanism can be ascribed to Fabry-Pérot lasing and coherent random lasing. The results have clearly demonstrated that the highly oriented ZnS NWs arrays indeed serve as an excellent nanoscopic laser cavity with room-temperature UV lasing.

There is considerable interest in further study of 1-D crystalline ZnS NWs. For material fabrication, new fabrication technologies are still developing to achieve high-crystalline quality ZnS NWs on various substrates (such as flexible substrates) with large scale. The high quality is needed to further investigate the fundamental optical and excitonic properties of ZnS NWs. Moreover, 1-D nanostructures consisting of two or more important functional materials are of prime importance for revealing unique properties and essential for developing potential nanoscale devices, such as ZnO, ZnSe, ZnTe, CdS and their ternary compounds like ZnS_xO_{1-x}, ZnS_xSe_{1-x}, and ZnS_xTe_{1-x}. It is known that metal ion doping of ZnS is one of the hottest research topics, e.g., manganese (Mn) doping yields an orange-red color at ~590 nm and copper (Cu)-doped ZnS is used in electroluminescent (EL) panels [100, 101]. Therefore, this idea can be adopted in the 1-D ZnS NWs. Although the

investigation about the optical and excitonic properties of 1-D crystalline ZnS NWs is just initiated a few years ago and the achievements are limited compared with other semiconductor materials such as ZnO and GaN, the results obtained are notable which indicates the unique properties and potential applications for various kinds of electronic application. Research down this line may help to advance UV photonic and sensing devices based on 1-D ZnS NWs and will receive more and more attentions due to its unique properties. There is still a lot of room for future development in this area.

References

1. Wagner R, Ellis W (1964) Vapor–liquid–solid mechanism of single crystal growth. Appl Phys Lett 4(5):89–90
2. Duan X, Huang Y, Agarwal R, Lieber CM (2003) Single-nanowire electrically driven lasers. Nature 421(6920):241–245
3. Huang MH, Mao S, Feick H, Yan H, Wu Y, Kind H, Weber E, Russo R, Yang P (2001) Room-temperature ultraviolet nanowire nanolasers. Science 292(5523):1897–1899
4. Wang X, Summers CJ, Wang ZL (2004) Large-scale hexagonal-patterned growth of aligned ZnO nanorods for nano-optoelectronics and nanosensor arrays. Nano Lett 4(3):423–426
5. Xiang J, Lu W, Hu Y, Wu Y, Yan H, Lieber CM (2006) Ge/Si nanowire heterostructures as high-performance field-effect transistors. Nature 441(7092):489–493
6. Zhou J, Gu Y, Fei P, Mai W, Gao Y, Yang R, Bao G, Wang ZL (2008) Flexible piezotronic strain sensor. Nano Lett 8(9):3035–3040
7. Chen R, Li D, Liu B, Peng Z, Gurzadyan GG, Xiong Q, Sun H (2010) Optical and excitonic properties of crystalline ZnS nanowires: toward efficient ultraviolet emission at room temperature. Nano Lett 10(12):4956–4961
8. Liu B, Chen R, Xu XL, Li DH, Zhao YY, Shen ZX, Xiong QH, Sun HD (2011) Exciton-related photoluminescence and lasing in CdS nanobelts. J Phys Chem C 115(26):12826–12830
9. Chen R, Bakti Utama MI, Peng Z, Peng B, Xiong Q, Sun HD (2011) Excitonic properties and near-infrared coherent random lasing in vertically aligned CdSe nanowires. Adv Mater 23(11):1404–1408
10. Tang ZK, Wong GKL, Yu P, Kawasaki M, Ohtomo A, Koinuma H, Segawa Y (1998) Room-temperature ultraviolet laser emission from self-assembled ZnO microcrystallite thin films. Appl Phys Lett 72(25):3270–3272
11. Law M, Greene LE, Johnson JC, Saykally R, Yang P (2005) Nanowire dye-sensitized solar cells. Nat Mater 4(6):455–459
12. Chen R, Xing GZ, Gao J, Zhang Z, Wu T, Sun HD (2009) Characteristics of ultraviolet photoluminescence from high quality tin oxide nanowires. Appl Phys Lett 95(6):061908
13. Wei ZP, Guo DL, Liu B, Chen R, Wong LM, Yang WF, Wang SJ, Sun HD, Wu T (2010) Ultraviolet light emission and excitonic fine structures in ultrathin single-crystalline indium oxide nanowires. Appl Phys Lett 96(3):031902
14. Utama MIB, Peng Z, Chen R, Peng B, Xu X, Dong Y, Wong LM, Wang S, Sun HD, Xiong Q (2011) Vertically aligned cadmium chalcogenide nanowire arrays on muscovite mica: a demonstration of epitaxial growth strategy. Nano Lett 11(8):3051–3057
15. Ziegler J, Xu S, Kucur E, Meister F, Batentschuk M, Gindele F, Nann T (2008) Silica-coated InP/ZnS nanocrystals as converter material in white LEDs. Adv Mater 20(21):4068–4073
16. Moreau JW, Weber PK, Martin MC, Gilbert B, Hutcheon ID, Banfield JF (2007) Extracellular proteins limit the dispersal of biogenic nanoparticles. Science 316(5831):1600–1603

17. Jiang X, Xie Y, Lu J, Zhu LY, He W, Qian YT (2001) Simultaneous in situ formation of ZnS nanowires in a liquid crystal template by gamma-irradiation. Chem Mater 13(4):1213–1218
18. Nakamura S (1998) The roles of structural imperfections in InGaN-based blue light-emitting diodes and laser diodes. Science 281(5379):956–961
19. Blachnik R, Chu J, Gałazka RR, Geurts J, Gutowski J, Hoenerlage B, Hofmann D, Kossut J, Levy R, Michler P, Neukirch U, Strauch D, Story T, Waag A (1999) Numerical data and functional relationships in science and technology. Springer, Berlin, New Series Edition, Ed. U. Rössler
20. Tran TK, Park W, Tong W, Kyi MM, Wagner BK, Summers CJ (1997) Photoluminescence properties of ZnS epilayers. J Appl Phys 81(6):2803–2809
21. Xiong Q, Wang J, Reese O, Lew Yan Voon LC, Eklund PC (2004) Raman scattering from surface phonons in rectangular cross-sectional w-ZnS nanowires. Nano Lett 4(10):1991–1996
22. Ma C, Moore D, Li J, Wang ZL (2003) Nanobelts, nanocombs, and nanowindmills of wurtzite ZnS. Adv Mater 15(3):228–231
23. Moore D, Wang ZL (2006) Growth of anisotropic one-dimensional ZnS nanostructures. J Mater Chem 16(40):3898–3905
24. Fang XS, Bando Y, Shen GZ, Ye CH, Gautam UK, Costa PMFJ, Zhi CY, Tang CC, Golberg D (2007) Ultrafine ZnS nanobelts as field emitters. Adv Mater 19(18):2593–2596
25. Gautam UK, Fang X, Bando Y, Zhan J, Golberg D (2008) Synthesis, structure, and multiply enhanced field-emission properties of branched ZnS nanotube-in nanowire core-shell heterostructures. ACS Nano 2(5):1015–1021
26. Ding J, Zapien J, Chen W, Lifshitz Y, Lee S, Meng X (2004) Lasing in ZnS nanowires grown on anodic aluminum oxide templates. Appl Phys Lett 85(12):2361–2363
27. Xu XJ, Fei GT, Yu WH, Wang XW, Chen L, Zhang LD (2006) Preparation and formation mechanism of ZnS semiconductor nanowires made by the electrochemical deposition method. Nanotechnology 17(2):426–429
28. Sun HY, Yu YL, Li XH, Li W, Li F, Liu BT, Zhang XY (2007) Controllable growth of electrodeposited single-crystal nanowire arrays: the examples of metal Ni and semiconductor ZnS. J Cryst Growth 307(2):472–476
29. Moore DF, Ding Y, Wang ZL (2004) Crystal orientation-ordered ZnS nanowire bundles. J Am Chem Soc 126(44):14372–14373
30. Shen G, Bando Y, Golberg D, Zhou C (2008) Heteroepitaxial growth of orientation-ordered ZnS nanowire arrays. J Phys Chem C 112(32):12299–12303
31. Biswas S, Ghoshal T, Kar S, Chakrabarti S, Chaudhuri S (2008) ZnS nanowire arrays: synthesis, optical and field emission properties. Cryst Growth & Des 8(7):2171–2176
32. Liang Y, Xu H, Hark SK (2010) Orientation and structure controllable epitaxial growth of ZnS nanowire arrays on GaAs substrates. J Phys Chem C 114(18):8343–8347
33. Haase M, Qiu J, DePuydt J, Cheng H (1991) Blue-green laser diodes. Appl Phys Lett 59(11):1272–1274
34. Lu F, Cai W, Zhang Y, Li Y, Sun F, Heo SH, Cho SO (2006) Well-aligned zinc sulfide nanobelt arrays: excellent field emitters. Appl Phys Lett 89(23):231928
35. Dai H, Wong EW, Lu YZ, Fan S, Lieber CM (1995) Synthesis and characterization of carbide nanorods. Nature 375(6534):769–772
36. Wong EW, Maynor BW, Burns LD, Lieber CM (1996) Growth of metal carbide nanotubes and nanorods. Chem Mater 8(8):2041–2046
37. Han W, Fan S, Li Q, Hu Y (1997) Synthesis of gallium nitride nanorods through a carbon nanotube-confined reaction. Science 277(5330):1287–1289
38. Lu M-Y, Song J, Lu M-P, Lee C-Y, Chen L-J, Wang ZL (2009) ZnO-ZnS heterojunction and ZnS nanowire arrays for electricity generation. ACS Nano 3(2):357–362
39. Feng QJ, Shen DZ, Zhang JY, Liang HW, Zhao DX, Lu YM, Fan XW (2005) Highly aligned ZnS nanorods grown by plasma-assisted metalorganic chemical vapor deposition. J Cryst Growth 285(4):561–565

40. Chan SK, Lok SK, Wang G, Cai Y, Wang N, Wong KS, Sou IK (2008) MBE-grown cubic ZnS nanowires. J Electron Mater 37(9):1433–1437
41. Li YQ, Tang JX, Wang H, Zapien JA, Shan YY, Lee ST (2007) Heteroepitaxial growth and optical properties of ZnS nanowire arrays on CdS nanoribbons. Appl Phys Lett 90(9):093127
42. Xiong QH, Chen G, Acord JD, Liu X, Zengel JJ, Gutierrez HR, Redwing JM, Voon L, Lassen B, Eklund PC (2004) Optical properties of rectangular cross-sectional ZnS nanowires. Nano Lett 4(9):1663–1668
43. Xiong QH, Gupta R, Adu KW, Dickey EC, Lian GD, Tham D, Fischer JE, Eklund PC (2003) Raman spectroscopy and structure of crystalline gallium phosphide nanowires. J Nanosci Nanotechnol 3(4):335–339
44. Toll JS (1956) Causality and the dispersion relation: logical foundations. Phys Rev 104(6):1760
45. Yu PY, Cardona M (1996) Fundamentals of semiconductors, physics and materials properties. Springer, Berlin
46. Klingshirn CF (2007) Semiconductor optics, 3rd edn. Springer, Berlin
47. Sun HD, Makino T, Segawa Y, Kawasaki M, Ohtomo A, Tamura K, Koinuma H (2002) Enhancement of exciton binding energies in ZnO/ZnMgO multiquantum wells. J Appl Phys 91(4):1993–1997
48. O'Connor DV, Phillips D (1984) Time-correlated single photon counting. Academic, London
49. Qadri S, Skelton E, Dinsmore A, Hu J, Kim W, Nelson C, Ratna B (2001) The effect of particle size on the structural transitions in zinc sulfide. J Appl Phys 89(1):115–119
50. Wang ZW, Daemen LL, Zhao YS, Zha CS, Downs RT, Wang XD, Wang ZL, Hemley RJ (2005) Morphology-tuned wurtzite-type ZnS nanobelts. Nat Mater 4(12):922–927
51. Wang YW, Zhang LD, Liang CH, Wang GZ, Peng XS (2002) Catalytic growth and photoluminescence properties of semiconductor single-crystal ZnS nanowires. Chem Phys Lett 357(3–4):314–318
52. Yang Y, Zhang WJ (2004) Preparation and photoluminescence of zinc sulfide nanowires. Mater Lett 58(29):3836–3838
53. Ye C, Fang X, Li G, Zhang L (2004) Origin of the green photoluminescence from zinc sulfide nanobelts. Appl Phys Lett 85(15):3035–3037
54. Geng BY, Liu XW, Du QB, Wei XW, Zhang LD (2006) Structure and optical properties of periodically twinned ZnS nanowires. Appl Phys Lett 88(16):163104
55. Yin LW, Bando Y, Zhan JH, Li MS, Golberg D (2005) Self-assembled highly faceted wurtzite-type ZnS single-crystalline nanotubes with hexagonal cross-sections. Adv Mater 17(16):1972–1977
56. Chai L, Du J, Xiong S, Li H, Zhu Y, Qian Y (2007) Synthesis of wurtzite ZnS nanowire bundles using a solvothermal technique. J Phys Chem C 111(34):12658–12662
57. Ye C, Fang X, Wang M, Zhang L (2006) Temperature-dependent photoluminescence from elemental sulfur species on ZnS nanobelts. J Appl Phys 99(6):063504
58. Gibbons DJ, Spear WE (1966) Electron hopping transport and trapping phenomena in orthorhombic sulphur crystals. J Phys Chem Solids 27(11–12):1917–1925
59. Zhai TY, Dong Y, Wang YB, Cao ZW, Ma Y, Fu HB, Yao HN (2008) Size-tunable synthesis of tetrapod-like ZnS nanopods by seed-epitaxial metal-organic chemical vapor deposition. J Sol State Chem 181(4):950–956
60. Zhai T, Gu Z, Fu H, Ma Y, Yao J (2007) Synthesis of single-crystal ZnS nanoawls via two-step pressure-controlled vapor-phase deposition and their optical properties. Cryst Growth & Des 7(8):1388–1392
61. Denzler D, Olschewski M, Sattler K (1998) Luminescence studies of localized gap states in colloidal ZnS nanocrystals. J Appl Phys 84(5):2841–2845
62. Yang Y, Yan H, Fu Z, Yang B, Xia L, Xu Y, Zuo J, Li F (2005) Photoluminescence investigation based on laser heating effect in ZnO-ordered nanostructures. J Phys Chem B 110(2):846–852

63. Lippens PE, Lannoo M (1989) Calculation of the band gap for small CdS and ZnS crystallites. Phys Rev B 39(15):10935–10942
64. Sun HD, Makino T, Tuan NT, Segawa Y, Kawasaki M, Ohtomo A, Tamura K, Koinuma H (2001) Temperature dependence of excitonic absorption spectra in ZnO/Zn0.88 Mg0.12O multiquantum wells grown on lattice-matched substrates. Appl Phys Lett 78(17):2464–2466
65. Sun HD, Makino T, Segawa Y, Kawasaki M, Ohtomo A, Tamura K, Koinuma H (2001) Biexciton emission from ZnO/Zn0.74 Mg0.26O multiquantum wells. Appl Phys Lett 78(22):3385–3387
66. Sun HD, Makino T, Tuan NT, Segawa Y, Tang ZK, Wong GKL, Kawasaki M, Ohtomo A, Tamura K, Koinuma H (2000) Stimulated emission induced by exciton-exciton scattering in ZnO/ZnMgO multiquantum wells up to room temperature. Appl Phys Lett 77(26):4250–4252
67. He TC, Chen R, Lin WW, Huang F, Sun HD (2011) Two-photon-pumped stimulated emission from ZnO single crystal. Appl Phys Lett 99(8):081902
68. Kasprzak J, Richard M, Kundermann S, Baas A, Jeambrun P, Keeling JMJ, Marchetti FM, Szymanska MH, Andre R, Staehli JL, Savona V, Littlewood PB, Deveaud B, Dang LS (2006) Bose-Einstein condensation of exciton polaritons. Nature 443(7110):409–414
69. Kavokin A, Malpuech G, Gil B (2003) Semiconductor microcavities: towards polariton lasers. Mrs Internet J Nitride Semiconductor Res 8(3):3
70. Savona V, Piermarocchi C, Quattropani A, Schwendimann P, Tassone F (1999) Optical properties of microcavity polaritons. Phase Transit 68(1):169–279
71. Weisbuch C, Nishioka M, Ishikawa A, Arakawa Y (1992) Observation of the coupled exciton-photon mode splitting in a semiconductor quantum microcavity. Phys Rev Lett 69(23):3314–3317
72. Viswanath AK, Lee JI, Kim D, Lee CR, Leem JY (1998) Exciton-phonon interactions, exciton binding energy, and their importance in the realization of room-temperature semiconductor lasers based on GaN. Phys Rev B 58(24):16333–16338
73. Liu B, Cheng CW, Chen R, Shen ZX, Fan HJ, Sun HD (2010) Fine structure of ultraviolet photoluminescence of tin oxide nanowires. J Phys Chem C 114(8):3407–3410
74. Lautenschlager P, Garriga M, Cardona M (1987) Temperature dependence of the interband critical-point parameters of InP. Phys Rev B 36(9):4813–4820
75. Varshni YP (1967) Temperature dependence of the energy gap in semiconductors. Phys (Amsterdam) 34(1):149–154
76. Lautenschlager P, Garriga M, Logothetidis S, Cardona M (1987) Interband critical points of GaAs and their temperature dependence. Phys Rev B 35(17):9174–9189
77. Makino T, Chia CH, Tuan NT, Segawa Y, Kawasaki M, Ohtomo A, Tamura K, Koinuma H (2000) Exciton spectra of ZnO epitaxial layers on lattice-matched substrates grown with laser-molecular-beam epitaxy. Appl Phys Lett 76(24):3549–3551
78. Bogani F, Carraresi L, Filoramo A, Savasta S (1992) Exciton-polariton relaxation in ZnSe single crystals. Phys Rev B 46(15):9461–9468
79. O' Neill M, Oestreich M, Rühle WW, Ashenford DE (1993) Exciton radiative decay and homogeneous broadening in CdTe/Cd0.85Mn0.15Te multiple quantum wells. Phys Rev B 48(12):8980–8985
80. Adu KW, Xiong Q, Gutierrez HR, Chen G, Eklund PC (2006) Raman scattering as a probe of phonon confinement and surface optical modes in semiconducting nanowires. Appl Phys Mater Sci Process 85(3):287–297
81. Ozaki S, Adachi S (1993) Optical constants of cubic ZnS. Jpn J Appl Phys 32(11A):5008–5013, Part 1: Regular Papers, Short Notes & Review Papers
82. Ong HC, Chang RPH (2001) Optical constants of wurtzite ZnS thin films determined by spectroscopic ellipsometry. Appl Phys Lett 79(22):3612–3614
83. Teke A, Özgür Ü, DoÄŸan S, Gu X, Morkoç H, Nemeth B, Nause J, Everitt HO (2004) Excitonic fine structure and recombination dynamics in single-crystalline ZnO. Phys Rev B 70(19):195207

84. Yoshida H, Yamashita Y, Kuwabara M, Kan H (2008) A 342-nm ultraviolet AlGaN multiple-quantum-well laser diode. Nature Photon 2(9):551–554
85. Suematsu Y (1985) Advances in semiconductor-lasers. Phys Today 38(5):32–39
86. Narukawa Y, Kawakami Y, Funato M, Fujita S, Nakamura S (1997) Role of self-formed InGaN quantum dots for exciton localization in the purple laser diode emitting at 420 nm. Appl Phys Lett 70(8):981–983
87. Zapien JA, Jiang Y, Meng XM, Chen W, Au FCK, Lifshitz Y, Lee ST (2004) Room-temperature single nanoribbon lasers. Appl Phys Lett 84(7):1189–1191
88. Yang HY, Yu SF, Yan J, Zhang LD (2010) Random lasing action from randomly assembled ZnS nanosheets. Nanoscale Res Lett 5(5):809–812
89. Chen R, Ling B, Sun XW, Sun HD (2011) Room temperature excitonic whispering gallery mode lasing from high-quality hexagonal ZnO microdisks. Adv Mater 23(19):2199–2204
90. Jiang Y, Zhang WJ, Jie JS, Meng XM, Zapien JA, Lee ST (2006) Homoepitaxial growth and lasing properties of ZnS nanowire and nanoribbon arrays. Adv Mater 18(12):1527–1532
91. Jiang Y, Meng XM, Liu J, Xie ZY, Lee CS, Lee ST (2003) Hydrogen-assisted thermal evaporation synthesis of ZnS nanoribbons on a large scale. Adv Mater 15(4):323–327
92. Ding Y, Wang XD, Wang ZL (2004) Phase controlled synthesis of ZnS nanobelts: zinc blende vs wurtzite. Chem Phys Lett 398(1–3):32–36
93. Fang XS, Ye CH, Zhang LD, Wang YH, Wu YC (2005) Temperature-controlled catalytic growth of ZnS nanostructures by the evaporation of ZnS nanopowders. Adv Funct Mater 15(1):63–68
94. Chen R, Sun HD, Wang T, Hui KN, Choi HW (2010) Optically pumped ultraviolet lasing from nitride nanopillars at room temperature. Appl Phys Lett 96(24):241101
95. Cao H, Zhao YG, Ho ST, Seelig EW, Wang QH, Chang RPH (1999) Random laser action in semiconductor powder. Phys Rev Lett 82(11):2278–2281
96. Cao H (2003) Lasing in random media. Waves Random and Complex Media 13(3):R1–R39
97. Cheng CW, Liu B, Yang HY, Zhou WW, Sun L, Chen R, Yu SF, Zhang JX, Gong H, Sun HD, Fan HJ (2009) Hierarchical assembly of ZnO nanostructures on SnO_2 backbone nanowires: low-temperature hydrothermal preparation and optical properties. ACS Nano 3(10):3069–3076
98. Yang HY, Yu SF, Yan J, Zhang LD (2010) Wide bandwidth lasing randomly assembled ZnS/ZnO biaxial nanobelt heterostructures. Appl Phys Lett 96(14):141115
99. Yu S, Yuen C, Lau S, Lee H (2004) Zinc oxide thin-film random lasers on silicon substrate. Appl Phys Lett 84(17):3244–3246
100. Jayanthi K, Chawla S, Chander H, Haranath D (2007) Structural, optical and photoluminescence properties of ZnS: Cu nanoparticle thin films as a function of dopant concentration and quantum confinement effect. Crys Res Technol 42(10):976–982
101. Jindal Z, Verma NK (2008) Photoluminescent properties of ZnS: Mn nanoparticles with in-built surfactant. J Mater Sci 43(19):6539–6545

Optical Properties of Nanocomposites

13

Timothy O'Connor and Mikhail Zamkov

Contents

1 Definition of the Topic

Optical characteristics of nanocomposites provide deeper insights into the overall function of these materials. This chapter describes steady-state and time-resolved optical properties of nanocomposites in the UV-Vis range derived through the analysis of a variety of nanoparticle architectures and the extrapolation of general trends from these examples.

2 Overview

Recent progress in controlling the size, morphology, and growth rate of inorganic nanocrystals synthesized via colloidal routes has enabled cost-effective methodologies for the creation of complex nanocomposite systems. These nanostructures are constructed through multistaged syntheses, wherein each step is accompanied by

T. O'Connor (✉) • M. Zamkov
Department of Physics, Bowling Green State University, Bowling Green, USA

Challa S.S.R. Kumar (ed.), *UV-VIS and Photoluminescence Spectroscopy for Nanomaterials Characterization*, DOI 10.1007/978-3-642-27594-4_13,

the addition of a new component, providing a greater degree of control over the optoelectronic properties that govern the overall functionality of the nano-object.

The characteristics of nanocomposites are usually tuned by adjusting the size, shape, and material composition of individual domains as well as the architecture of the overall nanostructure, as electronic interactions across material interfaces strongly contribute into the behavior of the complex nanocrystal.

By analyzing the outcome of steady-state and time-resolved optical measurements, this chapter deciphers the optoelectronic properties of nanocomposites during each stage of the synthesis, providing insights into the mechanism underlying the observed spectral phenomena. Meanwhile, the structural analysis of these nanocomposites using transmission electron microscopy (TEM) adds to procuring a relationship between the observed optical characteristics and the morphology of investigated nanocomposites.

3 Introduction

Inorganic nanocrystals represent one of the most fruitful grounds for the current research in nanoscience and nanotechnology, as they are relevant both to the fundamental understanding of the size- and dimensionality-dependent laws of nanoscale matter and to the bottom-up development of new functional materials, devices, and processes. Unique properties of these nanoparticles arise from the onset of carrier confinement in the two or three dimensions, such that the energy absorbed through optical or electrical excitations can be controllably trapped or channeled within the structure, which gives rise to enormous array of possible applications and new technologies, including lasing [1], photovoltaics, [2, 3] photocatalysis, [4, 5] LEDs, [6–11] bio-labels, [12–14] thermoelectric elements, [15, 16] field-effect transistors, [17–22] magnetic doping, [23, 24] and memory elements. [25–29].

Conjoining two or more materials in a single composite nanocrystal via low-cost colloidal routes further facilitates the design of nanostructures with "adjustable" electronic and optical properties, leading to a new degree of freedom in the development of multifunctional composites. [30–33] Adjacent domains of semiconductors having different band gap values and appropriately chosen band offsets could be used to trap electron–hole pairs in specific regions of the nanocrystal (type I confinement), thus forcing them to recombine therein with high efficiency. Alternatively, composite nanocrystals with a type II alignment of material band gaps, constructed in such a way that band edges of one domain lie lower in energy than the corresponding band edges of the other, facilitate spatial separation of electron–hole pairs (excitons) between different parts of the composite nanostructure, which can be harnessed for the development of photovoltaic and photocatalytic materials [34].

Nanostructures are also further classified by their material combination, separating them into semiconductor–semiconductor and metal–semiconductor systems. These composites can manifest in a variety of geometries such as core/shell, [30]

dot-in-a-rod, [35–38] barbell, [39–41] heterodimer, [42, 43] tetrapod, [44] and multibranched [45] nanocrystals. Frequently utilized material combinations for metal–semiconductor systems include Au/CdSe, [46, 47] Au/CdS, [48, 49] Pt/CdS [50], and Au/PbS [22], while semiconductor–semiconductor composites often utilize II–VI or III–V materials. The following sections analyze optical properties of these systems in more detail.

This chapter provides an overview of the optical properties of the aforementioned classifications of nanocomposites throughout their synthesis. These systems have been chosen as they comprise structures that demonstrate a range of general phenomenon typical of the various types of nanocomposites currently being researched. This chapter will begin with the simpler type I system, proceeding in increasing complexity through the type II system, and terminating with the analysis of the semiconductor–metal systems. The evolution of the optical properties will be presented, along with general conclusions that can be made using the information obtained from a number of examples.

4 Experimental and Instrumental Methodology

All nanoparticle types analyzed in this chapter are fabricated using "bottom-up" methodology via solution phase colloidal chemistry. These syntheses were carried out under argon or nitrogen environment at temperatures ranging between 30 °C and 450 °C. Owing to their colloidal stability, investigated nanocomposites are usually stored in nonpolar solvents.

Steady-state UV-vis absorption and photoluminescence spectra analyzed in this chapter were recorded using UV-vis and fluorescence spectrophotometers (e.g., CARY 50 and Jobin Yvon Fluorolog). Time-resolved transient absorption spectroscopy typically employs Ti:sapphire amplified laser system operating at a repetition rate of 0.1–200 kHz, which output is split into two components: monochromatic pump and broadband probe signals. Fluorescence lifetime measurements are usually performed using a time-correlated single-photon counting setup utilizing either a single-photon counting PCI card (e.g., Becker & Hickle GmbH), or a NIM bin-based amplification system comprising a differential amplifier, constant fraction discriminator, time-to-amplitude converter, and analog-to-digital converter units. The excitation of the sample is typically performed using a picosecond diode laser, which repletion rate is chosen to allow no more than one emission photon per 5–10 excitation pulses.

5 Key Research Findings

5.1 Semiconductor-Semiconductor Nanocomposites

Conjoining multiple semiconductor domains in a single nanocomposite provides a higher degree of customization in the development of unique optoelectronic

materials. By judiciously choosing the initial domains and the geometry in which they are assembled, such heteronanocrystals can be made to offer superior control over the spatial distribution of charge carriers across material interfaces, which determines the overall functionality of the quantum system. Conventionally, a heterojunction of two semiconductor materials can be classified as either type I, where both carriers are confined within the same semiconductor, or type II, where an electron and a hole are spatially separated in two different parts of the heterostructure. Due to highly stable emissions associated with nanocrystals in the first group [51–53], their properties are readily utilized in applications that require a coupling of quantum dots to organic moieties, such as in hybrid LEDs [8, 54, 55] or in vivo imaging, [13, 56] where the use of single-phase nanocrystals typically causes an irreversible loss of fluorescence [57, 58] or severe blinking [59–61]. Heterostructures of the second group benefit from an efficient separation of charges between the core and the shell, which makes them useful in photovoltaic applications [62–66], where spatial charge separation reduces an exciton dissociation potential, or QD-based lasers [1, 67, 68], where an electric dipole of a photogenerated pair Stark-shifts the biexciton level resulting in a desirable linear light amplification regime.

One common feature, characteristic to above-mentioned carrier localization types is a straightforward correspondence between a quantum dot emission range and the energy spacing between the two closest band edges of the semiconductor materials that form the heterostructure. Indeed, for both type I and type II heteronanocrystals, the energy of emitted photons is determined by the energy difference between the closest zero-angular momentum states, 1S(e) and 1S(h), of the adjoined materials.

5.1.1 Type I Nanocomposite Systems

Type I nanosystems are constructed by combining two semiconductor materials in such a manner that conduction and valence band edges of one material fall entirely within the band gap of the other semiconductor, creating a potential barrier at the interface. Likewise, semiconductor nanocomposites comprising more than one site of attachment are referred to as type I when the higher potentials surround the low band energy semiconductor. There is also a reverse type I system where the large band energy semiconductor is located at the center of the structure and is enclosed by the lower band gap semiconductor (see Fig. 13.1). As the name suggests, the direct and reverse systems have opposite effects on the localization of excitons created within them.

In type I nanocrystals, the potential energy restriction placed on the first material by the larger band gap of the second material confines photoinduced charges to the core of the nanocomposite. Restricting charge carriers to the central semiconductor will increase the quantum efficiency of the fluorescence emission, as the lower overlap of charge carriers with the surface states of the nanocomposite causes a decrease in trapping rate. Likewise, the growth of the semiconductor shell in a type I configuration helps protecting the optical characteristics of the core domain, as in this case the photooxidation of the shell material and associated ligands does not lead to the degradation of the core component.

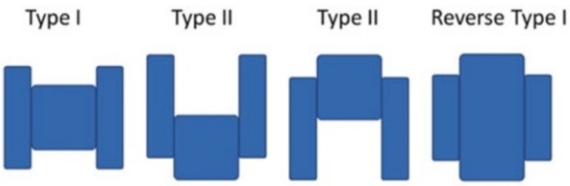

Fig. 13.1 Illustration of band-edge alignment in various system types

In reverse type I systems, the areas of lower potential energy reside on the outer edges of the heteronanocrystal such that electrons and holes are both pushed out of the central domain. In the case of a core/shell or a seeded tetrapod geometry, this would result in the injection of charge carriers from the core into the shell or arms, respectively. Reverse type I systems are less common than those with the direct type I configuration, as they generally have fewer practical uses; one known application of reverse type I systems is in LEDs which benefits from an enhanced tunability of the emission color in such nanocomposites.

CdSe/ZnSe/ZnS Core/Shell/Shell Nanocrystals

As an illustrative example of a type I nanocomposite system, CdSe/ZnSe/ZnS core/shell/shell nanocrystals will be analyzed in detail [69]. This system represents two type I systems within itself, but due to the main focus of a previous chapter on core/shell structures, the more complex core/shell/shell morphology was chosen to exemplify a broader scope of architectures.

Fabrication of CdSe/ZnSe/ZnS core/shell/shell heteronanocrystals was carried out one layer at a time, beginning with the synthesis of CdSe nanocrystals in colloidal solutions, onto which a thin ZnSe shell was then grown in a separate procedure. This step was then repeated for the growth of the ZnS shell, this time using the CdSe/ZnSe core/shell structures as seeds.

Each layer of the CdSe/ZnSe/ZnS system provides a unique aspect to the overall properties and function of the nanocomposite, with the core providing the greatest influence on the spectral character of the fluorescence. A CdSe core capped with original bulky ligands has relatively low emission quantum efficiency (typically less than 25 %) due to ligand oxidation and desorption, which promotes the interaction of the excitons with the surface states. This is mitigated by the inorganic surface passivation provided by the ZnSe and ZnS shell. The ZnSe shell is first grown to act as a transition, stress-relieve, layer between the CdSe core and the ZnS outer shell, as the lattice mismatch between the latter materials is high, roughly 12 %, and growth of ZnS directly onto CdSe would cause crystal defects, especially for shells exceeding two to three monolayers (MLs) in thickness. It should be mentioned that a sufficiently thick ZnSe shell would be able to provide adequate passivation, but ZnSe is not as stable a material and prone to photooxidation. The final ZnS shell results in comparable photoluminescence efficiencies, increased stability, and reduced biotoxicity, as ZnS is known as an innocuous material, making these nanocomposites applicable for biological labels and as well as nanocrystal LEDs.

The absorbance and emission profiles of the original CdSe cores are characteristic of binary nanocrystals exhibiting a typically sharp absorption edge and narrow

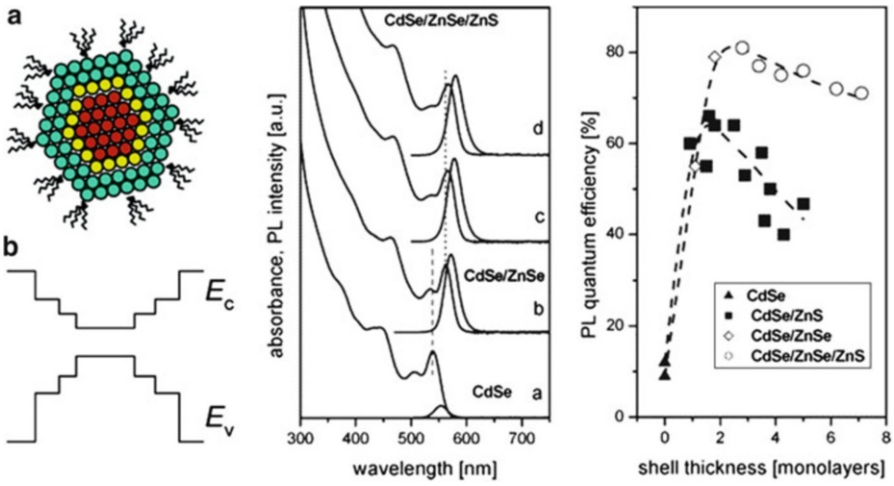

Fig. 13.2 (**a**) Schematic of core/shell/shell CdSe/ZnSe/ZnS nanocrystal. (**b**) Band gap energy diagram of CdSe/ZnSe/ZnS nanocrystal. (**c**) Absorbance and photoluminescence spectra of (a) CdSe cores, (b) CdSe/ZnSe core/shell with a two monolayer thickness for the ZnSe shell, (c) CdSe/ZnSe/ZnS core/shell/shell with a ZnS shell thickness of two monolayers, and (d) CdSe/ZnSe/ZnS core/shell/shell with a ZnS shell thickness of 4 monolayers. (**d**) Photoluminescence quantum efficiencies of various CdSe core/shell and core/shell/shell architectures depending on shell thickness (Reprinted with permission from Talapin et al. [69]. Copyright 2004 American Chemical Society)

emission width (Fig. 13.2). Growth of the ZnSe thin shell is marked by a drastic increase in photoluminescent quantum efficiency, and the associated bathochromatic (red) shift in both optical profiles due to the partial leakage of charge carrier wave packets into the shell. Upon grow minor red-shifting in both the absorbance and fluorescence occurs proportionate to the thickness of the shell as the overall volume of the nanocrystal has increased, allowing the wavefunctions to become slightly more delocalized. After the optimal thickness of the ZnS shell of roughly 2.5 monolayers is reached, the photoluminescence quantum efficiency of the ZnS layer, nanocomposites starts to decay when additional ZnS is added to the surface. The absorbance spectra show contributions from each individual structure, as is expected from multifunctional nanocrystal systems.

CdSe/CdS and CdSe/CdZnS Core/Giant Shells

Another example of a type I system is a core/shell and core/shell/shell structure that demonstrates an extreme case of charge carrier localization by implementing the growth of a giant shell around the core semiconductor [70] (Fig. 13.3). This giant shell (approximately 15–20 monolayers in thickness) not only provides means for inorganic passivation of the surface, increased stability, and increased quantum efficiency but also helps suppress nanocrystal blinking, a phenomenon best described as intermittency of fluorescence with on and off cycles lasting approximately several seconds. It is believed that nanocrystal blinking occurs when charge

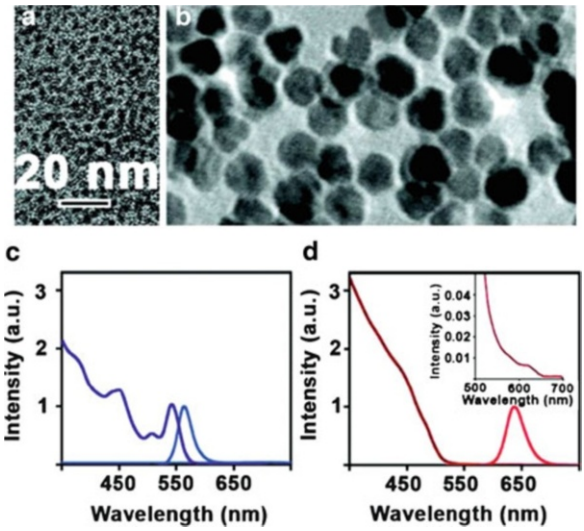

Fig. 13.3 Transmission electron microscopy (*TEM*) images for (**a**) CdSe nanocrystals and (**b**) CdSe/19CdS core/giant shells. (**c**) Absorption (*dark blue*) and PL (*light blue*) spectra for CdSe nanocrystals. (**d**) Absorption (*dark red*) and PL (*light red*) spectra for CdSe/19CdS core/giant shells (*inset*: absorption spectrum expanded to show contribution from core) (Reprinted with permission from Chen et al. [70]. Copyright 2008 American Chemical Society)

carriers get trapped on surface states whereby charging the nanocrystal, thus promoting Auger ejection or charge tunneling [59–61]. When the nanocrystal has built up charge, it will no longer fluoresce until it has regained its neutrality. Blinking must be mitigated before single nanocrystals become viable candidates for applications that require reliable single-photon emission, such as quantum informatics and biolabeling.

The synthesis of giant nanocrystals starts with the growth of CdSe seeds, 3–4 nm in diameter, then a very large shell that increases the particles diameter to 15–20 nm is fabricated by successive ion layer absorption and reaction (SILAR) [71] method. This shell can be composed of either a single material or an alloy of materials.

The absorbance profile is dominated by the shell semiconductor, as the ratio of shell to core material can reach 100:1 for nanocrystals that undergo ~20 monolayers of shell growth [70]. In the CdSe/CdS core/shell nanocrystals, this is manifested as the sharp onset of absorbance below 500 nm (Fig. 13.3d), which corresponds to the band gap of bulk CdS. Despite the presence of a thick CdS shell, which has dimensions that exceed the exciton Bohr radius for CdSe (≈ 6 nm), the emission of giant CdSe/CdS nanocrystals is dominated by the band-edge fluorescence of the core domain. This is a clear manifestation of a type I band-edge alignment, which confines photoinduced charges to CdSe. A slight increase in the wavelength of the CdSe emission upon shell growth is attributed to the minimal delocalization of charge carrier wavefunctions into the shell domain. Lastly, Fig. 13.4 shows the fluorescence intensity over time for core/shell nanocrystals, which exhibit blinking and the core/giant shell architectures, which have mitigated this intermittent fluorescence.

PbS/CdS Core/Shell Heteronanocrystals

PbS/CdS core/shell nanocomposites with the core component exceeding ≈ 3.2 nm in diameter represent another example of type I heterostructures, which show strong

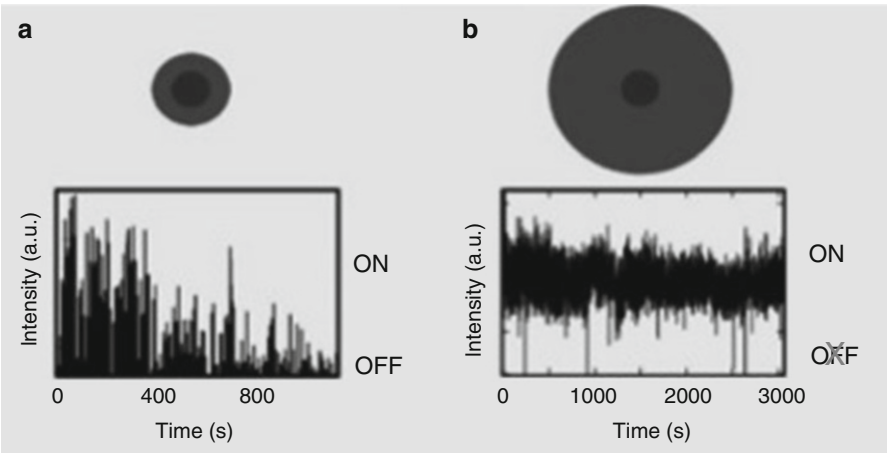

Fig. 13.4 (**a**) Fluorescence intensity over time for a blinking CdSe/CdS core/shell nanocrystal and (**b**) fluorescence intensity over time for a CdSe/CdS core/giant shell nanocrystal (Reprinted with permission from Chen et al. [70]. Copyright 2008 American Chemical Society)

band-edge fluorescence in the 1,000–2,500-nm spectral range. [72] It should be noted that PbS/CdS core/shell structures comprising smaller PbS cores (<3.2 nm in diameter) will yield type II systems due to the size tuning of the PbS 1S(e) band edge. Encapsulating larger PbS nanocrystals within a CdS shell not only enhances the emission yield of these materials but also improves the stability of the structure, which is otherwise quite susceptible to oxidation.

To initiate the synthesis, lead and sulfur precursors are reacted to create monodisperse PbS nanocrystal cores, into which a thin shell of CdS is implanted through $PbS^{2+} \rightarrow CdS^{2+}$ cation exchange. In this method, the nanocrystal cores are placed in a solution that contains an excess of Cd^{2+} cations. These Cd ions will diffuse into the outer layers of the PbS nanocrystals, replacing the Pb^{2+} and forming a thin shell of CdS. This method can be done at relatively low temperatures and slow growth conditions, allowing for the thickness of the shell to be accurately controlled. The thickness of the CdS shell can be controlled with a submonolayer precision by tuning either the temperature of the growth solution or the time of the exchange reaction [72, 73] According to the high-resolution (HR) TEM analysis of several PbS/CdS core/shell structures (Fig. 13.5), CdS shell grows uniformly on the surface of PbS nanocrystals without creating noticeable lattice defects, which is attributed to a relatively low lattice stress at the interface of PbS and CdS crystal phases (strain $\approx$ 1.7 %). A good lattice match at the core/shell boundary can also enable the growth of large CdS shells totaling 14–16 monolayers (ML).

The character of charge confinement in PbS/CdS core/shell nanocomposites is readily substantiated based on steady-state spectroscopy of excitonic transitions in these nanoparticles. According to Fig. 13.5, the $Pb^{2+} \rightarrow Cd^{2+}$ cation exchange in PbS nanocrystals results in blue-shifting of the absorption and emission features, which is attributed to the decreased length of the carrier confinement in PbS cores.

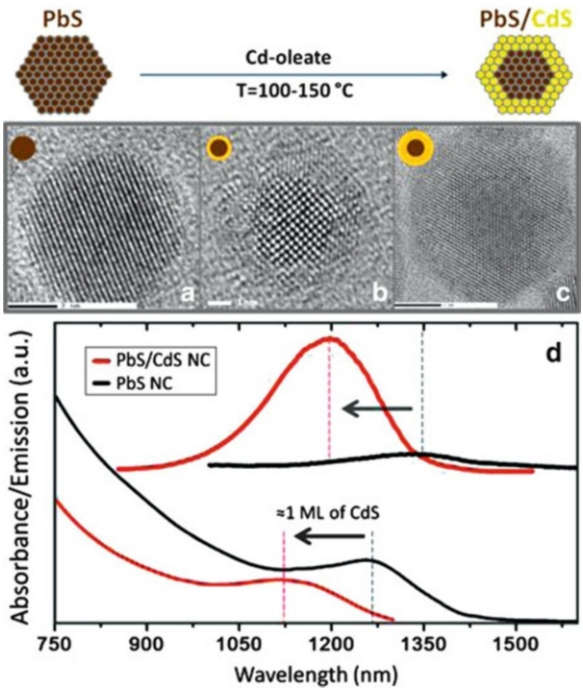

Fig. 13.5 TEM of (**a**) PbS nanocrystal, (**b**) PbS/CdS core/shell nanocrystal grown via cation exchange, (**c**) PbS/CdS core/shell nanocrystal (∼15 monolayers), and (**d**) absorbance and fluorescence of PbS (*black*) and PbS/CdS (one monolayer CdS via cation exchange) (*red*) vertically offset for clarity

The magnitude of this spectral shift is proportional to the reduction in the PbS diameter and can be used here for estimating the thickness of the PbS layer that was converted into the CdS shell. In addition to blue-shifting of excitonic transitions, the transformation of PbS nanocrystals into PbS/CdS core/shell structures is accompanied by a 5–10-fold increase in the emission intensity, which reflects a diminishing probability of core-localized charges to be trapped on nanocrystal surfaces. Such enhancement of the emission yield upon shell growth is consistent with the onset of the type I carrier localization in PbS/CdS core/shell heterostructures, for which both electrons and holes reside primarily in the core domain of the composite nanocrystal.

5.1.2 Type II Nanocomposites

By choosing the sizes and materials of each domain in a heteronanostructure, a staggered alignment of the band edges at the interfaces of two materials can be achieved. This type of architecture is commonly referred to as a type II system. When an exciton is created within a type II nanostructure, the offset band gaps create a potential gradient, driving the electron and hole away from each other and spatially separating their wavefunctions. Due to a smaller degree of electron–hole overlap, type II systems generally have weaker fluorescence characteristics and longer emission lifetimes.

Type II systems will also experience a red-shift of the fluorescence peak relative to the emission of their constituents originating from the recombination taking

place at the interface between materials, whereby electrons localized in the conduction band of one semiconductor will recombine with holes residing in the valence band of the other. This type of electron–hole recombination is also known as a "spatially indirect" recombination. The typical value of a Stokes shift in type II systems is thus dependent on the magnitude of the band-edge offset and can range from just a few nanometers for CdSe/CdTe nanocrystals to hundreds of nanometers for systems such as ZnSe/CdS or ZnTe/CdS.

CdSe-Seeded CdS Nanorods and Nanotetrapods: Quasi-type II Heterostructure

Heteronanorods and tetrapods are two common morphologies of type II nanocomposites. Both structures are usually fabricated by seeding the growth of CdS or CdSe nanorods from small-diameter CdSe, ZnTe, ZnSe, or CdTe nanocrystals, where a seed nanocrystal with wurtzite lattice structure yields nanorods while seeds with a zinc blende crystal lattice promote the growth of tetrapods [69]. More generally, however, the growth of the nanorods or tetrapods morphology is controlled by a combination of the seed lattice type, seed concentration [74], reaction temperature, and ligands. For instance site-specific ligands can suppress the growth along certain axes allowing for the desired shape to be created, while the size and length of nanorods can be controlled by concentration and reaction time. Similar to previously analyzed PbS/CdS core/shells nanostructures, CdSe/CdS heterostructures can transition between type I and type II systems depending on the size of core, where larger cores will yield a type II alignment of band edges.

In the case of CdSe nanocrystals, the growth of CdS linear extensions causes notable changes in the spectroscopic characteristics. The absorbance profiles of both nanorods and tetrapods will retain the excitonic edge associated the CdSe core, which is now red-shifted, due to the increase in the confinement length of CdSe excitons, but this feature is now overshadowed by the absorbance contribution of the CdS in the linear portions of the nanorods and tetrapods, manifesting as a sharp increase in absorbance around 450–460 nm, as is characteristic of CdS. This increase will be shaped as a shoulder or ledge, rather than a peak, due to a loss in dimensionality in the confinement of CdS excitations. Increasing the size of the rods or tetrapods will have a proportional effect on the absorbance profile, as the first spectral peak will shift redder and the CdS shoulder will be increased. The absorbance contribution of CdS is significantly larger than that of CdSe due to the high volume ratio of CdS material in the linear domains to CdSe in the core. These effects can be seen in Fig. 13.7a–b, where the absorbance contribution from the CdSe core is only recognizable after significant magnification. Tetrapods also experience a larger red-shift than the nanorods, originating from the morphological effects on electronic states and an intrinsic difference in energy levels of the types of CdSe wurtzite and zinc blende crystal lattices (Fig. 13.6).

Addition of the CdS domains onto CdSe core is also reflected in the emission of the CdSe/CdS nanocomposite, which undergoes a significant increase in photoluminescence. The large absorbance cross sections of the linear components

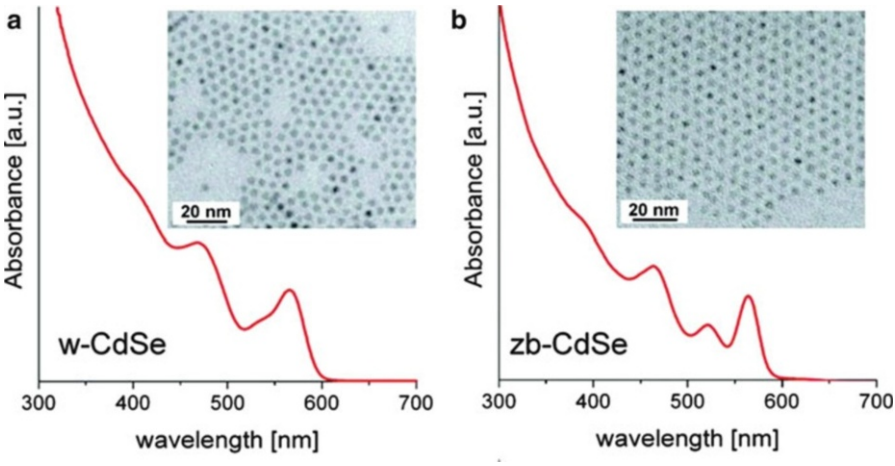

Fig. 13.6 (**a**) Absorption spectrum and TEM image of 4.4-nm CdSe nanocrystals with wurtzite lattice and (**b**) absorption spectrum and TEM image of 4.0-nm CdSe nanocrystals with zinc blende lattice (Reprinted with permission from Talapin et al. [69]. Copyright 2004 American Chemical Society)

act like antennae, increasing the number of excitons created, which will either recombine in the core (type I) or at the interface (type II). The type II fluorescence will manifest as a redder peak, as the indirect recombination is always a lower energy transition than direct recombination in either isolated semiconductor domain. Type II transitions are also accompanied by Stokes shift. In Fig. 13.7, graphs a and b, the associated Stokes shifts for nanorods and nanotetrapods are ~43 meV and ~78 meV, respectively. As the cores increase in size, this shift would become larger, due to the increasing difference in energy between the lowest absorption transition associated with CdSe and the decreasing energy of the inter-domain radiative decay.

Fluorescence lifetime also experiences a notable increase with the growth of linear extensions. Figure 13.7c and d illustrates the proportional relationship between the length of the linear structures and photoluminescent lifetimes. The trace of CdSe nanocrystals (black trace) is typical of binary nanocrystals, exhibiting nanosecond non-exponential decay. Upon the growth of rod or tetrapod "arms," the decay trend becomes nearly linear due to lower charge trapping probability, with tetrapods exhibiting lifetimes over twice as long as nanorods and nearly three times that of isolated CdSe nanocrystals.

Lastly, minor shifts in the optical spectra can be achieved by altering the dimensional parameters of the rods and tetrapods. As expected, large nanocomposites have reduced quantum confinement effects, as the carrier wavefunctions can spread out over or tunnel into a larger volume, but the spectral profiles are more sensitive to changes in dimensions that exhibit a higher degree of confinement. As a result, altering the diameter, or width, of the linear appendages initiates a more profound change than does altering the length.

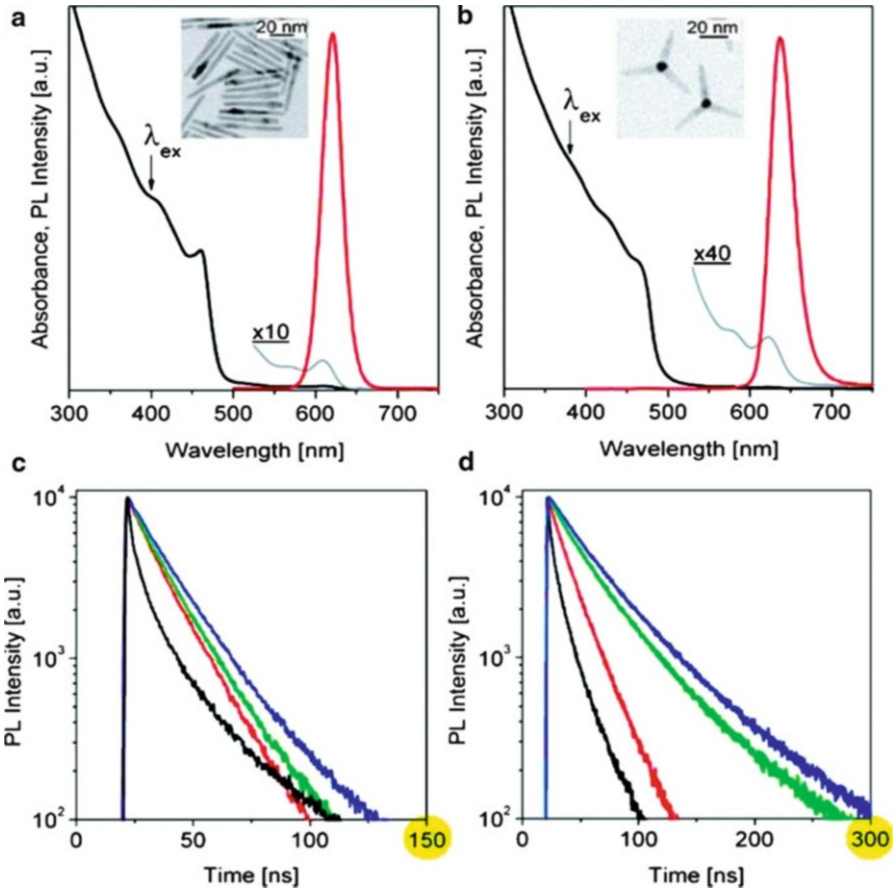

Fig. 13.7 (**a**) Absorption (*black*) and photoluminescent (*red*) spectra of 46-nm-long CdSe/CdS nanorods in toluene solution grown from 4.4-nm w-CdSe seeds. *Gray line* shows magnified absorption spectrum to elucidate the structure of the absorption onset. Absolute photoluminescent quantum efficiency of this sample was 80 %, measured at the excitation wavelength 514 nm. (**b**) Absorption (*black*) and PL (*red*) spectra of toluene solutions of CdSe/CdS nanotetrapods with 24-nm CdS legs grown from 4-nm zb-CdSe seeds. *Gray line* shows magnified absorption spectrum to emphasize structure of the absorption onset. Absolute PL quantum efficiency of this sample was 39 %, measured at the excitation wavelength 512 nm. (**c**) Fluorescence decay of 4.4-nm w-CdSe nanocrystals (*black*) and CdSe/CdS nanorods with different lengths: 12.2 nm (*red*), 24 nm (*green*), and 36 nm (*blue*). All samples were excited at 440 nm; emission was detected at the maxima of the PL spectra. (**d**) Fluorescence decay of 4.0-nm zb-CdSe nanocrystals (*black*) and CdSe/CdS nanotetrapods with arm length of 9.2 nm (*red*), 24 nm (*green*), and 38 nm (*blue*). All samples were excited at 440 nm; emission was detected at the maxima of the PL spectra (Reprinted with permission from Talapin DV, Mekis I, Götzinger S, Kornowski A, Benson O, Weller H. CdSe/ Reprinted with permission from Talapin et al. [69]. Copyright 2004 American Chemical Society.

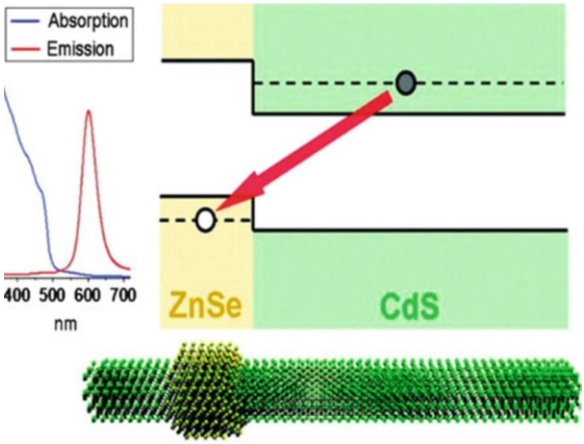

Fig. 13.8 Representation of the ZnSe/CdS type II band-edge offset and the separation of charge carriers across the interface, with electrons residing in the conduction band of CdS and holes in the valence band of ZnSe

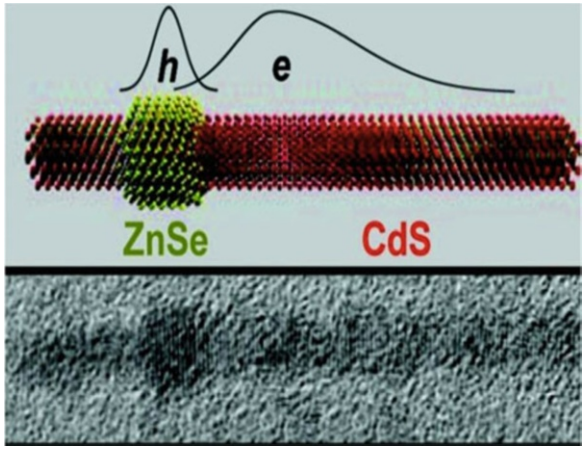

Fig. 13.9 Illustration of the domain-specific localization of electron and hole wavefunctions across the ZnSe/CdS heteronanorods (Reprinted with permission from Hewa-Kasakarage et al. [75], copyright 2009 American Chemical Society)

ZnSe/CdS (Core/Shell)-Seeded CdS Heteronanorods

ZnSe/CdS nanorods provide another example of a type II system, for which photoinduced holes are primarily localized in the ZnSe "dot" domains while electrons are delocalized along CdS "arms" (see Figs. 13.8 and 13.9) [36, 75]. These structures are fabricated in a three-step procedure, beginning with a ZnSe core, a thin shell consisting of a few monolayers of CdS, and finally a CdS nanorod "arm."

When an exciton is generated either in the core or "arm" domain of the ZnSe/CdS nanorod, the staggered band-edge alignment at the material interface leads to spatial separation of the charge carriers into different parts of the heterostructure. In spatially asymmetric nanostructures, such separation of charges could be near complete, which gives rise to unique optical properties associated with an induced electric dipole. In the case of ZnSe/CdS heteronanorods, the electron wavefunction

will spread out over the CdS domain while the hole is localized to the ZnSe component. Materials exhibiting such properties are applicable in photovoltaic technologies, where spatially separated carriers require less energy for dissociation; anisotropic light sources, where an induced electric dipole provides the capability for a high level of polarization; and optical modulators, where separation of carrier wavefunctions allows for switching of nanocrystal emission energies via quantum-confined Stark effect [75].

Figure 13.10 displays the optical properties of nanostructures after each fabrication stage involved in the synthesis of ZnSe/CdS heteronanorods. Spectral characteristics of ZnSe nanoparticles synthesized in the first reaction (Fig. 13.10a) are typical of monodisperse binary nanocrystals, recognized by a sharp absorption edge and a narrow emission bandwidth. The lingering, structureless tail, centered around 490 nm and noticeably extending into the infrared, is caused by the interaction of excitons with external media at trap states, as the surface of the nanocrystal is not optimally passivated by organic ligands at this stage. Figure 13.10, spectrum 2, demonstrates the increased contribution from trap states when the organic ligands are removed via heating, where the emission profile of unpassivated nanocrystals has lost considerable definition in its fluorescence peak.

Deposition of a thin CdS shell onto ZnSe nanocrystals results in the onset of a low-energy tail in the absorption profile (Fig. 13.10b), which extends over the visible range due to an onset of type II localization regime. This process is accompanied by quenching of type I violet emission in ZnSe nanocrystals and the appearance of a new emission feature in the visible range. This new peak originates from the radiative decay of excitons across the semiconductor heterojunction. Deep trap fluorescence associated with the original ZnSe cores can be still observed around 490 nm, as seen in Fig. 13.10d, spectrum 3, now joined by the contribution from interfacial trap states at roughly 475 nm. Together, these trap state features flank the emission peak corresponding to the spatially indirect ($1S_e$(CdS)-$1S_h$(ZnSe)) recombination in core/shell nanocrystals observed at 540 nm. As the shell increases in size, the portion of the emission spectra attributed to trap states begins to diminish (Fig. 13.10d, spectrum 4), and fluorescence lifetime continues to increase (Fig. 13.10e, trace 3).

The growth of short, 1–2-nm CdS extensions at the final stage of the synthesis leads to a near complete quenching of both deep and interfacial trap emissions, as well as continuous red-shifting of the spatially indirect fluorescence, as shown in the spectrum 5 of Fig. 13.10d. The diminishing contribution of traps to carrier relaxation for these structures is also evidenced by the increasing lifetime of the fluorescence intensity decay (Fig. 13.10e, trace 5).

Optical characteristics of high-aspect-ratio (ZnSe/CdS)/CdS heteronanorods are shown in Fig. 13.10c. Due to the delocalization of electronic wavefunctions into the increased volume of CdS, the emission of $\approx$ 100-nm heteronanorods undergoes a 10–15-nm red-shift from the peak position in short-branched (ZnSe/CdS)/CdS heterostructures (Fig. 13.10d, spectrum 5). Growth of linear CdS extensions is also accompanied by the 10–20-nm decrease in the spectral width of the emission, which is consistent with further quenching of trap state emission as well as the

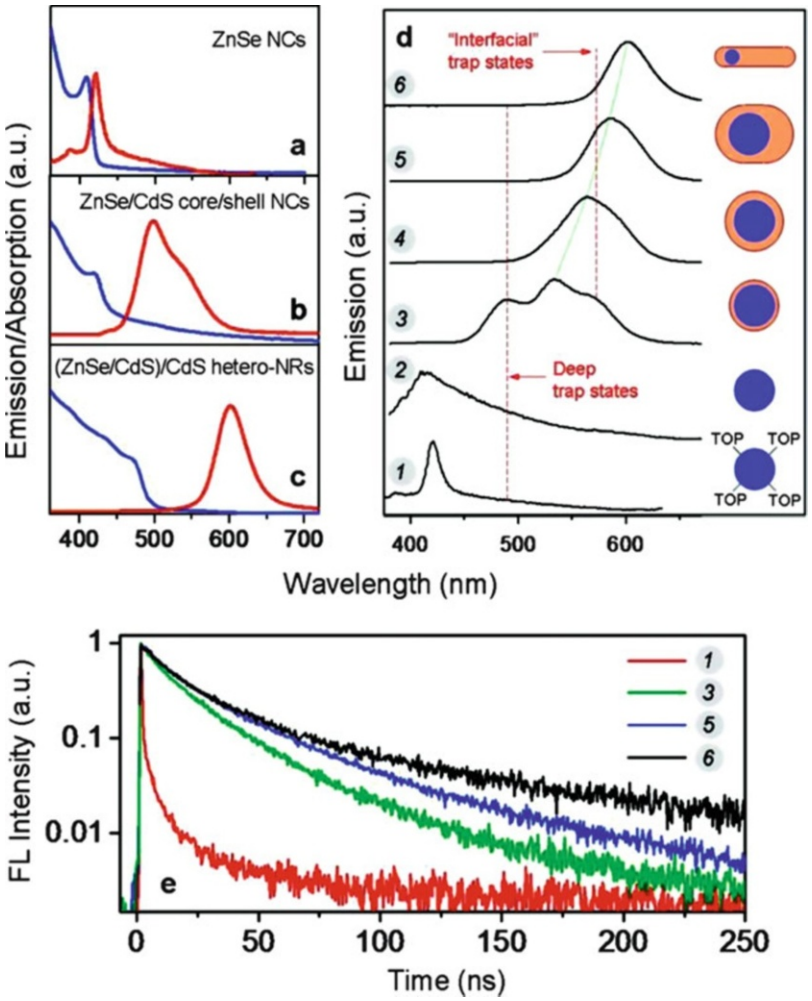

Fig. 13.10 Optical characteristics of nanocrystal and nanorod colloids. UV-vis absorption and steady-state fluorescence spectra for (**a**) 5-nm-diameter ZnSe nanocrystals; (**b**) ZnSe/CdS core/shell nanocrystals, fabricated by depositing teo to three monolayers of CdS; and (**c**) high-aspect ratio (ZnSe/CdS)/CdS heteronanorods. (**d**) Evolution of the fluorescence spectra during the three-stage synthesis, showing the trap state emission. Deep traps contribute to the emission near 490 nm as evidenced by the broad emission tail in passivated (spectrum 1) and unpassivated (spectrum 2) ZnSe nanocrystals. ZnSe/CdS core/shell nanocrystals with ca. 1 monolayer of CdS exhibit both deep and interfacial trap emission (spectrum 3). The former becomes quenched in thick-shell ZnSe/CdS nanocrystals (spectrum 4), while the latter is reduced in large-size (oblong) core/shell structures (spectrum 5) and becomes fully quenched in long (ZnSe/CdS)/CdS heteronanorods (spectrum 6). (**e**) Fluorescence intensity decay for ZnSe (*red*), thin-shell ZnSe/CdS nanocrystals (*green*), thick-shell ZnSe/CdS nanocrystals (*blue*), and (ZnSe/CdS)/CdS heteronanorods (black), measured by means of TCSPC technique (Reprinted with permission from Hewa-Kasakarage et al. [75]. Copyright 2009 American Chemical Society)

increase of CdS shell beyond the "saturation" value associated with the onset of type II localization regime.

The fluorescence intensity decay of (ZnSe/CdS)/CdS heteronanorods is shown in Fig. 13.10e, trace 6. It is expected that radiative relaxation of spatially separated excitons may exhibit unique relaxation times that arise from intrinsically different carrier decay mechanisms associated with a weak-confinement regime. Owing to a nonzero quantum yield and spatial separation of charges, fabricated heteronanorods provide a model system for testing such hypothesis. According to traces 5 and 6 in Fig. 13.10e, both short- and long-branched nanorods exhibit non-exponential radiative relaxation of excited carriers, which is usually expected of semiconductor quantum systems due to mixing of contributions from different single-exponential lifetimes corresponding to "on" and "off" blinking cycles [76]. The fluorescence lifetime of high-aspect-ratio heteronanorods appears to be longer than in short-branched heterostructures (Fig. 13.10e, traces 5 and 6), possibly the result of fewer carrier traps present at the ZnSe/CdS interface or smaller overlap between electron and hole wavefunctions brought by the delocalization of electrons in CdS. The overall character of carrier relaxation in high-aspect-ratio heteronanorods, however, appears to be similar to that of short heteronanorods or even core/shell nanocrystals, indicating that a mechanism of radiative recombination across the ZnSe/CdS heterojunction is majorly independent of the degree of charge separation.

ZnSe/CdS/ZnSe Nanobarbells and Transient Absorption Spectroscopy

In this section, we probe further into the optical properties of type II heterostructures by reviewing the time-dependent changes in the absorption spectra of ZnSe/CdS nanocomposites. To this end, the femtosecond transient absorption (TA) spectroscopy is employed to provide a more detailed picture of the ultrafast carrier dynamics in a barbell-like arrangement of ZnSe spheres and CdS nanorods [77]. In these experiments, excited state populations for both ZnSe and CdS materials were obtained through careful evaluation of measurements of the Stark effect and state-filling contributions into observed bleach recovery traces. It is reported that selective excitation of ZnSe tips results in an ultrafast transfer ($<$0.35 ps) of excited carriers into CdS domains, whereas resonant pumping of CdS portions of barbells leads to a comparatively slow injection of photoinduced holes into ZnSe domains ($\tau_h = 95$ ps). The observed interfacial electron transfer occurring under resonant pumping conditions is faster than CdSe/CdTe [26] and CdSe/CdS [27] heterostructures, regardless of the large spatial delocalization of corresponding wavefunctions across the ZnSe/CdS nanocomposite. This phenomenon, attributed to the near-epitaxial relationship between ZnSe and CdS crystalline domains, is expected due to a relatively small lattice mismatch (2.7 %) between junctioned lattices that reduces interfacial strain, thus lowering the occurrence interfacial defects.

Together, the fast spatial separation of photoinduced charges along the main axis of ZnSe/CdS barbell and the availability of both carriers for a chemical reaction with external media can be utilized for a number of optoelectronic applications.

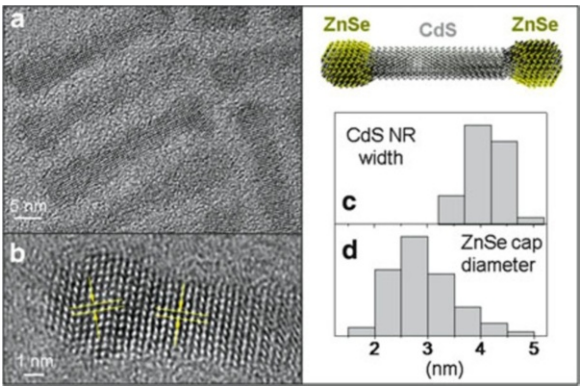

Fig. 13.11 Structural analysis of ZnSe/CdS barbells. (**a**) High-resolution transmission electron microscope (*TEM*) images of ZnSe/CdS heterostructures. (**b**) A typical ZnSe/CdS barbell showing unique directions of lattice planes for each of the material domains. (**c**) Statistical distributions of barbell widths and diameters of ZnSe tips (in (**d**)) (Reprinted with permission from Hewa-Kasakarage et al. [148]. Copyright 2010 American Chemical Society)

For instance, ZnSe/CdS is particularly well suited as a component for nanocomposites capable of photocatalytic water splitting since the electrochemical potentials of electrons and holes in ZnSe/CdS barbells straddle the H_2/H_2O and O_2/H_2O redox potentials [77, 78]. In addition, fast charge transfer between ZnSe and CdS domains can be harnessed in applications that rely on photoinduced electric dipoles to modulate the spectral response of the material, such as electroabsorption switching and modulation [79], as is also demonstrated in ZnSe/CdS nanorods exhibiting a photoinduced shift of the emission wavelength due to the quantum-confined Stark effect [75]. In the case of ZnSe/CdS barbells, the observed sub-picosecond electron transfer can enable switching rates of up to 1–2 THz, which exceed the present day characteristics of Ge-based electroabsorption modulators by an order of a magnitude [80].

Motion of excitons in the ZnSe and CdS domains of a barbell structure is confined in three and two dimensions, respectively, with a corresponding degree of confinement determined primarily by the size of ZnSe tips and widths of CdS nanorods. Accurate determination of these geometric parameters prior to spectroscopic characterization of the system is thus critical for establishing expected carrier energies in both materials. Average sizes of ZnSe and CdS domains are calculated using data from high-resolution (HR) transmission electron microscopy (TEM) measurements. Figure 13.11a and b displays typical HR-TEM images of several ZnSe/CdS heterostructures, where the barbell-like arrangement of materials can be identified by the characteristic direction of lattice planes in ZnSe tips compared to those in the CdS nanorods. Statistical analysis of approximately one hundred of such barbells shows a 5.7-nm increase of length along the 001 axis in comparison with the CdS nanorods used for seeding the growth of ZnSe, and the average tip size is 2.89 nm while the average width of barbells is roughly 4.1 nm.

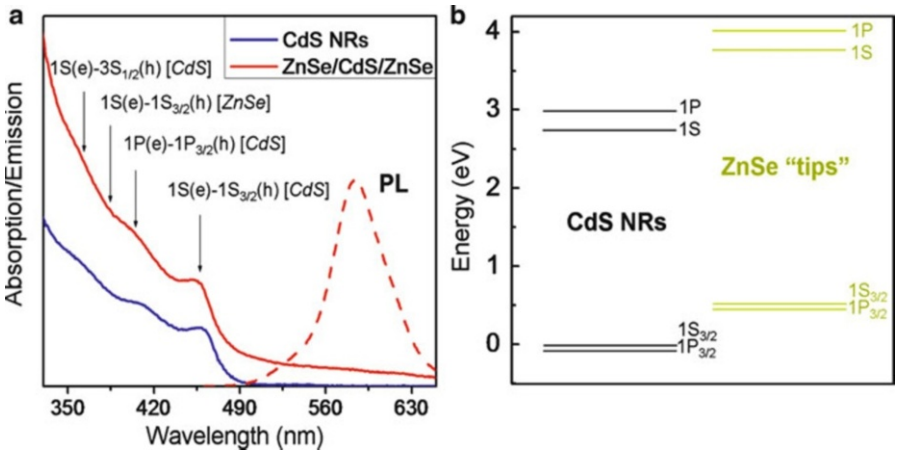

Fig. 13.12 Determination of excited state energies in ZnSe/CdS heterostructures. (**a**) Steady-state absorption and emission ($\lambda_{excitation} = 420$ nm) spectra of ZnSe/CdS barbells (*red*) and CdS nanorods (*blue*). Four lowest energy excited state transitions are identified in the absorption spectra. (**b**) Calculated excited state energies for ZnSe/CdS heterostructures comprising 4.1-nm-wide CdS nanorods and 2.85-nm ZnSe tips (Reprinted with permission from Hewa-Kasakarage et al. [148], copyright 2010 American Chemical Society)

Steady-state absorption measurements confirm the narrow distribution of barbell widths, inferred from the well-pronounced excitonic features related to the 1S(e)-$1S_{3/2}$(h) and 1P(e)-$1P_{3/2}$(h) transitions in CdS (Fig. 13.12a). The band-edge absorption in the ZnSe portion of barbells, which spectral position is expected to peak [81] at 384 nm, is not recognizable in this profile possibly due to the relatively small composition of ZnSe in the overall volume of the nanocomposite, though evidence of carrier absorption across the band gap of ZnSe is still provided by the observable change in the slope of the absorption curve below 380 nm and the apparent bleaching of the band-edge transition in time-resolved transient absorption measurements (Fig. 13.13c).

The relative alignment of $n = 1$ excited state energies in each component of the ZnSe/CdS heterostructure is shown in Fig. 13.12b. Excited electrons find the minimum of the conduction band in the 1S(e) state of CdS nanorods, which is positioned 0.80 eV lower than the 1S(e) energy of ZnSe tips. Meanwhile, photoinduced holes will localize in the $1S_{3/2}$(h) level of the ZnSe domain, which lies 0.53 eV above the valence band edge of CdS nanorods. As expected, the energy of the spatially indirect transition associated with the decay of carriers across the ZnSe/CdS interface is lower than the band gap of either ZnSe or CdS materials, accounting for the red-shifted emission of ZnSe/CdS heterostructures ($\hbar\omega = 2.1$ eV), as seen in Fig. 13.12a.

The photoinduced filling of excited states in nanocrystals leads to bleaching of interband optical transitions, such that absorption changes are proportional to the number of excited carriers:

$$\Delta A(\hbar\omega) = -\sum_i A_{0,i}(\hbar\omega - \hbar\omega_i)(n_i^e + n_i^h) \tag{13.1}$$

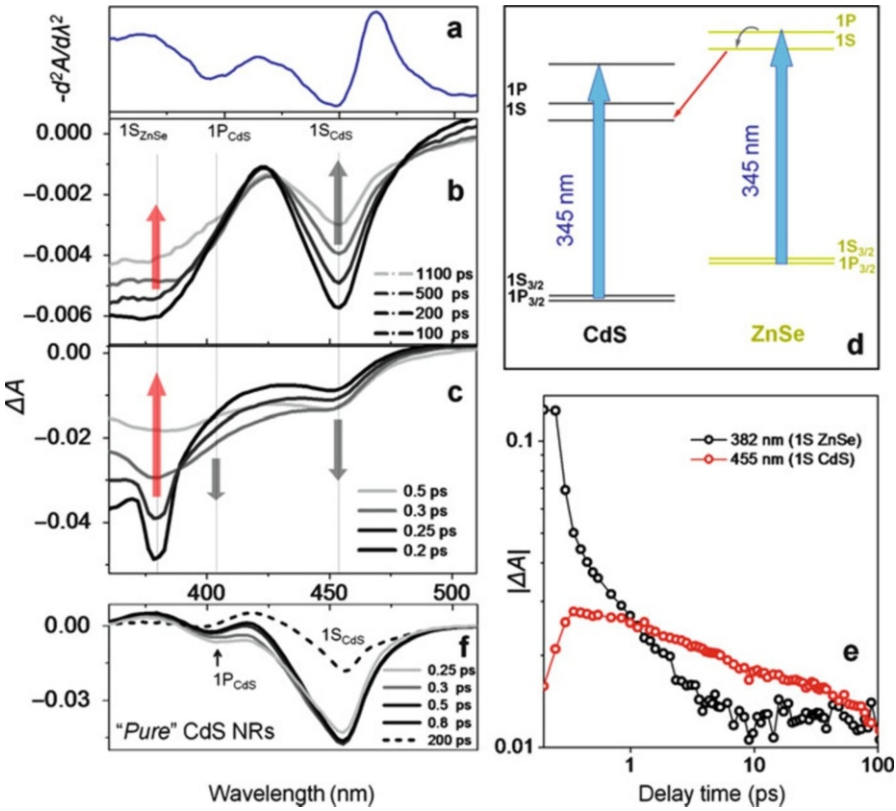

Fig. 13.13 Transient absorption measurements of ZnSe/CdS barbells resulting from resonant excitation of ZnSe domains ($\lambda_{pump} = 345$ nm). (**a**) Second derivative of the absorption profile. (**b**) and (**c**) Transient absorption spectra, $\Delta A = A(\text{pump + probe})\text{-}A(\text{probe})$, corresponding to long (**b**) and short (**c**) delay times. (**d**) Energy diagram of electronic states showing the maximum energy of pump photons (*blue arrows*) under resonant excitation of ZnSe domains. (**e**). Temporal dynamics of the transient absorption bleach recovery measured for band-edge excitons in CdS (*red*) and ZnSe (*black*) materials. (**f**). Transient absorption spectra of pure CdS nanorods ($\lambda_{pump} = 345$ nm) (Reprinted with permission from Hewa-Kasakarage et al. [148]. Copyright 2010 American Chemical Society)

where $A_{0,i}$ is an absorption profile of the ith transition and n_i^e and n_i^h are occupation numbers of electron and hole states involved in the transition. Since the effective masses of holes in CdS and ZnSe materials are approximately four to five times greater than those of electrons, their room-temperature occupation probabilities are small. As a result, the state-filling-induced absorption changes are dominated by electrons [82]. The contribution of holes into bleaching is further reduced due to exchange interaction that splits the 1S exciton into two different hole states, [83, 84]

such that the higher energy absorption transition states stay unoccupied until the lower energy hole state is completely filled, which occurs only when $\langle N \rangle >> 1$.

Another possible contribution into bleaching of nanocrystal optical transitions is due to local fields that alter transient spectra via Stark effect [85]. This leads to a spectral shift of absorbing transitions as well as changes in the corresponding oscillation strengths resulting from modifications in selection rules. In systems that produce a spatial separation of charges, such as the barbell nanostructures investigated here and type II systems in general, the contribution of the Stark effect can be particularly significant and its evaluation is necessary to properly assess the state-filling dynamics. As a semi-empirical approach to predicting the spectral changes in the transient absorption spectra of ZnSe/CdS barbells resulting from the Stark effect, a formalism [86, 87] is implemented that relates the effect of carrier-induced local fields in semiconductor nanocrystals with a repulsion between proximal transitions, such that the Stark effect contribution into ΔA can be modeled by the second derivative of the absorption profile.

The transient absorption spectroscopy of hexane-suspended ZnSe/CdS barbells is analyzed using two excitation regimes that correspond to the resonant pumping of the $n = 1$ transitions in CdS and ZnSe domains of the structure. Transient absorption spectra resulting from the quasi-resonant excitation of ZnSe tips are analyzed in Fig. 13.14. The wavelength of the pump beam, in this case, was set to 345 nm, which allows excitation across the two lowest energy transitions in the ZnSe domain: 1S(e)-$1S_{3/2}$(h) and 1P(e)-$1P_{3/2}$(h), denoted as $1S_{ZnSe}$ and $1P_{ZnSe}$, respectively, as well as three lowest transitions in CdS nanorods: 1S(e)-$1S_{3/2}$(h), 1P(e)-$1P_{3/2}$(h), and 1S(e)-$3S_{1/2}$(h), as shown in the energy diagram (Fig. 13.14d). Bleaching of band-edge transitions in both materials was observed as quickly as 200 fs after excitation (Fig. 13.14c) with spectral positions of bleach signals near the expected energies of $1S_{ZnSe}$ and $1S_{CdS}$ excitons (Fig. 13.13).

The modification of the bleach signals in the transient absorption induced by the Stark effect is estimated by comparing the second derivative of the absorption spectra (Fig. 13.14a) with the short-time transient spectra (Fig. 13.14c), revealing what initially seems to be a similarity in corresponding slopes both in the case of CdS (450–465 nm) and ZnSe (385–405 nm) transitions. However, if the short-time bleach has a significant contribution from the local fields, then the two maxima of d^2A/dt^2 would coincide with the photoinduced absorption ($\Delta A > 0$) in the transient absorption spectra, which is not observed here, as ΔA remains negative throughout the entire spectral window of the probe beam. Furthermore, the initial modification of transition energies attributed to the Stark effect typically diminishes within a few picoseconds, causing a noticeable shift of the bleach minima, yet spectral positions of $1S_{CdS}$ (450–465 nm) and $1S_{ZnSe}$ (370–395 nm) transitions are nearly constant within the entire nanosecond delay range (Fig. 13.14b). Based upon these observations, it is concluded that the influence of the Stark effect on transient absorption spectra for this nanocomposite is negligible, and the observed transient absorption bleach is attributed primarily to state filling in ZnSe and CdS domains.

Selective excitation of carriers into the CdS domain of ZnSe/CdS barbells is performed using 420-nm pump pulses, for which photon energies fall below the

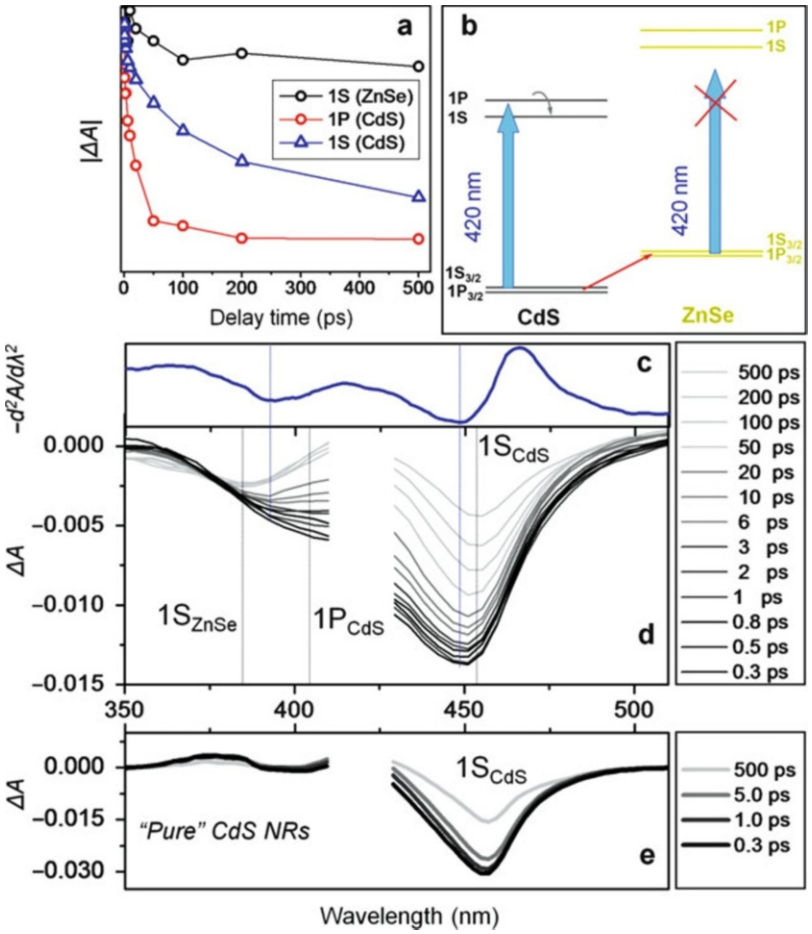

Fig. 13.14 Transient absorption measurements of ZnSe/CdS barbells resulting from selective excitation of CdS domains ($\lambda_{pump} = 420$ nm). (**a**) Temporal dynamics of the transient absorption bleach recovery for 1S(e)-$1S_{3/2}$(h) excitons in ZnSe (*black*), 1P(e)-$1P_{3/2}$(h) excitons in CdS (*red*), and 1S(e)-$1S_{3/2}$(h) excitons in CdS (*blue*). (**b**). Energy diagram of electronic states showing the maximum energy of pump photons (*blue arrows*) under selective excitation of CdS domains. Note that the average photon energy is not sufficient to induce absorption in ZnSe. (**c**) Second derivative of the absorption profile. (**d**) Transient absorption spectra of ZnSe/CdS barbells resulting from $\lambda_{pump} = 420$ nm excitation pulses. (**e**) Transient absorption spectra of pure CdS nanorods ($\lambda_{pump} = 420$ nm) (Reprinted with permission from Hewa-Kasakarage et al. [148], copyright 2010 American Chemical Society)

band gap of ZnSe tips. According to the energy diagram in Fig. 13.14b, these photons can only be absorbed through the excitation of 1S and 1P excitonic transitions in CdS nanorods, while excited states of the ZnSe component remain essentially unoccupied. Experimental evidence of the selective carrier injection into CdS portion of barbells is seen in the transient absorption spectra, where the

early-time bleach occurs primarily in the spectral range of the lower energy $1S_{CdS}$ transition. In addition to strong optical bleaching in CdS, a weak negative signal was also observed in the wavelength range of the $1S_{ZnSe}$ transition, which is energetically positioned 0.3 eV above those of excitation photons (Fig. 13.14d). Such above-the-threshold bleaching was attributed to the energy-independent effect of local fields (Stark effect) and not the state filling, as can be inferred by nearly identical behavior of the short-time transient absorption curve and the second derivative of the absorption profile (Fig. 13.14c). For instance, the effect of local fields on $1S_{ZnSe}$ and $1S_{CdS}$ bleaching signals can be easily identified in early time traces ($\Delta t < 1$ ps) as spectral shifts of both peaks by several nanometers from their longer-delay position ($\Delta t > 100$ ps), as indicated by the offsets of blue and gray lines in Fig. 13.14d. A sizable contribution of Stark effect into transient absorption is also identified by the remarkable similarity between ΔA ($\Delta t < 1$ ps) and $d^2A/d\lambda^2$ slopes throughout the most of the spectral range. Therefore, experimental TA data provides strong evidence for photoinduced charge transfer between the ZnSe and CdS nanocrystalline domains, which can be controllably performed in either direction by modulating the excitation wavelength, such that the resonant excitation of carriers in the ZnSe material leads to 350-fs injection of electrons into CdS, and the excitation of carriers in the CdS portion of barbells results in a slower transfer of holes into ZnSe.

5.2 Semiconductor-Metal Nanocomposites

Bulk heterojunctions of metal and semiconductor materials have long been of interest to fundamental science and device engineering due to the unique interaction of respective domains through the formation of the space-charge region, [88] which gives rise to numerous technological applications including Schottky barrier solar cells, solid-state lasers [89], light-emitting diodes [90], and field-effect transistors [91]. Recent progress in synthetic methodology of nanocomposite fabrication has extended the utility of metal–semiconductor heterojunctions to the nano realm, which has given rise to new opportunities for designing multifunctional materials with properties that cannot be obtained in the bulk phase. These hybrid nanocrystals attribute their properties not only to the size, shape, and configuration of the structure as a whole but also to the unique interaction of excitons in semiconductor materials and the characteristic surface plasmon resonance effect of the metal nanoparticles. These synergistic effects allow the nanostructures to function in ways well beyond their bulk and isolated individual forms [31, 46, 92–98]. Owing to these advances, a wide array of nanocomposite morphologies, including metal-core/semiconductor-shell heterostructures, [42, 99, 100] metal-tipped semiconductor nanocrystals (NCs), [46, 49, 101–107] and organically and non-epitaxially [99, 108, 109] coupled metal–semiconductor composites have been proposed in the past decade for manipulating energy at the nanoscale with potential application of these nanomaterials in areas of photovoltaics and solar fuel production, [110] lasers, [111] and Schottky detectors [112]. Other possible applications of

metal–semiconductor nanocomposites also include nanoscale wiring. For instance, semiconductor domains decorated with metal tips on both sides have been proposed for use as electrical interconnects in nanoscale circuitry [113], while semiconductors capped with a metal domain on one side can be harnessed as a charge separating unit in photovoltaic [114], or photocatalytic [74] composites.

Of a particular interest is a fundamental interaction between semiconductor excitons and surface plasmons of metal nanoparticles, which results from the modification of the exciton dipole moment due to local electromagnetic modes of surface plasmon [115, 116]. This interaction is enabled by the nanoscopic nature of both material domains and has a unique effect on optoelectronic properties of a composite metal–semiconductor system, which has been shown to dramatically alter the energy flow that occurs across metal–semiconductor junctions. Plasmon resonance is an energetic effect arising from oscillations of conduction electrons in metal nanoparticles due to interaction with the undulating electric field of light. As the frequency of light approaches a resonant value, the amount of light absorbed by the metal nanoparticle increases along with the amplitude of the electron oscillations, until the maximum magnitude is reached at the resonance frequency. The latter depends both on the size and composition of the metal nanoparticle as well as the dielectric constant of the surrounding medium. The surface plasmons of the metal domain interact with the excitons of the semiconductor by modifying the dipole moment of the exciton with its short-range electromagnetic modes [99, 115]. This interaction dramatically changes the flow of energy across the metal–semiconductor interface, which in turn alters the optoelectronic properties of the nanostructure. As an example, the generation of a plasmon radiative field in metals, caused by resonant oscillations of low-energy conduction electrons, can strongly influence the dynamics of excitons in conjoined semiconductor nanocrystals via two unique interaction mechanisms: plasmon–exciton energy transfer and modification of the local radiation field in semiconductor domains.

Exciton–plasmon interactions in the weak coupling regime are characterized by the presence of a substantial potential barrier at the interface of semiconductor and metal components and are achieved by implementing spacer molecules for non-epitaxial domain coupling. For these composites, the emission intensity in semiconductor domains may undergo an increase [117–124] due to the plasmon-induced enhancement of semiconductor radiative rates, [125, 126] an effect that shows promise in improving the process of light amplification in lasers [90, 127–130]. Likewise, the plasmon-induced enhancement of the electric field in semiconductor domains has been documented to increase the absorption cross section of semiconductor nanocrystals, [131, 132] thus promoting the development of light-concentrating nanocomposites in an effort to aid the energy harvesting mechanism in photovoltaic and photocatalytic applications [110, 132]. In addition to intensity enhancement, spectral modification of the semiconductor emission in semiconductor–metal composites has also been utilized for sensing target proteins attached to the linker moiety in Au/CdTe assemblies [133]. Finally, a weak exciton–plasmon interaction achieved through non-epitaxial coupling of metal and semiconductor domains using a core/shell morphology has been employed for controlling the spin

of Au nanoparticles [108], with a potential application of this phenomenon in quantum information and spintronics [134–136].

A particularly strong coupling between plasmons and excitons can be realized when metal and semiconductor domains are coupled directly, without spacing moiety in-between. The potential barrier between adjacent materials in this case becomes sufficiently small to allow inter-domain charge transfer, as well as a mixing of electronic states at the metal–semiconductor interface. Additionally, the enhanced electromagnetic field attributed to the metal plasmons in a strong coupling mode may procure further modifications to the carrier dynamics associated with shared oscillations of the excitation energy between the metal and semiconductor domains. This strong coupling interaction with the shared oscillations is known as Rabi oscillations [137]. Electronic interactions such as these alter the overall optoelectronic properties of hybrid nanocomposites, imparting the structure as a whole with significantly different effects and function than its isolated parts and giving metal–semiconductor hybrid systems a more diverse assortment of spectroscopic and emission characteristics than their previously analyzed semiconductor–semiconductor counterparts.

The spatial proximity of semiconductor and metal domains (so-called strong coupling regime) can significantly alter the optical characteristics displayed by the nanocomposite. For instance, the fluorescence of the semiconductor domain can either undergo suppression [138], which is the case in many directly coupled systems; enhancement [139], which commonly occurs when the two domains are separated by a spacer; or a partial suppression. The fluorescence quenching in metal–semiconductor nanocomposites can be attributed to the transfer of the exciton energy into the metal domain via FRET mechanism. Another possible reason for the suppression of fluorescence in metal–semiconductor composites is the ultrafast transfer of photoinduced charges from semiconductor nanocrystals to a metal. This type of nonradiative decay is common in materials such as Ag/ZnO and Au/CdS tipped nanorods or Au/PbS and Au/PbSe hybrid dimers and core/shell morphologies.

Fluorescence enhancement is observed less often than a complete nullification of emission, as these effects require more complicated architectures to be created [139]. Ordinarily, enhancement is observed when the metal–semiconductor domains are within close spatial proximity of each other while separated by a large potential barrier, effectively increasing the absorbance cross section without opening up nonradiative decay pathways, as seen in systems of Au nanoparticles chemically linked to CdTe nanowires [109]. Intermediate effects occur when precise morphological conditions are met, so the energy of the plasmons can instead be partially transferred to the semiconductor domain. For example, CdS nanorods conjoined with Au nanoparticles are known to completely quench the fluorescence, while Au nanocrystals with partial CdS shells grown over the core yield an intermediate enhancement.

The absorbance profile of the semiconductor nanocrystal component can likewise undergo significant changes upon coupling of the metal domain. The excitonic features of the semiconductor may experience broaderning [34, 139] rendering

the structural features of its spectrum less defined. While the individual contributions of each structural domain still greatly influences the shape of the spectrum, the overall spectral characteristics of metal–semiconductor nanocomposites are typically a nonlinear combination of its separate parts. This is reasoned to arise from mixing of electronic states between the two dissimilar materials, which modifies the density of states and alters the absorbance profile. It has also been observed that the degree in which the spectroscopic properties of a semiconductor are changed is strongly dependent on the size and number of metal domains.

5.2.1 CdS/Au Nanocomposites

Recently, Au/CdS and Au/CdSe heterostructures comprising gold domains grown onto cadmium chalcogenide semiconductor nanorods have emerged as a model system for studying the properties of metal–semiconductor nanocomposites [49, 101, 103, 104, 107]. Besides being a system of choice for advancing synthetic protocols and investigating plasmon–exciton interactions, these nanocomposites have been considered for applications in areas of solution-processed solar cells [140, 141] and nanoscale wiring [113]. For instance, it was demonstrated that CdSe nanorods capped with gold on both ends lead to a 10^5-fold increase in carrier conductivity as compared to pristine CdSe nanorods placed over metal contacts [113], which exemplifies the potential of these heterostructures as nanoscale electrical interconnects. On the other hand, CdS nanorods capped with gold at a single end can be harnessed as charge-separating units in photocatalytic and photovoltaic devices [114].

The effect of metal domains on the properties of semiconductor counterparts is best illustrated through the evolution of the absorption features during the synthesis of metal–semiconductor nanocomposites. The growth of small-diameter metal domains onto nanocrystals or nanorods is typically performed via reduction of $AuCl_3$ salts in a mixture of toluene, dodecyldimethylammonium bromide (DDAB), and dodecylamine (DDA) [46]. To promote the growth of large-size metal tips, either light-[104] or thermal-assisted [106] methods can be used. The latter approach relies on temperature controlled reduction of $AuCl_3$ on the surface of semiconductor nanorods in the presence of oleylamine. At roughly 60 °C, the threshold energy is reached for nucleation of Au particles, which initiate growth by attaching an ion to the semiconductor at defects in the crystal lattice. This creates a nucleation site allowing additional ions aggregate, eventually forming composite structures comprising small metal tips either ends with clusters of gold nucleated along the length of the rod (Fig. 13.17a). As the temperature is slowly increased, it becomes energetically unfavorable for the gold aggregates to remain along the linear semiconductor domain, and they begin to redissolve into solution. Through this process of Oswald ripening, the gold is transferred strictly to either end of the nanorod. Further controlled increase of the temperature continues to alter the energetics, now rendering the asymmetric forms of the nanocomposite.

The absorbance profile of metal–semiconductor nanocomposites comprising CdS nanorods coupled to Au domains grown via the aforementioned thermal-assisted approach is shown in Fig. 13.15. The spatial confinement of optical

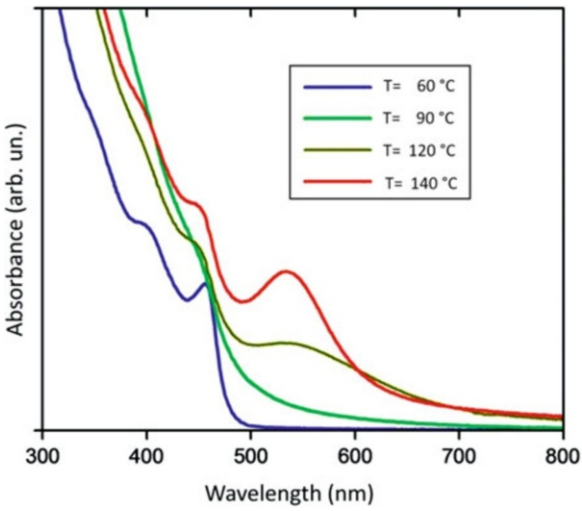

Fig. 13.15 Absorbance of Au/CdS nanocomposites of temperature-dependent morphologies (Reprinted with permission from Khon et al. [106]. Copyright 2010 American Chemical Society)

excitations in the transverse direction of CdS rods gives rise to a characteristic excitonic edge around 465 nm, which corresponds to the lowest energy transition, $1S(e)\text{-}1S_{3/2}(h)$, in these nanostructures [142]. The sharpness of the absorption edge in Fig. 13.15 confirms a narrow dispersion of nanorod widths, which agrees well with corresponding statistical distribution obtained from TEM images of these structures (Fig. 13.16a). The absorption spectra of isolated Au nanoparticles are examined in Fig. 13.18a. Since the excitation of surface plasmons in metals is a resonant process, its frequency is dependent on the composition, size, and shape of metal nanoparticles, as well as their dielectric environment. Changes in optical properties of Au/CdS nanocomposites during the growth of Au domains are summarized in Fig. 13.15. At $T = 90\ ^\circ C$, the absorption profile of Au/CdS nanoparticles exhibits noticeable changes from that of pure CdS nanorods, with the main difference occurring in the wavelength range above $\lambda = 550$ nm, where the absorption of heterostructures is increased. This red tail is attributed to the contribution from interfacial trap states as well as to optical transitions in small-size gold clusters forming on the surface of CdS nanorods. The disappearance of the excitonic feature in CdS NRs at this stage is attributed to the delocalization of carriers into small gold clusters and oleate complexes that form on the semiconductor surface. Spectral changes occurring during the initial heating of the mixture are accompanied by the visible change of the solution color from yellow to light brown, while further heating of the flask to above 100 °C results in additional darkening of the solution and correlated increase in the amplitude of the absorption tail (for $\lambda > 500$ nm). At this stage of the reaction, the average size of the Au tip reaches 4 nm, giving rise to a small absorption feature at $\lambda = 550$ nm, corresponding to the surface plasmon resonance in Au nanoparticles [143–145].

We now consider a more detailed analysis employing femtosecond transient absorption spectroscopy to investigate the dynamics of exciton–plasmon interaction in epitaxial composites of Au and CdS domains exhibiting strong domain

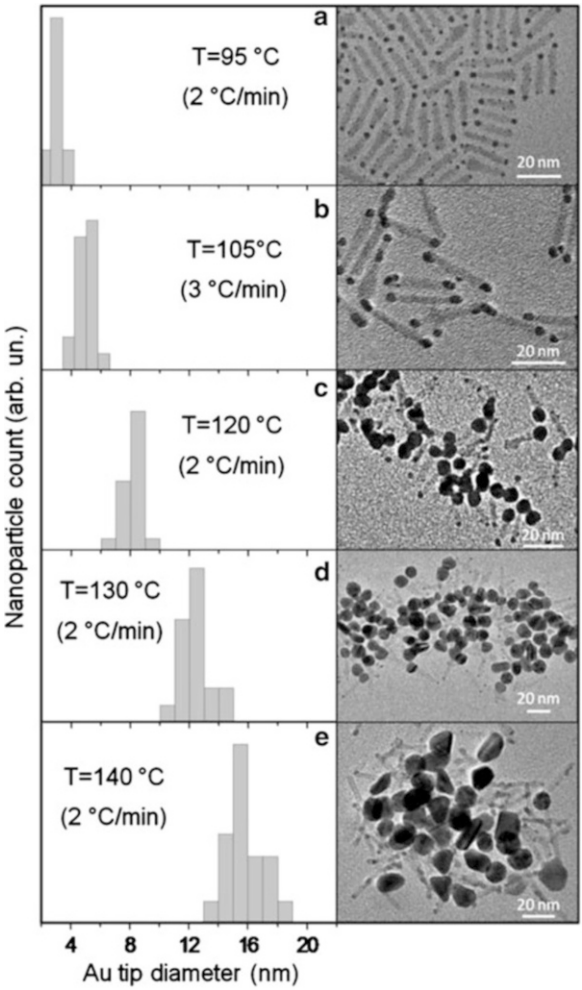

Fig. 13.16 Histogram (*left*) and TEM (*right*) of Au/CdS nanocomposites grown at five different temperatures. Average Au domain sizes are (**a**) d = 3.15 nm, (**b**) d = 4.87, (**c**) d = 8.7 nm, (**d**) d = 12.6 nm, and (**e**) d = 15.67 nm (Reprinted with permission from Khon et al. [106]. Copyright 2010 American Chemical Society)

coupling [138]. First, the steady-state and time-resolved optical properties of isolated Au and CdS nanocrystals are reexamined in Fig. 13.17. The absorbance of CdS nanorods (Fig. 13.17c) shows a characteristic excitonic edge at 465 nm, corresponding to the lowest energy 1S(e)-1$S_{3/2}$(h) transition in these structures.

The chirp-corrected transient absorption spectra (Fig. 13.17d), resulting from the excitation of CdS nanorods with 120-fs laser pulses (λ_{exc} = 340 nm), show an expected dominant bleaching associated with higher probability 1S(e)-1$S_{3/2}$(h) transitions as well as a lower magnitude bleaching corresponding to higher energy excitations between 1P(e)-1$P_{3/2}$(h) states. Spectral distortion due to the Shark effect was not observed in these measurements due to relatively low excitation intensities, corresponding to a linear power dependence regime. A negligible contribution of the Stark effect into the observed bleach dynamics is also consistent with the

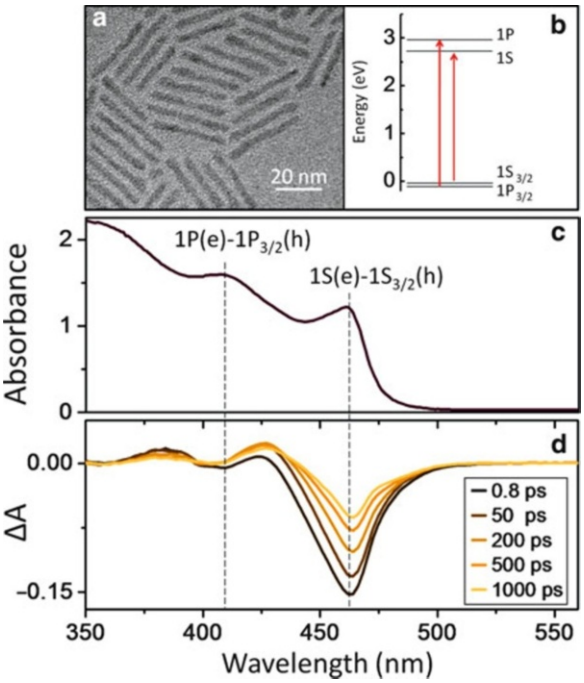

Fig. 13.17 (**a**) TEM image of CdS nanorods used for seeding the growth of Au domains. (**b**) Energy diagram showing the two lowest energy transitions in CdS NRs, corresponding to the excitation of 1S(e)-$1S_{3/2}$(h) and 1P(e)-$1P_{3/2}$(h) excitons, distinguishable in the absorbance spectra of CdS NRs (**c**), as the two broad-range peaks. (**d**). Temporal changes in the absorbance of CdS NRs induced by 340-nm excitation pulses. The negative signal around $\lambda \approx 465$ nm, known as spectral bleach, is produced by the excitation of 1S(e)$1S_{3/2}$(h) transitions, while a smaller negative signal at $\lambda \approx 410$ nm corresponds to the formation of 1P(e)$1P_{3/2}$(h) excitons (Reprinted with permission Khon et al. [138]. Copyright 2011 American Chemical Society)

absence of a positive transient absorption signal at early probe times ($\tau < 1$ ps). The observed changes in the absorption of CdS nanocrystals (ΔA) are chiefly the result of photoinduced electrons, as anticipated due to comparatively low effective masses of these carriers in bulk CdS [146, 147] and high degeneracy of hole states in CdS nanocrystals. The restoration of the 1S(e)-$1S_{3/2}$(h) bleach is achieved via both radiative decay and the trapping of excited carriers on nanorod surfaces, where approximately half of the initial carrier population in the 1S(e) excited state is recovered after 300 ps [148].

The absorption spectra of isolated Au nanoparticles are examined in Fig. 13.18. As a result of the resonant nature of surface plasmons, the frequency is dependent on the composition, size, and shape of metal nanoparticles, as well as their dielectric environment. To gain a better understanding of how the size of Au nanoparticles affects the transient and steady-state absorption of surface plasmons, samples consisting of three different Au nanoparticle diameters are compared. Furthermore, the Au nanoparticle diameters for these measurements are chosen to

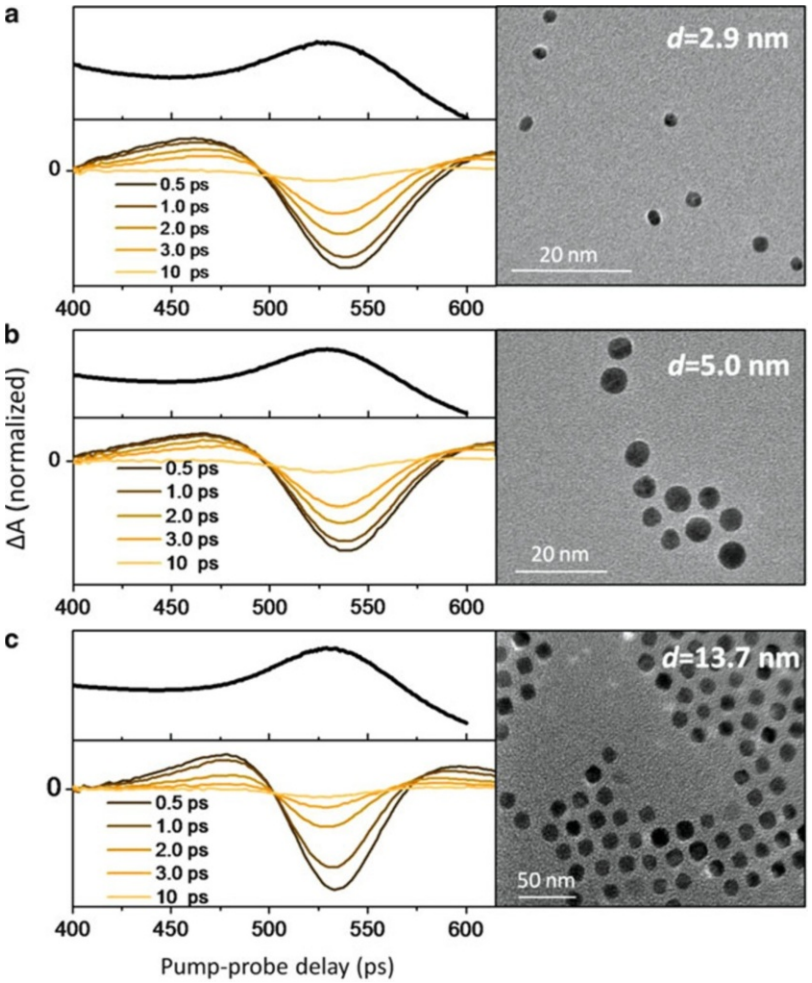

Fig. 13.18 Steady-state and transient absorption spectra of isolated Au domains, corresponding to three different nanoparticle sizes: (**a**) 2.9 nm, (**b**) 5.0 nm, and (**c**) 13.7 nm (Reprinted with permission Khon et al. [138]. Copyright 2011 American Chemical Society)

correspond with the size range of the Au domains in the heteroepitaxial Au/CdS nanocomposites soon to be examined. According to Fig. 13.18, plasmon resonance occurs in each of the three samples of isolated Au nanoparticles, observed as a broad-range absorption peak in the steady-state spectra with corresponding maxima in the vicinity of 530 nm. A moderate variation in the spectral position of the plasmon resonance between the individual measurements is consistent with the size-dependent characteristics of plasma oscillations according to Mie theory [149].

The transient absorption spectra ($\lambda_{exc} = 400$ nm) attributed to isolated Au nanocrystals of respective diameters show a pronounced bleach correlated to the

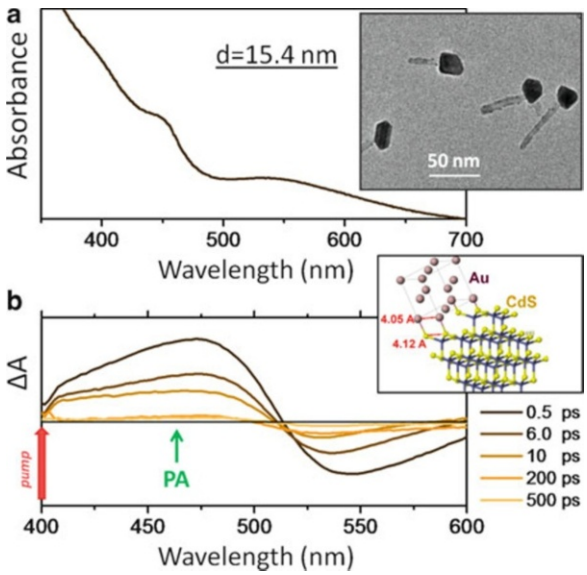

Fig. 13.19 (**a**) Steady-state absorption of Au/CdS heterostructures comprising 15.7-nm Au domains. A representative TEM image is shown in the *insert*. (**b**) Transient absorption spectra of 15.7-nm-Au/CdS nanocomposites resulting from the excitation at $\lambda = 400$ nm with 120 fs pump pulses. The recovery of ΔA shows an expected plasmonic feature, which resembles the corresponding TA dynamics of isolated Au nanoparticles. Surprisingly, bleaching of lowest energy excitons in CdS domains is not observed for any pump-probe delay (Reprinted with permission Khon et al. [138]. Copyright 2011 American Chemical Society)

steady-state absorption maxima. This negative ΔA signal in the transient absorption spectra of isolated Au nanoparticles has been previously ascribed to the excitation-induced broadening of the plasmon peak, which causes the transient absorption spectra to form a characteristic valley at the plasmon wavelength flanked by the two positive low amplitude peaks [150, 151]. Such broadening of the plasmon absorbance results from higher order multipole plasma oscillations (e.g., quadrapole) in Au nanoparticles induced by the excitation pulse. Notably, the central dip in the transient spectra is observed for all investigated gold samples, which further confirms the presence of resonant excited carrier oscillations in these nanoparticles.

To study the optical characteristics of exciton–plasmon interactions in Au/CdS composites, gold domains representing different diameters were grown directly onto colloidal CdS nanorods. To begin the assessment of the charge carrier dynamics, matchstick shaped Au/CdS nanocomposites comprising a large-diameter Au domain ($d = 15.4$ nm) were analyzed first (see Fig. 13.19). In order to achieve an efficient excitation of carriers in both domains of the heterostructure, a 400-nm excitation pulse is utilized, whereby delivering sufficient photon energy for the simultaneous excitation of 1S excitons in CdS ($\lambda = 465$ nm) and plasmons in Au domains ($\lambda = 530$ nm).

The transient absorption spectra of Au/CdS matchsticks in Fig. 13.19b shows spectrally broad bleaching of the absorption profile around $\lambda = 540$ nm, corresponding to plasmon oscillations in Au domains (note that *x*-scales in (a) and (b) are different). The magnitude of this bleach reaches its maximum in less than 500 fs, driven primarily by excitations of hot carriers and simultaneous fast cooling of the nonequilibrium carrier population via electron–electron interaction and subsequently recovers to $\Delta A(\lambda) = 0$ in 500 ps. While the observed plasmon bleaching kinetics are in agreement with the transient absorption spectra of isolated Au nanoparticles, there is now no evidence of bleaching at 465 nm, which would be associated with the formation of excitons in the CdS domain of the heterostructure. In fact, contrary to the transient absorption profile of pure CdS nanorods, which show a well-defined $1S(e)\text{-}1S_{3/2}(h)$ bleach ($\Delta A/A = -0.15$), the amplitude of Au/CdS nanocomposites in the same wavelength range is positive (green arrow in Fig. 13.19b) demonstrating a photodarkening effect, rather than bleaching.

The lack of excitonic features corresponding to $1S(e)\text{-}1S_{3/2}(h)$ transitions in Au/CdS composites can explain the regularly observed quenching of fluorescence emission in semiconductor domains [46, 152–155] However, a generally accepted explanation ascribing the origin of this fluorescence quenching in semiconductor domains to the photoinduced transfer of 1S(e) electrons into Au does not seem compelling considering the full suppression of the CdS bleach. If electron transfer was the dominant process depleting the population of 1S(e) states in CdS, a significant portion of excited electrons would still be present in the 1S(e) state after 500 fs, as the interfacial transfer rate of carriers is generally slow enough to be observed using transient absorption spectroscopy ($\tau(e) > 350$ fs, $\tau(h) > 650$ fs) [148, 156–159] Furthermore, electron transfer processes alone cannot account for the appearance of a positive transient absorption signal spanning such a broad wavelength range (400–520 nm), which is not present in the transient absorption spectra of isolated Au and CdS domains. The decay of the positive spectral feature provides hints as to the nature of the processes underpinning the carrier dynamics in Au/CdS nanocomposites, as the slow recovery (>100 ps) strongly suggests a contribution from the photoinduced absorption of excited carriers either in the Au or CdS domain.

Overall, the observed transient absorption spectra of Au/CdS composites comprising large-diameter gold domain (Fig. 13.19) are fundamentally different from those of its constituent isolated Au and CdS nanoparticles, exemplified both by the replacement of a bleaching signal in the semiconductor component with photoinduced absorption and the relatively weak bleaching of the surface plasmon feature in Au. To acquire a more informed understanding of the origin of this complex carrier dynamic, Au/CdS heterostructures constructed of smaller size Au domains are examined next.

Figure 13.20 shows the steady-state and transient absorption spectra of Au/CdS heterostructures comprising 5.3-nm Au nanoparticles. The steady-state spectra are rather featureless, exhibiting neither a surface plasmon peak nor the characteristic CdS absorbance edge. Furthermore, in the transient absorption spectra, bleaching of the surface plasmon resonance in Au domains is no longer identifiable, which

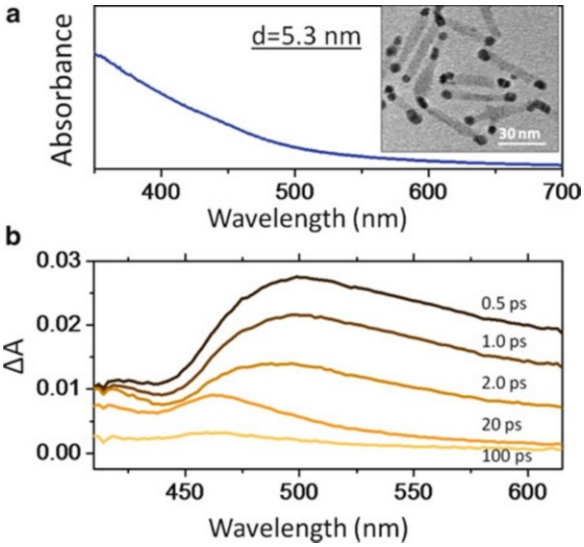

Fig. 13.20 (**a**) Steady-state absorption of Au/CdS heterostructures comprising 5.3-nm Au domains. A representative TEM image is shown in the insert. (**b**) Temporal evolution of the TA spectra for 5.3-nm-Au/CdS nanocomposites excited at $\lambda = 400$ nm. The TA trend contrasts the recovery dynamics observed in isolated Au and CdS nanoparticles, for which both excitonic and plasmonic features are manifested by the prominent dip in ΔA. Instead, the value of ΔA observed for Au/CdS nanocomposites remains positive throughout the entire spectral range of the probe beam (Reprinted with permission Khon et al. [138]. Copyright 2011 American Chemical Society)

strongly contrasts the dynamics of isolated nanoparticles (see Fig. 13.18) exhibiting an apparent plasmon bleach at $\lambda = 530$ nm. These dramatic alterations to the spectral profiles indicate that the nature of excited electron oscillations in smaller Au domains is now modified due to direct coupling of CdS nanocrystals.

In addition to the termination of the surface plasmon feature, the transient absorption spectra reveals a broad positive signal, which, in comparison with the transient absorption characteristics of 15.4-nm Au/CdS heterostructures, extends across the entire spectral range of the probe pulse. The recovery of this feature is too slow to be interpreted as a nonlinear modification of the spectral profile due to local fields and thus, similar to the case of 15.4-nm Au/CdS heterostructures, is attributed to the photoinduced absorption of excited carriers occupying electronic states within the CdS band gap. Note that decreasing the size of gold domains from 15.4 to 5.3 nm results in the onset of a semiconductor excitonic feature, appearing as a characteristic dip at $\lambda < 450$ nm, corresponding to the excitation of ground-state excitons, $1S(e)\text{-}1S_{3/2}(h)$, but this excitonic bleach is substantially weaker than that of pure CdS nanorods and is offset by the positive background of the broad photoinduced absorption.

Lastly, nanostructures in which the size of Au domains is only 2.7 nm (see Fig. 13.21) are considered. This specific architecture acts as a transitional system that spans the link between optical properties of pure CdS nanorods and those of

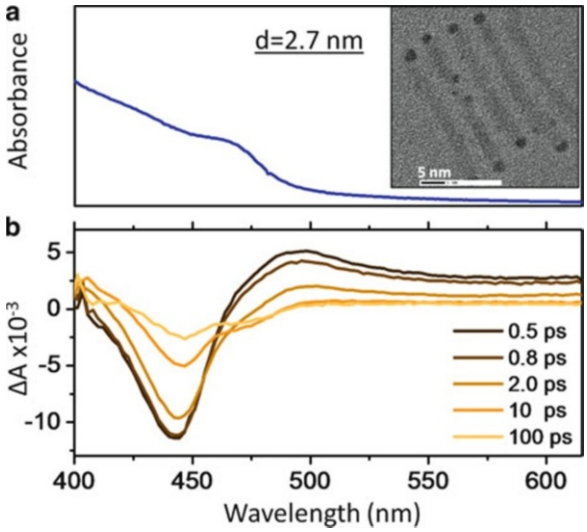

Fig. 13.21 (**a**) Steady-state absorption of Au/CdS heterostructures comprising 2.7-nm Au domains (a typical TEM image is shown in the *insert*). (**b**) Temporal evolution of the TA spectra for 2.7-nm Au/CdS nanocomposites resulting from the excitation at $\lambda = 400$ nm with 120 fs pump pulses. The negative ΔA signal at $\lambda \approx 445$ nm corresponds to bleaching of band gap transitions in CdS. Its spectral position is blue-shifted from the corresponding excitonic edge in the steady-state spectrum, which is believed to be caused by the positive contribution of the photoinduced absorbance into ΔA at the low-energy side of the excitonic peak. The absence of the plasmon bleach at $\lambda = 560$ nm is interpreted as a suppression of plasmon oscillations (Reprinted with permission Khon et al. [138]. Copyright 2011 American Chemical Society)

5.3-nm Au/CdS nanocomposites and exhibits several unique properties, including suppression of the plasmon bleach, suppression of excitonic features in CdS, and spectrally broad photoinduced absorption.

Similar to 5.3-nm Au/CdS heterostructures, transient absorption spectra of Au/CdS nanocomposites comprising 2.7-nm Au tips (Fig. 13.21b) do not indicate any spectral bleaching in the $\lambda = 530$ nm range. Also, just as in the case of nanocomposites with larger tip sizes, the suppression of plasmons in 2.7-nm Au/CdS heterostructures contrasts the carrier dynamics for the control sample of isolated 2.7-nm Au nanoparticles (Fig. 13.18), for which the presence of the plasmon resonance is observed in both steady-state and time-resolved absorption measurements.

To explain the observed suppression of plasmons in Au domains, we consider a "low-barrier" coupling between Au and CdS components, for which Au electrons with energies located above the Fermi level (plasmon band) are not sufficiently confined by the Au/CdS interface to exhibit resonant oscillations. The validity of this assumption is supported by the fact that the interface of the two nanosized domains consists of just a few monolayers and thus cannot form a substantial potential barrier and the fact that energies of conduction electrons in Au domains are raised relative to their respective positions in isolated Au nanoparticles due to

charging. Indeed, the photoinduced transfer of excited electrons from CdS to Au leaves Au domains with an excess negative charge, which equalizes the energy difference between the conduction states in both domains. As a result, electronic wavefunctions of conduction carriers in S and charged M domains partly overlap, giving rise to mixing of electronic states at the interface and corresponding changes in the density of states in both materials. For small-diameter Au nanoparticles, such mixing results in the delocalization of the plasma electrons into CdS portion of nanocomposites, which has a substantially greater volume, and therefore can significantly reduce the boundary effect in Au nanoparticles. Such delocalization-induced suppression of the plasmon resonance in Au NPs is further supported by steady-state absorption spectra of 2.7- and 5.3-nm Au/CdS nanocomposites through the absence of distinct plasmon features. These time-independent measurements rule out nonlinear excitation effects as a potential origin of plasmon suppression since excitation intensities used in steady-state absorption experiments are orders of magnitude below those used in ultrafast studies.

The proposed mixing of the electronic states at the interface of Au and CdS domains can also explain the existence of a positive transient absorption signal observed for all investigated Au/CdS samples. Indeed, due to strong coupling of semiconductor and metal domains, carrier excitations in CdS can lead to the population of CdS-modified conduction states of Au, which will then serve the role of interfacial trap states. This process can occur on a timescale faster than the pulse duration, as can be expected from the general nature of excitation processes in nanocrystals, and will therefore contribute into the "instantaneous" photoinduced absorption of Au/CdS nanocomposites, manifested by the positive ΔA.

While the suppression of plasmons in Au domains can be explained in terms of delocalization of conduction states across the Au/CdS interface, the absence of the excitonic features in the transient absorption and steady-state spectra can, likewise, be attributed to tunneling of CdS carriers into Au domains. Indeed, for small-diameter Au tips, the delocalization of CdS electrons into metal is limited to a few nanometers, which is insufficient to alter the character of quantum confinement in CdS, as can be confirmed by nearly unsuppressed CdS bleach in 2.7-nm Au/CdS spectra (Fig. 13.21b); meanwhile, large-size Au domains allow for a substantial delocalization of 1S(e) CdS wavefunctions into metal, thus leading to the suppression of excitonic features. Expectedly, the correlation between the degree of exciton suppression and the size of Au domains is opposite to that of plasmon suppression, which is the strongest when the size of Au tips is the smallest.

5.2.2 ZnSe- and ZnTe-Seeded CdS Nanorods Supporting Platinum Tips

The ZnTe/CdSe/CdS/Pt and ZnSe/CdS/CdS/Pt core/shell/rod/tip nanocomposites are one of the more complex nanocomposite structures, combining several type II semiconductor–semiconductor junctions with a metal–semiconductor interface [74]. These structures are capable of driving photocatalytic reactions for production of solar hydrogen. Excitons created by absorbed photons are quickly separated by the energy gradient of the type II semiconductor nanorod, where the electron is then injected into the Pt tip, which has a sufficient energy to reduce H_2O, producing H_2 gas.

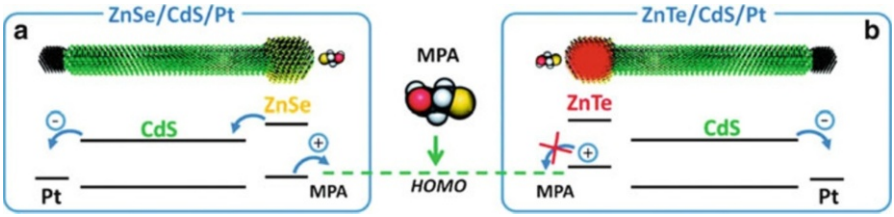

Fig. 13.22 Electronic level diagram showing a relative alignment of excited state energies in ZnSe/CdS/Pt (**a**) and ZnTe/CdS/Pt (**b**) heteronanocrystals. Upon excitation, an electron–hole pair is efficiently separated at hetero-interfaces of the two semiconductor materials with electrons residing in the CdS and holes in the ZnSe(Te) domain of the structure. Subsequently, photoinduced holes undergo further localization, character of which is determined by the relative alignment of hole energies at the semiconductor–ligand interface. For instance, in the case of ZnSe-terminated nanorods, the photoinduced hole is accepted by the ligand molecule mercaptopropionic acid (*MPA*) and expelled to the surface of the composite nanoparticle, while for ZnTe-terminated nanorods, the hole is confined inside the semiconductor domain (Reprinted with permission Acharya et al. [74]. Copyright 2011 American Chemical Society)

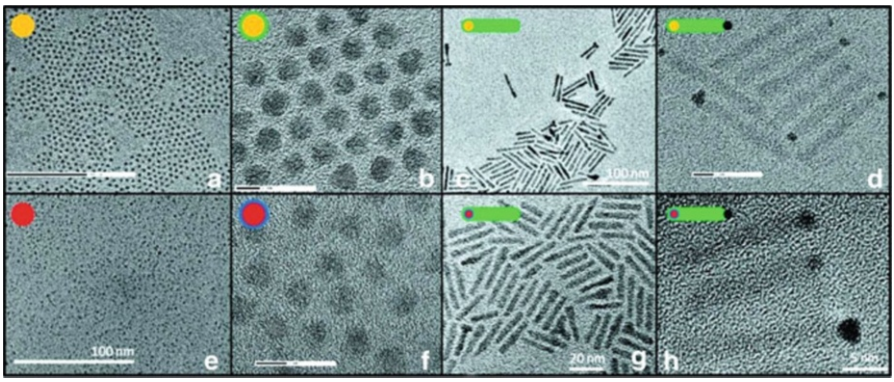

Fig. 13.23 Transmission electron microscope (*TEM*) images of ZnSe/CdS/Pt and ZnTe/CdS/Pt heteronanocrystals corresponding to the four consecutive stages of the growth protocol. (**a**) ZnSe seed NCs. (**b**) ZnSe NCs with a few monolayers of the CdS shell. (**c**) ZnSe/CdS nanorods grown from ZnSe/CdS core/shell NCs. (**d**) ZnSe/CdS nanorods after Pt deposition. (**e**) ZnTe NCs. (**f**). ZnTe/CdSe core/shell NCs. (**g**) ZnTe/CdSe/CdS nanorods grown from ZnTe/CdSe seeds. (**h**) ZnTe/(CdSe)/CdS nanorods after Pt deposition (Reprinted with permission Acharya et al. [74]. Copyright 2011 American Chemical Society)

While electrons undergo similar transitions in both ZnTe/CdSe/CdS/Pt and ZnSe/CdS/CdS/Pt systems through the charge transfer into a Pt tip, the photoinduced hole in ZnTe-seeded nanorods is bound to the core structure, while in ZnSe-seeded nanorods, it localizes on the surface (Fig. 13.22). This serves to protect the latter structure from photooxidation effects that would otherwise destroy the sulfide semiconductor, as is the fate of the ZnTe/CdSe nanorods.

The syntheses of both structures are similar to the previously covered protocols for ZnSe/CdS heteronanorods, which begins with the nucleation of the cores, followed

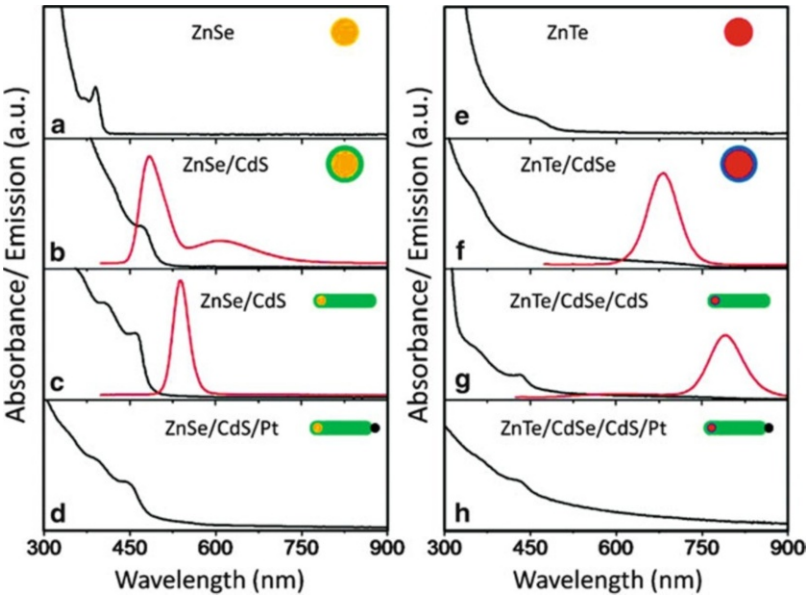

Fig. 13.24 Optical properties of fabricated heteronanocrystals. (**a**) The absorbance of ZnSe NCs showing an excitonic feature at $\lambda = 390$ nm. Band-edge emission was not observed for these samples. (**b**) ZnSe NCs overcoated with a 1-nm-thick shell of CdS, for which the onset of quasi-type II carrier confinement regime is evidenced through red-shifted absorption ($\lambda \approx 475$ nm) and emission peaks ($\lambda \approx 490$ nm). (**c**) Emission and absorbance of ZnSe/CdS nanorods grown from ZnSe/CdS core/shell NCs. (**d**) Absorbance of ZnSe/CdS nanorods after Pt deposition. (**e**)–(**h**) Emission and absorbance spectra associated with the four-step synthesis of ZnTe/CdS/CdS/Pt heteronanocrystals: (**e**) ZnTe NCs, (**f**) ZnTe/CdSe core/shell NCs, (**g**) ZnTe/CdSe/CdS nanorods grown from ZnTe/CdSe seeds, and (h) ZnTe/(CdSe)/CdS nanorods after Pt deposition (Reprinted with permission Acharya et al. [74]. Copyright 2011 American Chemical Society)

by the epitaxial growth of the shells, and continues with the anisotropic growth of an "arm." The reaction is now taken a step further to include the growth of small Pt tips onto one end of heteronanorods by reacting a Pt salt [74] (Fig. 13.23).

According to Fig. 13.24, ZnTe core nanocrystals initially exhibit an absorbance feature near 450 nm. The growth of the CdSe shell results in red-shifting of this absorbance feature and the onset of the type II emission around 700 nm (Fig. 13.24f).

The growth of the nanorod "arm" adds the familiar CdS absorbance edge at 450 nm, with the type II emission red-shifting further to about 800 nm (Fig. 13.24g). For clarification, as always, each step of the synthesis that increases the size in any or all directions that exhibit quantum confinement will result in a relatively small but detectable red shift of optical properties.

As ZnSe/CdS heteronanorods have already been analyzed in a previous section, only a brief summary will be provided here. For the detailed analysis of ZnSe/CdS structures, see section "CdSe Seeded CdS Nanorods and Nanotetrapods: Quasi-Type II Heterostructure." Growth of the CdS quenches the violet fluorescence of

the binary ZnSe core and introduces type II fluorescence of the ZnSe/CdS. As the CdS portions are synthesized, trap state emission is suppressed. Note that by this stage of the synthesis, the final absorption spectrum is similar to the superposition of each individual component of the spectra.

The most noticeable change in the optical characteristics resulting from deposition of Pt tips is the complete quenching of the fluorescence in both heteronanorod structures. This is caused by a combination of effects from photoinduced charge transfer of electrons into the metals Pt domain and the trapping of charge carriers at the CdS/Pt junction. The absorption spectra of both nanocomposites are also altered, marked by an apparent widening of the CdS excitonic feature spectra and an increase in low-energy emission observed as a long, featureless tail extending out into the infrared.

With this, we conclude the analysis of metal–semiconductor nanocomposites.

6 Future Perspectives

Design and synthesis of nanocomposite structures for enhancing optical properties of colloidal nanomaterials is a fast developing area of material science, which progress is fueled both by the fundamental significance of underlying intra-domain processes and the technological applicability of multicomponent nanostructures in the next generation optoelectronics.

The use of composite nanocrystals as fluorescent tags in biological and biomedical applications will continue to evolve. The two major avenues for the future expansion are viewed to be the employment of nontoxic semiconductors for core/shell nanocrystal bio-labels to aid either in vivo imaging applications or the development of composite nanocrystal probes for the transduction of electric potential changes in membranes of living cells (so-called action potential). The latter may lead to the construction of neural activity maps, which is of critical importance to the treatment of such neurological disorders as Alzheimer's or Parkinson's diseases.

Another possible avenue for the future development of nanocomposite's optical properties concerns the investigation and possible practical applications of the exciton–plasmon interactions in metal–semiconductor heterostructures. Indeed, such interaction allows for an enhanced harvesting of light through the plasmon-assisted mechanism, which energy is then transferred to the semiconductor counterpart. This may improve the efficiency of nanocrystal emitters in such devices as LEDS or lasers. On the other hand, plasmon's role of a light-harvesting antenna should enable an increased absorbance of light in photovoltaic and photocatalytic devices. At present, the exciton–plasmon interaction is well understood in a weak coupling regime, while strongly coupled exciton–plasmon interactions still present significant challenges both for the theoreticians in the attempt to describe the resulting system behavior and for experimentalists in their effort to fabricate functional metal–semiconductor tandems with strong exciton–plasmon coupling.

In addition to the aforementioned prospects for nanocomposite development, there are several other emerging directions that take an advantage of optical properties of multi-domain nanocrystals. The use of heterostructured nanorods appended with Pt tips, for instance, has been demonstrated to produce hydrogen from water under visible light. These structures may thus be developed as alternative catalysts for either H_2 production or CO_2 reduction under visible light. The use of composite nanocrystals has also been considered for such application as electroabsorption modulators, optical switches, and photodetectors. As always, the primary challenges on the way toward the realization of these prospects are synthetic in nature. The evolving ability to control the inter-domain stoichiometry and development of unified, scalable, and reproducible synthetic protocols is of paramount importance in establishing the control over optical properties of nanocomposites. Solving these challenges will undoubtedly contribute both to the technological applications of these multifunctional materials and to the fundamental understanding of electronic processes at composite nano-interfaces.

References

1. Klimov VI, Ivanov SA, Nanda J, Achermann M, Bezel I, McGuire JA, Piryatinski A (2007) Single-exciton optical gain in semiconductor nanocrystals. Nature 447:441
2. Hillhouse HW, Beard MC (2009) Solar cells from colloidal nanocrystals: fundamentals, materials, devices, and economics. Curr Opin Coll Int Sci 14:245
3. Gur I, Fromer NA, Geier ML, Alivisatos AP (2005) Air-stable all-inorganic nanocrystal solar cells processed from solution. Science 310:462
4. Borensztein Y, Delannoy L, Djedidi A, Barrera RG, Louis C (2010) Monitoring of the plasmon resonance of gold nanoparticles in Au/TiO_2 catalyst under oxidative and reducing atmospheres. J Phys Chem C 114:9008–9021
5. Amirav L, Alivisatos AP (2010) Photocatalytic hydrogen production with tunable nanorod heterostructures. J Phys Chem Lett 1:1051–1054
6. Coe S, Woo WK, Bawendi M, Bulovic V (2002) Electroluminescence from single monolayers of nanocrystals in molecular organic devices. Nature 420:800
7. Tessler N, Medvedev V, Kazes M, Kan SH, Banin U (2002) Efficient near-infrared polymer nanocrystal light-emitting diodes. Science 295:1506
8. Steckel JS, Snee P, Coe-Sullivan S, Zimmer JR, Halpert JE, Anikeeva P, Kim LA, Bulovic V, Bawendi MG (2006) Color-saturated green-emitting QD-LEDs. Angew Chem Int Ed 45:5796
9. Colvin VL, Schlamp MC, Alivisatos AP (1994) Light-emitting diodes made from cadmium selenide nanocrystals and a semiconducting polymer. Nature 370:354
10. Schlamp MC, Peng XG, Alivisatos APJ (1997) Improved efficiencies in light emitting diodes made with CdSe(CdS) core/shell type nanocrystals and a semiconducting polymer. Appl Phys 82:5837
11. Mattoussi H, Radzilowski LH, Dabbousi BO, Thomas EL, Bawendi MG, Rubner MF (1998) Properties of CdSe nanocrystal dispersions in the dilute regime: structure and interparticle interactions. J Appl Phys 83:7965
12. Medintz IL, Uyeda HT, Goldman ER, Mattoussi H (2005) Quantum dot bioconjugates for imaging, labelling and sensing. Nature Mat 4:435
13. Mattoussi H, Mauro JM, Goldman ER, Anderson GP, Sundar VC, Mikulec FV, Bawendi MG (2000) Self-assembly of CdSe – ZnS quantum dot bioconjugates using an engineered recombinant protein. J Am Chem Soc 122:12142

14. Bruchez JM, Moronne M, Gin P, Weiss S, Alivisatos AP (1998) Semiconductor nanocrystals as fluorescent biological labels. Science 281:2013
15. Wang RY, Feser JP, Lee JS, Talapin DV, Segalman R, Majumdar A (2008) Enhanced thermopower in PbSe nanocrystal quantum dot superlattices. Nano Lett 8:2283
16. Kovalenko MV, Scheele M, Talapin DV (2009) Colloidal nanocrystals with molecular metal chalcogenide surface ligands. Science 324:1417
17. Ridley BA, Nivi B, Jacobson JM (1999) All-inorganic field effect transistors fabricated by printing. Science 286:746
18. Lee S, Jeong S, Kim D, Park BK, Moon J (2007) Superlattices. Microstruct 42:361
19. Schneider JJ, Hoffmann RC, Engstler J, Soffke O, Jaegermann W, Issanin A, Klyszcz A (2008) A printed and flexible field-effect transistor device with nanoscale zinc oxide as active semiconductor material. Adv Mater 20:3383
20. Talapin DV, Mekis L, Gotzinger S, Kornowski A, Benson O, Weller H (2004) CdSe/CdS/ZnS and CdSe/ZnSe/Zns core-shell-shell nanocrystals. J Phys Chem B 108:18826
21. Talapin DV, Murray CB (2005) PbSe nanocrystal solids for n- and p-channel thin film field-effect transistors. Science 310:86
22. Lee JS, Shevchenko EV, Talapin DV (2008) Au-PbS core-shell nanocrystals: plasmonic absorption enhancement and electrical doping via interparticle charge transfer. J Am Chem Soc 130:9673
23. Erwin SC, Zu LJ, Haftel MI, Efros AL, Kennedy TA, Norris DJ (2005) Doping semiconductor nanocrystals. Nature 436:91
24. Salgueirino-Maceira V, Correa-Duarte MA (2007) Increasing the complexity of magnetic core/shell structured nanocomposites for biological applications. Adv Mater 19:4131
25. Son DI, Kim JH, Park DH, Choi WK, Li F, Ham JH, Kim TW (2008) Nonvolatile flexible organic bistable devices fabricated utilizing CdSe/ZnS nanoparticles embedded in a conducting poly N-vinylcarbazole. Nanotechnology 19:055204
26. Liz-Marzan LM, Mulvaney P (2003) The assembly of coated nanocrystals. J Phys Chem B 107:7312
27. Das BC, Batabyal SK, Pal AJ (2007) A bit per particle: electrostatic assembly of CdSe quantum dots as memory elements. Adv Mater 19:4172
28. Das BC, Pal AJ (2008) Memory applications and electrical bistability of semiconducting nanoparticles: do the phenomena depend on bandgap? Small 4:542
29. Ghosh B, Sahu S, Pal AJ (2008) Core-shell nanoparticles: an approach to enhance electrical bistability. J Phys Chem C 112:11290
30. Reiss P, Protiere M, Li L (2009) Core/shell semiconductor nanocrystats. Small 5:154
31. Cozzoli PD, Pellegrino T, Manna L (2006) Synthesis, properties and perspectives of hybrid nanocrystal structures. Chem Soc Rev 35:1195
32. Yao WT, Yu SH (2008) Synthesis of semiconducting functional materials in solution: from II-VI semiconductor to inorganic–organic hybrid semiconductor nanomaterials. Adv Funct Mater 18:3357
33. Talapin DV, Lee J-S, Kovalenko MV, Shevchenko EV (2010) Prospects of nanocrystal solids as electronic and optoelectronic materials. Chem Rev 110:389–458
34. Kumar S, Jones M, Lo SS, Scholes GD (2007) Nanorod heterostructures showing photoinduced charge separation. Small 3:1633
35. Carbone L, Nobile C, Giorgi MD, Sala FD, Morello G, Pompa P, Hytch M, Snoeck E, Fiore A, Franchini IR, Nadasan M, Silvestre AF, Chiodo L, Kudera S, Cingolani R, Krahne R, Manna L (2007) Synthesis and micrometer-scale assembly of colloidal CdSe/CdS nanorods prepared by a seeded growth approach. Nano Lett 7:2942
36. Dorfs D, Salant A, Popov I, Banin U (2008) ZnSe quantum dots within CdS nanorods: a seeded-growth type-II system. Small 4:1319
37. Lo SS, Khan Y, Jones M, Scholes GD (2009) Temperature and solvent dependence of CdTe/CdSe heterostructure nanorod spectra. J Chem Phys 131:084714

38. Zhong H, Scholes GD (2009) Shape tuning of type II CdTe-CdSe colloidal nanocrystal heterostructures through seeded growth. J Am Chem Soc 131:9170–9191
39. Shieh F, Saunders AE, Korgel BA (2005) General shape control of colloidal CdS, CdSe, CdTe quantum rods and quantum rod heterostructures. J Phys Chem B 119:8539
40. Halpert JE, Porter VJ, Zimmer JP, Bawendi MG (2006) Synthesis of CdSe/CdTe nanobarbells. J Am Chem Soc 128:12590
41. Kirsanova M, Nemchinov A, Hewa-Kasakarage NN, Schmall N, Zamkov M (2009) Synthesis of ZnSe/CdS/ZnSe nano-barbells showing photoinduced charge separation. Chem Mater 21:4305
42. Shi W, Zeng H, Sahoo Y, Ohulchanskyy TY, Ding Y, Wang ZL, Prasad PN (2006) A general approach to binary and ternary hybrid nanocrystals. Nano Lett 6:875
43. Heng Y, Chen M, Rice PM, Wang SX, White RL, Sun S (2005) Dumbbell-like bifunctional Au-Fe_3O_4 nanoparticles. Nano Lett 5:379
44. Carbone L, Kudera S, Carlino E, Parak WJ, Giannini C, Cingolani R, Manna L (2006) Multiple Wurtzite twinning in CdTe nanocrystals induced by methylphosphonic acid. J Am Chem Soc 128:748
45. Milliron DJ, Hughes SM, Cui Y, Manna L, Li JB, Wang LW, Alivisatos AP (2004) Colloidal nanocrystal heterostructures with linear and branched topology. Nature 430:190
46. Mokari T, Rothenberg E, Popov I, Costi R, Banin U (2004) Selective growth of metal tips onto semiconductor quantum rods and tetrapods. Science 304:1787
47. Mokari T, Sztrum CG, Salant A, Rabani E, Banin U (2005) Formation of asymmetric one-sided metal-tipped semiconductor nanocrystal dots and rods. Nature Mater 4:855
48. Carbone L, Kudera S, Giannini C, Ciccarella G, Cingolani R, Cozzoli PD, Manna L (2006) Selective reactions on the tips of colloidal semiconductor nanorods. J Mate Chem 16:3952
49. Menagen G, Macdonald JE, Shemesh Y, Popov I, Banin U (2009) Au growth on semiconductor NAnorods: photoinduced versus thermal growth mechanisms. J Am Chem Soc 131:17406–17411
50. Habas SE, Yang P, Mokari T (2008) Selective growth of metal and binary metal tips on CdS nanorods. J Am Chem Soc 130:3294
51. Peng XG, Schlamp MC, Kadavanich AV, Alivisatos AP (1997) Epitaxial growth of highly luminescent CdSe/CdS core/shell nanocrystals with photostability and electronic accessibility. J Am Chem Soc 119:7019
52. Hines MA, Guyot-Sionnest P (1996) Synthesis and characterization of strongly luminescing ZnS-capped CdSe nanocrystals. J Phys Chem 100:468
53. Dabbousi BO, RodriguezViejo J, Mikulec FV, Heine JR, Mattoussi H, Ober R, Jensen KF, Bawendi MG (1997) (CdSe)ZnS core-shell quantum dots: synthesis and optical and structural characterization of a size series of highly luminescent materials. J Phys Chem B 101:9463
54. Zhao JL, Zhang JY, Jiang CY, Bohnenberger J, Basche T, Mews A (2004) Electroluminescence from isolated CdSe/ZnS quantum dots in multilayered light-emitting diodes. J Appl Phys 96:3206
55. Nizamoglu S, Ozel T, Sari E, Demir HV (2007) White light generation tuned by dual hybridization of nanocrystals and conjugated polymers. Nanotechnology 18:065709
56. Bruchez M, Moronne M, Gin P, Weiss S, Alivisatos AP (2013) Semiconductor nanocrystals as fluorescent biological labels. Science 1998:281
57. Son DH, Hughes SM, Yin YD, Alivisatos AP (2004) Cation exchange reactions-in ionic nanocrystals. Science 306:1009
58. Costa-Fernandez JM, Pereiro R, Sanz-Medel A (2006) The use of luminescent quantum dots for optical sensing. Trends Anal Chem 25:207
59. Nirmal M, Dabbousi BO, Bawendi MG, Macklin JJ, Trautman JK, Harris TD, Brus LE (1996) Fluorescence intermittency in single cadmium selenide nanocrystals. Nature 383:802
60. Hohng S, Ha T (2004) Near-complete suppression of quantum dot blinking in ambient conditions. J Am Chem Soc 126:1324

61. Banin U, Bruchez M, Alivisatos AP, Ha T, Weiss S (1999) Evidence for a thermal contribution to emission intermittency in single CdSe/CdS core/shell nanocrystals; Chemla, D. S. J Chem Phys 110:1195
62. Li YC, Zhong HZ, Li R, Zhou Y, Yang CH, Li YF (2006) High-yield fabrication and electrochemical characterization of tetrapodal CdSe, CdTe, and $CdSe_xTe_{1-x}$ nanocrystals. Adv Funct Mater 16:1705
63. Zhou Y, Li YC, Zhong HZ, Hou JH, Ding YQ, Yang CH, Li YF (2006) Hybrid nanocrystal/polymer solar cells based on tetrapod-shaped $CdSe_xTe_{1-x}$ nanocrystals. Nanotechnology 17:4041
64. Zhang Y, Wang LW, Mascarenhas A (2007) "Quantum coaxial cables" for solar energy harvesting. Nano Lett 7:1264
65. Luque A, Marti A, Nozik AJ (2007) Solar cells based on quantum dots: multiple exciton generation and intermediate bands. Mrs Bull 32:236
66. Nemchinov A, Kirsanova M, Hewa-Kasakarage NN, Zamkov M (2008) Synthesis and characterization of type II ZnSe/CdS core/shell nanocrystals. J Phys Chem C 112:9301
67. Doose S (1856) Optical Amplification from Single Excitons in Colloidal Quantum Dots. Small 2007:11
68. Chan Y, Steckel JS, Snee PT, Caruge JM, Hodgkiss JM, Nocera DG, Bawendi MG (2005) Blue semiconductor nanocrystal laser. Appl Phys Lett 86:073102
69. Talapin DV, Mekis I, Götzinger S, Kornowski A, Benson O, Weller H (2004) CdSe/CdS/ZnS and CdSe/ZnSe/ZnS core-shell-shell nanocrystals. J Phys Chem B 108:18826–18831
70. Chen Y, Vela J, Htoon H, Casson JL, Werder DJ, Bussian DA, Klimov VI, Hollingsworth JA (2008) "Giant" multishell CdSe nanocrystal quantum dots with suppressed blinking. J Am Chem Soc 130:5026
71. Pathan HM, Lokhande CD (2004) Deposition of metal chalcogenide thin films by successive ionic layer absorption and reaction (SILAR) method. Bull Mater Sci 27:85
72. Pietryga JM, Werder DJ, Williams DJ, Casson JL, Schaller RD, Klimov VI, Hollingsworth JA (2008) Utilizing the lability of lead selenide to produce heterostructured nanocrystals with bright, stable infrared emission. J Am Chem Soc 130:4879–4885
73. Neo MS, Venkatram N, Li GS, Chin WS, Ji W (2010) Synthesis of PbS/CdS core-shell QDs and their nonlinear optical properties. J Phys Chem C 114:18037–18044
74. Acharya KP, Khnayzer RS, O'Connor T, Diederich G, Kirsanova M, Klinkova A, Roth D, Kinder E, Imboden M, Zamkov M (2011) The role of hole localization in sacrificial hydrogen production by semiconductor-metal heterostructured nanocrystals. Nano Lett 11:2919
75. Hewa-Kasakarage NN, Kirsanova M, Nemchinov A, Schmall N, El-Khoury PZ, Tarnovsky AN, Zamkov M (2009) Radiative recombination of spatially extended excitons in (ZnSe/CdS)/CdS heterostructured nanorods. J Am Chem Soc 131:1328
76. Fisher BR, Eisler HJ, Stott NE, Bawendi MG (2004) Emission intensity dependence and single-exponential behavior in single colloidal quantum dot fluorescence lifetime. J Phys Chem B 108:143
77. Hewa-Kasakarage NN, El-Khoury PZ, Tarnovsky AN, Kirsanova M, Nemitz I, Nemchinov A, Zamkov M (1837) Ultrafast carrier dynamics in Type II ZnSe/CdS/ZnSe nanobarbells. ACS Nano 2010:4
78. Grätzel M (2001) Photoelectrochemical cells. Nature 414:338–344
79. Miller DAB, Chemla DS, Damen TC, Gossard AC, Wiegmann W, Wood TH, Burrus CA (1984) Band-edge electroabsorption in quantum well structures – the quantum-confined Stark effect. Phys Rev Lett 53:2173–2176
80. Kuo1 Y, Lee1 YK, Ge Y, Ren S, Roth JE, Kamins TI, Miller DA, Harris JS (2005) Strong quantum-confined Stark effect in germanium quantum-well structures on silicon. Nature 437:334
81. Reiss P (2007) ZnSe based colloidal nanocrystals: synthesis, shape control, core/shell, alloy and doped systems. New J Chem 31:1843–1852

82. Hunsche S, Dekorsy T, Klimov V, Kurz H (1996) Ultrafast dynamics of carrier-induced absorption changes in highly-excited CdSe nanocrystals. Appl Phys B 62:3–10
83. Ekimov AI, Hache F, Schanne-Klein MC, Ricard D, Flytzanis C, Kudryavtsev IA, Yaveza TV, Rodina AV, Efros AL (1993) Absorption and intensity-dependent photoluminescence measurements on CdSe quantum dots: assignment of the first electronic transitions. J Opt Soc Am B 10:100–106
84. Nirmal M, Norris DJ, Kuno M, Bawendi MG, Efros AL, Rosen M (1995) Observation of the dark excitons in CdSe quantum dots. Phys Rev Lett 75:3728–3731
85. Klimov V, Hunsche S, Kurz H (1994) Biexciton effects in femtosecond nonlinear transmission of semiconductor quantum dots. Phys Rev B 50:8110–8113
86. Klimov VI (2000) Optical nonlinearities and ultrafast carrier dynamics in semiconductor nanocrystals. J Phys Chem B 104:6112–6123
87. Norris D, Sacra A, Murray C, Bawendi M (1994) Measurement of the size dependent hole spectrum in CdSe quantum dots. Phys ReV Lett 72:2612–2615
88. Many A, Goldstein Y, Grover NB (1965) Semiconductor surfaces. North Holland, Amsterdam
89. Nolte DD (1999) Semi-insulating semiconductor heterostructures: optoelectronic properties and applications. J Appl Phys 85:6259–6289
90. Ozgur U, Alivov YI, Liu C, Teke A, Reshchikov MA, Dogan S, Avrutin V, Cho SJ, Morkoc H (2005) A comprehensive review of ZnO materials and devices. J Appl Phys 98:041301
91. Storm HF (1969) Solid-state power electronics in the USA. IEEE Trans Electron Dev ED 16:957
92. Jun Y, Choi J, Cheon J (2006) Shape control of semiconductor and metal oxide nanocrystals through nonhydrolytic colloidal routes. Angew Chem Int Ed 45:3414–3439
93. Rajeshwar K, Tacconi N, Chenthamarakshan C (2001) Semiconductor-based composite materials: preparation, properties, and performance. Chem Mater 13:2765–2782
94. Cozzoli P, Manna L (2005) Tips on growing nanocrystals. Nature Mater 4:801–802
95. Yang J, Elim HI, Zhang Q, Lee JL, Ji W (2006) Rational synthesis, self-assembly, and optical properties of PbS-Au heterogeneous nanostructures via preferential deposition. J Am Chem Soc 128:11921
96. Dukovic G, Merkle MG, Nelson JH, Hughes SM, Alivisatos AP (2008) Photodeposition of Pt on colloidal CdS and CdSe/CdS semiconductor nanostructures. Adv Mater 20:4306–4311
97. Deka S, Falqui A, Bertoni G, Sangregorio C, Poneti G, Morello G, Giorgi M, Giannini C, Cingolani R, Manna L, Cozzoli PD (2009) Fluorescent asymmetrically cobalt-tipped CdSe@CdS Core@Shell nanorod heterostructures exhibiting room-temperature ferromagnetic behavior. J Am Chem Soc 131:12817–12828
98. Zanella M, Falqui A, Kudera S, Manna L, Casula MF, Parak WJ (2008) Growth of colloidal nanoparticles of group II–VI and IV–VI semiconductors on top of magnetic iron–platinum nanocrystals. J Mater Chem 18:4311–4317
99. Zhang JT, Tang Y, Lee K, Ouyang M (2010) Exciton-plasmon interactions in metal-semiconductor nanostructures. Science 327:1634–1638
100. Kim H, Achermann M, Balet LP, Hollingsworth JA, Klimov VI (2005) Synthesis and characterization of Co/CdSe core/shell nanocomposites: bifunctional magnetic-optical nanocrystals. J Am Chem Soc 127:544–546
101. Carbone L, Kudera S, Giannini C, Ciccarella G, Cingolani R, Cozzoli PD, Manna L (2006) Selective reactions on the tips of colloidal semiconductor nanorods. J Mater Chem 16:3952
102. Saunders AE, Popov I, Banin U (2006) Growth of colloidal nanoparticles of the group II-VI and IV-VI semiconductors on the top of magnetic ion-platinum nanocrystals. J Phys Chem B 110:25421
103. Menagen G, Mocatta D, Salant A, Popov I, Dorfs D, Banin U (2008) Selective gold growth on CdSe seeded CdS nanorods. Chem Mater 20:6900–6902

104. Carbone L, Jakab A, Khalavka Y, Sonnichsen C (2009) Light-controlled one-sided growth of large plasmonic gold domains on quantum rods observed on the single particle level. Nano Lett 9:3710–3714
105. Mokari T, Costi R, Sztrum CG, Rabani E, Banin U (2006) Formation of symmetric and asymmetric metal-semiconductor hybrid nanoparticles. Phys Stat Sol B 243:3952–3958
106. Khon E, Hewa-Kasakarage NN, Nemitz I, Acharya K, Zamkov M (2010) Tuning the morphology of Au/CdS nano-composites though temperature-controlled reduction of gold-oleate complexes. Chem Mater 22:5929
107. Costi R, Saunders AE, Banin U (2010) Colloidal hybrid nanostructures: a new type of functional materials. Angew Chem Int Ed 49:4878–4897
108. Zhang JT, Tang Y, Lee K, Ouyang M (2010) Tailoring light-matter-spin interactions in colloidal hetero-nanostructures. Nature 466:91–95
109. Lee J, Orazbayev A, Govorov AO, Kotov NA (2010) Solvent effect in dynamic superstructures from Au nanoparticles and CdTe nanowires: experimental observation and theoretical description. J Phys Chem C 114:1404–1410
110. Morfa AJ, Rowlen KL, Reilly TH, Romero MJ, Lagemaat VD (2008) Plasmon-enhanced solar energy conversion in organic bulk heterojunction photovoltaics. J Appl Phys Lett 92:013504
111. Oulton RF, Sorger VJ, Zentgraf T, Ma RM, Gladden C, Dai L, Bartal G, Zhang X (2009) Plasmon lasers at deep subwavelength scale. Nature 461:629–632
112. Jestl M, Maran I, Kock A, Beinstingl W, Gornik E (1989) Polarization-sensitive surface plasmon Schottky detectors. Opt Lett 14:719–721
113. Sheldon MT, Trudeau PE, Mokari T, Wang LW, Alivisatos AP (2009) Enhanced semiconductor nanocrystal conductance via solution grown contacts. Nano Lett 9:3676–3682
114. Maynadie J, Salant A, Falqui A, Respaud M, Shaviv E, Banin U, Soulantica K, Chaudret B (2009) Cobalt growth on the tips of CdSe nanorods. Angew Chem Int Ed 48:1814–1817
115. Drexhage KH, Wolf E (1974) Progress in optics. Amsterdam, The Netherlands, Vol. XII, p 163.
116. Achermann M (2010) Exciton-plasmon interactions in metal-semiconductor nanostructures. J Phys Chem Lett 1:2837–2843
117. Shimizu KT, Woo WK, Fisher BR, Eisler HJ, Bawendi MG (2002) Surface-enhanced emission from single semiconductor nanocrystals. Phys Rev Lett 89:117401
118. Farahani JN, Pohl DW, Eisler HJ, Hecht B (2005) Single quantum dot coupled to a scanning optical antenna: a tunable superemitter. Phys Rev Lett 95:17402
119. Bergman DJ, Stockman MI (2003) Phys Rev Lett 90:027402
120. Mertens H, Biteen JS, Atwater HA, Polman A (2006) Surface plasmon amplification by stimulated emission of radiation: quantum generation of coherent surface plasmons in nanosystems. Nano Lett 6:2622–2625
121. Okamoto K, Niki I, Shvartser A, Narukawa Y, Mukai T, Scherer A (2004) Surface plasmon enhanced light-emitters based on InGaN quantum wells. Nat Mater 3:601–605
122. Guo P-F, Wu S, Ren Q-J, Lu J, Chen Z, Xiao S-J, Zhu Y-YJ (2010) Phys Chem Lett 1:315–318
123. Gryczynski I, Malicka J, Jiang W, Fischer H, Chan WCW, Gryczynski Z, Grudzinski W, Lakowicz JR (2005) Surface-plasmon-coupled emission of quantum dots. J Phys ChemB 109:1088–1093
124. Pillai S, Catchpole KR, Trupke T, Zhang G, Zhao J, Green MA (2006) Surface plasmon enhanced silicon solar cells. Appl Phys Lett 88:161102
125. Muskens OL, Giannini V, Sanchez-Gil JA, Rivas JG (2007) Strong enhancement of the radiative decay rate of emitters by single plasmonic nanoantennas. Nano Lett 7:2871–2875
126. Wang Y, Yang T, Tuominen MT, Achermann M (2009) Radiative rate enhancements in hybrid metal-semiconductor nanostructures. Phys Rev Lett 102:163001
127. Noginov MA, Zhu G, Mayy M, Ritzo BA, Noginova N, Podolskiy VA (2008) Stimulated emission of surface plasmon polaritons. Phys Rev Lett 101:226806

128. Noginov MA, Zhu G, Belgrave AM, Bakker R, Shalaev VM, Narimanov EE, Stout S, Herz E, Suteewong T, Wiesner U (2009) Demonstration of a spaser-based nanolaser. Nature 460:1110–1112
129. Zheludev NI, Prosvirnin SL, Papasimakis N, Fedotov VA (2008) Lasing spaser. Nat Photonics 2:351–354
130. Englund D, Fattal D, Waks E, Solomon G, Zhang B, Nakaoka T, Arakawa Y, Yamamoto Y, Vuckovic J (2005) Efficient source of deterministically polarized single photons. Phys Rev Let 95:013904
131. Schaadt DM, Feng B, Yu ET (2005) Enhanced semiconductor optical absorption via surface plasmon excitation in metal nanoparticles. Appl Phys Lett 86:063106
132. Rand BP, Peumans P, Forrest SR (2004) Long-range absorption enhancement in organic tandem thin-film solar cells containing silver nanoclusters. J Appl Phys 96:7519–7526
133. Lee J, Hernandez P, Lee J, Govorov AO, Kotov NA (2007) Exciton-plasmon interactions in molecular spring assemblies of nanowires and wavelength-based protein detection. Nat Mater 6:291–295
134. Gupta JA, Knobel R, Samarth N, Awschalom DD (2001) Ultrafast manipulation of electron spin coherence. Science 292:2458–2461
135. Press D, Ladd TD, Zhang B, Yamamoto Y (2008) Complete quantum control of a single quantum dot spin using ultrafast optical pulses. Nature 456:218–221
136. Berezovsky J, Mikkelsen MH, Stoltz NG, Coldren LA, Awschalom DD (2008) Picosecond coherent optical manipulation of a single electron spin in a quantum dot. Science 320:349–352
137. Gómez DE, Vernon KC, Mulvaney P, Davis TJ (2010) Surface plasmon mediated strong exciton-photon coupling in semiconductor nanocrystals. Nano Lett 10:274–278
138. Khon E, Mereshchenko A, Tarnovsky AN, Acharya K, Klinkova A, Hewa-Kasakarage NN, Nemitz I, Zamkov M (2011) Suppression of the plasmon resonance in Au/CdS colloidal nanocomposites. Nano Lett 11:1792
139. Costi R, Saunders AE, Banin E, Angew U (2010) Colloidal hybrid nanostructures: a new type of functional materials. Chem Int Ed 49:4818–4897
140. Costi R, Saunders AE, Elmalem E, Salant A, Banin U (2008) Visible light-induced charge retention and photocatalysis and hybrid CdSe-Au nanodumbbells. Nano Lett 8:637–641
141. Zhao N, Liu K, Greener J, Nie Z, Kumacheva E (2009) Close-packed superlattices of side-by-side assembled Au-CdSe nanorods. Nano Lett 9:3077–3081
142. Scholes GD (2008) Insights into excitons confined to nanoscale systems: electron-hole interaction, binding energy and photodissociation. ACS Nano 2:523–537
143. Kelly KL, Coronado E, Zhao LL, Schatz GC (2003) The optical properties of metal nanoparticles: the influence of size, shape, and dielectric environment. J Phys Chem B 107:668–677
144. Link S, El-Sayed MA (1999) Size and temperature dependence of the plasmon absorption of colloidal gold nanoparticles. J Phys Chem 103:8410–8426
145. El-Sayed MA (2001) Some interesting properties of metals confined in time and nanometer space of different shapes. Acc Chem Res 34:257–264
146. Boernstein L (1998) Numerical data and functional relationships in science and technology. Group III, Condensed Matter, SubVolume C; Martienssen W (ed) Springer, Verlag
147. Dinger A, Petillon S, Grün M, Hetterich M, Klingshirn C (1999) Conduction band offset of the CdS/ZnSe heterostructure. Semi Sci Tech 14:595–598
148. Hewa-Kasakarage NN, El-Khoury PZ, Tarnovsky AN, Kirsanova M, Nemitz I, Nemchinov A, Zamkov M (2010) Ultrafast carrier dynamics in type II ZnSe.CdS.ZnSe nano- barbells. ACS Nano 4:1837–1844
149. Kreibig U, Vollmer M (1995) Optical properties of metal clusters. Springer, Berlin
150. Ahmadi TS, Logunov SL, El-Sayed MA (1996) Picosecond dynamics of colloidal gold nanoparticles. J Phys Chem 100:8053–8056

151. Logunov SL, Ahmadi TS, El-Sayed MAJ (1997) Electron dynamics of passivated gold nanocrystals probed by subpicosecond transient absorption spectroscopy. Phys Chem B 101:3713–3719
152. Yong KT, Sahoo Y, Choudhury KR, Swihart MT, Minter JR, Prasad PN (2006) Shape control on PbSe nanocrystals using noble metal seed particles. Nano Lett 6:709
153. Pacholski C, Kornowski A, Weller H (2004) Nanomaterials: site-specific photodeposition of silver on ZnO nanorods. Angew Chem Int Ed 43:4774
154. Mokari T, Aharoni A, Popov I, Banin U (2006) Diffusion of gold into in as nanocrystals. Angew Chem Int Ed 45:8001
155. Yong KT, Sahoo Y, Choudhury KR, Swihart MT, Minter JR, Prasad PN (2006) Control of the morphology and size of PbS nanowires using gold nanoparticles. Chem Mater 18:5965
156. Peng P, Milliron DJ, Hughes SM, Johnson JC, Alivisatos AP, Saykally RJ (2005) Femtosecond spectroscopy of carrier relaxation dynamics in a type II CdSe/CdTe tetrapod heteronanostructures. Nano Lett 5:1809–1813
157. Dooley CJ, Dimitrov SD, Fiebig T (2008) Ultrafast electron transfer dynamics in CdSe.CdTe donor-acceptor nanorods. J Phys Chem C 112:12074–12076
158. Lupo MG, Sala FD, Carbone L, Zavelani-Rossi M, Fiore A, Lüer L, Polli D, Cingolani R, Manna L, Lanzani G (2008) Ultrafast electron- hole dynamics in core/shell CdSe/CdS dot/rod nanocrystals. Nano Lett 8:4582–4587
159. Hewa-Kasakarage NN, Gurusinghe PG, Zamkov M (2009) Blue-shifted emission in CdTe/ZnSe heterostructured nanocrystals blue-shifted emission in CdTe/ZnSe heterostructured nanocrystals. J Phys Chem C 113:4362–4368

Biomedical and Biochemical Tools of Förster Resonance Energy Transfer Enabled by Colloidal Quantum Dot Nanocrystals for Life Sciences

14

Urartu Özgür Şafak Şeker and Hilmi Volkan Demir

Contents

1 Definition of the Topic

Semiconductor quantum nanocrystals (NCs) provide the ability to control and fine-tune peak emission wavelength using the size effect, with a broad optical absorption band (excitation window) increasing toward UV wavelength range. Quantum dots with different peak emission wavelengths can be excited at the same wavelength and offer longer fluorescence lifetimes, which make them desirable donor molecules for Förster resonance energy transfer (FRET)-based applications. In this chapter, the tools of FRET using these quantum dot nanocrystals in life science applications are addressed.

U.Ö.Ş. Şeker (✉) • H.V. Demir
Department of Electrical and Electronics Engineering, Department of Physics and UNAM—Institute of Materials Science and Nanotechnology, Bilkent University, Ankara, Turkey

Luminous! Centre of Excellence for Semiconductor Lighting and Displays, School of Electrical and Electronic Engineering, School of Physical and Mathematical Sciences, Nanyang Technological University, Singapore, Singapore

Challa S.S.R. Kumar (ed.), *UV-VIS and Photoluminescence Spectroscopy for Nanomaterials Characterization*, DOI 10.1007/978-3-642-27594-4_14,

2 Overview

Förster resonance energy transfer arises from the dipole–dipole interaction of donors and acceptors in their close proximity (typically less than 10 nm). FRET-based applications have been widely used in life sciences for a long time, especially utilizing fluorescent proteins and organic dyes as the donors and/or acceptors. FRET-based biological applications range from biosensing of a target molecule to the imaging of the transportation of a molecule within a cellular compartment. With the recent developments and improvements in nanotechnology, quantum dot nanocrystals have become the next generation fluorophores with their size-tunable emission properties and broadband absorption properties.

Quantum dot nanocrystals can be synthesized using both solvent and aqueous synthesis approaches. To conjugate the quantum dot nanocrystals with biomolecules and dye acceptors, surface functionalization is crucial. The surface functionalization may be carried out using a number of different approaches. The most popular chemical approach is the formation of carboxyl groups on the quantum dot surface by adding ligands during synthesis and activation of the carboxyl groups using carbodiimide chemistry based on NHS (*N*-hydroxysulfosuccinimide)/EDC (1-ethyl-3-(3-demethylaminopropyl)carbodiimide) activation. Another approach for the biomolecule conjugation to quantum dots relies on using conventional streptavidin-biotin interaction. Also, metal-affinity-based conjugation of biomolecules, especially proteins, is of great interest because of the simple application of this method. Thus far the protein-, peptide-, and DNA-conjugated quantum dots have been utilized in FRET applications for biosensing and imaging techniques.

In this chapter, we present how to utilize biomolecule-quantum dot conjugates in FRET applications for life sciences, which promise a number of new possibilities for biosensing and imaging.

3 Introduction

To track intracellular and extracellular events, many different labeling techniques have been employed. These include labeling the target biomolecule using a fluorescent reporter. This fluorescent molecule can be either another biological molecule such as a fluorescent protein and peptide, or more commonly a chemical dye molecule [1, 2]. Many dye molecules have been successfully designed, synthesized, and attached to certain biomolecules to track changes and processes in intracellular and extracellular environment [3, 4]. Many of these dye molecules have also been successfully utilized to make biochemical assays to determine the amount of a given molecule quantitatively and qualitatively [4, 5]. Although these approaches worked well in most cases, there have been certain limitations, which in turn make their potential limited for understanding the biological complexity and underpinning mechanisms. Most of the dye-protein labeling approaches need to be normalized with respect to the number of molecules used in the extracellular assays. This makes it hard to follow the changes upon interacting a labeled molecule,

as there is only one signal but many possible interactions. For biosensing applications, using only one labeled species can be problematic to track changes upon molecular interactions. Following up a single signal can cause nonspecific interaction errors. Considering all these factors, a more powerful technique, Förster resonance energy transfer – FRET, has found a large area of usability in biolabeling applications [6]. Förster resonance energy transfer, also sometimes referred to as the fluorescence resonance energy transfer in the community, is a phenomenon that takes place through the nonradiative transfer of the electronic excitation energy from an electronically excited donor to a fluorescence acceptor, which can only occur if the distance between the donor and acceptor species is smaller than twice Förster radii (typically corresponding to a distance of less than 10 nm) and if the emission of the donor spectrally matches the absorption of the acceptor. This phenomenon was first explained by Theodor Förster in 1948. Since then, FRET has been widely used in biological and biochemical applications, among which are protein–protein interactions, conformational change of proteins, DNA hybridization, and receptor–ligand binding [7].

For the protein–protein interaction studies, if the interaction is being carried out in an intracellular environment, generally both of the molecules are fused with a fluorescent protein such as green fluorescent protein (GFP) and red fluorescent protein (RFP), and through the change in FRET signal, the strength of the interaction can be quantified. Mostly, the FRET signal in intracellular protein–protein interaction type of these studies is monitored under fluorescence microscopy. Similarly, another approach relies on labeling both of the interacting molecules using conventional dye molecules that possess a good spectral overlap for FRET application. These approaches can be useful especially for extracellular FRET-based bioassays.

One of the popular utilization of FRET signal is for monitoring changes in the structure of a protein. In this approach, a protein molecule must be labeled in a site-specific manner with suitable fluorescence dyes, because any structural change that results in the folding of the protein will lead to a distance change between the dye molecules, and as long as the separation between the dye molecules satisfies the FRET conditions, one can easily correlate the structural rearrangement of the protein with the FRET signal. This event can be calibrated with reference molecules in such a way that FRET signal can be used as a molecularly sensitive nanoruler [8]. Similarly, upon the denaturation–renaturation of the proteins, the distance between the fluorescent labels can be changed, which can be followed through the change in the FRET signal [9]. Ligand–receptor binding was also characterized using FRET processes, where both ligands–receptors were labeled using fluorescent dyes [10]. This approach is now also widely utilized to analyze the molecular interaction in biological systems.

FRET applications have been carried out using a range of different materials dominantly including organic dyes, natural fluorophores (tryptophan, tyrosine, and phenylalanine), and fluorescent proteins, and enzyme catalyzed bio- and chemoluminescence reactions were also used [11–13]. However, one of the problems in most of these applications was the short fluorescent lifetime of the given molecules and materials, for which some other alternative dyes and materials were utilized [6].

The number of recent studies conducted to use nanoparticles in FRET studies is also increasing. Mostly metal- (e.g., gold) and semiconductor- (e.g., silicon) based nanoparticles as well as luminescent quantum dot nanoparticles have been used for their exceptional size-tunable properties [14]. With these, innovative improvements in nanotechnology, especially quantum dot nanocrystals, have been investigated to replace the currently available organic dye molecules. Compared to the organic dye molecules, these quantum dots have superior characteristics such as the size-tunable photoluminescence, relatively sharp emission spectrum, broad adsorption spectrum, and large Stokes shift, which make their emission band far from their absorption edge [15–17]. Using these unique properties of the quantum dots, they can be tuned to provide stronger spectral overlaps with a certain type of organic, natural, or inorganic acceptor. Today, many quantum dot nanocrystals, which can be utilized as FRET donors, are available in the market with a wide range of peak emission wavelength options. Also, the synthesis of these quantum dots can be easily achieved using the simple well-established recipes [18].

The applications of the quantum dot nanocrystals in biological and biomedical research have been covered in some other previous review papers and book chapters. However, in this chapter, rather than a general overview of the applications of the quantum dot nanocrystals, a more focused route into the FRET-based applications of the quantum dot nanocrystals is considered. This focused coverage aims at providing a rich source on the quantum dot-enabled FRET-based applications carried out for life sciences in the literature. This is especially important for a researcher in the biomedical and biotechnological research areas to envision novel applications exploiting quantum dot-based FRET as a powerful tool.

This chapter aims to cover the utilization of quantum dot-enabled FRET in biomedical and biochemical applications. In this sense, we are giving an overview starting from the basics of the quantum dots to the advanced applications of quantum dot-enabled FRET in life sciences by covering latest literature. This chapter starts with the synthesis and surface functionalization of the quantum dot nanocrystals, which is the key concept for their utilization in FRET-based processes. Subsequently, the use of these quantum dots is presented for FRET applications under two main titles, which are the most common applications of FRET processes: the biosensing and the bioimaging. Having different target molecules and utilizing different types of molecular recognition elements, biosensing applications are grouped as the antibody, protein, and nucleic acid-based applications.

4 Experimental and Instrumental Methodology

4.1 FRET Using Quantum Dot Nanocrystals

4.1.1 Semiconductor Quantum Dot Nanocrystals Synthesis

The first step toward the discovery and realization of the solution-phase formation of the colloidal quantum dots was taken just after the demonstration of the quantum confinement effect in semiconductor crystals. It was found that semiconductor

nanocrystals can be formed within the micellar structures. This first approach included the synthesis of the semiconductor nanocrystals at the water-oil interface using a surfactant. The researchers showed that by addition of the metal salts, one can easily synthesize the quantum dots within the room temperature limits; however, these initial attempts led to the formation of nanocrystals with poor crystalline structures in the early times [19].

Quantum dot nanocrystals are made of many different semiconductor materials, e.g., CdSe, ZnSe, CdZnSe, PbS, and InP, just to name a few. Later after the initial attempts for the synthesis of the quantum dot nanocrystals, Bawendi et al. demonstrated that high-quality quantum dot nanocrystals with high quantum yield and narrow size distribution can be obtained through a hot injection synthesis at high temperatures, which is considered as a revolutionary milestone in the synthesis of quantum dot nanoparticles [20, 21]. In this reaction scheme, the precursor materials which are organometallic precursors were injected into a boiling coordinating solvent, e.g., trioctylphosphine (TOP) and trioctylphosphine oxide (TOPO). This process results in the thermal decomposition of the precursor materials and the monomers form the first nucleus of the quantum dot nanocrystals. Following the nucleation by further addition of the precursor monomers from the solution, the crystal growth is achieved. In the mean time, further newly added monomers are incorporated onto the existing nuclei instead of forming new nuclei because of their lower unsaturated concentrations. As soon as the monomer concentration is decreased to a certain level, the growth of nanoparticles continues the Ostwald ripening process. In this process, the smaller particles with higher surface tension may dissolve and contribute to the growth of larger particles. This continues until the system is saturated by the formed quantum dot nanocrystals.

The formation of quantum dot nanocrystals can be controlled by the addition of certain surfactants and ligand molecules. The longer the reaction continues, the larger particles are formed. Because the size controls the peak emission wavelength of the quantum dot nanoparticles, one can optimize the reaction time to obtain quantum dots emitting at a desired wavelength. Cleaning of the synthesized nanocrystals is also important to remove the unreacted reagents, as there might be a high amount of acids, metals, and amines left unreacted in the solution. The synthesized nanocrystals are typically characterized using transmission electron microscopy, x-ray photoelectron spectroscopy, and wide-angle x-ray diffraction spectroscopy. Besides these, optical characterization of the particles must be carried out using absorption and fluorescence spectroscopy [22, 23].

Water is the crucial medium for all life forms and biological materials. To use synthesized nanocrystals in aqueous environments, there are two methods: one is to synthesize the quantum dot nanocrystals directly in an aqueous environment and the other is through the ligand exchange of solvent-based quantum dots. The successful synthesis of the aqueous quantum dot nanocrystals made of CdTe was first achieved by Nozik and Welles. During their synthesis of CdTe nanocrystals, Nozik et al. used 3-mercapto-1,2-propanediol and hexametaphosphate as the stabilizing agents. Alternatively, Welles et al. introduced different thiols such as mercaptoethanol and 1-thioglycerol in their aqueous synthesis [24].

Capping CdTe nanocrystals with TGA also makes it easy for their surface modification. Later, using aqueous routes of nanocrystals, various materials were synthesized; CdSe, CdS, CdTe, and HgTe are some of the aqueous NCs. Also, by applying different capping agents, especially thiols, the quantum efficiency of aqueous nanocrystals was increased up to 40–60% range. CdTe is now the most typically used material to make aqueous quantum dot nanocrystals, which has found many applications because of its simple synthesis while avoiding the need for any further modification toward water solubility. CdTe nanocrystals are synthesized from a Cd salt, most popularly from Cd $(ClO_4).6H_2O$. In the aqueous synthesis of CdTe, the salt is dissolved in water and a proper amount of thiol is added for stabilization and the flask is continuously stirred to sustain homogeneity. The control of the pH of the solution is achieved through dropwise addition of NaOH. In the mean time, the flask is heated for 30 min aerating with N_2. H_2Te gas is flown through the flask with the aid of N_2 flow. At the first stage, the precursor of CdTe is formed, and at the second stage, the precursors are refluxed at 100 °C under open air conditions by the aid of a condenser. During the reflux, CdTe NCs start to grow. Utilization of Al_2Te_3 as the Te source can be an alternative way for the CdTe nanocrystal synthesis, which can be more convenient but more expensive. During the synthesis of the CdTe nanocrystals, short chain thiols (namely thioglycolic acid, mercaptoacetic acid, 2-mercaptoethylamine, and cysteamine) with functional groups (e.g., amine, carboxyl, and hydroxyl) have been utilized [19, 25, 26].

4.1.2 Surface Modification of Quantum Dot Nanocrystals

In order to utilize the quantum dot nanocrystals in FRET applications, strategies for the conjugation with biomolecules and with certain dye molecules are needed. The conjugation of the quantum dot nanocrystals allows the dye and quantum molecule to be kept in the close proximity, which satisfies the nonradiative energy transfer. Commonly used approaches for the attachment of the fluorophores to a quantum dot for FRET applications can be grouped as follows.

4.1.3 Electrostatic Interaction of the Quantum Dot Nanocrystals with Fluorophores

In this approach, the quantum dot nanocrystals interact with the fluorophores through positively charged–negatively charged group interaction. In their study, Sun et al. found that aqueous CdTe solutions to yield high FRET efficiency while interacting with a polymer named poly (vinylcarbazole) in a blend. The interaction between these species was achieved through electrostatic interaction of the negatively charged CdTe and the positively charged polymer [27] Similarly, Osovsky et al. investigated the FRET process between CdTe NCs which are modified with two distinct functional groups, namely, positively charged cysteamine and negatively charged thioglycolic acid [28]. Here, the biomolecules were coupled with the quantum dots through electrostatic interaction using the charged groups on the backbone of the biomolecules. Also, quantum dot nanocrystal sensor complexes built up using single-strand DNA and the attachment of proteins are among the examples of biomolecule-quantum dot nanocrystals hybrid systems formed through

electrostatic interactions [29–33]. Although the electrostatic interaction is not very strong compared to metal affinity or chemical attachments, it is widely used for building FRET complexes using quantum dots because of the easiness of the method. However, if more stable structures are needed for FRET-operating systems, other approaches can be pursued.

4.1.4 Chemical Attachment of FRET Partners to Quantum Dot Nanocrystals

The outer shell surface of the quantum dots can be modified with amine or carboxylic acid groups, or during the synthesis of the quantum dot nanocrystals, these groups can be introduced. During the synthesis, thioglycolic acid can be used as the ligand at the outer shell and the quantum dots then become decorated with the carboxyl groups. The carboxylic acid group can be activated using the addition of EDC (1-ethyl-3-(3-demethylaminopropyl)carbodiimide). This reaction leads to the formation of O-acylisourea intermediate, which can react easily with the amine groups on the fluorescent biomolecule or the dye and forms a stable conjugate. In this reaction to prevent the hydrolysis of another intermediate molecule, NHS (*N*-hydroxysulfosuccinimide) can also be employed [34–36]. Amine-functionalized quantum dots can also be synthesized; for example, cysteamine can be employed as a capping agent, or via ligand exchange, the quantum dot nanocrystal surface can be decorated with cysteamine. In this case similar to the –COOH functionalization, the carboxyl-containing molecule can be activated, and quantum dot nanocrystal can be conjugated via amine coupling [37].

4.1.5 Metal Affinity Tag Enabled Assembly

Metal affinity tag is a commonly used peptide sequence for purification of the proteins using an affinity-based chromatography approach. The most common metal affinity tag is a hexahistidine molecule, which interacts strongly with the metal atoms. Nickel is the most widely used metal for its strong interaction with the imidazole groups on the histidine amino acids. However, it was also demonstrated that it can strongly interact with the semiconductor materials [38]. Especially fluorescence proteins and dye-labeled proteins tagged with 6xHis have been proven to form FRET couples with quantum dot nanocrystals. Park et al. investigated to synthesize thiolated nitrilotriacetate-capped CdSe/ZnS quantum dot nanocrystals, which were then shown to successfully capture the hexahistidine peptide conjugated with TAMRA dye [39]. Boeneman et al. achieved the assembly of a fluorescent protein mCherry on the surface of CdSe/ZnS NCs using the metal affinity tag as the linker molecule, which was later utilized in a FRET process successfully [40].

Other specific interactions were also used to conjugate fluorescent biomolecules and dye-labeled biomolecules to the quantum dot nanocrystals; for example, biotin–streptavidin interaction was widely used [41–43]. Other protein purification tags can also be employed for coupling proteins to the quantum dot nanocrystals, glutathione S-transferase; FLAG and strep-tag are the most promising ones for creating a protein-NC FRET couple [44].

4.2 Characterization Methods of the FRET Process

FRET process can be easily monitored using available fluorescence spectroscopy and time-resolved spectroscopy instruments. In fluorescence spectroscopy, the optical intensities of the donor and acceptor were measured separately, and then the optical intensity level of the mixture facilitating FRET must be measured. However, because the optical intensity level heavily depends on the molar ratio of the donor and acceptor in the solution, the optical intensity of the fluorescence signal must be carefully normalized for the three cases mentioned above. In fluorescence spectroscopy, only the change in the optical intensity change of the donor and acceptor molecules can be tracked.

An additional approach is to measure the fluorescence lifetime change of the donor and acceptor molecules. In this approach using a time-resolved fluorescence spectroscopy (e.g., time-correlated single photon count systems), the emission kinetics of the donor and acceptor are monitored and the decay lifetimes are measured. This leads to a more robust measurement of the FRET process, because the measurement changes in the emission kinetics are not as sensitive to the amount of the material that exists in the medium as the steady state measurements [45].

A time-resolved fluorescence spectroscopy tool needs to be equipped with a gated or pulsed laser source emitting at a suitable excitation wavelength, which can be used to excite the fluorescent materials subject to FRET process in the substrate medium. In order to focus the laser beam, a lens system is used and the beam is passed through a polarizer. Subsequently, the light is passed through a monochromator with a suitable slit aperture, and the photons can be counted using a high-precision time-correlated single photon counting system in the case of time-correlated single photon count systems [26].

5 Key Research Findings

5.1 Quantum Dot Nanocrystals Enabled Biosensors

5.1.1 Antibody–Antigen Interaction Using Quantum Dot Nanocrystal-Enabled FRET Processes

Nanobiosensors have been developed and/or improved in the last decade with better sensing capabilities and lower limits of detections [46]. Quantum dot nanocrystals have been widely used as the signal-generating parts of these sensing systems. FRET process is the best way to harness the optical properties of QD photoluminescence (PL). Quantum dots are versatile donors for FRET applications, and they can generate very efficient FRET processes when they are coupled with a proper acceptor [7, 47, 48]. Today, many researchers are interested in using quantum dots as donors for FRET applications for their favorable optical properties, which are mentioned earlier. Especially high-quantum-yield (QY) ratios of these quantum dots make them popular for FRET applications because a high QY allows for detecting at longer FRET distances. Also, the sharp and size-tunable emission of

the quantum dots allows minimizing the cross talk between the acceptor and donor emission wavelengths during measurements. Quantum dots are ideal for multiplexed FRET configurations as more than one quantum dot emitting at different wavelengths can be excited at the same wavelength without an overlap with their respective PLs [6]. One of the important requirements for the biosensors is specificity. In this respect, the quantum dots provide very large surface areas which enable them to be easily functionalized for recognition elements using a number of different conjugation methods [18].

Quantum dot-based FRET has been used in biosensing applications to monitor different types of specific biological and biochemical events. In biosensing studies, one of the most studied and well-established approaches is based on utilizing molecular recognition elements to detect specific molecules such as antibody–antigen systems. In an antibody-based sensing system, typically a sandwich type of assay is utilized to capture an antigen. Here, two antibodies with affinity to the same target can be used. In this case, the first antibody is labeled with a quantum dot, and the second antibody, reporter antibody, is labeled with a dye molecule [49]. If a target antigen is added into the solution, it binds both the antibodies, which finally creates a FRET-controlled quenching of the quantum dot with the dye molecule, and the loss in PL of the quantum dot depends on the concentration of the target antigen [50]. This assay configuration may, however, cause some problems including a possible heterogonous A–D separation due to the bigger size of the antibody, which can then result in mixed antibody avidity [51]. For example, Wei et al. tested this configuration by conjugating a monoclonal antibody specific for estrogen receptor β (ER-β) to a quantum dot emitting at 565 nm and polyclonal anti-ER-β reporter antibody labeled with Alexa Fluor 633 dye. They characterized the system by adding ER-β into the solution. The loss in PL of the quantum dot was observed upon formation of the sandwich. The FRET distance between A and D was calculated to be 8–9 nm, which is a proof of the larger size of the molecules [52]. Detection of the FRET signal between an antigen and an antibody can be improved using a specific separation approach, which was achieved through a capillary electrophoresis. In their study, Li et al. accomplished the labeling of mouse IgG and goat anti-mouse IgG with water-soluble CdTe QDs emitting at 532 nm (donor) and 632 nm (acceptor). FRET process was observed by separating noninteracting and well interacting FRET pairs using CE equipped with a fluorescence detector [53]. In contrast to this approach, the competition between a phage display-selected anti-TNT (2,4,6-trinitrotoluene) single-chain Fv fragment attached to CdSe/ZnS core/shell QDs (emitting at 530, 555, and 570 nm) and a quencher dye (Black Hole Quencher-10)-labeled TNT analogue (TNB) was used to yield FRET-based quenching. As shown in Fig. 14.1, upon binding of TNT existing in the sample to the scFv fragment around the quenched quantum dot bound to TNB-BHQ-10, TNB-BHQ-10 was exchanged with TNT, which allowed a concentration-based increase in the quantum dot emission after termination of the quenching via FRET process [54].

Proteomic applications of antibodies are of great interest for detection of many diseases. Autoimmune diseases can be characterized using antibody profiling of the

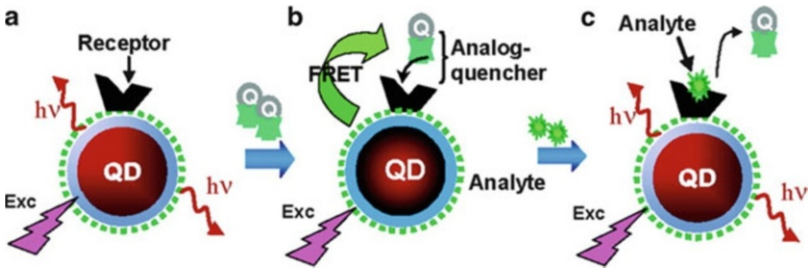

Fig. 14.1 Schematic of the TNT sensor (**a**) QD conjugate of the TNT receptor, (**b**) FRET between QD and quencher-labeled analogue molecule, and (**c**) replacement of the quencher-labeled analogue and recovering the QD fluorescent emission (Reprinted with permission from Goldman, E. R. et al. A hybrid quantum dot-antibody fragment fluorescence resonance energy transfer-based TNT sensor. J. Am. Chem. Soc. 127, 6744-6751 (2005). Copyright (2005) American Chemical Society)

disease markers, which is crucial for the diagnosis of the disease at early stages. In this manner, Sukhanova et al. demonstrated a sandwich-type assay by using the FRET effect enabled between orange emitting quantum dot nanocrystals and FITC dye. Quantum dots were assembled on microbeads and covered with a human DNA topoisomerase I (topol), which was used to detect anti-topol antibodies as they were one of the markers of systemic sclerosis. After the addition of the human plasma followed by the addition of FITC-labeled secondary anti-topol antibodies, the readout gave a FRET signal upon the existence of any anti-topol antibody in the human blood plasma [55].

5.1.2 Monitoring Nucleic Acid Assembly and Functionality Using Quantum Dot Nanocrystal-Enabled FRET Processes

Conjugation of the nucleic acids with quantum dot nanocrystals is a popular approach to build biosensors. Using the FRET process, the quantum dot nanocrystal–nucleic acid conjugates were used to detect the existence of certain nucleic acid sequences via sequence-controlled hybridization. Also, nucleic acid aptamers were utilized in this type of applications, which have specific recognition capabilities toward a specific molecule (e.g., protein, peptide, and DNA) via their corresponding three-dimensional structure. Compared to the dye-labeled protein-quantum dot conjugates, the dye-labeled thiolated DNA-quantum dot configuration makes more sensitive FRET sensors [56].

Molecular beacons are the well-known examples for the quantum dot-nucleic acid conjugations facilitating FRET process. In a molecular beacon, a single-stranded DNA (ssDNA) molecule is conjugated to a quantum dot nanocrystal from one end, and a quencher molecule is attached to the other end. The ssDNA molecule is generally designed in a way that can hybridize to forming a stem loop at the end. Generally, this stem-loop sequence contains a specific sequence that targets another specific region. Upon hybridization of the stem-loop sequence with the target probe, the stem loop opens and the distance between quantum dot nanocrystal

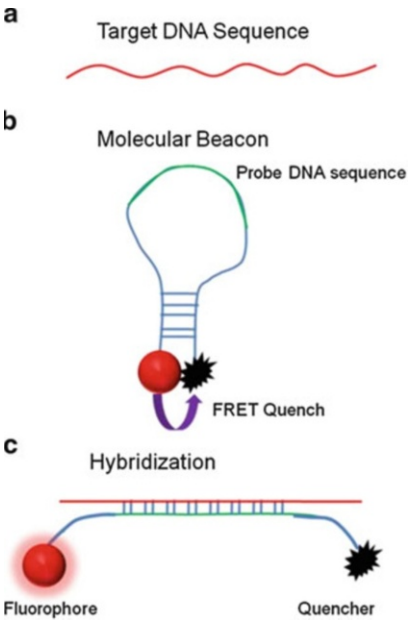

Fig. 14.2 Schematics of a molecular beacon and its working principle

and quencher molecule increases, turning on the emission of the quantum dot upon the decrease in the FRET efficiency of the quantum dot with the quencher. Cady et al. studied the optimum conditions of molecular beacon configuration using quantum dot nanocrystal as the fluorophore (Fig. 14.2).

The attachment chemistry of quantum dot nanocrystal to ssDNA is crucial for the molecular beacon. Although streptavidin–biotin-based attachment is easy, using a zero-length linker, EDC chemistry is promising and provides a better fluorescence intensity. Depending on the emission wavelength of the quantum dot, using a dye molecule as a quencher is more promising instead of using gold nanoparticles, although it is a good quencher. However, the spectral overlap with the dye must be well-defined [57]. Wu et al. demonstrated the importance of the linker to conjugate DNA molecule to quantum dot after surface treatments for FRET-based sensing applications on a glass surface. Amine-functionalized DNA was attached to the carboxyl-containing quantum dots using NHS/EDC chemistry. Using a zero-length linker, they avoided any possible steric hindrance due to the size of the conjugates on the glass slide surface, where they achieved a 3 nm quantum dot conjugate in size and 70% FRET efficiency during DNA detection via specific DNA hybridization of the target DNA molecule with a surface-bound reporter [58]. Similarly, using thiols is also very useful as a linker for quantum dot-DNA conjugates in FRET applications [56]. Quantum dot molecular beacons were also formed using quantum dot nanocrystals emitting at different wavelengths, which brought about a promising approach for the multiplexed quantum dot molecular beacon systems. In a multicolor quantum dot nanocrystal scheme, molecular beacons were able to detect a target DNA down to 8 ng in a sample solution, which was comparable to

that of the currently available organic dyes with a higher stability and a lesser background signal [59].

Single quantum dot-based DNA nanosensors have been very popular since the demonstration of its first usage. In this scheme, a dye molecule was attached to quantum dot nanocrystals by using appropriate conjugation chemistry. Cy5 and quantum dot nanocrystals emitting at 605 were found to have an excellent overlap, and in most of the following studies, this pair was used for FRET-enabled sensing. In the demonstration by Zhang et al., this configuration was found to be more sensitive than a molecular beacon approach [60].

DNA aptamers are molecular recognition elements functioning through their three-dimensional structures. They were selected using a system called SELEX. Using an aptamer molecule selected for adenosine triphosphate (ATP) binding, Chen et al. built quantum dot nanocrystal-enabled FRET-based systems to sense ATP in solution, which has an alternative configuration. In the nanosensor, a streptavidin-coated quantum dot nanocrystal (605 nm), a 3′-biotin-modified DNA, 3′-Cy5-labeled DNA, and a capture DNA involving an ATP-binding aptamer that contains specific binding sequences for 3′-biotin-modified DNA were used. In the absence of ATP, the capture DNA was bound to the 3′-Cy5-labeled DNA and 3′-biotin-modified DNA, which later was bound to the streptavidin-coated quantum dot nanocrystal complex via biotin. In this first configuration, the bound 3′-Cy5-labeled DNA came into the close proximity with the quantum dot, resulting in the quenching of the quantum dot due to the FRET process. However, if ATP was introduced, it competed with the 3′-Cy5-labeled DNA and released it. This resulted in an obvious increase of the quantum dot emission [61].

This alternative approach might be extended into sensing DNA–DNA, DNA–protein, and DNA–small molecule interactions (e.g., minerals and vitamins). Moreover, a nanosensor for cocaine detection was realized using a similar approach based on a DNA aptamer specific for cocaine. This sensor, however, was built in two different configurations. A quantum dot nanocrystal emitting at 605 nm was conjugated with a DNA molecule displaying a cocaine-specific aptamer sequence and could also hybridize with a DNA fragment conjugated with Cy5. In the absence of the cocaine, the Cy5-conjugated DNA fragment was bound to the quantum dot nanocrystal conjugated backbone, and the FRET process between Cy5 and quantum dot nanocrystal causes the quantum dots to be quenched. Upon the addition of cocaine into the medium, it was bound to the aptamer sequence which has caused the dissociation of the Cy5-labeled DNA fragment and triggered the increase of quantum dot PL upon turning down the FRET process. Furthermore, the same process was improved by introducing another dye-labeled (Iowa Black RQ) DNA fragment. This secondary fragment (Iowa Black RQ) DNA can bound to the DNA attached to the quantum dot nanocrystal and formed a sandwich shown as in Fig. 14.3 in the absence of cocaine which resulted in quenching the emission of Cy5. In the presence of cocaine, the aptamer was bound to cocaine, which resulted in the release of Iowa Black RQ-labeled DNA. After this, the fluorescence of Cy5 became detectable as a sign of cocaine [62].

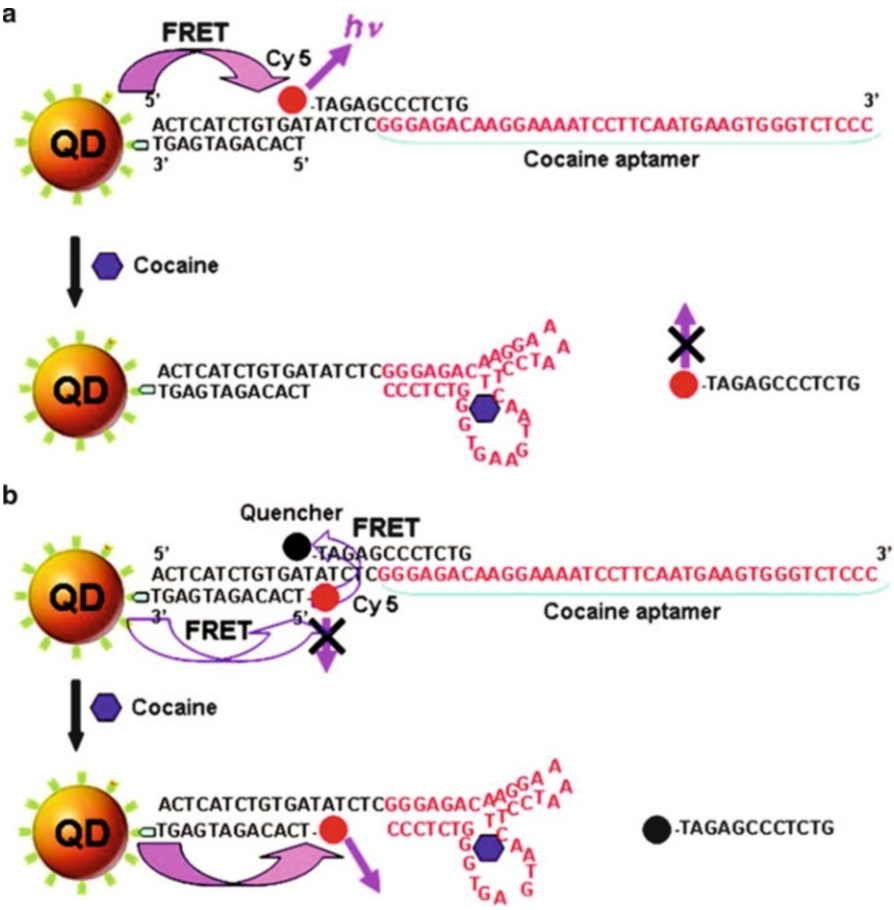

Fig. 14.3 Schematic of the cocaine sensor: (**a**) Signal-off configuration of the QD-based cocaine sensor, where the QD emission was quenched at first and later increased upon cocaine binding. (**b**) Signal-on configuration of the QD-based cocaine sensor, where the QD emission was quenched upon cocaine binding (Reprinted with permission from Johnson, L. W. & Zhang, C. Y. Single Quantum-Dot-Based Aptameric Nanosensor for Cocaine. Anal Chem 81, 3051–3055, doi: 10.1021/Ac802737b (2009). Copyright (2009) American Chemical Society)

Detection of the platelet-derived growth factor (PDGF) using an aptamer DNA conjugated with quantum dot nanocrystals was also realized, where the FRET was switched off and on by the attachment and release of the black hole quencher to the quantum dot-conjugated DNA sequence upon the absence and existence of PDGF in the sample [63]. Alternatively, unlabeled DNA can be also captured to its specific capture agent, and detection of target DNA can be achieved. In this configuration, the capture DNA was conjugated to a quantum dot nanocrystal using polyethylene glycol (PGE) linker. PEG linker helped to adjust the distance of capture DNA to quantum dot nanocrystal, which helped to adjust FRET distance between quantum

dot nanocrystal and dye, ethidium bromide (EtBr), a molecule labeled to target DNA. To detect the unlabeled DNA, the sample was introduced into the solution and the hybridization took place. Later, EtBr was added to the solution and it formed a fluorescent complex with unlabeled DNA. Upon the formation of the complex, FRET occurred between the quantum dot nanocrystal and the complex, which gave a rise in the fluorescent emission of ethidium bromide [64]. In another innovative approach, it was proposed to detect the DNA hybridization using a two-step FRET system. In this route, a positively charged conjugated polymer was used as the light-harvesting antenna in the solution. It was bound to negatively charged CdTe QDs, upon which FRET process took place and the outer surface of QD-antenna complex became positively charged. This complex was then interacted with the labeled DNA fragments in solution. The second FRET process took place between the dye-labeled DNA molecule and quantum dot-conjugated polymer complex. It was also noted that ssDNA and double-stranded DNA (dsDNA) created different slopes in linearly increasing ratio of dye to quantum dot nanocrystal emission intensities because of the difference in their binding strength to QD-polymer complex [65].

A tumor marker, mucin 1, is a glycoprotein that was expressed on most epithelial cells. This marker was known to be a good indicator for early cancer diagnosis. A nanosensor that involved a specific DNA aptamer for a MUC1 was constructed, where the DNA aptamer was bound to the quantum dot through EDC/NHS chemistry. The quencher ssDNA, which involved the Iowa Black quencher dye, was able to hybridize with the MUC1 DNA aptamer; however, in the presence of MUC1, the aptamer was unfolded into ssDNA. Therefore, both the quencher ssDNA and quantum dot-modified ssDNA were able to attach on the aptamer. This hybridization brought the quencher DNA and the quantum dot in close proximity resulting in FRET-enabled quenching of the quantum dot, which was shown to be MUC1 concentration dependent [66].

Besides using chemical conjugation or streptavidin–biotin conjugation, for the assembly of ssDNA to quantum dot nanocrystals, the electrostatic interaction was also employed to build FRET facilitating system to probe micrococcal nuclease activity detection. In this configuration, CdSe/ZnS nanoparticles were functionalized with an enzyme, lysozyme, to prepare positively charged quantum dots to assemble a negatively charged dye-labeled ssDNA. The dye-labeled ssDNA was a substrate for nuclease activity on the outer surface of the quantum dot nanocrystal. When the complex was brought in contact with the micrococcal nuclease, the nuclease digested the ssDNA and caused the release of the dye molecule. This process was monitored as a decrease in the emission of the dye molecule upon deterioration of the FRET process through nuclease activity [33].

To detect the target DNA more precisely, a DNA binding and cleaving enzyme, nicking endonuclease, was utilized by Xu et al. In the assay, they used a linker DNA, which was fully complementary to the target DNA. First, the target DNA and the linker DNA were brought together and they formed a dsDNA, which had a site for the endonuclease to recognize. The endonuclease cleaved dsDNA and the target DNA was released, and this recycle was repeated for many times by resulting in the

cleavage of many linker DNAs. In the second stage, first the enzyme was denatured, and then the quantum dot-conjugated probe I DNA and rhodamine B-conjugated probe II DNA were added, while the uncleaved linker DNA was hybridized with the quantum dot nanocrystal-probe I. Subsequently, the hybrid was sandwiched with rhodamine B-probe II and led to the FRET process. Because the ssDNA target can be used for many cycles, this assay was found to be capable of DNA detection down to 1nM level [67].

In addition, for the detection of the target DNA molecules in solution, also the DNA methylation was probed using a quantum dot-based FRET process in another approach, which is an important tool to detect cancer and monitor tumor behavior for targeted therapy. For this purpose, a sensitive and fast methodology was developed and the established method was called MS-qFRET. In this approach, the genomic DNA was extracted from the sample and subjected to sodium bisulfite conversion. First, the reaction converted the unmethylated cytosines to uracil and the methylated ones were not affected. Second, the sample genomic DNA was amplified with polymerase chain reaction (PCR) using biotin and organic red-emitting fluorophore labeled forward and reverse primers. Finally, the streptavidin-coated nanocrystal was assembled with the biotin and dye-tagged sample DNA. During the PCR reaction, elongation was interrupted by uracils (converted from unmethylated cytosines). Thus, the higher ratio of methylation led to the longer DNA sequence and increased the number of dye molecules that were attached. Consequently, the methylation ratio was determined from the quenching of quantum dot nanocrystals upon FRET with the dye molecules within the close proximity [68]. Suzuki et al. also demonstrated a multipurpose approach using DNA-conjugated quantum dot nanocrystal system for FRET process, which aimed at responding to nucleolytic cleavage, DNA polymerization, and pH change. DNA digestion was monitored upon specific cleavage of the DNA molecule by a nuclease. However, depending on the construction strategy of the DNA-quantum dot nanocrystal conjugates, two distinct FRET patterns were observed. In DNA elongation experiment, upon addition of the Klenow fragments and their elongation with dye-labeled dUTPs, the increased fluorescence of the quantum dot nanocrystals was observed. By the attachment of fluorescein dye to the amine-functionalized quantum dot nanocrystals using Traut's reagent, a FRET-based pH-sensitive sensor was constructed [69].

A nanocrystal-based FRET sensor has also been constructed for the detection of RNA. In their work, Bakalova et al. demonstrated a siRNA sensor to test the effectiveness and activity of the siRNA fragments with the aim of using them in RNA interference applications in mammalian cells. For that, they conjugated their designed siRNA sequence with a cross-linker to the carboxyl-coated quantum dot. They amplified the mRNA extracted from the target sample and labeled Cy5-labeled nucleotides, while the mRNA sequence was amplified. Cy5-labeled mRNA was used as a reporter during the hybridization with the siRNA-modified quantum dots. If the siRNA fragment is a good candidate for the target mRNA and hybridizes with the siRNA conjugated to quantum dot nanocrystals, then a FRET process took place between Cy5 on mRNA and the quantum dot nanocrystal

conjugated to siRNA. This led to an increase in the emission of Cy5. However, if the increase in the emission of Cy5 was limited or cannot be detected, then a mismatch was observed instead of the hybridization. Compared to the available techniques, this approach is faster and promising as a route for siRNA screening [70].

Another similar experiment was carried out to test the drug candidates for AIDS, where the sequence-specific interaction between regulatory protein Rev of HIV virus and portion of *env* gene within RNA gene (Rev-responsive element, RRE) was targeted. Since this interaction is vital for the HIV-1 replication, any attempt to destroy this interaction may lead to the discovery of new drugs for HIV. With this motivation, Zhang et al. proposed a sensor, which probes the interaction between the RRE RNA and a 17-mer peptide derived from Rev. In this configuration, RRE RNA was labeled with a biotin and later conjugated to the streptavidin-coated quantum dot emitting at 605 nm. Rev peptide was modified with Cy5 from its N-terminus. FRET process took place when the Cy5-Rev peptide was bound to the QD-RRE RNA, with an increase in Cy5 emission. The inhibitory effect of the proflavin was tested within the system, where the proflavin was expected to dissociate the Cy5-Rev peptide and decrease the Cy5 emission upon corruption of the FRET process. However, due to the long red tail of proflavin emission, it was not possible to see the decrease in emission of Cy5, only the expected increase in the quantum dot emission was detected. Using correct dichroic and band-pass filters, the leaking long red tail of proflavin emission was filtered, and a distinct suppressed emission from Cy5 was obtained when proflavin triggered the dissociation of Cy5-Rev peptide from RRE RNA-conjugated nanocrystals [71].

Nanocrystal-based FRET research was carried out in solution as the ensemble measurements. However, it was found that it is possible to enhance FRET signal between the donor quantum dot and the acceptor dye-attached DNA by using capillary electrophoresis system. This enhancement phenomenon was observed because of the deformation of the DNA molecule in the capillary flow [72]. Therefore, it can be useful to search for the methodologies other than these ensemble measurements to enhance the FRET signal, which is possibly as important as the conjugation strategies and linkers to be utilized.

5.1.3 Monitoring Protein Involved FRET Processes

Many applications of biosensors in the literature heavily depend on the utilization of proteins as the recognition elements of the biosensor of interest [73]. They have also been utilized in many different FRET applications, and dye-conjugated proteins served as the acceptor or donor molecules. In some of these studies, the proteins were used without any dye conjugation as they already have a self-fluorescence originated from amino acids such as tryptophan, tyrosine, and phenylalanine [74, 75]. Sarkar et al. have showed this phenomenon by conjugating human serum albumin (HAS) to a CdS quantum dot emitting at 510 nm. In this configuration, when HAS was used as a donor and the quantum dot was as an acceptor, FRET was facilitated between the tryptophan at the position of Trp214 and the quantum dot. HSA was conjugated to CdS nanocrystal, and upon thermal

folding/unfolding, which basically modulated the distance between the quantum dot and Trp214, the steady state PL and time-resolved PL were monitored so that a structural nanosensor was introduced to track protein-folding intermediates [76]. Since FRET signal occurred at distances lower than 10 nm, it is possible to track the changes in the conformation of a given protein labeled at appropriate regions with proper acceptor–donor dye choices. Depending on the conformation of the protein, the distance between the labeled regions may facilitate FRET, if the conformation of the protein is changed, and the distance and hence the FRET signal between the labeled residues change, too. The FRET signal being a nanoruler for the molecular distances can thus act as a probe for tracking the changes in the protein structure.

The phenomenon of using the structural changes as a probe in conjugation with an eventual change in the FRET signal was also tested using a model protein, maltose-binding protein (MBP). Hybrid assemblies of the maltose-binding protein and quantum dots were shown to be a model biosensor. Maltose-binding protein from *Escherichia coli* was attached to quantum dots emitting at 560 nm via His-tag expressed at the C-terminus of the protein. Later, the MBP-quantum dot assembly was brought in contact with a dye-labeled maltose analogue molecule, β-cyclodextrin-QSY9 (dark quencher). Then β-cyclodextrin-QSY9 was bound to the saccharide-binding site of MBP. Upon binding of the β-cyclodextrin-QSY9, the quantum dot emission was quenched because of the FRET between β-cyclodextrin-QSY9 and the quantum dot. When maltose molecules were added to the solution, the cyclodextrin-QSY9 dissociated and the maltose was bound to the MBP maltose-binding site, which gave rise to a signal increase in the quantum dot emission by virtue of the breakdown of the FRET-based quenching. Consequently, the maltose concentration-dependent increase in the quantum dot emission was observed. Utilizing the distance dependence nature of FRET in this configuration, another approach was put forth. In this technique, possible problems derived from the donor–acceptor distance restrain can be overcome by the utilization of a multiple step FRET process. In the second configuration, a two-step FRET process was employed where MBP was both conjugated to the quantum dot emitting at 530 nm as the donor and a Cy3 dye as the acceptor emitting at 570 nm. First, the FRET process took place from the quantum dot to the Cy3 dye, and the second FRET process occurred between the Cy3 and the β-cyclodextrin-Cy3.5. The second FRET process resulted in the quenching of the Cy3. Again, addition of maltose molecules replaced the β-cyclodextrin-Cy3.5, and removal of this molecule was detected as an increase in the emission of Cy3 in a maltose concentration-dependent manner. This system was well studied from different aspects including the concentration dependency and the utilization of different donor and acceptor molecules for optimal functioning [77–79].

Detection of the enzymatic activity by manipulating the FRET process between the quantum dot and an acceptor molecule was also demonstrated as biosensors. Protease activity has been one of the most detected phenomena in the biosensor literature. Also, protease sensors were proposed and implemented using quantum dot-enabled FRET processes. Chang et al. proposed a structure where gold nanoparticles (AuNPs) were conjugated with the quantum dot nanocrystal by

exploiting a peptide linker (GGLGPAGGCG), which was a proper target for a protease called collagenase XI. Decoration of the surface of the quantum dot with AuNPs quenched the optical emission. Protease was added into the solution, and the peptide linkers were digested by collagenase, and the AuNPs were released from the close proximity of the quantum dots, which led to the increased QD emission [80]. A similar strategy was also realized to detect type IV collagenase, which finds applications in tumor invasion and metastasis [81]. In a mechanistic study, nonradiative quenching of the quantum dots due to the proximal gold nanoparticles was investigated by means of distance control between the quantum dots and AuNPs using a peptide sequence (YEHK), which was recognized to exhibit a rodlike structure, with its second structure enabling a rigid nature. In this approach, the chain length was changed, and it was concluded that the quantum dot quenching arose due to the long-distance dipole–metal interaction [82].

Attachment of a dye molecule to a quantum dot is one of the most popular approaches, which were also explained in the previous section. Similarly, various peptide sequences were employed as mentioned above. For example, Shi et al. followed a similar approach and functionalized the surface of quantum dots with a short peptide (RGDC) terminated with rhodamine Red-X, which quenched the quantum dot emission in the close proximity. Upon addition of collagenase and subsequent cleavage of the peptide, FRET was ceased, consequently increasing the quantum dot emission and quenching of the rhodamine Red-X [83]. Using the same quantum dot-RGDC-rhodamine Red-X, the effect of the inhibitory activity of various chemical agents was tested in vitro, where the inhibition of the enzymatic activity of trypsin was tracked [84]. *Clostridium botulinum* is attributed to be one of the well-known pathogens and is being characterized by the extracellular production of a toxin called botulinum, composed of a light and heavy chain dimer and activated just after the posttranslational modifications. Posttranslational modifications through proteolysis produce the chains by breaking disulfide bond between them. Sapsford et al. proposed a quantum dot nanosensor to detect the activity, thus the presence of the toxin. The light chain of the toxin (LcA) was used as the target molecule, which showed an endopeptidase activity. His-tagged peptide targets were prepared into which an LcA binding side and a helix spacer were incorporated, which were labeled with a Cy3 and resultantly caused the quenching of quantum dots. Sapsford et al. utilized two approaches. The first was the popular metal affinity conjugation of the peptide to the quantum dot, and they assayed the LcA activity through the increase in the PL emission of the quantum dots upon detachment of the Cy3-containing part of the peptide. They also proposed another approach in which the LcA protein and the substrate peptides containing Cy3 and His-tag were mixed. Upon proteolytic activity of LcA, the peptide was broken down into parts. Therefore, upon addition of the QD, undigested peptides were stuck on them. This attachment caused decrease in the PL emission and read out as the signal for the LcA activity when compared to the initial peptide concentration [85].

Caspase is an important protease with its particular relevance to cancer research and one of the key signs of apoptosis. Boeneman et al. constructed a nanosensor to detect caspase-3 activity in vitro. A cleavage site for caspase-3 protease activities

was incorporated into a fluorescent protein mCherry through protein engineering, which was terminated with His-tag sequence to attach the protein to the quantum dot. The kinetics of FRET process was monitored as a function of proteolytic activity of caspase-3 in real time so that the Michaelis–Menten descriptors for caspase-3 were extracted as well [40]. Similar to this approach, Prasuhn et al. demonstrated a caspase-3 sensor by utilizing a chemical dye, Texas Red, as the acceptor molecule [86]. Biswas et al. designed and implemented an alternative protease sensor for in vivo applications. In this design, elastine-like peptide (ELP) and TAT sequence were also incorporated in addition to the protease cleavage site, dye molecules, and quantum dot. The penetration of the quantum dot was carried out using the ELP peptide and TAT sequence. The quantum dots were conjugated with an organic dye, Alexa 568, through a cysteine group contained by a peptide expressing protease cleavage site and attached to ELP and TAT. The quantum dot conjugate cargo was delivered into the HeLa cells and monitored under a fluorescence microscopy. Later, the cells were transfected with a proviral plasmid pNL4-3.HSA.R-E- to induce the production of noninfectious HIV viruses. Following the delivery of the quantum dot probe, the cleavage of the peptide with the HIV-1 Pr was monitored as a decrease in the intensity of Alexa dye. Inhibition of HIV-1 Pr upon addition of ritonavir, saquinavir, and indinavir was detected as an increase in the FRET efficiency in a dose-dependent manner [87].

Kinase-enabled protein phosphorylation is recognized as one of the key cellular processes any dysfunction of the kinases has been related to in the development of a disease state, and kinases are important for cell signaling and cancer biology. Ghadiali et al. exploited quantum dot nanocrystals attached with reporter peptides involving serine, tyrosine, and threonine amino acids, where the attachment was achieved through using His-tagged peptides. In the existence of kinase, the corresponding amino acids were phosphorylated, and FRET partner dye-labeled anti-phospho-amino acid antibody was brought in contact with the quantum dot-peptide conjugate. While the anti-phospho-amino acid antibody was bound to the phosphorylated peptides, the quantum dot emitting at 605 and Alexa Fluor emitting at 670 were brought in close proximity satisfying the FRET conditions [88]. The same group also constructed another sensor to monitor the activity of the histone acetyltransferase (p300 HAT). They utilized the same approach for the kinase sensor and synthesized a target peptide mimicking H4 N terminal histone sequence including His-tag. The peptide sequence was first incubated with the p300 HAT and acetylated at the Lys_6 position. Later, dye-labeled acetyl lysine specific antibody recognized the target peptide and was bound to it, causing a FRET-based quenching of the quantum dot, which was monitored as a sign of HAT activity [89].

Being responsible for the β-lactam antibiotic resistance in bacteria, detection of β-lactamase is crucial for clinical samples. In their work, Xu et al. proposed a quantum dot-enabled assay method, which relied on a signal-off type of FRET interaction. In this approach, CdSe/ZnS quantum dot nanocrystals were decorated with streptavidin, and the Cy5 dye-conjugated and biotin-modified β-lactam molecules were synthesized. To eliminate steric hindrance, which arose due to the deep binding pocket of streptavidin (SA), a linker was also introduced to the β-lactam

molecules after the biotin modification. After the conjugation of quantum dot-SA with biotinylated linker-β-lactam-Cy5 complex, the quantum dot emission was observed to quench indicating the formation of the nanosensor. Meanwhile, the lactamase was added into the nanosensor solution and, due to the degradation of β-lactam, Cy5 was released into the solution and diminished the FRET process, which in turn resulted in an increase in the quantum dot emission (by fourfolds in this case) [90].

Lipid-coated quantum dots have been developed to be utilized as a probe for lipid exchange at the cellular interface. In order to understand the capability of the lipid-coated quantum dot nanocrystals for this purpose, a quantum dot-based architecture that facilitated FRET process was proposed. This lipid-coated quantum dot structure was composed of a quantum dot coated with DMPE, a phospholipid that displayed an available amine group. Through the further modification of the amine group, an infrared dye Cys5.5 was conjugated to the quantum dot surface. For a second nanoparticle conjugate to mimic a natural high-density lipoprotein (HDL), the particle was further incubated with apolipoprotein (apoA $\sim$ 1). First, the QD-HDL without Cy5.5 was tested for the lipid exchange ability with the Cy5.5-HDL and Cy5.5-micelles. These two particles were mixed, and it was observed that because of the exchange of the lipids, Cy5.5 was also transferred to the QD-HDL structure, which was observed as a decrease in the emission of the QDs due to the FRET process between the QD and the Cy5.5 dye. The effectiveness of the Cy5.5-labeled QD-HDL particles was tested for their functionality by incubating them with living j774a.1 macrophage cells. Upon the adhesion of the Cy5.5-labeled QD-HDL nanoparticles, Cy5.5-lipid exchange with the cell membrane caused the FRET to disappear. This process was observed in the course of transferring the quantum dot conjugates from the cell membrane into the cellular organelles [91]. The schematic of the approach was displayed in Fig. 14.4.

Rakovich et al. realized a FRET facilitating system to increase the light-harvesting efficiency of the bacteriorhodopsin (bR) embedded into the purple membranes (PM) of a bacteria *Halobacterium salinarum*. Quantum dot nanoparticles conjugated with PM were tested for their effectiveness by monitoring the FRET-based quenching of the quantum dots. The formation of the FRET-processing QD-PM assembly increased the light-driven transmembrane pumping by enhancing light-harvesting capability of bR [92] (Fig. 14.5).

Seker et al. proposed and constructed a film-based biosensing approach where the quantum dots emitting at 640 nm were used as the acceptor and the quantum dots emitting at 560 were used as the donor for FRET process. Negatively charged CdTe quantum dots were layer by layer assembled using polyelectrolytic peptides. The thermodynamics of the assembly process of the peptides was investigated as well as the structural features of the peptides to form the most reliable film combination. Supramolecular assembly of the peptide pairs with different chain lengths was tested for most reliable design of the FRET facilitating quantum dot nanocomposites. Once the best peptide constructs were realized, control of the FRET efficiency was achieved using trypsin enzyme. Trypsin enzyme cleaved specifically the linker peptides, which triggered the destruction of peptidic thin

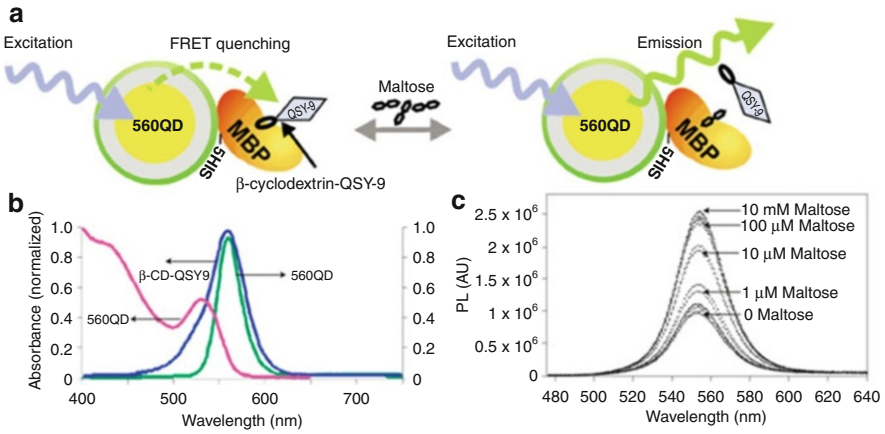

Fig. 14.4 (**a**) QD-FRET sensor schematics, (**b**) spectral properties of the sensor: absorption (*pink*) and emission spectra (*green*) of MBP-conjugated 560QD, along with the absorption spectra (*blue*) of beta-CD-QSY9. (**c**) 560QD-10MBP maltose sensing (Reprinted by permission from Macmillan Publishers Ltd: [Nature Materials] (79), copyright (2003))

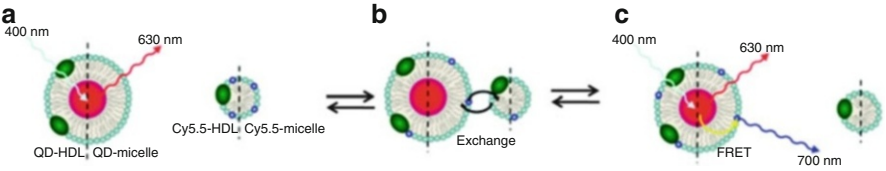

Fig. 14.5 The schematic of FRET facilitating lipid-coated quantum dots: (**a**) HDL-coated QD and QD micelle with Cy5.5-HDL and Cy5.5-micelle without FRET, (**b**) Cy5.5 dye exchange between the HDL-QD and HDL-micelle, and (**c**) FRET between the Cy5.5 and QD in both QD-micelle and QD-HDL configuration (Reprinted with permission from Skajaa, T. et al. Quantum Dot and Cy5.5 Labeled Nanoparticles to Investigate Lipoprotein Biointeractions via Forster Resonance Energy Transfer. Nano Lett 10, 5131–5138 (2010). Copyright (2010) American Chemical Society)

film. In the study, instead of the PL intensities of the donor and acceptor quantum dots, the change in the fluorescence lifetime of these QDs was used as the readout signal. Following the release of the donor quantum dots from the peptidic film, the remaining acceptor quantum dots exhibited a substantially decreased lifetime [93] (Fig. 14.6).

5.2 Quantum Dot Nanocrystals Enhanced Bioimaging

Quantum dot-based FRET processes were incorporated in many different biosensing designs, some of which were discussed above. In some of these applications, the quantum dot-based FRET sensors were also delivered into the cells

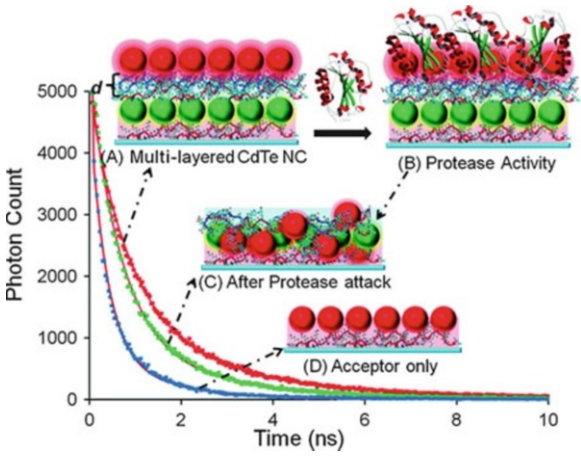

Fig. 14.6 Peptidic FRET facilitating nanocomposite film: (**a**) PL decay of the multilayered structure facilitating FRET, (**b**) the proteolyic digestion of the peptide film, and (**c**) PL decay following the rearrangement of the peptide film as a result of the proteolyic digestion, and (**d**) PL decay of the acceptor alone (Reprinted with permission from Seker, U. O. S. et al., Peptide-Mediated Constructs of Quantum Dot Nanocomposites for Enzymatic Control of Nonradiative Energy Transfer. Nano Letters 11, 1530–1539 (2011). Copyright (2011) American Chemical Society)

to monitor any specific cellular process. For imaging applications, the same approach for constructing biosensors was followed, and the formed constructs of the quantum dots were delivered into the cells to track cellular function or to deliver biomolecules or drugs, which were later monitored by the FRET signal in real time.

Shaheen et al. utilized the FRET process involving quantum dots to monitor the state of the condensation and decondensation of the plasmid DNA (pDNA). pDNA was attached to the quantum dot nanocrystal, and FRET was achieved between this conjugate and rhodamine-labeled polycations. The pDNA-polycation core was then encapsulated into a lipid vehicle, which was called the tetra-lamellar multifunctional envelope-type nanodevice (T-MEND) to transfect HeLa cells. Following the penetration of the loaded T-MEND into the cell, the release of the pDNA was tracked by imaging the change in the FRET signal using a confocal microscope, which has also scanned the T-MEND device in z-stack to detect the condensation/decondensation of the pDNA embedded into the T-MEND device. This method brings about a new and feasible approach for the optimization of the gene delivery tools for gene therapy using the FRET signal as a guide [94].

Bagalkot et al. constituted a hybrid quantum dot system, which was conjugated with an A10 RNA aptamer, to recognize the extracellular domain of the prostate-specific membrane antigen (PSMA). Aptamer-QD conjugate was loaded with an anticancer drug named as doxorubicin. Studies showed that this system facilitates two distinct FRET processes. First, a FRET process occurred between the quantum dot and the doxorubicin molecule, where the quantum dot served as a donor. Second, a FRET process took place between the aptamer molecules and doxorubicin molecules where the doxorubicin acted as a donor. This multi-FRET system

was first delivered into the PSMA-expressing prostate adenocarcinoma cell lines with the help of A10 RNA aptamer molecule through molecular recognition. After the delivery of the particle cargo, the doxorubicin was released into the cellular environment. Release of the doxorubicin reverted the PL emission of the quantum dot. Upon release of the doxorubicin, PL of doxorubicin was also recovered as it was dissociated from the A10 RNA aptamer. Therefore, both the delivery of the quantum dot composite and the release of the drug were monitored through imaging; additionally, the therapy of the cells was succeeded with the released drug [95].

The localization of the protein in living cells is important for the protein distribution. The available techniques can give some idea about the existence of these proteins but not about their interaction depending on their localization. As a solution, with the method Kang et al. proposed, it is possible to track the existence of neighboring proteins. In this work, nucleolin protein was labeled with a dye-modified aptamer molecule, AS1411 targeting nucleolin. On the other hand, integrin was marked with a quantum dot nanocrystal. To recognize the integrin, the quantum dot was decorated with an RGD sequence, which exhibits a high affinity toward integrin protein. Following the assembly of the quantum dot and dye molecules, a FRET process between the dye and the quantum dot was tracked. Using the microscopy analysis, the expression levels of integrin and nucleolin were determined. This approach allows to co-localize various proteins in a native cell, which are important to determine the function of some of the important genes [96]. Intracellular imaging of levels of a given material was also achieved using quantum dot-enhanced FRET, for which Wang et al. used a calcium-modulating protein (CaM)-QD sensor to track the intracellular Ca^{+2} level based on FRET [97].

6 Conclusions and Future Perspective

Quantum dot nanocrystals have been exploited in FRET applications for probing different biological processes. FRET-based labeling systems were designed typically using quantum nanocrystal as the donors, while the organic dye molecules or fluorescent proteins were utilized as the acceptors. Also nanoparticles like silica nanoparticles and gold nanoparticles were used as the acceptor species. To satisfy the FRET conditions, donors and acceptors were conjugated using different approaches. Most popularly, the quantum dots and acceptor species were conjugated using a chemical bonding approach, where the carboxyl-functionalized quantum dots were activated using NHS/EDC and then active amine-binding quantum dots were linked. Streptavidin-coated quantum dots were also commonly conjugated with the biotin-labeled acceptors, or as an alternative approach, the conjugation was obtained using electrostatic interaction between the quantum dot donors and dye acceptors.

Many assays were designed and realized for quantum dot-based FRET applications. Antibody–antigen interactions, protein–protein interactions, and enzymatic activities were successfully monitored using quantum dot-enabled FRET systems,

where a pre-quenched quantum dot was typically used as the donor and an increase in the quantum dot PL was observed upon interaction of the targeted entities. Similarly, in the design of molecular beacons or DNA-hybridization assays, the same approach was used, which is commonly known as the signal-off mode FRET system. Additionally, another FRET mode, in which initially the quantum dot emission was not quenched and the acceptor was not in the close proximity of the donor or was quenched by a secondary acceptor due to its interaction with another molecule, the FRET conditions were later satisfied only upon the interaction with the targeted molecule.

Most of the previous studies in the literature focused on using the quantum dot nanocrystals as the donor molecules because of their long fluorescence lifetime, which makes the resulting FRET efficiency higher. Although there are challenges in using quantum dots as the acceptors, utilizing biological reactions (e.g., those based on chemoluminescence and bioluminescence) can enable the quantum dots to emit in the absence of a physical light. This kind of approaches can lead to the development of innovative bioassay systems.

Although there have been fascinating efforts put into action to improve the capabilities of the quantum dots, there are still challenges especially for the in vivo delivery of these dots. There have been numerous different approaches and tools developed and optimized for a simple delivery of the quantum dots. Utilization of lipid transfection, direct microinjection, and electroporation are among the widely studied approaches in this area [98–100]. The surface chemistry of the quantum dots affects the delivery in the cellular environment. For that reason, utilization of protein and peptide-integrated quantum dots is becoming more important. Biomolecules are generally recognized to be biocompatible compared to the chemical linkers. For example, signaling molecule-functionalized quantum dots can be used for the transportation of the quantum dots across the cellular membrane to the nucleus of the cells.

FRET-based approaches to track any given biochemical reaction occurring within the cell are capable of creating a new era for the proteomics. Given the fact that metabolic engineering needs real time monitoring of the metabolic flux analysis of a molecule of interest, quantum dots can be used to construct in vitro assays facilitating FRET. Not only for diagnosis but also for therapy, the quantum dots could be successfully utilized while carrying drug cargo into the target cell compartment, and the real time delivery of the drug molecule and its effectiveness could be monitored. In this way, the quantum dot FRET-based drug screening approaches could possibly be established. However, there is one important challenge to be addressed about their toxicity. In order to bear with the toxicity of the quantum dots, various attempts were made using cell-based experiments focused on the fate of the quantum dots within the cell, especially about distribution and accumulation of the quantum dots [101–103]. To overcome these disadvantages, strategies were tested to reduce toxicity of the quantum dots including negatively charged surface and biocompatible surface coatings. Another reported approach was based on using less toxic materials instead of Cd for the synthesis of semiconductor nanoparticles such as ZnO and ZnSe [104, 105].

To sum up, semiconductor colloidal quantum dots make one of the most popular and promising tools in biomedical and biochemical applications, potentially enabling game-changing detection and imaging systems for life sciences. Quantum dot-based FRET applications allow for the flexibility of carrying out detection and imaging studies at a wide range of wavelength choice at high efficiency levels with their broadband absorption and long fluorescence lifetimes, compared to the available organic dyes. With the ease of their surface functionalization, the colloidal quantum dots are capable of serving as efficient FRET donors for a wide range of applications with a potential high impact of emerging commercial production lines toward biomedical diagnostic and therapy tools.

References

1. Luo SL, Zhang EL, Su YP, Cheng TM et al (2011) A review of NIR dyes in cancer targeting and imaging. Biomaterials 32:7127–7138
2. Yuca E, Karatas AY, Seker UOS, Gungormus M et al (2011) In vitro labeling of hydroxyapatite minerals by an engineered protein. Biotechnol Bioeng 108:1021–1030
3. Sameiro M, Goncalves T (2009) Fluorescent labeling of biomolecules with organic probes. Chem Rev 109:190–212
4. Vendrell M, Lee JS, Chang YT (2010) Diversity-oriented fluorescence library approaches for probe discovery and development. Curr Opin Chem Biol 14:383–389
5. Margulies D, Hamilton AD (2010) Combinatorial protein recognition as an alternative approach to antibody-mimetics. Curr Opin Chem Biol 14:705–712
6. Sapsford KE, BertiI L, Medintz L (2006) Materials for fluorescence resonance energy transfer analysis: beyond traditional donor-acceptor combinations. Angew Chem Int Ed 45:4562–4588
7. Mutlugun E, Nizamoglu S, Demir HV (2009) Highly efficient nonradiative energy transfer using charged CdSe/ZnS nanocrystals for light-harvesting in solution. Appl Phys Lett 95:033106
8. Krukenberg KA, Street TO, Lavery LA, Agard DA (2011) Conformational dynamics of the molecular chaperone Hsp90. Q Rev Biophys 44:229–255
9. Ratzke C, Mickler M, Hellenkamp B, Buchner J et al (2010) Dynamics of heat shock protein 90 C-terminal dimerization is an important part of its conformational cycle. Proc Natl Acad Sci USA 107:16101–16106
10. Huttunen R, Shweta ME, Lahdenranta M et al (2011) Single-label time-resolved luminescence assay for estrogen receptor-ligand binding. Anal Biochem 415:27–31
11. Rajdev P, Mondol T, Makhal A, Pal SK (2011) Simultaneous binding of anti-tuberculosis and anti-thrombosis drugs to a human transporter protein: a FRET study. J Photochem Photobiol B-Biol 103:153–158
12. Liu S, He J, Jin HL, Yang F et al (2011) Enhanced dynamic range in a genetically encoded $Ca^{(2+)}$ sensor. Biochem Biophys Res Commun 412:155–159
13. Breton B, Sauvageau E, Zhou J, Bonin H et al (2010) Multiplexing of multicolor bioluminescence resonance energy transfer. Biophys J 99:4037–4046
14. Li M, Cushing SK, Wang QY, Shi XD et al (2011) Size-dependent energy transfer between CdSe/ZnS quantum dots and gold nanoparticles. J Phys Chem Lett 2:2125–2129
15. Michalet X, Pinaud FF, Bentolila LA, Tsay JM et al (2005) Quantum dots for live cells, in vivo imaging, and diagnostics. Science 307:538–544
16. Burda C, Chen XB, Narayanan R, El-Sayed MA (2005) Chemistry and properties of nanocrystals of different shapes. Chem Rev 105:1025–1102
17. Rosi NL, Mirkin CA (2005) Nanostructures in biodiagnostics. Chem Rev 105:1547–1562

18. Hildebrandt N (2011) Biofunctional quantum dots: controlled conjugation for multiplexed biosensors. ACS Nano 5:5286–5290
19. Mattoussi H (2010) In: Klimov VI (ed) Nanocrystal quantum dots, Ch 10. CRC Press, pp 369–393
20. Murray CB, Kagan CR, Bawendi MG (2000) Synthesis and characterization of monodisperse nanocrystals and close-packed nanocrystal assemblies. Annu Rev Mater Sci 30:545–610
21. Murray CB, Norris DJ, Bawendi MG (1993) Synthesis and characterization of nearly monodisperse Cde (E = S, Se, Te) semiconductor nanocrystallites. J Am Chem Soc 115:8706–8715
22. Pandey G, Dixit S (2011) Growth mechanism and optical properties determination of CdS nanostructures. J Phys Chem C 115:17633–17642
23. Miao SD, Hickey SG, Rellinghaus B, Waurisch C et al (2010) Synthesis and characterization of cadmium phosphide quantum dots emitting in the visible red to near-infrared. J Am Chem Soc 132:5613–5615
24. Rogach AL, Gaponik N (2008) In: Semiconductor nanocrystal quantum dots. Synthesis, assembly, spectroscopy and applications (Rogach AL ed). Springer, pp 73–99
25. Gupta S, Uhlmann P, Agrawal M, Lesnyak V et al (2008) Covalent immobilization of quantum dots on macroscopic surfaces using poly(acrylic acid) brushes. J Mater Chem 18:214–220
26. Gaponenko SV, Ozel T, Nizamoglu S, Sefunc MA et al (2011) Anisotropic emission from multilayered plasmon resonator nanocomposites of isotropic semiconductor quantum dots. ACS Nano 5:1328–1334
27. Sun HZ, Ning Y, Zhang H, Zhang JH et al (2009) Synthesis and characterization of CdTe nanoparticle/polymer functional composites. J Nanosci Nanotechno 9:7374–7378
28. Osovsky R, Shavel A, Gaponik N, Amirav L et al (2005) Electrostatic and covalent interactions in CdTe nanocrystalline assemblies. J Phys Chem B 109:20244–20250
29. Qiu T, Zhao D, Zhou G, Liang Y et al (2010) A positively charged QDs-based FRET probe for micrococcal nuclease detection. Analyst 135:2394–2399
30. Lee J, Choi Y, Kim J, Park E et al (2009) Positively charged compact quantum dot-DNA complexes for detection of nucleic acids. Chemphyschem 10:806–811
31. Kim YS, Jurng J (2011) Gold nanoparticle-based homogeneous fluorescent aptasensor for multiplex detection. Analyst 136:3720–3724
32. Lu H, Schops O, Woggon U, Niemeyer CM (2008) Self-assembled donor comprising quantum dots and fluorescent proteins for long-range fluorescence resonance energy transfer. J Am Chem Soc 130:4815–4827
33. He ZK, Qiu T, Zhao D, Zhou GH et al (2010) A positively charged QDs-based FRET probe for micrococcal nuclease detection. Analyst 135:2394–2399
34. Liu W, Howarth M, Greytak AB, Zheng Y et al (2008) Compact biocompatible quantum dots functionalized for cellular imaging. J Am Chem Soc 130:1274–1284
35. Mattoussi H, Susumu K, Uyeda HT, Medintz IL et al (2007) Enhancing the stability and biological functionalities of quantum dots via compact multifunctional ligands. J Am Chem Soc 129:13987–13996
36. Pinaud F, King D, Moore HP, Weiss S (2004) Bioactivation and cell targeting of semiconductor CdSe/ZnS nanocrystals with phytochelatin-related peptides. J Am Chem Soc 126:6115–6123
37. Lee CM, Jang D, Cheong SJ, Kim EM et al (2010) Surface engineering of quantum dots for in vivo imaging. Nanotechnology 21:285102
38. Peelle BR, Krauland EM, Wittrup KD, Belcher AM (2005) Design criteria for engineering inorganic material-specific peptides. Langmuir 21:6929–6933
39. Grailhe R, Park HY, Kim K, Hong S et al (2010) Compact and versatile nickel-nitrilotriacetate-modified quantum dots for protein imaging and forster resonance energy transfer based assay. Langmuir 26:7327–7333

40. Medintz IL, Boeneman K, Mei BC, Dennis AM et al (2009) Sensing caspase 3 activity with quantum dot-fluorescent protein assemblies. J Am Chem Soc 131:3828–3829
41. Medintz IL, Boeneman K, Deschamps JR, Buckhout-White S et al (2010) Quantum dot DNA bioconjugates: attachment chemistry strongly influences the resulting composite architecture. ACS Nano 4:7253–7266
42. Kizek R, Ryvolova M, Chomoucka J, Janu L et al (2011) Biotin-modified glutathione as a functionalized coating for bioconjugation of CdTe-based quantum dots. Electrophoresis 32:1619–1622
43. Nikiforov TT, Beechem JM (2006) Development of homogeneous binding assays based on fluorescence resonance energy transfer between quantum dots and Alexa Fluor fluorophores. Anal Biochem 357:68–76
44. Terpe K (2003) Overview of tag protein fusions: from molecular and biochemical fundamentals to commercial systems. Appl Microbiol Biotechnol 60:523–533
45. Demir HV, Seker US, Ozel UOST (2011) Peptide-mediated constructs of quantum dot nanocomposites for enzymatic control of nonradiative energy transfer. Nano Lett 11:1530–1539
46. Willner I, Gill R, Zayats M (2008) Semiconductor quantum dots for bioanalysis. Angew Chem Int Ed 47:7602–7625
47. Cicek N, Nizamoglu S, Ozel T, Mutlugun E et al. (2009) Structural tuning of color chromaticity through nonradiative energy transfer by interspacing CdTe nanocrystal monolayers. Appl Phys Lett 94:061105
48. Krull UJ, Algar WR, Tavares AJ (2010) Beyond labels: a review of the application of quantum dots as integrated components of assays, bioprobes, and biosensors utilizing optical transduction. Anal Chim Acta 673:1–25
49. Su XG, Li YB, Ma Q, Wang XY (2007) Fluorescence resonance energy transfer between two quantum dots with immunocomplexes of antigen and antibody as a bridge. Luminescence 22:60–66
50. Su XG, Ma Q, Wang XY, Wan Y et al (2005) Fluorescence resonance energy transfer in doubly-quantum dot labeled IgG system. Talanta 67:1029–1034
51. MattoussiI H, Medintz L (2009) Quantum dot-based resonance energy transfer and its growing application in biology. Phys Chem Chem Phys 11:17–45
52. Lee EK, Wei OD, Lee M, Yu X et al (2006) Development of an open sandwich fluoroimmunoassay based on fluorescence resonance energy transfer. Anal Biochem 358:31–37
53. Zhao YD, Li YQ, Wang JH, Zhang HL et al (2010) High-sensitivity quantum dot-based fluorescence resonance energy transfer bioanalysis by capillary electrophoresis. Biosens Bioelectron 25:1283–1289
54. Goldman ER, Medintz IL, Whitley JL, Hayhurst A et al (2005) A hybrid quantum dot-antibody fragment fluorescence resonance energy transfer-based TNT sensor. J Am Chem Soc 127:6744–6751
55. Rogach AL, Sukhanova A, Susha AS, Bek A et al (2007) Nanocrystal-encoded fluorescent microbeads for proteomics: antibody profiling and diagnostics of autoimmune diseases. Nano Lett 7:2322–2327
56. Zhou DJ, Piper JD, Abell C, Klenerman D et al. (2005) Fluorescence resonance energy transfer between a quantum dot donor and a dye acceptor attached to DNA. Chem Commun 38:4807–4809
57. Cady NC, Strickland AD, Batt CA (2007) Optimized linkage and quenching strategies for quantum dot molecular beacons. Mol Cell Probe 21:116–124
58. Wu CS, Cupps JM, Fan XD (2009) Compact quantum dot probes for rapid and sensitive DNA detection using highly efficient fluorescence resonant energy transfer. Nanotechnology 20:305502
59. Ozkan M, Kim JH, Chaudhary S (2007) Multicolour hybrid nanoprobes of molecular beacon conjugated quantum dots: FRET and gel electrophoresis assisted target DNA detection. Nanotechnology 18:195105

60. Zhang CY, Yeh HC, Kuroki MT, Wang TH (2005) Single-quantum-dot-based DNA nanosensor. Nat Mater 4:826–831
61. Deng L, Chen Z, Li G, Zhang L et al (2008) A new method for the detection of ATP using a quantum-dot-tagged aptamer. Anal Bioanal Chem 392:1185–1188
62. Johnson LW, Zhang CY (2009) Single quantum-dot-based aptameric nanosensor for cocaine. Anal Chem 81:3051–3055
63. Oh MK, Kim GI, Kim KW, Sung YM (2009) The detection of platelet derived growth factor using decoupling of quencher-oligonucleotide from aptamer/quantum dot bioconjugates. Nanotechnology 20:175503
64. Zhou D, Ying L, Hong X, Hall EA et al (2008) A compact functional quantum dot-DNA conjugate: preparation, hybridization, and specific label-free DNA detection. Langmuir 24:1659–1664
65. Jiang G, Susha AS, Lutich AA, Stefani FD et al (2009) Cascaded FRET in conjugated polymer/quantum dot/dye-labeled DNA complexes for DNA hybridization detection. ACS Nano 3:4127–4131
66. Cheng AKH, Su HP, Wang A, Yu HZ (2009) Aptamer-based detection of epithelial tumor marker Mucin 1 with quantum dot-based fluorescence readout. Anal Chem 81:6130–6139
67. Wang LB, Xu LG, Zhu YY, Ma W et al (2011) Sensitive and specific DNA detection based on nicking endonuclease-assisted fluorescence resonance energy transfer amplification. J Phys Chem C 115:16315–16321
68. Carraway HE, Bailey VJ, Easwaran H, Zhang Y et al (2009) MS-qFRET: a quantum dot-based method for analysis of DNA methylation. Genome Res 19:1455–1461
69. Suzuki M, Husimi Y, Komatsu H, Suzuki K et al (2008) Quantum dot FRET Biosensors that respond to pH, to proteolytic or nucleolytic cleavage, to DNA synthesis, or to a multiplexing combination. J Am Chem Soc 130:5720–5725
70. Bakalova R, Zhelev Z, Ohba H, Baba Y (2005) Quantum dot-conjugated hybridization probes for preliminary screening of siRNA sequences. J Am Chem Soc 127:11328–11335
71. Johnson LW, Zhang CY (2007) Quantifying RNA – peptide interaction by single-quantum dot-based nanosensor: an approach fair drug screening. Anal Chem 79:7775–7781
72. Johnson LW, Zhang CY (2006) Quantum dot-based fluorescence resonance energy transfer with improved FRET efficiency in capillary flows. Anal Chem 78:5532–5537
73. Sriram R, Yadav AR, Mace CR, Miller BL (2011) Validation of arrayed imaging reflectometry biosensor response for protein-antibody interactions: cross-correlation of theory, experiment, and complementary techniques. Anal Chem 83:3750–3757
74. Amniai L, Lippens G, Landrieu I (2011) Characterization of the AT180 epitope of phosphorylated Tau protein by a combined nuclear magnetic resonance and fluorescence spectroscopy approach. Biochem Biophys Res Commun 412:743–746
75. Garai K, Frieden CC (2010) The association-dissociation behavior of the ApoE proteins: kinetic and equilibrium studies. Biochemistry 49:9533–9541
76. Sarkar R, Narayanan SS, Palsson LO, Dias F et al (2007) Direct conjugation of semiconductor nanocrystals to a globular protein to study protein-folding intermediates. J Phys Chem B 111:12294–12298
77. Medintz IL, Deschamps JR (2006) Maltose-binding protein: a versatile platform for prototyping biosensing. Curr Opin Biotechnol 17:17–27
78. Medintz IL, Konnert JH, Clapp AR, Stanish I et al (2004) A fluorescence resonance energy transfer-derived structure of a quantum dot-protein bioconjugate nanoassembly. Proc Natl Acad Sci USA 101:9612–9617
79. Medintz IL, Clapp AR, Mattoussi H, Goldman ER et al (2003) Self-assembled nanoscale biosensors based on quantum dot FRET donors. Nat Mater 2:630–638
80. Chang E, Miller JS, Sun JT, Yu WW et al (2005) Protease-activated quantum dot probes. Biochem Biophys Res Commun 334:1317–1321

81. Liu HY, Liang GX, Abdel-Halim ES, Zhu JJ (2011) A sensitive and selective quantum dots-based FRET biosensor for the detection of cancer marker type IV collagenase. Anal Methods 3:1797–1801
82. Pons T, Medintz IL, Sapsford KE, Higashiya S et al (2007) On the quenching of semiconductor quantum dot photoluminescence by proximal gold nanoparticles. Nano Lett 7:3157–3164
83. Shi LF, De Paoli V, Rosenzweig N, Rosenzweig Z (2006) Synthesis and application of quantum dots FRET-based protease sensors. J Am Chem Soc 128:10378–10379
84. Shi LF, Rosenzweig N, Rosenzweig Z (2007) Luminescent quantum dots fluorescence resonance energy transfer-based probes for enzymatic activity and enzyme inhibitors. Anal Chem 79:208–214
85. Sapsford KE, Granek J, Deschamps JR, Boeneman K et al (2011) Monitoring botulinum neurotoxin A activity with peptide-functionalized quantum dot resonance energy transfer sensors. ACS Nano 5:2687–2699
86. Prasuhn DE, Feltz A, Blanco-Canosa JB, Susumu K et al (2010) Quantum dot peptide biosensors for monitoring caspase 3 proteolysis and calcium ions. ACS Nano 4:5487–5497
87. Biswas P, Cella LN, Kang SH, Mulchandani A et al (2011) A quantum-dot based protein module for in vivo monitoring of protease activity through fluorescence resonance energy transfer. Chem Commun 47:5259–5261
88. Ghadiali JE, Cohen BE, Stevens MM (2010) Protein kinase-actuated resonance energy transfer in quantum dot-peptide conjugates. ACS Nano 4:4915–4919
89. Ghadiali JE, Lowe SB, Stevens MM (2011) Quantum-dot-based FRET detection of histone acetyltransferase activity. Angew Chem Int Ed 50:3417–3420
90. Xu CJ, Xing BG, Rao HH (2006) A self-assembled quantum dot probe for detecting beta-lactamase activity. Biochem Biophys Res Commun 344:931–935
91. Skajaa T, Zhao YM, van den Heuvel DJ, Gerritsen HC et al (2010) Quantum dot and Cy5.5 labeled nanoparticles to investigate lipoprotein biointeractions via forster resonance energy transfer. Nano Lett 10:5131–5138
92. Rakovich A, Sukhanova A, Bouchonville N, Lukashev E et al (2010) Resonance energy transfer improves the biological function of bacteriorhodopsin within a hybrid material built from purple membranes and semiconductor quantum dots. Nano Lett 10:2640–2648
93. Seker UOS, Ozel T, Demir HV (2011) Peptide-mediated constructs of quantum dot nanocomposites for enzymatic control of nonradiative energy transfer. Nano Lett 11:1530–1539
94. Harashima H, Shaheen SM, Akita H, Yamashita A et al (2011) Quantitative analysis of condensation/decondensation status of pDNA in the nuclear sub-domains by QD-FRET. Nucleic Acids Res 39:E48–U108
95. Bagalkot V, Zhang L, Levy-Nissenbaum E, Jon S et al (2007) Quantum dot - Aptamer conjugates for synchronous cancer imaging, therapy, and sensing of drug delivery based on Bi-fluorescence resonance energy transfer. Nano Lett 7:3065–3070
96. Kang WJ, Ko MH, Lee DS, Kim S (2009) Bioimaging of geographically adjacent proteins in a single cell by quantum dot-based fluorescent resonance energy transfer. Proteomics Clin Appl 3:1383–1388
97. Wang QL, Chen B, Liu P, Zheng MZ et al (2009) Calmodulin binds to extracellular sites on the plasma membrane of plant cells and elicits a rise in intracellular calcium concentration. J Biol Chem 284:12000–12007
98. Choi Y, Kim K, Hong S, Kim H et al (2011) Intracellular protein target detection by quantum dots optimized for live cell imaging. Bioconjug Chem 22:1576–1586
99. Srinivasan C, Siddiqui S, Silbart LK, Papadimitrakopoulos F et al (2009) Dual fluorescent labeling method to visualize plasmid DNA degradation. Bioconjug Chem 20:163–169
100. Delehanty JB, MattoussiI H, Medintz L (2009) Delivering quantum dots into cells: strategies, progress and remaining issues. Anal Bioanal Chem 393:1091–1105

101. Su YY, Peng F, Jiang ZY, Zhong YL et al (2011) In vivo distribution, pharmacokinetics, and toxicity of aqueous synthesized cadmium-containing quantum dots. Biomaterials 32:5855–5862
102. Clift MJD, Brandenberger C, Rothen-Rutishauser B, Brown DM et al (2011) The uptake and intracellular fate of a series of different surface coated quantum dots in vitro. Toxicology 286:58–68
103. Qu Y, Li W, Zhou YL, Liu XF et al (2011) Full assessment of fate and physiological behavior of quantum dots utilizing *Caenorhabditis elegans* as a model organism. Nano Lett 11:3174–3183
104. Reddy KM, Feris K, Bell J, Wingett DG, et al. (2007) Selective toxicity of zinc oxide nanoparticles to prokaryotic and eukaryotic systems. Appl Phys Lett, 90:213903
105. Xie RG, Chen K, Chen XY, Peng XG (2008) InAs/InP/ZnSe Core/Shell/Shell quantum dots as near-infrared emitters: bright, narrow-band, non-cadmium containing, and biocompatible. Nano Res 1:457–464

Probing Photoluminescence Dynamics in Colloidal Semiconductor Nanocrystal/ Fullerene Heterodimers with Single Molecule Spectroscopy

15

Zhihua Xu and Mircea Cotlet

Contents

1 Definition of the Topic

Single molecule optical spectroscopy (SMS) allows for the characterization of photoluminescence intensity and lifetime of a isolated colloidal semiconductor nanocrystal, which provide valuable information about its intrinsic structural defects and interactions with the external nanoenvironment. In this chapter, we describe the application of SMS for the study of photoluminescence blinking and photoinduced charge transfer in colloidal semiconductor nanocrystals.

Z. Xu
Department of Chemical Engineering, University of Minnesota Duluth, Duluth, MN, USA

M. Cotlet (✉)
Brookhaven National Laboratory, Upton, NY, USA

Challa S.S.R. Kumar (ed.), *UV-VIS and Photoluminescence Spectroscopy for Nanomaterials Characterization*, DOI 10.1007/978-3-642-27594-4_15,

2 Overview

Colloidal semiconductor nanocrystals, or quantum dots (QDs), exhibit size-dependent, narrow-band, and high quantum yield photoluminescence (PL). QDs have demonstrated their utilization in applications spanning from biological imaging, lasing, to electronics. Under steady-state photoexcitation, the PL emitted by individual QDs shows strong intermittency or blinking, switching frequently between bright (on) and dark (off) states. The existence of such dark states not only reduces the overall PL quantum yield of QDs, but also impairs their optoelectronic usages.

Photoinduced charge transfer (CT) between quantum dots and the external environment is not only closely related to the PL properties of quantum dots, but also a critical process in QD-based optoelectronic devices, such as solar cells and light-emitting diodes. Unfortunately, the intrinsic heterogeneity and fluctuation dynamics of photoinduced CT in quantum dots are usually obscured by the conventional ensemble-based measurements, such as transient photoluminescence and absorption spectroscopy.

Here we describe a single molecule spectroscopy (SMS) study of the photoluminescence blinking and of the photoinduced CT in colloidal quantum dots using a series of self-assembled quantum dot-fullerene heterodimers. This work provides deep insight into the external charge trap effect on the PL blinking dynamics, and on the heterogeneity of photoinduced charge transfer at the level of individual quantum dot.

3 Introduction

Colloidal semiconductor nanocrystals, or quantum dots (QDs), are a class of nanomaterials whose properties are largely dependent on their physical dimensions. Owing to the unique tunability of their optoelectronic properties, these nanomaterials have found widespread applications in biological imaging [1–3], lasing [4–8], and electronics [9–14]. The attractiveness of quantum dots for device applications also results from their solution-based processability, which is compatible with the inexpensive roll-to-roll fabrication procedures.

Quantum dots synthesized by colloidal chemistry are usually composed of a nanoscale semiconductor core covered by a layer of organic ligands [15, 16]. Commonly used semiconductor cores include cadmium selenide (CdSe), cadmium sulfide (CdS), indium phosphide (InP), etc. The surface ligand molecules improve the long-term stability of the nanocrystals in solution, at the same time preventing uncontrolled growth and agglomeration of nanoparticles into aggregates. The ligands also provide electronic passivation of the nanocrystals by reducing dangling bonds on the surface, which are an important source for reducing the photoluminescence quantum yield of quantum dots by facilitating nonradiative recombination channels. In order to further passivate the surface of quantum dots, a thin layer of a wide bandgap semiconductor, such as zinc sulfide (ZnS), can be grown on the surface of the semiconductor core, forming a so-called core/shell quantum dot [17].

The applications of quantum dots heavily rely on their size-tunable PL emission. However, under steady-state photoexcitation, the photoluminescence (PL) emitted by individual QDs shows strong intermittency or blinking, switching frequently between bright (on) and dark (off) states [18]. The existence of such dark states not only reduces the overall PL quantum yield of QDs, but also impairs their usage such as dynamic single molecule fluorescent reporters. Given the scientific and technological impact of QDs in various fields, the origin of QD PL blinking has been the research focus since its discovery, but has yet to be fully understood [19].

Recently, quantum dots have also been combined with dyes, fullerenes, TiO_2, or with conductive polymers to yield donor-acceptor (DA) charge transfer systems for dye-sensitized cells or hybrid solar cells [12, 13, 20]. However, the power conversion efficiency of such QD-based devices remains quite low. Tremendous efforts have been devoted to unveil the fundamentals of photovoltaic processes, such as charge separation/recombination in QD-based devices, mainly by ensemble-averaged optical methods, such as ultrafast transient photoluminescence and absorption. However, the ensemble-based measurements are unable to resolve the intrinsic heterogeneity and the fluctuation dynamics of charge transfer, which are important information for developing efficient quantum dot-based solar cells.

Given the potential of widespread applications for semiconductor QDs, the PL blinking and charge transfer mechanisms of quantum dots have attracted intense attention within the scientific community, leading to significant progresses. In this chapter, we review single molecule spectroscopy studies of PL blinking and charge transfer dynamics for semiconductor quantum dots, with emphasis on the recent research done in our group. The chapter is organized as follows: First, the ensemble-based PL measurements of core/shell CdSe/ZnS quantum dots are summarized. Then a surface-based assembly method is introduced for the fabrication of electron transfer donor-bridge-acceptor (DBA) heterodimers based on a CdSe/ZnS QD and a fullerene (fullerene-malonic acid-hexadduct, FMH) and aminoalkanethiol linkers with varying linker length. These heterodimers with controllable donor-acceptor distance provide a model system for the single molecule spectroscopy of charge transfer. Finally, the progresses on single molecule exploration of (1) the external trap effect on PL blinking characteristics, and of (2) the photoinduced electron transfer between QDs and electron acceptors are reviewed [21, 22].

Using single molecule spectroscopy to study the photoluminescence emitted by QDs and DBA heterodimers, we found that charge transfer followed by charge recombination is an important mechanism in determining the blinking behavior of QDs when the external trap is properly coupled with the excited state of QD, leading to a quasi-continuous distribution of on-states and an early falloff from a power-law distribution for both on- and off-times associated with quantum dot photoluminescence blinking. By varying the linker length and the QD core size, we demonstrate control of the electron transfer rate and of the magnitude of fluctuations in rate at the level of individual DBA heterodimer. SMS has allowed us to distinguish between two electron transfer fluctuations, one attributed to the

variation of the trap state in the QDs and the other to molecular motions within the DBA heterodimer. By reducing the linker length and the QD core size we were able to diminish electron transfer fluctuations in such self-assembled DBA heterodimers.

4 Experimental and Instrumental Methodology

4.1 Chemicals

Carboxyl-ended core/shell CdSe/ZnS QDs (QD ITK) emitting at 605 nm (QD605), 565 nm (QD565), and 525 nm (QD525) were purchased from Invitrogen. Aminoalkanethiols, 16-Amino-1-hexadecanethiol hydrochloride, 11-amino-1-undecanethiol hydrochloride, and 6-Amino-1-hexanethiol hydrochloride were purchased from Dojindo, and 1-ethyl-3-(3-dimethylaminopropyl)-carbodiimide hydrochloride (EDC) and 3-Aminopropyltrimethoxysilane (APTMS) were purchased from Sigma Aldrich. The synthesis of the fullerene-malonic acid-hexadduct (FMH) is reported elsewhere [23].

4.2 Heterodimer Fabrication

The stepwise surface assembly procedure of QD-FMH dimers for single molecule spectroscopy measurements included five steps: (1) Coverglass cleaning, (2) Surface silanization, (3) Fullerene FMH coupling, (4) Linker coupling, and (5) QD conjugation. Coverglasses (VWR) were cleaned by soaking in *Piranha* solution of 30 % (v/v) hydrogen peroxide and 70 % (v/v) sulfuric acid for about 15–30 min, followed by thoroughly rinsing by deionized water. After drying by nitrogen gas, clean coverglasses were incubated in a dessicator together with 20 μL APTMS under vacuum (20 KPa) for 15–120 min, and later on baked by heat treatment (90 °C) in an oven for about 1 h [24]. The amine-modified coverglasses were then covered by 100 μL mixed aqueous solution of the FMH (0.04 mg/mL) and EDC (5 mg/mL) and incubated for 30 min. The surface of the glass slides was further treated by 100 μL mixed aqueous solutions of EDC (5 mg/mL) and different aminoalkanethiols (0.01 mg/mL) for 30 min. In a final step, the glass surface was incubated with a diluted solution of quantum dots (0.5 nM) for about 1 min. Following each of last three steps, the coverglasses were thoroughly rinsed by deionized water to remove any excess chemical.

4.3 Single Molecule Fluorescence Spectroscopy

Single molecule fluorescence spectroscopy (SMS) was performed on a home-built scanning-stage confocal fluorescence microscope (Olympus IX81) coupled with a laser system delivering 460 nm pulses at 8 MHz repetition rate and consisting

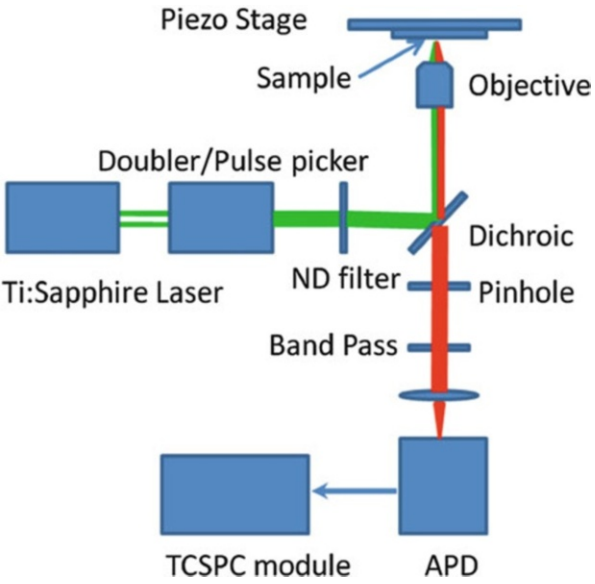

Fig. 15.1 Schematic representation of the scanning-stage confocal single molecule fluorescence microscope used in the studies reported herein

of a frequency doubled, pulsed-picked Ti:Sapphire laser, Tsunami Spectra-Physics, pumped by a Millenia Spectra Physics 532 nm CW laser (Fig. 15.1). The excitation laser beam entering the microscope was reflected by a dichroic mirror (Di01-R442, Semrock), and focused on the sample by a 100x, 1.4 NA oil-immersion objective lens (Olympus Japan). Fluorescence from single molecules immobilized on coverglass was collected by the same objective lens, filtered from laser excitation by the dichroic and by a band pass filter (FF01-583/120, Semrock), spatially filtered by a 75 μm pinhole and focused on a single photon counting avalanche photodiode (APD, MPD Picoquant). The signal from the APD was measured by a time-correlated single photon counting analyzer (PicoHarp 300, PicoQuant). Single molecule fluorescence intensity and lifetime trajectories were recorded using the proprietary time-tagged time-resolved mode of PicoHarp 300, with each single molecule trajectory recorded for 60 s. Lifetimes were calculated from decay histograms containing, on average, 1,000 total photons, by using the Maximum Likelihood Estimation method [25].

Antibunching or photon correlation experiments were performed using a classical Hanbury-Twiss and Brown type experiment in combination with pulsed excitation [26]. Antibunching experiments were used to demonstrate that the nanoclusters we investigate are true single DBA heterodimers. Antibunching was set up in the confocal arrangement described above by adding a 50/50 non-polarizing beam splitter into the detection path, thus splitting the collected fluorescence and focusing it onto two APD detectors. The signals from the APDs were split and either fed into a router (PicoQuant PRT402) connected to a time analyzer (PicoHarp300) to measure PL intensity and PL lifetimes or directly fed into a second time analyzer (PicoHarp300) for photon pair correlation experiments.

In this later case, the time analyzer measures the time interval between photons detected by the APDS. For a repetition rate of 8 MHz of the excitation laser, laser pulses are displaced with 128 ns time intervals such that a histogram of the interphoton arrival times is determined by the laser repetition rate with interphoton arrival times multiples of the laser repetition frequency. For a single emitter, such as a single QD, the probability to emit tow photons upon the absorption of a single photon is zero for low excitation powers (100 nW) and, as a result, the histogram of interphoton arrival times exhibits no peak at zero time.

4.4 Photoluminescence Lifetime Autocorrelations

The photon-by-photon analysis method allows one to retrieve the dynamics of fluorescence lifetime fluctuations for a single fluorescent species when single molecule fluorescence data are collected in the so-called time-tagged time-resolved (TTTR) mode [25, 27]. In TTTR mode, for each detected photon one registers the delay time (t_n) with respect to the laser excitation pulse and the time lag (T_n) with respect to the previously detected photon. For a single molecule, if the lifetime does not fluctuate, the probability distribution of t_n is monoexponential, with a mean value equal to the fluorescence lifetime ($\tau_0 \sim k^{-1}$). If the lifetime fluctuates, the probability distribution of t_n becomes multi-exponential. The dynamics of the lifetime fluctuations can be retrieved from the second order correlation of fluorescence lifetimes $ACPL^2(t) = \langle \Delta k^{-1}(t) \Delta k^{-1}(0) \rangle$ with $\Delta k^{-1}(t) = k^{-1}(t) - \langle k^{-1} \rangle$ and with $ACPL^2(t)$ calculated on a photon-by-photon basis. For a single fluorescent molecule not showing lifetime fluctuations, $ACPL^2(t) = 0$. If the single molecule reversibly switches between two states with different lifetimes ${k_1}^{-1}$ and ${k_2}^{-1}$, the autocorrelation of lifetimes becomes $ACPL^2(t) = \left[n_{12} n_{21} (k_1^{-1} + k_2^{-1}) / (n_{12} + n_{21}) \right] \exp[-(n_{12} + n_{21})/t]$ with n_{12}, n_{21} as interconversion rates. A single exponential fit applied to $ACPL^2(t)$ will yield the time scale of the interconversion between the two states.

5 Key Research Findings

5.1 Ensemble Spectroscopic Measurements

The water-soluble carboxyl-ended core/shell CdSe/ZnS QDs and the materials used for fabricating the QD-FMH heterodimers, namely, the water-soluble fullerene derivative (FMH), and the aminoalkanethiol linkers, are shown in Fig. 15.2a. The UV–VIS absorption and PL spectra of QDs used in these studies are shown in Fig. 15.2b, and they demonstrate size-dependent absorption and PL emission properties from a CdSe QD core. The absorption spectrum of FMH is shown in Fig. 15.2b and indicates very low absorbance in the visible spectral range with no PL detected from an aqueous solution of FMH, and this is similar to other fullerene derivatives reported in literature [28].

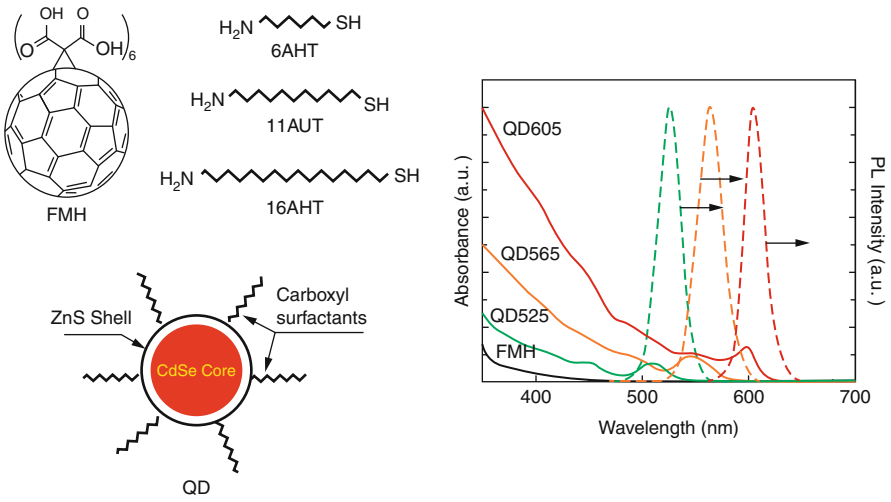

Fig. 15.2 Structures of FMH, CdSe/ZnS QD and aminoalkanethiols linkers, UV–vis spectrum of FMH (*black*), UV–vis (*line*) and PL (*dash*) spectra of QD525 (*green*), QD565 (*orange*) and QD605 (*red*) (reproduced in part from reference [21])

Due to lack of overlap between the PL spectra of QDs and the absorption spectrum of FMH, energy transfer from QDs to FMH is excluded. Therefore, charge transfer from QDs to FMH should be the primary photoinduced interaction under optical excitation at 460 nm. This interaction can be further narrowed down to electron transfer (ET) considering the positioning of the electronic energy levels for CdSe QDs (conduction band −4.3 eV, valence band −6.4 eV for a 4.4-nm-sized CdSe QD) [29] and for fullerene (lowest unoccupied molecular level, LUMO, −4.7 eV, highest occupied molecular level, HOMO, −6.8 eV) which do not favor hole transfer [30].

When QDs and FMH are mixed in aqueous solution, without aminoalkanethiols, quenching of the PL of QDs by FMH is low (15 %), as shown by Fig. 15.3a, and presumably due to the weak electronic coupling between QDs and FMH, with both components having carboxyl groups on their surface. To enhance the electronic coupling, aminoalkanethiol linkers of varying length were used to conjugate QD and FMH components: 16-Amino-1-hexadecanethiol hydrochloride (16AHT), 11-amino-1-undecanethiol hydrochloride (11AUT), and 6-Amino-1-hexanethiol hydrochloride (6AHT). Specifically, the amine end of the linker couples with a carboxyl group of the FMH through a standard coupling reaction assisted by 1-Ethyl-3-(3-dimethylaminopropyl)-carbodiimide (EDC), while the thiolated end of the linker binds to the ZnS surface of the core/shell QD [31]. This procedure enhances quenching of QDs by FMH in solution, up to 42 % for the shortest linker, as shown in Fig. 15.4b, thus indicating enhanced ET and therefore, successful linking of QDs and FMHs by aminoalkanethiols.

Enhanced ET was also confirmed by transient PL lifetime measurements in solution (Fig. 15.4). PL decays measured by the time-correlated single photon counting method using 460 nm excitation and 605 nm detection and for solution

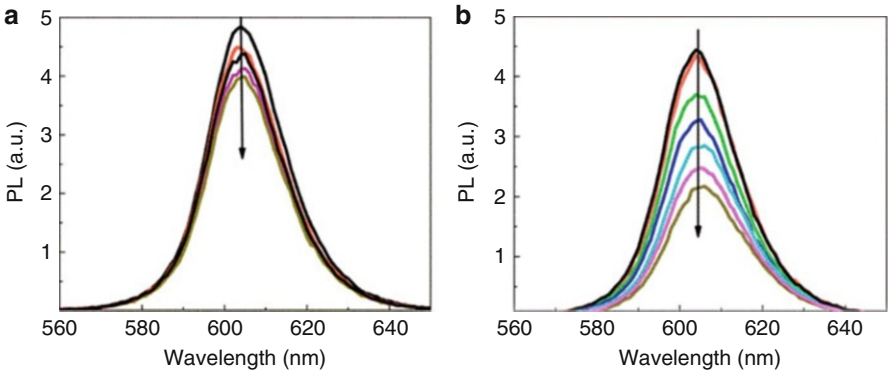

Fig. 15.3 (**a**) PL spectra of QD605 (80 nM) mixed with FMH at various concentrations (0–4.8 μM). (**b**) PL spectra of QD605 mixed with 0–4.8 μM FMH in the presence of EDC and 6AHT linker

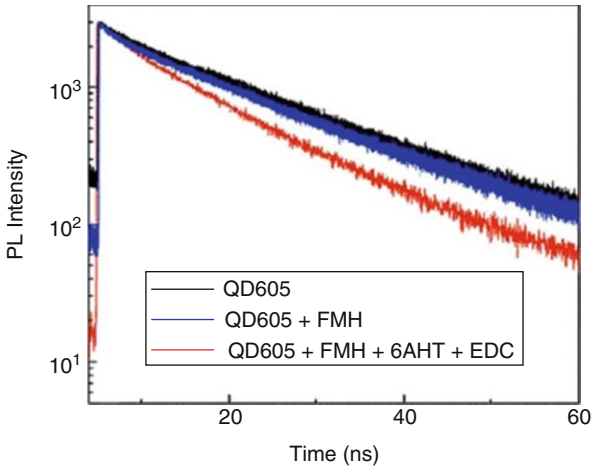

Fig. 15.4 PL lifetime of QD605 (*black*), QD605 mixed with FMH (*blue*), and QD605 blended with FMH, EDC, and 6AHT (*red*)

samples containing QD605 (80 nM), QD605 mixed with FMH (at 80 nM and 4.8 μM concentrations, respectively), and QD605 mixed with FMH (80 nM and 4.8 μM, respectively) in the presence of 6AHT (80 μM) and EDC (4 mM) are shown in Fig. 15.5, and they are characterized by average PL lifetimes of 16.7, 16.2, and 12.9 ns, respectively. These PL decays indicate enhanced ET from QD605 to FMH in the presence of 6AHT linker and EDC, similar to the PL spectra from Fig. 15.3a, b. We note that control experiments showed negligible PL quenching of QDs in the presence of either EDC or aminoalkanethiols.

Further evidence for the presence of enhanced ET when QDs and FMH are coupled with the linker is given by solution ensemble transient absorption measurements. These experiments were performed using a Helios fs-Transient Absorption Spectrometer (Newport) and an excitation laser system based on a regenerative

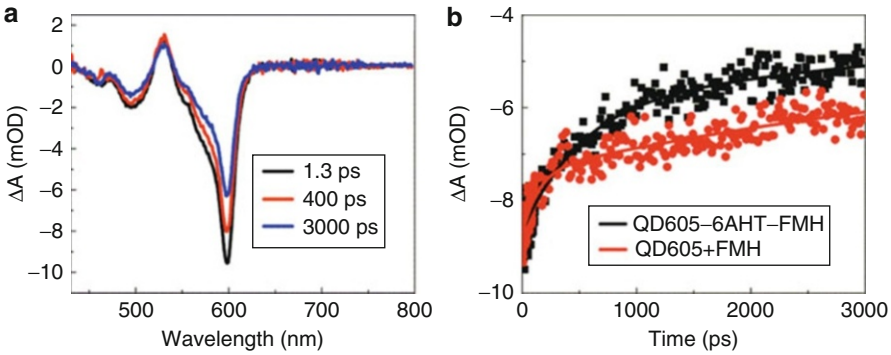

Fig. 15.5 (**a**) Transient absorption spectra of QD605 recorded following 460 nm laser pulse excitation; (**b**) bleaching recovery profiles at 595 nm of QD605 (400 nM) blended with FMH (20 μM) (Red), and QD605(400 nM) blended with FMH (20 μM), EDC (20 mM) and 6AHT (400 μM) (black)

amplifier system (SpitFire Pro, Newport Spectra Physics, 1 kHz repetition rate, 120 fs pulse width) and a TOPAS optical parametric amplifier (Newport Spectra Physics). Figure 15.5a shows the transient absorption spectra of QD605 at different (delay) times following 460 nm laser pulse excitation. The two peaks at 595 and 495 nm can be attributed to bleaching of the ground state transitions corresponding to the s- and p-states respectively, similar to that reported in [32]. By mixing QDs with FMH, linkers, and EDC, this does not change the shape of the transient spectra. The dynamics of the bleaching recovery was recorded at 595 nm for QD samples and no visible change was detected upon adding FMH onto the QD solution. Significant faster recovery was observed only after adding EDC and linker (6AHT) to the mixed QD605/FMH solution (see Fig. 15.5b). The same phenomenon has been observed from CdSe QDs and TiO_2 complexes, and attributed to photoinduced electron transfer from CdSe QDs to TiO_2 [32].

5.2 Surface-Based Assembly of QD-FMH Heterodimers

Although coupling of QDs and FMH can be achieved in solution and it is found to enhance ET, the limited yield of the EDC coupling reaction and the unavoidable cross-linking between QDs and FMH in solution result in uncontrollable stoichiometry leading to the coexistence of isomers, dimers, trimers, and even larger structures, making QD-FMH conjugates highly heterogeneous and unpractical for single molecule characterization.

To circumvent this heterogeneity, we designed a stepwise surface-based assembly procedure that yields QD-FMH dimers of high purity, and this is schematically shown in Fig. 15.6. The surface assembly starts with vacuum deposition of low molecular weight amine-ended silane (3-aminopropyltrimethoxysilane, APTMS) on a substrate (cover glass) and with the density of amine groups on the surface controlled by the deposition time. Next, FMH is immobilized on the surface through EDC coupling

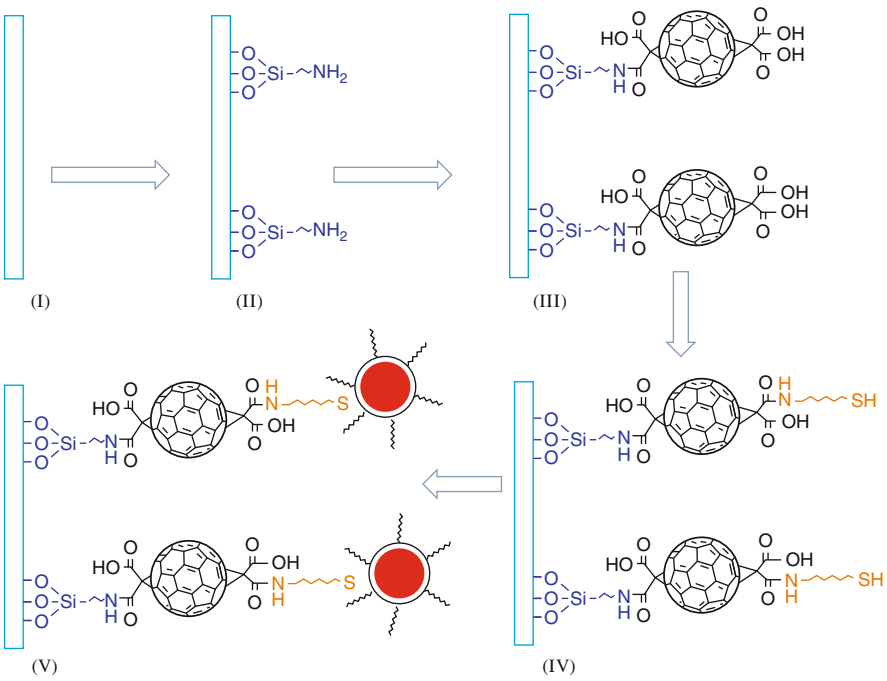

Fig. 15.6 Step-wise surface-based assembly of QD-FMH dimers. Steps I–V are described in the main text. Drawing of QDs and FMH is not to scale "(reproduced in part from reference [21])

between the amine groups present on the surface and carboxyl groups of FMH. A second EDC coupling reaction connects an aminoalkanethiol linker to the immobilized FMH, specifically the amine group of the linker and an available carboxyl group in FMH. In a final step, carboxyl-ended CdSe/ZnS QDs are coupled to the immobilized and thiolated FMHs. Since the size of a functionalized core/shell CdSe/ZnS QD is about 8–12 nm and therefore, by far larger than that of FMH (~1 nm), binding of multiple QDs to a single immobilized FMH is excluded due to the steric repulsion effect on this surface configuration. Conversely, by controlling the surface coverage of FMHs we ensured that a single QD couples to only one immobilized FMH.

Figure 15.7a is a confocal fluorescence lifetime microscopy (FLIM) image (sample area of 20 × 20 μm) of isolated QD605 isomers immobilized on a silane (APTMS) functionalized glass surface by the EDC. The sample was produced by incubating a silanized glass surface with a 100 μL aqueous solution of 0.5 nM QD605 for about 1 min, followed by thorough washing with deionized water. It is noteworthy that the density of immobilized QDs increases with the increase of the APTMS deposition time, with the immobilization of QD attributed probably to the specific binding between APTMS and QD isomers, given the large affinity between the amine group of APTMS and the Zn^{2+} from the QD surface. A control sample consisting of a non-silanized coverglass did not show the presence of QD isomers by FLIM, confirming the above statement. However, as shown in

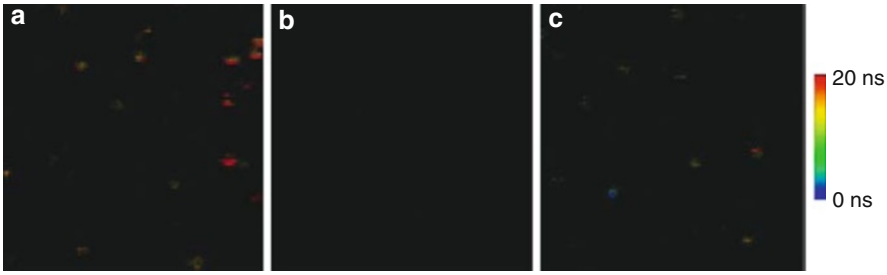

Fig. 15.7 Confocal FLIM images of (**a**) silanized cover glass treated with QD605, (**b**) silanized glass treated with FMH and EDC, followed by treatment with QD605 and (**c**), silanized glass treated with FMH and EDC, followed by treatment with 16AHT and EDC, and finally followed by treatment with QD605

Fig. 15.7b, QDs cannot be immobilized after the silanized surface was treated by the mixed solution of FMH and EDC (step III in Fig. 15.6). This proves that the amine groups of APTMS bind specifically to FMH, with FMH repulsing carboxyl-functionalized QDs. As demonstrated by the FLIM image from Fig. 15.7c, the affinity between the QDs and the glass surface is reestablished by further coupling thiol linkers on FMH (step IV in Fig. 15.6). Thus, these control experiments indicate negligible nonspecific binding of QDs directly to the coverglass surface or to non-thiolated, but immobilized FMH. Furthermore, antibunching experiments confirmed that the detected fluorescence signals from self-assembled QD-linker-FMH were indeed from single QD emitters.

Representative PL decays measured from isolated QD605 isomers and DBA dimers of varying linker length are shown in Fig. 15.8. The majority of individual QD605 isomers exhibit single exponential PL decays with PL lifetimes around 20 ns, while about 10 % show multi-exponential PL decays with shorter lifetimes. This 10 % population of QDs will be addressed later on in this work. Individual DBA dimers show multi-exponential PL decays with PL lifetimes significantly shorter than those observed for QD isomers and with average PL lifetimes exhibiting a clear linker length dependency, suggesting the successful fabrication of QD-FMH dimers based on the surface assembly approach and distance-dependent quenching of QD's photoluminescence by electron transfer (ET) to fullerene.

5.3 Photoluminescence Blinking

Under steady-state photoexcitation, the PL emitted by individual QDs shows strong intermittency or blinking, switching frequently between bright (on) and dark (off) states [18]. The existence of such dark states not only reduces the overall PL quantum yield of QDs, but also impairs their usage such as dynamic single molecule fluorescent reporters. The origin of QDs PL blinking has been the research focus since its discovery [19], and significant progress has been made in the synthesis of QDs with suppressed blinking [33–37].

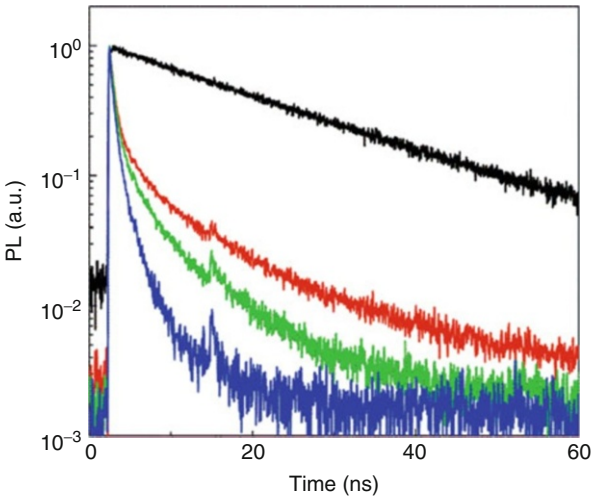

Fig. 15.8 Single molecule PL decays from a QD isomer (*black* color), and from DBA heterodimers, QD-16AHT-FMH (*red*), QD-11AUT-FMH (*green*), and QD-6AHT-FMH (*blue*), with average PL lifetimes of 20, 7, 4 and 2 ns, respectively (reproduced in part from reference [22])

A widely accepted physical model describing photoluminescence blinking in isolated QDs is the Auger recombination model [18, 38]. In this model, a photoexcited QD becomes positively charged due to electron ejection to long-lived trap sites, and efficient Auger recombination keeps the now charged QD in the off-state. The QD returns to the on-state when the trapped electron recombines with a hole to render the QD neutral.

While regarded as a major step toward understanding the blinking of QDs, this particular model does not necessarily explain the unique power-law distribution exhibited by the on- and off-times associated with blinking [39]. Furthermore, it has been recently reported that depending on the QD type and embedding nanoenvironment, power law distributions for the on- and off-times can exhibit exponential cutoffs at long time scales [40]. Such truncated power-law distributions have been explained by modified Auger recombination models invoking scenarios like the existence of a distribution of trap states [41], fluctuating electron tunneling barrier [39], spectral diffusion of on- and off-state associated energies [42, 43], or spatial diffusion of ejected electrons [44]. However, recent experimental reports addressing the radiative decay times of negatively charged excitons (trions) [45], the PL quantum yield of biexcitons [46], and the optical excitation intensity dependence of the PL decay dynamics [47] suggest that Auger recombination might not be the sole mechanism responsible for the off-states of QDs. For example, an alternate model has been proposed in which nonradiative recombination is induced by short-lived hole traps as a process dominating during QD's off-time and without invoking long-lived charge raps [48]. Nevertheless, all current models emphasize an important role of the charge carrier traps in regulating the photoluminescence of individual QDs. Traps are generally defined as defective sites located either in the core/shell structure (internal traps), such as crystalline defects and surface dangling bonds [43, 49], or in the local nanoenvironment of a QD (external traps) [50, 51] and which are energetically

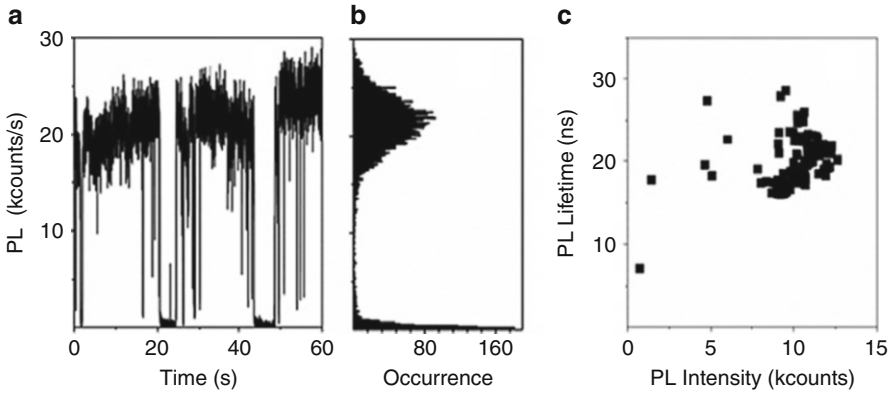

Fig. 15.9 (**a**) Single molecule PL intensity trajectory, (**a**) (10 ms bin time), corresponding intensity histogram, (**b**) (10 ms bin time), and correlation of PL intensity versus PL lifetime, (**c**) (500 ms bin time), for an isolates QD isomer (reproduced from reference [22])

favorable to accept photogenerated electrons or holes. Although it is commonly accepted that proper surface passivation of QDs can lead to suppressed blinking by reducing the amount of surface traps [52], the exact nature of these traps and how they affect the blinking dynamics of an isolated QD are still open questions.

Here we use the QD-FMH dimers with the electron donating core/shell CdSe/ZnS QD and the electron accepting fullerene FMH as a model system to investigate the effect of external charge traps (FMH) on the blinking dynamics of QDs. As discussed before, the favorable energy band alignment between the CdSe QD and fullerene makes electron transfer the dominant interaction between a photoexcited CdSe QD and fullerene [20, 53, 54]. Thus, for the QD-FMH dimers, the fullerene moiety functions as a single external electron trap toward the QD, and the location of this trap is controlled by the length of the aminoalkanethiol bridge.

Figure 15.9a is a so-called "classic" time-trajectory of the PL intensity from an isolated QD isomer, featuring a typical "two-state" telegraph-like, on-off blinking. Switching of the PL intensity between an "on-state" and an "off-state" is also demonstrated by the histogram of the PL intensity (Fig. 15.9b) derived from Fig. 15.9a, which features two distinct peaks: one corresponding to the "on" state (peak at ~22 counts/ms) and the second corresponding to the "off" state (peak at ~1count/ms). Figure 15.9c is the correlation of PL intensity versus PL lifetime for this particular QD isomer, for which the majority of data points exhibit high PL intensity correlated with long PL lifetime and therefore, corresponding to the "on" state. Data in connection with the off-state that would be featured as very short PL lifetimes are not present in this plot, most probably due to the limited temporal resolution of our single molecule microscope (0.3 ns). Instead, some data points associated with low PL intensity and long PL lifetime are present and are most probably related to the fast blinking dynamics within the binning time (here 500 ms per calculated single molecule PL lifetime) [55].

Oppositely to an isolated QD isomer, the QD-FMH heterodimers feature non-typical on-off blinking, for example, multiple rather than a two-state behavior. This is shown in Fig. 15.10a, d, g for isolated dimers of the type QD-16AHT-FMH, QD-11AUT-FMH, and QD-6AHT-FMH, respectively. The corresponding histograms of the PL intensity trajectories of the QD-FMH heterodimers are shown in Fig. 15.10b, e, and h, and all feature prominent peaks for the off-state (peaks at ~1count/ms), but rather broad distribution for the on-states. These multiple on-states were further confirmed by correlations of the type PL intensity versus PL lifetime as those shown in Fig. 15.10c, f, i. These correlations are consistent with the observation of multi-exponential decaying of PL from QD-FMH dimers, as shown in Fig. 15.8. The "on-states" explored by QD-FMH dimers feature low PL intensity and short PL lifetimes, in contrast with the "on-state" of the QD isomers which is associated with high PL intensity and long PL lifetimes. Similar multistate blinking characteristics with correlated PL intensity and PL lifetime values have been reported previously for streptavidin-coated QDs, and attributed to a distribution of positive charge traps at the core-shell interface or shell surface (internal traps) [56]. Photogenerated charges can migrate between different surface traps leading to a variation of radiative and nonradiative recombination rate.

Recalling that the majority of the probed QD isomers exhibit two-state PL blinking behavior, the observed multistate blinking of isolated QD-FMH heterodimers should be associated with the presence of the single external electron trap, the fullerene FMH. To induce multistate blinking, the ET rate in a specific QD-FMH heterodimer should vary as a function of time. In fact, fluctuating single molecule ET dynamics has been reported for a variety of donor-acceptor systems, such as QDs co-adsorbed with organic molecules [57] or with fullerenes [58], QDs deposited on TiO_2 [59], organic fluorophores adsorbed to TiO_2 nanoparticles [60, 61] or organic only QD-FMH molecules [25, 62–66]. We discuss the origins of fluctuating ET in QD-FMH heterodimers in detail in the next paragraph.

The dynamics of PL blinking in isolated QD isomers and QD-FMH dimers can be analyzed by building the probability distributions of on-times, $P(t_{on})$, and off-times, $P(t_{off})$, with the so-called "threshold method." The threshold method has been previously applied to both two-state and multistate blinking QDs [50, 67, 68]. In this method, a threshold is set to separate the "on" and "off" levels in a time-trajectory of the PL intensity, for example here at a value equal to the standard deviation of the PL intensity above the mean value of the background signal. For the multistate QDs or QD-FMH heterodimers, extra care was taken to determine the background signal (measured from dark regions of the sample featuring no PL signals) due to the existence of on-states of low PL intensity. $P(t_{on})$ and $P(t_{off})$ were calculated according to

$$P(t_i) = \frac{N(t_i)}{N^{tot}} \times \frac{1}{\Delta t_i^{ave}} \tag{15.1}$$

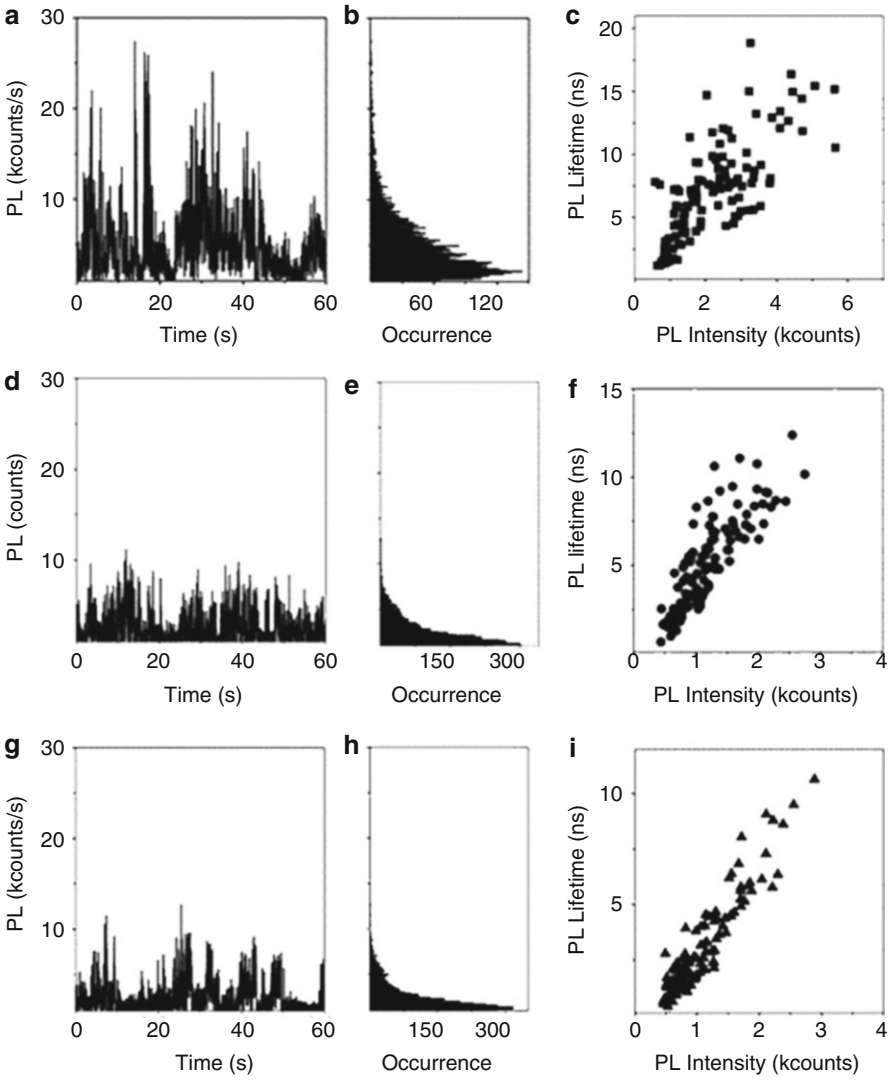

Fig. 15.10 Single molecule PL intensity trajectories, PL intensity histograms, and correlations of PL intensity versus PL lifetime for QD-FMH heterodimers, namely QD-16AHT-FMH (**a**–**c**), QD-11AUT-FMH (**d**–**f**) and QD-6AHT-FMH (**g**–**i**). PL intensity and histograms in panels **a**, **d**, **g** and **b**, **e**, **h** are shown using 10 ms bin time while PL intensity versus PL lifetime correlations in panels **c**, **f**, **i** are shown using 500 ms bin time (reproduced from reference [22])

where i = on or off, $N(t_i)$ is the number of "on" or "off" events of duration time t observed for a particular molecule, N^{tot} is the total number of "on" or "off" events observed for the molecule, and Δt_i^{ave} is the average of the time intervals to the preceding and following events.

Rather than analyzing probability distributions of isolated molecules, which usually feature poor statistics due to the limited number of blinking events, we decided to build the so-called ensemble-like distributions $P(t_{on})$ and $P(t_{off})$ [51, 59] as shown in Fig. 15.11a, b, respectively. Each of these distributions includes blinking events captured from single molecule PL time trajectories of 60 s and of equal bin time (10 ms) from a population of 50 isolated molecules. For isolated QD isomers and for the time scale probed here, both $P(t_{on})$ and $P(t_{off})$ follow inverse power-law distributions as described by Eq. 15.2 [39]

$$P(t) = bt^{-m} \tag{15.2}$$

with power exponents $m_{on} = 1.35$ and $m_{off} = 1.55$, respectively (see Table 15.1).

For QD-FMH dimers, P(ton) exhibits a power law dependency at short times, followed by an exponential decay dependency at longer times, a behavior that can be modeled with a truncated power-law function as described by Eq. 15.3 [41, 42, 69]

$$P(t) = bt^{-m} \exp(-\frac{t}{\tau_{on}}) \tag{15.3}$$

with τ_{on} the crossover time from power law to exponential decay behavior. By reducing the linker length in QD-FMH dimers, from 16AHT to 11AUT and to 6AHT, τ_{on} decreases from 770 ms to 430 ms and to 250 ms, respectively (Table 15.1). $P(t_{off})$ distributions of QD-FMH dimers (Fig. 15.11) also show deviation from a power law dependency at longer times. However, these distributions do not fit well by a truncated power law model as described by (Eq.15.2). A more appropriate model is a modified truncated power law model including a stretch exponential bending tail at longer times as described by Eq. 15.4 (see results in Fig. 15.11 and Table 15.1), [70]

$$P(t) = bt^{-m} \exp\left[-\left(\frac{t}{\tau_{off}}\right)^{n}\right] \tag{15.4}$$

An exponential falloff behavior for $P(t_{on})$ from a power law dependency has been previously observed for isolated QDs and reported to be dependent on temperature, excitation wavelength, and laser power. Such behavior was attributed to charge ejection to external traps assisted by Auger ionization [40], phonon [50, 68], and biexcitons [69]. For the QD-FMH dimers investigated here, electron transfer is most likely the mechanism responsible for the exponential falloff of $P(t_{on})$. Similar decrease of τ_{on} as observed here for the QD-FMH dimers has been reported for QDs co-adsorbed with electron-accepting molecules or with TiO_2 nanoparticles [59, 71].

A recently proposed diffusion-controlled electron transfer (DCET) model explains the PL blinking of QDs, in particular the dependency of τ_{on} on the excitation intensity and temperature according to [42, 70]

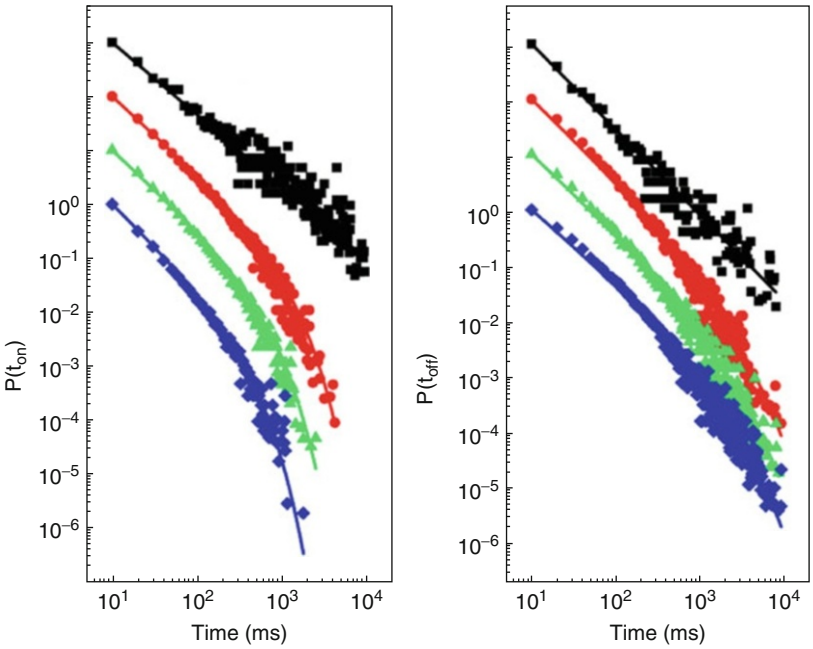

Fig. 15.11 "Ensemble"-like probability distributions of (*left*) on-times, $P(t_{on})$ and (*right*) off-times, $P(t_{off})$ for QD isomers (*black squares*) and QD-FMH dimers, QD-16AHT-FMH (*red circles*), QD-11AUT-FMH (*green triangles*), and QD-6AHT-FMH (*blue rhombs*). Each distribution sums blinking events from 50 molecules, with each molecule observed for 60 s (10 ms bin time). For clarity, $P(t_{on})$ and $P(t_{off})$ are normalized and offset. Fits according to Eqs. 15.2, 15.3, and 15.4 are drawn as solid lines and the obtained parameters are listed in Table 15.1 (reproduced from reference [22])

Table 15.1 Parameters derived from fitting the distributions $P(t_{on})$ and $P(t_{off})$ from Fig. 15.11 with the models described by Eqs. 15.2, 15.3, and 15.4

Molecule	m_{on}	τ_{on} (ms)	m_{off}	τ_{off} (ms)
QD isomer	1.35	NA	1.55	NA
QD-16AHT-FMH	1.45	770	1.45	910
QD-11AUT-FMH	1.46	430	1.4	830
QD-6AHT-FMH	1.55	250	1.3	770

$$1/\tau_{on} = \frac{E_a}{2Dk_BT} = \frac{(\Delta G + \lambda)^2}{8\lambda Dk_BT} \tag{15.5}$$

Here E_a is the activation energy for ET taking place from the excited state of QD to the trap state, a property which is determined by the free energy, ΔG, and by the reorganization energy, λ, and D is the diffusion time constant of the QD's excited state which is dependent on the excitation intensity and temperature. For a QD,

coupling of a good electron acceptor, such as fullerene, increases the driving force for ET (ΔG becomes more negative) and the reorganization energy, λ, is expected to decrease by reducing the donor-acceptor separation distance [72], thus both leading to the reduction of the activation energy E_a. According to Eq. 15.5 one would expect a smaller τ_{on} for the QD isomer than for QD-FMH dimers and an increase of τ_{on} for DBA dimers with reduced linker length. However, data from Table 15.1 do not follow the predictions of the DCET model. One potential reason might be related to the fact that this particular model is built upon the assumptions of slow electron transfer between the QD's excited state and long-lived shallow traps, and of Auger recombination dominating the charge separation state. For our QD-FMH dimers, coupling of an external electron acceptor like fullerene FMH to a QD can lead to fast forward and backward (charge recombination) electron transfer. Therefore, the fullerene acts more like a short-lived "deep" trap for the QD, inducing a blinking dynamics beyond the scope of the DCET model.

Fast charge recombination in the case of our QD-FMH dimers is supported by the clear deviation of $P(t_{off})$ from a power law distribution (reduced τ_{off}) which indicates lower possibility of long off-times compared to QD isomers. Furthermore, charge recombination is much faster at isolated donor/acceptor interfaces, for example, QD-FMH dimers, than in bulk donor-acceptor heterojunction films where separated charge carriers can diffuse away from each other [73]. Similarly, charge recombination in QD-FMH dimers should be faster than that in the case of a QD interacting with multiple electron acceptors, such as in the case of QDs spin-coated on TiO_2 film which were found to exhibit longer τ_{off} than QD isomers [59]. Fast charge recombination has also been demonstrated between isolated QDs and TiO_2 nanoparticles dispersed in solution [74], and the dynamic coupling of a QD with an isolated TiO_2 nanoparticle was found to lead to suppressed blinking [74].

For our QD-FMH dimers, a $P(t_{off})$ exhibiting a stretched exponential dependency at longer times suggests complex charge recombination dynamics [75]. Compared with the direct electron tunneling during forward electron transfer, for example, from QD to fullerene FMH, it is not uncommon to speculate that charge recombination follows more complicated dynamics at donor-acceptor interface [76].

Fast electron transfer/recombination in QD-FMH dimers inevitably suppresses Auger recombination, and their blinking dynamics appears to be incompatible with theoretical models invoking long-lived external charge traps. Similar charge transfer/recombination mechanisms can exist in a QD adsorbed with low energy moieties, such as oxygen [77]. For example, around 10 % of the probed QD isomers were found to exhibit multistate blinking, similar to QD-FMH dimers. One such example of a so-called "bad" QD isomer is shown in Fig. 15.12. For such multistate blinking QD isomers, trap-induced charge transfer/recombination might be another important mechanism in determining the dynamics of PL blinking. As such, further understanding of the multistate blinking characteristics of QDs may, therefore, rely on the refinement of current models or the development of new ones invoking short-lived charge traps [48].

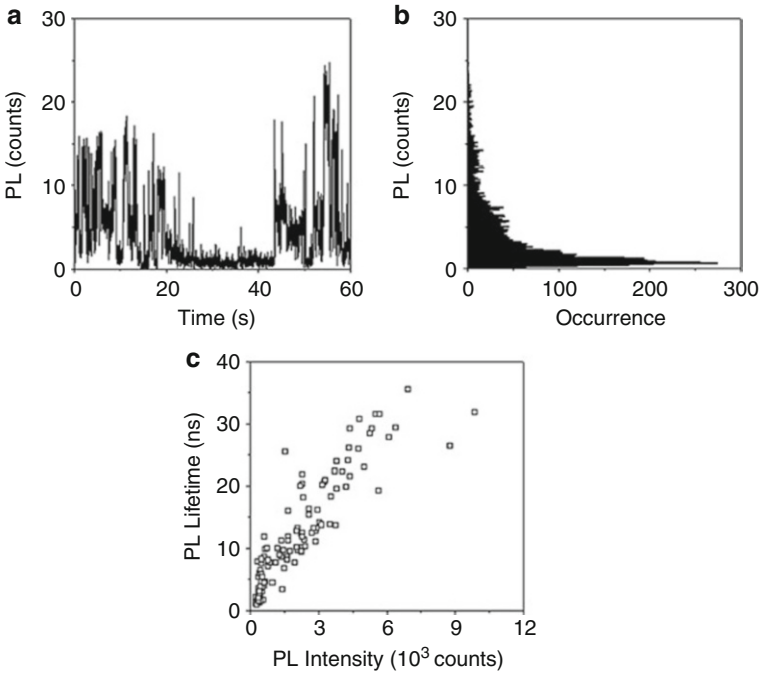

Fig. 15.12 PL intensity trajectory (**a**), PL intensity histogram (**b**), and correlations of PL intensity versus PL lifetime (**c**) for a single QD isomer exhibiting multi-state blinking behavior

5.4 Photoinduced Electron Transfer

Single molecule spectroscopy (SMS) is a powerful method to unveil the inhomogeneous dynamics of CT obscured by ensemble-averaging, and it has been successfully applied to a variety of systems including organic donor-bridge-acceptor systems, dyes adsorbed on TiO_2 or proteins [25, 61, 76, 78–80]. A limited number of SMS studies address charge transfer between QDs and acceptor materials, such as TiO_2 or an ensemble of dyes adsorbed on a QD [59, 71, 81].

The QD-bridge-FMH heterodimers fabricated by the surface-based assembly procedure reported in the previous paragraph provide a model system for the single molecule exploration of photoinduced electron transfer between QDs and electron acceptors, which is an essential process in QD-based solar cells. By varying the linker length and the QD size, it is possible to control the rate and the magnitude of fluctuations of the photoinduced electron transfer at the level of individual dimer, and with SMS, it is possible on the other hand to unveil both static and dynamic heterogeneity in ET, as will be shown below.

Representative PL intensity and PL lifetime trajectories of a single QD605 isomer and of single DBA heterodimers of the type QD605-16AHT-FMH,

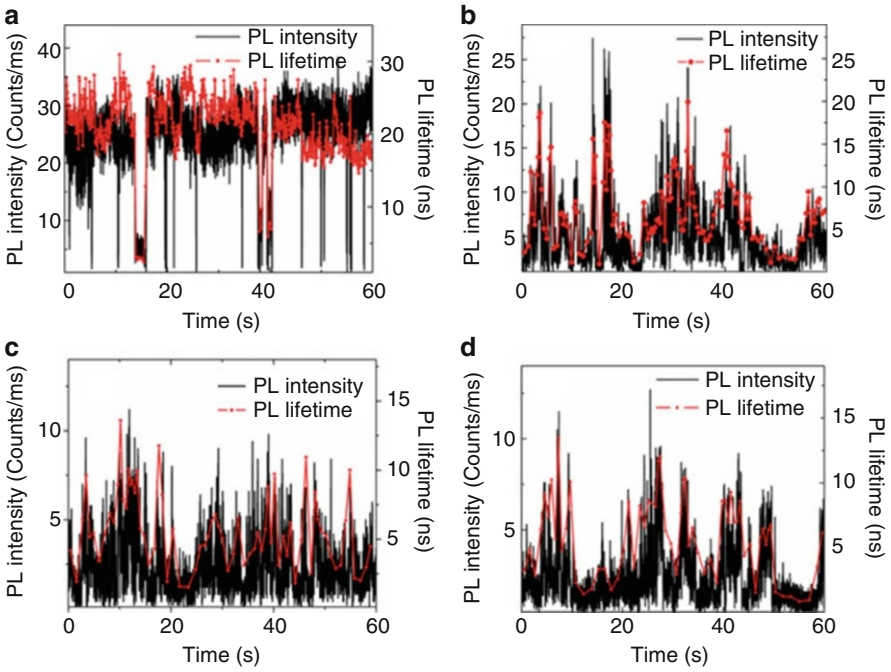

Fig. 15.13 Single molecule trajectories of the PL intensity (*black*) and lifetime (*red*) measured from (**a**) QD605 isomer and from dimers, (**b**) QD605-16AHT-FMH, (**c**) QD605-11AUT-FMH and (**d**), QD605-6AHT-FMH (reproduced from reference [21])

QD605-11AUT-FMH, and QD605-6AHT-FMH are shown in Fig. 15.13. The PL intensity trajectory of a QD605 isomer shows the typical "on-off" blinking, similar to that depicted in Fig. 15.9 – a behavior that can be regarded as a signature for the presence of a single emitting nanocrystal. The corresponding PL lifetime fluctuates in time and in correlation with the PL intensity, that is, high intensity states tend to exhibit longer PL lifetime, suggesting variations in the nonradiative recombination rate [56]. The PL intensity and lifetime trajectories of QD-FMH dimers also show correlated fluctuations, but the corresponding PL intensity and lifetime values are suppressed when compared to that of the QD605 isomer, suggesting enhanced nonradiative recombination due to photoinduced electron transfer from QD to FMH. Compared to the QD isomer, the dimers exhibit different blinking dynamics, as discussed in the previous paragraph: the PL intensity distributes continuously between "on" and "off" states, suggesting inhomogeneous electron transfer between QD and FMH.

The inhomogeneity of ET in QD-FMH dimers is better seen in the PL lifetime histograms from Fig. 15.14 that were constructed from PL lifetime trajectories measured from each 50 individual QD605 isomers (Fig. 15.13a) and from each 50 individual QD605-FMH dimers of a given linker length (Fig. 15.14b–d). For QD605 isomers, the lifetimes distribute symmetrically around 20 ns with a standard

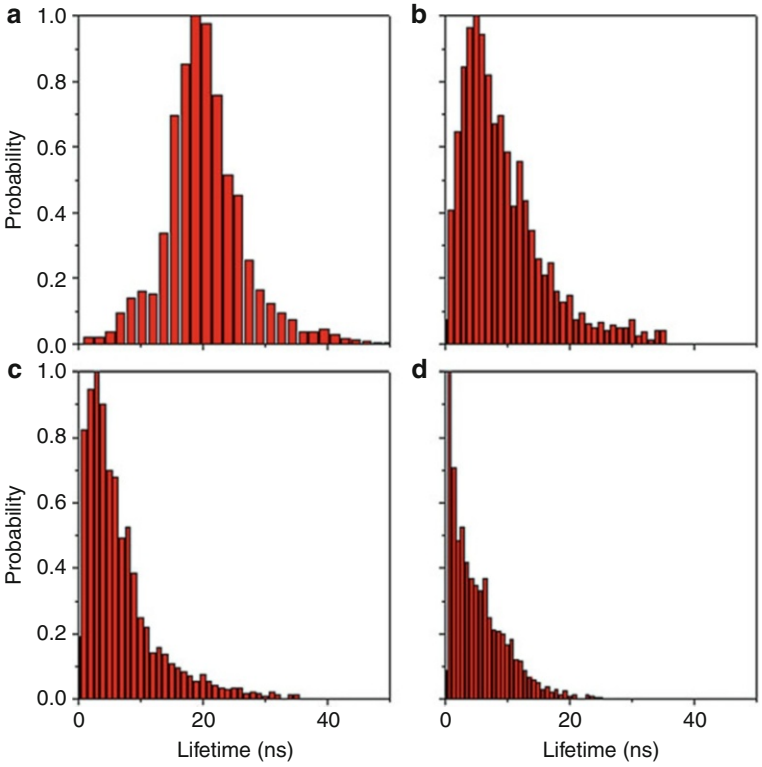

Fig. 15.14 Histograms of single molecule PL lifetimes constructed from each 50 individual trajectories measured from (**a**) QD605 isomers, from dimers, (**b**) QD605-16AHT-FMH, (**c**) QD605-11AUT-FMH, (**d**) QD605-6AHT-FMH (reproduced from reference [21])

deviation σ∼6.5 ns. For dimers, the lifetime histograms are asymmetric and with peak values diminished to 5 ns (σ∼6.7 ns) for QD605-16AHT-FMH, 3 ns (σ∼5.9 ns) for QD605-11AUT-FMH, and 1 ns (σ∼4.4 ns) for QD605-6AHT-FMH, indicating enhanced electron transfer rate and suppressed ET fluctuation with reducing linker length.

As a comparison, the PL lifetime histogram constructed from 50 individual QD isomers spin-coated on top of an FMH thin film, a condition where QD and FMH are not linked by a molecular bridge, is shown in Fig. 15.15. This histogram features a peak at 20 ns and a rather wide standard deviation (σ∼7.6 ns) compared to those of the heterodimers (Fig. 15.14b–d). However, it is rather similar to PL lifetime distributions observed for QDs deposited on TiO_2 film [59]. This suggests that the dimer structure significantly reduces the magnitude of fluctuations of ET between QD and FMH.

The inhomogeneity of electron transfer in QD-FMH dimers leads to a distribution of PL lifetimes and ET rates seen here as static heterogeneity. The linker length effect on electron transfer rate k_{ET} can be calculated from the intensity-weighted average PL

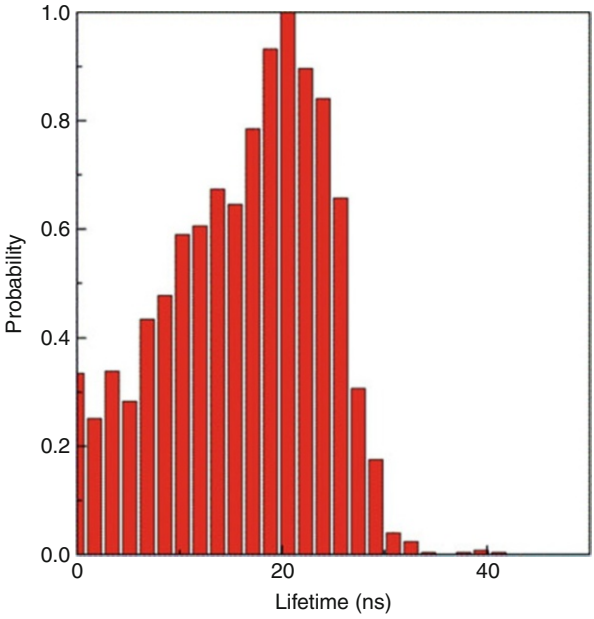

Fig. 15.15 Histograms of single molecule PL lifetimes constructed from each 50 individual trajectories measured from QD605 isomers spincoated on a FMH film (reproduced in part from reference [21])

lifetime, τ_{av} for QD-FMH dimers from the lifetime histograms from Fig. 15.14b–d. The average PL lifetime τ_{av} of QDs and QD-FMH dimers was calculated using

$$\tau_{av} = \frac{\sum_i a_i \tau_i^2}{\sum_j a_j \tau_j} \tag{15.6}$$

where a_i is the occurrence probability of lifetime τ_i in the PL lifetime histogram. The average ET rate k_{ET} for QD-FMH dimers can then be calculated based on

$$k_{ET} = 1/\tau_{av} - (k_R + k_{NR}) \tag{15.7}$$

where k_R and k_{NR} are the radiative and nonradiative recombination rates for QD isomers, which can be calculated using the average PL lifetime estimated for QD isomers. We found that the average ET rate exhibits an exponential dependence on linker length as shown in Fig. 15.16, with an attenuation coefficient $\beta \sim 0.1$ Å^{-1}, calculated from $\ln k_{ET} = \ln k_0 - \beta R$, with R linker length. For organic only DBA systems with flexible alkane bridges, bulk measurements in solution reported $\beta \sim 0.8$ Å^{-1} [66]. For QD-FMH dimers, a small β might indicate collapsed/folded aminoalkanethiol linkers due to the solvent-free environment in which the single molecule experiments were performed.

The electron transfer is not only influenced by the D-A electronic coupling, but also by the driving force (energy band offset) between D and A moieties. The unique size-dependent energy bandgap of QDs provides another effective

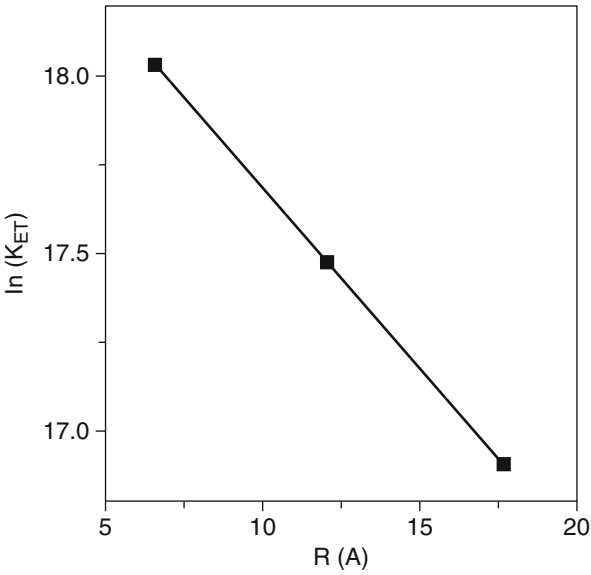

Fig. 15.16 Electron transfer rate, k_{ET} versus linker length, R, calculated for QD605-FMH dimmers on the basis of single molecule experiments (reproduced in part from reference [21])

way to control single molecule ET in QD-FMH dimers. By decreasing the QD's core size from 4.4 to 2.5 nm, the conduction band is expected to be uplifted by around 0.2 eV [29], resulting in an increase of the ET driving force. PL lifetime histograms constructed from trajectories corresponding to 50 each individual QD isomers and 50 each individual QD-16AHT-FMH dimers with QDs of different colors (sizes), namely, QD605 (core size 4.5 nm), QD565 (3.2 nm), and QD525 (2.5 nm), are shown in Fig. 15.16ac–c, respectively.

Figure 15.18 shows the average ET rate versus QD's core size calculated based on the histograms from Fig. 15.17a–c. The ET rate increases from 2.2×10^7 s^{-1} for QD605-16AHT-FMH to 4.9×10^8 s^{-1} for QD525-16AHT-FMH, consistent with the size-dependent ET observed from CdSe QDs to TiO_2 [32]. One interesting phenomenon associated with the size-dependent ET rate is that ET fluctuations are suppressed in dimers with smaller QD size. The standard deviation of the PL lifetime is 6.7 ns for QD605-16AHT-FMH, 1.4 ns for QD565-16AHT-FMH, and 0.8 ns for QD525-16AHT-FMH, respectively. This suppression of ET fluctuation in dimers with smaller QD size leads to stable charge generation rate which can have a positive impact on the application of these dimers in molecular electronics.

The time scale of ET fluctuations in QD-FMH dimers can be unraveled by using a photon-by-photon analysis method capable of probing fluctuations in single molecule lifetimes from as short as few microseconds, up to seconds [27, 78]. As described in previous paragraphs, the photon-by-photon method does this by computing autocorrelations of the PL lifetimes (ACPLs) measured from a single molecule on a photon-by-photon basis (see detailed description in previous paragraph). Typical ACPLs for a single QD isomer and a QD-FMH dimer are shown in Fig. 15.19, and they can be roughly described by a single exponent decay (Fig. 15.19a)

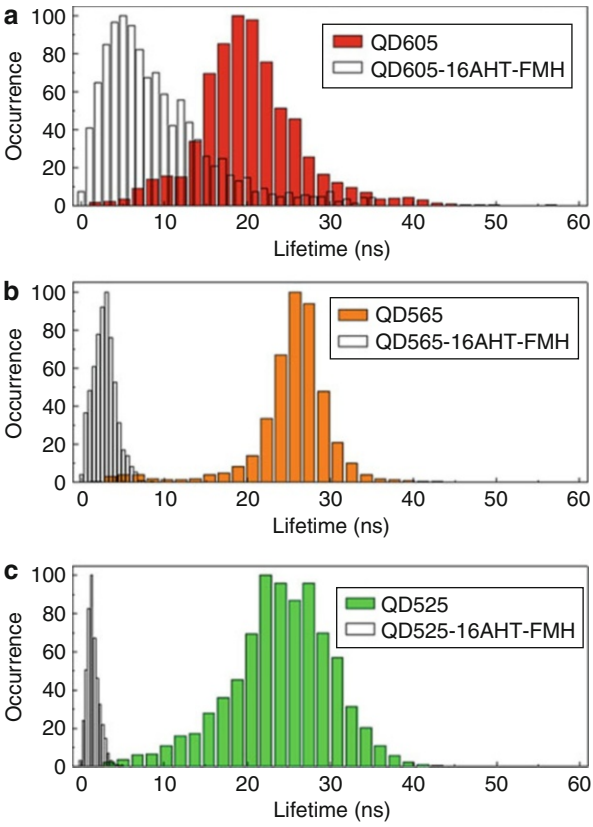

Fig. 15.17 Histograms of single molecule PL lifetimes constructed from each 50 individual trajectories measured from QD isomers and QD-FMH dimers using QDs of different sizes: (**a**) QD605 isomer (*red*) and QD605-16AHT-FMH dimer (*black*); (**b**) QD565 isomer (*orange*) and QD565-16AHT-FMH dimer (*black*); (**c**) QD525 isomer (*green*) and QD525-16AHT-FMH dimer (*black*) (reproduced from reference [21])

and a biexponent decay (Fig. 15.19b), respectively. Fluctuations in the PL lifetime of individual QDs isomers have been previously explained by invoking dynamic distribution of the charge trap state [56, 82]. The variation in the trap state not only leads to fluctuations in the nonradiative recombination rate, but also to variations in the QD's electronic states, as manifested by spectral diffusion [64] – a phenomenon that could influence the electron transfer to FMH. Therefore, the long time decay (after 10 ms) of the ACPLs of QD isomer and QD-FMH dimer can be attributed to fluctuations of the charge trapping state in QDs, consistent with recent findings that spectral diffusion dynamics of single QDs is slower than 10 ms [83]. In this assumption, it is understandable the observation of suppressed ET fluctuations in dimers with smaller QD sizes, because these dimers have larger ET driving force and hence will be less prone to fluctuation of the electronic states of the QD. Compared to a QD isomer, the ACPLs of QD-FMH dimers exhibit a significant decay before 10 ms. These fast ET fluctuations might be due to the complicated thermally induced molecular motions, similar to that previously reported for organic DBA systems [65, 66]. We observed that reducing linker length in dimer results in suppression of ET fluctuations, which indicates that linker motion plays an important role for defining and controlling the magnitude of ET fluctuation.

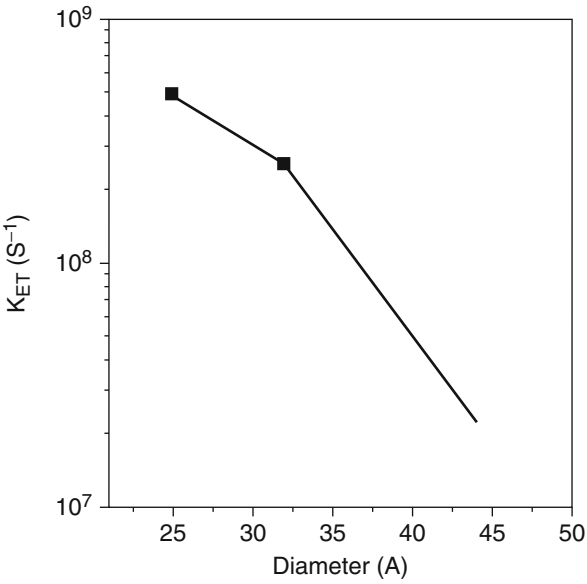

Fig. 15.18 Electron transfer rate versus QD core size calculated for QD-FMH dimers on the basis of single molecule experiments (reproduced from reference [21])

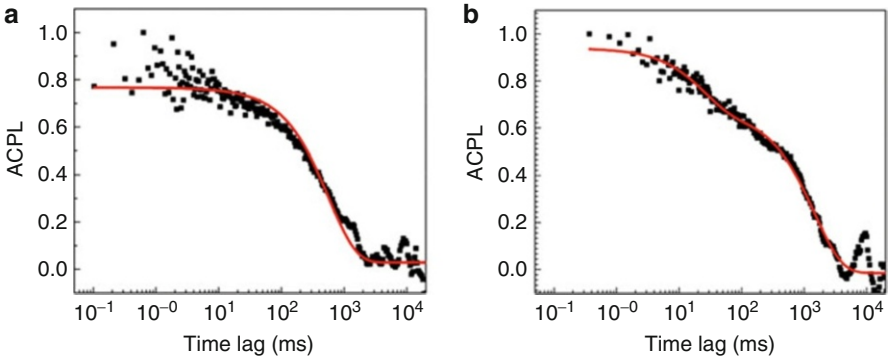

Fig. 15.19 Photon-by-photon autocorrelations of PL lifetimes (ACPLs) measured from individual (**a**) QD605 isomer and (**b**) QD605-16AHT-FMH dimer. Shown in red are single exponential (panel **a**, 572 ms) and biexponential (panel **b**, 25 ms, 1,490 ms) decay fits (reproduced from reference [21])

6 Conclusion and Future Perspective

We have successfully fabricated a series of donor-bridge-acceptor heterodimers composed of core/shell CdSe/ZnS quantum dots and fullerene FMH via a novel surface-based stepwise self-assembly approach. The QD-FMH heterodimers exhibit controlled electron transfer properties, including controlled ET rate and reduced ET rate fluctuation when compared to similar components assembled

without a molecular linker. A thorough comparison of the single molecule spectroscopic behavior of the QD-FMH heterodimer and QD isomers has provided deeper insight into the PL blinking mechanism of core/shell QDs. For example, by comparing the PL blinking characteristics between QDs and QD-FMH dimers with varying interparticle linker length, we found that external charge traps that are properly coupled to the excited state of a QD have a significant effect on the QD's PL blinking dynamics. Charge transfer followed by charge recombination between a QD and an external trap leads to a quasi-continuous distribution of the on-states and an early cutoff of $P(t_{on})$ and $P(t_{off})$ distributions from an inverse power-law behavior. This multistate blinking was also observed in some 10 % of the probed QD isomers and attributed to trap-induced charge transfer/recombination with traps supposedly in the form of defects located at the QD surface. An evaluation of the blinking dynamics of QD isomers and QD-FMH dimers in view of the diffusion-controlled ET model suggests the need to refine such models addressing the presence of not only long-lived shallow traps but also short-lived deep ones.

Single molecule spectroscopic characterization of the electron transfer in QD-FMH dimers not only revealed the linker length and QD size effect on the average ET rate, but unveiled the static and dynamic inhomogeneity of ET, otherwise obscured in ensemble-averaged experiments. We have successfully identified two distinct ET fluctuation regimes that were attributed to variation of the trap state in the QDs and to molecular motions within dimers. Reducing linker length and QD size has been found to limit fluctuations of ET in these dimers. With excellent, size-dependent light absorption properties conferred by the incorporated QDs, the DBA dimers are promising power generating units for molecular electronics.

While we and others have found that PL blinking behavior of individual quantum dots is closely related to photoinduced charge transfer, further experimental and theoretical investigations are needed to understand the exact relationship, which is of significant importance for the widespread applications of quantum dots.

Acknowledgments We would like to thank Dr. H.L. Wang from Los Alamos National Laboratory in New Mexico for providing the fullerene compound and our colleagues from Brookhaven National Laboratory, Dr. M. Sfeir for helping with transient absorption experiments and Drs. M. Hybertsen and Q. Wu for helpful discussions and suggestions in connection with some of the data reported here. We also thank the Office of Science of the United States Department of Energy for funding this research under Contract No. DE-AC02-98CH10886.

References

1. Chan WCW, Nie SM (1998) Quantum dot bioconjugates for ultrasensitive nonisotopic detection. Science 281(5385):2016–2018
2. Medintz IL et al (2005) Quantum dot bioconjugates for imaging, labelling and sensing. Nat Mater 4(6):435–446
3. Klostranec JM, Chan WCW (2006) Quantum dots in biological and biomedical research: Recent progress and present challenges. Adv Mater 18(15):1953–1964

4. Klimov VI et al (2000) Optical gain and stimulated emission in nanocrystal quantum dots. Science 290(5490):314–317
5. Brumer M et al (2006) Nanocrystals of PbSe core, PbSe/PbS, and PbSe/PbSexS1-x core/shell as saturable absorbers in passively Q-switched near-infrared lasers. Appl Opt 45(28):7488–7497
6. Vezenov DV et al (2005) A low-threshold, high-efficiency microfluidic waveguide laser. J Am Chem Soc 127(25):8952–8953
7. Klimov VI et al (2007) Single-exciton optical gain in semiconductor nanocrystals. Nature 447(7143):441–446
8. Darugar Q, Qian W, El-Sayed MA (2006) Observation of optical gain in solutions of CdS quantum dots at room temperature in the blue region. Appl Phys Lett 88(26)
9. Colvin VL, Schlamp MC, Alivisatos AP (1994) Light-emitting-diodes made from cadmium selenide nanocrystals and a semiconducting polymer. Nature 370(6488):354–357
10. Dabbousi BO et al (1995) Electroluminescence from CdSe quantum-dot polymer composites. Appl Phys Lett 66(11):1316–1318
11. Choudhury KR, Song DW, So F (2010) Efficient solution-processed hybrid polymer-nanocrystal near infrared light-emitting devices. Org Electron 11(1):23–28
12. Nozik AJ (2002) Quantum dot solar cells. Physica E 14(1–2):115–120
13. Huynh WU, Dittmer JJ, Alivisatos AP (2002) Hybrid nanorod-polymer solar cells. Science 295(5564):2425–2427
14. Gur I et al (2005) Air-stable all-inorganic nanocrystal solar cells processed from solution. Science 310(5747):462–465
15. Murray CB, Norris DJ, Bawendi MG (1993) Synthesis and characterization of nearly monodisperse Cde (E = S, Se, Te) semiconductor nanocrystallites. J Am Chem Soc 115(19):8706–8715
16. Peng ZA, Peng XG (2001) Formation of high-quality CdTe, CdSe, and CdS nanocrystals using CdO as precursor. J Am Chem Soc 123(1):183–184
17. Dabbousi BO et al (1997) (CdSe)ZnS core-shell quantum dots: synthesis and characterization of a size series of highly luminescent nanocrystallites. J Phys Chem B 101(46):9463–9475
18. Nirmal M et al (1996) Fluorescence intermittency in single cadmium selenide nanocrystals. Nature 383(6603):802–804
19. Frantsuzov P et al (2008) Universal emission intermittency in quantum dots, nanorods and nanowires. Nat Phys 4(7):519–522
20. Brown P, Kamat PV (2008) Quantum dot solar cells. Electrophoretic deposition of CdSe-C-60 composite films and capture of photogenerated electrons with nC(60) cluster shell. J Am Chem Soc 130(28):8890–8891
21. Xu ZH, Cotlet M (2011) Quantum dot-bridge-fullerene heterodimers with controlled photoinduced electron transfer. Angew Chem Int Ed 50(27):6079–6083
22. Xu Z, Cotlet M (2011) Photoluminescence blinking dynamics of colloidal quantum dots in the presence of controlled external electron traps. Small 8(2):253–258
23. Hirsch A et al (1994) Regiochemistry of multiple additions to the fullerene core – synthesis of a T-H-symmetrical hexakisadduct of C-60 with bis(ethoxycarbonyl)methylene. J Am Chem Soc 116(20):9385–9386
24. Anderson AS et al (2008) Functional PEG-modified thin films for biological detection. Langmuir 24(5):2240–2247
25. Cotlet M et al (2004) Probing conformational dynamics in single donor-acceptor synthetic molecules by means of photoinduced reversible electron transfer. Proc Natl Acad Sci USA 101(40):14343–14348
26. Weston KD et al (2002) Measuring the number of independent emitters in single-molecule fluorescence images and trajectories using coincident photons. Anal Chem 74(20):5342–5349
27. Yang H, Xie XS (2002) Probing single-molecule dynamics photon by photon. J Chem Phys 117(24):10965–10979
28. Pichler K et al (1991) Photophysical properties of solid films of fullerene C-60. J Phys Condens Matter 3(47):9259–9270

29. Greenham NC, Peng XG, Alivisatos AP (1996) Charge separation and transport in conjugated-polymer/semiconductor-nanocrystal composites studied by photoluminescence quenching and photoconductivity. Phys Rev B 54(24):17628–17637
30. Liu DF et al (2007) Chemical conjugation of fullerene C-60 to CdSe nanocrystals via dithiocarbamate ligands. J Phys Chem C 111(48):17713–17719
31. Ravindran S et al (2003) Covalent coupling of quantum dots to multiwalled carbon nanotubes for electronic device applications. Nano Lett 3(4):447–453
32. Robel I, Kuno M, Kamat PV (2007) Size-dependent electron injection from excited CdSe quantum dots into TiO_2 nanoparticles. J Am Chem Soc 129(14):4136–4137
33. Hohng S, Ha T (2004) Near-complete suppression of quantum dot blinking in ambient conditions. J Am Chem Soc 126(5):1324–1325
34. Fomenko V, Nesbitt DJ (2008) Solution control of radiative and nonradiative lifetimes: a novel contribution to quantum dot blinking suppression. Nano Lett 8(1):287–293
35. Chen Y et al (2008) "Giant" multishell CdSe nanocrystal quantum dots with suppressed blinking. J Am Chem Soc 130(15):5026–5027
36. Mahler B et al (2008) Towards non-blinking colloidal quantum dots. Nat Mater 7(8):659–664
37. Wang XY et al (2009) Non-blinking semiconductor nanocrystals. Nature 459(7247):686–689
38. Efros AL, Rosen M (1997) Random telegraph signal in the photoluminescence intensity of a single quantum dot. Phys Rev Lett 78(6):1110–1113
39. Kuno M et al (2001) "On"/"off" fluorescence intermittency of single semiconductor quantum dots. J Chem Phys 115(2):1028–1040
40. Shimizu KT et al (2001) Blinking statistics in single semiconductor nanocrystal quantum dots. Phys Rev B 6320(20):205316
41. Verberk R, van Oijen AM, Orrit M (2002) Simple model for the power-law blinking of single semiconductor nanocrystals. Phys Rev B 66(23):233203
42. Tang J, Marcus RA (2005) Diffusion-controlled electron transfer processes and power-law statistics of fluorescence intermittency of nanoparticles. Phys Rev Lett 95(10):107401
43. Pelton M et al (2007) Evidence for a diffusion-controlled mechanism for fluorescence blinking of colloidal quantum dots. Proc Natl Acad Sci USA 104(36):14249–14254
44. Margolin G et al (2006) Power-law blinking quantum dots: stochastic and physical models. Fractals Diffus Relax Disord Complex Syst Part A 133:327–356
45. Jha PP, Guyot-Sionnest P (2009) Trion decay in colloidal quantum dots. ACS Nano 3(4):1011–1015
46. Zhao J et al (2010) Challenge to the charging model of semiconductor-nanocrystal fluorescence intermittency from off-state quantum yields and multiexciton blinking. Phys Rev Lett 104(15):157403
47. Rosen S, Schwartz O, Oron D (2010) Transient fluorescence of the off state in blinking CdSe/CdS/ZnS semiconductor nanocrystals is not governed by auger recombination. Phys Rev Lett 104(15):157404
48. Frantsuzov PA, Marcus RA (2005) Explanation of quantum dot blinking without the long-lived trap hypothesis. Phys Rev B 72(15):155321
49. Wang XY et al (2003) Surface-related emission in highly luminescent CdSe quantum dots. Nano Lett 3(8):1103–1106
50. Knappenberger KL et al (2008) Excitation-wavelength dependence of fluorescence intermittency in CdSe nanorods. ACS Nano 2(10):2143–2153
51. Wang S et al (2006) Fluorescence blinking statistics from CdSe core and core/shell nanorods. J Phys Chem B 110(46):23221–23227
52. Antelman J et al (2009) Suppression of quantum dot blinking in DTT-doped polymer films. J Phys Chem C 113(27):11541–11545
53. Biebersdorf A et al (2006) Semiconductor nanocrystals photosensitize C-60 crystals. Nano Lett 6(7):1559–1563
54. Guldi DM et al (2004) Versatile organic (fullerene) – inorganic (CdTe nanoparticle) nanoensembles. J Am Chem Soc 126(44):14340–14341

55. Schlegel G et al (2002) Fluorescence decay time of single semiconductor nanocrystals. Phys Rev Lett 88(13):137401
56. Zhang K et al (2006) Continuous distribution of emission states from single CdSe/ZnS quantum dots. Nano Lett 6(4):843–847
57. Issac A, Jin SY, Lian TQ (2008) Intermittent electron transfer activity from single CdSe/ZnS quantum dots. J Am Chem Soc 130(34):11280–11281
58. Song NH et al (2011) Poisson-distributed electron-transfer dynamics from single quantum dots to C60 molecules. ACS Nano 5(1):613–621
59. Jin SY, Lian TQ (2009) Electron transfer dynamics from single CdSe/ZnS quantum dots to TiO_2 nanoparticles. Nano Lett 9(6):2448–2454
60. Biju V et al (2004) Intermittent single-molecule interfacial electron transfer dynamics. J Am Chem Soc 126(30):9374–9381
61. Wang YM et al (2009) Probing single-molecule interfacial electron transfer dynamics of porphyrin on TiO_2 nanoparticles. J Am Chem Soc 131(4):1479–1487
62. Cotlet M et al (2004) Probing the influence O-2 on photoinduced reversible electron transfer in perylenediimide-triphenylamine-based dendrimers by single-molecule spectroscopy. Angew Chem Int Ed 43(45):6116–6120
63. Bell TDM et al (2005) Electron transfer at the single-molecule level in a triphenylamine-perylene imide molecule. Chemphyschem 6(5):942–948
64. Neuhauser RG et al (2000) Correlation between fluorescence intermittency and spectral diffusion in single semiconductor quantum dots. Phys Rev Lett 85(15):3301–3304
65. Davis WB, Ratner MA, Wasielewski MR (2001) Conformational gating of long distance electron transfer through wire-like bridges in donor-bridge-acceptor molecules. J Am Chem Soc 123(32):7877–7886
66. Closs GL, Miller JR (1988) Intramolecular long-distance electron-transfer in organic-molecules. Science 240(4851):440–447
67. Kuno M et al (2000) Nonexponential "blinking" kinetics of single CdSe quantum dots: a universal power law behavior. J Chem Phys 112(7):3117–3120
68. Knappenberger KL et al (2007) Expitation wavelength dependence of fluorescence intermittency in CdSe/ZnS core/shell quantum' dots. Nano Lett 7(12):3869–3874
69. Peterson JJ, Nesbitt DJ (2009) Modified power law behavior in quantum dot blinking: a novel role for biexcitons and auger ionization. Nano Lett 9(1):338–345
70. Tang J, Marcus RA (2005) Mechanisms of fluorescence blinking in semiconductor nanocrystal quantum dots. J Chem Phys 123(5):054704
71. Cui SC et al (2008) Interfacial electron transfer dynamics in a single CdTe quantum dot-pyromellitimide conjugate. J Phys Chem C 112(49):19625–19634
72. Marcus RA (1993) Electron-transfer reactions in chemistry – theory and experiment (Nobel lecture). Angew Chem Int Ed Engl 32(8):1111–1121
73. Wu XY, Bell TDM, Yeow EKL (2009) Electron transport in the long-range charge-recombination dynamics of single encapsulated dye molecules on TiO_2 nanoparticle films. Angew Chem Int Ed 48(40):7379–7382
74. Hamada M et al (2010) Blinking suppression in CdSe/ZnS single quantum dots by TiO_2 nanoparticles. ACS Nano 4(8):4445–4454
75. Tang J (2008) The effects of anomalous diffusion on power-law blinking statistics of CdSe nanorods. J Chem Phys 129(8):084709
76. Guo LJ, Wang YM, Lu HP (2010) Combined single-molecule photon-stamping spectroscopy and femtosecond transient absorption spectroscopy studies of interfacial electron transfer dynamics. J Am Chem Soc 132(6):1999–2004
77. Koberling F, Mews A, Basche T (2001) Oxygen-induced blinking of single CdSe nanocrystals. Adv Mater 13(9):672–676
78. Yang H et al (2003) Protein conformational dynamics probed by single-molecule electron transfer. Science 302(5643):262–266

79. Sauer M (2003) Single-molecule-sensitive fluorescent sensors based on photoinduced intramolecular charge transfer. Angew Chem Int Ed 42(16):1790–1793
80. Holman MW et al (2004) Studying and switching electron transfer: from the ensemble to the single molecule. J Am Chem Soc 126(49):16126–16133
81. Huang J et al (2008) Photoinduced ultrafast electron transfer from CdSe quantum dots to rebipyridyl complexes. J Am Chem Soc 130(17):5632–5633
82. Verberk R, van Oijen AM, Orrit M (2002) Simple model for the power-law blinking of single semiconductor nanocrystals. Phys Rev B 66(23):233202
83. Marshall LF et al (2010) Extracting spectral dynamics from single chromophores in solution. Phys Rev Lett 105(5):053005

Index